AD-A129 821 DIODE DYNAMICS BEAM GENERATION AND TRANSPORT AND PLASMA EROSION OPENING SWITCH DEVELOPMENT(U) JAYCOR ALEXANDRIA VA P F OTTINGER 17 MAY 83 JAYCOR-J207-83-C-001 1/9

UNCLASSIFIED N00173-80-C-0202 F/G 9/1 NL

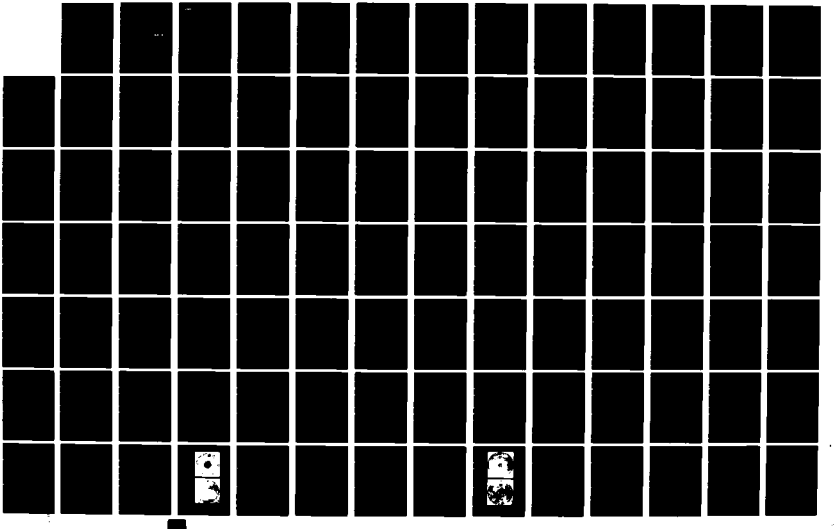

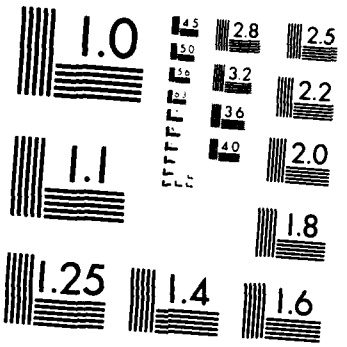

DIODE DYNAMICS, BEAM GENERATION AND TRANSPORT AND PLASMA EROSION OPENING SWITCH DEVELOPMENT

JAYCOR Project No. 6188
Contract No. N00173-80-C-0202
Report No. J207-83-C-001

JAYCOR

A

205 South Whiting Street
Alexandria, Virginia 22304

JAYCOR

DIODE DYNAMICS, BEAM GENERATION AND TRANSPORT AND PLASMA EROSION OPENING SWITCH DEVELOPMENT

JAYCOR Project No. 6188
Contract No. N00173-80-C-0202
Report No. J207-83-C-001

FINAL REPORT

P. F. Ottinger

Submitted to:

Naval Research Laboratory
Washington, DC 20375

UNCLASSIFIED

SECURITY CLASSIFICATION OF THIS PAGE (When Data Entered)

REPORT DOCUMENTATION PAGE

READ INSTRUCTIONS BEFORE COMPLETING FORM

1. REPORT NUMBER: J207-83-C-001
2. GOVT ACCESSION NO.:
3. RECIPIENT'S CATALOG NUMBER:

4. TITLE (and Subtitle): DIODE DYNAMICS, BEAM GENERATION AND TRANSPORT AND PLASMA EROSION OPENING SWITCH DEVELOPMENT

5. TYPE OF REPORT & PERIOD COVERED: FINAL REPORT Jan 14 '80 - Apr 14 '83

6. PERFORMING ORG. REPORT NUMBER: J207-83-C-001

7. AUTHOR(s): P. F. Ottinger

8. CONTRACT OR GRANT NUMBER(s): N00173-80-C-0202

9. PERFORMING ORGANIZATION NAME AND ADDRESS:
JAYCOR
205 South Whiting Street
Alexandria, VA 22314

10. PROGRAM ELEMENT, PROJECT, TASK AREA & WORK UNIT NUMBERS:

11. CONTROLLING OFFICE NAME AND ADDRESS:
Naval Research Laboratory
4555 Overlook Avenue, SW
Washington, DC 20375

12. REPORT DATE: May 17, 1983

13. NUMBER OF PAGES: 677

14. MONITORING AGENCY NAME & ADDRESS (if different from Controlling Office):
Naval Research Laboratory
4555 Overlook Avenue, SW
Washington, DC 20375

15. SECURITY CLASS. (of this report): UNCLASSIFIED

15a. DECLASSIFICATION/DOWNGRADING SCHEDULE:

16. DISTRIBUTION STATEMENT (of this Report)

NRL Code 4701-1 copy
4702-1 copy
4703-1 copy
4770-1 copy

Defense Documentation Center-12 copies
Bldg. 5, Cameron Station
Alexandria, VA 22314

17. DISTRIBUTION STATEMENT (of the abstract entered in Block 20, if different from Report)

18. SUPPLEMENTARY NOTES

19. KEY WORDS (Continue on reverse side if necessary and identify by block number)

Diode Physics
Intense Ion Beams
Relativistic Electron Beam
Beam Transport
Plasma Erosion Opening Switch

20. ABSTRACT (Continue on reverse side if necessary and identify by block number)

This document summarizes the JAYCOR research program in the areas of diode physics, beam transport and plasma erosion opening switches. Each of these areas are outlined and reports are provided for details.

DD FORM 1 JAN 73 1473 EDITION OF 1 NOV 65 IS OBSOLETE
S/N 0102-LF-014-6601

UNCLASSIFIED

SECURITY CLASSIFICATION OF THIS PAGE (When Data Entered)

TABLE OF CONTENTS

1.0 INTRODUCTION

This final report covers work performed by JAYCOR under contract to the Naval Research Laboratory (NRL) over a period of 39 months from 01/14/80 through 04/14/83. The original contract (JAYCOR Proposal 8351-11, March 1979) was funded with a start date of 01/14/80 and subsequently modified three times (JAYCOR Proposals 8206-29, January 1981; Proposal 8207-12, August 1981; and Proposal 8800-02, April 1982). A no-cost extension of the contract was also granted to extend the contract from 01/14/83 to 04/14/83.

The work performed under this contract involved research in the areas of diode physics, beam transport and plasma erosion opening switches. The research was conducted on-site at NRL by JAYCOR as part of NRL's Light-Ion Inertial Confinement Fusion (ICF) program for the Department of Energy (DOE) and NRL's Defense Nuclear Agency (DNA) program for Nuclear Weapons Effects Simulation (NWES). Results of the JAYCOR effort in these programs significantly aided NRL in successfully accomplishing its tasks. As with any research project the goals and needs of the program often shift during the performance period of the contract. This is reflected here, for example, in that the original proposal contains no mention of plasma erosion opening

switch work, yet it was a dominate part of the work at the end of the performance period. Similarly, when the contract began, beam transport was identified as a major part of the work, but was not mentioned in the Statement of Work in the last modification.

Here all aspects of the work performed under this contract are reported. Because of the length of the performance period of this contract, most of the work has already been presented at scientific conferences or documented in reports and published journal articles. For this reason each area of research is only summarized to tie the various reports, etc., together. Each such summary is then followed by an extensive collection of reports where all the technical details are included. There were three major areas of research. Section 2 will deal with the diode physics research area, Section 3 will deal with the investigation of intense beam transport and, finally, Section 4 will involve plasma erosion opening switch research.

2.0 DIODE PHYSICS

The continuing development of diode physics understanding has been the main thrust of the work under this contract. The production and focusing of intense light-ion beams for ICF purposes and the generation of intense e-beams for Bremsstrahlung production are two of the major goals of the program. Over the course of this contract many areas of diode physics have been investigated both experimentally and theoretically. Ion production efficiency has been studied in detail including scaling to high voltage and power. Focusing of high brightness beams to small areas has also been investigated as well as techniques to improve beam brightness. Methods for increasing the critical current which can be driven through a pinched beam diode for a given anode-cathode gap have also been studied in order to prevent premature gap closure. New diode concepts have been tested including the equatorial pinch-reflex diode (EPRD), the series diode, the magnetically insulated splitter concept* and the paravector-potential diode. Problems involving magnetically insulated flow have been addressed on numerous occasions and

---

*J. Shannon et al., 1983 IEEE International Conference on Plasma Science, (San Diego, CA, 1983).

finally new diagnostics have been developed. Results in each of these areas is summarized here and technical details can be found in the attached reports.

The pinch-reflex diode (PRD) is the mainstream diode concept in the program. High ion production efficiency is attained by pinched electron flow reflexing along the anode surface allowing for enhanced ion emission. Particle-in-cell (PIC) codes have provided a great deal of insight into the operation of such a diode. Scaling laws for the impedance and ion production efficiency have been derived analytically and verified by experiments and numerical simulations using the PIC codes. The two-dimensional electric and magnetic field profiles and current flow patterns obtained from the code runs have helped develop an understanding of how the diode operates and more importantly how to improve or manipulate diode operation.

For example, attempts at beam focusing using shaped anodes and self-magnetic field focusing effects was greatly aided by information derived from the code results. This led to the focusing of 0.5 TW deuteron beams produced on the NRL Gamble II generator to current densities of ~ 300 kA/cm^2. Numerical simulations have also been used to study small-area pinch-reflex diode operation in the 3-5 Ω range in order to guide experiments on Gamble II at NRL. The

results led to successful production of high-brighness proton beams (.4 MA, 1MV) from 20 cm axial PRD's at a source power brighness of $\gtrsim$ 10 TW/cm^2 rad^2.

Another important aspect of the reseach involved demonstration that the PRD operation could be successfully scaled to higher voltage and higher power. Experiments were performed on the Aurora generator at Harry Diamond Laboratory to investigate high voltage operation and on the Pithon generator at Physics International to study high power operation. On Aurora high impedance diodes (10~35) were used to generate $\gtrsim$ 50 kA ion beam at $\lesssim$ 5 MV with ion production efficiencies of ~20%. This agrees well with numerical simulations and the theoretical scaling of $I_i/I_e \sim (m_e/2m_i)^{\frac{1}{2}} (\gamma+1)^{\frac{1}{2}}$ R/D, however, in this small R/D, high impedance diode, code results show that electron reflexing is less important than in the large R/D, low impedance diode. The R/D enhancement here is attributed to prolonged electron lifetime in the diode gap due to complicated electron trajectories as they drift across the diode gap. Thus scaling to high impedance, high voltage operation was successful.

Scaling to high power was achieved on Pithon. Ion beams with currents of 1 MA at 1.8 MV were extracted in a 130 kJ, 100 ns pulse with a peak power approaching 2 TW. The ion production efficiency was ~60% with a anode source

current density an average of ~20 kA/cm^2. These results agreed well with theoretical and numerical predictions. Focusing to current densities of 150 kA/cm^2 was also achieved on Pithon.

Since high impedance (which here is meant to be ~4 Ω) operation is required for machines like PBFA-I at Sandia and generally high impedance implied low ion production efficiency for PRD's, attempts were made to find ways of improving I_i/I_e for 4 Ω operation. The magnetic dam concept uses a wire carrying a current in the gap behind the anode foil to relfect electrons entering this gap back into the AK gap at a larger radius than they entered. This is accomplished by having the wire current flow in the opposite direction to the normal diode current flow. This technique, however, as studied, increased both the electron and ion current leaving I_i/I_e essentially unchanged.

The use of a finite J_θ in the diode shank was also studied numerically to see if I_i/I_e could be increased. Numerical simulations predict that the ratio of the effective ion current to total diode current can be significantly increased by introducing a small but finite azimuthal current into the tip of the cathode shank of a high impedance (4 Ω) axial pinch-reflex diode. Such a current generates large tangential magnetic fields along the electron-emitting cathode surfaces. These fields, in turn,

impart finite angular momentum to the electrons as they are injected into the anode-cathode gap. The resultant particle self-fields alter electron trajectories in such a way as to boost electron space charge near certain portions of the ion-emitting anode surface. The net consequence is a modification of the radial profile of ion emission which enhances the net ion current transmitted through the interior of the hollow cathode shank.

Introducing a conducting anode ring on the surface of the anode was also investigated. The modification consists of covering the anode foil with a conducting annulus which has an inner diameter slightly smaller than the inner diameter of the cathode. The annulus (typically Ta or Al) is then compared with the electron range and is ..ot electrically connnected to the machine inner conductor. Experimental observations of diode operation for such a configuration included (1) better symmetry of pinching and more reliable centering, (2) significant increase in impedance for a given anode-cathode gap, (3) higher ion-production efficiency for a given impedance and (4) better late-time impedance behavior even for very small anode-cathode gaps. Computer simulation codes indicate that the suppression of ion emission in the region of the metallic annulus in turn suppresses electron emission from the cathode tip resulting in a diode behavior which is

consistent with the experimental observations.

The radial or a barrel-shaped version of the axial PRD, which is called the equatorial pinch-reflex diode (EPRD), also provides for improved ion production efficiency. This diode easily coupled to PBFA-I and showed flat impedance behavior and good power flow characteristics. The important feature here, however, is that the impedance is controlled by R/D where R is the diode radius and the ion production efficiency is controlled by H/D where H is the height of the diode. Thus I_i/I_e could be increased by simply raising H. This is limited by the ability to effectively turn on the larger anode area. Experimental and numerical code results verified this scaling. Beam focusing with this diode is also expected to be easier than with the axial PRD, because of uniform J_i in the EPRD as opposed to $J_i \sim 1/r$ in the axial PRD. The magnetic binding of the ion orbits in the AK gap then is proportional to height in the EPRD and thus acts as a lens whereas in the PRD magnetic binding is the same at all radii and must be compensated for.

For relativistic electron beam (REB) production a technique was developed for exceeding the critical current or effectively reducing the impedance of a pinched beam diode. Typically, the current drawn from REB diodes is equal to the critical current, $I_c(kA)=8.5\ R/D(\gamma^2-1)^{\frac{1}{2}}$ where R and D are the cathode radius and the effective anode-cathode

gap and is the usual relativistic factor. Theoretical studies indicate that I can be exceeded by almost a factor of 2 by shaping of the anode structure and selectively controlling ion emission. These predictions were tested experimentally on the NRL Gamble II generator. A radial electric field was introduced by extending the anode coaxially with the cathode. The resulting radial-gap-to-axial-gap ratio was then varied. In addition, information was controlled by either using graphite-coated metal surfaces to suppress ion production or, insulators designed for easy flashover. Results indicated that the impedance can indeed be controlled by these techniques in agreement with the theoretical predictions. This allows the diode gap to be set at a larger value to obtain the same impedance without anode shaping thus helping to prevent premature gap closure.

The ability to focus intense light-ion beams extracted from PRD's has been studied both experimentally and theoretically. Focus control with megampere-level ion beams requires analysis of radially and time-dependent self-magnetic field effects in the diode. Focus-compensating techniques include electrode shaping and proper account of electrode plasma motion. This anode plasma motion has been studied experimentally and theoretically with a 1-D hydrocode and shows rapid expansion

near the axis with peak velocities as high as 30 cm/μsec due to pressure gradients and $\underline{J}x\underline{B}$ forces. Attention must also be paid to uniform anode and cathode turn-on and subsequent ion beamlet pinching in the vacuum gap between the anode and cathode foils. Experimentally it was found that the source brightness can be improved by minimizing this vacuum gap and thus ion beamlet pinching predicted by theory. In particular an ion-beam-divergence half angle $\Delta\theta$ of 0.05 radians was achieved with a planar diode. This implies a source-power brightness of $P/\Delta\theta^2 \sim 10^{13}$ $W/cm^2 rad^2$. Focusing of such bright beams is still being investigated.

Although closing the axial anode-cathode gap improves beam brightness, it does not eliminate filamentation as source of beam divergence. In addition, it forces reduction of the diode impedance and leads to premature gap-closure. In order to overcome these limitations a diode concept incorporating both axial and radial electric fields was studied both experimentally and by computer simulation. The new geometry incorporates anode shaping as in the REB experiments. The anode is extended axially in the form of a cylinder so that it surrounds the cathode shank azimuthally and allows for a controllable radial anode-cathode gap. The diode impedance is primarily determined by the emission, and subsequent pinching on axis of electrons off the extended cathode shank. This allows for electron orbit mixing which

may mean less rippling of the E-field lines in the ion production region of the diode. Such ripples have been observed in computer simulations to have scale lengths of the order of an electron Larmor radius for the case of thin-walled hollow cathodes emitting axially. In addition, since the axial gap is no longer as important for electron emission, the ion-current-neutralizing gas region inside the cathode can be extended axially all the way to the cathode tip thus further minimizing E-field rippling while at the same time minimizing the axial in vacuo ion flow.

Experimentally, it was found that by suppressing ion production from the radial structure one can avoid severe ion beam filamentation in the azimuthal direction. In particular, in focusing geometry significant improvement in the beam divergence was observed, i.e., smaller aiming errors when such an axial-radial geometry is employed. Good impedance control was also experimentally achieved by varying the radial anode-cathode gap.

By increasing the electron emission area the possibility of cathode plasma filmentation by thermal-resistive instability is reduced. Electron current flow drawn off a hollow cylindrical cathode in a pinch-reflex ion diode is observed in general to have a filamentary structure. Such filamentation can lead to nonuniform anode turn-on and ion emission. Consequently,

ion beam brightness is degraded. In this context a purely growing thermal-resisitive instability in the cathode plasma was examined. The instability causes current filamentation and grows on a time scale comparable to the electron-ion energy equilibration time. Since the peak growth rate scales with J_0, increasing the emitting area should reduce the growth. Electron inelastic collisions have a stabilizing influence on the instability.

Electromagnetic PIC code development has begun and eventually will be very valuable in studying diode phenomena such as electromagnetic instabilities in the diode flow. Preliminary results for bi-polar flow in planar diodes indicate that indeed the electron-ion flow is filamented and may be an inherent source of ion beam divergence.

Other diode concepts which have been studied are the para-vector-potential diode, the series diode and the magnetically insulated splitter. The para-vector-potential diode is designed to allow for a very tight electron beam pinch. Analytic theory numerical simulations and experiments show that a combination of a bias current pinch and an ion induced pinch allows efficient pinching of electron beams generated in large aspect ratio diodes. In the new diode geometry electrons flow radially inward along vector-potential field lines which lie close to the anode. As these electrons do not touch the anode, there is no

plasma formation and consequent loss of energy to accelerated ions. Entering a region close to the axis in which an anode plasma does exist these electrons undergo an ion induced pinch to still smaller radii. Since the bulk of the flow occurs long vector-potential field lines, this new diode is called the Paravector-potential diode.

The concept of a series REB diode has been investigated in the past by researchers from several groups including those from Physics International Co. and Maxwell Laboratories, Inc. It involves driving two or more REB diodes in series from a single source in order to proportion the total available generator voltage between each diode. This is particularly useful for producing a low energy e-beam source. Recent experiments have shown that two REB diodes could be successfully driven in series when the center floating electrode which must act as the anode for one diode and the cathode for the other diode was mechanically held rigid by a 1 μH inductor. The voltage of the floating electrode was inferred from measurements of the current flowing through the inductor. The 1.5 MV generator voltage was divided approximately equally between the two 12 cm diameter hollow-cathode diodes when 300 kA flowed through each diode. Similar electron beam induced damage was also observed on each anode.

Annular electron beams have been produced using a magnetically insulated splitter concept.* This three-diimensional configuration was used on NRL's Gamble II vacuum diode to convert the coaxial generator output to a triaxial output. It in turn, drives a double-edged annular cathode where ideally the electrons from the outer edge pinch inward while electrons from the inner edge pinch outward. The results was an annular electron beam whose average diameter is determined both by the relative inductances associated with the inner and outer anode return current paths and by the relative impedances of the inner and outer cathodes.

Experiments were performed at power levels of up to 1.5 TW and energies of 40-60 kJ. Typical voltages were 1-1.5 MV with currents of 0.6-1.2 MA. The typical 10 cm diameter diode geometry was varied to determine impedance behavior beam quality and beam shape. In addition to controlling anode-cathode gap spacings, cathode annulus width and return path inductances, ion production from the anode was also controlled, by selectively using high and low atomic weight materials, in an attempt to effect beam positioning.

---

*J. Shannon et al., 1983 IEE International Conf. on Plasma Science, (San Diego, CA, 1983).

The low prepulse (< 10 kV) and fast risetime (< 20 ns) of the Gamble II outut voltage pulse, generally produced well behaved azimuthally symmetric beams although electron beam filaments originating from the magnetic nulls between the magnetically insulated posts could be observed. Finally, two concentric tri-plate feeds producing annular beams of 5 and 15 cm diameter were tested. The two beams were smooth and well-behaved and, as expected, could be controlled independently of each other. Such a technique can eventually lead to the capability of producing large-area, low impedance electron beams with very little current loss to anode-produced ions.

The important issue which affects the design of pulsed power devices in general is vacuum magnetic insulation. Two particular cases that were studied in detail were electron leakage power loss in a tri-plate transmission line and steady state magnetically insulated charge flow in coaxial geometry. In the first case numerical simulations were conducted using a PIC code to model the steady-state behavior of electron flow in an applied B radial diode and in its adjacent tri-plate transmission line (TTL). Particular attention was paid to the magnitude of the electron current flowing from the cathode to the anode surface in the TTL. The electron current flow was restricted mainly to the transition region in the TTL into

which there is "seepage" of the B_z field that is imposed in the diode gap. This finding highlights the importance of that region to diode designers.

In the second problem a vectorized FORTRAN computer program was written to calculate steady-state electron and ion fluxes as well as radial profiles of the magnetic and electric fields for specific practical radial diode and magnetically insulated vacuum feed line parameters. The numerical formulation is derived in part from the theoretical treatment of the topic by K. D. Bergeron. However, it differs from the treatment in several important respects including: a correction in one of the key scaling expressions a restructuring of the boundary conditions to allow for specific parametric solutions and a more careful consideration of the regions near the anode and cathode surfaces and near the electron sheath boundary. In deriving these results analytic approximations for the fields in these "special" regions were developed. These approximate solutions permitted numerical treatment of the singularities there. Matching the approximations between the regions also provided first-order guesses for the gross steady-state operating characteristics.

Finally, as with any experimental research program development of new diagnostics plays a vital role. Some of the new diagnostics that have been developed include a method for measuring beam profiles, and trajectories of intense ion beams, a nuclear diagnostic technique for measuring proton beams and an inductive voltage monitor. First a new diagnostic method of measuring beam profiles and trajectories of intense ion beams as a function of time was developed. The technique employs fast photograhy in conjunction with fast scintillators. Prior to detection, the excessive intensity of the direct ion beam is reduced by means of Rutherford scattering. A time resolution of a few nanoseconds and a spatial resolution of a few millimeters has been achieved. Using this technique focusing properties of planar and spherical pinch reflex diodes have been investigated. A low energy electron beam precursor has been detected. A simple model for its production was developed.

A 50-kJ proton beam consisting of 6×10^{16} protons with energy ~5 MeV was inferred from neutron measurements using the $^{7}Li(p,n)\ ^{7}Be$ reaction from an intense multi-MeV ion beam generated with a pinch-reflex diode configuration on the Aurora generator. In addition, a carbon-ion component was indicated by measurements of nuclear activation induced in the aluminum cathode.

Ion beam directed onto thick LiCl targets produced neutrons by the $^{7}Li(p,n)^{7}Be$ reaction which has a threshold at 1.9 MeV. Cross sections and angular distributions for this reaction are well known (1), and the resultant neutron energies are appropriate for time-of-flight (TOF) measurements. Intensities of 2×10^{12} neutrons/sr in the direction of the ion beam were deduced from Rh-activation counter measurements. Proton energies of ~5 MeV were determined from neutron TOF measurements for a 13.8-m flight path in the forward direction. This energy was consistent with the measured diode voltage. These results require a beam intensity of 6×10^{16} protons. An average current of 70 kA was deduced for the duration of the voltage pulse. The corresponding proton power was 0.4 TW.

An inductive voltage monitor was also developed to provide an independent and more direct measurement of the voltage across the diode. Previously the diode voltage was inferred by correcting the capacitive voltmeter by LI for the inductance between the voltmeter and the dicde. This inductive correction is not always well known so that the new inductive monitor can provide a good calibration.

This summary of the diode physics research performed during the past 39 months highlights the important aspects and advances of the program. Many of the details were omitted for the sake of brevity but can be found in the

following collection of reports.

2.1 List of Reports on Diode Physics

2.1.a Contributed Papers

1. "Finite Axial Magnetic Field Effects in the Electron Reflexing Double Diode," R. J. Barker and Shyke A. Goldstein, Bull. Am. Phys. Soc. 24, 950 (1979).

2. "Investigation of Inductive Effects Due to Internal Diode Flow," A. T. Drobot and Shyke A. Goldstein, Bull. Am. Phys. Soc. 24, 1033 (1979).

3. "Multiterawatt Pinch Reflex Ion Diode Performance," S. J. Stephanakis, J. R. Boller, G. Cooperstein, S. A. Goldstein, D. D. Hinshelwood, D. Mosher, W. F. Oliphant and F. C. Young, Bull. Am. Phys. Soc. 24, 1031 (1979).

4. "High Current Density Reflex Diode Experiments," R. A. Meger, Shyke A. Goldstein, D. D. Hinshelwood and G. Cooperstein, Bull. Am. Phys. Soc. 24, 976 (1979).

5. "Ion Beam Generation Experiments on the Aurora Accelerator," R. A. Meger, G. Cooperstein, A. T. Drobot, Shyke A. Goldstein, D. Mosher, F. C. Young, S. E. Graybill, G. A. Huttlin, K. G. Kerris and A. G. Stewart, 1980 IEEE International Conf. on Plasma Science, (Madison, WN, May 1980), p. 58.

6. "Nuclear Diagnosis of Ion Beams from Aurora," F. C. Young and R. A. Meger, 1980 IEEE International Conf. on Plama Science, (Madison, WN, May 1980), p. 59.

7. "Electrode Plasma Evolution in a Multiterawatt Pinch Ion Diode," R. D. Genuario, J. Maenchen, R. Stringfield, G. Cooperstein, D. Mosher, S. J. Stephanakis and S. A. Goldstein, 1980 IEEE International Conf. on Plasma Science, (Madison,

WN May 1980), p. 13.

8. "Quartz Gauge Measurements of Intense Pulsed Ion Current Densities from a Pinch-Reflex Diode on the Pithon Genertor," J. Maenchen, R. D. Genurio, V. Bailey, D. Mosher and S. A. Goldstein, 1980 IEEE International Conf. on Plasma Science, (Madison WN, May 1980), p. 13.

9. "Pinch Reflex Ion Diode Performance at 3-5 TW," G. Cooperstein, J. R. Boller, S. A. Goldstein, D. Mosher, W. F. Oliphant, S. J. Stephanakis, F. C. Young, R. D. Genuario and J. E. Maenchen, 1980 IEEE Iinternational Conf. on Plasma Science, (Madison WN, May 1980), p. 97.

10. "Ion Production from Small-Area Pinch-Reflex Diodes," S. J. Stephanakis, G. Cooperstein, D. Mosher, W. F. Oliphant, F. C. Young and S. A. Goldstein, 1980 IEEE International Conf. on Plasma Science, (Madison WN, May 1980), p. 98.

11. "Numerical Simulation of Ion Production from the Aurora Diode," A. T. Drobot, R. J. Barker and Shyke A. Goldstein, 1980 IEEE International Conf. on Plasma Science, (Madison WN, May 1980), p. 58.

12. "Experimental Study of the Pinched Beam Ion Diode," F. L. Sandel, 1980 IEEE International Conf. on Plasma Science, (Madison, WN, May 1980), p. 84.

13. "Computer Simulations of a Magnetically Insulated Radial Diode," R. J. Barker, Shyke A. Goldstein and A. Drobot, 1980 IEEE International Conf. on Plasma Science, (Madison WN, May 1980), p. 97.

14. "Radial-Enhancement Pinch-Reflex Ion Diodes," S. J. Stephanakis, S. A. Goldstein, D. Mosher and W. F. Oliphant, Bull. Am. Phys. Soc. 25, 900 (1980).

15. "Production of Light-Ion Beams on a Super Power Generator," J. Maenchen, R. Genuario, R. Stringfield, J. Kishi, G. Cooperstein, D. Mosher, S. J. Stephanakis, F. C. Young, S. A. Goldstein and D. Hinshelwood, Bull. Am. Phys. Soc. 25, 945 (1980).

16. "Ion-Diode Experiments in Positive Polarity on Aurora," F. C. Young, R. A. Meger, D. P. Bacon, J. J. Condon, G. Cooperstein, S. A. Goldstein, D. Mosher, S. E. Graybill, G. A. Huttlin, K. G. Kerris, A. G. Stewart, D. A. Whittaker, R. Bixby and M. S. Litz, Bull. Am. Phys. Soc. 25, 899 (1980).

17. "Diode Geometry Effects on the Aurora Ion Diode," R. A. Meger, A. T. Drobot, Shyke A. Goldstein and F. C. Young, Bull. Am. Phys. Soc. 25, 900 (1980).

18. "Numerical Simulation of Ion Beam Production in Positive Polarity," A. T. Drobot, R. A. Meger and Shyke A. Goldstein, Bull. Am. Phys. Soc. 25, 900 (1980).

19. "Magnetic Insulation in Axial Diodes," R. J. Barker and Shyke A. Goldstein, Bull. Am. Phys. Soc. 25, 900 (1980).

20. "Ion Beam Experiments on the Aurora Generator," F. C. Young and R. A. Meger, High Energy X-Ray Source Technology Conf., Albuquerque, NM, July 8-11, 1980.

21. "Computational Studies of a Radial Pinch-Reflex Diode," R. J. Barker and S. A. Goldstein, Bull. Am. Phys. Soc. 25, 921 (1981).

22. "Ion Source Brightness of Pinch Reflex Diodes," S. J. Stephanakis, Shyke A. Goldstein and P. F. Ottinger, Bull. Am. Phys. Soc. 26, 921 (1981).

23. "Aurora Modifications for Positive Polarity In Diode Operation," J. R. Boller, J. D. Shipman, Jr., J. K. Burton, G. Cooperstein, R. A. Meger, G. A. Huttlin and A. G. Stewart, 1981 IEEE International Conference on Plasma Science, (Santa Fe, NM, May 1981), p. 5.

24. "Modified Aurora Ion-Diode Experiments," R. A. Meger, F. C. Young, A. T. Drobot, R. J. Barker, J. J. Condon, G. Cooperstein, Shyke A. Goldstein, R. Bixby, G. A. Huttlin, K. G. Kerris and D. A. Whittker, 1981 IEEE International Conf. on Plasma Science, (Santa Fe, NM, May 1981), p. 6.

25. "Effects of Conducting Anode Rings on Pinch Reflex Diode Behavior," S. J. Stephanakis, R. J. Barker, S. A. Goldstein and W. F. Oliphant, 1981 IEEE International Conf. on Plasma Science, (Santa Fe, NM, May 1981), p. 8.

26. "Anode Plasma Expansion in Pinch-Reflex Diode," D. Colombant and Shyke A. Goldstein, 1982 IEEE International Conf. on Plasma Science, (Ottawa, Canada, May 1982), p. 81.

27. "Focusing of Ion Beams from High-Brightness Pinch-Reflex Diodes," S. J. Stephanakis, D. Mosher, F. C. Young and Shyke A. Goldstein, IEEE International Conf. on Plasma Science, (Ottawa, Canada, May 1982), p. 81.

28. "Cathode Plasma Filamentation in Pinch-Reflex Diodes," P. F. Ottinger, Shyke A. Goldstein, J. Guillory and V. K. Tripathi, Bull APS 27, 1121 (1982).

29. "Ion Energy Losses in Pinch-Reflex Diodes," F. C. Young, S. J. Stephanakis and Shyke A. Goldstein, Bull. Am. Phys. Soc. 27, 11212 (1982).

30. "Experimental Study of Exceeding the Critical Current in an REB Diode," S. J. Stephanakis, Shyke A. Goldstein, R. J. Barker, J. R. Boller

and G. Cooperstein, Bull. Am. Phys. Soc 27, 992 (1982).

31. "Theoretical Study of Exceeding the Critical Current in an REB Diode," R. J. Barker, Shyke A. Goldstein, S. J. Stephanakis and G. Cooperstein, Bull Am. Phys. Soc. 27, 991 (1982).

32. "Series REB Diode Experiment," J. R. Boller, S. J. Stephanakis, Shyke A. Goldstein and G. Cooperstein, Bull. Am. Phys. Soc. 27, 991 (1982).

33. "Comparison of Diode Voltage and Ion Energy for an Intense Pulsed Ion-Beam Diode," F. C. Young, S. J. Stephanakis, J. R. Boller and Shyke A. Goldstein, 1983 IEEE International Conf. on Plasma Science, (San Diego, CA, May 1983).

34. "Ion Beams from Axial Pinch-Reflex Diodes with Radial Electric Fields," S. J. Stephanakis, F. C. Young, Shyke A. Goldstein, R. J. Barker and T. J. Renk, 1983 IEEE International Conf. on Plasma Science, (San Diego, CA, May 1983).

35. "Ion Beams from Axial Pinch-Reflex Diodes with Radial Electric Fields," S. J. Stephanakis, F. C. Young, Shyke A. Goldstein, R. J. Barker and T. J. Renk , 1983 IEEE International Conf. on Plasma Science, (San Diego, CA, May 1983).

36. "Annular Electron Beam Production on Gamble II Using a Magnetically Insulated Splitter," W. F. Oliphant, R. J. Barker, J. R. Boller, G. Cooperstein, Shyke A. Goldstein and S. J. Stephanakis, 1983 IEEE International Conf. on Plasma Science, (San Diego, CA, May 1983).

2.1b Unpublished Technical Reports

1. "Computer Simulation of Intense Electron Beam Generation in a Hollow Cathode Diode," R. J. Barker, S. A. Goldstein and Roswell Lee, NRL

Memorandum Report 4279 (September 1980).

2. "Vector-Potential Flow in Relativistic Beam Diodes," D. P. Bacon, S. A. Goldstein, R. Lee and G. Cooperstein, NRL Memorandum Report 4326 (1980).

3. "Computational Study of Magnetic Dam Effects in a High Impedance Diode," R. J. Barker, Shyke A. Goldstein and A. T. Drobot, NRL Memorandum Report 4642 (October 1981).

4. "Steady State Numerical Solution of Magnetically Insulated Charge Flow in a Coaxial Geometry," R. J. Barker and P. F. Ottinger, NRL Memorandum Report 4654 (December 1981).

5. Production of Intense Light-Ion Beams from a Superpower Generator," F. C. Young, G. Cooperstein, S. A. Goldstein, D. Mosher, S. J. Stephanakis, W. R. Oliphant, J. R. Boller, J. Maenchen, R. D. Genuario and R. N. Stringfield, NRL Memorandum Report 4726 (1982).

6. "The Use of Finite J_θ for Increasing the Ion Efficiency of High Impedance Diodes" R. J. Barker and Shyke A. Goldstein, NRL Memorndum Report 4773 (April 1982).

7. "Numerical Study of Electron Leakage Power Loss in a Tri-Plate Transmission Line," R. J. Barker and Shyke A. Goldstein, NRL Memorandum Report 4837 (June 1982).

8. "Effects of Partial Suppression of Ion Emission in Moderate Impedance Diodes," R. J. Barker and Shyke A. Goldstein, NRL Memorandum Report 4915 (September 1982).

1. "Numerical Simulation and Modeling of Electron and Ion Flow in Pulsed Power Diodes," A. T. Drobot, R. J. Barker, Roswell Lee, A. Sternlieb, D. Mosher and Shyke A. Goldstein, Proc. of the Third International Topical Conf. on High Power Electron and Ion Beam Research and Tech., (Novosibirsk, USSR, July 3-6, 1979), p. 647.

2. "Theory and Experiments of Terawatt Light-Ion Beams," D. Mosher, D. G. Colombant, G. Cooperstein, A. T. Drobot, S. A. Goldstein, R. A. Meger, P. F. Ottinger, F. L. Sandel, S. J. Stephanakis and F. C. Young, Proc. of the Topical Meeting on Inertial Confinement Fusion, (San Diego, CA, Feb. 26-28, 1980), p. 100.

3. "Focus Control in High-Current Light-Ion Diodes," D. Mosher, G. Cooperstein and S. A. Goldstein, Proc. of the Topical Meeting on Inertial Confinement Fusion, (San Diego CA, Feb. 26-28, 1980), p. 104.

4. "Progress in Light-Ion-Beam Research for ICF," G. Cooperstein, S. A. Goldstein, D. Mosher, R. J. Barker, J. R. Boller, D. G. Colombant, A. T. Drobot, R. A. Meger, W. F. Oliphant, P. F. Ottinger, F. L. Sandel, S. J. Stephanakis, F. C. Young, G. Ginet, D. A. Hammer, S. Humphries, Jr., J. M. Neri, R. Pal and R. N. Sudan, Proc. of the 8th International Conf. on Plasma Physics and Controlled Nuclear Fusion Research, (Brussels, July 1-10, 1980), p. 401.

5. "Light-Ion Production and Focusing with Pinch-Reflex Diodes," G. Cooperstein, S. A. Goldstein, R. A. Meger, D. Mosher, W. F. Oliphant, F. L. Sandel, S. J. Stephanakis, F. C. Young, and H. U. Karow, Proc. of the 4th International Topical Conf. on High-Power Electron and Ion-Beam Research and Technology, (Palaiseau, France, June 29-July 3, 1981), p. 53.

6. "Electromagnetic and Quasi-Static Simulation of Ion Diodes," A. T. Drobot, A. Palevsky, R. J. Barker, S. A. Goldstein G. Craig and D. Mosher, Proc. of the 4th International Topical Conf. on

High-Power Electron and Ion-Beam Research and Technology, (Palaiseu, France, June 29-July 3, 1981), p. 363.

7. "High Impedance Ion-Diode Experiment on the Aurora Pulser," R. A. Meger, F. C. Young, A. T. Drobot, G. Cooperstein, Shyke A. Goldstein, D. Mosher, S. E. Graybill, G. A. Huttlin, K. G. Kerris, and A. G. Stewart, J. Appl. Phys. 52, 6084 (1981).

8. "NRL Light-Ion Beam Research For Inertial Confinement Fusion," G. Cooperstein, Shyke A. Goldstein, D. Mosher, R. J. Barker, J. R. Boller, D. G. Colombant, A. Drobot, R. A. Meger, W. F. Oliphant, P. F. Ottinger, F. L. Sandel, S. J. Stephanakis, and F. C. Young, Laser Interaction and Related Plasma Phenomena, Vol. 5, edited by J. J. Schwartz, H. Hora, M. Lubin and B. Yaakobi, (Plenum, NY, 1981), p. 105.

9. "Light-Ion Inertial-Confinement-Fusion Research at NRL," G. Cooperstein, R. J. Barker, D. G. Colombant, A. Drobot, Shyke A. Goldstein, R. A. Meger, D. Mosher, W. F. Oliphant, P. F. Ottinger, F. L. Sandel, S. J. Stephanakis and F. C. Young, in Plasma Physics and Controlled Nuclear Fusion Research 1982, Vol. V, (IAEA, Baltimore, 1982).

10. "Measurements of Intense Ion Beams by a Novel Diagnostic Method," A. E. Blaugrund, S. J. Stephanakis, and S. A. Goldstein, J. of Appl. Phys. 53, 7280 (1982).

11. "High-Intensity Light-Ion Beam Research at NRL," G. Cooperstein, R. J. Barker, D. G. Colombant, A. Drobot, Shyke A. Goldstein, R. A. Meger, D. Mosher, P. F. Ottinger, F. L. Sandel, S. J. Stephanakis, and F. C. Young, in the Proceedings of the US-Japan Seminar on Theory and Application of Multiply Ionized Plasmas Produced by Laser and Particle Beams (Japan 1982).

12. "Pinch-Beam Diode Scaling on the Aurora Pulser," R. A. Meger and F. C. Young, J. Appl. Phys. 53, 8543 (1982).

13. Status of Light-Ion Inertial Fusion Research at NRL," G. Cooperstein, P. F. Ottinger, S. A. Goldstein, R. J. Barker, D. G. Colombant, R. A. Meger, J. M. Neri, D. Mosher, F. L. Sandel, S. J. Stephanakis and F. C. Young in Laser Interaction and Related Plasma Phenomena, Vol. 6, edited by H. Schwartz H. Hora, M. Lubin and B. Yaakobi, (Plenum Press, NY, 1982).

14. "Production of Intense Light-Ion Beams on a Multiterawatt Generator," J. W. Maenchen, F. C. Young, R. Stringfield, S. J. Stephanakis, D. Mosher, S. A. Goldstein, R. D. Genuario and G. Cooperstein, J. Appl. Phys. 54, 89 (1983).

15. "Thermal-Resistive Current Filamentation in the Cathode Plasma of a Pinch-Reflex Diode," V. K. Tripathi, P. F. Ottinger and J. Guillory, to be published in J. of Appl. Phys.

2P14 Finite Axial Magnetic Field Effects in the Electron Reflexing Double Diode.* ROBERT J. BARKER and SHYKE A. GOLDSTEIN, JAYCOR.—The anode foil double diode configuration has been the object of repeated experimental and theoretical studies in the quest for intense electron and ion sources. The electron reflexing inherent in such a device lends itself to a natural enhancement of otherwise space charge limited current densities. The imposition of an axial magnetic field has been shown to significantly alter the performance of these devices. Computer simulations have now been conducted to shed light on the detailed physics of electron and ion behavior in these diodes for imposed magnetic fields in the kilogauss to megagauss range. Particular attention was given to the possible impact of such fields on the limits of the current bootstrapping phenomenon which has been observed in similar reflexing configurations.

* Work performed at the Naval Research Laboratory, Washington, D.C. and supported in part by the U.S. Dept. of Energy

6D13 INVESTIGATION OF INDUCTIVE EFFECTS DUE TO INTERNAL DIODE FLOW*, A.T. Drobot, Science Applications, Inc., McLean, VA. 22102, and Shyke A. Goldstein, JAYCOR, Alexandria, Va. 22304

Inductive effects are important in treating the behavior of low impedance pulsed power diodes because of time dependent internal electron and ion flows. Rough estimates, based on current-voltage traces from experimental data[1], indicate that the potential drop across the diode due to internally generated inductive fields is a significant fraction of the applied diode voltage. We are in the process of developing an inductive simulation code to treat this problem. Our understanding of the importance of inductive effects and progress on the numerical modeling will be presented.

*Work performed at the Naval Research Laboratory.

[1] S. J. Stephanakis et al., Bull. Am. Phys. Soc. 23, 907 (1978); and also S.J. Stephanakis et al., 1979 IEEE Int'l. Plasma Sciences Conf., Montreal, Canada p. 79 (IEEE cat. # 79CH1410-0 NPS).

6D1 Multiterawatt Pinch Reflex Ion Diode Performance*. S. J. STEPHANAKIS, J. R. BOLLER, G. COOPERSTEIN, SHYKE A. GOLDSTEIN†, D. D. HINSHELWOOD†, D. MOSHER, W. F. OLIPHANT, F. C. YOUNG, Naval Research Laboratory, Washington, D. C., and R. D. GENUARIO and J. E. MAENCHEN, Physics International Co., San Leandro, CA--Preliminary results of pinch reflex ion diode performance on the PITHON generator will be presented. Diode impedance and ion production efficiency results will be discussed. Sub-electron-range plastic foil anodes of 100 cm^2 area and hollow cathodes are used in a geometry similar to that employed in recent NRL GAMBLE II experiments to which the results will be compared.

*Work supported by the U. S. Defense Nuclear Agency
†JAYCOR, Inc., Alexandria, VA 22304

3B4 High Current Density Reflex Diode Experiments* R. A. MEGER, SHYKE A. GOLDSTEIN, D. D. HINSHELWOOD, JAYCOR, Inc., and G. COOPERSTEIN, Naval Research Laboratory-- Large area reflex diodes with solid anode foils have been shown to produce bipolar electron current densities in excess of Child-Langmuir flow [illegible] strong magnetic fields[1]. Ions partially neutralize the electron space charge near the cathode and allow increased electron emission. In this way the diode current "bootstraps" itself up to many times the Child-Langmuir current density. By using a small cathode area reflex diode (<0.02 cm^2) in a strong magnetic field (~30 kG), current densities in excess of 10^7 A/cm^2 ($I \sim 10^4 I_{CL}$) have been observed[2] on the NRL GAMBLE I facility (~1 MV, I~ 300 kA). Ions should comprise as much as 10% of this current. Experiments are in progress to measure electron and ion current fluxes within the diode with applications to high specific power deposited on targets for Inertial Confinement Fusion research.

*Work supported by U. S. Department of Energy

[1] D. S. Prono, et al., PRL 37, 21 (1976)
[2] G. Cooperstein, et al., Bull. Am. Phys. Soc. 23, 790, (1978).

3A5 Ion Beam Generation Experiments on the Aurora Accelerator*. R. A. MEGER†, G. COOPERSTEIN, A. T. DROBOT‡, SHYKE A. GOLDSTEIN†, D. MOSHER, F. C. YOUNG, Naval Research Laboratory and S. E. GRAYBILL, C. A. HUTTLIN, K. G. KERRIS, A. G. STEWART, Harry Diamond Laboratories -- An ion diode has recently been installed on one arm of the Aurora accelerator. First experiments have been performed at the 1.3 TW level (~1/3 available power for one arm) and have produced ~50 kJ of 5 MeV protons. About 10^{13} neutrons per shot were observed when the ~70 kA, 140 ns duration proton beam was incident on a thick LiCl target. The diode consisted of a 10 cm diameter cylindrical cathode separated from a polyethylene anode by ~5 cm in a pinch-reflex diode configuration. The diode impedance during ion acceleration was ~25 ohms. Ion production efficiency was ~30%. This high efficiency (~7 times bipolar flow) was expected from computer simulation of a high impedance small-aspect-ratio diode(1). The high efficiency appears to be the result of electron orbit lengthening due to $\vec{E}\times\vec{B}$ drifts when the total current exceeds the Alfvén current.

These experiments represent an effort by the NRL Light Ion Beam Research Group in collaboration with Harry Diamond Laboratories to scale results on lower-impedance machines (the NRL GAMBLE II and the Physics International PITHON machines)(2) to higher voltage and impedance diodes at high beam energy levels. Although the ion efficiencies are less than on lower impedance machines, the "stiffer", high-voltage beam can be ballistically focused to smaller spot sizes in long focal length geometries. Initial pulsed-power work on the Aurora accelerator shows that the positive-polarity operation required for beam transport is practical. Power multiplication by a factor of 5 through axial beam bunching during transport might be achieved by ramping the diode voltage. Additional energy may be obtained by overlapping ion beams from the four arms of Aurora.

This paper will summarize the present experimental results. The next three papers will detail the following aspects of the research effort. First, the computer simulation results will be presented; second, the Aurora accelerator modifications, accelerator diagnostics, and polarity reversal experiments will be described; and finally, the ion diagnostics will be presented in detail. Discussions will include the initial low power work as well as scaling to higher power and positive polarity.

*Work supported by Defense Nuclear Agency
†JAYCOR, Inc., Alexandria, VA 22304
‡Science Applications, Inc., McLean, VA 22102

[1] Shyke A. Goldstein and Roswell Lee, 1078 (Private communication).
[2] S. J. Stephanakis, et al, Bull. Am. Phys. Soc. 24, 1031 (1979).

3A8 Nuclear Diagnosis of Ion Beams from Aurora*, F. C. YOUNG and R. A. MEGER†, Naval Research Laboratory.

Intense multi-MeV ion beams have been generated with a pinch-reflex diode configuration on the Aurora generator. A 50-kJ proton beam consisting of 6×10^{16} protons with energy ~5 MeV has been inferred from neutron measurements using the $^{7}Li(p,n)^{7}Be$ reaction. In addition, a carbon-ion component is indicated by measurements of nuclear activation induced in the aluminum cathode.

Ion beams directed onto thick LiCl targets produced neutrons by the $^{7}Li(p,n)^{7}Be$ reaction which has a threshold at 1.9 MeV. Cross sections and angular distributions for this reaction are well known (1), and the resultant neutron energies are appropriate for time-of-flight (TOF) measurements. Intensities of 2×10^{12} neutrons/sr in the direction of the ion beam were deduced from Rh-activation counter measurements. Proton energies of ~5 MeV were determined from neutron TOF measurements for a 13.8-m flight path in the forward direction. This energy is consistent with the measured diode voltage. These results require a beam intensity of 6×10^{16} protons. An average current of 70 kA is deduced for the duration of the voltage pulse. The corresponding proton power is 0.4 TW.

Delayed radioactivity induced in the aluminum cathode provided evidence for the production of energetic carbon ions. Gamma-ray pulse-height analysis of the cathode after beam bombardment showed 3.32-, 2.14- and 1.17-MeV gamma rays with 30-min half-lives. This radioactivity is characteristic of ^{34m}Cl. The most likely source for this activity is from the $^{27}Al(^{12}C,2n)^{34m}Cl$ reaction (2) which has a carbon-ion threshold energy of 4.9 MeV. Carbon ions of up to 30 MeV may be produced in these experiments by the acceleration of multiply-ionized atoms from the polyethylene anode foil. Cross sections reported for this reaction(2) have been used to estimate that ~10^{13} carbon ions are required to account for the observed activity if the carbon-ion energy is 20 MeV (i.e. C^{+7}). If the ion energy is less (greater), then the number of carbon ions is larger (smaller).

Further experiments with improvements and refinements of these ion diagnostics are planned, including neutron intensity measurements by delayed counting of Mn-foil activations. Also, positive-polarity operation will allow direct ion current measurements with a Rogowski loop.

*Work supported by the Defense Nuclear Agency, Washington, D. C.

†JAYCOR, Inc., Alexandria, VA

1. H. Liskien and A. Paulsen, Atomic Data and Nuclear Data Tables 15, 217 (1975).
2. I. M. Ladenbauer-Bellis, I. L. Preiss and C. E. Anderson, Phys. Rev. 125, 606 (1962)

1E2 ELECTRODE PLASMA EVOLUTION IN A MULTITERAWATT PINCH ION DIODE*

R. O. Genuario, J. Maenchen, R. Stringfield
Physics International Company
San Leandro, California 94577

G. Cooperstein, D. Mosner, S. Stephanakis
Naval Research Laboratory
Washington, D.C. 20375

S. A. Goldstein
Jaycor, Inc.
Del Mar, CA. 92014

Recent scaling of ion production from Pinch-Reflex diodes to high power[1] have made it a leading candidate for ICF applications. Ballistic focusing over ~ .3 m has been proposed as a means of achieving high beam-power density prior to injection into a plasma channel for transport to the pellet. For ballistic focusing to be effective, the plasma boundaries of the anode and cathode must evolve in such a manner as to compensate for orbit bending in the time-dependent electric and magnetic fields of the inter-electrode gap. Suitable foil electrode geometries can be designed only when the plasma motion (which reduces the gap as the fields rise) is known.

A series of experiments have been performed at the 3-5 TW level on the PITHON generator using a Pinch-Reflex ion diode to investigate electrode-plasma motion holographically. The pulsed-ruby laser-holographic-interferometry system produces a sequence of four dual exposure transmission holograms. Each of the four frames has an exposure time of 5 ns, with a separation variable from 10 ns to 100 ns. The density range accessible to this system for our geometry is 10^{17} $cm^{-3} < n_e < 10^{21}$ cm^{-3}. Electrode plasma evolution as a function of radius and time for plastic anode foils will be presented.

*Work supported by the Defense Nuclear Agency.

[1] S. Stephanakis et al. Bull. Am. Phys. Soc. Vol 24, No. 8, (1979).

121

QUARTZ GAUGE MEASUREMENTS OF INTENSE PULSED ION CURRENT DENSITIES FROM A PINCH-REFLEX DIODE ON THE PITHON GENERATOR

J. Maenchen, R. D. Genuario, V. Bailey
Physics International Company
San Leandro, California 94577

D. Mosher
Naval Research Laboratory
Washington, D.C. 20375

S. A. Goldstein
Jaycor
Del Mar, California 92014

In the field of light ion beam ICF, the shock wave coupled from a beam into a target is an essential parameter governing the implosion. Standard diagnostics used to quantify ion beams during the extraction, focusing, and transport phases of an experiment provide pulsewidth, voltage, total current, and current density over selected areas, all of which can be combined via a hydrodynamic code to derive the target stress. This paper discusses recent work to directly monitor the pressure pulse produced in an aluminum target loaded by an ion beam using an x-cut quartz piezo-electric detection system. This stress pulse is unfolded with the aid of the PISCES[1] material response code to yield the local current density. Stress profile and inferred current density data for Pinch Reflex diode operation at 5 TW on the PITHON generator are presented.

The quartz gauges are laminate of an aluminum beam absorber and an x-cut quartz guard ring gauge. The diagnostic signal extracted is a direct measure of the shock transmitted from the aluminum into the quartz. The shock signature may be predicted using the known ion voltage, current history and focusing geometry to provide a detailed deposition profile boundary. The free parameter used to match the experimental and simulation waveforms is the local ion beam current density. Details of the calculations as well as comparisons of simulation and experimental data for an ion beam on the PITHON generator will be presented.

*Work supported by the Defense Nuclear Agency.

[1]PISCES™ IDL-Physics International Co. registered trademark.

406 Pinch Reflex Ion Diode Performance at 3-5 TW*, G. COOPERSTEIN, J. R. BOLLER, SHYKE A. GOLDSTEIN[†], D. MOSHER, W. F. OLIPHANT, S. J. STEPHANAKIS, F. C. YOUNG Naval Research Laboratory, Washington, D. C. and R. D. GENUARIO and J. E. MAENCHEN, Physics International Co., San Leandro, CA -- Pinch-Reflex diodes of 100 cm² area have recently[(1,2)] produced .7 MA currents of 1.3 protons using the NRL GAMBLE II device at 1.5 TW and 1 MA of 2 MV protons and deuterons using the Physics International Co. PITHON generator at 3 TW. Ongoing experiments on PITHON are being scaled to the 5 TW level.

At 3 TW, more than 100 kJ of ions were extracted from 12 cm-diameter planar anode foils with 60% power and energy efficiency. Beam pulse durations of 100 ns were obtained with anode-cathode gaps ≥3 mm and anode-cathode transmission foil gaps ≥1 cm. Curving the anode plane to a spherical section with a 12.7 cm radius of curvature did not diminish the ion current. In both cases, diode impedance was controlled to ± 0.05 Ω by varying the anode-cathode gap. This impedance control with the observed small gaps indicates that programmed-voltage waveforms for ion beam bunching during transport and sophisticated focusing geometries can be employed.

Preliminary results of scaling the diode behavior to both higher power (up to 5 TW) and smaller cathode areas (25 cm²) as well as preliminary focusing results will be presented. Results will be compared to theoretical predictions and requirements for pellet fusion systems.

*Work supported by the U.S. Defense Nuclear Agency
[†]JAYCOR, Inc., Alexandria, VA 22304

[1]G. Cooperstein, S. A. Goldstein, D. Mosher, W. F. Oliphant, F. L. Sandel, S. J. Stephanakis and F. C. Young, Proc. 3rd International Topical Conference on High Power Electron and Ion Beam Research and Technology, 3-6 July 1979, Novosibirsk.
[2]S. J. Stephanakis, J. R. Boller, G. Cooperstein S. A. Goldstein, D. D. Hinshelwood, D. Mosher, W. F. Oliphant, F. C. Young, R. C. Genuario and J. E. Maenchen, Bull. Am. Phys. Soc. 24, 1031, 1979.

4C9 Ion Production from Small-Area Pinch-Reflex Diodes*, S. J. STEPHANAKIS, G. COOPERSTEIN, D. MOSHER, W. F. OLIPHANT and F. C. YOUNG, Naval Research Laboratory, and SHYKE A. GOLDSTEIN, JAYCOR, Inc. -- Proton and deuteron beams are produced with greater than 50% efficiency when Pinch-Reflex diodes are driven by the multiterawatt NRL GAMBLE II and Physics International Co. PITHON generators.[1] In these experiments, diodes with aspect-ratios of 15-20 operate at 1-2 ohm impedance levels which are well-matched to the generators. Ion currents of about 1 MA are extracted from the 100 cm^2 anode areas employed.

Diodes operating at somewhat higher impedance levels may be more appropriate for inertial-confinement-fusion systems because of greater ease in focusing a large number of ion beams to the pellet. In the Sandia Laboratories PBFA I system,[2] modular vacuum-transmission lines which transport energy at 1 TW in each of 36, 4 Ω, 30 ns generators may be individually terminated in ion diodes. In order to minimize the distance between the various diodes and the pellet, diodes employed should not exceed about 6 cm in diameter. Beams extracted from such smaller diodes may also be easier to focus into z-discharge transport channels[3] in order to obtain ion beam bunching.

With these considerations in mind, the GAMBLE II generator was used to drive 6 cm diameter Pinch-Reflex diodes at the 1 TW level. The geometry employed was a factor-of-two scale-down in diameter from diodes previously discussed. Electrode gaps were adjusted to lower-aspect ratio (~6) to provide diode operation in the 3-5 ohm range. Ion-production performance is discussed for several diode configurations. Results are compared to experiments with larger-area diodes and to theoretical predictions.

*Work supported by the Department of Energy

[1]Stephanakis, S. J. et al, Bull. Am. Phys. Soc., 24, (8) Oct. 1979.

[2]Yonas, G. et al, Proc. 3rd International Topical Conference on High Power Electron and Ion Beam Research and Technology 3-6 July 1979, Novosibirsk.

[3]Mosher, D. et al, ibid.

3A6 Numerical Simulation of Ion Production from the Aurora Diode*, A. T. DROBOT, Science Applications, Inc., McLean, VA 22102, R. J. BARKER and SHYKE A. GOLDSTEIN, JAYCOR, Alexandria, VA 22304 -- This paper will present the physical interpretation, based on numerical simulations, of the small-aspect-ratio diode used in the recent experiments at the Aurora facility.[1] Modeling the geometry used in the actual experiments and assuming a diode voltage that varies from 2 to 5 MeV, the numerical simulation predicts an electron current of 220 kA and an ion current >60 kA, at 5 MeV, in good agreement with the experimentally observed values. The ion efficiency obtained in the simulation exceeds bipolar Child-Langmuir by a factor of ~7. The purpose of the simulation was to investigate the details of ion and electron flow and to identify the mechanisms responsible for the enhanced ion efficiency as a function of rising voltage in this high impedance diode. The prolonged electron lifetime in the anode-cathode gap, which is responsible for the high ion efficiency, may be due to magnetic or electrostatic reflexing, and/or 2D electron flow.

The electron flow in the diode used on Aurora has been simulated at several voltages to obtain information about the early field structure to determine how the anode plasma is generated at the reflexing foil. The possible mechanisms are heating of the foil, flashover due to electric field strength, or flashover due to embedded charge. The simulations indicate that there is a factor of ~1.5 difference in the diode impedance for pure electron flow when the foil is non-conducting, I=92 kA at 5 MeV, and when the foil is conducting, I=145 kA.

To generalize these studies to other high impedance diodes, Z ~ 5 ohms, we shall also be reporting the results of diode configurations with aspect ratios ranging from R/d=1, as on Aurora, to r/d=10. Because the ion efficiency and beam quality are two important aspects in considering high-impedance-ion-diode sources for inertial confinement fusion applications we shall also discuss methods for improving the efficiency of ion production and maintaining high beam quality.

*Work performed at the Naval Research Laboratory and partially supported by the Defense Nuclear Agency and the Department of Energy.

[1]R. A. Meger, G. Cooperstein, A. T. Drobot, Shyke A. Goldstein, D. Mosher, F. C. Young, S. E. Graybill, G. A. Huttlin, K. G. Stewart, "Ion Beam Generation Experiments on the Aurora Accelerator", (see these proceedings).

315 Experimental Study of the Pinched Beam Ion Diode*
F. L. SANDEL, JAYCOR, Inc., Alexandria, VA 22304 -- An extensive experimental study of the pinched beam ion diode has been reported[1]. This included, among other topics, the mechanisms of anode plasma formation and the effect of anode composition on the ion yield, diode impedance behavior, ion beam reproducibility and focusibility. Furthermore, control of the diode impedance to establish voltage ramping and beam bunching was demonstrated. In order to apply these devices as light-ion ICF drivers the emitted ion beams and their behavior during subsequent propagation and focussing must be understood in more detail. In particular, to obtain good focussing and efficient injection into beam transport systems, a detailed knowledge of the magnetic structure of the beam, both radial and axial, is required. The fields change substantially as the beam undergoes magnetic neutralization in gases or focuses either ballistically or due to self magnetic fields. Also, the field structure necessarily depends on the distribution of ion yield at the anode plane.

Experiments have been conducted on the GAMBLE I accelerator in which moderate ($\leq$ 40 kA net current) ion beams are extracted from hollow cathodes and allowed to propagate in conducting drift tubes. Situations studied include propagation in vacuum, through ion transmitting foils separating the diode and vacuum drift regions and through ion transmitting foils separating the diode from a gas-filled drift region. The net current in the propagating beam was measured with an axial array of high speed current sensors. Locally, the beam was sampled with biased ion collector probes. The effect of axially movable return current planes on the axial distribution of net current was studied. Additionally, the radial magnetic structure of the beam was studied with an array of magnetic probes. In this way the degree of local beam current neutralization and the distribution of beam return current was determined. Experiments are in progress to determine the spatial distribution of the ion yield on the anode and the ion species present. Progress in these areas will also be reported.

*Work performed at the Naval Research Laboratory and supported by the Department of Energy.

[1] F. L. Sandel, Proc. IEEE Conference on Plasma Science, June 4-6, 1979, Montreal, Canada.

4C8 Computer Simulations of a Magnetically Insulated Radial Diode*, R. J. BARKER and Shyke A. GOLDSTEIN, JAYCOR, Alexandria, VA and A. DROBOT, Science Applications, Inc., McLean, VA.

Experimental investigations[1] have been performed on the use of a radially configured diode as an azimuthally symmetric source of light ions for inertial confinement fusion applications. This group has conducted computer simulations on a typical radial geometry in order to attempt explanations of the various observed phenomena. In particular, possible mechanisms that affect magnetic insulation of electron flow and change the ion production efficiency have been examined. These questions hinge on the behavior of electron flow into and within the radial gap. In this connection, the detailed structure of the imposed and self-magnetic fields can critically modify the overall operating characteristics of the device.[2]

The numerical simulation code[3] employed for these studies is 2½-D (r,z) particle-in-cell (PIC) and treats the proton and electron macroparticles in a fully relativistic manner. Using a quasi-steady state approach, the fields are taken as $E = -\nabla\phi$ and $B = \nabla \times A$. Poisson's equation yields ϕ and A_θ respectively from ρ and J_θ, while B_θ is found directly through radial integration of Ampere's Law over the mesh. This electrostatic and magnetostatic field solving is accomplished over an irregularly bounded region through the application of a capacitance matrix technique.

These simulation studies have focused on the coupling of electron flow from large radii in the vacuum feed into the radial diode gap itself. This would seem to be an attractive mechanism for enhancing electron space charge and thus ion emission in the gap. The characteristics of this electron flow were found to depend critically on the structure of the high azimuthal and axial magnetic fields present in the feed and in the gap. As a test case, a cathode shank radius of 5.0 cm was chosen with an anode collar inner radius of 5.5 cm (i.e. - a 0.5 cm radial gap). The gap length was 6.4 cm while the vacuum feeds were taken as 1.0 cm wide and were modeled out to a radius of 10.0 cm. An insulating B_z of 20 kG was imposed uniformly between the radii of 5.0 and 5.5 cm and was forced to decay linearly to zero at R = 6.5 cm. For such a geometry with a potential difference of 2 MV the vacuum feed electrons were not seen to enter the gap. Instead, net electron currents of about 2.5 MA were observed in the gap both for the case with as well as for the case without electron emission in the vacuum feed.

*Work performed at the U. S. Naval Research Laboratory and supported in part by the U. S. Department of Energy.

1. D. J. Johnson, Recent Light Ion Beam Production and Focusing Experiments, APS Plasma Physics Division Meeting, 12-16 Nov 1979, Boston, MA.
2. R. J. Barker and S. A. Goldstein, Finite B_z Effects on Current Bootstrapping in the Electron Reflexing Diode, APS Plasma Physics Division Meeting, 12-16 Nov 1979, Boston, MA.
3. Robert J. Barker, Shyke A. Goldstein, and Roswell Lee, 2½ Dimensional Numerical Simulations of Current Bootstrapping in the Electron Reflexing Diode, IEEE International Conference on Plasma Science, 4-6 June 1979, Montreal, Canada.

4F 15 Radial-Enhancement Pinch-Reflex Ion Diodes.* S.J. STEPHANAKIS, SHYKE A. GOLDSTEIN†, D. MOSHER, and W.F. OLIPHANT, Naval Research Laboratory.--Pinch-Reflex diodes exhibit ion efficiencies exceeding 50% when operated below about 2 Ω at the 1 TW level. Unfortunately, the same designs experience factors-of-two reduction in efficiency when diode gaps are adjusted for operation above 3 Ω. We report here on Gamble II experiments involving modified 5 Ω, 6-cm diameter ion diodes appropriate for PBFA operation. A metal ring at the anode potential and concentric with the smaller diameter cathode stalk was added to enhance the radial electric field at the cathode tip. Computer simulation indicates that the resulting modification to electron trajectories enhances anode reflexing thus promoting increased ion emission. Radial-Enhancement diode performance characteristics with a range of anode-cathode and enhancement ring-cathode gaps are presented.

*Work supported by the Department of Energy.
†JAYCOR, Inc., Alexandria, VA 22304

6D 15 Production of Light Ion Beams on a Superpower Generator. J. MAENCHEN, A. SERNAS, R. STRINGFIELD, J. KISHI, Physics International Co., S COOPERSTEIN, D. MOSHER, S. STEPHANAKIS, F. YOUNG, Naval Research Laboratory†, S. GOLDSTEIN, D. HINCHELWOOD, Jaycor.--Experimental investigations into the production and ballistic focusing of proton and deuteron beams are presented. A Pinched-Reflex ion diode developed by the Naval Research Laboratory (NRL) on the Gamble 1 and 2 accelerators, was matched to the PITHON generator at Physics International Company. The PITHON generator parameters are 5 TW, 2.5 MV, 1 Ω for 100 ns with minimal prepulse. We present the results of diode performance and the study of the evolution of the plasma electrode surfaces.

*Work supported by the Defense Nuclear Agency.

4F 9 Ion-Diode Experiments In Positive Polarity on Aurora.* F.C. YOUNG, R.A. MEGERT, D.P. BACON†, J.J. CONDON, G. COOPERSTEIN, S.A. GOLDSTEIN†, D. MOSHER, Naval Research Lab., S.E. GRAYBILL, G.A. HUTTLIN, K.G. KERRIS, A.G. STEWART, D.A. WHITTAKER, R. BIXBY, M.S. LITZ, Harry Diamond Lab., and C.W. MENDEL, Sandia National Lab.--The NRL light-ion-beam research group has continued Aurora experiments in conjunction with HDL. Negative-polarity experiments[1] have been extended to positive polarity to allow diagnosis of ion beams with a Rogowski coil. Ion currents of up to 70 kA have been measured at diode voltages of 4 MV for a duration of 150 ns (FWHM). These results are consistent with measurements of neutrons produced by the $^{7}Li(p,n)^{7}Be$ reaction. The ion power of 0.3 TW is 1/4 of that delivered to the diode in these experiments. With the use of plasma erosion switches, increased ion production was measured for A-K gaps as small as 2 cm. Ion-beam production was observed to double as the A-K gap was reduced from 5 to 2 cm.

*Work supported by the Defense Nuclear Agency.
†JAYCOR, Inc., Alexandria, VA 22304
[1]See abstracts 3A5 thru 3A8 in IEEE Inter. Conf. on Plasma Science, Madison, WI, 1980, p. 58.

4F 10 Diode Geometry Effects on the Aurora Ion Diode.* R.A. MEGERT, A.T. DROBOT†, SHYKE A. GOLDSTEIN†, and F.C. YOUNG, Naval Research Laboratory.--A high-impedance ion-diode experiment is in progress on the Aurora generator.[1] Proton beams of up to 70 kA net current and V < 5 MV have been generated using small-aspect-ratio, azimuthally-symmetric ion-diode configurations. Scaling of the ion-beam-generation efficiency with the aspect ratio will be presented and compared with theory. Variations on the diode geometry, such as the imposition of small magnetic fields[2] or radial electric fields, can result in increased ion-generation efficiency. In addition, non-planar focusing anodes may affect the ion-beam density distribution. Preliminary results of experiments with such diode variations will be compared to computer simulations.

*Work supported by the Defense Nuclear Agency.
†JAYCOR, Inc., Alexandria, VA 22304
‡Science Applications, Inc., McLean VA 22102
[1]F.C. Young, et al., see abstract this conference.
[2]R.J. Barker and Shyke A. Goldstein, see abstract this conference.

4F 11 Numerical Simulation of Ion Beam Production In Positive Polarity.* A.T. DROBOT, Science Applications, Inc., R.A. MEGER and SHYKE A. GOLDSTEIN, JAYCOR, Inc.--Results of numerical simulations corresponding to the NRL experiments at the AURORA facility will be reported. The cases considered are variations of the pinch-reflex-diode configurations run in positive polarity. These include focusing geometry, radial electric field flux compression, and partial turn on of the anode plasma. The results will be compared to experimental data and contrasted with previous theoretical work for negative polarity.

*Work supported by the Defense Nuclear Agency and the Department of Energy as part of the Naval Research Laboratory Light Ion Beam Program.

4F 12 Magnetic Insulation in Axial Diodes.* R.J. BARKER and SHYKE A. GOLDSTEIN, JAYCOR.--High impedance axial diodes (5-25 Ω) are under development as light ion sources for use with the AURORA pulsed power generator. Thus far, the observed ion production efficiencies of these devices have fallen far short of their low impedance (1-2 Ω) pinch-reflex axial diode predecessors. It has been suggested that the introduction of some degree of magnetic insulation of the electron flow in the axial A-K gap could result in a significant increase in electron space charge near the anode enhancing the net ion emission. This technique has proven extremely successful for producing high ion efficiencies (> 80%) in the radial diodes tested at Sandia Laboratories. Theoretical and numerical studies of the magnetically insulated radial diode have isolated the key elements responsible for its high efficiency. Present studies are focused on how these elements can be incorporated into axial diode geometries. Numerical simulations of possible configurations are being conducted with the 2½-D quasistatic DICE2D PIC code.

*Work supported by the Defense Nuclear Agency and the Department of Energy as part of the Naval Research Laboratory Light Ion Beam Program.

ION BEAM EXPERIMENTS ON THE AURORA GENERATOR

F. C. Young and R. A. Meger*

Naval Research Laboratory
Washington, DC 20375

The operation of an ion diode on one arm of Aurora has been recently studied experimentally and theoretically by the NRL Light Ion Beam Research Group in collaboration with Harry Diamond Laboratories. Experiments at 1.2 TW (into an under-matched diode with the Marx-charging voltage reduced to 90 kV) have produced 40 kJ of 5 MeV protons with ~ 30% efficiency. These experiments represent an effort to scale results from the lower-impedance NRL GAMBLE II and Physics International PITHON machines to higher-voltage and higher-impedance diodes. Analysis of proton and carbon-ion beams by nuclear techniques will be described. Other experimental and theoretical results will be summarized.

*JAYCOR, Inc., Alexandria, VA 22304

4E5 Computational Studies of a Radial Pinch-Reflex Diode.* R.J. BARKER†, and SHYKE A. GOLDSTEIN†, Naval Research Laboratory -- The low impedance axial pinch-reflex diode as well as the magnetically insulated radial diode have both proven to be extremely efficient sources for intense light ion beams. Typically, seventy to ninty percent of the power passing through these diodes is imparted to the ion beam. Computer simulations have been initiated on a new diode concept which combines NRL's pinch-reflex phenomenon with a radial geometry compatible with Sandia National Laboratories' PBFA I pulsed power generator. In this radial PRD, an anode foil forms a cylindrical band completely surrounding the cathode shank. Electrons reflexing through the anode foil plasma enhance ion emission there while prolonging their own lifetimes in the A-K gap. The equatorially focused ion flow is then ballistically directed towards a target on the diode's central axis. These simulations are being conducted with the PREMAS computer code, the follow-on to NRL's DIODE2D.

*Work supported by the Department of Energy
†JAYCOR, Inc., Alexandria, VA 22304

4E6 Ion Source Brightness of Pinch Reflex Diodes.* S.J. STEPHANAKIS, SHYKE A. GOLDSTEIN†, P.F. OTTINGER†, D. MOSHER, Naval Research Laboratory -- Experimental results on the NRL Gamble II generator indicate that intense light ion beams exiting pinch reflex diodes possess power brightness $P_B = P/\langle\alpha\rangle^2$ approaching 10^{13} watts/cm^2, where P is the ion power density and $\langle\alpha\rangle$ the mean angle of divergence of the ions produced at a given point on the anode surface. Source brightness limitations are associated with undulations of the anode plasma surface and filamentation of the electrode plasmas and/or the vacuum flow in the diode. In addition, beam focusability is affected by lack of brightness due to time-dependent magnetic bending of the ions in the diode. All these effects have been studied experimentally and theoretically. The results of this study will be presented.

*Work supported by the Defense Nuclear Agency and the Department of Energy

†JAYCOR, Inc., Alexandria, VA 22304

1C1 Aurora Modifications for Positive Polarity Ion Diode Operation.* J. R. BOLLER, J. D. SHIPMAN, Jr.†, J. K. BURTON‡, G. COOPERSTEIN, R. A. MEGER‡, Naval Research Laboratory and G. A. HUTTLIN, A. G. STEWART, Harry Diamond Laboratories -- One of the four arms of the Aurora generator is being modified to enhance its usefulness in support of the NRL Light Ion Beam Program while retaining the capability of being returned to its original configuration for use as a bremsstrahlung source. The goal of the modification is to maximize the peak electrical power that could be extracted from one arm of Aurora operating in positive polarity and delivered to a 5-10 Ohm ion diode load. The present configuration consists of a 22 Ω oil insulated Blumlein in series with a segmented insulator vacuum tube and a 7 m long 47 Ω vacuum coax with either an ion diode or 35 Ω bremsstrahlung load at its output. The main change that will be made to accomplish this goal is the removal of 5 meters of vacuum coax to allow the ion diode to operate near the tube. Preliminary power flow studies using a transmission line code indicate that this will both improve the efficiency of power flow into the relatively low impedance ion diode load and will produce a voltage ramp for bunching. Also, it will alleviate many of the electron emission problems associated with the operation of the long magnetically insulated vacuum coax in positive polarity. This shortened vacuum feed along with plasma erosion switches at the load will lower the peak inductive voltage across the tube insulator thus helping to reduce flashover problems in positive polarity. Resistive and possibly capacitive grading of the insulator is also being studied. To facilitate monitoring of voltages, currents and other diagnostics located on the center conductor of the vacuum feed, a 40 μH coil will be installed in the oil just after the prepulse switch for the purpose of carrying the signal cables from the center conductor to the outer conductor. This shunt inductance is calculated to reduce the peak power of the one arm by only 9%. Experimental results will be presented and compared with power flow calculations to analyze the effects of the modifications. Possible additional modifications for further increasing power flow efficiency and reducing the maximum voltage stresses on the tube insulator will also be discussed.

*Work supported by the Defense Nuclear Agency
†Sachs/Freeman Associates, Inc., Bowie, MD 20715
‡JAYCOR, Inc., Alexandria, VA 22304

1C2 Modified Aurora Ion-Diode Experiments* R. A. MEGER†, F. C. YOUNG, A. T. DROBOT‡, R. J. BARKER†, J. J. CONDON, G. COOPERSTEIN, SHYKE A. GOLDSTEIN†, Naval Research Laboratory and R. BIXBY, G. A. HUTTLIN, K. G. KERRIS, D. A. WHITTAKER, Harry Diamond Laboratories.

The production of intense light-ion beams on the high impedance Aurora accelerator is being studied as a potential driver for inertial confinement fusion. In the past, measurements of proton beams from various ion diodes have been made with the accelerator operating in both negative[1] and positive[2] polarity. Based on the success of these experiments, the transmission line of the accelerator is being modified[3] to increase power delivery to the ion diode in positive polarity.

Positive polarity experiments to date have produced ion beams with net currents of $\leq$ 70 kA out of $\sim$ 300 kA total diode current at proton energies of $\geq$ 2 MeV. The peak proton current has been shown to follow a simple reflex diode scaling[4] of $I_i/I_e \sim [M_e(\gamma-1)/2M_i]^{\frac{1}{2}} R/D_{eff}$ where M_e and M_i are the electron and ion masses, γ is the relativistic factor for electrons, R is the cathode radius and D_{eff} is the effective anode-cathode gap allowing for plasma closure. Experiments have shown that diode operation is sensitive to the presence of a prepulse. Plasma erosion switches and flashover prepulse suppressors have been used to divert the accelerator prepulse from the ion diode and to sharpen the risetime of the main voltage pulse at the diode. In this manner anode-cathode gaps as small as 2 cm have been used without gap closure during the 150 nsec voltage pulse.

In this paper, the new ion-diode geometry will be described; the results of computer simulations of the diode operation based on this geometry will be shown; and preliminary experimental results with the modified accelerator and new diode geometry will be presented.

*Work supported by the Defense Nuclear Agency
†JAYCOR, Inc., Alexandria, VA 22304
‡Science Applications, Inc., McLean, VA 22102
[1]R. A. Meger, et al, IEEE Conference Record-Abstracts, 1980 International Conference on Plasma Science, Madison, Wisconsin, p. 58.
[2]F. C. Young, et al, Bull. Am. Phys. Soc. 25, 899 (1980).
[3]See J. R. Boller, et al, these proceedings.
[4]Shyke A. Goldstein and R. Lee, PRL 35, 1079 (1975).

1C9 Effects of Conducting Anode Rings on Pinch Reflex Diode Behavior.*, S.J. STEPHANAKIS, R.J. BARKER†, S.A. GOLDSTEIN†, M.F. OLIPHANT, Naval Research Laboratory -- The pinch reflex diode consists of a hollow cathode and a thin-dielectric, free-standing, foil-anode. The electrons from the cathode impinge on the anode foil and proceed to pinch predominantly radially onto the diode axis after reflexing several times through the anode foil. For this pinching process to occur, the presence of an anode plasma is required. This plasma is provided by the surface-flashing and/or heating of the anode foil. This plasma is also the source of intense beams of ions (usually protons) which can carry a significant fraction of the total diode current for large-aspect-ratio diodes.[1]

We will report on a modification to the "standard" diode which generally improves its performance and increases its ion production efficiency for a given diode impedance. The modification consists of covering the anode foil with a conducting annulus which has an inner diameter slightly smaller than the inner diameter of the cathode. The annulus (typically Ta or Al) is thin compared with the electron range and is not electrically connected to the machine inner conductor. Experimental observations of diode operation for such a configuration include:

(1) Better symmetry of pinching and more reliable centering,

(2) Significant increase in impedance for a given anode-cathode gap,

(3) Higher ion-production efficiency for a given impedance, and

(4) Better late-time impedance behavior even for very small anode-cathode gaps.

Computer simulation codes indicate that the suppression of ion emission in the region of the metallic annulus in turn suppresses electron emission from the cathode tip resulting in a diode behavior which is consistent with the experimental observations. Both the experimental results and the simulation results will be presented and discussed.

*Work supported by the Defense Nuclear Agency and the Department of Energy
†JAYCOR, Alexandria, VA 22304

[1]Goldstein, S.A., G. Cooperstein, R. Lee, D. Mosher, and S.J. Stephanakis, Phys. Rev. Letters, 40(23), 1978.

4A4 Anode Plasma Expansion in Pinch-Reflex Diode.* D. COLOMBANT and SHYKE A. GOLDSTEIN**, Naval Research Laboratory, Washington, DC 20375--Anode plasma motion is characterized experimentally[1] by several distinct stages. In the first one, which lasts for about 10 nsec for the diode parameters in Ref. 1, no expansion velocity larger than 1 cm/μsec is observed. In the second stage, the anode plasma accelerates toward the cathode and velocities are of the order of 10 cm/μsec. In a third stage, the plasma is observed to reach velocities up to 30 cm/μsec and then to recede.

In this presentation, we report attempts at simulating the behavior of this anode plasma. We use a 1D slab MHD model in order to follow the time-dependence of the anode plasma expansion and in particular to study the effects of the pressure gradient vs. (jxB) acceleration. The electron and ion experimental current traces are used in the calculation and thus make the model reasonably accurate for this part. The major unknowns relate to the initial conditions of the anode material after flashover e.g. its thickness, temperature, resistivity and chemical composition of polyethylene which was the material used in Ref. 1. Attempts have been made to determine the sensitivity of the calculation to these different unknowns. Changes in the equation of state seem to influence in a significant way the anode plasma motion. In fact, the qualitative picture which has emerged from this study is that in the early stages, the material vaporized from the anode is still made up of heavy C_2H_4 molecules. As energy is fed into this layer of material, it goes first into internal energy, mostly into vibrational states of the molecules. Then, these heavy molecules are dissociated into lighter components before turning into carbon and hydrogen atoms. When dissociation is almost complete, ionization takes place. During these early phase transitions, little energy is left for kinetic motion. This explains the experimental observation of reduced anode plasma motion in the first stage. When the plasma is finally formed of lighter components (ions and electrons), much larger acceleration of the plasma takes place. This acceleration is due at first to pressure gradient terms (this points out the importance of knowing the pressure in the early stages) and after some time to the (jxB) term. Respective roles of these two terms will be presented. Other mechanisms like magnetic diffusion are also included in the calculation and their roles are also examined.

* Work supported by Department of Energy
**Present address: JAYCOR, Inc., Alexandria, VA

[1] F.C. Young, G. Cooperstein, S.A. Goldstein, D. Mosher, S.J. Stephanakis, W.F. Oliphant, J.R. Boller, J. Maenchen, R.D. Guenario, and R.N. Stringfield, NRL Memorandum Report 4725, 1982.

4A3 Focusing of Ion Beams From High-Brightness Pinch-Reflex-Diodes*. S. J. STEPHANAKIS, D. MOSHER, F. C. YOUNG, Naval Research Laboratory, Washington, DC 20375 and SHYKE A. GOLDSTEIN, JAYCOR, Inc., Alexandria, VA 22304--We have reported in the past[1] that the source brightness of ion beams produced in pinch-reflex-diodes can be improved by minimizing the vacuum gap that the ions traverse between the anode and the cathode. In particular, an ion-beam-divergence half angle $\Delta\theta$ of 0.05 radians was achieved with a planar diode. This implies a source-power brightness:

$$B_\rho \equiv P/\langle\Delta\theta\rangle^2 \sim 10^{13}\ \mathrm{W/cm^2 rad^2}.$$

A 5 cm dia. pinch-reflex diode with a spherical-section anode (5.1-cm radius of curvature) and a similarly-curved cathode transmission foil has been used recently on the NRL Gamble II generator. For the electrical parameters of the experiment (~ 400 kA of ~ 1 MeV protons) and the diode geometry used, calculations of ion focusing predict (see figure)

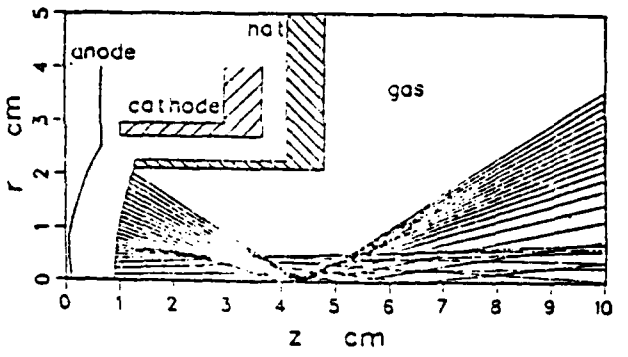

current densities exceeding 1 MA/cm^2 at about 4 cm from the anode-foil apex. Experimentally, measurements of Kα x-rays from aluminum targets, gold-foil heating viewed with x-ray diodes and a total-stopping ion calorimeter are being used to infer the ion current density. A description of the experiment will be presented, and the results of the investigations will be reported.

*Work supported by the Defense Nuclear Agency and the Department of Energy.

[1] S. J. Stephanakis, et al., Bull. Am. Phys. Soc. 26 921 (1981).

9D 12 Cathode Plasma Filamentation in Pinch-Reflex Diodes.* P.F. OTTINGER**, SHYKE A. GOLDSTEIN**, and J. GUILLORY**, Naval Research Laboratory and V.K. TRIPATHI, University of Maryland--Filamentation of the current flow in pinch-reflex diodes is a source of divergence for the ion beams extracted from such diodes. For ICF applications one would like to minimize beam divergence in order to maximize beam focusability. Since filamented electron flow is observed even when ion production is suppressed, it is suspected that unstable current flow in the cathode plasma is responsible for filamentation. Possible mechanisms for this unstable behavior have been studied including the thermal-resistive and ionization instabilities. Both these instabilities result from current-perturbation-ennancement of the local conductivity which, in turn, intensifies the current perturbation. Results of these analyses will be presented and compared with experimental findings.

* Work performed at the Naval Research Laboratory and the University of Maryland and supported by the Department of Energy and the Defense Nuclear Agency.

**JAYCOR, Inc., Alexandria, VA 22304

9D 11 Ion Energy Losses in Pinch-Reflex Diodes.* F.C. YOUNG, S.J. STEPHANAKIS, and SHYKE A. GOLDSTEIN+, Naval Research Laboratory--The energy of MeV protons or deuterons from pinch-reflex diodes is 200-300 kev less than the measured diode voltage.[1] This discrepancy is being investigated using the time-of-flight technique with d-d neutrons to make precision ion-energy measurements. Thin deuterated polyethylene (CD_2) targets are used so that the duration of the neutron signal is dominated by the duration of the energetic ion pulse. Selective CD_2 coating of the anode and judicious positioning of CD_2 targets are used to evaluate different mechanisms which could account for the observed energy loss. Mechanisms investigated include: 1)resistive voltage drop in the anode plasma, 2)multiple charge-exchange reactions in the anode plasma sheath, and 3)inductive or return-current effects in the anode structure. The results of measurements to evaluate such energy-loss mechanisms will be discussed.

*Work supported by the U.S. DOE and the U.S. DNA.
+JAYCOR, Inc., Alexandria, VA 22304
[1]F. C. Young, et.al., NRL Memorandum Report No. 4322, 1980; and F. C. Young, et.al., Bull. Am. Phys. Soc. 26, 920 (1981).

4E 10 Experimental Study of Exceeding the Critical Current in an REB Diode.* S.J. STEPHANAKIS, SHYKE A. GOLDSTEIN+, R.J. BARKER+, J.R. BOLLER, AND G. COOPERSTEIN, Naval Research Laboratory--Typically, the current drawn from REB diodes is equal to the critical current $I_c(kA)=8.5\ R/D(\gamma^2-1)$ where R and D are the cathode radius and the effective anode-cathode gap and γ is the usual relativistic factor. Recent theoretical studies (see abstract by R.J. Barker, et.al.) indicate that I_c can be exceeded by almost a factor of 2 by shaping of the anode structure and selectively controlling ion emission. These predictions were tested experimentally on the NRL Gamble II generator. A radial electric field was introduced by extending the anode coaxially with the cathode. The resulting radial-gap-to-axial-gap ratio was then varied. In addition, ion formation was controlled by either using graphite-coated metal surfaces to suppress ion production or, insulators designed for easy flashover. Results to date indicate that the impedance can indeed be controlled by such techniques in agreement with the theoretical predictions. The implications of these results for both REB and ion research will be discussed.
*Work Supported by the Defense Nuclear Agency
+JAYCOR, Inc., Alexandria, VA 22304

4E 9 Theoretical Study of Exceeding the Critical Current in an REB Diode* R.J. BARKER+, SHYKE A. GOLDSTEIN+, S.J. STEPHANAKIS, and G. COOPERSTEIN, Naval Research Laboratory--Numerical simulations have been completed using NRL's PREMAS computer code which show that diode currents nearly twice the critical current and many times the 1-D, Child-Langmuir prediction can be realized in an REB diode through appropriate shaping of the anode structure and through attention to ion emission surfaces. Furthermore, as has been shown previously for a radial diode with cathode radius, R, anode-cathode (A-K) gap, D, and cathode tip half-width, c, the ion-to-electron current ratio scales like c/D instead of the R/D scaling typical for a pinched beam diode. Electron backscatter from the solid anode surface is also introduced to test its effect on the diode's operation (see abstract of N. Pereira, Maxwell Labs, Inc.). Experiments on NRL's Gamble II generator compare well with these findings (see abstract by S. J. Stephanakis, et.al., this bulletin).
*Work Supported by the Defense Nuclear Agency.
+JAYCOR, Inc., Alexandria, VA 20304.

4E 8 Series REB Diode Experiments.* J.R. BOLLER, S.J. STEPHANAKIS, SHYKE A. GOLDSTEIN+, AND G. COOPERSTEIN, Naval Research Laboratory--The concept of a series REB diode has been investigated in the past by researchers from several groups including those from Physics International Co. and Maxwell Laboratories Inc. It involves driving two or more REB diodes in series from a single source in order to proportion the total available generator voltage between each diode. Recent experiments at NRL have shown that two REB diodes could be successfully driven in series when the center floating electrode, which must act as the anode for one diode and the cathode for the other diode, was mechanically held rigid by a 1 μH inductor. The voltage of the floating electrode was inferred from measurements of the current flowing through the inductor. The 1.5 MV generator voltage was divided approximately equally between the two 12 cm diameter hollow-cathode diodes when 300 kA flowed through each diode. Similar electron beam induced damage was also observed on each anode.
*Work supported by the Defense Nuclear Agency
+JAYCOR, Inc., Alexandria, VA 20304

Comparison of Diode Voltage and Ion Energy for an Intense Pulsed Ion-Beam Diode,* F.C. Young, S.J. Stephanakis, J.R. Boller and Shyke A. Goldstein,+ Naval Research Laboratory, Washington, DC 20375 -- A comparison is made of the voltage applied to an intense pulsed ion-beam diode and the energy of deuterons emitted from the diode. Previous experiments have indicated that the energy of MeV protons or deuterons from pinch-reflex diodes is less than the measured diode voltage[1] and that the ions are created in the diode region with this reduced energy.[2] We have measured the energy of deuterons from diodes operating at peak voltages ranging from 0.5 to 1.5 MV. The deuteron energy is determined by neutron time-of-flight (TOF) using d-d neutrons. Deuterons from a CD_2-coated anode bombard a thin CD_2 target located at the cathode to produce neutrons which are detected at 0°. Measured voltage and ion current traces are used to calculate the neutron TOF trace. The deuteron energy is determined by adjusting the magnitude of the voltage so that the calculated TOF trace agrees temporally with the measured trace. Corrections for distortion of the TOF trace due to lead shielding around the detector[3] are necessary to fit the measured neutron trace. The peak deuteron energy is determined to a precision of 5 to 10% for a flight path of 7.7 m. The diode voltage is deduced from a capacitive voltmeter with an inductive correction for the difference between the voltmeter and diode locations. The deuteron energy is observed to scale with the diode voltage but with a value of only 75% of the diode voltage.

An independent measurement of the voltage between the anode and cathode was made with an inductive voltage monitor.[4] The diode voltage deduced from this monitor is less than the corrected voltage from the capacitive voltmeter and is consistent with the ion energy from neutron TOF. The discrepancy between these ion energy and voltage measurements is being investigated.

---

* Work supported by the Defense Nuclear Agency and the Department of Energy.

+ JAYCOR, Inc. Alexandria, VA 22312.

1 F.C. Young, S.J. Stephanakis, G. Cooperstein, D. Mosher, F.L. Sandel, P.G. Blauner and S.A. Goldstein, NRL Memo Report 4322 (1980); and F.C. Young, D. Mosher, S.J. Stephanakis, and S.A. Goldstein, Phys. Rev. Lett. 49, 549 (1982).

2 F.C. Young, S.J. Stephanakis and S.A. Goldstein, Bull. Am. Phys. Soc. 27, 1121 (1982).

3 R.J. Leeper and J. Chang, IEEE Trans. Nucl. Sci. NS-29, 798 (1982).

4 J.R. Boller, S.J. Stephanakis and G. Cooperstein, Bull. Am. Phys. Soc. 27, 991 (1982).

Ion Beams from Axial Pinch-Reflex Diodes with Radial Electric Fields†, S.J. Stephanakis, P.C. Young, Shyke A. Goldstein[a], R.J. Barker[b], and T.J. Renk[c], Naval Research Laboratory, Washington, DC 20375 -- In the past we have reported that in order to produce light ion beams of high brightness from pinch reflex diodes, it is necessary to minimize the distance that these ions traverse in vacuo under the influence of their self-magnetic field. Although closing the axial anode-cathode gap improves beam brightness, it does not eliminate filamentation as a source of beam divergence. In addition, it forces reduction of the diode impedance and leads to premature gap-closure.

In order to overcome these limitations a diode concept incorporating both axial and radial electric fields is being studied both experimentally and by computer simulation. The new geometry incorporates an anode which is extended axially in the form of a cylinder so that it surrounds the cathode shank azimuthally and allows for a controllable radial anode-cathode gap. The diode impedance is primarily determined by the emission, and subsequent pinching on axis, of electrons off the extended cathode shank. This allows for electron orbit mixing which may mean less rippling of the E-field lines in the ion production region of the diode. Such ripples have been observed in computer simulations to have scale lengths of the order of an electron Larmor radius for the case of thin-walled hollow cathodes emitting axially. In addition, since the axial gap is no longer as important for electron emission, the ion-current-neutralizing gas region inside the cathode can be extended axially all the way to the cathode tip thus further minimizing E-field rippling while at the same time minimizing the axial in vacuo ion flow.

Experimentally, we have found that by suppressing ion production from the radial structure we can avoid severe ion beam filamentation in the azimuthal direction. In particular, in focusing geometry we have observed significant improvement in the beam divergence, i.e., smaller aiming errors, when such an axial-radial geometry is employed. We have also experimentally achieved good impedance control by varying the radial anode-cathode gap.

These experimental results as well as some computer simulation results will be presented and discussed.

† Work supported by the Defense Nuclear Agency and the Department of Energy

a)JAYCOR, Inc., Alexandria, VA 22304
b)Present Address: Mission Research Corp., Alexandria, VA 22312
c)NRL/NRC Cooperative Research Associate

Annular Electron Beam Production on Gamble II Using a Magnetically Insulated Splitter,* W.F. Oliphant, R.J. Barker,** J.R. Boller, G. Cooperstein, Shyke A. Goldstein,*** and S.J. Stephanakis, Naval Research Laboratory, Washington, DC 20375 -- Annular electron beams have been produced on the NRL Gamble II generator using a magnetically insulated splitter concept.[1] This three-dimensional configuration is used on the Gamble II vacuum diode to convert the coaxial generator output to a triaxial output. It, in turn, drives a double-edged annular cathode where ideally the electrons from the outer edge pinch inward while electrons from the inner edge pinch outward. The result is an annular electron beam whose average diameter is determined both by the relative inductances associated with the inner and outer anode return current paths and by the relative impedances of the inner and outer cathodes.

Experiments were performed at power levels of up to 1.5 TW and energies of 40-60 kJ. Typical voltages were 1-1.5 MV with currents of 0.6-1.2 MA.

The typical 10 cm diameter diode geometry was varied to determine impedance behavior, beam quality and beam shape. In addition to controlling anode-cathode gap spacings, cathode annulus width and return path inductances, ion production from the anode was also controlled, by selectively using high and low atomic weight materials, in an attempt to effect beam positioning.

The low prepulse (< 10 kV) and fast risetime (< 20 ns) of the Gamble II output voltage pulse, generally produced well behaved azimuthally symmetic beams although electron beam filaments originating from the magnetic nulls between the magnetically insulated posts could be observed.

Finally, two concentric triplate feeds producing annular beams of 5 and 15 cm diameter were tested. The two beams were smooth and well-behaved and, as expected, could be controlled independently of each other. Such a technique can eventually lead to the capability of producing large-area, low impedance electron beams with very little current loss to anode-produced ions.

* Work supported by the Defense Nuclear Agency, Washington, DC 22305.

** Present Address: Mission Research Corp., Alexandria, VA 22312

***Jaycor, Inc., Alexandria, VA 22304

[1] J. Shannon et.al., Invited Paper, these Proceedings.

COMPUTER SIMULATION OF INTENSE ELECTRON BEAM GENERATION IN A HOLLOW CATHODE DIODE

Introduction

Several years ago at the Naval Research Laboratory, Cooperstein, et al., observed some interesting anode damage patterns during runs of the Gamble I low-impedance diode.[1] The experimental arrangement is depicted in Fig. 1. A simple carbon hollow cathode opposed a flat plate porous graphite anode. (Note that only the small D carbon witness plate location is of interest here.) Large external magnetic field coils maintained the entire configuration in a 30 kG solenoidal magnetic field. A number of discharges were run in the 600 kV to 1 MV range. After a typical experiment, examination revealed that a perfect circular groove had been cut into the anode surface. The dimensions of the groove were such that the cathode could neatly fit into it. Furthermore, upon closer examination there was an even finer pattern of damage inside the groove. A radial cross-section had the shape of a straight-sided "W". The groove was decidedly deeper at the edges than along the center.

The close correspondence between the cathode radius and the damage radius was attributed to the effect of the strong axial magnetic field. This effect alone, however, could not explain the sheer magnitude of the damage. Some 100 kA/cm^2 of electron current density would have been required to pulverize the anode material. Standard one-dimensional analysis cannot explain the emission of such high current densities from the cathode.

Manuscript submitted June 16, 1980

Nevertheless, their existence has been established. A possible explanation is that electron emission is enhanced through a two-dimensional intensification of the electric field near the cathode face edges.[2,3] This enhanced edge emission would also explain the "W" shape of the anode groove cross-section. The computer simulations described below were conducted to test this theory.

The Simulation Code

The computer code utilized in these studies is a modified version of the DIODE2D code developed at the Naval Research Laboratory during the mid-1970's by one of the authors (R.E.L.). That original code performed numerous accurate and efficient one- and two-dimensional electrostatic diode simulations.[4,5] These results encouraged the expansion of the program to allow the full treatment of radial and axial self-magnetic fields as well as the inclusion of an imposed axial magnetic field. As in the original code, great emphasis was placed upon optimizing the numerics of the new code for use on NRL's vector machine, the Texas Instrument Advanced Scientific Computer. The coding work was completed by another of the authors (R.J.B.) in August of 1978. Since then, work to improve its efficiency has continued simultaneous to its application to a variety of problems of interest including the one presented herein. The capabilities of the code and its limitations are outlined below.

The code is 2½ dimensional, particle-in-cell (PIC). Inhomogeneities are allowed in the radial (r) and axial (z) spatial dimensions. Complete azimuthal symmetry is assumed. On the other hand, all three momentum components (r, θ, z) are retained. This retention of the theta momentum is a prerequisite for the treatment of radial and axial magnetic fields in the simulation. The "particles" in this model are axially-centered rings of

charge with all other degrees of freedom. In reality they are macroparticles carrying many times an elementary charge but retaining the physical charge-to-mass ratios of the protons and electrons which they represent. Area weighting (i.e., linear interpolation) is used to couple these charges with the electric and magnetic fields calculated over a fixed set of grid-points in the region of interest. The fields thus interpolated to the particle positions act on these charge-current rings by way of the relativistic Lorentz force equation.

The fields are treated electrostatically and magnetostatically. In this sense the code does not perform a true "simulation" since Maxwell's equations are not observed. Rather the treatment is "quasistatic". Equilibrium solutions to various diode geometries are sought. The "timesteps" which appear in the code are actually snapshots of the system while it seeks to relax toward its steady-state operation. It is this steady state which is of primary interest. In order to determine the electric field within the diode region particle charge densities are distributed over a fixed grid and the discrete Poisson's equation is solved.[6] The same technique is used to determine the axial and radial components of the self-magnetic field from the azimuthal current densities. In both cases the code permits irregular conducting boundaries inside the computational region. The treatment of such internal boundaries entails the use of a "capacitance matrix".[7] The internal surfaces thus created are held at predetermined electric potential values while magnetic flux from all but the imposed fields is excluded from them. Direct radial integration of the axial current densities over the mesh yields the azimuthal magnetic field via Ampere's Law. The outer radial boundary of the diode region may be either conducting or free-space. The electrostatic potential, ϕ, is set constant along all conducting boundaries. Along radial

free-space boundaries, ϕ is graded logarithmically and along axial ones, linearly. For A_θ, when a free-space outer radial boundary is chosen, the external source-free cylindrical vector potential eigenvectors are matched up with their internal, source-consistent counterparts there. The algorithm also permits the imposition of a temporally and spatially uniform axial magnetic field. This feature was essential to the completion of this particular study.

At the start of a typical computer run, the computational diode region is a complete vacuum, devoid of particles. The electric potential is pre-set along the entire boundary as well as along all internal conducting surfaces. A fixed value is similarly set for the imposed axial magnetic field (B_z). The emission of the ions is permitted anywhere along the conducting high voltage boundary (anode) surface. Electrons are emitted along the front face of the cathode surface. The value of the perpendicular electric field at a given emission point determines the total charge (i.e., number of particles) that will be emitted there. At the beginning of a timestep, the electric field at a surface specifies the net charge density on the surface via Gauss' Law. The surface integral of this density over a cell width around a given grid point yields the net charge which is emitted there for this timestep. Prior to the actual particle-pushing the electric field is recalculated taking into account the newly emitted charge.

The emitted particles are then pushed according to the relativistic Lorentz force law using the area weighted electric and magnetic field values interpolated at the particle position from the four nearest grid points. After the pushing in each timestep the charge and current density associated with each particle is distributed over the four nearest gridpoints using the same linear interpolation scheme in reverse. This yields a complete array of

values for the charge density, ρ, and the current density, $\vec{J}$, over the computational mesh. Poisson solving these arrays yields ϕ and A_θ from which E_R, E_z, B_R and B_z are calculated. The azimuthal component of $\vec{B}$ is obtained through direct integration of J_z over the grid. Quantities of interest are then extracted and output via diagnostic subroutines. The code then cycles to the next timestep for particle emission.

Finally, it would be noted that the numerics of the particle pushing as well as the potential solving has been completely "vectorized". Thus the momentum, position, and field components associated with the entire ensemble of particles are treated as macro-vector quantities. Arithmetic operations performed with them are accomplished in a completely vector-array format. This property of the code permits efficient running times on the most advanced scientific computers. (Of course, the interpolation of ρ, $\vec{J}$, $\vec{E}$, and $\vec{B}$ values between particle positions and grid points requires random accessing of array points and this process cannot be vectorized.)

The Computer Experiment

Configuration Under Study

The diode configuration modeled in this simulation was chosen specifically for its significant distortion of the internal electric field. Any emission enhancement resulting from this distortion should be relatively easy to see. Figure 2 provides a scale drawing of the actual geometry of the diode modeled. The hollow-cathode projects into the computational region from the left-hand boundary. A cylindrical anode cup completely surrounds it radially and to the right. One-quarter centimeter separates the cathode face from the anode disc plate while radial gap between these two coaxial electrodes is one and one-quarter centimeters wide. The cathode itself measures 1.27 centimeters in outer radius with a wall thickness of 0.14 cm. It

projects 0.08 cm into the 2-D computational region. A conducting plug fills the cathode interior to within 0.08 cm of the edge face and thus coincides with the computational region's inner left boundary. The upper half of the region's left boundary is left "open" with the electrostatic potential graded logarithmically with radius.

The vacuum diode equipotential surfaces are depicted in Fig. 3. Of particular interest in this plot is the manner in which these surfaces are compressed near the edges of the cathode face. This bunching gives rise to the electric field enhancement at these points and to the resulting enhanced electron emission there.

Operational Parameters

For all of the runs discussed herein, the diode voltage is initialized at 120 kV and climbs linearly over 50 timesteps to a steady state plateau value of 600 kV. The timestep, Δt, itself is fixed at 1.6×10^{-12} second. The two-dimensional numerical mesh over which the particles move measures 128 cells in the radial dimension and 64 cells in the axial. In addition, a monolayer of "guard cells" completely surrounds the mesh to yield a total of 130 × 66 cells overall. All boundary surfaces run between neighboring rows of gridpoints rather than along them. (Gridpoints are defined as the cell centers.) The electrostatic potentials on these boundaries are held fixed relative to the full diode potential at any given timestep throughout the simulation. The cell widths (or gridpoint spacings) are 0.0195 and 0.00521 centimeters for ΔR and ΔZ, respectively. The front face of the cathode emits electrons over six radial cells. This emission profile provided adequate resolution for this experiment. Finally, a solenoidal magnetic field is imposed and is assumed to have been on long enough to have

completely penetrated the anode and the cathode before particle emission is initiated.

For the first 300 timesteps of the simulation, only electron emission was permitted. By that time, an electrons-only steady state had been attained. The program diagnostics were then examined to determine which regions of the anode surface were being bombarded by the largest electron current densities. At timestep 301, ion emission was turned on over those regions. (In the physical diode, these are the areas where the most heating of the anode surface has occurred.)[8] The computer simulation then continues until the net ion and electron currents equilibrate. The numerical data presented in the next section are taken from this final timestep with the device in its steady-state operation.

Results

In order to gauge the specific effect of a strong imposed solenoidal magnetic field, B_z, on diode operation, the same diode was simulated with and without B_z = 30 kG. In both cases the plateau voltage is set at 600 kV. In Case 1, B_z is set equal to zero. The major phenomenum to be observed in this case is the two-dimensional electric field enhanced emission of electrons. The results are graphically presented in Fig. 4. After 300 timesteps of electrons-only operation, the equilibrium profiles of electron emission current density at the cathode face and the electron impact current density at the anode are plotted as shown. It is quite clear that the compression of electrostatic equipotential liner at the cathode face edges (see Fig. 3) has had its effect. Electron emission is up by a factor of about 2.5 at the edges as compared to the center of the cathode face. A peak electron current density of over 78 kA/cm^2 is observed at the edge. The sharpness of this profile degenerates markedly before hitting the anode face. Virtually all

of the double-peaked definition is lost. The distribution is relatively diffuse with a maximum density of only about 24 kA/cm^2. A net current of 37.6 kA now flows through the diode. Since the critical current is about 82 kA, only very weak pinching can occur.

At timestep 301, ion emission begins on the anode face in the region where the electrons have been arriving. The addition of protons into the system has a substantial effect (see Fig. 5). At equilibrium, the total current through the diode has jumped to 61.5 kA. The electron emission profile has about the same shape but it now exceeds 90 kA/cm^2 at the cathode face edges. Similarly, the anode electron impact plot is still diffuse but it now peaks at about 32 kA/cm^2. Note also that the self-pinching of the electron beam is more pronounced. The mean radius of the beam has decreased by about one millimeter in its passage across the two and a half millimeter gap.

For the diode simulation Case 2, a thirty kilogauss solenoidal magnetic field, B_z, is imposed. The results of the runs are plotted in Figs. 6 and 7. As in the previous case, only electrons flow through the system during the first 300 timesteps. Figure 6 reveals once again a double peaked emission distribution at the cathode with a maximum value of about 96 kA/cm^2. The truly dramatic change is found in the anode profile. The beam's radial diffusion while crossing the gap has been sharply restricted by the imposed B_z. The anode impact plot has about the same shape as the plot of the electron emission. It peaks at about 83 kA/cm^2. In this steady state about 40 kA is flowing through the diode. The results become more marked after ions are permitted into the system (see Fig. 7). Peak electron emission rises to 108 kA/cm^2 while a maximum of 92 kA/cm^2 of electron current density is being deposited at the anode face. (Note that the total diode current is

59.2 kA in steady state. This is less than that recorded for the $B_z = 0$ case for the simple reason that ion emission was artifically limited to fewer points on the anode face for this run.)

These results indicate the following: (a) Electron emission is enhanced at the cathode face edges. (b) Protons flowing in the system substantially increase net diode current figures. (c) A strong imposed B_z significantly reduces the self-pinching of the electron beam as well as its radial diffusion.

Comparison of Results to Theory and Experiment

The computational results just presented gain significance only through comparison with the predictions of theory as well as with the findings of experiment. The first question is that of electron emission enhancement due to two-dimensional electric field distortions. In a one-dimensional analysis, in the absence of ions the Child-Langmuir emission law predicts that for an infinite flat plate vacuum diode with gap separation, d (in centimeters), and potential difference, V (in volts), electrons will be emitted uniformly over its cathode surface with a current density[9] of

$$J_{CL} = 2.34 \times 10^{-6} V^{3/2} d^{-2}$$

For the diode treated in this paper, V equals 600 kV while d is 0.25 centimeters. The formula thus yields $J_{CL} \approx 17.4$ kA/cm^2. This prediction comes fairly close to the 20-24 kA/cm^2 measured near the center of the cathode face. One would physically expect those interior regions to most closely resemble the one-dimensional model. At the edges, on the other hand, the electron emission exceeds the one-dimensional J_{CL} prediction by a factor of 4 to 5.

The introduction of protons into the system modifies the theoretical predictions. This new condition is termed one-dimensional bi-polar flow. The new electron emission current density, J_{BP}, is approximated by

$$J_{BP} = 1.86\ J_{CL}$$

Thus, it predicts about 32 kA/cm^2 for the diode operating with ions and electrons. This agrees quite well with the 32-42 kA/cm^2 seen in the simulation for the inner cathode face emission. However, it is off by a factor of 2.5 to 3 from the edge emission figures. The two-dimensional field enhancement effects have to drastically change the physics there from the simple 1-D analysis.

The second major question concerns the effect of the 30 kilogauss solenoidal magnetic field on the electron current densities impacting the anode face. Experimental corroboration for the computational results presented herein was derived from the previously mentioned observations obtained from a series of runs by the Gamble I device at NRL in the mid 1970's. These empirical results were presented by Cooperstein to the 1976 meeting of the Plasma Physics Division of the American Physical Society. Of those results, one of particular interest here is shown in Fig. 8. Using a diode configuration closely approximating that modeled in this computer simulation, a double peaked damage pattern was observed on the anode face at very nearly the radius of the hollow cathode after each discharge. Such damage could result if the anode material was being pulverized by the electron beam. The pulverization of carbon requires the deposition of 2 kcal/g. Assuming a mean graphite density of 2.5 g/cc this translates to 5 kcal/cc. The electron beam in the computer simulation was delivering a peak power of 54 j/cm^2-sec over an area of roughly 1.1 cm^2. Thus the experimentally observed damage could

be obtained to a depth of about one millimeter if the simulated beam were maintained for approximately forty nanoseconds. According to Fig. 8, the experimental voltage and current peaks were 1 MV and 200 kA, respectively. Comparing this to the 600 kV and 60 kA of the simulation would indicate that the experimental diode could have achieved the observed damage in twenty nanoseconds or less.

In short, the correlation between experiment and simulation is very good. The empirical results can now be better understood as a consequence of the combined effects of two-dimensional electric field electron emission enhancement as well as of the electron path stiffening caused by the strong axial magnetic field.

References

1. G. Cooperstein, D. A. Hammer, I. M. Vitkovitsky, S. J. Stephanakis, J. J. Condon, and Shyke A. Goldstein, Bulletin of the American Physical Society, San Francisco, 1976, p. 1096.
2. Edward Ott, Thomas M. Antonsen, Jr., R. V. Lovelace, Phys. Flu. 20, 1180 (1977).
3. J. Chen and R. V. Lovelace, Phys. Flu. 21, 1623 (1976).
4. S. A. Goldstein, R. C. Davidson, J. G. Siambis, and Roswell Lee, Phys. Rev. Lett. 33, 1471 (1974).
5. Shyke A. Goldstein and Roswell Lee, Phys. Rev. Lett. 35, 1079 (1975).
6. Robert J. Barker, Banach Center Publications 3, 255 (1975), Warsaw, Poland.
7. B. L. Buzbee, F. W. Dorr, and J. A. George, Technical Report CS-71-195, Computer Science Department, Stanford University, Stanford, California (1970).
8. Shyke A. Goldstein, G. Cooperstein, Roswell Lee, D. Mosher, and S. J. Stephanakis, Phys. Rev. Lett. 40, 1504 (1978).
9. Robert K. Parker, Technical Report AFWL-TR-73-92, USAF Weapons Lab., Albuquerque, New Mexico (1973).

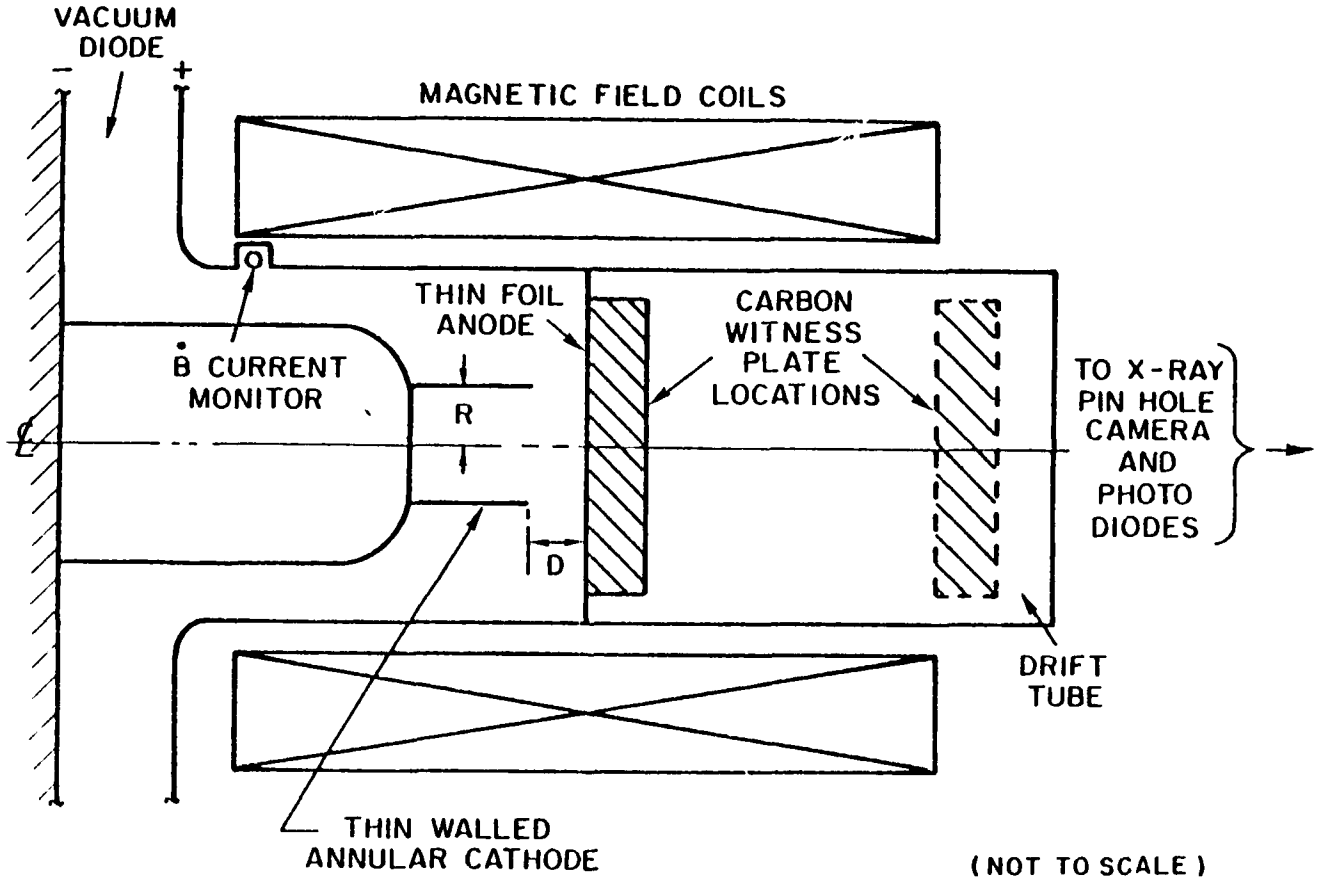

Fig. 1 - Experimental arrangement

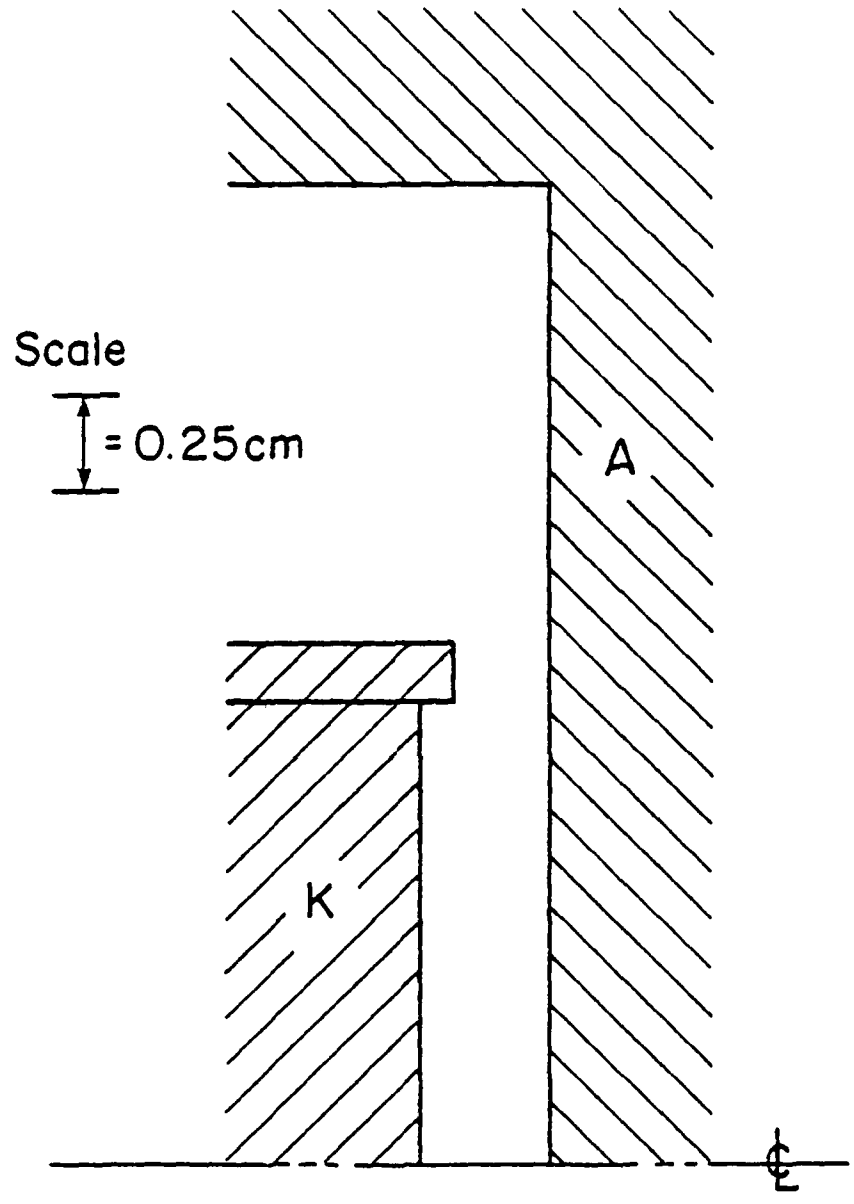

Fig. 2 - Scale drawing of diode

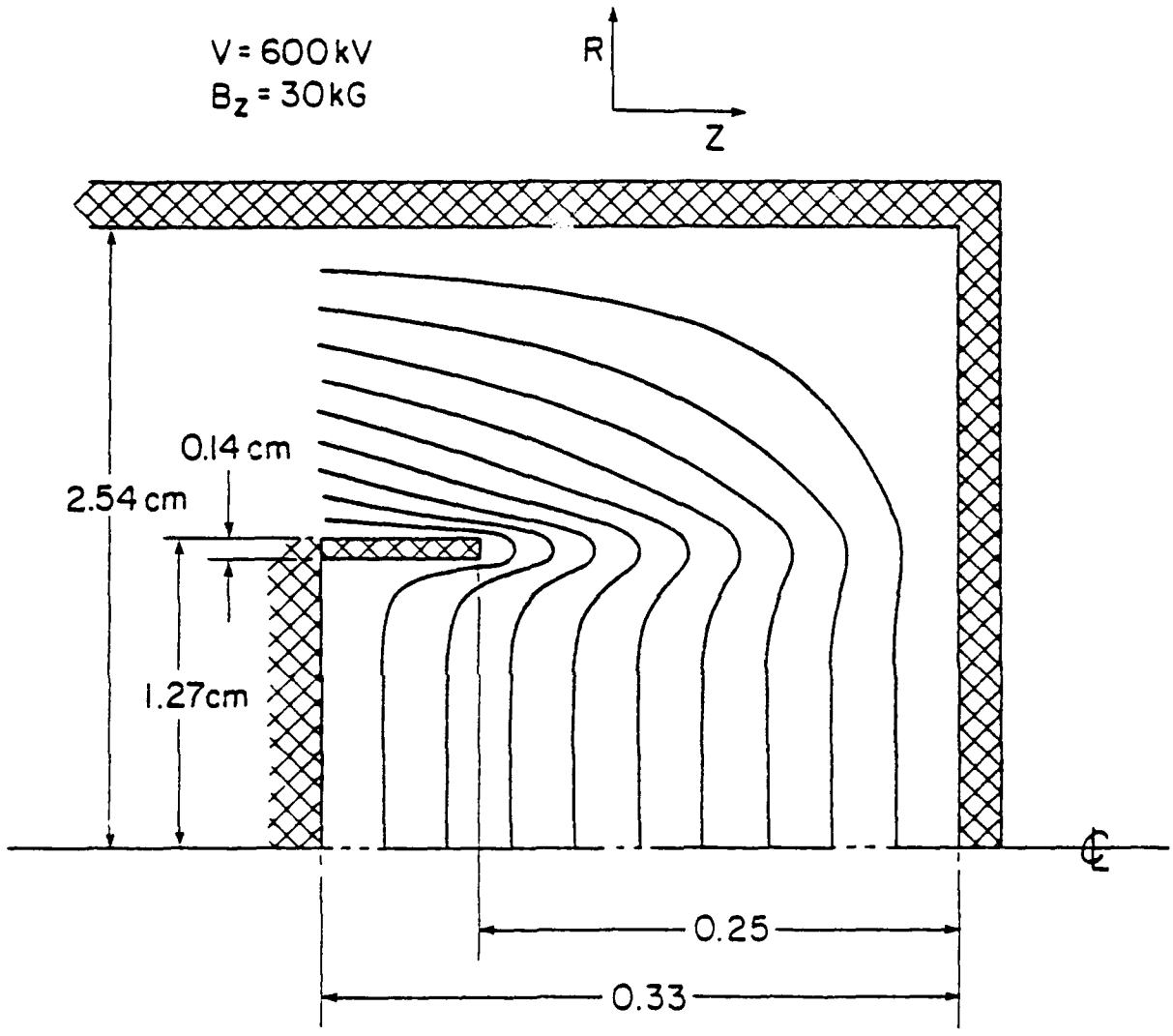

Fig. 3 - Vacuum equipotential plot

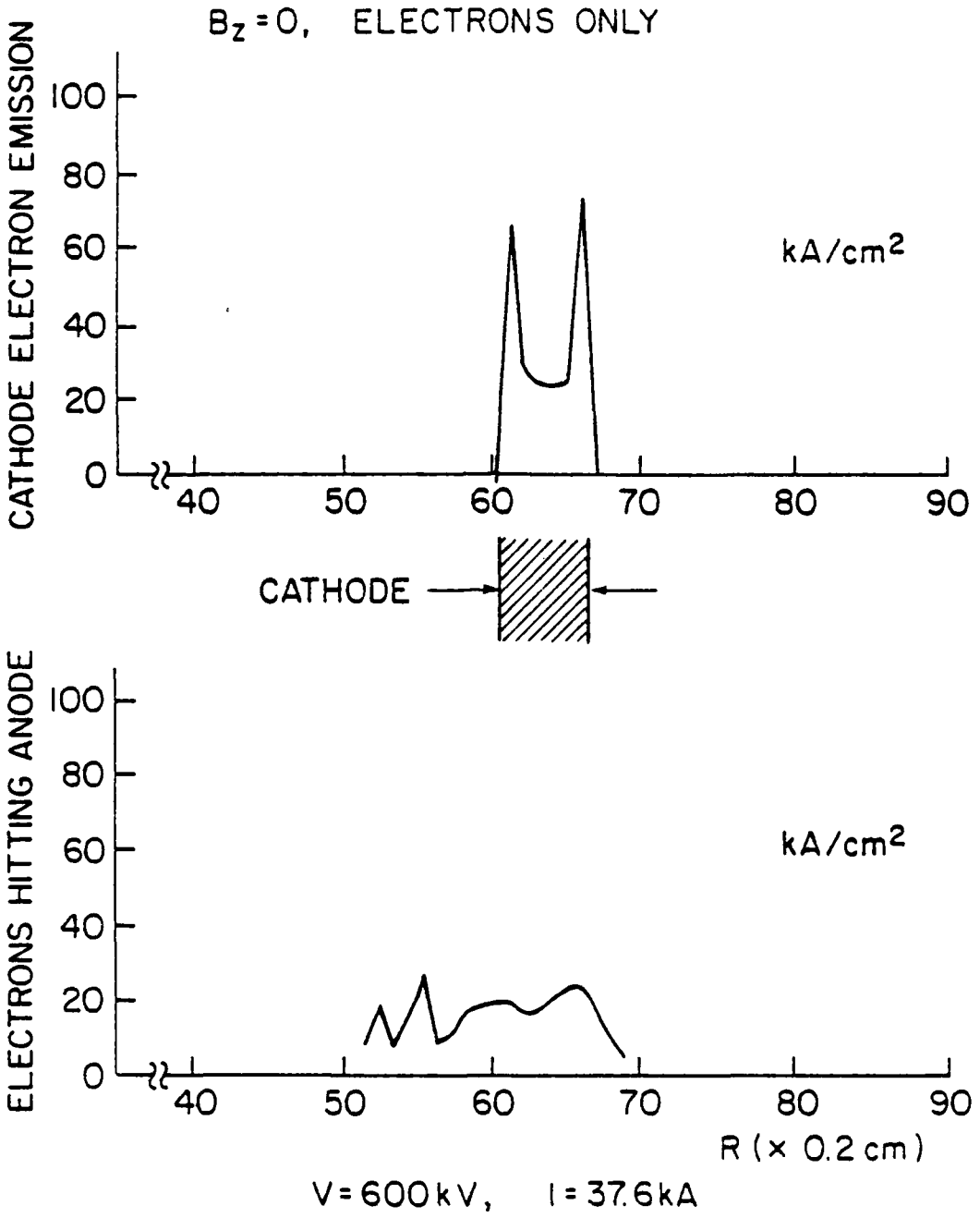

Fig. 4 - Steady-state current density for case 1 with only electrons

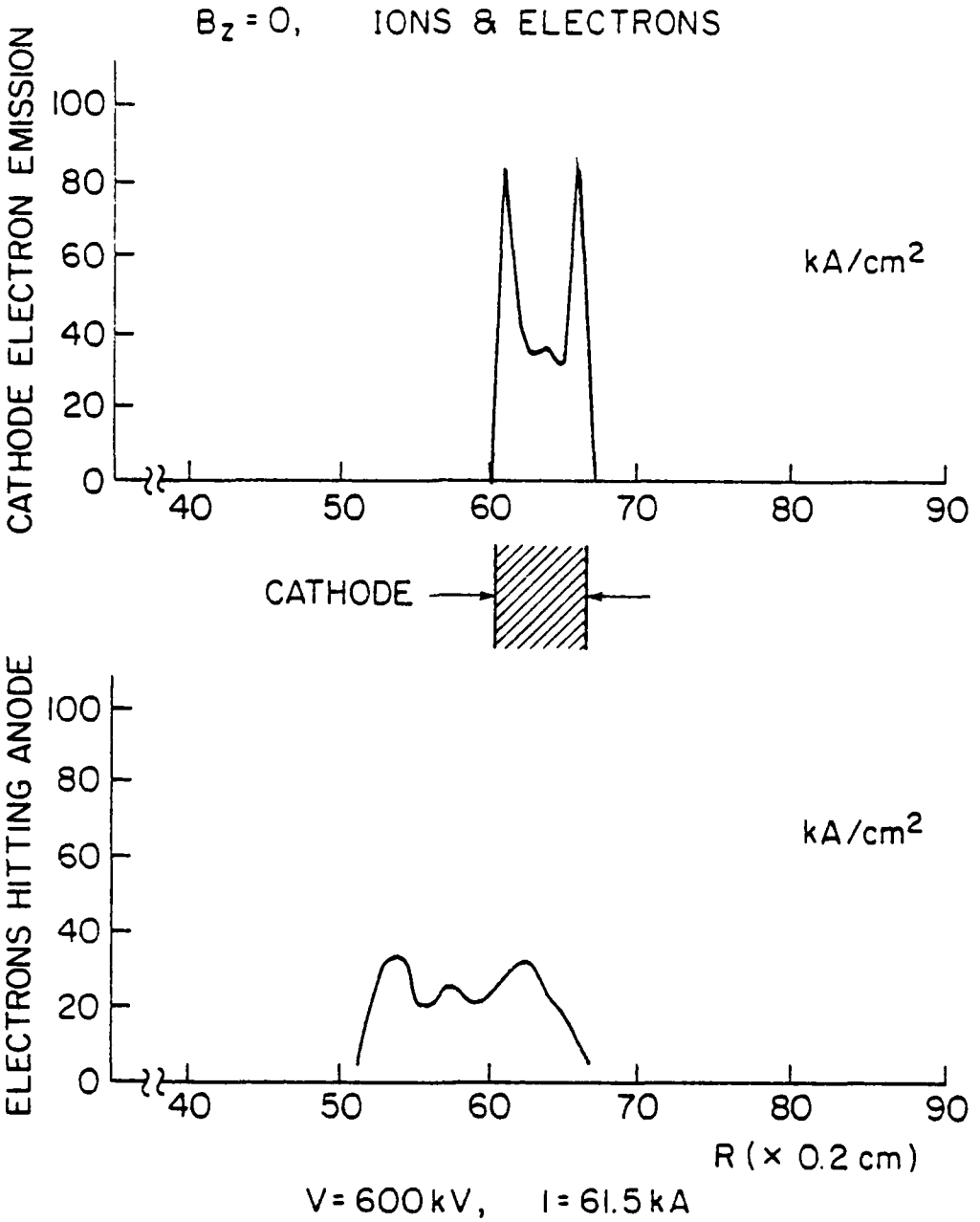

Fig. 5 - Steady-state current density for case 1 with electrons and ions

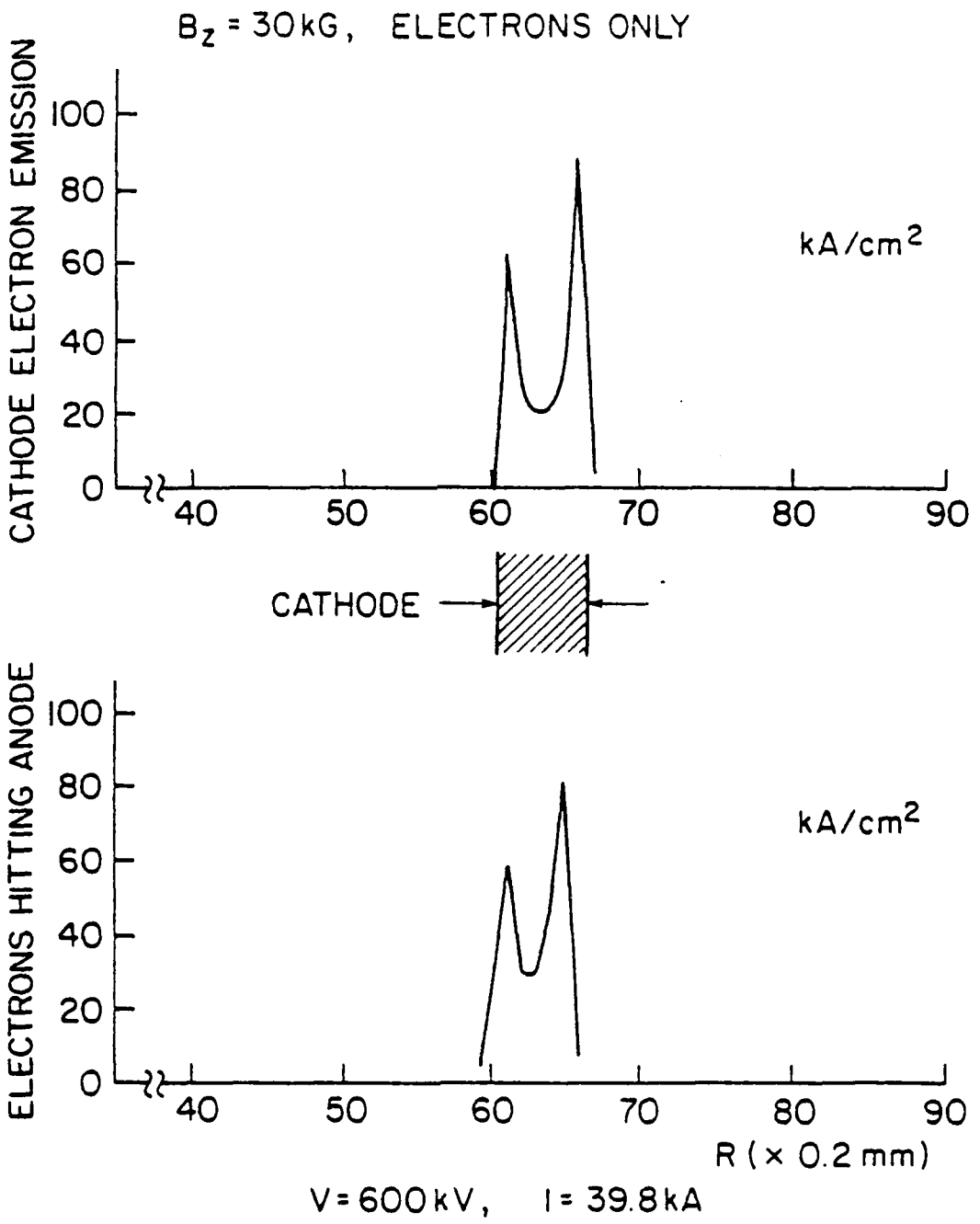

Fig. 6 - Steady-state current density for case 2 with only electrons

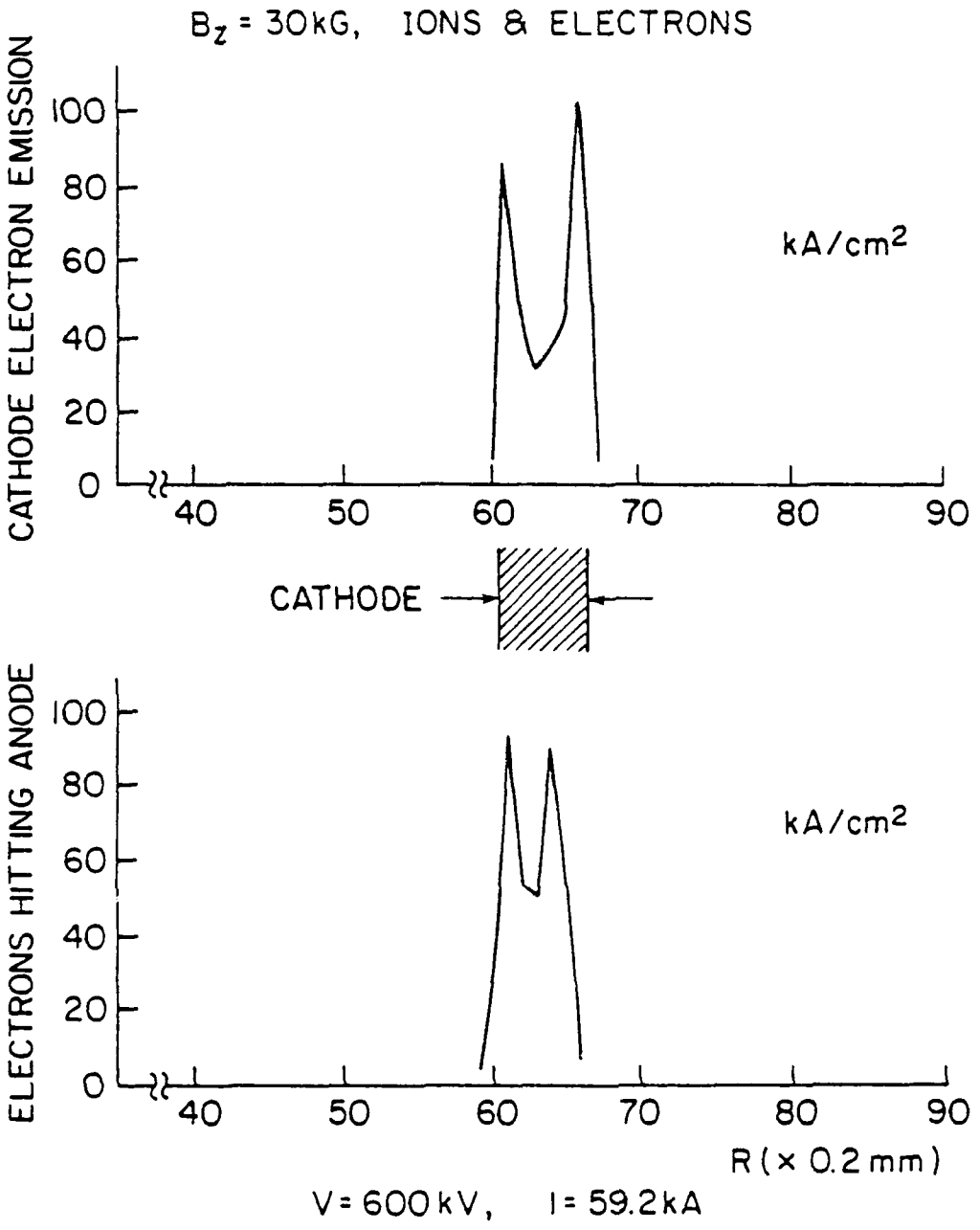

Fig. 7 - Steady-state current density for case 2 with electrons and ions

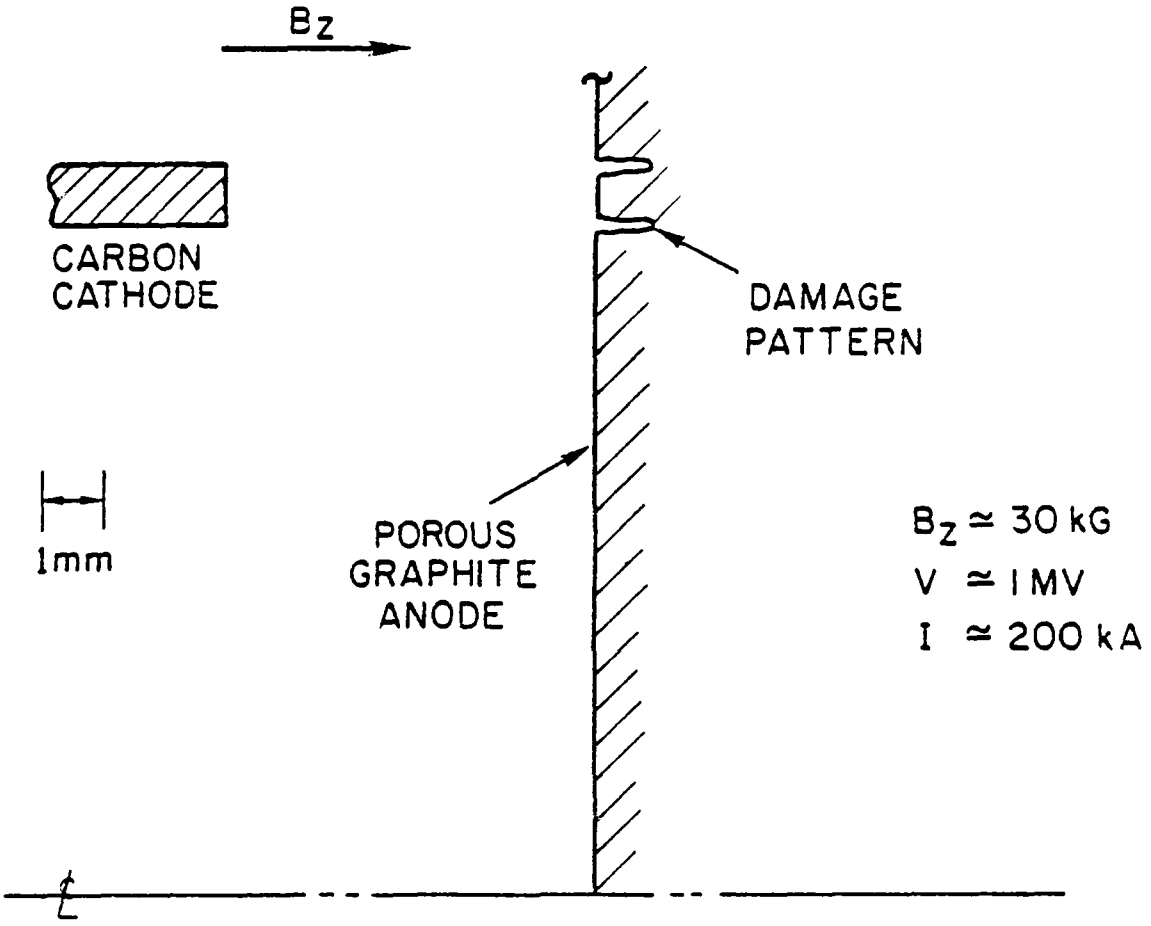

Fig. 8 - Witness plate damage

VECTOR-POTENTIAL FLOW IN RELATIVISTIC BEAM DIODES

I. INTRODUCTION AND THEORY

Pinched electron flows in diodes have been used as a means of concentrating relativistic electron beam kinetic energy onto small areas. Inertial confinement fusion with relativistic electron beams has been a prime motivation for experimental and theoretical efforts directed at maximizing the electron power concentration. During recent studies it was found that hollow cathodes generate a collapsing hollow ring[1] that pinches because of an ion induced pinch.[2,3] Prior to these discoveries, it was speculated that the electron flow pinches in vacuum[4,5] due to the self-magnetic field generated by the electron flow current when it exceeded a critical current for pinching.[6] It has been shown that the relativistic effects[7] of unneutralized electron flows under self-magnetic fields do not generate a tightly pinched electron flow, but rather a weakly pinched one. The reason for this is that

$$|\underline{E}|_{SELF} > |\underline{B}|_{SELF} \tag{1}$$

and electrons do not $\underline{E} \times \underline{B}$ drift under such conditions. The models[4,5] for vacuum pinching, however, can be made self-consistent by adding a mysterious current flowing on the diode axis. This current adds to the total magnetic field reversing inequality (1). The resulting electron flow is described by a force-free flow which has been coined[4,5] Para-Potential Flow (PPF). One may then summarize the ion induced pinch and the PPF described above for generating pinched electron flow as two ways of reversing inequality (1). The ion induced pinch introduces ions that reduce the electric field while the PPF scheme

Manuscript submitted May 21, 1980

introduces a bias current that increases the magnetic field. The latter shall be called a bias current pinch since the PPF is only one of a family of electron flows that $\underline{E} \times \underline{B}$ drift towards the diode axis.

There is a definite advantage of bias current pinches over ion induced pinches for low impedance ($\lesssim 1\ \Omega$) generators. The ion current that flows in low impedance pinched beam diodes restricts[2,8] the electron power to a finite level ($\sim 10^{12}$ W) and is thus an unacceptable power drain for electron beam fusion (but is an interesting source of power for ion beams[2,9]). Historically, there were many attempts to generate bias current pinches. These included the use of (1) tapered hollow cathodes[10], (2) a plasma column on the diode axis,[11] (3) an externally driven rod on the diode axis,[12] (4) two concentric cathodes[13] and recently (5) multiple cathodes.[14]

Here, we report on a new technique that is a combination of a bias current pinch and an ion induced pinch (Figure 1). This technique allows one either to minimize the ion current or to concentrate it near the axis. In addition, electron injection into the diode is radial rather than the axial emission of electrons from cathodes used to date. The radial injection was attemped as a smooth transition for electrons from the cathode to the equipotential surfaces (see the electron trajectories shown in Figue 1). Since electrons must cross equipotentials starting from the cathode (where the potential $\phi \equiv 0$) on their way to motion along the equipotential surfaces near the anode, they cannot be characterized by a PPF theory. A more general theory which is restricted only to cold electron flow[7] shows that the

mechanical momentum of the electron fluid is related to the magnetic field by

$$\vec{\nabla} \times \vec{P} = -\frac{e}{c} \vec{B} \tag{2}$$

Since $\vec{B} = \vec{\nabla} \times \vec{A}$, and A is free to be defined within the addition of any $\vec{\nabla}\chi$, one may realize

$$\vec{P} = -\frac{e}{c} \vec{A} \tag{3}$$

by choosing $\vec{\nabla}\chi = 0$. Thus the electron mechanical momentum vector lies along the vector potential. Hence the name Paravector-potential (PVP) diode.

The actual solutions of the electron flow for the geometry of Figure 1 near the inner edge of the outer cathode and the anode edge are ratner complicated. The exact solutions at smaller radii will depend on an analytic continuation of the flow pattern from the regions of the corners into the smooth region of the flat anode. A family of solutions which are exact solutions of the generalized equation[7] is given by a treatment similar to that of the reference.

The solutions are based on the existence of a region of zero electric field ((a) in Figure 1), an electron sheath of thickness d_1 (region (b)), and a vacuum region of thickness d_2 (region (c)). The magnetic field in region (a) is derived from the bias current of the center cathode, and ions flowing to it from the anode. Electrons from the outer cathode flow without being lost on the anode at radii

between the two cathodes. Using the forms of the electric and magnetic fields of the electron flow as derived by Goldstein, et al.,[7] the thickness of the electron flow d_1, and the thickness of the flow-anode vacuum gap. d_2, are found as functions of radius.

$$d_1 = r\left(\frac{I_o}{I_c}\right) F\left(\frac{I_t}{I_c}\right) \tag{4}$$

$$d_2 = r\left(\frac{I_o}{I_c}\right)\left(\gamma_o - \frac{I_t}{I_c}\right) G\left(\frac{I_t}{I_c}\right) \tag{5}$$

Here r is the radius, $I_o = \frac{m_e c^3}{e} = 17$ kA, I_c is the center current, $\gamma_o = 1 + \left|\frac{eV_o}{M_e c^2}\right|$, V_o the diode voltage, and the functions F and G are given by

$$F(x) = \tfrac{1}{2} \ln(x + (x^2 - 1)^{\frac{1}{2}}) \tag{6}$$

$$G(x) = \tfrac{1}{2}\left\{\frac{x + (x^2-1)^{\frac{1}{2}}}{x^2 + x(x^2-1)^{\frac{1}{2}} - 1}\right\} \tag{7}$$

Over the range $2 \leq x \leq 3$, $F(x)$ and $G(x)$ are approximately 0.8 and 0.25, respectively.

It is important to note that for a given diode voltage, the gaps are totally defined by the ratio $\frac{I_t}{I_c}$. The physical anode-cathode spacing in region (a) does not enter into the result.

Since d_2 must be positive (or else the electrons will strike the anode), I_c must be greater than $\frac{1}{\gamma_o} I_t$. As d_2 is the distance between the flow and the anode, it provides a measure of the axial anode perturbations that the diode can tolerate. For example, for diode

parameters of 1 MV, 1 MA, and $\frac{I_t}{I_c} = 2.4$, the spacing $d_2 = (0.006)r$ while d_1 is a factor of 5 greater. Thus, at a radius of 4 cm, one can tolerate anode imperfections on the order of 0.02 cm.

If only electron flow existed, then the space charge effect of the flow from the outer cathode as it came opposite the inner cathode would have decreased the electron flow from the inner cathode, thus decreasing the bias current, resulting in the loss of the electrons on to the anode opposite the inner cathode. Taking into account that an anode plasma is being produced opposite the inner cathode by the electron beam heating of the anode surface, it is seen that ion flow may provide space-charge neutralization negating the effect of the radial electron flow and replacing the partially-suppressed electron current. The sum of the electron and ion currents in the center cathode represents the needed bias current. The presence of the ion flow allows an ion induced pinch to continue the pinching of the electron flow to radii smaller than the inner cathode. Numerical simulation[15,16] has shown that, in this region, the drifts of electrons (such as the $\vec{\nabla B}$ drift) are a prime cause for finite pinch radius. The use of smaller hole cathodes is known[17] to generate smaller pinches and was also tried in the experiments reported here.

In the numerical simulation studies an extension of the r, z, semi-static, particle-in-cell code was used to find the self-consistent, numerical solutions of electron and ion flows. In Figure 2, the diode geometry and vacuum equipotentials are shown for diode parameters close to those used in the experiments. When self-consistent

particle flows are generated in this diode, the equipotential field lines (Figure 3) are drastically altered and shifted toward the anode in close agreement with analytic theory. The only constraint imposed was that ions on the anode were generated only at radii smaller than that of the inner cathode.

The basic concept of the PVP diode led to the design of a series of diodes used in conjunction with the GAMBLE I and GAMBLE II generators operated in positive polarity. The diode performance was studied over wide variations of voltage and total-to-center current ratio, I_t/I_c. In agreement with thoery, it was found that given a total to inner current ratio less than γ_o, then the radially injected electrons will flow inward without striking the anode at large radii providing there are no gaps or projections to perturb the equipotential surfaces. If the needed bias current is not provided, then a self-correcting phenomenon was observed in which excess radially injected electrons are lost immediately to the anode edge. The rest then flow in without striking the anode at large radii resulting in a current of $\gamma_o I_c$ near the anode axis. The other predicted phenomenon observed was the interaction of the radial electron flow with the bias flow. Instead of continually rising during the voltage pulse, the bias current clamped at the value it had at the time the radial flow started.

II. EXPERIMENTAL APPARATUS

The PVP diode design has worked over the course of more than 80 shots. A scale drawing of the latest geometry is shown in Figure 4.

The cathodes (shown solid) were made from brass and mounted on a 36 cm diameter, 2.5 cm thick aluminum insert (shown cross-hatched) that fit the door of both of the GAMBLE relativistic beam generators, which were operated in positive polarity. The door insert had a 4.4 cm diameter hole on axis (originally 2.5 cm) and 1.0 cm slit 22.9 cm long cut through it (originally 19.7 cm) for viewing a diameter of the anode. The taper of the inner cathode was varied from 6° to 30° with a variety of inner and outer diameters. The most recent inner cathode was the 8.2/1.3 cm (O.D./I.C.), 12° tapered hollow cathode shown in Figure 4. The outer cathode was a 22.9 cm I.D., 25.4 O.D. brass ring. Shots using annular brass inserts to close the radial gap or tailor the emmission surface have been taken. The anodes were originally flat aluminum disks (Figure 5a) 20 cm in diameter which were held onto the center conductor of GAMBLE I or GAMBLE II by 6 insulating bolts at a large radius. On later shots, the anode diameter was increased to close the radial gap. Spacers allowed the anodes to be positioned so as to be in the plane of the outer cathode. Later, in an attempt to reduce the edge damage, the outer edge was beveled at 45° (Figure 5b) to give the non-radially emitted electrons more distance in which to turn. Only in the last series of shots was the outer edge geometry changed to that shown in Figures 4 and 5c - the anode edge being relatively sharp and the anode beveled at negative 45°. In this configuration, the axial electric field was reduced with the result that most of the current flowed radially. The anode was a 20.3 cm diameter, stainless steel outer structure (shown with fine hatching)

which held an aluminum insert (shown with large hatching). The space behind the insert was present to prevent shock damage to the stainless holder and the hub of the generator. The stainless holder was mounted with a single ¼" - 20 screw into the generator. The entire anode surface was covered with either 2 μm aluminized KIMFOL polycarbonate foil or 6 μm aluminized mylar, aluminum side towards the cathode. The covering provided the anode with a smooth, continuous potential surface.

The main diagnostics were a diode voltage monitor, $\dot{B}$ loops monitoring the current flowing from the center cathode and also from the total cathode assembly, anode witness plate damage, and x-ray production monitored by a time-integrated x-ray pinhole camera and calibrated p-i-n diodes.

III. OBSERVATIONS

Series I - GAMBLE I shots #5828-5836

This series of shots used 20.0 cm diameter flat aluminum anodes mounted with six bolts at a diameter of 18.4 cm. The bolts were counterbored so as not to protrude out of the plane of the anode. An insert into the outer cathode made the radial gap 5 mm (See Figure 5e). The anode was varied from being inserted 0.5 mm into the plane of the outer cathode to being withdrawn 0.5 mm from it. The inner cathode was an 8.4/3.9 cm (O.D./I.D.), 6° tapered hollow cathode and the anode-cathode gap was 5.2 mm at the inner diameter.

The voltage on these shots was low($\lesssim$400 kV) and the bias current criterion was not met. Only 100 kA out of the 235 kA total current flowed in the center cathode which, according to the theory of PVP flow,

could bring in 80 kA from the outer cathode leaving 55 kA to strike the anode rim. Anode rims showed existence of radial flow through their extensive damage. The inner edges of the screw holes showed evidence that the beam had struck them on its way in lending support for the existence of radial flow.

The other conclusion from this series of experiments is that the vary large area anode (314 cm^2) could not turn on an anode plasma during the 50 ns pulse time so that an ion induced pinch could not take place. This is in agreement with the areal velocity[3] on aluminum ($\sim$ 2 cm^2/ns·100 kA) which brought the collapsing hollow ring from a radius of 10 cm to a radius of 9 cm.

Series II - GAMBLE I Shots #5837 and 5845

For these shots, the same aluminum anodes were used as well as the same inner cathode. However, the outer cathode had finger stock mounted on its inner edge instead of an insert (Figure 5f). The inner cathode provided the required bias current and was nearly equal to $\frac{1}{\gamma_o} I_t$ for almost the total pulse time. The anodes showed little edge damage and had a rear-surface spall of 1.1 cm diameter on axis. The x-ray pinhole photograph for shot #5845 shows a 7 mm (FWHM) pinch. Figure 6 shows the front (top) and back of the anode for shot #5845. Note the slight damage at the inner edge of the screw holes. Figures 7 and 8 show the diode parameters for the same shot. It is significant to note that the outer cathode did not turn on for 10-20 ns after the start of the current pulse. When the outer cathode did turn on, the inner cathode current was clamped at its then current value and

remained nearly equal to $\frac{1}{\gamma} I_t$ for the rest of the pulse. The value at which the inner current clamped was a factor of two below its operating value when used without the outer cathode. This agrees with our theoretical expectations of the effect of the radial electron flow on the behavior of the inner cathode.

Series III - GAMBLE I Shots #5847-5851

These shots were identical to the shots in Series II with the addition of a TRW streak camera looking at the ions emitted from the anode. The ions struck the silvered side of an optically-thin slab of Pilot-B scintillator covering a diameter. The scintillator was viewed with the streak camera. The streak camera photographs showed that there were no ions emitted at large radii (compared to the outer radius of the inner cathode) although there were some ions coming from just outside the inner cathode.

Series IV GAMBLE I Shots #5861-5868

These shots had a 45° beveled outer cathode insert (Figure 5g) and a 20.3 cm or 20.6 cm diameter, 45° beveled anode (Figure 5c). The reduced radial gap meant that the voltage was again low and the required bias current not supplied. This geometry did not prove successful.

Series V - GAMBLE II Shots #1731-1735

For the first series of shots on the higher power GAMBLE II generator, 20.6 cm diameter, 45° beveled anodes (Figure 5c) and an outer cathode with finger stock mounted on its inner edge (Figure 5f) were used. On none of these shots was the $\frac{1}{\gamma_o} I_t$ bias current supplied

Nevertheless, shot #1735 appeared to be a relative success.

Figures 9 and 10 show the diode parameters for shot #1735. The diode operated at 750 kV, 900 kA with a flat, 0.8 Ω impedance during the plateau of the voltage pulse. Two things should be noticed: The bias current required (350 kA) to vacuum pinch all of the outer current was never supplied, and there was no delay time between the start of the inner and outer currents. Even so, 400 kA out of an outer current of 650 kA should have vacuum pinched.

Figure 11 shows the front (top) and back of the anode plate for shot #1735. Although there was a great deal of damage to the anode edge due to the 250 kA of excess current, most of the anode outside of the inner cathode radius is relatively undamaged. Most of the apparent damage seen in Figure 11 is aluminum melted by the pinch and deposited on the anode surface. The x-ray pinhole photograph confirms this as it shows relatively little x-rays coming from the region between the anode edge and the inner cathode compared to x-rays from the anode edge. This provides additional support for our theoretical expectation that $\gamma_o I_c$ will pinch with the excess outer current sloughing off to the anode edge.

Series VI - GAMBLE II Shots #1745-1748

These shots were identical to the last series except that the outer cathode had no finger stock insert (Figure 5d) in order to open the radial gap, and the inner cathode was a 2.5 cm I.D., 2.9 cm O.D., 30^o tapered, hollow cathode. The sharp-edged center cathode tended to either not supply very much current, or to short out. However, for

shot #1748, the biasing criteria was satisfied through the peak of the voltage pulse (1 MV) but was not satisfied during the voltage fall. Again, the x-ray photograph shows little radiation between the anode edge and the inner cathode.

Series VII - GAMBLE I shots #6431-6447

This last series of shots used the geometry shown in Figure 4, the design of which was based on considerations described earlier. The electrical characteristics and x-ray photographs showed that this new geometry almost always met the biasing criterion and that there were few or no x-rays from the anode edge. Also, this diode operated with a shot-to-shot reproducibility of 10% in current and voltage. Figures 12 and 13 are the averaged diode behavior for the five shots 6442-6446. As was typical of the earlier successful GAMBLE I shots, there is a 10-20 ns time delay between the start of the total current and the start of the outer current.

In order to study the ion current, the anode was modified by drilling a 1.3 cm diameter hole on axis and mounting a 2 cm diameter disk of 120 μm polyethylene over the hole. The anode was recessed slightly over the central 2 cm so that the polyethylene disk would not protrude. The mylar anode covering was cut away to expose this disk. The result of activation measurements on this system indicates that ion current densities of approximately 4 kA/cm^2 flow in the 2.5 cm diameter hole of the center cathode. These preliminary results will be further investigated.

IV. CONCLUSIONS

A comparison of analytic theory, numerical simulation results, and experiments indicates that bias current pinching via paravector-potential flow may indeed be realized. Detailed geometries of diodes specifically designed to allow a smooth transition from a PVP flow at large radii to an ion induced pinch flow at small radii were studied. With careful optimization, it may be possible to create very efficient electron pinches from large aspect ratio diodes.

It has been shown that the PVP diode concept allows the multiplication of the total current of a single, tapered, hollow cathode by a factor of γ_o without changing the geometry of the hollow cathode. In addition a fraction $(1- {}^{1}/\gamma_o)$ of this current may be electron current independent of the diode aspect ratio or impedance. This contrasts with single, hollow cathodes which rely on ion induced pinching and contain a smaller fraction of their total current in electron current. The same diode may, however, operate with a bias current exceeding $\frac{1}{\gamma_o} I_t$ by allowing efficient ion production inside the center cathode. Preliminary results are encouraging and will be investigated further.

V. ACKNOWLEDGMENTS

The authors wish to thank Dr. A. E. Blaugrund for the ion streak measurement and E. Bellafiore, A. Robinson, and J. W. Snider for their expert assistance.

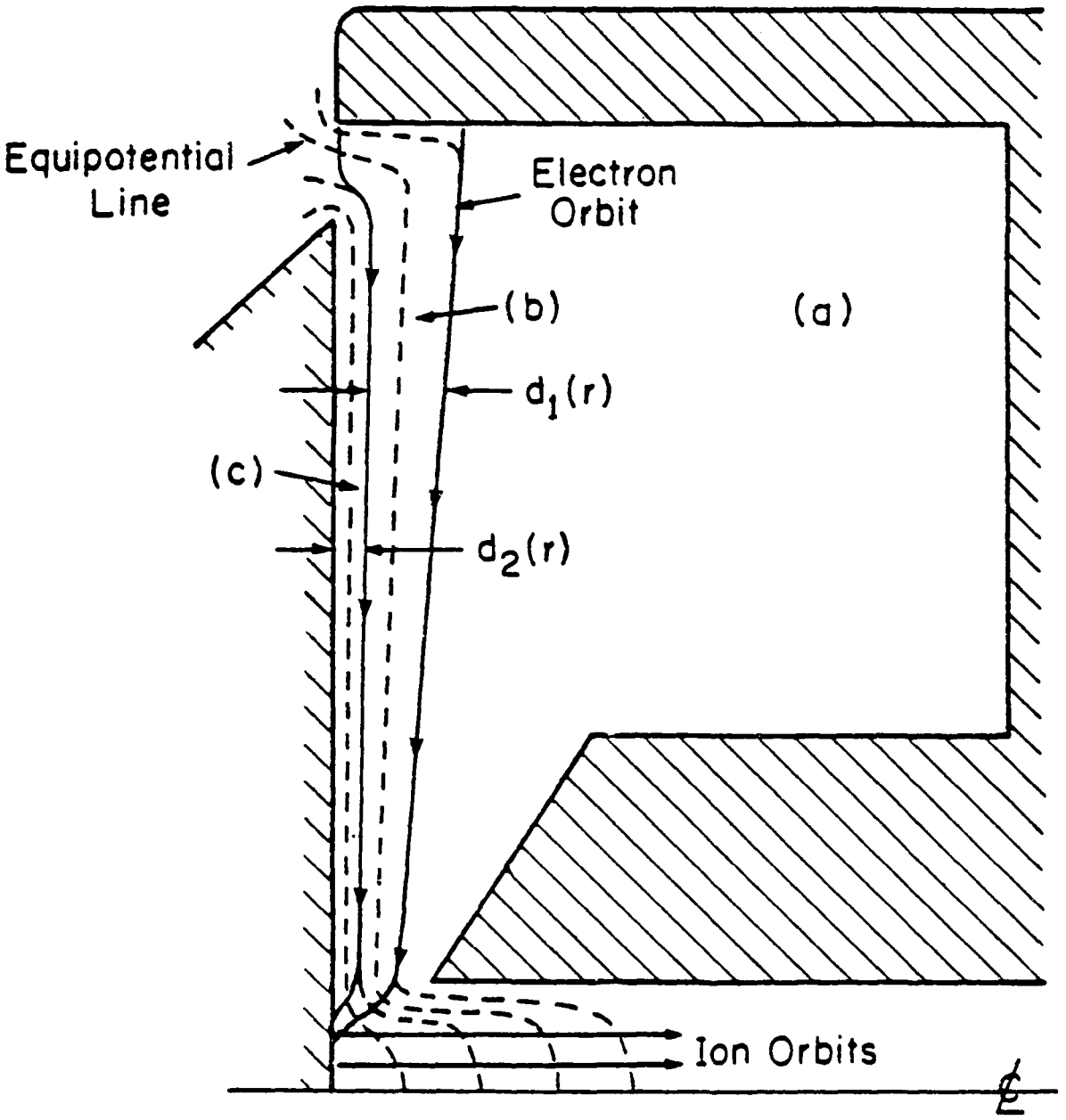

Fig. 1 — A conceptual drawing of the PVP diode.

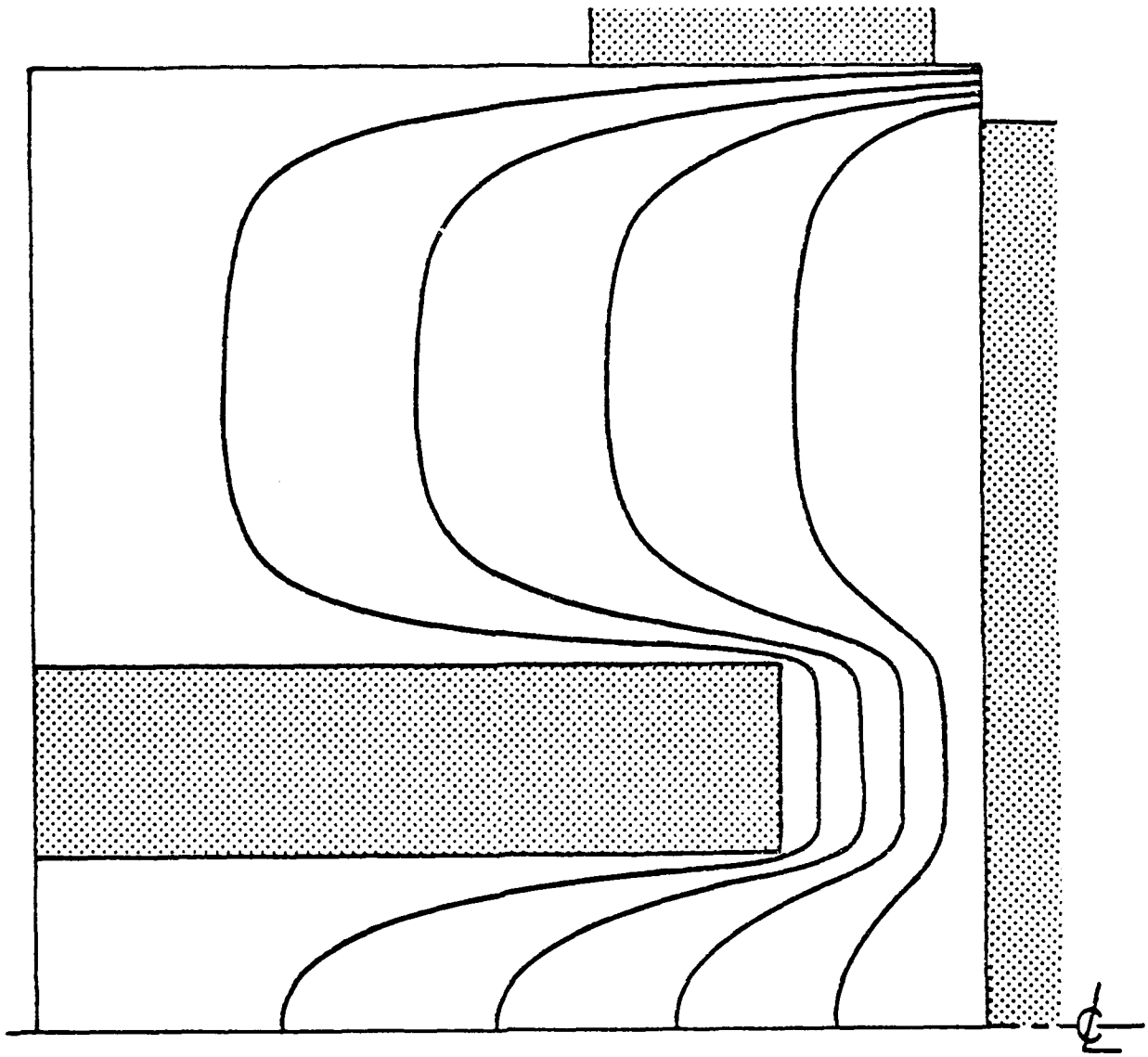

Fig. 2 — Numerical simulation of equipotential field lines prior to electrical emission.

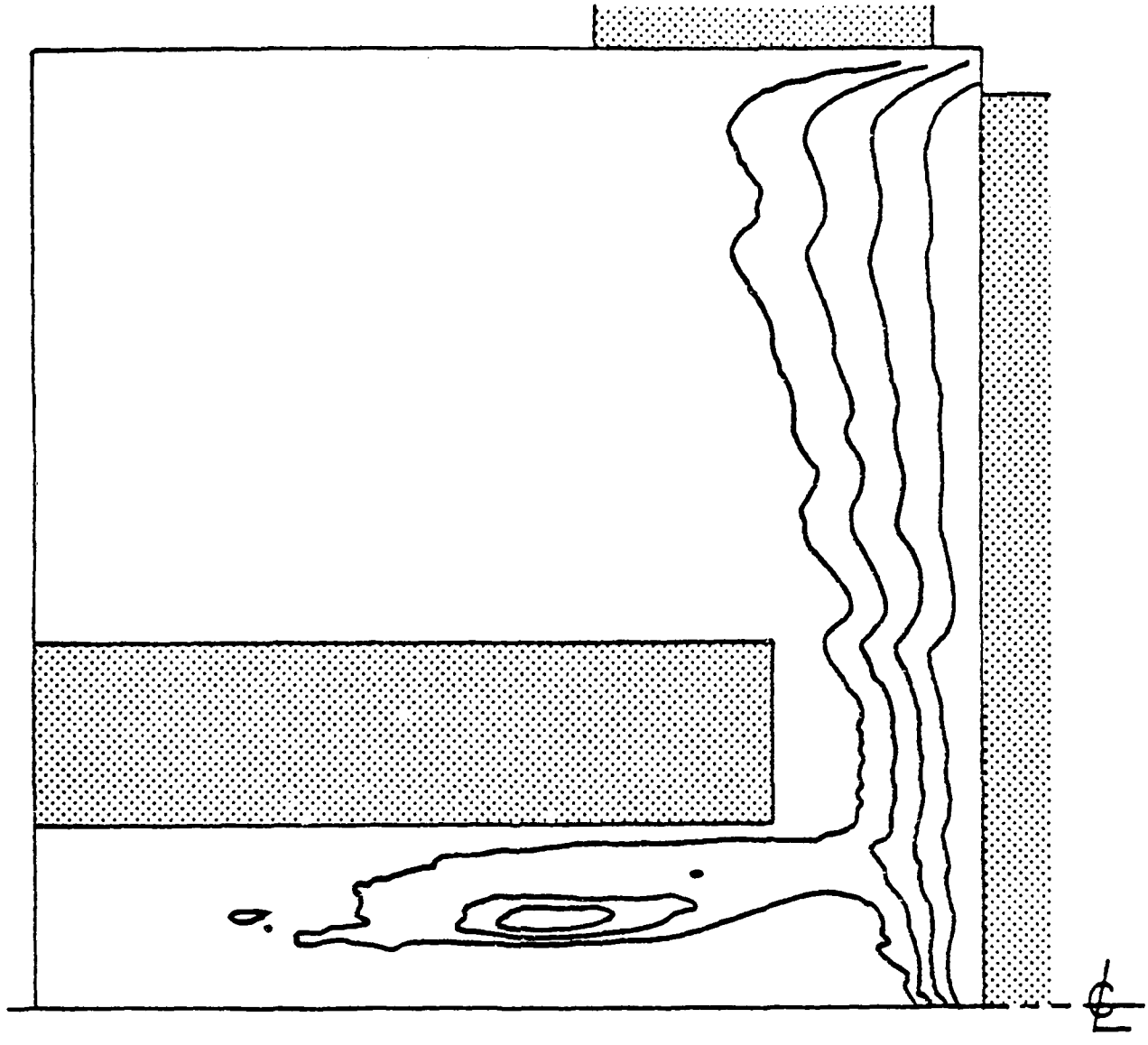

Fig. 3 — Numerical simulation of equipotential field lines after 2.5 ns of electron emission.

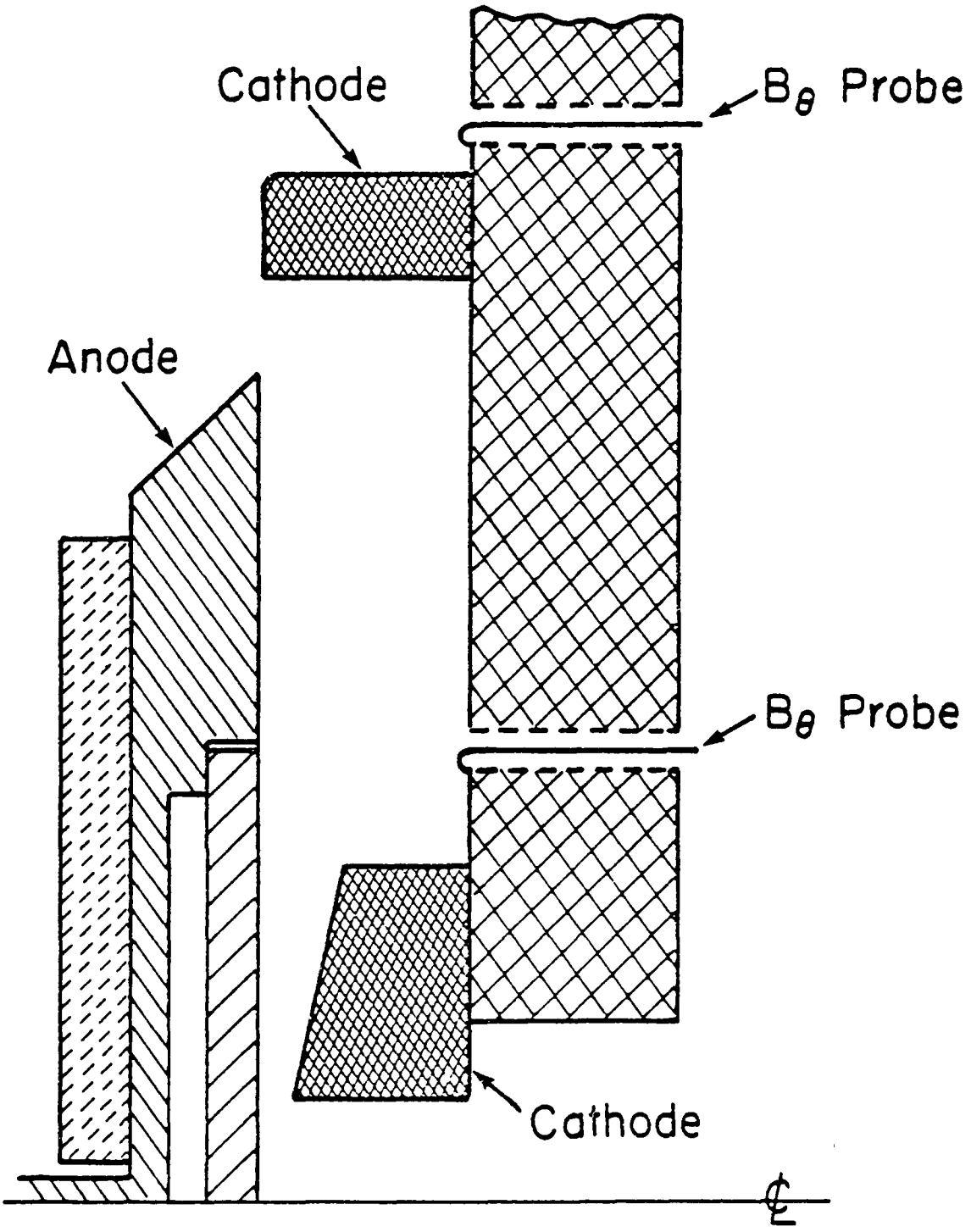

Fig. 4 — Scale drawing of latest PVP diode.

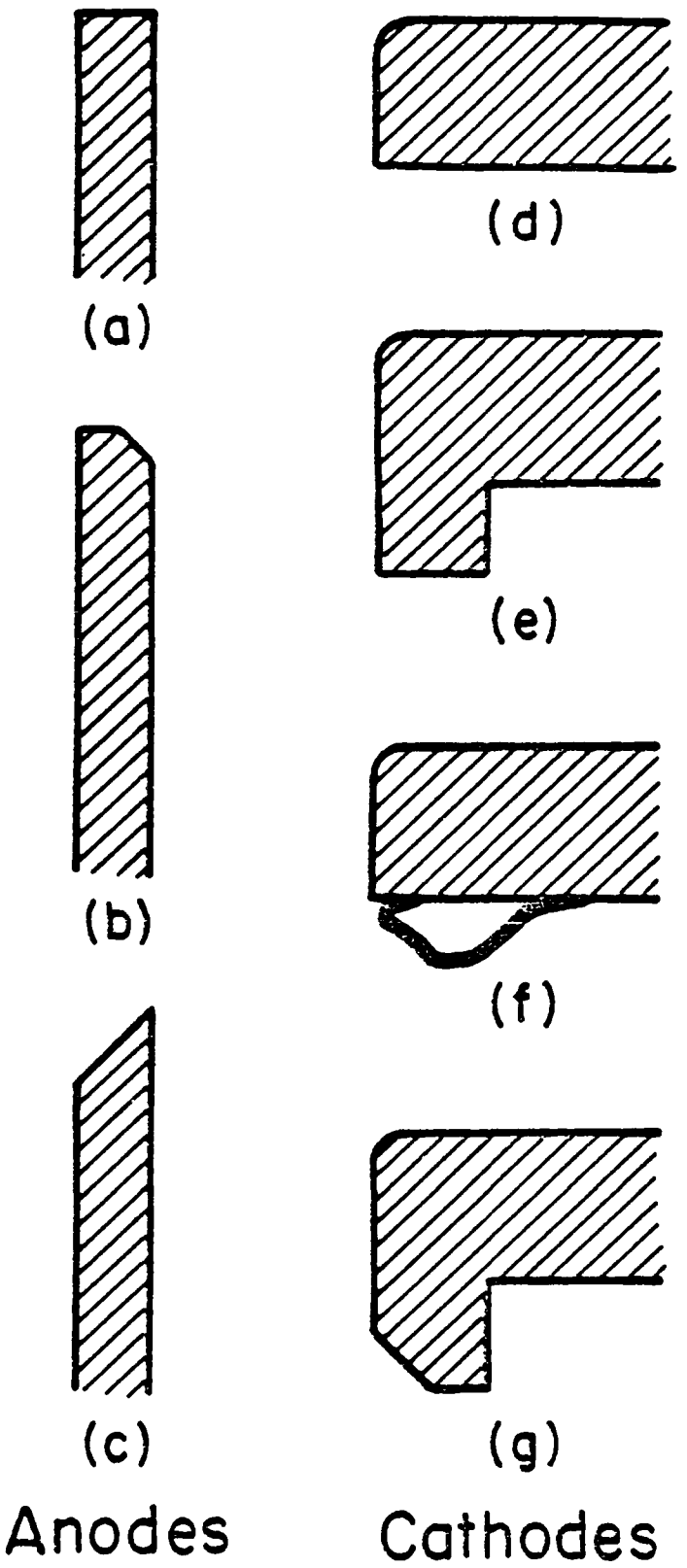

Fig. 5 — Anode and outer cathode geometries used in these experiments.

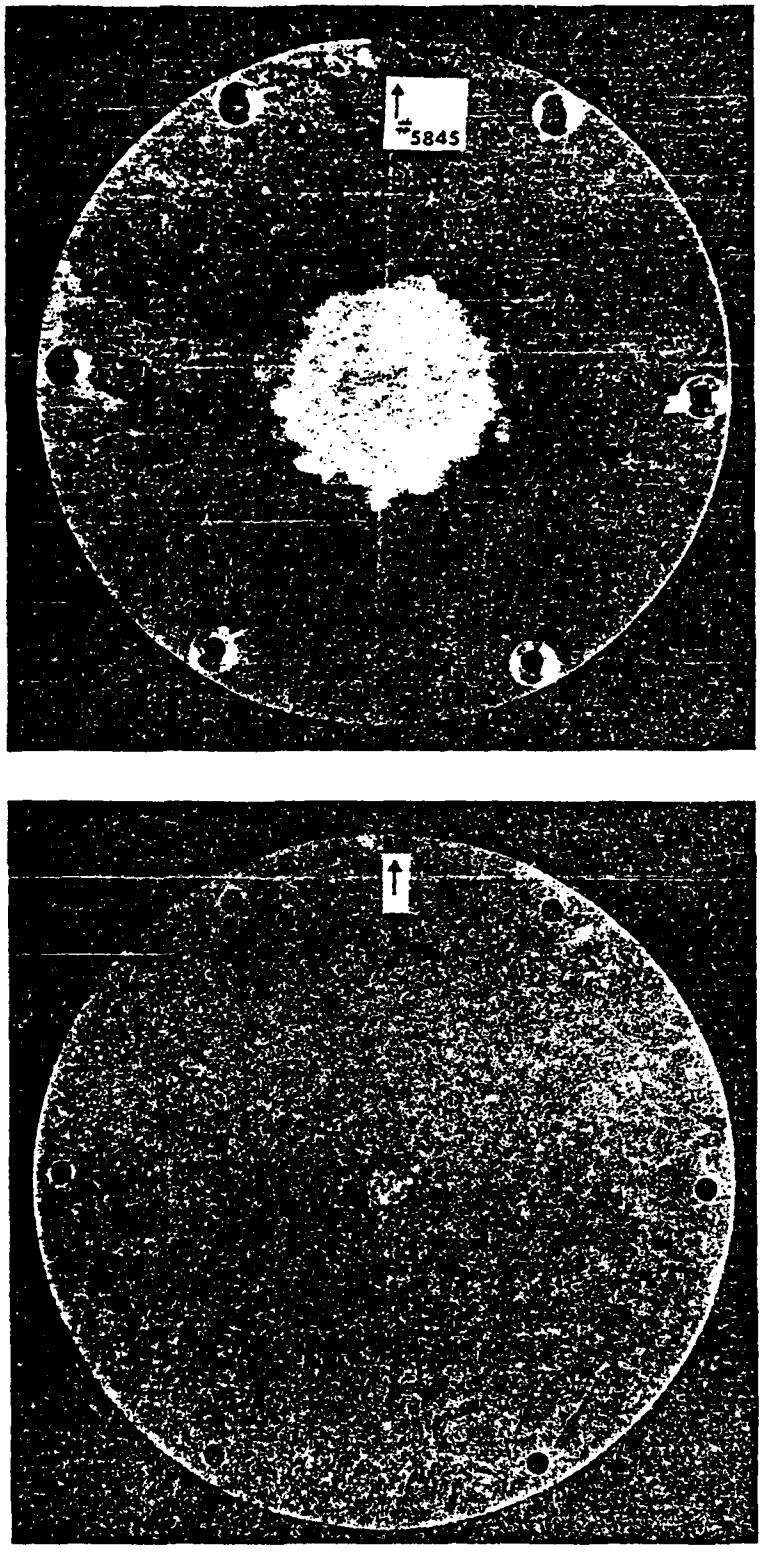

Fig. 6 — Aluminum anode for shot #5845.

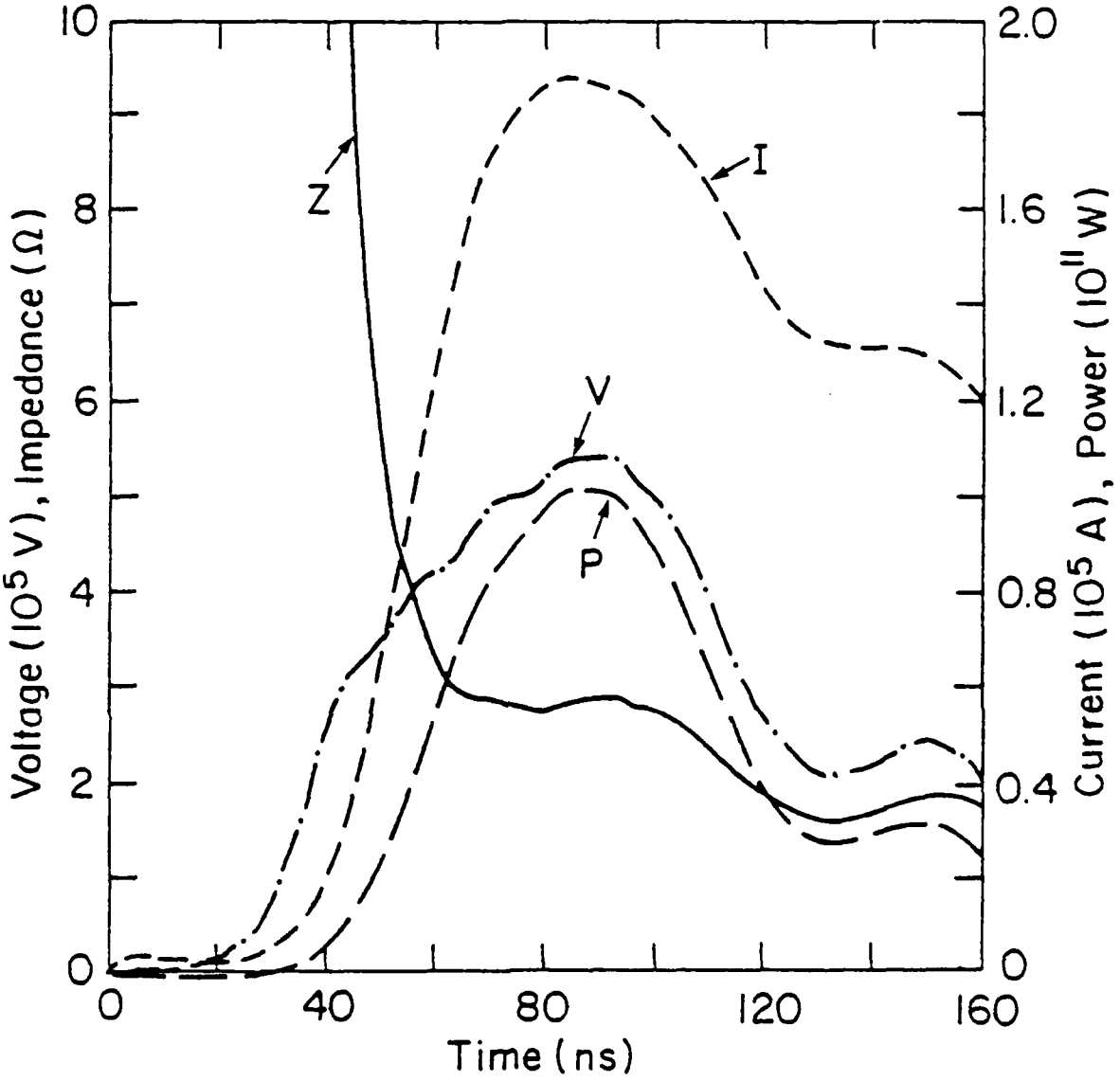

Fig. 7 — Overall diode parameters for shot =5845.

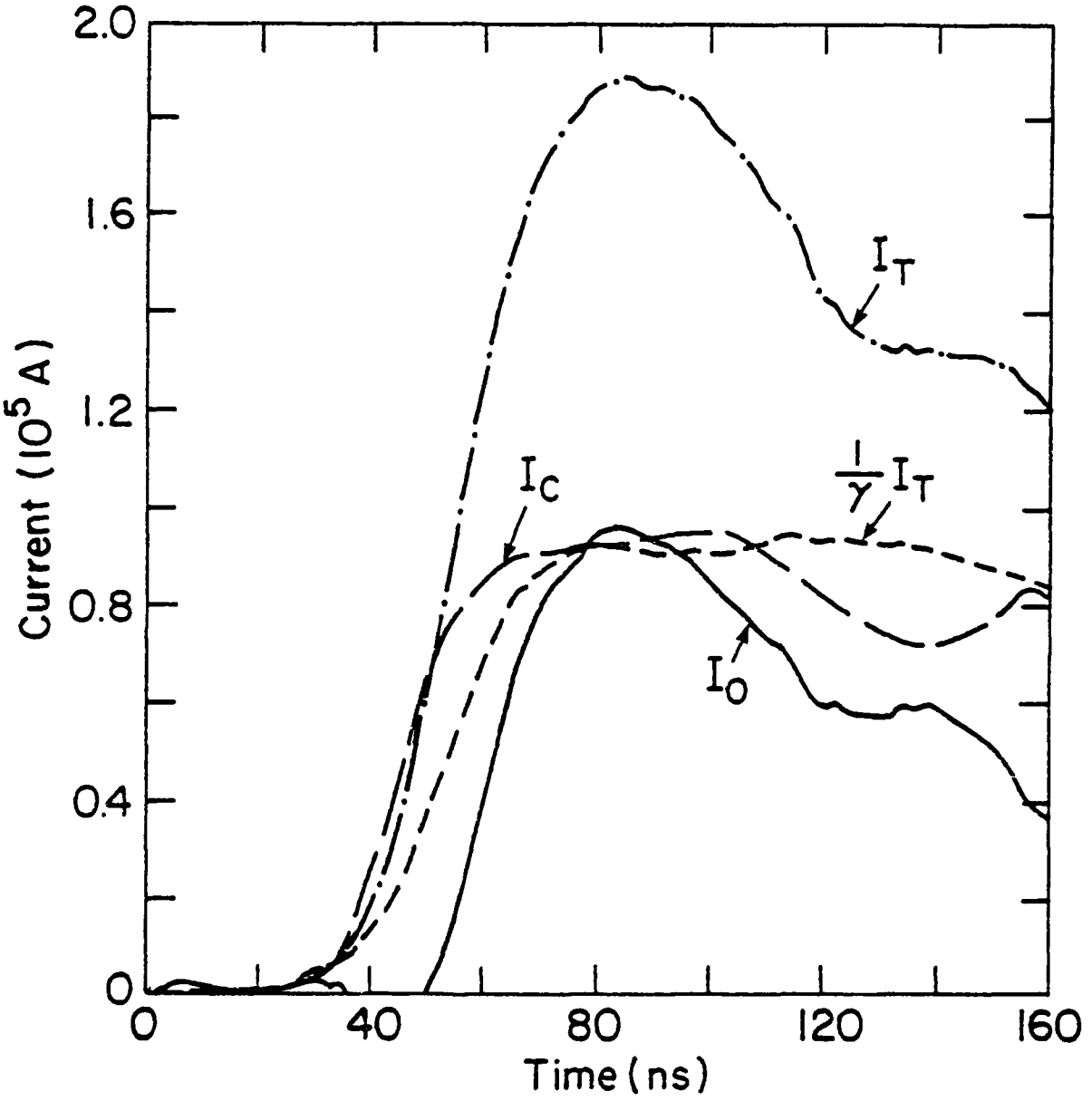

Fig. 8 — Inner, outer, total and theoretical bias current for shot #5845.

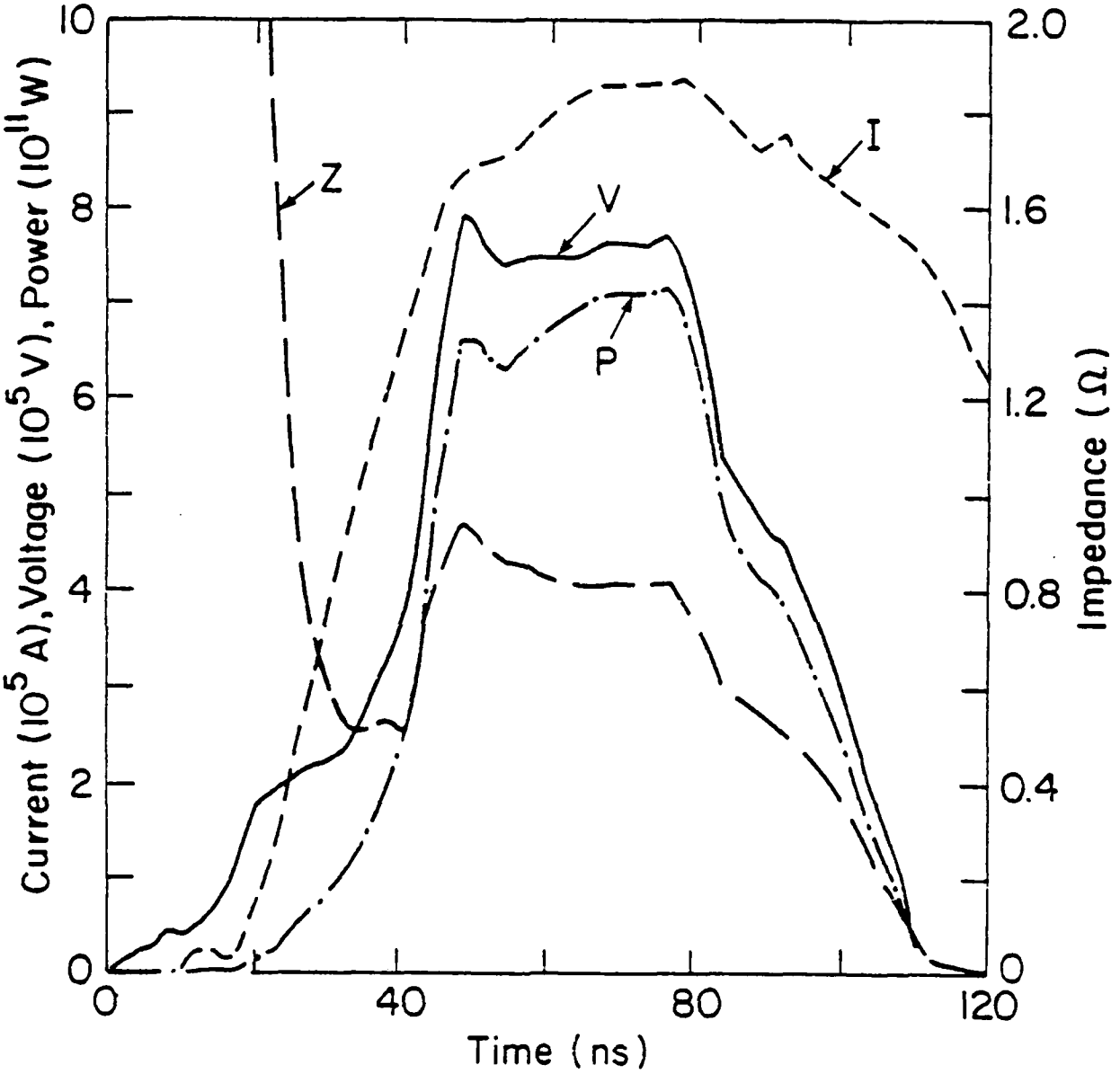

Fig. 9 — Overall diode parameters for shot #1735.

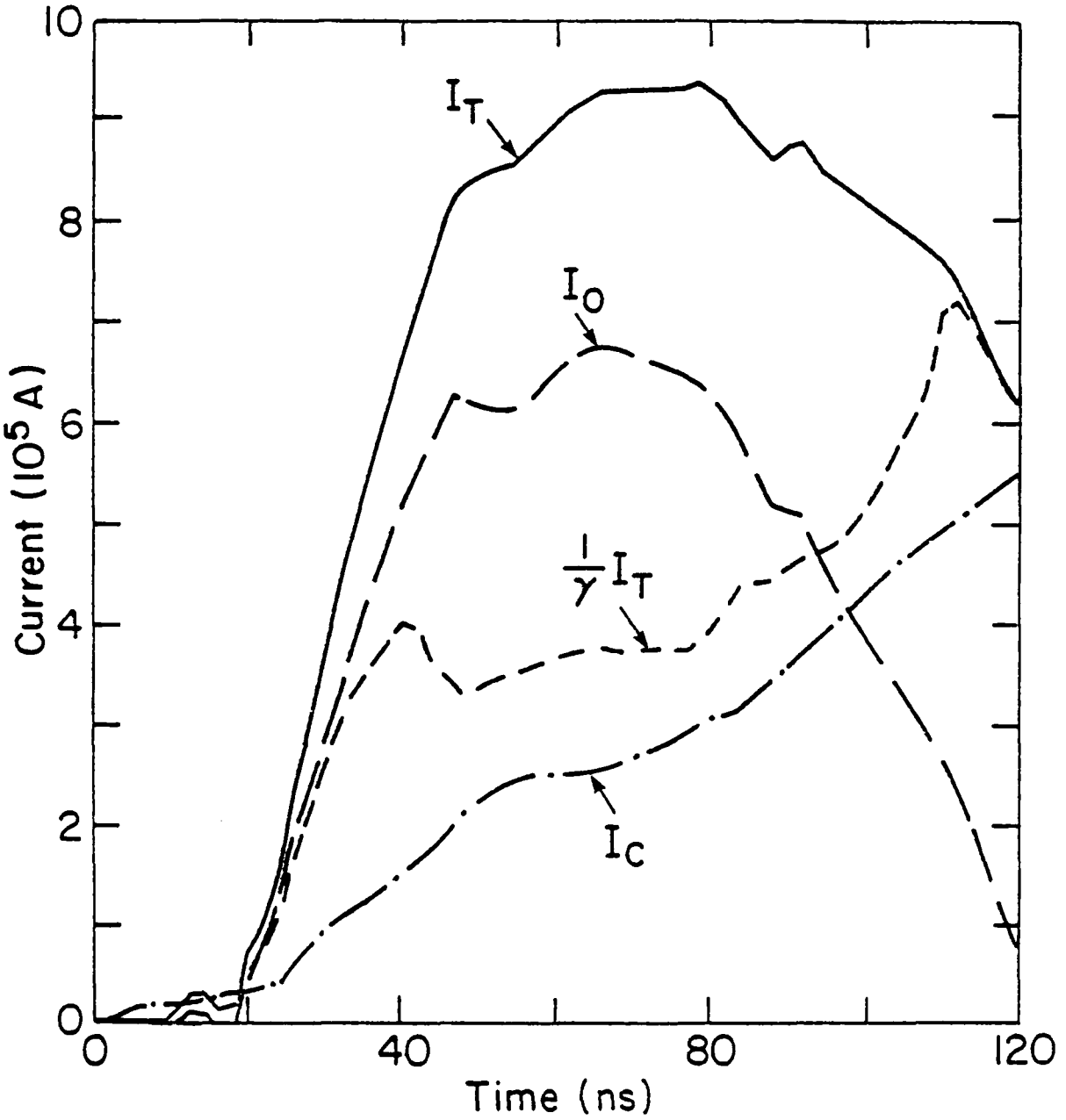

Fig. 10 — Inner, outer, total, and theoretical bias current for shot =1735.

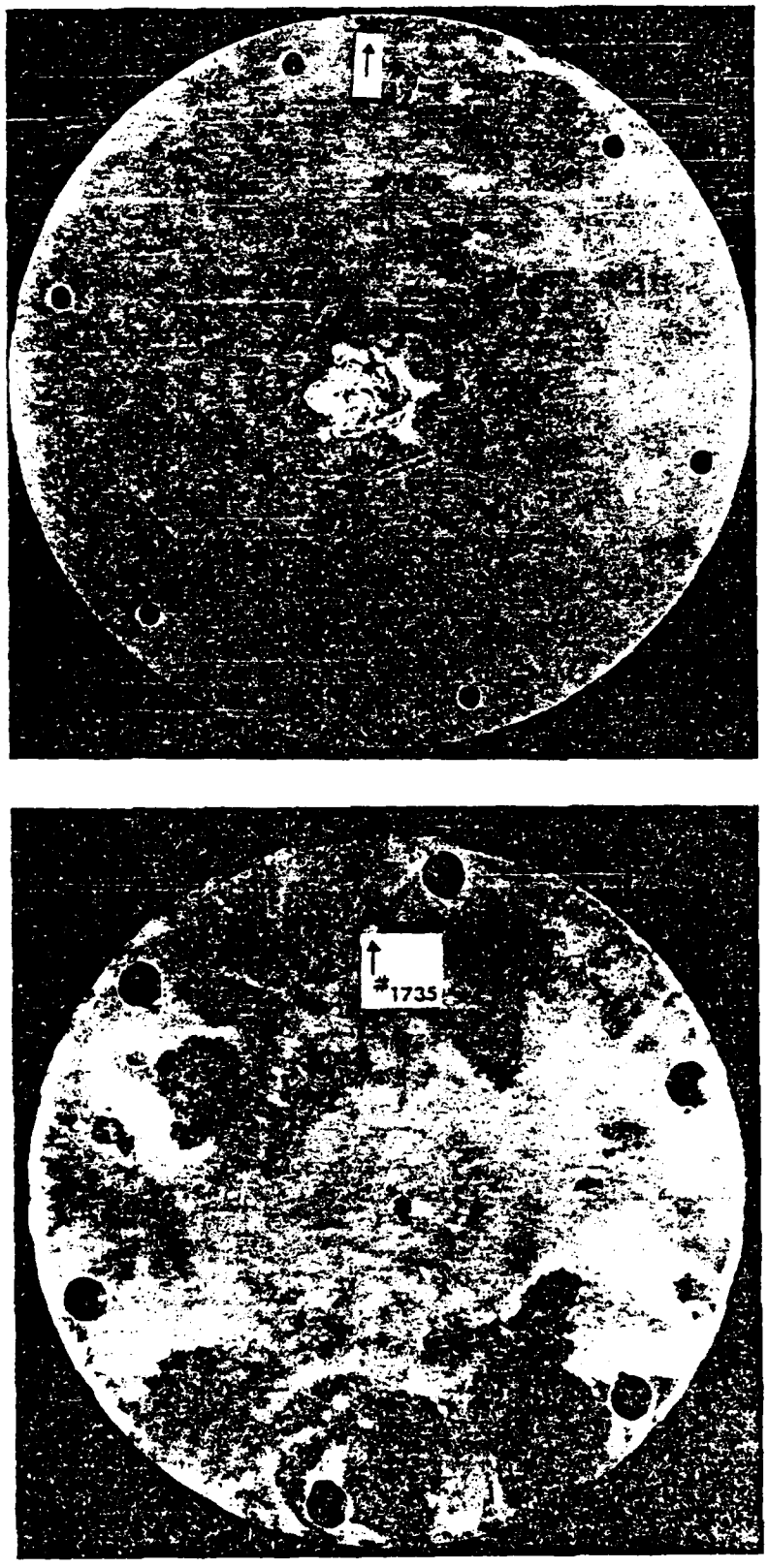

Fig. 11 — Aluminum anode for shot #1735.

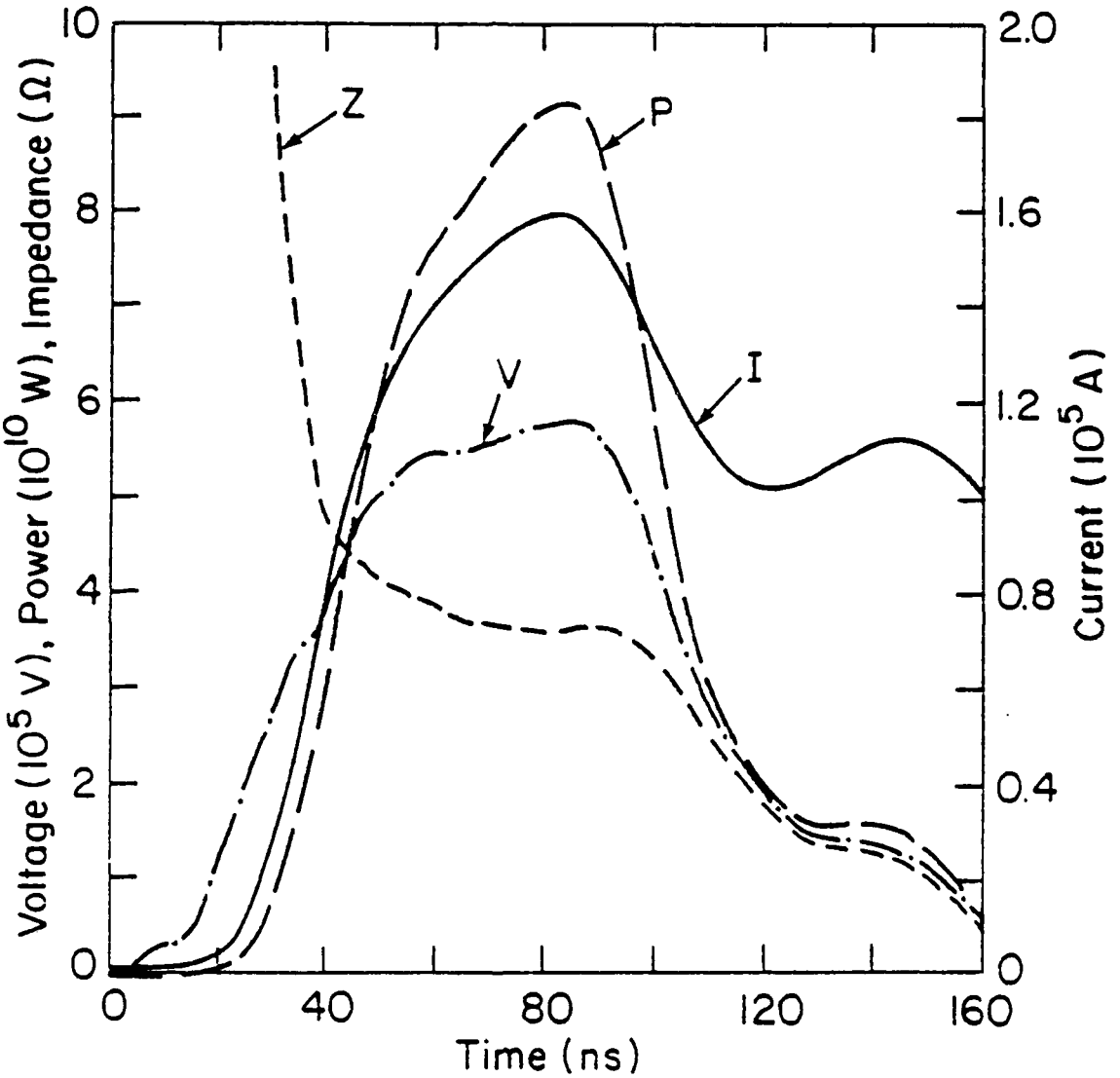

Fig. 12 — Average overall diode parameter for shots #6442-6446.

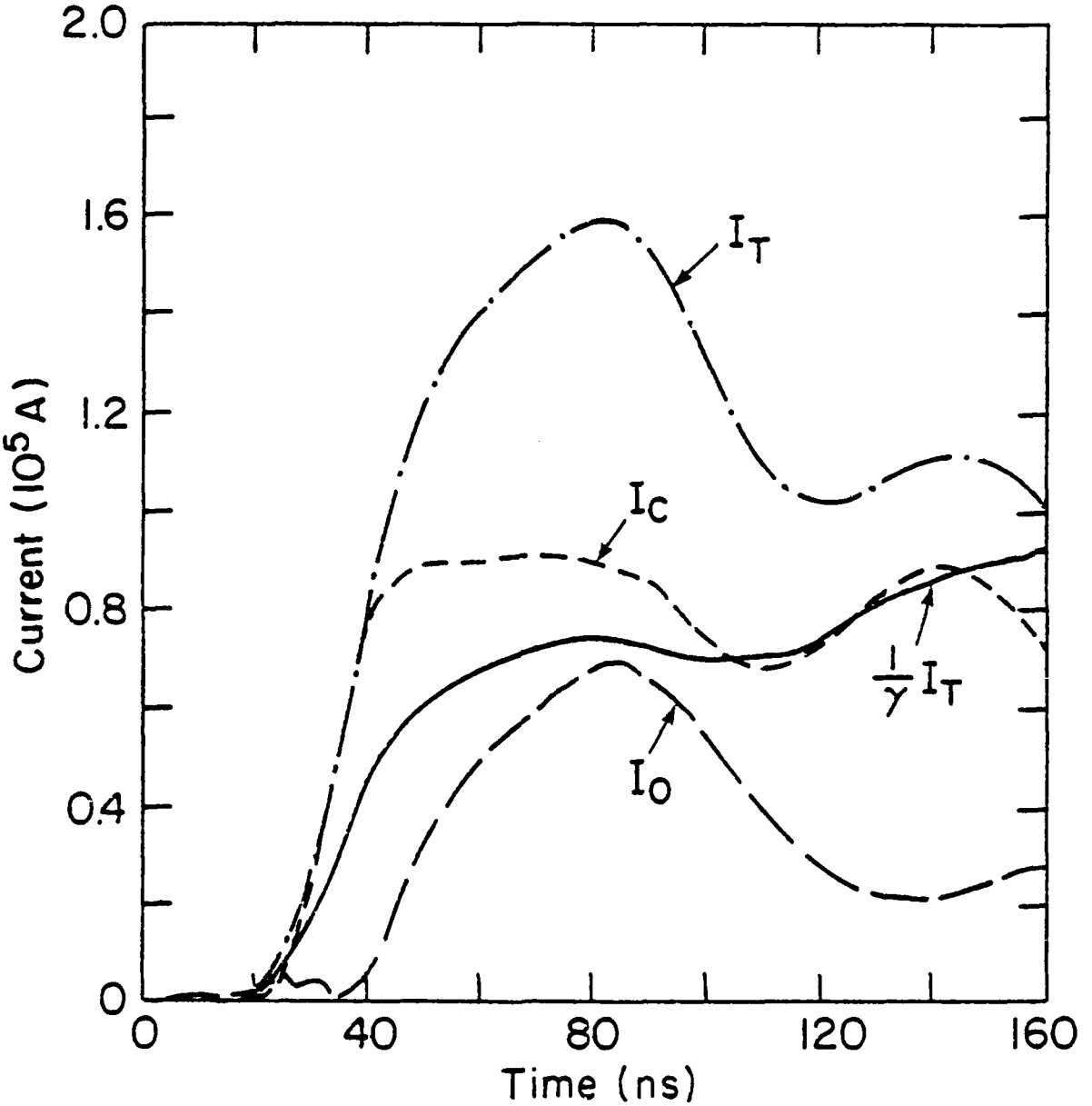

Fig. 13 — Average inner, outer, total, and theoretical bias current for shots #6442-6446.

REFERENCES

1. Blaugrund, A. E. and Cooperstein, G., Phys Rev Lett 34, 461 (1975).
2. Goldstein, Shyke A. and Lee, Roswell, Phys Rev Lett 35, 1979(1975).
3. Blaugrund, A. E., Cooperstein, G. and Goldstein, S. A., Phys of Fluids 20, 1185 (1977).
4. de Packh, D. and Ulrich, P. B., J. of Electronics and Control 10. 139 (1961), and de Packh, D., Naval Research Laboratory, Radiation Project Internal Report No. 5, 1968 (unplublished).
5. Creedon, J. M., J. Appl. Phys 46, 2946 (1975); and Phys Int'l Co. Report No. PIIR-17-72, 1972 (unpublished).
6. Friedlander, F., et al, Varian Associates Report No. DASA 2173, 1968 (unpublished).
7. Goldstein, S. A. et al, Phy Rev Lett 33, 1471 (1974).
8. Poukey, J. W., in Proc of the Int'l Topical Conf on Electron Beam Research and Technology, Albuquerque, NM, 1975, edited by Gerald Yonas (U. S. Dept. of Commerce, Washington, DC, (1976, p 247.
9. Stephanakis, S. J., et al, Phys Rev Lett 37, 1543 (1976).
10. de Packh, First experimental work on PPF cathodes on GI, (unpublished).
11. Yonas, G. et al, Phys Rev Lett. 30, 164 (1973).
12. Read, Michael, PhD Thesis, Cornell University (1976).
13. Cooperstein, G. in NRL Memorandum Report No. 3006, p. 60 (1975); and G. Yonas (private communication)
14. Mendel, C. W. and Goldstein, Steven (private communications).

15. Lee, Roswell, Goldstein, Shyke A. and Bacon, D. P., Bull. Am. Phys. Soc. 23, 762, (1978).

16. Quintenz, J. P., J. Appl. Phys. 49, 4377 (1978).

17. Johnson, D. J., et al, J. Appl. Phys. 49, 4634 (1978).

COMPUTATIONAL STUDY OF MAGNETIC DAM EFFECTS IN A HIGH IMPEDANCE DIODE

I. INTRODUCTION

The NRL Light Ion Fusion Program has experimentally demonstrated high efficiencies for the production of light ion beams using low impedance diodes. On Gamble II in 1-2 ohm operation well over 70% of the diode power is typically carried by the ions.[1,2] Current and planned experiments call for the design and use of diodes on the high impedance pulsed power generators of Harry Diamond Lab's AURORA and Sandia National Lab's PBFA II modules. Since impedance matching is essential for efficient transfer of power from the machine to the diode, these new diodes must be designed for 4-20 ohm operation. Unfortunately, it has been experimentally determined that efficiencies of only 20-50% can be obtained in this operating regime using traditional axial diode configurations.[3] The development of techniques for boosting these relatively low ion production efficiencies is today the subject of intense research and speculation. This paper reports on the results of one such theoretical effort. Although the specific diode design which was simulated did not achieve the desired boost of ion efficiency, an examination of its shortcomings clearly indicates both a cause as well as possible solutions. These observations bear on high impedance axial diodes in general and lend a new insight into their peculiarities which may eventually assist in a design breakthrough.

Specifically, the diode geometry under consideration here would be suitable for operation on AURORA. It is drawn to scale in Figure 1 with all significant dimensions given, as indicated, in centimeters. Although the latest NRL/AURORA ion diode has an anode stalk almost 25 cm in radius, its cathode shank remains about 5 cm in radius. The differences caused by modifications to the electric field beyond R = 7 cm are assumed to be minor, since they do not directly effect electron motion in the active anode-cathode (A-K) gap. The diode modeled was chosen for positive polarity operation. That is, the resultant ion beam would be traveling through the cathode shank in a direction away from the generator and pulse-forming line. The inner and outer radii of the vacuum feed line are 8.0 and 10.0 centimeters, respectively. The anode is a simple hollow cylinder with a wall one-half centimeter thick which is capped by two 4 mil. polyethylene foils separated by a one-quarter centimeter vacuum gap. It is important that the electron beam traveling through the cell behind the anode foil be charged and current neutralized. It is widely believed that a gas fill at several torr pressure could provide the assumed neutralization. A thin wire is located along the anode's central axis and is electrically connected to it via the inner foil. Current of arbitrary magnitude may be fed through this wire from an external source which is independent of the pulsed power generator. Such a current of I_w amperes will create an azimuthal magnetic field behind the foil of

Manuscript submitted August 24, 1981.

AD-A129 821 DIODE DYNAMICS BEAM GENERATION AND TRANSPORT AND PLASMA EROSION OPENING SWITCH DEVELOPMENT(U) JAYCOR ALEXANDRIA VA P F OTTINGER 17 MAY 83 JAYCOR-J207-83-C-001 2/0

UNCLASSIFIED N00173-80-C-0202 F/G 9/1 NL

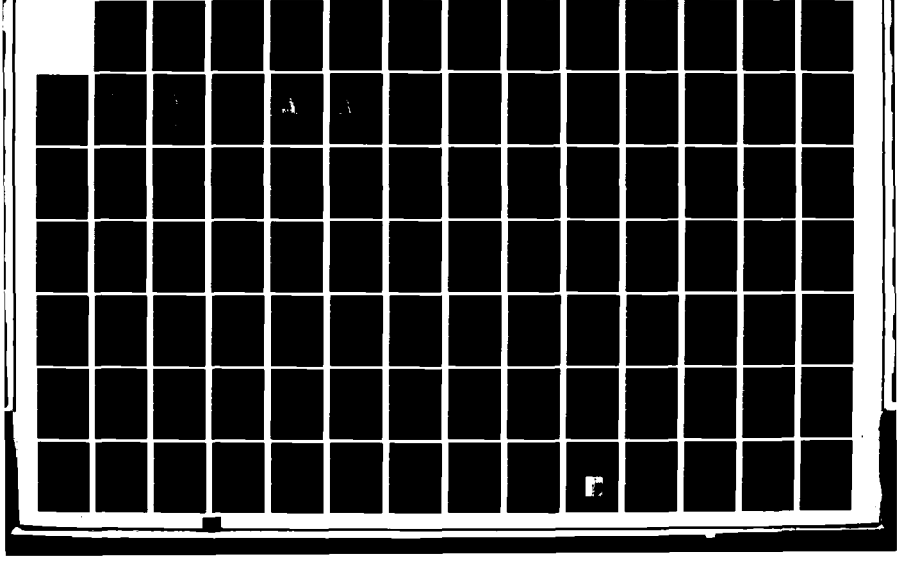

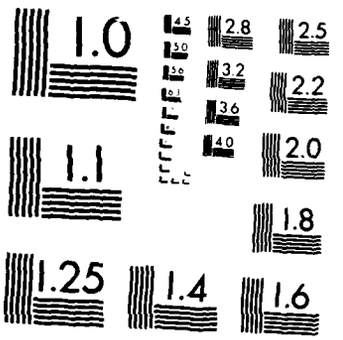

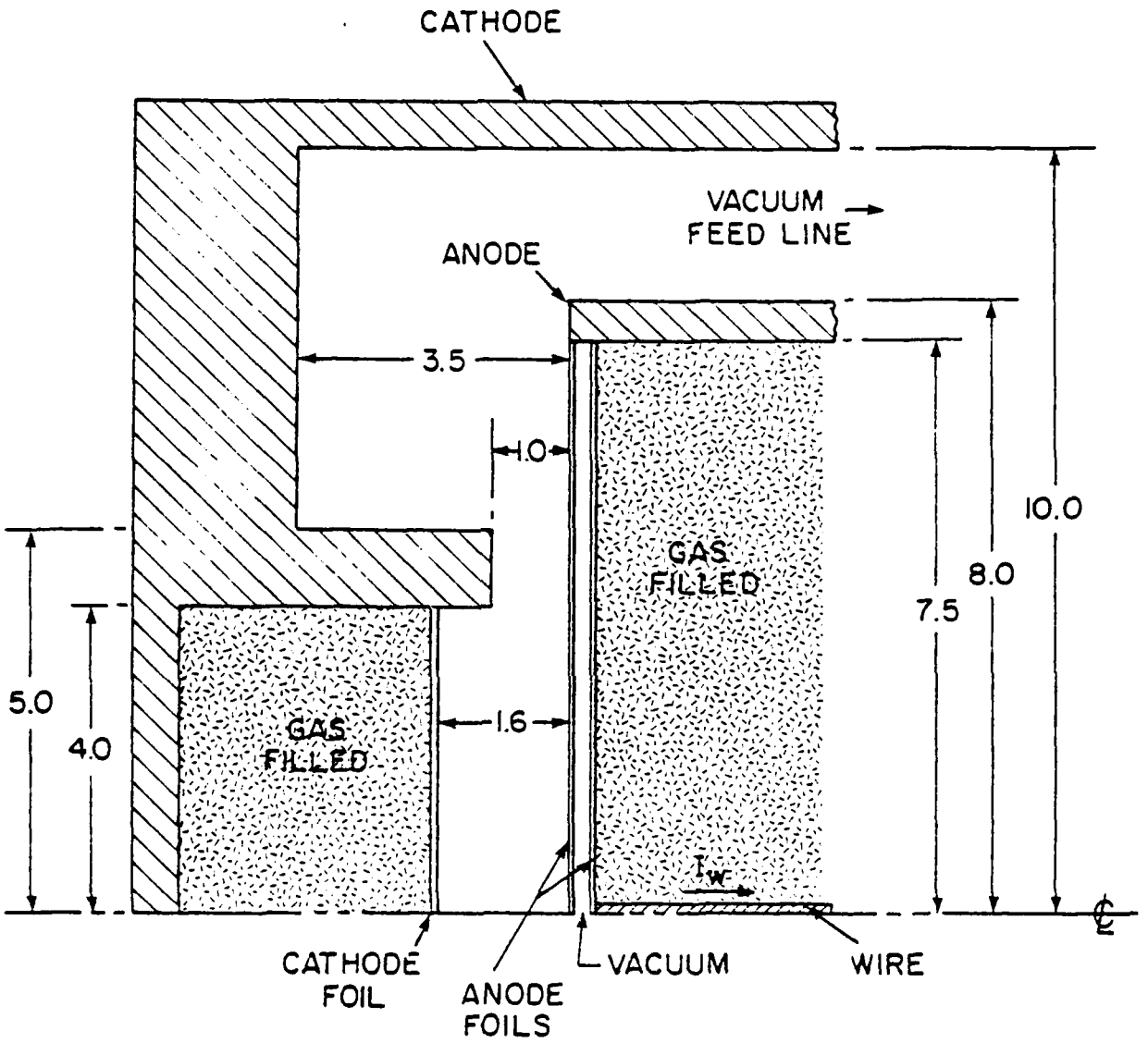

Fig. 1 — A scale drawing of the magnetic dam diode. (All dimensions are in centimeters.)

magnitude $\frac{0.2I_w}{r}$ gauss. If sufficiently strong, this B_θ can bend the trajectories of electrons entering the anode gas cell near r = 0 in such a way as to "reflect" them out of the anode foil again at a higher radius. This effective barrier against axial electron flow is the essence of the magnetic dam concept. It is seen as a possible mechanism for increasing the average lifetime of a typical electron in the anode-cathode (A-K) gap. This should increase electron space charge for a given electron current, increasing the net ion emission.

In the given diode, the A-K gap was chosen to be one centimeter to allow approximately 6-8 ohm impedance at the fixed 4 megavolts applied. Finally, the hollow cathode has an outer radius of 5.0 cm. with 1.0 cm. shank thickness. A 4 mil polyethylene foil is recessed 0.6 cm into the shank to enclose a low-pressure gas fill similar to that of the anode and serving a similar charge/current neutralization role for the emerging ion beam. This cathode gas cell plays no part whatsoever in this simulation.

The analysis of this diode begins in Section II with a theoretical discussion of the "magnetic dam" principle. This will explain the motivation for conducting the simulation. Section III will transition into the actual numerics of the modeling, examining the details of the code that was employed. Specific approximations and assumptions used in the model will be pointed out. This report will conclude in the fourth section with a presentation of the simulation results complete with suggestions for follow-on work.

II. THEORY OF THE MAGNETIC "DAM"

The treatment of electron trajectories in an azimuthal magnetic field and in the absence of an electric field may be derived from an analysis of ion orbits due to Goldstein and Ottinger.[4] The particle orbits may be determined from a simple conservation of energy principle. Consider an electron traveling at velocity, $\vec{v}$, impinging on the anode foil at some angle, θ, and entering the anode gas cell at radius, R_o, as shown in Figure 2. In the gas cell, it is assumed to be acted upon only by the azimuthal magnetic field there. Its energy must therefore remain constant and

$$\gamma = (1 - \frac{v^2}{c^2})^{-\frac{1}{2}} = \text{constant},. \qquad (1)$$

where

$$v^2 = v_r^2 + v_z^2 . \qquad (2)$$

For an electron which has just crossed a cathode-anode gap with electric potential difference, V, in megavolts, it may be further written that

$$\gamma = 1 + \left| \frac{V}{0.511} \right| . \qquad (3)$$

From Figure 2,

$$v_{z_o} = v \sin\theta . \qquad (4)$$

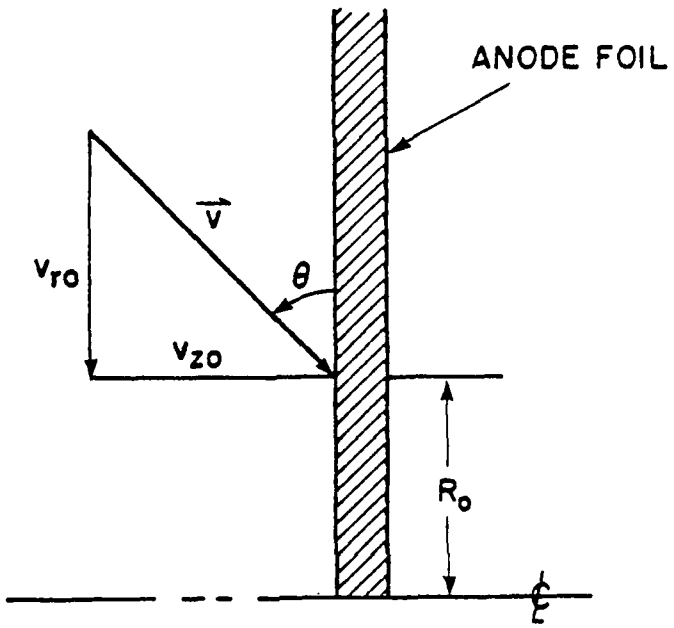

Fig. 2 — Geometry of electron penetration into the anode gas cell

Combining Eqs. (1), (3), and (4) yields

$$v_{zo} = c \sin\theta \sqrt{1 - \left(\frac{0.511}{v+0.511}\right)^2} \qquad (5)$$

Furthermore, Eqs. (2) and (4) give a direct expression for the time dependence of the electron's radial velocity in the gas cell,

$$v_r(t) = \pm \sqrt{v_{zo}^2 \sin^{-2}\theta - v_z^2(t)} \quad . \qquad (6)$$

The force acting upon the electron is given by the relativistic Lorentz Law to be

$$\gamma m_o \frac{dv_z}{dt} = -\frac{e}{c} \vec{v}_r \times \vec{B}_\theta(r) = -\frac{e}{c} \frac{dr}{dt} B_\theta(r) \quad . \qquad (7)$$

where m_o is the electron rest mass. This equation may be rearranged and integrated from the foil entry point $(0,R_o,0)$ out to some point along the electron's trajectory in the cell to yield

$$v_z(t) - v_{zo} = \frac{-e}{m_o c \gamma} \int_{R_o}^{r} B_\theta(r)\, dr \quad . \qquad (8)$$

As stated previously, the magnetic field in the gas cell generated by a current, I_w, flowing through the axial wire is simply $B_\theta(r) = 0.2\, I_w/r$. Equation (8) may thus be rewritten as

$$v_z = v_{zo}\left(1 - \chi(r)\right) \qquad (9)$$

where

$$\chi(r) \equiv \frac{0.2\, e}{m_o\, c\, v_{zo}\, \gamma} I_w \ln\frac{r}{R_o} \qquad (10)$$

with I_w expressed in amperes and all other quantities in c.g.s. units. The orbit expression linking r explicitly to z is simply the ratio of the respective velocity components given in Eqs. (6) and (9),

$$\frac{dr}{dz} = \frac{v_r}{v_z} = \pm \frac{\sqrt{\sin^{-2}\theta - 1 + \chi(r)\,(2-\chi(r))}}{1 - \chi(r)} \qquad (11)$$

The integration of Eq. (11) yields the exact trajectory of an electron traversing the gas-filled anode for specific values of θ, V, I_w, and R_o.

It is instructive to calculate sample orbits for various combinations of parameters. In all cases, V is fixed at 4.0 megavolts in order to correspond to realistic AURORA ion diode operations. Useful choices for I_w can be estimated by a rather simple calculation. Consider a 4 MeV

electron with an entrance angle of 90° beginning its gas cell trajectory at a radius of 1.0 centimeter. Assume that it remains in a uniform azimuthal magnetic field of magnitude equal to that found at the exact center of its circular gyration in the actual gas cell. Therefore, for a desired exit radius of 5.0 centimeters, the value of B_ϑ (r) at r = 3.0 cm. is taken as a constant over the entire electron trajectory. In order to generate the field strength needed for a 2.0 centimeter relativistic gyroradius, a wire current of 63.75 kiloamps is required. This reasoning leads to the following selection of values for I_w to be tested: 65 kA, 130 kA, and 300 kA.

For the first set of sample orbits, an entrance angle of $\vartheta = 90°$ is chosen. This choice leads to an orbit equation given by

$$\frac{dr}{dz} = \pm \frac{\sqrt{\chi(r)\ (2-\chi(r))}}{1-\chi(r)} \qquad (12)$$

The trajectories for R_o = 1.0 and R_o = 2.0 cm. are plotted in Figure 3. It can be seen that I_w = 65 kA generates too weak a field to reflect electrons with R_o greater than 1.0 cm. back into the A-K gap. The orbit for R_o = 1.0 cm is marginal. On the other hand, I_w = 130 kA produces the desired effect for R_o less than 2.0 cm and the I_w = 300 kA case is even better.

In a realistic pinch reflex diode configuration such as that being modeled, one expects to see a focused electron flow in which electrons magnetically self-pinch to smaller radii as they cross the gap. It is therefore important to attempt a similar orbit calculation for non-normally incident electrons. A reasonably straightforward, yet probably illustrative example would be electrons entering the gas cell at 45°. This choice of ϑ reduces Equation (11) to

$$\frac{dr}{dz} = \frac{\pm\sqrt{1+\chi(r)\ (2-\chi(r))}}{1-\chi(r)} \qquad (13)$$

A new set of sample orbits is calculated and shown in Figure 4.

Comparison of the two sets of plots reveals immediately that non-perpendicular injection leads to electrons exiting the gas cell at significantly lower radii. This is reasonable considering the longer period of time a given electron spends in regions of relatively higher magnetic field strength. Their orbits consequently experience greater bending. The overall effect for all but the 65 kA cases is the satisfactory reflection of all electrons with $R_o \leq 2.0$ cm back into the anode-cathode gap where they can enhance ion emission.

III. THE NUMERICAL SIMULATION

A. The Simulation Code

The computer code utilized in these studies is a 2-D version of the 2½-D DIODE2D[5] particle-in-cell (P.I.C.) code. Inhomogeneities are allowed in the radial (r) and axial (z) spatial dimensions. Complete azimuthal symmetry is assumed. In addition , the r- and z- momentum components are retained. The "particles" in this model are axially-centered rings of charge. In reality they are macroparticles carrying many times an elementary charge

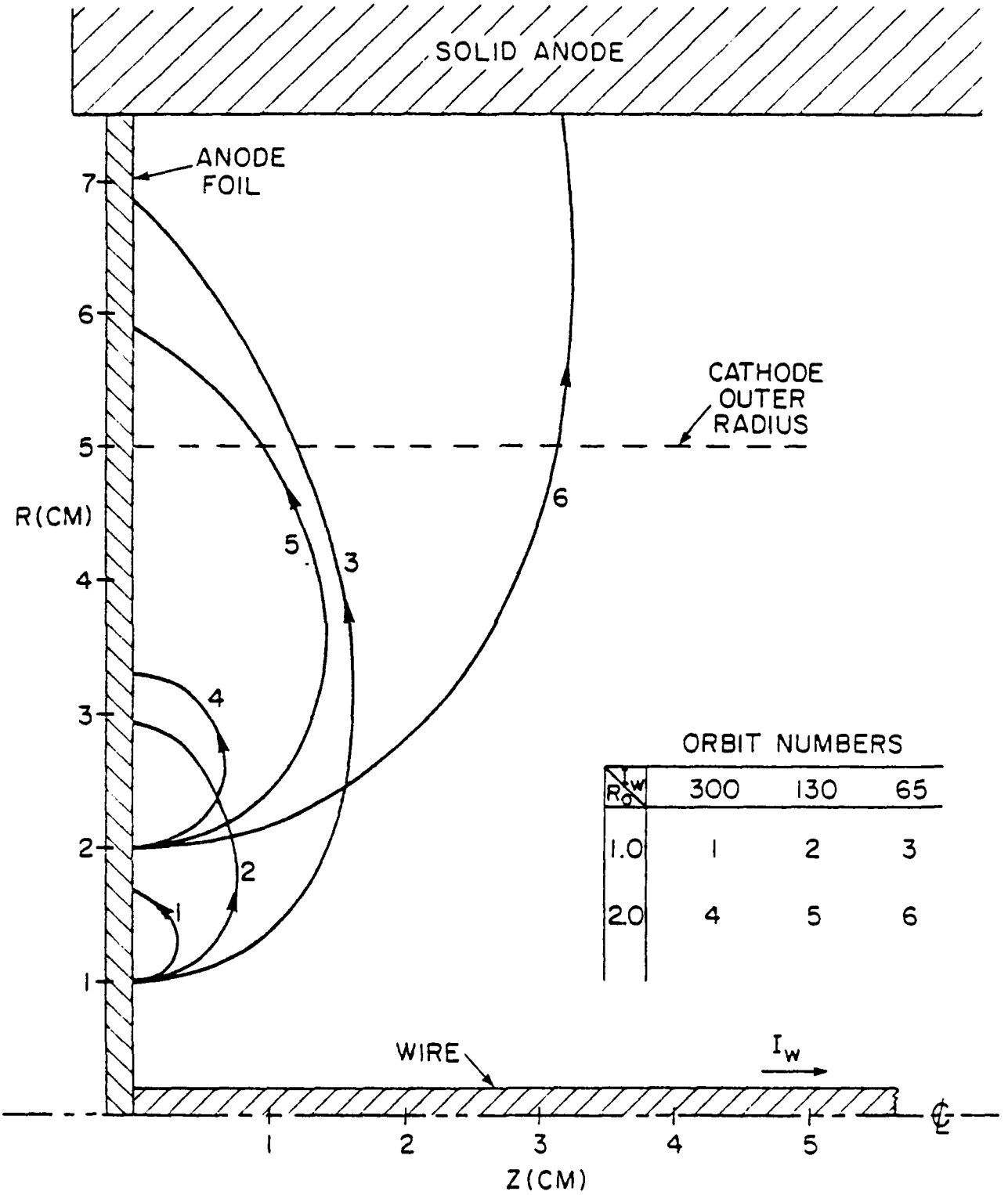

Fig. 3 — Sample 4 MeV electron orbits for 90° injection

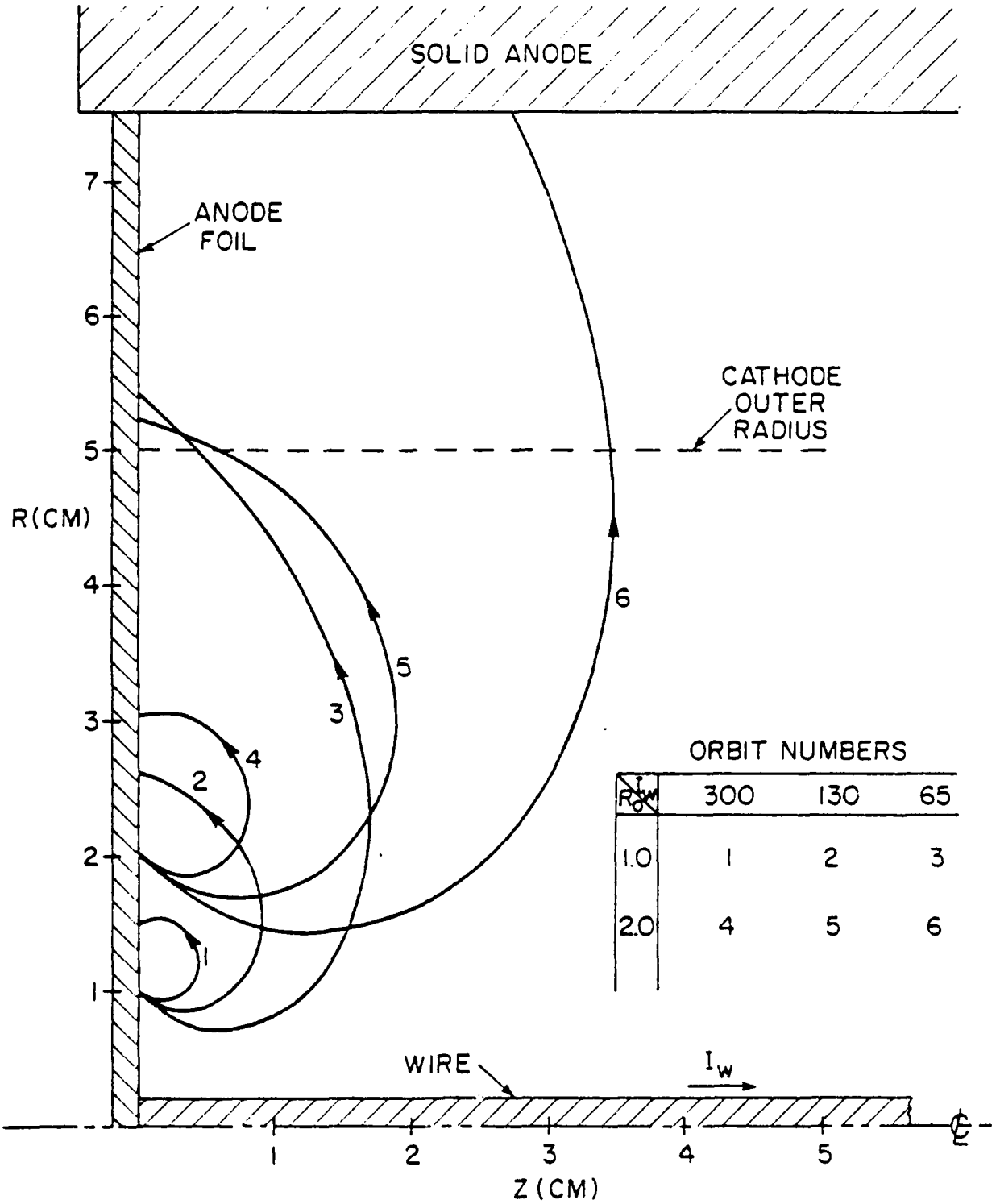

Fig. 4 — Sample 4 MeV electron orbits for 45° injection

but retaining the physical charge-to-mass ratios of the protons and electrons which they represent. Area weighting (i.e., linear interpolation) is used to couple these charges with the electric and magnetic fields calculated over a fixed set of grid-points in the region of interest. The fields thus interpolated to the particle positions act on these charge-current rings by way of the relativistic Lorentz force equation. The field treatment is electrostatic. In this sense the code does not perform a true "simulation" since the time-dependent equations are not observed. Rather the treatment is "quasistatic". Equillibrium solutions to various diode geometries are sought. The "timesteps" which appear in the code are actually snapshots of the system while it seeks to relax toward its steady-state configuration. In order to determine the electric field within the diode region, particle charge densities are distributed over a fixed grid and the discrete Poisson's equation is solved.[6] The code permits irregular conducting boundaries inside the computational region. The treatment of such internal boundaries entails the use of a "capacitance matrix". The internal surfaces thus created are held at predetermined electric potential values. Direct radial integration of the axial current densities over the mesh yields the azimuthal magnetic field via Ampere's Law. The outer radial boundary of the diode region may be either conducting or free-space. The electrostatic potential, φ, is set constant along all conducting boundaries. Along radial free-space boundaries, φ is graded logarithmically and along axial ones, linearly.

At the start of a typical computer run, the computational diode region is a complete vacuum devoid of particles. The electric potential is pre-set along the entire boundary as well as along all internal conducting surfaces. The emission of the ions is permitted anywhere along fixed regions of the anode surface. Electrons are emitted along the entire cathode, including the inner and outer shank surfaces. The value of the perpendicular electric field at a given emission point determines the total charge (i.e., number of particles) that will be emitted there. At the beginning of a timestep, the electric field at a surface specifies the net charge density on the surface via Gauss' Law. The surface integral of this density over a cell width around a given grid point yields the net charge which is emitted there for that timestep. Prior to the actual particle-pushing the electric field is recalculated taking into account the newly emitted charge.

All particles are then pushed according to the relativistic Lorentz force law using the area weighted electric and magnetic field values interpolated at the particle position from the four nearest grid points. After pushing in each timestep a position check is performed on each particle to determine if it is inside a conductor or outside the mesh boundaries. If so, the particle is appropriately absorbed and so recorded. On the other hand if it is an electron in an anode foil, then it is passed to a scattering subroutine which employs a one-step Monte Carlo algorithm to calculate energy loss and deflection. Upon completion of this sorting process, the charge and current density associated with each unabsorbed particle is distributed over the four nearest grid points using the same linear interpolation scheme in reverse. This yields a complete array of values for the charge density, ρ, and the current density, J_z, over the computational mesh. Poisson solving these arrays yields φ from which E_ρ and E_Z are calculated. The azimuthal component of $\vec{B}$ is obtained through direct integration of J_z over the grid. Quantities of interest are then extracted and output via diagnostic

subroutines. The code then cycles to the next timestep for particle emission.

Finally, it should be noted that the numerics of the particle pushing as well as the potential solving has been completely "vectorized". Thus, the momentum, position, and field components associated with the entire ensemble of particles are treated as macro-vector quantities. Arithmetic operations performed with them are accomplished in a completely vector-array format. This property of the code permits efficient running times on the most advance scientific computers. (Of course, the interpolation of $\vec{\rho}$, $\vec{J}$, $\vec{E}$, and $\vec{B}$ values between particle positions and grid points requires random accessing of array points and this process cannot be vectorized.)

B. The Computational Experiment

At the outset of this simulation, as with any other, great care was taken to minimize the numerical complexity/cost while preserving all aspects of the essential physics to be treated in the problem. It was this desire to minimize expense that motivated the use of a 2-D version of DIODE2D rather than its standard 2½-D form. (The standard version allows for solution of self B_r and B_z field components which are never generated here.) The second most significant economization involved the minimization of the physical size of the computational region. It was deemed uneconomical as well as physically unimportant to fill the entire diode cavity with the numerical grid. As can be seen from Figure 1, that would result in a mesh measuring about six centimeters axially by ten radially and would waste computational effort by including space devoid of particles. Instead, the axial extent of the grid was bounded by the plane of the cathode foil and by the inner anode foil. Similarly, its radial limit was set as the inner radius of the anode cylinder. The only obstacle to this reduction of grid extent was the free-space part of the new, artificial boundary. DIODE2D's field solving algorithm requires fixed potential values along all the boundaries. For the full diode with its conducting walls this is, of course, no problem. Even the open segment of the vacuum feed line entrance is trivial, since a simple logarithmic potential grading can be used there (assuming the presence of no particles there). The setting of potential values along the new, ad hoc boundaries cannot be accomplished intuitively. Instead, a two-step process is employed. First, a capacitance matrix field-solve is carried out for the entire diode cavity as pictured in Figure 5. It is assumed that no "sources" (i.e. charges or currents) are present anywhere. Then the new "boundaries" are located as indicated by the dotted lines, and the free-space potential values are noted. Finally the new computational region is set up with those values imposed along the appropriate edges. As long as no particles stray too "near" those ends, φ should remain fairly constant there. In any case, the bulk ion and electron flow should be too "remote" to feel any peripheral abnormalities. The vacuum potential solution for the actual simulation grid is shown in Figure 6. Note that the axial scaling is much finer than the radial in order to more fully appreciate the field profiles.

The final computational grid is depicted in Figure 7. It is spanned by 66 data cells in the axial dimension and 77 radially. Poisson-solving is accomplished on the interior 64 X 75 mesh, leaving a monolayer of "guard" cells along the boundary. Simple Gaussian field emission of electrons is permitted all along the heavy-lined surfaces of the cathode as shown in the

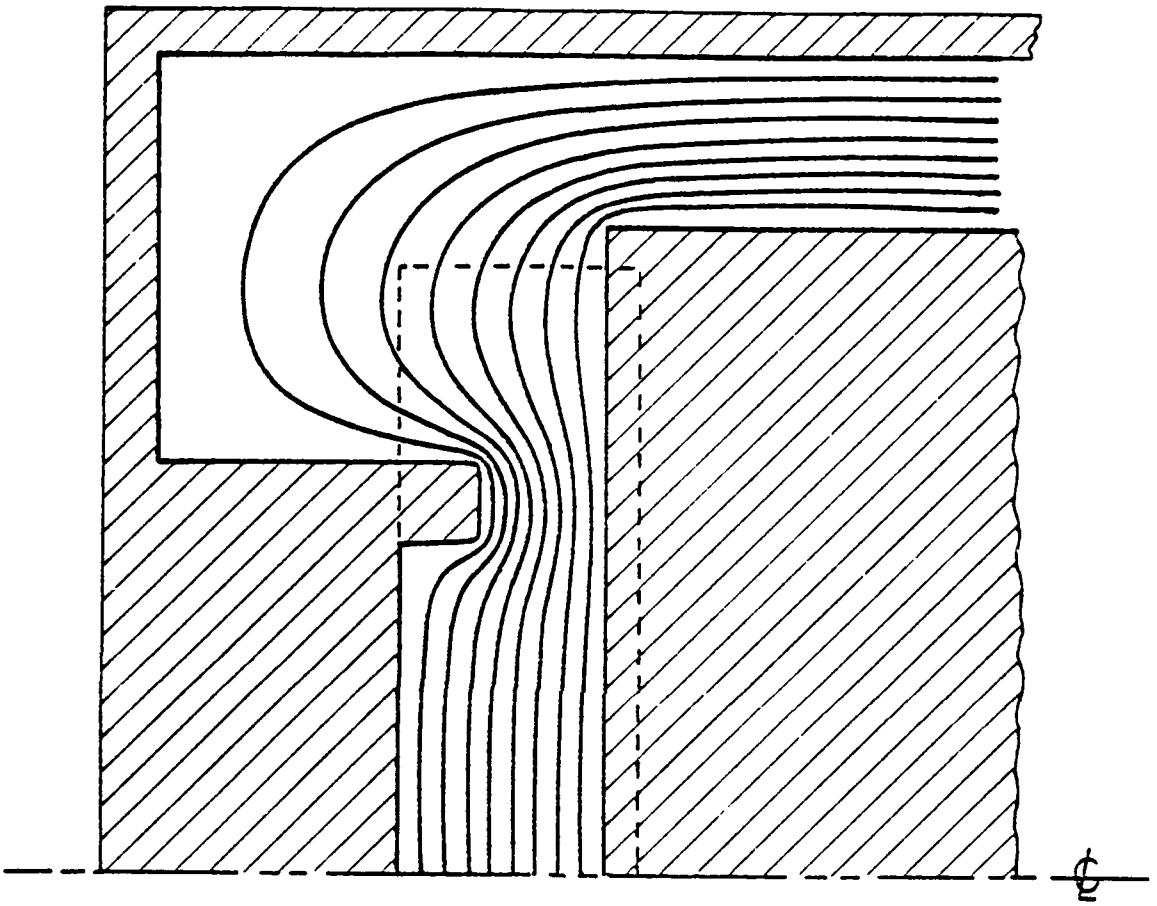

Fig. 5 — Vacuum equipotential plot for the entire diode

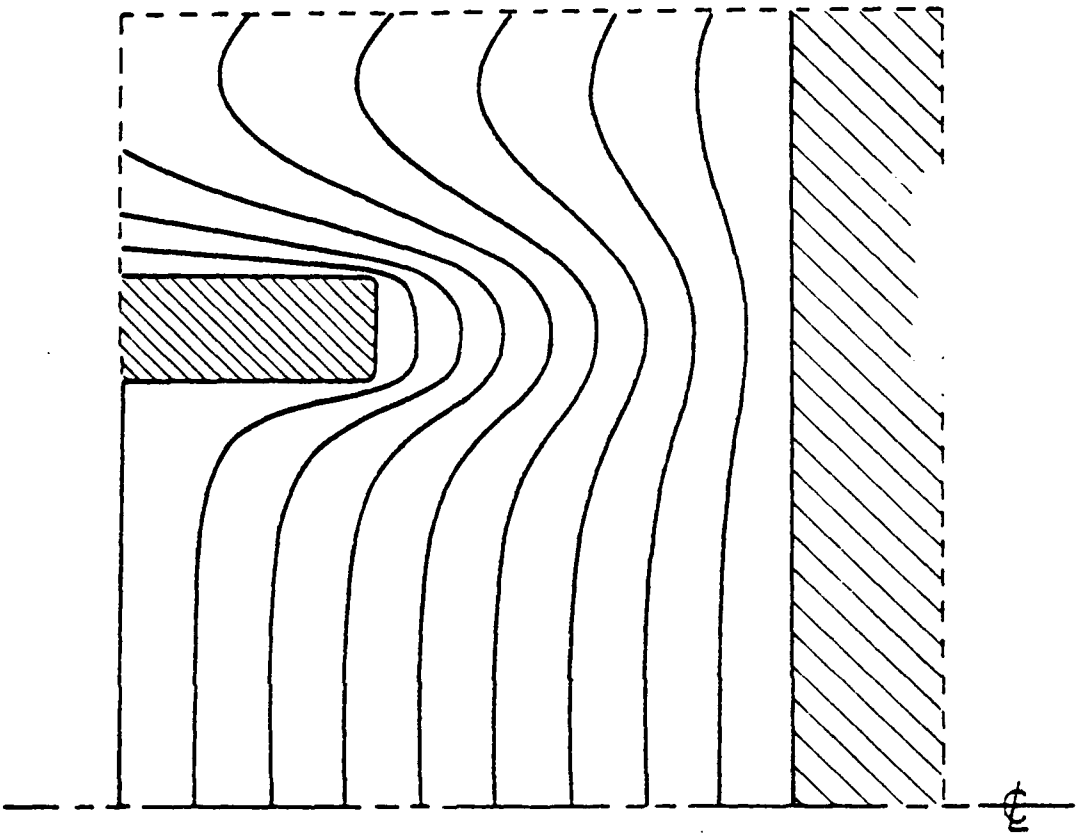

Fig. 6 — Vacuum equipotential plot for the restricted computational region

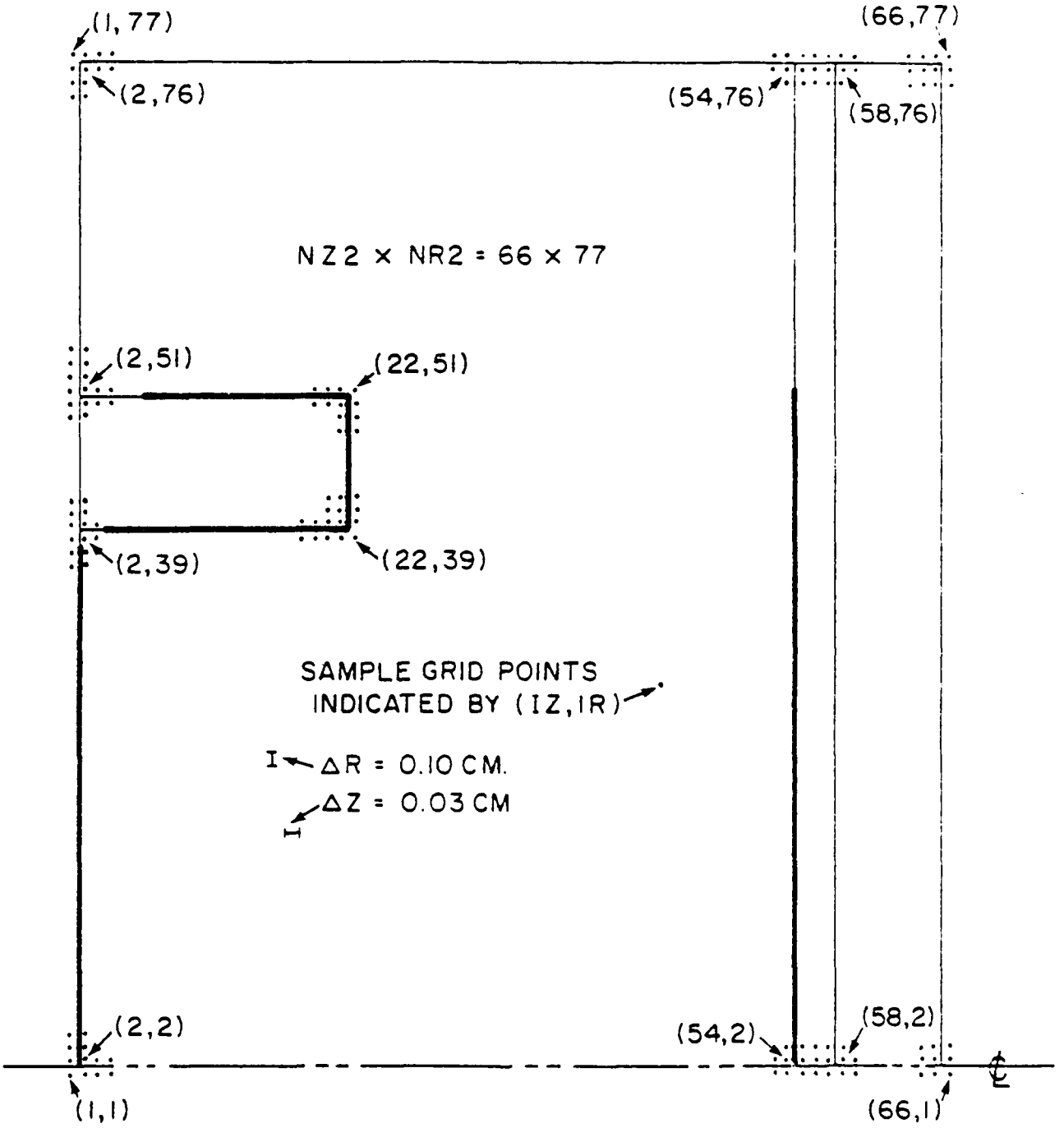

Fig. 7 — The numerical computation grid

figure. The same is true for ion emission along the outer surface of the anode foil. Note that no electron emission is allowed in either the region around point (2,39) of the inner cathode shank surface or along the rear of the outer shank. Electric field values are expected to be too imprecise there. The timestep was fixed at 1.5×10^{-12} second for most of the runs presented although smaller timesteps were used near steady state to test the stability of the equilibria. Another interesting point is the numerical "thickness" of the outer anode foil. Although physically treated as 4.0 mil thick polyethelene by DIODE2D's electron scattering algorithm, this foil spans three full cells spatially. This is an artifact to ensure that no electron will be able to traverse the foil in a single timestep. Since no fields act on particles inside the foil, this false thickness does not impact on the physics of the simulation itself. Among the most important of the code diagnostics are a complete record of time-averaged emission and absorption profiles for each of the surfaces, sample particle position plots, and electrostatic equipotential plots.

The numerical implementation of the physics of the magnetic dam involved non-trivial manipulation and reorganization of the standard DIODE2D algorithms. The region inside the gas cell, behind the inner anode foil was designed to be completely free of all electric and magnetic fields except for the azimuthal B-field due to the current-carrying wire along the axis. Therefore, no solutions of Poisson's equation nor radial integrations of Ampere's law were necessary there. Only $B_\theta = 0.2\ I_w/r$ need be enforced. Thus, no extension of the field-solving and charge/current apportionment mesh was called for. Instead, the standard electron-absorbing character of the rightmost boundary was changed to complete transparency to electron flow. The particle accounting routines in the simulation were charged, such that an electron hitting that edge was <u>not</u> removed from the "active" particle list. Instead, it was given a special "label" which told the particle pushing subroutine to act on it only with a B_θ appropriate to its radial displacement, r, and to the I_w chosen for the wire current.

IV. RESULTS

In the initial simulation runs, the diode voltage was set at four megavolts and electron emission was turned on all along those cathode surfaces indicated in Figure 7. To limit the diode impedance, proton emission along the anode foil was not permitted beyond a radius of 5.0 centimeters. The early development of electron and ion flow patterns proceeded as illustrated in Figures 8a and 8b. In each plot of sample particle positions, note that the axial and radial dimension scales are not the same. Each frame measures 7.5 cm radially and just under two centimeters axially. The lower border of each frame is the diode centerline. In looking at these pictures, bear in mind that these are glimpses of a quasi-static simulation of particle flows trying to relax into a steady state. They do not represent the actual evolution of the physical system. Only the <u>final</u> picture for each set of parameters may coincide with experimentally realizable diode operation. It is those final steady-state pictures which comprise the core of the simulation results. One other thing to bear in mind is that in a physical diode, ion emission is not generally initiated simultaneously with electron emission. Rather, time integrated electron flow to the anode foil deposits either sufficient amounts of energy over the impact regions to cause vaporization

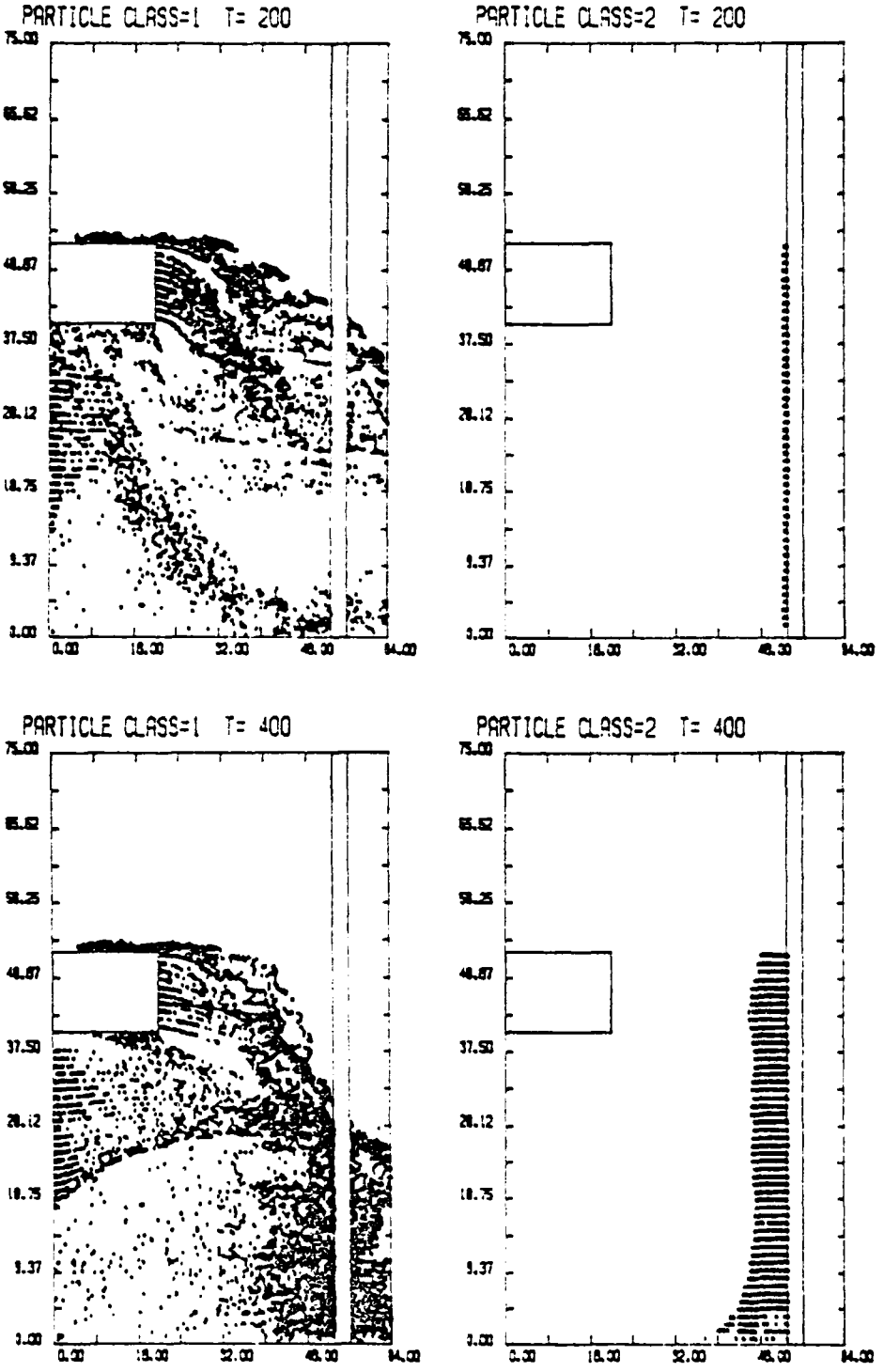

Fig. 8a — Early time evolution of the $I_w = 0$ case

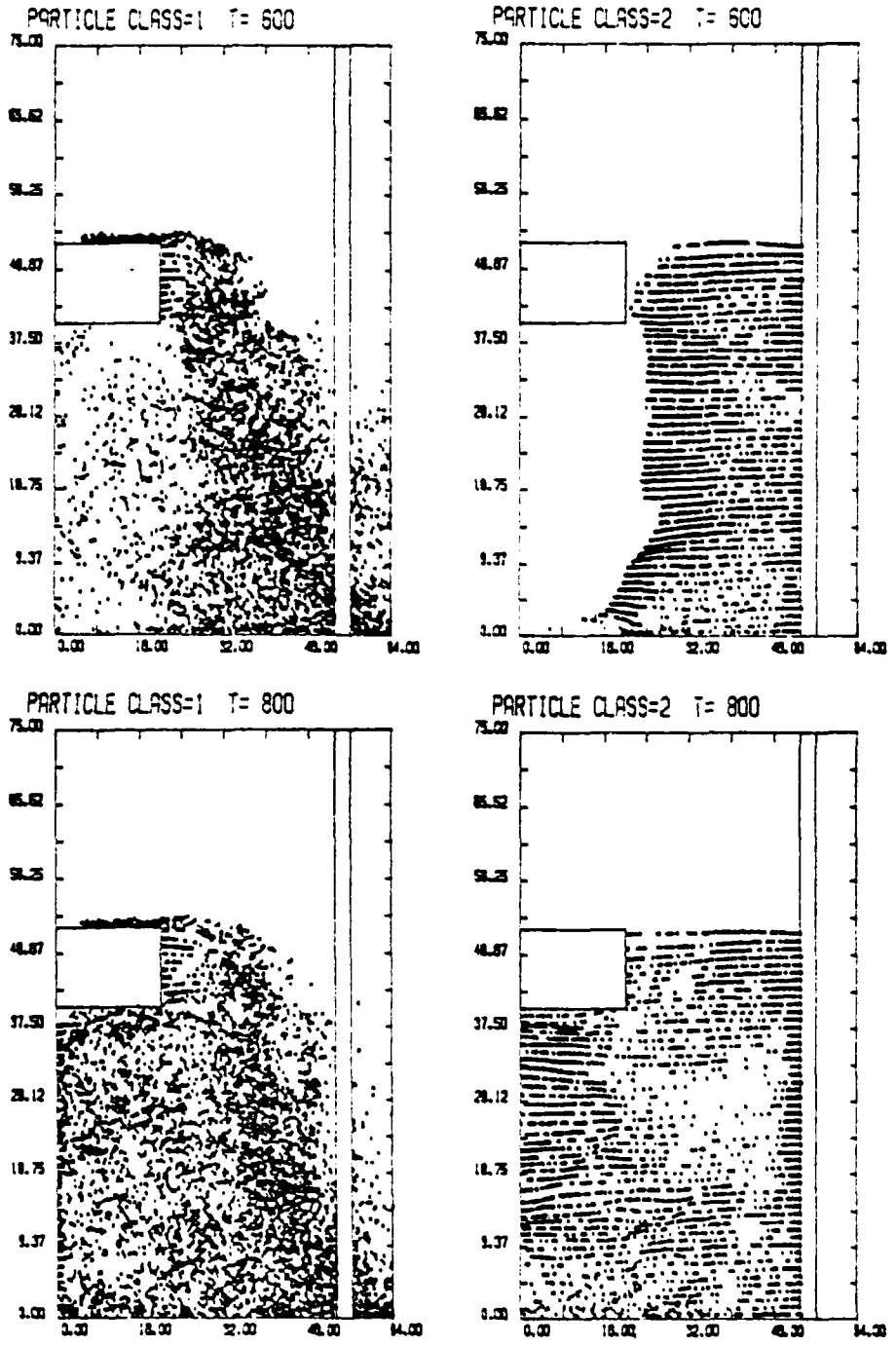

Fig. 8b — Late time evolution of the $I_w = 0$ case

and ionization or sufficient amounts of charge to cause surface flashover and ionization. In either case, the anode plasma thus formed acts as the source for protons in the diode.

Keeping in mind that only the equilibrium state will be "correct" it is nevertheless instructive to follow the sequence of events in Figure 8. At T = 200 Δt the newly emitted ions have bearly moved. The electron flow governed by its strong self-fields takes the form of two distinct streams. The numerical restriction of particle emission strictly to data cell centers allow for streamline tracing in all but the turbulent regions. In this far-from-steady condition, the electron current emitted is about 580 kiloamps, while that collected is a mere 240 kA. Emitted ion current is erratic, but appears to be around 150 kA. At T=400 Δt, the ions have advanced significantly with those at lower radii making up the vanguard due to the electric field enhanced by the focused electron charge near R = 0 at the anode. Attracted by the previously unneutralized ion space charge, the electron flow has unified into a single, neatly reflexing stream. (Note that in this run, the inner anode foil which forms the rightmost boundary of each frame is taken to be an electron-absorbing, solid conductor.) Notice that the regions or densest electron space charge at lower radii correspond to the space occupied by the advancing ion front. The net emitted and collected electron currents are 600 and 300 kiloamps, respectively, while ion emission has risen to about 350 kA. Turning to Figure 8b, T= 600 Δt reveals the ion front racing along near its full velocity. It is just about to make contact with face of the cathode shank. Two important characteristics of the electron flow deserve mention: 1) this flow is strongly pinched toward the center of the anode without much apparent reflexing (very typical of high impedance diodes), and 2) most of the electron space-charge is concentrated in regions containing ion charge. At this time $(I_e)_{emit}$ = 600 kA, $(I_e)_{coll}$ = 300 kA, and $(I_i)_{emit}$ = 230 kA. Finally, by T = 800 Δt, the near-equilibrium flow has set in. Electrons completely fill the inner diode cavity. The strongly pinched electron flow remains while the ion streams are fairly uniform. A word of caution -- the sparsely dotted area in the ion picture is an artifact of the non-random particle plotter; it does not translate to an actual absence of ions there. This configuration was allowed to continue for additional 200 timesteps. At that point (see Figure 9), the equillibrium currents were I_e = 326 kA and I_i = 287 kA. This total current of 613 kiloamps translated to an impedance of 6.5 Ω which was too low for our desired operating regime.

In order to correct this, ion emission from the anode foil was "turned off" opposite the cathode shank. This could be accomplished experimentally by overlaying the anode foil with a metal foil there. Protons were then only injected from R = 0 out to the last cell just below the shank inner radius, R = 4.0 cm. The system evolved for another 1000 timesteps to the flow pattern depicted in Figure 10. Very little change from the electron flow of Figure 9 can be detected. At this stage, note that the inner anode foil is still taken to be a solid, electron-absorbing surface. The new quasi-static currents were I_e = 264 kA and I_i = 214 kA, yielding a net impedance of 8.4 Ω for the diode. This was chosen as the reference steady-state against which the magnetic dam results are to be compared.

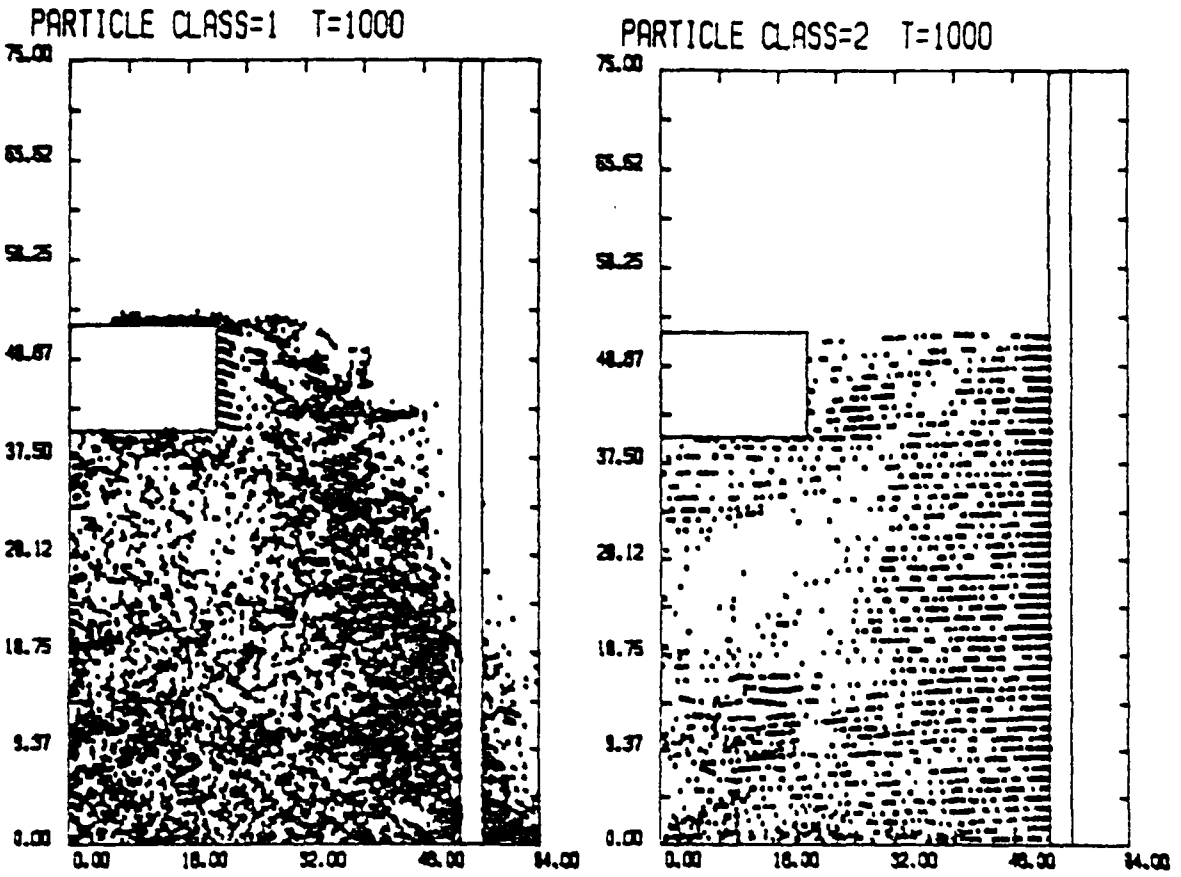

Fig. 9 — Steady-state particle positions for $I_w = 0$

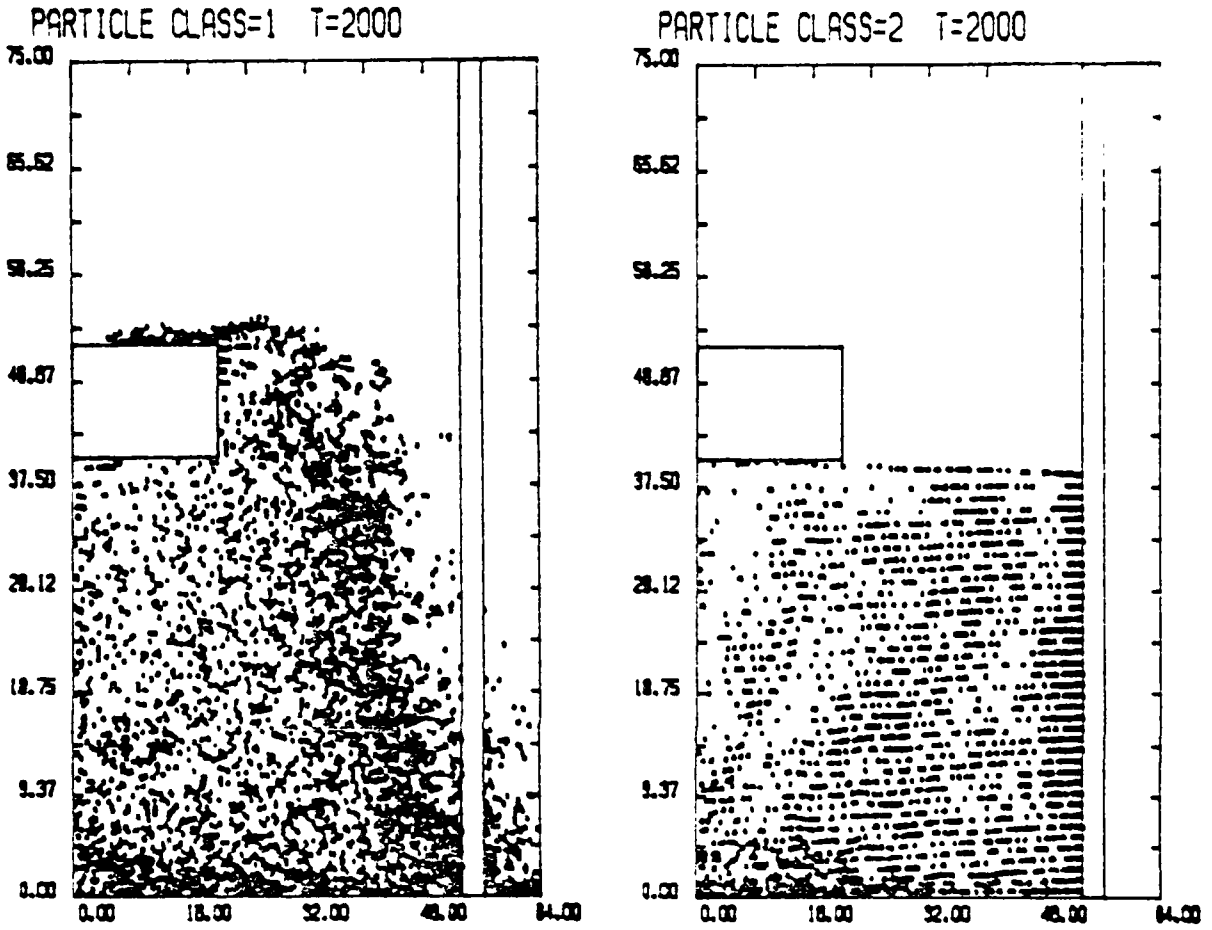

Fig. 10 — Steady-state particle positions for $I_w = 0$ with restricted ion emission

Retaining the same voltage, geometry and emission surfaces as those used for the 8.4 Ω reference case, the magnetic dam was then "turned on" by sending 65 kA through its central wire. The new particle positions for T= 2400 Δt are shown in Figure 11. There are two things immediately apparent: first, the radial deflection of the electron flow due to the gas cell is unacceptably large as might have been predicted from Figures 3 and 4 and, second, an improved particle position plotter is required in which the z - range is extended into the "gas cell" so that the electrons there can be plotted. To remedy the first problem, I_w was doubled to 130 kiloamps. In order to alleviate the second, the axial width of the plotting page was increased from 64 ΔZ to 100 ΔZ = 3.0 centimeters. Before moving on to this new case, it was recorded that the quasi-static currents were I_e = 309 kA and I_i = 232.5 kA. A true steady-state had not been reached, but it was decided not to invest additional funds to pursue such a non-promising run.

In addition to the doubling of I_w, the double anode foil configuration was eliminated for the remainder of the simulation runs. Referring back to Figure 1, the inner foil to which the wire was originally attached has now been completely removed. The quarter-centimeter vacuum gap is now treated numerically the same as the rest of the gas cell with the wire now running all the way to the outer anode foil. To accomplish this change in physical set-up required only the shifting of the electron "flag" setting boundary from Z = 64 Δ Z to Z = 56 Δ Z (See discussion at end of Section III). The original double-foil configuration probably contributed little to the magnetic dam physics but only served the practical experimental purpose of retaining a solid I_w current path for use after vaporization of the outer, proton-source anode foil.

As already stated, the first run using this new configuration was carried out for the case of I_w = 130 kiloamperes. Snapshots of the equilibrium electron and ion flows are shown in Figure 12. It appears that significant electron flow still extends beyond the right boundary, 1.32 centimeters from the anode foil. Referring back to Figure 4, this should not be surprising. Electron trajectories beginning at R = 2.0 cm at 45° extend almost 1.9 cm. into the gas cell. The even steeper angle injection suggested by the cathode-to-anode electron streaming should easily account for even wider ranging electrons at lower radii. One particularly disappointing aspect of the picture is the configuration of the electron charge density at the anode. An enhanced electron cloud can clearly be seen behind the anode foil, in the gas cell. Only a very thin electron layer appears in front of the foil where it is needed to enhance the ion emission. This observation is borne out in the equilibrium diode currents of I_e = 330 kA and I_i = 244 kA. The ion current increase is modest over the I_w = 0 case. Much more significant, however, is the even greater increase in the electron current. The net result has been a decrease in diode impedance of over one ohm while the ion production efficiency has actually dropped slightly. This is a crucial point which will be discussed later.

One obstacle that may be impeding the increase of ion efficiency is the wide disparity between the strengths of the oppositely directed B_θ fields on either side of the anode foil. These fields are proportional to the respective axial currents which, inside R=5.0 cm, are -574 kA on the left-hand side, and +130 kA on the right-hand side. Clearly, any electron

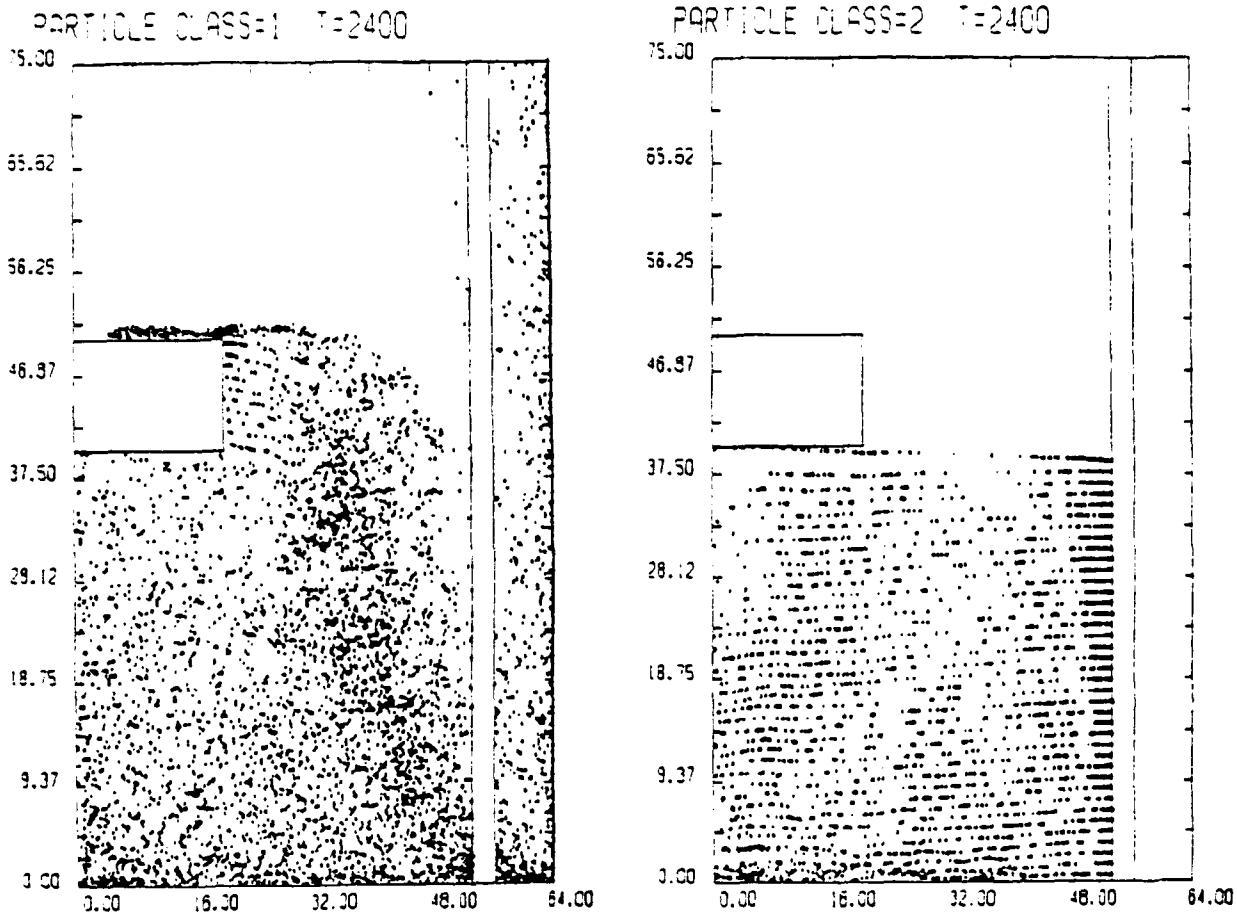

Fig. 11 — Quasi-equilibrium particle positions for I_w = 65 kA

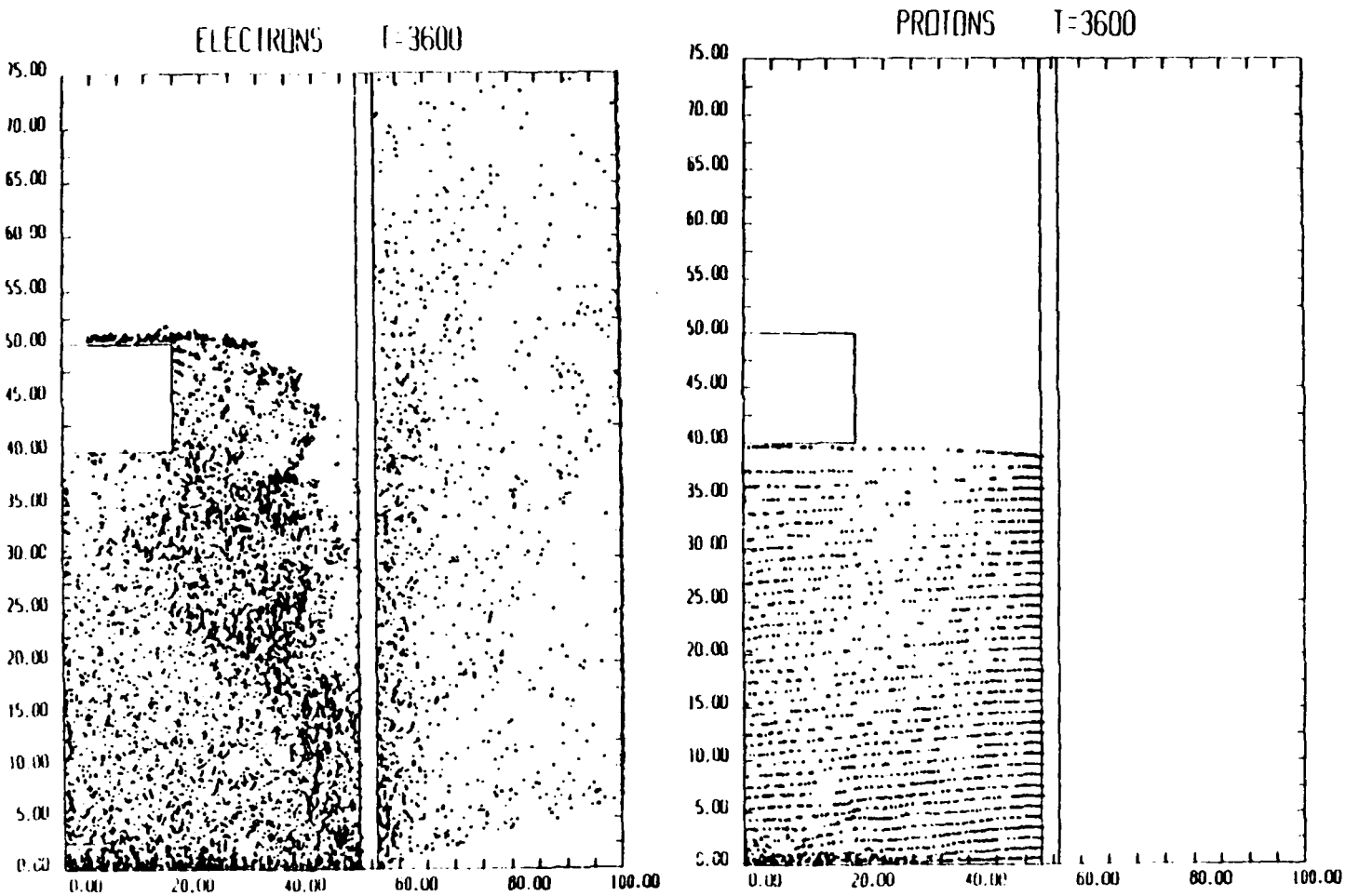

Fig. 12 — Steady-state particle positions for I_w = 130 kA

reflected back into the A-K gap will be quickly turned back into the gas cell. It "r" position will also be increased, resulting in a net outward radial electron flow. Thus, judging from the orbits of Figure 3 and 4, a typical electron might be bent back into the anode-cathode gap once below a radius of four centimeters. There, it will see a reverse B_θ approximately three times as great as that in the dam gas cell. After a gap drift time relatively short in comparison to that in the gas, the electron will be reflected back through the foil into a B_θ considerably weaker than that it had experienced in its previous trek through the gas. Thus, this "relative dwell time" problem snowballs with increasing radius as the gas B_θ decreases, while the gap B_θ increases. Reflected electrons spend progressively less a fraction of their time in the gap and progressively more in the gas at larger values of "r" where the larger electron gap dwell times would be felt over larger ion emission areas. In an attempt to redress this imbalance, a larger value of I_w was tested.

Although it would probably be somewhat difficult to accomplish experimentally, the current in the anode cell wire was boosted to 300 kA and the simulation was allowed to continue. A steady state was arrived at about T = 4800 Δt. The respective new flow patterns are presented in Figure 13. It would appear that an almost symmetric electron space-charge now hovers around the anode foil above about 1.5 centimeters radius. However, a large fraction of the electrons still penetrate a centimeter or more into the gas cell before reflection. This is in agreement with the predictions of Figure 4. The new currents are I_e = 338 kA and I_i = 256.5 kA yielding an even lower impedance and only slightly greater ion efficiency than those for the I_w = 130 kA case. The problem seems to be essentially the same as that for the previous case. An additional difficulty is suggested by the serious distortion of the mainstream shank electron flow away from the upper anode foil. This could easily cause degradation of the resultant ion emission.

All of these numerical results are summarized in Table 1. In this table, the term "ion production efficiency" is simply defined as I_{ion}/I_{diode}. Given the fixed voltage of the device, this ratio represents that fraction of the net diode power that has been imparted to the ions. The final two items in the tables are the total specie charges, Q, present in the diode/gas cell system. When these quantities have only small fluctuations during a simulation, one knows that the diode has reached an equilibrium state. Note the jump in Q_e when electrons are allowed to fill the gas cell for the I_w = 65 kA case. The steady reduction of Q_e in the subsequent two cases is indicative of the decreased volume accessible to the electrons in their more constrained excursions into the gas cell. Both I_i and Q_i steadily increase for increasing I_w, establishing the effectiveness of the dam at enhancing ion emission. The disappointing stagnation of the ion efficiency, combined with the consistent drop in diode impedance, however, indicates a proportional enhancement of electron emission.

The modest nature of the ion emission enhancement is obviated by Figure 14. For the higher values of I_w, otherwise significant gains in J_i on some regions of the anode foil are offset by the strong suppression of emission in other regions. This suppression is probably due to the deflection of the main cathode-shank-to-anode electron stream away from certain areas of the anode foil face. Nevertheless, there is a net gain in ion current. Thus, the true

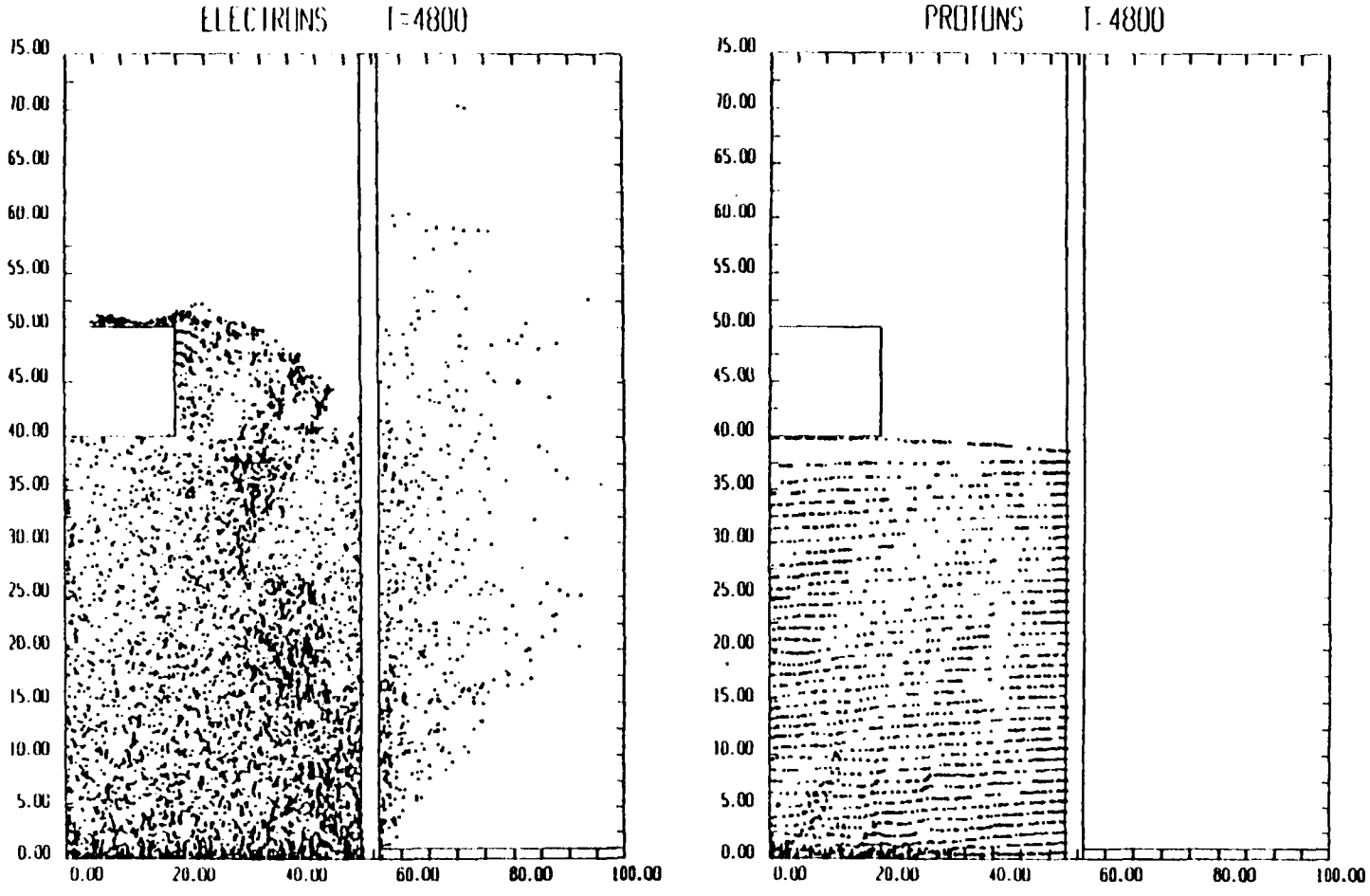

Fig. 13 — Steady-state particle positions for I_w = 300 kA

Table 1

I_{wire}(kA)	0	65	130	300
Simulation Timestep	2000	2400	3600	4800
$I_{electron}$(kA)	263.5	309	330	338
I_{ion}(kA)	214	232.5	244	256.5
I_{diode}(kA)	477.5	541.5	574	594.5
Ion Efficieny	0.448	0.429	0.425	0.431
Diode Impedence	8.4	7.4	7.0	6.7
Net Electron Charge (kilostatcoulombs)	-613	-898	-879	-782
Net Ion Charge (kilostatcoulombs)	+498	+539	+593	+615

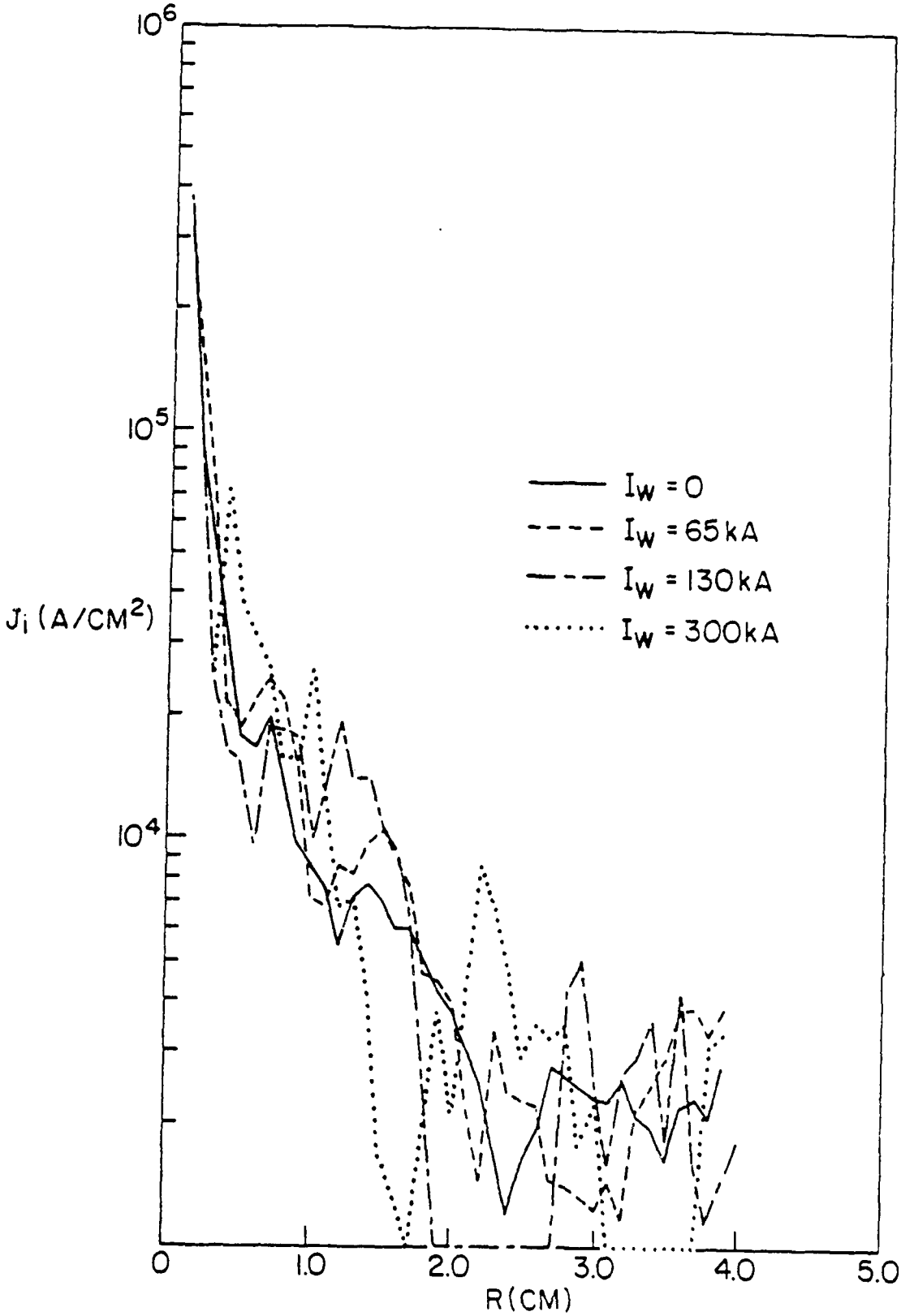

Fig. 14 — Emitted ion current density profiles along anode foil

obstacle to higher ion efficiency is the steady, net gain in electron current which results in a mild "bootstrapping"[7] of the total diode current with increasing I_w.

Some insight into the cause of this phenomenon may be derived from a comparision of the respective equilibrium equipotential plots for each of the four cases. These are presented in Figure 15. The plot for I_w = 65 is something of an anamoly. This is understandable, since it has not yet reached a true steady state. The other three plots, however, show a definite migration of the potential contours toward the face of the cathode shank. This corresponds to an increased emission there. Electron emission also increased along the cathode foil for larger values of I_w. Interestingly enough, the inner and outer shank surfaces showed a decrease in emitted electron current, perhaps due to the stronger insulating B_θ fields which accompanied the larger net diode currents.

In order to propose more meaningful solutions, it is first necessary to more closely isolate the source of the excess I_e. For that purpose, the radial profiles of emitted electron current densities along the cathode shank face are plotted in Figure 16. Above 4.7 centimeters, the curves are virtually identical. On the lower half of the face, however the difference is marked. This agrees with the electric field enhancement there suggested in Figure 15. In fact, a full 75% of each increase is accounted for by the increase of I_e from the shank face. Specifically, $(I_e)_{total}$ increased 66.5 kA between the I_w = 0 and I_w = 130 kA cases; the shank face electron emission had increased by 49 kA. The total increase between I_w =130 kA and I_w =300 kA amounted to only 8kA of electron current; 6 kA of this difference can be attributed to the shank face. Simply stated, it appears that enhanced ion emission at higher radii increases the positive ion space charge in the A-K gap near the shank face sufficiently to enhance electron emission there. This, in turn, prohibited any increase in net ion production efficiency.

In conclusion,therefore, the dam diode pictured in Figure 1 does not appear to be effective in boosting ion efficiency in its present form. It does produce enhanced ion current but does not simultaneously reduce the diode electron current. A large part of the blame rests on the rapid outward radial migration of electrons along the anode foil and on the large disparity between typical electron lifetimes in the gas cell versus those in the gap. This limits the number of electrons available in the upper A-K gap to neutralize the positive space charge arising there due to the increased ion flow. Hence electric fields and electron emission along the lower face of the cathode shank are made larger.

A modification which could possibly rectify this situation would be to invert the radial dependence of the magnetic field strength in the anode gas cell. If it were directly rather than inversely proportional to radius, then electron gyroradii would progressively decrease as they moved outward, increasing the "dwell time" of electron space charge in the crucial region between R = 3.0 and R = 5.0 centimeters. That would accomplish both an enhancement of ion emission over relatively large surface areas of the anode foil and also a probable suppression of electron emission along the cathode shank face located only one centimeter away. A possible alternative, and one easier to realize experimentally, is to absorb all electrons hitting the anode

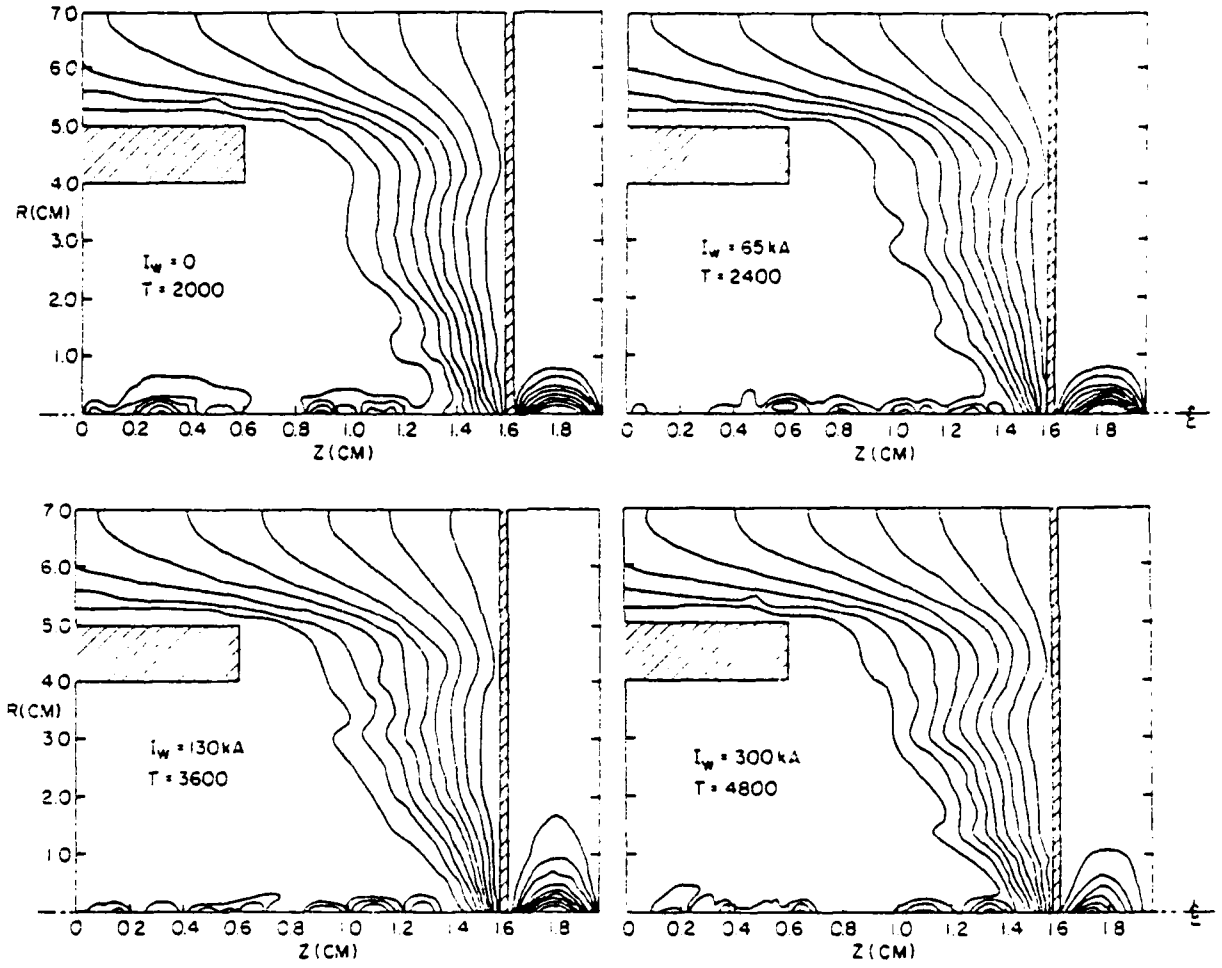

Fig. 15 — Steady-state equipotential contours for the four cases

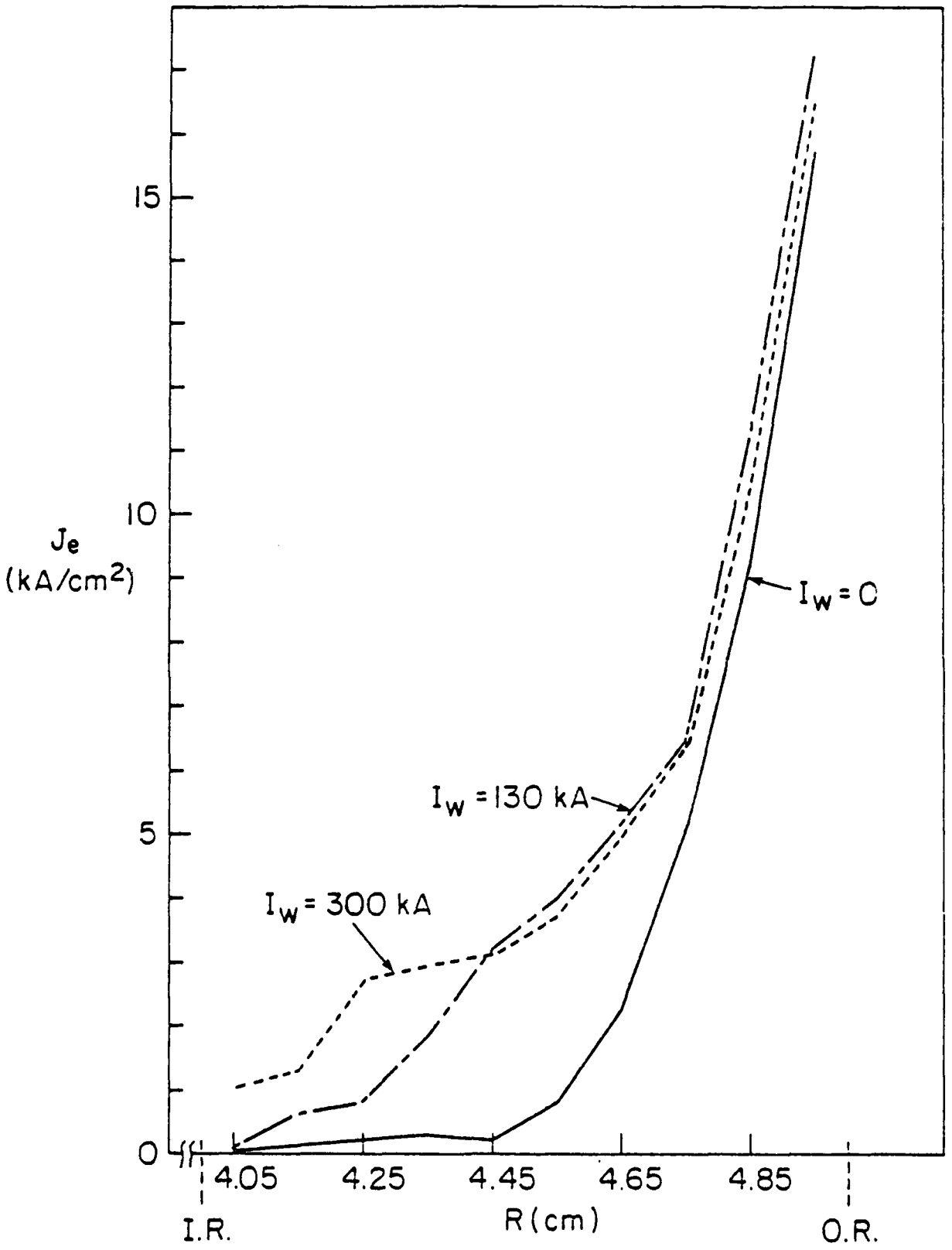

Fig. 16 — Radial profiles of electron emission along face of cathode shank

foil above, say, 3.0 centimeters while leaving the dam field inversely proportional to radius. This reduces the electron space charge near the anode foil above r=3, reducing the ion emission above r=3, reducing ion space charge in the gap above r=3, reducing electric field strengths at the cathode shank face, reducing electron emission there. This mandates an increase of this diode's impedance for a fixed gap and voltage. Both of the above modifications will be simulated in future computational experiments to test their ability to boost the ion production efficiency.

REFERENCES

1. S. J. Stephanakis, D. Mosher, Shyke A. Goldstein, W. F. Oliphant, Roswell Lee, and G. Cooperstein, Bull. Am. Phys. Soc. 22, 1130 (1977).

2. S. J. Stephanakis, J. R. Boller, G. Cooperstein, Shyke A. Goldstein, D. D. Hinshelwood, D. Mosher, W. F. Oliphant, F. Sandel, and F. C. Young, Bull. Am. Phys. Soc. 23, 907 (1978).

3. S. J. Stephanakis, J. R. Boller, G. Cooperstein, Shyke A Goldstein, D. D. Hinshelwood, D. Mosher, W. F. Oliphant, F. C. Young, R. D. Genuario, and J. E. Maenchen, Bull. Am. Phys. Soc. 24 , 1031 (1979).

4. S. A. Goldstein and P. F. Ottinger, JAYCOR Report No. TPD200-80-003-FR, (1980).

5. R. J. Barker, A. T. Drobot, Roswell Lee, and S. A. Goldstein, Proc. 9th Conference on the Numerical Simulation of Plasmas, Evanston, Ill. (1980).

6. R. J. Barker, Banach Center Publications 3, 255, Warsaw, Poland (1975).

7. R. J. Barker, S. A. Goldstein, and R. E. Lee, IEEE Int. Conf. on Plasma Science, Montreal, Canada (1979).

STEADY STATE NUMERICAL SOLUTION OF MAGNETICALLY INSULATED CHARGE FLOW IN COAXIAL GEOMETRY

I. INTRODUCTION

Impressive results have been achieved experimentally with the production of intense proton fluxes in radial diodes.[2-4] The high ion production efficiencies of these devices make them attractive candidates for use as driver sources in future ion beam inertial confinement fusion systems. In addition, magnetically insulated, coaxial vacuum feed lines[5-8] form an integral part of pulsed power systems for a wide variety of applications. Clearly, a computer code capable of predicting current flow in coaxial systems for realistic values of operational parameters would be a valuable tool. At the present time the only relativistic, two-specie, cylindrical geometry, theoretical formulation using cycloidal electron orbits is that of K. D. Bergeron.[1] Its foundation rests on the steady-state magnetic insulation model formulated independently by Sudan and Lovelace,[9,10] and at about the same time by Ron, Mondelli, and Rostoker.[11] In this model, electrons form a cloud near the cathode in which each electron traces an individual, single-arc trajectory which begins and terminates on the solid cathode surface (See Fig. 1.) All of these electrons see the full steady-state, self-consistent electric and magnetic fields during their entire orbit and all orbits are identical. There exists a competing magnetic insulation model formulated by Antonsen and Ott[12] and foreshadowed in the work of Creedon[13] and Buneman.[14] This model assumes that all electrons in the cathode sheath have been emitted from the cathode surface onto electrostatic equipotential contours during an adiabatically rising diode voltage pulse. In the equilibrium state, they $\vec{E} \times \vec{B}$ drift along their respective contours in a Brillouin[15] type flow, never again intersecting the cathode (See Fig. 1). This formulation is based on a vanishingly small Larmor radius approximation. The cylindrical geometry $\vec{E} \times \vec{B}$ drift model has recently been treated by Swegle and Ott.[16]

Manuscript submitted on September 9, 1981.

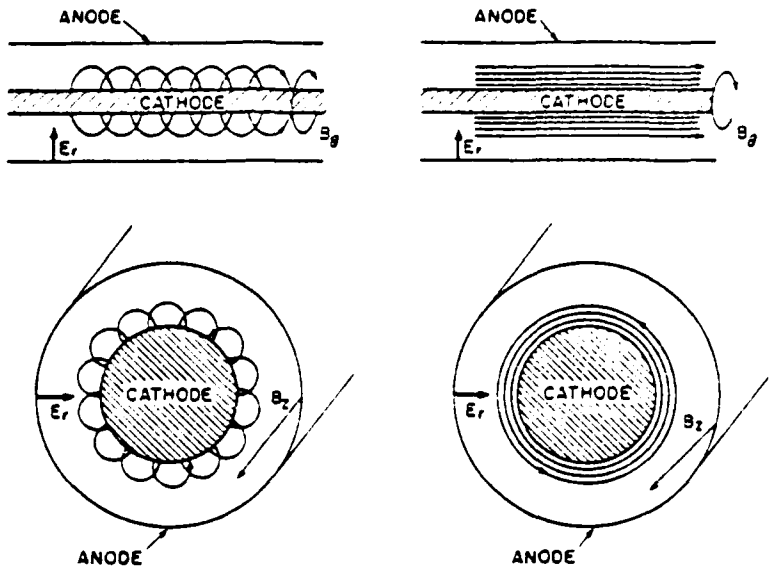

Fig. 1 — Two models for magnetically insulated electron flow: large orbit flow (left) and small larmor radius or Brillouin flow (right).

Both equilibrium models have equal physical validity. When applied to a given problem, they have led to very similar solutions,[17] however, stability properties could differ considerably. No sufficiently extensive analytic comparison has been performed on both models to justify the exclusion of one or the other for specific parameter ranges. However, there are conceptual weaknesses regarding the initiation of Brillouin flow in coaxial geometry. Certainly it can be postulated that appropriate injection mechanisms can be experimentally contrived, but this is not very satisfying when faced with the analysis of a general, uncontrived device. In addition, for the case of a radial diode with strong B_z insulation, the $\vec{E} \times \vec{B}$ drift is axial. In time, this would deplete any initial Brillouin electron population. Injection and replenishment problems do not exist for the Sudan and Lovelace formulation. For that reason, it was chosen for use in this analysis. In reality, it seems probable that some mixture of the two distributions exists in magnetically insulated coaxial lines with the Antonsen and Ott picture dominating early in time and progressively giving way to Sudan and Lovelace electrons later in the pulse. A number of computer simulations have been conducted which seem to support such a picture.[18]

II. THE THEORETICAL MODEL

Cross-sections of both polarity types of the coaxial geometry treated in this analysis are depicted in Fig. 2. Unless otherwise stated, the central conductor is assumed to be the cathode in the following discussion. The analysis for the case of a central anode is identical except for magnetic field boundary conditions discussed at the end of this section. The major assumptions of the model are as follows:

(1) All emitted electrons are confined to an azimuthally symmetric electron sheath of radius, r_S, and execute identical single-arc trajectories out to that radius. The magnetic insulation field, $\bar{B}$, moderately exceeds the critical insulation field (defined as that field value at which electron orbits just graze the anode surface), so that $r_S < r_A$, where r_A is the anode radius and the critical fields are defined as

$$(B_z)_{crit} = \frac{m_0 c^2}{e} \left(\frac{2 r_A}{r_A^2 - r_c^2} \right) \sqrt{U_0^2 - 2U_0} ,$$

and

$$(B_\theta)_{crit} = \frac{m_0 c^2}{e} \frac{0.2 \sqrt{U_0^2 + 2U_0}}{r_c \, 2 \ln \left(\frac{r_A}{r_c} \right)} .$$

Here r_c is the cathode radius and U_0 is the diode voltage multipled by $\frac{e}{m_0 c^2}$.

(2) The time-scale is such that the self-magnetic fields do not significantly penetrate the anode and cathode surfaces.

(3) The electrons are treated relativistically and the ions nonrelativistically (a reasonable approximation for voltages below 10 MV).

(4) The ion current is strictly radial. This implies no significant ion contribution to the self magnetic field. (The angular deflection suffered by an ion is on the order of $\sqrt{\frac{m_0}{M_0}} \frac{B}{B_{crit}}$ radians. Therefore, even if $B = 4B_{crit}$ an ion would experience less than 0.1 radian deflection.)

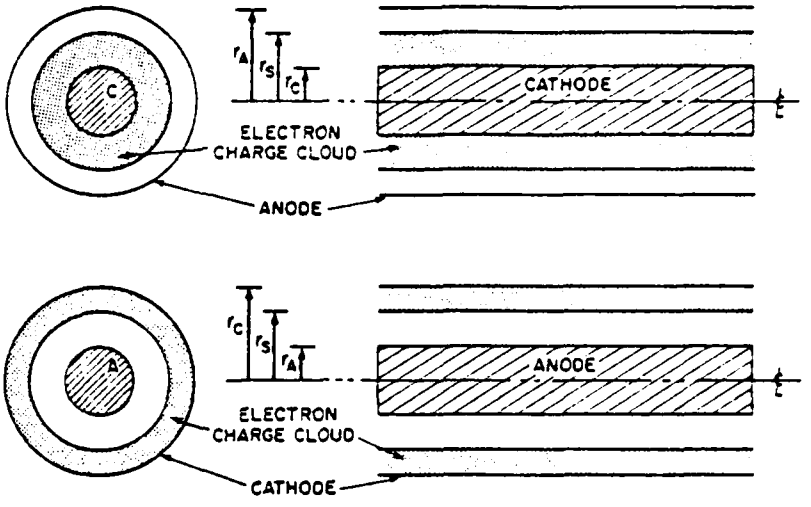

Fig. 2 — Coaxial, magnetic insulation geometries of the negative polarity (top) and positive polarity (bottom) types.

One characterizes the electron (ion) beam by a velocity $\bar{v}$ ($\bar{V}$), charge density $n(N)$, and current density $\bar{j} = n\bar{v}(\bar{J} = N\bar{V})$. Conservation of relativistic electron energy requires that

$$\gamma m_0 c^2 - e\phi(r) = m_0 c^2, \tag{1}$$

where $\gamma = \left[1 - \frac{v^2}{c^2}\right]^{-1/2}$. Conservation of canonical momentum demands that

$$\gamma m_0 v_{\theta} - \frac{e}{c} A_{\theta} = 0, \tag{2}$$

where the θ subscript refers to the $\bar{E} \times \bar{B}$ direction. Finally, conservation of ion energy states that

$$V_r = \sqrt{\frac{2e}{M_0}}\sqrt{\phi_0 - \phi}, \tag{3}$$

where ϕ_0 is the imposed diode voltage. Continuity of diode current flux provides two additional constants, $F = r|J_r|$ and $f = -r|j_r|$. Employing all of these relations allows one to reduce Poisson's equation and Ampere's law to

$$\nabla^2\phi(r) = \frac{4\pi}{r}\left[2\left|\frac{f}{v_r}\right| - \left|\frac{F}{V_r}\right|\right], \tag{4}$$

and

$$(\bar{\nabla} \times (\bar{\nabla} \times \bar{A}(r)))_{\theta} = -4\pi\left|\frac{2f}{cr v_r}\right| v_{\theta}. \tag{5}$$

The factors of two for the electron flux terms reflect the presence of both radially inward and radially outward components to the electron current in the electron cloud. This doubling of the electron flow is specifically mentioned by Bergeron if Ref. 1; however, it is not present in his Eqs. (35) and (36).

Numerical considerations encourage the substitution of appropriately scaled dimensionless variables in place of those appearing in Eqs. (4) and (5). Following Bergeron, the terms employed in this analysis are $U \equiv \frac{e}{m_0 c^2}\phi$, $W \equiv \frac{e}{m_0 c^2} A_\theta$ [or $W \equiv -\frac{e}{m_0 c^2} A_z$ for an *azimuthal* insulating field], and $\lambda \equiv \frac{4\pi}{cB_0}\sqrt{\frac{M_0}{m_0}}\,|F|$. The electron flux term is modified by the additional factor of two mentioned above, giving $\lambda \equiv \frac{8\pi}{cB_0}\,|f|$. A significant modification to Bergeron's treatment can be found in the new scale chosen for the independent radial variable. It is here defined as $\rho \equiv \frac{eB_0}{m_0 c^2} r$ where B_0 is chosen to be some typical magnetic field strength. In contrast, Bergeron scales r to the electron gyroradius in the presence of the magnetic field at the cathode surface. Such a scaling provides one with a simple boundary condition for the first derivation of W at ρ_c, namely $\left.\frac{dW}{d\rho}\right|_{\rho=\rho_c} = 1$. However, the value of $\overline{B}$ at $\rho = \rho_c$ is known *a priori* only for the case of an azimuthal insulation field with the cathode as the central conductor. In addition, the possibility of the magnetic field strength approaching and even equaling zero at the cathode surface for the other cases cannot be discarded. Such an eventuality would make nonsense of any solutions using Bergeron's scaling and may, at least in part, explain the lack of closed solutions Bergeron noted in some parameter regimes.

Given these definitions, Eqs. (4) and (5) reduce to

$$\rho\,\frac{d^2U}{d\rho^2} + \frac{dU}{d\rho} = \frac{\lambda(1+U)}{\sqrt{U^2 - 2U - W^2}} - \frac{\lambda}{\sqrt{U_0 - U}}, \tag{6}$$

and

$$\rho\,\frac{d^2W}{d\rho^2} + \frac{dW}{d\rho} = \frac{\lambda W}{\sqrt{U^2 + 2U - W^2}} + \epsilon\,\frac{W}{\rho}, \tag{7}$$

with $\epsilon = 0$ for azimuthal insulation and $\epsilon = 1$ for the axial case. The boundary conditions for axial insulation are

$$U(\rho_c) = W(\rho_c) = \left.\frac{dU}{d\rho}\right|_{\rho_c} = 0, \tag{8}$$

at the cathode while at the anode

$$U(\rho_A) = U_0 \text{ and } \left.\frac{dU}{d\rho}\right|_{\rho_A} = 0. \tag{9}$$

The conditions governing the first derivative of U follow directly from the assumption of space charge limited, Gaussian emission at both surfaces. (However, if an equilibrium solution is sought for which $\Lambda = 0$, then the value of the electric field at the anode cannot be assumed to vanish.) Such an emission mechanism in turn presumes a sufficiently dense plasma to exist at both surfaces. We now have a set of two second order equations in U and W, with two additional unknowns, λ and Λ. Six boundary conditions are therefore necessary for a solution. In addition to the five conditions stated in Eqs. (8) and (9), for the case of axial magnetic insulation, the final condition results from conservation of the magnetic flux,

$$\Phi_M = \int_S \bar{B} \cdot d\bar{a} = \oint_C \bar{A} \cdot d\bar{S},$$

over a fixed cross sectional surface area, S, enclosed by the line contour, C. Specifically, it is assumed that the insulating B-field is present before emission begins and that any diffusion of the field into the electrodes is insignificant over the time scale of the voltage pulse. For the case of an initially uniform, axial insulating field, B_0, which is taken as the scaling field for ρ, this condition implies

$$W(\rho_A) = \frac{\rho_A^2 - \rho_c^2}{2\rho_A}. \tag{10}$$

On the other hand, for an azimuthal insulating field, magnetic flux is not conserved. In place of Eq. (10) one is given the known magnetic field strength at the surface of the central conductor,

$$B_{c.c.} = 0.2\,\frac{I_{c.c.}}{R_{c.c.}}, \tag{11}$$

where $B_{c.c.}$ is in gauss, $R_{c.c.}$ is the radius of the central conductor measured in centimeters and $I_{c.c.}$ is the current in amperes flowing through the central conductor. Therefore, the final boundary condition for the azimuthal field case is simply

$$\left.\frac{dW}{d\rho}\right|_{\rho_{c.c.}} = \frac{B_{c.c.}}{B_0}, \tag{12}$$

where B_0 is the arbitrary scale field and $\rho_{c.c.}$ may be either ρ_A or ρ_c, depending upon the geometry chosen. (When $B_0 = B_{c.c.}$ and $\rho_{c.c.} = \rho_c$, this reduces to Bergeron's boundary condition.) For the case of a magnetically self-insulated vacuum feed line, the value of $I_{c.c.}$ is a known (or at least independently derivable) quantity. On the other hand, $I_{c.c.}$ is not known *a priori* for a radial diode. In this device, the central conductor current will generally be a function of the axial dimension, z. Furthermore, the total current, $I_{c.c.}$, flowing through the diode will be entirely due to ion flow through the A-K gap and will be given in statamps by

$$I_{c.c.} = 2\pi |rJ_r| L,$$

or

$$I_{c.c.} = 2\pi L\left[\frac{cB_0}{4\pi}\sqrt{\frac{2m_0}{M_0}}\,\Lambda\right], \tag{13}$$

where L is the axial half-length of the gap. In order to clarify the distinctions between the axial versus the azimuthal boundary conditions and unknowns, they are grouped accordingly in Table 1.

For both cases, the numerical integration of Eqs. (6) and (7) begins at the cathode radius, ρ_c. For a configuration with B_z insulation, values are guessed for λ, Λ, and $W'(\rho_c)$. Then U, U', and W are integrated out to the anode radius and their boundary values are compared to those given in (9) and (10). Repeated guesses for λ, Λ, and $W'(\rho_c)$ are made until a match-up at ρ_A is achieved. For B_θ insulation with the cathode as the central conductor, an additional starting condition is given in the form of Eq. (12). This simplifies the problem considerably. Only the two anode conditions given by Eq. (9) must be matched and only values for λ and Λ must be sought by iterative guesses. Finally, for the azimuthal case with the anode as the central conductor, the guessed parameters become λ, $W'(\rho_c)$, and $I_{c.c.}$. The three conditions which must be matched at ρ_A are now given by Eqs. (9) and (12). It

Table 1. Matrix of Knowns, Unknowns, and Boundary Conditions.

Insulating B-field Type	AXIAL		AZIMUTHAL			
Relative A-K Positions	either		cathode inside		cathode outside	
Ions Present ?	Yes	No	Yes	No	Yes	No
Input Parameters	$(B_z)_o$	$(B_z)_o$	L	$I_{c.c.}$	L	$I_{c.c.}$
Input $\rho = \rho_c$ Guesses	j, J, and W'	j, W'	j, J	j	j, J and W'	j, W'
Output Quantities to be matched at $\rho=\rho_A$ and at $\rho = \rho_S$	U, U', and W	U, W	U, U'	U	U, U', and W'	U, W'
Universal Input	r_A, r_C, φ_o, LAZ, LCIN, and LIONS					
Universal Output	Radial Profiles of φ and B					

where: r_A (r_C) = anode (cathode) radius in centimeters,
φ_o = A-K potential difference in volts,
$(B_z)_o$ = imposed insulating axial magnetic field strength in gauss,
L = axial length of A-K gap in centimeters,
$I_{c.c.}$ = current flowing in the central conductor in amperes, and
j (J) = electron (ion) current density at cathode in amp/cm^2.

will be shown in the next section that analytic solutions are available for the region between ρ_A and ρ_S. This allows for numerical solution matching at ρ_S instead of at ρ_A with a considerable gain in accuracy.

A problem arises when solutions are sought for radial diodes in which both axial *and* azimuthal magnetic insulating fields are present. If no B_z is imposed in the A-K gap, then only pure azimuthal insulation is possible and no conflict can arise. When an axial insulation case with ion flow is being studied, however, it is inevitable that a B_θ be generated as well. The strength of this B_θ in the A-K gap can be predicted directly from the value of Λ obtained in the pure B_z solution. If this field strength is comparable to or greater than the imposed B_z, the numerical formulation presented here has more limited value for predicting actual diode operating characteristics. (See Appendix B.)

III. THE COMPUTATIONAL FORMULATION

As previously stated, the solution of Eqs. (6) and (7), combined with the boundary conditions in Eqs. (8) and (9), will be carried out as a three-parameter "shooting" problem. Values must be guessed for λ, Λ, and $\left.\frac{dW}{d\rho}\right|_{\rho_c}$ and the equations then integrated from ρ_c to ρ_A. The correctness of a given guess is determined by the accuracy with which generated function values match with known solutions at ρ_A and ρ_S. In undertaking the numerical integration of Eqs. (6) and (7), special attention must be paid to three separate values of ρ at which certain terms on the right hand side become singular. Specifically, the denominator of the electron current term vanishes at $\rho = \rho_c$, since both U and W are defined to be equal to zero there. It also vanishes at the electron sheath boundary, $\rho = \rho_S$, as would be expected, since this quantity represents the radial component of the electron velocity. The final singularity occurs at $\rho = \rho_A$ where the ion current term in Eq. (6) becomes infinite. Brute force numerical procedures cannot cope with integrations in the neighborhood of these singular points. Instead, analytic treatments expanding about the singularities produce approximate explicit solutions valid in the pathological regions near ρ_c and ρ_S. This technique provides the numerical quadrature with tractable starting values at $\rho = \rho_c + \Delta\rho$. The numerics may be relied upon from that point up to about $\rho = \rho_S - \Delta\rho$ at which radius another analytic approximation advances the solution to ρ_S. Beyond that point, λ equals zero. Equations (6) and (7) have straightforward analytic solutions spanning $\rho_S < \rho \leqslant \rho_A$ which can be used to accurately advance U, W $\left[\text{or } \frac{dW}{d\rho}\right]$, and $\frac{dU}{d\rho}$ at $\rho = \rho_S$ out to the anode radius. In this manner, the numerical singularity at $\rho = \rho_A$ need never be faced directly.

The numerical solution of Eqs. (6) and (7) begins with the derivation of an explicit functional expression for the radial variations of U and W in the immediate vicinity of the cathode surface. For $\rho = \rho_c - r$ where $r << \rho_c$, the equations can be expanded and solved in terms of a triple power series with solutions

$$U = \left[\frac{r}{\rho_c}\right] \sum_{n=0}^{\infty} a_n^{(1)} \left[\frac{r}{\rho_c}\right]^n + \left[\frac{r}{\rho_c}\right]^{4/3} \sum_{n=0}^{\infty} a_n^{(4/3)} \left[\frac{r}{\rho_c}\right]^n + \left[\frac{r}{\rho_c}\right]^{5/3} \sum_{n=0}^{\infty} a_n^{(5/3)} \left[\frac{r}{\rho_c}\right]^n, \tag{14}$$

$$W = \left(\frac{r}{\rho_c}\right) \sum_{n=0}^{\infty} b_n^{(1)} \left(\frac{r}{\rho_c}\right)^n + \left(\frac{r}{\rho_c}\right)^{4/3} \sum_{n=0}^{\infty} b_n^{(4/3)} \left(\frac{r}{\rho_c}\right)^n + \left(\frac{r}{\rho_c}\right)^{5/3} \sum_{n=0}^{\infty} b_n^{(5/3)} \left(\frac{r}{\rho_c}\right)^n. \tag{15}$$

Straightforward calculus and algebra may then be used to isolate the leading order terms,

$$U = \frac{3}{2}\left[\frac{3\lambda^2\rho_c^2}{4}\right]^{1/3}\left(\frac{r}{\rho_c}\right)^{4/3} + \left[\frac{b_c^2\rho_c^2}{20} - \frac{9\Lambda\rho_c}{20U_0^{1/2}}\right]\left(\frac{r}{\rho_c}\right)^2, \tag{16}$$

and

$$W = (-1)^{\epsilon+1} b_c r\left[1 - \frac{1}{2}\left(\frac{r}{\rho_c}\right) + \frac{9}{28}\left[\frac{2\lambda^2\rho_c^2}{9}\right]^{1/3}\left(\frac{r}{\rho_c}\right)^{4/3}\right], \tag{17}$$

where the term $b_c \equiv \dfrac{B(\rho_c)}{B_0}$ is presently unknown and where the solutions are only valid for

$$\frac{r}{\rho_c} < Min\left[\frac{40}{9}\left[\frac{10}{3}\right]^{1/2}\frac{\lambda V_0^{3/4}}{\Lambda^{3/2}\rho_c^{1/2}},\ \frac{9\lambda}{2b_c^3\rho_c^2}\right]. \tag{18}$$

Equation (18) places an upper limit on the initial step size. All but the ion term in Eq. (16) had been predicted by the leading order terms of an expression due to Goldstein[19] which corrected the Child-Langmuir emission law to include transverse magnetic field effects. The first derivatives of equations (16) and (17) are simply

$$U' = \frac{dU}{d\rho} = \frac{dU}{dr} = 2\left[\frac{3}{4}\frac{r}{\rho_c^2}\right]^{1/3}\lambda^{2/3} + \frac{r}{10}\left[b_c^2 - \frac{9\Lambda}{\rho_c U_0^{1/2}}\right], \tag{19}$$

and

$$W' \equiv \frac{dW}{d\rho} = \frac{dW}{dr} = (-1)^{\epsilon+1} b_c\left[1 - \frac{r}{\rho_c} + \frac{3}{4}\left[\frac{2}{9}\lambda^2\rho_c^2\right]^{1/3}\left(\frac{r}{\rho_c}\right)^{4/3}\right]. \tag{20}$$

For purposes of the overall numerical quadrature of Eqs. (6) and (7), the gap region between ρ_c and ρ_A is divided up into some predetermined number of identical, one-dimensional cells of width, $\Delta\rho$. The above approximations are used to advance the solution of U, W, U', and W' over the first $\Delta\rho$ away from the $\rho = \rho_c$ singularity point.

The bulk of the remaining numerics is accomplished using a proven predictor-corrector scheme. Unfortunately, this scheme requires a knowledge of functional values at four prior spatial steps in order to advance an additional $\Delta\rho$. In order to obtain those additional values at the start of the integration, a

fourth-order Runga Kutta scheme is employed.[20] For this, as well as for the predictor-corrector, the set of two second-order D.E.'s is reduced to a set of four first-order D.E.'s as follows:

$$U' \equiv X, \tag{21}$$

$$X' = \frac{\lambda(1+U)}{\rho\sqrt{S}} - \frac{\lambda}{\rho\sqrt{U_0 - U}} - \frac{X}{\rho}, \tag{22}$$

$$W' \equiv Y, \text{ and} \tag{23}$$

$$Y' = \frac{\lambda W}{\rho\sqrt{S}} + \frac{W}{\rho^2} - \frac{Y}{\rho}, \tag{24}$$

where $S \equiv U^2 + 2U - W^2$. Each expression is then in the form $\eta' = f_\eta(\rho, U, W, X, Y)$ and can be advanced one $\Delta\rho$ at a time using the standard R-K approximation,

$$\eta_{n+1} = \eta_n + \frac{1}{6}(k_{\eta 1} + 2k_{\eta 2} + 2k_{\eta 3} + k_{\eta 4}),$$

where

$$k_{\eta 1} = \Delta\rho f_\eta(\rho_n, U_n, W_n, X_n, Y_n),$$

$$k_{\eta 2} = \Delta\rho f_\eta(\rho_n + \frac{1}{2}\Delta\rho, U_n + \frac{1}{2}k_{U1}, W_n + \frac{1}{2}k_{W1}, \ldots),$$

$$k_{\eta 3} = \Delta\rho f_\eta(\rho_n + \frac{1}{2}\Delta\rho, U_n + \frac{1}{2}k_{U2}, W_n + \frac{1}{2}k_{W2}, \ldots),$$

$$k_{\eta 4} = \Delta\rho f_\eta(\rho_n + \Delta\rho, U_n + k_{U3}, W_n + k_{W3}, \ldots).$$

Thereafter, the Adams-Bashforth-Moulton predictor-corrector scheme[21] advances the variables in a two-step process:

$$(\eta_{n-1})_{\text{predicted}} = \eta_n + \frac{\Delta\rho}{24}(55\eta'_n - 59\eta'_{n-1} + 37\eta'_{n-2} - 9\eta'_{n-3}),$$

and

$$(\eta_{n-1})_{\text{corrected}} = \eta_n + \frac{\Delta\rho}{24}(9\eta'_{n+1} + 19\eta'_n - 5\eta'_{n-1} + \eta'_{n-2})$$

where η'_{n+1} has been calculated using the predicted value for η_{n-1}. An error check is accomplished by monitoring the magnitude of $|(\eta_p - \eta_c)/\eta_p|$ where η_p and η_c are the predicted and corrected values of η, respectively.

The above predictor-corrector process is continued until the electron sheath radius, ρ_S, is reached. At that point, another analytic approximation must be found in order to correctly advance the function values past the numerical singularity there. This is accomplished by expanding Eqs. (6) and (7) about ρ_S in a power series. One may write $\rho = \rho_S - r$, $U = U_S + \hat{U}$, and $W = W_S + \hat{W}$ where

$$\rho_S >> r > 0,$$

$$\hat{U} = a_0 r^{\alpha_0} + a_1 r^{\alpha_1} + a_2 r^{\alpha_2} + \ldots,$$

$$\hat{W} = b_0 r^{\beta_0} + b_1 r^{\beta_1} + b_2 r^{\beta_2} + \ldots,$$

and

$$U_S^2 + 2U_S - W_S^2 = 0.$$

Equations (6) and (7) can then be expanded and solved. The leading terms of the solutions are

$$U = U_S + a_0 r + a_1 r^{3/2} + a_2 r^2, \tag{25}$$

and

$$W = W_S + b_0 r + b_1 r^{3/2} + b_2 r^2, \tag{26}$$

where

$$2(1 + U_S)a_0 - 2W_S b_0 > 0,$$

$$a_1 = \frac{4\lambda(1 + U_S)}{3\rho_S[2(1 + U_S)a_0 - 2W_S b_0]^{1/2}},$$

$$b_1 = \frac{4\lambda W_S}{3\rho_S[2(1 + U_S)a_0 - 2W_S b_0]^{1/2}},$$

$$a_2 = \frac{(a_0 - \Lambda/(U_0 - U_S)^{1/2})}{2\rho_S},$$

and

$$b_2 = \frac{(b_0 - \epsilon W_S/\rho_S)}{2\rho_S}.$$

As is obvious from Eqs. (25) and (26), the coefficients a_0 and b_0 are merely the negative first derivatives of U and W, respectively at ρ_S (i.e., $a_0 = -U_S' = -X_S$ and $b_0 = -W_S' = -Y_S$). Having used Eqs. (25) and (26) to obtain U_S, W_S, X_S and Y_S, the numerical integration of Eqs. (6) and (7), with λ now set equal to zero, may resume. In the RADBER code, however, explicit analytic expressions are used to match all functions of interest at ρ_S from the known values at the anode radius.

Beyond the electron sheath radius, the key deterministic equations for the electrostatic and magnetostatic potentials become

$$\rho \frac{d^2U}{d\rho^2} + \frac{dU}{d\rho} = \frac{\Lambda}{\sqrt{U_0 - U}}, \tag{27}$$

and

$$\rho \frac{d^2W}{d\rho^2} + \frac{dW}{d\rho} = \epsilon \frac{W}{\rho}. \tag{28}$$

Equation (27) takes the same form as the equation treated by Langmuir in his 1913 paper[22] and later treated in greater depth for coaxial geometry in a subsequent paper by Langmuir and Blodgett.[23] The solution to the equation is therefore

$$U = U_0 - \left[\frac{9}{4}\,\rho\beta^2\Lambda\right]^{2/3} \tag{29}$$

where $\beta = \Sigma A_n \gamma^n$ and $\gamma \equiv \ln\left[\frac{\rho}{\rho_A}\right]$. The first 14 values of the coefficients, A_n, are listed in Blodgett's paper. Knowing the values of U_0, Λ, ρ_A, and ρ_S, a value for U_S may be calculated using Eq. (29). This value is then compared to that found via the numerical integration of Eq. (6) out from ρ_c. The closeness of the match is used to measure the accuracy of the original set of parameter guesses. For the case where $\Lambda = 0$ (i.e., no ion flow) Eq. (27) becomes

$$\rho\,\frac{d^2U}{d\rho^2} + \frac{dU}{d\rho} = 0, \tag{30}$$

with solution

$$U = U_S + X_S\rho_S \ln\left[\frac{\rho}{\rho_S}\right], \tag{31}$$

and the same matching procedure for U_S may be carried out. Similarly, the solutions to Eq. (28) take the form

$$W = \begin{cases} \left[W_S - \dfrac{a_{01}}{\rho_S}\right]\dfrac{\rho}{\rho_S} + \dfrac{a_{01}}{\rho}, & \epsilon = 1 \\ W_S + a_{02}\ln\left[\dfrac{\rho}{\rho_S}\right], & \epsilon = 0 \end{cases} \tag{32}$$

Matching the solutions for the first derivatives at $\rho = \rho_S$ demands that $a_{01} = \frac{1}{2}\,(W_S\rho_S - Y_S\rho_S^2)$ for the $\epsilon = 1$ case and $a_{02} = Y_S\rho_S$ for the $\epsilon = 0$ case. Equations (29), (31), and (32) may be used to obtain values for U_S, X_S, W_S, and Y_S in terms of known quantities. Depending upon the specific configuration under study, some subset of those four values (see Table 1) are matched to the corresponding values on the cathode side of the electron sheath boundary as obtained from Eqs. (25) and (26). The closeness of that fit at $\rho = \rho_S$ of the two sets of solutions forms the final, most accurate test of the validity of the original parameter guesses.

IV. APPROXIMATE ANALYTIC SOLUTION

For the case of low voltages and with geometries whose anode-cathode gap is much smaller than the radius of the outer conductor, complete, approximate analytic solutions can be obtained by matching the analytic solutions near the cathode given in Eqs. (16)-(20) with the solutions valid near the electron sheath radius given in Eqs. (25) and (26). The solutions are matched at $\rho_1 = (\rho_c + \rho_S)/2$ by requiring that U, W, U', and $B/B_0 = (W' + \epsilon W/\rho)$ all be continuous at $\rho = \rho_1$. At $\rho = \rho_S$ the solution given in Eqs. (25) and (26) is also matched in the same manner with the solution valid for $\rho_S \leqslant \rho \leqslant \rho_A$. There one finds

$$U = U_0 - \left(\frac{9}{4}\,\Lambda\rho_A\right)^{2/3}\left(\frac{r}{\rho_A}\right)^{4/3}, \tag{33}$$

and

$$W = \begin{cases} \dfrac{b_A}{2}\left[\rho - \dfrac{\rho_S^2}{\rho}\right] + \dfrac{\rho_S W_S}{\rho}, & \text{for } \epsilon = 1 \\ W_S + \rho_A b_A \ln\left[\dfrac{\rho}{\rho_S}\right], & \text{for } \epsilon = 0 \end{cases}, \tag{34}$$

where $r \equiv \rho_A - \rho$ and $b_A \equiv B(\rho_A)/B_0$. Equation (33) is equivalent to the limit of Eq. (29) for $r \ll \rho_A$. Likewise, Eq. (34) follows from Eq. (32) when a_0 is obtained by imposing the boundary conditions at $\rho = \rho_A$ instead of at $\rho = \rho_S$. For $\epsilon = 1$, flux conservation fixes the value of $W(\rho = \rho_A)$ (see Eq. (10)) and yields $b_A = [(\rho_A^2 - \rho_c^2)/(\rho_A^2 - \rho_S^2) - 2\rho_S W_S/(\rho_A^2 - \rho_S^2)]$. For the azimuthal field case ($\epsilon = 0$), on the other hand, $b_A = Y_A$ in agreement with Eq. (32) since the field outside the sheath is constant. In order to complete the overall solution for this analytic approximation one must also use the relationship, $U_S^2 + 2U_S - W_S^2 = 0$, and also $b_c = 1$ for the $\epsilon = 0$ case. There is now enough information with which to construct a composite solution.

For the case where the central conductor is the cathode, one finds that for both $\epsilon = 0$ or 1, an analytic solution is possible as long as the diamagnetic electron current does not significantly alter the magnetic field. In this case B_0 is approximately given by the applied field,

$$\frac{J(\rho_A)}{J_{CL}} = \left[\frac{6}{7}\right]^{3/2} \frac{d^2(U_S/U_0)^{3/2}}{[d - (U_S^2 + 2U_S)^{1/2}](U_S^2 + 2U_S)^{3/4}}, \tag{36}$$

$$\frac{j(\rho_c)}{j_{CL}} = \frac{6}{7}\left[\frac{3}{7}\right]^{1/2} \frac{d^2(U_S/U_0)^{3/2}}{(U_S^2 + 2U_S)}, \tag{37}$$

and

$$\rho_S - \rho_c = (U_S^2 + 2U_S)^{1/2}, \tag{38}$$

where $d = \rho_A - \rho_c$ and $j_{CL} = \left[\frac{m_i}{m_e}\right]^{1/2} J_{CL} = (2e/m_e)^{1/2}\ \phi_0^{3/2}/9\pi(r_A - r_c)^2$. The sheath potential needed to complete Eqs. (36)-(38) is defined by the transcendental equation

$$U_0 = \frac{U_S}{7}\left[1 + \frac{6d}{(U_S^2 + 2U_S)^{1/2}}\right]. \tag{39}$$

The ion production efficiency of the diode, $\eta = J/(J + j)$, can be easily obtained from Eqs. (36) and (37). Plots of J and $\rho_S - \rho_c$ are shown in Figs. (3) and (4) as solid lines. The validity of the results becomes suspect beyond $e\phi_0/m_e c^2 \sim 1$. Note that $|\rho_A - \rho_c| = d << \rho_A$ was also assumed which implies these results only apply to large radius structures with small anode-cathode gaps (i.e., large aspect ratio devices). For higher voltages and smaller aspect ratio devices the RADBER code is needed since in these cases the simple matching technique used to form the composite analytic solution is no longer possible. This results from the decreasing range of validity of the expansions used to obtain the solution. In any case, however, these approximate solutions may be used to provide reasonable starting parameter guesses for the RADBER code.

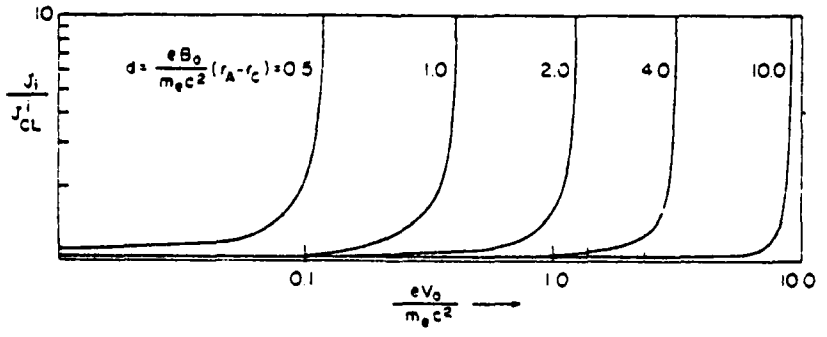

Fig. 3 — Analytic estimates for ion current enhancement

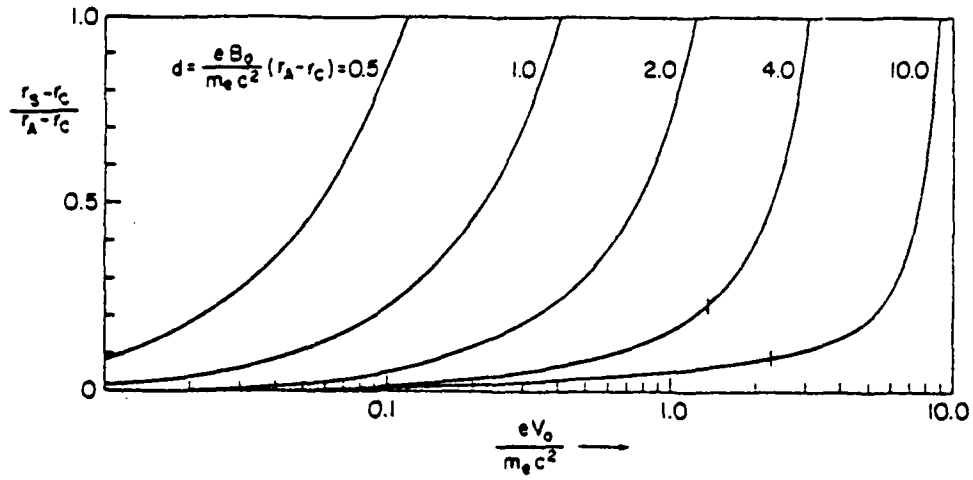

Fig. 4 — Analytic estimates for electron sheath thickness

V. THE NUMERICAL TREATMENT

The RADBER computational package consists of a main core program and four subprograms: START, PRIME, BOUND, and MATCH. All of these program elements are listed in their entirety in Appendix A. They are written in a version of FORTRAN compatible with the Texas Instruments Advanced Scientific Computer.[24] Every effort was made to avoid non-standard terminology. Nevertheless, the need for minor changes can be anticipated when implementing this code at any other computer facility. Particularly prone to such changes are the data input/output statements. For that reason, I/O formats were left as simple as possible. A particularly strong point of the code is its vectorized format. This allows for the simultaneous, step-by-step integration of U' and W for a large number of λ and Λ guesses in a "shotgun" fashion. The average cost for the complete integration of Eqs. (6) and (7) over 500 steps from ρ_c to ρ_4 for a single $(\lambda, \Lambda, W'(\rho_c))$ guess was about $0.025. (CPU rates are over $900/hour on the ASC at NRL.)

The basic flow chart for RADBER is shown in Fig. 5. In the main program, data input begins with a choice for the parameter, NDR, the number of radial steps across the anode-cathode gap. The default value, as shown, is 500. The specific physical and numerical parameters for the problem under study are fed in through the NAMELIST's, GUESS and GIVEN. For the sake of practicality, the code

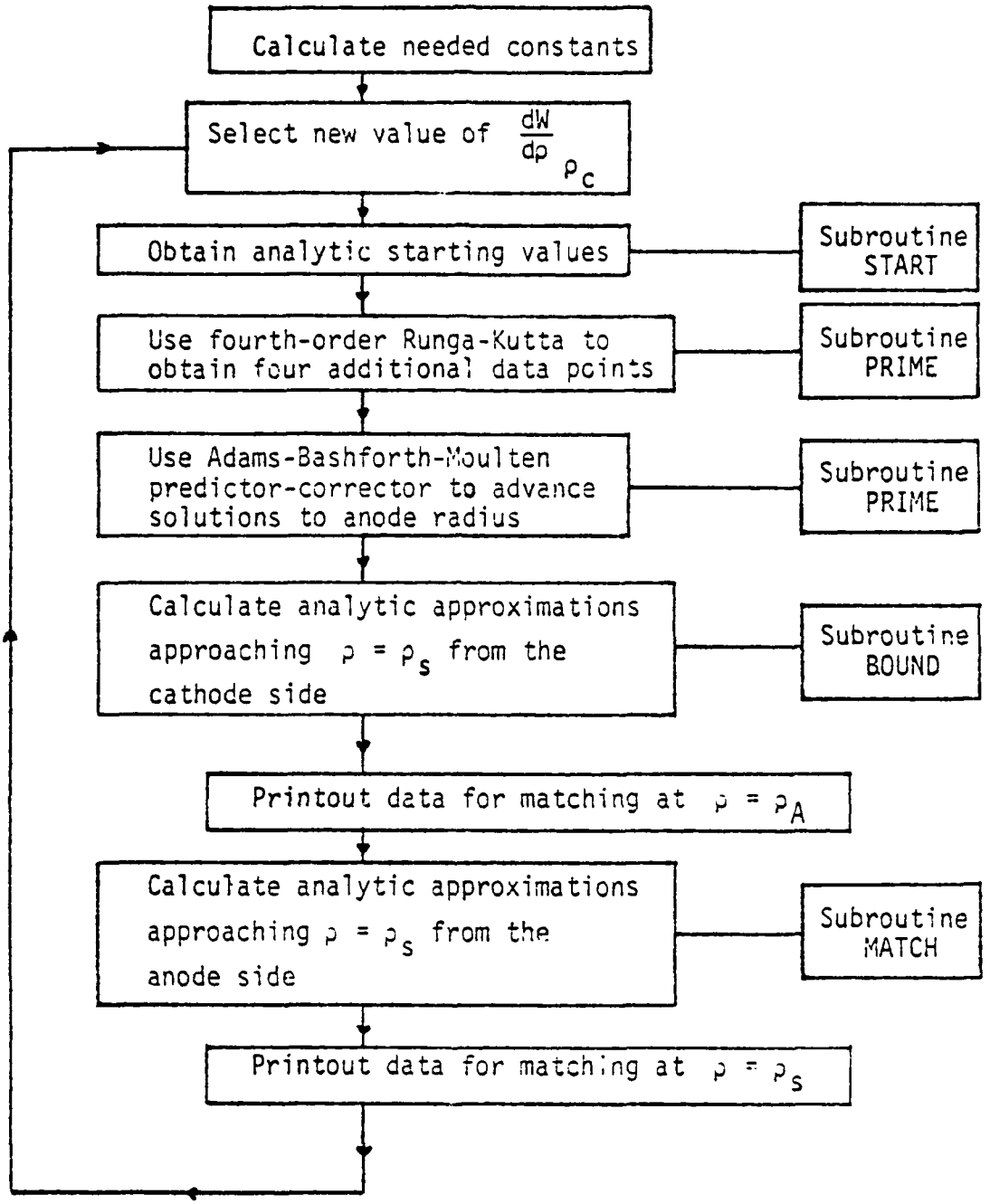

Fig. 5 — RADBER flow chart

accepts guesses for the actual current densities, j and J, at the cathode rather than for the dimensionless fluxes, λ and Λ. In GUESS, the range of guesses for the triplets, $(j, J, W''(\rho_c))$ are specified. The minimum guess for the electron current density is AMIN in amperes per cm.^{2} A total of NA values of j are then tried in the program, each one DELA greater than the next. Similarly, there are NB guesses for J in amps/cm^2 beginning with BMIN and increasing in steps of DELB. The product NA multiplied

by NB must equal exactly 100 for the program as presently written. Finally, the slopes of W at the cathode radius are guessed as some fraction, FMIN, FMIN + DELF, FMIN + 2 DELF, etc., of the scale magnetic field, B_0. There is no limit on the number, NF, of these which can be tested with the 100 (j,J) guesses under consideration. The significance of the integers, I1, I2, and I3 will be explained when the OUTPUT section of the program is discussed.

In NAMELIST, GIVEN, the cathode and anode radii are specified in centimeters by RC and RANODE, respectively. The potential difference between the two electrodes is given in volts by U_0. The scale magnetic field strength, B_0, in gauss, is arbitrary, but can conveniently be chosen as the vacuum, imposed field strength for an axial insulation field problem or as the vacuum value near the cathode for an azimuthal insulating field. The parameter, GAPLEN, is only significant when azimuthal insulation in a radial diode configuration (i.e., the cathode is the central conductor) is under study. In that case, it is equal to the axial length of the A-K gap in centimeters. In a similar sense, CURCEN need only be specified for the case of azimuthal insulation with no ion flow present. It is equal to the axial current assumed to be present in the central conductor in amperes. The logical variables, LAZ, LCIN, and LIONS specify the overall nature of the problem under consideration as follows:

a. LAZ = .TRUE. implies an azimuthal magnetic insulation field,

b. LCIN = .TRUE. implies the cathode is the central conductor, and

c. LIONS = .TRUE. implies the presence of ion (proton) flow.

Finally, ERROR is a decimal fraction to be chosen as the maximum allowable percentage difference tolerable in predictor-corrector steps before a given step iteration there is stopped.

RADBER then uses the above NAMELIST inputs in order to calculate constants and parameters utilized throughout the rest of the program. These set of one hundred guesses for (j,J) are then attempted for each guess of $\frac{dW}{d\rho}(\rho = \rho_c)$. That is, the entire remainder of the program is cycled through once for each value of $W'(\rho_c)$. This iteration begins at statement number 400. The 100

integrations from ρ_c to ρ_4 for each (j,J) pair are carried out simultaneously. Quadrature over the first $\Delta\rho$ is accomplished in the subroutine, START, using the analytic approximations of Eqs. (16)-(20). From that point and over the next 4 $\Delta\rho$, fourth-order Runga-Kutta is employed to generate a finite length string of starting values for the master predictor-corrector scheme. Both here, as well as in the main integrator, the values for the second derivatives of $U(\rho)$ and $W(\rho)$ are calculated via Eqs. (6) and (7) in the subroutine, PRIME. That subroutine also locates the electron sheath radius, ρ_s, by monitoring the value of $U^2 + 2U - W^2$ and finds the effective anode radius for a given (j,J) by pinpointing the value of ρ for which $U(\rho) = U_0$. The Adams-Bashforth-Moulton predictor-corrector algorithm integrates "over" $\rho = \rho_S$, ignoring any functional discontinuities there. It simply forges ahead in a brute force manner, setting λ equal to zero between ρ_S and ρ_4. For some choices of parameter ranges, this may lead to serious errors propagating in the quadrature beyond $\rho = \rho_S$. For that reason, the array, IFLAG, stores the integer number of the radial step over which the electron sheath boundary was encountered. The final test for the validity of the various $(j,J,W'(\rho_c))$ guesses is accomplished through matching of the potentials and the fields at $\rho = \rho_S$.

After the predictor-corrector has blindly pushed all 100 integrations out to $\rho = \rho_4$, the program looks back to find the function values at the two data points immediately preceeding each of the 100 respective ρ_S's. Having stored those values in the COMMON block, FIT, the program then calls the subroutine, BOUND, to calculate U, $U'(=X)$, W, and $W'(=Y)$ at ρ_S (approaching from the cathode side) via the analytic approximations given in Eqs. (25) and (26). Specifically, the lowest order terms of those equations may be rearranged to yield

$$U_S = U_{n-1} + X_S r + a_1 r^{3/2}, \tag{40}$$

$$W_S = W_{n-1} + Y_S r + b_1 r^{3/2}, \tag{41}$$

where the subscript $(n-1)$, signifies the function value at the second data point before the recorded ρ_S. Equation (40) is multiplied by W_S and (41) by $(1 + U_S)$. Subtraction of the resultant equations leads to the expression

$$r = \frac{W_{n-1}(1 + U_S) - W_S(1 + U_{n-1})}{X_S W_S - Y_S(1 + U_S)}. \tag{42}$$

but, since $U_S^2 + 2U_S - W_S^2 = 0$,

$$r = \frac{(U_S^2 + 2U_S)^{1/2}(1 + U_{n-1}) - W_{n-1}(1 + U_S)}{Y_S(1 + U_S) - X_S(U_S^2 + 2U_S)^{1/2}}. \tag{43}$$

Using the known values of U_n as reasonable first guesses for U_S, Eq. (43) yields a first predicted value for r. That value can then be fed into (25) to obtain a corrected value for U_S and the process continued until reasonable convergence is achieved. As written, the subroutine BOUND performs a number of iterations equal to the integer, ITER, which is a fixed parameter in the CALL statement.

At that point in the RADBER program, a pause is made in the computations in order to output the results of the full integration to $\rho = \rho_A$. The format of this primary output depends upon the parameters and geometry under consideration as indicated in Table 1. In all cases the guessed values for j and J (A and B) in amps/cm^2 are listed as are the values found for r_S and r_A in centimeters as well as the values of the electric potential and electric field at $\rho = \rho_A$ in volts and volts/cm respectively. Depending upon the geometry being studied, $W(\rho_A)$ or $W'(\rho_A)$ may be listed along with the value it must have in a true steady state. The table thus created allows a quick evaluation of the merits of the (j,J) guesses tried for the given value of $W'(\rho_c)$. In addition, immediately following that table are listed complete radial profiles for the electric potential in volts and for the insulating magnetic field in gauss from ρ_c to ρ_A for the 11th, 12th, and 13th (j,J) guesses. These profiles provide invaluable information about how well-behaved the steady state conditions are for typical current density choices.

Having completed those pieces of data output, RADBER moves on to a comparison of the function values at the sheath boundary obtained by numerical integration on the cathode side and by analytic evaluation in the electron-free region on the anode side. The analytically obtained values are calculated in the subroutine, MATCH, using Eqs. (29)-(32) along with the values for ρ_S, X_S, and Y_S obtained in the subroutine, BOUND. These pairs of values to be matched at the sheath boundary are tabulated as the final block of output in a given $W'(\rho_c)$ cycle. The table heading clearly indicates which values should be compared to which (e.g., US1 to US2). It is useful to use this sheath boundary matching to fine-tune $(j,J,W'(\rho_c))$ guesses after some coarse fit to the chosen parameters has been

established in the $\rho = \rho_A$ matching table. The process suggested for this iterative improvement of guesses is illustrated by the examples given in Appendix B and Appendix C.

VI. CONCLUSIONS

The RADBER computer code which has resulted from the extensive theoretical, computational, and numerical efforts outlined above stands as a unique tool for analyzing numerous practical, high-voltage devices. It provides the experimenter with reliable predictions for electron and ion flow profiles as well as electric and magnetic field characteristics in coaxial, cylindrical geometry. Appendix A which follows this section provides a complete FORTRAN listing of the code. Appendix B illustrates the details of how the code is applied to a specific problem and how the iterative "shooting" technique is used to converge to the correct answer. The device chosen in this first sample case is a simple radial diode. Its treatment points out the danger of applying RADBER to a mixed axial-azimuthal insulation field. Finally, the much simpler problem of electron flow in a vacuum transmission line is treated for three different voltages in Appendix C. The solution has direct application to a power loss problem experienced in a more complicated coaxial geometry. Taken together, the two sample treatments explicitly demonstrate the versatility of the code.

ACKNOWLEDGMENTS

The authors are indebted to Shyke A. Goldstein and A. T. Drobot for numerous valuable discussions during the course of this work.

Appendix A

THE RADBER COMPUTER CODE

```
C
C
C-----------------------------------------------------------------------
C          THE RADBER PROGRAM
C-----------------------------------------------------------------------
C
      PARAMETER NDR=750
C
      LOGICAL LAZ,LCIN,LIONS
      INTEGER IFLAG(100)
      REAL*8 R,DR,RC,RANODE
C
      DIMENSION X(100,NDR),Y(100,NDR),XP(100,NDR),YP(100,NDR),URA(100)
     &   ,U(100,NDR),W(100,NDR),UU(100),UW(100),XX(100),YY(100)
     &   ,AC(100),BC(100),  SCA(100),SCB(100),SCC(100),SCD(100),
     &   SCE(100),SCF(100),SCG(100),SCH(100)
C
      COMMON /COEF/ A(100),B(100),RS(100),RA(100),AFLAG(100),
     &   R,DR,RC,RANODE,RINV,U0,B0,EBYMC2,EMRAT,C,GAPLEN
      COMMON /SWITCH/ LAZ,LCIN,LIONS
      COMMON /FIT/ UN(100),WN(100),XN(100),YN(100),UNM1(100),WNM1(100),
     &   XNM1(100),YNM1(100),RNM1(100),RSTAR(100),USTAR(100),WSTAR(100),
     &   XSTAR(100),YSTAR(100)
      COMMON /ITCHY/ SCRA(100),WS(100),US(100),ES(100)
C
      NAMELIST /GUESS/ AMIN,DELA,NA,BMIN,DELB,NB,FMIN,DELF,NF,I1,I2,I3
      NAMELIST/GIVEN/RC,RANODE,U0,B0,GAPLEN,CURCEN,ERROR,LAZ,LCIN,LIONS
C
C          IN NAMELIST 'GIVEN' -
C            GAPLEN, RC, AND RANODE ARE IN CENTIMETERS,
C            U0 IS IN VOLTS,
C            B0 IS IN GAUSS,
C            CURCEN IS IN AMPERES,
C            ERROR IS A DECIMAL FRACTION, AND
C            LAZ=.TRUE. FOR AN AZIMUTHAL INSULATION FIELD.
C            LCIN=.TRUE. FOR THE CATHODE AS THE CENTRAL CONDUCTOR
C            LIONS=.TRUE. FOR THE PRESENCE OF ION FLOW
C
C
C********** SUPPLY NEEDED CONSTANTS **********************************
C
      SIXINV=1.00/6.00
      C=2.9979E10
      PI=3.1416E0
      EMRAT=SQRT(1.6726E-24/(2.0*9.1095E-28))
      EBYMC2=4.8032E-10/(9.1095E-28*C*C)
C
C********** INITIALIZE AND SCALE THE VARIABLES ***********************
C
C*** FIRST READ IN THE DEFAULT PARAMETERS ***
C
      READ(5,GUESS)
      READ(5,GIVEN)
C
C*** THEN SUPPLY THE SPECIFIC VALUES ***
C
      READ(5,GUESS)
      READ(5,GIVEN)
      ASCALE = 8.0 * PI * RC * 3.0E9 / (C * B0)
      BSCALE = ASCALE * 0.5 * EMRAT
      RANODE = EBYMC2*B0*RANODE
      RC = EBYMC2*B0*RC
      U0 = EBYMC2*U0/3.0E2
      DR=(RANODE-RC)/DFLOAT(NDR)
      FACT=DR/24.0
      WRITE(6,GUESS)
      WRITE(6,GIVEN)
C
C****GENERATE THE CURRENT FLUX COEFFICIENTS **********************
C
      DO 2 I=1,NA
      AA= (AMIN+DELA*(I-1))*ASCALE
      DO 2 J=1,NB
      AC(I+NB*(J-1)) = AA
      BC(I+NB*(J-1)) =(BMIN+DELB*(J-1) )*BSCALE
 2    CONTINUE
```

```
C
C********** CALCULATE CORRECT W(RA) OR WP(RA) **********
C
      IF(LAZ) GO TO 500
      WFAC=(RANODE**2-RC**2)/(2.0*RANODE)
      GO TO 501
  500 IF(LCIN) GO TO 502
      IF(LIONS) GO TO 503
      WFAC=B0*0.2*CURCEN*EBYMC2/RANODE
  501 DO 504 I=1,100
  504 WRA(I)=WFAC
      GO TO 502
  503 WFAC=0.05*EBYMC2*C*B0*GAPLEN/(EMRAT*RANODE)
      DO 505 I=1,100
  505 WPA(I)=WFAC*B(I)
  502 CONTINUE
C
C********** ITERATE OVER CHOICES FOR CATHODE B-FIELD **********
C
      IT=0
  400 IT=IT+1
      F=FMIN+DELF*(IT-1)
      R=RC
      IF(LAZ.AND.LCIN.AND..NOT.LIONS) F=0.2*CURCEN*EBYMC2/RC
      ICORR=0
      DO 1 I=1,100
      RS(I)=0.0
      RA(I)=0.0
      AFLAG(I)=1.0
      IFLAG(I)=0
      A(I)=AC(I)
      B(I)=BC(I)
    1 CONTINUE
C
C********** USE ANALYTIC APPROXIMATIONS TO GENERATE INITIAL **********
C*****I**** VALUES AT RC+DR          **********K**********
C
      R=R+DR
      RINV=1.0/R
C
      CALL START(U,X,W,Y,F)
C
C********** TH ORDER RUNGA-KUTTA FOR STARTING VALUES **********
C
      DO 4 I=1,4
C
      DO 5 J=1,100
      SCA(J)=DR*X(J,I)
    5 SCB(J)=DR*Y(J,I)
      DO 6 J=1,100
      SCC(J)=DR*(X(J,I)+SCA(J)*0.5)
    6 SCD(J)=DR*(Y(J,I)+SCB(J)*0.5)
      DO 7 J=1,100
      SCE(J)=DR*(X(J,I)+0.5*SCC(J))
    7 SCF(J)=DR*(Y(J,I)+0.5*SCD(J))
      DO 8 J=1,100
      SCG(J)=DR*(X(J,I)+SCE(J))
    8 SCH(J)=DR*(Y(J,I)+SCF(J))
C
      DO 9 J=1,100
      U(J,I+1)=U(J,I)+(SCA(J)+2.0*SCC(J)+2.0*SCE(J)+SCG(J))*SIXINV
    9 W(J,I+1)=W(J,I)+(SCB(J)+2.0*SCD(J)+2.0*SCF(J)+SCH(J))*SIXINV
C
      CALL PRIME(U(1,I),W(1,I),X(1,I),Y(1,I),XP(1,I),YP(1,I),I,IFLAG)
C
      DO 10 J=1,100
      SCG(J)=DR*XP(J,I)
   10 SCH(J)=DR*YP(J,I)
C
      R =R+0.5*DR
      RINV=1.0/R
C
      DO 11 J=1,100
      UU(J)=U(J,I)+0.5*SCA(J)
```

```
      UU(J)=U(J,I)+0.5*SCB(J)
      XX(J)=X(J,I)+0.5*SCG(J)
   11 YY(J)=Y(J,I)+0.5*SCH(J)
C
      CALL PRIME(UU,WW,XX,YY,SCA,SCB,I,IFLAG)
C
      DO 12 J=1,100
      SCA(J)=DR*SCA(J)
   12 SCB(J)=DR*SCB(J)
C
      DO 13 J=1,100
      UU(J)=U(J,I)+0.5*SCC(J)
      WW(J)=W(J,I)+0.5*SCD(J)
      XX(J)=X(J,I)+0.5*SCA(J)
   13 YY(J)=Y(J,I)+0.5*SCB(J)
C
      CALL PRIME(UU,WW,XX,YY,SCC,SCD,I,IFLAG)
C
      DO 14 J=1,100
      SCC(J)=DR*SCC(J)
   14 SCD(J)=DR*SCD(J)
C
      R=R+0.5*DR
      RINV=1.0/R
C
      DO 15 J=1,100
      UU(J)=U(J,I)+SCE(J)
      WW(J)=W(J,I)+SCF(J)
      XX(J)=X(J,I)+SCG(J)
   15 YY(J)=Y(J,I)+SCD(J)
C
      CALL PRIME(UU,WW,XX,YY,SCE,SCF,I,IFLAG)
C
      DO 16 J=1,100
      X(J,I+1)=X(J,I)+(SCG(J)+2.0*SCA(J)+2.0*SCC(J)+DR*SCE(J))*SIXINV
   16 Y(J,I+1)=Y(J,I)+(SCH(J)+2.0*SCB(J)+2.0*SCD(J)+DR*SCF(J))*SIXINV
C
    4 CONTINUE
C
      CALL PRIME(U(1,5),W(1,5),X(1,5),Y(1,5),XP(1,5),YP(1,5),5,IFLAG)
C
C**********************************************************
C     AT THIS POINT WE HAVE COMPLETE DATA FOR THE
C          FIRST FIVE POINTS.
C**********************************5555**********************
C********* THE ADAMS-BASHFORTH-MOULTEN PREDICTOR-CORRECTOR
C
      DO 100 J=6,NDR
C
      R=R+DR
      RINV = 1.0/R
C
      DO 20 I=1,100
C
      X(I,J)=X(I,J-1)+FACT*(55.0*XP(I,J-1)-59.0*XP(I,J-2)
     &                +37.0*XP(I,J-3)-9.0*XP(I,J-4))
      Y(I,J)=Y(I,J-1)+FACT*(55.0*YP(I,J-1)-59.0*YP(I,J-2)
     &                +37.0*YP(I,J-3)-9.0*YP(I,J-4))
      U(I,J)=U(I,J-1)+FACT*(55.0*X(I,J-1)-59.0*X(I,J-2)
     &                +37.0*X(I,J-3)-9.0*X(I,J-4))
      W(I,J)=W(I,J-1)+FACT*(55.0*Y(I,J-1)-59.0*Y(I,J-2)
     &                +37.0*Y(I,J-3)-9.0*Y(I,J-4))
   20 CONTINUE
C
      CALL PRIME(U(1,J),W(1,J),X(1,J),Y(1,J),XP(1,J),YP(1,J),J,IFLAG)
C
C********* THE CORRECTOR.
C
  101 CONTINUE
C
      DO 40 I=1,100
      SCA(I)=U(I,J-1)+FACT*(9.0*X(I,J)+19.0*X(I,J-1)
     &                -5.0*X(I,J-2)+X(I,J-3))
      SCB(I)=W(I,J-1)+FACT*(9.0*Y(I,J)+19.0*Y(I,J-1)
     &                -5.0*Y(I,J-2)+Y(I,J-3))
   40 CONTINUE
```

```
      DO 30 I=1,100
      X(I,J)=X(I,J-1)+FACT*(9.0*XP(I,J)+19.0*XP(I,J-1)
     &                -5.0*XP(I,J-2)+XP(I,J-3))
      Y(I,J)=Y(I,J-1)+FACT*(9.0*YP(I,J)+19.0*YP(I,J-1)
     &               -5.0*YP(I,J-2)+YP(I,J-3))
 30   CONTINUE
C
      CALL PRIME(SCA, SCB, X(1,J),Y(1,J),XP(1,J),YP(1,J),J,IFLAG)
C
C********** ERROR CHECK
C
      ICORR=ICORR+1
      IF(ICORR.GT.1000) GO TO 102
      DO 41 I=1,100
      SCC(I)=ABS((U(I,J)-SCA(I))/U(I,J))
 41   SCD(I)=ABS((W(I,J)-SCB(I))/W(I,J))
      DO 42 I=1,100
      U(I,J)=SCA(I)
 42   W(I,J)=SCB(I)
      DO 43 I=1,100
      IF(SCC(I).LT.ERROR) GO TO 43
      GO TO 101
 43   CONTINUE
      DO 44 I=1,100
      IF(SCD(I).LT.ERROR) GO TO 44
      GO TO 101
 44   CONTINUE
C
 100  CONTINUE
C
 102   CONTINUE
C
C*** USE ANALYTIC FIT AT SHEATH BOUNDARY **********************
C
      DRSING=SNGL(DR)
      DO 601 I=1,100
      IF((DR*RS(I)).GE.(DR*RA(I))) GO TO 603
      GO TO 600
 603  IF(RA(I).EQ.0.0) GO TO 600
 602  UN(I)=1.0
      WN(I)=1.0
      XN(I)=0.0
      YN(I)=DRSING/ABS(DRSING)
      UNM1(I)=1.0
      WNM1(I)=1.0
      XNM1(I)=0.0
      YNM1(I)=YN(I)
      RNM1(I)=SNGL(RC)
      GO TO 601
 600  IF(IFLAG(I).LE.7) GO TO 602
      UN(I)=U(I,IFLAG(I)-1)
      WN(I)=W(I,IFLAG(I)-1)
      XN(I)=X(I,IFLAG(I)-1)
      YN(I)=Y(I,IFLAG(I)-1)
      UNM1(I)=U(I,IFLAG(I)-2)
      WNM1(I)=W(I,IFLAG(I)-2)
      XNM1(I)=X(I,IFLAG(I)-2)
      YNM1(I)=Y(I,IFLAG(I)-2)
      RNM1(I)=SNGL(RC+DR*(IFLAG(I)-2))
 601  CONTINUE
C
      CALL BOUND(DRSING,AC,BC,U0,5)
C
C*** SCALE SELECTED VARIABLES INTO CGS UNITS ******************
C
      USCA=3.0E2/EBYMC2
      RSCA=1.0/(B0*EBYMC2)
      DO 210 I=1,100
      A(I)= AC(I)/ASCALE
      B(I)= BC(I)/BSCALE
      RS(I)=RS(I)*RSCA
      RA(I)=RA(I)*RSCA
      U(I,NDR)=U(I,NDR)*USCA
      YP(I,NDR)=Y(I,NDR)*B0
```

```
      IF(LAZ) GO TO 210
      YP(I,NDR)=YP(I,NDR)+U(I,NDR)*B0/RANODE
  210 CONTINUE
C
C**************** THE OUTPUT ***************************************
C
      BCATH = FLOAT0.001
      WRITE(6,999) BCATH
  999 FORMAT('1',///,20X,'FOR A MAGNETIC FIELD NEAR THE CATHODE OF',
     &    E18.5,' KILOGAUSS :',//)
      IF(LAZ) GO TO 201
      WRITE(6,1000)
 1000 FORMAT(3X,'I',9X,'A',11X,'B',14X,'RS',10X,'RA',11X,'E(RA)',
     &    7X,'U(RA)',11X,'U(RA)',7X,'URA',//)
      DO 200 I=1,100
  200 WRITE(6,1001) I,A(I),B(I),RS(I),RA(I),X(I,NDR),U(I,NDR),U(I,NDR)
     &    ,URA(I)
 1001 FORMAT(1X,I3,4(3X,2E12.4),/)
      GO TO 202
  201 IF(LCIN) GO TO 203
      WRITE(6,1002)
      DO 204 I=1,100
  204 WRITE(6,1001) I, A(I),B(I),RS(I),RA(I),X(I,NDR),U(I,NDR)
     &    ,YP(I,NDR),URA(I)
 1002 FORMAT(3X,'I',9X,'A',11X,'B',14X,'RS',10X,'RA',11X,'E(RA)'
     &    ,7X,'U(RA)',10X,'BT(RA)',6X,'BTRA',//)
      GO TO 202
  203 WRITE(6,1003)
      DO 205 I=1,100
  205 WRITE(6,1001) I,A(I),B(I),RS(I),RA(I),X(I,NDR),U(I,NDR)
 1003 FORMAT(2X,'I',12X,'A',16X,'B',15X,'RS',13X,'RA',12X,
     &    'E(RA)',8X,'U(RA)',//)
  202 CONTINUE
C
C********** CALCULATION OF SAMPLE B-FIELD PROFILES
C
      IF(LAZ) GO TO 251
      R=RC
      DO 250 I=1,NDR
      R=R+DR
      RINV=1.0/R
      YP(1,I)=(Y(I1,I)+U(I1,I)*RINV) * B0
      YP(2,I)=(Y(I2,I)+U(I2,I)*RINV) * B0
  250 YP(3,I)=(Y(I3,I)+U(I3,I)*RINV) * B0
      GO TO 253
  251 CONTINUE
      DO 252 I=1,NDR
      YP(1,I) = B0 *  Y(I1,I)
      YP(2,I) = B0 *  Y(I2,I)
  252 YP(3,I) = B0 *  Y(I3,I)
  253 CONTINUE
C
C*** SCALING OF THE POTENTIAL ***************************************
C
      DO 260 I=1,NDR
      U(I1,I) = U(I1,I) * USCA
      U(I2,I) = U(I2,I) * USCA
  260 U(I3,I) = U(I3,I) * USCA
C
      WRITE(6,1006) I1,I2,I3
 1006 FORMAT(1X,/////,1X,'PHI AND B-FIELD PROFILES FOR (A,B) CHOICES',
     &    I4,',',I4,', AND',I4,'  .',///)
C
      DO 300 I=1,NDR,2
  300 WRITE(6,1005) I,U(I1,I),YP(1,I),U(I2,I),YP(2,I),U(I3,I),YP(3,I)
 1005 FORMAT(1X,I3,3(3X,2E14.5))
C
C*** COMPARE VALUES AT ELECTRON SHEATH BOUNDARY *********************
C
      CALL MATCH(RSTAR,URA,YSTAR,XSTAR,BC)
C
      WRITE(6,1010)
```

```
 1010 FORMAT(1X,/////,1X,'MATCHING VALUES AT SHEATH BOUNDARY',//,
     &   3X,'I',9X,'RS',13X,'US1',8X,'US2',12X,'ES1',
     &   8X,'ES2',12X,'WS1',9X,'YS1',9X,'WS2',//)
C
Cxxx SCALE RSTAR INTO CENTIMETERS xxxxxxxxxxxxxxxxxxxxxxxx555x
C
      DO 650 I=1,100
  650 RS(I)=RSTAR(I)*RSCA
C
      DO 700 I=1,100
  700 WRITE(6,1004) I,RS(I),USTAR(I),US(I),XSTAR(I),ES(I),
     &                WSTAR(I),YSTAR(I),W_(I)
C
 1004 FORMAT(1X,I3,2X,E12.4,2(3X,2E12.4),3X,3E12.4,/)
      IF(IT.LT.NF) GO TO 400
C
      STOP
C
      END



C
C
C
C-----------------------------------------------------------------------
C           SUBROUTINE BOUND
C-----------------------------------------------------------------------
C
      SUBROUTINE BOUND(DR,A,B,U0,ITER)
C
      LOGICAL LAZ,LCIN,LIONS
C
      DIMENSION A(100),B(100),R(100),SCR1(100)
C
      COMMON /FIT/ UN(100),WN(100),XN(100),YN(100),UNM1(100),WNM1(100),
     &   XNM1(100),YNM1(100),RNM1(100),RSTAR(100),USTAR(100),WSTAR(100),
     &   XSTAR(100),YSTAR(100)
      COMMON /SWITCH/ LAZ,LCIN,LIONS
      COMMON /ITCHY/ A1(100),B1(100),A2(100),B2(100)
C
      EPS=1.0
      IF(LAZ) EPS=0.0
      F = 1.0
      IF(.NOT.LCIN) F=-1.0
C
Cxxx MAKE ZEROETH-ORDER GUESSES xxxxxxxxxxxxxxxxxxxxxxxxxxxxxxxxxx
C
      DO 1 I=1,100
      R(I)=DR
      USTAR(I)=UN(I)
      WSTAR(I)=WN(I)
      XSTAR(I)=XN(I)
    1 YSTAR(I)=YN(I)
C
Cxxx ITERATE FOR SOLUTIONS xxxxxxxxxxxxxxxxxxxxxxxxxxxxxxxxxxxxxx
C
      DO 2 IT=1,ITER
C
Cxxx CALCULATE A1 AND B1 xxx
C
      DO 3 I=1,100
      A2(I)=F*4.0*A(I)/(3.0*(R(I)+RNM1(I)))
    3 B2(I)=F*(2.*USTAR(I)*YSTAR(I)-2.*XSTAR(I)*(1.+USTAR(I)))
C
      DO 20 I=1,100
      IF(B2(I).GT.0.0) GO TO 20
      B2(I)=1.0E20
   20 CONTINUE
C
      DO 4 I=1,100
      A1(I)= A2(I)*(1.0+USTAR(I))/SQRT(B2(I))
```

```
 4    B1(I)= A2(I)*USTAR(I)/SQRT(B2(I))
C
C*** CHECK FOR NEGATIVE VALUES OF 'USTAR' ********************
C
      DO 30 I=1,100
      IF(USTAR(I).GT.0.0.AND.USTAR(I).LT.U0) GO TO 30
      USTAR(I)= (1.0E-3)*U0
 30   CONTINUE
C
C*** CALCULATE R-CORRECTED ***
C
      DO 5 I=1,100
      A2(I)= SQRT(USTAR(I)*(2.0+USTAR(I)))
  5   B2(I)= 1.0 + USTAR(I)
C
      DO 6 I=1,100
  6   RSTAR(I)= (A2(I)*(1.0+UNM1(I))-UNM1(I)*B2(I)) /
     &          (YSTAR(I)*B2(I) - XSTAR(I)*A2(I))
C
      DO 14 I=1,100
 14   IF((RSTAR(I).F).GE.0.0) R(I)=RSTAR(I)
C
C*** CALCULATE A2 AND B2 ***
C
      DO 7 I=1,100
  7   SCR1(I)=-0.5/(R(I)+RNM1(I))
C
      DO 8 I=1,100
      A2(I)=SCR1(I)*(XSTAR(I)+B(I)/SQRT(U0-USTAR(I)))
  8   B2(I)=SCR1(I)*(YSTAR(I)+2.0*EPS*USTAR(I)*SCR1(I))
C
C*** CORRECT THE PREDICTED VALUES ***
C
      DO 9 I=1,100
      XSTAR(I)=XNM1(I)+1.5*A1(I)*SQRT(F*R(I))+2.0*A2(I)*R(I)
  9   YSTAR(I)=YNM1(I)+1.5*B1(I)*SQRT(F*R(I))+2.0*B2(I)*R(I)
C
      DO 10 I=1,100
      USTAR(I)=UNM1(I)+R(I)*(XSTAR(I)-A1(I)*SQRT(F*R(I))-A2(I)*R(I))
 10   USTAR(I)=UNM1(I)+R(I)*(YSTAR(I)-B1(I)*SQRT(F*R(I))-B2(I)*R(I))
C
  2   CONTINUE
C
      DO 12 I=1,100
 12   RSTAR(I)=RNM1(I)+R(I)
C
      RETURN
C
      END
C
C
C
C-----------------------------------------------------------------
C          SUBROUTINE PRIME
C-----------------------------------------------------------------
C
      SUBROUTINE PRIME(U,W,X,Y,XP,YP,IT,IFLAG)
C
      DIMENSION S(100),U(100),W(100),X(100),Y(100),XP(100),YP(100)
C
      COMMON /ITCHY/SCA(100),SCB(100),SCC(100),SCD(100)
      COMMON /COEF/ A(100),B(100),RS(100),RA(100),AFLAG(100),
     &   R,DR,RC,RANODE,RINV,U0,B0,EBYMC2,EMRAT,C,GAPLEN
      COMMON /SWITCH/ LAZ,LCIN,LIONS
C
      LOGICAL LAZ,LCIN,LIONS
      INTEGER IFLAG(100)
      REAL*8 R,DR,RC,RANODE
```

```
C
C********** FIND THE ELECTRON SHEATH RADIUS **************************
C
      DO 1 I=1,100
 1    S(I)=2.0*U(I)+(U(I)+U(I))*(U(I)-U(I))
      DO 2 I=1,100
      IF(S(I).GT.1.0E-8) GO TO 2
      S(I)=1.0
      A(I)=0.0
      IF(IFLAG(I).EQ.0) IFLAG(I)=IT
 2    CONTINUE
C
      DO 7 I=1,100
 7    SCB(I)=A(I)+RS(I)
C
      DO 3 I=1,100
      IF(SCB(I).NE.0.0) GO TO 3
      RS(I)=R
 3    CONTINUE
C
C********** FIND THE 'ANODE RADIUS' **********************************
C
      DO 4 I=1,100
      IF(U(I).LT.U0) GO TO 4
      A(I)=0.0
      B(I)=0.0
      AFLAG(I)=0.0
      X(I)=0.0
      Y(I)=0.0
 4    CONTINUE
C
      DO 5 I=1,100
 5    SCA(I)=AFLAG(I)+RA(I)
C
      DO 6 I=1,100
      IF(SCA(I).NE.0.0) GO TO 6
      RA(I)=R
 6    CONTINUE
C
      DO 10 I=1,100
 10   SCA(I)= 1.0/SQRT(S(I))
      DO 11 I=1,100
 11   SCB(I)=A(I)*SCA(I)
      DO 12 I=1,100
      XP(I)=SCB(I)*(1.0+U(I))
 12   YP(I)=SCB(I)*U(I)
      DO 13 I=1,100
 13   SCA(I) = U0-U(I)
      DO 14 I=1,100
      IF(SCA(I).GT.0.0) GO TO 14
      SCA(I)=1.0
 14   CONTINUE
      DO 15 I=1,100
 15   SCC(I)=1.0/SQRT(SCA(I))
      DO 16 I=1,100
 16   SCA(I)=XP(I)-B(I)*SCC(I)
      DO 17 I=1,100
 17   SCB(I) = YP(I)
      IF(LAZ) GO TO 19
      DO 18 I=1,100
 18   SCB(I)=SCB(I)+AFLAG(I)*U(I)*RINU
 19   CONTINUE
      DO 20 I=1,100
      SCC(I)=SCA(I)-X(I)
 20   SCD(I)=SCB(I)-Y(I)
      DO 21 I=1,100
      XP(I)=SCC(I)*RINU
 21   YP(I)=SCD(I)*RINU
C
      RETURN
C
      END
```

```
C
C
C
C-----------------------------------------------------------------------
C          SUBROUTINE MATCH
C-----------------------------------------------------------------------
C
      SUBROUTINE MATCH(RSTAR,URA,YSTAR,XSTAR,BC)
C
      LOGICAL LAZ,LCIN,LIONS
      REAL*8 R,DR,RC,RANODE
C
      COMMON /COEF/ A(100),B(100),RS(100),RA(100),AFLAG(100),
     &              R,DR,RC,RANODE,RINV,U0,B0
      COMMON /SWITCH/ LAZ,LCIN,LIONS
      COMMON /ITCHY/ SCA(100),SCB(100),SCC(100),SCD(100)
C
      DIMENSION RSTAR(100),URA(100),YSTAR(100),XSTAR(100),
     &          BC(100),RAT(100),RATINV(100),G(100),BETA(100),
     &          BETAP(100)
C
C*** DETERMINE NEEDED CONSTANTS ***************************
C
      RASING=SNGL(RANODE)
      DO 1 I=1,100
      RAT(I)=RASING/RSTAR(I)
 1    G(I)=1.0
      DO 2 I=1,100
 2    RATINV(I)=1.0/RAT(I)
      DO 3 I=1,100
      IF(RATINV(I).GT.0.0) G(I)=ALOG(RATINV(I))
 3    CONTINUE
C
C*** MATCH THE MAGNETIC VARIABLE **************************
C
      IF(LAZ) GO TO 4
C
      DO 5 I=1,100
 5    SCA(I)= 2.0*URA(I) - YSTAR(I)*(RASING-RSTAR(I)*RATINV(I))
      DO 6 I=1,100
      IF(RAT(I).NE.1.0) GO TO 7
      GO TO 6
 7    SCB(I) = SCA(I)/ (RAT(I)+RATINV(I))
 6    CONTINUE
      GO TO 8
C
 4    CONTINUE
      DO 9 I=1,100
 9    SCB(I) = URA(I)*RAT(I)/B0
C
 8    CONTINUE
C
C*** MATCH THE ELECTRICAL VARIABLES ************************
C
      IF(.NOT.LIONS) GO TO 20
C
      DO 10 I=1,100
      BETA(I) = G(I)*( 1.0 - G(I)*( 0.400 - G(I)*( 9.1666E-2
     &   - G(I)*( 1.4242E-2 - G(I)*( 1.6793E-3 - G(I)*( 1.6122E-4
     &   - G(I)*( 1.2935E-5 - G(I)*( 8.8769E-7 - G(I)*( 5.4619E-8
     &   - G(I)*( 2.9484E-9 - G(I)*( 1.3603E-10 - G(I)*( 7.1101E-13
     &   - G(I)*( 2.6644E-13 + G(I)* 1.2526E-15))))))))))))
 10   CONTINUE
C
      DO 11 I=1,100
      BETAP(I) = ( 1.0 - G(I)*( 0.8 -G(I)*( 2.75E-1 - G(I)*(
     &   5.6968E-2 - G(I)*( 8.3964E-3 - G(I)*( 9.6733E-4
     &   - G(I)*( 9.0544E-5 - G(I)*( 7.1015E-6 - G(I)*( 4.9157E-7
     &   - G(I)*( 2.9484E-8 - G(I)*( 1.4963E-9 - G(I)*( 8.5321E-12
     &   - G(I)*( 3.4637E-12 + G(I)* 1.7536E-14))))))))))))))/RSTAR(I)
 11   CONTINUE
```

```
C
      DO 12 I=1,100
 12   SCC(I) = U0 - (ABS(9.0*RSTAR(I)*BETA(I)*BETA(I)*BC(I))/4.0)
     &                **(2.0/3.0)
      DO 13 I=1,100
 13   SCD(I)= -(2.0/3.0)*(U0 - SCC(I))*(1.0/RSTAR(I)
     &          + 2.0*BETAP(I)/BETA(I))
      GO TO 14
C
 20    CONTINUE
C
      DO 15 I=1,100
 15   IF(RAT(I).GT.0.0) G(I)=ALOG(RAT(I))
      DO 16 I=1,100
 16   SCC(I) = U0 - XSTAR(I)*RSTAR(I)*G(I)
C
 14   RETURN
C
      END
```

Appendix B

SAMPLE SOLUTION FOR A RADIAL DIODE

In order to provide an example of the iterative "shooting" technique solution process, the radial diode depicted in Fig. 6 was modeled. Two megavolt operation of such a geometry should make the case interesting to those in the light ion beam research area. The desired configuration was specified by the following choice of variables:

a. LAZ = .FALSE.,

b. LCIN = .TRUE.,

c. LIONS = .TRUE.,

d. RC = 5.0,

e. RANODE = 5.5,

f. UØ = 2.0E6, and

g. BØ = 2.0E4.

As for the numerical factors, NDR was left at 500 and ERROR was chosen as 0.02.

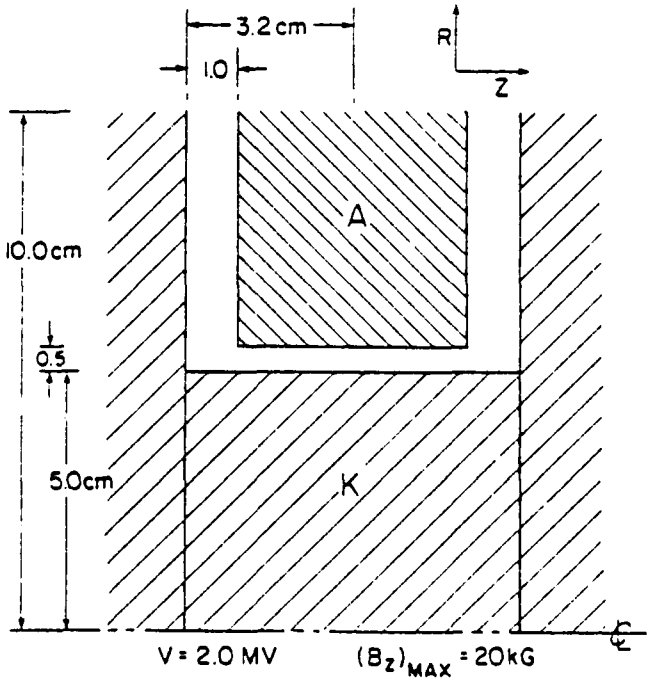

Fig. 6 — The radial diode test case

A quasi-static computer simulation of this diode has been completed[25] and the numerical results indicate an electron current density at the cathode of approximately 3.8×10^4 amps/cm^2 with a complementary ion current density of about 1.3×10^4 amps/cm^2. Due to the geometric electric field enhancement at the anode surface, it can be assumed that this ion current is too high. In the simulation, the axial magnetic field strength at the cathode surface was found to go slightly negative. Such field reversal cannot be expected if the electron and ion currents are significantly reduced. Given the high voltages of this test case, the approximate solutions presented in Figs. 3 and 4 do not provide any additional assistance in choosing reasonable guesses. As a first test for RADBER, therefore, it was decided to search the following parameter ranges:

(a) $(B_z)_{\text{cathode}} = 4$, 5, 6, 7, and 8 kilogauss.

(b) Ten equispaced values of $2.0 \times 10^4 \leqslant j \leqslant 4.25 \times 10^4$ amps/cm^2.

(c) Ten equispaced values of $0.3 \times 10^4 \leqslant J \leqslant 0.75 \times 10^4$ amps/cm^2.

In examining the numerical results from the program it is important to note that in cases such as this where the electron sheath boundary will lie close to the anode surface, the matching of values at $\rho = \rho_A$ is extremely unreliable due to the sharp discontinuities in U'' and W'' at $\rho = \rho_S$. As a general rule, therefore, one must perform the matching tests at $\rho = \rho_S$. After good matches are found there, the corresponding tables for $\rho = \rho_A$ may or may not add corroboration but they can never be used to overrule the ρ_S test results. Similarly, the sample ϕ and B_z profiles are to be trusted completely only *inside* the electron sheath.

An examination of the matching results for this first parameter search yielded, as might be expected, only a few promising candidates. By far most of the values to be compared at $\rho = \rho_S$ differed by at least factors of two. From this mass of data, however, the best matches were extracted for presentation in Table 2. The closest fit seems to be reached for $(B_z)_{\text{cath}} = 7$ kG, $j = 2.75 \times 10^4$ and $J = 0.35 \times 10^4$. The next logical search region seems to be:

TABLE 2. SAMPLE RADIAL DIODE OUTPUT

BZ	JE	JI	(US)IN	(US)OUT	(XS)IN	(XS)OUT	(WS)IN	(WS)OUT
5.0	2.50	0.40	2.36	3.89	0.552	0.559	3.21	5.54
5.0	4.00	0.55	2.95	3.89	0.443	0.688	3.82	5.52
6.0	2.70	0.40	2.85	3.76	0.703	0.956	3.72	5.25
6.0	3.50	0.45	3.36	3.91	0.532	0.340	4.25	5.58
7.0	2.25	0.30	3.23	3.87	0.855	0.612	4.11	5.44
7.0	2.75	0.35	3.48	3.86	0.772	0.694	4.36	5.41
7.0	3.50	0.40	3.74	3.85	0.293	0.776	4.63	5.38
8.0	2.50	0.30	3.66	3.73	0.906	0.871	4.55	5.08

WHERE IN THIS TABLE AS WELL AS IN TABLES 3, 4, AND 5:
BZ IS IN KILOGAUSS,
JE AND JI ARE IN UNITS OF 10,000 AMP/CMSQ, AND
US, XS, AND WS ARE ALL DIMENSIONLESS.

(a) $(B_z)_{cath}$ = 6.5, 7.0, and 7.5 kG.

(b) Ten equispaced values for $2.0 \times 10^4 \leqslant j \leqslant 3.8 \times 10^4$.

(c) Ten equispaced values for $0.25 \times 10^4 \leqslant J \leqslant 0.43 \times 10^4$.

The RADBER-generated matching values at $\rho = \rho_S$ provided the results listed in Table 3. The best overall answers seem to be for $(B_z)_{cath} = 7.5$ kG, $j = 2.80 \times 10^4$, and $J = 0.33 \times 10^4$. For those parameters, the worst match occurs for W_S. However, the jump in those values of W_S compared to their neighbors in the table suggests that the program is searching in a sensitive region of parameter space. Such "sensitivity" often implies that one is close to the correct answer in the search. To further delineate the correct range, it seems reasonable to check adjacent $(B_z)_{cath}$ values. For the third test search, therefore, the following ranges are chosen:

(a) $(B_z)_{cath} = 7.25$, 7.50, 7.75, and 8.00 kG.

(b) Ten equispaced values of $1.7 \times 10^4 \leqslant j \leqslant 3.5 \times 10^4$.

(c) Ten equispaced values of $0.25 \times 10^4 \leqslant J \leqslant 0.43 \times 10^4$.

TABLE 3. SAMPLE RADIAL DIODE OUTPUT

BZ	JE	JI	(US)IN	(US)OUT	(XS)IN	(XS)OUT	(WS)IN	(WS)OUT
6.5	2.00	0.29	2.98	3.89	0.790	0.526	3.85	5.51
6.5	2.20	0.31	2.81	3.86	0.788	0.635	3.68	5.42
6.5	3.00	0.39	3.38	3.89	0.688	0.604	4.26	5.50
6.5	3.20	0.41	3.43	3.86	0.643	0.732	4.32	5.43
7.0	2.00	0.29	2.76	3.60	0.350	0.981	3.63	4.95
7.0	2.20	0.31	2.94	3.66	0.860	0.962	3.81	5.03
7.0	2.40	0.33	3.09	3.69	0.357	0.959	3.97	5.08
7.0	2.60	0.35	3.21	3.70	0.341	0.975	4.09	5.09
7.0	2.80	0.35	3.55	3.29	0.732	0.559	4.44	5.50
7.0	3.00	0.37	3.60	3.86	0.674	0.698	4.49	5.42
7.5	2.00	0.27	3.06	3.67	0.938	0.390	3.93	5.01
7.5	2.20	0.29	3.23	3.71	0.934	0.384	4.11	5.07
7.5	2.40	0.31	3.36	3.72	0.914	0.399	4.24	5.09
7.5	2.60	0.33	3.46	3.71	0.880	0.934	4.35	5.08
7.5	2.80	0.33	3.75	3.87	0.667	0.641	4.65	5.43
7.5	2.80	0.35	3.54	3.69	0.835	0.938	4.43	5.03
7.5	3.00	0.35	3.78	3.82	0.530	0.734	4.67	5.31

The best matches are listed in Table 4. Clearly the most tantalizing results are those for the 8.0 kilogauss case. For that fixed value of $(B_z)_{cath}$ a close match for each of the three variables tested can be found within the given (j,J) matrix. More importantly, all of the matches fall on the line $j = 2.10 + 10\,(J - 0.27) = 10J - 0.60$. Two possibilities suggest themselves; either *the* solution falls on a similar line for an adjacent magnetic field value or it lies on an adjacent (j,J)-line unresolved by the coarse mesh but at the same field value. The former alternative will be tested first by examining the same (j,J) mesh for the values, $(B_z)_{cath} = 7.9, 8.1, 8.2, 8.3, 8.4, 8.5$. The major results are listed in Table 5. The coalescence of circled solutions indicates a finer scale search in the region delineated by:

(a) $(B_z)_{cath} = 8.3, 8.4, 8.5, 8.6, 8.7$ kG.

(b) Ten equispaced values of $1.65 \times 10^4 \leqslant j \leqslant 2.55 \times 10^4$.

(c) Ten equispaced values of $0.225 \times 10^4 \leqslant J \leqslant 0.315 \times 10^4$.

No tabulated results are necessary for this run since a "hit" was scored in the $\rho = \rho_S$ matching results for the parameter combination $(B_z)_{cath} = 8.7$ kG, $j = 2.25 \times 10^4$ amps/cm^2, and $J = 0.275 \times 10^4$

TABLE 4. SAMPLE RADIAL DIODE OUTPUT

BZ	JE	JI	(US)IN	(US)OUT	(XS)IN	(XS)OUT	(WS)IN	(WS)OUT
7.25	2.10	0.29	3.00	3.66	0.899	0.928	3.87	5.02
7.25	2.30	0.31	3.16	3.70	0.895	0.924	4.04	5.07
7.25	2.50	0.33	3.29	3.71	0.878	0.939	4.17	5.09
7.25	2.90	0.35	3.68	3.86	0.678	0.671	4.57	5.42
7.25	3.10	0.35	3.81	3.91	0.321	0.338	4.70	5.58
7.25	3.10	0.37	3.70	3.82	0.605	0.807	4.60	5.32
7.50	2.50	0.31	3.56	3.83	0.859	0.723	4.45	5.33
7.50	2.70	0.33	3.63	3.81	0.801	0.792	4.52	5.27
7.50	2.90	0.33	3.83	3.89	0.459	0.501	4.73	5.52
7.50	2.90	0.35	3.68	3.77	0.734	0.879	4.57	5.19
7.50	3.10	0.35	3.83	3.85	0.366	0.726	4.72	5.37
7.50	3.10	0.37	3.71	3.73	0.662	0.975	4.60	5.09
7.50	3.30	0.37	3.82	3.78	0.288	0.888	4.71	5.22
7.50	2.90	0.39	3.22	3.26	0.908	1.374	4.09	4.40
7.50	3.10	0.39	3.53	3.52	0.813	1.207	4.41	4.75
7.75	2.10	0.27	3.29	3.72	0.972	0.841	4.17	5.07
7.75	2.30	0.29	3.43	3.73	0.950	0.855	4.32	5.10
7.75	2.50	0.31	3.54	3.73	0.910	0.891	4.43	5.08
7.75	2.70	0.31	3.83	3.87	0.627	0.610	4.72	5.43
7.75	2.70	0.33	3.62	3.70	0.856	0.947	4.51	5.04
7.75	2.90	0.33	3.84	3.82	0.517	0.762	4.74	5.30
8.00	2.10	0.27	3.26	3.59	1.011	0.958	4.14	4.82
8.00	2.30	0.29	3.40	3.61	0.994	0.977	4.29	4.85
8.00	2.50	0.31	3.52	3.60	0.960	1.012	4.41	4.84
8.00	2.70	0.33	3.61	3.58	0.911	1.063	4.50	4.80
8.00	2.90	0.35	3.67	3.54	0.849	1.125	4.56	4.74
8.00	3.10	0.37	3.72	3.49	0.778	1.197	4.61	4.65
8.00	3.30	0.39	3.75	3.42	0.701	1.276	4.64	4.55

TABLE 5. SAMPLE RADIAL DIODE OUTPUT

BZ	JE	JI	(US)IN	(US)OUT	(XS)IN	(XS)OUT	(WS)IN	(WS)OUT
7.9	2.30	0.29	3.42	3.66	0.977	0.932	4.30	4.95
7.9	2.50	0.31	3.53	3.65	0.940	0.968	4.42	4.94
7.9	2.70	0.33	3.61	3.63	0.889	1.020	4.50	4.90
7.9	2.90	0.35	3.68	3.59	0.826	1.085	4.57	4.83
7.9	3.10	0.37	3.72	3.54	0.754	1.160	4.61	4.74
7.9	3.30	0.39	3.75	3.47	0.677	1.241	4.64	4.64
7.9	3.50	0.41	3.76	3.40	0.599	1.133	4.65	4.52
8.1	2.10	0.27	3.24	3.53	1.026	0.998	4.12	4.71
8.1	2.30	0.29	3.39	3.55	1.011	1.018	4.28	4.75
8.1	2.50	0.31	3.51	3.55	0.980	1.053	4.40	4.74
8.1	2.70	0.33	3.60	3.53	0.932	1.102	4.49	4.71
8.1	2.90	0.35	3.67	3.49	0.873	1.163	4.56	4.65
8.1	3.10	0.37	3.72	3.44	0.802	1.233	4.61	4.56
8.2	2.10	0.27	3.22	3.47	1.040	1.035	4.10	4.61
8.2	2.30	0.29	3.38	3.50	1.028	1.056	4.26	4.65
8.2	2.50	0.31	3.50	3.50	0.999	1.091	4.39	4.64
8.2	2.50	0.33	3.20	3.16	1.030	1.314	4.08	4.18
8.2	2.70	0.33	3.59	3.48	0.954	1.139	4.48	4.61
8.2	2.90	0.35	3.66	3.44	0.897	1.198	4.56	4.55
8.3	1.90	0.25	3.01	3.36	1.045	1.058	3.83	4.44
8.3	2.10	0.27	3.21	3.41	1.054	1.069	4.03	4.51
8.3	2.30	0.29	3.37	3.44	1.045	1.092	4.25	4.55
8.3	2.50	0.31	3.49	3.44	1.018	1.127	4.38	4.55
8.3	2.70	0.33	3.59	3.42	0.975	1.174	4.48	4.52
8.3	2.90	0.35	3.66	3.39	0.918	1.232	4.55	4.46
8.4	1.90	0.25	2.99	3.29	1.057	1.088	3.86	4.34
8.4	2.10	0.27	3.19	3.35	1.069	1.101	4.07	4.41
8.4	2.30	0.29	3.35	3.38	1.062	1.125	4.23	4.45
8.4	2.50	0.31	3.48	3.39	1.037	1.160	4.37	4.45
8.4	2.70	0.33	3.58	3.37	0.996	1.207	4.47	4.42
8.5	1.90	0.25	2.97	3.23	1.067	1.117	3.84	4.24
8.5	2.10	0.27	3.17	3.29	1.082	1.131	4.05	4.31
8.5	2.30	0.29	3.34	3.32	1.077	1.156	4.22	4.35
8.5	2.50	0.29	3.00	2.92	1.069	1.365	3.88	3.82
8.5	2.50	0.31	3.47	3.33	1.056	1.192	4.35	4.35

amps/cm^2. For that choice, RADBER found the following: $r_S = 5.445$, $(U_S)_{in} = 3.438$, $(U_S)_{out} = 3.381$, $(X_S)_{in} = 1.104$, $(X_S)_{out} = 1.096$, $(W_S)_{in} = 4.324$, and $(W_S)_{out} = 4.397$. It is interesting to note that the matching at $\rho = \rho_A$ yielded $r_S = 5.445$, $r_A = 5.497$, $E_A = -0.0053$, $\phi_A = 2.0$ MV, and $W_A = 5.435$. Only the value for W_A is significantly displaced from its proper value of 5.600. A final fine-tuning run is called for not so much to obtain better values for the parameter guesses but rather to obtain useable profiles for the quantities $\phi(r)$ and $B_z(r)$. For this final run, it was decided to pick:

(a) $(B_z)_{cath} = 8.675$, 8.700, and 8.725 kG.

(b) Ten equispaced values of $2.05 \times 10^4 \leqslant j \leqslant 2.50 \times 10^4$.

(c) Ten equispaced values of $0.255 \times 10^4 \leqslant J \leqslant 0.300 \times 10^4$.

The results of that run clearly indicate a best choice of parameters as $[(B_z)_{cath}, j.J)] = [8.725$ kG, 22.0 kA/cm^2, 2.75 kA/cm^2]. For that combination, matching at $\rho = \rho_S$ yielded $(U_S)_{in} = 3.306$, $(U_S)_{out} = 3.268$, $(E_S)_{in} = 1.116$, $(E_S)_{out} = 1.152$, $(W_S)_{in} = 4.188$, $(W_S)_{out} = 4.235$, and $r_S = 5.436$ cm. The percentage errors in each of the respective quantities are $\Delta_U = 1.2\%$, $\Delta_E = 3.2\%$, and $\Delta_W = 1.1\%$. Given the 2% error margin chosen for the predictor-corrector, it is mathematically pointless to seek a closer match. The radial profiles of the electrostatic potential and axial magnetic field values supplied by RADBER for that chosen solution are plotted in Fig. 7. Note that the nature of the B-field profile is qualitatively identical to those plotted by Ron, et al., (see Ref. 11). On the other hand, the E-field inferred from the curve of $\phi(r)$ in Fig. 7 sharply differs from that cited in the above journal article. The difference exists because the presence of ions was not treated in Ref. 11. Ion emission at the anode surface requires that the electric field strength go to zero there.

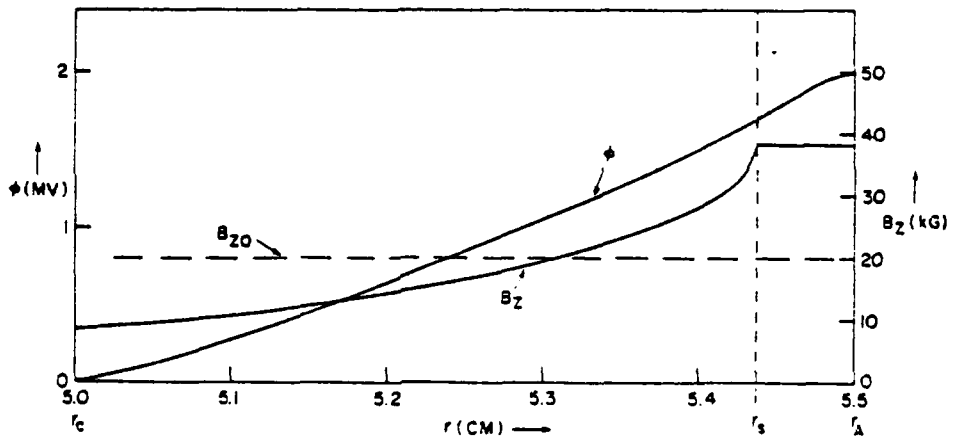

Fig. 7 — Profiles of ϕ and B_z in the 4-K gap of the radial diode.

These RADBER results represent a very significant departure from the results of the full DIODE2D computer simulation of the radial diode under study. Instead of a slightly negative B_z at the cathode surface, RADBER predicts 8.725 kG. Instead of an electron current density of 38 kA/cm^2, RADBER finds 22 kA/cm^2. Finally, and most dramatically, we are left with only 2.75 kA/cm^2 of ion current density compared to DIODE2D's 13.0 kA/cm^2. These observed differences, however, may be attributed to two major causes:

(1) The electric field near the anode of the actual simulated radial diode is enhanced due to 2-D distortions which cannot be modeled by RADBER's one-dimensional treatment.

(2) The DIODE2D simulation accurately treated the azimuthal magnetic insulation present in the actual diode as well as the axial one. Given the currents of over a megampere flowing through the cathode shank, very large values of B_θ could be expected. This additional field component could easily have modified the results of the simple 1-D model by the degree shown. As an additional reference point, simple Child-Langmuir bi-polar analysis predicts an electron current density of just under 50 kA/cm^2 and a corresponding J of 1.2 kA/cm^2. It is interesting that both densities are off by factors of two from the RADBER results but in opposite directions.

In conclusion, therefore, RADBER, has given a reliable order-of-magnitude estimate for the current flow through the system. It also gives an investigator some appreciation for the degree to which combined axial and azimuthal insulation can modify a simple axial insulation prediction. Of course, RADBER can also be used to predict a purely azimuthal insulation result for this same diode in order to give even more insight into the overall physics of its operation. Such further studies would be valuable for specific diode designers.

Appendix C

SAMPLE SOLUTION FOR A VACUUM TRANSMISSION LINE

As part of the NRL Light Ion Fusion Research Program, high power diodes were tested for use as intense ion beam sources on the AURORA pulsed power generator at the Harry Diamond Laboratory. For these tests, the machine was operated in positive polarity so that the magnetically insulated coaxial feed line which transmits the power from the generator to the diode has a configuration qualitatively similar to that pictured in the lower half of Fig. 2. A significant difference, however, is that in the actual transmission line the outer conductor is conical rather than cylindrical. The specific geometry is drawn to scale in Fig. 8 with all dimensions given in centimeters. In recent ion diode runs on this device, clear evidence was found that significant amounts of electron current were impacting the outer circumference of the end of the inner conductor (anode). This could represent a significant loss of power that could have been usefully applied to the generation of ions in the diode instead. The 250 kiloamperes of current flowing through the anode stalk had been assumed to be quite sufficient for generating a strong enough azimuthal B-field to insulate any electron flow in the line. Apparently it may not be. The RADBER code can now be used to check the physics of the assumption.

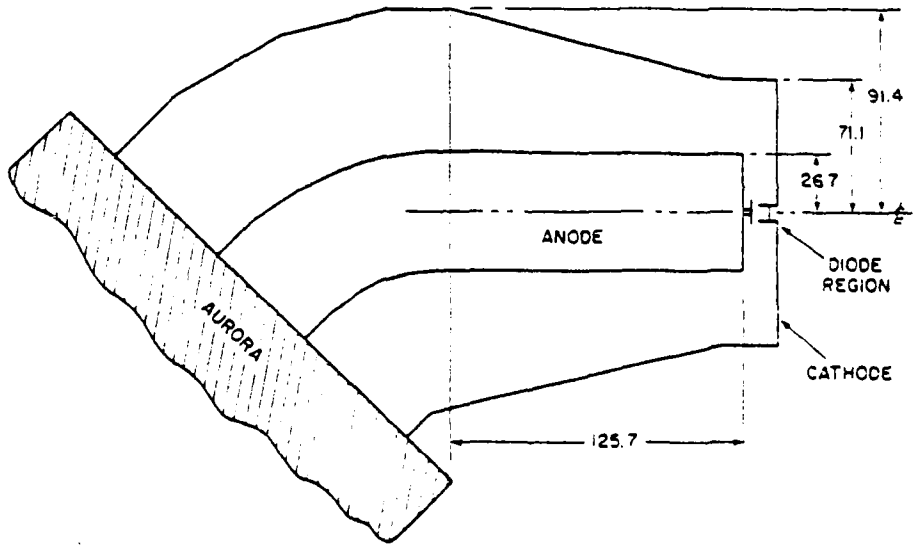

Fig. 8 — Modified AURORA magnetically insulated transmission line (MITL)

Quite differently from the case treated in Appendix B, the solutions at $\rho = \rho_S$ proved to be extremely erratic in the immediate vicinity of the true solution. This is to be expected judging from the sharp discontinuity in the slopes of both the electric field and the magnetic field for this case. On the other hand, the sharpness of the jumps in j space are a useful aide in pinpointing the solution after coarse tuning of the parameter guesses is accomplished through matching at $\rho = \rho_4$. For the 3 MV case, the correct steady state values for r_S, j, and $(B_\theta)_{cath}$ are 70.51 cm, 3.90 amp/cm^2, and 0.689 kG respectively. Similarly, for $\phi_0 = 4$ MV, they are 70.33 cm, 4.735 amp/cm^2, and 0.677 kG. Finally, for $\phi_0 = 5$ MV, the corresponding numbers are 70.03 cm, 6.315 amp/cm^2, and 0.663 kG. In Fig. 9 are plotted the profiles of ϕ and B_θ near the cathode for all three cases. Notice the pronounced discontinuity in the slope of each B_θ at its respective electron sheath boundary compared to the relatively smooth transition of ϕ across the same boundaries. In vacuum, the B_θ has a simple r^{-1} dependence while $\phi(r)$ is proportional to ln r.

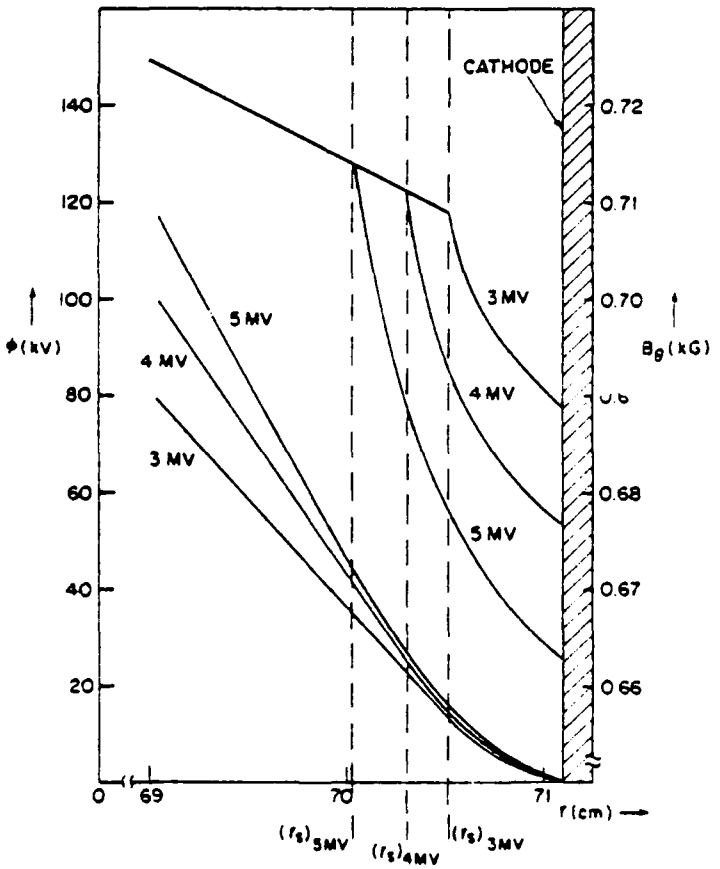

Fig. 9 — Profiles of ϕ and B_θ for the modified AURORA MITL

The weakest insulation can probably be expected near the end of the anode stalk where the damage was experimentally observed. Cylindrically coaxial equilibrium solutions will be sought for that region using RADBER for total voltages, ϕ_0, of 3.0, 4.0 and 5.0 mV. Assuming 250 kA of axial current in the anode stalk demands a vacuum B_ϑ of approximately 0.7032 kG at the lower cathode radius of 71.1 cm. That value will be used as the scale B-field, B_0. RADBER's numerical variables must then be set as follows:

a. LAZ = .TRUE.

b. LCIN = .FALSE.

c. LIONS = .FALSE.

d. ERROR = 0.01

e. RC = 71.1

f. RANODE = 26.7

g. UØ = 3.0E6, 4.0E6, and 5.0E6

h. BØ = 0.7032E3

i. CURCEN = 2.50E5.

This problem is somewhat simpler than that of the radial diode since no ion current is present. Thus, only two parameters, j and $(B_\vartheta)_{\text{cath}}$, must be guessed. Similarly, only two resultant parameters, U and $W' = Y$, must be matched at $\rho = \rho_S$ and $\rho = \rho_A$. As a starting point for parameter guesses, simple Child-Langmuir theory predicts about 6.2, 9.5 and 13.3 amps/cm^2 of emitted electron current density for $\phi_0 = 3.0$, 4.0 and 5.0 MV respectively. With such low values for j, relatively little departure from the vacuum B_ϑ of 0.70 kG can be expected. This in turn would lead to values of ρ_S very close to ρ_c. Because of that, finer resolution must be used in the numerical integration so that a value of $NDR = 750$ is chosen. The details of the numerical solution search process paralleling that used in Appendix B will not be given here. It is sufficient to note that the reduction of the work from a three-point to two-point shooting problem permitted convergence to a solution for each of the three voltages within three iterations of guesses.

These solutions indicate that there is very little to fear from power losses to electron flow in this feed line. The electron sheathes at the cathode surface are all on the order of only one centimeter thick compared to a radial anode-cathode separation of almost forty-five centimeters. The source of the experimentally-observed damage patterns is now believed to be some phenomenon associated with the plasma erosion switches used near the diode assembly.

REFERENCES

1. K.D. Bergeron, Phys. Fluids 20, 688 (1977).

2. D.J. Johnson, et al., Phys. Rev. Lett. 42, 610 (1979).

3. P. Dreike, et al., J. Appl. Phys. 47, 85 (1976).

4. S. Humphries, Jr., et al., J. Appl. Phys. 47, 2382 (1976).

5. M.Y. Wang and M.S. DiCapua, J. Appl. Phys. 51, 5610 (1980).

6. B. Goplen, R.E. Clark, and S.J. Flint, Mission Research Corporation Report MRC/WDC-R-001 (1979).

7. A.A. Kolomenskii, E.G. Krastelev and B.N. Yablokov, Sov. Tech. Phys. Lett. 3, 247 (1977).

8. J.D. Smith, Proc. 1st Inter. Conf. on Electron Beam Research and Technology 1, 472 (1976).

9. R.N. Sudan and R.V. Lovelace, Phys. Rev. Lett. 31, 1174 (1973).

10. R.V. Lovelace and E. Ott, Phys. Fluids 17, 1263 (1974).

11. A. Ron, A.A. Mondelli and N. Rostoker, IEEE Trans. Plasma Science, PS-1, 85 (1973).

12. T.M. Antonsen, Jr. and E. Ott, Phys. Fluids 19, 52 (1976).

13. J.M. Creedon, J. Appl. Phys. 46, 2946 (1975).

14. O. Buneman, Proc. Camb. Philos. Soc. 50, 77 (1954).

15. L. Brillouin, Phys. Rev. 67, 260 (1945).

16. J. Swegle and E. Ott, Phys. Fluids 24, 158 (1981).

17. I.D. Smith, P. D'A. Champney and J.M. Creedon, Proc. IEEE Inter. Pulsed Power Conf., Lubbock, Texas (1976).

18. A.T. Drobot, private communication.

19. Shyke A. Goldstein, J. Appl. Phys. 47, 894 (1976).

20. S.D. Conte and Carl de Boor, *Elementary Numerical Analysis* 2d ed. (McGraw-Hill, New York, 1972), p. 338.

21. F.S. Acton, *Numerical Methods That Work* (Harper & Row, New York, 1970), p. 146.

22. I. Langmuir, Phys. Rev. Series 2 2, 450 (1913).

23. I. Langmuir and K.B. Blodgett, Phys. Rev. Series 2 22, 347 (1923).

24. *ASC FORTRAN Reference Manual*, Texas Instruments, Inc., Publication No. 930044-3 (1978).

25. R.J. Barker, S.A. Goldstein, and A.T. Drobot, Proc. IEEE Int. Conf. on Plasma Science, Montreal, Canada (1979).

PRODUCTION OF INTENSE LIGHT ION BEAMS FROM A SUPERPOWER GENERATOR

I. INTRODUCTION

Recent technological advances in the production and focusing of intense pulsed light ion beams (hydrogen, deuterium, and carbon) have raised the attainable intensities from levels of 1 A/cm^2 into the MA/cm^2 regime.[1-3] The present achievements of high-power ion beams and the potential for continued advancements in this field make them prime candidates as drivers for inertial confinement fusion (ICF). Requirements of an ICF system that are met by an ion beam driver[4-6] include: (1) ions can be produced at high efficiency in extraction geometries appropriate to ICF ignition,[7-9] and (2) beam power density delivered on target can be significantly larger than the source density through velocity bunching of the ions during transport,[10] by geometrical shaping of the ion source,[8] or by externally magnetically focusing the extracted ion beam.[7] A specific advantage of an ion beam driver for ICF is that the ion energy deposition profile in the target is more favorable than those of either laser photons or relativistic electrons[11].

A variety of diode configurations to produce light ion beams for ICF have been discussed in the literature.[1] In this paper, experimental investigations into the production and ballistic focusing of proton and deuteron beams from one such diode are presented. The pinch-reflex diode,[8] developed by the Naval Research Laboratory (NRL) on the Gamble II accelerator, was matched to the PITHON generator[12] at Physics International Company. In addition to diode physics studies, the coupling between a biconic magnetically insulated vacuum transmission line and a small pinch-reflex diode at high stress ($E > 2 \times 10^6$ V/cm) has been investigated.

The early motivation for this work stemmed from computational modeling of the pinch-reflex diode toward ICF applications. The PITHON generator parameters may satisfy requirements for a single module in a multi-ion-beam target irradiation concept based on beam bunching during transport in Z-pinches[13] and multi-beam overlap on target. Two experimental sessions were performed with this generator: The first studied the scaling of diode performance and ballistic focusing at higher powers and longer pulselengths than previously available;[2] the second studied the detailed shape evolution of the electrode plasma surfaces--information essential for design of a diode to produce a high quality focused ion beam.[14]

Manuscript submitted November 10, 1981.

In this paper we present the results of these studies. The generator and diode are discussed in Sec. II. The beam diagnostics employed to evaluate ion species, current density profile and history, time-integrated beam geometry, and anode plasma surface evolution are described in Sec. III. The principal results of the two experimental sessions are presented and discussed in Sec. IV. Conclusions of this work are presented in Sec. V.

II. EXPERIMENTAL APPARATUS

A. Accelerator

The PITHON accelerator, shown schematically in Fig. 1, is a water dielectric multi-stage coaxial transmission line driven by a 40-stage, 1.5-MJ, oil-insulated, twin Marx generator. The 2.3 Ω intermediate storage capacitor is charged to a voltage above the open circuit Marx potential (through ringup), then discharged via a single-site, self-breaking water switch into a 1.3-Ω pulse forming line (PFL). Multi-site water output switches provide a low-inductance energy transfer from the PFL to a tapered 1.0 Ω first transformer in a pulse of about half the PFL voltage and twice the duration.

A common problem in pulsed power accelerators is a low-voltage, long-duration "prepulse" loading the diode prior to the main high voltage pulse. This phenomenon is due to capacitive coupling between sequential inner conductor stages of the accelerator and can often lead to diode shorting and nonreproducibility. This coupling is reduced in PITHON by a low permittivity epoxy "prepulse slab" between the first and second transformers (see Fig. 1). For a shot yielding a 2-MV output pulse, this technique reduces the prepulse level at the vacuum interface from over 300 kV to below 10 kV thus allowing the use of a wide variety of field-emission-diode loads.

Multi-site, gas-insulated switches connecting the transformers through the prepulse slab close on the leading edge of the high voltage pulse. There are two interchangeable second transformers which connect this slab to the water-vacuum interface with characteristic impedances of 0.75 and 1.0 Ω. Both interfaces allow penetration of a "transit time isolator" cable shield through the water from the high-voltage vacuum cathode to the grounded outer shell. Through this isolator the ion-beam diagnostic signals, floating at the 2- to 2.5-MV cathode potential, can be extracted with less than 50-mV noise.

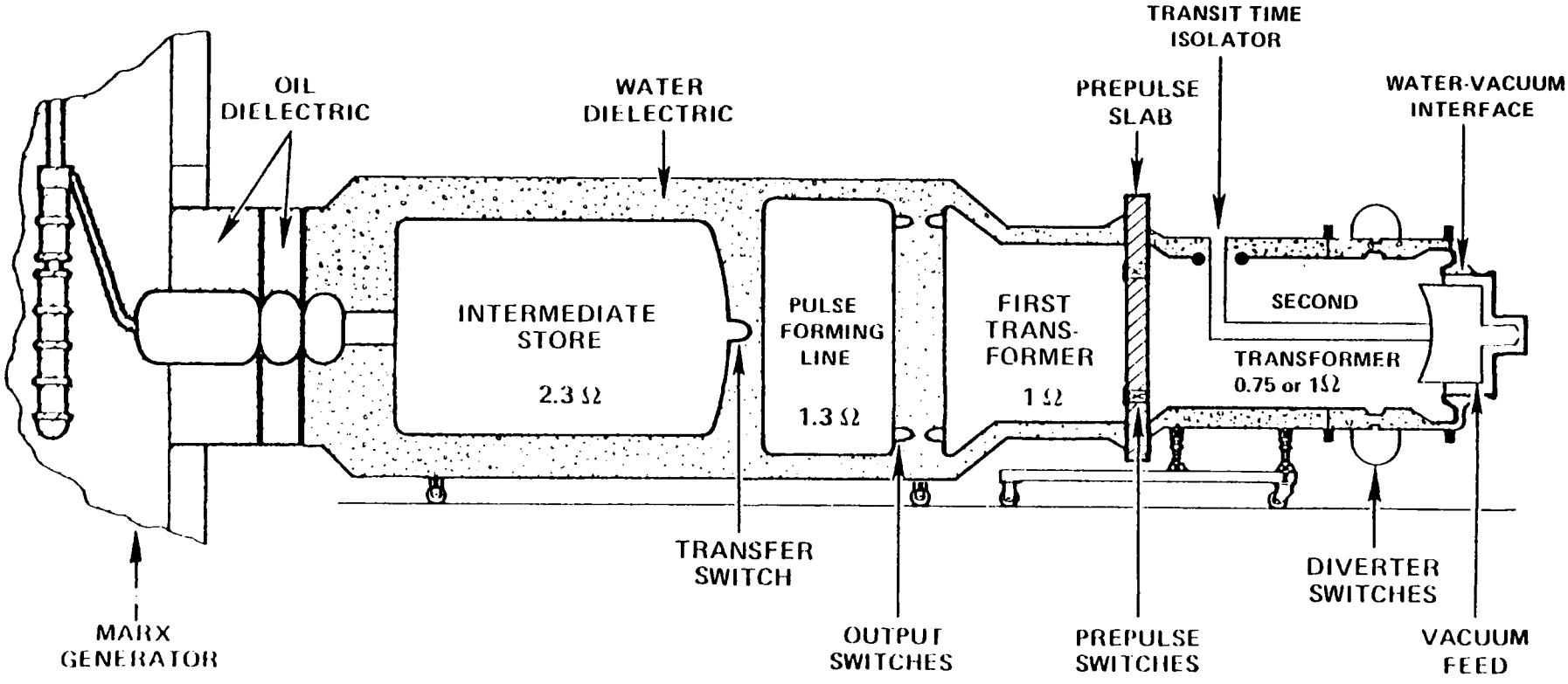

Fig. 1 — Schematic of the PITHON waterline

The vacuum feed connecting the second transformer to the diode is shown in Fig. 2. The shaded area is the water-dielectric transmission line, which carries the electromagnetic wave. The line bends radially inward and flares to reduce the electric field stress on a graded axially-stacked epoxy interface separating water from vacuum. Interface voltage and current diagnostics (V_T and I_T) are located at the flare in several azimuthal locations. On the vacuum side of this interface, the energy pulse is carried by an electromagnetic wave and by electrons. The total current can be measured on the anode and is monitored at the vacuum interface (I_0) and at the diode (I_D). The total inductance between these monitors is about 30 nH. A dielectric surface flashover switch interrupts the cathode side of the feed to further reduce the prepulse on the diode to about 5 kV.

B. Diode Structures

Two independent cathode and anode configurations were tested in these experiments. The diode structures used in the first run are shown in Fig. 3. Following the vacuum feed from the flashover switch toward the axis, a sudden transition is made from a radial biconic to a coaxial feed. The center conductor is the cathode shank, a 0.6-cm-thick wall stainless-steel cylinder. The outer coax anode shell is aluminum and can be adjusted for concentricity and axial spacing. This coax section terminates in the pinch-reflex diode: a thin hollow cathode tip opposite a grounded planar or spherical anode.

A planar pinch-reflex diode is shown in Fig. 3a. The anode assembly is a disk of 0.012-cm-thick polyethylene (CH_2) held 5 mm from a carbon backing plate by an outer insulating annulus and a central carbon button. When this foil flashes early in the electrical pulse, an anode plasma spreads across the foil and expands into the anode-cathode gap. Ions are accelerated toward the cathode from the low-density front of this moving plasma and are deflected radially inward by their self-magnetic field toward a time-varying collection of foci. The ion beam current (I_{ion}) is measured by a Rogowski coil sheltered behind the cathode tip. The ions entering the cathode pass through a 1.8-μm-thick polycarbonate (Kimfol*) foil pressure window and propagate current- and charge-neutralized in a 1-Torr-nitrogen drift chamber.

*available from Kimberly Clark Corp., Lee, MA, 01238

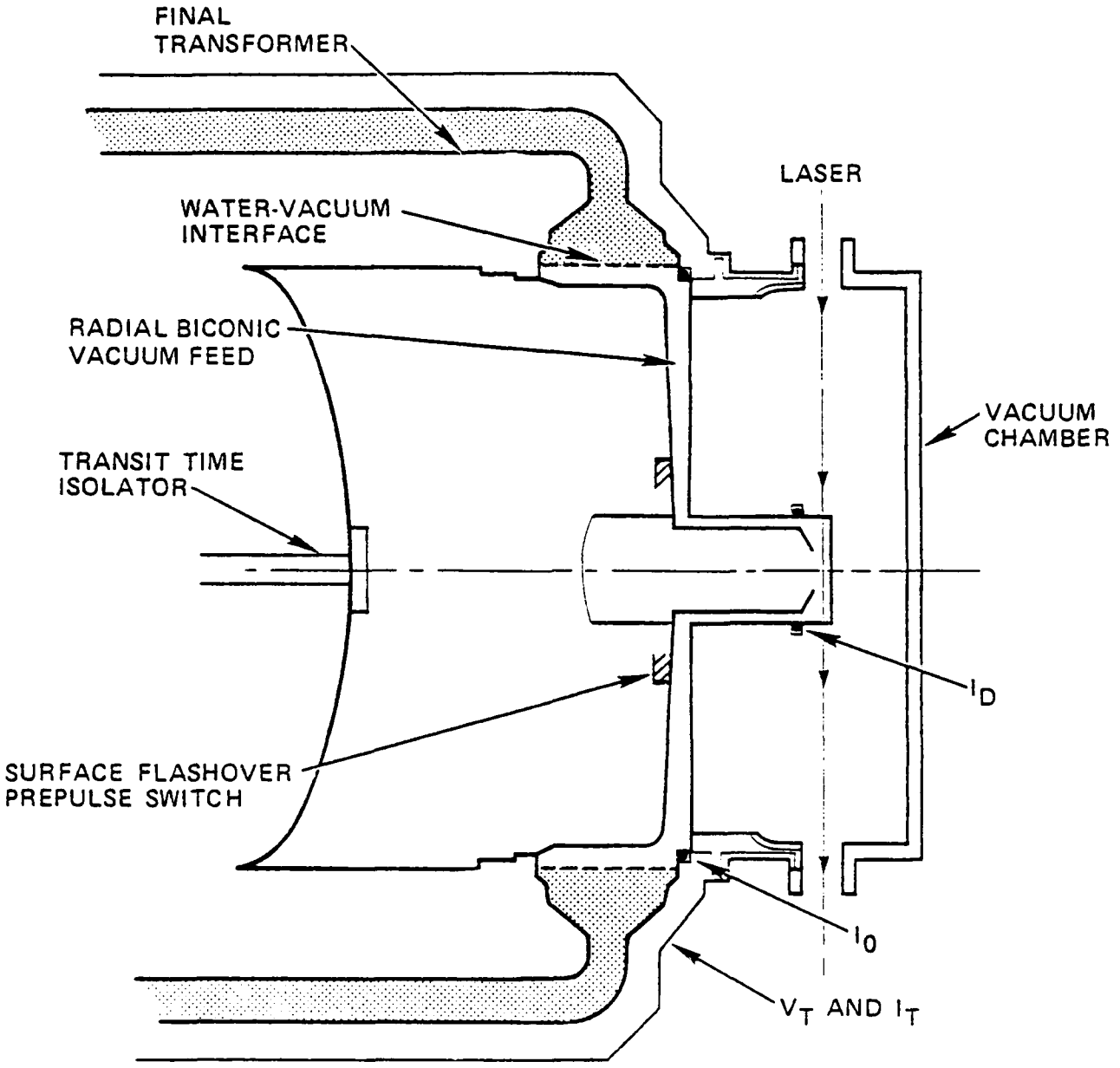

Fig. 2 — Schematic of the vacuum feed interface on PITHON

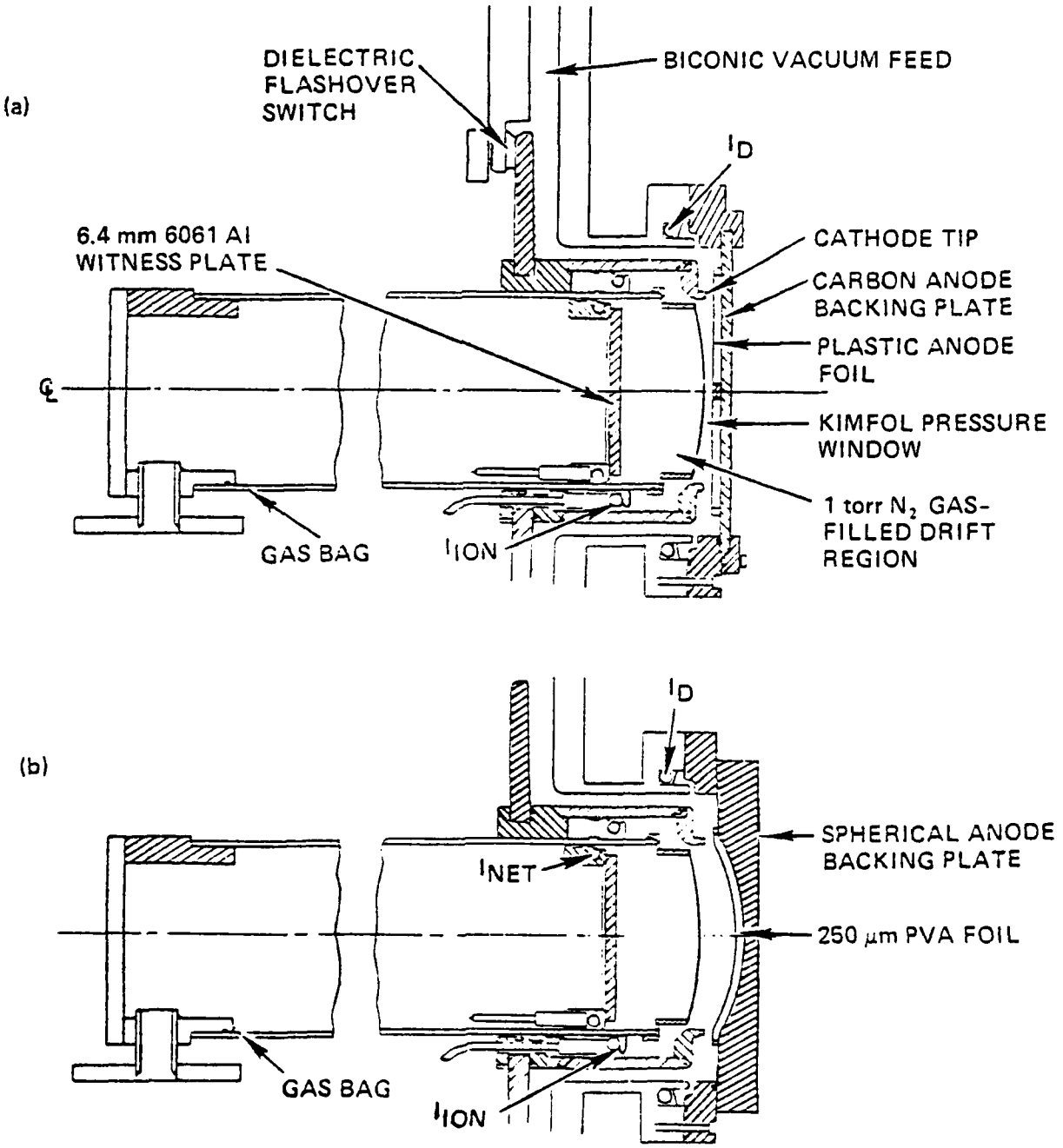

Fig. 3 — Pinch-reflex diode assemblies for the first experimental session in (a) planar geometry and (b) focusing geometry

The focusing configuration of the pinch-reflex diode in the first experimental session is shown in Fig. 3b. Anode foils of 0.025-cm-thick polyvinyl-acetate (PVA), deformed into a spherical section with a 12.7-cm radius-of-curvature, were mounted onto similarly machined carbon backing plates to maintain a 5-mm foil-plate separation (see Fig. 3b). An extended tip cathode was used to define the 100-cm^2 diode area for pinch-reflex electron operation with a 3- to 4-mm anode-cathode gap. The initial ion velocity is directed toward a geometric focus located substantially inside the planar-diode focal length. The intent of this design is to create a high-current-density ion-beam focus which is less sensitive to self-deflection variations during the pulse[14] and from shot to shot.

The diode structures used in the second session were somewhat different from those shown in Fig. 3 and are displayed in Fig. 4. The coax gap was increased to form a higher inductance but constant characteristic impedance 5-Ω transition from the biconic into the coaxial feed. This design represents an attempt to improve the vacuum power flow into the diode structure. The thick stainless-steel cathode shank was severely distorted after a few PITHON shots in the first run and has been replaced with disposable spun aluminum cylinders in this design. By sealing the inner cathode volume with Kimfol glued to the tip of the ion Rogowski assembly, the inside of the cathode is pressurized to 1-Torr nitrogen while the surrounding volume is at ambient 10^{-5} Torr pressure. Variation of cathode radius was engineered by spinning a smooth taper on the cathode tip. Figure 4a shows a 100-cm^2 cathode bore, while Fig. 4b shows a smaller 30-cm^2 area diode.

The coax length was extended to allow access for direct viewing across the diode gap with a ruby laser holographic system. Planar diodes were used and disposable anode backing plates were fabricated of spun aluminum in which an array of viewing slots were machined. The slots were made as symmetric as possible consistent with direct viewing to avoid return current asymmetries. Finally, a 7.6-cm-diam central carbon insert was pressed into the backing plate to minimize bremsstrahlung and to reduce aluminum buildup on the reusable diode hardware.

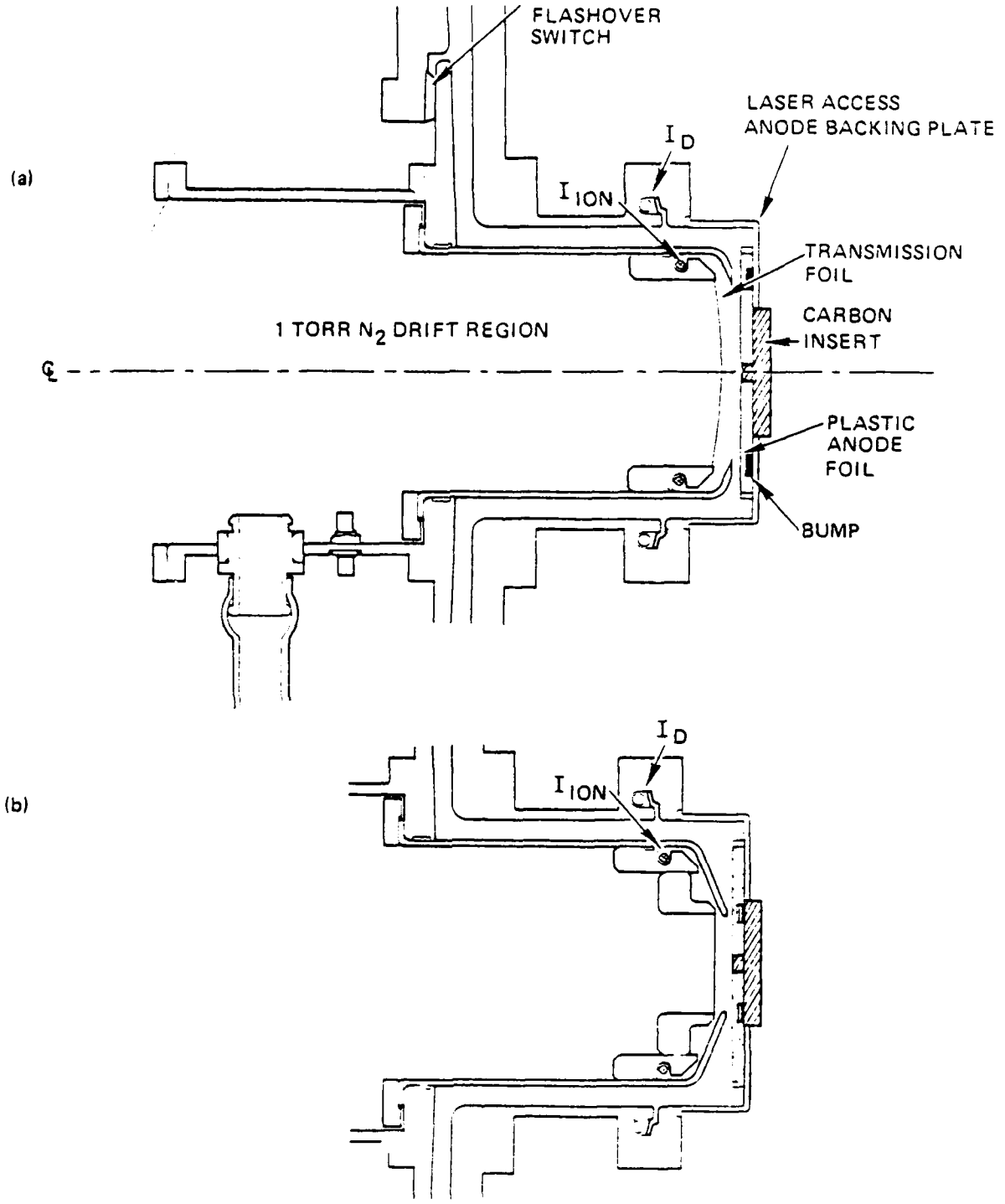

Fig. 4 — Pinch-reflex diode assemblies for the second experimental session for (a) a 100-cm^2 area diode and for (b) a 30-cm^2 area diode

III. DIAGNOSTICS

In this section the generator, beam, and plasma diagnostics will be described and data reduction procedures will be discussed. These include: generator voltage and current detectors distributed in the vacuum feed; bremsstrahlung diagnostics for the electron-beam pinch history and time-integrated x-ray profile; a Rogowski coil to measure the ion-beam current; a "shadow box" diagnostic for spatial-profiling of the ion beam; nuclear-reaction diagnostics for ion-beam duration and fluence; and interferometric laser holography for evolution of the anode and cathode plasmas.

A. Electrical Measurements

The accelerator diagnostics for voltage and various currents are shown in Fig. 2. The injected voltage is measured by balanced capacitive dividers (V_T) at several azimuthal locations in the water, displayed separately to evaluate wave symmetry, and averaged to calculate impedance, power and energy. The injected current is monitored both in the water adjacent to the voltage probes (I_T) and in the vacuum (I_0) at the entrance to the radial biconic transmission line with dB/dt and segmented Rogowski probes, respectively. The difference between these measurements affords insight into water or vacuum arcs in the interface and transition regions. The total diode current (I_0) is measured with a self-integrating Rogowski coil[15] as is the ion current (see Figs. 3 and 4). These current monitors have risetimes of less than 5 ns and integration times greater than 3.4 μs . Several designs are employed to shield the epoxy encapsulated coils from particle bombardment and UV irradiation while minimizing the monitor inductance. On most shots, valid ion current measurements are obtained from power onset to peak. All current monitors are bench tested and cross-calibrated in short circuit shots. The data are monitored through a 200-MHz bandwidth 7912R transient digitizer system controlled by a PDP 11/40 computer and are reduced numerically.

B. X Rays

The ion power and energy on each shot are qualitatively correlated with the yield of bremsstrahlung radiation and the symmetry and size of the electron pinch as evidenced by its x-ray image. Because the bremsstrahlung yield scales with diode potential, a large x-ray signal with a large FWHM (40-60 ns) indicates a high-voltage, long-impedance-lifetime shot.

The time-resolved x-ray output from the electron pinch is monitored with an optical photodiode (PDX) coupled to a plastic scintillator. The unit is rigidly mounted outside the vacuum chamber at 180° to the diode axis. Similarly mounted is an x-ray pinhole camera to record hard photons ($E > 30$ keV) from the diode region through a 0.05-cm-diam 20° tapered pinhole. This camera images the diode onto a stack of Kodak No-Screen, XR5, and Polaroid Type 52 films coupled to a variety of intensifier screens. This wide range of film sensitivities to x rays affords good contrast over the variation of bremsstrahlung intensity across the diode image. Lithium fluoride thermoluminescent detector (TLD) capsules monitor the time-integrated bremsstrahlung dose at the photodiode from the entire anode. Serious current losses in the vacuum feed were correlated with the photographic, TLD, and PDX data as well as with visual damage following a shot.

C. Ion Imaging

The location of the ion-beam focus was determined by using ballistic reconstruction of ion trajectories from the edges of ion-induced melt damage patterns recorded on the rear witness plate of a shadowbox[2] (see Fig. 5). The interpretation of this data is based on several key assumptions. These are: the ions are accelerated from a planar anode plasma with initial velocity vectors parallel to the axis; as they cross the anode-cathode gap each ion is magnetically deflected by the field of a calculated ion-current-density profile.[16] Upon crossing the cathode foil and entering the 1-Torr-nitrogen drift chamber, the ions are assumed to be charge and current neutralized and hence execute straight-line orbits through a focal region and expand into the shadowbox. The current neutrality premise has been verified by measurements of the net-current fraction in the gas (I_{net}/I_{ion}) of less than 2% on both Gamble II (Ref. 2) and PITHON. The damage patterns on the witness plate of the shadowbox are projections of the ion beam through the front apertures (see Fig. 5). The patterns, which are time-integrated records, often form teardrop or oval shapes. The radial variation is attributed to the change in focal length during the pulse due to time-varying diode fields. The azimuthal width of the damage is due to the divergence of the ion beam from the anode plasma, asymmetries in the source, and scattering through the transmission foil. The computer reconstruction, shown in Fig. 5, traces the recorded damage areas back through the front-plate apertures, through the focus and onto the anode

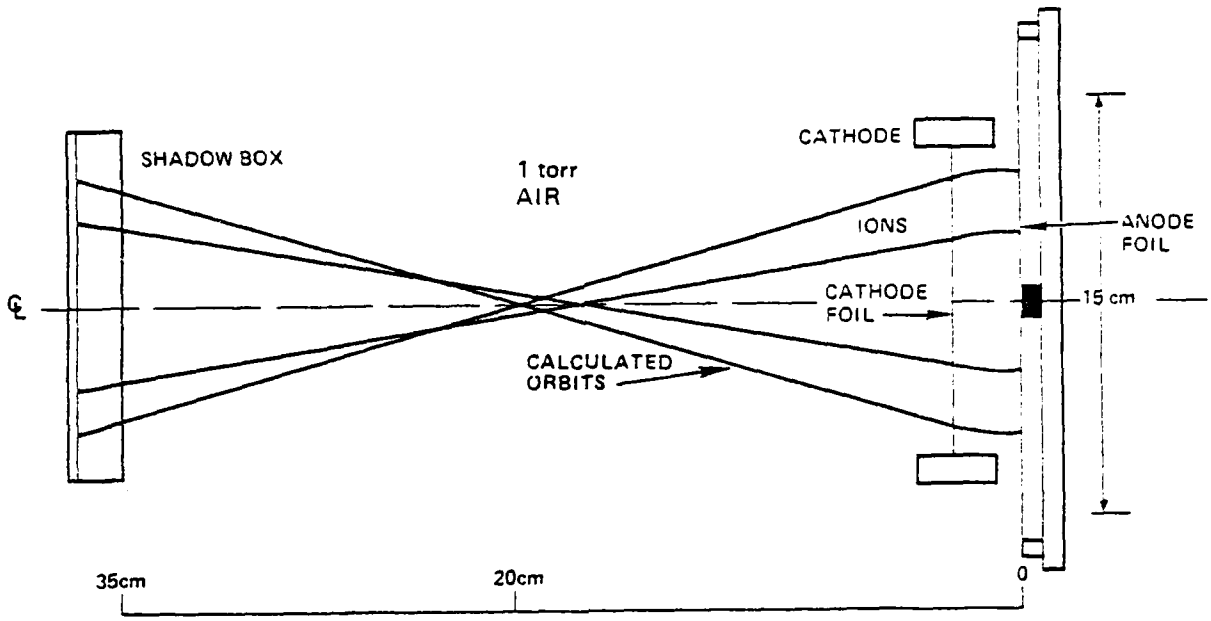

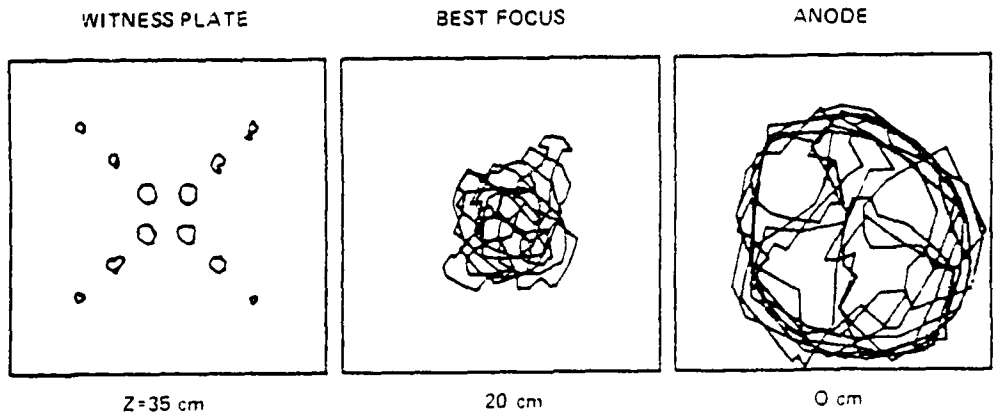

Fig. 5 — Shadowbox geometry and reconstruction of ion-beam trajectories for planar-diode Shot 1676

surface. The large damage patterns at the smallest radii on the witness plate are due to the time-varying focal spot moving through the shadowbox location and are not useful in planar geometry reconstructions.

D. Nuclear Diagnostics

The intensity and duration of proton or deuteron currents were also monitored by nuclear-reaction techniques. For proton beams, a prompt γ-ray diagnostic[17] was employed utilizing the $^{19}F(p,\alpha\gamma)^{16}O$ reaction. Teflon (CF_2) targets were placed in the ion-beam path, and 6-MeV prompt γ rays were measured with a fast scintillator (NE-111) and photomultiplier (XP-2020) detector housed in a 3.2-cm-thick lead enclosure located 4 m from the ion diode at 95° to the diode axis behind a one meter-thick concrete shielding wall. This wall differentially shields the diode bremsstrahlung and improves the γ-ray-to-bremsstrahlung ratio. Measured and calculated signals for this detector on a shot with a CH_2 anode and Teflon target are compared in Fig. 6. This detector could not be calibrated absolutely as the attenuation of the prompt-γ signal by the concrete shielding wall is difficult to estimate.

The total yield of deuteron beams was determined by measuring neutrons from the $D(d,n)^3He$ and $^{12}C(d,n)^{13}N$ reactions. Deuteron beams, produced by using CD_2 coated PVA foil anodes, were directed onto thick CD_2 targets to produce these reactions. Because the ion beam was directed into the generator in these experiments, neutron measurements were confined to recoil angles greater than 90°. Total neutron yields were measured with two rhodium activation detectors[18] located 17 m from the diode at 175° to the diode axis. These detectors viewed the diode through a 30-cm-diam hole in a concrete shielding wall located 8.3 m from the diode. This geometry minimized the number of room-scattered neutrons which reached the detectors and allowed the intensity of the direct collimated neutron beam to be scaled inversely with the square of the source-to-detector distance, even at 17 m. These rhodium activation detectors were calibrated with a ^{252}Cf neutron source as described in Ref. 18. Deuteron intensities were inferred from measured neutron intensities by using $D(d,n)^3He$ and $^{12}C(d,n)^{13}N$ reaction yields. Thick-target yields for these reactions were calculated from measured cross sections[19,20] and published stopping powers[21] and are presented in Fig. 7. Above 1 MeV, the $^{12}C(d,n)^{13}N$ reaction contributes significantly to the neutron yield.

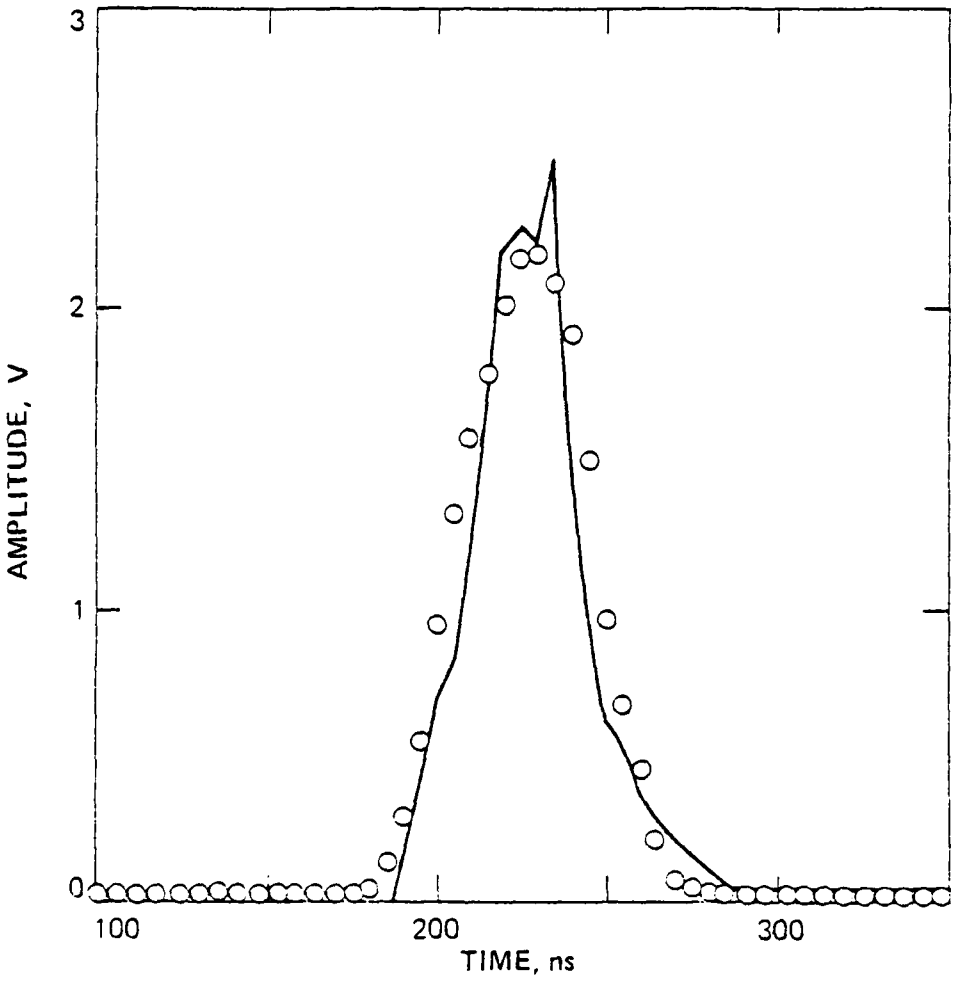

Fig. 6 — Prompt-γ signals measured on Shot 1665 (solid line) and calculated (open circles) for protons on a thick CF_2 target. The calculated trace has been normalized in amplitude to the measured signal. Good agreement in pulse width and shape is shown.

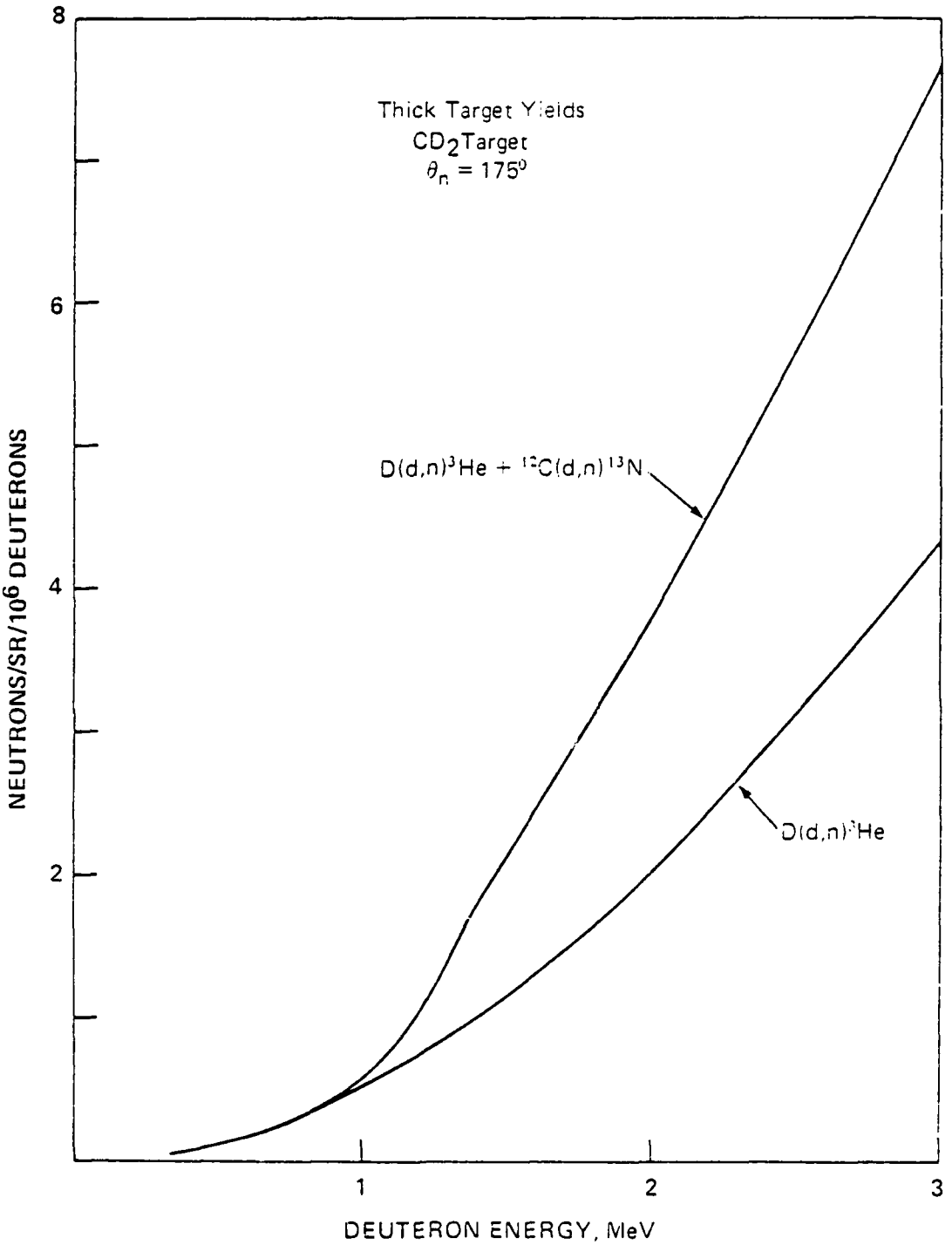

Fig. 7 — Thick-target yields for the $D(d,n)^3He$ and $^{12}C(d,n)^{13}N$ reactions at 175°

The neutron time-of-flight (TOF) technique was used with the $D(d,n)^3He$ reaction to determine neutron energies and to monitor the duration of the deuteron beam. Neutron energies were determined with a TOF detector located 16.8 m from the diode in the same geometry as the rhodium activation detectors. This detector consisted of a fast scintillator (NE-111) quenched with 5% piperidine[22] and photomultiplier (XP-2020) mounted within a 7.6-cm-thick lead shield. To operate this detector in the linear range, the light incident on the photomultiplier was attenuated with an ND-1 filter. The time history of the deuteron beam was determined using a TOF detector with a relatively short flight path as described in Ref. 23. For this purpose, a detector was located 3.2 m from the diode at 160° to the diode axis. This detector consisted of a similar fast quenched scintillator (NE-111), an ND-2 filter, and a photomultiplier (XP-2020) mounted within a 10-cm-thick lead shield. Typical traces from these two TOF detectors are shown in Fig. 8 along with calculated neutron pulse shapes for these detector locations. For the detector at 16.8 m, the time interval from the peak of the bremsstrahlung to the peak of the neutron signal was used to determine the neutron energy. An energy of 1.9 ± 0.2 MeV, consistent with the diode voltage, was determined from this trace after correcting for the x-ray flight time. For the detector at 3.2 m, the duration of the neutron signal gives a measure of the duration of the deuteron beam. The width (FWHM) of this neutron pulse is 60 ns, which compares favorably with the duration of the ion pulse based on the measured diode voltage and ion-current traces for this shot.

E. Interferometric Holography

The final diagnostic to be described is the interferometric holography system[24] used to monitor the anode and cathode plasma motions in the interelectrode gap. The system configuration is schematically illustrated in Fig. 9. The system employs a 6-ns ruby laser pulse, which is split into four beams. These are delayed by path length into 10-ns increments to form a train of four laser pulses over a 30-ns interval. Each of these four beams is split into a scene and reference beam. Each scene beam passes through the pinch-reflex diode and then through lenses and mirrors to form a real image of the diode on a glass holographic film plate. The reference beams are directed to the film without passing through the diode, overlapping their respective scene beams to produce an array of four holograms on the film plane. Two such sets

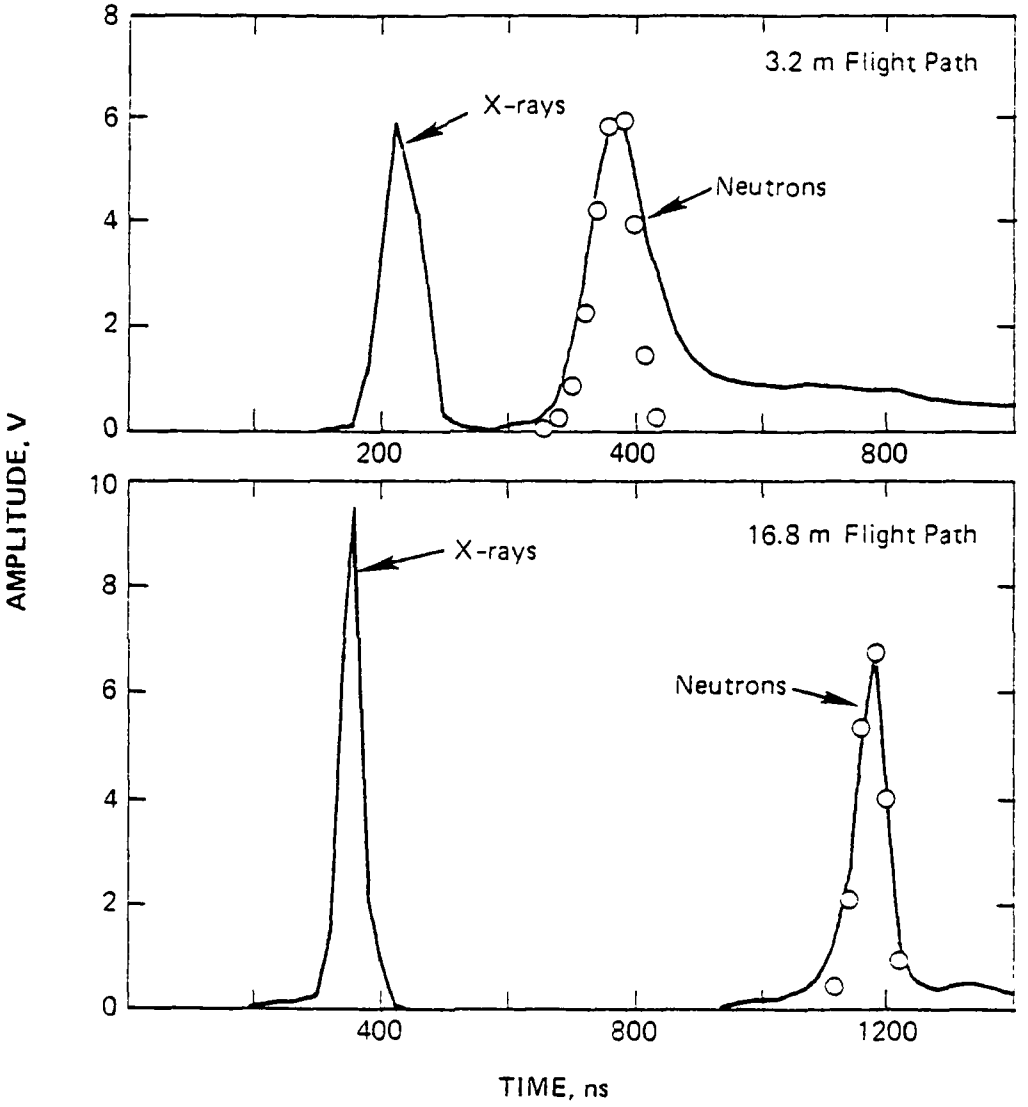

Fig. 8 — Neutron TOF traces for Shot 1692. Calculated neutron pulse shapes at 3.2 m and 16.8 m are plotted as open circles. The calculations are normalized in amplitude to the measured neutron responses.

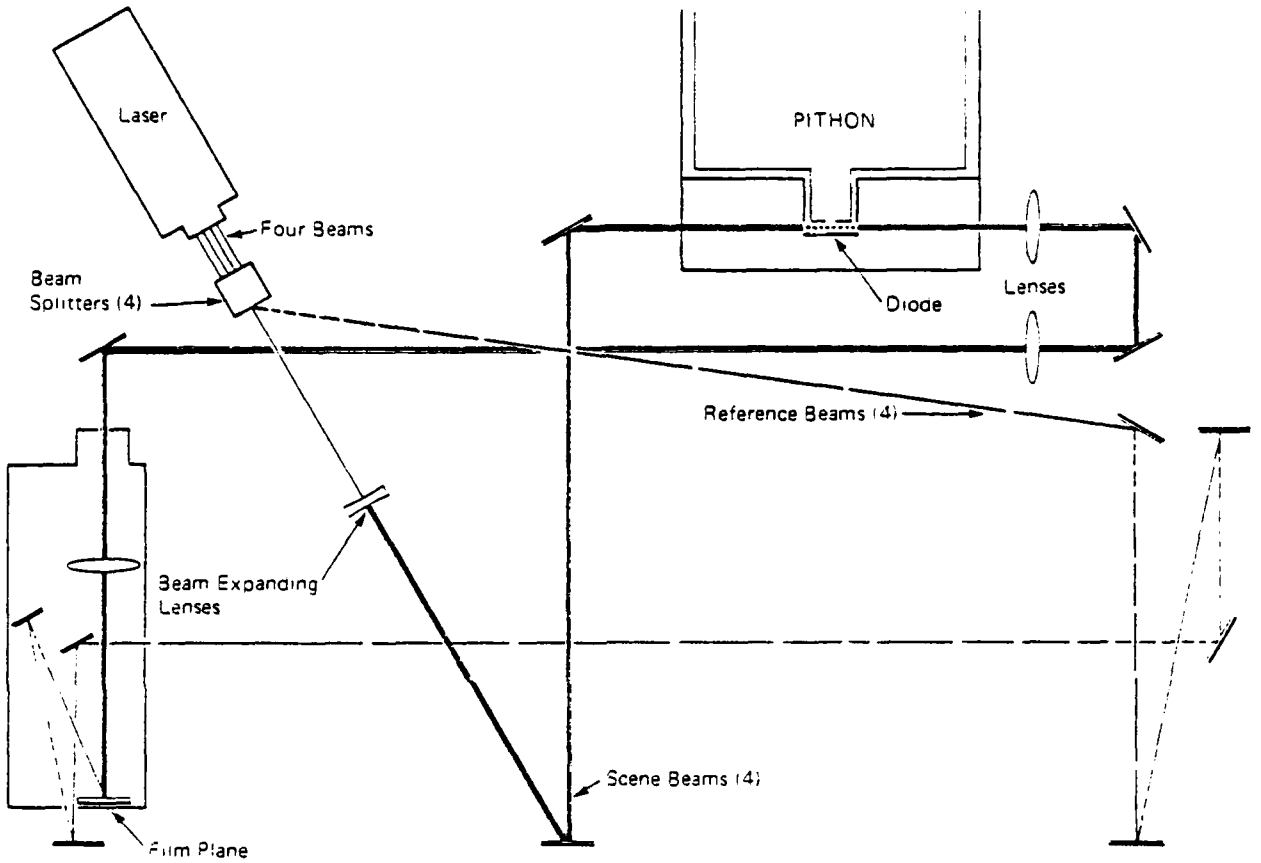

Fig. 9 — Ion-diode laser interferometric holography system

of holograms are superposed: one made before the shot and the other during the shot. The two sets of interference patterns overlap to form four Moire patterns. The differences between a superposed pair of holograms are due to optical-path-length variations in the scene beam where it passes through the diode plasma.

By shining light through a developed interferometric hologram, both an image of the diode and series of fringes can be seen. As an aid to data interpretation, a uniformly changing optical-path-length difference between the two hologram sets is introduced by slightly tilting one of the mirrors in the system after the first set is exposed. This produces a reference array of uniformly spaced straight fringes on the image where no plasma is present. Additional changes in the optical path length caused by plasma result in bending of the fringes: the bending of a fringe over the distance of one reference fringe spacing corresponds to an additional wave length of path difference due to the plasma. The corresponding plasma density can be estimated by the relation:

$$n_e \, \Delta X = 3.2 \times 10^{17}/cm^2/\text{fringe shift}$$

where ΔX is the total path length through a uniform plasma of density n_e. The largest plasma line density measurable by this technique is that for which the index of refraction equals zero (i.e. $2.3 \times 10^{21}/cm^2$). The maximum density observable in this experiment is estimated to be between 10^{19} and 10^{20} due to ray-tracing effects: large-angle refraction of the laser beam by higher-density plasmas reduces the light intensity entering the optical system and the exposure level on the film.

Unfolding the detailed radial-density profile is not possible with this technique. Figure 10a shows the diode area with the laser-viewing slots machined out of the anode: the shaded area is the laser-beam cross section, and the clear holes are the observable diode regions. It is important to note that the view through a hole pair is a chord across a disk system which may not be axially symmetric: a thin plasma ripple in an orientation other than the laser axis will appear to be a large-area plasma motion. Further, anode plasma which crosses the visual anode-cathode gap inside the cathode inner radius does not necessarily contact the cathode plasma lifting off the hollow

(a)

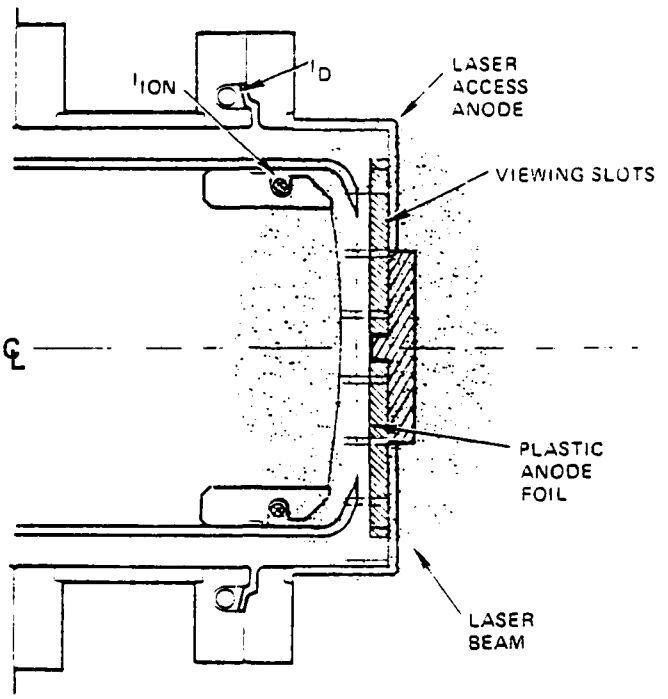

(b)

LASER PHOTO

Fig. 10 — (a) Ion-diode laser diagnostic detail, and (b) reconstructed holographic interferogram

emission ring. Despite these limitations, the system presents new information about the plasma surface evolution which is important for the design of high-focus-quality diodes.[25]

IV. EXPERIMENTAL RESULTS

A variety of experimental goals were addressed in the two pulsing sessions. The first session extended scaling of the pinch-reflex ion diode to the higher power and longer pulselength of the PITHON generator. Both planar and spherical anode foils were tested. The second session utilized modified accelerator impedance and vacuum feed hardware. Emphasis was placed on determining the electrode plasma evolution in the diode, the scaling of diode parameters with cathode radius, and the consequences of diode modifications.

A. Planar Diode Experiments

The important scaling parameters studied in these experiments were the ion efficiency, the ion turn-on time, and the diode-impedance lifetime. The PITHON generator was chosen for these scaling studies for its similarity to Gamble II in minimal prepulse, similar impedance (1.0 versus 1.5 Ω) and voltage risetime, yet larger peak voltage and pulsewidth. These similarities suggested the physics of the pinch-reflex diode would be the same and detailed comparisons could be made between equivalent power PITHON and Gamble II shots. These comparisons, performed during the first session, confirmed the baseline similarity between the accelerators. The scaling variables are then the 70% larger and 30% longer FWHM power pulses available on PITHON. Theoretical calculations[8] based on the generator open-circuit-voltage waveforms predicted a doubling of the Gamble II ion currents to about 1.0 MA of protons from a pinch-reflex diode on PITHON.

A typical waveform data set from the first experimental session (Shot 1662) is shown in Fig. 11. The injected voltage and current measured at the water-vacuum interface (see Fig. 2) have 2.1-MV (V_T) and 2.0-MA (I_0) peak values at a mean impedance of 1.2 Ω. These signals indicate a 4-TW power pulse of 88-ns FWHM containing 340 kJ is injected into the vacuum feed structure. The voltage impressed on the diode (V_D) is less than the injected voltage by the L(dI/dt) inductive drop due to the wave passing through the

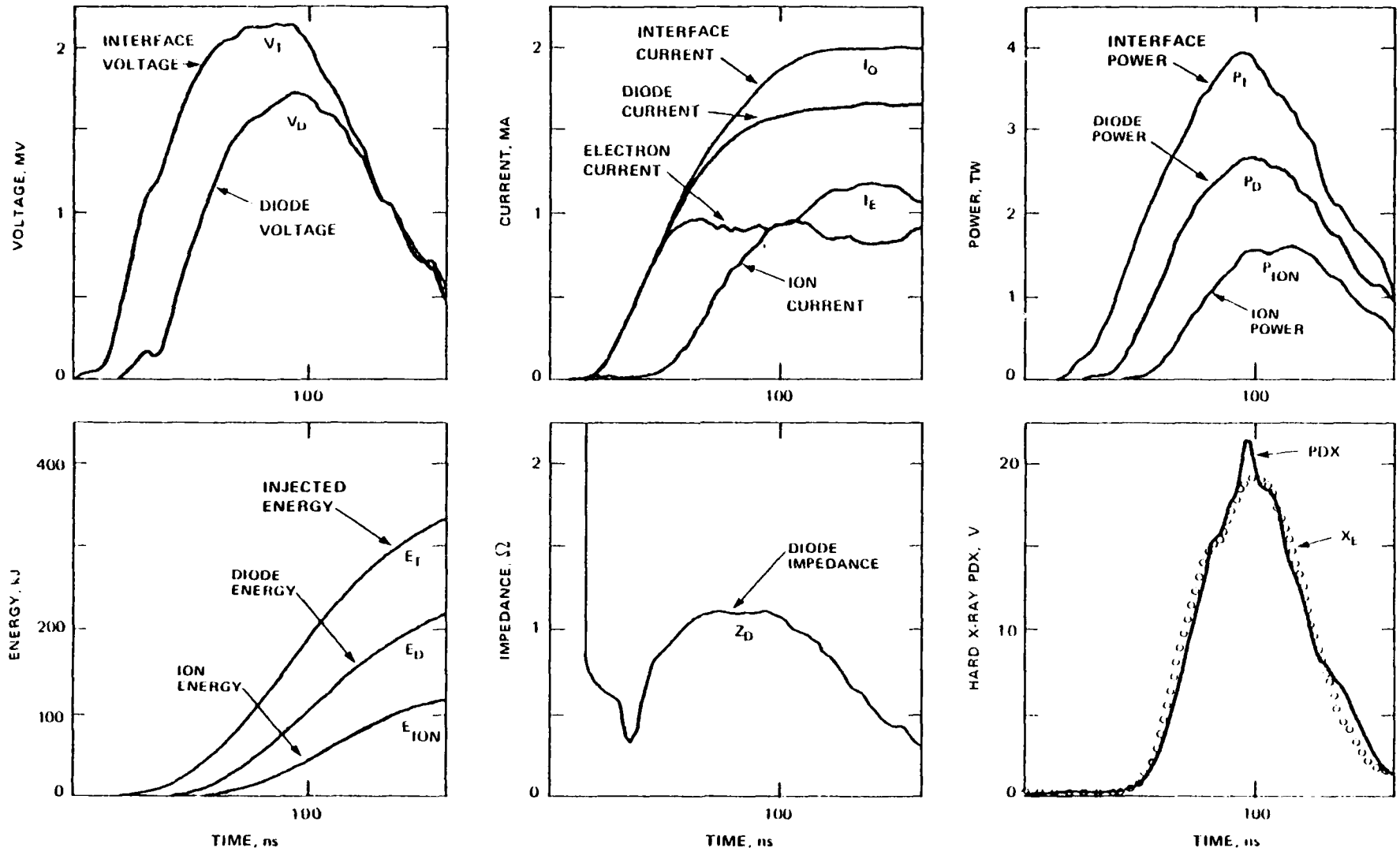

Fig. 11 — Measured waveforms for Shot 1662 at 4 TW

vacuum feed. The effective inductance is determined to be 30 nH by defining the potential across a shorted diode to be zero. There is a current loss in the vacuum feed shown by the difference between the interface (I_0) and diode (I_D) current waveforms. The total electron current in the system (I_E) is defined as the difference between the interface (I_0) and ion (I_{ion}) currents. Despite the losses in the vacuum feed, 2.7 TW and 230 kJ were coupled into the diode on this shot. The ion-beam current entering the 100-cm^2 cathode bore (0.9 MA at 1.7 MV) begins 22 to 26 ns after the diode current, a delay characteristic in all these experiments. The resulting peak ion power and energy are 1.6 TW and 125 kJ respectively. These data correspond to an average source current density of 12 kA/cm^2, which is in agreement with numerical predictions.

The diode-impedance lifetime is an important consideration in scaling the ion diode toward an eventual ICF application. The velocity bunching desired for power multiplication requires carefully programmed voltage and impedance histories. The diode impedance shown in Fig. 11 reaches a plateau near 1.1 Ω for 40 ns then slowly falls until the end of the applied pulse. Accurate impedance control was provided by anode-cathode gap adjustment, with shot-to-shot variations of 0.2 Ω obtained throughout the experimental sessions.

The ion Rogowski coil located inside the cathode provided timing of the formation of an anode plasma on the cathode side of the anode foil. Frequently a low-level signal is seen starting with the diode current (see Fig. 12), due perhaps to a small anode-foil hot spot or to electrons emitted from the ion Rogowski holder and transmission foil. Several explanations for the 22 to 26-ns delay for ion turn-on are possible. One conjecture, based on pinched-electron-beam-diode physics[26] is that before the anode foil flashes, forming a plasma and bringing the floating dielectric foil to ground potential, the electron beam passes through the anode foil and pinches on the backing plate. Previous pinched-electron-beam experiments[27] on PITHON have measured pinch areal velocities of 5 cm^2/ns, or a value of 20 ns for the present 100-cm^2 experiments, which is consistent with the measured delay. The resulting high field stress on the foil adjacent to the central button could then cause surface flashover. If this mechanism is responsible for anode-plasma formation, the small-area (30 cm^2) diodes tested should exhibit a much smaller delay in ion turn-on time of roughly 8 ns. These results, presented

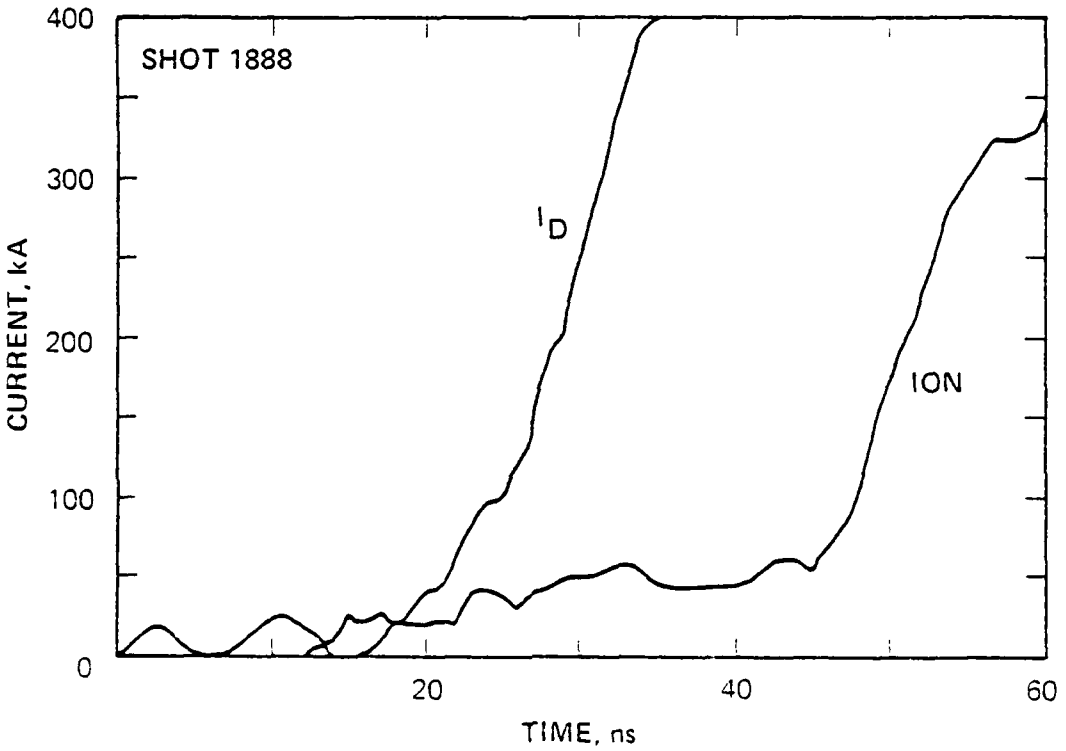

Fig. 12 — Early-time behavior of the diode- and ion-current traces

AD-A129 821 DIODE DYNAMICS BEAM GENERATION AND TRANSPORT AND PLASMA EROSION OPENING SWITCH DEVELOPMENT(U) JAYCOR ALEXANDRIA VA P F OTTINGER 17 MAY 83 JAYCOR-J207-83-C-001 3/8

UNCLASSIFIED N00173-80-C-0202 F/G 9/1 NL

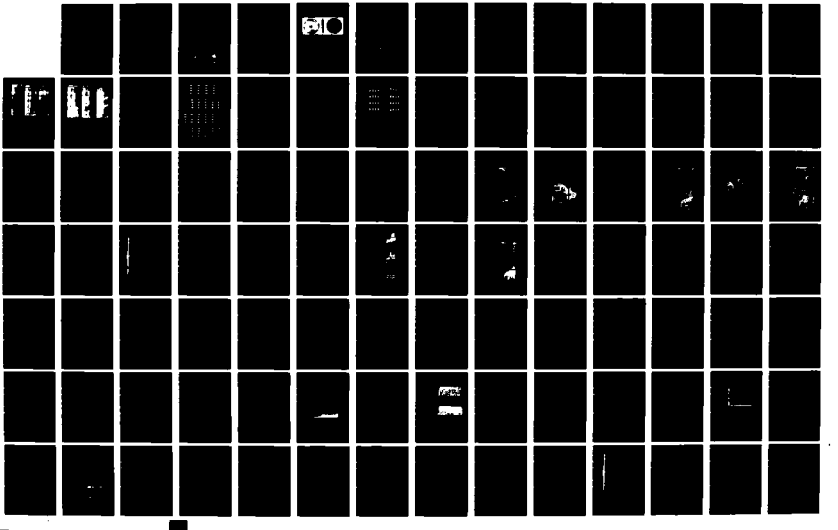

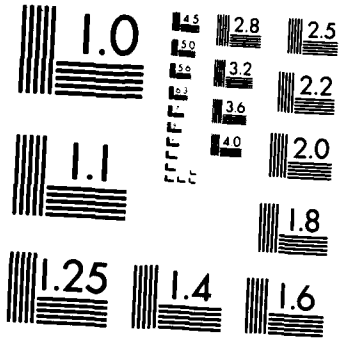

later, show no discernible change in the delay of ion turn-on. An alternative explanation for the ion delay is that it represents the inherent delay of surface flashover.[28] For these large and small area diodes, the difference in delay would be ± 5 ns which is within the shot-to-shot variation.

The radiation diagnostics provide corroboration of the relative timing and waveshape of the diode voltage, injected current, and ion current. The x-ray photodiode signal (PDX) for Shot 1662 is shown in Fig. 11 and compared with a calculated waveform (X_E). The theoretical scaling[29] for x-ray production from electron beams is given by $X_E = I_E(V_D)^{2.8}$, which is a sensitive measure of voltage waveshape. The calculated waveform was normalized in magnitude and shifted in time for the comparison, and the shapes of the two signals agree reasonably well. This agreement provides an independent check on how well the measured voltage and electron current pulse shapes represent the actual wave shapes at the diode. Similarly, the agreement between the measured and calculated prompt-γ nuclear radiation signals[17], shown in Fig. 6, indicates that the diode voltage and ion current pulse shapes are correctly timed and are of reasonable proportion.

The ratio of the ion current to the diode current provides a direct measure of the pinch-reflex-diode efficiency for ion production. At maximum power the efficiency on Shot 1662 is 60% for an ion current of 900 kA. Bremsstrahlung measurements, as described in the next paragraph, indicate that the electron beam formed a well-centered pinch with good coupling of the injected energy to the diode on this shot.

Bremsstrahlung diagnostics were used to study the symmetry of power flow and current loss in the vacuum feed and diode regions. Measurements for two different classes of shots are compared in Fig. 13. A well-centered pinch with bremsstrahlung from only the central 2 cm of the 12-cm-diam anode is observed in the x-ray pinhole photograph in Fig. 13a. For this shot, the x-ray photodiode signal (PDX) is substantial for the entire diode pulse duration, and the energy at the vacuum interface (E_T) shows good coupling of the injected power to the diode. A second class of shots is shown in Fig. 13b where the power flow is asymmetric and the electron pinch is not well centered. The x-ray pinhole image shows flutes extending onto the aluminum backing plate, and bremsstrahlung from the coax feed at 9-cm radius is seen. Intense bremsstrahlung emission from aluminum and stainless steel, relative to

A. GOOD QUALITY PINCH
SHOT 1867

X-RAY PINHOLE

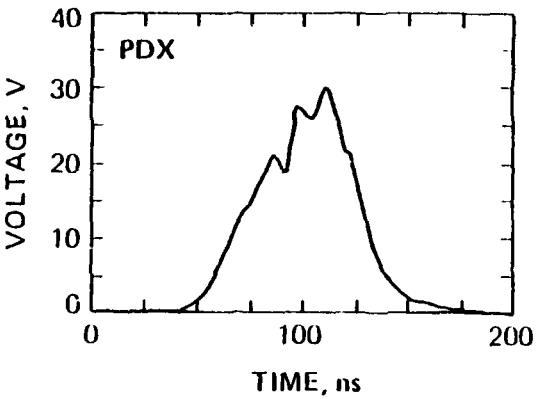

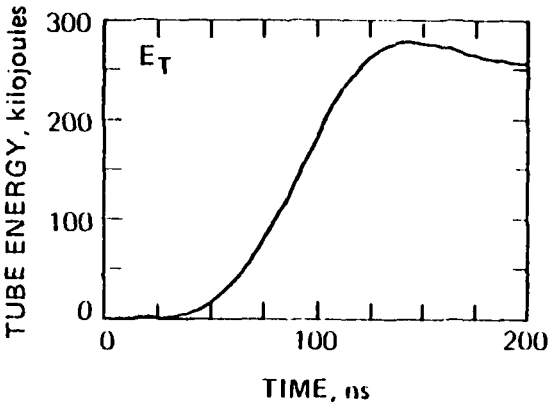

B. POOR PINCH
SHOT 1874

X-RAY PINHOLE

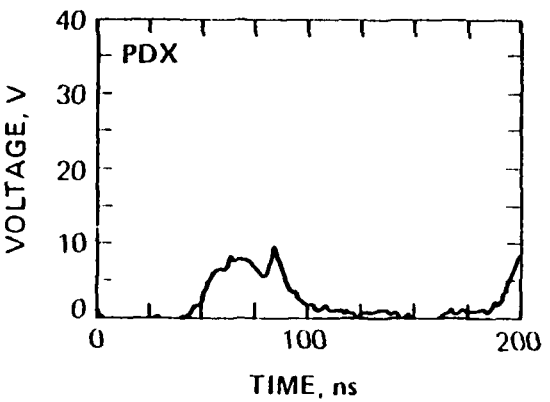

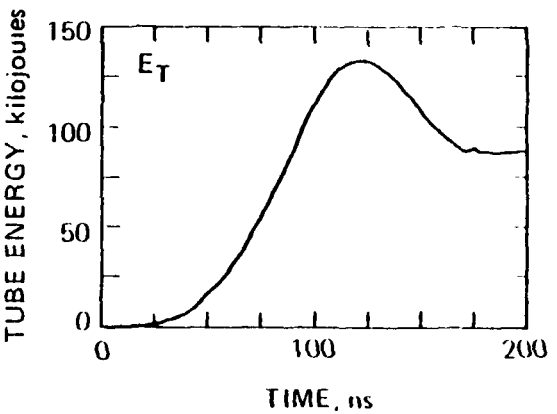

Fig. 13 — Comparison of x-ray pinhole images, x-ray photodiode traces and total energy at the vacuum interface for shots with (a) a good quality pinch and (b) a poor pinch

carbon, allows electron losses in the vacuum feed at low current density to have intensities comparable to the intense central pinch on carbon. On this shot the PDX trace is smaller in amplitude and narrower in pulsewidth, indicating a reduction in diode voltage. Also, a significant fraction of the injected energy is reflected off the load. Visual damage to the feed hardware was consistent with the origins of x rays indicated in Fig. 13 on these two shots.

The shadowbox diagnostic was used to determine the time-averaged location and size of the focus as indicated previously in Fig. 5. A model developed to predict the best focus location[14] yielded a minimum spot size at about 18 cm from the anode foil for the voltage and current values of a typical 3-TW shot. The ballistic reconstruction shown in Fig. 5 gives a best focus at 20 cm, in good agreement with this prediction. Witness plate targets of 6.4-mm-thick aluminum (6061-T6) placed at this location showed centered front surface damage and backspalls about 1 cm in diameter (see Fig. 14).

B. Focusing Diode Experiments

Experiments investigating geometric focusing of high power ion beams from a pinch-reflex ion diode, which were first performed at NRL on Gamble II (Ref. 8), were extended to higher power in the present experiments on PITHON. It is important to note that the voltage, current, and impedance characteristics of the focusing diodes are essentially the same as those of the planar diodes. The ions are magnetically deflected in passage across the anode-cathode gap, then drift ballistically in the 1-Torr gas to an actual focus at about 9 cm from the anode foil, inside the geometric focus located at 12.7 cm. This magnetic bending is demonstrated by shadowbox reconstructions shown in Fig. 15. The damage patterns extrapolate back through the focus to cover the entire anode plane. The focal spot is seen to be within a 3-cm-diam circle, corresponding to an areal beam reduction from the anode source of 14. A preliminary estimate of the focused current density can be made by assuming the entire measured ion current is uniformly distributed over this disk of least confusion. The calculation yields an ion current density of 150 kA/cm^2 over the 7-cm^2 spot. Peak focused current densities could be significantly larger. Witness-plate targets located at the focus exhibit multiple layered backspalls through plates of 6.4-mm-thick aluminum (6061-T6), consistent with higher focused current densities than found in the planar-geometry shots.

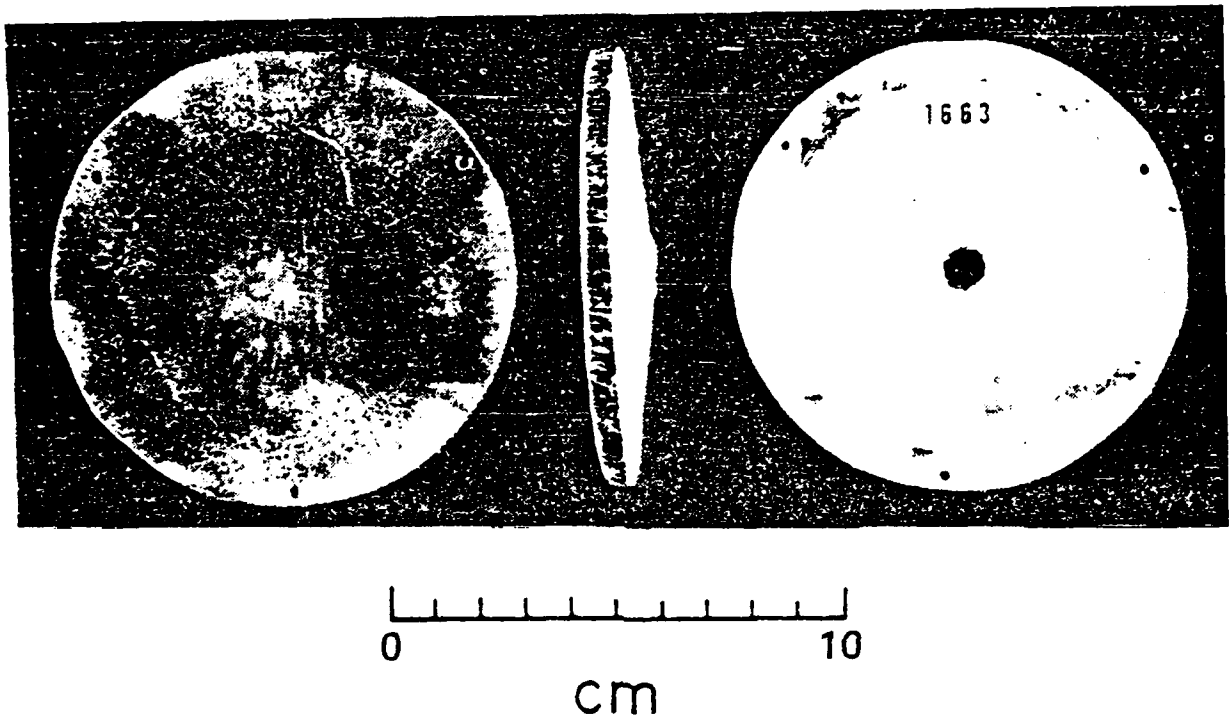

Fig. 14 — Witness plate damage on Shot 1663 for a 6.4-mm-thick aluminum (6061-T6) plate located at the approximate proton self-focus of a planar pinch-reflex diode

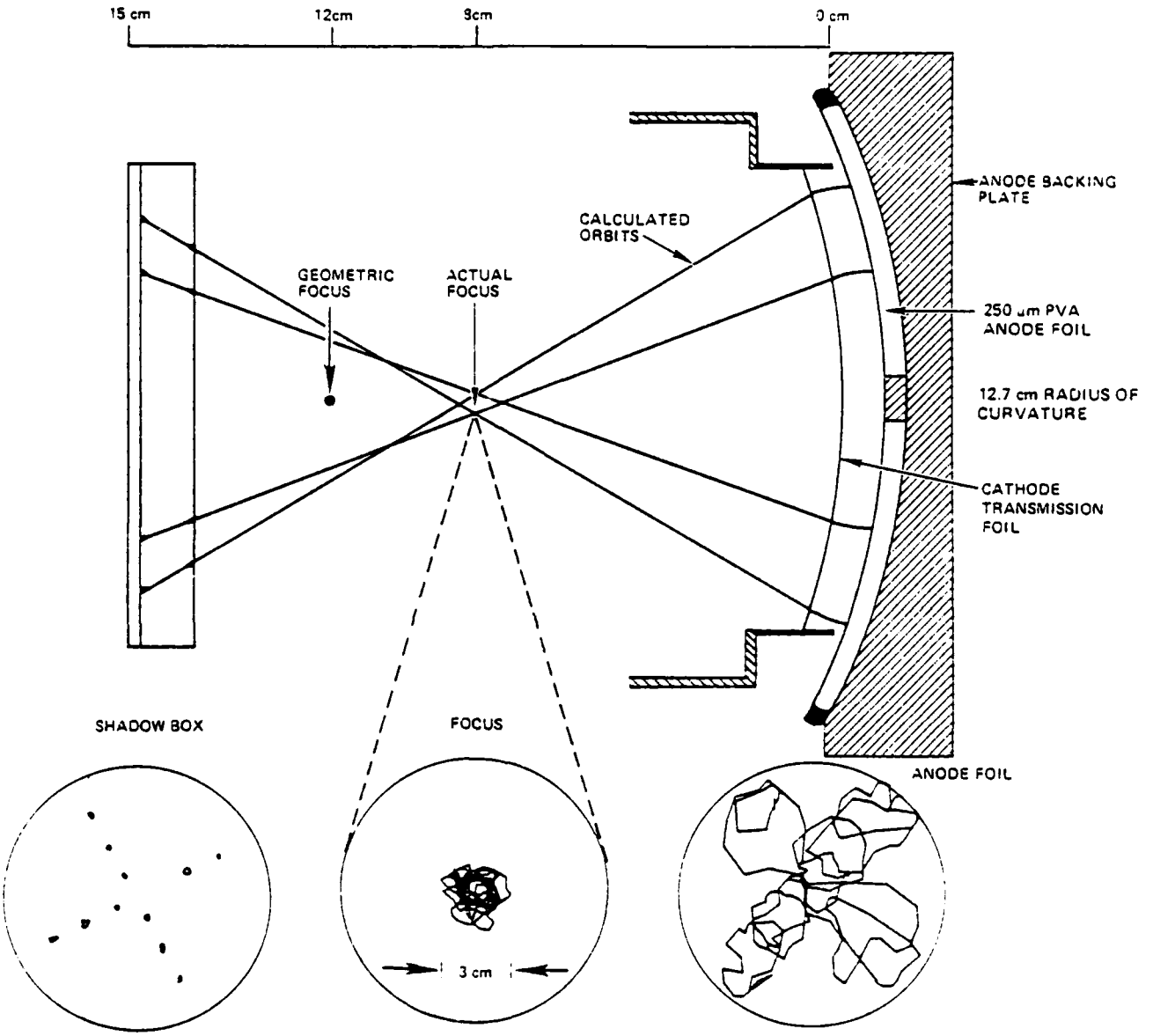

Fig. 15 — Shadowbox geometry for a focusing pinch-reflex diode and reconstruction of ion trajectories for Shot 1863

C. Results from Neutron Measurements

The energy of neutrons from the $D(d,n)^3He$ reaction was determined by the TOF technique. However, this measurement could not be used to determine the deuteron energy (i.e., diode voltage) because the neutron energy is insensitive to the deuteron energy for the d-d reaction at the 175^o measurement angle. Furthermore, the focusing of deuterons in the diode introduces an uncertainty in the neutron emission angle. Neutron energy determinations are consistent with deuteron energies given by the diode voltage. The measured ion current and diode voltage were used to calculate neutron responses as shown in Fig. 8 (Ref. 23). The shapes of the measured and calculated responses are in good agreement. The low energy tail on the trace at 3.2 m is attributed to scattered neutrons.

For both the planar and focusing diode experiments the measured neutron yields are about 1/3 of yields calculated using the measured ion current and diode voltage corrected for energy loss in the Kimfol. For the planar-diode geometry, the calculated yields are based on the combined thick-target yields for the $D(d,n)^3He$ and $^{12}C(d,n)^{13}N$ reactions at 175^o as shown in Fig. 7. For the focusing-diode geometry, a broad range of neutron emission angles (140^o-180^o) exists due to the angular spread of the deuterons incident on the CD_2 target. In this case the calculated yield is based on thick-target yields at different angles weighted by an ion-current-density profile[16] determined from numerical simulations. The difference between the measured and calculated neutron yields may be attributed to several factors: 1) The measured ion current may include significant proton or carbon-ion components which contribute very little to the neutron output; 2) Ion energy losses in the region from the anode to the CD_2 target,[30] which have not been taken into account in the neutron-yield calculation, may reduce the ion energy on target and hence the neutron yield; and 3) Enhanced deuteron stopping[31] in the hot dense plasma target may lead to a reduced neutron output, particularly in the focusing diode geometry. A quantitative assessment of the importance of these factors in the present experiments is not possible.

The largest neutron yield at 175^o was obtained with the planar-diode geometry because the d-d neutron yield peaks at 180^o. For this diode, neutron yields of up to 4.5×10^{11}/sr were measured. At the diode voltage of 1.7 MeV corresponding to this yield, approximately 50% of these neutrons are from the

D(d,n) reaction (see Fig. 7). The corresponding total neutron yield into 4 π, corrected for the anisotropy of neutron emission, is 3.7×10^{12} with 50% from the D(d,n) reaction.

With the focusing-diode geometry, time-integrated neutron yields were used to determine focused current density by comparing neutron yields from different area CD_2 targets. For this purpose, the measured neutron output was scaled to the current measured by the ion Rogowski coil. The fraction of deuterons incident on targets as small as 0.75 cm^2 was determined by comparing the neutron yield with the yield measured on 100-cm^2 area targets. On the 0.75 cm^2 area target, the neutron yield was still about 50% greater than that observed without any CD_2 target. To correct for variations in neutron output in these measurements due to shot-to-shot variations in voltage and current, the measured yields were scaled to yields calculated from the measured diode voltages and ion currents. A deuteron current density of 150 kA/cm^2 at peak ion voltage was determined from these measurements. If the ion current is only 1/3 deuterons, as suggested by comparisons between measured and calculated neutron yields, then the total ion current density may be 2 to 3 times larger than this value.

D. Power Flow Studies

Problems in power flow from the PITHON accelerator to the pinch-reflex ion diode occurred in the magnetically insulated vacuum transmission line where a vacuum flow of electrons crossed the feed, reaching the anode before entering the diode. To inhibit electron leakage, the vacuum biconic and coax sections were designed with a characteristic impedance gradually decreasing to a value several times larger than the ion-diode impedance. A parapotential (Brillouin) flow analysis[32] for this configuration predicts that the entire electromagnetic-wave energy is transported as boundary current in the electrodes, with no vacuum electron flow possible. This analysis was found to be inadequate in these experiments. The diode impedance early in the pulse is independent of the dielectric anode foil, and is that of a simple pinched-beam diode with an interelectrode spacing of 8.5 mm, or an impedance of 5 Ω. This value is very close to the vacuum-feed-coax impedance of 6.5 Ω, and the Brillouin flow analysis breaks down. Several shots with larger diode gaps (hence with diode impedance greater than the feed impedance) lead to large-area current loss in the vacuum feed section and no appreciable power reached

the diode. Analysis of hardware damage for the first experimental configuration indicated that serious electron losses were occurring near the abrupt transition between radial and coax lines. A number of polishing, cleaning, and coating techniques were tried with little improvement to power flow.

The second experimental session required an extended coax section for diagnostic access, so an increased electrode spacing was designed to enhance the magnetic insulation in the coax region. The transition junction from biconic to coax was designed to be a constant characteristic impedance of 9.2 Ω . Even so, current loss was again observed beginning 37 ± 11 ns after current turn-on; a similar delay as in the first session, although the fractional loss was larger in the second session.

Several vacuum-feed modifications were studied in an attempt to increase power flow to the diode. These include a "bump" behind the anode foil, Aerodag versus oil on the coax cathode shank, a smooth conductive covering of the radial-line anode discontinuities, a smooth shorting of the diode current monitor, a Krylon coating on the anode side of the vacuum feed, and enhancement of the cathode tip. The "bump" is a grounded aluminum annulus typically 1-cm wide mounted behind the plastic anode foil on the backing plate opposite the cathode tip (see Fig. 4). Its purpose is to lower the early time Langmuir-Child electron diode impedance and trap the vacuum flow of electrons emitted in the feed. A sequence of shots taken without the bump, ranging from 2 to 3.5 TW, all showed an early-time current loss between injected (I_0) and diode (I_D) current monitors (see Fig. 16a). Shots with a smoothly curved cathode, as in Fig. 4, produced poor pinches without the bump. Shots taken with a bump did not show the early-time current loss (see Fig. 16b). All low-power shots taken with the large-area (100 cm^2) cathode and the bump produced excellent pinches.

At the 4.5-TW level, the bump was not sufficient to ensure good pinches. Smoothly covering the anode discontinuities with copper tape in the radial feed and with stainless-steel tubing in the coax feed (bypassing I_D) produced better pinches and larger PDX signals of greater FWHM. No shots without this modification produced good pinches at higher power, while 7 out of 11 shots were excellent with the anode discontinuities covered. Unfortunately, these modifications eliminated the diode-current measurement,

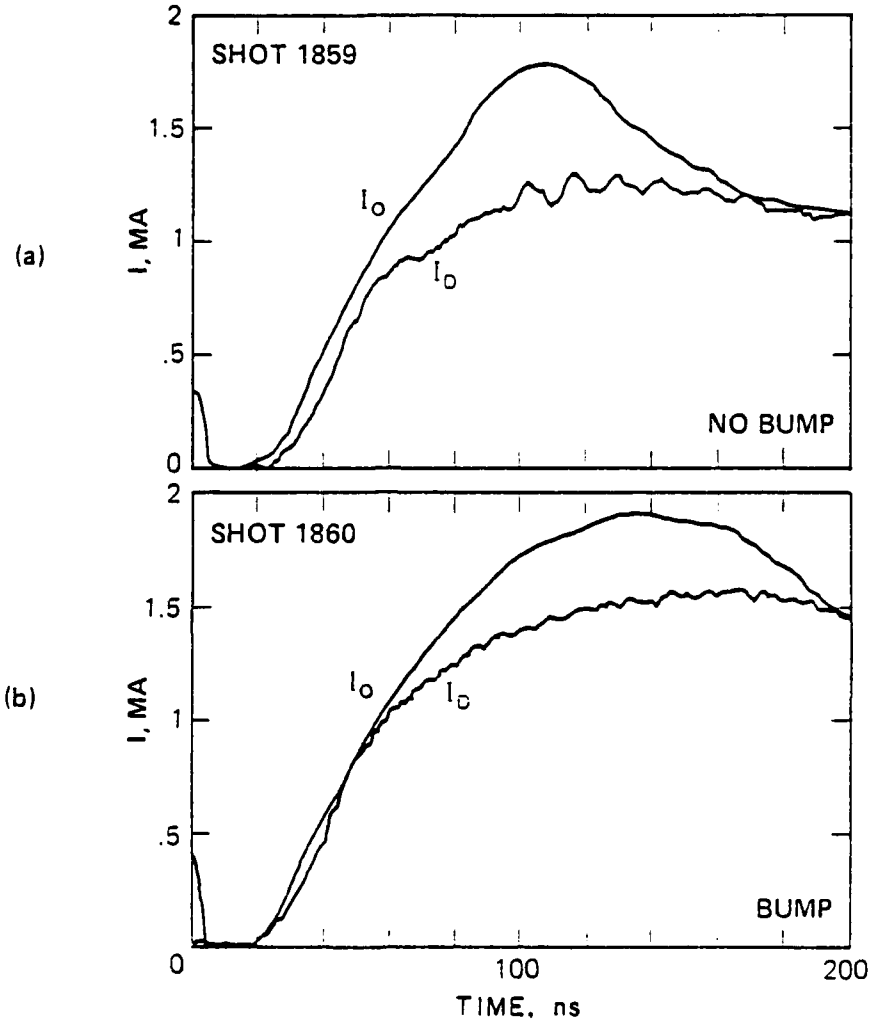

Fig. 16 — Comparison of the injected current and diode current (a) on a shot without the bump (No. 1859) and (b) a shot with the bump (No. 1860). Without the bump, the current loss in the vacuum feed is larger.

hence the inductive voltage correction and an upper bound on ion power and energy were unattainable on these shots.

The first experimental session utilized a cathode shank which tapered abruptly from the coax vacuum feed to an extended enhanced cathode tip. Early-time current losses were observed, but the deviations between injected and coupled currents were less than for the hardware shown in Fig. 4. A shot was performed in the second session at 5-TW matched-load power to evaluate cathode-tip-enhancement effects on power flow. A 1-cm-long, 5-mm-wide enhanced lip was welded to the hollow taper cathode, a standard bump was employed, and the diode current monitor engaged. Power loss was again observed, but the pinch was quite good, indicating that this configuration compensates at least in part for the anode-discontinuity effect at high power.

Observations from this study indicate that the modifications to the hardware designed to alleviate the power-flow problem were not effective, suggesting that the geometric transition from radial to coax feed is dominant in power flow over a variation of characteristic impedance. Further, electrode surface is not important, while a well-designed cathode emission tip and a low early-time diode impedance are essential for coupling power from the generator to the diode.

E. Small-Area Diodes

A modification to the diode design was tested to evaluate the performance of smaller-radius diodes with larger ion-current source densities. The hollow taper cathode, shown in Fig. 4, was configured to vary in radius. Shots were taken at 100 cm^2, reported above, and at 30-cm^2 area (see Fig. 4b).

Several small-area diode shots were taken at anode-cathode spacings from 2.6 to 5.6 mm. The small anode-cathode spacings shorted early in the pulse while the large spacings caused the power to dissipate in the lower-impedance vacuum feed. An intermediate spacing of 3.5 mm lead to efficient coupling of the injected energy into the diode without shorting or power loss in the structure. In this case, the diode impedance history was 1.4 Ω for 50 ns before collapsing (see Fig. 17). A source-area-averaged ion current density of 20 kA/cm^2 at peak power was obtained. The ion-current onset times for this small-area diode were slightly earlier than for the large-area diode as presented in Sec IV A.

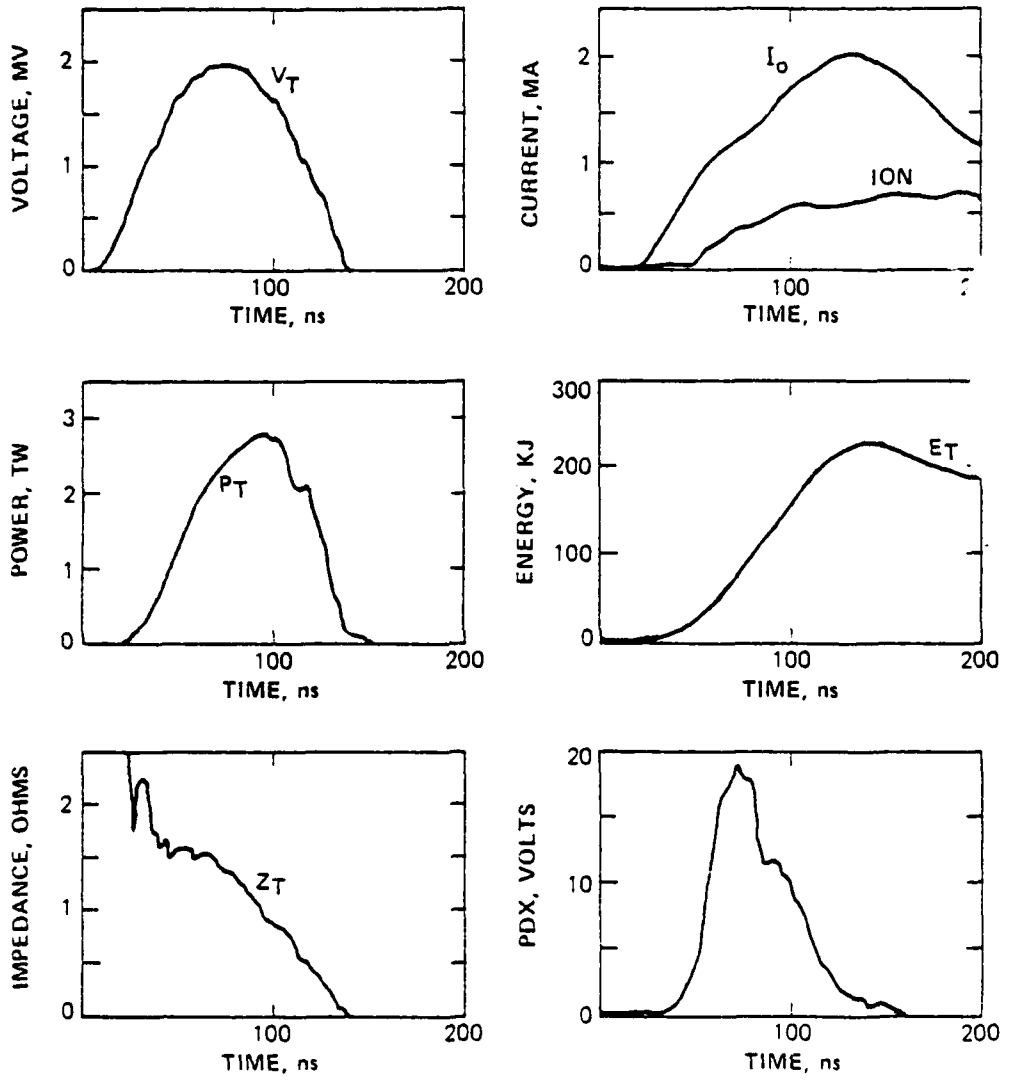

Fig. 17 — Measured waveforms for a 3-TW, 30-cm^2 area pinch-reflex diode shot (No. 1884)

F. Holographic Interferometry

Plasma evolution in the pinch-reflex ion diode was investigated with the holographic interferometry system during the second experimental session. Exposures were made through slots cut in the current return housing of the anode (Fig. 10) to allow a side view of the cathode and anode. The left side of each rectangular slot is defined by the cathode tip, and the right side by the anode foil.

Holograms measured on three different shots are presented in Figs. 18 and 19 and must be compared only in a general way. One can see in Fig. 18 that early in time the plasma density is too small to produce observable fringe shifting. As peak power is approached, significant fringe bending is noticeable near the anode, with smaller effects near the cathode. The greatest effect is near the axis of the diode. One can see in Fig. 19 that later in time significant plasma motion has occurred. The first two holograms (exposures D and E) are for the same shot. For these exposures, optically opaque plasmas have advanced from the electrodes, narrowing the slit through which the laser light can pass to the point that Fraunhofer single-slit diffraction of the light becomes important. Light is clearly visible far outside the borders of the rectangular viewing slits cut in the diode housing. In the slot viewing the diode axis, the plasma has become opaque to the laser light incident during the shot by the time the power pulse has dropped to 40% of its peak value. The adjacent holes have narrowed substantially. A hologram taken after the total collapse of power on another shot, exposure F, shows total opacity everywhere between the electrodes.

Holographic measurements were made on the large-area diode (100 cm^2) for four similar shots at intervals spanning most of the power pulse. The timing of the laser-pulse exposures on these shots is shown in Fig. 20. A tracing of each of the four holograms on these shots was made to show the contour corresponding to a line density of $3.2 \times 10^{17}/cm^2$, or one fringe shift. These tracings are shown in Fig. 21. The accuracy of the contours is estimated to be $\pm$ 0.5 mm of the 3.5 mm anode-cathode gap. Contours for greater fringe shifts were in most cases impossible to extract because large density gradients caused the fringes to run together.

It is clear from the single-fringe-shift reconstructions in Fig. 21 that the plasma fronts expanding from the anode foil and cathode tip are fairly

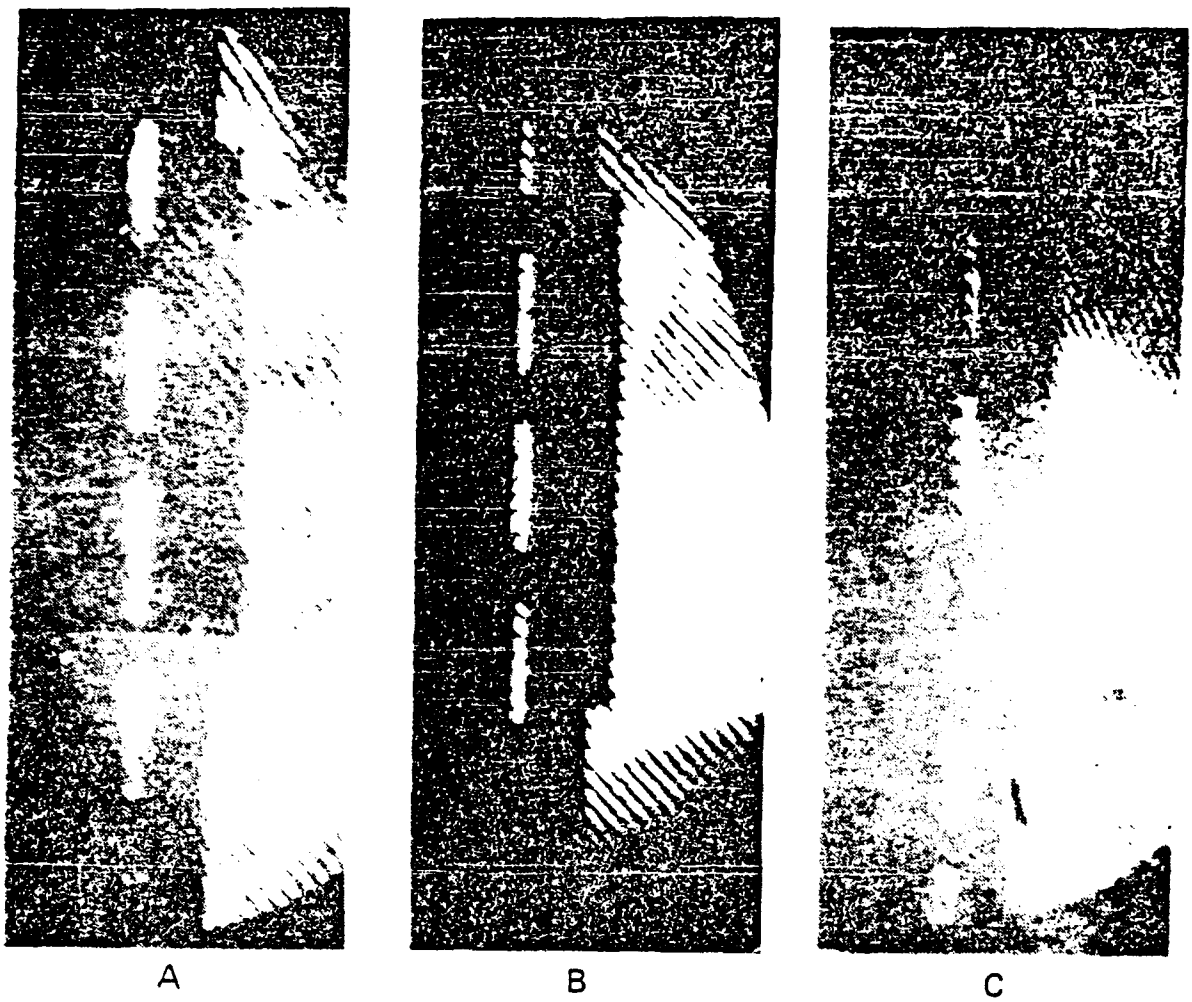

Fig. 18 — Holograms showing plasma formation early in the power pulse for the large-area diode. The timing of the laser-interferometer exposures is indicated by the vertical lines labeled A, B and C on the corresponding power pulse.

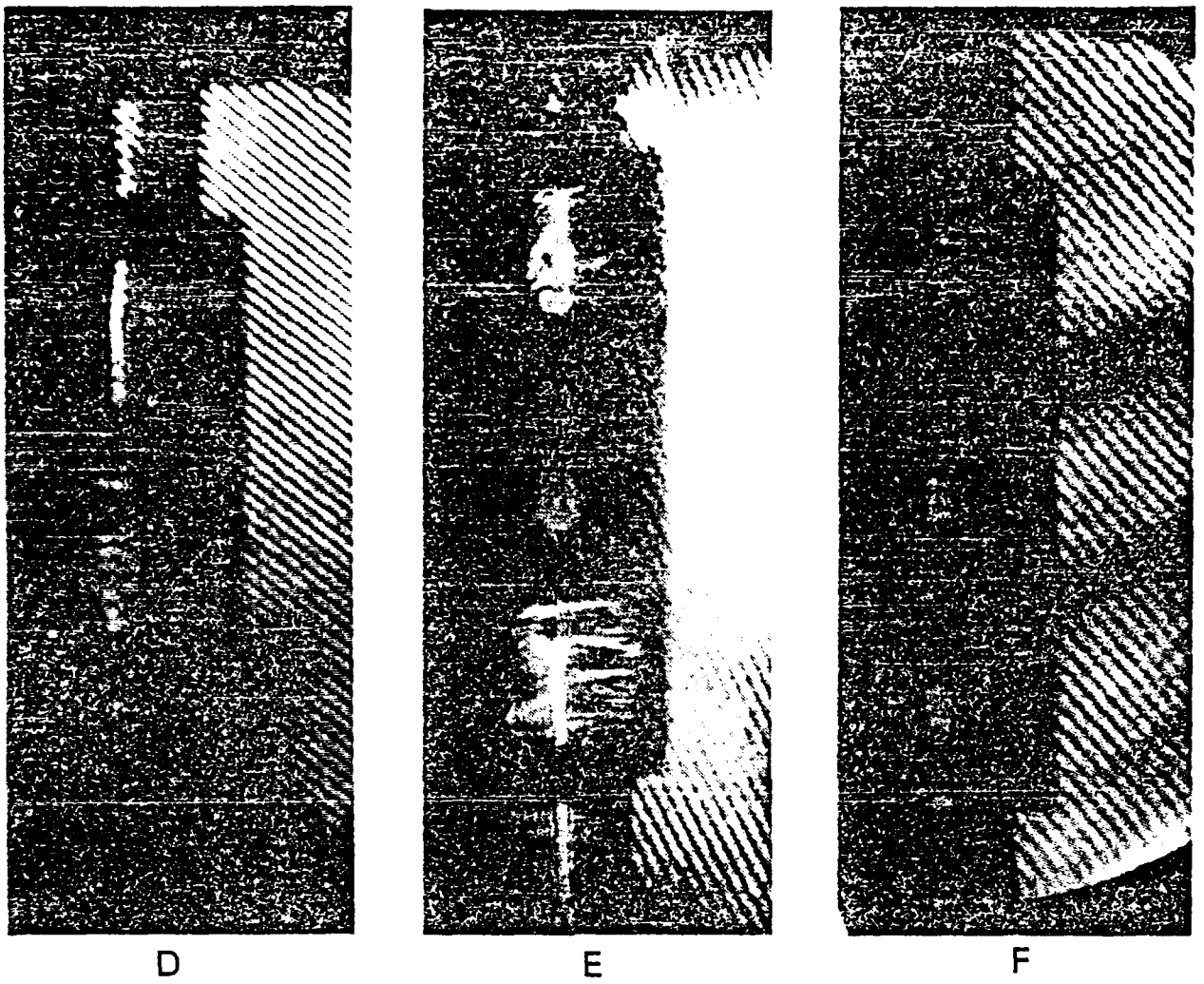

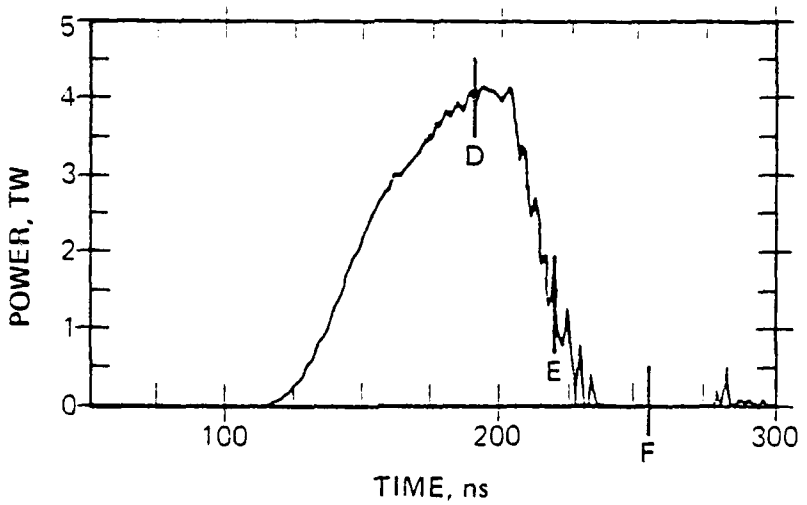

Fig. 19 — Holograms showing late-time plasma evolution for the large-area diode. The timing of the laser interferometer exposures is indicated by the vertical lines labeled D, E and F on the corresponding power pulse.

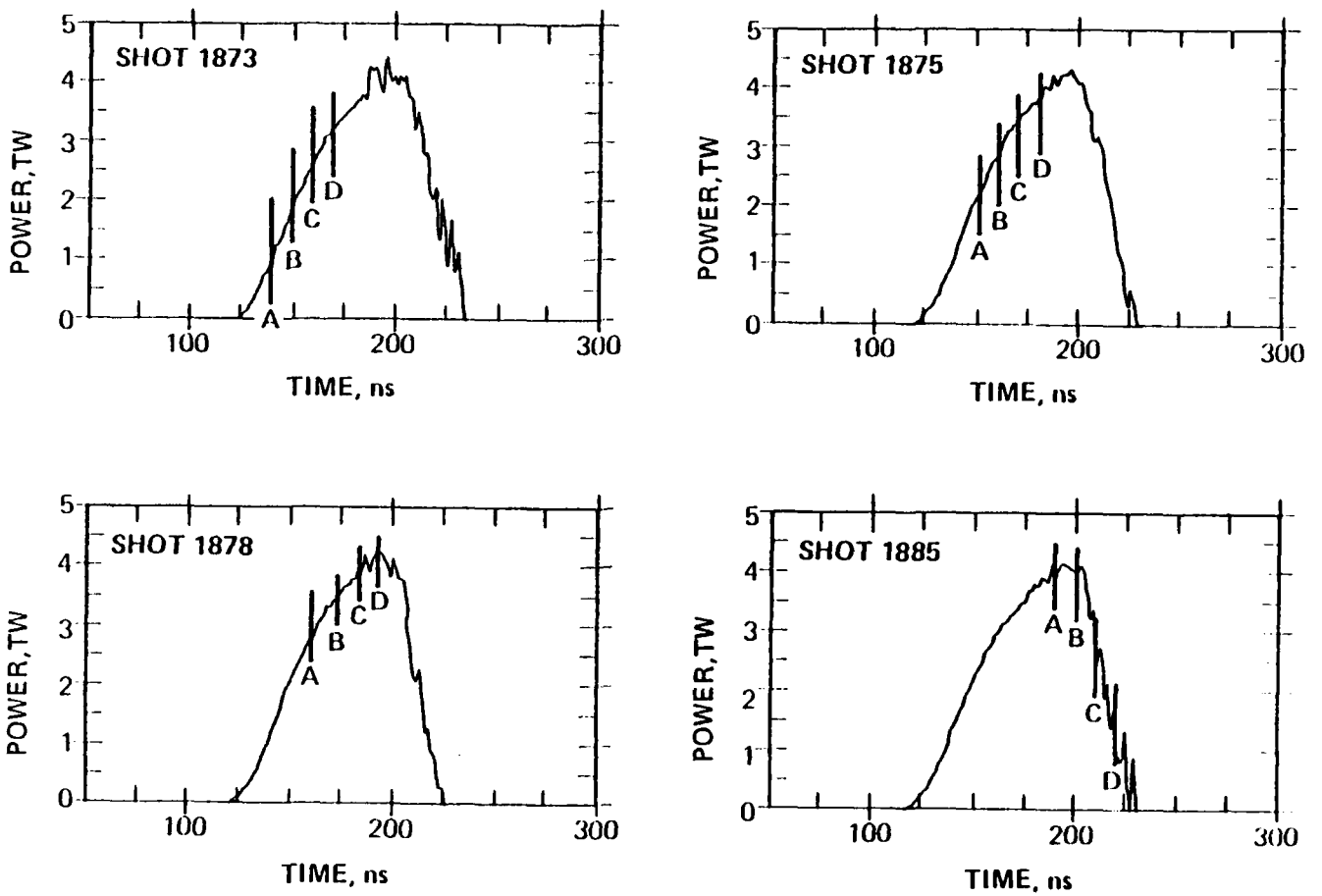

Fig. 20 — Timing of the laser-interferometer exposures relative to the power pulse on four different pinch-reflex diode shots. The vertical lines labeled A, B, C and D indicate the times at which the exposures are recorded on each shot.

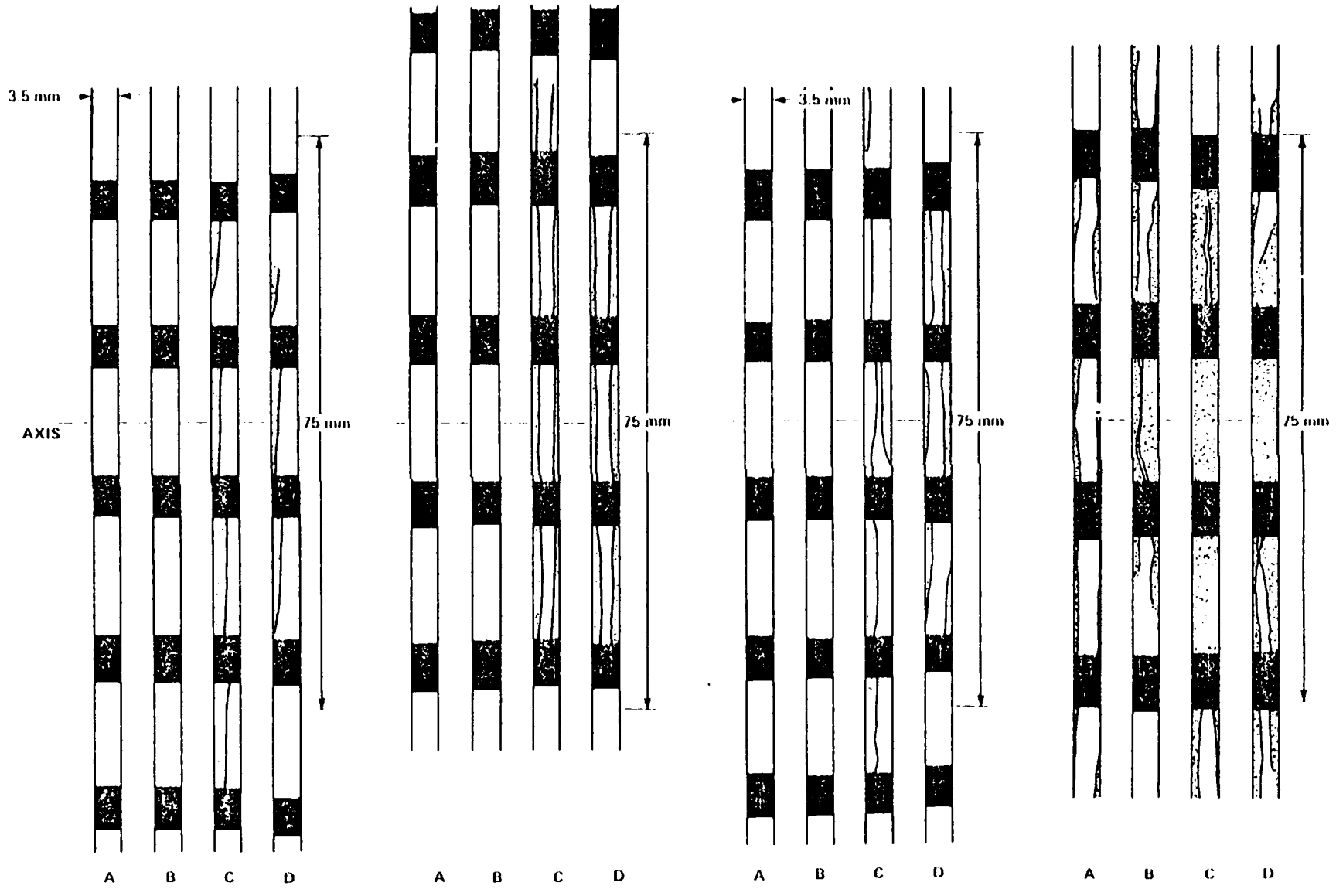

Fig. 21 — Single-fringe-shift reconstructions corresponding to the holograms measured on (a) Shot 1873, (b) Shot 1875, (c) Shot 1878 and (d) Shot 1885. The shaded regions indicate plasma line densities greater than $3.2 \times 10^{17}/cm^2$.

regular with gentle surface fluctuations and are not, in general, cylindrically symmetric. The absence of sharp plasma protrusions argues for a reasonable beam emittence, although a smoother and more regular plasma surface is required for high-focus-quality beam development. The important points to notice are that the plasmas expand from the boundary surface as the power pulse approaches its peak, that they are reasonably uniform and approach one another at increasing velocities, and that the center velocity appears greater than the larger-radius plasma motions.

The contours of Shot 1885 (Fig. 21d), showing the plasma behavior during the power collapse, indicate a considerable change between the first and second frames, both of which were taken near peak power. The plasma closure velocity implied on axis is 27 cm/μs; off axis at a radius of 3 cm the velocity is 7 cm/μs between frames A and B, and 10 cm/μs between frames B and C. The line density off axis is seen to decrease in the last frame, allowing light to again pass through holes that were formerly opaque. This phenomenon may be due to the anode plasma being compressed by magnetic pressure. Alternatively, the anode and cathode plasmas may never have met in the earlier frames, but the opacity there may have been caused by surface fluctuations or ripples that blocked the laser line-of-sight.

The plausibility of the magnetic-pressure mechanism can be determined by calculating the time required for the plasma pressure to be overcome by the rising magnetic pressure in the diode gap. Energy is deposited into the anode plasma continuously throughout the pulse, increasing the particle kinetic energy. The decreasing diode impedance means that early in time the current (and hence magnetic field) is low so $nkT >> B^2/2\mu$. Later the impedance decreases and the magnetic pressure increases more quickly than the plasma thermal energy. Rough parameters appropriate to the diode at the time of impedance collapse could be 2 MA flowing within a 3-cm radius, a plasma density of about $10^{18}/cm^3$ of CH_2 components, and a temperature of 5 eV. The magnetic pressure for these values is 67 MPa while the thermal pressure is 0.75 MPa, clearly much smaller. These yield an acceleration of 120 $cm/\mu s^2$ and a time of 16 ns for anode and cathode plasmas to each move 1.5 mm. This value is comparable to the observed 10-ns time scale of plasma motion across the diode. While plasma surface fluctuations cannot be ruled out as the source of diode opacity after peak power, the most likely explanation is the

ejection of plasma from the diode into the hollow cathode cavity and back to the anode location by magnetic pressure from the diode short circuit.

In addition to the 3-TW, 100-cm^2 diode shots, several shots at 2 to 2.5-TW diode power with a small-area (30 cm^2) diode were holographically monitored (Fig. 22). On Shot 1886 (Fig. 22a) interferograms of the diode during the ascent to peak power were recorded, indicating little plasma motion before peak power and with noticeable motion within a radius of 3 cm during the last two frames at peak power. The closure velocity on axis between the last two frames is 21 cm/μs.

On two other small-diameter shots, arcs occurred in different parts of the feed early in time. On Shot 1379, the arc formed well upstream from the diode in the coaxial vacuum feed. A perturbation in the reference fringes on one side of the diode is the only indication of the event (Fig. 22b). On Shot 1380, the arc was in the diode, resulting from too small an electrode separation. The diode was opaque to laser light even in the first hologram and hence density contour mapping was not possible.

V. SUMMARY OF RESULTS

In this paper, we have presented recent technological advances in intense pulsed ion-beam development. The pinch-reflex diode has been successfully scaled up to multiterawatt operation on the PITHON accelerator. Pulsed proton and deuteron beams have been produced in both planar and spherically focusing geometries with 1.0-MA of 1.8-MeV light ions measured at a peak power of 1.8 TW yielding a 130-kJ light ion beam in 100 ns.

Focusing of intense ion beams by electrode shaping and by self-magnetic field deflection has been shown at large radii to follow simple theoretical modeling with several corroborating diagnostics. Spherical electrode shaping served to compress the ion beam from an 11-cm-diam anode surface to a 3-cm-diam focal spot located, due to magnetic bending, inside the geometric focus. Small-area diode tests at lower power demonstrated that impedance lifetime is not a problem at higher source-current-density levels. Further, these results suggest that a smaller-area pinch-reflex diode of higher power density may be suitable for injection into a plasma transport channel.

The most serious problem encountered in these experiments was independent

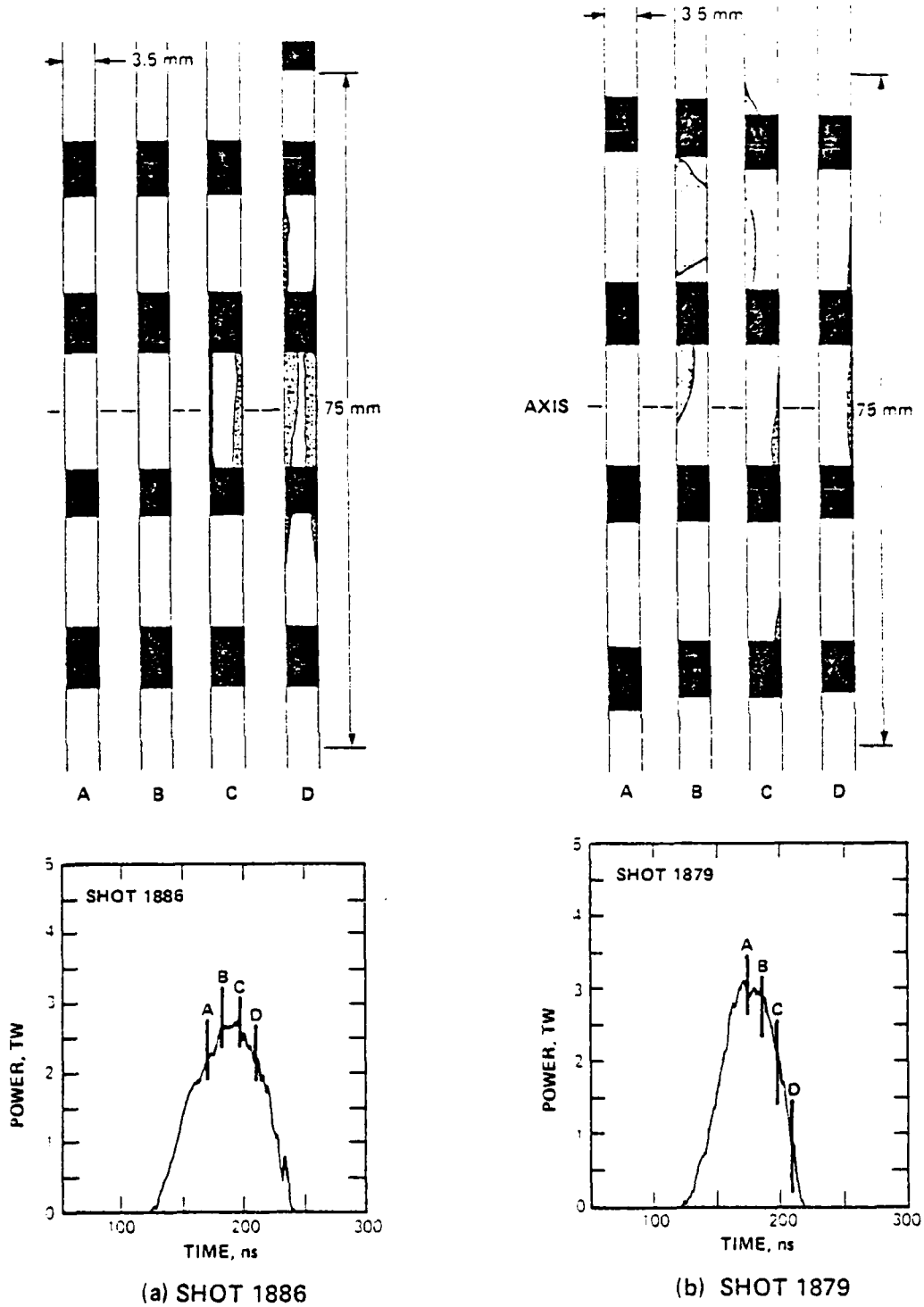

Fig. 22 — Single-fringe-shift reconstructions for (a) Shot 1886 and (b) Shot 1879. The timing of the laser interferometer exposures is indicated by the vertical lines labeled A, B, C and D on the corresponding power pulses. The shaded regions indicate plasma line densities greater than $3.2 \times 10^{17}/cm^2$.

of the pinch-reflex diode but concerned the coupling of power from the accelerator interface through the vacuum feed structure to the diode. These losses were found to be geometric, that is, independent of electrode surface, and occurred principally between the biconic-to-coax transition and the diode. Reducing the early-time diode impedance, smoothing the vacuum feed of resonant grooves, and enhancing the cathode emission tip all served to increase the power flow to the diode.

Beam diagnostics were developed to survive the harsh bremsstrahlung and impulse environment of a 3-TW pinch-reflex diode. Measurements of nuclear-reaction products provided total ion yields and pulse-shape evaluations. Total beam Rogowski coil monitors were developed to perform through the time of peak power. The shadowbox technique provided beam-focus location and local-beam divergence.

A first study of the spatial evolution of the anode and cathode plasmas in a 3-TW pinch-reflex diode was performed on multiple shots spanning the power pulse. Surfaces at constant line density ($3 \times 10^{17}/cm^2$) are observed to expand from the electrodes at times approaching peak power in fairly uniform though nonsymmetric profiles and accelerate toward one another. After peak power, significant anode-plasma surface fluctuations and a high velocity (up to 30 cm/μs) axial plume were observed. During the power pulse collapse a high density ($n > 10^{18}/cm^3$) plasma bridges the anode-cathode gap over the central 7.5-cm diameter. On some shots the high density plasma is later seen to open suggesting magnetic plasma confinement. The knowledge of the anode and cathode shapes at peak power suggests that further research into the formation of more uniform plasmas is necessary for development of a highly focused ion diode. The measured evolution of the shapes of the anode and cathode plasmas is the information required to design a first iteration modification to the simple spherically focusing anode.

REFERENCES

1. See for example: G. Yonas, 4th ANS Topical Meeting on Technology of Controlled Nuclear Fusion, October 14-17, 1980, Valley Forge, Pennsylvania; and S. Humphries, Jr., SAND 80-0402, Sandia Laboratories, 1980.
2. G. Cooperstein, S.A. Goldstein, D. Mosher, R.J. Barker, J.R. Boller, D.G. Colombant, A. Drobot, R.A. Meger, W.F. Oliphant, P.F. Ottinger, F.L. Sandel, S.J. Stephanakis, and F.C. Young, in Laser Interaction and Related Plasma Phenomena, H. Schwarz, H. Hora, M. Lubin and B. Yaakobi, Editors (Plenum, New York, 1981), Vol. 5, p. 105.
3. V.M. Bystritsky and A.N. Didenko, Uspekhi Fizicheskikh Nauk 132, 91 (1980).
4. J.W. Shearer, Nucl. Fusion 15, 952 (1975).
5. M.J. Clauser, Phys Rev. Lett. 35, 849 (1975).
6. R.O. Bangerter and D.J. Meeker, in Proc. 2nd Int. Topical Conf. on High Power Electron and Ion Beam Res. and Tech.,J.A. Nation and R.N. Sudan, Editors, (Cornell University, Ithaca, New York, 1977), p. 183.
7. J. Maenchen, L. Wiley, S. Humphries, Jr., E. Peleg, R.N. Sudan, and D.A. Hammer, Phys. Fluids 22, 555 (1979).
8. S.A. Goldstein, G. Cooperstein, Roswell Lee, D. Mosher and S.J. Stephanakis, Phys. Rev. Lett. 40, 1504 (1978).
9. S. Humphries, Jr., J. Appl. Phys. 51, 1876 (1980).
10. P.F. Ottinger, D. Mosher, and S.A. Goldstein, Phys. Fluids 23, 909 (1980).
11. D. Mosher, G. Cooperstein, S.J. Stephankis, S.A. Goldstein, D.G. Colombant, and Roswell Lee, Report No. 3658, Naval Research Laboratory, 1977.
12. G. Frazier, in Proc. NSWC Pulse Power Systems Workshop (Cornell University, Ithaca, New York, Sept. 1976).
13. D. Mosher, D. G. Colombant, and S.A. Goldstein, Comments Plasma Phys. 6, 101 (1981).
14. D. Mosher, Bull. Am. Phys. Soc., Ser. II, 25, 900 (1980).
15. D.G. Pellinen, Marco S. DiCapua, S.E. Sampayan, H. Gerbracht, and M. Wang, Rev. Sci. Instrum. 51, 1535 (1980).

16. A. Drobot, Roswell Lee, S.A. Goldstein, and G. Cooperstein, IEEE Conf. Record Abstracts, 1979 IEEE Int. Conf. on Plasma Sci. (Montreal, Canada, June 4-6, 1979), IEEE No. 79CH1410-0 NPS, p. 78.
17. F.C. Young, W.F. Oliphant, S.J. Stephanakis, and A.R. Knudson, IEEE Trans. Plasma Sci. PS-9, 24 (1981).
18. F.C. Young, IEEE Trans. Nucl. Sci. NS-22, 718 (1975).
19. H. Liskien and A. Paulsen, Nuclear Data Tables 11, 569 (1973).
20. H.W. Lefevre, C.A. Burke, and R.M. Bahnsen, Report No. RLO-1925-44, University of Oregon, 1971.
21. H.H. Andersen and J.F. Ziegler, Stopping Powers and Ranges in all Elements, (Pergamon Press, New York, 1977), Vol. 3.
22. J.G. Pronko, T.R. Fisher, and L.F. Chase, Nucl. Instr. and Meth. 163, 227 (1979).
23. F.C. Young, D. Mosher, S.J. Stephankis, S.A. Goldstein, and D. Hinshelwood, Memo Report No. 3823, Naval Research Laboratory, 1978.
24. K. Triebes and R. Huff, Bull. Am. Phys. Soc., Sec. II, 19, 976 (1974).
25. D. Mosher, G. Cooperstein, and S.A. Goldstein in Technical Digest of Conf. on Inertial Confinement Fusion (San Diego, California, February 26-28, 1980), IEEE No. 80CH1536-2 QEA, p. 104.
26. A.E. Blaugrund, G. Cooperstein and S.A. Goldstein in Proc. Int. Topical Conf. on Electron Beam Res. and Tech. G. Yonas, Editor, SAND76-5122, (Albuquerque, New Mexico, Feb., 1976) Vol. I, p. 233.
27. R.D. Genuario and V.L. Bailey, Appl. Phys. Lett. 33, 694 (1978).
28. J.C. Martin "Nanosecond Pulse Techniques," SSWA/JCM/704/49, Internal Report, AWRE, Aldermaston, England, 1970.
29. H.W. Koch and J.W. Motz, Rev. Mod. Phys. 31, 4 (1959).
30. F.C. Young, S.J. Stephanakis, G. Cooperstein, D. Mosher, F.L. Sandel, P.G. Blauner and S.A. Goldstein, Naval Research Laboratory Report 4322, 1980.
31. E. Nardi, E. Peleg and Z. Zinamon, Appl. Phys. Lett. 39, 46 (1981).
32. J. Creedon, J. Appl. Phys. 48, 2946 (1975).

THE USE OF FINITE J_θ FOR INCREASING THE ION EFFICIENCY OF HIGH IMPEDANCE DIODES

I. INTRODUCTION

The efficient generation of intense beams of energetic light ions is a central objective of the NRL Light Ion Fusion Research Program.[1] Over the past several years, focused ion current densities of over 100 kA/cm^2 from terrawatt-level beams have been achieved with magnetically insulated radial diodes at Sandia National Laboratories[2] as well as with pinch-reflex axial diodes at the Naval Research Laboratory.[3] Using diodes of below 2 ohm impedance, ion beam efficiencies of over 70% were achieved in both of the above configurations[4,5] (i.e., — over 70% of the power travelling through the diodes was carried by the light ions generated therein). The question of ion efficiency is critical to the goal of a practical light ion driven inertial confinement fusion (ICF) reactor. As much as possible of a given pulsed power generator's energy must be imparted to the ion beam exiting the diode in order to minimize the number of beam sources necessary for successful pellet ignition as well as to maximize the overall reactor efficiency. These efficiency considerations are well met by the low impedance diodes.

Unfortunately, the high current densities of the ion beams produced by low impedance diodes are not compatible with the focusing and transport systems presently under study for bringing the beams to bear on the proposed fusion targets.[6] In addition, there are strong arguments in favor of the use of high impedance generators in present reactor scenarios.[7] High impedance diodes must be matched to such generators to ensure efficient power transmission but these diodes are plagued by relatively low ion production efficiencies. These low efficiencies are a direct consequence of established diode theory. It has been found semiempirically[8] that the total current flowing through a pinched-beam diode may be approximated by

Manuscript submitted January 28, 1982.

$$I = I_e + I_i \approx 9(\gamma^2 - 1)^{1/2} \frac{R}{D} \left[1 + \left(\frac{eV}{2m_i c^2} \right)^{1/2} \frac{R}{D} \right] \tag{1}$$

where $\gamma = 1 + \frac{V(\text{in } MV)}{0.511}$, R = cathode radius, D = axial anode-cathode ($A-K$) gap, V = diode voltage, and m_i = ion (proton) mass. Implicit in this formula is an ion-to-electron current ratio given by

$$\frac{I_i}{I_e} \geq 0.5 \frac{v_i}{c} \frac{R}{D} \tag{2}$$

where v_i is the mean ion velocity.[9] Thus, for a fixed voltage, increasing the diode impedance translates to decreasing the aspect ratio, R/D. That, in turn, results in a decrease of the current ratio I_i/I_e and a lowering of the ion production efficiency, $I_i/(I_e + I_i)$. This is the crux of the problem addressed by this research. Stated in other terms, Eq. (2) expresses the inverse dependence of the specie current ratio on the ratio of respective species lifetimes in the $A-K$ gap. By increasing the relative electron lifetime over the standard parapotential flow model[10,11] through some modification of the diode field structures, one can hope to significantly beat the R/D limit. The modification studied herein involves the introduction of finite azimuthal current flow in the cathode shank which gives rise to strong tangential magnetic fields along the electron-emitting shank surface. For the J_θ values tested, this technique produced positive results in increasing the effective ion efficiency, η_i, of a 4Ω diode. The same J_θ values tested in a 25Ω diode did not substantially effect its η_i but did modify the density profile of the resultant ion beam. The rationale underlying the finite J_θ techniques as well as the results of the cases tested are presented below.

II. THEORY AND NUMERICAL IMPLEMENTATION

The theories quoted in the previous section assume a predominantly radial flow of electrons cascading from the cathode face at radius, R, down toward the center of the anode. For diode potentials in excess of 1 MV, electrons are quickly accelerated to very near the speed of light, c. Their gap lifetimes, τ_e, are thus on the order of R/c. On the other hand, due to their much greater mass, protons experience little deflection from an axial trajectory across the $A-K$ gap of width, D. They have life-

times, τ_i, of about $D/\bar{v}_i$ where $\bar{v}_i$ is the average ion velocity. Allowing for oscillations in the electron flow yields a pessimistic electron-to-ion τ ratio equal to the current ratio of Eq. (2). In order to increase this ratio, a thin hydrogen-rich foil may be substituted in place of a solid anode. The thickness of the foil is such as to allow an electron to pass through it without excessive energy loss. Behind the foil, a virtual cathode and/or a strong B_θ acts to reflect the electrons back into the $A-K$ gap.[12,13] In such a case, τ_e increases with N, the number of reflections through the foil experienced by a typical electron. That is the essence of the pinch reflex diode (PRD) (see Figure 1) pioneered by NRL. Alternately, the entire diode may be reconfigured from an axial to a radial $A-K$ gap geometry as in Figure 2. In such a diode a combination of imposed B_z and self-generated B_θ magnetic fields constrain electron flow to form an azimuthally symmetric negative space-charge cloud stretching some distance from the cathode into the radial gap. Given the proper choice of operating voltage and other parameters, few electrons will reach the anode ($\tau_e \to \infty$) and virtually all of the current in this "radial diode" will be carried by the ions in their near-radial trajectories across the gap.[14,15]

With reference to the previously mentioned problem of low ion production efficiency in high impedance diodes, it was reasoned that a possible solution might be to combine the τ_e enhancement created by the electron reflexing anode foil with that arising from the electron flow constraints imposed by the magnetic fields such as those found in a radial diode. Specifically, the standard axial pinch-reflex geometry of Figure 1 might be retained while imposing an azimuthal current density, J_θ, in the tip of the cathode shank.[16] Experimentally, this could be achieved by cutting an azimuthally symmetric pattern of spiral gaps into the shank tip.[17] Increasing the pitch and/or the density of the spirals would increase the effective I_θ component of the net cathode current. This I_θ would give rise to a strong B_r along the intense electron emission region at the tip of the cathode which field would impart a finite angular momentum to those electrons. Several consequences can be expected. First of all, depending upon the strength of $(B_r)_{CATHODE}$, net electron emission along the cathode tip will be reduced due to tangential magnetic field effects (longer electron space-charge retention near the emitting surface).[18] If the impedance remains fixed, this would demand an increase in the ion efficiency. Secondly, finite

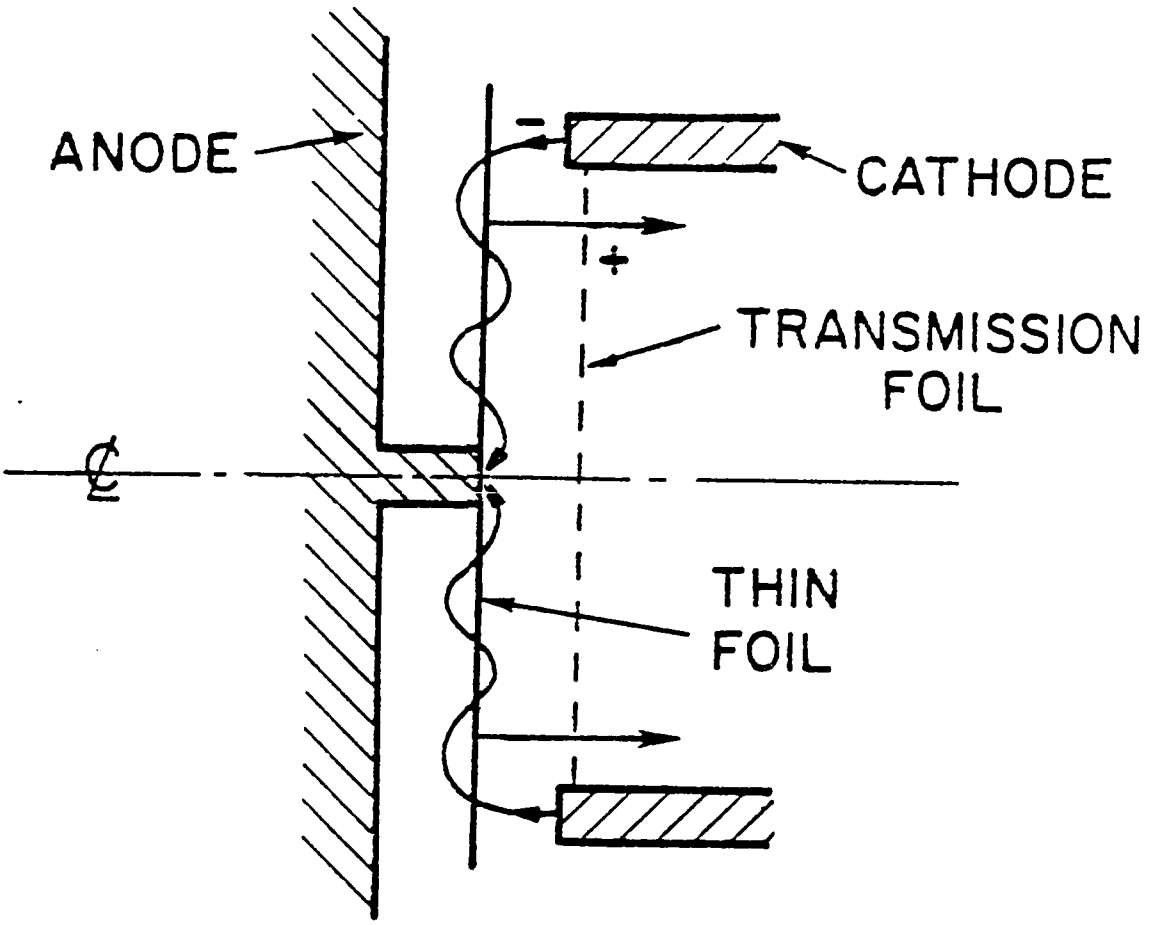

Fig. 1 — The pinch-reflex diode

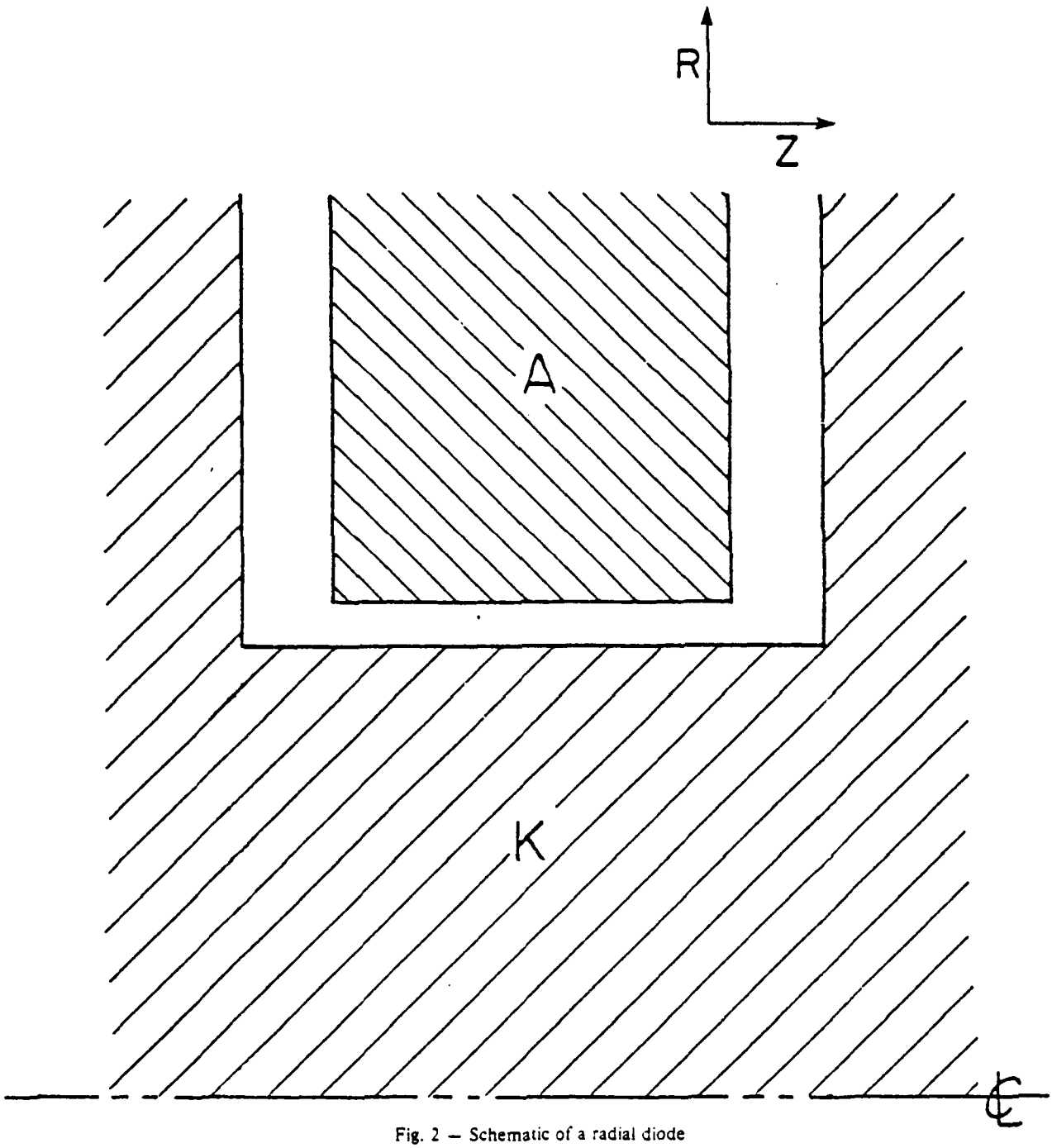

Fig. 2 — Schematic of a radial diode

angular momentum will prohibit electrons from reaching $R = 0$ and thus will inhibit the formation of large electron space-charge accumulations along the diode's central axis. (Such a charge build-up is common in pinch-reflex diodes).[19] This should depress the ion emission peak at the center of the anode and likewise limit the growth of the anode plasma "pimple" at zero radius,[20] thus lowering the average divergence of the ion beam. Thirdly, the additional degree of freedom in the electron motion necessarily complicates the particle's trajectory through the $A-K$ gap. Convoluted figure-eight electron orbits have been observed to increase τ_e in conventional PRD's;[21] the effect should be much more pronounced here. Finally, there is a possibility of noticable magnetic insulation of the electron flow near the anode plasma surface due a combination of electron diamagnetic effects and foil flux exclusion. The resultant formation of an electron charge layer near the ion-emitting surface is a key mechanism for efficient ion production in radial diodes.[22] There are thus four reasons for optimism over this proposed modification for high impedance axial diode design.

NRL's DIODE2D computer code was employed to numerically simulate the steady-state operating conditions for such a J_4-diode (JTD) for various sets of parameters. The details of the code may be found elsewhere.[23] It is sufficient here to point out that DIODE2D calculates equilibrium electric and magnetic field strengths over an $NZ \times NR$ mesh of discrete data points on a pre-determined computational region corresponding to an arbitrary $R-Z$ planar cross-section passing through the diode's centerline. Complete azimuthal symmetry is assumed. A finite number of macro-electrons and macro-protons having correct, physical charge-to-mass ratios are advanced timestep-by-timestep across the mesh in a relativistically covariant manner. A steady-state solution is sought both for field structures as well as for particle flows. No time-dependent phenomena are actually treated.

The dimensions of the diode numerically modeled here come from actual experimental apparatus designed by NRL personnel for light ion beam research on the AURORA and PBFA-I pulsed power generators. At the U.S. Army's Harry Diamond Laboratories (HDL), one of the four 50-ohm lines of the AURORA machine was fitted with a custom designed PRD.[24] The experimental arrangement is depicted in Figure 3. Details of the diode structure at the tip of the device are shown in Figure 4. All

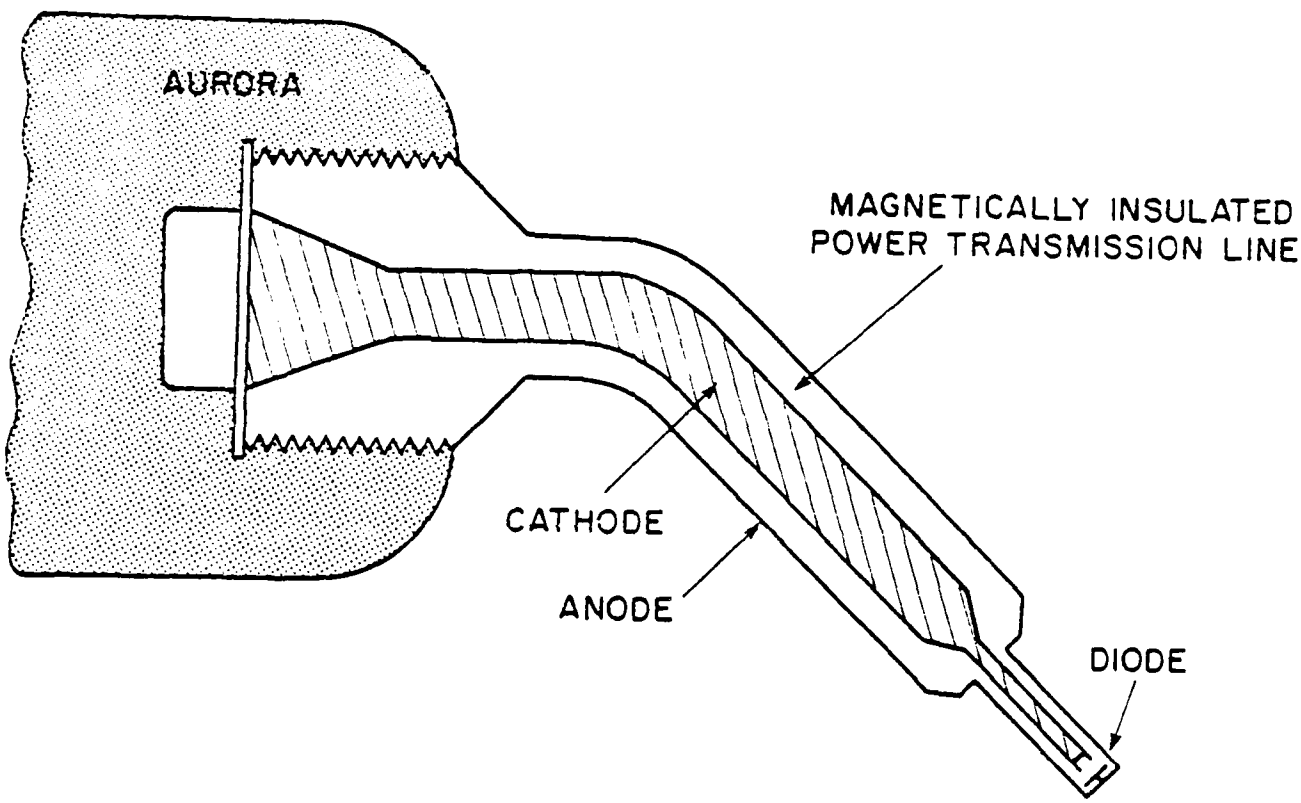

Fig. 3 — The NRL-AURORA ion diode experiment

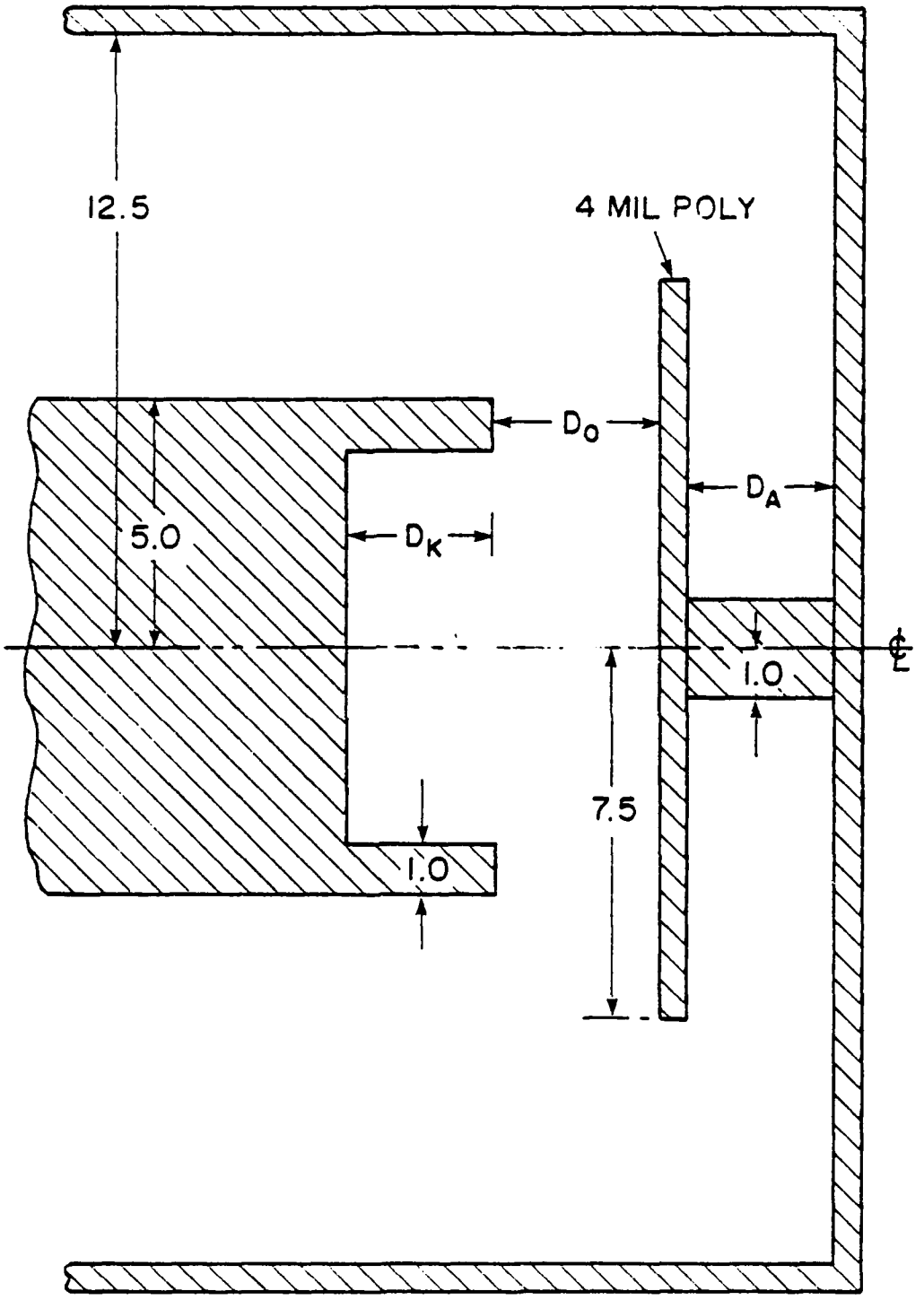

Fig. 4 — The diode to be modeled

radial dimensions are given in centimeters. Of the three, variable axial dimensions indicated, the most significant is D_0, the anode-cathode ($A-K$) gap. For a fixed cathode radius of five centimeters, the value of D_0 essentially determines the diode impedance and efficiency for a given applied voltage via Eqs. (1) and (2). It may be further noted that the diode of Figure 4 is in a "negative polarity" configuration corresponding to the early experimental runs on AURORA. The cathode is the central conductor of the coaxial line and the resultant ion beam is accelerated toward the machine, making beam diagnostics very difficult and beam transport impossible. In more recent experiments, the central conductor was switched to positive polarity[25] and the anode foil and cathode appropriately reversed. Such a change in polarity can be expected to significantly modify the source-free electric field structure only at large radii and probably have little impact on the dynamics of particle flows in the active $A-K$ gap below five centimeters radius. This relative isolation of the active particle flow region from the large radius field structure similarly encouraged the use of the same diode structure of Figure 4 to model the 4-6 ohm PRD being designed by NRL for use on the individual lines of PBFA-I at Sandia Labs. Only the diode voltage and axial dimensions were changed. Specifically, the AURORA simulations were conducted with $D_0 = 3.3$ cm at 5.0 MV while those for PBFA-I were with $D_0 = 0.66$ cm at 2.0 MV.

The volume that must be simulated using the DIODE 2D code extends radially from the central axis to the inner radius of the anode shell and axially from the plane corresponding to the recessed foil face of the cathode out to the inner plane surface of the vacuum vessel, anode shell. Since it presumes azimuthal symmetry, the computer code only deals with a single $R-Z$ planar cross-section extending out from the centerline. This computational region is presented in Figure 5. The grid points are shown as dots and correspond to the center of their respective rectangular data cells. Given the monolayer of guard cells completely surrounding the entire region in which particles are "allowed," a total of $(NZ + 2) \times (NR + 2) = 66 \times 52 = 3{,}432$ mesh points are used. The bottom boundary corresponds to the central axis ($R = 0$) of the diode. The right and upper boundaries represent the anode shell and are maintained at the full anode potential. The left boundary is kept at zero voltage up to cell 22 and

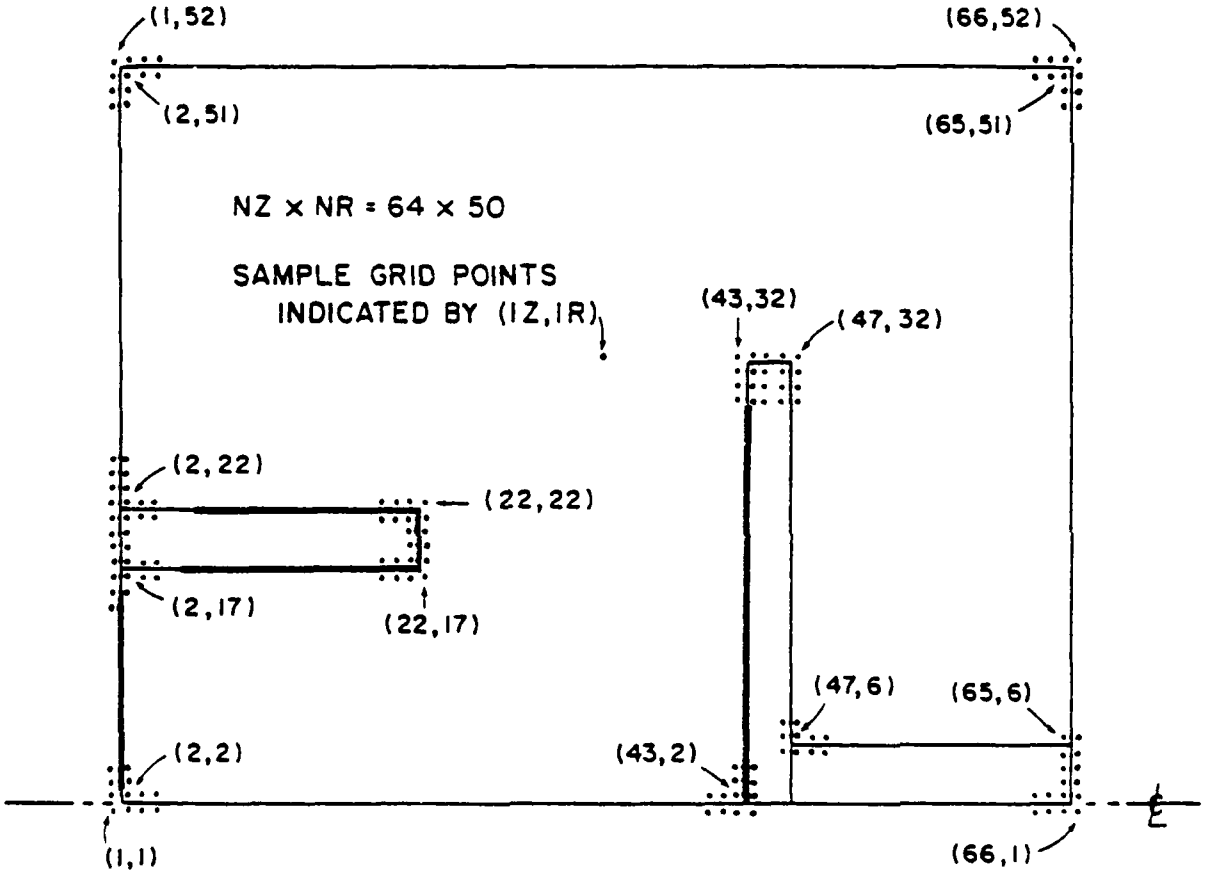

Fig. 5 — Set-up of the numerical simulation region

then increased logarithmically up to the anode voltage. Perfectly conducting cathode and anode surfaces are included in the computational region as shown in Figure 5. They are treated numerically via a capacitance matrix technique described elsewhere (see Ref. 26). On the order of 10^4 macroelectrons and 10^4 macroprotons participate in the simulation at steady state. These macroparticles are emitted at their respective electrodes along the heavy-lined surfaces. Axial currents in the cathode shank and in the anode stalk are treated rigorously as a function of z in order to ensure an accurate distribution of B_θ throughout the diode. The results of these numerical simulations as well as a summary of the conclusions which could be drawn from them are presented in the following two sections.

III. RESULTS

1. AURORA

The first diode modeled was one appropriate for use on the AURORA machine. The diode voltage was fixed at 5 MV. The axial spacing between grid points was set to $\Delta Z = 0.15$ cm, yielding an $A-K$ gap, D_0, of 3.3 cm (see Figure 4). For a cathode radius of 5.0 cm, Eq. (1) predicts a diode current of 156.7 kA yielding an impedance of 32 ohms. Equation (2) predicts an ion efficiency, η_i, of only 0.0725 $\left[= \frac{I_i}{I_e + I_i}\right]$. These predictions fall far short of observed results. A diode with the above geometry and voltage was tested experimentally and computationally by NRL and the results were just recently published.[27] The numerical simulation quoted in that paper found a steady-state diode current of 205 kA of which 40 kA were carried by protons. This amounts to a diode impedance of 24 ohms and an ion efficiency, η_i, of about 0.195. The average experimental results reported in the same paper were $I_{diode} \approx 250$ kA (20 ohms) and $\eta_i \approx 0.20$. It should be noted that the experiment started with an $A-K$ gap of 4.9 cm but that gap closure due to electrode plasma expansion was expected to have narrowed that to about 3.3 cm by the time of peak current in the power pulse. Those findings clearly contradict Eqs. (1) and (2). High impedance operation gives rise to new diode phenomena not properly treated in that earlier analysis. The need for a more complete theoretical treatment still exists. Until one is found, numerical simulation is the best nonexperimental tool available for analysis.

As an additional "benchmark" for the results to be reported here, a numerical simulation was carried out on the same diode but in positive polarity. The results were: I_e = 182 kA, I_i = 56 kA, I_{diode} = 238 kA, Z = 21 ohms, and η_i = 0.235. This is in agreement with the negative polarity experiment indicating that changes in the electric field configuration along the far boundaries of the diode have little effect on the physics of the $A-K$ gap. Higher currents were achieved here than in the negative polarity simulation probably because no electron emission along the cathode shank had been permitted in that earlier run. The electron particle plot of Figure 6 shows very significant electron flow from the shank. To test the effects of J_θ in the shank, a negative polarity was again assumed in the diode to conform to the quoted experiments.

The azimuthal current was imposed in the cathode shank in a very straightforward manner. Referring back to Figure 5, a constant, predetermined value of J_θ was assumed in each of the data cells in the rectangular region stretching from IZ = 6 through IZ = 21 and from IR = 18 through IR = 21 (i.e., —a cross-sectional area of 2.4 cm^2). As a first test for the idea, a value of J_θ = 1 kA/cm^2 was arbitrarily chosen giving 2.4 kA of azimuthal current flowing through the shank. The effect of this small I_θ was quite pronounced. In a simulation of electron-only flow, a net current of 209 kA was achieved (diode impedance of 24 ohms). A sampling of electron positions in the steady state for that case is presented in Figure 7. The shaping of the electron flow by the shank's B-field is clearly discernable. Notice, in particular the intense stream of electrons from the top rear of the shank arcing up and across the gap along the field lines. There also seem to be electrons that are emitted from the inside shank surface and then flung upward behind the foil. The net effect is an increase in the mean radius of electron impact on the anode foil. Thereafter in the simulation, proton emission was turned on along the entire front face of the anode foil. The new equilibrium with both species present yielded the following: I_e = 244 kA, I_i = 41 kA, I_{net} = 285 kA, Z = 17.5 ohms, and η_i = 0.144. Thus, the ion production efficiency decreased by 0.091 or almost 40% while the impedance dropped by about 17% compared to the J_θ = 0, "benchmark" case. This was unexpected but an examination of the sample particle plots of Figure 8 suggests two causes. First of all, the electron stream is illuminating only a

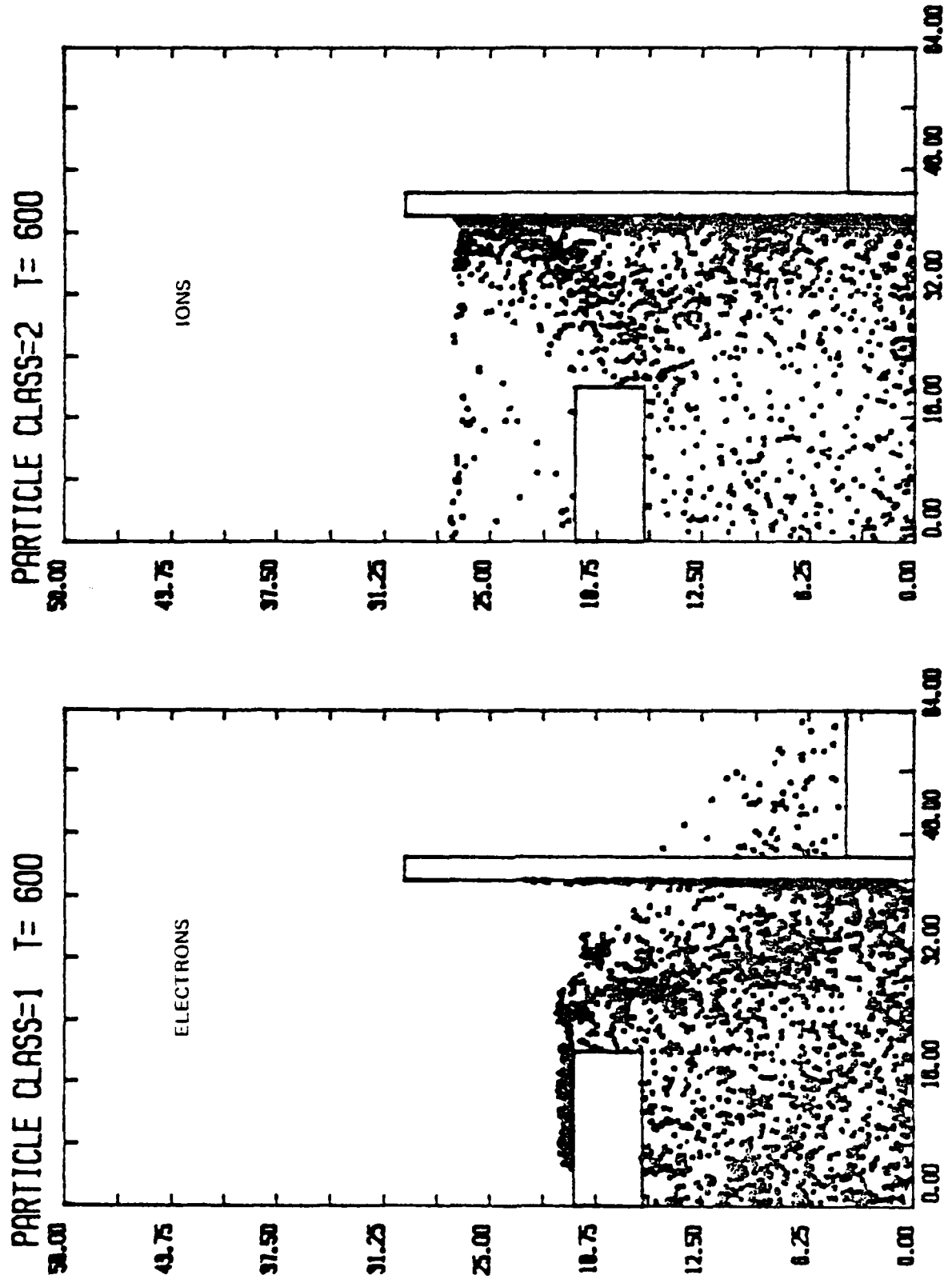

Fig. 6 — AURORA electron and ion flow for $J_0 = 0$.

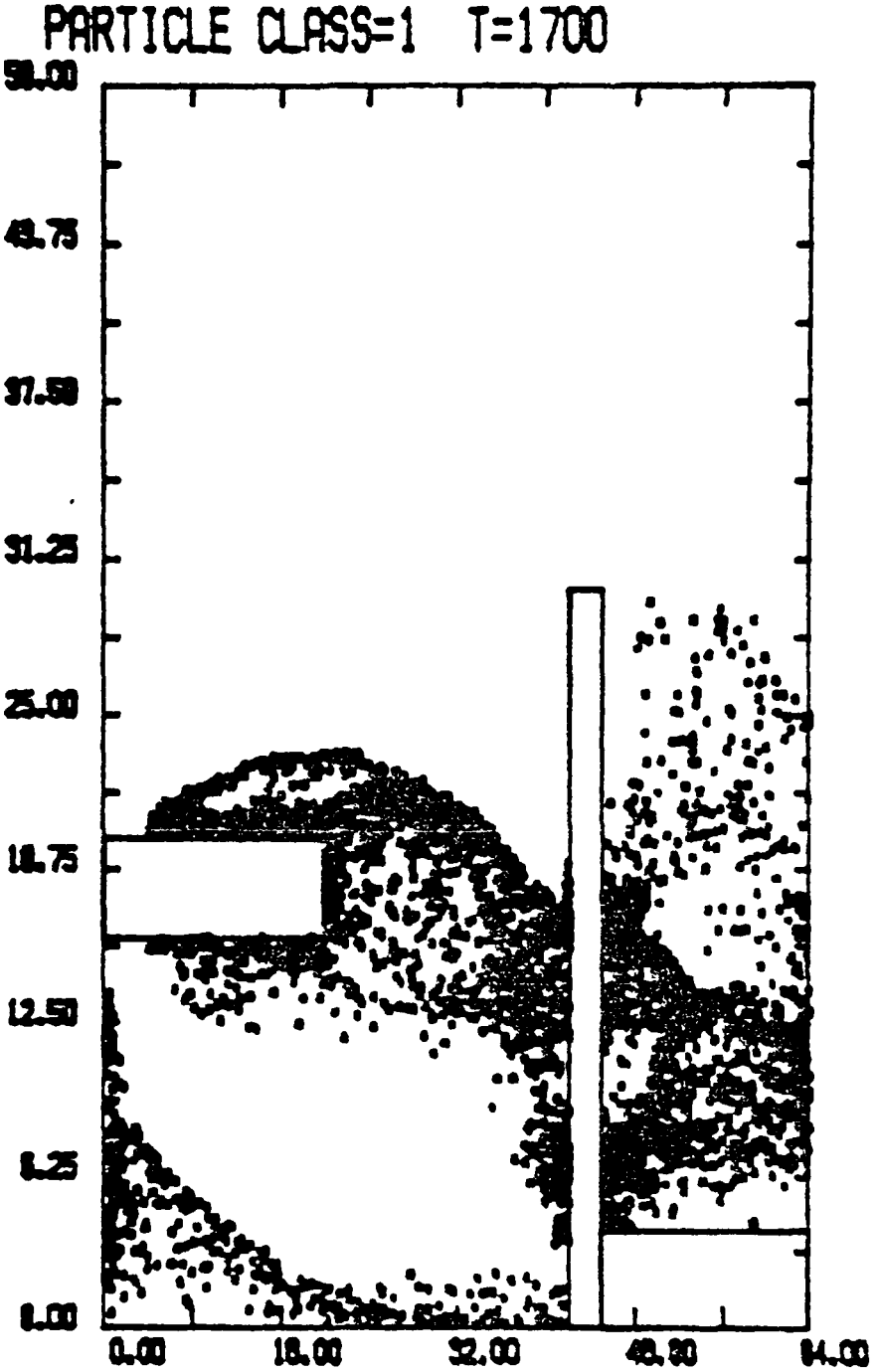

Fig. 7 — AURORA electrons-only flow for J_g = 1 kA/cm^2

relatively small area of the anode. This is lowering η_i. Secondly, the shank magnetic field is still enhancing the net shank electron emission by keeping large numbers of electrons emitted in the rear of the shank from hitting the forward portions of the shank and lowering emission there as is normally the case. This "layering" of the shank electron flow can be seen in Figure 8.

In order to remedy this situation, a better choice for J_s was sought. The simulation code was reset to the electrons only equilibrium and J_s was set to 10 kA/cm^2 or a total azimuthal shank current of about 24 kA. The results can be seen in Figure 9. This case was not run to equilibrium. The net effects were in a beneficial direction albeit to an extreme. The mean radius of electron impact on the anode foil was indeed increased. In addition, although emission on the outer surface of the shank was again enhanced, emission on both the inner surface as well as along the cathode tip was greatly curtailed due to direct magnetic insulation. The net electron current fell to about 60 kA.

As a reasonable intermediate choice J_s was taken as 4 kA/cm^2 yielding I_s = 4.8 kA. This case was run and again both the impedance and the efficiency dropped. Specifically, the observed steady-state currents were I_e = 257 kA, I_i = 34 kA, and I_{diode} = 291 kA giving an impedance of 17.2 ohms and an ion efficiency of 0.117. As shown in Figure 10, the cause of the problem seems to be very similar to that for the J_s = 1 kA/cm^2 case. Once again although the shank B-field is reducing emission at the shank tip, it is also preventing much of the normal self-suppression of electron emission over the bulk of the outer shank surface. One improvement is the larger average radius of electron impact on the anode foil. This confirms the ability of the shank J_s to radially direct the $A-K$ gap electron flow. Still, the anode foil area illuminated by the electrons is rather narrow and most electrons appear to transit immediately to the solid anode surface in the rear without reflexing again through the foil. This tightly restricted nature of the electron flow and resultant ion flow is illustrated by the plots in Figure 11. These radial profiles of ion current density collected at the cathode show distinct regions of enhancement. All three curves show peaks near the central axis due to the strong flow of tightly pinched electrons emitted from the rear cathode foil surface inside the shank. All three likewise have peaks between R = 4 cm and R = 5 cm corresponding to ions collected by the protruding cathode

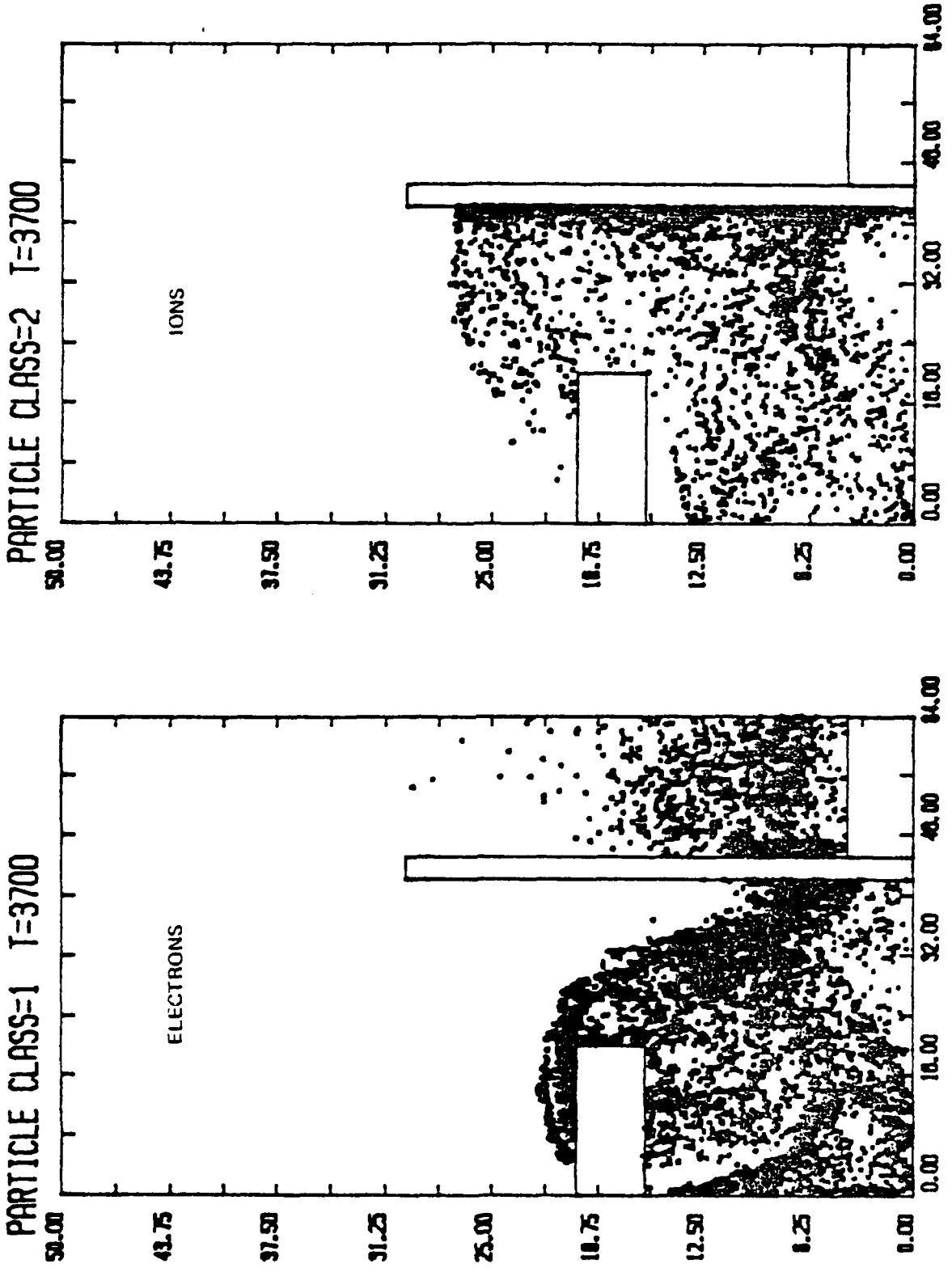

Fig. 8 — AURORA electron and ion flow for $J_0 = 1$ kA/cm^2

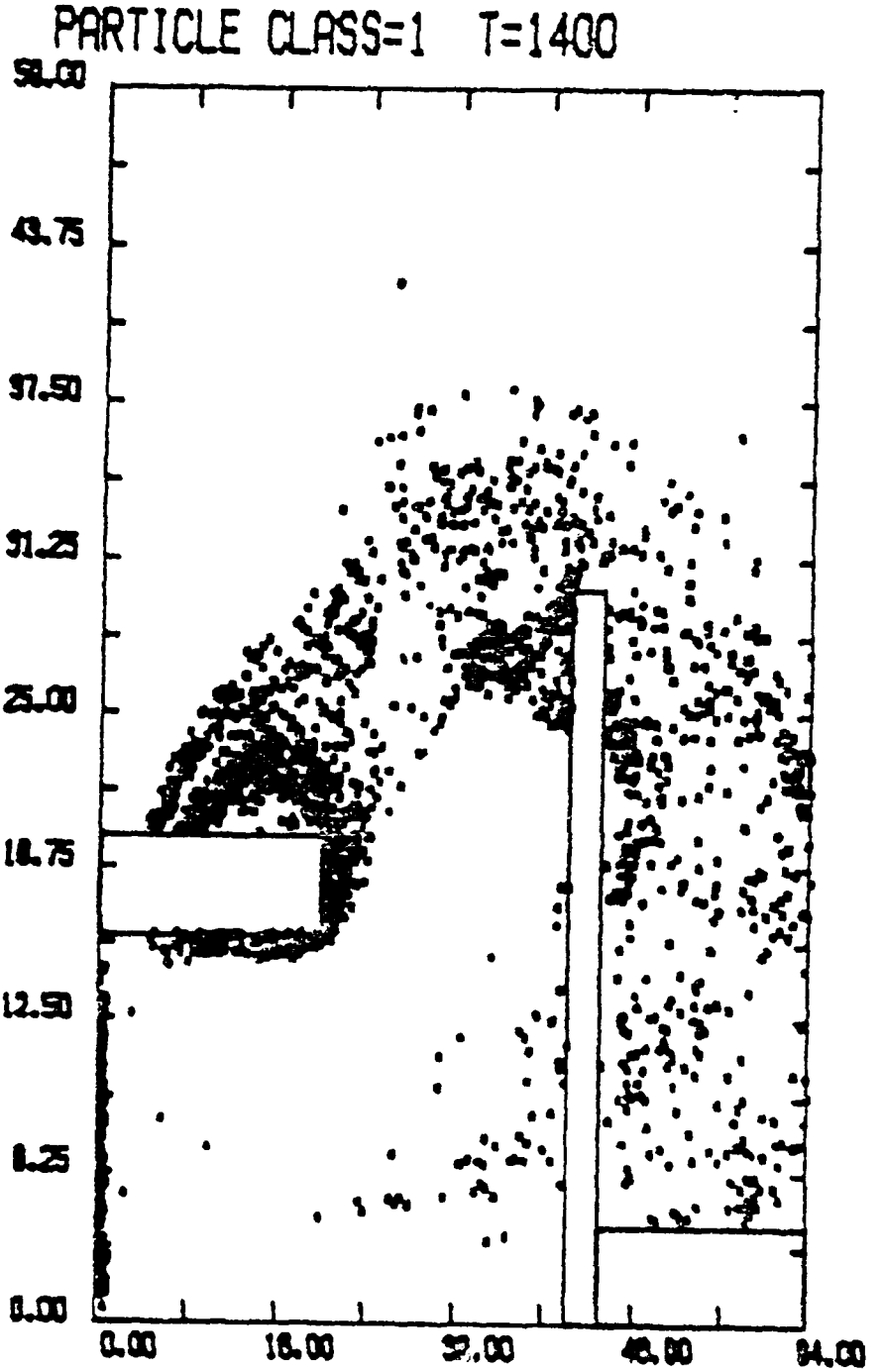

Fig. 9 — AURORA electrons-only flow for J_0 = 10 kA/cm^2

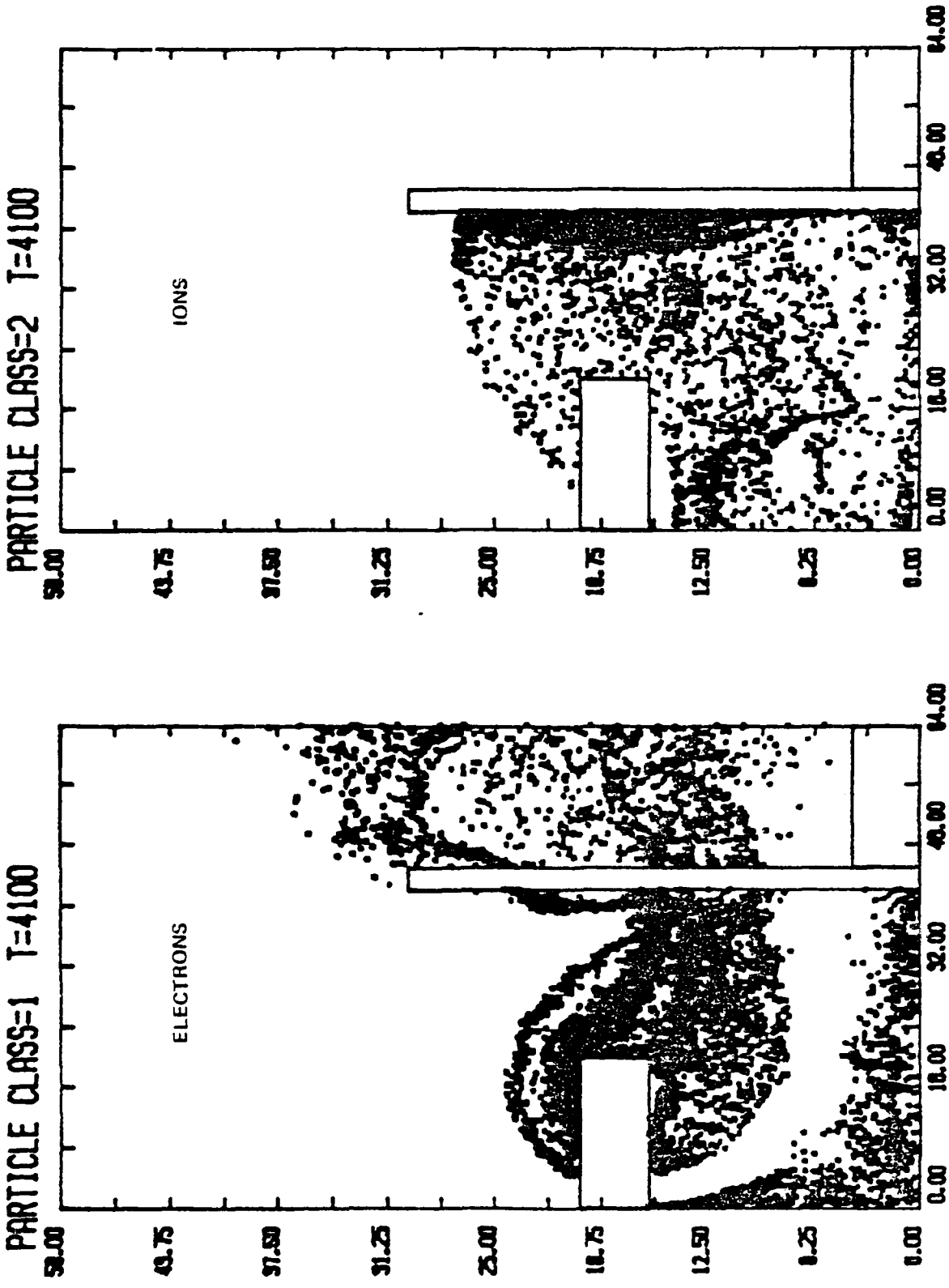

Fig. 10 — AURORA electron and ion flow for $J_0 = 4$ kA/cm^2

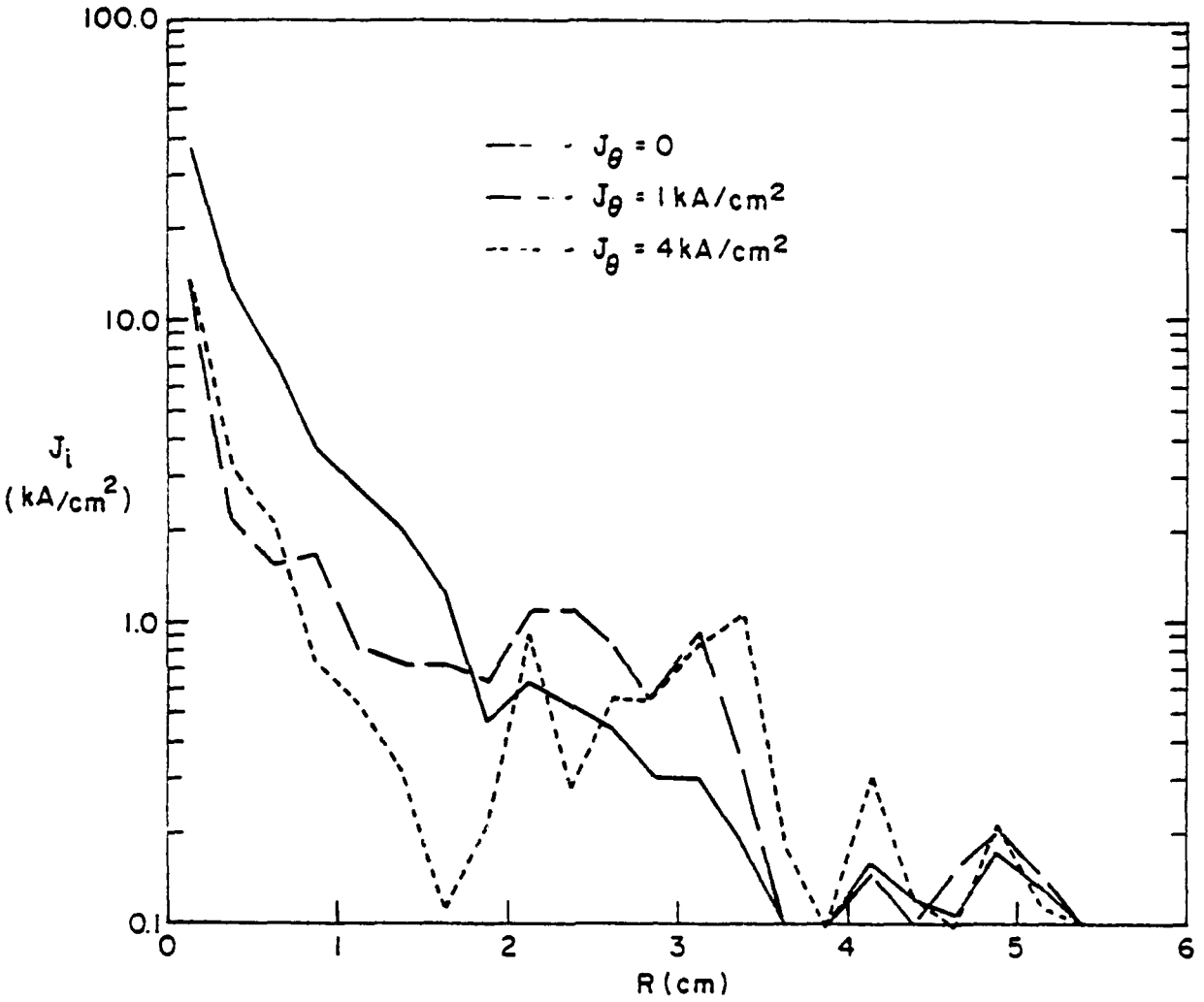

Fig. 11 — Radial profiles of AURORA ion current density collected at cathode

shank. However, in terms of net ion current collected at the various radii, the $J_s = 4\ kA/cm^2$ profile indicates that most of the ion current is flowing in a hollow cylindrical shell. This capability to shape the ion current density emerging from the diode may prove useful for future applications. Unfortunately it is clear that whatever other benefits $(J_s)_{shank}$ may offer for the AURORA diode, an improvement in ion production efficiency does not appear to be among them.

2. PBFA-I

Much of the on-site experimental effort of the NRL Light Ion Fusion Group has been dedicated to the design of an ion-efficient, 3-5 Ω diode for use on individual modules of the PBFA-I pulse power generator at Sandia National Laboratories. This work has been conducted on the GAMBLE-II machine at NRL.[28] A typical diode configuration used in that research is illustrated in Figure 12. The outer radius of the cathode shank was 3 cm while its thickness varied between 4 and 8 mm. An $A-K$ gap of approximately 5 mm was maintained although electrode plasma expansion gap closure at a normal rate of 3 cm/μsec over the 40 ns power pulse probably created an effective $A-K$ gap of 3.8 mm. The effective diode voltage was about 1.8 MV. For these parameters and a gap of 5 mm, Eqs. (1) and (2) predict an impedance of 7.1 ohms and an ion efficiency, η_i, of 0.186. An effective gap of 3.8 mm changes these to 5.1 ohms and $\eta_i = 0.245$ respectively. Experimentally, the diode ran at from 3 to 5 ohms and achieved 0.25 to 0.35 ion efficiencies in 40% of the shots (see Figure 13). The theoretical predictions using $D_0 = 3.8$ mm were quite close. Numerical simulations were conducted for a similar 4 ohm diode at 1.8 MV and a η_i of about 0.40 was observed.[29] Therefore, theory, experiment, and numerical simulation all call for between 0.25 and 0.40 ion efficiency.

To numerically test the effects of a shank J_s on diode performance in this lower impedance regime of 3-5 ohms, the same model diode as that used for the AURORA simulations (see Figure 4) was employed except that the voltage was lowered to 2 MV and D_A, D_0, and D_s were set equal to 0.60., 0.66, and 0.57 cm respectively. For those parameters, theory predicts 4.9-ohm operation and an η_i of at least 0.247. The experimental and numerical results from the actual GAMBLE-II diode would

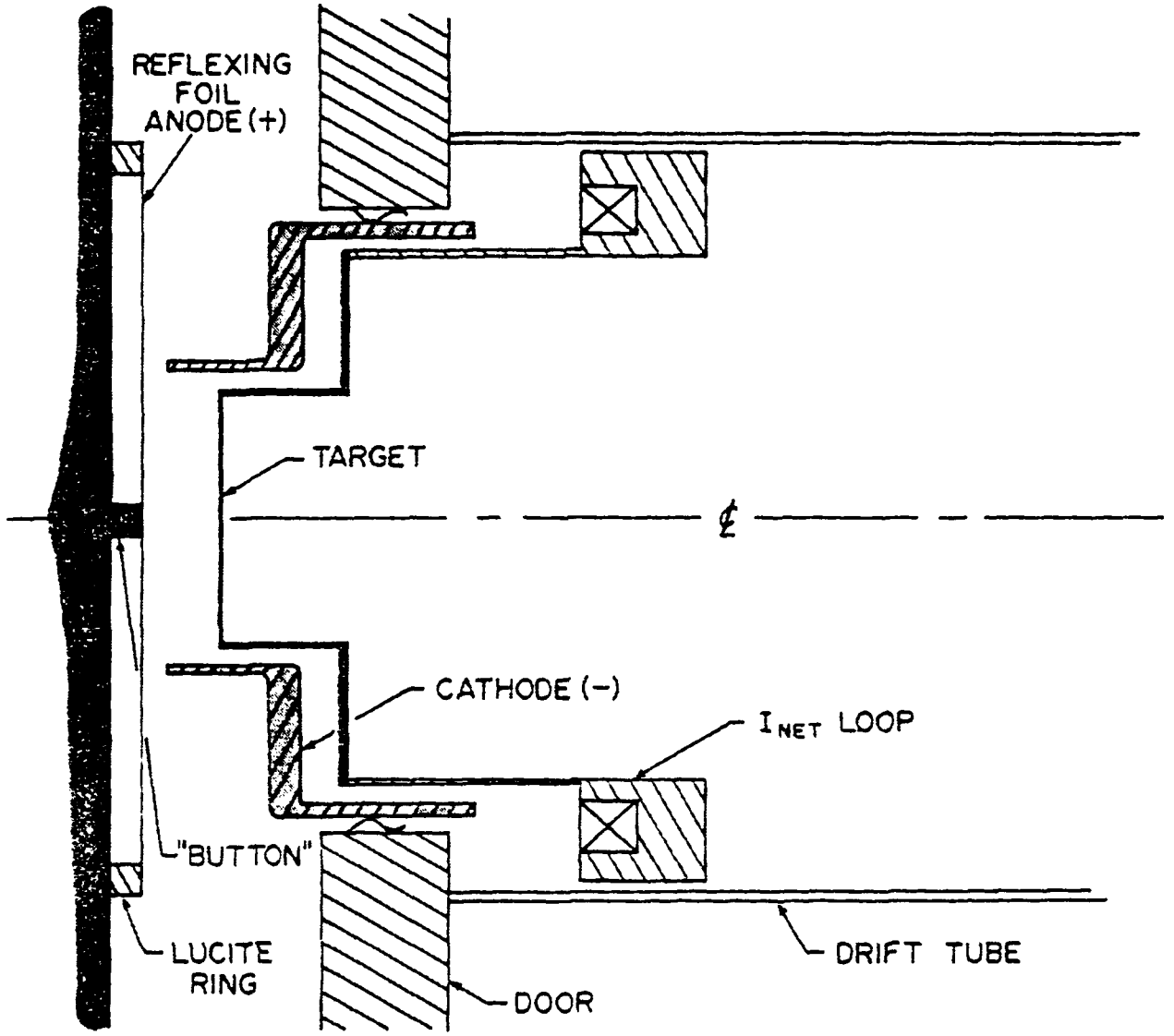

Fig. 12 — The high impedance Gamble II Test Diode for PBFA-I (courtesy of G.J. Stefanakis and D Mosher).

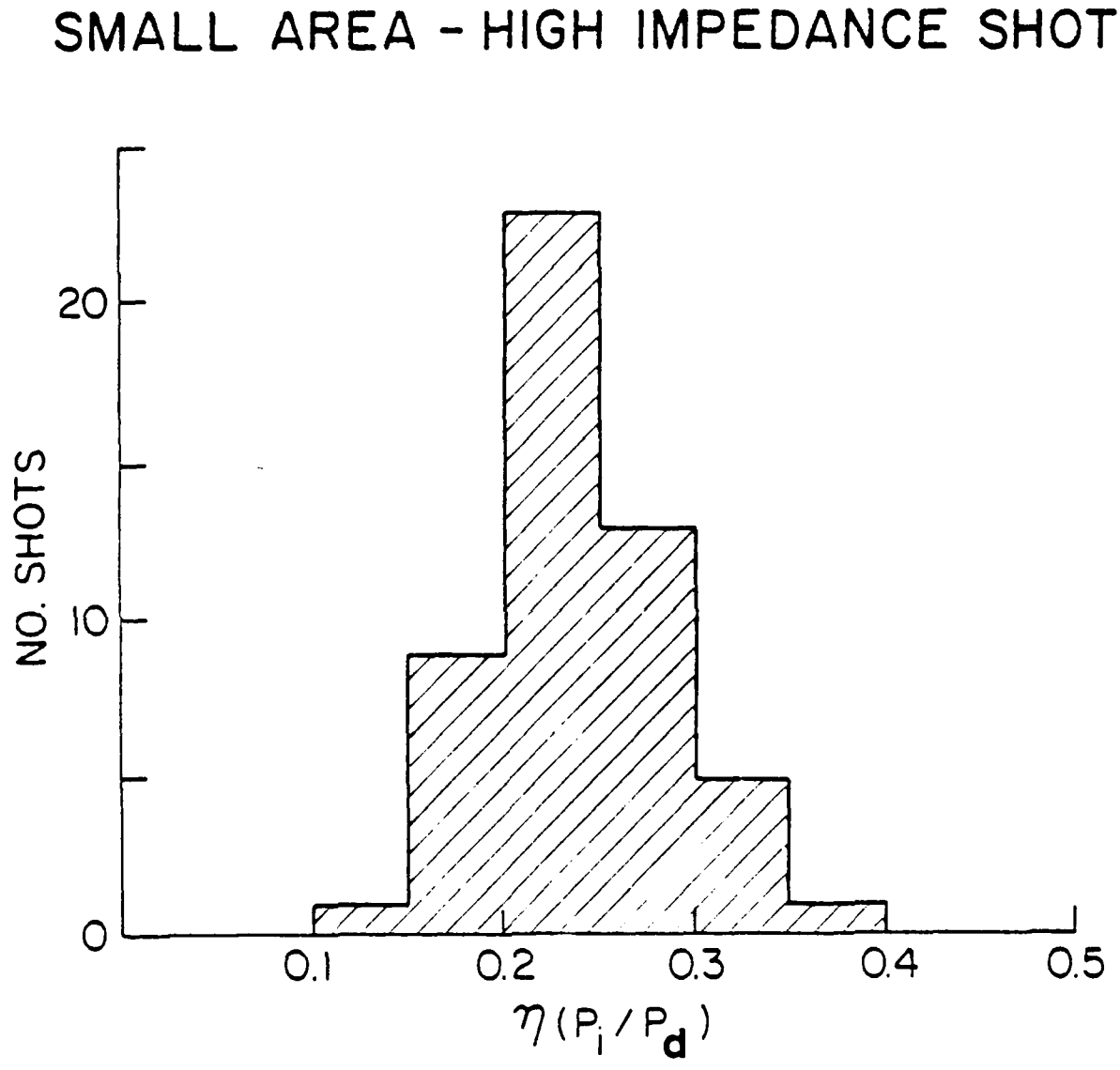

Fig. 13 — Statistical distribution of η, for the 4Ω diode (courtesy of S. J. Stefanakis).

indicate that those predictions are pessimistic. The computational results which follow will use the numerical run cited in the previous paragraph as a $J_\theta = 0$ "benchmark."

The total simulation was run in such a way as to sequentially test the following cases: (a) $J_\theta = 0$ with only electrons, (b) $J_\theta = 2$ kA/cm^2 with only electrons, (c) $J_\theta = 2$ kA/cm^2 with ions and electrons, and (d) $J_\theta = 4$ kA/cm^2 with ions and electrons. The traces of the electron and ion currents collected by the opposing electrodes during this run are plotted in Figure 14. The near-steady state at $T = 400$ for electron flow in the $J_\theta = 0$ case was used as the starting point for the imposed J_θ tests. This azimuthal current density was again imposed on the numerical mesh points in the rectangular cathode shank cross-section extending from $IZ = 6$ through $IZ = 21$ and from $IR = 18$ through $IR = 21$. With the new axial grid spacing of $\Delta Z = 0.03$ cm, this amounts to an area of 0.48 cm^2. The first test case, with $J_\theta = 2$ kA/cm^2, therefore amounts to a net azimuthal current of 0.96 kA. This shank current component was "turned on" at $T = 400$. At $T = 600$, ion emission was initiated along the front anode surface. The test for this particular value of J_θ was terminated at $T = 1200$, well before a steady state had been achieved. The reason for the early termination was the poor development of the electron flow pattern in the diode. This is illustrated by the sequence of sample electron position snapshots shown in Figure 15. The first shot depicts the electrons-only flow for $J_\theta = 0$ at $T = 400$. A substantial amount of reflexing through the anode foil is apparent as is a significant loss of electrons directly to the solid anode surface behind the foil. A stream of electrons emitted from the recessed cathode foil inside the shank can also be seen. Note that the electron mainstream initially impacts the anode foil almost exactly opposite the cathode shank face (i.e.-between 4.0 and 5.0 cm in radius). The electrons-only flow with $J_\theta = 2$ kA/cm^2 in the second shot of the series embodies the same electron flow characteristics as the $J_\theta = 0$ case but with significantly more radial pinching. Few electrons are impacting the anode foil opposite the shank face. In fact, a distinct gap has opened in the flow above a radius of 4.2 cm within a millimeter of the foil surface. Finally, in the last of the three segments of Figure 15, the electron flow is shown at a time when the main ion flow has traveled about halfway toward the recessed cathode foil. Only the anode foil below 3.0 cm in radius is being illuminated by

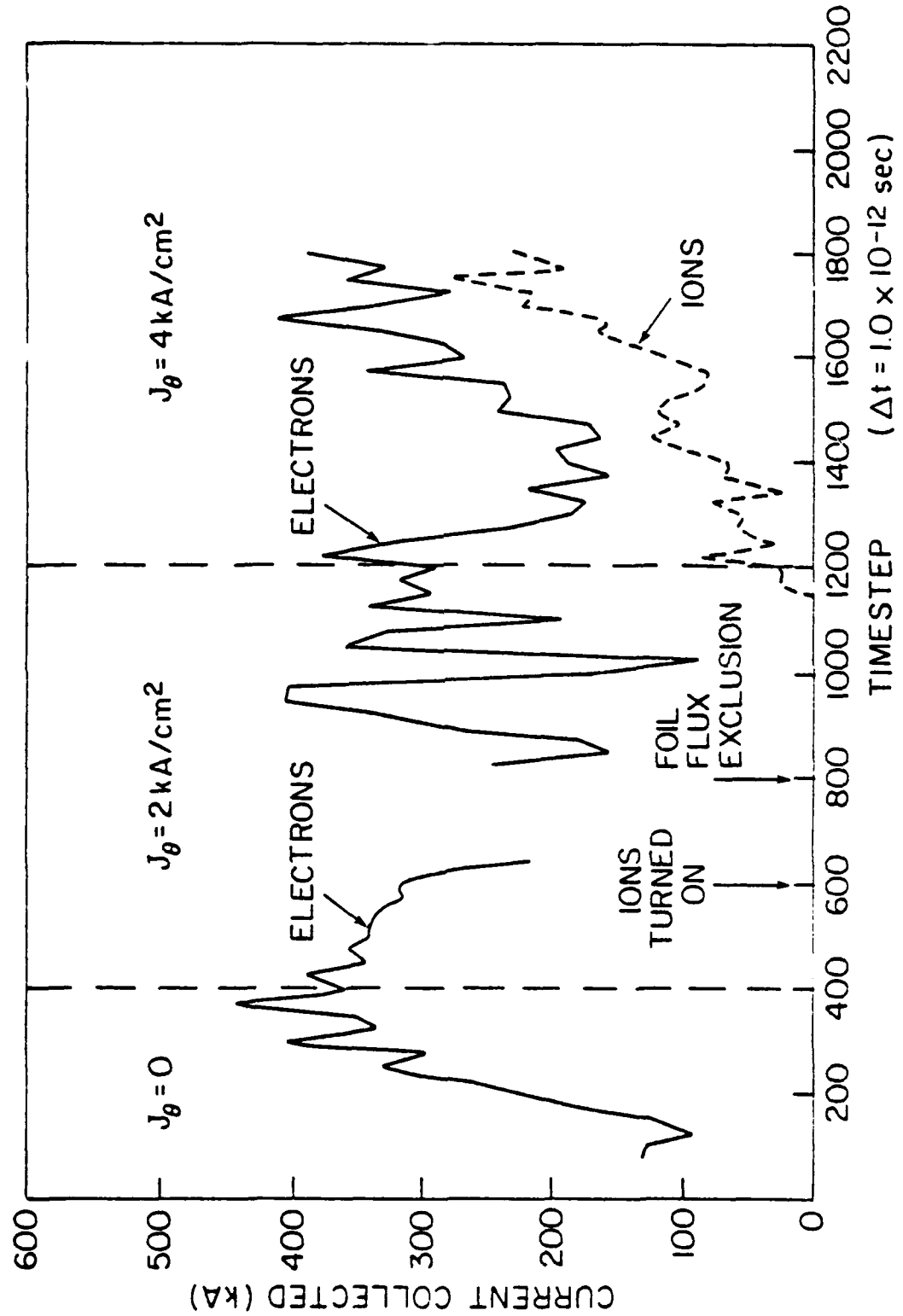

Fig. 14 — Temporal traces of collected electron and ion currents from the PBFA-I diode simulation

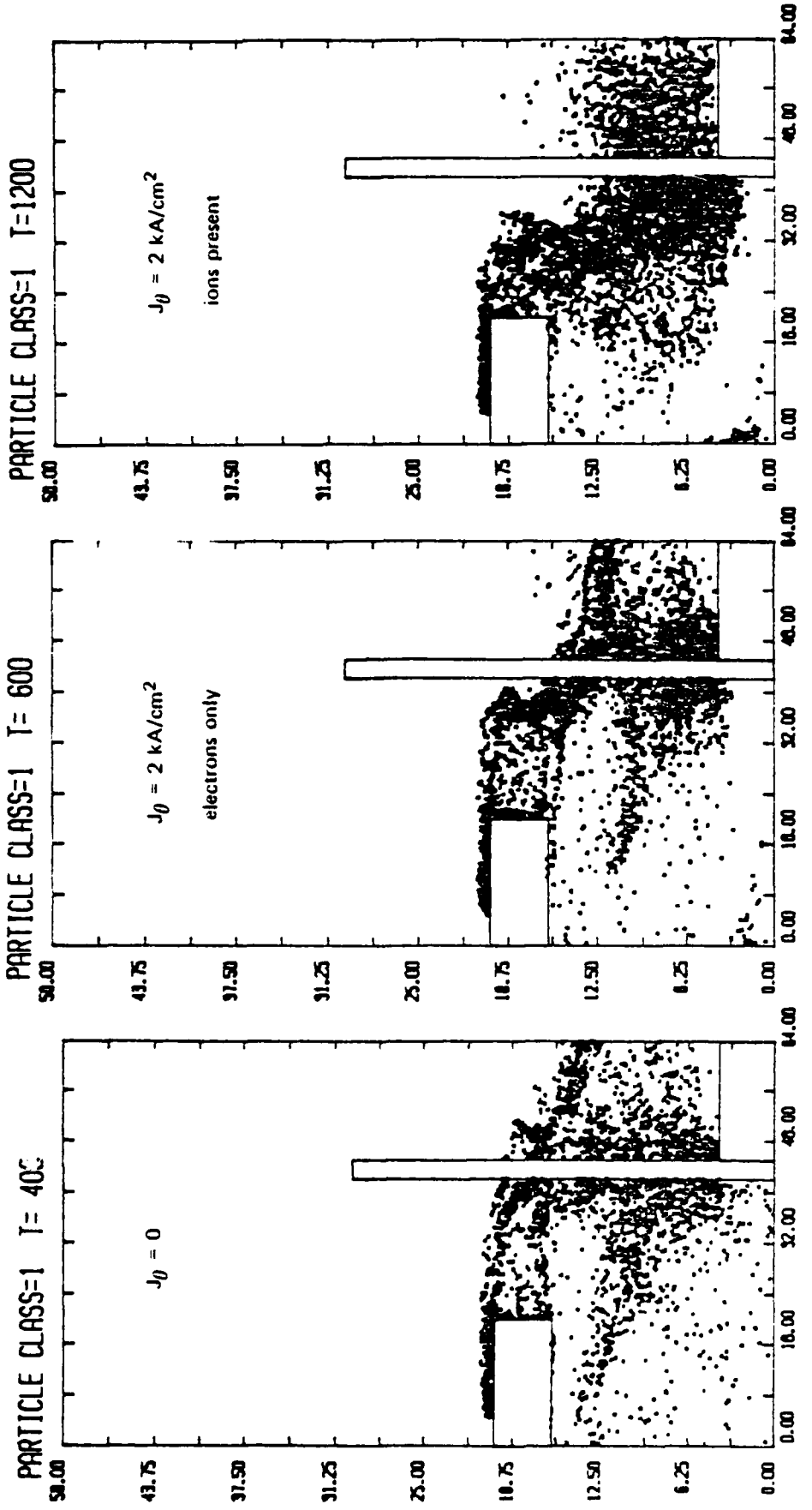

Fig. 15 — Comparison of PBFA-I electron flow patterns

electron impacts. This translates to no enhancement of ion emission over the large anode foil areas at larger radii.

In order to remedy the electron flow pattern problem, the beneficial effects of elevated J_s are recalled (see Figure 9). At $T = 1200$, the azimuthal shank current density was doubled to 4.0 kA/cm^2. When equilibrium was reached at $T = 2600$, the sample electron and ion flow appeared as shown in Figure 16. There is a definite improvement of anode illumination by electrons compared with the $J_s = 2$ kA/cm^2 case as indicated by Figure 17 which provides radial profiles of accumulated numbers of electron hits (not necessarily absorptions) across the face of the anode foil. The numbers given are relative and may be normalized to the total electron current in each case if so desired. For the purposes of this comparison, take I_e to be the same for each case. The $J_s = 4$ kA/cm^2 profile yields the most sharply peaked hollow electron beam at the highest mean radius. The sharpness of the profile is not unlike that observed in hollow cathode diodes having strong applied axial magnetic fields.[30] The equilibrium total currents were $I_e = 322$ kA and $I_i = 232$ kA yielding an impedance of 3.6 ohms and an ion production efficiency of 0.42 compared to the $J_s = 0$ benchmark of 4.0 ohms and $\eta_i = 0.40$.

The observed gain in net ion efficiency of 0.02 is insignificant, especially when taken in combination with the 0.4 ohm drop in diode impedance. There is a difference, however, between the total ion current flowing in a diode and the net ion current which can be extracted from a diode through the hollow cathode shank. Only the latter is useful from a practical, experimental standpoint. This distinction is crucial in judging the merits of the *J*-theta diode. Plotted in Figure 18 are the radial profiles of ion current density striking the cathode for both the $J_s = 0$ case (a $1/r$ profile with a central plateau corresponding to the location of the anode foil support button) and for the $J_s = 4$ kA/cm^2 case. For $J_s = 0$, a full 22% of the total ion current is lost to the cathode shank. This reduces the *effective* ratio of useful (extractable) ion current to total diode current to 0.31, in good agreement with the previously mentioned experimental observation of 0.25 to 0.35 ion efficiencies in 40% of the 4Ω shots actually conducted on GAMBLE-II. In comparison, for $J_s = 4$ kA/cm^2, only 11% of the total ion current is lost to the shank, leaving an *effective* ion efficiency of 0.374. This amounts to an improvement of over

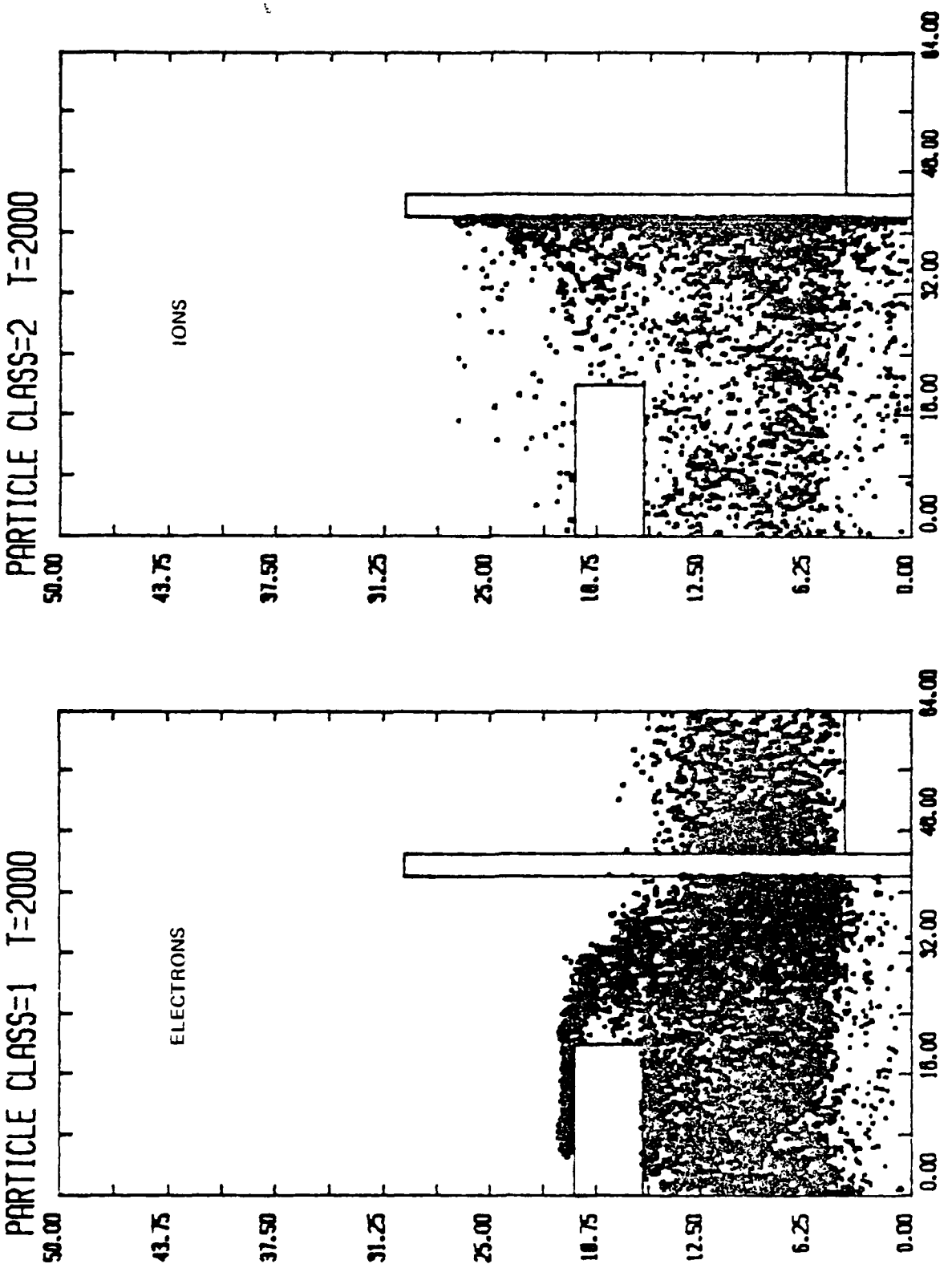

Fig. 16 — PBFA-I electron and ion flow for $J_0 = 4$ kA/cm^2

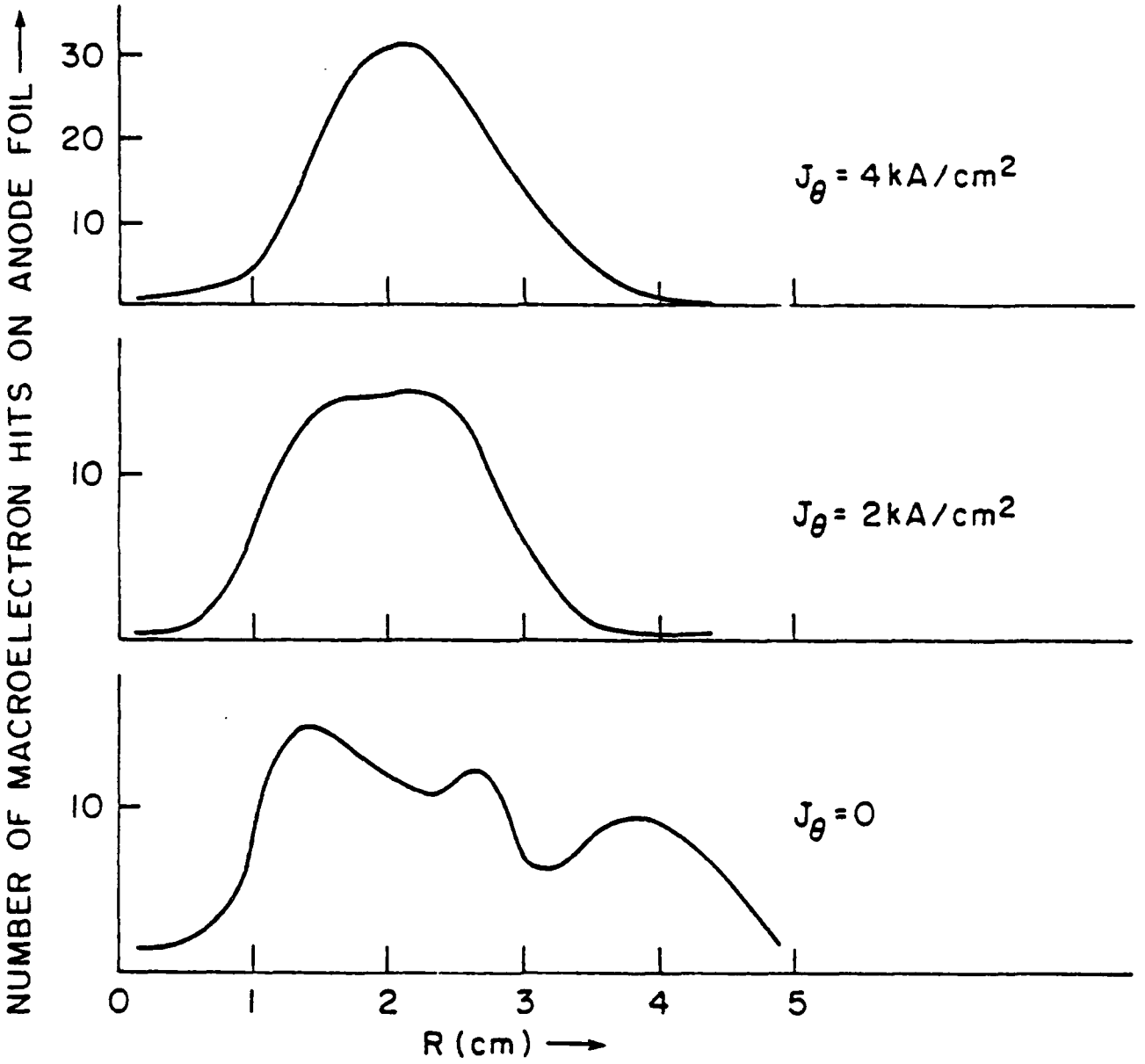

Fig. 17 — Comparative radial profiles of electron impacts on anode foil

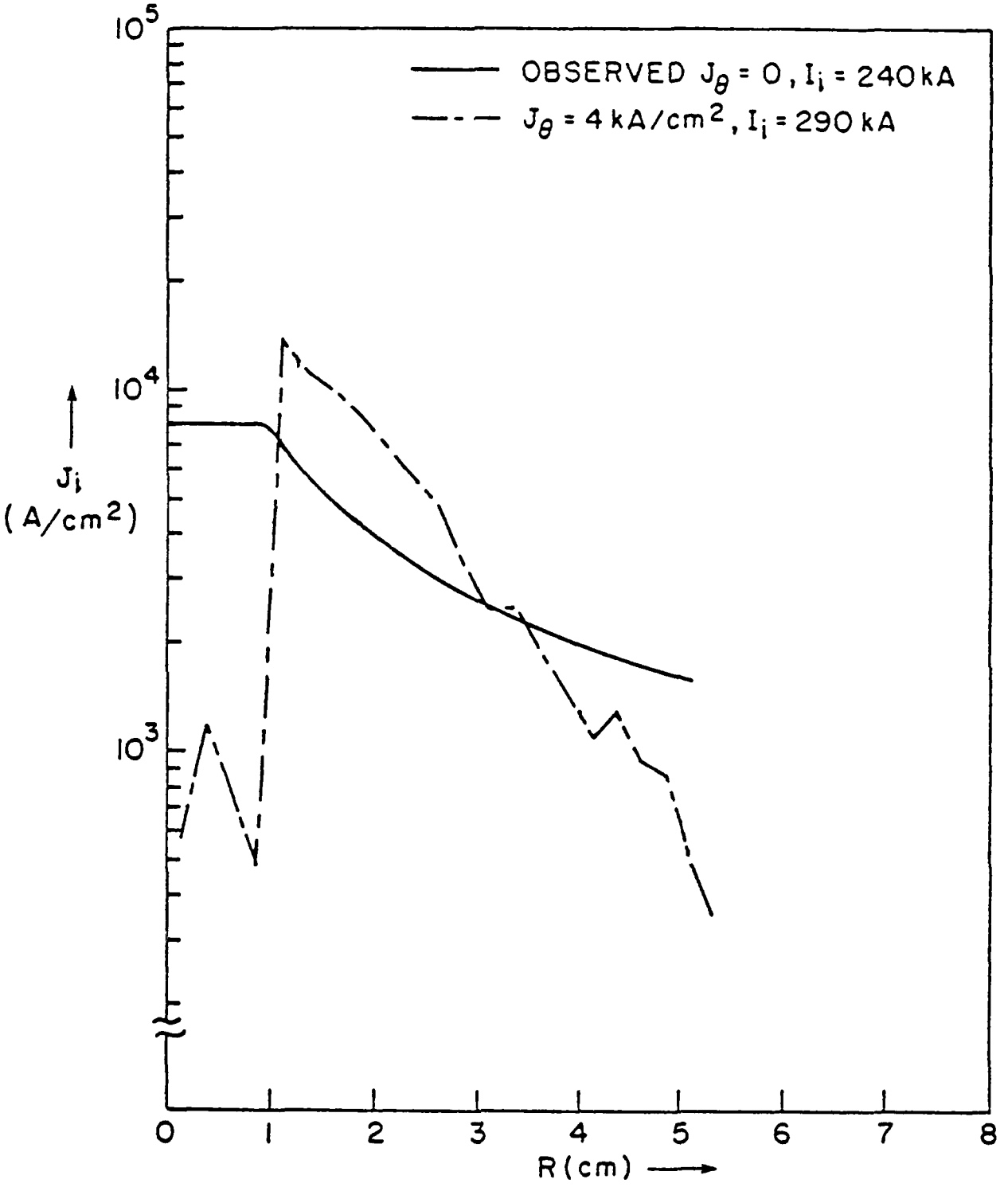

Fig. 18 — Radial profiles of PBFA-I ion current density

20% in $(\eta_i)_{effective}$ and thereby recommends this J_θ-diode for experimental testing on GAMBLE-II for possible use on PBFA.

In addition to this favorable result regarding enhanced effective ion production, several other results merit mention. Comparison of Figure 18 to the corresponding AURORA J_i profiles of Figure 11 show a hollowing of the ion beam. The central axis current density peak dissappears. Since shank electrons with their finite angular momentum cannot reach $R = 0$, this indicates that significantly more electrons are being emitted from the recessed cathode foil on the AURORA diode. These *can* reach $R = 0$ and enhance ion emission there. Another difference between the two impedance regimes is the nature of the cathode shank electron flow. On AURORA, the imposition of J_θ actually enhanced electron emission on the shank by lifting the flow away from the surface. This phenomenon does not manifest itself in the 4Ω runs. Finally, there was some question whether any actual magnetic insulation of the electron flow from the anode foil was taking place. The answer was obtained by measuring the strength of the radial component of the magnetic field one-half data cell (0.015 cm) from the magnetic-flux-excluding surface of the anode foil. Figure 19 shows that, as expected, very high fields are to be found over large areas of the foil. This is typical of the diamagnetic field enhancement observed in magnetically insulated radial diodes.[31]

IV. CONCLUSIONS

The major results of all of the above computer simulations are summarized in Table 1. The imposition of a relatively small azimuthal current in the hollow cathode shank of a 4-ohm axial diode has been numerically shown to increase the *effective* ion production efficiency of the diode by over 20%. This positive result recommends the further study of the new concept both theoretically and experimentally. Additional simulations should be conducted to examine diode equilibria for other values of J_θ. Experimentally, an actual J_θ-diode has been constructed as shown in Figure 20. Its cathode shank is approximately six centimeters in diameter with 48 slots 3/8 inch deep, 0.045 inch wide, and angled at 20° cut around its periphery in order to generate a J_θ by spiraling the current flowing through the

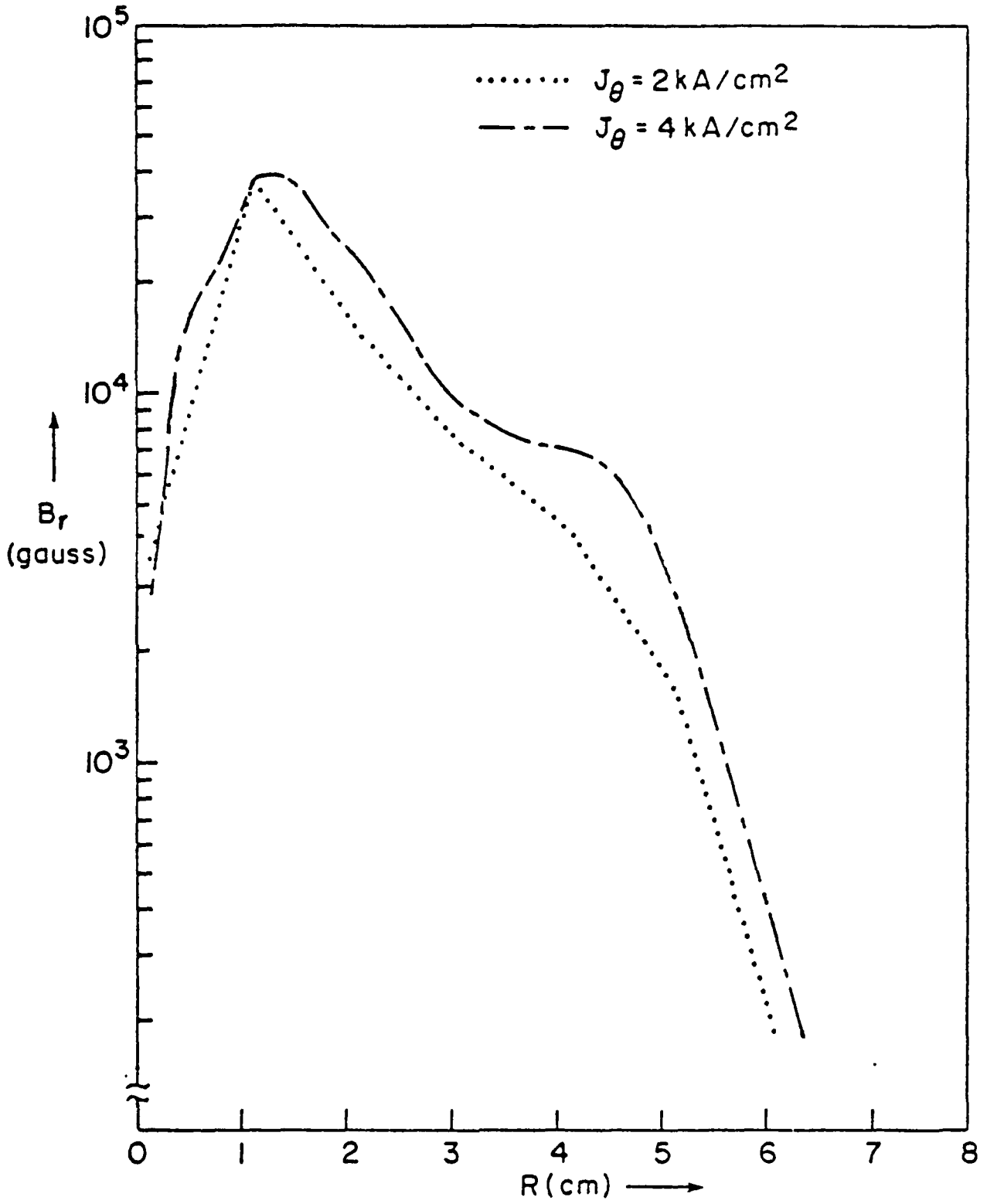

Fig. 19 — Radial profiles of B_R near PBFA-I anode foil

Table 1 – Summary of Major Results

	AURORA (5 MV)				PBFA (2 MV)	
J_θ (kA/cm^2)	0 ($^{neg.}_{pol.}$)	0 ($^{pos.}_{pol.}$)	1	4	0	4
I_e (kA)	165	182	244	257	300	322
I_i (kA)	40	56	41	34	200	232
$(I_i)_{eff}$ (kA)	35	50	35	30	150	207
I_{diode} (kA)	205	238	285	291	500	555
Z (ohms)	24.4	21.0	17.5	17.2	4.0	3.6
η_i	0.195	0.235	0.144	0.117	0.40	0.42
$(\eta_i)_{eff}$	0.171	0.210	0.123	0.103	0.30	0.37

shank. Three shots were conducted using this diode on GAMBLE-II but diagnostic difficulties prevented the gathering of enough useful information for proper evaluation. Additional shots will be attempted as circumstances permit.

For diodes with impedances in the neighborhood of twenty ohms, no evidence of ion efficiency boosting via a shank J_θ has been obtained. However, even for that case the azimuthal current component does significantly modify the radial profile of the extractable ion current density. Such a capability to change the shape of the ion beam which emerges from the diode may prove useful in the future for optimizing this beam for transport away from the diode through plasma channels.

ACKNOWLEDGMENTS

The authors are indebted to R.A. Meger and S.J. Stephanakis for their valuable assistance in the preparation of this report.

JDT REFERENCES

1. G. Cooperstein, S.A. Goldstein, D. Mosher, and R.J. Barker, et al., NRL Memo Report 4387 (1980).

2. D.J. Johnson, G.W. Kuswa, A.V. Farnsworth, Jr., and J.P. Quintenz, et al., Phys. Rev. Lett. 42, 610 (1979).

3. G. Cooperstein, S.A. Goldstein, and D. Mosher, et al., in Proceedings 3rd International Topical Conference on High Power Electron and Ion Beam Research and Technology, Novosibirsk, USSR (1979).

4. D.J. Johnson, Bull. Am. Phys. Soc. 24, 925 (1979).

5. S.J. Stephanakis, J.R. Boller, G. Cooperstein, S.A. Goldstein, D.D. Hinshelwood, D. Mosher, F.W. Oliphant, F. Sandel, and F.C. Young, Bull. Am. Phys. Soc. 23, 907 (1978).

6. D.G. Colombant, S.A. Goldstein, and D. Mosher, Phys. Rev. Lett. 45, 1253 (1980).

7. R.A. Meger, F.C. Young, G. Cooperstein, S.A. Goldstein, and D. Mosher, NRL Memo Report 4477 (1981).

8. D.J. Johnson, S.A. Goldstein, R. Lee, and W.F. Oliphant, J. Appl. Phys. 49, 4634 (1978).

9. S.A. Goldstein and R. Lee, Phys Rev. Lett. 35, 1079 (1975).

10. S.A. Goldstein, R.C. Davidson, J.G. Siambis, and R. Lee, Phys. Rev. Lett. 33, 1471 (1974).

11. D.P. Bacon, S.A. Goldstein, R. Lee, and G. Cooperstein, NRL Memo Report 4326 (1980).

12. M.M. Widner, J.W. Poukey, and J.A. Halbleib, Sr., Phys. Rev. Lett. 38, 548 (1977).

13. J.W. Shearer, Lawrence Livermore Lab Report UCRL-52129 (1976).

14. R.J. Barker and P.F. Ottinger, NRL Memo Report 4654 (1981).

15. R.J. Barker and S.A. Goldstein, to appear as an NRL Memo Report (1982).

16. R.J. Barker and S.A. Goldstein, Bull. Am. Phys. Soc. 25, 900 (1980).

17 Suggested independently for other applications by F. Sandel in 1978.

18. S.A. Goldstein, J. Appl. Phys. 47, 894 (1976).

19. A.E. Blaugrund, G. Cooperstein, and S.A. Goldstein, Phys. Fluids 20, 1185 (1977).

20. D. Mosher, Bull. Am. Phys. Soc. 25, 900 (1980).

21. J.W. Poukey, J.R. Freeman, and G. Yonas, J. Vac. Sci. Technol. 10, 954 (1973).

22. S. Humphries, Jr., Plasma Physics 19, 399 (1977).

23. R.J. Barker, A.T. Drobot, R. Lee, and S.A. Goldstein, Proc. 9th Conf. on the Numerical Simulation of Plasmas, Evanston, Ill. (1980).

24. R.A. Meger, A.T. Drobot, S.A. Goldstein, and F.C. Young, Bull. Am. Phys. Soc. 25, 900 (1980).

25. F.C. Young and R.A. Meger, et al., Bull. Am. Phys. Soc. 25, 899 (1980).

26. R.J. Barker, Banach Center Publications 3, 255, Warsaw, Poland (1975).

27. R.A. Meger, F.C. Young, and A.T. Drobot, et al., NRL Memo Report 4477 (1981) and J. Appl. Phys. 52, 6084 (1981).

28. S.J. Stephanakis, S.A. Goldstein, D. Mosher, and W.F. Oliphant, Bull. Am. Phys. Soc. 25, 900 (1980).

29. A.T. Drobot, private communication.

30. R.J. Barker, S.A. Goldstein, and R.E. Lee, NRL Memo Report 4279 (1980).

31. R.J. Barker, S.A. Goldstein, and A.T. Drobot, Proc. IEEE Conf. on Plasma Science, Madison, Wisc. (1980).

NUMERICAL STUDY OF ELECTRON LEAKAGE POWER LOSS IN A TRI-PLATE TRANSMISSION LINE

I. INTRODUCTION

There exist two major alternate geometries for intense light ion beam sources (diodes) to be used in light ion inertial confinement fusion reactor scenarios. They are the axial pinch-reflex diode (PRD) pioneered at the Naval Research Laboratory[1] and the magnetically insulated radial diodes under development at Sandia National Laboratories[2] and Cornell University.[3] Each of the two diode types have their respective advantages and disadvantages. The low impedance (0.5-2.0 ohm) PRD's tested on the Gamble II pulsed power generator at NRL proved themselves capable of delivering over 70% of the net power flowing through the diodes to the light ion (H^+ and D^+) beams.[4] They owed their high ion production efficiencies to the theoretically established benefits of large aspect ratios[5] (cathode radius/A-K gap) and multiple reflections of electrons through the anode foil.[6] The geometry of the PRD (pinch-reflex diode) produced an axially flowing ion beam which could then be directed to illuminate a fusion pellet target located some distance away.[7] In some current fusion reactor conceptual designs this can be considered an advantage since the ion beam source could then be located far enough away from the fusion reactor vessel to protect them from possible radiation and blast damage. In addition, there would be no limit to the number of individual axial diode ion beam sources which could be arrayed around a central target to deliver as much beam power as necessary to the target. Unfortunately, theoretical analysis has revealed that lower current ion beams lend themselves more efficiently to transport over multi-meter distances.[3] To maintain a given power level while boosting transport efficiency, higher impedance ion diode sources are desirable. Over the past several years NRL has pursued an experimental ion diode development program under DNA sponsorship at the Harry Diamond Laboratory (HDL). In that work, diode impedances range from 10 to 40

Manuscript submitted April 9, 1982.

ohms to more closely match the 50 ohm characteristic impedance of the single arm of the AURORA pulsed power generator used there (compared to the 1.5 ohms of NRL'S GAMBLE II). To achieve the higher impedances, lower aspect ratio PRD's were employed and this necessarily lowered the diode's ion production efficiency. Efficiencies of only 20% to 30% were observed.[9, 10] Various techniques are being tested to improve this performance.[11, 12]

Magnetically insulated radial diodes offer a different set of pros and cons. They have been shown to operate at better than 75% ion production efficiency.[13] Since ion flow is focused to the diode centerline, beam transport is not a consideration and low impedances may be employed. This also means that target ignition will take place inside the diode which could result in damage to the device. The power feed geometry for the radial diode may also lead to other difficulties. Figure 1 presents a conceptualization of a possible radial diode test apparatus. As shown in the cutaway view, a large number of individually charged power modules are arrayed around the circumference of the device. They are so designed to dump their stored electrical energy simultaneously into the large disc-like triplate transmission line (TTL) which fills the central portion of the machine. This triplate consists of an anode disc sandwiched between two equispaced cathode discs. The interplate separation may also vary with radius. The TTL (triplate transmission line) terminates in the center with an azimuthally-symmetric radial diode. A possible configuration for that central region is illustrated in Figure 2. The symmetry of the power flow to such a diode is one key consideration.[14] Another is the highly inductive character of the TTL itself. This high inductance can cause a severe lowering (via L . dI/dt) of the voltage across the diode as compared to the voltage output of the individual pulsed power modules. Furthermore, the resistance divided by the

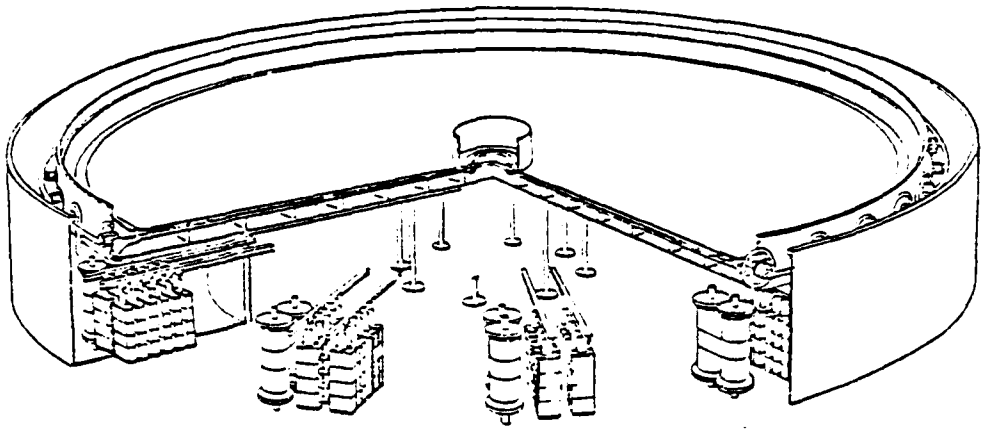

Fig. 1 — Conceptual reactor configuration using tri-plate transmission line and radial diode (courtesy, Sandia Laboratories)

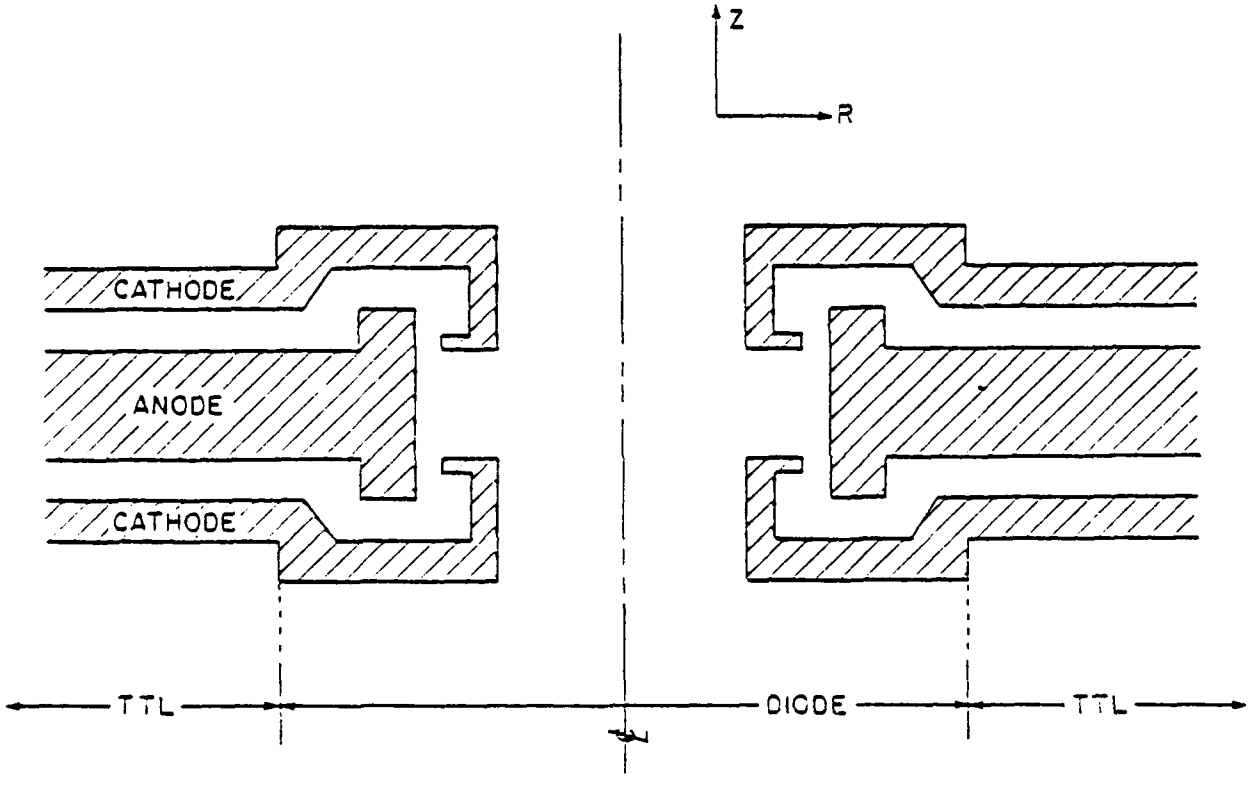

Fig. 2 — Central region of the reactor configuration

inductance of the TTL circuit can lead to a phase shift between the peak voltage across the diode and the peak current flowing through the diode, with unfortunate consequences for the power characteristics of the device. Those problems have been and are being studied elsewhere. This report focuses on yet another possible TTL power loss mechanism, namely that of direct electron flow through the vacuum gap between the plates. The properties of magnetic insulation are well enough understood to ensure that an adequately insulated TTL could be designed with sufficiently large gap spacings for known values of diode current and voltage. However, there is likely to be a transition region in the TTL in the immediate vicinity of the radial diode into which will seep a finite value of the axial magnetic field imposed in the diode's A-K gap. The physics of electron flow in such a transition region cannot readily be dealt with by analytic treatment. For that purpose, this numerical simulation was undertaken.

II. THE RADIAL DIODE AND TTL

The ideal diode and triplate transmission line geometry chosen for analysis is depicted in Figure 3 (drawn to scale). The cathode consists of a solid shank 5.0 centimeters in diameter and 6.4 centimeters long sandwiched axially between two infinite parallel plates. The anode takes the form of a flat annular collar, mounted symmetrically and coaxially to the cathode shank. The anode's inside diameter of 5.5 centimeters yields a radial anode-cathode gap of 0.5 centimeter while its 4.4 centimeter thickness allows a clearance of 1.0 centimeter from each of the parallel cathode plates. An electrical potential difference of 2.0 megavolts is maintained between the electrodes. In addition, a field coil structure is assumed such that a constant and uniform background B_{zo} of 20.0 kilogauss permeates the diode gap

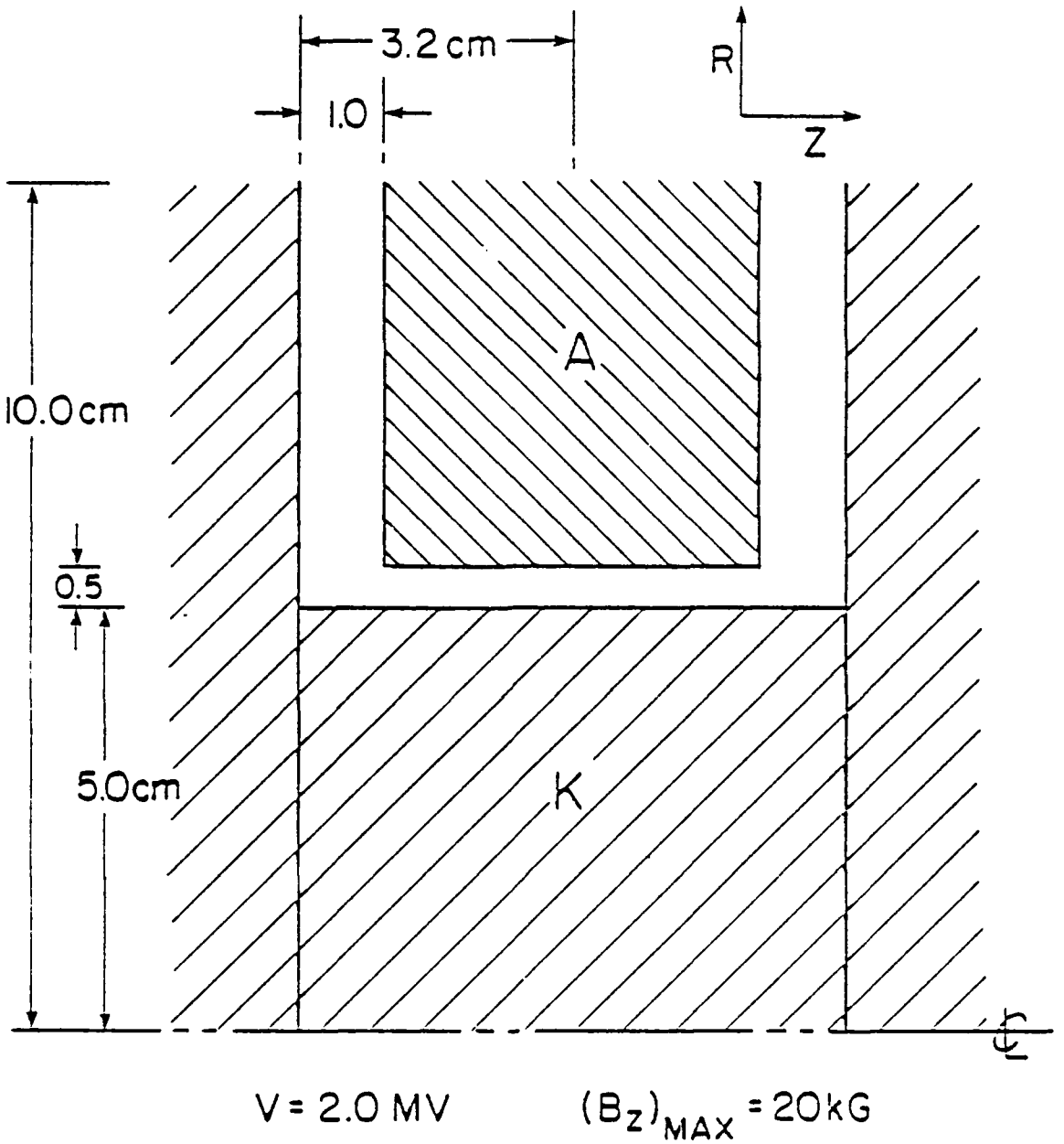

Fig. 3 — The radial diode and TTL modeled

completely from R = 5.0 to R = 5.5 centimeter. This field is further assumed to decrease in strength linearly with increasing radius inside the adjacent TTL, until it reaches zero at R = 6.5 cm.

The geometry under consideration may be subdivided into three separate gap regions as shown in Figure 4. Each half of the "infinite" triplate shall be called Region I. It is primarily the diode current flowing axially through the cathode shank which generates an azimuthal magnetic field in this region to insulate the electron flow. Region II consists of the radial anode-cathode gap which is the heart of the radial diode. There too an insulating B_θ arises from the cathode shank current. Note, however, that I_z must go to zero at the diode's center plane. B_θ must vanish with it there. For that reason, it is the strong applied axial magnetic field, B_{zo}, which must be relied upon to insulate the electrons in the diode. The azimuthal field component there serves primarily to complicate the electron flow. Finally, there is the transition volume of Region III. In the lower third of that region, $\vec{B}$ will closely resemble that of II but $\vec{E}$ will be weaker and no longer totally radial. In the upper two-thirds there is a fairly sharp B_z gradient which should act to prevent any TTL electrons from entering II. Exactly where those reflected electrons go is the central question treated herein. Before plunging into the numerics, it is first illuminating to derive some zeroeth-order predictions for Region I and II from simple analytic theory.

Throughout most of Region II, the vacuum electric field has a uniform value of $(E_r, E_z) = (1.33 \times 10^4, 0.0)$ statvolts/cm, while in $(E_r, E_z) = (0.0, 0.666 \times 10^4)$ statv/cm. In the absence of B_z and B_θ in II, the expected space-charge limited electron flow (ignoring ions) may be approximated by the Langmuir-Compton[15] expression

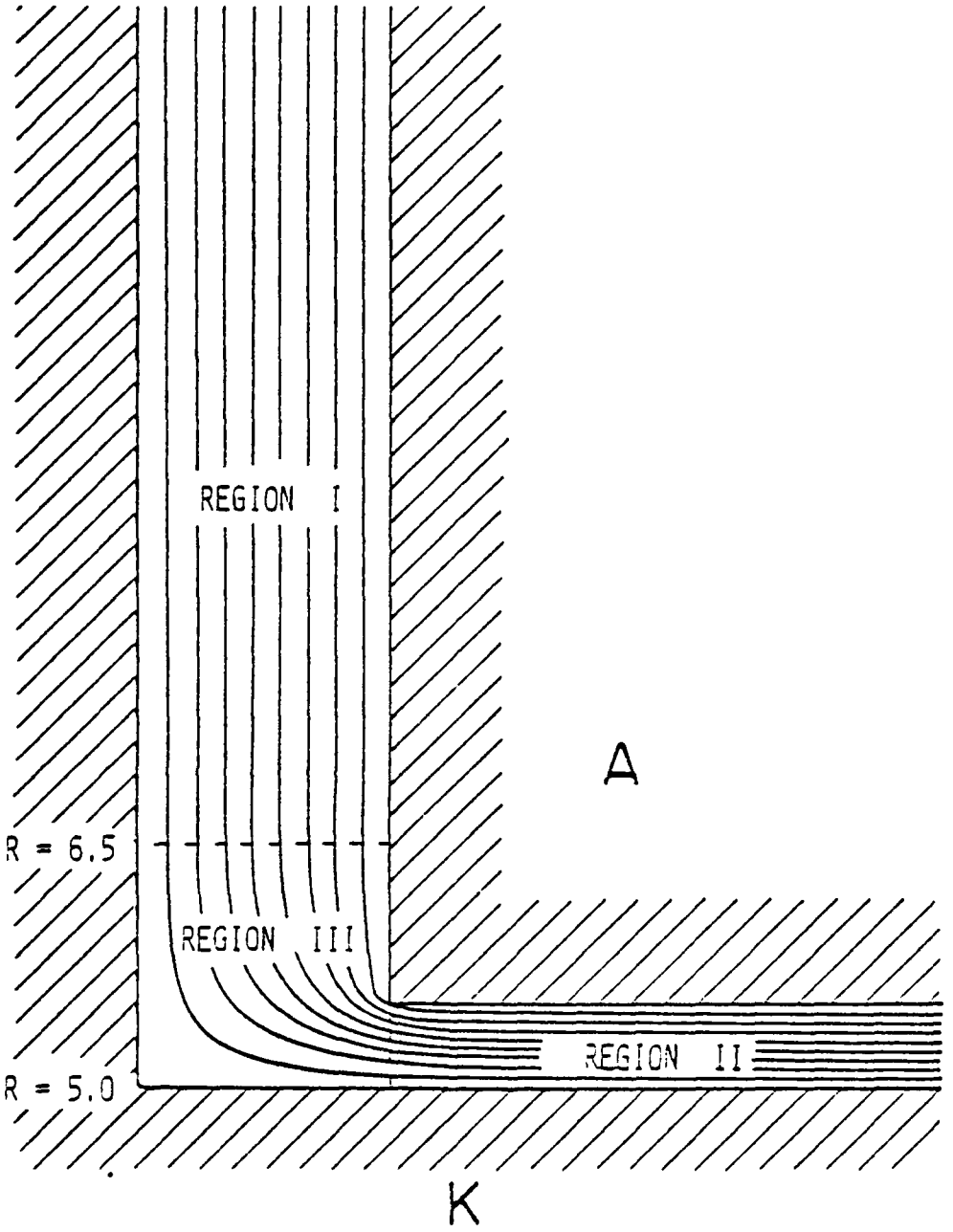

Fig. 4 — The three major regions under study

$$I_e = 14.7\times10^{-6}\,\frac{L\,V^{3/2}}{r\,\alpha_1^2}\ \text{amps} \qquad (1)$$

with $\alpha_1 \equiv \delta - \left(\frac{2}{5}\right)\delta^2 + \left(\frac{11}{120}\right)\delta^3 - \left(\frac{47}{3300}\right)\delta^4 + 0.00158\,\delta^5 \ldots$ where $\delta \equiv \ln\left(\frac{r}{r_e}\right)$, r = collector radius = 5.5 cm, r_e = emitter radius = 5.0 cm, L = length of emitting shank = 4.4 cm, V = diode voltage = 2.0 MV. For the given values of radii, δ = 0.09531 and α_1 = 0.09176. This predicts an electron current of 3.95 megamperes in the radial A-K gap (N.B. - This ignores those portions of the cathode shank in Region III). Significant electron emission can also be expected along the parallel cathode side plates of Region I. The space-charge limited electron current density emitted there can be approximated from the relativistic expression attributed to Friedlander, et.al.[16]

$$J_e = 2.72\times10^3\left[\sqrt{\frac{eV}{mc^2}+1} - 0.8471\right]^2 d^{-2}\ \text{amps/cm}^2 \qquad (2)$$

where d = arode-cathode plate separation = 1.0 cm. For the two megavolts applied, this predicts J_e = 5.1024 kA/cm^2. In the simulation that follows, electron emission is permitted on these surfaces between R = 5.2 and R = 9.5 cm. This yields an emission area of 198.6 cm^2 in each TTL or a total diode feed line electron current of about 2.0 megampere. Ignoring the effects of magnetic fields, this apparatus as modeled would therefore have a total electron current of about six megamperes. Substituting an electron-ion bipolar current in the A-K gap raises the figure there by about a factor of 1.86 and thereby boosts the total diode current to about 9.35 megamperes.

In order to gauge the effect of magnetic insulation in Region I a parallel can be drawn with the analysis of the "critical current" in an

idealized parallel plate axial diode.[17] In that device, the axial current flow generates an axial magnetic field which causes emitted electrons to bend toward the center axis. If this B_θ (and therefore this I_z) is large enough, the electron will not reach the anode plate. Ignoring the effects of the emitted electron space-charge, a simple estimate can be made for the "critical current," I_c, necessary to produce an electron trajectory which just grazes the anode surface:

$$I_c = 8500\ \beta\gamma\ \left(\frac{R}{d}\right)\ \text{amperes} \qquad (3)$$

where R = the radius of emission, d = A-K gap, and β and γ have their standard relativistic definitions. Here $\beta_{max} = 0.98$, $\gamma_{max} = 4.9$, and d = 1.0 cm so that the equation becomes

$$I_c = 4.08 \times 10^4\ R\ \text{amperes} \qquad (4)$$

The axial current taking part in the physics of Eq. 4 may be considered to consist only of the total cathode shank current (i.e. - one half of the net Region II current). By definition, the insulated electron flow in the TTL can contribute no net axial current. The previous, crude estimate of electrons-only I_{II} of 3.95 MA leads to an axial current of 1.98 MA which implies, via Eq. 4, magnetic insulation out to a radius of about 48.5 centimeters. However, in a properly functioning radial diode, the current prediction of Eq. 1 will not hold true. The relativistic electron gyroradius in the imposed 20 kG axial magnetic field is only 0.41 cm, well below the 0.50 cm width of the gap. Thus, magnetic insulation should prevail and estimates for diode performance should be sought directly from the literature on magnetically

insulated coaxial charge flow. In one of the most recent comprehensive treatments on the subject,[18] it was noted that the critical field for insulation is given by

$$B_c = \frac{mc^2}{e}\left(\frac{2\, r_A}{r_A^2 - r_c^2}\right) \left(V_o^2 + 2\, V_o\right)^{1/2} \qquad (5)$$

where r_A is the anode radius, r_c is the cathode radius and $V_o = \frac{e}{mc^2}\phi_o$. For ϕ_o= 2 MV, V_o equals 3.9 and B_c becomes 17 kG, well below the chosen value of B_{zo} = 20 kG in the diode under consideration. There also appears in Reference 18, rough parametric plots of ion current values for various combinations of diode characteristics. From those plots, it may be crudely approximated that the ion current in Region II should be about 2-3 times the Langmuir-Blodgett ion current, I_{LB}. This I_{LB} will be equal to the previously predicted 3.95 MA for electrons multiplied by the square root of the electron-proton mass ratio, m_e/m_i. This leads to a Region II ion current of about 200-300 kA and a half-current of 100-150 kA which in turn implies magnetic insulation in the TTL out to a radius of only 2.45 to 3.68 cm. This translates to no insulation at all in the TTL since its lower radius is 5.0 cm. Only the full numerical simulation can accurately show what the true outcome will be.

III. THE COMPUTATIONAL EXPERIMENT

The numerical simulation of the radial diode was carried out with the latest version of NRL's DIODE2D computer code.[19] This code is two and one-half dimensional (i.e., particles are allowed two spatial coordinates, r and z, as well as three canonical momentum components P_r, P_z and P_θ). The computational "particles" are azimuthally-symmetric charge/current rings with

charge-to-mass ratios corresponding exactly to that of electrons and protons. The motion of these macroparticles is treated completely relativistically. DIODE2D is a particle-in-cell (PIC) code in which macroparticle charges and current densities are area-weighted over the four nearest grid points on the computational mesh. In its electrostatic, magnetostatic treatment, DIODE2D solves Poisson's equation to obtain $\phi(r,z)$ and $A_\theta(r,z)$ respectively from $\rho(r,z)$ and $J_\theta(r,z)$.[20] From these the self-consistent fields are given by $\vec{E} = -\nabla\phi$ and $\vec{B} = (B_r, B_z)_{self} = \vec{\nabla} \times \vec{A}$. The azimuthal component of the self-magnetic field, B_θ, is found directly through radial integration of Ampere's Law over the mesh. Regularly shaped conductor regions which exclude electric field and magnetic flux may be overlayed on the computational mesh by utilizing a capacitance matrix technique[21] in the Poisson solving algorithm. This optional capability was essential for this particular simulation. A static and spatially non-uniform axial magnetic field is imposed on the computational mesh in a manner presented in the treatment below.

Figure 5 depicts the layout of the computational mesh used to model the combined radial diode and TTL of Figure 4. Due to its left-to-right symmetry, only the left-half of the device is modeled on the computer. Thus, the current values tabulated in Section IV for the numerical model must be multiplied by two to apply to the entire diode. In setting up the computational mesh primary attention was paid to ensuring needed spatial resolution of field and particle motions in all regions of interest. As presented in Section II, the electron gyroradius in the radial gap is approximately 0.41 cm. A minimum of four cells per gyroradius is desired so Δr is fixed at 0.1 cm. Considerations regarding the fast fourier transform technique employed in the Poisson solver allow increased generosity with the

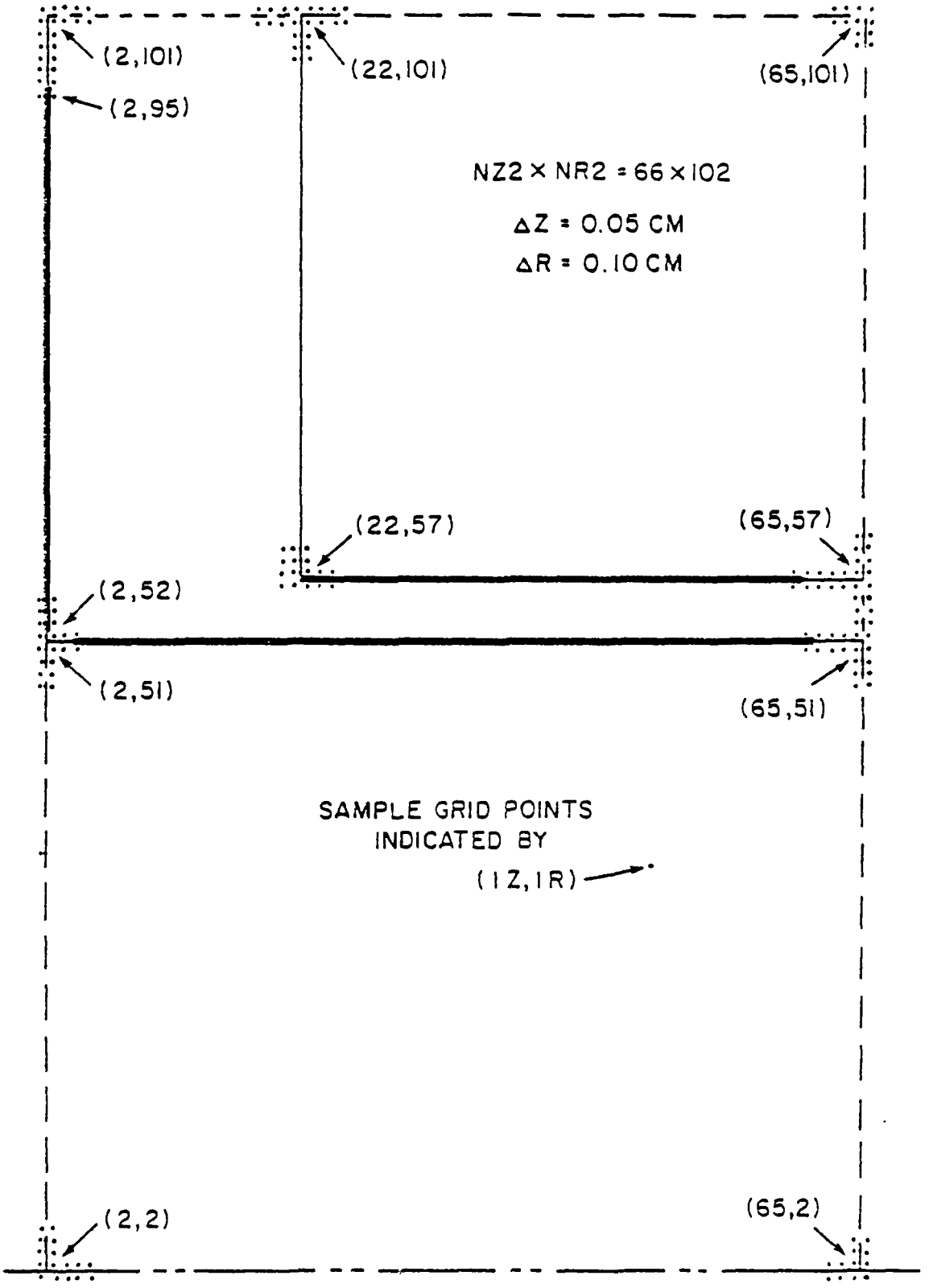

Fig. 5 — Layout of the numerical grid

number of axial gridpoints so that a Δz of 0.05 cm is chosen. For the specified diode dimensions this yields a computational mesh spanning 64 cells in z and 100 cells in r.

The temporal resolution employed in the simulation plays an equally significant role and, if misjudged, may lead to gross numerical instabilities. Once again, the electron gyromotion is a determining factor. Its frequency, f_G, is estimated to be approximately 5.6×10^{10} hertz and proper representation of electron motion demands that $f_G \cdot \Delta t << 1.0$. At the same time, it is desirable to follow the simulation through several ion anode-to-cathode crossing times in order to assure that a believable steady state has been reached. For the given voltage of 2 MV, about 1.2×10^{-9} second is consumed by an ion traversing the radial gap. In order to keep the cost of the simulation at a reasonable level, this crossing time should correspond to no more than 1000 timesteps. These upper and lower brackets suggest a timestep of $\Delta t = 2.0 \times 10^{-12}$ second. For this choice, $f_G \Delta t \simeq 0.11$ and the ion crossing time equals 600 timesteps.

Particles are injected into the diode gap using the space charge limited emission condition. (Just enough charge is emitted so that the component of the electric field normal to the emission surface vanishes.) In this simulation, electron emission is permitted up to a radius of 9.5 cm as well as all along the axial cathode surface to within 0.2 cm of the diode center plane. Emission was suppressed at the extrema of the computational mesh because of expected distortion of field values near the boundaries. In contrast ion emission is restricted to the inner axial anode surface except for the region with 0.2 cm of the diode center plane. Emitting sufaces are indicated by the heavy lines in Figure 5. Since only the left half of the

diode is being simulated complete symmetry demands that any particles impacting the right-hand computational boundary are perfectly reflected back into the simulation mesh.

The question of electric and magnetic boundary conditions is not trivial to handle properly. Since no particle emission is permitted closer than 0.5 cm (5 data cells) to the outer radial boundary of the TTL, there is no serious problem in assuming no change to the source-free, static potential solution there during the entire simulation. For that reason, the electrostatic potential, ϕ, rises linearly in z from o to ϕ_o across the 1 cm gap along that boundary (see Figure 4). (The magnetostatic boundary condition there is irrelevant since there is no B_z imposed in Region I.) The right boundary of Region II is more difficult. It clearly does not remain source-free during the simulation. Unfortunately, the capacitance matrix in the Poisson-solver must be recalculated every time the boundary values of the potentials change. This is a costly procedure. Rather than pay the price of matrix recalculation, it was decided to freeze the values of ϕ along that boundary as well at their source-free, logarithmically-spaced values (as in Figure 4). In addition, no self magnetic flux penetration across that diode centerplane is permitted. These conditions do some violence locally to the $\vec{E}$ and $\vec{B}$ field structure there but the gross dynamics of Region II should remain unaltered.

IV. RESULTS

To better understand the physics of the device, two distinct simulations were conducted. In the first, a benchmark for the radial diode operation was sought by permitting electron emission only on the cathode shank. This provided better estimates for the ideal magnetic insulation to be expected in the TTL region and it gave a reference figure for the maximum operating power

of the diode itself. The second simulation allowed electron emission all along the cathode surface in the TTL as well as along the shank. Sample particle position plots were generated to depict the nature of the electron flow there in conjunction with plots of the radial profile of electron current densities striking the anode surface in the TTL. Direct measurement was made of the electron current flowing in Region I to yield the percentage of total power which never reached the diode.

Case I, which simulated only the radial diode, was run over 1200 timesteps of 2.0×10^{-12} second each. The electron and ion currents of the half-diode being modeled are depicted in Figure 6. (Multiply by 2 to obtain full diode currents.) During the first 400 timesteps, only electron (no ions) were permitted in the system. The dots on the plot represent emitted electron current. The solid lines are the collected ion and electron currents as indicated. Note that the electron flow was completely insulated in the diode during electron-only operation. A steady electron current of about 75 kA continued to be emitted by the cathode shank but an equal electron current was continuously absorbed by the shank. This is characteristic of ideal magnetic insulation.[22,23] A constantly replenished cloud of electrons is formed adjacent to the cathode surface and extends some finite radial distance into the A-K gap. This is illustrated in the sample electron position plot of Figure 7. (Note again that only half of the diode is shown. The other half is completely symmetric about the center-plane.) No net current is flowing through the diode. Therefore, the TTL is completely uninsulated. Electrons in that region are free to migrate toward the anode limited only by the self-fields they may generate.

At $T = 400\ \Delta t$, ion emission was "turned on" all along the cylindrical anode surface. The resultant neutralization of electron space charge caused a

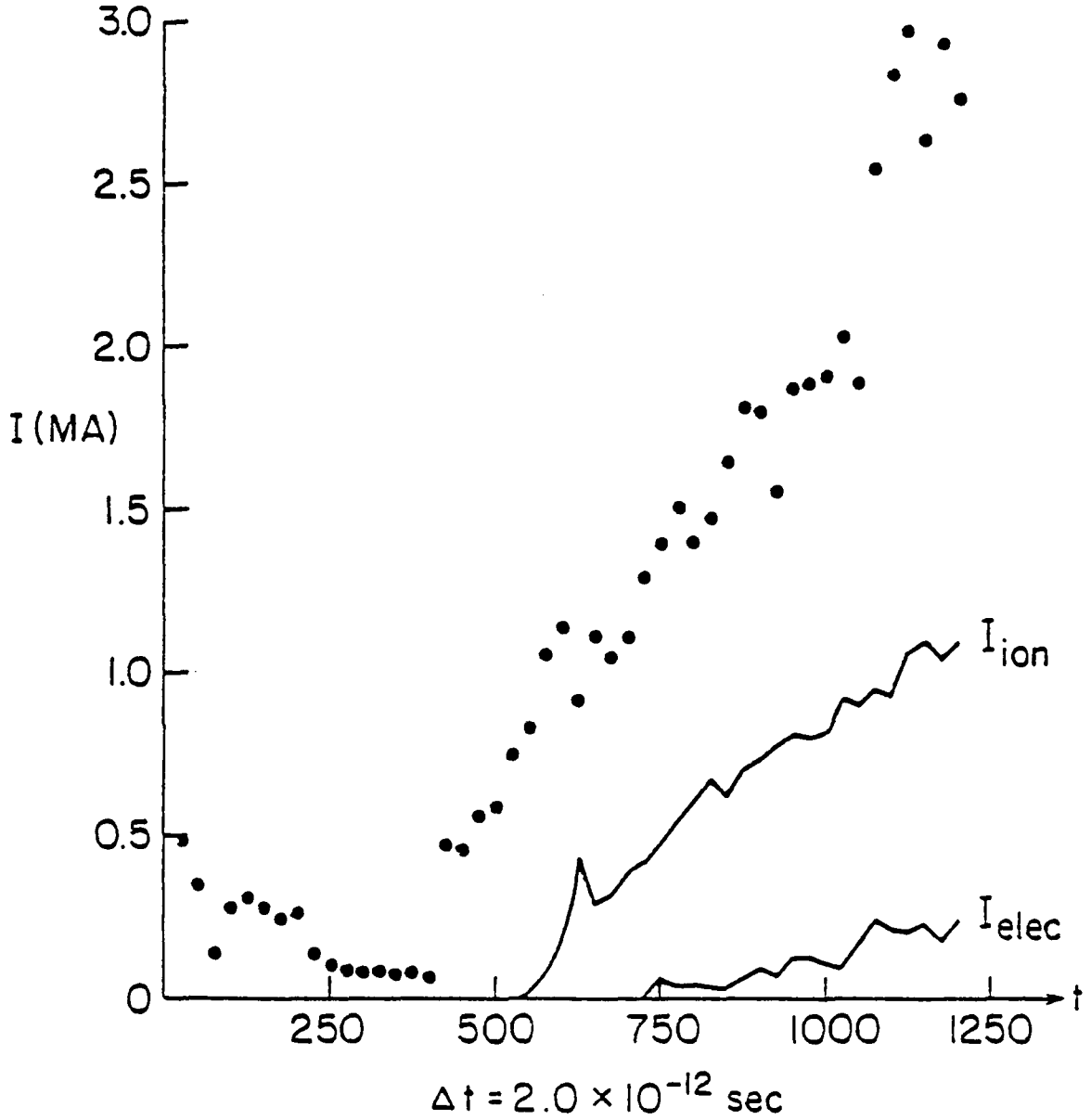

Fig. 6 — Electron and ion currents in the radial diode "Benchmark" case

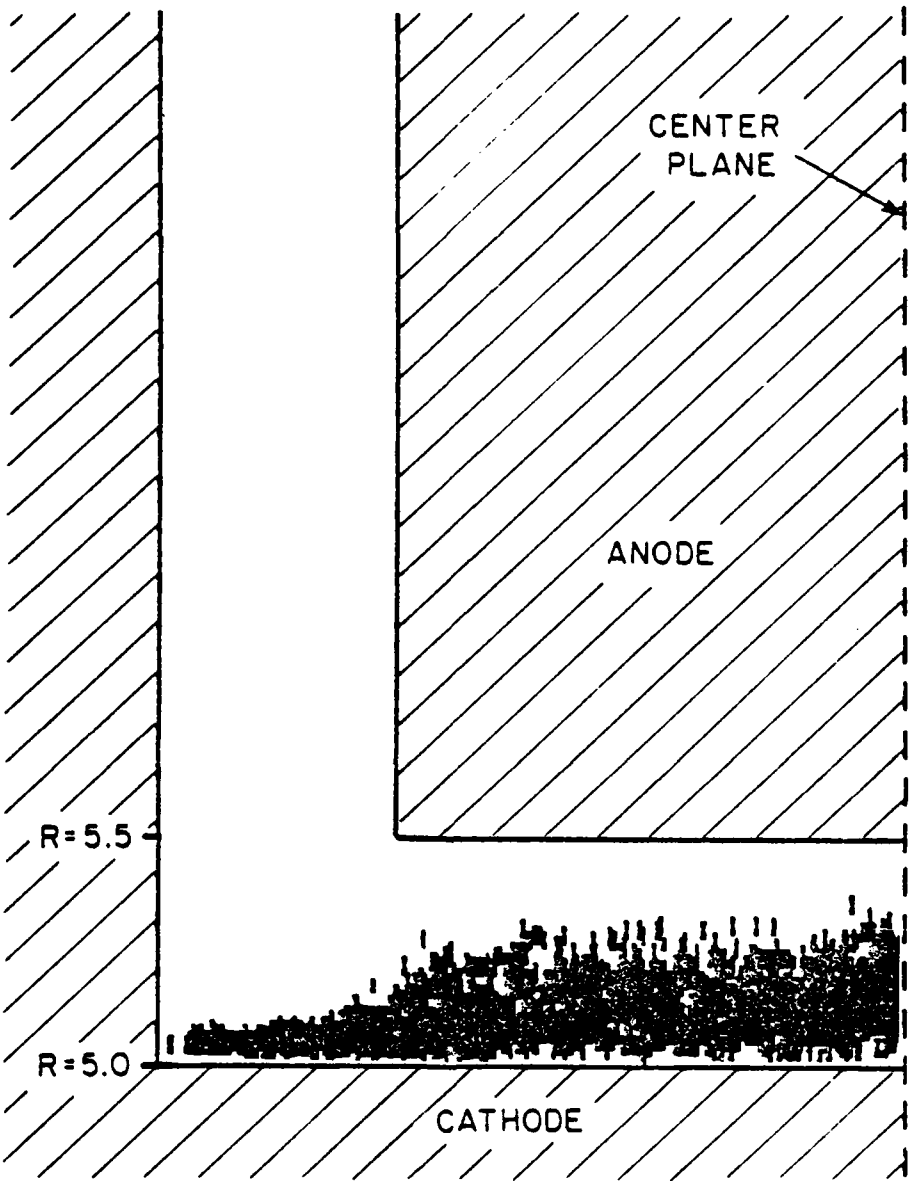

Fig. 7 — Sample electron positions with electrons-only flow in the "Benchmark" case

sharp increase of electron emission as seen in Figure 6. In the new equilibrium state formed by the two-specie flow, almost 3 MA was continuously emitted and reabsorbed by the cathode half-shank to maintain the enlarged negative space-charge cloud depicted in Figure 8. The densest portion of the cloud is now within one millimeter of the anode surface. This accounts for the steady-state ion half-current of about 1.1 MA, far above the simple Langmuir-Blodgett prediction of 100-150 kA. In contrast, the net electron half-current is a mere 250 kA compared to the nearly 2 MA L.-B. estimate. The net current flowing through one-half of the diode is thus about 1.35 MA. According to Eq. 4, this should provide magnetic insulation in the TTL out to a radius of about 33 cm if the imposed axial magnetic field were not present. However, B_z cannot be ignored. It is the key to ion-efficient operation of the radial diode.[24] In combination with the diamagnetic self-fields generated by charge circulation in the electron cloud, the imposed B_z forms an axial magnetic field in the A-K gap whose average radial profile is as shown in Figure 9. The net field gradient is mild in the electrons-only case but exceeds 140 kG/cm when full two-specie flow is present. The field strength peak of almost 70 kG near the anode surface in Region II acts as an effective barrier against electron penetration there. The details of the role this B-field plays in the A-K gap physics is discussed elsewhere.[25] Of primary importance here is the "spill-over" of this field into Region II, the lower end of the TTL.

In the model chosen for this simulation, the imposed 20 kG field is spacially uniform between R=5.0 and R=5.5 cm. It decays linearly to zero with increasing radius between R=5.0 and R=6.0 cm in the TTL. To that background field must be added the particle self-fields. Sample values of the net $B_z(r,z)$ are presented in Figure 10 for the cases with and without ions . Note

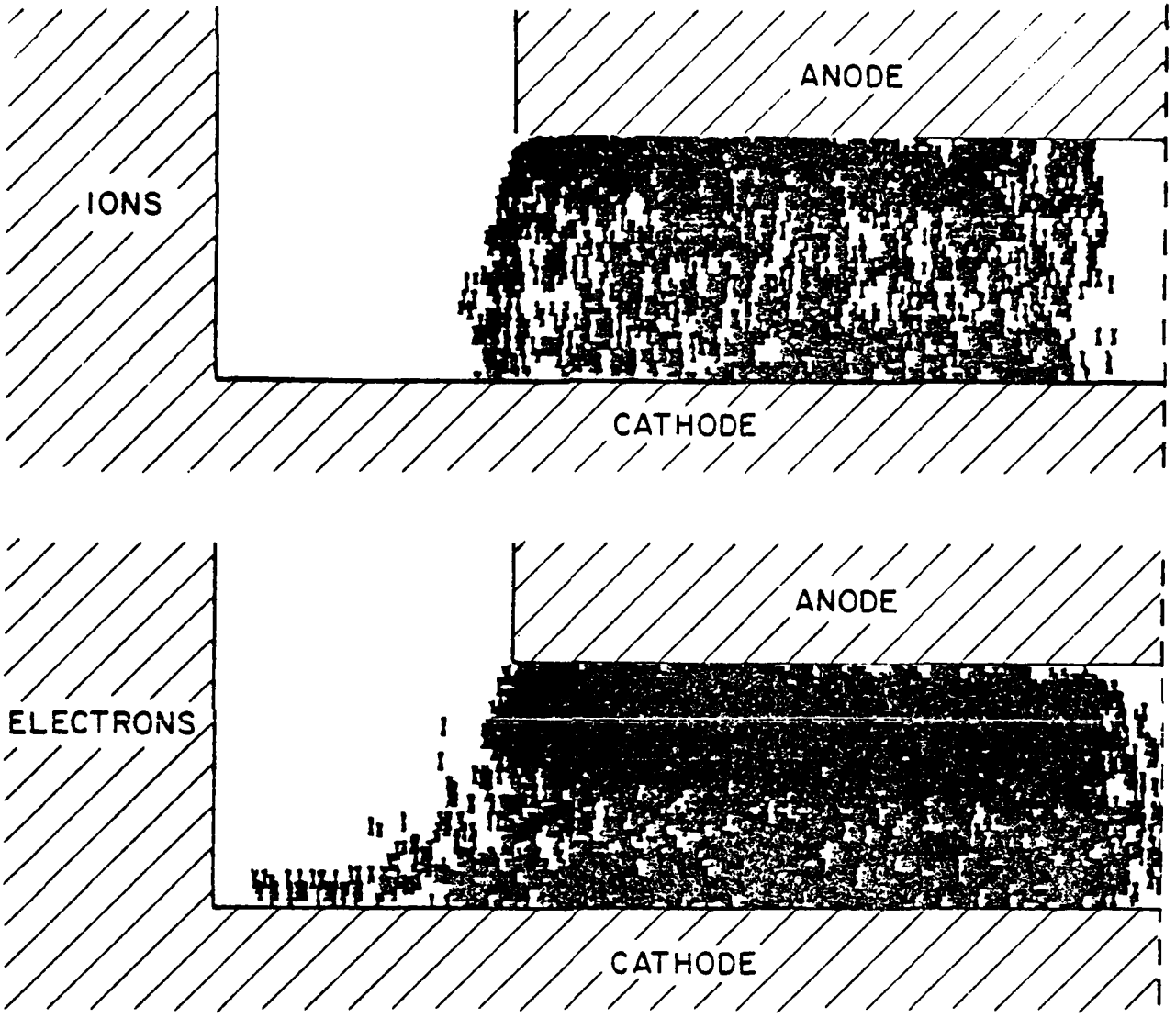

Fig. 8 — Sample ion and electron positions for the full, equilibrium "Benchmark" case

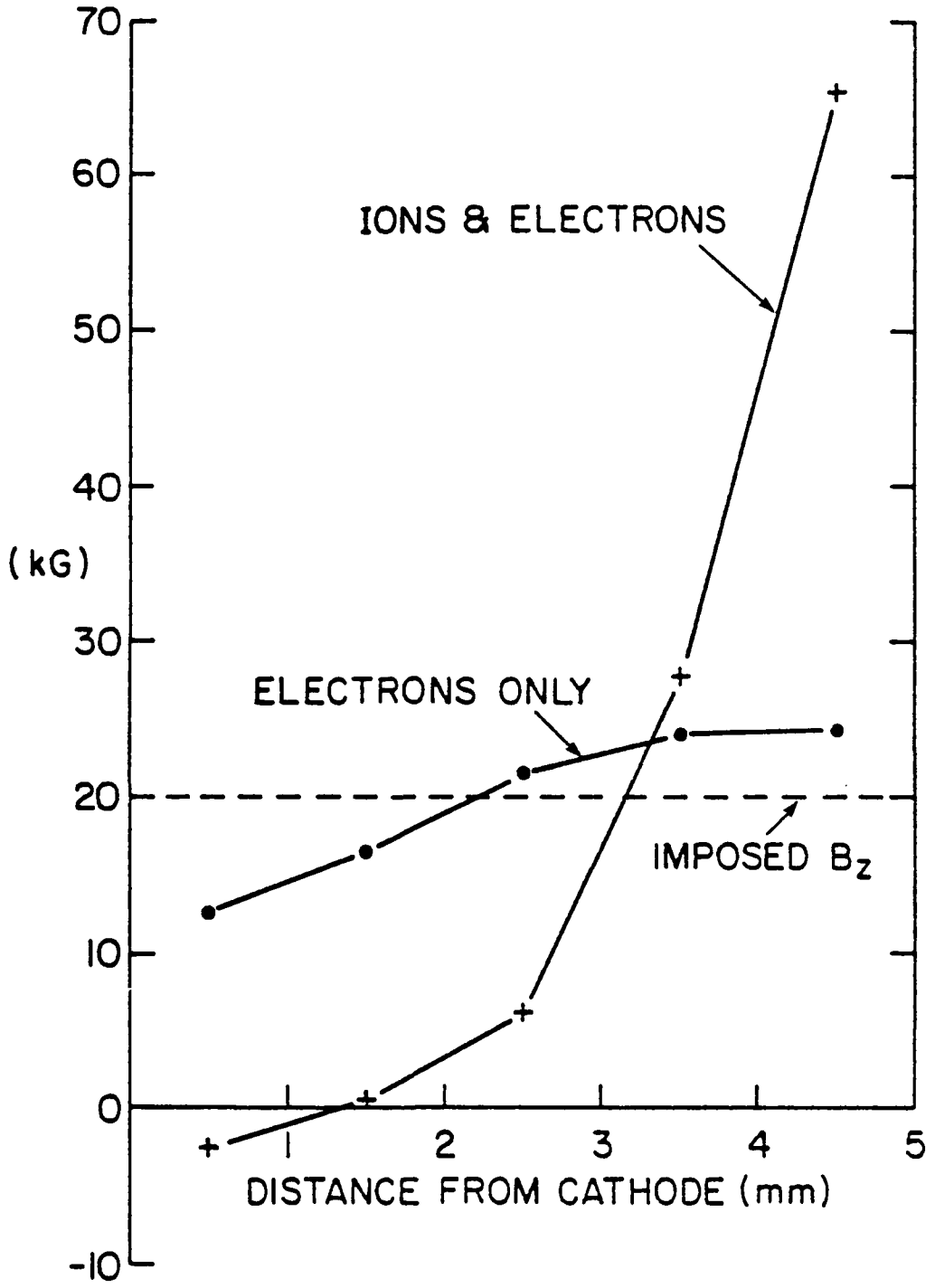

Fig. 9 — Radial profile of B_z in the A-K gap (averaged in the z = direction) for the "Benchmark" case

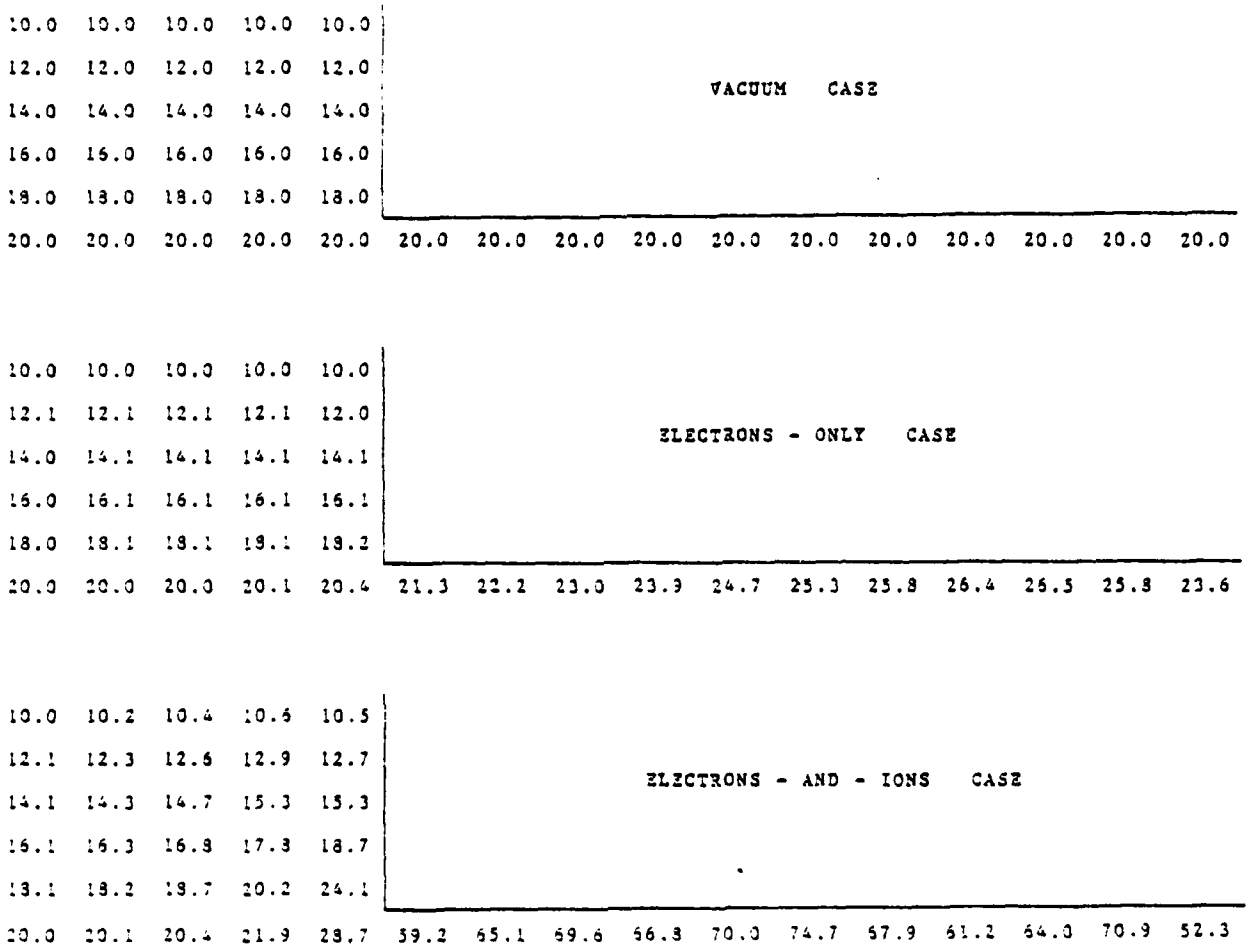

Fig. 10 — Sample values of B_z near the anode for the pure radial diode "Benchmark" case

that the Region II fields are hardly modified at all in the electrons-only steady state. The addition of ions into the system, as already pointed out, does make a significant difference. Particularly on the anode side of Region III, the values of B_z are elevated, resulting in a somewhat steeper magnetic gradient. The modification of the fields there, though significant, is quite small in comparison to the tripling of B_z inside Region II. Therefore, it is the imposed field gradient in the TTL that will be responsible for loss of insulation there. Over most of the axial distance, that gradient is little changed by current flows in the diode.

The second simulation run, Case II, tested the full combination of the radial diode and the TTL. Figure 11 provides the corresponding point plot of emitted electron current as well as traces of collected ion and electron currents. Once again, the numerical model was run for the first 400 timesteps without any ions present. The plot shows about 620 kA of electron current continuously emitted in the steady state with a full 450 kA of it being collected by the anode. This leaves about 170 kA of electrons to sustain any recirculating electron cloud in Region II or in the TTL (compared with 75 kA in Case I). The fate of the 450 kA net flow can be deduced from the sample electron position plot of Figure 12. Electrons appear to be bridging the TTL gap out to a radius of about 7.5 centimeters or more. The fact that electrons make it across at all is consistent with the previously determined lack of electron-only current flow across the radial diode gap. Any B_θ insulation in the TTL must therefore arise from the electron current bridging the gap there. A simple estimate may be obtained for the minimum insulation radius by equating the critical current of Eq. 4 with the net TTL current below a

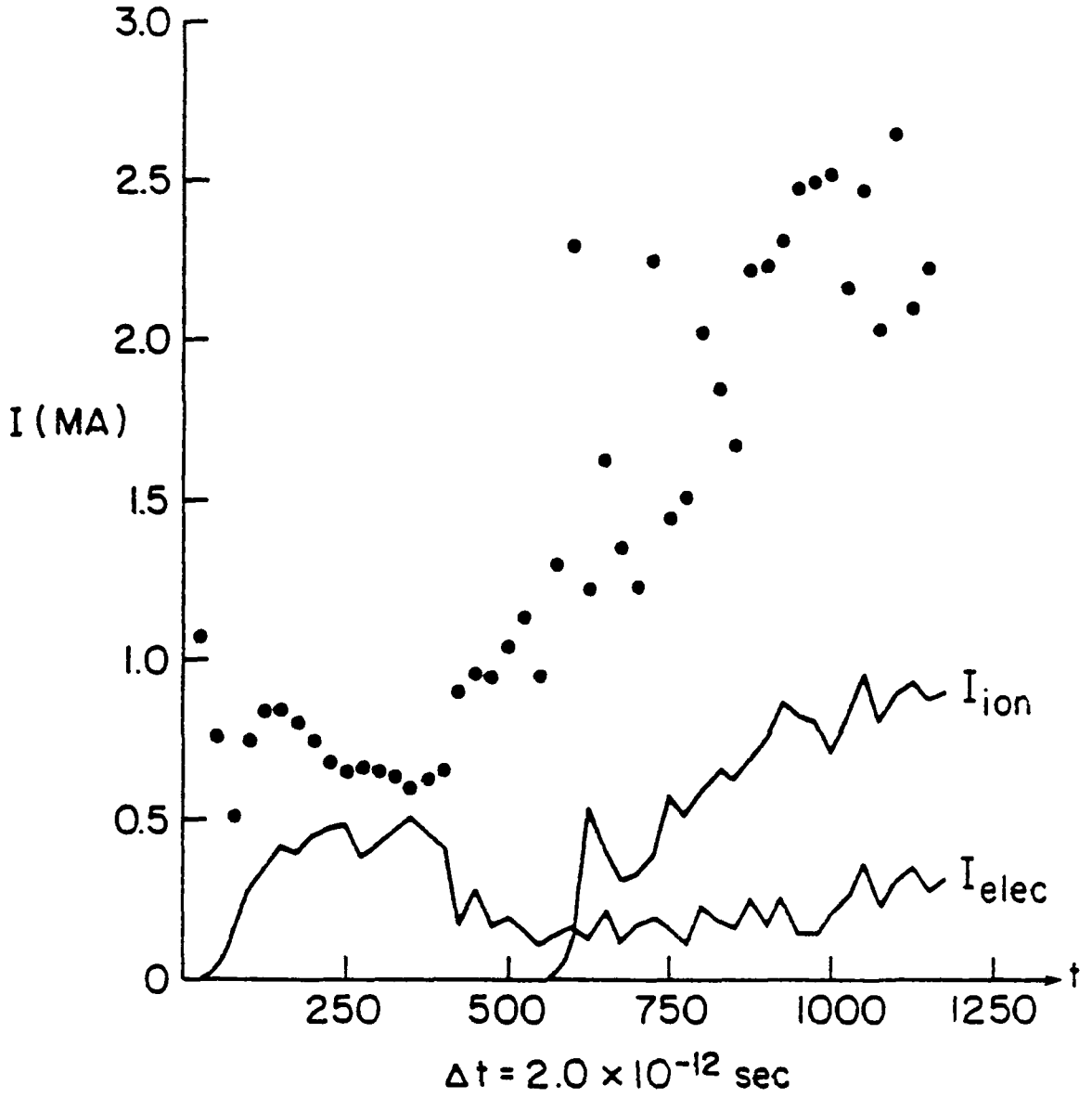

Fig. 11 — Electron and ion currents in the full radial diode-TTL case

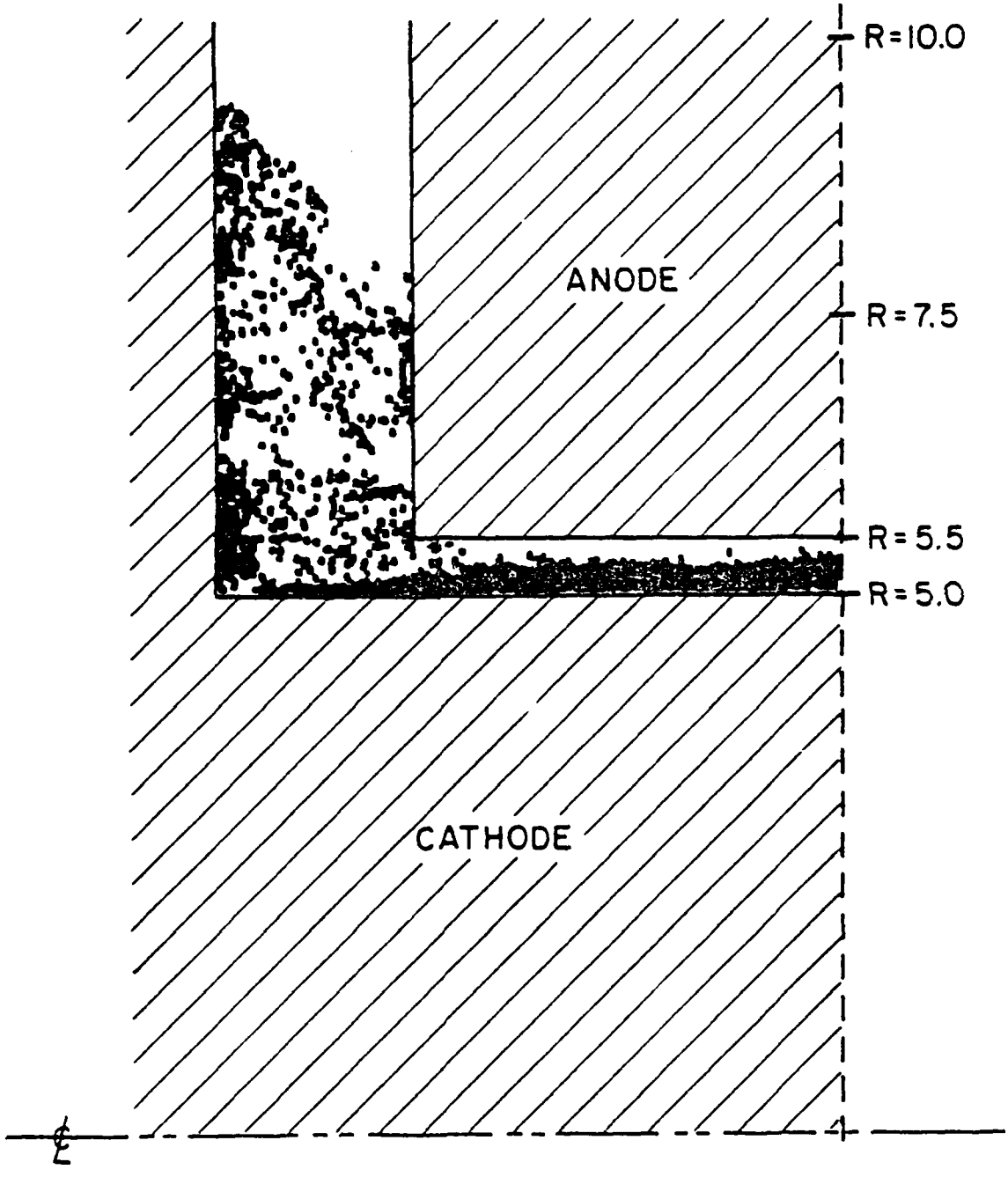

Fig. 12 — Sample electron positions with electrons-only flow in the diode-TTL case

radius, R, assuming a uniform J_e of 5.1 kA/cm^2 as determined from Eq. 2. This produces the expression:

$$\pi (r^2 - 5.5^2)\ 5.1\text{x}10^3 = 4.08\text{x}10^4\ R \qquad (6)$$

which yields a minimum radius of about 6.9 centimeters, in agreement with what is observed in the simulation. For a more complete picture of the electron flow pattern in the TTL, the emitted and collected electron current densities, J_e, were plotted in Figure 13. An integration of the collected current yields 425 kA, which accounts for essentially all of the net 450 kA of electron current flowing through the device. Furthermore, the primary peak of collected J_e lies below 6.5 cm in radius in agreement again with the theoretical estimate of 6.9 cm. It is also interesting to note the profile of the emitted j_e. As expected, the highest peak lies above R=9.0 cm where the electron emission region begins and the surface E-fields are highest due to two-dimensional distortions in the equipotential line there. At that high radius, however, the B_ϑ is more than adequate to prevent the emitted electrons from reaching the anode. They are bent around to strike the cathode again at around R=8.0 cm, causing a virtual shut-off of emission there due to a buildup of negative space-charge. The emission profile is much more steady below R=7.5 cm where B_ϑ is not strong enough to confine electron flow near the cathode.

As in the previous case which looked only at the radial diode, ion emission in Region II was "turned on" at T=400 Δt. The relaxation of the system to a new steady state can be traced in Figure 11. By T=1200 Δt , the ion half-current collected has settled to about 925 kA while that of the electrons is about 300 kA. Figure 14 depicts a sample set of electron and ion

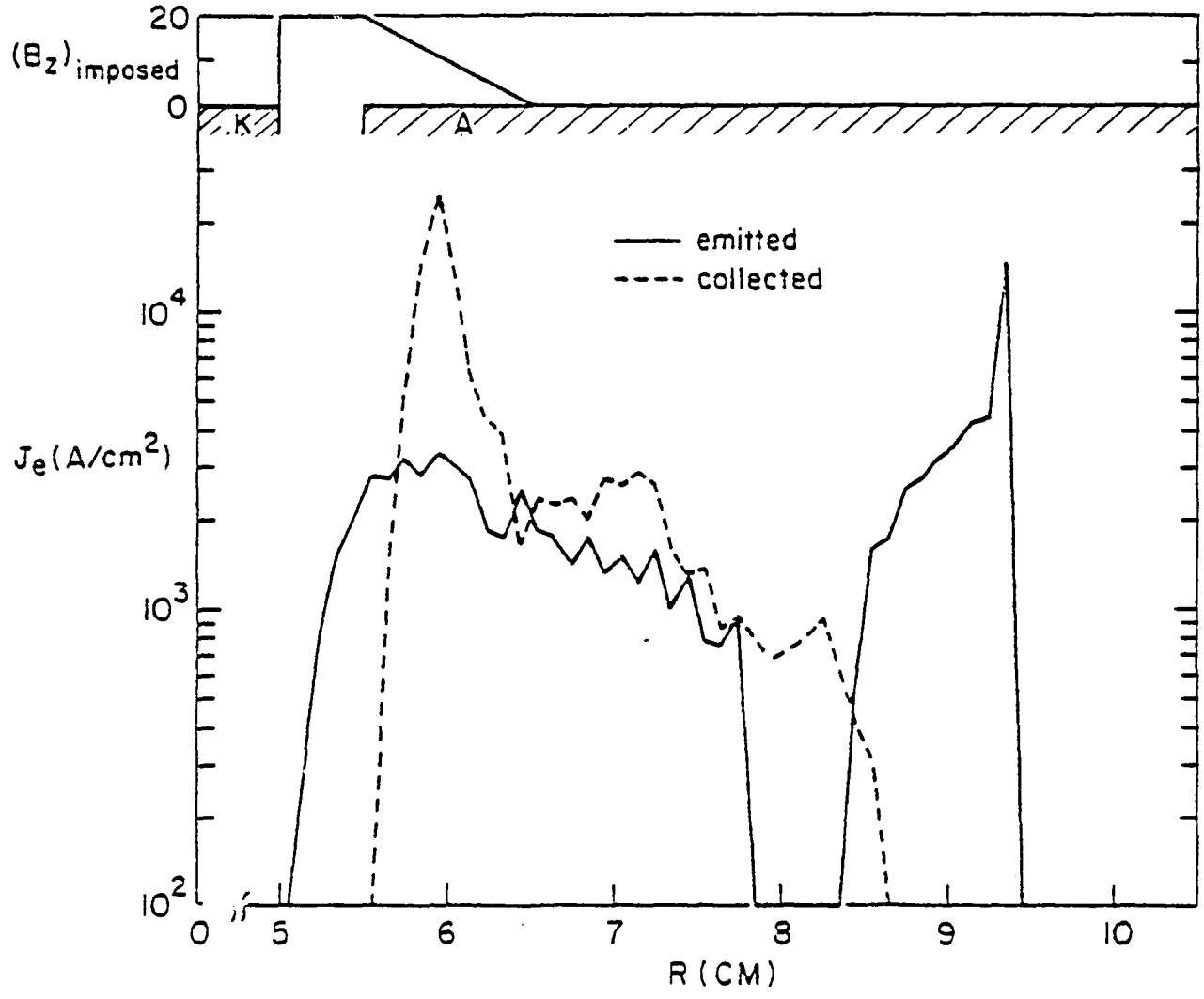

Fig. 13 — Radial profiles of emitted and collected electron current densities in the TTL for electrons-only flow

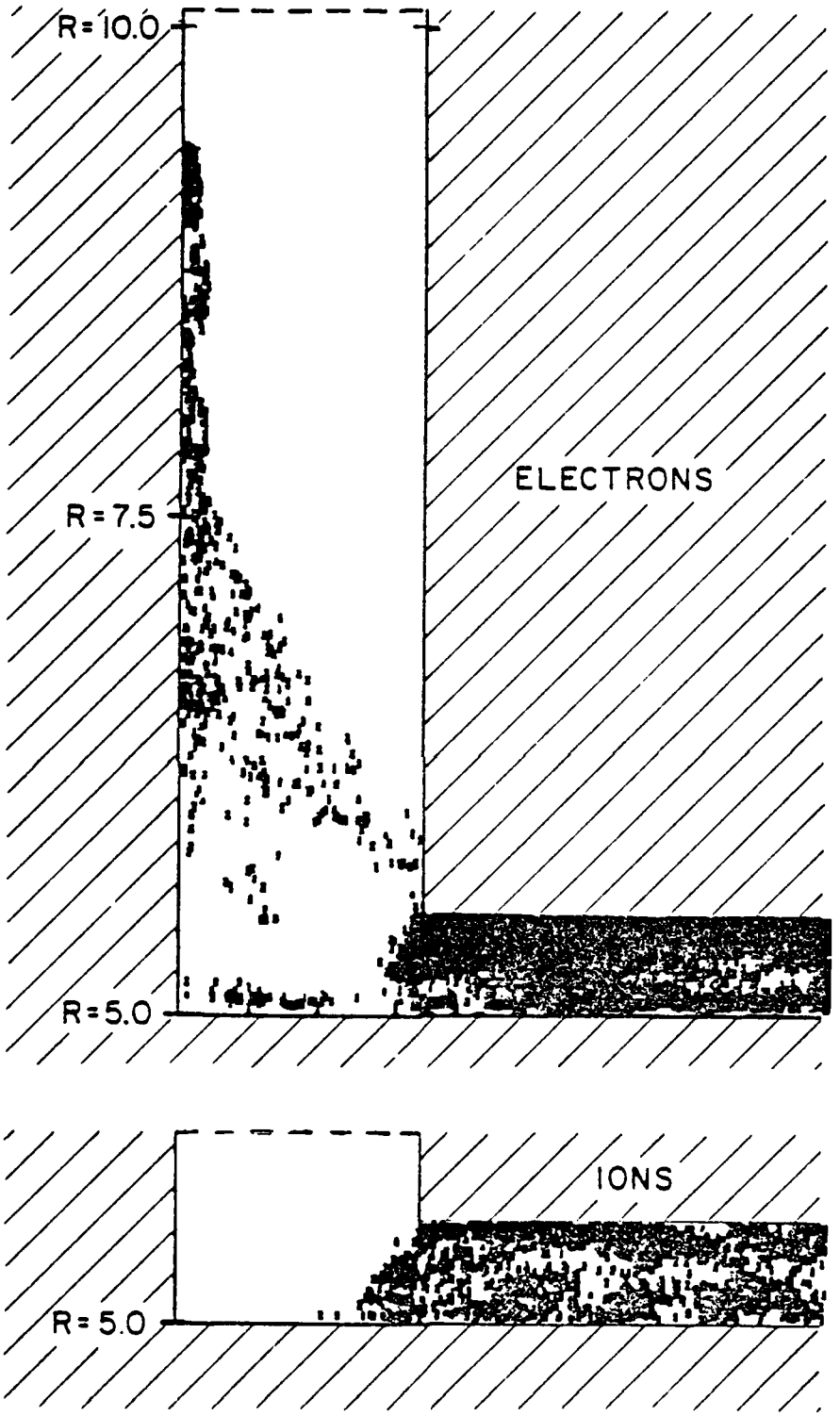

Fig. 14 — Sample ion and electron positions for the full, equilibrium diode-TTL case

positions at equilibrium. The electron plot is very different from that of Figure 12. As previously stated, an ion half-current of about 1.0 MA is more than adequate to insure magnetic insulation throughout the TTL in the absence of any B_z. Thus it is no surprise to see electrons there confined to a thin sheath near the cathode surface down to about 6.5 cm, where the applied axial B-field begins to rise in value from zero to a full 20 kG at R=5.5 cm. In that annular band between 5.5 and 6.5 cm, a very significant leakage of electron current to the anode occurs. This shorting should not manifest itself were it not for the applied B_z gradient there. To quantify the amount of power lost due to this leakage, the radial profiles of the electron current density emitted and collected in the TTL are plotted in Figure 15. The emission profile is quite irregular. Peaks and troughs alternate down the entire length. Enhanced emission at one point leads to negative charge buildup downstream in the electron sheath, causing reduced emission there. On the other hand, the collected J_e plot consists of a single, intense band below R=6.5 cm as could be guessed from the sample position plot of Figure 14. A total of about 205 kA of electron current is impacting there in the TTL. This corresponds to a full two-thirds of the net electron current flowing through the entire device. What is even more disturbing is that 0.41 terawatts out of a total of 2.45 TW flowing through the half-diode modeled are being lost in the TTL.

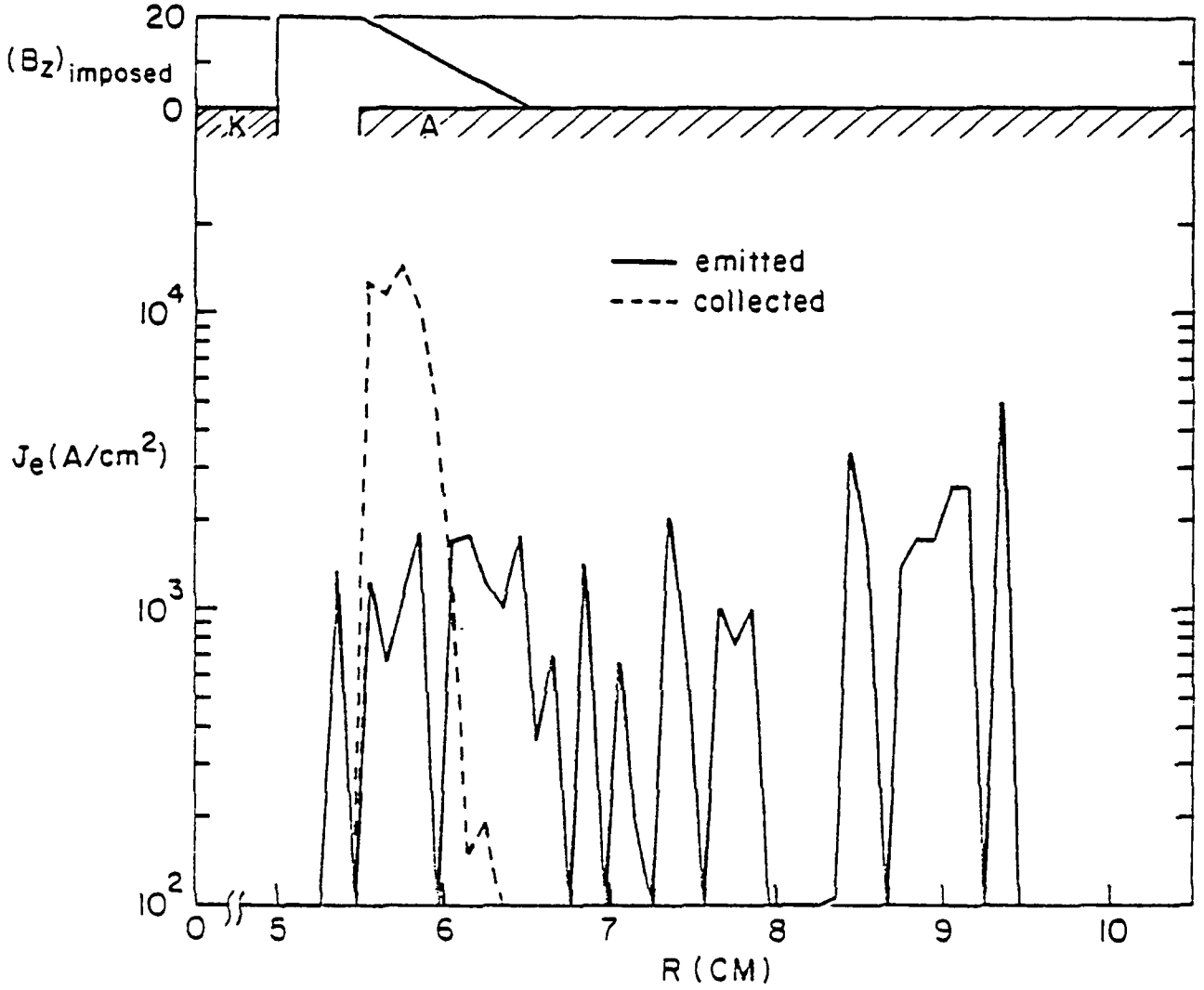

Fig. 15 — Radial profiles of emitted and collected electron current densities in the TTL for the full diode-TTL case

V. CONCLUSIONS

The major findings of this set of numerical simulations are summarized in Table 1. As stated in the introduction, the optimization of net ion production efficiency is a central objective of pulsed power diode research. The table shows a loss of almost 20% of the net input power in the TTL for the configuration modeled. The loss can be attributed to the steep gradient in B_z in the transition region between the TTL and the radial diode. The result is about an 8% drop in the total ion production efficiency of the TTL-diode combination. That can probably be tolerated for most practical applications. However, any experimental configuration different from that shown in Figure 3 will experience a different and possibly greater power loss in the TTL. One must clearly exercise care in setting the TTL gap and in shaping any imposed magnetic field profiles in the transition region.

Table 1 — Summary of results

	CASE I		CASE II	
ions present ?	no	yes	no	yes
$(I_e)_{emitted}$	0.15 MA	6.0 MA	1.24 MA	5.0 MA
$(I_e)_{collected\ in\ TTL}$	-	-	0.9 MA	0.4 MA
$(I_e)_{collected\ in\ diode}$	-	0.5 MA	0	0.2 MA
$(I_i)_{collected}$	-	2.2 MA	-	1.85 MA
$\eta_{i_D} = \left(\frac{I_i}{I_i + I_e}\right)_D$	-	0.815	-	0.902
$\eta_D = \frac{P_D}{P_D + P_{TTL}}$	1.0	1.0	0	0.833
$(\eta_i)_{net} = \eta_{i_D} \cdot \eta_D$	-	0.815	-	0.751

REFERENCES

1 S. J. Stephanakis, D. Mosher, S. A. Goldstein, et.al., Bull. Am. Phys. Soc. 22, 1130 (1977).

2 D. J. Johnson, G. W. Kuswa, A. V. Farnsworth, Jr., J. P. Quintenz, et.al., Phys. Rev. Lett. 42, 610 (1979).

3 P. Dreike, C. Eichenberger, S. Humphries, and R. Sudan, J. Appl. Phys. 47, 85 (1976).

4 S. J. Stephanakis, J. R. Boller, G. Cooperstein, S. A. Goldstein, et.al., Bull. Am. Phys. Soc. 23, 907 (1978).

5 S. A. Goldstein and R. E. Lee, Phys. Rev. Lett. 35, 1079 (1975).

6 J. W. Shearer, Lawrence Livermore Lab Report UCRL-52129 (1976).

7 P. F. Ottinger, S. A. Goldstein, and D. Mosher, NRL Memo Report No. 4548 (1981).

8 D. G. Colombant, S. A. Goldstein, and D. Mosher, Phys. Rev. Lett. 45, 1253 (1980).

9 S. J. Stephanakis, J. R. Boller, G. Cooperstein, et. al., Bull. Am. Phys. Soc. 24, 1031 (1979).

10 R. A. Meger, F. C. Young, A. T. Drobot, et. al., NRL Memo Report 4477 (1981).

11 R. J. Barker, S. A. Goldstein, and A. T. Drobot, NRL Memo Report No. 4642 (1981).

12 R. J. Barker and S. A. Goldstein, to appear as a NRL Memo Report (1982).

13 Particle Beam Fusion Progress Report April 1978 through December 1978, Sandia National Labs, SAND 79-1011 (1979).

14 D. B. Seidel and J. P. VanDevender in Particle Beam Fusion Progress Report June 1979 - December 1979, Sandia National Labs, SAND 80-0974 (1980).

15 I. Langmuir and K. T. Compton, Rev. of Modern Physics 3, 191 (1931).

16 F. Friedlander, R. Hechtel, H. Jory, et.al., Megavolt-Megampere Electron Gun Study, DASA 2173, Varian Associates, Palo Alto, CA (1968).

17 Robert K. Parker, Technical Report AFWL-TR-73-92, U. S. Air Force Weapons Laboratory, Albuquerque, NM (1973).

18 K. D. Bergeron, Phys. Fluids 20, 693 (1977).

19 R. J. Barker, A. T. Drobot, R. E. Lee, and S. A. Goldstein, Proc. 9th Conf. on Numerical Simulation of Plasmas, Evanston, IL (1980).

20 R. J. Barker, Banach Center Publication 3, 255; Warsaw, Poland (1975).

21 B. L. Buzbee, F. W. Dorr, and J. A. George, Technical Report CS-71-195, Computer Science Dept., Stanford University, Stanford, CA (1971).

22 R. N. Sudan and R. V. Lovelace, Phys. Rev. Lett. 31, 1174 (1973).

23 R. V. Lovelace and E. Ott, Phys. Fluids 17, 1263 (1974).

24 A. Ron, A. A. Mondelli, and N. Rostoker, IEEE Trans. Plasma Science, PS-1, 85 (1973).

25 R. J. Barker, S. A. Goldstein, and A. T. Drobot, IEEE Int. Conf. on Plasma Science, Madison, WI (1980).

EFFECTS OF PARTIAL SUPPRESSION OF ION EMISSION IN MODERATE IMPEDANCE DIODES

I. INTRODUCTION

The efficient generation of intense beams of energetic light ions is a central objective of the NRL Light Ion Fusion Research Program.[1] Over the past several years, focused ion current densities of over 100 kA/cm^2 from terrawatt-level beams have been achieved with magnetically insulated radial diodes at Sandia National Laboratories[2] as well as with pinch-reflex axial diodes at the Naval Research Laboratory.[3] Using diodes of below 2 ohm impedance, ion beam efficiencies of over 70% were achieved in both of the above configurations[4,5] (i.e., over 70% of the power coupled to the diodes was carried by the light ions generated therein). The question of ion efficiency is critical to the goal of a practical light ion driven inertial confinement fusion (ICF) reactor. As much as possible of a given pulsed power generator's energy must be imparted to the ion beam exiting the diode in order to minimize the number of beam sources necessary for successful pellet ignition as well as to maximize the overall reactor efficiency. These efficiency considerations are well met by the low impedance diodes.

Unfortunately, the high current densities of the ion beams produced by low impedance diodes are not compatible with the focusing and transport systems presently under study for bringing the beams to bear on the proposed fusion targets.[6] In addition, there are strong arguments in favor of high voltage, the use of high impedance generators in present reactor scenarios.[7] Diodes matched to such generators must likewise be of high impedance to ensure efficient power transmission but such diodes are plagued by relatively low ion production efficiencies. These low efficiencies are a direct consequence of established diode theory. It has been found semiempirically[8] that the total current flowing through a pinched-beam diode may be approximated by

$$I = I_e + I_i \approx 9(\gamma^2 - 1)^{1/2}\frac{R}{D}\left[1 + \left[\frac{eV}{2m_ic^2}\right]^{1/2}\frac{R}{D}\right] \tag{1}$$

where $\gamma = 1 + \dfrac{V(\text{in } MV)}{0.511}$, R = cathode radius, D = axial anode-cathode (A-K) gap, V = diode voltage, and m_i = ion (proton) mass. Implicit in this formula is an ion-to-electron current ratio given by

$$\frac{I_i}{I_e} \geqslant 0.5\frac{v_i}{c}\frac{R}{D} \tag{2}$$

where v_i is the mean ion velocity.[9] Thus, for a fixed voltage, increasing the diode impedance translates to decreasing the aspect ratio, R/D. That, in turn, results in a decrease of the current ratio I_i/I_e and a lowering of the ion production efficiency, $I_i/(I_e + I_i)$. This is the crux of the problem addressed by this report. The essence of the proposed solution is an attempt to decouple the impedance from its R/D dependence while exploiting the theorized efficiency enhancement gained through a decreased gap size, D.

For fixed values of R, D, and voltage, the net diode current can be changed from that predicted in Eq. (1) by restricting the emission of electrons from the cathode and ions from the anode respectively.

Manuscript submitted July 23, 1982.

As a starting point, take the standard pinch-reflex diode (PRD) geometry shown in Figure 1. Typical electron and ion trajectories are as sketched. The predominant flow of electrons originates from the cathode shank tip. Electrons emitted there stream to the thin, polyethylene anode foil (pinching radially as they cross the $A-K$ gap if the critical diode current is exceeded[10]). They then pass through the foil with an appropriate loss of energy. Finally they are reflected back through the foil by the large azimuthal magnetic field, B_θ, which is present between the foil and the solid anode surface. This reflection (or "reflexing") process continues as the electrons cascade toward the diode's central axis where they are funneled off through the anode stalk. The hydrocarbon anode plasma formed along the foil meanwhile acts as a rich source of protons which are accelerated in the opposite direction toward the cathode. Proton emission can be expected everywhere the anode plasma has formed including regions along the foil at larger radii than the outer radius of the cathod shank. Ions emitted at radii above the inner radius of the cathode shank are useless for light ion research for two major reasons. First of all, their trajectories differ so little from straight lines that, assuming a planar anode foil, they will probably all hit and be absorbed by the solid cathode shank and thus be unavailable for extraction from the diode. Secondly, their presence near the cathode tip will further increase the emission of electron current with presumably detrimental results to the overall ion production efficiency.

These considerations lead one to conclude that significant benefit could be derived by suppressing the emission of ions from those outer regions of the anode foil face. This is accomplished experimentally by covering the plastic anode foil beyond the inner cathode radius with a thin metal foil (on Gamble II, first tantalum then aluminum was used[11]). This concept has been tested at NRL with very favorable results[12] which will be discussed later. The numerical simulations reported herein modeled the steady-state operation of those experimental diodes. The empirical data showed that suppression of the peripheral ion emission both decoupled the diode impedance from R/D (thus allowing a smaller D for a given impedance) and also significantly enhanced the ion efficiency in comparison to a diode with the same impedance but with larger D and full anode ion emission. The computer runs confirmed the impedance decoupling from R/D but failed to detect any significant ion efficiency enhancement. However, the numerically observed ion efficiency of the diode with ion suppression and small D does agree with the experimental results. Furthermore, the simulation suggests a possible physical mechanism whereby the true magnitude of the net ion current could have been partially masked in the "benchmark" (i.e., full anode ion emission) experiments by a comoving electron current.

II. THE DIODE AND ITS NUMERICAL MODEL

The actual Gamble II experimental diode configuration is drawn in Figure 2. For the discussions presented later in this report, it is particularly important to note the structure of the inner cathode assembly. The "target" is a sheet of KIMFOL stretched over an inner cylindrical cathode shank of radius 2.25 cm. Only the ions flowing within that radius can be extracted from the diode and counted in the experimental $(I_{NET})_{ion}$ measurements. For ease of numerical modeling, the actual diode of Figure 2 was simplified slightly to the form depicted in Figure 3. The anode foil radius was shortened from about 6.0 cm to 3.7 cm. Since that is still almost a centimeter larger than the cathode outer radius the electric field structure along the electron-emitting cathode shank and along the anode's ion-emitting regions opposite the cathode shank should not be significantly modified. In addition, the axially bounding, solid cathode and anode surfaces are taken as completely planar and parallel. The front surface of the cathode "door" (see Figure 2) coplanar with the "target" face. Finally, the thickness of the cathode shank is taken as 0.35 cm while in the experiments it was usually 0.25 cm. The extra millimeter allows for somewhat better numerical resolution over the all-important tip of the shank where most of the net electron current is emitted. Having fixed the essential geometry, it is a straightforward process to implement the numerical model.

NRL's DIODE2D computer code was employed to numerically simulate the steady-state operating conditions for this diode for various sets of parameters. The details of the code may be found elsewhere.[13] It is sufficient here to point out that DIODE2D calculates equilibrium electric and magnetic field strengths over an $NZ \times NR$ mesh of discrete data points on a predetermined computational region

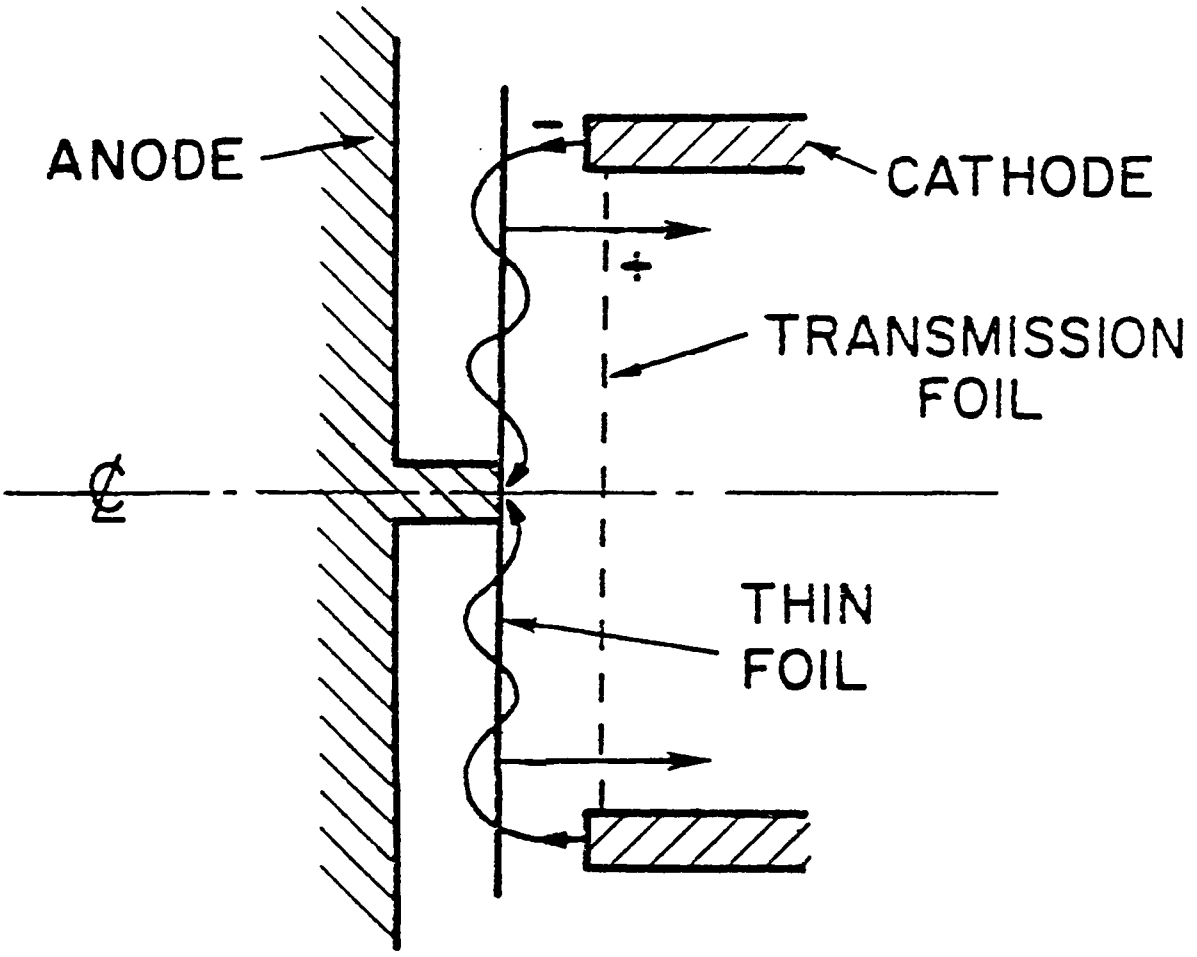

Fig. 1 — The pinch-reflex diode

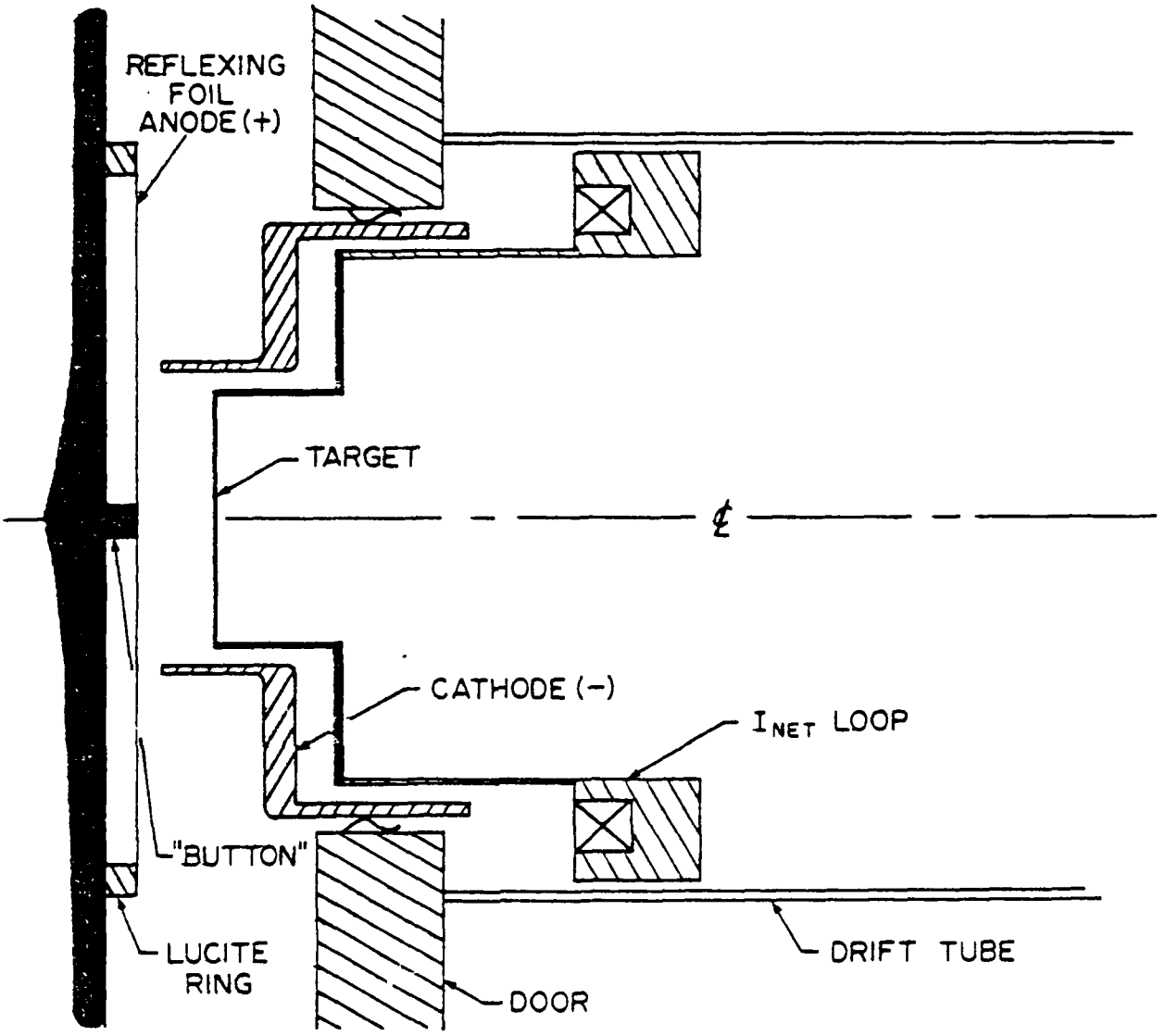

Fig. 2 — The high impedance Gamble II test diode for PBFA-I
(courtesy of S. J. Stephanakis)

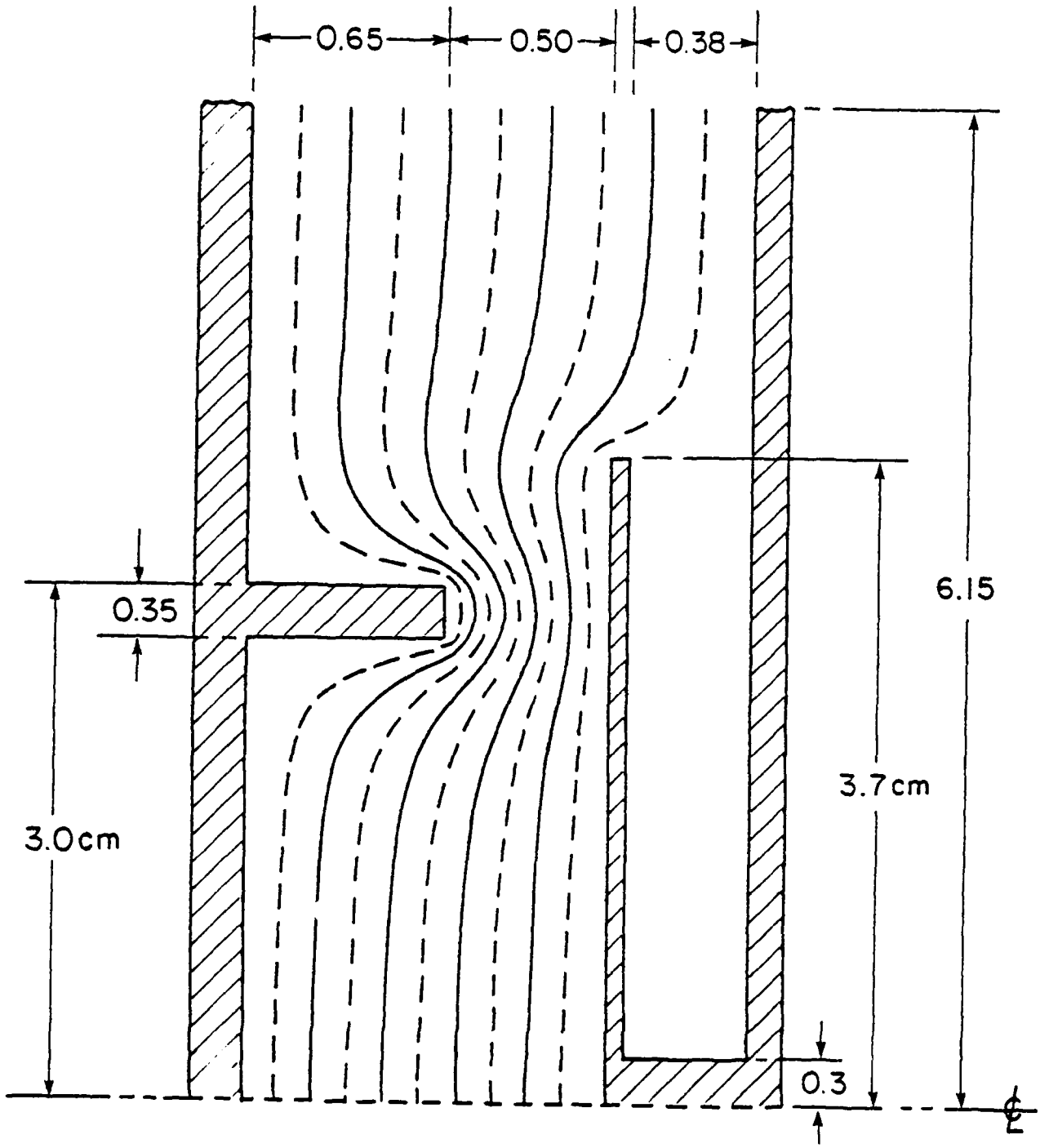

Fig. 3 — Specific geometry of the diode as modeled and its electrostatic equipotential contours with no space charge present

corresponding to an arbitrary $R - Z$ planar cross-section passing through the diode's centerline. Complete azimuthal symmetry is assumed. A finite number of macroelectrons and macroprotons having correct, physical charge-to-mass ratios are advanced timestep-by-timestep across the mesh in a relativistically covariant manner. A self-consistent, steady-state solution is sought both for field structures as well as for particle flows. No time-dependent phenomena are actually treated.

The physical volume simulated by the DIODE2D code extends radially outward from the central axis to a distance of 6.15 cm in the vacuum gap and axially forward from the plane corresponding to the solid cathode face out to the opposing plane surface of the solid anode. Since it presumes azimuthal symmetry, the computer code only deals with a single $R - Z$ planar cross-section extending out from the centerline. This computational region is presented in Figure 4. The grid points are shown as dots and correspond to the centers of their respective rectangular data cells. Counting the monolayer of guard cells which completely surround the numerical region in which "particles" are "allowed," a total of $(NZ + 2) \times (NR + 2) = 66 \times 125 = 8,250$ data cells are used. The bottom boundary corresponds to the central axis ($R = 0$) of the diode. The right boundary corresponds to the solid anode plane and is maintained at the full anode potential, V. The left boundary is kept at zero voltage since it represents the solid cathode plane. Finally, the upper boundary is simply a source-free, vacuum interface between what may be loosely described as the "diode region" and the pulsed power transmission line. The electrostatic potential is therefore graded linearly from zero to V along that upper boundary. Perfectly conducting cathode and anode surfaces are included in the computational region as shown in Figure 4. Those surfaces are treated numerically via a capacitance matrix technique described elsewhere.[14] On the order of 10^4 macroelectrons and 10^4 macroprotons participate in the simulation at steady state. These macroparticles are emitted at their respective electrodes along the heavy-lined surfaces. Axial currents in the cathode shank and in the anode stalk are treated rigorously as a function of z in order to ensure an accurate distribution of B_θ throughout the diode. The results of these numerical simulations as well as a summary of the conclusions which can be drawn from them are presented in the following two sections.

III. SIMULATION RESULTS

In order to test the theorized effects of selective ion emission suppression on the performance characteristics of the diode of Figure 2, three specific test cases were simulated. In all three cases, the diode voltage was fixed at 1.8 MV in accordance with the capabilities of the Gamble II machine. Cases I and II were both run with an A-K (anode-cathode) gap of 5 mm just as shown in Figure 3. Case I corresponded to a "benchmark" run in which no suppression of ion emission on the anode foil was attempted. Protons were emitted along the anode mesh from cells $(IZ,IR) = (48, 2)$ through $(48, 65)$ just as indicated by the heavy line in Figure 4. In Case II, the imposition of a metal foil annulus over the outer anode face was simulated by shutting off ion emission beyond cell $(48, 49)$. Finally, for Case III, the restricted ion emission was retained while all axial dimensions in the simulation were reduced by a factor of 0.70. This changed the A-K gap to 3.5 mm and reduced the diode impedance back to its value in Case I. The detailed results of these simulations are as follows.

Case I was run 4400 timesteps, Δt, of 1.5×10^{-12} seconds each until an equilibrium state was reached. In order to determine the true steady-state values of the quantities of interest a new statistical technique was applied to the numerical data. Specie current values were tabulated at intervals of $25\Delta t$ over the last 200 steps. These values were then subjected to the same type of least squares error analysis and data reduction methods as is normally reserved for the treatment of experimental observations. The details of this new computational approach are presented in the Appendix. The equilibrium ion and electron currents for this "benchmark" case were 230 ± 6 kA and 147 ± 6 kA respectively. Given the diode voltage of 1.8 MV, this yields an impedance of 4.77 ± 0.11 ohms for the device, well within the desired operating regime of 4-5 Ω. The net ion efficiency, $\eta_i \equiv I_{ion}/I_{diode} = I_{ion}/(I_{ion} + I_{electron})$, is then 0.390 ± 0.016. This is in excellent agreement with the 40% ion efficiency recently reported[15] for a numerical simulation of a 2.0 MV, 4 ohm PRD (pinch-reflex diode) having an R/D of 7.58 compared with an R/D of 6.0 for this run. It differs significantly, however from the 0.24

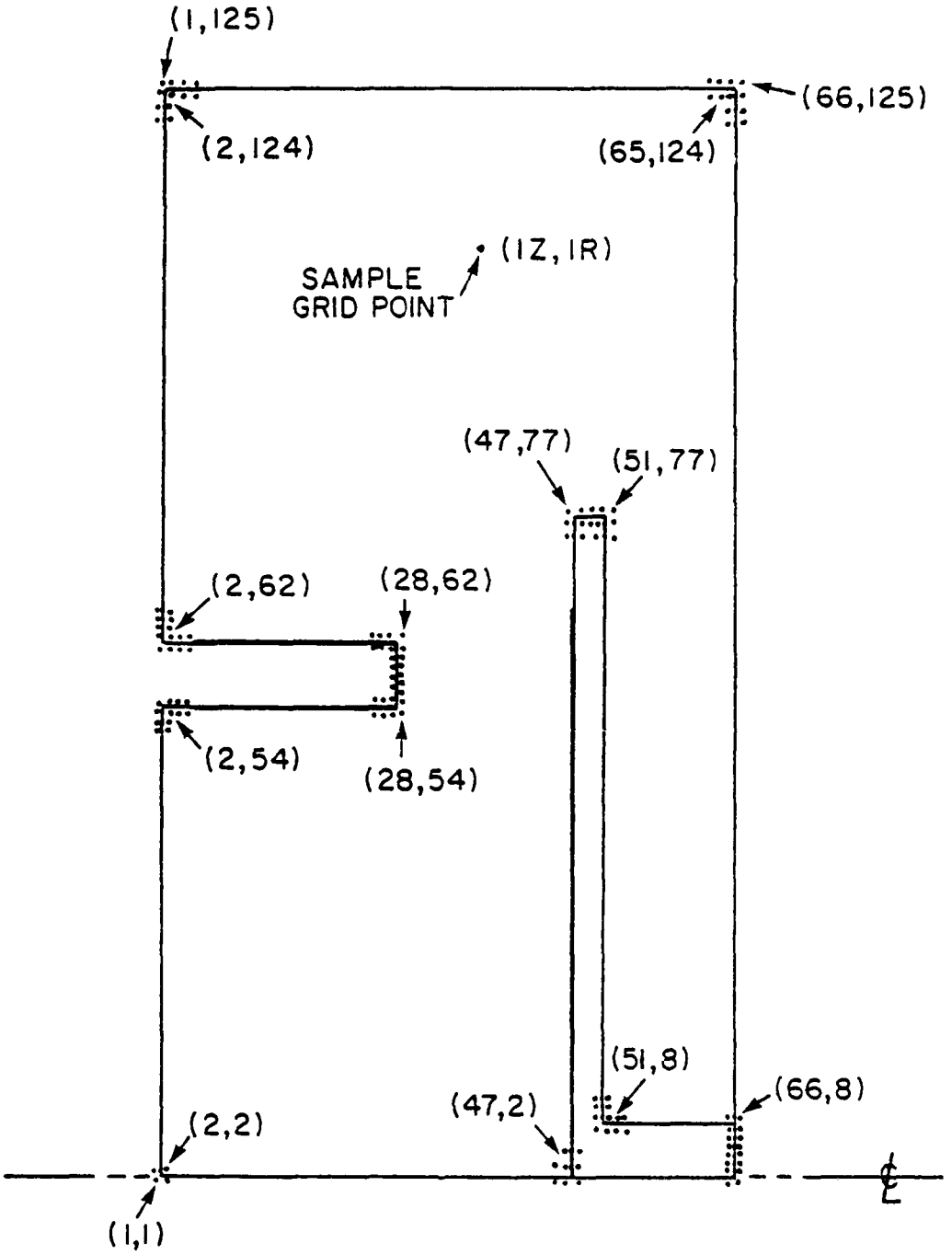

Fig. 4 — Set-up of the numerical simulation region

AD-A129 821 DIODE DYNAMICS BEAM GENERATION AND TRANSPORT AND PLASMA EROSION OPENING SWITCH DEVELOPMENT(U) JAYCOR ALEXANDRIA VA P F OTTINGER 17 MAY 83 JAYCOR-J207-83-C-001 4/8

UNCLASSIFIED N00173-80-C-0202 F/G 9/1 NL

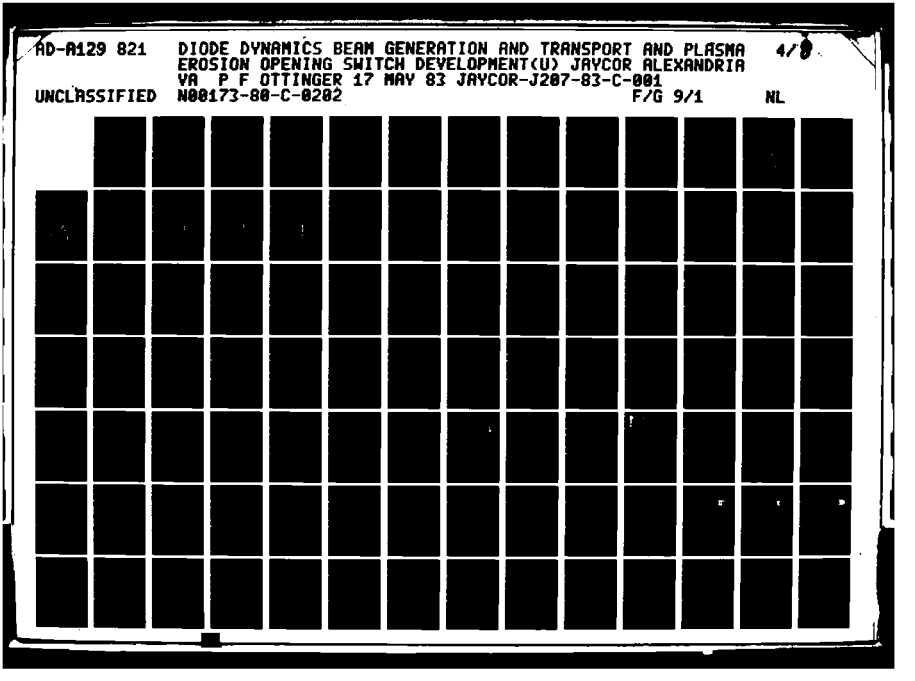

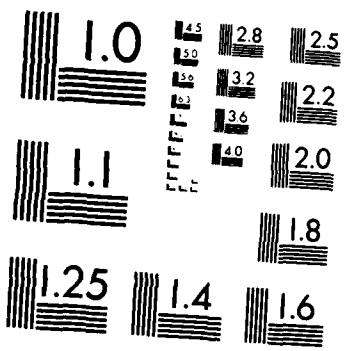

average ion efficiency reported from a series of Gamble II experimental runs[16] (see Figure 5). At least part of this discrepancy between the numerical and experimental results can be explained by examining Figure 2. The location of the I_{NET} Rogowski coil loop in the experimental set-up shows that it is measuring only that portion of the ion current which hits the "target" inside the cathode shank. Any ions hitting the cathode beyond a radius of 2.25 cm are not counted. To properly compare the numerical results to the experiment, this "effective" ion current must be calculated. Figures 6 and 7 present radial profiles of the emitted and collected ion current densities flowing in the steady state diode. Integrated from these profiles are not only the total ion currents but also the effective currents falling within $R = 2.25$ cm (indicated by the dotted lines). This shows that the empirically measured number should be 119 kA, not 147 kA. This still implies an ion efficiency of 0.316. Although much closer to the experimental data, it is still far from "good" agreement. A more complete explanation for the poor correlation can be found by examining the nature of the electron currents in the diode. That new phenomenon will be discussed after the numerical results for Cases II and III are presented.

Having completed the benchmark run, the next step was to test the effect of restricted ion emission while holding all other diode parameters constant. The maximum radius for ion emission along the anode foil was reduced from $R = 3.2$ cm to $R = 2.4$ cm. Just as for Case I, Case II was run to equilibrium at $t = 4400$ timesteps. At that point, using the same statistical data reduction technique, the currents were found to be $I_e = 186 \pm 3$ kA and $I_i = 83 \pm 2$ kA. These figures imply a diode impedance of 6.69 ± 0.08 ohms and a net ion efficiency of 0.309 ± 0.007. As expected, the impedance has been very significantly raised in spite of the constant A-K gap size, $D = 5$ mm. Once again, to correlate the ion efficiency to the experimental results, the radial profiles of the emitted and collected ion current densities are presented in Figures 8 and 9. An effective I_i of 79 kA is then observed to strike within the "target" radius of 2.25 cm. Interestingly enough, the effective ion efficiency has dropped a mere two percentage points to $(\eta_i)_{eff} = 0.294$ in spite of the 2 ohm impedance rise.

Finally, for Case III the restricted ion emission radius of 2.4 cm was retained while the gap was reduced from 5.0 to 3.5 mm. The observed steady-state diode currents were $I_e = 247 \pm 3$ kA and $I_i = 130 \pm 4$ kA yielding an impedance of 4.77 ± 0.07 ohms and a total ion efficiency of 0.345 ± 0.012. Thus, as expected, the impedance of Case I has been restored in spite of the decreased gap size, D. Although it had been hoped that the ion efficiency would increase, a drop of almost 0.05 was instead recorded. Hopes that a comparison of the effective ion currents would be more optimistic were likewise disappointed. Figures 10 and 11 record the corresponding Case III ion emission and collection profiles. They show that the effective ion current is 119 kA — *exactly* the same as for Case I. Thus the simulations of Case I and Case III share identical impedances *and* identical efficiencies. This is in sharp contrast with the experimental data. The same diode as modeled in Case III fired 28 separate times on Gamble II yielded the modified efficiency data shown in Figure 12 (overlapped with the Case I data). With an average effective ion efficiency of 0.34, it represents a clear departure from the experimental data garnered from the diode without emission restriction and with $D = 5.0$ mm although the average impedances was nearly identical for the two cases. On the other hand, the Case III efficiency figure of 0.34 is in reasonable agreement with the 0.316 measured numerically for both cases.

As previously mentioned, at least a partial explanation for the disagreement between simulation and experiment may rest in the diode's electron flow patterns. The DIODE2D computer code is not electromagnetic; rather, it is electrostatic-magnetostatic. Inductive electric fields are not generated by the particle currents as they should be due to temporal variations in B_θ. This limitation allowed sustained electron currents of huge magnitude to arise between the inside cylindrical surface of the cathode shank and the "target" plane inside the shank. The ability of the ion flow in a diode to draw in electrons to neutralize its space charge is well established.[17] How this neutralizing fill of electron charge maintains itself in the A-K gap is not well understood. At least in this simulation, part of that charge is constantly replenished by the cathode-to-cathode electron currents herein observed. For Case I, this electron current comoving with the ions hitting the "target" region has a magnitude of almost 200 kA.

For Case II it is only about 120 kA. While for Case III it increases slightly again to around 140 kA. It is probable that the inclusion of a physical, inductive E-field would greatly reduce the size of those reverse currents. It is questionable if they would be eliminated entirely. If only 20 kA of electron current were left comoving with the ion beam in the detector region for the Case I numerical simulation, the experimentally recorded efficiency of 0.24 would be achieved. It thus seems quite possible that such comoving electrons may be masking some of the true ion current being extracted from the diode in the Case I Gamble II experiment. This theory remains to be tested. Figures 13, 14, and 15 provide plots of sample electron positions (each particle carries the same predetermined amount of charge) for the equilibria of Cases I, II, and III respectively. They show how electron space charge fills the entire interior of the diode. Unfortunately, they do not show explicit flow patterns inside the cathode radius. One thing that does seem clear is the difference in cathode-tip-to-anode-foil electron flow. For Case I, without ion emission suppression, the ion space charge in the gap between the tip and the foil allows electrons to stream almost directly across, thus illuminating the foil face out to about 3 cm with significant negative space charge. Electrons hugging that surface out to large radii encourage enhanced ion emission. On the other hand, Figures 14 and 15 show that elimination of the ion space charge fill near the cathode tip causes much of the electron stream there to pinch radially inward early in its transit of the gap. Thus the mainstream of the electron flow on the average for Cases II and III stays further away from the foil face than in Case I. This reduces expected ion emission and can apparently reduce the ion efficiency benefits of decreasing the gap size, D.

IV. CONCLUSIONS

From the results summarized in Table 1, one may conclude that selective ion emission suppression definitely allows the use of smaller A-K gaps (therefore, higher R/D ratios) for a fixed diode impedance. This can be beneficial for all light ion beam work in which efficient generator-to-diode power transmission dictates a high diode impedance since a smaller A-K gap means that the ions must spend less time subject to the trajectory-bending effects of the strong electric and magnetic fields found in the diode. The resultant impact on ion beam quality is illustrated in Figures 16, 17, and 18 which plot sample proton equilibrium positions for Cases I, II, and III respectively. The ions are emitted only at data cell centers along the anode face. Thus they are initially spaced out evenly in coaxial, laminar streams. The relative smoothness of each stream may be followed across the gap by tracing from point to point. Significantly less erratic stream behavior is observed in Figure 18 (Case III) with its 3.5 mm gap than for either of Cases I and II in Figures 16 and 17. Although this confirms at least one positive effect of partial ion emission suppression, the simulations did not show any decoupling of the effective ion production efficiency from the diode impedance as was found in the corresponding Gamble II experiments. Although the simulation results are clouded by unrealistically large electron currents comoving with the ion beam, the physical existence of electron currents even an order-of-magnitude smaller than those numerically observed would be sufficient to explain the discrepancy between experiment and simulation.

Two distinct elements of follow-on research should be undertaken. First of all, the simulations described herein should be repeated using a fully electromagnetic computer code. The PREMAS computer code (the successor of DIODE2D at NRL) is currently being upgraded to include time dependent electric and magnetic field solving algorithms. It can be applied to this problem as soon as that coding and debugging is complete. Secondly, an experimental diagnostic technique to separate out the pure ion beam current from any comoving electron component should be designed. The Gamble II runs could then be repeated with such a new diagnostic in place.

ACKNOWLEDGMENTS

The authors are indebted to S. J. Stephanakis for his scientific collaboration, technical advice, and infinite patience over the course of this research and in the preparation of this report.

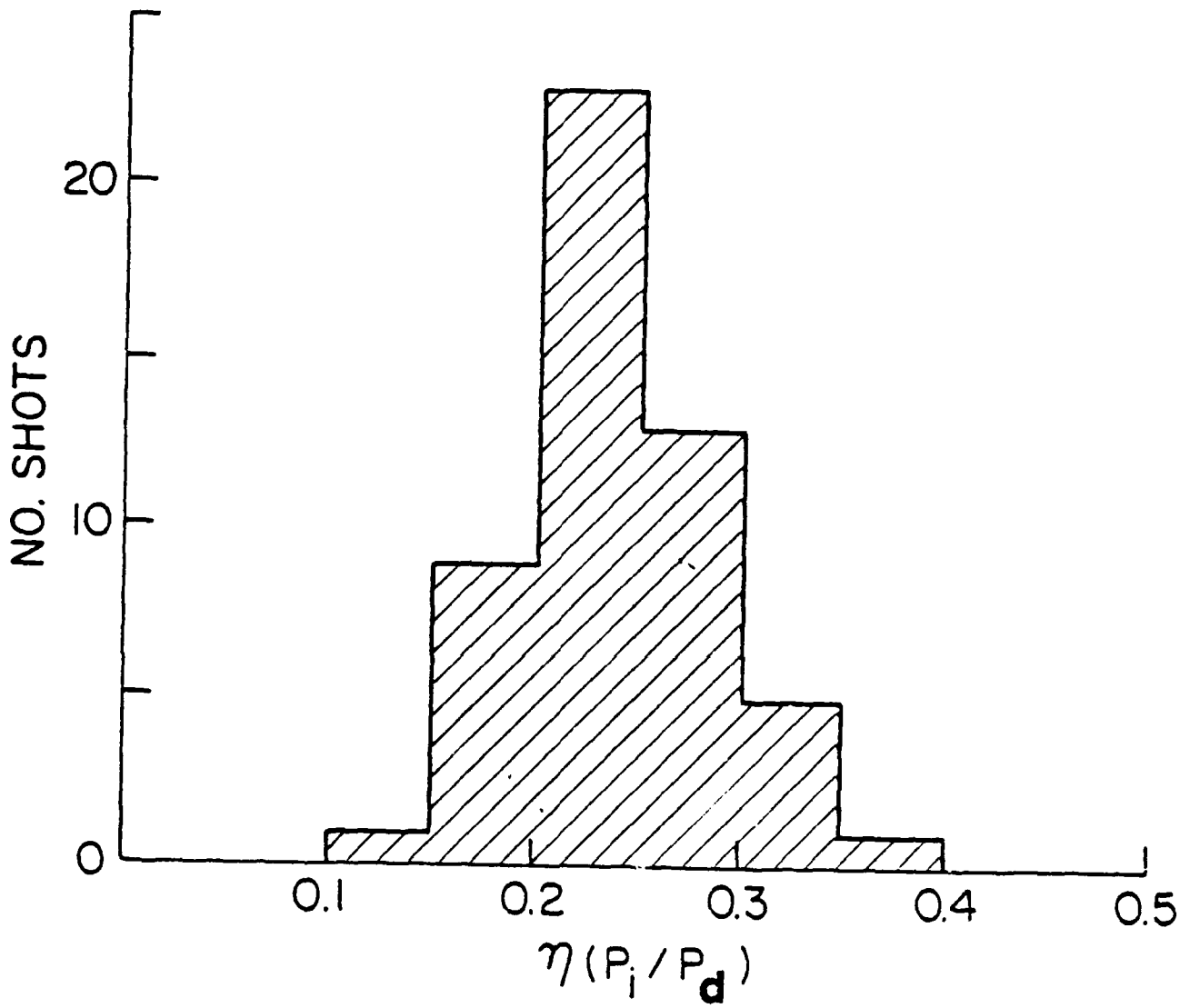

Fig. 5 — Statistical distribution of η_i for the 4Ω Gamble I diode with no ion emission suppression (courtesy of S. J. Stephanakis)

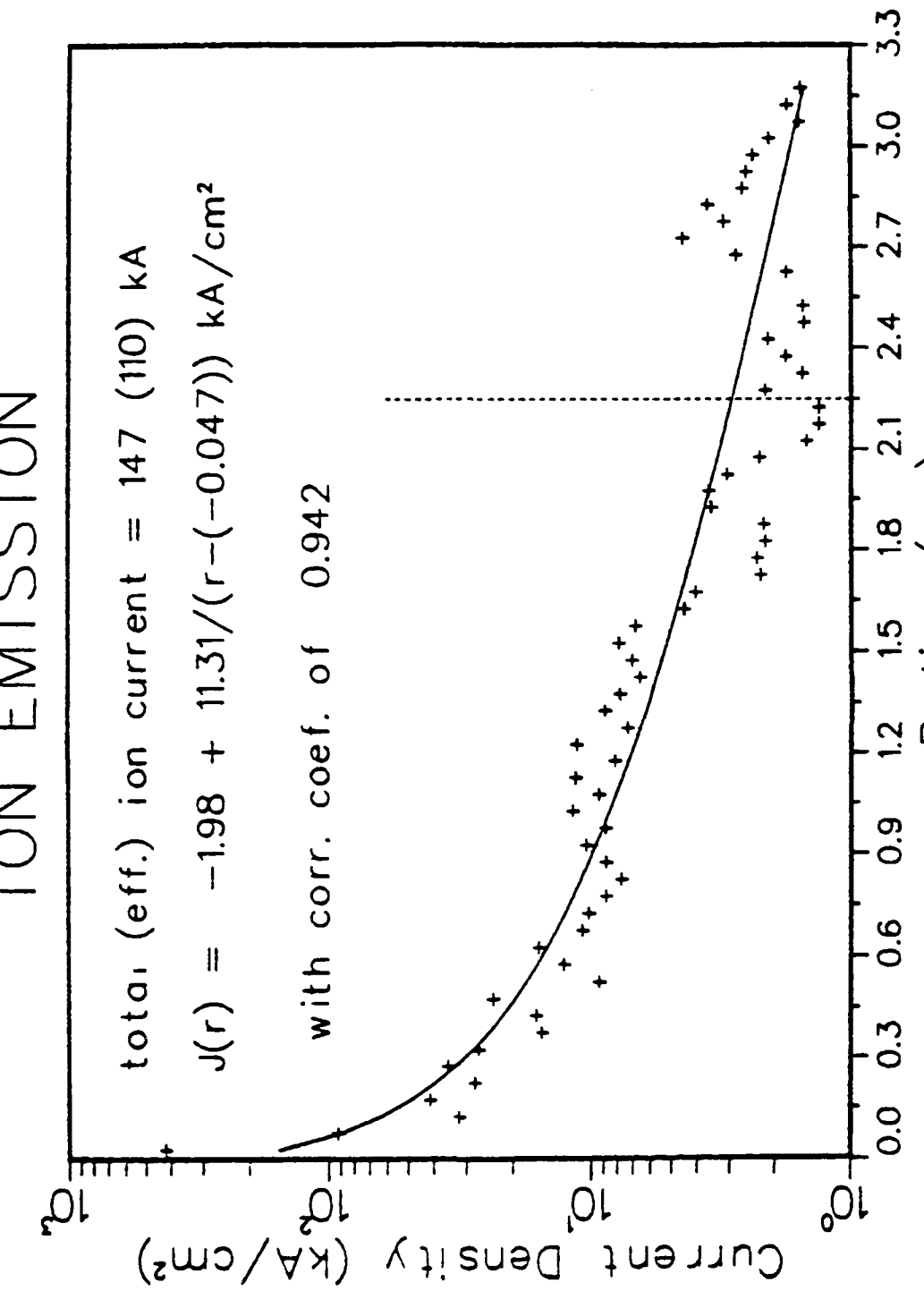

Fig. 6 – Radial profile of emitted ion current density for Case I

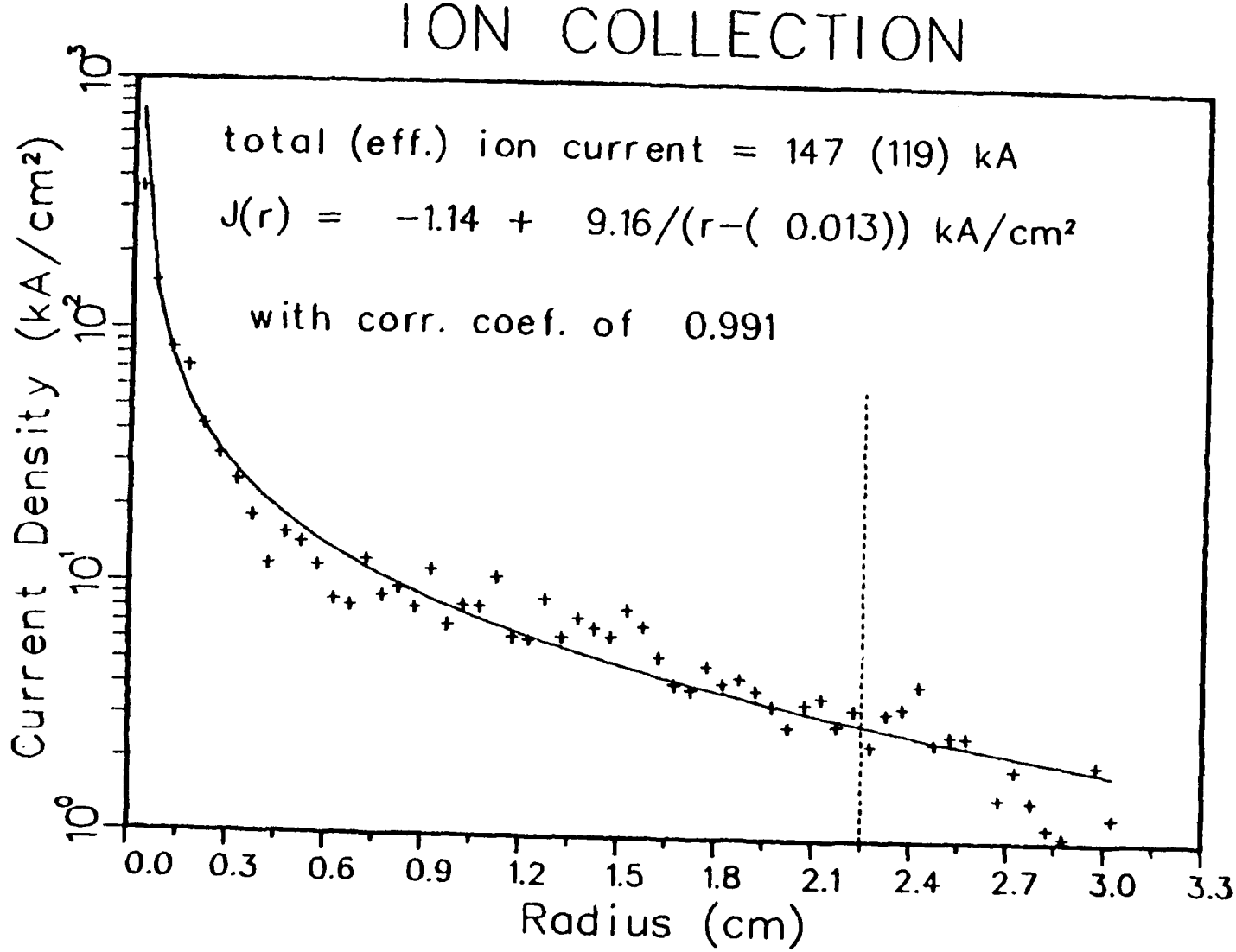

Fig. 7 — radial profile of collected ion current density for Case I

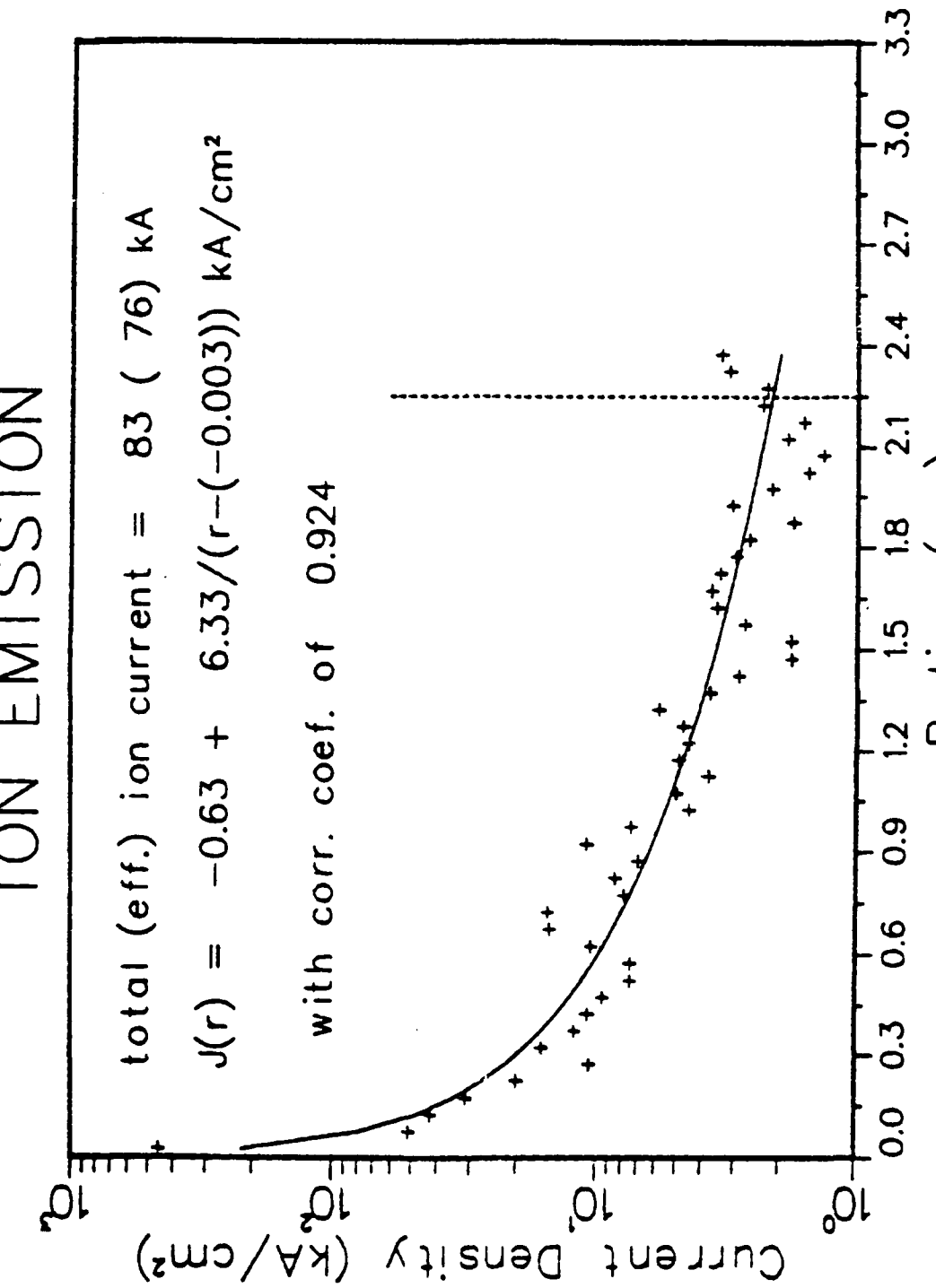

Fig. 8 — Radial profile of emitted ion current density for Case II

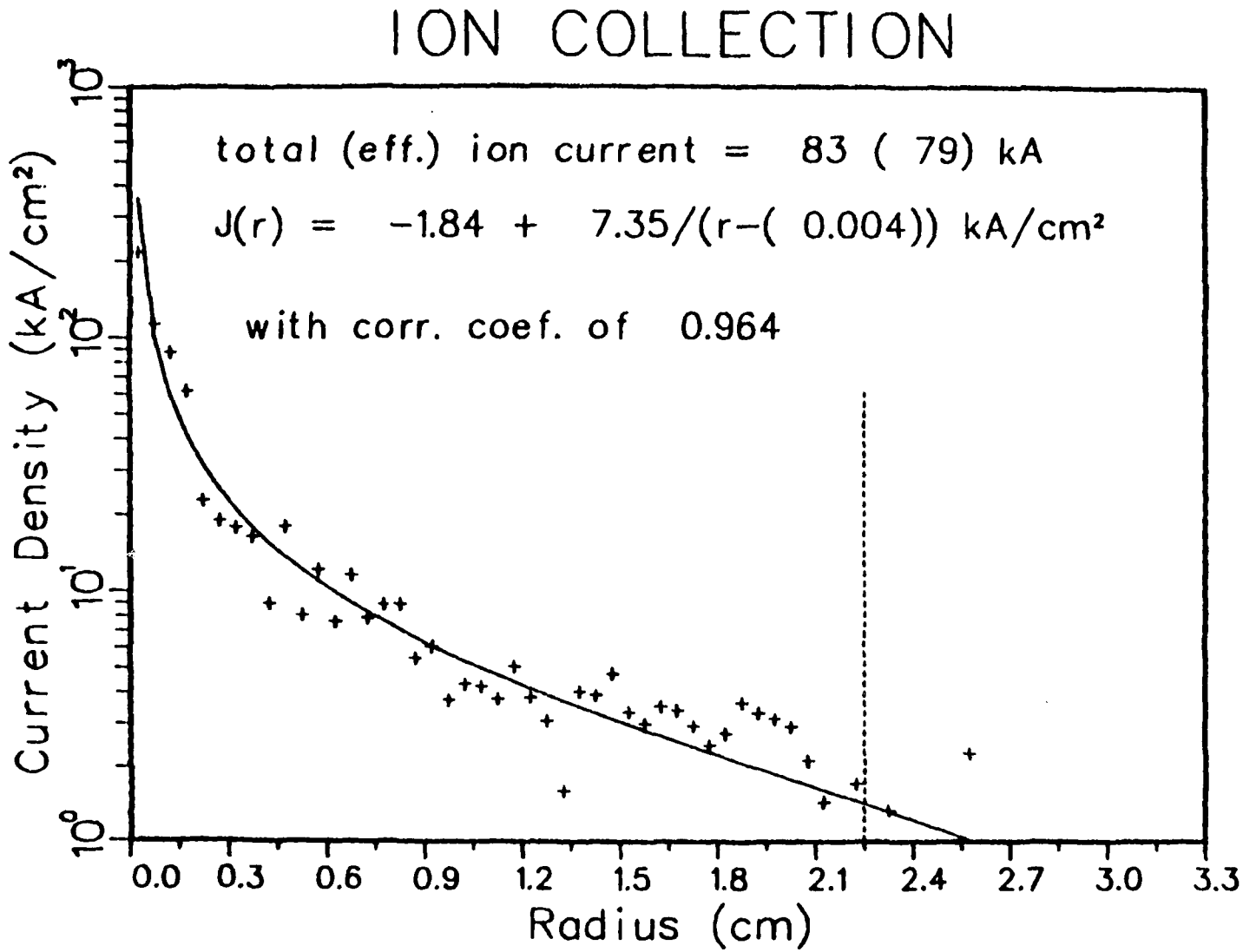

Fig. 9 — Radial profile of collected ion current density for Case II

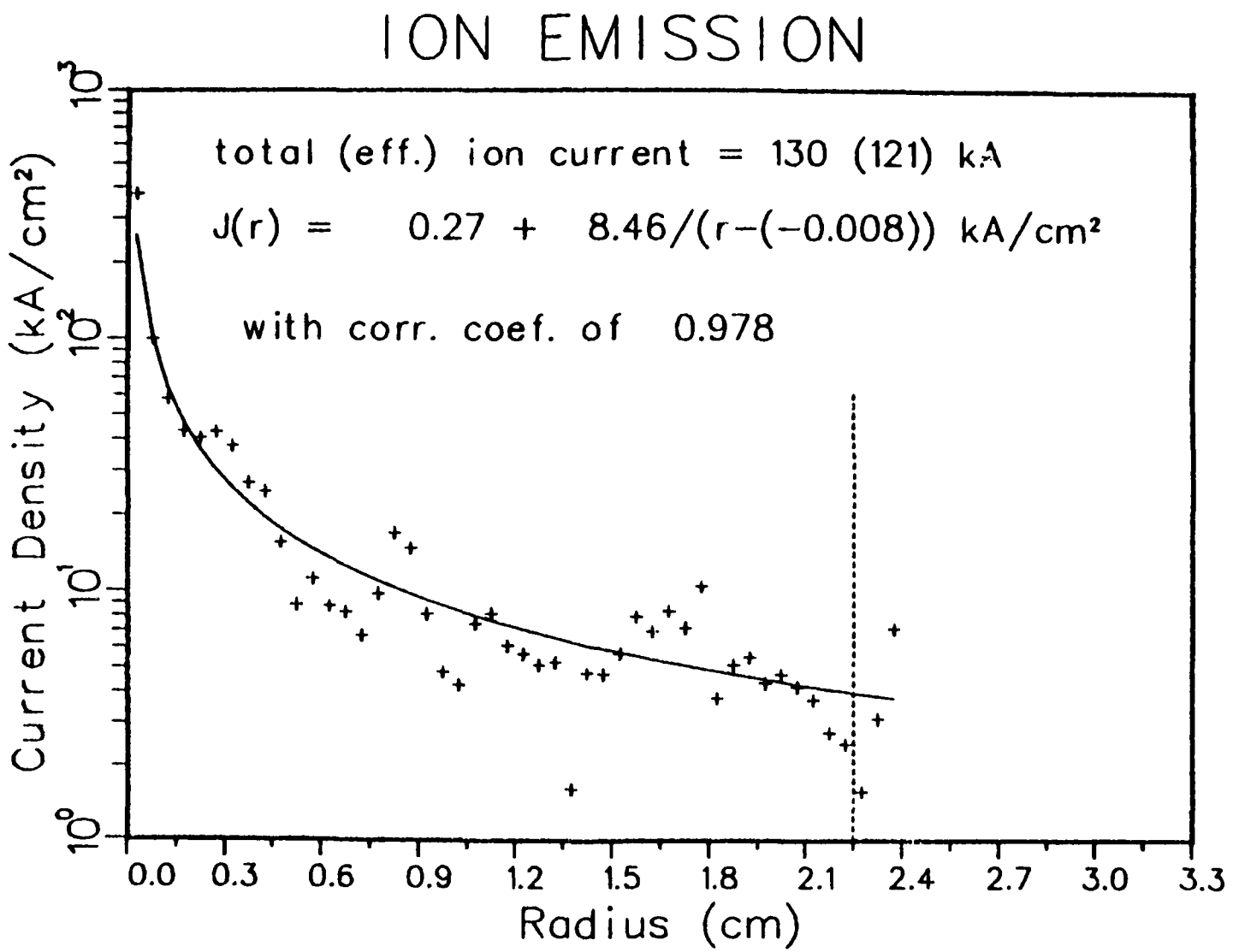

Fig. 10 — Radial profile of emitted ion current density for Case III

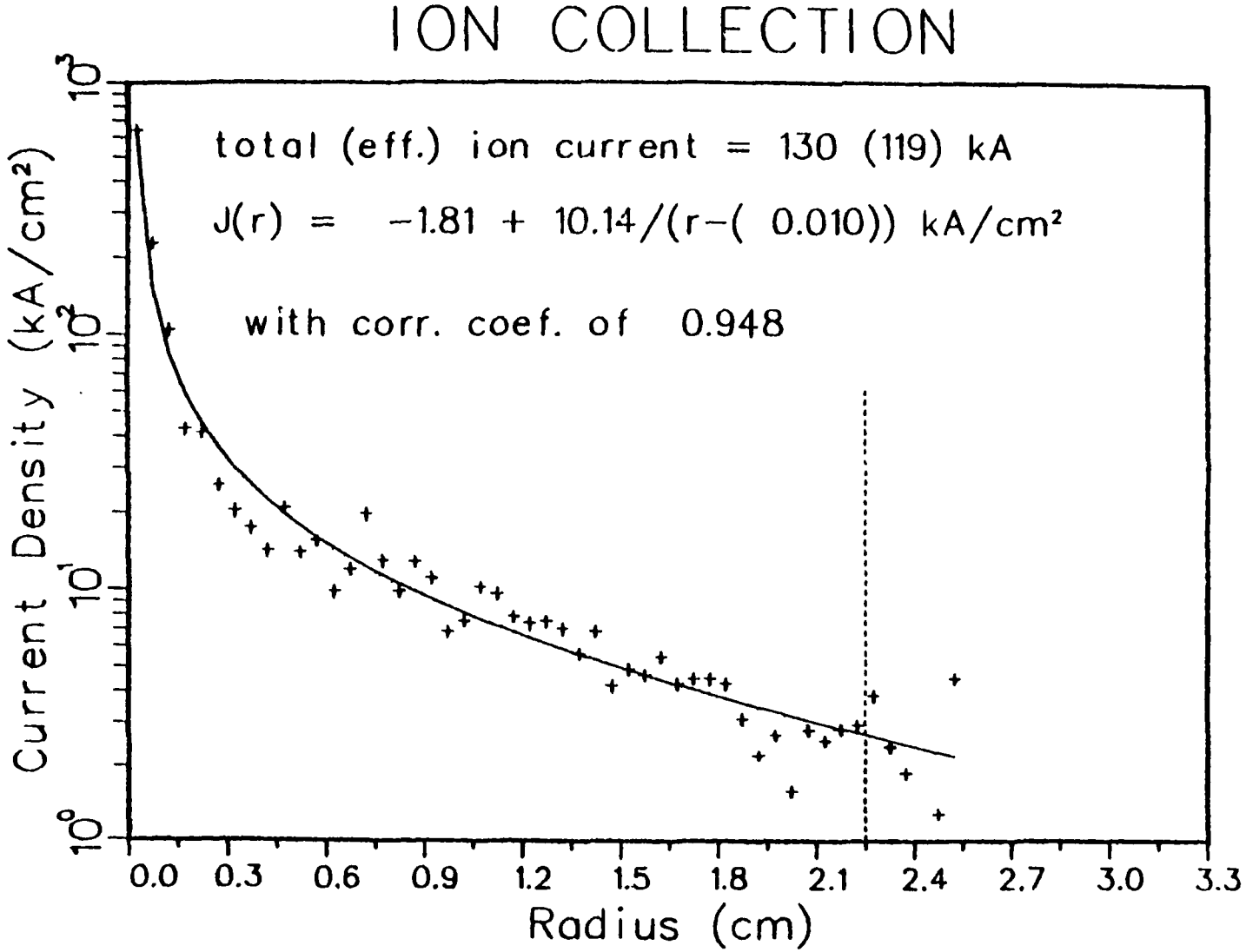

Fig 11 — Radial profile of collected ion current density for Case III

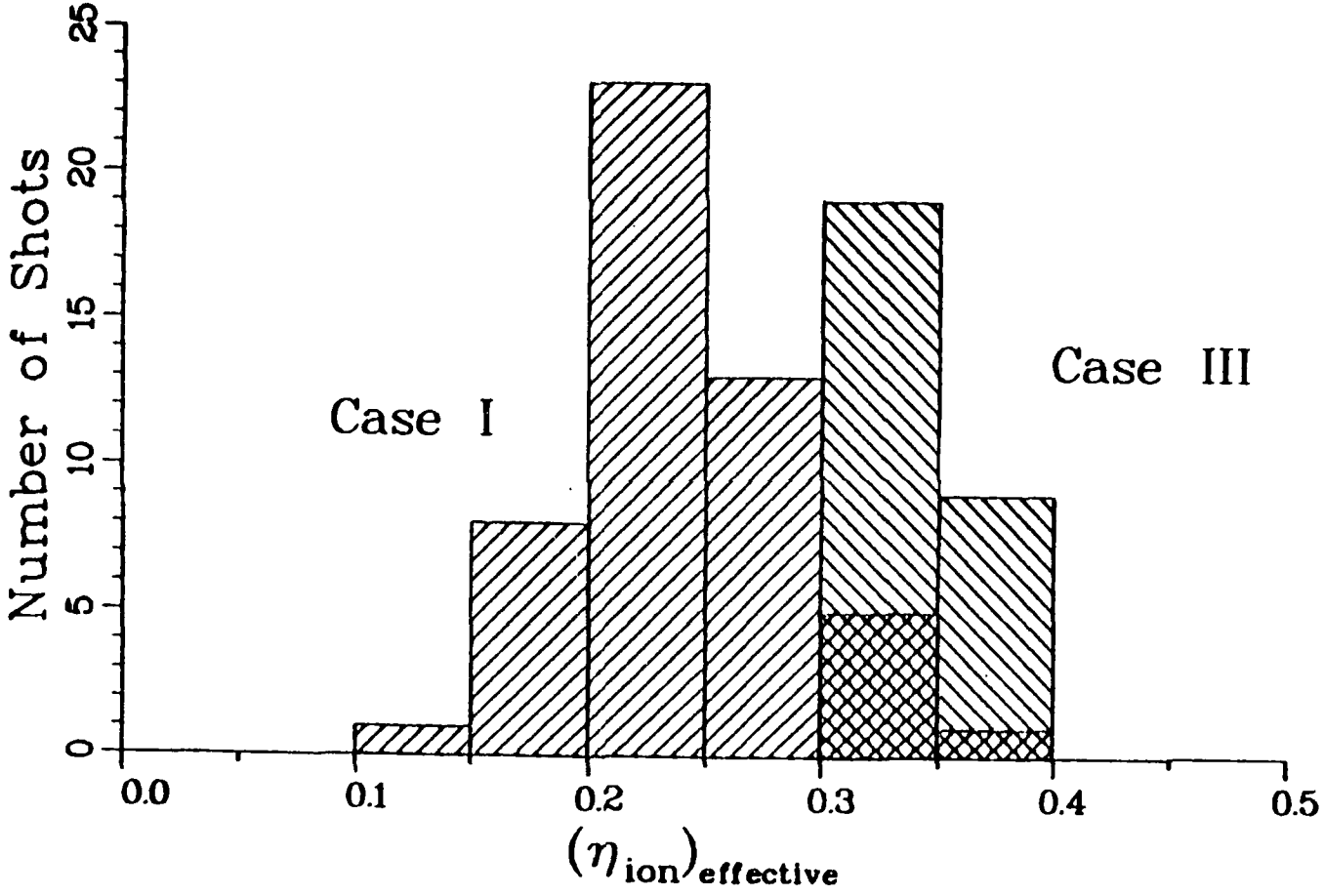

Fig. 12 – Comparison of η_i data collected on Gamble II for 4 Ω diodes with (right) and without (left) selective ion emission suppression

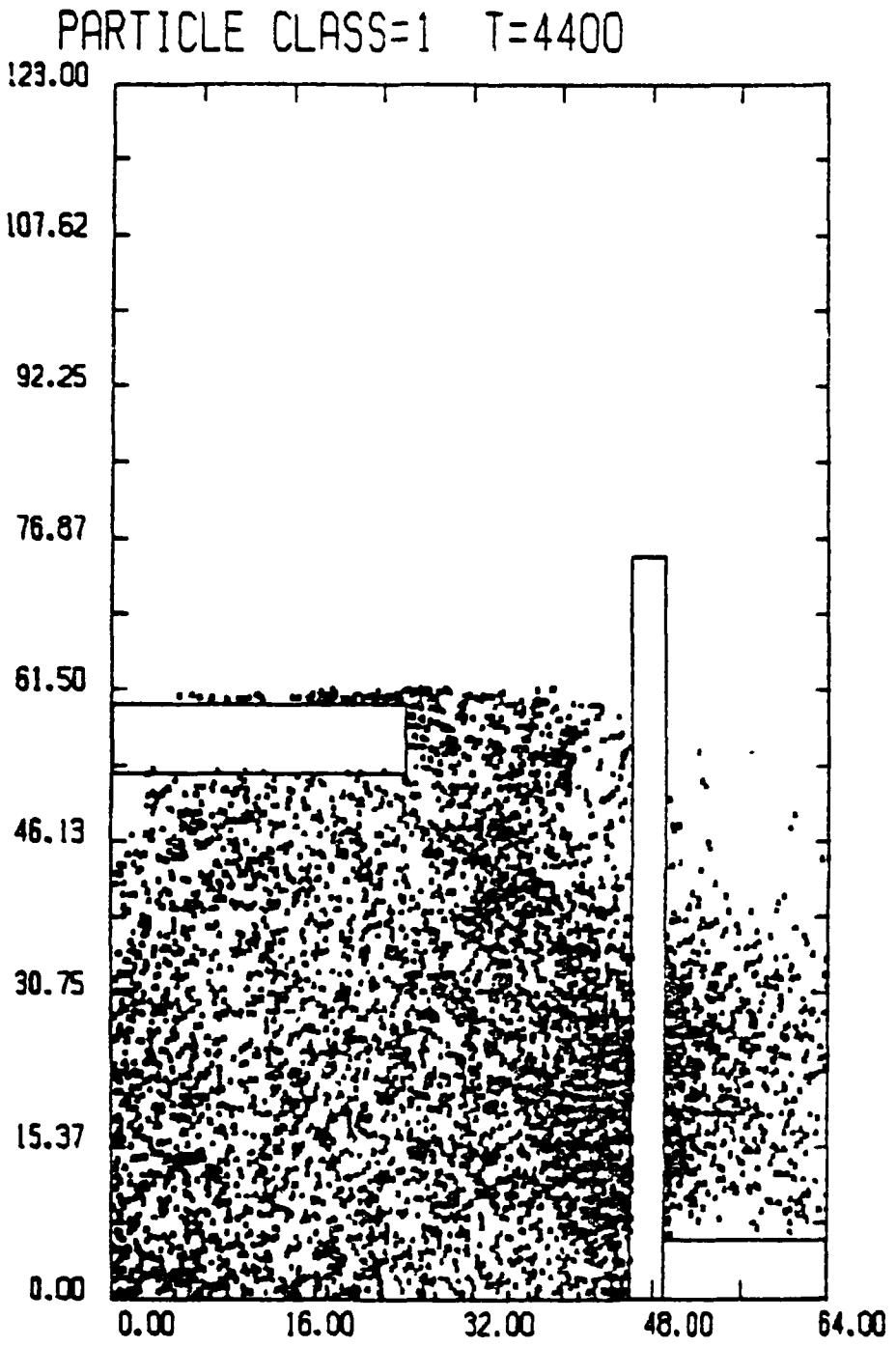

Fig. 13 — Sample steady-state electron plot for Case 1

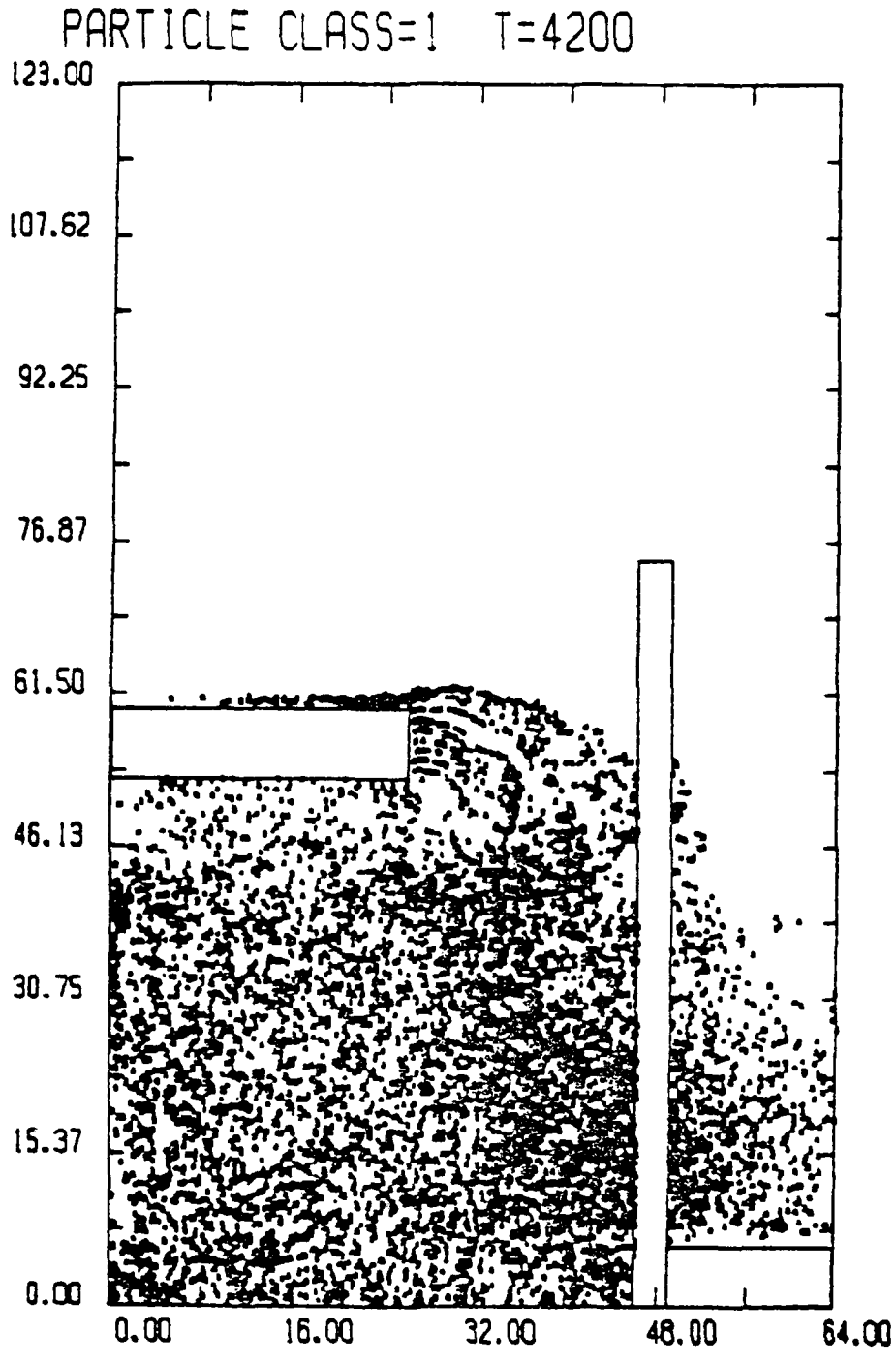

Fig. 14 — Sample steady-state electron plot for Case II

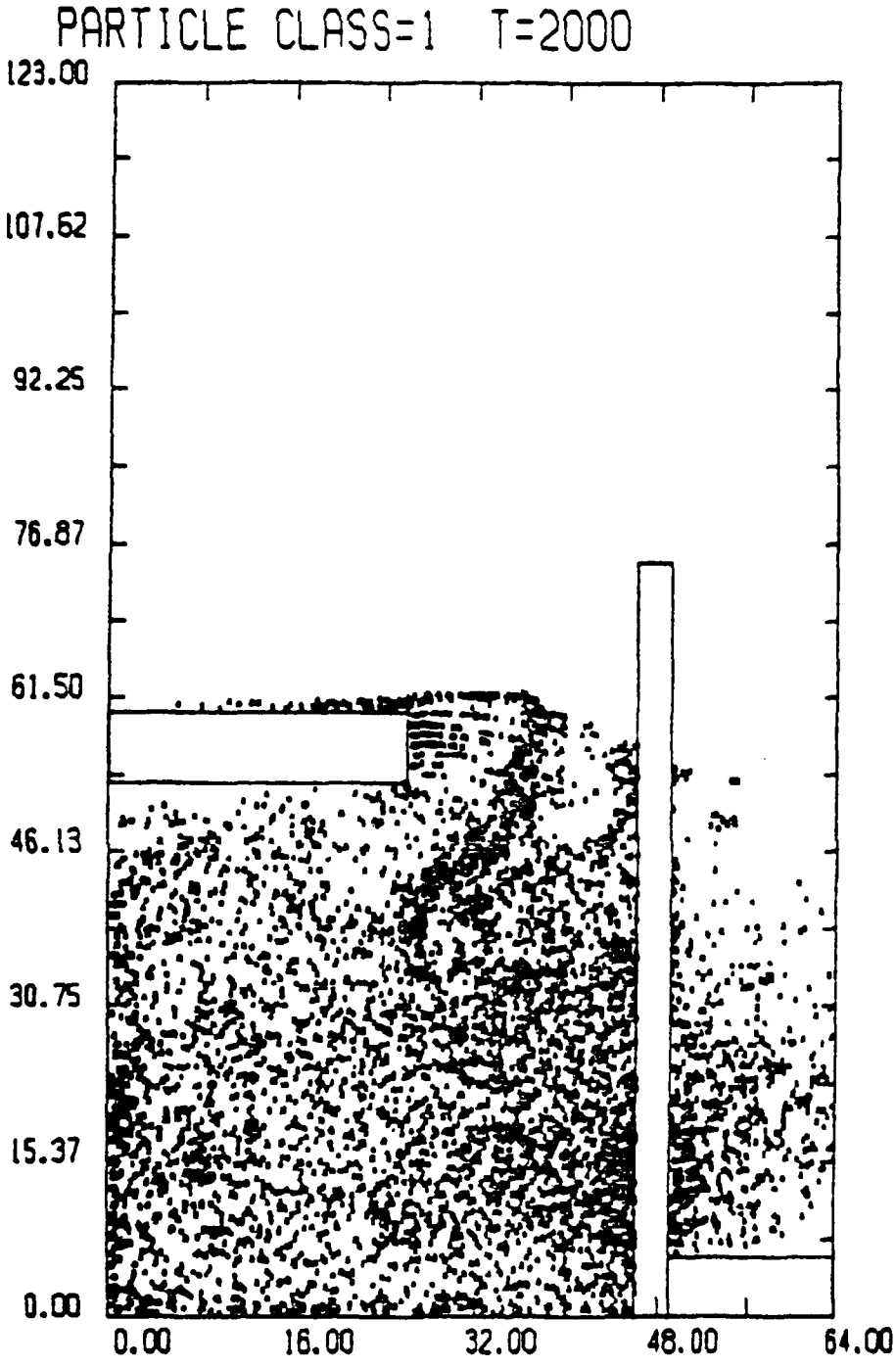

Fig. 15 — Sample steady-state electron plot for Case III

Table 1 — Summary of Computational Results

(ALL AT 1.8 MV)	D = 5.0 MM		D = 3.5 MM
	FULL EMIT CASE I	PART EMIT CASE II	PART EMIT CASE III
$I_{electron}$ (kA)	230 ± 6	186 ± 3	247 ± 3
I_{ion} (kA)	147 ± 6	83 ± 2	130 ± 4
I_{diode} (kA)	377 ± 8	269 ± 3	377 ± 5
$(\eta_{ion})_{net}$	0.39 ± 0.02	0.31 ± 0.01	0.35 ± 0.01
$(I_{ion})_{effective}$	119	79	119
$(\eta_{ion})_{effective}$	0.32	0.29	0.32
Z_{diode} (OHMS)	4.77 ± 0.11	6.69 ± 0.08	4.77 ± 0.07

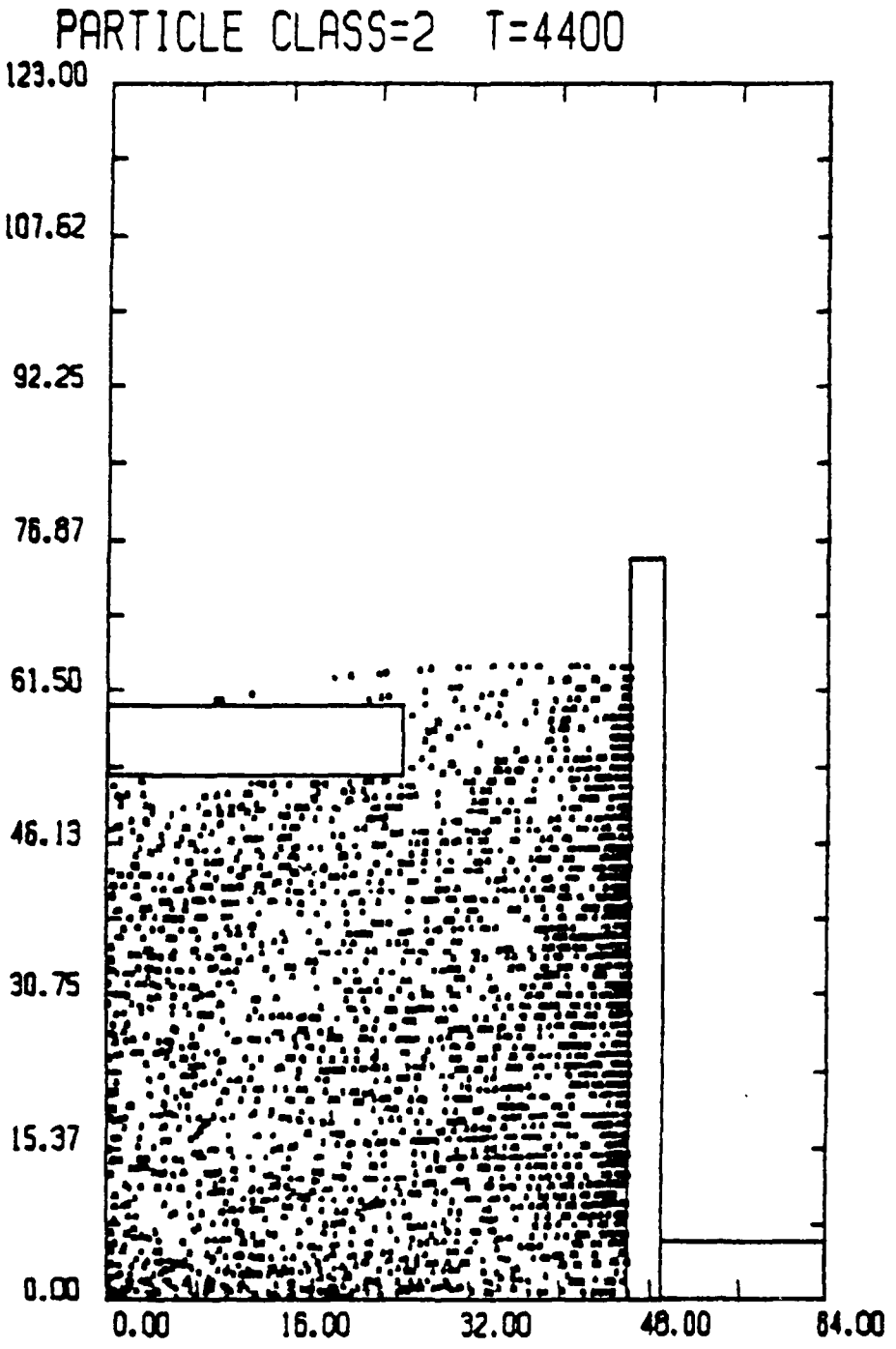

Fig. 16 — Sample steady-state ion plot for Case I

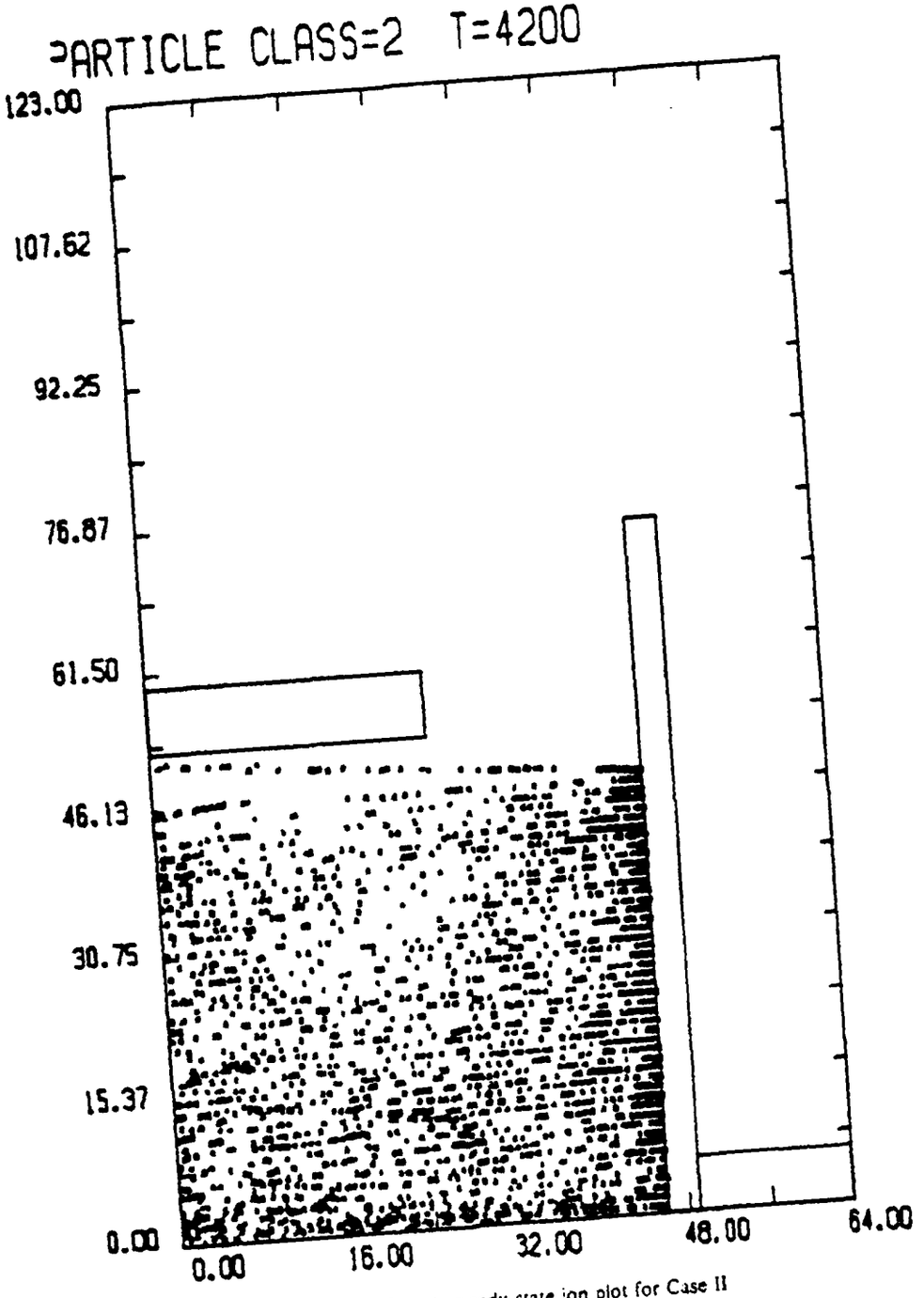

Fig. 17 — Sample steady-state ion plot for Case II

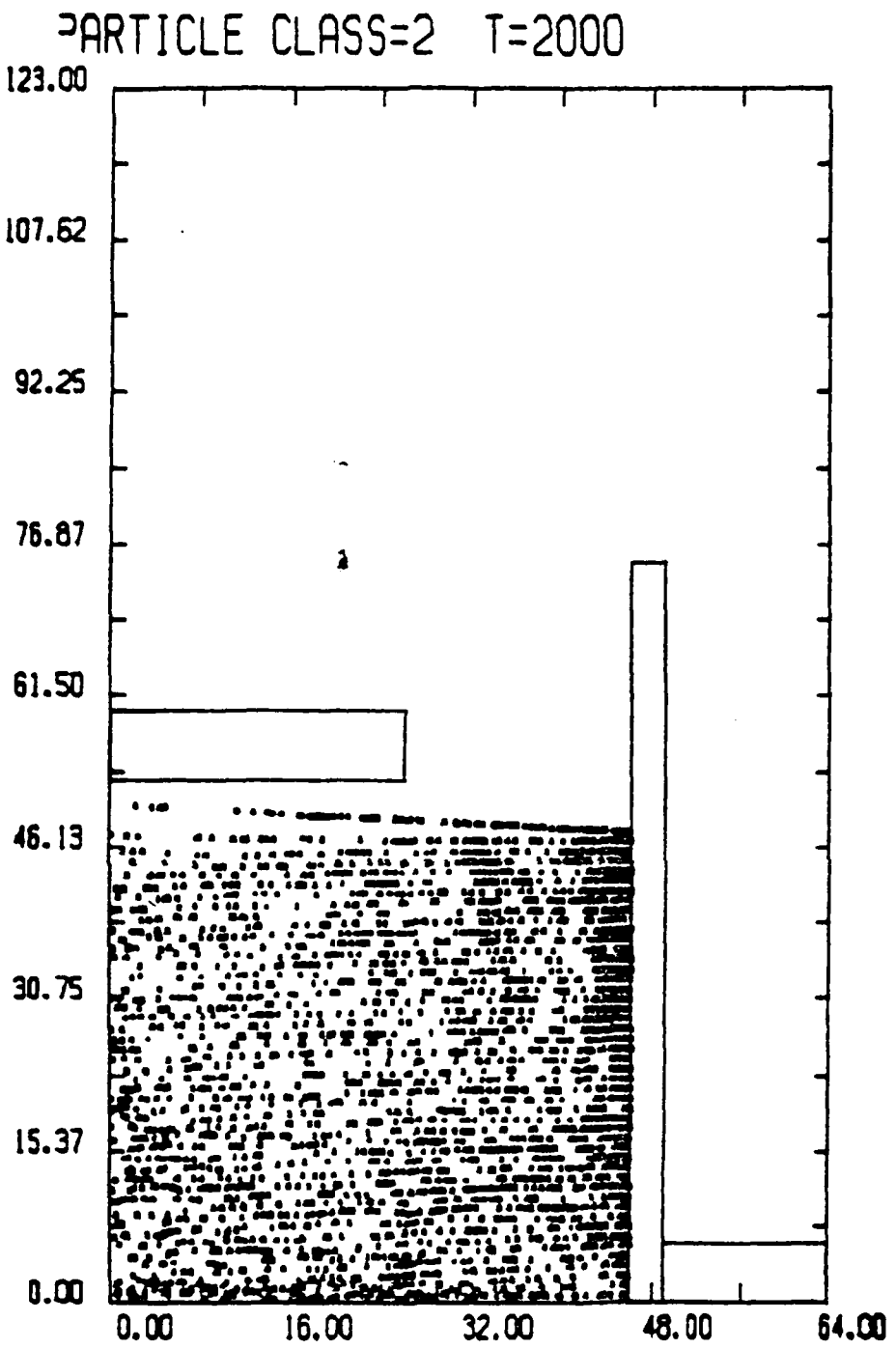

Fig. 18 — Sample steady-state ion plot for Case III

Appendix

STATISTICAL TREATMENT OF COMPUTATIONAL DATA

Whenever numerical predictions extracted from computer simulations are cited in the literature they are almost always presented without any indication of the error brackets associated with those predictions. Conventional error analysis such as that performed routinely for experimental data is traditionally ignored by many computational physicists. When one analyzes a given physical system using a computer simulation code, the numerical data distilled from the code is just as prone to systematic and random sampling errors as that gleaned from a physical experiment. Programming flaws in the code as well as physical flaws and resolution limits in the simulation model will introduce systematic errors into the resulting data. Similarly, when dealing with a computer code which attempts to find the steady-state operating conditions of a given system, periodic sampling of the parameters of interest as they relax into their equilibrium values will give rise to random errors around the "true" values. Both types of errors can be quantified in order to allow an outside observer to know how much weight he should give to the computational results.

The identification and minimization of gross systematic errors contained in the algorithms of a given computer code is normally accomplished once and for all before a given code is accepted for use in production simulation runs. Careful debugging using a variety of standard test cases can eliminate numerical deviations from true physics that go beyond established assumptions for the systems to be modeled. In addition to computer programming bugs, there are also the finite resolution limitations inherent in any digitized model. Some of these, such as standard numerical "round-off" errors can be made insignificant through clever coding of the numerical algorithms. Other sources of error such as the finite number of spatial data points and the finite number of particles used, give rise to actual "minimum errors" which can have significant sizes compared with the values of interest and which can only be lowered by changing the numerical parameters or by rewriting sections of the computer code itself. Any potential user of the simulation results must rely upon the professional abilities of the individual computational physicist regarding the removal of all "bugs" from his code. On the other hand, the user must be aware that there *will* definitely be some systematic errors due to numerical discreteness.

The treatment of random sampling errors is less a question of computational talents then of scientific rigor. Observationally obtained data is inherently bracketed by error bars. Only a finite number of samples of data can be obtained from a given system. Like its physical counterpart, a numerical system cannot be truly static. It will oscillate around an equilibrium state and it is at various points on these "ripples" that the diagnostic data is output from the program. Therefore, random sampling errors must occur and they can be quantified using conventional, statistical treatments. The data reduced for presentation in this report may be used to illustrate the procedure. The major macroscopic quantity monitored in these simulations is the net current flowing through the diode. This current is made up of an electron and an ion component. For each specie component, the emitted current and the collected current are measured separately. Therefore, there are four "subcurrents" that are directly monitored and must be analyzed separately. In a given DIODE2D simulation run, the subcurrents and net charges in the system are tallied every 25 timesteps. After some specific "risetime" is passed, these quantities begin to oscillate around certain plateau values. Such behavior signals the system's arrival at an equilibrium state. At that point, the last eight subcurrent data values spanning the last 200 timesteps are reduced to arrive at approximate steady state predictions for the diode being modeled.

To illustrate the data reduction procedure, the ion current of Case II in this report will be analyzed. The last eight collected ion current values (25 Δt apart) were found to be 83, 81, 87, 84, 82, 78, 93, and 80 kA respectively. This yields a mean value, $<I_{icoll}>$, of 83.5 kA. To determine the random sampling error associated with that value, the mean value of the square, $<I_{icoll}^2>$, is found to be 6991.5 kA^2 from which the variance,

$$\sigma_{icoll} = \sqrt{<I_{icoll}^2> - <I_{icoll}>^2} \tag{A.1}$$

is computed to be 4.387 kA. The standard deviation of the mean of the given eight values is then simply

$$(\sigma_{icoll})_m = \frac{1}{\sqrt{8}}\,\sigma_{icoll} = 1.55 \text{ kA}. \tag{A.2}$$

Thus, on the basis of the computer-supplied data, the collected ion current for Case II can be written as $(I_i)_{coll} = 83.5 \pm 1.6$ kA. In exactly the same manner, the last eight emitted ion current values of 97, 99, 112, 73, 48, 85, 77, and 76 kA reduce to a steady-state prediction of $<I_{i_{emit}}> = 83.4 \pm 6.5$ kA. The much larger standard deviation stems directly from the higher residuals of each data point with respect to their mean value. To arrive at a specific prediction for the net equilibrium ion current flowing through the diode, the weighted average is taken of the emitted and collected ion currents using the method of least squares with

$$I = \frac{<I_{emit}>/(\sigma_{emit})_m^2 + <I_{coll}>/(\sigma_{coll})_m^2}{1/(\sigma_{emit})_m^2 + 1/(\sigma_{coll})_m^2} \tag{A.3}$$

and

$$\frac{1}{\sigma_m^2} = \frac{1}{(\sigma_{emit})_m^2} + \frac{1}{(\sigma_{coll})_m^2}. \tag{A.4}$$

Applying these formulae lead to the result quoted in the text of this report, $I_{ion} = 83 \pm 2$ kA.

An identical analysis is then applied to find the electron current and its error brackets. The net diode current is then simply

$$I_{diode} = I_{ion} + I_{electron} \tag{A.5}$$

with

$$(\sigma_{diode})_m^2 = (\sigma_{ion})_m^2 + (\sigma_{electron})_m^2. \tag{A.6}$$

From this quantity flows the expressions for the diode impedance, z, and ion production efficiency η_i. For the impedance, one may write $z = V/I_{diode}$ where V is the constant diode voltage. The standard deviation from the mean of this quantity is then given by

$$(\sigma_z)_m^2 = \left[\frac{V}{I_{diode}^2}\right]^2 (\sigma_{diode})_m^2. \tag{A.7}$$

Similarly, the ion production efficiency, $\eta_i = I_{ion}/I_{diode}$, has a standard deviation found from the expression,

$$(\sigma_{\eta_i})_m^2 = \left[\frac{I_{ion}}{I_{diode}^2}\right]^2 (\sigma_{diode})_m^2 + \left[\frac{(\sigma_{ion})_m}{I_{diode}}\right]^2. \tag{A.8}$$

The above equations summarize the error analysis which flows naturally from the reduction of raw, numerical data. It provides a simple framework for the statistically valid presentation of steady-state computer simulation code results for diode physics research.

For this specific problem of light ion diode error analysis, another element of statistical analysis, namely — curve fitting, was employed. Its purpose was to obtain the best possible analytic approximation for the radial profile of the ion current density exiting the diode. Such an explicit representation for $J(r)$ is useful particularly for theoreticians attempting to model the transport of the emerging ion beam away from the diode through a predetermined transport channel.[18,19] Previous simulations have observed an approximate inverse proportionality of the current density to the radius.[20] A functional form of

$$J(r) = J_0 + a(r - r_0)^{-1} \tag{A.9}$$

is therefore chosen as the starting point. The raw data of averaged ion emission and collection at each mesh point in the r-dimension along the anode and cathode respectively are first plotted as single points (see Figures 6-11). Then a curve of form (A.9) is fitted to it. In order to obtain that curve, the method of least squares[21] is employed. The three unknowns in the equation are then given by

$$J_0 = D^{-1} \begin{vmatrix} \Sigma\ J_i r_i^2 & \Sigma\ r_i & \Sigma\ J_i r_i \\ \Sigma\ J_i r_i & N & \Sigma\ J_i \\ \Sigma\ J_i^2 r_i & \Sigma\ J_i & \Sigma\ J_i^2 \end{vmatrix} \tag{A.10}$$

$$r_0 = D^{-1} \begin{vmatrix} \Sigma\ r_i^2 & \Sigma\ r_i & \Sigma\ J_i r_i^2 \\ \Sigma\ r_i & N & \Sigma\ J_i r_i \\ \Sigma\ J_i r_i & \Sigma\ J_i & \Sigma\ J_i^2 r_i \end{vmatrix}$$

$$a = J_0 r_0 + D^{-1} \begin{vmatrix} \Sigma\ r_i^2 & \Sigma\ J_i r_i^2 & \Sigma\ J_i r_i \\ \Sigma\ r_i & \Sigma\ J_i r_i & \Sigma\ J_i \\ \Sigma\ J_i r_i & \Sigma\ J_i r_i & \Sigma\ J_i^2 \end{vmatrix}$$

where

$$D = \begin{vmatrix} \Sigma\ r_i^2 & \Sigma\ r_i & \Sigma\ J_i r_i \\ \Sigma\ r_i & N & \Sigma\ J_i \\ \Sigma\ J_i r_i & \Sigma\ J_i & \Sigma\ J_i^2 \end{vmatrix}$$

and where the summations are from $i = 1$ to $i = N$ (N being the number of radial data points), r_i is the radius of the "i"th point, and J_i is the observed $J(r_i)$. The "goodness" of the fit of the data to the curve thus generated can be gauged by comparing the root mean square deviation of the data points from the curve to the root mean square deviation of those same points from their average value $\langle J \rangle = N^{-1} \Sigma\ J_i$. The resultant "correlation coefficient" may then be expressed as[22]

$$\sqrt{1 - \frac{\Sigma\ (J_i - J_0 - a(r_i - r_0)^{-1})^2}{\Sigma\ (J_i - \langle J \rangle)^2}}. \tag{A.11}$$

It should be noted that in practice some care must be exercised in the application of (A.11) to the problem in question. Near $r = 0$, the values of J become quite large so that deviations from the smoothed fit tend to be exaggerated. To avoid that distortion, the data at $r = r_1$ is ignored in the calculation of (A.11) as presented in Figures 6 through 11.

REFERENCES

1. G. Cooperstein, R.J. Barker, et al., in Proceedings of the United States-Japan Symposium on the Theory and Application of Multiply Ionized Plasmas Produced by Laser and Particle Beams, Japan (1982).

2. D.J. Johnson, G.W. Kuswa, A.V. Farnsworth, Jr., and J.P. Quintenz, et al., Phys. Rev. Lett. 42, 610 (1979).

3. G. Cooperstein, S.A. Goldstein, and D. Mosher, et al., in Proceedings of the 3rd International Topical Conference on High Power Electron and Ion Beam Research and Technology, Novosibirsk, USSR (1979).

4. D.J. Johnson, Bull. Am. Phys. Soc. 24, 925 (1979).

5. S.J. Stephanakis, J.R. Boller, G. Cooperstein, S.A. Goldstein, D.D. Hinshelwood, D. Mosher, W.F. Oliphant, F. Sandel, and F.C. Young, Bull. Am. Phys. Soc. 23, 907 (1978).

6. D.G. Colombant, S.A. Goldstein, and D. Mosher, Phys. Rev. Lett. 45, 1253 (1980).

7. R.A. Meger, F.C. Young, A. T. Drobot, G. Cooperstein, S.A. Goldstein, and D. Mosher, NRL Memo. Report 4477 (1981).

8. D.J. Johnson, S.A. Goldstein, R. Lee, and W.F. Oliphant, J. Appl. Phys. 49, 4634 (1978).

9. S.A. Goldstein and R. Lee, Phys. Rev. Lett. 35, 1079 (1975).

10. A. E. Blaugrund, G. Cooperstein, and S.A. Goldstein, Phys. Fluids 20, 1185 (1977).

11. S.J. Stephanakis, private communication.

12. S.J. Stephanakis, R.J. Barker, S.A. Goldstein, and W.F. Oliphant, IEEE Conf. on Plasma Science 1C9, Santa Fe, New Mexico (1981).

13. R.J. Barker, A.T. Drobot, R. Lee, and S.A. Goldstein, Proc. 9th Conf. on the Numerical Simulation of Plasmas, Evanston, Ill. (1980).

14. R.J. Barker, Banach Center Publications 3, 255, Warsaw, Poland (1975).

15. R.J. Barker and S.A. Goldstein, NRL Memo. Report 4773 (1982).

16. S.J. Stephanakis, S.A. Goldstein, D. Mosher, and W.F. Oliphant, Bull. Am. Phys. Soc. 25, 900 (1980).

17. R.J. Barker, S.A. Goldstein, and A.T. Drobot, NRL Memo. Report 4642 (1981).

18. D.G. Colombant, D. Mosher, and S.A. Goldstein, NRL Memo. Report 4252 (1980)

19. P.F. Ottinger, S.A. Goldstein, and D. Mosher, NRL Memo. Report 4548 (1981).

20. R.A. Meger, F.C. Young, et al., NRL Memo. Report 4477 (1981).

21. H.D. Young, *Statistical Treatment of Experimental Data,* McGraw-Hill, New York (1962).

22. E.L. Crow, F.A. Davis, and M.W. Maxfield, *Statistics Manual,* Dover, New York (1960).

NUMERICAL MODELING AND SIMULATION OF ELECTRON AND ION FLOW IN PULSED POWER DIODES

A.T. Drobot,[a] R.J. Barker,[b] Roswell Lee,[b]
A. Sternlieb,[c] D. Mosher and Shyke A. Goldstein,[b]
Plasma Physics Division
Naval Research Laboratory
Washington, D.C. 20375

I. INTRODUCTION

Pulsed power diodes have recently been used to generate intense ion beams with power levels approaching 1.0 TW [1]. As discussed in the papers presented by Drs. Cooperstein and Mosher in this conference, these beams are being considered for driving inertial-confinement-fusion pellets. The characteristics of the ion beams that can be generated are important in determining their suitability for focussing, transport and axial compression. The quality of the beams produced is a strong function of the detailed flow of electrons and ion in the diode itself and can be influenced by the specific geometry of the diode region. Because the behavior of diodes is a complicated nonlinear problem, numerical simulation modeling is required. Several simulation codes have been developed and used to study the flow of electrons and ions in a variety of devices and diode loads.

Using a one-dimensional, relativistic P.I.C. code, the time-dependent behavior of a reflex double diode has been studied. The important feature of these simulations was the inclusion of a lumped-element model of the generator circuit and its coupling to the particle dynamics through the diode boundary conditions [2]. The results of this investigation are presented in Section II. Modified versions of the DIODE2D electro-and magneto-static 2 1/2-dimensional (R,Z) code with relativistic dynamics were used to study reflex and pinch-reflex diode configurations [3]. We describe the important features of the code in Section III and the results of simulations in Sections IV and V for the reflex and pinch-reflex configurations respectively.

II. REFLEX DOUBLE DIODE

In order to understand the time-dependent dynamics of ion and electron flow in a reflex double diode, it is necessary to describe the coupling between the power generator and the diode itself. A one-dimensional model of the reflex diode coupled to a lumped parameter circuit equation for the generator has been

fluctuations in the particle emission.

In the algorithm, a 1-D particle in cell code is coupled in series to the generator circuit. The diode current is advanced in time as dictated by the circuit equation. The emitted electron and ion currents are found from the total diode current and the absorbed electron and ion currents in such a way that space-charge-limited emission is enforced for both species.

This algorithm was tested on a simple Child-Longmuir diode and agreed with the well known solution. The circuit equation employed was,

$$\frac{dI}{dt} = \frac{1}{L_G}[V_{ext} - R_G I - V_D],$$

where I is the total diode current, V_{ext} is the applied voltage, V_D is the voltage drop across the diode electrodes, (supplied by the simulation code), and R_G, L_G are lumped impedance and inductance of the generator.

A simulation using the same circuit equation but a double reflex diode was run for a number of cases. Typical results are shown in Figure 1, which contains the I and V_D vs. time characteristics. In this case, the diode voltage rises very rapidly to the generator voltage of 600 kV because of the initially high diode impedance. As the diode current rapidly bootstraps itself, the diode voltage drops and a near steady state value of 300 kV is achieved.

The asympotic diode voltage corresponds to an electron energy which would give about 4 reflexings in the polyethylene foil of the anode. This result is in good agreement with both the theoretical and experimental understanding of double reflex-diode operation in 1-D.

III. THE DIODE2D SIMULATION CODE

The steady state flow of electrons and ions in a diode is modeled by an electro- and magneto-static particle-in-cell simulation code. Several other groups, most notably Poukey and Quintenz at Sandia Laboratories, have developed similar codes to study diode problems. The important features of the code reported on here include:

i) A fast Poisson solver which calculates the electric potential due to internal changes in the presence of complicated boundaries and externally-applied voltages.

ii) A similar solver for the vector potential A_θ when self-induced beam rotation is important as in the case of the

reflex diode immersed in a B_z magnetic field with conducting boundaries.

iii) Relativistic treatment of the particle dynamics.

iv) The introduction of temporal and spatial smoothing to reduce the noise level caused by the use of a finite number of simulation macro particles.

v) The treatment of particle scattering in the reflexing foil including inelastic energy losses and angular scattering.

vi) A wide variety of diagnostics to help in the interpretation of the simulation results.

The equations that are solved in the simulation are:

$$\nabla^2\phi = -4\pi\rho; \qquad \vec{E} = -\vec{\nabla}\phi,$$

where ρ is the charge density due to the ions and electrons in the diode. The Poisson equation for ϕ is solved in difference form on a uniform mesh in (R,Z) geometry by a fast Fourier transform in Z and Gaussion elimination in R. The applied voltages are imposed through boundary conditions on ϕ. The capacitive matrix method is used to account for the internal diode structure (that is, electrode shapes which do not conform to the mesh). In the case where an externally applied axial magnetic field is present, the vector potential A_θ is solved for by:

$$\nabla^2 A - \frac{A_\theta}{R^2} = \frac{4\pi}{C} J_\theta; \qquad \vec{B} = B_0 \hat{Z} + \vec{\nabla} \times \vec{A},$$

where J_θ is the azimuthal current due to electrons and ions is the diode. The azimuthal component of magnetic field is solved from Amperes Law.

$$B_\theta = \frac{4\pi}{CR}\int_0^R dR' R' J_z (R',Z)$$

The electron and ion equations of motion are advanced using the Boris pusher [4] and the self consistent electric and magnetic fields as described above. The field quantities used for the particle equations of motion are interpolated from the four nearest cell points and the current and charge density contributions are determined by the inverse process. To reduce the noise level due to the finite number of particles in the simulations, local averages in are taken of the form:

$$\rho'(R,Z_i) = \alpha\,\rho(R,Z_{i-1}) + (1 - 2\alpha)\rho(R,Z_i) + \alpha\,\rho(R,Z_{i+1}),$$

where the index i refers to a particular mesh point. The coefficient α can be varied but is typically set to $\alpha = 1/4$. Since a steady state is desired, temporal smoothing is also included to reduce fluctuations. This has the form:

$$\rho'^{T+1} = (1 - \beta)\, \rho^{T+1} + \beta\, \rho'^{T}$$

where the primed quantities are used in the field solvers and the unprimed values calculated directly from the particle contributions. The charge and current density are both averaged in this way.

The particle emission is assumed to be space-charge limited. The electric field perpendicular to an emission surface is determined from the Poisson solver and the appropriate amount of charge introduced in the cell adjacent to the surface to reduce that field to zero. Poisson's equation is then resolved with the emitted charge contribution before any further particle advancement. In the reflexing foil, energy reduction as well as angular scattering is included.

Particle energy loss in the foil is calculated by table look up of the range-energy data from Spencer [5] using the length of the path traversed in crossing the foil. The angular scattering is implemented in a Monte-Carlo sense by redirecting the exit angle of a particle by randomly selecting the scatter angle according to the range and energy of the particle.

This code was run on the Texas Instruments-ASC vector computer which has a cycle time of 40 nsec per operation. The code was fully vectorized and used $\sim$ 23 μsec per particle push per time step. In a typical simulation we used approximately 15,000 particles and mesh sizes ranging from 32x40 to as large as 128x130. The code can be run in such a way that the charge attributed to the macroparticles is variable.

IV. REFLEX DIODE SIMULATIONS

In a reflex diode, the detailed phenomenon of ion emission enhancement by "bootstrapping" due to the electron reflexing is not well understood. The simulations described here were motivated by the possibility of very high ion-current densities, $J_i > 10^6$ Amps/cm^2, which may be achieved with a small area reflex diode immersed in a strong axial magnetic field. The high current densities may be useful for beam-target experiments. Experimentally, it has been found that electron current densities as high as $J_e = 10^7$ Amps/cm^2 can be achieved from a 1.6 mm diameter rod cathode in reflex geometry [6].

In the simulations conducted, it was found that the bootstrapping of the

diode. If too much flux was permitted to leave the diode, so that

$$\int^{S} E \cdot dA \approx Q_e$$

over the interior region of the diode, the resulting charge imbalance prevented bootstrapping. If, on the other hand, the geometry forced near charge neutrality the exponentiation of electron and ion current could be realized. The simulation results for a geometry in which bootstrapping was achieved are presented. The diode configuration shown in Figure 2 has a small-diameter cathode of radius 0.1cm and a foil-cathode spacing of 0.1cm. The diode geometry was specifically designed to exclude as little flux as possible from the interior. A 125μm polyethylene foil was used for reflexing the electrons, a voltage of 600kV was applied to the diode, and a uniform external field of B_z = 100kG was imposed. The simulation was conducted for 0.5nsec to determine the transient response of the diode currents. The peak electron and ion densities generated are shown in table below. They correspond to the values achieved at the end of the simulation run. The total diode current was ∿ 70kA with I_i = 20kA and I_e = 50kA.

	emitted (A/cm^2)	absorbed (A/cm^2)
$(J_e)max$	1.25×10^7	2.32×10^6
$(J_i)max$	1.77×10^6	4.83×10^6

The time history of the electron and ion currents is shown in Figure 3. It can be seen that the electron current rises monotonically throughout the run and that the ion current has a corresponding increase. The ion current density absorbed at the cathode is shown in Figure 4 and has a peak value on axis of ∿ 5MA/cm^2. It appears from these simulations that very high ion current densities can be generated by such reflex diodes at modest power levels.

V. PINCH-REFLEX DIODE SIMULATIONS

Recent experimental and theoretical work has shown that the pinch-reflex diode can be a highly efficient source of ions that are suitable for light ion beam fusion applications. The enhanced ion currents in the pinch-reflex diode are caused by an increase of the electron lifetime in the anode-cathode gap by taking advantage of the high aspect ratio pinched electron flow and by reflexing of electrons that would otherwise be lost because they cross the anode at radii greater than the pinch radius. The reflexing is done through a thin foil placed between the solid anode and the hollow, high-aspect-ratio cathode

and is caused by the magnetic field due to the total diode current which runs in an axially placed rod connecting the thin foil to the solid anode. The ions that are generated on the cathode side of the thin reflexing foil exit the diode through a transmission foil placed across the inner radius of the hollow cathode. To focus the ion beam generated by this diode, it is desirable to have the radial velocity profile of the exiting ions directly proportional to the radius. If this condition is achieved, then all of the ions generated will have the same focal point if the ion beam is current neutralized after leaving the diode.

We have conducted simulations of electron and ion flow in pinch-reflex diodes using the configuration shown in Figure 5. The typical diode dimensions had an R/d = 20 aspect ratio where R = 6.4cm was the outer radius of the hollow cathode and d = .32cm the separation of cathode from the anode foil. The thickness of the cathode shank was 0.8cm. The scattering foil in these calculations was assumed to be 125μm thick polyethylene. It was assumed that the region between the reflexing foil and the solid anode was filled with ions and that the resulting charge neutralization made it unnecessary to solve for the electrostatic fields in that region. The sequence of events for a simulation at 1.5MeV is shown in Figures 6 and 7. These figures show the time evolution for a simulation done on a 32 × 40 mesh. The positions of the electrons are shown in (R,Z) configuration space at various points in time. Early in time (step 200), the electrons (one in 10 is plotted on the figure) have transited the diode and reflexed twice through the foil. By time step 400, the electrons have reflexed several times and have established the pinched flow along the diode side of the reflexing foil. At step 2000, the pinched electron flow is well established and the electrons fill the diode gap. At the conclusion of the run, step 3800, the electron flow has come to an average steady state. The corresponding ion positions are shown in Figure 7. At step 400, the ions have not crossed the diode gap and are clumped along the anode foil. As can be seen at step 1000, the ion emission occurs in filaments with a separation of two electron Larmor radii corresponding to the locations where electrons reflex through the foil. By step 2000, scattering has destroyed the coherent electron clumps at the foil so that the ion emission is more uniform. At the end of the run, the ion density assumes a fairly uniform radial profile as can be seen from the plot of particle positions at step 3800. The ion current profile arriving at the cathode transmission foil is shown in Figure 8. Some adjustment of diode geometry will be necessary to produce a more uniform current flow.

A summary of the simulations carried out for this general geometry appear in the table below.

Voltage MeV	Cathode Thickness Δ_s cm	kA			
		I_i^{tot}	I_i^{foil}	I_e^{tot}	I_e^{foil}
1.5	0.8	436	370	423	346
1.5	1.6	438	306	402	319
2.0	0.8	573	494	409	307

The simulations were all for R/d = 20 and the same position of transmission and reflexing foil relative to the cathode face as shown in Figure 5. The simulation results are in reasonable agreement with the NRL experimental data for R/d = 20 with respect to total ion and electrons currents [1]. The geometry was significantly different and so it is difficult to make a more concrete statement. The location of the transmission foil is further removed from the cathode face in the experiments and this may have an effect on the diode behavior. In the simulations, an electron current of ~200kA is seen flowing from the cathode shank to the transmission foil. Changes in this flow with the cathode foil moved further back are difficult to predict. Further simulations that are closer to the actual experimental configurations are being conducted and direct comparison can then be made with experiments.

REFERENCES

a) Science Applications, Inc., McLean, Virginia 22102

b) Jaycor, Alexandria, Virginia 22304

c) University of Maryland, College Park, Maryland 20742

[1] G. Cooperstein, Proc., IEEE Int'l Conference on Plasma Science, Montreal, Canada, p.80, June 1979. (IEEE Cat.#79CH1410-0 NPS); also see proceedings of this conference.

[2] A. Sternlieb, Shyke A. Goldstein, and Roswell Lee, University of Maryland Technical Report 79-059, December 1978 (to be published).

[3] Roswell Lee, Shyke A. Goldstein and D.P. Bacon, Bull. Am. Phys. Soc. 23, 762, (1978); also R.J. Barker, Roswell Lee, and Shyke Goldstein, Bull. Am. Phys. Soc. 23, 762 (1978).

[4] J. Boris, Proc. IV Int'l Conf. on Plasma Simulation, Naval Research Laboratory, Washington, D.C. (1974).

[5] L.V. Spencer, Energy Dissipation by Fast Electrons, NBS Monograph 1, Washington, D.C. 1959.

[6] G. Cooperstein, Shyke A. Goldstein, J.J. Condon, D.D. Hinshelwood, D. Mosher and S.J. Stephanakis, Bull. Am. Phys. Soc. 23, 800, (1978).

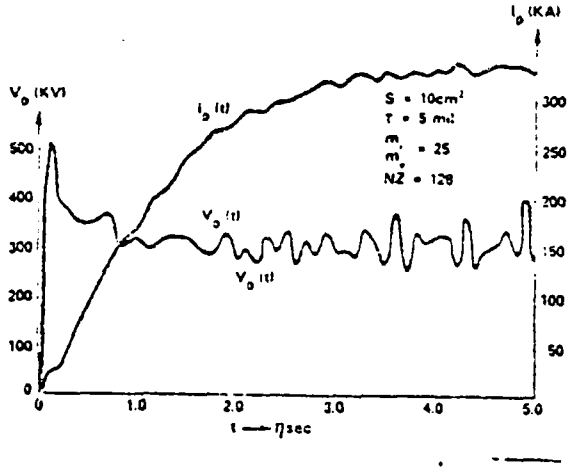

Fig. 1. Current and voltage characteristics of a double-reflex-diode from a self-consistent 1-D simulation.

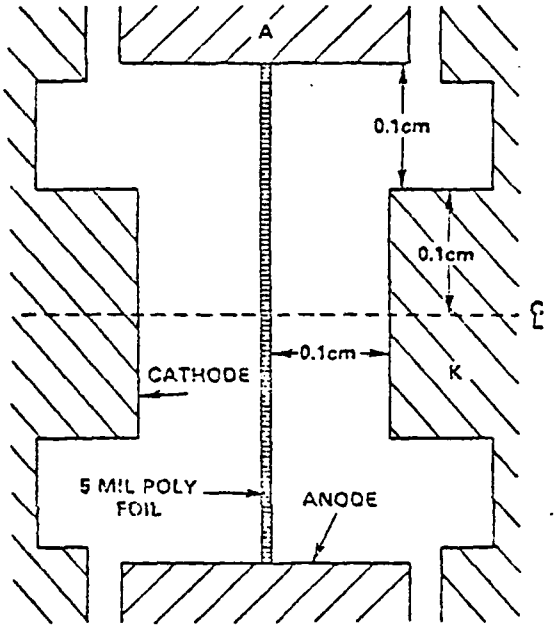

Fig. 2. The configuration of the reflex geometry used in the simulation. The simulation was done on a 128×50 mesh with a ~10000 particles and $\Delta T = 0.25 \times 10^{-13}$ sec.

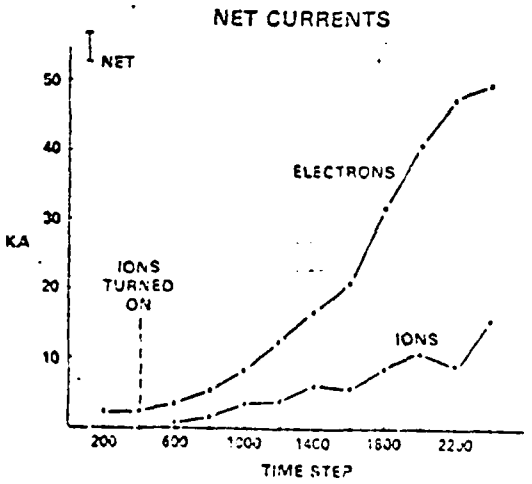

Fig. 3. Time history of the ion and electron current in the reflex diode showing "bootstrapping."

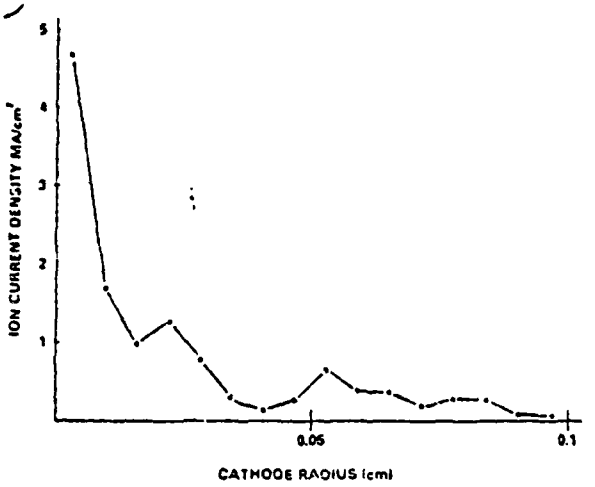

Fig. 4. The ion current density profile at the cathode. The total current was ~20kA.

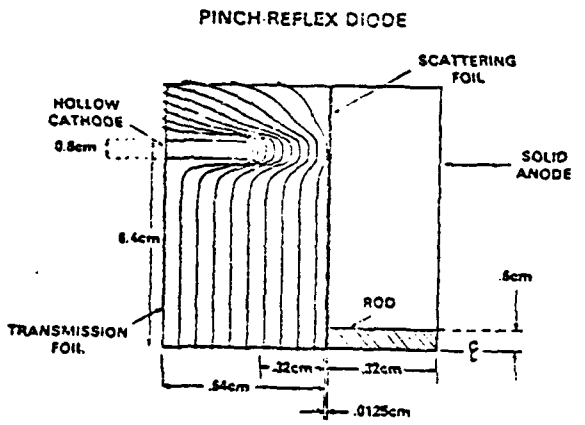

Fig. 5. Configuration used for pinch-reflex-diode simulations showing equipotential lines due to applied voltage of 1.5 MeV. Simulation was done on a 32×40 mesh with ~15000 particles, $\Delta T = 5\times10^{-13}$ sec and $M_i/M_e = 1837$.

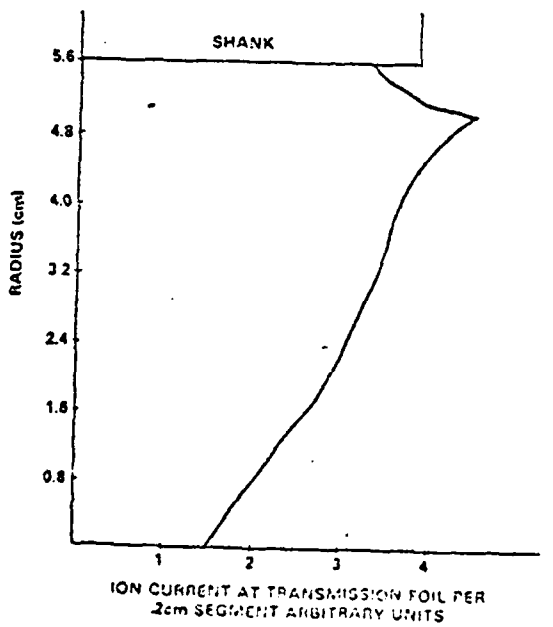

Fig. 8. The current profile of ions arriving at the transmission foil in radial segments of 0.2cm. Total ion current was 370kA.

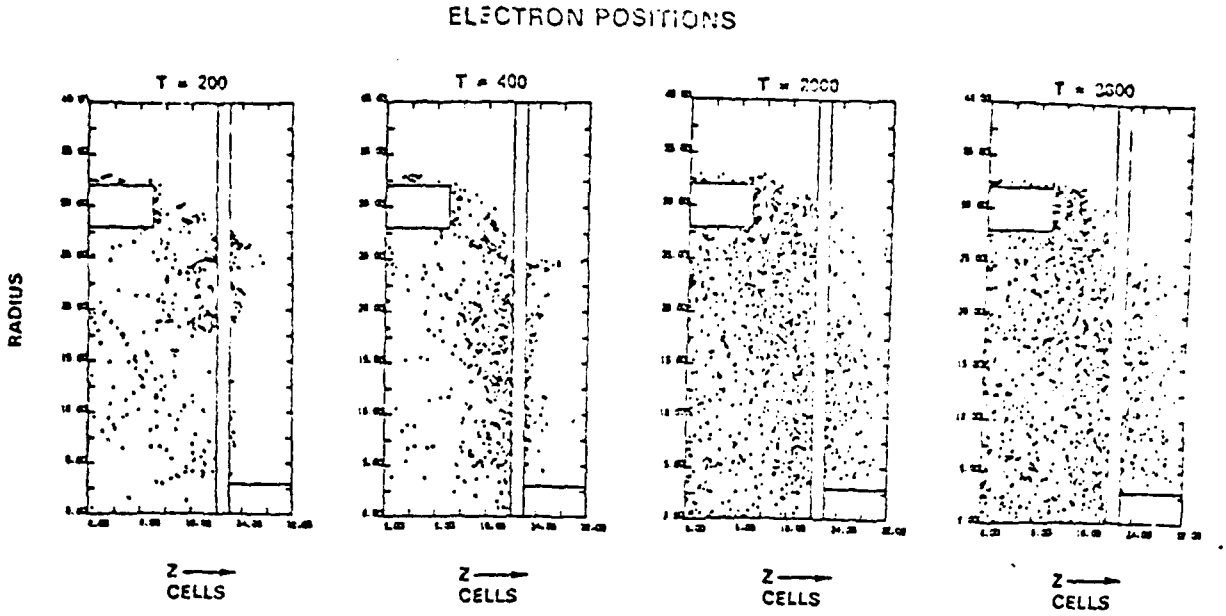

Fig. 6. Time history of the electron positions of the diode. One in ten is plotted on these graphs.

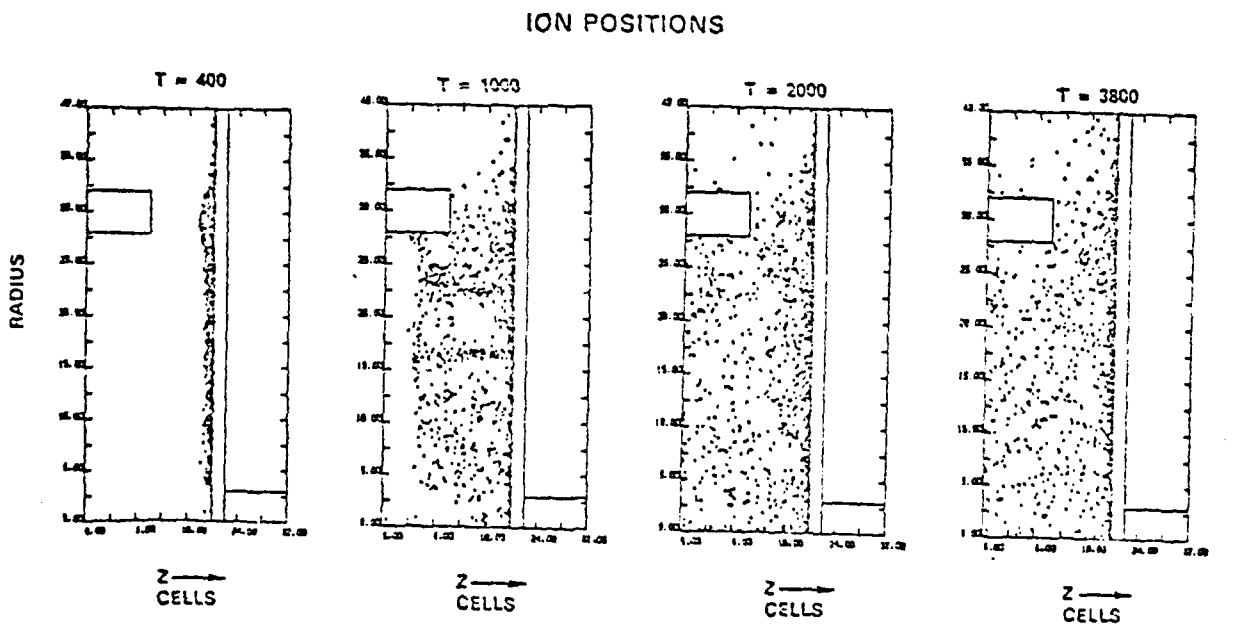

Fig. 7. The time history of the ion positions in the pinch-reflex diode corresponding to the electron history in Fig. 6.

THC1 Theory and experiments of terawatt light ion beams

DENIS G. COLOMBANT, G. COOPERSTEIN, A. DROBOT, SHYKE A. GOLDSTEIN, [illegible] MOSHER, P. [illegible] NARIS, and F. [illegible] Laboratory, Washington, D.C. 20375; and R. GULLICKSON, Physics International Co., 2700 Merced St., San Leandro, Calif. 94577

The use of light ion beams (protons, deuterons, etc.) for ICF was proposed a few years ago[1] and is based on the discovery that intense ion beams (>1 TW/cm²) can be used to generate hot plasma efficiently (>50%) with megampere currents at the megavolt level. Preliminary results of ballistic focusing[1] of the ion beams as well as a scheme for transporting[2] the beam in a plasma Z discharge were presented at the 1978 CLEOS/ICF meeting.[3] Recently, a systematic theoretical and experimental study has established those results to above 100 kJ in the ion beams, and first experiments of ion beam transport were performed.[4]

Based on these studies, two different approaches have emerged that for regulating the problem of using a few modules for the generation and overlap of the ion beams to achieve megajoule energies[3] on target. One approach calls for using pulse power techniques for pulse compression, magnetic insulation flow in vacuum transmission lines, and a small ion diode in close proximity (≲20 cm) to the target. The second approach involves the use of plasma channels (a few meters long) for pulse compression of the ion beams by bunching and overlapping the beams in a field-free region. There may be about ten modules.

In this paper we summarize the major results of a combined experimental and theoretical study of each approach. For convenience, we divide the problem of ion beam delivery into three parts: (a) ion beam source, (b) focusing, and (c) transport.

(a) The highest current density of protons at the source was in excess of 10 kA/cm² in the pinch-reflex diode, which matches with self-magnetic insulation. This diode[1] has been studied by numerical simulation techniques and in experiments on the generators GAMBLE 2 and PITHON. The comparison between theory and experiments of the time dependence of total current, voltage, and ion current shows good agreement for both proton and deuteron beams. New studies show that static and inductive effects play a role in the electron flow pattern that affects the details of ion beam divergence in the diode (a few degrees). The ion current efficiency for diode impedances near 1 Ω was ~70% for protons and 60% for deuteron beams. The maximum energy of the ion beam exceeded 100 kJ, and the peak power was ~2 TW. Typical diagnostics include neutron production in beam target interactions producing a $\lesssim 10^{14}$ neutrons.

(b) Two modes of focusing were studied, self-magnetic focusing and ballistic focusing.[4] The diode magnetic fields are large enough to bend the ion orbits so that self-ion pinching in diode was observed. However, in the mode of ballistic focusing curved anodes dominate over the magnetic field effect.[1] Behind the thin cathode foil a gaseous medium of a few torr was used to provide space charge and current neutralization (95% neutralization observed). The focal distances were near 10 cm and based on neutron time of flight from small (CD_2)$_n$ targets, ~300 kA/cm² focal spots were observed.

(c) The magnetic field of a plasma Z discharge is used to provide the required focusing and beam confinement field after focusing. Channel transport of the ions by the discharge electric fields and single-particle processes are discussed. The effects of ion and electron flow instabilities are divided into two groups: (a) fields and low-velocity waves that affect ion transport and (b) high-velocity waves that affect ion energies below 10 MeV. The single-particle energy losses and channel densities below 2×10^{19} ions/cm³ are calculated.

Energy losses in the electric field that provides the return current (≲ 1 kV/cm) and are reduced for lower plasma densities that allow higher current densities. The plasma density is high enough to provide collisional damping of many plasma instabilities and only for $J_i > 10^6$ A/cm² do these effects become important. However, as such current densities for ~50-nsec pulses are approached, a lower limit to the plasma density ($\gtrsim 2 \times 10^{14}$ ions/cm³) is established. The physics for that process is the $J \times B$ expansion forced by the magnetic field action on the return current in the plasma. During such expansion the frozen-in magnetic flux expands with the plasma, and the ion beam is allowed to expand to larger radii, reducing its current density.

The above effect is not severe during a 50-nsec pulse for 5×10^{14} ions/cm³ and becomes less of a problem as the beam bunches during transport, since the expansion is linear with the current density but squared with pulse time. We thus conclude that ion beam density of 10^6 A/cm² may be transported with a convenient window of gas pressure. Experiments were performed with 50 kA in wall-ablated Z pinches, and ion beam propagation over 1 m was observed with efficiency of ≲50%. The uncertainty is due to unknown energy losses in the gas. (25 min)

1. G. Cooperstein *et al.*, in *Digest of Topical Meeting on Inertial Confinement Fusion* (Optical Society of America, Washington, D.C., 1979), paper WB6; S. A. Goldstein *et al.*, Phys. Rev. Lett. 40, 1504 (1978).
2. S. A. Goldstein *et al.*, in *Digest of Topical Meeting on Inertial Confinement Fusion* (Optical Society of America, Washington, D.C., 1979), paper WB7.
3. J. H. Nuckolls, in *Digest of Topical Meeting on Inertial Confinement Fusion* (Optical Society of America, Washington, D.C., 1978), paper TuA5.
4. D. Mosher *et al.*, in *Digest of Topical Meeting on Inertial Confinement Fusion* (Optical Society of America, Washington, D.C., 1980), paper THC5.

THC5 Focus control in high-current light ion diodes

D. MOSHER, G. COOPERSTEIN, and SHYKE A. GOLDSTEIN, U.S. Naval Research Laboratory, Washington, D.C. 20375

Megampere currents of 1–2-MeV protons and deuterons have recently been extracted from 100-cm² pinch-reflex diodes coupled to >1-TW transmission line generators.[1] Utilization for ICF requires that many such beams be transported and combined onto the pellet. Other research has demonstrated that centimeter-diameter Z-discharge plasma channels conducting toward the target can be used to transport the beam extracted from each module provided that ions can be efficiently focused onto the entrance aperture of each channel.[2,3] For practical reasons, it is desired to limit the externally driven discharge current to ≲100 kA. Thus, only beams with sufficiently small transverse energy can be confined and transported. For ions of a few mega-electron-volts, the angle of injection into the channel should not exceed ~15°. Thus, ions extracted from a 5–10-cm beam diode must be brought to focus ≳10–20 cm downstream, requiring an aiming-angle accuracy of ≲4–2°. This degree of focus control with megampere-level ion beams requires analysis of radially and time-dependent self-magnetic-field effects in the diode. Focus-compensating techniques involving electrode shaping and electrode-plasma motion are the subject of this paper.

In the paraxial-ray limit appropriate for small-angle focusing, the problem can be analyzed using

$$\theta_i(r,t) = \theta_0(r) - \omega_c(r,t)\Delta(r,t)/v(t),$$

where θ_i is the angle between the direction of an ion exiting the cathode foil and the z axis, θ_0 is the ion launch angle at the anode surface and normal to it, ω_c is the ion cyclotron frequency associated with diode B_θ fields, v is the ion velocity determined from the accelerating voltage, and Δ is the anode-cathode gap determined from contouring and plasma motion of the two electrodes. Since the cathode foil separates the vacuum diode from a field-free low-pressure-gas-filled focusing drift section, ions exiting the diode execute straight-line ballistic orbits to the focus. Good focusing is then described by $\theta_i = -r/F$, where F is a fixed distance separating the cathode foil and focus.

Experiments and particle-in-cell computations[4] show that the diode magnetic field increases slower than linearly with r. Diode geometries for which Δ increases with r are presented. These compensate for unfavorable $B_\theta(r)$ variations as shown by analytic and computational techniques. The time variations of B_θ and v for desired accelerating-voltage pulses increase magnetic bending of ions with time. Analysis indicates that the time variation in focus location can be reduced by the natural reduction of Δ with time due to electrode-plasma motion. Currently interesting ICF scenarios require anode-cathode foil closure velocities of 4–8 cm/μsec, values within the range of experimental observation. (12 min)

1. G. Cooperstein *et al.*, at Third International Topical Conference on High Power Electron and Ion Beam Research and Technology, Novosibirsk, U.S.S.R., 3–6 July 1979.
2. D. Mosher *et al.*, Ref. 1.
3. J. R. Freeman *et al.*, Ref. 1.
4. A. T. Drobot *et al.*, Ref. 1.

Reprint from

"PLASMA PHYSICS
AND CONTROLLED
NUCLEAR FUSION RESEARCH
1980"

VOL. II

INTERNATIONAL ATOMIC ENERGY AGENCY
VIENNA, 1981

PROGRESS AT NRL AND CORNELL IN LIGHT ION BEAM RESEARCH FOR INERTIAL-CONFINEMENT FUSION*

G. COOPERSTEIN, S.A. GOLDSTEIN†, D. MOSHER, R.J. BARKER†, J.R. BOLLER, D.G. COLOMBANT, A. DROBOT††, R.A. MEGER†, W.F. OLIPHANT, P.F. OTTINGER†, F.L. SANDEL†, S.J. STEPHANAKIS, F.C. YOUNG
Naval Research Laboratory, Washington, D.C.

G. GINET, D.A. HAMMER, S. HUMPHRIES, Jr.§, J.N. NERI, R. PAL, R.N. SUDAN
Laboratory of Plasma Studies, Cornell University, Ithaca, New York, United States of America

Abstract

PROGRESS AT NRL AND CORNELL IN LIGHT ION BEAM RESEARCH FOR INERTIAL-CONFINEMENT FUSION.

Proof-of-principle and scaling experiments for light-ion-driven inertial-confinement fusion are in progress at NRL. Important advances have been made in the areas of ion production with pinch-reflex diodes and of beam focusing and transport. At Cornell, light-ion beams of Li^{+1}, B^{+1} and C^{+1} have been produced and work on producing low-divergence ion beams has progressed.

1. INTRODUCTION

Proof-of-principal and scaling experiments for light-ion-driven inertial-confinement fusion are in progress using generators which are appropriate for use as ignition-system modules. Intense beams extracted from ion diodes already have particle energies, currents and pulse durations which could satisfy system requirements related to ion production, focusing and transport to an ICF target [1]. Recent results in light-ion-beam research at NRL and Cornell are summarized below.

---

* Work supported in part by US Department of Energy and US Defense Nuclear Agency.
† JAYCOR, 205 S. Whiting Street, Suite 500, Alexandria, VA 22304.
†† Science Applications, Inc., 8400 Westpark Drive, McLean, VA 22101.
§ Sandia Laboratories, Albuquerque, NM 87115.

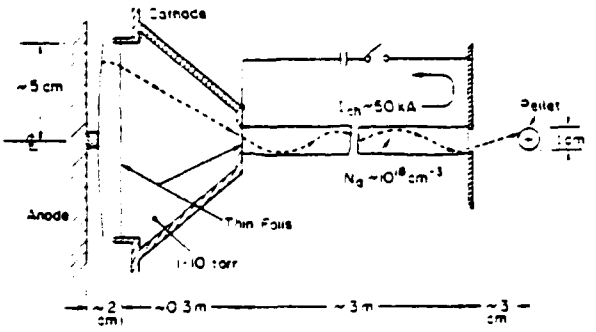

FIG.1. Conceptual schematic of VRL light-ion inertial-confinement fusion approach.

centimeters to the pellet with low divergence because of the small transverse velocity. Several ion beams can then be overlapped onto the pellet.

2.1. Ion Production

In the most recent positive polarity experiments [2] on upgraded [3] GAMBLE II at 1.3 TW, ~ 60% conversion efficiency from generator power to ion power was achieved using a planar version of the curved pinch-reflex ion diode schematically illustrated in Fig. 1. A thin CH_2 foil stretched across a dielectric ring is electrically connected to the positive electrode by a 1-cm-diameter rod on the diode axis. Plasma formation due to surface flashover causes the plastic foil to become a conductor early in the pulse and provides a source of ions. This geometry enhances ion emission by increasing the electron path length (and therefore lifetime) relative to that of ions by forcing the electrons to reflex through the thin foil as they pinch in radially. This reflexing in the vacuum gap behind the foil is due to the azimuthal self-magnetic field caused by the return-current flow through the center conductor. In front of the foil, the electrons reflex in the self-consistent diode fields. The ions that are produced on the back of the anode foil do not carry diode current because the back plate is at anode potential. Results of the numerical simulation of this diode configuration are discussed elsewhere [4].

Typical diode electrical characteristics on GAMBLE II are shown in Fig. 2a for a 6-cm cathode radius, a 0.4-cm anode-cathode gap spacing, and a 0.5-cm vacuum gap behind the 0.01-cm CH_2 anode foil. Ion currents of 0.5 MA have been

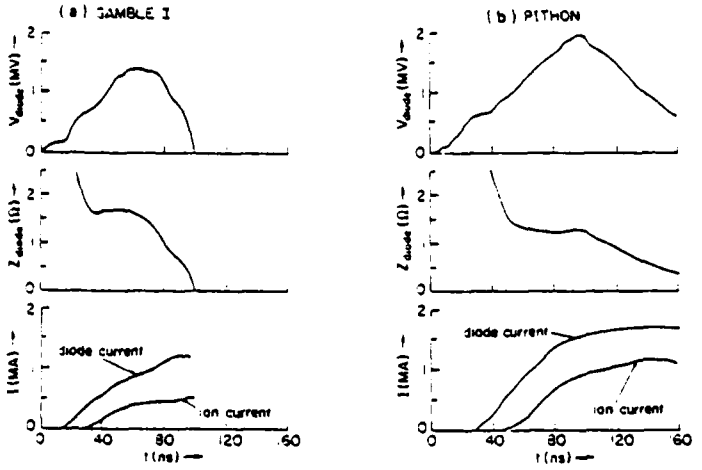

FIG.2. Diode electrical characteristics for Gamble II and Pithon.

measured with 0.9-MA total diode currents. This corresponds to an average source-ion current density of 5 kA/cm^2. The net current signal (the current entering the cathode foil) is interpreted as the total ion current flowing in the anode-cathode gap. The location of the Rogowski coil used to make this measurement is illustrated in Fig. 3.

In other ion production experiments [5], a pinch-reflex ion diode similar to that used on GAMBLE II was successfully operated at 3 TW on the Physics International PITHON generator. The main difference between the geometry used on GAMBLE II and that used on PITHON was that PITHON presently only operates in the negative polarity mode. Deuteron-current measurements were made in the conventional manner by coating the anode foil with CD_2 and using both nuclear activation and neutron time-of-flight detectors to detect the neutrons produced from a greater than one-range-thick CD_2 target placed behind the cathode.

Typical diode electrical characteristics on PITHON are shown in Fig. 2b for a 6-cm cathode radius, a 0.3-cm anode-cathode gap spacing, and a 0.5-cm vacuum gap behind the 0.01-cm CH_2 anode foil. Peak diode voltages of 2 MV at 1.5-MA diode current were obtained with flat impedance behavior even though the pulse length was almost twice as long as that on GAMBLE II. Ion currents of up to 1 MA were obtained corresponding to peak ion powers approaching 2 TW. Over 100 kJ

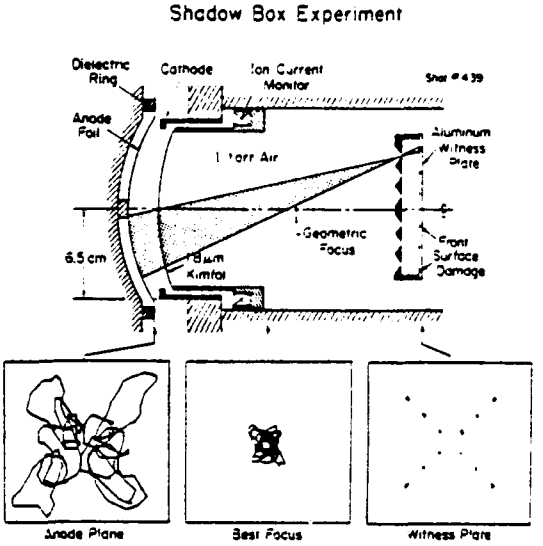

FIG.3. Geometric focus geometry showing ion current monitor and ion pinhole shadow box.

of ions were produced out of just over 200 kJ of electrical energy delivered to the diode. Impedance control and electrical reproducibility were excellent. When deuterons were produced, the neutron yield approached 10^{13} from the D-D and D-carbon reaction occurring in the CD_2 target. These results demonstrate that pinch-reflex ion diodes can successfully be operated at higher voltages and currents as well as longer pulse lengths.

The voltage and ion currents produced on PITHON are in the range required for a single module of a multi-module pellet ignition system. The long impedance lifetimes and high reproducibility associated with the ∿ 1-cm gaps between the anode and cathode transmission foils indicate that programmed-voltage waveforms for beam bunching during transport can be employed. Focus-perturbing effects associated with time-varying B_θ fields in the diode region can be controlled for these ∿ 1-cm diode gaps by electrode shaping and naturally occurring gap closure [6].

An ion diode has recently been installed on one arm of the AURORA accelerator at HDL. First experiments have been performed at the 1.3-TW level (∿ 1/3 available power for one arm) and have produced ∿ 50 kJ of 5-MeV protons [7]. About 10^{13}

neutrons per shot were observed when the ∿ 70-kA, 140-ns-duration proton beam was incident on a thick LiCl target. The diode consisted of a 10-cm-diameter cylindrical cathode separated from a polyethylene anode by ∿ 5 cm in a pinch-reflex diode configuration. The diode impedance during ion acceleration was ∿ 25 ohms. Ion production efficiency was ∿ 30%. This high efficiency (∿ 7 times bipolar flow) appears to be the result of electron-orbit lengthening due to ∇B drifts when the total diode current exceeds the Alfvén current.

These experiments represent an effort to scale results on lower-impedance machines (GAMBLE II and PITHON) to higher -voltage and -impedance diodes at high beam energy levels. Although the ion efficiencies are less than on lower-impedance machines, the "stiffer" high-voltage beam can be ballistically focused to smaller spot sizes in long focal-length geometries. Initial pulsed-power investigations on the AURORA accelerator show that the positive-polarity operation required for beam transport is practical. Additional energy may be obtained by overlapping ion beams from the four arms of AURORA.

2.2. Beam Focusing

In order to achieve high ion current densities, a 0.025-cm-thick spherical-section plastic anode foil with a 12.7-cm radius of curvature was used on GAMBLE II as shown in Fig. 3. In this short-focal-length geometry, the ion launch angle at the anode exceeds the magnetic deflection in the diode. Focal spot broadening due to radial- and temporal-field effects is thus minimized. When the anode was coated with CD_2, the observed focus was close to the geometric focus. By using small CD_2 targets and measuring neutrons from D-D and D-carbon reactions with activation counters and time-of-flight detectors, peak deuteron current densities of about 300 kA/cm^2 were inferred. Typical neutron yields were a fraction of 10^{12} neutrons from 0.5-1 cm^2 targets.

Important new experimental results for focusing are provided by a pinhole shadowbox diagnostic shown in Fig. 3. Small ion beamlets are produced by masking off all of the beam drifting in the neutralizing background except for that protion emerging through 1-mm-diameter holes placed along two diameters at right angles. When the shadowbox is placed further from the diode than the center of the ion focus, these orbits can be projected from the damage spots back through the pinhole to the focus and then to the anode plane. The radial extent (typically a few millimeters) of each damage pattern reflects the time-variation of deflection angle due to time-varying diode fields. The significantly smaller observed azimuthal extent

of damage compared with the radial extent of damage suggests that with proper aspheric anode and cathode shapes, focusing of ion beams to areas much less than the present 1-3 cm^2 should be possible.

For the present ion transport experiments on GAMBLE II, the planar, pinch-reflex diode configuration previously discussed was used to bring a 0.5-MA, 1.4-MV proton beam to a narrow-angle focus (~ 50 kA/cm^2) 20-30 cm downstream from the diode [8,9]. The long focal length was achieved by magnetic self-focusing acting alone in the diode gap in the flat-anode geometry. This configuration was employed to inject ions into the transport channel since larger-angle injection required excessive transport-channel currents.

2.3. Beam Transport

The transport section consisted of a copper pipe containing an insulating ceramic liner filled to the 0.2-2 torr air background pressure of the focusing-drift section. The inside diameter of the ceramic liner defines the diameter of the wall-stabilized discharge. Discharge-channel diameters of 1.6-4.5 cm were employed. The discharge current rose to about 50 kA in less than 1 μsec after which time the ion beam was injected into the channel. This channel current was enough to provide radial confinement for ions entering the channel with the maximum 10° angle. Measurements of transport efficiency were provided by diagnosis of 6-MeV gamma rays produced by the interaction of beam protons with fluorine [9]. Collimated scintillator-photomultiplier detectors were used to detect the gamma rays produced in 50%-transparent Teflon screens placed at the entrance and exit apertures of the transport system.

The results of the analysis of the prompt γ-signals indicate that 100-kA-level beams were transported over 1 meter distances with 50 to 80% efficiencies. The calculated efficiencies have large uncertainties associated with unknown ion energy losses occurring in the diode, focusing and transport sections.

Theoretical analysis of the plasma response to beam passage using a MHD code indicates that the channel plasma density must be $\geq 10^{18}$ nucleons/cm^3 in order to prevent excessive channel $\vec{J}\times\vec{B}$ force expansion during beam passage [10]. Ion energy loss due to the stopping power of the plasma sets the upper limit on the plasma density. Additional ion energy losses occur in the electric field generated by return currents and plasma expansion although such losses may be reduced or

even converted into an energy gain by injecting the beam into an imploding channel [11]. In expanding channels, the transportable beam current is limited to under 1 MA for each arm of a modular system unless a larger-diameter channel followed by a final-focussing stage is employed [12]. These considerations combined with pellet requirements set a lower limit on the number of modules [1,2].

Other theoretical considerations [13] show that small electric fields and modifications of the radial profile of B_θ produced by beam passage do not seriously affect beam bunching. Analysis also shows that growth of sausage-like modes in the channel do not seriously affect beam transport and that velocity space instabilities are either quenched by collisional effects or do not grow to levels which will inhibit good beam transport. Further theoretical analysis is underway.

3. CORNELL ION BEAM ICF PROGRAM

Ion beam ICF research at Cornell has been concerned recently with the generation of ion beams other than protons, and with studies of ion beam divergence both in magnetically insulated ion diodes and during beam propagation. Some experiments and theoretical modeling which address these topics are described below.

3.1. Generation of Li^{+1}, B^{+1} and C^{+1} Beams

Most intense light-ion-beam work to date has involved proton or deuteron beams. The anode in such work is typically a hydrocarbon plastic. It has been suggested that heavier ions, such as Li or C, should be superior to protons as light-ion ICF drivers because of their substantially higher specific energy deposition than protons of comparable energy [14]. Lithium ionization potentials are such that it is likely to exist as a pure singly-charged species in an anode plasma, whereas it may be that C^{+4} can be made the principal species in a carbon beam. This raises the possibility of an 8-MeV C^{+4} beam using the 2-MV PBFA I accelerator now nearing completion, and 16 MeV using the 4-MV PBFA II accelerator scheduled for operation in the middle 1980's.

In recent exploratory experiments, 200-300 keV beams which were predominantly Li^{+1}, B^{+1} and C^{+1} were produced using lithium fluoride (LiF), boron nitride (BN) and Teflon ($(CF_2)_n$), respectively, as the anode plasma source in a magnetically insulated (MI) diode. The diode used for these experiments is of the type described by Maechen et al. [15]. Briefly, it

has a concentric "racetrack" design with the anode inside the cathode. One flat side of the anode has the anode plasma-source material mounted on it opposite a set of extraction slots in the cathode. The cathode serves as a single-turn coil to provide the magnetic insulation. The diode is driven directly by a Marx generator providing beam pulses which are typically 200-300 nsec wide with a diode gap spacing of 4 mm. Current densities and species determinations with the different anodes were made using magnetically insulated, biased Faraday cups with and without 2-μm mylar "filters", magnetic mass spectroscopy combined with time-of-flight analysis, and secondary ion mass spectroscopy. The results indicated that beams consisting of (74 ± 10)% Li^{+1}, (72 ± 14)% B^{+1}, and (86 ± 8)% C^{+1} were produced using the LiF, BN and $(CF_2)_n$ anodes, respectively. The balance of these 40-60 A/cm^2 beams was protons, apparently from hydrocarbons due to the diffusion pump oil in the system. For reference when a polyethylene ($(CH_2)_n$) anode is used, 50-80% of the extracted beam is protons and the remainder is C^{+1}. For further details of these experiments, see Ref. 16.

3.2. Beam Divergence Studies

In any intense ion beam for use as an ICF driver, an important parameter for determining how well the beam can be focused is $j/\Delta\theta^2$. Here j is the current density which must be maximized, and $\Delta\theta$ is the beam divergency angle which must be minimized. Experiments on two different generators have achieved proton beam divergence angles of $2\frac{1}{2}^\circ \pm \frac{1}{2}^\circ$ at 200-300 keV and $\leq 1^\circ$ at 500-600 keV in magnetically insulated diodes operating at > 100 A/cm^2. In the lower voltage experiment, which used the diode described in Sec. 3.1, it was demonstrated that the anode configuration as represented by the type and thickness of the plastic, and the configuration of holes used to induce surface flashover, affected both the divergence angle and the current density. Divergence angles as low as 2° were measured, using several Faraday cups and many pulses to obtain a current density profile of a propagating beamlet obtained by masking the cathode. In the higher voltage experiment, a similar diode using a virtual cathode formed by metal vanes inserted into the diode gap was used [17]. By appropriate adjustment of the vanes, a uniform $\geq$ 200 A/cm^2, beam was produced. A divergence angle of $\leq 1^\circ$ was estimated by placing a screen mesh consisting of 0.38-mm wires in the beam path a distance of 10 cm from the cathode and observing the shadow of the screen in damage produced on aluminum 1.3 cm further downstream.

In a MI diode the ion beam is extracted through a drift space formed by slots in the cathode. Prompt charge neutralization by electrons is necessary to prevent beam expansion. In practice this occurs by (i) secondary electron emission from the side walls through ion bombardment and (ii) by extraction of electrons from the magnetized layer of electrons near the cathode. For successful space-charge neutralization [18] the wall-emitted electrons are thermalized, probably by micro-instabilities, and electron extraction from the magnetized layer is possible only if the magnetic field B drops off such that the axial potential gradient $|d\phi/dx| > B$. In any event, a space-charge potential $e\phi_o \geq 2m_e u_i^2$ builds up in the sheath [19] near the beam exit region to accelerate electrons. In a magnetic field-free region the electrons have a mean velocity approximately equal to the beam velocity and thermal velocity of the same order. When beams propagate across a magnetic field and space-charge neutralization from surrounding walls is inadequate, the electrons can acquire much higher thermal energy [20]. At a minimum, the ions are deflected in the direction transverse to propagation by $e\phi \sim 2m_e u_i^2$ so that the minimum divergence of the beam after propagating a distance $\sim a_o(m_i/Zm_e)^{\frac{1}{2}}$ is $\Delta\theta \sim \alpha(Zm_e/m_i)^{\frac{1}{2}}$, where α is of order unity and a_o is the initial beam radius.

Experiments have been performed using an "Applied Bθ-diode" [21] as a beam source in which a weakly focusing 2-10 kA, 300-keV proton beam is propagated over distances up to 40 cm in vacuum or low pressure (0.1 torr) helium gas. From the observed beam-ion flux density profiles as a function of axial distance, we conclude that it is charged neutralized. Measurement by Rowgowski loops show that the net current during the beam pulse was less than 5%. Severe beam distortion is observed when the beam is a thin ($\leq$ 1 cm) annulus. Substantial beam spreading is observed when the full 10-k 5-cm annular thickness beam is propagated, as compared to 1.25-cm-thick 2-kA annular sections of the beam.

Studies in all of these areas are continuing.

REFERENCES

[1] SUDAN, R.N., Bull. Am. Phys. Soc. 24, 925 (1979); JOHNSON, D.J., ibid.; MOSHER, D., ibid.; and GOLDSTEIN, S.A., et al., in Digest of Topical Meeting on ICF (Opt. Soc. of Am., Wash. DC, 1980), paper THC1.

[2] COOPERSTEIN, G., et al., in Laser Interaction and Related Plasma Phenomena, edited by H. Hora, H. Schwarz and B. Yaakobi, (Plenum Press, New York, 1980).

[3] BOLLER, J.R., BURTON, J.K., and SHIPMAN, Jr., J.D., in Proceedings of the IEEE Second International Pulsed Power Conference (Lubbock, Texas, 1979).
[4] DROBOT, A.T., et al., in Proceedings 3rd International Topical Conference on High Power Electron and Ion Beam Research and Technology (Novosibirsk, USSR, 1979).
[5] STEPHANAKIS, S.J., et al., Bull. Am. Phys. Soc. 24, 1031 (1979).
[6] MOSHER, D., COOPERSTEIN, G., and GOLDSTEIN, S.A., in Digest of Topical Meeting on ICF (Opt. Soc. of Am., Wash. DC, 1980) paper THC5.
[7] MEGER, R.A., et al., in Record, 1980 IEEE Int. Conf. on Plasma Sci. (Madison, Wisconsin, 1980) p. 58.
[8] SANDEL, F.L., et al., Bull. Am. Phys. Soc. 24, 1031 (1979).
[9] YOUNG, F.C., et al., NRL Memorandum Rep. 4171 (1980).
[10] COLOMBANT, D.C., et al., Bull. Am. Phys. Soc. 24, 1032 (1979). Submitted for publication.
[11] GOLDSTEIN, S.A. and TIDMAN, D.A., in Record, 1980 IEEE Int. Conf. on Plasma Sci. (Madison, Wisconsin, 1980) p. 96.
[12] OTTINGER, P.F., GOLDSTEIN, S.A., and MOSHER, D., ibid., p. 95.
[13] OTTINGER, P.F., ibid, p. 57; OTTINGER, P.F., MOSHER, D. and GOLDSTEIN, S.A., Phys. of Fluids 23, 909 (1980); also MOSHER, D., Ref. [1].
[14] See, for example, SUDAN, R.N. Phys. Rev. Lett. 41, 476 (1978).
[15] MAENCHEN, J., et al., Phys. Fluids 22, 555 (1979).
[16] NERI, J.M., et al., Appl. Phys. Lett 37, 101 (1980).
[17] NERI, J.M., et al., in Record, 1980 IEEE Int. Conf. on Plasma Sci. (Madison, Wisconsin, 1980) p. 57.
[18] SUDAN, R.N., in Proceedings of the Int. Conf. on Plasma Physics (Nagoya, Japan, 1980); also Cornell University Laboratory of Plasma Studies Report No. 280 (May 1980).
[19] HUMPHRIES, Jr., S., Appl. Phys. Lett. 32, 792 (1978).
[20] DREIKE, P.L., et al., Phys. Rev. Lett. 41, 1328 (1978).
[21] PAL, R., et al., in Record, 1980 IEEE Int. Conf. on Plasma Sci. (Madison, Wisconsin, 1980) p. 83.

DISCUSSION

J.P. WATTEAU *(Chairman)*: Does pressure have any effect on the ion-beam transport through the channel?

G. COOPERSTEIN: For the present experiments, which have total ion currents of ~ 100 kA at current densities of ~ 50 kA · cm^{-2}, the transport

efficiency appears to be independent of pressure from 0.5 to 2.0 torr. However, channel hydrodynamic response calculations indicate difficulties in transporting ion beams much in excess of 1 MA · cm^{-2}. We shall have to wait for experiments at higher current densities in order to observe the effect of the pressure. It is calculated that for transport of 1 MA of protons in hydrogen the density (n_i) should be $(1-3) \times 10^{18}$ cm^{-3}.

Printed by the IAEA in Austria

LIGHT ION PRODUCTION AND FOCUSING WITH PINCH-REFLEX DIODES†

G. Cooperstein, Shyke A. Goldstein*, R.A. Meger*, D. Mosher,
W. F. Oliphant, F. L. Sandel*, S. J. Stephanakis,
F. C. Young and H. U. Karow**

Naval Research Laboratory
Washington, DC 20375 USA

ABSTRACT

Light-ion ICF requires the development of diodes which can efficiently produce high-brightness ion beams, and which can aim the ions in a narrow cone towards a cm-diameter fusion target or transport-channel. Since candidate ion species span protons to carbon ions, diode behavior must be studied in a range of acceleration voltages (2-8 MV) and impendances (1-10 Ω) . NRL has developed a broad experimental data base using pinch-reflex diodes (PRD) on a variety of generators to address the issues of ion production efficiency and beam brightness.

I. INTRODUCTION

At the last meeting of this conference [1] we reported on 12 cm diameter PRDs used on the NRL Gamble II generator to produce over 700 kA of protons at 1.3 MeV and to focus 0.5 TW deuteron beams to about 300 kA/cm^2. A summary of our main PRD results since that meeting follows. High-power (~ 3 TW), low-impedance (~ 1 Ω) ion-diode behavior was studied on the PITHON generator in collaboration with Physics International Co. Greater than 100 kJ of protons or deuterons were produced with 60-70% efficiency at ion powers approaching 2 TW using a 12-cm diameter PRD [2]. The evolution of the electrode plasmas in the presence of high diode self-magnetic fields was measured on PITHON using four channel holography [3]. The scaling of PRD behavior to high-voltage (~ 5 MV) and high-impedance (5-20 Ω) operation is being studied on the AURORA generator in collaboration with Harry Diamond Laboratory. Experiments performed on one arm of AURORA yielded 60 kA of 5 MeV protons from a 20 Ω PRD [4]. These experiments are continuing in positive polarity on one arm that has been modified [5] to maximize power flow and ion efficiency at a lower diode impedance (5-10 Ω). Experiments designed to study PRD operation on PBFA I modules at the 4 Ω and 0.8 TW level were performed on the NRL Gamble II device. Ion- production efficiencies of about 40% have been obtained with 6 cm-diameter PRDs. Efficiencies of about 70% are obtained when the same diode is operated at 1 Ω , i.e., ion-current densities at the anode

averaged 30 kA/cm^2 [6]. A new ion beam target measurement technique has been developed to allow determination of stopping powers of intensely focused deuteron beams [7]. Recent experiments have concentrated on determining the controlling factors for maximizing ion beam source brightness. This paper will review the highlights in each of these areas.

II. PITHON EXPERIMENTS

In order to study the scaling of low impedance (~ 1 Ω) PRD performance at higher powers and longer pulse lengths than available on Gamble II, experiments were performed on the PITHON generator operated at 3 TW. The evolution of anode-cathode (A-K) plasma surfaces, information essential for the design of high power focusing ion diodes, was also determined. Both planar and curved (focusing PRD) diode configurations, similar to the Gamble II designs previously reported [2,8], were studied.

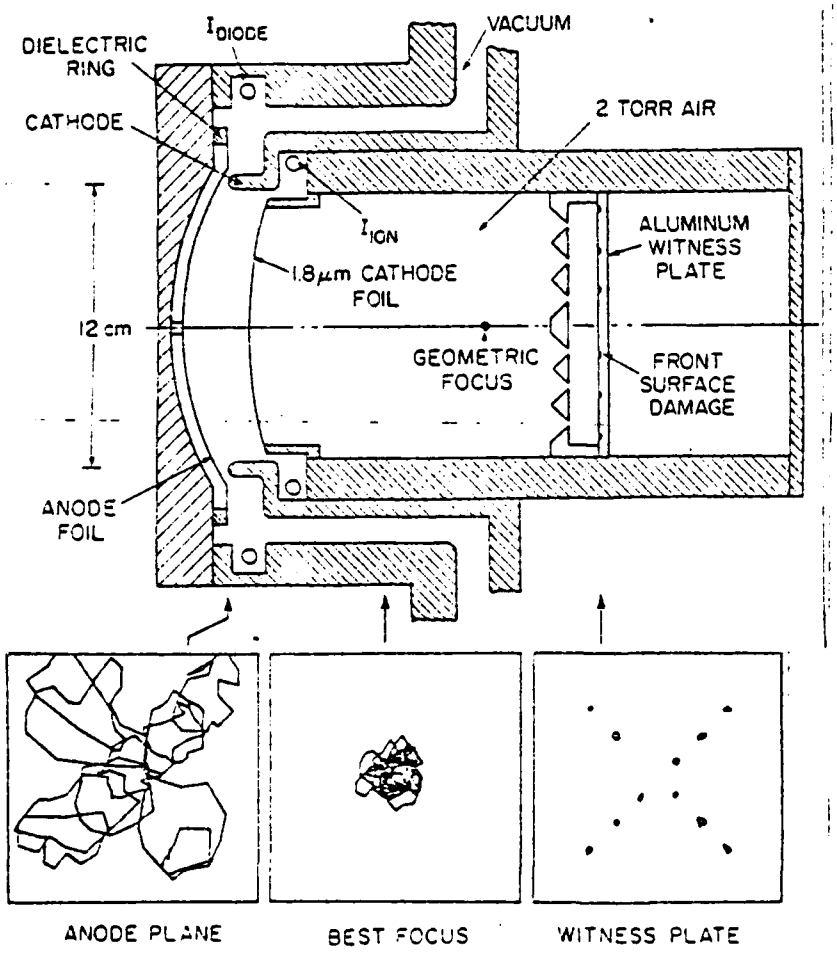

Fig. 1. PITHON focusing geometry with ion shadowbox ballistic reconstruction.

The focusing PRD illustrated in Fig. 1 is similar to the planar diode except that the anode foil and backing plate form a 12 cm radius-of-curvature spherical section. The shadowbox diagnostic and damage patterns shown in Fig. 1 will be discussed later. The PRD geometry enhances ion emission by increasing the electron path length (and therefore lifetime) relative to that of ions by forcing the electrons to reflex through the thin foil as they pinch in radially. The ions, emitted perpendicular to the anode plasma, are accelerated through the diode potential while being radially deflected inward by their self-magnetic field. They then

pass through the thin cathode foil into a gas filled drift tube where space-charge and current neutralization allow them to drift ballistically toward a focus. A main difference between the geometries used on Gamble II and PITHON was that PITHON operates only in the negative-polarity mode. Because the transmission cathode is operated at high potential, special techniques for diagnostic access and gas filling were required. Deuteron current measurements were made by coating the anode foil with CD_2 and using both nuclear activation techniques and neutron time-of-flight detectors for neutrons produced from greater than range-thick CD_2 targets in the drift space.

Typical diode electrical characteristics are shown in Fig. 2 for the planar version of the diode shown in Fig. 1. It had a 12 cm cathode diameter, a 0.3 cm A-K gap spacing, and a 0.5 cm vacuum gap behind a 0.01 cm CH_2 anode foil. Peak diode voltages of 2 MV at 1.5 MA diode current were obtained with flat impedance behavior even for the 100 ns PITHON pulse. Ion currents of 1 MA were obtained with peak ion powers approaching 2 TW. Over 100 kJ of ions were produced out of about 200 kJ of electrical energy delivered to the diode. Shot-to-shot impedance control and electrical reproducibility were excellent. When deuterons were produced, the neutron yield approached 10^{13} from the d-d and d-carbon reactions occurring in the CD_2 target. The inferred deuteron current was consistent with the ion current measured by the Rogowski coil outside the cathode.

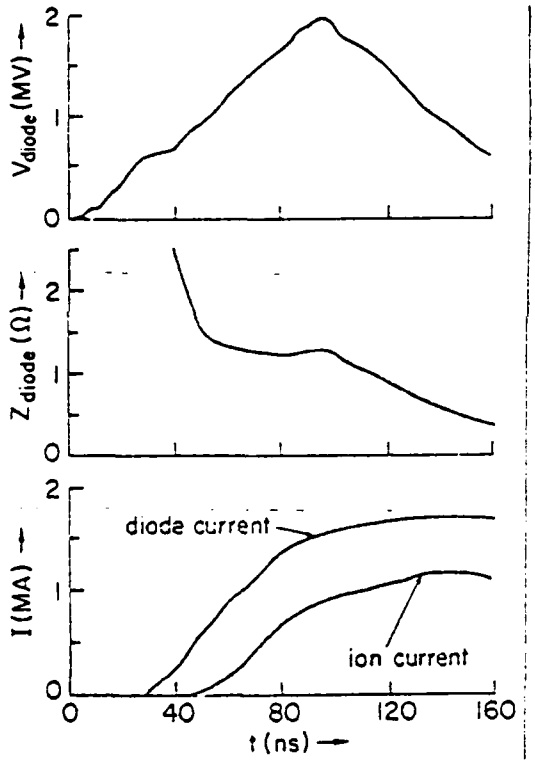

Fig. 2. PITHON electrical characteristics.

Approximately the same diode electrical parameters were obtained using the focusing electrode structure shown in Fig. 1. Here, the magnetic deflection of the ions in the vacuum causes the focus to occur about 4 cm closer to the diode than the geometric focus. The ion pinhole shadowbox was used to determine the time-averaged location and diameter of the best focus. The ion orbits are projected from each damage spot on the witness plate back through the corresponding pinhole through the focus to the cathode plane. The radial extent of each damage pattern reflects the

time-variation of deflection angle due to time-varying diode fields, gap closure and time-variations of anode-emission angle due to anode-plasma expansion. The smaller-observed azimuthal extent of damage reflecting other beam-divergence phenomena suggests that with proper aspheric electrode shapes, the ion focus diameter could be reduced to the 1 cm diameter scale desired for beam-target interaction experiments.

The diode used for holographic measurement of the electrode-plasma surfaces is somewhat different from the above diodes. The cathode was terminated in a smooth taper which allowed variation of the cathode radius. Both 6 and 12 cm diameter cathodes were tested. The anode was designed to allow direct viewing access of the diode A-K gap through an array of viewing holes.

The Physics International four-channel, 6 ns, ruby laser interferometric holography system was used to study the spatial and temporal evolution of the anode and cathode plasmas of diodes operated at 2-3 TW. The four laser pulses were separated by 10 ns each and data was taken on a number of shots in order to span the entire 100 ns power pulse. Preliminary analysis of surfaces of constant line density ($3 \times 10^{17}/cm^2$) show uniform expansion until a time near peak power. After peak power, anode plasma surface fluctuations and high velocity (up to 30 cm/μs) axial plumes were observed. During the power pulse collapse a high density ($n > 10^{18}/cm^3$) plasma bridges the anode-cathode gap. On some shots this high density plasma is later seen to open suggesting that magnetic field pressure is driving it back. Knowledge of the anode and cathode shapes at peak power suggests further research into techniques for forming more uniform plasmas is necessary for development of high-performance focusing ion diodes. The measured evolution of these shapes provides information required to design modifications to the simple spherical-section electrodes tested.

III. AURORA EXPERIMENTS

Ion diode experiments were performed on one of the four arms of the AURORA accelerator in order to scale results from lower-impedance generators to higher-voltage and higher-impedance operation at power levels above 1 TW. Initial experiments were performed in negative polarity with a 20 Ω PRD placed at the end of the 7 meter long, 50 Ω coaxial-magnetically-insulated transmission line driven by a 20 Ω oil insulated Blumlein. When the diode was operated at 1.3 TW (1/3 available power for one arm) 50 kJ of 5 MeV protons were produced. About 10^{13} neutrons per shot were observed when the 60 kA, 140 ns-duration

proton beam was incident on a thick LiCl target. The diode consisted of a 10 cm diameter cathode separated from a polyethylene anode by ~ 5 cm in a pinch-reflex diode configuration. The diode impedance during ion acceleration was ~ 20 ohms. Ion production efficiency was ~ 25% . This high efficiency (~ 6 times bipolar flow) appears to be the result of electron-orbit lengthening due to ∇B drifts when the total diode current exceeds the Alfven current.

When these experiments were repeated in positive polarity only ~ 0.8 TW could be coupled into a similar diode geometry. These reduced power results combined with the need to develop lower impedance (5-10 Ω) , more efficient ion diodes, and the need for improved diagnostic access to the positive center conductor have stimulated a reversible upgrade of one arm of the accelerator. First, a 5 meter long section of the vacuum coax was removed and an ion diode mounted just downstream of the tube insulator stack. Second, an inductive isolator carrying several coaxial cables was installed in the oil behind the insulator stack to allow direct diagnostic access to the center high voltage conductor.

The modified diode geometry with the new voltage and current diagnostics is illustrated in Fig. 3. The plasma erosion switches [9], supplied by C. Mendel of Sandia National Laboratories, are used to both suppress prepulse and to sharpen beamfront risetime. This installation allows the PRD to operate at the 2 cm A-K gaps required for 5-10 Ω operation. Preliminary experimental results are very encouraging. These demonstrate that > 1.5 TW has been delivered to the ion diode with ion yields matching or exceeding the negative-polarity results.

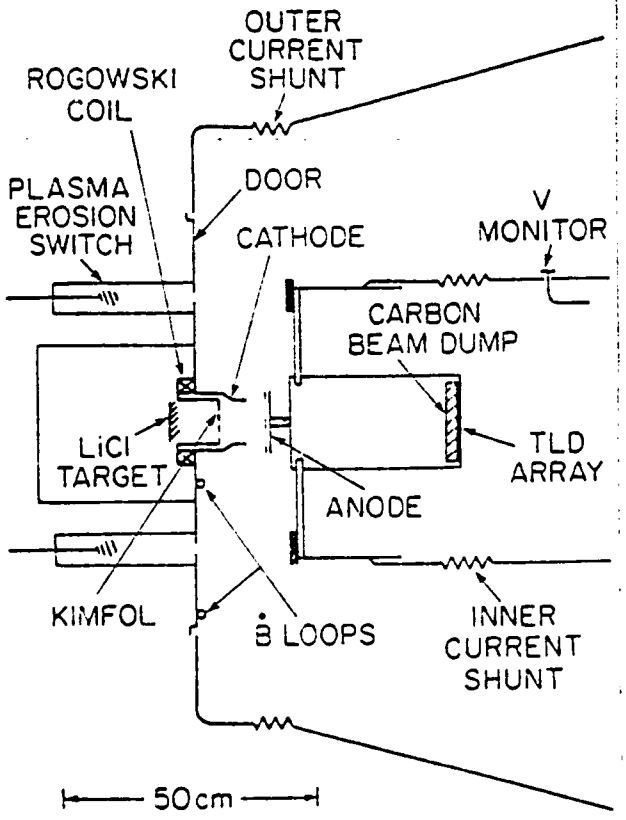

Fig. 3. Pinch-reflex ion diode on modified arm of AURORA.

The present plans with the installed modifications call for delivery of ~ 2.5 TW into a 5 Ω PRD and use of the resultant proton and deuteron beams in focusing,transport and

bunching experiments. Ultimately, it would be possible [10] to further upgrade one arm of AURORA to deliver 10 TW into a 5 Ω PRD. This power level is appropriate for one module of a multi-module light ion ICF system [11].

IV. GAMBLE EXPERIMENTS

Gamble II experiments have concentrated on studying PRD operation for PBFA I modules, developing beam-target interaction diagnostics and investigating beam brightness issues.

Experiments designed to develop efficient PRDs for operation on the 0.8 TW, 4Ω PBFA I modules have been performed on Gamble II. A variety of designs were tested for improved ion production efficiency at the desired impedance. About 40% efficiency was obtained with a 6 cm diameter PRD which had the portion of the anode foil opposite the cathode covered with a metal annulus of inner diameter slightly smaller than the inner diameter of the cathode. Experimental observations of the diode operation for this configuration include: 1) better symmetry of pinching and more reliable centering, 2) significant increase in impedance for a given A-K gap, 3) higher ion-production efficiency for a given impedance, and 4) better late-time impedance behavior even for very small A-K gaps.

This 6 cm diameter PRD geometry was also used with a smaller A-K gap (~ 2.5 mm) to obtain ion production efficiencies of about 70% at 1 Ω impedance levels. This resulted in average ion current densities at the anode of about 30 kA/cm^2. These small diameter, low-impedance experiments are designed to improve ion source brightness by increasing ion current density, without correspondingly increasing beam divergence.

A new beam-target interaction diagnostic has been developed and successfully used with focused deuteron beams from Gamble II PRDs. The goal was to measure the deuteron stopping power of target plasmas that are heated by the beam. The technique is based on using neutron time-of-flight (TOF) measurements from the d(d,n)^{3}He reaction to determine the deuteron energy loss. Deuterons are focused to high current density onto a sub-range layered target consisting of mylar foil coated on front and rear with a thin layer of CD_2. The TOF of neutrons from the two CD_2 targets is used to determine the deuteron energy loss in the stopping foil which has been heated by the intense ion beam. The ratio of neutron yields from the two CD_2 targets provides an independent determination of the energy loss if the thickness of these two targets is accurately known.

Preliminary experiments show evidence of enhanced stopping power at 100 kA/cm^2 level deuteron current densities. A more accurate experiment

is in progress to accurately determine the enhancement factor, current density and target temperature.

Recent experiments with 6 cm-diameter PRDs on Gamble II suggest that the ion-beam brightness is worse than anticipated from theoretical computations of diode time-variations described above and scattering. New beam diagnostics can separate design-correctable systematic focus variations from beam divergence associated with asymmetry and instability of the electrode plasmas and charged-particle flow. We have measured beam divergence angles about 3-times higher than the calculated half/angle of 0.03 rad [11].

An example of a new, time resolved intense ion beam diagnostic capable of measuring the diode exit angles of ions which are produced at different radii is given elsewhere in these proceedings [12].

The time integrated ion shadowbox technique is another diagnostic useful for determining diode phenomena important for focusing (Fig. 4). Here, the time-averaged ion-diode exit angle (θ) is measured as a function of cathode exit radius (r_c) for four shots with a 6 cm diameter (2R) PRD operated at 0.6 TW with a 1.2 cm anode cathode foil separation (Δ). Constant (θ) at large radius is due to the constant magnetic field associated with a 1/r ion current density distribution at the anode. The minimum angle at small radius is due to an expanding anode plasma caused by concentrated electron beam heating near the diode axis. The theoretical curve shown by the solid line is calculated assuming a Gaussian expansion profile of the anode plasma using a pinch radius measured from x-ray pinhole photographs. The reasonable agreement of experiment to theory corroborates the simple theoretical models used to predict ion divergence angles caused by magnetic bending and gross electrode plasma motion.

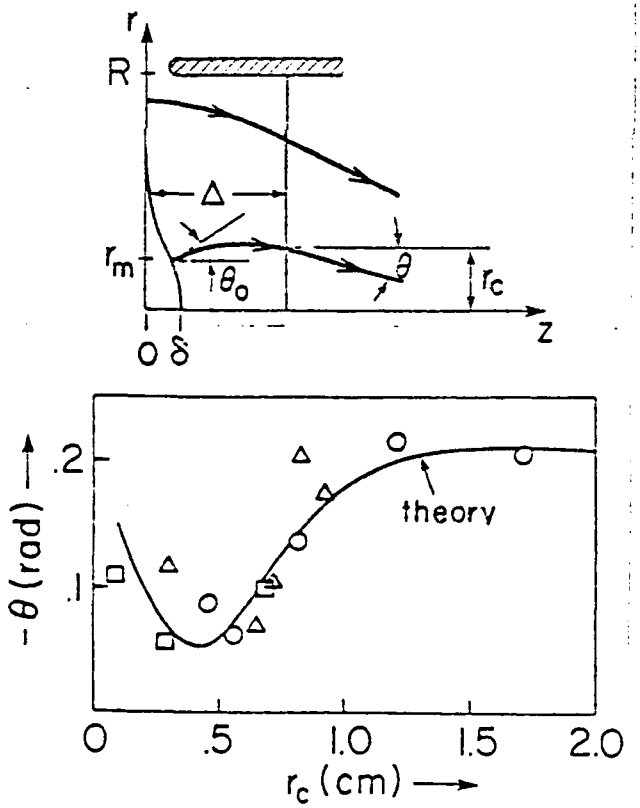

Fig. 4. Shadowbox analysis of Gamble II data.

Most of our present PRD experiments on Gamble II are designed to determine which aspects of the diode geometry affect beam brightness.

Electrode damage, anode bremsstrahlung and electromagnetic-code simulation point to the existance of filamentation instabilities as the main source of small-scale electric- and magnetic-field structures responsibile for enhanced divergence. Therefore, we are systematically studying variations of the anode and cathode geometry to determine their effect on beam divergence. Examples include variation of anode plastic foil thickness and the use of plastic foils backed by high and low Z conducting foils. These changes affect anode plasma formation. Examples of cathode variations include the use of highly polished or plated surfaces and scalloped cathode surfaces designed to enhance electron temperature in the azimuthal direction. The presence of a weak B_z field in the diode may slow growth of filamentation [13]. This effect will also be investigated. These studies will hopefully lead to diodes which generate the higher-brightness beams needed for light-ion ICF.

REFERENCES

†Work supported in part by Department of Energy, Washington, DC 20545 and Defense Nuclear Agency, Washington, DC 20305.

*JAYCOR, 205 S. Whiting Street, Suite 500, Alexandria, VA 22304
**Permanent Address: Kernforschungszentrum, Karlsruhe, W. Germany.

[1] G. Cooperstein, S.A. Goldstein, D. Mosher, F.W. Oliphant, F.L. Sandel, S.J. Stephanakis and F.C. Young, in the Proceedings of the 3rd International Topical Conference on High Power Electron and Ion Beam Research and Technology, Novosibirsk, USSR (1979).
[2] G. Cooperstein, S.A. Goldstein, D. Mosher, R.J. Barker, J.R. Boller, D.G. Colombant, A. Drobot, R.A. Meger, W.F. Oliphant, P. F. Ottinger, F.L. Sandel, S.J. Stephanakis and F.C. Young, Proc. of the Fifth Workshop on Laser Interaction and Related Plasma Phenomena, Laboratory for Laser Energetics, Rochester, NY, Nov. 1979.
[3] J.E. Maenchen, R. Genuario, R. Stringfield, G. Cooperstein, D. Mosher, S.J. Stephanakis, F.C. Young and S.A. Goldstein, to be pub.
[4] R.A. Meger, F.C. Young, A.T. Drobot, G. Cooperstein, S.A. Goldstein, D. Mosher, S.E. Graybill, G.A. Huttlin, K.G. Kerris, and A.G. Stewart, to be published in the J. Appl. Phys. 1981.
[5] J.R. Boller, J.D. Shipman, Jr., J.K. Burton, G. Cooperstein and R.A. Meger, in Conf. Rec. Abstracts (Proc. 1981 IEEE Int. Conf. on Plasma Science, Santa Fe, NM) IEEE Cat 81 CH1640-2 NPS, p. 5.
[6] S.J. Stephanakis, R.J. Barker, S.A. Goldstein and W.F. Oliphant, op. cit 4, p. 8.
[7] F.C. Young, S.A. Goldstein and S.J. Stephanakis, op. cit. 4, p. 91.
[8] S. A. Goldstein, G. Cooperstein, Roswell Lee, D. Mosher and S. J. Stephanakis, Phys. Rev. Lett. 40,1504 (1978).
[9] C.W. Mendel, and S.A. Goldstein, J. of Appl. Phys. 48, 1004 (1977).
[10] P. Champney and I. Smith, private communication.
[11] D. Mosher, D.G. Colombant, S.A. Goldstein and P.F. Ottinger, these proc.
[12] A.E. Blaugrund, S.J. Stephanakis and S.A. Goldstein, these proc.
[13] P. F. Ottinger, private communication.

ELECTROMAGNETIC AND QUASI-STATIC SIMULATIONS OF ION DIODES*

A. T. Drobot and A. Palevsky
Science Applications, Inc., McLean, VA

R. J. Barker and Shyke A. Goldstein
Jaycor, Inc., Alexandria, VA

G. Craig
Lawrence Livermore National Laboratory, Livermore, CA

D. Mosher
Naval Research Laboratory, Washington, D.C.

ABSTRACT

Two types of numerical simulations of ion diodes have been performed, one with the DIODE-2D magneto- and electro-static code, and the other with the MASK electromagnetic code. We present a brief description of the two codes and results of recent simulations. These include quasi-static simulations of pinch-reflex-diodes, which indicate that efficiencies approaching 50% may be achieved in operation at 4Ω and 1.8 MeV, and electromagnetic simulations of bi-polar flow in planar diodes, which indicate that the electron-ion flow filaments and may be an inherent source of ion beam divergence.

I. INTRODUCTION

The extraction of ion beams from pulsed power diodes at MA currents and MeV energies is presently the subject of intense research activity for Inertial Confinement Fusion (ICF) with ion beam drivers. The theoretical and experimental concern is the development of an ion source which satisfies the stringent requirements for ICF pellet ignition. In this context, the efficiency of the ion source, the beam brightness, the beam power, and the time dependent behavior of the ion energy distribution have all been recognized as important issues. Since the electron and ion flow is complicated and difficult to predict analytically, we have resorted to detailed numerical simulations of diode behavior. This paper describes results from numerical simulations of pinch-reflex-diode configurations, which have been used experimentally to generate light ion beams on GAMBLE-II at the Naval Research Laboratory and at the AURORA facility. To date most of the numerical simulations we have conducted have used the DIODE-2D quasi-static code. As the awareness of the physics issues concerning pulsed power ion diodes has evolved, it has become clear that while a quasi-static code may be adequate for describing diode operation in a rough overall sense (i.e., impedance scaling) it lacks the physics input to answer reliably more delicate

questions. To improve the situation we are adapting an electromagnetic code, MASK, for studying ion diode behavior. Preliminary simulation results of bi-polar flow in planar diodes indicate that electromagnetic effects may be responsible for filamentation of electron and ion flow and hence act as an inherent source of beam divergence.

A brief description and a discussion of the assumptions underlying the quasi-static simulations is presented in Section II. The results of numerical simulations of the pinch-reflex-diode with the quasi-static code appear in Section III. They describe diode operation at voltages ranging from 1.8 MeV to 5.0 MeV and impedances from 4 to 20 Ω. The indication is that efficiencies approaching 50% may be possible at 4Ω and 1.8 MeV. In Section IV we discuss the approach to electromagnetic numerical simulations and in Section V show the results from a model problem of bi-polar flow in planar geometry. Finally in Section VI we discuss some of the outstanding issues of numerical and analytical modeling of ion-beam diodes.

II. THE DIODE-2D QUASI-STATIC CODE

The DIODE-2D code uses a particle-in-cell model of electron and ion flow in conjunction with a two dimensional (R,Z) azimuthally symmetric electro- and magneto-static field solver to simulate steady state behavior. This kind of code has been used extensively by us and others in the past and detailed descriptions exist [1]. The limit in which the results are expected to be valid occurs when the electron and ion flows are in steady state equilibrium. The code's approach to equilibrium is through a sequence where test particle orbits are integrated one step at a time using the relativistically correct equations of motion and fields caalculated in the static approximation with charge and current densities due to the ensemble of test particles at that time step. That is:

$$\nabla^2 \phi(\vec{x},t) = 4\pi \rho(\vec{x},t), \quad \vec{E}(\vec{x},t) = -\vec{\nabla} \phi(\vec{x},t) \tag{1}$$

$$\vec{\nabla} \times \vec{B}(\vec{x},t) = \frac{4\pi}{c} \vec{J}(\vec{x},t) \quad , \tag{2}$$

where the equations are solved on a mesh with the charge density, ρ, and the current density, $\vec{J}$, found from the macro particles in the simulation. The flexibility of the code comes from the inclusion of boundary conditions for generalized geometries, space charge limited emission from designated surfaces, foil scattering algorithms, and diagnostics. While the transient behavior exhibited by the code does not represent the physically correct evolution, when convergence to steady state occurs, the code provides correct equilibrium solutions. We have used the code by specifying the diode geometry, fixed applied voltage, external magnetic fields, and regions of particle emission

and run until a steady state or near steady state was achieved. In that case the results unabiguously satisfy the assumptions of our model. In cases where no steady state is reached the results are open to interpretation.

III. PINCH-REFLEX-DIODE SIMULATIONS

The NRL light ion group has been experimentally generating proton beams at the AURORA facility with currents >50 kA at 5 MeV [2] and on GAMBLE-II at the lower voltage of 1.8 MeV with ion currents of ∿160 kA and efficiencies approaching 40% [3]. The interest in such intermediate impedance pinch-reflex-diodes is possible use on PBFA-I at Sandia. Quasi-state simulations were carried out in geometries that correspond to the experimental configurations. As a typical example, the diode geometry that was used on the AURORA experiments in positive polarity is shown in Fig. 1a, which also contains a contour map of the equipotentials. The important elements of the diode are the cathode shank, which acts as a primary source of electrons, the reflexing foil, which is a source of ions, the flux excluder, which limits the electron flow in vacuum from reaching the solid anode, and the return current rod, which helps to reflect electrons magnetically into the active anode cathode gap. Electron and ion flow patterns are shown in Figs. 1b and 1c and were taken at the same timestep as the equipotentials in Fig. 1a. It is quite clear that for the emission characteristics specified the flow in vacuum contributes significantly to the electron space charge. With no ion emission behind the foil, electron reflexing is improved by the existence of a virtual cathode. The results from a series of runs with various impedances, regulated by altering the cathode-foil gap, are shown below.

Voltage MeV	Impedance Ω	Efficiency $\eta = I_i/I_{tot}$	Cathode Radius cms	Comments
1.8	4.8	.40	6.0	
1.8	4.8	.32	3.0	
1.8	6.7	.28	3.0	
3.0	26.0	.12	6.0	
4.0	6.7	.48	5.0	
4.0	8.4	.43	5.0	
4.0	20.0	.13	6.0	ion emission for R < 3.3 cm
5.0	24.0	.20	6.0	

The results indicate that ion production improves with higher voltage for fixed impedance and with lower impedance for fixed voltage. The results are in good qualitative agreement with experimental observation. We have found some reasons for concern, however, because the simulations do not settle down to a steady state other than in an average sense. There are large

of ∿25. This may indicate the presence of instabilities or nonsteady flow.

IV. ELECTROMAGNETIC SIMULATION CODE

To gain an understanding of physics issues that cannot be treated under steady state assumptions, a version of MASK [4] has been adopted for treating diode problems. MASK is a 2D-3V particle-in-cell code with relativistic particle dynamics and a two dimensional electromagnetic field solver. The algorithms used are similar to those in other 2D EM particle codes [5]. However, adaptation to diode simulation required the generalization of boundary conditions and geometry, the inclusion of space charge limited emission, and the coupling between the simulation space and a lumped parameter generator model. As in the static case, the code integrates particle orbits in time with fields in the force equation interpolated from a grid at each step. The fields, however, are advanced in concert with the particles by time integration of Maxwell's equations:

$$\frac{\partial}{\partial t}\vec{E}(\vec{x},t) = c\,\vec{\nabla} \times \vec{B}(\vec{x},t) - 4\pi\,\vec{J}(\vec{x},t)$$

$$\frac{\partial}{\partial t}\vec{B}(\vec{x},t) = -c\,\vec{\nabla} \times \vec{E}(\vec{x},t) \quad .$$

where the expressions $\vec{\nabla} \cdot \vec{E} = 4\pi\rho$ and $\vec{\nabla} \cdot \vec{B} = 0$ serve only as initial conditions. Within the limits of the finite difference approximation for the integrations, the code self-consistently treats the time dependent behavior in the diode. This includes inductive as well as radiative effects and the correct transient evolution of the electron-ion flow. The major drawback in the use of this code is the limitation on timestep imposed by numerical considerations. This limitation is not introduced by the fact that the code is electromagnetic but by the particle and emission dynamics. For large currents and large current densities both the EM and quasi-static codes are constrained by spatial resolution in the emission region and by timestep in correctly following particle trajectories in large magnetic fields.

V. BI-POLAR DIODE FLOW

As a test problem we used the electromagnetic code to simulate a simple planar diode with electron and ion flow. The diode with its driving generator circuit is shown in Fig. 2. The boundary conditions were space charge limited emission for electrons at $x = 0$ and for ions at $x = d$ where $d = 4.8$ mm. With an applied voltage of 2.0 MV and an artificially fast rise time of 0.5 ns we followed the evolution of the electron and ion flow for 2 ns. For this simple problem steady state, as measured by the total current drawn, was achieved shortly after one ion crossing time, when the voltage

across the diode plateaued at 1 MeV. The total current and the ratio of electron to ion current were in excellent agreement with bi-polar theory. The flow, however, exhibited pronounced structure as shown in Figs. 3a through 3d, which are plots of electron and ion phase space of momentum component vs. distance across the A-K gap. The average of the P_x momentum component is again in excellent agreement with bi-polar theory, but P_y, which should be small, indicates a mean divergence of $P_{yth}/P_x \cong .03$ for the ions, and $P_{yth}/P_x \cong .2$ for the electrons as they exit the diode. A test run with electrons only showed no such filamentary structure. If the electromagnetics were turned off the electron-ion flow was again quiescent. A test for finer spatial resolution resulted in the same behavior. A preliminary conclusion is that an electromagnetic filamentation instability may exist even for such simple electron-ion flow.

VI. DISCUSSION AND CONCLUSION

The results we have presented from simulations of pinch-reflex-diodes with the quasi-static code are in good agreement with experimentally observed efficiencies and impedances. They show that efficiencies of ~50% can be achieved. Because the simulations do not always achieve a steady state, which is the underlying assumption of the quasi-static model, we are developing an electronmagnetic code for diode simulation. This will include inductive and electromagnetic effects which may be important. It is hoped that such a code will yield more reliable information on the ion beam profile and distribution function as it leaves the diode. A preliminary simulation of bi-polar flow in a planar diode indicates that electromagnetic effects influence the ion divergence because of filamentation in the electron-ion flow. Since this is an initial result, it is now important to develop the theoretical understanding of the origin of instability and turbulence in diode flow. Even though the step to electromagnetic simulations may be an improvement, physics phenomena remain which have not been included. Among these are the formation and control of anode and cathode plasmas and three dimensional effects. Symmetry breaking perturbations of the electron and ion emission plasma sheaths are a source of ion beam divergence and must eventually be modeled. At present we are planning to exercise the EM code to fully understand its limitations and to apply it to the simulation of pinch-reflex-diodes in geometries corresponding to the NRL experiments.

REFERENCES

*Work supported in part by the Department of Energy and the Defense Nuclear Agency.

[1] R.J. Barker, A.T. Drobot, Roswell Lee, and Shyke A. Goldstein, Proceedings 9th Conf. on Numerical Simulation of Plasmas, Northwestern University, Evanston, Illinois, June 30-July 2, 1980.

[2] R. A. Meger, R.C. Young, A.T. Drobot, G. Cooperstein, Shyke A. Goldstein, D. Mosher, S.E. Graybill, G.A. Huttlin, K.G. Kerris, and A.G. Stewart, to be published in J. App. Phys., Sept. 1981.

[3] G. Cooperstein, Shyke A. Goldstein, D. Mosher, R.J. Barker, J.R. Boller, D. Colombant, A.T. Drobot, R.A. Meger, W.F. Oliphant, P.F. Ottinger, F.L. Sandel, S.J. Stephanakis, and F.C. Young, Proc. 5th Workshop on Laser Interaction and Related Plasma Phenomena, Laboratory for Laser Energetics, Rochester, N.Y., Nov. 1979: and G. Cooperstein, Shyke A. Goldstein, D. Mosher, W.J. Oliphant, S.J. Stephanakis, F.C. Young, F.L. Sandel, and H.U. Karow, these proceedings.

[4] A. Palevsky and A.T. Drobot, Proceedings 9th Conf. on Numerical Simulation of Plasmas, Northwestern University, Evanston, Illinois, June 30-July 2, 1980.

[5] Good examples are: A.B. Langdon and B.F. Lasinski, Methods in Computational Physics Vol 16, Academic Press, N.Y. 1976; and J.P. Boris, Proc. 4th Conf. on Numerical Simulation of Plasmas, Naval Research Laboratory, Washington, D.C. 1970.

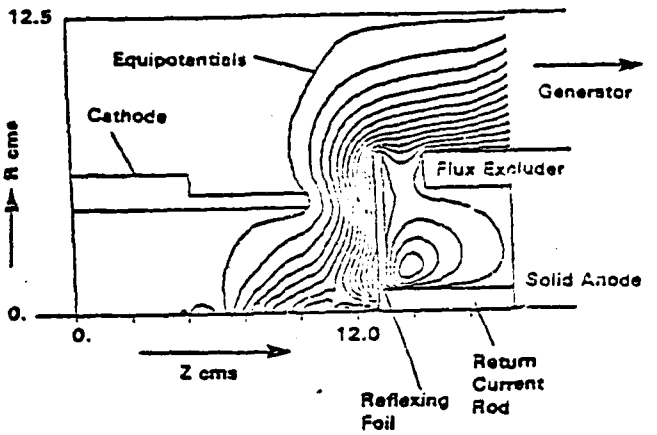

(a) Diode configuration showing equipotentials for a case run at 4 MeV.

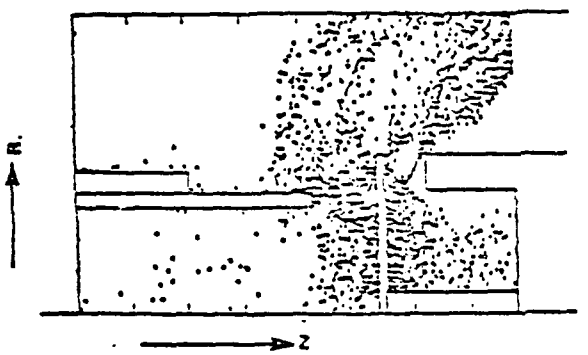

(b) Sample electrons projected on the (R,Z) plane.

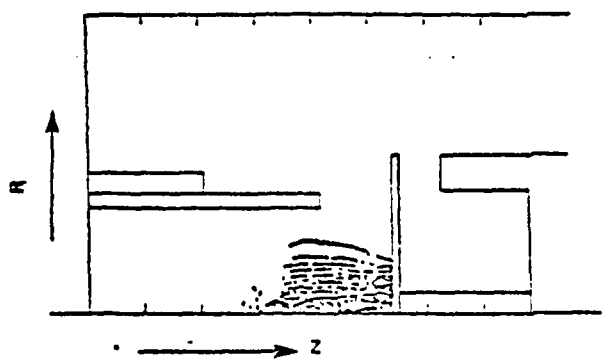

(c) Sample ions projected on the (R,Z) plane.

Figure 1. Simulation of AURORA pinch-reflex-diode in positive polarity.

High-impedance ion-diode experiment on the Aurora pulser

R. A. Meger,[a] F. C. Young, A. T. Drobot,[b] G. Cooperstein, Shyke A. Goldstein,[a] and D. Mosher
Naval Research Laboratory, Washington D.C. 20375

S. E. Graybill, G. A. Huttlin, K. G. Kerris, and A. G. Stewart
Harry Diamond Laboratories, Adelphi, Maryland 20783

(Received 20 April 1981; accepted for publication 8 May 1981)

Proton beams with currents >50 kA at 5 MeV in a ≤160-ns FWHM pulse have been extracted from an ion diode operated on the Aurora pulser. This current corresponds to an efficiency (proton current/total current) of 20%, which compares favorably with numerical simulation. The simulation indicates that the ion current is enhanced over the Child-Langmuir value due to increased electron lifetime in the diode. The proton beam directed onto a LiCl target provides a source of 1.8×10^{12} neutrons/sr/pulse in the forward direction from the ^{7}Li(p,n) ^{7}Be reaction.

PACS numbers: 52.50.Dg, 52.70.Nc, 29.25.Cy, 29.25.Dz

I. INTRODUCTION

There is increasing interest in the development of intense light-ion beams as drivers for thermonuclear pellets in inertial-confinement-fusion (ICF) applications.[1,2] This approach requires the production of a number of intense beams of a few MeV/nucleon, focusing and transport of each beam, then overlapping of the beams onto a target with sufficient power density to implode and ignite it.

One technique for producing intense light-ion beams uses the azimuthally symmetric pinch-reflex diode.[1,3] This diode uses the self-fields of the charged-particle flow to enhance ion production and to aid in focusing the ions. This diode operates most efficiently with a large aspect ratio (cathode radius/anode-cathode gap) and a low diode impedance ($Z<2\ \Omega$). Experiments on low-impedance generators have produced ion currents of up to 700 kA at 1.3 MV with 60% ion efficiency (ion current/total current)[1] and ion currents of 900 kA at 1.8 MV with comparable efficiency.[4,5] The high current density associated with these low-voltage, high-current ion beams puts limitations on the focusing and transport of such beams to ICF targets.[6,7]

Experiments at order-of-magnitude higher impedance levels and at power levels comparable to these low-impedance experiments have been carried out on the Aurora generator at the Harry Diamond Laboratories. In general, higher-impedance generators are more efficient in delivering energy from the capacitative store to the diode and can deliver higher power levels. Inductive voltage losses in the vacuum diode are reduced due to lower currents, and the increase stiffness of beams extracted from high-impedance diodes shouls improve their ability to be focused. Focused current densities required for pellet impulsion are reduced for higher-energy ion beams provided that the beam species is properly matched to pellet-deposition requirements. The advantages must be weighed against theoretical predictions of lower ion-production efficiencies for high-impedance diodes.

The experiments described here employed a low-aspect-ratio modification of the conventional pinch-reflex diode in order to better match the high-impedance Aurora pulse line. Computer simulation of the aurora diode showed enhanced ion production when operating at diode currents exceeding the Alfvén current. The Aurora experiments have demonstrated similar enhanced ion-production efficiencies ($\sim$20%). The ion diode was driven by a 160-ns FWHM pulse from one of the 50-Ω vacuum transmission lines on the generator. The diode operated at about 5 MV and 200 kA ($Z\sim25\ \Omega$). The mismatch of this ion diode to the 50-Ω transmission line limited the peak power to less than 1.5 TW and the total diode energy to less than 200 kJ. Average proton currents of >50 kA at 5 MeV were inferred from neutron activation and time-of-flight measurements using the ^{7}Li(p,n) ^{7}Be reaction. A carbon ion component of >1% of the proton intensity was also observed. Ion-imaging measurements indicated that the ion beam originated near the axis of the anode and was affected by an unknown focusing or defocusing mechanism in the anode-cathode region. It was shown that reflexing of electrons through the anode foil was not of primary importance to the enhanced ion production. The experimental results are consistent with computer simulations, which indicate that the ion production is enhanced as a result of prolonged electron lifetime in the diode due to the complicated trajectories of the electrons.

The paper will detail the theoretical simulations and experimental measurements of ion-diode studies on the Aurora generator in negative polarity. Section II presents the results of the numerical simulations. Section III describes the experimental hardware and diagnostics. The experimental results are presented in Sec. IV. Section V summarizes the experimental and theoretical studies. A more detailed report of this work may be obtained by requesting NRL Memo Report No. 4477.

II. THEORY AND SIMULATION

The high-impedance diode used in the Aurora experiments exhibits a ion-production efficiency much higher than the prediction from bipolar Child-Langmuir flow. The most

[a]JAYCOR, Alexandria, VA 22304.
[b]Science Applications Inc., McLean, VA 22102.

important aspect of the current flow established in the diode is that the total diode current exceeds the Alfvén current, $I_A(\mathrm{A}) = 17\,000\beta\gamma$, where β and γ are the usual relativistic factors for electrons at the full diode voltage. In this case, the electron flow pinches in the region of the anode-cathode gap. The electrons no longer have trajectories which take them directly from the cathode to the anode; rather they perform complicated figure-eightlike orbits through the axis of symmetry. A combination of $\vec{E} \times \vec{B}$ and $\vec{\nabla} B \times \vec{B}$ motion caused by the applied electric field and the self-magnetic field of the diode current combine to produce these complicated electron trajectories. As a result, the electron lifetime in the anode-cathode gap is enhanced. The ion-production efficiency is determined by the total charge balance in the diode and the relative average lifetimes of electrons and ions in the gap. The ions travel in essentially straight lines and move more slowly than the relativistic electrons, but the longer path length of the electrons allows a larger fraction of the current than predicted by Child-Langmuir theory to be carried by the ions.

For the diode used in the Aurora experiments, it is difficult to calculate analytically the ion-generation efficiency. Therefore, numerical simulations were used to model the diode behavior. The diode configuration used in the simulations is similar to that used in the experiments and is shown in Fig. 1. Electron emission was limited to the face of the cathode, and the anode-cathode gap was fixed at 3.3 cm. The anode foil was modeled as a 0.175-cm-thick polyethylene conducting disk acting as a space-charge-limited ion source on the cathode side. The on-axis support rod and back plate of the anode were assumed to be perfectly absorbing surfaces for electrons.

The results of simulations at diode voltages of 3 and 5 MV are presented in Table I and Fig. 2. The total diode current is comparable to the Alfvén current in the 3-MeV case, but is significantly greater than the Alfvén current for the 5-MeV case. In both cases, the electron beam pinches,

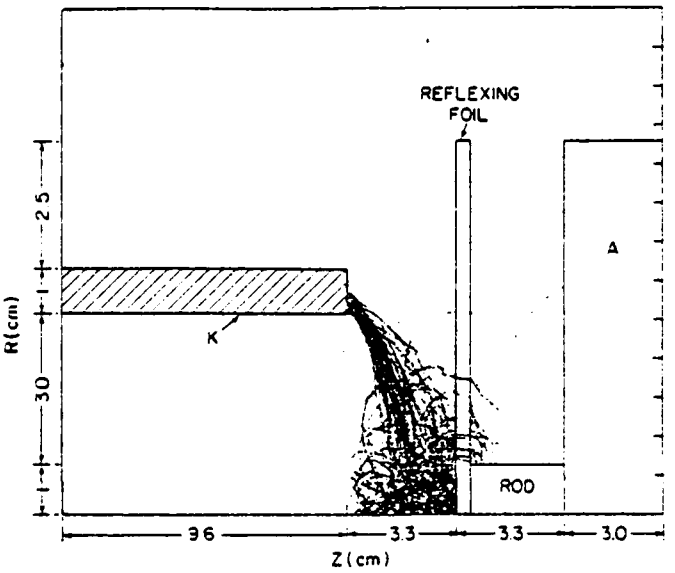

FIG. 1. Pinch-reflex-diode geometry used for the numerical simulations. Only the region to the right of the hollow cathode was simulated. Test electron orbits, shown for the 5-MeV case, illustrate the complicated trajectories. The orbits have been projected onto the (r,z) plane.

but the pinch is stronger and there is less reflexing through the anode foil for the 5-MeV case. The ion efficiency is significantly greater than the Child-Langmuir efficiency in both cases and reaches 20% for the 5-MeV case. Radial profiles of the ion current density at the front face of the cathode are shown in Fig. 2(a). The ion current density is peaked on axis in both cases and reaches at least 10 kA/cm^2 for 5 MeV. Radial velocities of the ions at the cathode face are presented in Fig. 2(b). For the 3-MeV case, defocusing of the ion orbits is indicated by the maximum outward radial velocity of 0.6 cm/μs combined with an axial velocity of 2.3 cm/μs. However, for the 5-MeV case the maximum outward radial velocity is reduced and the axial velocity is increased to 3.1 cm/μs

TABLE I. Results from numerical simulations.

Quantity calculated		3-MeV case	5-MeV case
Diode currents (kA):	Electron	100	165
	Ion	14	40
	Total	114	205
Alfvén current (kA)		116	183
Electron currents absorbed by the anode (kA):	Front foil	50	125
	Support rod	35	40
	Back plate	14	0
Diode impedance (Ω):		26	24
Ion efficiency (%):		12	20
Child-Langmuir efficiency		4.6	8.0
Ion current density on axis at cathode plane (kA/cm^2):		1	10

so that the ion beam is less divergent. Also, at large radii the radial velocity is directed inward, corresponding to ion focusing.

Electron orbits for the 5-MeV case are shown in Fig. 1. The pinching effect on the electrons can be seen clearly as well as the figure-eightlike drift motion of the electrons. Such electron motion is characteristic of the ∇B drift of primary electrons in this diode.

III. EXPERIMENTAL PROCEDURE

A. Hardware

In this experiment a single arm of the Aurora simulator[8] was used with an extension section to bring the beam out in the horizontal plane.[9] The Marx generator was operated in negative polarity at the 90-kV charge level, well below the maximum 120-kV charge available. The electrical pulse from the generator was transmitted to the ion diode through a 7-m-long, magnetically insulated coaxial transmission line which has a geometric impedance of 50 Ω.

The locations of voltage and current probes along this transmission line are shown in Fig. 3. A single resistive-divider voltage monitor (V_T) was located in the oil, and three

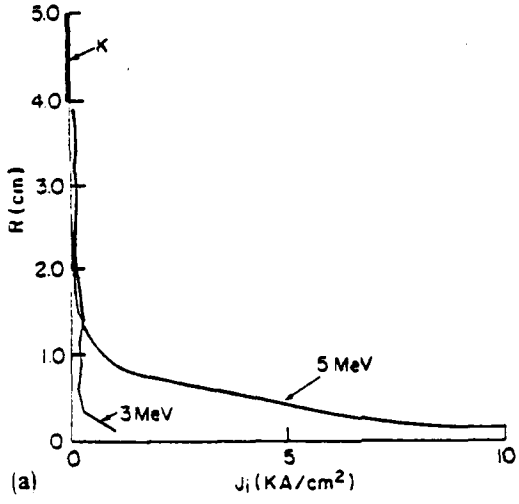

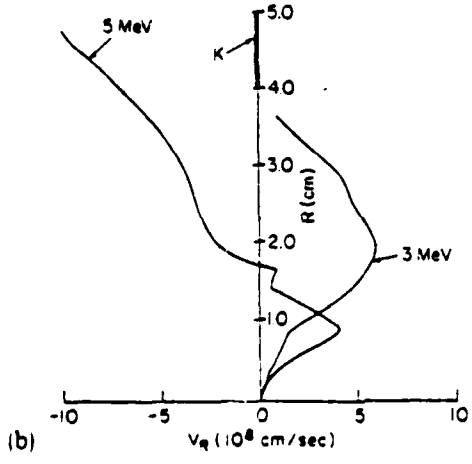

FIG. 2. (a) Radial profiles of ion-current density at the plane of the front surface of the cathode. (b) Radial velocity profiles of the ions at the plane of the front surface of the cathode.

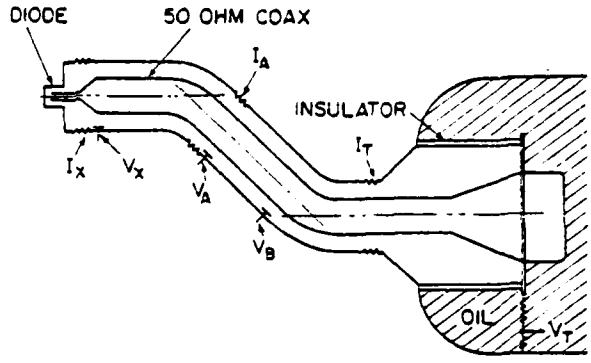

FIG. 3. One arm of the Aurora generator from the oil region to the ion diode. The resistive voltage divider in the oil is indicated as well as various resistive current shunts and capacitive voltage monitors in the vacuum coax.

capacitive dividers were located along the vacuum line. Only the farthest upstream capacitive monitor V_B gave reproducible signals. Current measurements were made with 7-mΩ resistive current monitors spaced along the outer coax. The V_T monitor measured a peak of about 10 MV, while V_B measured a peak of 6 MV and the current shunt I_T measured 190 kA. These values suggest that the diode was operating below the 50-Ω geometric coaxial line impedance.

An enlarged view of the ion-diode end of the coaxial transmission line is shown in Fig. 4. The 53-cm-diam. center stalk tapers to 10 cm while still in the 1.2-m-diam. chamber. After a 50-cm-long section, the outer conductor is reduced to 25 cm to recover the 50-Ω line impedance. A prepulse switch is located on the center stalk just downstream of the large-diameter transition as shown in Fig. 4. The switch consists of a series of polycarbonate plastic insulators and aluminum field grading rings which capacitively attenuate the prepulse applied to the diode. The cathode was mounted on the 10-cm-diam. inner stalk and was aligned with the anode mounted on an aluminum plate in the 25-cm-diam. vacuum region. A 35-cm-long vacuum chamber with a graphite dump for the electron beam was located downstream of the anode.

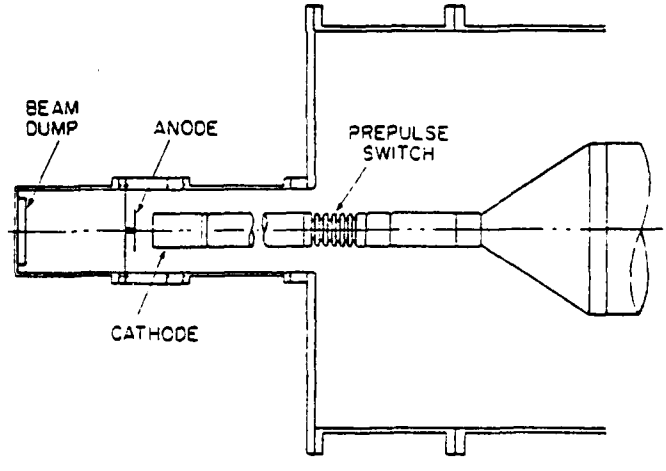

FIG. 4. Diode end of the vacuum coax as used in this experiment.

The cathode and anode used in these experiments are illustrated in Fig. 5. The cathode consisted of a 10-cm-diam., 6-mm-thick wall aluminum tube with a rounded edge. An aluminum witness plate was recessed inside the cathode. On most shots, lithium chloride (LiCl) was deposited on the witness plate to provide a neutron source through the $^7Li(p,n)^7Be$ reaction. The anode consisted of 100-μm-thick polyethylene (CH_2) foil stretched between a 0.8-mm-thick, 15-cm-diam. aluminum ring and a 2.5-cm-diam. central aluminum disk. The outer edge of the center disk and the inner edge of the ring were sharp to enhance surface breakdown of the CH_2 foil. The center disk was covered with various thicknesses of CH_2. An aluminum round-head screw clamped the anode onto a 1.9-cm-diam., 0.17-mm-thick, 6-cm-long aluminum tube. The entire anode was bolted onto a 1.5-mm-thick aluminum plate. The anode structure was made of thin aluminum to limit debris from the shot as well as to allow many reflexes of electrons through the structure (the range of 5-MeV electrons in aluminum is 1.1 cm).

B. Diagnostics

X-ray and neutron diagnostics used in this experiment are indicated schematically in Fig. 6. Because the machine was operated in negative polarity and there was no access to the center stalk, all ion diagnostics were remote or delayed. X-ray diagnostics consisted of a collimated scintillator-photodiode and a pinhole camera, both directed at the diode region.

Neutron diagnostics consisted of a neutron time-of-flight (TOF) detector and neutron-activation detector, as indicated in Fig. 6. The TOF detector was used to determine the proton energy in the diode. This detector was deployed at 10° to the anode-cathode axis and 13.8 m from the LiCl target. At this angle the proton energy for the $^7Li(p,n)^7Be$ reaction is a sensitive function of the neutron energy. Neutron intensities were measured with a Rh-activation counter[10] and an array of Mn-activation foils. The Rh detector was deployed at 155° to the ion-beam direction and Mn-foil samples were placed at several different locations, as noted in Fig. 6. The Rh counter was calibrated with a Californium-252 neutron source. This activation detector has been described elsewhere,[11] and calibrations with similar neutron sources have been described previously.[10] Measurements with Mn-foil activations provided neutron intensities at dif-

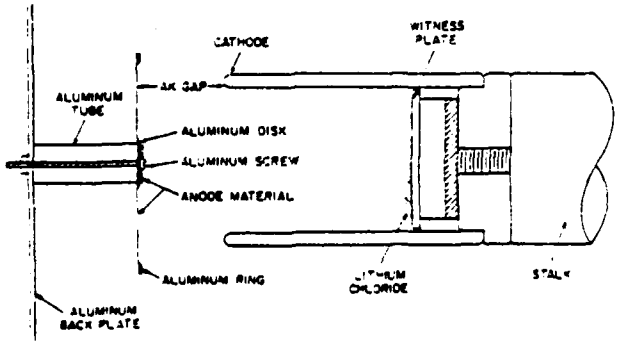

FIG. 5. Detailed anode-cathode geometry used in this experiment.

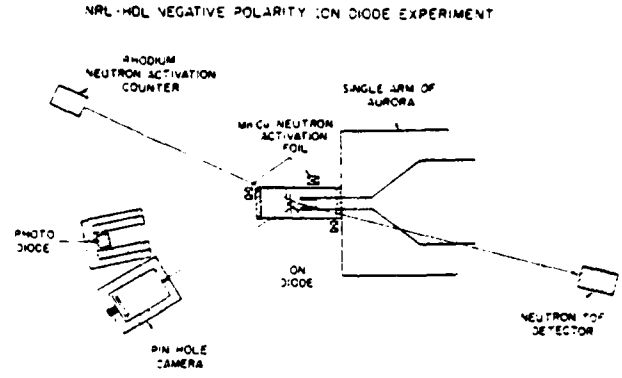

FIG. 6. Schematic arrangement of the x-ray and neutron diagnostics.

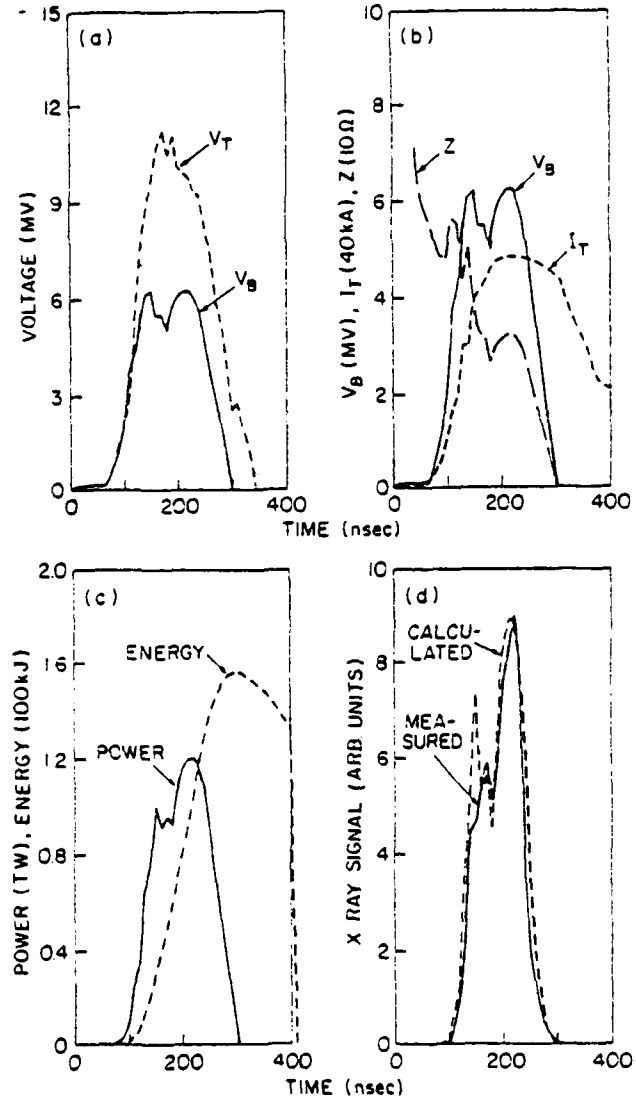

FIG. 7. Electrical characteristics measured on shot 2978. (a) Voltage waveshapes measured by the resistive divider in the oil V_T and a capacitive monitor in the vacuum transmission line V_B. (b) Voltage V_B, current I_T, and effective line impedance $Z = V_B/I_T$. (c) Power P and energy E derived from V_B and I_T. (d) Comparison of the measured x-ray pulse shape with the x-ray response calculated from V_B and I_T.

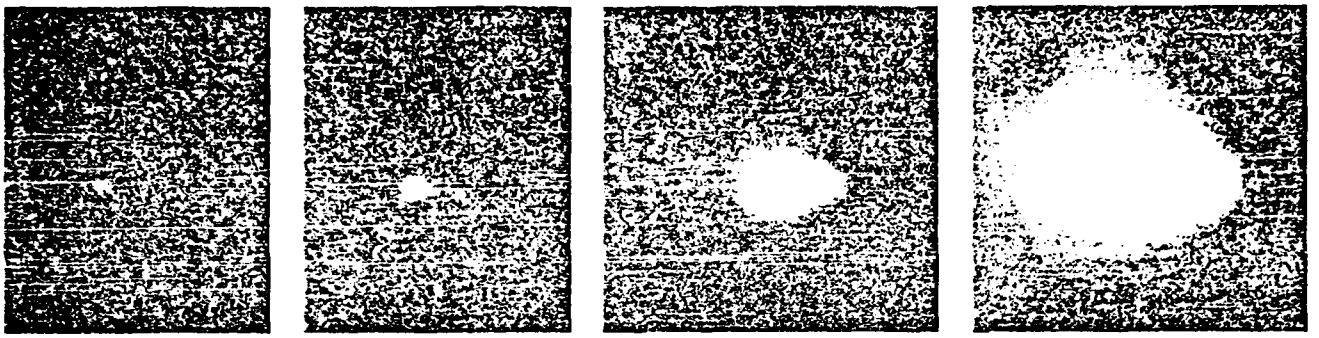

FIG. 8. X-ray pinhole photographs at four different film sensitivities for shot 2978. Film sensitivity increases from left to right. On the left, only the aluminum screw head on the front of the anode (see Fig. 5) is seen. Next, some of the thin aluminum anode supporting tube and more of the central aluminum anode disk are apparent. The outer aluminum anode ring is evident in the third image. The last image indicates that the aluminum back plate was irradiated by a diffuse spray of electrons.

ferent angles and distances from the target on a single shot. Foils of Mn-Cu(81% Mn) 2.5 cm in diameter and 50 μm thick were placed in the center of a cylindrical 7.6×7.6-cm CH_2 moderator and exposed to neutrons on a shot. The 156-min half-life γ-ray activity induced in the foil by the $^{55}Mn(n,\gamma)^{56}Mn$ reaction was measured after the shot. Mn activations were used to demonstrate the inverse-square scaling of neutron emission with distance from the LiCl target out to a distance of 1 m. The calibrated Rh counter was used to provide absolute neutron intensities and to calibrate the Mn activation detectors.

The trajectories of ions emitted from the diode were diagnosed by measurements with a pinhole shadowbox placed within the cathode.[1] The shadowbox consisted of a 6-mm-thick stainless-steel plate which contained an array of 1-mm-diam. apertures mounted 2.6 cm in front of a polished aluminum witness plate. The pattern of damage produced on the witness plate located behind the pinhole array allowed one to determine orbits for ions entering the pinholes at different radii. The aluminum witness plate will melt if more than 100 A/cm^2 of 5-MeV protons are deposited, and it will vaporize when the current density exceeds 1.4 kA/cm^2. The front aperture plate of the shadowbox was coated with LiCl to provide simultaneous neutron diagnostics.

Measurements of residual radioactivity on the cathode were made after each shot to provide additional information about the ion beam. The γ-ray activity of the cathode stalk was measured with a cylindrical 7.6×7.6-cm NaI detector. Counting of the cathode could be initiated 15 min after the shot. Pulse-height spectroscopy was used to determine the γ-ray energies associated with radioactive species produced by ion bombardment of the cathode.

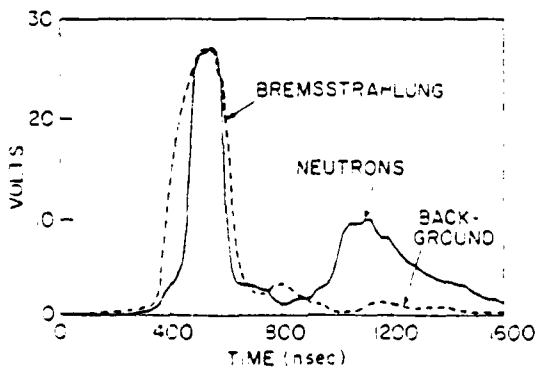

FIG. 9. Neutron time-of-flight traces measured for shot 2978 and for a shot without a LiCl target.

IV. EXPERIMENTAL RESULTS

A. Typical results

Experimental results will be presented by discussing a single shot (No. 2978) in detail. The ion diode used on the shot had a 4.9-cm anode-cathode (AK) gap. The anode consisted of an 86-μm-thick CH_2 foil on top of the center field-enhancing disk and aluminum screw head. A shadowbox was recessed 10.5 cm inside the cylindrical aluminum cathode and had a LiCl target mounted on its front surface.

The electrical characteristics measured on this shot are presented in Fig. 7. The voltage (V_T) measured in the oil just before the insulator stack, and the voltage measured by a capacitive monitor (V_B) in the vacuum transmission line, are compared in Fig. 7(a). The 40% drop in peak voltage between V_T and V_B is the result of impedance mismatches between the Blumlein (21 Ω), the oil-to-vacuum insulator stack (100 Ω), and the vacuum coax (50 Ω). Voltages measured closer to the ion diode have waveshapes similar to V_B. No direct measurement of the cathode voltage was made. The voltage V_B was combined with the current I_T just downstream of the diode insulator to give an effective line impedance $Z = V_B/I_T$, as shown in Fig. 7(b). The calculated impedance at this location has a plateau of about 30 Ω for about 100 ns during the pulse. Figure 7(c) shows the power and energy derived from V_B and I_T. The peak power of 1.2 TW is typical for this run. At the end of the voltage pulse, these probe measurements indicate an integrated power flow of about 160 kJ past this point in the coaxial line. The diode voltage was lower than V_B and the diode current higher than I_T due to the impedance mismatch between the transmission line and the ion diode. Transmission line computer code studies[12] indicate that the current is about 250 kA in the diode region. This result, coupled with the 5-MV diode voltage implied from the TOF measurements (to be discussed),

suggests that the diode was operating close to 20-Ω impedance.

The signal measured by x-ray scintillator photodiode for this shot is shown in Fig. 7(d). The shape of this signal is compared with a theoretical scaling[13] for x-ray production from electron beams given by $I_T(V_B)^{2.8}$. The calculated signal was normalized in magnitude and positioned in time for comparison with the measured signal. The agreement between the shapes of the two signals provides an independent check on how well the measured voltage and current waveshapes agree with the actual waveshapes across the diode.

The results of x-ray measurements with the pinhole camera are shown in Fig. 8. Images were recorded with four different film sensitivities through a 1.9-mm-diam. pinhole. The pictures obtained on this shot are typical of the experiment. The pinch was well centered on all shots, seemingly striking the central disk or screw head on the anode. In no case were bright regions observed from the aluminum back plate except near the center.

Neutron TOF measurements for this shot and for a shot without a LiCl target are compared in Fig. 9. The neutron pulse is readily detected above the tail of the bremsstrahlung signal. The width of the neutron pulse is due primarily to the duration of proton emission from the diode and to the neutron energy spread produced by protons stopping in the thick LiCl target. Proton energies were determined in two ways. First, the time interval from the peak of the x-ray pulse to the peak of the neutron pulse gives a measure of the average proton energy. Second, the time interval from the peak of the x-ray pulse to the 50% point on the leading edge of the neutron pulse gives an estimate of the maximum proton energy. Proton energies were extracted from these time measurements by using the kinematics of the ^{7}Li(p,n) ^{7}Be reaction.[14] The results for this shot are compared with averages for 12 shots in Table II. We conclude that a proton energy of 5 MeV is characteristic of this experiment.

The neutron yield measured by the Rh-activation detector for this shot was 4.3×10^{11} neut/sr at 155° compared to an average of 2.8×10^{11} neut/sr for 18 shots. The larger yield may be due in part to the higher-than-average proton energy on this shot. With no LiCl, the neutron yield was only 0.5–1.0×10^{10} neut/sr. In this case, neutron production presumably results from ion bombardment of the aluminum witness plate and cathode.

Proton intensities were determined from the neutron intensities using thick-target nuclear reaction yields which were calculated from published cross sections[14] and stopping powers.[15] The thick-target yields on a LiCl target are displayed in Fig. 10. These yields include only the ground-state reaction. The contribution from the first excited state is less than 10% at these energies. Note that this reaction has a threshold at 1.9 MeV and that the reaction yield is forward peaked. In the backward direction, where the Rh detector was located, the yield is not sensitive to the angle of the emitted neutrons. For shot 2978, the observed neutron output corresponds to 5.4×10^{16} protons at 5 MeV. This result is relatively sensitive to the proton energy and ranges from 3.1×10^{16} protons at 5.9 MeV (maximum energy from TOF) to 8.1×10^{16} protons at 4.6 MeV (average energy from TOF). For all 18 shots, the average number of protons is 3.7×10^{16}. We conclude that up to 5×10^{16} protons are produced with energies of about 5 MeV.

The trajectories of ions from the diode were inferred from the shadowbox results on this shot. The damage patterns produced by ions on the witness plate are outlined in Fig. 11. In this figure, these images have been projected by straight-line trajectories back through the corresponding witness plate apertures toward the anode-cathode region. Ion trajectories traced from the larger-radii holes in the shadowbox appear to converge closer to the anode that those of ions passing through the smaller-radii apertures. All of the ions appear to come from the central region of the anode.

TABLE II. Proton energies from neutron time of flight.

Timing procedure	Shot 2978	Average of 12 shots	
	E (MeV)	E (MeV)	Range (MeV)
Peak to peak	4.6	4.4	4.0–5.5
Peak to 50% rise	5.9	5.2	4.6–5.9

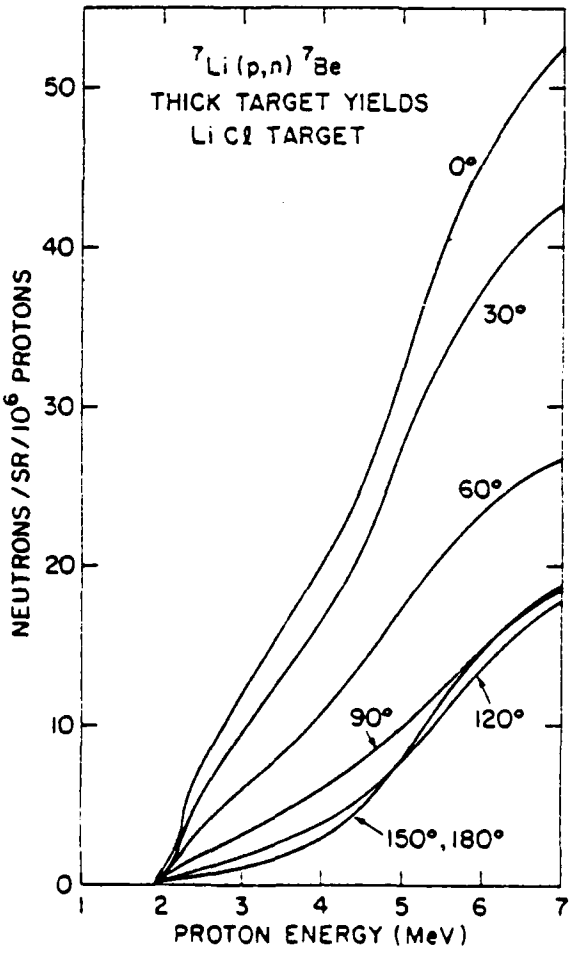

FIG. 10. Calculated thick-target yields for the ^{7}Li(p,n) ^{7}Be reaction on a LiCl target.

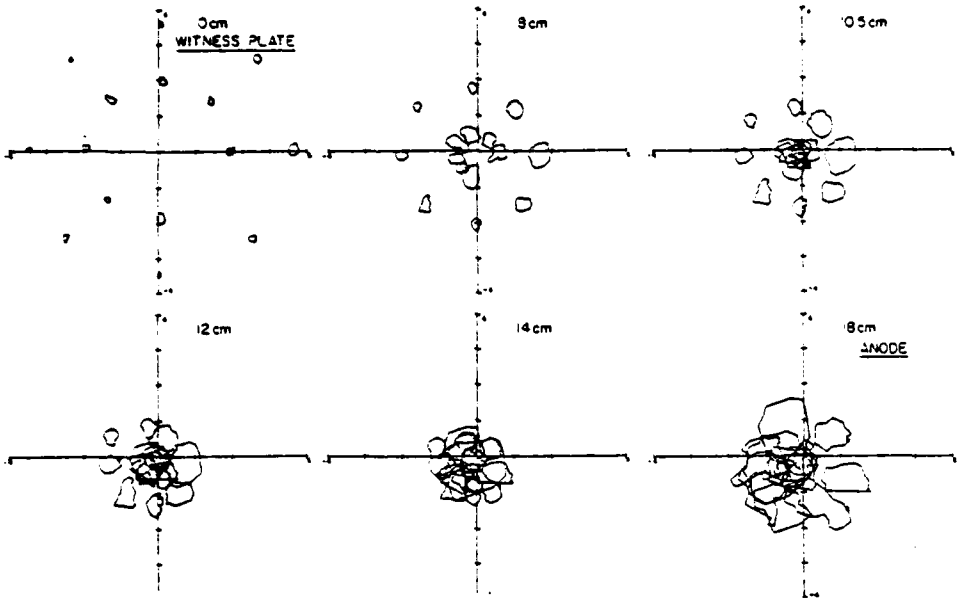

FIG. 11. Ion damage patterns observed on a shadowbox witness plate projected back through the shadowbox apertures toward the anode. The actual witness-plate damage is outlined at 0 cm. Projections of this damage through the corresponding apertures are shown on planes at various distances from the witness plate. The projections at 8 and 10.5 cm indicate that ions at the smaller radius are converging faster than ions at the larger radius. The inner-radius projections pass through an apparent best focus at 10.5 cm and begin to diverge as one approaches the anode located at 18 cm. The outer-radius projections have an apparent best focus very near the anode plane. The scale on these projections is 1 cm/division.

The projections at different radii suggest that ion focusing is going on within the anode-cathode gap with a significant fraction of the ions crossing the axis several centimeters in front of the anode.

B. Cathode activation

Radioactivity induced on the cathode after a shot could not be understood solely by proton bombardment but required the presence of an energetic carbon component in the beam. A pulse-height spectrum of the delayed γ-ray activity measured on the aluminum cathode with the NaI detector is shown in Fig. 12. Invariably, the most intense γ rays observed were annihilation quanta (0.51 MeV) resulting from positron activity produced by a variety of nuclear reactions. The decay of these γ rays could not be characterized by a single half-life. The γ rays at 1.18, 2.13, and 3.30 MeV dominate the high-energy region of this spectrum. A half-life of 32 min was measured for the decay of the 2.13- and 3.30-MeV γ rays. These results indicate that this activity is ^{34m}Cl. This identification was confirmed by Ge spectroscopy of the cathode activity, as summarized in Table III. For this measurement, counting could not be initiated until 100 min after a shot so short half-life activities were not detected. Gamma-ray energies were measured to a precision $\pm$ 1 keV, and the values agree with those recommended from the literature for ^{34m}Cl (see Table III). Note that the intense 146-keV γ ray from ^{34m}Cl was observed by Ge spectroscopy, but not in the NaI spectrum (see Fig. 12). In addition, γ rays associated with ^{63}Zn and ^{7}Be were also observed. The ^{7}Be activity results from the ^{7}Li(p,n) ^{7}Be reaction in the LiCl target. The ^{63}Zn activity results from the ^{63}Cu(p,n) ^{63}Zn reaction on a copper impurity in the aluminum cathode. The ^{34m}Cl activity cannot be accounted for by a proton-induced reaction but can result from the ^{27}Al(^{12}C,αn) ^{34m}Cl reaction due to a carbon component in the ion beam. The cross section[16] for this reaction rises rapidly with carbon-ion energy to a peak at 30 MeV. If the carbon ions were produced in the $+6$ charge state and accelerated through 5 MV to give an energy of 30 MeV, the number of ions required to account for the maximum observed activity would be 3×10^{14}. For lower-energy ions, this number increases due to the reduced cross section. Also, this value represents a lower limit because radioactive

TABLE III. Results from Ge spectroscopy of the aluminum cathode.

Observed gamma lines (keV)	Recommended gamma energies (keV)	Radionuclide	Source reaction	Threshold energy (MeV)
3303	3303.5[a]			
2127	2127.5[a]			
1176	1175.8[a]	^{34m}Cl	^{27}Al(^{12}C,αn) ^{34m}Cl	4.9
510	511.0[b]			
145.7	145.7[c]			
669	669.6[d]	^{63}Zn	^{63}Cu(p,n) ^{63}Zn	4.2
961	961.9[d]			
477	477.6[b]	^{7}Be	^{7}Li(p,n) ^{7}Be	1.9

[a] R. W. Kavanagh, A. Gallmann, E. Aslanides, F. Jundt, and E. Jacobs, Phys. Rev. 175, 1426 (1968).
[b] J. B. Marion, Nucl. Data A4, 301 (1968).
[c] T. F. Ward and P. K. Kuroda, J. Inorg. Nucl. Chem. 33, 609 (1971).
[d] R. Colle, R. Kishore, and J. B. Cumming, Phys. Rev. C 9, 1819 (1974).

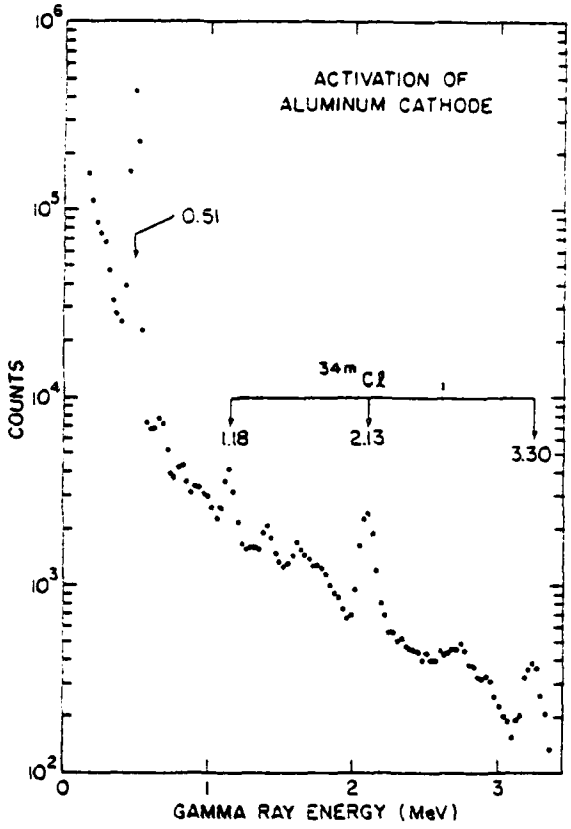

FIG. 12. Pulse-height spectrum of the γ-ray activity induced on the cathode after a shot as measured with a NaI detector. The energies of the more intense peaks in this spectrum are identified. The spectrum was measured 53 min after a shot for a duration of 4 min.

material vaporized off the cathode during the shot is not measured. We conclude that more than 3×10^{14} carbon ions per shot are generated in these experiments.

C. Variation of diode parameters

The behavior of the diode was studied for several variations of diode parameters. These studies included variations of the anode-cathode gap, the number of prepulse insulators, and the anode structure. The AK gap study was aimed at ion-production-efficiency scaling. The prepulse insulator was varied to examine the effects of a large prepulse on the diode impedance. The anode structure study was made to evaluate the importance of electron reflexing through the anode.

The AK gap study consisted of five shots with gaps ranging from 2.8 to 7.0 cm. For gaps greater than 4.8 cm, the voltage and current traces did not change significantly with the gap spacing. For gaps less than 4 cm, the voltage rise time and peak value did not change, but the voltage decayed more rapidly after the peak. For example, the full width at half-maximum of voltage V_B dropped from about 160 ns for gaps greater than 4.8 cm to about 100 ns for a 2.8-cm gap. Likewise the peak current as measured by I_T was 30 kA higher for the small gap. These observations indicate that the diode impedance is falling rapidly during the latter half of the pulse. The ion diagnostics showed a decrease in the number of neutrons and ^{34m}Cl nuclei produced for smaller gaps [see Fig. 13(a)]. No energetic neutrons were observed in the TOF detector for gaps less than 4.8 cm. The decrease in neutron and ^{34m}Cl production may be due to either the production of

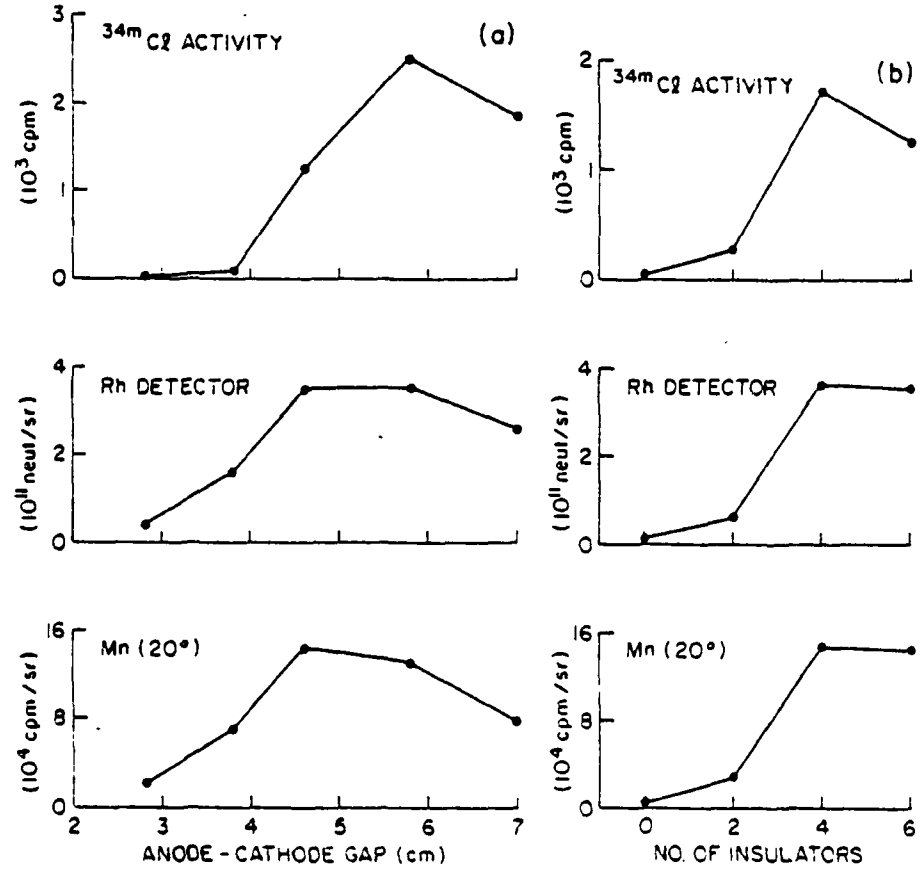

FIG. 13. Dependence of the cathode activation (^{34m}Cl) and neutron production (Rh and Mn detectors) on (a) the anode-cathode gap and (b) the number of prepulse insulators.

fewer ions or to a reduced voltage across the diode. The TOF measurements indicate that it is probably the latter. In this case, the strong energy dependence of the cross sections for these diagnostics causes the reduced outputs.

One constraint on the efficient coupling of a low-impedance diode to the Aurora generator is the presence of a prepulse in the diode. An oscillating prepulse of 150–200 kV peak voltage and about 1-μs period was measured on the vacuum transmission line beginning about 2 μs before the main voltage pulse. Prepulse can cause anode and cathode plasmas to form and begin to close the diode gap. As a consequence, the diode may short out prematurely when the main pulse appears at the diode. To minimize this effect, an insulator flashover switch was located behind the cathode (see Fig. 4) to capacitively attenuate the prepulse level at the diode. By changing the number of insulators in this switch, the prepulse voltage on the diode could be decreased by an order of magnitude. Shots were taken with 0, 2, 4, and 6 insulators in this switch, for a 5-cm AK gap. The diode behavior was similar for 4 and 6 insulators. For 2 insulators, the rise of the main voltage pulse V_B to its peak did not change significantly, but after the peak, the voltage collapsed rapidly. For no insulators (no prepulse switch), the voltage rise time increased, the peak voltage decreased by about 1 MV, and a rapid decay followed the peak and shortened the pulse to 135 ns FWHM. For the configurations with none and two insulators, peak diode currents of about 230 kA were well above the average of 190 kA for the entire run, indicating lower-impendance operation. Also, no energetic neutrons were observed in the TOF detector for these two insulator configurations. The dependence of the neutron intensity and cathode activatic (measurements on the number of insulators in the prepulse switch is shown in Fig. 13(b). The decrease in neutron and ^{34m}Cl production is consistent with lowering of the diode voltage due to gap closure.

Ion production in these experiments depends on the interaction of electrons with the anode foil. Reflexing of electrons through the anode foil may enhance ion production. In these negative-polarity experiments, the CH_2 anode foil acts as a ground plane as well as a plasma source for ions (see Fig. 5). Electrons from the cathode may reflex through the anode foil due to the magnetic field produced by current in the anode stalk. The gyroradius of 5-MeV electrons in the magnetic field at the cathode radius resulting from a 150-kA current is about 3 cm. For an anode stalk longer than 3 cm, electrons can reflex through the anode without interacting with the aluminum plate supporting the anode. In addition, a virtual cathode may be formed in the vacuum region behind the support plate and reflect electrons back toward the anode. These two potential reflexing mechanisms complement one another.

Several shots with different anode structures were made to examine the role of electron reflexing in the diode. First, a series of shots with anode stalk lengths ranging from 3 to 12.8 cm was made for AK gaps of 5 cm. No significant differences in the voltage, current, neutron output, and ^{34m}Cl production were observed. X-ray pinhole images indicated that the longer stalks were radiating along their entire length. This suggests that current is being conducted along the anode stalk to the aluminum support plate. Finally, shots were taken with the anode foil placed directly on the anode support plate and the thickness of the support plate adjusted to allow or suppress electron reflexing. The aluminum support plate thickness was increased to 3 mm (from 1.5 mm) and backed with a 13-mm-thick carbon plate to suppress electron reflexing. Under this condition the neutron yield was reduced by about one-half of that measured on shots with a thin support plate. These observations indicate that electron reflexing is, at best, only weakly enhancing the ion production.

V. SUMMARY OF RESULTS

The ion diode experiments on Aurora described in this paper have produced up to 5×10^{16} protons with energies of about 5 MeV and proton pulse durations of up to 160 ns. The corresponding average proton current is >50 kA or 20% of the total current in the diode. These numbers give about 40-kJ energy in the proton beam. The 20% ion generation efficiency is in agreement with computer simulations. In addition to protons, a carbon-ion component of greater than 3×10^{14} ions was extracted from the CH_2 anode foil. The energy of these ions was not determined, but their number may be larger depending on their charge state and hence their energy.

The enhancement of the ion-production efficiency over the Child-Langmuir limit is attributed to increased electron lifetime in the diode. Previous experiments[1] with pinch reflex diodes have indicated enhanced ion production can result from electron reflexing through an anode foil. However, it was demonstrated that electron reflexing is not the dominant enhancement mechanism in the present experiments. Experimentally, the electron beam pinches on the anode, and the ions appear to originate primarily from a small area (2–4 cm^2) on the anode axis. Both of these results are supported by computer simulation. Moreover, the simulation indicates that electrons in the diode undergo complicated figure-eightlike orbits.

Analysis of the shadowbox measurements indicates that the ions have a relatively large divergence from a localized region on axis within the anode-cathode gap. This result suggests some focusing mechanism at work in the diode. These observations are consistent with the computer simulations.

Experiments with various prepulse switches and AK gaps indicate that the diode is sensitive to the prepulse voltage level in the 25–200-kV range. Gap closure may have occurred late in the pulse for AK gaps less than 4 cm or for large prepulse levels. Such closure can result from the motion of anode or cathode plasmas produced by the prepulse 1.5 μs before the main voltage pulse.

The 5-MeV proto beam in this experiment was directed onto a LiCl target to provide an intense neutron source through the ^{7}Li$(p,n)^7$Be reaction. Neutron intensities of up to 4.3×10^{11} neutrons/sr/pulse were measured at 155° in the laboratory. This corresponds to 1.8×10^{12} neutrons/sr/pulse at 0° based on the thick-target yields for this reaction (see Fig. 10). The angle-integrated neutron intensity is 10^{13} neutrons/pulse. These neutron yields could be increased by

a factor of 5 by replacing the LiCl target with a pure lithium target.

ACKNOWLEDGMENTS

The authors would like to acknowledge a preliminary computer simulation performed by Roswell Lee, which provided the impetus for performing the initial experiments, as well as the invaluable technical assistance of J. Negri and T. Robinson at the Naval Research Laboratory and D. Whittaker, C. Casaere, T. Cassady, A. Poirier, and the entire Operations and Maintenance crew at the Harry Diamond Laboratories. The support of K. W. Marlow of NRL with the Ge-spectroscopy measurements is acknowledged. This research was supported by the United States Defense Nuclear Agency.

[1]G. Cooperstein, Shyke A. Goldstein, D. Mosher, R. J. Barker, J. R. Boller, D. G. Colombant, A. Drobot, R. A. Meger, W. F. Oliphant, P. F. Ottinger, F. L. Sandel, S. J. Stephanakis, and F. C. Young, in *Laser Interaction and Related Phenomena*, edited by H. Schwarz, H. Hora, M. Lubin and B. Yaakobi (Plenum, New York, 1981), Vol. 5, p. 105.

[2]G. Yonas, Sci. Am. 239, 50 (1978); P. A. Miller, D. J. Johnson, T. P. Wright, and G. W. Kuswa, Comments Plasma Phys. 5, 95 (1979).

[3]Shyke A. Goldstein and R. Lee, Phys. Rev. Lett. 35, 1079 (1975).

[4]S. Stephanakis, J. R. Boller, G. Cooperstein, Shyke A. Goldstein, D. D. Hinshelwood, D. Mosher, W. F. Oliphant, and F. C. Young, Bull. Am. Phys. Soc. 24, 1031 (1979).

[5]G. Cooperstein, J. R. Boller, Shyke A. Goldstein, D. Mosher, W. F. Oliphant, S. J. Stephanakis, F. C. Young, R. D. Genuario, and J. E. Maenchen, IEEE Conference Record-Abstract, 1980 Intl. Conf. on Plasma Science, Madison, Wisconsin, 1980, p. 97 (unpublished).

[6]D. G. Colombant, Shyke A. Goldstein, and D. Mosher, Phys. Rev. Lett. 45, 1253 (1980).

[7]D. Mosher, D. G. Colombant, and Shyke A. Goldstein, Comments Plasma Phys. 6, 101 (1981).

[8]B. Bernstein and I. Smith, IEEE Trans. Nucl. Sci. 20, 294 (1973).

[9]S. E. Graybill, Harry Diamond Laboratories Technical Report No. 1862, 1978 (unpublished).

[10]F. C. Young, IEEE Trans. Nucl. Sci. NS-22, 718 (1975).

[11]F. C. Young and S. J. Stephanakis, NRL Memorandum Report No. 3104, August 1975 (unpublished).

[12]G. Huttlin, Harry Diamond Laboratories Internal Report No. HDL-R-290-80-2 (unpublished).

[13]H. W. Koch and J. W. Motz, Rev. Mod. Phys. 31, 4 (1959).

[14]H. Liskien and A. Paulsen, At. Nucl. Data Table 15, 57 (1975).

[15]H. H. Andersen and J. F. Ziegler, *The Stopping and Ranges of Ions in Matter*, Vol. 3 (Pergamon, New York, 1977).

[16]I. Landenbauer-Bellis, I. L. Preiss, and C. E. Anderson, Phys. Rev. 125, 606 (1962).

From: LASER INTERACTION AND RELATED PLASMA PHENOMENA, Vol. 5
Edited by Helmut J. Schwarz, Heinrich Hora,
M. Lubin, and B. Yaakobi
(Plenum Publishing Corporation, 1981)

NRL LIGHT ION BEAM RESEARCH FOR INERTIAL CONFINEMENT FUSION†

G. Cooperstein, Shyke A. Goldstein*, D. Mosher
R. J. Barker*, J. R. Boller, D. G. Colombant,
A. Drobot**, R. A. Meger*, W. F. Oliphant,
P. F. Ottinger*, F. L. Sandel*, S. J. Stephanakis,
and F. C. Young

Naval Research Laboratory
Washington, DC 20375

ABSTRACT

There is presently great interest in using light ion beams to drive thermonuclear pellets. Terrawatt-level ion beams have been efficiently produced using conventional pulsed power generators at Sandia Laboratory with magnetically-insulated ion diodes and at the Naval Research Laboratory with pinch-reflex ion diodes. Both laboratories have recently focused ion beams to pellet dimensions. This paper reviews recent advances made at NRL in the area of ion production with pinch-reflex diodes, and in the areas of beam focusing and transport. In addition, modular generator and beam requirements for pellet ignition systems are reviewed and compared with the latest experimental results. These results include the following: (1) production of ≥ 100 kJ proton and deuteron beams with peak ion powers approaching 2 TW on the PITHON generator in collaboration with Physics International Co., (2) focusing of 0.5 TW deuteron beams produced on the NRL Gamble II generator to current densities of about 300 kA/cm^2, and (3) efficient transport of 100 kA level ion beams over 1 meter distances using Z-discharge plasma channels.

† Work supported by Defense Nuclear Agency, Washington, DC 20305 and Department of Energy, Washington, DC 20545
* JAYCOR, 205 S. Whiting Street, Suite 500, Alexandria, VA 22304
** Science Applications, Inc., 8400 Westpark Dr., McLean, VA 22101

1. INTRODUCTION

The use of light ion beams (protons, deuterons, etc.) for inertial confinement fusion has been seriously pursued following the theoretical prediction[1-3] and the experimental documentation[4], that small-area diodes ($\sim$ 100 cm^2) can be used to generate ion beams efficiently at the megavolt-megampere level. Soon after this, results of ballistic beam focusing experiments were presented[5] and a technique for transporting ions in a plasma Z-discharge was introduced[6]. Recently, terrawatt-level ion beams with focused ion current densities in excess of 100 kA/cm^2 have been produced using water-dielectric transmission-line generators at Sandia Laboratories (SANDIA) with magnetically-insulated ion diodes[7] and at the Naval Research Laboratory (NRL) with pinch-reflex ion diodes[8].

Target designs for light ion beams[9] call for delivery of about 2 MJ to an $\sim$ 1 cm diameter pellet in an $\sim$ 10 ns time scale in order to achieve high-gain thermonuclear ignition. Present pulsed power technology provides up to 10 TW single generator modules from which up to 300 kJ of ions can be extracted in 50-100 ns. Thus, a large number of modules and the means to transport energy from these modules onto the pellet are needed. Additionally, compression of the pulse to the pellet-implosion time-scale is required.

Two different approaches addressing these problem areas have emerged. An approach researched by SANDIA[10] involves pulsed-power techniques for shortening the accelerating-voltage pulse, and self-magnetically insulated flow of electromagnetic energy in vacuum transmission lines which terminate in small ion diodes close to the pellet. Packing of transmission lines near the target, coupling of diodes to the lines, and ion-beam focusability will be investigated with the 36 short pulse, 1 TW PBFA I modules now in construction at SANDIA. For pellet ignition, this approach will require on the order of 100 modules.

A second approach, researched by NRL, involves the extraction and focusing of beams from self-insulated pinch-reflex ion diodes, coupled with transport of these focused beams in $\sim$ 1 cm diameter Z-discharge transport channels. Pulse compression during transport to the pellet-implosion time-scale is achieved by increasing the accelerating voltage with time. These techniques are appropriate for modules operating up to the 10 TW level with a 50-100 ns pulse duration. The number of modules required for this approach is on the order of 10.

In the present report, major results of a combined experimental and theoretical study of the second approach are reviewed with concentration on recent advances made at NRL in the area of ion production using pinch-reflex diodes, and in the areas of beam focusing and transport.

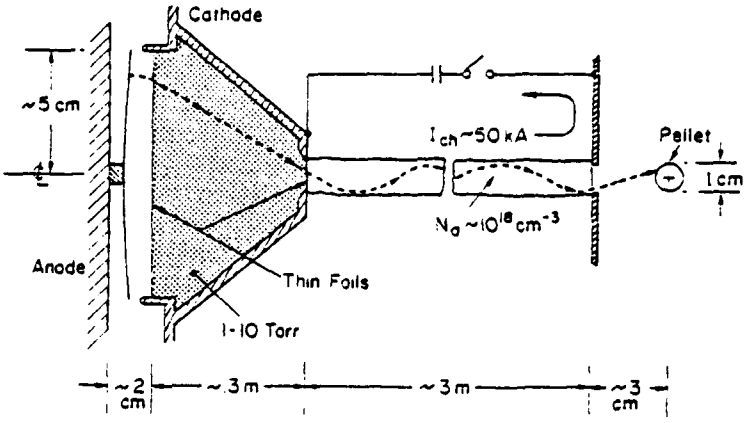

Fig. 1. Conceptual schematic of NRL Light-Ion Inertial Confinement Fusion Approach.

A conceptual schematic of the NRL approach is shown in Fig. 1. The diode and transport system together with the pulsed power generator (not shown) is one module of a multi-module pellet-ignition system. A pinch-reflex ion diode (∿ 10 cm in diameter) produces the ions and properly aims them towards the transport system entrance aperture. The ion beam then free streams in a gas-filled chamber towards an ∿ 1 cm diameter focus. The gas in the drift region allows the ion beam to be highly charge- and current-neutralized. Inside the channel, the ions are confined radially by the azimuthal magnetic field produced by the discharge of an external capacitor bank. The ∿ 50 kA current in the channel is sufficient to provide radial confinement for ions entering the channel with transverse velocities below about 15% of their axial velocity. The plasma density in the channel must be sufficiently high to provide inertial resistance to channel expansion forces during beam transit and sufficiently low to prevent excessive energy loss of the beam during transport. Beam power multiplication of about a factor-of-five is achieved during transport to the pellet by ramping the accelerator voltage in time. Beams emerging from the channel propagate the last few centimeters to the pellet with low divergence because of the small transverse velocity. Several ion beams can then be overlapped onto the pellet.

The second section of this paper discusses ion production in pinch-reflex ion diodes including recent experiments[11] in collaboration with Physics International Co. on the PITHON generator. In these experiments, greater than 100 kJ of protons and deuterons were produced with peak ion powers approaching 2 TW. In Sec. 3, the self-focusing of ion beams with planar diode geometries is reviewed

and ion focusing experiments with curved geometries are reviewed in Sec. 4. In these experiments, 0.5 TW deuteron beams produced on the NRL Gamble II generator were focused to current densities of about 300 kA/cm^2. In Sec. 5, the numerical simulation of pinch-reflex ion diodes is discussed. Theoretical work on ion orbits in the transport channel is reviewed in Sec. 6, and in Sec. 7 results of recent transport experiments are discussed. In these experiments, high current ion beams have been efficiently transported 1 meter distances using Z-discharge plasma channels. The MHD response of the channel induced by beam passage is then considered in Sec. 8. In Sec. 9, bunching of ion beams in transport channels is briefly discussed. Finally, the results of this research are used to determine a range of system parameters which are appropriate for driving high-gain pellets with proton or deuteron beams.

2. ION PRODUCTION

Self-pinched electron flow and laminar ion flow in a large-aspect-ratio electron-beam diode are conceptually illustrated in Fig. 2. After an initial phase leading to self-pinched flow[12], the electrons primarily originate from the edge of the cathode and flow under the dominant influence of the self-magnetic fields towards the diode axis ending up in a tight pinch at the center of the anode plane. The ions, which are primarily protons originating from the desorbed gases making up the anode plasma, are only slightly bent

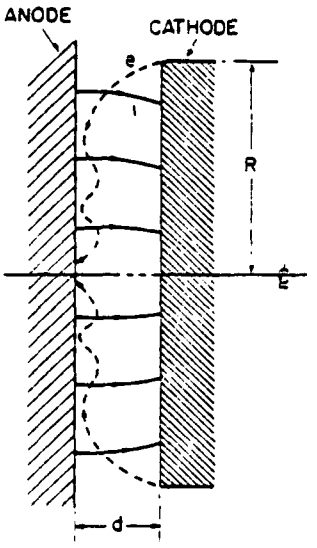

Fig. 2. Conceptual schematic of electron and ion flow in large-aspect-ratio (R >> d) vacuum diode.

by the diode's self-magnetic fields due to their heavier mass. Thus ions flow in almost straight lines toward the cathode as they accelerate up to the diode voltage. The enhanced ion currents come about because of the additional electron space charge in the diode caused by the large electron path length (R) relative to the ion path length (d). For the simple diode configuration shown in Fig. 2 analytical theory predicts[1] and numerical simulation confirms[13] an ion to electron current ratio of

$$\frac{I_i}{I_e} > \frac{R}{d}\left(\frac{eV}{2m_i c^2}\right)^{\frac{1}{2}}$$

where R is the diode radius, d is the anode-cathode gap spacing, V is the diode voltage and m_i is the ion mass.

Early experimental results[14] with R ≈ 6 cm and d ≈ 0.4 cm giving $(I_i/I_e) \sim 1/2$ were in excellent agreement with this theory. These demonstrated 0.8 MeV proton currents of up to 200 kA. Using spherical section electrode structures, focused deuteron current densities of up to 70 kA/cm^2 were obtained[15]. These early results were obtained at 0.5 TW with the Gamble II generator operated for the first time in positive polarity. In positive-polarity operation, the cathode is mounted on the door of the generator so that ions accelerated through the diode potential can be injected into a drift tube region through a thin cathode transmission foil.

In the most recent positive polarity experiments[8] on upgraded[16] Gamble II at 1.5 TW, ~ 60% conversion efficiency from generator power to ion power was achieved using the refined diode design illustrated in Fig. 3. A thin CH_2 foil stretched across a dielectric ring is electrically connected to the positive electrode by a 1 cm-diameter rod on the diode axis. Plasma formation due to surface flashover causes the plastic foil to become a conductor early in the pulse and provides a source of ions. This geometry enhances ion emission by increasing the electron path length (and therefore lifetime) relative to that of ions by forcing the electrons to reflex through the thin foil as they pinch in radially. This reflexing is not due to spatial charge building up in the vacuum gap behind the foil because this is quickly neutralized by ions from the anode plasma. Rather, it is due to the azimuthal self-magnetic field caused by the return current flow through the center conductor. Thus, electron reflexing is magnetically induced behind the foil. In front of the foil, the electrons reflex in the self-consistent diode fields. The ions that are produced on the back of the anode foil do not carry diode current because the back plate is at anode potential. Results of the numerical simulation of this diode configuration will be presented in Sec. 5.

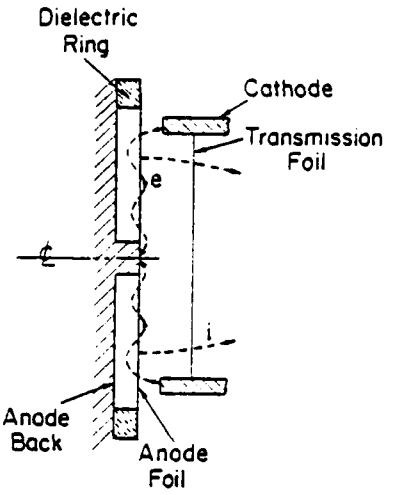

Fig. 3. Pinch-reflex diode schematic.

Typical diode electrical characteristics are shown in Fig. 4a for a 6 cm cathode radius, a 0.4 cm anode-cathode gap spacing, and a 0.5 cm vacuum gap behind the 0.01 cm CH_2 anode foil. Ion currents of 500 kA have been measured with 1 MA total diode currents. This corresponds to an average source ion current density of 5 kA/cm^2. After passing through a phase associated with establishing the charged-particle flow illustrated in Fig. 3, the diode impedance remains well matched to the 1.5 ohm output impedance of the Gamble II generator. Closure of the anode-cathode gap due to electrode plasma motion usually occurs near the end of the electrical power pulse. The diode impedance can be adjusted by varying the cathode emitting area, the anode-cathode gap spacing, or the applied voltage. The natural voltage ramp which occurs demonstrates that accelerating voltages appropriate for ion bunching during transport to fusion pellets can be achieved with these generators. The net current signal (the current entering the cathode foil) is interpreted as the total ion current flowing in the anode cathode gap. The location of the Rogowski coil used to make this measurement will be illustrated later in Fig. 6. On a few selected shots, the measured net current exceeded 700 kA at 1.3 MV out of 1.1 MA of total diode current. Carbon activation[17] by proton beams indicates that greater than 50% of the net-current signal is due to protons. The interpretation of these results is limited by an unknown correction for deuteron activation. When the anode is coated with CD_2, neutron time-of-flight measurements show that greater than 50% of the net current takes the form of deuterons. Up to 10^{12} neutrons have been measured on Gamble II. This data is consistent with ion

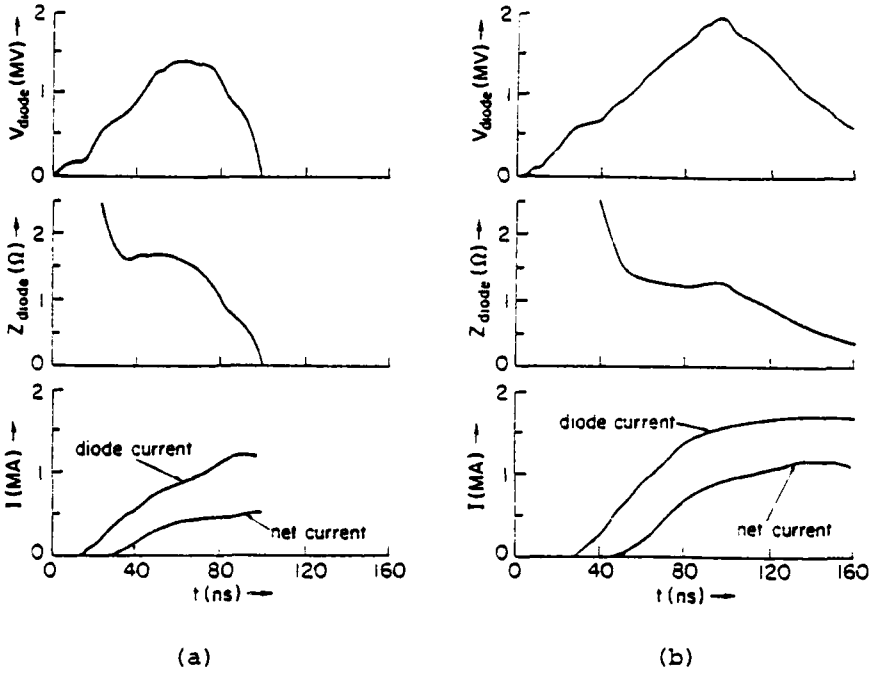

Fig. 4. Diode electrical characteristics for (a) Gamble II and (b) PITHON.

energies of at most 300 kV lower than the diode voltage of 1.3 MV. Several mechanisms are being investigated as a source of this loss.

In the most recent ion production experiments[11], a pinch-reflex ion diode, similar to that used on Gamble II (Fig. 3), was successfully operated at 3 TW on the Physics International PITHON generator. The main difference between the geometry used on Gamble II and that used on PITHON was that PITHON presently only operates in the normal negative polarity mode. Because the cathode was now at a 2 MV potential, this required special techniques to be able to both read out the ion current monitors and to fill the drift region behind the cathode with gas. Deuteron current measurements were made in the conventional manner by coating the anode foil with CD_2 and using both nuclear activation and time-of-flight neutron detectors to detect the neutrons produced from a (greater than one range thick) CD_2 target placed behind the cathode.

Typical diode electrical characteristics are shown in Fig. 4b for a 6 cm cathode radius, a 0.3 cm anode-cathode gap spacing, and a 0.5 cm vacuum gap behind the 0.01 cm CH_2 anode foil. Peak diode voltages of 2 MV at 1.5 MA diode current were obtained with flat impedance behavior even though the pulse length was almost twice as long as that on Gamble II. Ion currents of up to 1 MA were obtained

corresponding to peak ion powers approaching 2 TW. Over 100 kJ of ions were produced out of just over 200 kJ of electrical energy delivered to the diode. Impedance control and electrical reproducibility were excellent. When deuterons were produced, the neutron yield approached 10^{13} from the D-D and D-carbon reactions occurring in the CD_2 target.

As will be discussed in the last section, the voltage and ion currents produced on PITHON are in the range for a single module of a multi-module pellet ignition system. The long impedance lifetimes and high reproducibility associated with the $\sim$ 1 cm gaps between the anode and cathode transmission foil indicates that programmed-voltage waveforms for beam bunching during transport can be employed. Focus perturbing effects associated with time varying B_θ fields in the diode region can be controlled for these $\sim$ 1 cm diode gap by electrode shaping and naturally occurring gap closure as discussed in the next section.

3. ION FOCUSING IN PLANAR GEOMETRY

The processes believed to be important in ion focusing are schematically illustrated in Fig. 5. Ions traversing the vacuum gap are radially accelerated inward by the azimuthal magnetic field of the diode current flow. Particle-in-cell codes predict that the predominant electron flow in the diode is close to the anode surface where most of the potential drop across the diode takes place. Thus, the electron current contributes to the angular deflection of ions only for a small fraction of the vacuum space. The ions are radially

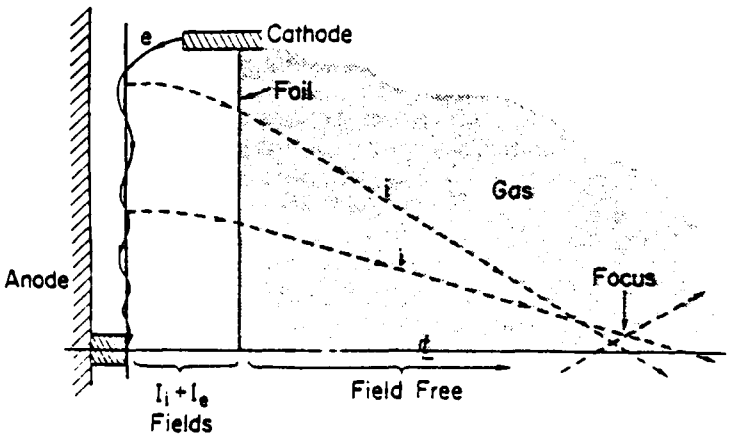

Fig. 5. Light ion focusing schematic.

accelerated primarily by their own current. If the ion current density were approximately uniform over the anode surface, then the resulting linear $B_\theta(r)$ would cause the ions to be pointed towards an approximately-common focus as they enter the cathode transmission foil. Scattering during passage through the 1.8 μm polycarbonate (KIMFOL) foil is about 20 mrad for 1 MeV protons. Beam induced breakdown of the low pressure gas filling the drift region to the right of the cathode foil allows beam current neutralization. The magnetic field acting on the ions is reduced by a factor of 50 by this neutralization. The ions have therefore nearly straight-line trajectories in this region and free stream towards the focus.

One major limitation to tight focusing is asymmetry in power and charged particle flow in the diode. This can be overcome by careful experimental design which results in well-centered electron pinches and centered symmetric ion focal spots. Another major limitation is the actual radial distribution of ion current which may direct ions emitted at different radii to different foci. In principle, for a given diode voltage and current, the shapes of the anode and cathode surfaces can be adjusted to correct for focus-perturbing effects of non-uniform ion current distributions. For instance, the launch angle can be changed by curving the anode surface. The radial deflection due to diode magnetic fields can also be changed by varying the axial position of the cathode foil as a function of radius. The anode-foil thickness can also be varied as a function of radius to vary the degree of electron reflexing and thus control the emitted ion current profile. A final major limitation to tight focusing is the time variation in the focusing magnetic fields which cause a change in focus location with time. This effect can be partially offset by the natural reduction of the anode-cathode (AK) gap due to electrode plasma motion. Thus, as the diode current increases, the increasing radial acceleration of the ions can be offset by the reduction of AK gap with time. In principle, both the initial AK gap spacing and the cathode foil material could be chosen to minimize this time variation effect.

Long focal lengths (i.e. large f-numbers) are achieved by magnetic self-focusing acting alone in a flat-anode geometry. This configuration is employed to inject ions into transport channels since larger-angle injection requires excessive transport-channel currents. Spherically-curved anodes in conjunction with self-magnetic forces are used to obtain shorter focal-lengths appropriate for target studies with the highest-focused current densities.

Three sets of focusing experiments in planar geometry were performed on Gamble II with electrical characteristics similar to those of Fig. 4a.

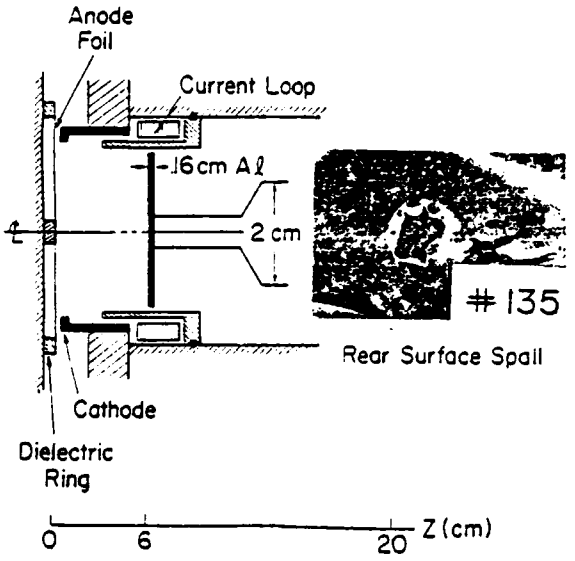

Fig. 6. Self-focusing in planar geometry with no cathode foil.

The first self-focusing experiments were performed with the planar diode geometry illustrated in Fig. 6 where a 0.01 cm thick CH_2 anode foil stretched across a dielectric ring was used with a 12 cm diameter hollow cathode without a cathode transmission foil. The ion beam was observed to self-focus 6 cm from the anode as indicated by the 1 cm^2 rear surface spall produced on a 0.16 cm thick aluminum witness plate. No spall was observed when the witness plate was placed a few centimeters to either side of this position. The focus location was in agreement with self-consistent analytical and numerical calculations for the self-focusing of a 500 kA, 1.3 MV proton beam. These calculations consist of solving ion orbit equations in the diode electromagnetic fields (determined from current and voltage measurements) and in the focusing/drift region magnetic fields (determined from net current measurements).

In the second set of self-focusing experiments, the 1.8 μm thick cathode foil was placed at 4 mm from the cathode face as shown in Fig. 7, and the drift tube was evacuated. A Rogowski coil in the evacuated drift tube measured a net current of about ½ the total ion current. The ion self-focus, as determined from the rear surface spall of the witness plate, moved from 6 cm to about 12 cm from the anode plane, again consistent with the predicted location for this reduced net current in the drift section. The origin and nature of this net current has been discussed[18].

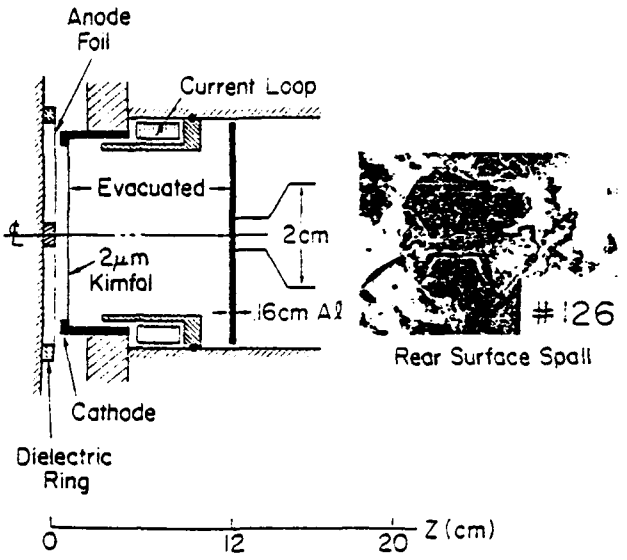

Fig. 7. Self-focusing in planar geometry with cathode foil and evacuated drift tube.

The final self-focusing experiments were performed with the cathode foil 2.8 cm from the anode and with the drift tube region behind the foil filled with 2 Torr of air. The large separation between the anode and the cathode foil insured that negligible electron current flowed from the cathode foil to the anode. This experiment is illustrated in Fig. 8. The cathode foil was bowed by the air pressure in the drift tube. The Rogowski coil surrounding the cathode foil support structure monitored the total current flowing into the cathode foil. The second Rogowski coil in the drift tube read less than 2% of the current read by the first for drift tube pressures between 0.2 to 3 Torr. With gas in the drift section, an aluminum witness plate placed at the 20 cm predicted focus location showed a 3 cm diameter rear surface spall. Computer analysis predicting ion orbits indicates that the 2-3 cm diameter focus spot size is consistent with axial motion of the best-focus location due to the time variation of diode current and voltage. That is, although the current and voltage values may be appropriate for tight focusing at peak power, the beam is under-focused early and over-focused late in time. No spall occurred a few centimeters to either side of this position and moving the cathode foil moved the focus location as predicted. It is important to note that damage patterns associated with focusing in the neutralizing gas backgrounds of this last set of experiments were typically well centered and symmetrical, whereas, focal spots obtained in vacuum display azimuthal irregularities and beam filamentation. Aluminum

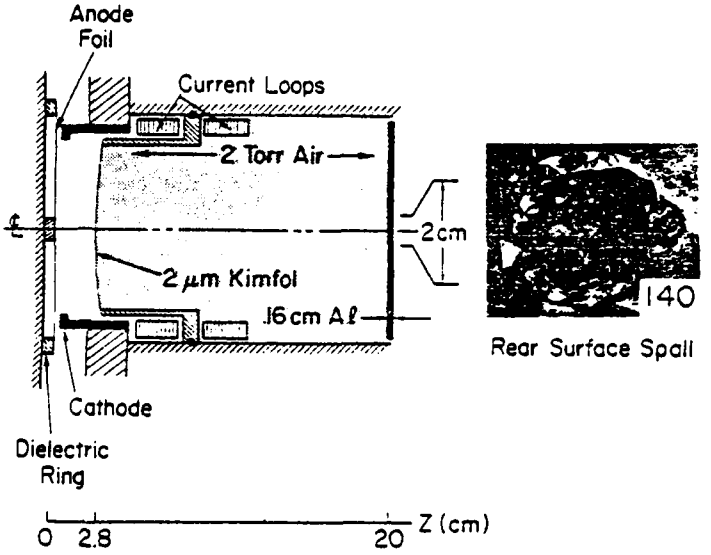

Fig. 8. Self-focusing in planar geometry with cathode foil and gas in drift tube.

K_α x-ray pinhole photographs[7] showed a peak current density of about 50 kA/cm^2.

4. ION FOCUSING IN CURVED GEOMETRY

In order to achieve high ion current densities for beam target experiments, a 0.025 cm thick spherical-section plastic anode foil with a 12.7 cm radius of curvature was used. As shown in Fig. 9, the same cathode geometry previously shown was employed except for the closer proximity of the thin cathode transmission foil to the cathode surface. In this short-focal-length geometry, the ion launching angle dominates over the magnetic deflection in the diode. Focal spot broadening due to radial and temporal field effects is thus minimized. Aluminum witness plates placed at the best focus location exhibit smaller area spall patterns (1-1.5 cm diameter) than in flat geometry with gas. When the anode was coated with CD_2, the observed focus was close to the geometric focus because of the small magnetic deflection of deuterons. By using small CD_2 targets and measuring neutrons from D-D and D-carbon reactions with activation counters and time-of-flight detectors, peak deuteron current densities of about 300 kA/cm^2 over 0.5-1 cm^2 were inferred. Typical neutron yields were a fraction of 10^{12} neutrons.

Important new experimental results for focusing are provided by a pinhole shadowbox diagnostic shown in Fig. 10. Small ion

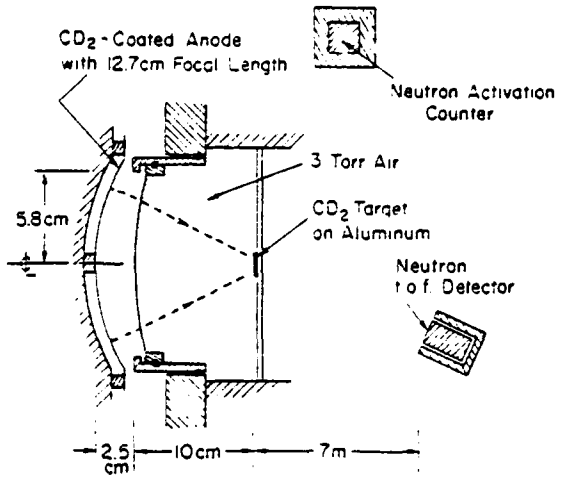

Fig. 9. Geometric focus experiments.

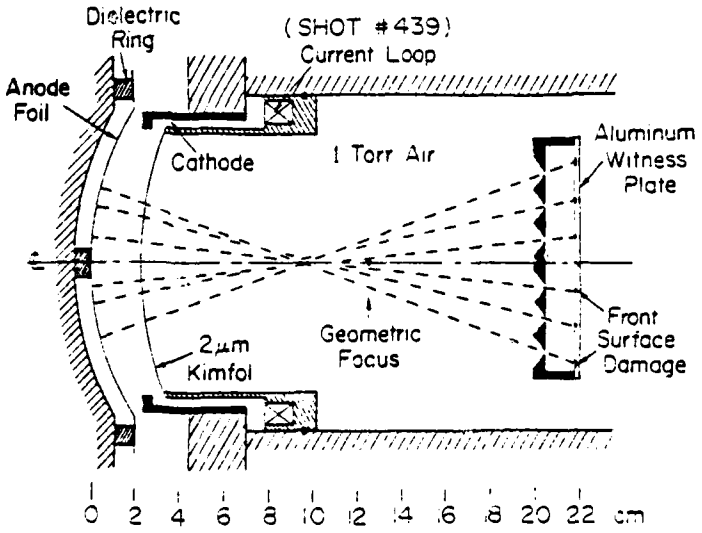

Fig. 10. Ion pinhole shadowbox.

beamlets are produced by masking off all of the beam drifting in the neutralizing background except for that portion emerging through 1 mm diameter holes placed along two diameters at right angles. Damage patterns produced on a aluminum witness plate 1 cm behind the pinhole array (shown as solid spots in the figure) allow one to determine ballistic orbits for ions entering pinholes at various radii. When the shadowbox is placed further from the diode than the center of the ion focus, these orbits can be projected from the damage spots back through the pinhole to the focus. These are shown as dashed lines in the figure. In this manner, the best focus location and the radial dependence of ion deflection angle can be determined. Additionally, the radial extent (typically a few millimeters) of each damage pattern reflects the time-variation of deflection angle due to time-varying diode fields. The preliminary Gamble II results with protons demonstrate that radial deflections of damage patterns (shown in Figure 10) are consistent with the measured focus location. Diode deflection angles were found to be roughly proportional to radius. Also, the significantly smaller observed azimuthal extent of damage compared with the radial extent of damage suggests that with proper aspheric anode and cathode shapes, focusing of ion beams to areas very much less than the present 1-3 cm^2 should be possible.

5. NUMERICAL SIMULATION OF PINCH-REFLEX ION DIODES

Numerical simulations of electron and ion flow in pinch-reflex diodes were conducted for the configuration shown in Fig. 11 using the NRL DIODE2D simulation code.[19] The initial equipotential lines are also shown in the figure. The diode dimensions modeled in the simulation had an R/d=20 aspect-ratio where r=6.8 cm was the outer radius of the hollow cathode and d=0.32 cm was the separation of the cathode face from the anode foil. The thickness of the cathode shank was 0.8 cm and the scattering foil was assumed to be 125 μm thick polyethylene. The distance between the reflexing foil and the solid anode was 0.29 cm. This space was assumed to be filled with ions which charge neutralize the reflexing electrons, making it unnecessary to solve for the electrostatic fields in that region. The distance from the reflexing foil back to the ion transmission foil inside the hollow cathode was 0.7 cm. These new simulations were carried out on a finer 64×40 mesh rather than the 32×40 mesh used in previously reported results.[20] The simulations also assumed azimuthal symmetry and were done in (R,Z) geometry with a time step of 0.25 psec.

The time evolution of the electron and ion flow in the diode is shown in Fig. 12 for a simulation done at 1.5 MV. The positions of the electrons and ions are shown in (R,Z) configuration space at four different times. Early in time (step 500), the electrons (one in 10 is plotted on the figure) had transited the diode and

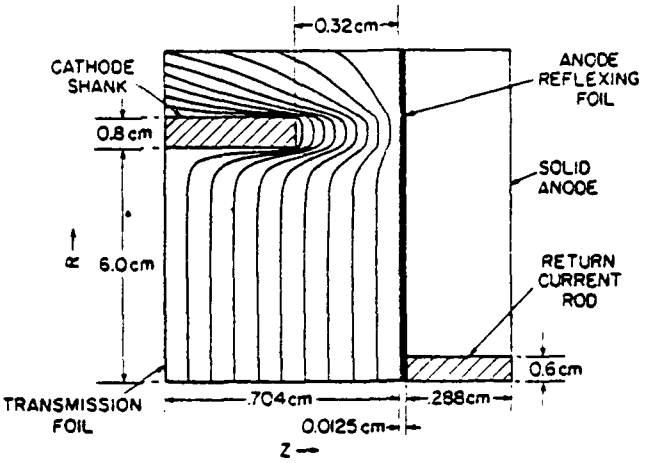

Fig. 11. Configuration used for pinch-reflex diode simulation showing equipotential lines due to applied voltage.

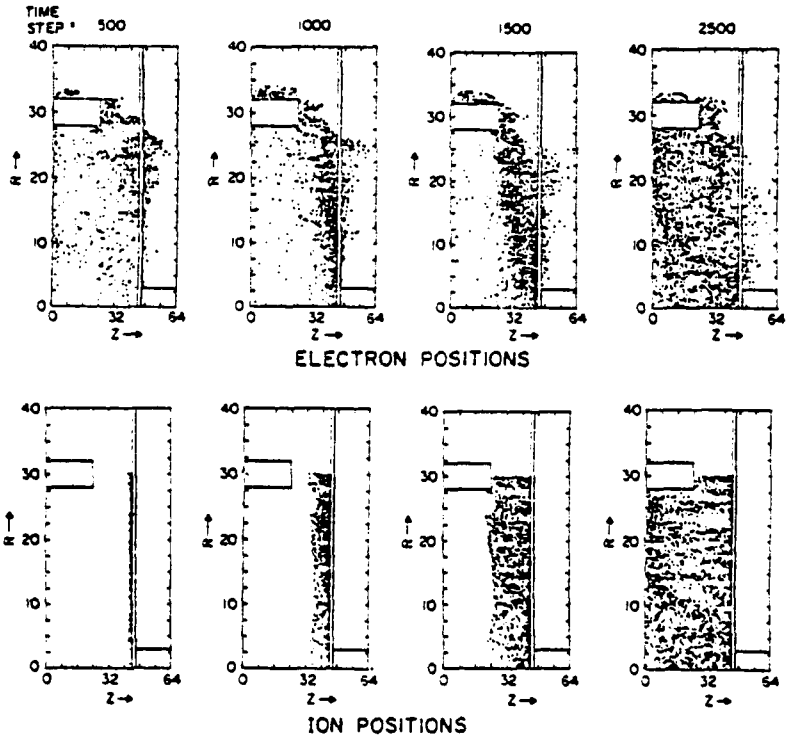

Fig. 12. Time history of the electron and ion positions in the diode.

reflexed several times through the foil. The ions had not yet crossed the diode gap and were clumped along the anode foil. By time step 1000, the electrons had established the pinched flow along the diode side of the reflexing foil. At step 1500, the pinched electron flow was well established and the electrons filled the diode gap. However, electrons did not flow along the foil except at low radii because of the tendency for electrons to follow ions at large radii to provide space charge neutralization. At step 2500 all the ions had now crossed the gap and a quasi-steady state was established. The flow pattern shown at step 2500 persisted for the remainder of the run which was taken to step 4000.

In the quasi-steady state the equipotential lines are piled up near the anode foil so that most of the potential drop occurs over a distance much less than the 0.32 cm gap between the cathode face and the anode foil. This justifies the assumption of Sec. 3 that the ion bending between the anode and cathode foil is primarily due to the self-magnetic field of the ions. The current density profile of the ions arriving at the cathode transmission foil is shown in Fig. 13. This current profile, which is the result of averaging the arriving ion current for 500 time steps, shows a 1/R dependence as predicted by analytic theory[2] for planar diodes. The simulation for this case assumed that ion emission occurred along the reflexing foil up to a radius of 6.4 cm. In this case, the net ion current was 590 kA and the electron current 330 kA. In order to determine if the average ion current density could be increased by suppressing ion emission at large radii, a case where emission was allowed only up to a radius of 3.0 cm was also

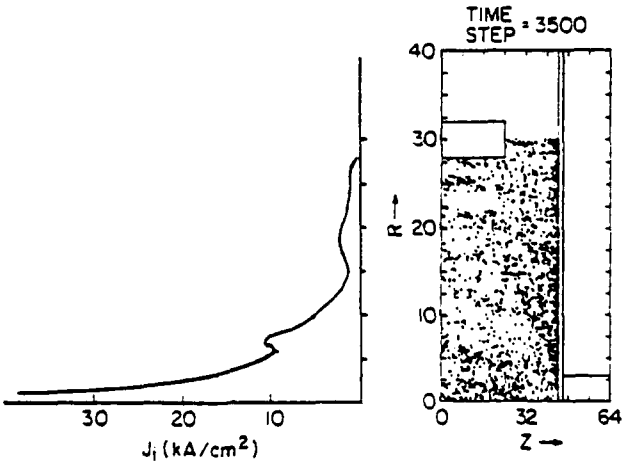

Fig. 13. Ion current density profile at the cathode and ion positions in the quasi-steady state.

simulated. In this case, the total diode current remained close to 900 kA and the total ion current decreased by about a factor of 2.

The simulation results are in reasonable agreement with the NRL experimental data with respect to total ion and electron currents. The geometry was different enough so that it is difficult to make a more quantitative statement. The transmission foil is further removed from the cathode face in the present Gamble II experiments than in the simulation and this may affect the diode behavior. Further simulations that are closer to the actual experimental configurations are being conducted so that a more direct comparison with experiments can be made.

6. ION ORBITS IN Z-DISCHARGE CHANNELS

As shown in Fig. 14, ions enter the discharge channel with a range of injection angles up to θ_M determined by the anode radius and distance to the focus. The externally-applied current flowing through the channel must be sufficient to confine ions with maximum transverse kinetic energy, that is, ions which enter the channel with the maximum injection angle at the maximum injection radius, r_s. The required discharge current can be determined from conservation of ion energy and P_z conical momentum

$$V_r^2 + V_z^2 = V_o^2 \; ; \qquad V_z = V_o \cos\theta + \frac{q}{m}\int_{r_o}^{r} B_\theta(r')dr' \quad ,$$

where $\frac{1}{2}mV_o^2$ is the energy of an ion with charge q, θ is the injection angle and r_o is the injection radius. In order for the magnetic

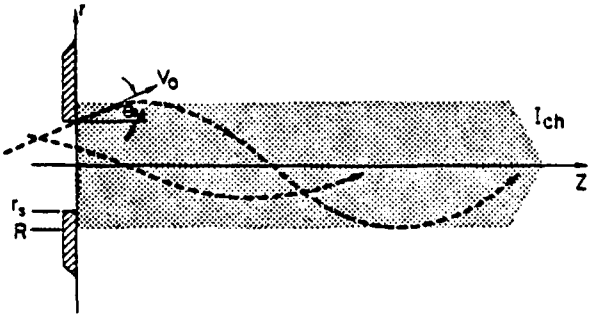

Fig. 14. Ion orbits in a Z-discharge channel.

field to be just sufficient to confine a maximum-transvere-energy ion to the channel radius (R), V_r must vanish when r = R for initial conditions $\theta = \theta_M$ and $r_o = r_s$. Substituting into the previous equation, results in the expression

$$q \int_{r_s}^{R} B_\theta \, dr = mV_o \, (1-\cos\theta_M) \quad . \tag{1}$$

Defining an ideal channel as one carrying a uniform discharge current so that $B_\theta \sim r$ when $r \leq R$, Eq. (1) takes the form

$$I_{ch}(A) = \frac{10^{-3} V_o (1-\cos\theta_M)}{1 - (r_s/R)^2} \tag{2}$$

for protons where I_{ch} is in amperes when V_o is in cm/s. This result indicates that megampere discharge currents are required to confine ions injected with large angles. Protons of 5 MeV with $\theta_M = 0.2$ radians require about 120 kA for confinement within the channel when $r_s/R = 2/3$.

Analytical and computational techniques have been used to determine the effects of various forms of nonideal channel behavior on ion confinement and beam bunching.[21] Axial electric fields associated with plasma currents and expansion disrupt confinement and reduce beam power multiplication due to bunching only if large enough to strongly slow the beam during transport. Radially non-uniform net currents develop as the beam passes through the background because of beam-induced MHD expansion of the channel. The effects of the resulting B_θ fields on beam confinement are discussed in Sec. 8. Channels which taper to smaller radius as they approach the pellet were investigated as a means of increasing the beam current density. A WKB-like analysis for the ion motion shows that only a small improvement in current density due to radial beam compression can be achieved before disruption of axial compression by bunching. Both analytic and numerical calculations were performed to determine ion confinement in a channel with a large amplitude m = 0 sausage instability. Fig. 15 shows one result of this work. The channel B_θ was modeled as $\sim r$ inside the channel radius R(z), and $\sim 1/r$ outside. With every change in axial location $\Delta z = \lambda$, the value of R changed abruptly and randomly to simulate the non-linear development of the instability. A large number of ion orbits were numerically determined for a range of injection angles up to θ_M and injection radii up to r_s. The figure shows a cross-section of beam ion density at various axial locations along the channel. The case shown corresponds to $r_s = 0.4$ cm, R = 0.6 cm, $E_i = 5$ MeV, $\theta_M = 0.2$ radians, $I_{ch} = 120$ kA, $\lambda = 3.8$ cm, $\Delta R_{rms}/\bar{R} = 1$. This high

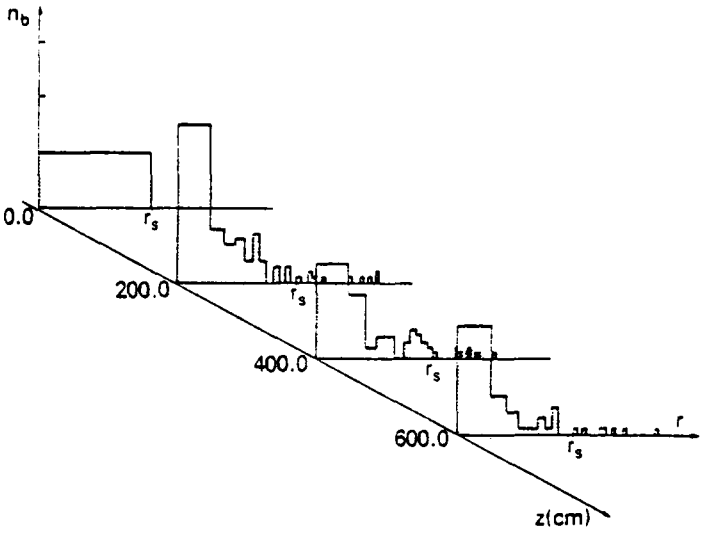

Fig. 15. Beam density profile at various axial locations along a sausage unstable channel.

degree of fluctuation is required for radial loss of half the beam ions after transporting 6 m. When ΔR_{rms} is decreased by about a factor of 2, only about 9% of the beam is lost at 6 m. Good radial confinement is predicted for all cases in which the axial wave length of the instability is much smaller than the betatron wavelength of the ion in the channel. Electrostatic and electromagnetic microinstabilities driven by the relative streaming between the beam ions and the channel plasma have been discussed previously.[22]

7. ION TRANSPORT EXPERIMENTS

Figure 16 illustrates the experimental configuration for transport experiments on Gamble II. The planar, pinch-reflex diode configuration shown previously in Fig. 8 was used to bring a 0.5 MA, 1.4 MV proton beam to a narrow-angle focus ($\sim$ 50 kA/cm^2) 20-30 cm downstream from the diode. The transport section consisted of a copper pipe containing an insulating ceramic liner filled to the 0.2-2 Torr air background pressure of the focusing-drift section. The inside diameter of the ceramic liner defines the diameter of the wall-stabilized discharge. A discharge channel diameter of 4.5 cm was employed. The discharge current was provided by a 20 kV, 10 kJ capacitor bank. The current rose to about 50 kA in 15 μs after which time the ion beam was injected into the channel. This current satisfies Eq. (2) for the injection angles employed in the experiment. Measurements of transport efficiency were provided by diagnosis of 6 MeV gamma rays produced by the interaction of beam protons with fluorine[23]. Collimated scintillator-

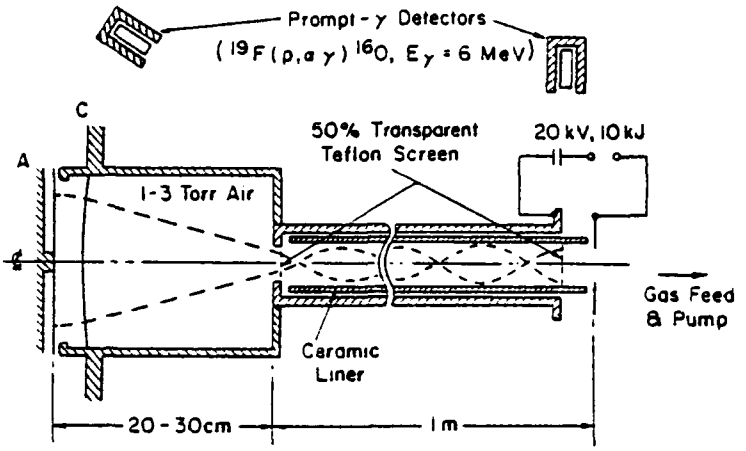

Fig. 16. Ion transport experiment schematic.

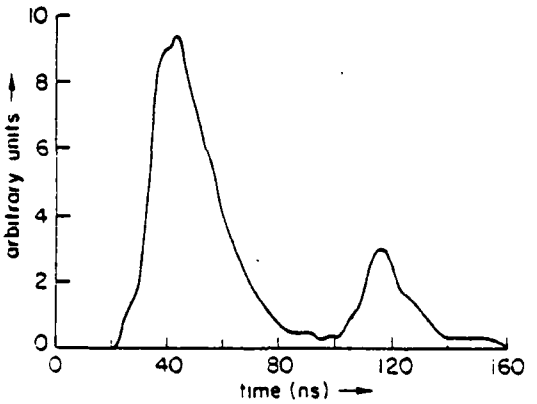

Fig. 17. Prompt-γ signal from two 50% transparent teflon targets placed on meter apart in the channel.

photomultiplier detectors were used to detect the gamma rays produced in 50% transparent teflon screens placed at the entrance and exit apertures of the transport system.

The signal shown in Fig. 17 was obtained with a single detector placed about 4 m from both screens and behind about 0.5 m of concrete. Signals from the two screens are separated by the ion time-of-flight through the 1 m discharge channel. Because the teflon screens are 50% transparent, the second signal must be multiplied by a factor of 2 in order for comparison with the signal from the entrance aperture. Since the gamma-ray production cross-section is a strong function of the proton energy, the transport efficiency could not be immediately inferred from the ratio of signals associated with the two screens. Assuming no ion energy loss during transport, experimental results indicated a lower limit of 50% transport efficiency. If an energy loss of 200 kV is assumed, which is consistent with the relative timing between the prompt-γ signals shown in Fig. 17, then the particle transport efficiency in the channel is about 80%. A more concrete example of the ability to transport ion beams is provided by witness plates at the exit aperture. Aluminum plates 0.16 cm thick exhibited rear surface spalls with widths less than the channel diameter. Null experiments, measurements without channel current, did not show evidence of ion transport.

In more recent transport experiments a smaller 1.6 cm diameter channel was used with a much faster risetime (0.5 μs) capacitor bank than previously employed. Preliminary results indicate that proton beams with current densities of several tens of kA/cm^2 were efficiently transported over 1 m distances. Unlike the large diameter channel transport experiments, shots were taken with the ion beam injected into the channel while the channel plasma was still radially imploding. On these shots, the shapes and relative timing of the input and output prompt-γ signals suggest that the protons may have gained rather than lost energy in the channel. This observation would be consistent with recent theoretical predictions[24] that the transported ion beam could gain energy from the fields associated with a radially imploding Z-pinch plasma. This phenomenum is presently under investigation.

8. RESPONSE OF THE CHANNEL TO BEAM TRANSIT

As the focused ion beam transits the transport channel, it heats the background plasma by collisional deposition and induces plasma-electron return currents which resistively heat the plasma. Since the electromagnetic fields induced by the beam can vary substantially from those assumed to confine the beam ions, it is important to determine how the self-consistent fields alter beam confinement and energy loss during transport. To answer these

questions, a 1-D radial, time-dependent MHD code has been developed[25]. The code solves the usual conservation equations for particle number, momentum and energy. The $\vec{\nabla} \times \vec{B}$ and $\vec{\nabla} \times \vec{E}$ Maxwell's relations, and electron transport equations (using classical coefficients for electrical and thermal conduction) close the set of equations. The beam is specified by its current density in space and time and the particle energy as a function of time. Collisional beam deposition and plasma-electron return-current heating are included as is bremsstrahlung radiation cooling. Development of radial profiles in time for background density, electron and ion temperature, azimuthal magnetic field and radial velocity are shown in Fig. 18 for a 50 kA discharge in deuterium carrying 600 kA of 5 MeV protons in a 50 ns pulse. Since the plasma is initially at rest, no radial velocity profile is shown in Fig. 18a. The initial temperature distribution is thus determined by an equilibrium pressure balance condition. Once the beam enters the channel, the plasma pressure and $\vec{j} \times \vec{B}$ forces acting on the plasma push material out of the channel interior and pile it up against the steep density gradient at the channel edge. The initial magnetic field profile corresponds to uniform current density arising from the long times and the low conductivities associated with channel creation. Once the beam heats the channel (Fig. 18b), the conductivity rises quickly and magnetic field lines become frozen in the plasma. The magnetic field is then convected out of the center of the channel along with the plasma flow.

A primary criterion for maintenance of beam confinement is suggested by Eq. (1) and is given by the integral extended from r_o to R. If the value of the integral is reduced, ions injected with large r_o or θ_o can reach the high density edge of the channel and be lost. For low beam current cases, the plasma channel response to the beam is sufficiently gentle not to disrupt confinement. However, in the high-current cases, ions with larger transverse energy are lost.

The evolution of the confinement integral with time does not depend sensitively on the ion energy. This behavior can be understood qualitatively by examining the plasma equation of motion.

$$\rho \frac{dV_r}{dt} = - \frac{\partial p}{\partial r} - j_z B_\theta \approx j_b B_\theta \qquad (3)$$

The final expression on the right hand side of Eq. (3) results from the dominance of the $\vec{j} \times \vec{B}$ term over the pressure term and good beam current neutralization. For a maximum allowed acceleration given by $2R/\tau^2$, where τ is the beam duration, Eq. (3) yields

$$I_b I_{ch} < 300\, \rho\, R^4/\tau^2 \qquad (4)$$

for maintenance of beam confinement. In Eq. (4), the currents are

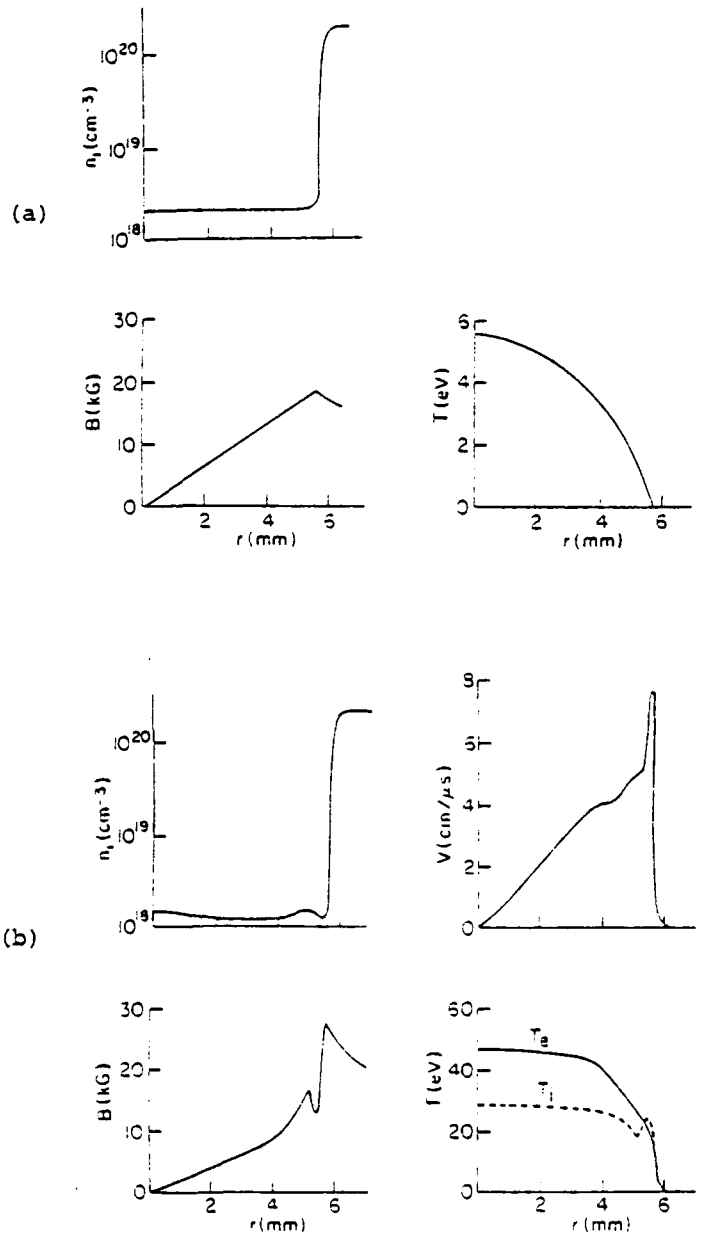

Fig. 18. Initial (a) and final (b) radial profiles in time for background plasma density, azimuthal magnetic field, electron and ion temperature ($T_i = T_e$ initially), and radial plasma velocity (V=0 initially).

in amperes and the terms of the right-hand-side are in cgs units. This condition is in qualitative agreement with the results of the MHD code. Because of the greater primary beam deposition, lower-voltage ion beams require lower background density. Thus, the maximum allowed value of $I_b I_{ch}$ is reduced with lower ion voltage. This indicates that less power can be transported in channels carrying lower-voltage ions unless the channel current can be significantly reduced. However, the channel current is determined primarily by the spread of injection angles and θ_M is unlikely to be reduced for less-stiff lower-energy ions. Additionally, Eq. (4) is easier to satisfy with the beam in the bunched state since $I_b T$ remains constant as T is reduced. If a final focusing stage after transport can be employed[26], then the beam can be transported with a radius larger than the pellet size. In this case the constraints of Eq. (4) can be considerably relaxed because of the strong R^4 dependence.

A second important consideration for beam transport channels is the total energy loss suffered by the beam during transport. The energy loss consists of both that due to primary deposition and that due to slowing in the electric field produced by return currents and plasma expansion. For the example considered in Fig. 18, the 5 MV protons lose about 200 kV/m. This energy loss could be reduced or possibly turned into an energy gain[24] if the channel plasma during beam injection is imploding with a velocity of $\sim 10^7$ cm/sec using a 100 kA channel current.

9. BEAM BUNCHING DURING TRANSPORT

Since the time of flight of the ions through the channel to the pellet usually exceeds the beam pulse duration, applying an accelerating voltage ramp at the diode can result in power multiplication (PM) by beam bunching[27]. Since the pulsed-power technology employed results in ion emission times of 50-100 ns and the desired irradiation time on the pellet is about 20 ns, as much as a factor-of-5 bunching is desirable. For purely axial motion, ions accelerated by the ideal voltage waveform

$$\Phi(t) = \frac{\Phi_o}{(1-t/t_a)^2} \; ; \; 0 \leq t \leq T < t_a \qquad (5)$$

all arrive at the target at the same time t_a. In reality, errors in voltage shape, $\delta\Phi$, and the spread in ion injection angles contribute to a spread in arrival times, δt_a, thus limiting the degree of power multiplication to a factor $T/\delta t_a$. For a desired PM factor of 5, analysis indicates that $\delta\Phi/\Phi \leq 0.15$ and $\theta_M \leq 0.3$ radians are sufficient for parameters of interest.

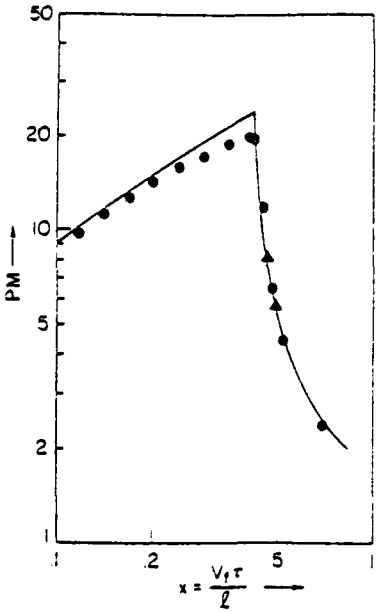

Fig. 19. Theoretically achievable power multiplication predicted by analytic modeling (solid curve) and macroparticle code.

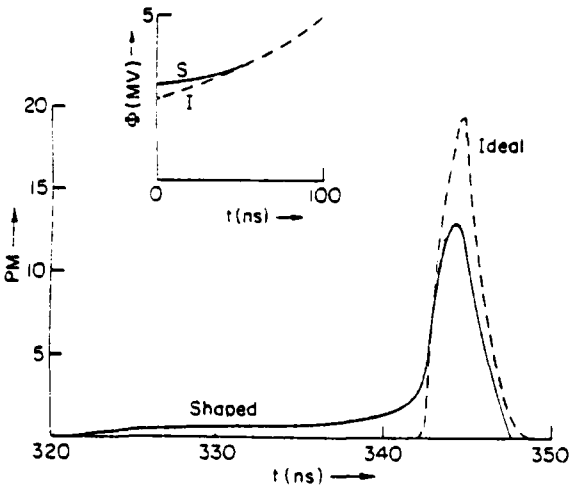

Fig. 20. Bunched pulse shaping.

Figure 19 compares analytic modeling of achievable power multiplication with a macroparticle code, where λ is the distance to the target and V_f is the ion speed at $t = \tau$. Below $x = 0.414$, PM is limited by the spread in injection angles $\theta_M = 0.2$ radians. Above this value, PM is determined by a maximum voltage ramp $\Phi_f/\Phi_o = 2$ in order to control the energy spectrum of ions depositing in the pellet.

Figure 20 compares the time variation of power on target using two voltage waveforms and the parameter set $r_s = 0.4$, $R = 0.6$ cm, $\lambda = 7.5$ m, $\theta_M = 0.2$ radians. Peak power multiplication is achieved by employing the ideal voltage. In that case, the power multiplication is limited by the dispersion in injection angles. When the accelerating voltage is higher than the ideal early in time, some ions arrive early on target. This results in a shaped foot which may be desirable for some inertial-confinement-fusion target configurations.

10. SYSTEM REQUIREMENTS FOR INERTIAL CONFINEMENT FUSION

Pulsed power, ion focusing, transport, bunching and beam-target interaction considerations can be combined in order to determine an acceptable set of system parameters for the ignition of a high-gain fusion pellet. High voltage beams are easily focused because of their relative insensitivity to time-varying magnetic fields in the diode. However, their long range in materials leads to inefficient energy coupling to fusion targets. Low voltage beams suffer from excessive energy loss in the transport channel and difficulty in focusing. For any voltage, channel hydrodynamic response calculations indicate difficulty in transporting ion beams much in excess of 1 MA without employing a final focusing stage. Thus, for a fixed power and energy requirement delivered to the target, MHD considerations establish a lower limit on the number of channels which can be used to transport ion beams to the target. An upper limit on the number of channels which can be used is set by considerations that include channel creation energy and beam overlap problems. These points are considered in Fig. 21 which defines an acceptable parameter range for a 2 MJ ion beam incident on a high-gain pellet. The SANDIA PBFA concept has design objectives in the lower right-hand corner of the window. Research at NRL concentrates primarily on parameters of the upper left. Table 1 summarizes an acceptable range of system parameters based on the considerations discussed above. Parameters based on two pellet requirements and two ion pulse durations are shown. The stored energy is an estimate of the total electrical energy stored in the Marx generators required to provide the total ion beam energy. The shorter-duration beams require higher powers in the diode but also require less bunching in order to achieve power on target. The focused power represents the total focused ion beam power for all the modules into the entrance of all the channels.

AD-A129 821 DIODE DYNAMICS BEAM GENERATION AND TRANSPORT AND PLASMA EROSION OPENING SWITCH DEVELOPMENT(U) JAYCOR ALEXANDRIA VA P F OTTINGER 17 MAY 83 JAYCOR-J207-83-C-001 5/8

UNCLASSIFIED N00173-80-C-0202 F/G 9/1 NL

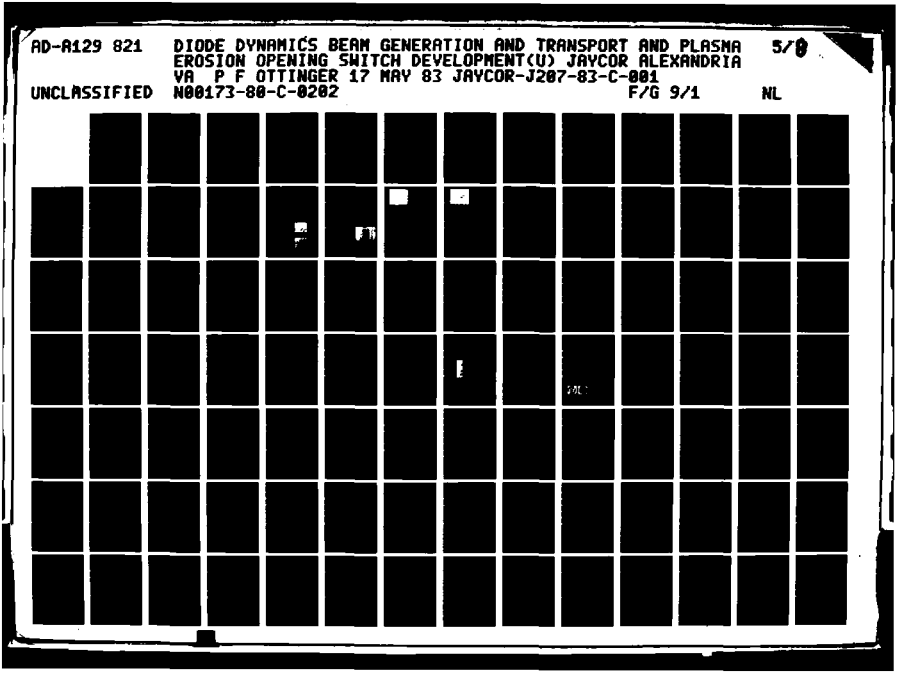

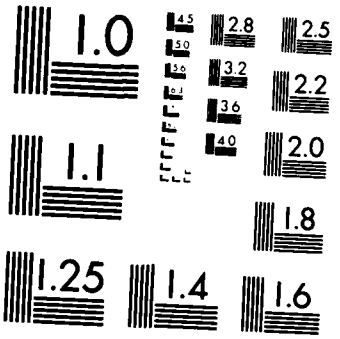

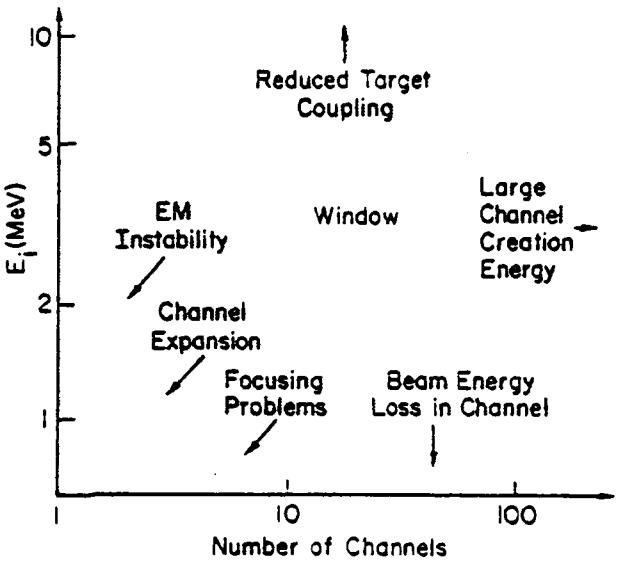

Fig. 21. Channel number considerations for protons in hydrogen.

Table 1. Ignition System Parameter

ENERGY ON PELLET (MJ)	3		2	
POWER ON PELLET (TW)	200		100	
STORED ENERGY (MJ)	24		16	
PULSE DURATION (ns)	100	50	100	50
FOCUSED POWER (TW)	35	70	23	45
POWER MULTIPLICATION	6	3	4.5	2
FOCUSED CURRENT (MA)				
5 MeV PEAK	7	14	4.5	9
2 MeV PEAK	18	35	12	23
MIN. BUNCHING LENGTH (m)				
5 MeV PROTONS	6	2.5	6	2
2 MeV DEUTERONS	3	1	2.5	0.8

Focused current represents the total current transported by all channels. Using 1 MA as the current which can be transported in any given channel, the focused current numbers represent an estimate of the minimum number of channels required to transport the total beam. The minimum channel length (i.e. stand-off distance) is arrived at by determining the smallest transport length which can achieve the desired degree of power multiplication (PM) using an accelerating voltage which varies by no more than a factor of 2. This bunching length may be estimated from[21]

$$\frac{V_c T}{\ell} = \frac{0.414}{1-1/PM} \quad .$$

The scaling of ℓ with PM results from the fact that smaller lengths than necessary for optimal bunching are sufficient for moderate power multiplication factors.

Extension of these results to ion species other than Z = 1 requires further investigation of transport properties. Higher voltage beams can transport at lower beam current to achieve beam powers comparable to Z = 1. Channel currents are uncertain. From Eq. (1), I_{ch} is proportional to the larger values of m/q. However, it tends to be reduced by the smaller values of θ_M permitted by better focusing control.

In the near future scaling of present results will be attempted in the following areas. Diode behavior at the 3-5 TW level on PITHON will be studied in order to check ion beam efficiency and focusability. The physics of higher voltage (up to 10 MV) diodes operating at impedances up to 20 ohms will be studied on the Harry Diamond Laboratory Aurora generator.[28] Transport of ion beams will be performed in longer channels where beam bunching may be investigated. Larger diameter channels with a final focusing stage will be studied in order to achieve transport of higher current, longer duration ion beams. The effect of imploding plasma discharges on the energy of the transported ion beam will be investigated. These experiments will provide the MA/cm^2 level fluxes required for relevant ICF beam target studies.

ACKNOWLEDGMENT

The authors are indebted to R. Genuario and J. Maenchen for their essential contribution to the ion beam experiments on PITHON.

REFERENCES

1. Shyke A. Goldstein and R. Lee, Phys. Rev. Lett. 35, 1079 (1975).
2. J. W. Poukey, J. R. Freeman, M. J. Clauser, and G. Yonas, Phys. Rev. Lett. 35, 1806 (1975).
3. J. W. Poukey, J. Vac. Sci. Technol. 12, 1214 (1975).
4. A. E. Blaugrund, G. Cooperstein, J. R. Boller and Shyke A. Goldstein, Bull. Am. Phys. Soc. 20, 1252 (1975).
5. P. A. Miller, C. W. Mendel, D. W. Swain, and S. A. Goldstein, in Proceedings of the International Topical Conference on Electron Beam Research and Technology, Albuquerque, New Mexico (1975), p. 619; G. Cooperstein, S. J. Stephanakis, J. R. Boller R. Lee, and Shyke A. Goldstein, in Proceedings of the 1976 IEEE International Conference on Plasma Science, Austin, Texas (1976), (IEEE Cat. 76CH1083-5-NPS), p. 126.
6. Shyke A. Goldstein, D. P. Bacon, D. Mosher and G. Cooperstein, Proceedings of the Second International Topical Conference on High Power Electron and Ion Beam Research and Technology, Ithaca, New York (1977) p. 71.
7. D. J. Johnson, G. W. Kuswa, A. V. Farnsworth, Jr., J. P. Quintenz, R. J. Leeper, E. J. T. Burns, and S. Humphries, Jr., Phys. Rev. Lett. 42, 610 (1979); D. J. Johnson, Bull. Am. Phys. Soc. 24, 925 (1979).
8. G. Cooperstein, Shyke A. Goldstein, D. Mosher, F. W. Oliphant, F. L. Sandel, S. J. Stephanakis and F. C. Young in Proceedings 3rd International Topical Conference on High Power Electron and Ion Beam Research and Technology, Novosibirsk, USSR (1979).
9. R. O. Bangerter and D. J. Meeker, in Proceedings of the Second International Topical Conference on High Power Electron and Ion Beam Research and Technology, Ithaca, New York (1977), p.183; J. H. Nuckolls, in Proceedings of the Topical Meeting on Inertial Confinement Fusion, San Diego, CA (1978), (Optical Society of America 78CH1310-2QEA).
10. G. Yonas, Sci. Am. 239, No. 5, 50 (1978); P. A. Miller, D. J. Johnson, T. P. Wright and G. W. Kuswa, Comments on Plasma Physics and Controlled Fusion, 5, 95 (1979).
11. S. J. Stephanakis, J. R. Boller, G. Cooperstein, Shyke A. Goldstein, D. D. Hinshelwood, D. Mosher, W. F. Oliphant, F. C. Young, R. D. Genuario and J. E. Maenchen, Bull. Am. Phys. Soc. 24, 1031 (1979).
12. A. E. Blaugrund, G. Cooperstein, and Shyke A. Goldstein, Phys. Fluids 20, 1195 (1977).
13. J. W. Poukey, in Proceedings of the International Topical Conference on Electron Beam Research and Technology, Albuquerque, New Mexico (1975), p. 247.

14. S. J. Stephanakis, D. Mosher, G. Cooperstein, J. R. Boller, J. Golden, and Shyke A. Goldstein, Phys. Rev. Lett. 37, 1543 (1976).
15. Shyke A. Goldstein, G. Cooperstein, Roswell Lee, D. Mosher and S. J. Stephanakis, Phys. Rev. Lett. 40, 1504 (1978).
16. J. R. Boller, J. K. Burton, and J. D. Shipman, Jr., in Proceedings of the IEEE Second International Pulsed Power Conference, Lubbock, Texas (1979).
17. F. C. Young, J. Golden, and C. A. Kapetanakos, Rev. Sci. Instr 48, 432 (1977).
18. Shyke A. Goldstein, A. T. Drobot, in Proceedings of 1979 IEEE International Conference on Plasma Science, Quebec (1979), (I Cat. 79CH1410-ONPS), p. 161.
19. R. Lee and Shyke A. Goldstein, NRL Memorandum Report 3702 (197 D. Mosher, G. Cooperstein and Shyke A. Goldstein, NRL Memoran Report 4130 (1979).
20. A. T. Drobot, R. J. Barker, R. Lee, A. Sternlieb, D. Mosher an Shyke A. Goldstein, in Proceedings of the 3rd International Topical Conference on High Power Electron and Ion Beam Research Technology, Novosibirsk, USSR (1979).
21. P. F. Ottinger, D. Mosher, Shyke A. Goldstein, in Proceedings the 1979 IEEE International Conference on Plasma Science, Que (1979), (IEEE Cat. 79CH1410-ONPS), p. 105, and to be publishe in Phys. Fluids (1980).
22. P. F. Ottinger, D. Mosher and Shyke A. Goldstein, Phys. Fluids 22, 332 (1979); P. F. Ottinger, D. Mosher and Shyke A. Goldstein, NRL Memorandum Report 4088 (1979), and submitted t Phys. Fluids.
23. J. Golden, R. A. Mahaffey, J. A. Pasour, F. C. Young, C. A. Kapetanakos, Rev. Sci. Instrum. 49, 1384 (1978).
24. Shyke A. Goldstein and D. A. Tidman, private communication.
25. D. G. Colombant, Shyke A. Goldstein, D. Mosher, in Proceedings of the 1979 IEEE International Conference on Plasma Science, Quebec (1979), (IEEE Cat. 79CH1410-ONPS), p. 105.
26. P. F. Ottinger, Shyke A. Goldstein and D. Mosher, private communication.
27. D. Mosher, Shyke A. Goldstein, Bull. Am. Phys. Soc. 23, 800 (1978).
28. B. Bernstein, I. Smith, IEEE Trans. Nucl. Sci. 20, 294 (1973).

INTERNATIONAL ATOMIC ENERGY AGENCY

9th INTERNATIONAL CONFERENCE ON PLASMA PHYSICS AND CONTROLLED NUCLEAR FUSION RESEARCH

Baltimore, USA, 1–8 September 1982

IAEA-CN-41/ N-2

LIGHT-ION INERTIAL-CONFINEMENT-FUSION RESEARCH AT NRL+

G. Cooperstein, R. J. Barker*, D. G. Colombant, A. Drobot**,

Shyke A. Goldstein*, R. A. Meger*, D. Mosher, P. F. Ottinger*,

F. L. Sandel*, S. J. Stephanakis and F. C. Young

Naval Research Laboratory

Washington, DC 20375

LIGHT-ION INERTIAL-CONFINEMENT-FUSION RESEARCH AT NRL

ABSTRACT

High-brightness proton beams (.4 MA, 1 MV) have recently been extracted from 20 cm^2 axial pinch-reflex diodes (PRDs) mounted on the NRL Gamble II generator. A source power brightness of > 10 TW/cm^2rad^2 was achieved in these experiments. A new barrel-shaped equitorial PRD that can be coupled to PBFA-II has also been operated on Gamble II and has demonstrated 50% proton efficiency with predominately azimuthally-symmetric charged-particle flow. In other experiments the stopping power of deuterons in hot plasmas was measured using a PRD on Gamble II. Results show about 40% enhancement in stopping power over that in cold targets when the beam was focused to about .25 MA/cm^2. Research is also being performed on transporting ion beams in large-diameter channels ($\gtrsim$ 2.5 cm) and on a post-transport, plasma-filled, magnetic focusing section to bring the beam to pellet dimensions.

1. INTRODUCTION

Recent NRL experiments and theory have investigated key aspects of two ignition-system configurations for light-ion-drivers on Sandia's PBFA-II [1]. The first configuration uses groups of modules to drive small-area disc-like axial ion diodes each of which focuses a beam into a z-discharge transport channel about 2 m long and a few cm in diameter [2]. Each channel is terminated in a short, higher-current discharge which magnetically focuses the beam onto the pellet [3], and thus allows larger-diameter beams to be transported and then focused. Such a system is schematically illustrated in Fig. 1. The second configuration ties all 36 modules to a single barrel-shaped radial ion diode with 1 m dimensions surrounding the pellet located on the diode axis of symmetry.

Section II will review recent high brightness diode experiments on Gamble II. The new barrel-shaped equitorial PRD concept and preliminary Gamble II results will be reviewed in Section III. Section IV will discuss the energy loss experiments of deuteron beams in subrange Mylar and aluminum targets. Finally, transport considerations in large diameter channels, and final focusing concepts and experiments will be discussed in Section V.

2. ION BEAM BRIGHTNESS STUDIES

Beam power brightness at the diode imposes the ultimate limit on the ability to focus ion beams onto targets. The PRD, which has been previously described [4,5], has been studied with respect to its performance as a source of high current density, low divergence ion beams. Electron-filamentation instabilities, which may occur in the electrode plasmas and vacuum gap are currently under investigation. Changes in diode

geometry and electrode materials are being investigated experimentally in order to determine their effects on the instabilities.

In recent 1 TW diode experiments on Gamble II, .6 TW proton beams were extracted from 20 cm^2-area anode foils. The ion beam brightness was measured crudely by a shadowbox technique [5,6] that uses multiple pinhole images of the ion beam. With the multiple hole shadowbox one can reconstruct the ion source pattern and its divergence. The ion source exhibited 10 to 20 beamlets 1 cm in diameter for this small radius diode. The beam divergence changed drastically when the gap, Δ, between the anode and the cathode inner foil was changed. The half angle of the diverging beam cone, $\delta\theta$, was measured to be ~ .1 rad at a gap of 1.5 cm and ~ .05 rad at a gap of .5 cm.

A simple calculation to explain beam divergence versus gap width was performed assuming that the total ion beam current (450 kA) was distributed equally among 15 sources each having a diameter of 1 cm. Self-pinching of these ion beamlets by self-magnetic fields would result in $\delta\theta=.08\Delta/\sqrt{V}$ for protons at a voltage V measured in MV. The experimental results at V = 1.2 MV show that $\delta\theta$ agrees well with the predicted value at the larger gap of Δ=1.5 cm. At the smaller gap, however, the experimental divergence cannot be explained by this magnetic self-pinching effect.

Two other mechanisms which could increase the beam divergence have been identified. The first is associated with plasma hydrodynamics when the anode plasma is formed at discrete spots and expands in a two dimensional manner generating bulges on the anode. Such spotty structure is clearly seen in the shadowbox pinhole images. The second mechanism is filamented electron beam flow. The resultant space charge structure introduces azimuthal and radial components to the electric field in addition to the axial field. The filamented electron flow could also result in azimuthal magnetic deflections of the beam ions.

The beam brightness ($JV/\delta\theta^2$) observed for V = 1.2 MV, J = 20 kA/cm^2 and $\delta\theta$~ .05 rad is ~ 10 TW/cm^2rad^2. Holding J constant, scaling up the voltage to 3 MV, reducing $\delta\theta$ appropriately ($\delta\theta\sim1/\sqrt{V}$) and assuming a factor-of-4 bunching during transport without brightness loss, leads to a modular-beam brightness of about 250 TW/cm^2rad^2. If 40% of the solid angle surrounding a pellet is subtended by final-focus exit apertures, on target modular power densities approaching 100 TW/cm^2might then be achievable with existing PRDs.

3. EQUITORIAL-PINCH-REFLEX DIODE

A new version of the NRL PRD has been designed to operate on the radial triplate geometry of Sandia's PBFA-I. A conceptual schematic is shown in Fig. 2. This diode produces two cylindrically-symmetric sheet beams of electrons which flow from top and bottom by self-magnetic pinching and reflexing action on the anode foil to a common line pinch around the equator of the diode, hence the name equitorial-pinch-reflex diode (EPRD).

Although this diode appears to be a simple topological variation of the conventional PRD, there are basic conceptual differences. There is no electron-space-charge-density enhancement as occurs with the conventional axial PRD because there is no radially converging electron flow towards the diode axis. This lack of electron convergence leads to a constant ion current density rather than one that increases inversely with the distance from the diode axis as in the axial PRD; hence the EPRD has better focusing properties.

Another major difference and advantage of the EPRD over the conventional PRD is that the ratio of ion current to electron current, I_i/I_e, is decoupled from the diode impedance Z. For a given anode-cathode gap spacing, D, and diode radius, R, the impedance of a EPRD of height H is proportional to D/R as with the conventional PRD, however, I_i/I_e is proportional to H/D (i.e., the electron path length/the ion path length) and is independent of diode radius or diode impedance. Thus, for any current equal to or above the critical current, the ion production efficiency can be made arbitrarily large by increasing the separation between the two disc cathodes. These properties were verified using a particle-in-cell code [7].

The EPRD has been tested on NRL's Gamble II generator by driving only the upper half of the diode shown in Fig. 2 in a coaxial-feed geometry. The anode radius was 7 cm and typical anode-cathode gaps were 3.5 to 6 mm. Initial experiments [8] have shown the diode to be an efficient ion source and a good electrical match to the accelerator. Net ion currents on the order of 400 kA have been measured with diode impedances of 1.5-2 Ω. Predominately azimuthally-symmetric electron and ion current flow has been observed. The diode impedance has been shown to be a linear function of anode-cathode gap but practically independent of diode axial height as predicted by theory. Shadowbox results show a time-averaged half-angle divergence of 1-2° from areas not containing filaments. Experiments to reduce beam filamentation are in progress. Sandia National Laboratory is presently testing a high power diode of similar design on PBFA-I [9].

4. ENERGY LOSS EXPERIMENT

Theoretical research [10] indicates that, at the ionization levels of ICF pellet plasmas, the stopping power of light ions may be enhanced by a factor-of-two over that in the cold target. In this section, measurements of the energy loss of MeV deuterons in plasmas formed by focusing intense Gamble II ion beams (1 MeV, .2 MA, 20 ns) onto subrange-thick targets are presented. The results demonstrate that the stopping power of the heated target is enhanced over that of the cold target.

For these energy-loss measurements, a spherically-contoured PRD is used to produce a 250 kA/cm^2 focused deuteron beam while a planar anode foil version of the diode is used to produce a 50 kA/cm^2 deuteron beam. The .01 cm thick plastic anode foil is coated with deuterated polyethylene (CD_2) to provide the deuterons.

The experimental technique for determining the deuteron-energy loss uses neutron time-of-flight (TOF) with a

multilayered target [11]. The target consists of a subrange stopping foil sandwiched between .3-μm and 1.0-μm thick layers of CD_2. Measurements of the d-d neutron TOF from the two CD_2 targets are used to determine both the incident deuteron energy and the deuteron energy loss in the stopping foil on each shot. The thickness of the stopping foil is adjusted so that neutrons from the two CD_2 targets can be resolved. In these experiments, 6.4-μm Mylar and aluminum stopping foils are used. The time interval between the peak of the ion power and the peak of the first neutron pulse determines the neutron energy from the front CD_2 target and, by kinematic calculation, the incident deuteron energy. The time separation of the two neutron peaks provides a direct measure of the deuteron energy loss in the stopping foil.

The results of stopping-power measurements using both planar and spherical diodes are presented in Fig. 3. For each case, the measurements are compared to the cold-target energy loss deduced from measurements of stopping cross sections by Andersen and Ziegler [12]. The measured energy losses are significantly larger than cold-target values in all cases except for the planar diode with a Mylar target. In this case, the measurements are consistent with cold-target values.

The deuteron energy losses deviate from that in a cold-target when sufficient ionization occurs in the stopping medium. Hydrocode calculations which model this experiment [13] indicate that the target has expanded to about 2-mm thickness at the peak of the power pulse, and that the electron temperature is 4 to 5 eV at 50 kA/cm^2 and 13 to 17 eV at 250 kA/cm^2 for an aluminum stopping foil. Similar results for Mylar are ~3 eV at 50 kA/cm^2 and 9 to 11 eV at 250 kA/cm^2. The calculated energy losses at peak power are shown as solid triangles in Fig. 3, and are in reasonable agreement with the measurements. For the experimental conditions where a significant number of free electrons are produced in the stopping foil, the measured deuteron stopping is enhanced (Fig. 3b, c and d). If the energy deposition produces less ionization, the measured energy loss is consistent with cold-target stopping (Fig. 3a).

5. TRANSPORT AND FINAL FOCUSING

Intense light-ion beam transport in z-discharge channels provides accelerator standoff from ICF targets and allows time-of-flight bunching of the beam to higher intensity. Stability constraints [14] combined with channel expansion and beam-energy loss constraints [15] define an operational window for ion transport. Results show that a larger operational window exists for the higher-atomic-weight species. This is a consequence of their lower currents at equivalent transported power levels. Raising the channel density somewhat above the optimum for minimum beam-energy loss during transport relaxes the two-stream and channel-filamentation stability constraints and the channel-expansion constraint while only slightly modifying the energy-loss constraint. Increasing the beam radius relaxes the two-stream stability constraint and considerably reduces the channel-expansion and beam energy-loss constraints.

It is determined that multi-terawatt beams can be transported a few meters in large-radius channels with beam divergence half angles of .1 to .2 radians. Such angles are presently attainable with PRDs. If time-of-flight bunching during transport and final focusing after transport are employed, less than 10 (and as few as 4) channels are required to deliver the power needed to ignite a pellet.

Theoretical results show factor-of-ten increases in final-focused ion-current density for beams transported in hollow channels. Channels which carry discharge current in the channel interior result in beam-brightness loss during transport and hence cannot be compressed as well by the final focusing cell. Focusing cells which are 1/8 of an ion-betatron-wavelength long focus the beam an additional 1/8-wavelength beyond the exit of the focusing cell. This 1-2 cm drift length is the stand-off distance separating the cell exit from the pellet. High plasma densities can be employed in the short focusing cell without excessive beam-energy loss in order that the plasma-MHD response can be minimized.

A final-focus system was designed and fielded on the Gamble II accelerator [16]. A discharge of ~ 100 kA was initiated by an external capacitor bank along the Lexan insulator which was filled with 5-10 Torr of air. Channel currents were chosen to match a 1/4 betatron wavelength for the ions with the 8 cm channel length. A convex pinch-reflex type anode was used to partially offset the self pinching of the ion beam in the diode and provide a nearly parallel trajectory injected ion beam. When aluminum witness plates were used, focusing was evidenced by rear surface spall which only appeared over the exit-aperture region when the focusing current was turned on. Further experiments with shadowboxes placed downstream of the exit-aperture confirmed that a well defined focal position existed and that no large scale mixing of the ion orbits in the 1/4 betatron wavelength focusing cell occurred during focusing. Results agree well with theoretical predictions. Eventually, experiments will be performed with this final-focusing system placed at the exit of the transport system.

REFERENCES

† Work supported by Department of Energy, Washington, DC 20545 and Defense Nuclear Agency, Washington, DC 20305

* JAYCOR, Inc., 205 S. Whiting St., Alexandria, VA 22304

**Science Application, Inc., 8400 Westpark Drive, McLean, VA 22101

[1] KUSWA, G.W., QUINTENZ, J.P., SEIDEL, D.B., JOHNSON, D.J., MENDEL, Jr., C.W., BURNS, E.J.T., FEHL, D., LEEPER, R.J., PERRY, F.C., MILLER, P.A., WIDNER, M.M., and FARNSWORTH, Jr., A.V., in the Proceeding of the 4th Int. Conf. on High-Power Electron and Ion-Beam Research and Technology, Palaiseau, France (1981), p.3.

[2] SANDEL, F.L., STEPHANAKIS, S.J., YOUNG F.C., and OLIPHANT, W.F., ibid., p. 129; MOSHER,D., COLOMBANT, D.G., GOLDSTEIN, S.A., and OTTINGER, P.F., ibid., p. 19; GOLDSTEIN, S.A., COLOMBANT, D.G., MOSHER, D., OTTINGER, P.F., and SANDEL, F.L., ibid., p. 113.

[3] OTTINGER, P.F., GOLDSTEIN S.A., and MOSHER, D., 1980 IEEE Int. Conf. on Plasma Science, Madison, Wisconsin (1980), p. 95.

[4] GOLDSTEIN, S.A., COOPERSTEIN, G., LEE, R., MOSHER D.,and STEPHANAKIS, S.J., Phys. Rev. Lett. 40, 1504 (1978).

[5] COOPERSTEIN, G., GOLDSTEIN, S.A., MOSHER, D., BARKER, R.J., BOLLER, J.R., COLOMBANT, D.G., DROBOT, A., MEGER, R.A., OLIPHANT, W.F., OTTINGER, P.F., SANDEL, F.L., STEPHANAKIS, S.J., and YOUNG, F.C., in Laser Interaction and Related Phenomena, edited by H. Schwarz, H. Hora, M. Lubin and B. Yaakobi, Vol. 5 (Plenum, New York, 1981), p. 105.

[6] STEPHANAKIS, S.J., GOLDSTEIN, S.A., OTTINGER, P.F., MOSHER, D., Bull. Am. Phys. Soc. 26, 921 (1981).

[7] BARKER, R.J., and GOLDSTEIN, S.A., Bull. Am. Phys. Soc. 26 , 921 (1981).

[8] SANDEL, F.L., private communication.

[9] OLSEN, J.N., private communication.

[10] MEHLHORN, T.A., J. Appl. Phys. 52, 6522 (1981); NARDI, E., PELEG, E., and ZINAMON, Z., Appl. Phys. Lett. 39, 46 (1981); MOSHER, D., in ERDA Summer Study of Heavy Ions for Inertial Fusion LBL-5543, 1976, p. 39.

[11] YOUNG, F.C., 1982 IEEE Int. Conf. on Plasma Science, Ottawa, Canada (1982), p. 27.

[12] ANDERSEN, H.H., and ZIEGLER, J.F., The Stopping and Ranges of Ions in Matter, Vol. 3 (Pergamon Press, New York, (1977).

[13] MEHLHORN, T.A., private communication.

[14] OTTINGER, P.F., GOLDSTEIN, S.A., and MOSHER, D., NRL Memo Report 4548, July 1981.

[15] MOSHER, D., COLOMBANT, D.G., and GOLDSTEIN, S.A., Comments Plasma Physics 6, 101 (1981).

[16] MEGER, R.A., GOLDSTEIN, S.A., OTTINGER, P.F., MOSHER, D., STEPHANAKIS, S.J., and YOUNG, F.C., Bull. Am. Phys. Soc. 26, 921 (1981).

MODULAR LIGHT-ION ICF

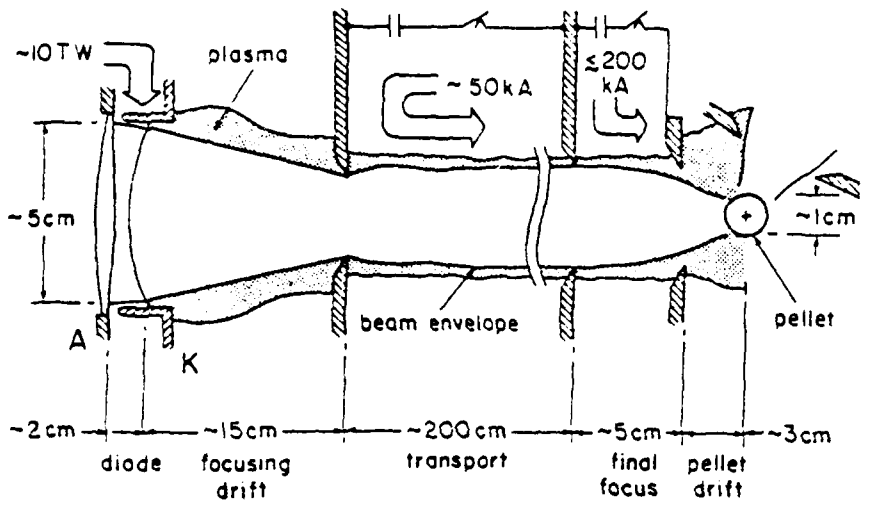

Fig. 1 Schematic of modular light-ion ICF system.

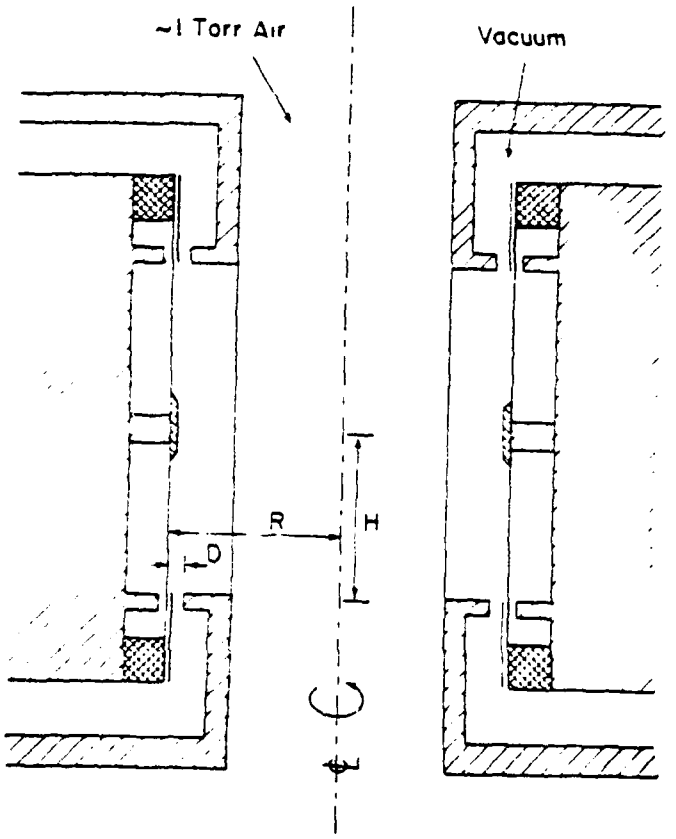

Fig. 2 Equitorial-pinch-reflex diode.

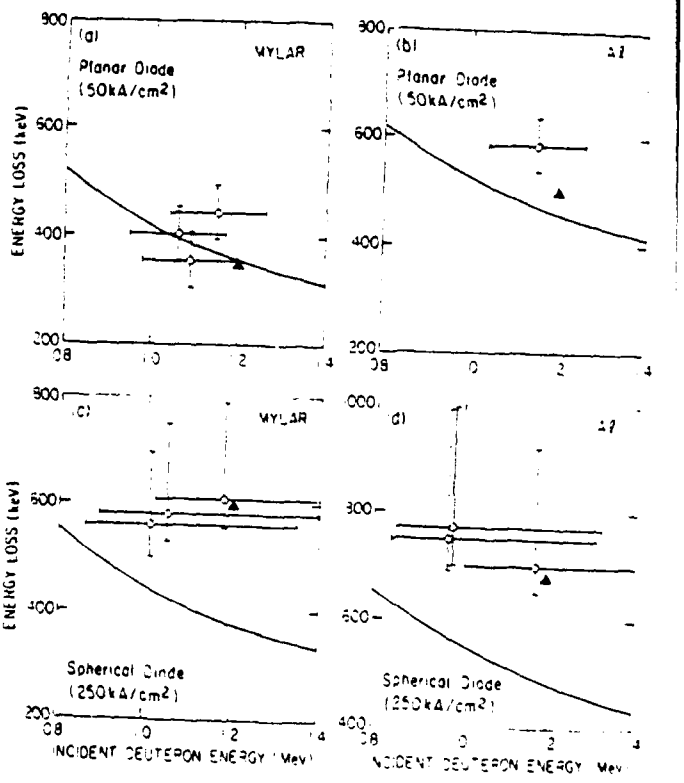

Fig. 3 Comparison of energy loss measurement with planar (a and b) and spherical (c and d) diodes with energy losses curves calculated for cold-target.

Measurements of intense ion beams by a novel diagnostic method

A. E. Blaugrund,[a] S. J. Stephanakis, and Shyke A. Goldstein[b]
Naval Research Laboratory, Washington, D.C. 20375

(Received 17 November 1981; accepted for publication 16 June 1982)

A new diagnostic method capable of measuring beam profiles and trajectories of intense ion beams as a function of time has been developed. The technique employs fast photography in conjunction with fast scintillators. Prior to detection, the excessive intensity of the direct ion beam is reduced by means of Rutherford scattering. A time resolution of a few nanoseconds and a spatial resolution of a few millimeters has been achieved. Using this technique focusing properties of planar and spherical pinch reflex diodes have been investigated. A low energy electron beam precursor has been detected. A simple model for its production is presented.

PACS numbers: 52.70.Nc, 29.15.Cy, 41.80.Gg

I. INTRODUCTION

The use of light ion beams for inertial confinement fusion requires extremely powerful beams of particles converging on a small pellet. Present estimates[1] indicate that 10–100 TW beams have to be focussed onto a pellet a few millimeters in diameter. The first intense ion beams were produced several years ago on the NRL Gamble II accelerator.[2] Since then, steady progress has been made both in this laboratory[3] and elsewhere.[4] The most intense ion beams produced in a magnetically insulated diode by the PROTO II generator[5] were 1.6 MA of protons at 1.7 MV. In experiments with the pinch reflex diode conducted on the PITHON generator,[6] 1 MA of protons at 1.8 MV were obtained. This is still a long way from the power density required for pellet ignition, and work towards achieving this goal is in progress in several laboratories. Clearly, these efforts require diagnostic techniques capable of measuring the ion composition of the beam, the particle energies, the current density and its distribution in space, as well as the directions of motion of the ions. Since the temporal behavior of these quantities has to be known, the data have to be measured and recorded in a time resolved way. The large number of parameters necessitates the use of a method in which a large number of data points can be recorded simultaneously. One such method which suggests itself immediately is high speed photography in conjunction with fast scintillators. Unfortunately, scintillators placed directly in the path of ion currents of tens of kiloamperes per square centimeter cease to function almost immediately. Efforts to reduce the ion current density incident on the scintillator by means of screens or pinhole arrays have proved unsuccessful. This failure can easily be understood on the hand of the following argument: in order to ensure proper functioning of a plastic scintillator for the duration of the beam pulse, the current density of protons striking the scintillator should be less than a few A/cm^2,[7] i.e., at least 10^4 times less than present day beam current densities. If such a reduction has to be achieved by expansion of a beamlet passing through a pinhole (even assuming that such an expansion does take place), the beamlet diameter has to increase by a factor of 100 before reaching the scintillator. In order to prevent the pinhole from closing under the impact of the powerful ion beam, the pinhole diameter cannot be much less than 1 mm. Expanding the diameter of such a beamlet by a factor of 100 would mean a spatial resolution of 100 mm, which would render the measurement useless.

In this work we present a time resolved ion beam diagnostic method using fast photography and scintillators. The desired reduction in the ion flux incident on the scintillator is achieved by Rutherford scattering: the direct beam hits a scatterer and only deflected ions are allowed to reach the scintillator. The differential scattering cross section per unit solid angle for light ions scattered by heavy nuclei through an angle θ is given by

$$\sigma_R(\theta) = \frac{\sigma_0}{\sin^4\frac{1}{2}\theta}, \tag{1}$$

with $\sigma_0 = (Zze^2/16\pi\epsilon_0 E)^2$ (mks units), where Z is the atomic number of the scattering atom, ze the charge of the scattered ions, E the kinetic energy of the ions, and $\epsilon_0 = 8.84\times 10^{-12}$ F/m is the permittivity of vacuum. The specific functional dependence of σ_R on Z, E, and θ can be exploited to obtain desired properties for the diagnostic method. So, for example, the desired ion flux incident on the scintillator can be achieved by an appropriate choice of the atomic number of the scattering material.

Using a simple electronic streaking camera, distributions of ions along a beam diameter were measured with a time resolution of about 2 ns and a spatial resolution of 3–4 mm. In other experiments, the direction of motion of the ions at a few selected radii within the beam was recorded as a function of time.

II. THE METHOD

The desired reduction in ion flux and the required spatial and temporal resolution can be achieved in a variety of geometrical arrangements. Figure 1 schematically shows three possible geometries. In each case the ion beam passes through a long and narrow slit before impinging on a scatterer. The width d of the slit is chosen as small as possible. However, it should be large enough so that hydrodynamic motion of the slit jaws under beam bombardment does not significantly interfere with the passage of the beam pulse.

[a] Jaycor, Alexandria, VA 22304; Permanent address: Weizmann Institute of Science, Rehovot, Israel.
[b] Jaycor, Alexandria, VA 22304.

 0021-8979/82/117280-10$02.40

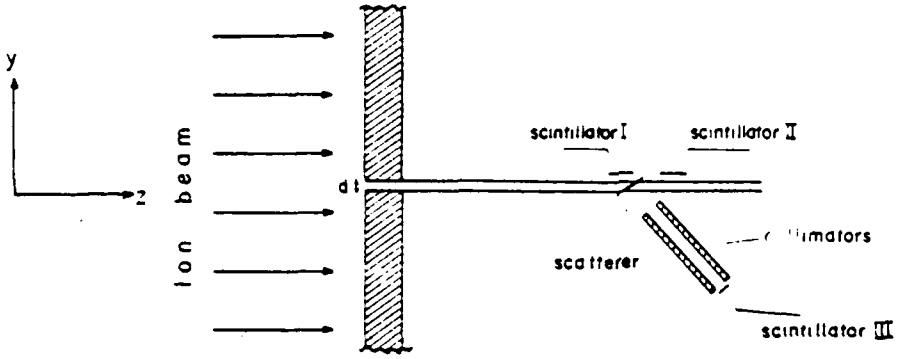

FIG. 1. Schematic diagram of the Rutherford scattering method showing three possible geometries. I: reflection geometry with proximity focusing; II: transmission geometry with proximity focussing; III: transmission geometry with collimation. The entrance slit, the scatterer, and the scintillator extend along the x direction over the entire beam diameter.

The length of the slit in the x direction (see Fig. 1) should be large enough to let an entire beam diameter reach the scatterer. The latter has the form of a long and narrow strip large enough to intercept the beam passing through the slit. The different geometries can be classified into four general categories: the scattered ions can be observed either in reflection or in transmission and spatial resolution can be achieved either by proximity focussing or by collimation (see Fig. 1). Since in reflection the incident and the scattered particles are on the same side of the scatterer, both thin and thick scatterers can be used. In transmission only thin foil scatterers can be employed. In proximity focussing (scintillators I and II in Fig. 1), the scintillator has the form of a long and narrow strip parallel to the scatterer and is placed as close as possible to the scatterer, while still remaining shielded from the direct beam. The spatial resolution is determined by and is of the order of the distance traveled by the ion from the scatterer to the scintillator. The finite dimension d of the beam puts a limit to the proximity and therefore limits the resolution. Because of the pronounced forward peaking of the Rutherford cross section the resolution can be improved by mainly looking at ions scattered through small angles, even at the expense of increasing the distance traveled by the ions from the scatterer to the scintillator. The optimal choice of the scattering angle and of the distance will be discussed later. In the collimation method the scattered ions reach the scintillator through a row of collimator tubes (preferably adjacent collimators with thin walls and square or rectangular cross sections). Here, the spatial resolution is determined by the size of the collimators in the x direction and by their length and distance from the scatterer. In principle, any desired resolution can be achieved, provided that the flux of ions reaching the scintillator is sufficient for detection. Proximity focussing and collimation can be used in conjunction with both reflection and transmission scattering, thus giving the four general geometrical categories.

In the work described here two geometries were tried successfully, viz., transmission scatterer with a collimator array and reflection scatterer with proximity focussing. The latter method offers many practical advantages:

(1) One can use a thick scatterer, thus making its mounting and handling easier. Also, many materials which are usually not available as thin foils can serve as scatterers.

(2) When proximity focussing is used there is no need for a rather delicate array of collimator tubes, which is easily damaged by the debris produced by a high power ion beam. (On the other hand, the use of collimators eliminates the necessity of an entrance aperture. This makes possible the use of high speed framing photography, producing two-dimensional records of the beam cross section).

(3) For a thick reflection scatterer the light output of the scintillator depends only weakly on the ion energy (see following paragraphs) and is therefore primarily a measure of the ion current density in the beam. This is an advantage when one wants to measure the beam profile as a function of time while the diode voltage is changing.

Since the achievable spatial resolution of a few millimeters was deemed sufficient for our purpose, practically all experiments were done using a thick reflection scatterer in conjunction with proximity focussing and it will be this method that we shall describe here in detail.

Let us first consider the factors determining the spatial resolution of the proximity focussing. Assume a thin pencil beam moving in the z direction in the x-z plane (see Fig. 2). Let this beam be scattered at point 0 by a scatterer. The narrow strip scintillator, placed parallel to the x axis and at a distance s from the scatterer, determines together with the scatterer the plane of scattering which makes an angle α with the x-z plane. $\delta = s \sin \alpha$ is the distance between the scintillator and the beam plane. Let OP^0 be the trajectory of scattered particles incident on the scintillator at a right angle at the point P^0 and let OP be another trajectory in the scattering plane making an angle β with OP^0 and reaching the scintillator at a point P. We shall define the spatial resolution as twice the distance between the point P^0 and a point P^1 in which the flux of scattered particles is one half that at point

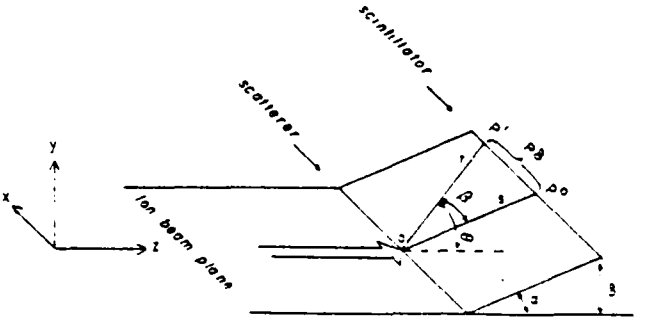

FIG. 2. Geometrical quantities determining the spatial resolution in proximity focussing.

P^0. It is clear that for a given angle α the resolution distance $2P^0P^1$ is proportional to δ, which should, therefore, be chosen as small as possible. Let us now determine how the resolution depends on the angle α. We introduce a dimensionless resolution $2R$, where $R = P^0P^1/\delta$. For an isotropic scattering process the scattered intensity per unit area of scintillator $I(P^1)$ at any point P will be inversely proportional to the square of the distance to the scattering point 0. Therefore,

$$\frac{I(P^1)}{I(P^0)} = \frac{s^2\cos\beta}{r^2} = 0.5, \tag{2}$$

where s and r denote the distance OP^0 and OP^1, respectively. Simple trigonometry immediately leads to the result

$$R = \frac{0.77}{\sin\alpha}. \tag{3}$$

For optimum resolution R should be minimum, i.e., $\alpha = 90°$. This is obvious since $\alpha = 90°$ also means the shortest distance between the scatterer and the scintillator. This is the essence of proximity focussing. The Rutherford scattering cross section σ_R is far from isotropic. Its strongly forward peaked distribution suggests that angles $\alpha < 90°$ may result in improved spatial resolution. Since the scattering cross section $\sigma_R \sim 1/\sin^4\frac{1}{2}\theta$ one gets, instead of Eq. (2),

$$\frac{I(P^1)}{I(P^0)} = \frac{s^2\cos\beta\sin^4\frac{1}{2}\alpha}{r^2\sin^4\frac{1}{2}\theta} = 0.5. \tag{4}$$

Let us start by assuming that the optimum angle is very much smaller than 90° so that the approximation $\sin\alpha \simeq 2\sin\frac{1}{2}\alpha$ is acceptable and that the same approximation may be used for the scattering angles θ. Then one gets, instead of Eq. (3),

$$R^2 \simeq (1 + b^2)^{1/2} - b, \tag{5}$$

where $b = \frac{1}{2}(1 + \cos^2\alpha)$. Equation (5) means that the best resolution is obtained for very small angles α. In spite of the approximations used in Eq. (5), it deviates by less than 10% from the exact result for the full range of angles $0° \leqslant \alpha \leqslant 90°$. Figure 3 shows the dependence of R on the angle α. It can be seen that the dependence is not very strong and that the optimum at $\alpha = 0$ is not very pronounced.

Clearly, in practice, the angle α cannot be made very small. Aside from the finite dimensions of the beam, of the scatterer, and of the scintillator, which determine a range of angles rather than a single angle α, it should be remembered that the scattering process is used here to reduce the flux of ions incident on the scintillator. Since $\sigma_R \to \infty$ when $\theta \to 0$, using angles $\alpha \simeq 0$ would defeat the very purpose of the method. However, for $\alpha = 40°$ the resolution is only 10% worse than the theoretical optimum. Therefore, the spatial resolution in proximity focussing will be

$$2R\delta \simeq 2\delta[(1 - b^2)^{1/2} - b]^{1/2}, \tag{6}$$

where δ should be chosen as small as possible, within the limitations of the experiment. For $\alpha = 40°$ and $\delta \simeq 3.5$ mm, $2R\delta \simeq 5$ mm.

For a thick scatterer, ions deflected at large angles β generally lose more energy in the scatterer (and therefore produce less light in the scintillator) than the ones scattered at $\beta = 0$. This effect tends to improve the spatial resolution. Experimentally, the resolution obtained with a thick scatterer is about 30% better than the value calculated using Eq. (6).

Let us now consider the dependence of the light output of the scintillator on the properties of the ion beam (particle flux and energy), on the properties of the scatterer (atomic number Z), and on the geometry of the experimental arrangement (distance δ and range of angles α).

For low enough ion current densities incident on the scintillator, the light flux produced is approximately proportional to the power density of the ions reaching the scintillator.[8] As the power density rises, the scintillator response becomes nonlinear, reaching saturation and then even declining to zero.[7] The sensitivity of the light recording system should be such that an observable record is produced while the scintillator still functions in its linear range. For an electronic streaking camera the sensitivity is determined by the product of the gathering power of the input optics, the light amplification of the image converter, the streaking speed, the efficiency of light transfer from the fluorescent screen to the recording film, and the sensitivity of the photographic film. For any given beam intensity the desired ion flux on the scintillator can be achieved by choosing the angles α and the atomic number of the scattering material ($\sigma_R \sim Z^2$). A linear dependence of scintillator output on the incident ion power will be assumed in the following.

It will now be shown that the light output of a scintillator operating in conjunction with a thick scatterer in reflection is, to a rough approximation, independent of the ion energy and is, therefore, approximately proportional to the ion current. Assume again a thin pencil beam stricking a thick scatterer at point 0 and consider only ions scattering in the y-z plane through an angle α and reaching the scintillator at point P^0 (see Fig. 2). (This restriction is strictly valid for the collimation method only.) Also, assume that the specific energy loss dE/dz of ions moving through the scatterer material is independent of ion energy. Admittedly, this is a rather coarse approximation. However, the stopping range of 0.1–1.2 MeV protons is roughly proportional to their energy.[9] Let E_0 be the energy of the ions incident on the scatterer, E_z the energy of ions scattered at the depth z in the scatterer, and E_α their energy when reaching the scintillator. Under

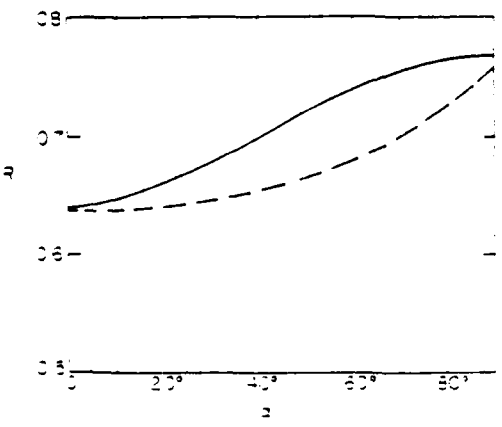

FIG. 3. Dimensionless resolution R as a function of the angle α. Numerical solution of Eq. (4): broken line; approximate analytical expression [Eq. (5)]: solid line.

the above assumptions, $E_z = E_0 - z\,dE/dz$ and $E_{zz} = E_0 - az\,dE/dz$, where a is a dimensionless factor ($a > 1$) which depends on the angle α and on the inclination of the scatterer surface to the beam direction. The maximum depth z_m from which ions can still reach the scintillator is determined by $E_{zz} = 0 = E_0 - az_m\,dE/dz$ from which follows that z_m is proportional to E_0. Therefore, the average energy $\bar{E}_z$ at scattering is also proportional to E_0. Since the scattering cross section $\sigma_R \sim E_z^{-2}$, the number of scattered ions $N \sim \sqrt{\bar{E}_z^{-2}} z_m \sim E_0^{-1}$, i.e., NE_0 is independent of E_0. Since the ion energy flux incident on the scintillator is proportional to $N\bar{E}_{zz} \sim NE_0$, this energy flux is also independent of E_0. Thus, under the above assumptions, the light output of the scintillator is independent of the kinetic energy of the ions and depends linearly on their current. Although for proximity focussing scattering outside the $y-z$ plane cannot be entirely neglected, it can safely be said that even there the light output of the scintillator depends only weakly on the particle energy. For an ion beam pulse in which the particle energy strongly varies as a function of time, this feature of the diagnostic can be attractive.

In the diagnostic method presented here the desired reduction in ion current density reaching the scintillator is achieved by means of Rutherford scattering. We shall now derive the expression for this reduction factor. Consider a beam of infinite cross section composed of light ions moving along the z direction and let the current density i within the beam be constant. Let this beam pass through a narrow slit (width d) extending along the x direction and let it impinge upon a scatterer parallel to the x axis. The scattered ions are detected by a narrow strip of scintillator placed parallel to the x axis at a distance s from the scatterer (see Fig. 2). The scatterer and the scintillator define the scattering plane which makes an angle α with the plane of the beam. Assume the surface of the scintillator to be perpendicular to the scattering plane. The current density of ions i_α incident on the scintillator is given by

$$i_\alpha = \frac{8idnz_m\sigma_0}{s}\int_0^{\pi/2}\frac{d\beta}{(1-\cos\alpha\cos\beta)^2} = \frac{8idnz_m\sigma_0}{\delta}\left[\cot\alpha + (\pi-\alpha)\csc^2\alpha\right], \tag{7}$$

where n is the number of scattering nuclei per m^3 and $\delta = s\sin\alpha$ is the distance of the scintillator from the median plane of the beam.

$$\sigma_0(m^2) = 1.30\times10^{-31}Z^2z^2/E^2\ (\text{MeV}).$$

For 1-MeV protons, scattered by copper ($Z = 29$) and for $d = 1$ mm, $\delta = 3.5$ mm, and $\alpha = 40°$, the reduction factor is

$$i_\alpha/i = 6.7\times10^{-4}.$$

Here, z_m was assumed to be one half the range of 1-MeV protons in copper. These are the approximate values of the parameters used in our experiments. The reduction factor can easily be increased or reduced by up to an order of magnitude by a suitable choice of the atomic number of the scattering material.

III. THE EXPERIMENTAL ARRANGEMENT

Proton beams of several hundreds of kiloamperes at 1–1.5 MV were produced in a pinch reflex diode[3] on the upgraded Gamble II generator[10] operating in positive polarity. Both planar and curved (focussing) anode foils approximately 10 cm in diameter were used. In Fig. 4 a planar pinch reflex diode with the diagnostic equipment in the drift tube is shown. The current densities encountered in these experiments ranged from a few kiloamperes per square centimeter to more than 100 kA/cm^2, depending on the diode geometry and on the distance from the diode. The experimental arrangement for detecting the ions by the Rutherford scattering method is shown in Fig. 5. The beam aperture, the support for the scatterer, the support for the scintillator and for the optical mirror were machined from two solid blocks of

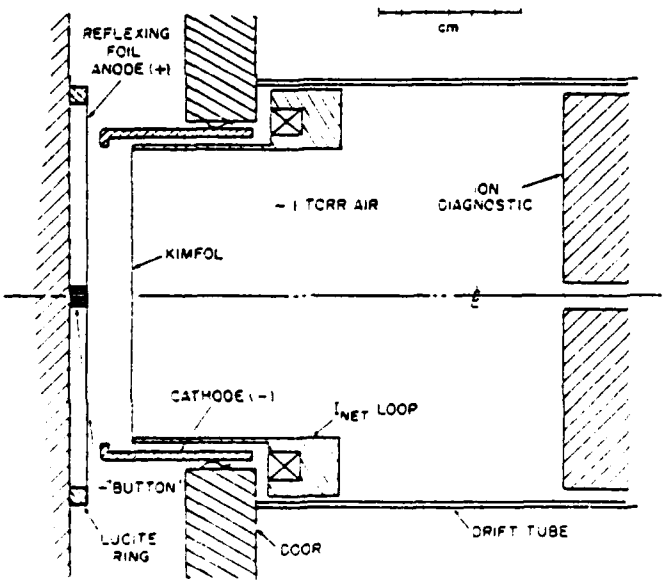

FIG. 4. Schematic diagram of a planar pinch reflex diode, the drift tube, and the diagnostic equipment.

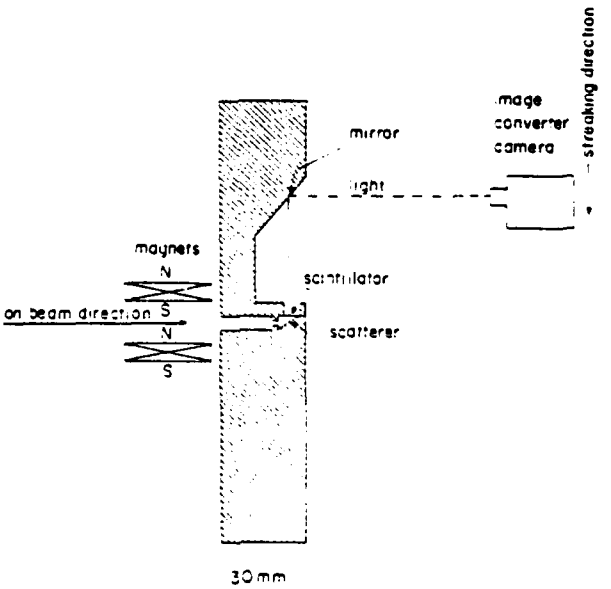

FIG. 5. Cross section through the entrance aperture, the scatterer, and the scintillator support. Note the magnets in front of the entrance aperture.

aluminum which together formed the structure shown in Fig. 5. This structure could be taken apart for installing the scatterer and the scintillator. The beam aperture had the form of a narrow slit, 1 mm wide and 10 cm long. This aperture extended along a diameter of the circularly symmetric ion beam. The scatterer was an approximately 8 mm wide and 10 cm long strip of metal (usually thicker-than-range copper tape) which intercepted the entire beam passing through the aperture. Its surface made a 30° angle with the beam direction. The NE 102 scintillator was 4.5 mm wide, 10 cm long, and 40 μm thick. It was positioned above the scatterer, with its surface parallel to the plane of the incident beam and at a distance of 3.5 mm from it. The scattering angles α ranged from 30° to 70°, but because of the forward peaking of the scattering the average angle was $\alpha \simeq 40°$. In order to minimize the background due to x rays and fast electrons the thickness of the scintillator was chosen approximately equal to the range of the protons. On the surface facing the scatterer the scintillator was coated with approximately 1000 Å of aluminium in order to prevent light produced by the ion beam striking the scatterer from reaching the camera. The light of the scintillator was recorded by a TRW model 1D image converter camera with a model 12b streak plug-in unit. The objective lens had an f number of 2 and the fluorescent screen of the camera was photographed through an f1.4 lens on 3000 ASA Polaroid film. The scintillator-to-film demagnification was approximately 1/4 and the streaking speed was 0.5 mm/ns. The reduction factor $i_s/i = 6.7 \times 10^{-4}$ calculated in the previous section applies approximately to this experimental arrangement. The fact that here the scattered particles are not normally incident on the scintillator surface reduces the ion current density on the scintillator by another factor of sin α. However, as a consequence of this the ion energy is deposited in a layer thinner by a factor sin α so that the energy dissipated per unit mass of scintillator material remains the same and this additional reduction in current density serves no useful purpose. However, this particular orientation of the scintillator surface was chosen for its simplicity in machining the support and in mounting the scintillator. This was particularly important since both the scatterer and the scintillator had to be replaced after every shot.

The diagnostic equipment shown in Fig. 5 fitted into a 15-cm-diam drift tube filled with approximately 1 Torr of air. Beyond a certain minimum distance from the pinch reflex diode the equipment could be positioned anywhere along the drift tube. The minimum distance varied from 6 to 12 cm, depending on the presence of deflection magnets (see further) and of a Rogowski coil which measured the net ion current (see Fig. 4). The ion beam entered the drift tube through a 2-μm-thick Kimfol[11] near the cathode. This foil separated the air in the drift tube from the vacuum in the diode. The air was required to space charge and current neutralize the ion beam and thus facilitate its nearly ballistic propagation down the drift tube.

In most of the experiments a set of permanent magnets were placed before the entrance aperture of the Rutherford diagnostic equipment. These magnets produced a transverse magnetic field of about 1.5 kG over 2 cm, which prevented electrons preceding or accompanying the ion beam from reaching the scatterer. The function of these magnets will be discussed in the next section.

IV. MEASUREMENTS

In the first experiments using the Rutherford diagnostic method it was discovered that the ion beam is preceded by a hollow electron beam. Figure 6 shows two streak photographs taken at a distance of 20 cm from the anode of a spherical diode. The two photographs were obtained under similar experimental conditions except that the photograph in Fig. 6(b) was taken with a 1.5-kG transverse magnetic field preceding the entrance aperture of the diagnostic equipment. Figure 6(a) shows two distinct parts in the signal. In Fig. 6(b) it can clearly be seen that the magnetic field totally removes the early part of the signal without affecting it at later times. This indicates that the first part of the signal in Fig. 6(a) is due to electrons, as opposed to the second part which is due to ions. By covering the scintillator with absorbers of various thicknesses it was determined that these electrons have an energy of 40–80 keV. In the transverse magnetic field of 1.5 kG such electrons have a Larmour radius of rotation of about 0.5 cm and would therefore be unable to reach the scatterer, in agreement with the observations. The time delay between the appearance of the electrons and of the ions is due to the largely different transit times and is consistent with both beams being produced in the diode at the same instant. From the relative light intensities produced by the two beams and taking into account transmission

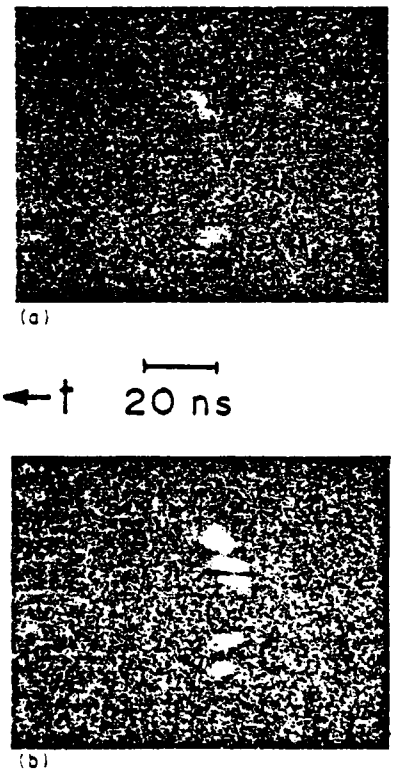

FIG. 6. Streak photographs taken using the Rutherford scattering method: spherical pinch reflex diode. Diagnostics positioned beyond the focal point. (a) Without magnetic field; (b) with transverse magnetic field. The sharp black lines are fiducial marks.

through the entrance aperture, differences in scattering cross sections, and scintillator response, it follows that the flux of electrons is about an order of magnitude smaller than that of the ions. This indicates an electron current of the order of 20 kA.

The interaction of the electron flow with the gas in the drift tube is responsible for partial ionization and generation of a net current I_e, which is about one half of the electron current[12] for the present experiment. The magnetic field associated with this net current allows the electron beam to propagate from the cathode to the diagnostic apparatus. The magnetic field produced by the net current can confine electrons with an emission angle of less than θ given by[13]

$$I_e(\mathrm{A}) = \tfrac{1}{2}\theta^2 \cdot 17 \cdot 10^3 (\gamma^2 - 1)^{1/2},$$

where γ is the relativistic mass ratio. For $I_e = 10$ kA and $\gamma = 1.1$ (50 keV electrons), $\theta \simeq 1.5$ rad, which shows that most of the electrons propagate. On the other hand, note that a much more intense electron beam would not propagate because of the Alfvén limit.[14] Of course, beyond the entrance aperture and on the way to the scatterer the electron beam is no more confined by its own magnetic field and therefore it is strongly attenuated (by a factor of approximately 40) before reaching the scatterer. This was taken into account while deducing the electron current from the ratio of light emitted in the scintillator by the electrons and the ions. A possible mechanism for production and emission of such energetic electrons from the diode will be discussed later.

If the beam, on its way to the scintillator, is intercepted by a beam stop, generally a distinct shadow will appear on the scintillator. By choosing the proper size and location of the beam stop various goals can be achieved: thus, placing narrow (1 mm wide) beam stops directly under the scintillator produces very thin and sharp dark lines in the streak photographs which can be used as geometric fiducial marks. Two such fiducial marks are shown both in Figs. 6(a) and 6(b).

A narrow beam stop immediately preceding the scatterer produces a dark line from the width of which the spatial resolution of the diagnostic equipment can be deduced. In this way, a spatial resolution (FWHM) of 3.5 mm was determined for the diagnostic equipment used here, in good agreement with theoretical predictions.

Placing a narrow beam stop some way upstream (e.g., at the entrance aperture of the equipment) will again produce a distinct shadow on the scintillator, provided the beam particles move along straight lines and the beam is not excessively convergent or divergent at the point of observation. In Fig. 6(b) two such shadows were produced by two 5-mm-wide beam stops placed at the entrance aperture of the diagnostic equipment. From the radial position of these shadows, as measured on the scintillator, and from the known radial positions of the beam stops and their distance from the scintillator, the direction of motion of the ions at these radii in the beam can be determined. Thus, in the measurement shown in Fig. 6(b), protons entering the diagnostic equipment at radii $r = \pm 20$ mm diverge with an angle of 13° with the beam axis. It can be seen that this angle remains almost constant throughout the beam pulse. By placing an array of narrow beam stops at selected radii divergence (or convergence) angles can be measured as a function of radius and of time. At the same time variations of beam intensity as a function of radius and time can be deduced from the light intensity of the scintillator in the intervals between the shadows of beam stops. This technique very much enhances the power of this diagnostic method.

In order to be able to make accurate relative measurements of beam intensities, the scintillator must be used in its linear range. Also, the streak image should be recorded on a wide dynamic range transparent film. These requirements can only be satisfied by using an image converter camera with a sufficiently high light gain. Such cameras are readily available commercially. Unfortunately, such a camera was not available in our experiments so that high speed 3000 ASA, nontransparent, low dynamic range Polaroid film had to be used. Also, the scintillator, while not totally saturated, had to be used in a range where deviations from linearity are not negligible. All this made reliable intensity ratio measurements impossible. However, interesting qualitative observations could still be made.

In Fig. 7 a streak photograph taken without a transverse magnetic field again shows an electron beam preceding the ion beam. The dark lines in the lower half of the picture are produced by 2-mm-wide beam stops of varying thickness (see legend) placed directly under the scintillator. They deviate from straight lines because of image converter overloading and distortion. The dark band shown at the upper edge of the streak picture is due to an 8-mm-wide beam stop (24-mg/cm^2-thick polyvinylchloride) placed at the entrance aperture of the equipment. This dark band, which clearly shows in the ion part of the picture, is very diffuse and can barely be seen in the electron part of the streak. This pheno-

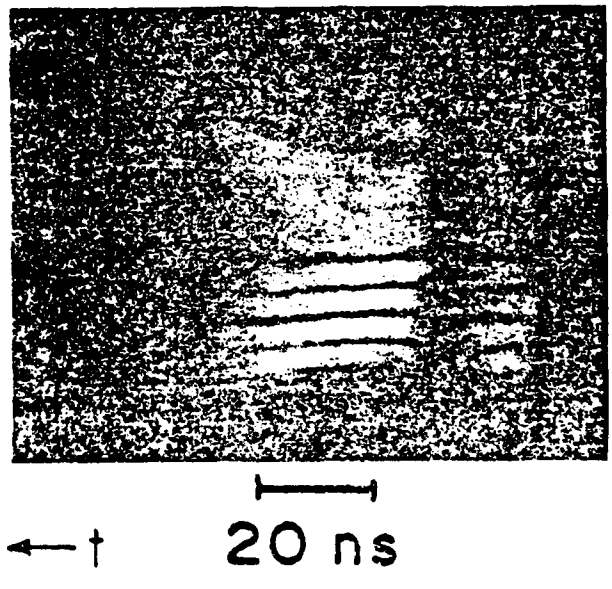

FIG. 7. A streak photograph taken with various thicknesses absorbers. Upper edge: 8 mm wide, 24 mg/cm^2 thick vinyl tape placed over the entrance aperture 28 mm from the scintillator; all other absorbers 2 mm wide and placed directly under the scintillator. From center to bottom: 24 mg/cm^2 thick vinyl, 5 mg/cm^2 aluminum, 10 mg/cm^2 aluminum, 1.1 mg/cm^2 aluminum, 2.2 mg/cm^2 aluminum. The dark lines near the edges of the streak picture are artifacts due to light reflections.

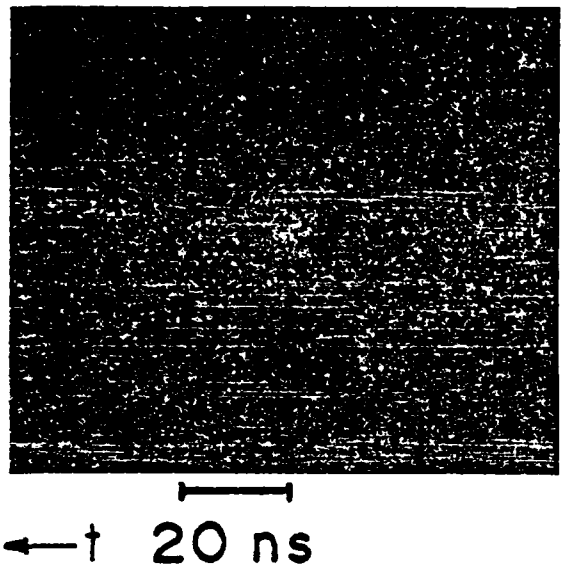

FIG. 8. A streak photograph of a convergent ion beam from a spherical reflex diode taken beyond the focal point. The two sharp dark lines at the center are fiducial marks. The other dark lines are due to beam stops placed at the entrance aperture (see text and Fig. 10).

menon cannot be explained by assuming that the PVC is highly transparent to the electrons since the same thickness of PVC placed directly under the scintillator (center of streak in Fig. 7) produced a sharp black shadow both in the ion and in the electron part of the picture. Thus, the diffuseness of the shadow can only be due to the fact that the particles incident on the beam stop do not move in parallel trajectories. The self-magnetic field of a 20-kA beam of 50-keV electrons would produce enough bending of the electrons to explain the diffuseness of the shadow. This result is entirely consistent with the estimates of electron energy and current presented in the preceding paragraphs.

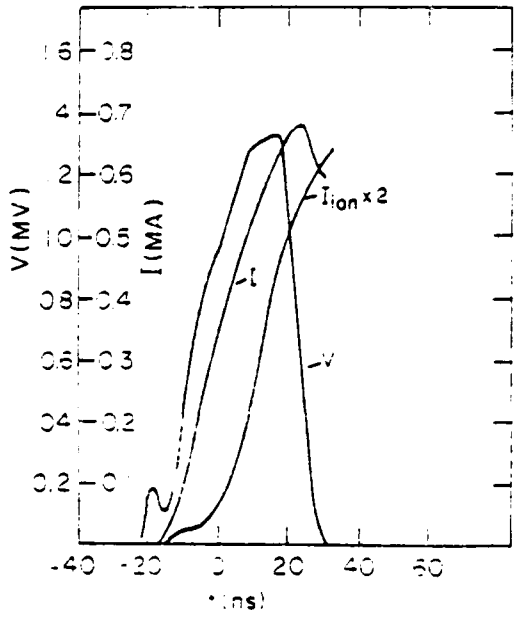

FIG 9. Diode voltage, diode current, and ion current waveforms. Zero time corresponds to the onset of ion current in the streak photograph, corrected for the ion time of flight.

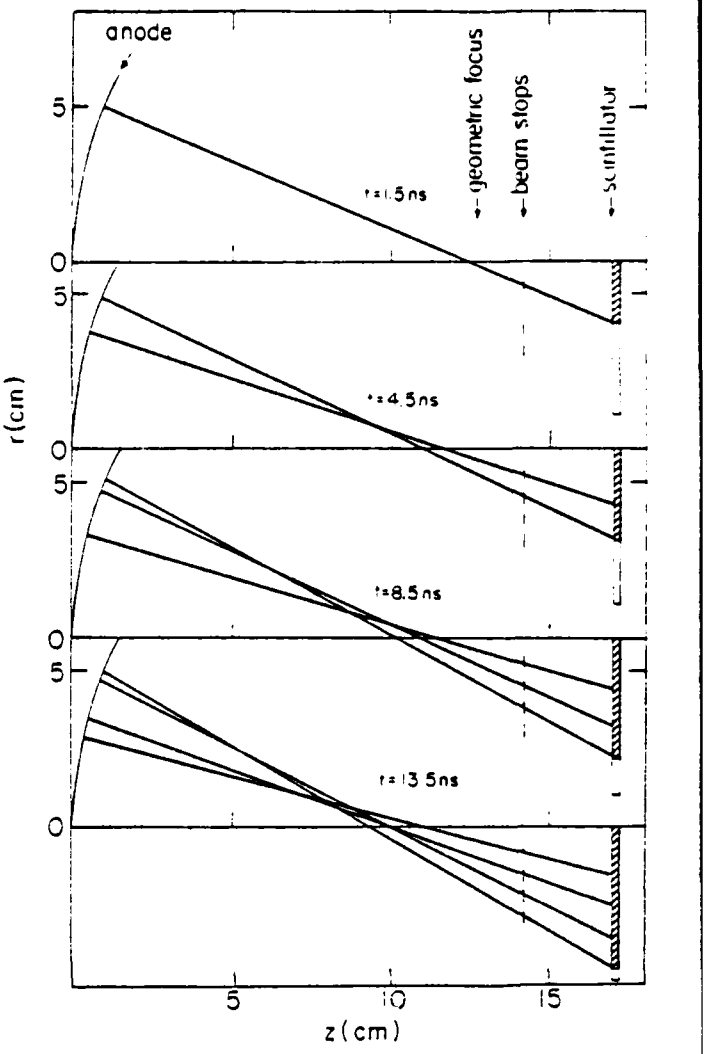

FIG. 10. Reconstruction of the ion trajectories, using data shown in Fig. 8. The shaded area of the scintillator corresponds to the illuminated part of it.

The technique of beam stops placed at the entrance to the Rutherford scattering equipment was used to determine the focusing properties of a spherical pinch reflex diode.[3] The anode foil had a radius of curvature of 127 mm, the anode-to-cathode distance was 5 mm, and the anode-to-Kimfol distance was 28 mm. Figure 8 shows a streak photograph taken with beam stops placed at $r = \pm 7.5, 14.5, 21.5$, and 28.5 mm at a distance of 142 mm from the apex of the spherical diode. The distance between the beam stops and the scintillator was 28 mm. The two thin dark lines visible at the center of the photograph are fiducial markers placed under the scintillator at $r = \pm 3$ mm. Figure 9 shows the diode voltage, diode current, and the ion current entering the drift tube. Zero time marks the onset of the ion current in the streak photograph (corrected for the time of flight of the ions). An analysis of the shadows produced by the beam stops on the scintillator and a reconstruction of the ion trajectories are shown in Fig. 10. It can be seen that as time progresses and the diode current rises the ion trajectories are bent more and more towards the diode axis, deviating from

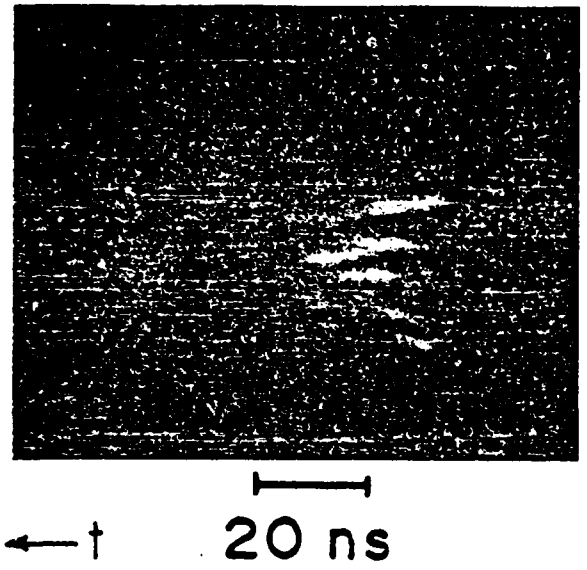

FIG. 11. A streak photograph of an ion beam from a planar pinch reflex diode.

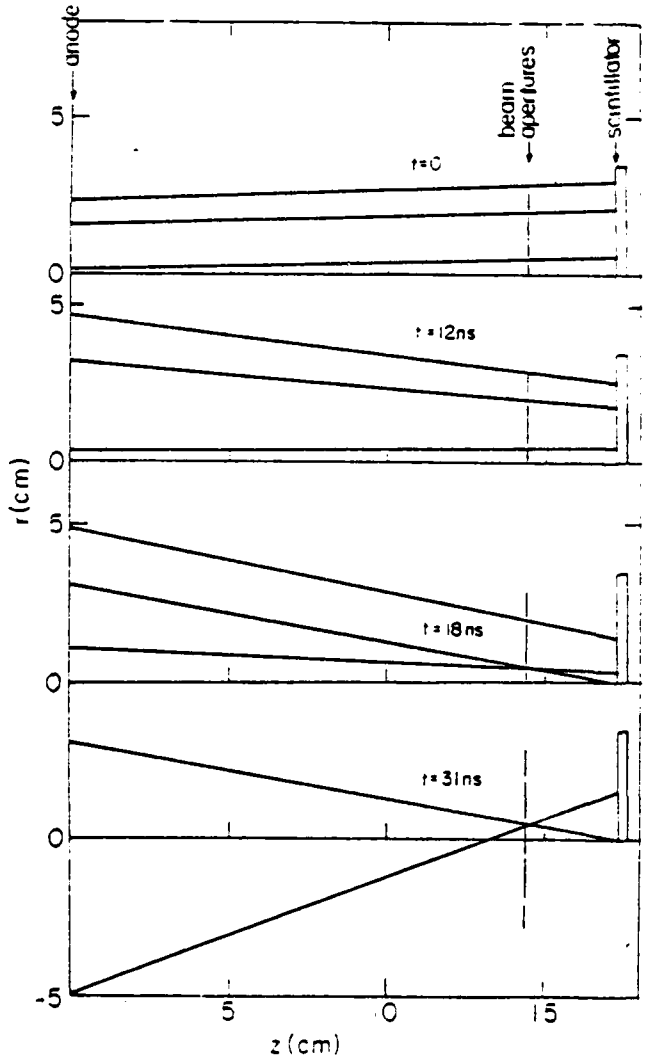

FIG. 12. Reconstruction of the ion beam trajectories using data shown in Fig. 11.

the geometric focus. The shaded area of the scintillator in Fig. 10 corresponds to the illuminated part of it. The edge of the illumination corresponds to ion emission from the outer radius of the anode ($r = 5$ cm). Because the trajectories are bent more and more as the diode current rises, the illuminated diameter of the scintillator increases with time. This can clearly be seen in the photograph in Fig. 8.

Figure 11 shows a streak photograph obtained with an ion beam from a planar pinch reflex diode. Here, 2-mm-wide apertures rather than beam stops were placed at the entrance aperture, producing narrow beamlets on the scintillator. Figure 12 shows the reconstruction of the ion trajectories from the data of Fig. 11 at four different times in the beam pulse. Initially, the ion beam is almost parallel to the diode axis, possibly with a slight divergence. As time progresses, the trajectories are again bent inward more and more by the rising magnetic field.

V. THEORETICAL DISCUSSION

A. Generation of the electron precursor beam

The rising azimuthal magnetic field inside the diode produces electric fields of inductive origin. This change of magnetic flux allows for nonconservation of kinetic energy of electrons emitted from one part of the cathode (say, C_1 in Fig. 13) and crossing to another part of it (say, C_2). In Fig. 13 we show the diode geometry and two possible orbits of electrons emitted from C_1 at, say, different times and different diode voltages. The electron orbit C_1C_2 encloses the magnetic flux ϕ_C in the cross section $C_1C_0C_2C_1$. Since an inductance can be assigned to that loop the voltage $V_{C_1C_2}$ between C_1 and C_2 is simply $d\theta_c/dt = L_C dI_V/dt$, where L_C is the inductance of that loop and I_V the current as measured by the I_{NET} loop near C_0. In the present series of experiments this inductance was about 3 nH. Typically $dI_V/dt \simeq 1.5\times10^{13}$ A/s, and thus $V_{C_1C_2} \simeq 50$ kV. The stream of electrons through the cathode at point C_2 will thus have a typical energy of 50 keV. The very thin (2 μm) cathode foil of polycarbonate reduces the energy only by a few kiloelectron volts.

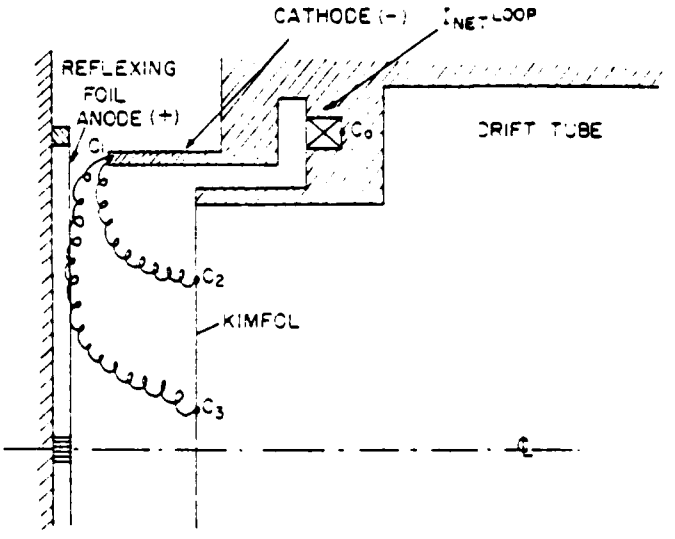

FIG. 13. Diode geometry, showing individual electron trajectories (schematic) and the Rogowski coil for measuring I_V.

The energy of the electrons entering the drift tube depends on their exact trajectories, which in turn, change with changing diode voltage and expanding plasma. Thus, the above figure for the electron energy only represents a rough estimate which should, however, be accurate to within a factor of two. This energy estimate is in agreement with the experimental results quoted previously.

The acceleration of these electrons is the result of the rising self-magnetic field of the ions and will thus be limited to about 15–20 ns during which the ion current rises steeply (see Fig. 9). This, too, is in agreement with the observed duration of the electron pulse.

The propagation of these electrons through the gas in the drift tube has already been discussed in a preceding paragraph. This propagation is made possible by the self-magnetic field of the electron beam. The rise of the ion current in the drift tube may eventually reverse the sign of the magnetic field in the plasma, thus preventing further propagation of the electrons. At this stage it is difficult to decide whether this effect also contributes to the sudden termination of the electron signals in the streak photographs.

TABLE I. Measured and calculated deflection angles of ions emerging from a planar pinch reflex diode.

t (ns)	I_i (kA)	r (cm)[a]	$\sin\theta^b$ measured	$\sin\theta^c$ calculated
~0	15	0.2	−0.03	0.01
		1.6	−0.03	
		2.4	−0.02	
12	110	0.5	0.0	0.09
		3.3	0.09	
		4.7	0.12	
18	200	1.1	0.04	0.16
		3.1	0.18	
		4.9	0.19	
31	300	3.1	0.18	0.23
		4.9	0.35	

[a] Reconstructed emission radius.
[b] A negative sign indicates a divergent angle.
[c] Using Eq. (8).

B. Bending of the ion trajectories

The angles at which the ions emerge from an ion diode are determined by the direction and magnitude of the electric and magnetic fields in the diode. The ions are launched from the anode plasma perpendicular to its surface and are bent towards the diode axis by the azimuthal self-magnetic field. Consider a planar ion diode. Early in the pulse the anode plasma surface is still very close to the planar anode foil and the ions will be launched in the axial direction. Since the ion current and its self-magnetic field are still low, the ions will emerge from the diode nearly parallel to its axis.

In the pinch reflex diode the anode plasma expands faster near the diode axis than off axis.[6] Later in the pulse this may result in a sloping plasma surface. Thus, ions emitted from that surface some distance from the axis may be launched with an outward velocity component. In experiments performed with a similar diode on the PITHON generator[15] this plasma motion was measured. Very little plasma expansion was observed during the initial 50 ns of the pulse. Thus, it seems that in our experiments this effect can be neglected.

As the azimuthal magnetic field in the diode increases the ion trajectories are bent more and more towards the axis. This bending can easily be estimated. The electron current crosses the diode gap near the outer radius ($R = 5$ cm) and then flows toward the center near the anode foil (see Fig. 4). Thus, the azimuthal magnetic field acting on the ions is almost exclusively due to the flow of ions crossing the diode gap z_A. For an ion current density $i \sim 1/r$ (as corroborated by numerical simulation[16]), the magnetic field is independent of the radius r and equals $H = I_i/(2\pi R)$, where R is the anode plasma radius, and I_i the total ion current. For small deflections the radial momentum P_r of singly charged ions after traversing the anode-cathode distance z_A is given by $P_r = -eBz_A$, where $B = \mu_0 H$ is the magnetic induction in the diode and e the proton charge. The angle θ that the ion trajectories make with the diode axis at the entrance to the drift tube is given by

$$\sin\theta = P_r/P \simeq eBz_A/(2\ \mathrm{MeV})^{1/2}, \tag{8}$$

where P is the total ion momentum, M the ion mass, and V the accelerating potential. For 200 kA of 1-MeV protons and for $z_A = 2.8$ cm, Eq. (8) gives for the deflection angle $\sin\theta = 0.16$. Since the ion current in the drift tube is to a large degree (>98%) neutralized the additional trajectory bending in the drift tube contributes less than 10% to the total measured deflection.

Reconstructed ion trajectories from a planar pinch reflex diode are shown in Fig. 12. The trajectories were reconstructed from the streak photograph in Fig. 11 (see Sec. V) neglecting trajectory bending in the drift tube. Table I shows the angles that the reconstructed trajectories make with the diode axis for four different times during the pulse. The estimated error in $\sin\theta$ is ± 0.02. For $t \simeq 0$ all three trajectories are almost parallel to the diode axis, as expected. For $t = 12$ ns and $t = 18$ ns the two outer trajectories are almost parallel to each other, in agreement with a diode magnetic field independent of the radius. The measured values of $\sin\theta$ are about 20% higher than the calculated ones. Part of this discrepancy may be attributed to the small trajectory bending by the residual magnetic field in the drift tube. The trajectories originating at small radii show much smaller deflection angles. This disagreement is not surprising since the assumption of $i \sim 1/r$ must break down for small values of r. For $t = 31$ ns the agreement with theory is less satisfactory. Possibly, anode plasma expansion and trajectory bending in the drift tube start playing an increasingly important role.

VI. DISCUSSION AND CONCLUSIONS

Intense proton beams from a pinch reflex diode have been measured using our new Rutherford scattering diag-

nostic method. The new method enabled us to measure, as a function of time, ion trajectories of beams emitted by planar and spherical pinch reflex diodes. It was shown that focussing properties of these diodes are dominated by the seif-magnetic field of the ions crossing the anode-cathode gap. For not too small emission radii the agreement between predicted and measured angles of ion trajectories in planar diodes is satisfactory, except very late in the pulse. This result is consistent with a $1/r$ dependence of the ion current density.[16] In spherical (focussing) diodes the magnetic field is largely responsible for the deviation of the focus from its geometric location.

In the course of the experiments, a low energy precursor electron beam was discovered. A simple model for the production mechanism of such an electron beam was developed. In this model acceleration of electrons by inductively produced electric fields is proposed. The predictions of the model are in qualitative agreement with the observed behavior of the electrons.

The Rutherford scattering diagnostic method presented here makes possible the simultaneous measurement of current density profiles and directions of motion of beam particles as a function of time for mega-electronvolt ion beams in the range 1 kA/cm^2–1 MA/cm^2. Spatial resolution of the order of a millimeter and time resolution of the order of a few nanoseconds can relatively easily be achieved. At very high power densities the hydrodynamic expansion of slit jaws and scatterer material may constitute a problem.

The method seems to be very powerful and versatile and variants of the basic technique can be adapted to requirements of different experiments. For example, time resolved frame photographs of a full cross section of an ion beam can be obtained by intercepting the full cross section of the beam by a scatterer and viewing the scatterer through a two-dimensional array of collimators capped by a scintillator.

Rapid progress towards inertial confinement fusion employing intense light ion beams will heavily depend upon sophisticated diagnostic techniques. It is hoped that the Rutherford scattering diagnostic method will contribute to the advancement of this field of research.

ACKNOWLEDGMENT

The skillful technical support of J. R. Boller is gratefully acknowledged.

[1]Gerold Yonas, Proceedings of the 3rd International Topical Conference on High Power Electron and Ion Beam Research and Technology, Novosibirsk, July 1979, p. 390 and references therein.

[2]A. E. Blaugrund, G. Cooperstein, J. R. Boiler, and Shyke A. Goldstein, Bull. Am. Phys. Soc. 20, 1252 (1975); S. J. Stephanakis, D. Mosher, G. Cooperstein, J. R. Boller, J. Golden, and Shyke A. Goldstein, Phys. Rev. Lett. 37, 1543 (1976).

[3]G. Cooperstein, Shyke A. Goldstein, D. Mosher, F. W. Oliphant, F. L. Sandel, S. J. Stephanakis, and F. C. Young, Proceedings of the 3rd International Topical Conference on High Power Electron and Ion Beam Research and Technology, Novosibirsk, July, 1979, p. 567.

[4]D. J. Johnson, Bull. Am. Phys. Soc. 24, 925 (1979).

[5]D. J. Johnson, R. J. Leeper, and J. P. Quintenz, Bull. Am. Phys. Soc. 25, 899 (1980).

[6]D. G. Colombant, G. Cooperstein, A. Drobot, Shyke A. Goldstein, R. A. Meger, D. Mosher, P. Ottinger, F. L. Sandel, S. J. Stephanakis, F. C. Young, J. Maenchen, and R. Genuario, Topical Meeting on Inertial Confinement Fusion, Feb. 1980, IEEE Cat. No. 80 CH 1536-2, QEA, p. 100.

[7]J. G. Pronko, D. Kohler, and L. F. Chase, Nucl. Instrum. Methods 164, 491 (1979).

[8]The response of a scintillator is proportional to the particle current density but, for ions, only approximately proportional to their energy. However, except for very slow ions, the deviation from linearity is small and will be neglected here.

[9]H. H. Andersen and J. F. Ziegler, *The Stopping and Ranges of Ions in Matter*, Vol. 3 (Pergamon, New York, 1977).

[10]J. R. Boller, J. K. Burton, and J. D. Shipman, Jr., Proceedings of the IEEE International Pulsed Power Conference, Lubbock, Texas (1979).

[11]Kimfol ($C_{16}H_{14}O_3$), a product of DuPont de Nemours & Co.

[12]R. J. Briggs, J. C. Clark, T. J. Fessenden, R. E. Hester, and E. J. Lauer, Proceedings of the 2nd International Conference on High Power Electron and Ion Beam Research and Technology, Cornell University, October 1977, p. 319.

[13]D. A. Hammer and N. Rostoker, Phys. Fluids 13, 1831 (1970); P. A. Miller, D. J. Johnson, T. P. Wright, and G. W. Kuswa, Comm. Plasma Phys. 5, 95 (1979).

[14]The ion current propagating in the drift tube creates enough ionization to largely neutralize its own magnetic field. It does not, therefore, prevent the electron propagation until, possibly, towards the end of the electron pulse.

[15]J. Maenchen (private communication).

[16]A. T. Drobot, R. J. Barker, Roswell Lee, A. Sternlieb, D. Mosher, and S. A. Goldstein, Proceedings of the 3rd International Topical Conference on High Power Electron and Ion Beam Research and Technology, Novosibirsk, July 1979, p. 647.

U.S.-Japan Seminar on
Theory and Application of Multiply Ionized Plasmas
Produced by Laser and Particle Beams
May 3-7, 1982

HIGH-INTENSITY LIGHT-ION BEAM RESEARCH AT NRL+

G. Cooperstein, R. J. Barker*, D. G. Colombant, A. Drobot**, Shyke A. Goldstein*, R. A. Meger*, D. Mosher, P. F. Ottinger*, F. L. Sandel*, S. J. Stephanakis and F. C. Young

Naval Research Laboratory, Washington, DC 20375

ABSTRACT

High-brightness proton beams (.4 MA, 1 MV) have recently been extracted from 20 cm^2 axial pinch-reflex diodes (PRDs) mounted on the NRL Gamble II generator. A source power brightness of > 10 TW/cm^2rad^2 was achieved in these experiments. A new barrel-shaped equitorial PRD that can be coupled to PBFA-II has also been operated on Gamble II and has demonstrated 50% proton efficiency with predominately azimuthally-symmetric charged-particle flow. In other experiments the stopping power of deuterons in hot plasmas was measured using a PRD on Gamble II. Results show about 40% enhancement in stopping power over that in cold targets when the beam was focused to about .25 MA/cm^2. Research is also being performed on transporting ion beams in large-diameter channels ($\gtrsim$ 2.5 cm) and on a post-transport, plasma-filled, magnetic-focusing section to bring the beam to pellet dimensions.

I. INTRODUCTION

Recent NRL experiments and theory have investigated key aspects of two ignition-system configurations for light-ion-drivers on PBFA-II.[1,2] The first configuration ties all 36 modules to a single barrel-shaped radial ion diode with 1 m dimensions surrounding the pellet located on the diode axis of symmetry. The barrel diameter must be small enough to permit focusing to pellet dimensions but large enough to permit time-of-flight bunching of the beam from the power-pulse duration to the pellet-driving time. The second configuration uses groups of modules to drive small-area disc-like axial ion diodes each of which focuses a beam into a z-discharge transport channel[3] about 2 m long and a few cm in diameter. Each channel is terminated in a short, higher-current discharge which magnetically focuses the beam onto the pellet.[2,4] Beam transport allows the diode focusing length to be much less than the bunching length and the post-transport magnetic-focusing allows larger-diameter beams to be transported and then focused. Such a system is schematically illustrated in Fig. 1

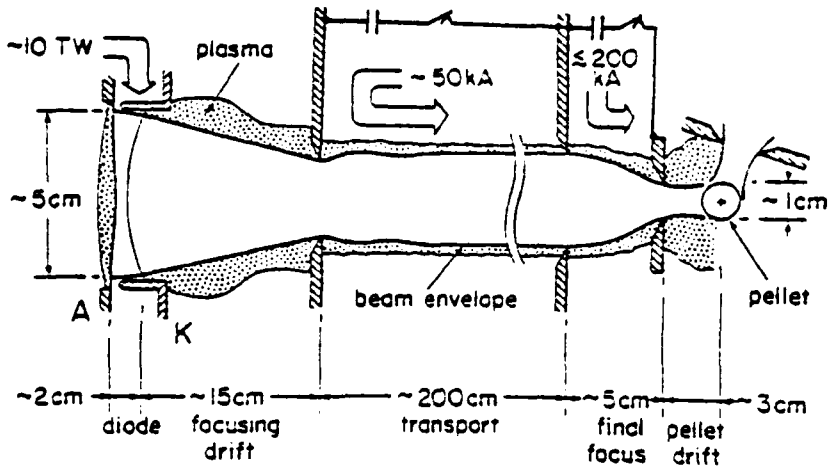

Fig. 1. Schematic of modular Light-Ion ICF system.

Ongoing research is evaluating pinch-reflex diodes (PRDs) for both ignition system configurations. Barrel-shaped equitorial PRD experiments on the NRL Gamble II device operating at 1.2 MV and .8 MA have demonstrated 50% proton efficiency with predominately azimuthally-symmetric charged-particle flow, average beam-divergence half-angles in the $1\text{-}2^{o}$ range between filaments, and good agreement with theoretical scaling laws.[5] This low divergence leads to a high brightness beam as defined in Sec. II. A high-power diode of similar design is now being tested on PBFA-II.[6] High-brightness proton beams (.4 MA, 1 MV) have recently been extracted from 20 cm^2 axial PRDs mounted on Gamble II. A source power brightness of 10 TW/cm^2rad^2 was achieved by minimizing the vacuum gap between the anode and cathode-transmission foils, thereby reducing the disruptive effects of filamentation in the vacuum gap.[7] Similar diodes have produced nearly 2 TW, 100 kJ proton and deuteron beams with 70% ion production efficiency on the Physics International PITHON generator.[8]

Other experiments on Gamble II have employed 20 cm^2 axial PRDs to measure the energy loss of deuteron beams in subrange Mylar and aluminum targets located at the beam focus. These targets are sandwiched between thin CD_2 layers so that ion-energy loss could be determined from time-of-flight analyses of the two neutron pulses. Results show about 40% enhancement in stopping power[9] over that in cold targets when the beam is focused to about .25 MA/cm^2. Results of these and other lower-current-density measurements are in excellent agreement with calculated stopping due to free and bound electrons at ionization levels expected from ion-target heating.[10] Factor-of-two enhancements over cold stopping for light- and heavy-ion beams are predicted at target temperatures expected for break-even pellets.

New stability constraints have recently been combined with channel-MHD and energy-loss constraints to define an operational window for transport of various light-ion species. Calculations of two-stream- and filamentation-instability growth rates show that multi-terawatt beams can be transported a few meters in channels a few centimeters in diameter.[2,11] Less than 10 channels would be sufficient to transport PBFA-II level beams and ignite a pellet provided that final magnetic focusing can be utilized to focus each transported beam. A proof-of-principle experiment for final focusing has been carried out on Gamble II using a 100 kA discharge channel 4 cm in diameter and 8 cm long mounted in front of the diode.[12] Experiments in which a transported beam will be focused are planned.

Section II will review recent high brightness diode experiments on Gamble II. The new barrel-shaped equitorial PRD concept and preliminary Gamble II results will be reviewed in Section III. Section IV will discuss the energy loss experiments of deuteron beams in subrange Mylar and aluminum targets. Finally transport considerations in large diameter channels and final focusing concepts and experiments will be discussed in Section V.

II. ION BEAM BRIGHTNESS STUDIES

Beam power brightness at the diode imposes the ultimate limit on the ability to focus ion beams onto targets. The PRD which has been previously described[13,14] and which is illustrated in Fig. 2 has been studied

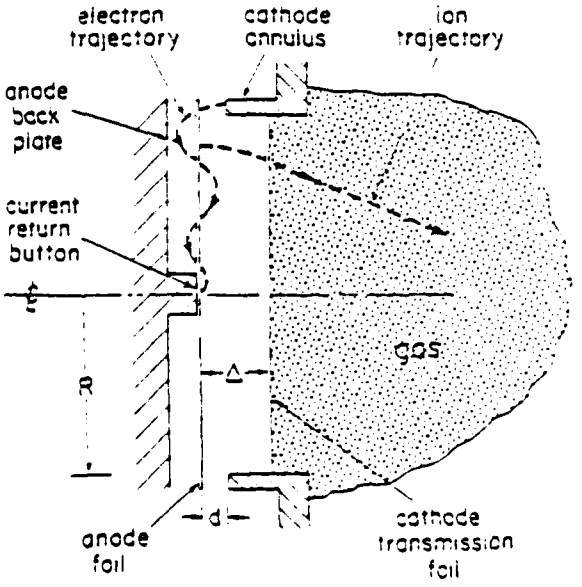

Fig. 2. Pinch-reflex-diode.

with respect to its performance as a source of high current density, low divergence ion beams. Both experimental and theoretical efforts are underway. Electron-filamentation instabilities which may occur in the electrode plasmas and vacuum gap are currently under investigation. Small-scale perturbations in diode electromagnetic fields associated with such instabilities can degrade brightness. In addition to their effects on beam brightness, varying electromagnetic fields and electrode-plasma motion also introduce time-dependent aberrations in the focusing properties of the diode. Changes in diode geometry and electrode materials are being investigated experimentally in order to determine their effects on the instabilities.

Provided that ion efficiency is not reduced and beam-divergence is not degraded, diode-beam brightness can be increased by reducing the diode radius. In recent 1 TW diode experiments on Gamble II, .6 TW proton beams were extracted from 20 cm^2-area anode foils. The ion beam brightness was measured crudely by a shadowbox technique[7] that uses multiple pinhole images of the ion beam. The recording plates used were either brass or cellophane. The brass is heated up by the impinging ion beam causing zinc to collect on the surface. Small features of ion beamlets can be clearly recorded provided their current density is high ($J_i \sim 10^3 A/cm^2$). The cellophane is more sensitive and records current densities down to 10 A/cm^2. Using these plates with the multiple hole shadowbox mounted far enough from the diode one can reconstruct the ion source pattern and its divergence. The ion source exhibited 10 to 20 beamlets for this small radius diode. Each beamlet had a size of about 1 cm in diameter. The beam divergence changed drastically when the gap, Δ, between the anode and the cathode inner foil was changed. The half angle of the diverging beam cone, $\delta\theta$, was measured to be ~ .1 rad at a gap of 1.5 cm and ~ .06 rad at a gap of .5 cm. The divergence was observed as a conic structure with no preference to radial or azimuthal direction.

A simple calculation to explain beam divergence versus gap width was performed assuming that the total ion beam current (450 kA) was distributed equally among 15 sources each having a diameter of 1 cm. Self-pinching of these ion beamlets by self-magnetic fields would result in $\delta\theta = .08\Delta/\sqrt{V}$ for protons at a voltage V measured in MV. The experimental results at V = 1.2 MV show that $\delta\theta$ agrees well with the predicted value at the larger gap of Δ=1.5 cm. At the smaller gap the plasma motion from the

cathode (2×10^6 cm/s) and anode (5×10^6 cm/s) reduce Δ from its initial value of .5 cm to a lower value of about .2 cm at peak power. The calculated divergence is then .015 rad compared with the observed divergence of .05 rad. The larger experimental divergence cannot be explained by magnetic fields and must therefore be due to electric fields.

Two mechanisms have been identified for distortion of equipotentials. The first is associated with plasma hydrodynamics when the anode plasma is formed at discrete spots and expands in a two dimensional manner generating bulges on the anode. Since the conductive anode plasma prevents electric field penetration it distorts the equipotential structure close to its surface. Such spotty structure is clearly seen in the shadowbox pinhole images and was also observed using interferometry on the PITHON experiment.[8] The second mechanism is electron beam filamentation in vacuum. The resultant space charge structure introduces azimuthal and radial components to the electric field in addition to the axial field.

The two mechanisms mentioned would have caused large divergences ($\delta\theta \sim .2$ rad) if the electric field would have been compressed against the anode plasma where the ions are launched. The PRD, however, operates by screening the ion beam space charge with the relativistic electrons that pinch and reflex through the anode plasma. This action allows the equipotentials to be spread across the entire diode gap unlike the magnetically insulated diode that only operates at high ion current density when the equipotentials are pushed against the anode plasma. The observed lower $\delta\theta$ of .05 rad is a clear experimental demonstration that even at this average ion source current density of 20 kA/cm^2 the PRD is operating as a space charge enhanced source rather than an electric field enhanced source.

The beam brightness ($JV/\delta\theta^2$) observed for V = 1.2 MV, J = 20 kA/cm^2 and $\delta\theta \sim .05$ rad is ~ 10 TW /cm^{2}rad^2. Scaling this figure up with voltage to the 3 MV level and assuming a factor-of-4 bunching during transport without brightness loss, leads to a modular-beam brightness of about 250 TW/cm^{2}rad^2. If 40% of the solid angle surrounding a pellet is subtended by final-focus exit apertures, on target power densities approaching 100 TW/cm^2 might then be achievable with existing PRDs.

III. EQUITORIAL-PINCH-REFLEX DIODE

A new version of the NRL PRD has been designed to operate on the

radial triplate geometry of PBFA-I. A conceptual schematic is shown in Fig. 3. This diode produces two cylindrically-symmetric sheet beams of electrons which flow from top and bottom by self-magnetic pinching and reflexing action on the anode foil to a common line pinch around the equator of the diode, hence the name equitorial-pinch-reflex diode (EPRD).

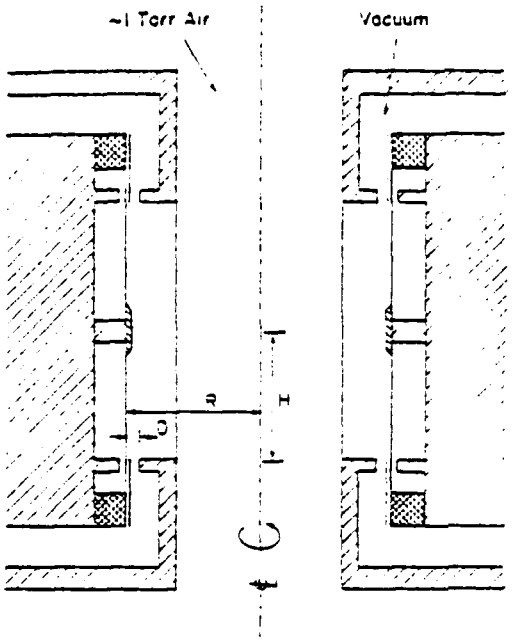

Fig. 3. Equitorial-pinch-reflex diode.

Although this diode appears to be a simple topological variation of the conventional PRD, there are a number of basic conceptual differences. There is no electron-space-charge-density enhancement as occurs with the conventional axial PRD because there is no radially converging electron flow towards the diode axis. This lack of electron convergence leads to a constant ion current density rather than one that increases inversely with the distance from the diode axis as in the axial PRD. These ions produce an azimuthal focusing magnetic field in the gap between the anode and cathode foils which increases proportionally to the distance from the equator. This in turn leads to a natural self-focusing of the ion beam even from a flat anode foil. Any additional spherical curvature of the anode foil simply adds to this natural self-focusing in a manner similar to simple geometric optics. This self-focusing is in contrast to the conventional PRD where the self-magnetic field from the ion current leads to a constant bending angle which must be compensated for by an aspheric focusing anode foil.

The other major difference and advantage of the EPRD over the conventional PRD is that the ratio of ion current to electron current, I_i/I_e, is decoupled from the diode impedance Z. In contrast, in a conventional PRD I_i/I_e scales like R/D and Z scales like D/R, which lead to high ion efficiency only for low impedance diodes (i.e., R/D>>1). For a given anode-cathode gap spacing, D, and diode radius, R, the impedance of the EPRD is proportional to D/R as with the conventional PRD, however, I_i/I_e is proportional to H/D (i.e., the electron path length/the ion path length) and is independent of diode radius or diode impedance. Thus, for any current equal to or above the critical current, the ion production efficiency can be made arbitrarily large by increasing the separation between the two disc cathodes. These properties were verified using a particle-in-cell code.

The EPRD has been tested on NRL's Gamble II generator by driving only the upper half of the diode shown in Fig. 3 in a coaxial-feed geometry. The Gamble diode is designed for negative-polarity operation of Gamble II to allow optical alignment. This arrangement requires diagnostic connections through transit-time-insulator cables installed in the coaxial water line. The anode radius is 7 cm and several anode foil materials including Mylar, polyvinyl acetate and polyethylene are being studied as ion sources. Anode lengths of 5, 10 and 15 cm have been used to provide configurations where the electron path length in the diode is respectively less than, comparable to, and greater than the diode radius. Typical anode-cathode gaps are 3.5 to 6 mm. Diagnostics include x-ray pinhole cameras, probes for measurement of net ion current, total diode current and diode voltage, arrays of ion collector probes, ion beam pinhole imaging to determine beam uniformity, direction and divergence, and various witness plate configurations. A differentially-pumped cylindrical neutralizing gas cell can be deployed inside the cathode-foil cylinder for studying radial convergence of the ion beam under near field-free conditions.

Initial experiments have shown the diode to be an efficient ion source and a good electrical match to the accelerator. Net ion currents on the order of 400 kA have been measured with diode impedances of 1.5-2 Ω. Azimutnally-symmetric electron and ion current flow has been observed. The diode impedance has been shown to be a linear function of anode-cathode gap but practically independent of diode axial height as predicted by theory. Definite limits to the anode surface area which can be uniformly turned on

at a given diode power level have been observed. Filamentation of mode number ~ 100 has been observed at the cathode with concomitant filamentation with mode number ~ 10 in the electron flow down the anode. Enhanced ion production has been observed from anode areas containing these filaments. Imaging of ion beamlets shows time-averaged half-angle divergence of 1-2° from areas not containing filaments while ions from filamented areas have 10-15° time-averaged half-angle divergences, principally in the azimuthal direction. Experiments to reduce the beam filamentation are in progress. Sandia National Laboratory is presently testing a high power diode of similar design on PBFA-I.[6]

IV. ENERGY LOSS EXPERIMENT

Theoretical research[15] indicates that at the ionization levels of ICF pellet plasmas the stopping power of light ions may be enhanced by a factor-of-two over that in the cold target. In this section, measurements of the energy loss of MeV deuterons in plasmas formed by focusing intense Gamble II ion beams (1 MeV, .2 MA, 20 ns) onto subrange-thick targets are presented. The results demonstrate that the stopping power of the heated target is enhanced over that of the cold target.

For these energy-loss measurements, a spherically-contoured PRD (Fig. 4) is used to produce an intense deuteron beam focus about 4 cm

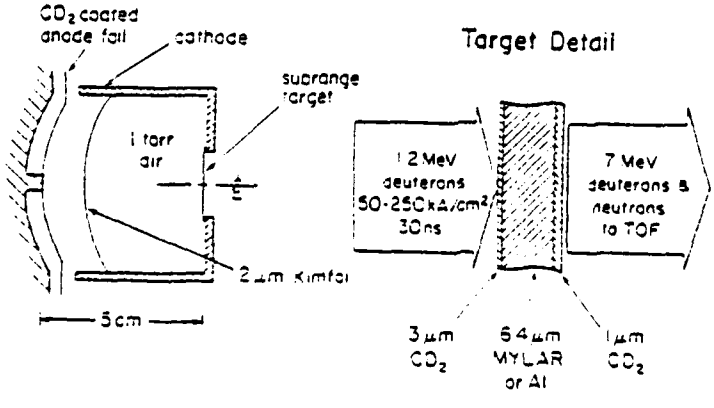

Fig. 4. Experimental set up for energy-loss measurements.

from the anode. The .01 cm thick plastic anode foil is coated with deuterated polyethylene (CD_2) to provide deuterons. A planar anode foil version of the diode is used for lower current density experiments. With planar anodes, the ion beam is focused onto targets about 10 cm from the center of the anode.

The experimental technique for determining the deuteron-energy loss uses neutron time-of-flight (TOF) with a multilayered target.[9] The target consists of a subrange stopping foil sandwiched between .3-μm and 1.0-μm thick layers of CD_2 (Fig. 4). Measurements of the d-d neutron TOF from the two CD_2 targets are used to determine both the incident deuteron energy and the deuteron energy loss in the stopping foil on each shot. Neutrons are detected in the forward-beam direction and reaction kinematics[16] are used to extract deuteron energies. The thickness of the stopping foil is adjusted so that neutrons from the two CD_2 targets can be resolved. In these experiments, 6.4-μm Mylar and aluminum stopping foils are used.

Figure 5 shows a typical trace from the neutron TOF detector.

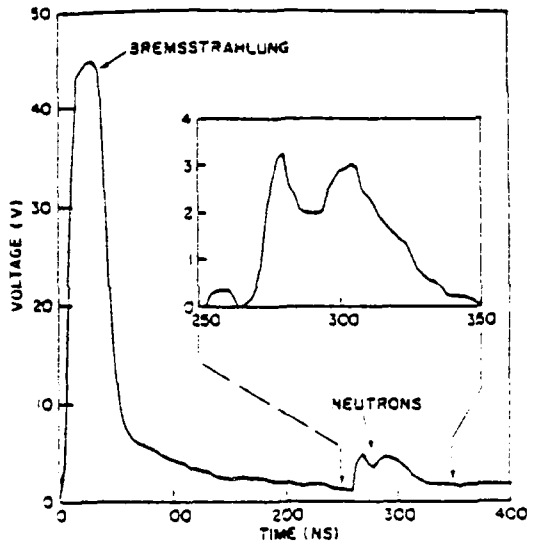

Fig. 5. Neutron TOF trace for Mylar stopping foil, spherical diode and 7.6 m flight path.

Bremsstrahlung radiation from the diode saturates the detector output, but neutron responses from the CD_2 targets are TOF delayed and are resolved about 260 ns after the bremsstrahlung signal. Neutrons are emitted primarily during the time of high voltage and current so that the neutron output is maximum at peak ion power. The time interval between the peak of the ion power and the peak of the first neutron pulse therefore determines the neutron energy from the front CD_2 target and, by kinematic calculation, the incident deuteron energy. A small correction (< 5%) is made to the TOF measurement for the flight time of deuterons from the anode to the target. The neutron signal is shown in the insert of Fig. 5. The flat background from the bremsstrahlung tail has been subtracted from the trace in the insert. The time separation of the two neutron peaks provides a direct measure of the deuteron energy loss in the stopping foil.

Focused ion current densities of 50 kA/cm^2 for the planar diode and 250 kA/cm^2 for the spherical diode are estimated for these experiments using previous proton results [14] using the measured total ion currents. Uncertainties of ±30% are assigned to the current densities obtained in this way. The results of stopping-power measurements using both planar and spherical diodes are presented in Fig. 6. For each case, the measurements

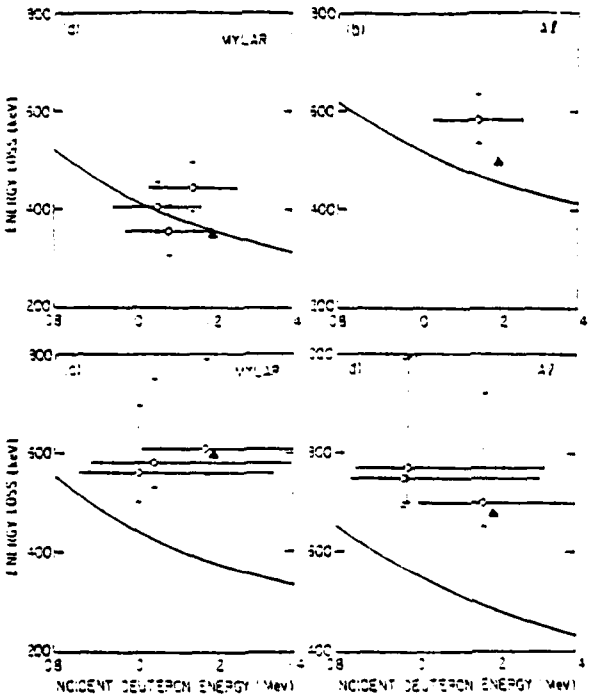

Fig 6. Comparison of energy loss measurements with planar (a and b) and spherical (c and d) diodes with energy losses (curves) calculated for cold-target.

are compared to the cold-target energy loss deduced from measurements of stopping cross sections by Andersen and Ziegler.[17] The measured energy losses are significantly larger than cold-target values in all cases except for the planar diode with a Mylar target. In this case, the measurements are consistent with cold-target values.

The deuteron energy losses deviate from that in a cold-target when sufficient ionization occurs in the stopping medium. The average ionization for aluminum and polyethylene with internal energy density parameterized from "SESAME"[18] are shown in Fig. 7. It is assumed that the free-electron production for Mylar is similar to that for CH_2. The internal energies corresponding to the experimental conditions for planar and spherical diodes are also indicated. It was calculated that ~ 75% of the deposited energy is converted into internal energy during the beam pulse. The rest is in kinetic expansion and radiation losses. This fraction is based on LASNEX hydrocode calculations which model this experiment.[10]

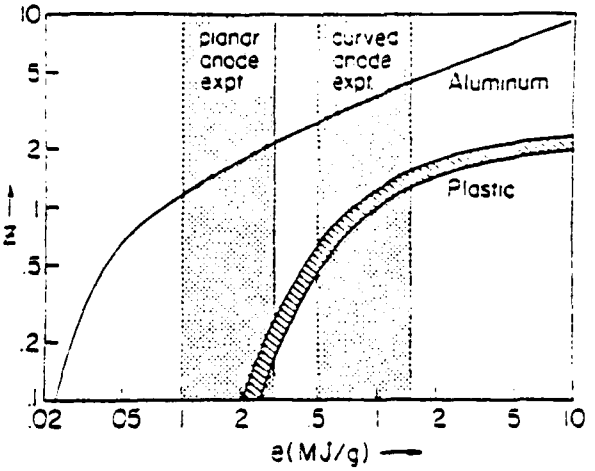

Fig. 7. Average ionization state (z) versus internal energy density (e) for aluminum and plastic (CH_2).

These calculations indicate that the target has expanded to about 2-mm thickness at the peak of the power pulse, and that the electron temperature is 4 to 5 ev at 50 kA/cm^2 and 13 to 17 eV at 250 kA/cm^2 for an aluminum stopping foil. Similar results for Mylar are ~3 eV at 50 kA/cm^2 and 9 to 11 eV at 250 kA/cm^2. The calculated energy losses at peak power are shown as solid triangles in Fig. 6, and are in reasonable agreement with the measurements. For the experimental conditions where a significant number of free electrons are produced in the stopping foil, the measured deuteron stopping is enhanced (Fig. 6b, c and d). If the energy deposition produces less ionization, the measured energy loss is consistent with cold-target stopping (Fig. 6a).

V. TRANSPORT AND FINAL FOCUSING

Intense light-ion beam transport in z-discharge channels provides accelerator standoff from ICF targets and allows time-of-flight bunching of the beam to higher intensity. Stability constraints combined with channel expansion and beam-energy loss constraints define an operational window for ion transport. The stability constraints are derived from the requirements to avoid significant growth of the electron-beam ion two-stream instability, the beam-filamentation instability and the channel-filamentation instability.[19] The channel-expansion constraint results from demanding that the $\underset{\sim}{J}\times\underset{\sim}{B}$-driven radial expansion of the channel occurs on a time scale longer than the beam-pulse duration.[20] Finally, the beam energy-loss constraint requires that no more than 25% of the beam energy is lost during transport.

The constraints have been derived for arbitrary beam-ion species in

order to evaluate the advantages of higher-atomic-weight ions. The beam energy, beam radius and channel density are also free parameters which have been varied in order to determine their effects on the operational window. In all cases, the channel gas was taken as deuterium. This allows the use of a simple model for channel heating and has the advantage of reduced radial acceleration due to the passing beam at the same stopping-power as hydrogen.

Results for beams of H^+, D^+, He^{+2} and C^{+6} show that a larger operational window exists for the higher-atomic-weight species. This is a consequence of their lower currents at equivalent transported power levels. Raising the channel density somewhat above the optimum for minimum beam-energy loss during transport relaxes the two-stream and channel-filamentation stability constraints and the channel-expansion constraint while only slightly modifying the energy-loss constraint. Increasing the beam radius relaxes the two-stream stability constraint and considerably reduces the channel-expansion and beam energy-loss constraints.

It is determined that multi-terawatt beams can be transported a few meters in large-radius channels with beam divergence half angles of .1 to .2 radians. Such angles are presently attainable with PRDs. If time-of-flight bunching during transport and final focusing after transport are employed, less than 10 (and as few as 4) channels are required to deliver the power needed to ignite a pellet. Such a system is conceptually illustrated in Fig. 1.

Theoretical results show factor-of-ten increases in final-focused ion-current density for beams transported in hollow channels. Channels which carry discharge current in the channel interior result in beam-brightness loss during transport and hence cannot be compressed as well by the final focusing cell. Focusing cells which are 1/8 of an ion-betatron-wavelength long focus the beam an additional 1/8-wavelength beyond the exit of the focusing cell. This 1-2 cm drift length is the stand-off distance separating the cell exit from the pellet. High plasma densities can be employed in the short focusing cell without excessive beam-energy loss in order that the plasma-MHD response can be minimized. These high densities combined with a thin transmission foil at the exit of the cell discourage pellet preheat from focusing-cell plasma plumes.

A final-focus system was designed and fielded on the Gamble II

accelerator.[12] Figure 8 shows a schematic representation of the channel.

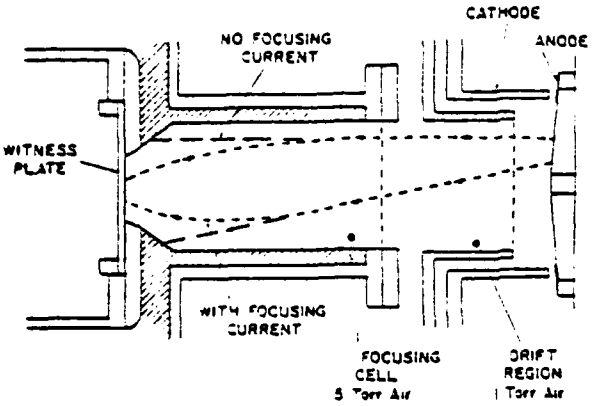

Fig. 8. Final focusing experiment mounted on front of Gamble II diode.

A discharge of ~ 100 kA was initiated by an external capacitor bank along the Lexan insulator (shaded region in Fig. 8) which was filled with 5-10 Torr of air. Channel currents were chosen to match a 1/4 betatron wavelength for the ions with the 8 cm channel length. No attempt in these early proof-of-principle experiments was made to synchronize the ion beam injection with the time dependent channel current density distribution. A convex pinch-reflex type anode was used to partially offset the self pinching of the ion beam in the diode and provide a nearly parallel trajectory injected ion beam. When aluminum witness plates were used, rear surface spall only appeared over the aperture region when the focusing current was turned on. Further experiments with shadowboxes placed downstream of the aperture confirmed that no large scale mixing of the ion orbits in the 1/4 betatron wavelength focusing cell occurred during focusing. Further experiments where the channel current distribution is optimized for a given beam injection condition are planned. Eventually, experiments will be performed with this final-focus system placed at the exit of the transport system.

REFERENCES

+Work supported by Department of Energy, Washington, DC 20545 and Defense Nuclear Agency, Washington, DC 20305
*JAYCOR, Inc., 205 S. Whiting St., Alexandria, VA 22304
**Science Application, Inc., 8400 Westpark Drive, McLean, VA 22101

[1] G. W. Kuswa, J. P. Quintenz, D. B. Seidel, D.J. Johnson, C. W. Mendel, Jr., E. J. T. Burns, D. Fehl, R. J. Leeper, F. C. Perry, P. A. Miller, M. M. Widner, and A. V. Farnsworth, Jr., in the Proceeding of the 4th Int. Conf. on High-Power Electron and Ion-Beam Research and Technology, Palaiseau, France (1981), p.3.

[2] D. Mosher, D. G. Colombant, S. A. Goldstein and P. F. Ottinger, ibid., p. 19.

[3] F. L. Sandel, S. J. Stephanakis, F. C. Young and W. F. Oliphant, ibid., p. 129.

[4] P. F. Ottinger, S. A. Goldstein and D. Mosher, 1980 IEEE Int. Conf. on Plasma Science, Madison, Wisconsin (1980), p. 95; S. A. Goldstein, D. G. Colombant, D. Mosher, P. F. Ottinger and F. Sandel, in the Proceeding of the 4th Int. Conf. on High-Power Electron and Ion-Beam Research and Technology, Palaiseau, France (1981), p. 113.

[5] F. L. Sandel, private communication; R. J. Barker and S. A. Goldstein, Bull. Am. Phys. Soc. 26, 921 (1981).

[6] J. N. Olsen, private communication.

[7] S. J. Stephanakis, S. A. Goldstein, P. F. Ottinger, D. Mosher, Bull. Am. Phys. Soc. 26, 921 (1981).

[8] F. C. Young, G. Cooperstein, S. A. Goldstein, D. Mosher, S. J. Stephanakis, W. F. Oliphant, and J. R. Boller, J. Maenchen, R. D. Genuario and R. N. Stringfield, NRL Memorandum Report 4726 (1981).

[9] F. C. Young, D. Mosher, S. J. Stephanakis, S. A. Goldstein, and T. A. Mehlhorn, 1982 IEEE Int. Conf. on Plasma Science, Ottawa, Canada.

[10] T. A. Mehlhorn, private communication.

[11] P. F. Ottinger, D. Mosher and S. A. Goldstein, 1982 IEEE Int. Conf. on Plasma Science, Ottawa, Canada.

[12] R. A. Meger, Shyke A. Goldstein, P. F. Ottinger, D. Mosher, S. J. Stephanakis, and F. C. Young, Bull. Am. Phys. Soc. 26, 921 (1981).

[13] S. A. Goldstein, G. Cooperstein, R. Lee, D. Mosher and S. J. Stephanakis, Phys. Rev. Lett. 40, 1504 (1978).

[14] G. Cooperstein, S. A. Goldstein, D. Mosher, R. J. Barker, J. R. Boller, D. G. Colombant, A. Drobot, R. A. Meger, W. F. Oliphant, P. F. Ottinger, F. L. Sandel, S. J. Stephanakis and F. C. Young, in Laser Interaction and Related Phenomena, edited by H. Schwarz, H. Hora, M. Lubin and B. Yaakobi (Plenum, New York, 1981), Vol. 5 p. 105.

[15] T. A. Mehlhorn, J. Appl. Phys. 52, 6522 (1981); E. Nardi, E. Peleg and Z. Zinamon, Appl. Phys. Lett., 39, 46 (1981); D. Mosher in ERDA Summer Study of Heavy Ions for Inertial Fusion LBL-5543, 1976, p. 39 (unpublished).

[16] H. Liskien and A. Paulsen, Atomic and Nuclear Data Tables 15, 57 (1975).

[17] H. H. Andersen and J. F. Ziegler, The stopping and Ranges of Ions in Matter, Vol. 3 (Pergamon Press, NY 1977).

[18] B. I. Bennett, J. D. Johnson, G. I. Kerly, G. T. Rood, "Recent Developments in the SESAME Equation-of-State Library,." Los Alamos Scientific Laboratory Report LA 7130, 1978 (unpublished).

[19] P. F. Ottinger, S. A. Goldstein and D. Mosher, NRL Memo Report 4543, July 1981.

[20] D. Mosher, D. G. Colombant and S. A. Goldstein, Comments Plasma Physics, 6, 101 (1981).

Pinched-beam ion-diode scaling on the Aurora pulser

R. A. Meger[a] and F. C. Young
Naval Research Laboratory, Washington, D.C. 20375

(Received 25 January 1982; accepted for publication 4 August 1982)

A pinched-beam ion diode has been operated on the Aurora pulser in positive polarity at impedances ranging from 10 to 35 Ω. Ion generation efficiencies of 20% were observed with ion energies ranging from 2.5 to 5 MeV. The ion current scaled inversely with the anode-cathode gap, and a peak value of 65 kA was measured for the smallest gap. A plasma erosion switch was used to decrease prepulse voltage and gap closure in the diode.

PACS numbers: 52.50.Dg, 52.70.Nc, 29.25.Cy, 29.25.Dz

I. INTRODUCTION

Progress in the field of intense pulsed light ion-beam generation has been rapid over the last few years, and high power ion beams are being investigated at several laboratories.[1] The Naval Research Laboratory (NRL) has concentrated its efforts on the pinch-reflex type of ion diode.[2] Experiments with this diode have been performed on the Gamble I and Gamble II accelerators at NRL,[3] the PITHON accelerator at Physics International,[4] the Aurora accelerator at the Harry Diamond Laboratories,[5] the SIDONIX and THALIE machines at Valduc,[6] and the REIDEN IV accelerator at Osaka.[7] With these machines a large range of diode impedances and ion energies have been investigated. Ion beams have been produced with diodes operating at impedances of 1 to 35 Ω. Ion-generation efficiencies (ion current/diode current) of up to 60% have been achieved at the lower-impedance level. For higher-impedance diodes, efficiencies of up to 20% at 20 Ω and 5 MV have been measured. The dependence of the ion-beam output on various pinched-beam-diode parameters is being studied in order to understand the scaling of such diodes with impedance and voltage.

The Aurora pulser is normally operated at high impedance (35 Ω) in negative polarity for bremsstrahlung production.[3] Ion-diode experiments in negative polarity on this machine have been reported.[5] Since then the accelerator has been modified to operate in positive polarity. In this paper, experiments on Aurora in positive polarity using a pinch-reflex-diode geometry are reported with emphasis on scaling of the ion-generation efficiency in the 10 to 35-Ω impedance regime. First, a simple scaling relationship for the ion efficiency of pinched-beam diodes is presented. Then the experimental measurements and results are described. In particular, it is shown that the diode efficiency is 20% at 10 Ω and 2.5 MV. Finally, the experimental results are compared with the expected scaling of the ion-beam-generation efficiency.

II. ION-GENERATION-EFFICIENCY SCALING

For a cylindrical-geometry pinched-beam diode, the ratio of the ion current density j_i to the electron current density j_e at nonrelativistic electron voltages is given by $j_i/j_e = (M_e/M_i)^{1/2}(R/D)$ where R is the cathode radius, D is the diode gap, and M_e and M_i are the electron and ion masses.[9] The ion current is enhanced by the factor R/D due to the different pathlengths of electrons ($\sim R$) and ions ($\sim D$) as they traverse the diode gap. For relativistic electron voltages, this expression becomes[10]

$$j_i/j_e = (M_e/M_i)^{1/2}[(\gamma+1)/2]^{1/2}(R/D), \tag{1}$$

where γ is the relativistic factor for electrons at the full diode voltage. Physically the relativistic correction results from electron-velocity saturation at relativistic energies while the ion velocity still increases with γ. This effect provides some enhancement of the ion current. For example, the ratio of ion-to-electron current is increased by a factor of 2.3 for a diode operating at 5 MV compared to the same diode at nonrelativistic voltages.

For a pinched-beam-diode with a reflexing anode foil (cylindrical hollow cathode and thin planar anode foil), the ion current is enhanced further due to the reflexing of electrons through the anode foil in conjunction with electron pinching on axis. Enhancements by a factor of 2 to 3 have been determined from experiments[11] and have been predicted from computer simulations[12,13] for diodes operating at 1 MV with R/D values of 10 to 20. For diodes operating at higher voltage and smaller values of R/D, electron reflexing is less important, but similar ion-current enhancement has been observed. This enhancement was attributed to prolonged electron lifetime in the diode due to compiicated electron trajectories as they drift across the diode gap.[5] In this paper, experimental results for a pinch-reflex diode with R/D values of 1 to 2 will be compared to the scaling predicted by Eq. (1).

III. EXPERIMENTAL PROCEDURE

These experiments were performed on the Aurora accelerator operated in positive polarity to allow direct diagnostic access to the ion beam. The Marx generator was charged to + 90 kV out of a possible charge of + 120 kV. The lower charge level was used to minimize possible damage to the Blumlein in positive polarity and to limit the voltage across the diode insulator. Only one of four vacuum transmission lines on the generator was used. Copper sulphate dummy loads were installed in the oil on the three unused lines.

The output end of the transmission line on the accelerator with the diode is shown in Fig. 1. The Blumlein output breaks down an oil prepulse switch, putting the voltage pulse

[a] JAYCOR, Alexandria, VA 22304.

 0021-8979/82/128543-06$02.40

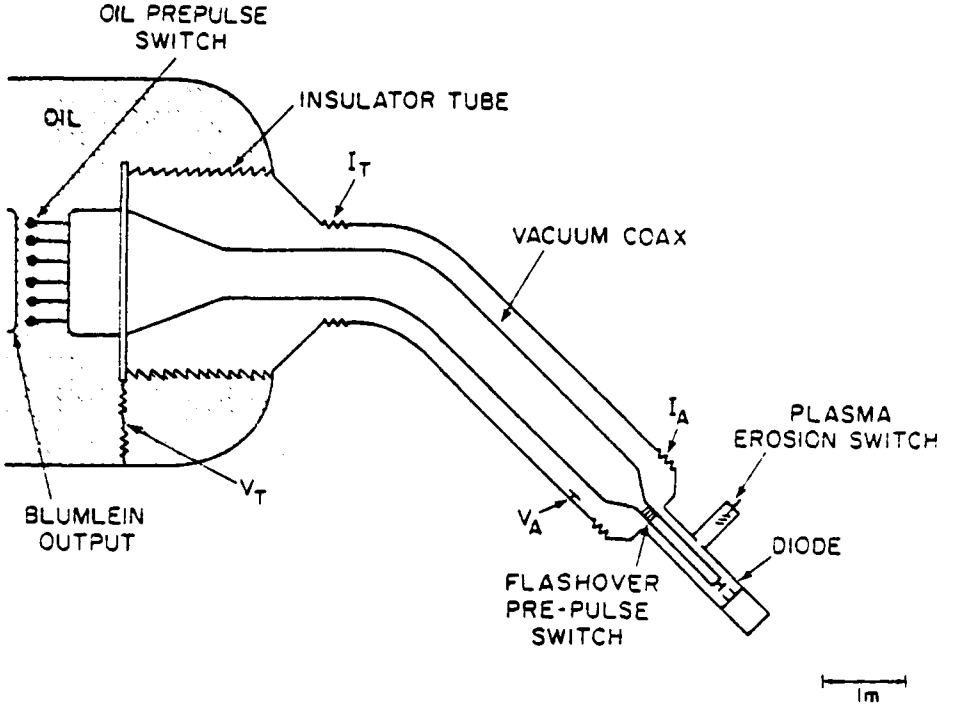

FIG. 1. One arm of the Aurora pulser from the oil region to the ion diode. The location of the resistive voltage divider V_T, the current shunt I_A, the flashover prepule switch, and the plasma-erosion-switch system are shown.

across the cylindrical insulator tube. This pulse propagates 7 m along a magnetically insulated 50-Ω coaxial transmission line. The 1.2-m o.d. coaxial conductor is reduced to a 25-cm diam vacuum chamber at the front end while the 58-cm i.d. conductor is tapered to 10 cm. The ion diode is mounted one meter into this smaller diameter coax. A flashover prepulse switch mounted on the inner conductor, as shown in Fig. 1, lowers the $\sim$200-kV prepulse on the transmission line to less than 50 kV. On some shots a plasma erosion switch (PES) was used to futher suppress the prepulse as well as to sharpen the risetime of the main pulse.

The PES system consists of three plasma guns of the type developed by Sandia National Laboratory.[14] These guns are mounted to inject plasma radially toward the center conductor as shown in Fig. 2. Several microseconds before the main power pulse arrives, the guns inject columns of carbon plasma with electron densities in the 10^{11}–10^{12} cm^{-3} range and with a velocity of $\sim 10^7$ cm/s. These columns provide a low impedance shunt in parallel with the ion diode. This protects the ion-diode load from the machine prepulse as well as shorting out some fraction of the main voltage pulse. Some of the charge transmitted through the plasma columns is provided by background ions which come from a sheath region near the outer conductor (negative electrode). As this sheath grows, the impedance of the PES increases rapidly. The increasing magnetic field is the coaxial region from the main power pulse causes the PES to open completely, and the remainder of the power pulse is delivered to the diode load. The voltage risetime across the load becomes the PES opening time which is less than the 100-ns accelerator voltage risetime. The fraction of the main voltage pulse, which is diverted through the erosion switch, can be controlled by adjusting the injected plasma density. This is done by altering the distance of the plasma guns from the center conductor and the firing time of the guns. Similar switches have been used on other pulsed-power machines.[15,16]

The ion diode used in these experiments is shown in Fig. 3. The anode consists of a 127-μm thick polyethylene (CH_2) foil stretched on a 12-cm diam aluminum ring and supported by a thin-wall (0.17-mm) aluminum tube. The cathode is a 10-cm i.d., 6.4-mm thick aluminum cylinder with a rounded

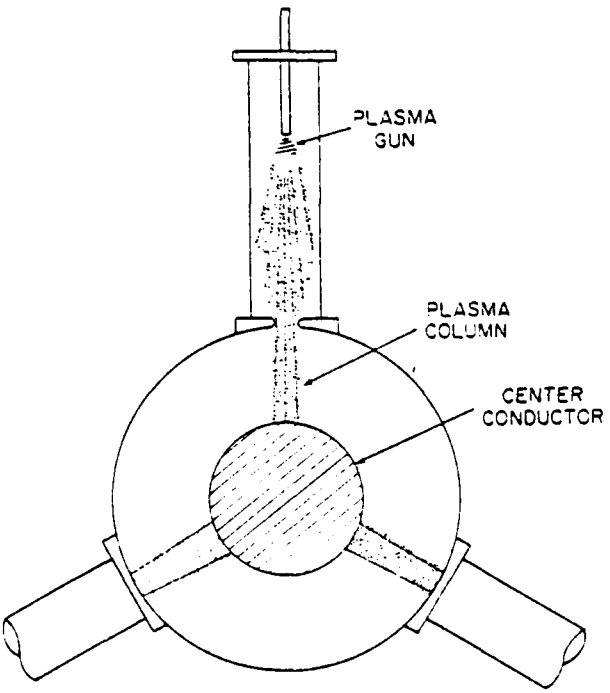

FIG. 2. Cross-sectional schematic of the plasma-erosion-switch system.

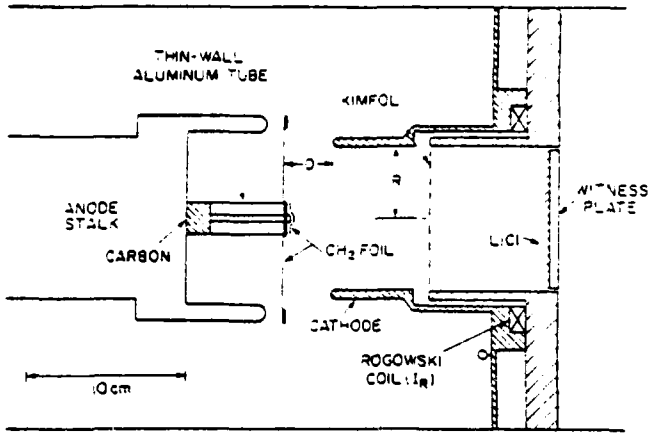

FIG. 3. Details of the ion diode used in positive polarity.

end. On some shots a 1.8-μm thick aluminized Kimfol[17] foil is located inside the cathode, followed by an aluminum witness plate coated with LiCl for neutron diagnostics. A Rogowski coil is mounted behind the cathode to measure the ion current incident on the Kimfol. This probe remains at ground potential with the generator configured in positive polarity.

The locations of the accelerator electrical diagnostics are shown in Fig. 1. The resistive voltage divider V_T, located in oil near the insulating tube, provides the most reliable voltage monitor. Capacitive voltage probes located in the vicinity of V_4 in the magnetically insulated transmission line suffer from electron emission or collection and do not provide useable data. Resistive current shunts located on the outer conductor provide reliable signals but do not measure current due to electrons flowing in the vacuum along the surface of the outer conductor. The magnitude of such electron current is expected to be small at the relatively low electric fields present in the large diameter coax region.

The remote electron and ion-beam diagnostics used in the experiment are similar to the previous negative-polarity experiments.[5] Time-integrated x-ray emission from the diode was imaged with a pinhole camera, while a scintillator photodiode measured the time-resolved x-ray signal. The ion diagnostics are based primarily on measurements of neutrons from the ^{7}Li$(p, n)^7$Be reaction resulting from proton bombardment of the LiCl target. Neutron intensities were measured with a Rh-activation detector[18] and with Mn-activation detectors.[19] Neutron energies were measured with the time-of-flight (TOF) technique for flight paths of 10 to 15.2 m in the forward direction. These energy measurements were used to determine the ion voltage for the diode.

IV. RESULTS

Approximately 50 shots have been taken with anode-cathode (AK) gaps ranging from 1.5 to 5.5 cm with and without the plasma erosion switches. Pinching of the electron beam on the anode axis as in the negative-polarity experiments[5] was confirmed by x-ray images from the pinhole camera. For a 2.0-cm AK gap, the diode operated at 2.5 MeV and 10 Ω (inferred from neutron TOF and total current measurements), while for a 5-cm AK gap the diode operated at 5 MeV and 35 Ω.

The large variation of the diode load impedance modified the power flow in the accelerator significantly. At low impedance the mismatch between the diode and the accelerator limited the amount of power delivered to the load. In addition, the voltage measured across the insulator tube was found to be dependent on the load impedance. Figure 4 shows the behavior of the tube voltage for two shots with AK gaps of 5.5 and 3.0 cm. The large-AK-gap shot (No. 3057) ran at a higher tube voltage and impedance than the smaller-AK-gap shot (No. 3509). In general, shots with lower peak tube voltage had longer-duration voltage pulses. This behavior of the tube voltage may be a consequence of the insulator design. The insulator was built for negative-polarity operation. Using it in positive polarity degrades the voltage standoff by about a factor of 2.[20] Also, the insulator flashover process is time and voltage dependent, with higher voltages giving faster breakdown. For high-impedance diode configurations, insulator flashover limited power flow into the diode; while at lower impedances, accelerator coupling limited the power flow. In all cases the peak power was less than 1 T W.

Electrical measurements are presented in Fig. 5 for a shot with a 4.0-cm AK gap and with the PES system. Voltage and current traces measured near the insulator tube and the corresponding power are given in Fig. 5(a). The voltage (V_T) peaks at 7.5 MV and has a FWHM of 150 ns. The current (I_T) increases during the voltage pulse to a peak of 180 kA before this monitor shorts. The injected peak power is 0.8 T W. Current traces (I_4 and I_R) measured near the diode are displayed in Fig. 5(b). The peak value of I_4 is similar to I_T, but the trace is delayed by the transit time of the transmission line. The ion current (I_R) rises to a peak of 29

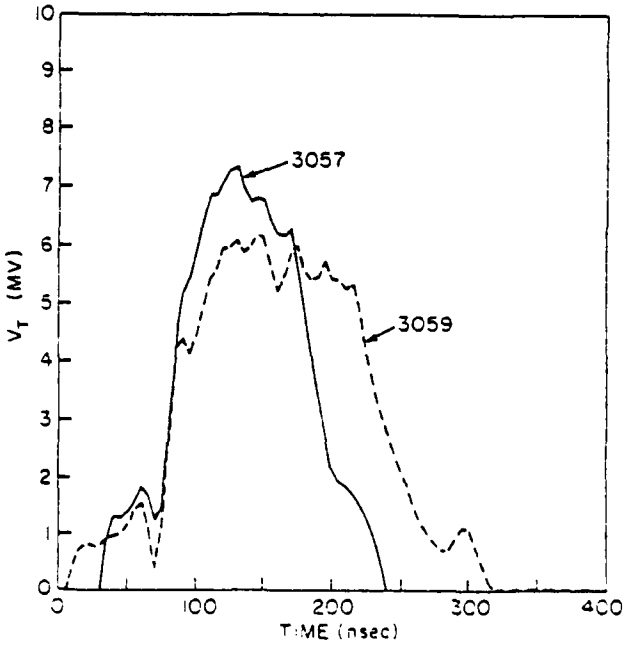

FIG. 4. Measured tube voltages V_T for a 5.5-cm-AK-gap shot (No. 3057) and for a 3.0-cm-AK-gap shot (No. 3059).

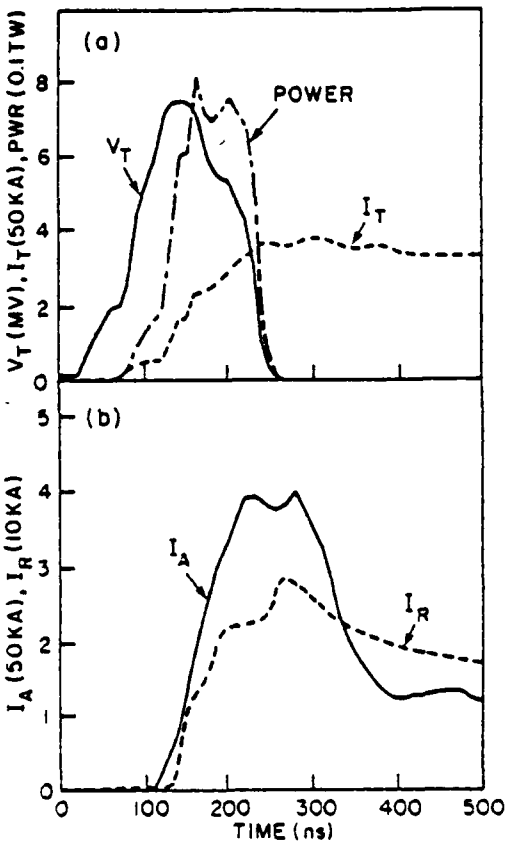

FIG. 5. Electrical traces measured (a) near the insulator and (b) near the diode for a 4.0-cm-AK-gap shot (No. 3058). The power trace in (a) is given by $I_T V_T$.

kA corresponding to an ion efficiency (I_A/I_R) of 16%. Peak values of these currents are nearly simultaneous and these values are used to characterize the ion efficiency.

The dependences of the peak shunt current I_A and peak Rogowski-coil current I_R on the AK gap are displayed in Figs. 6 and 7, respectively. In both cases, an inverse relationship between current and AK gap is observed. The shunt current measures the total diode current except for vacuum electron flow past the shunt. This electron flow is expected to be small in the large-diameter vacuum coax region where the shunt resistor is located. The Rogowski coil measures the net ion current passing through the coil and does not record current lost in front of the coil or current shielded by comoving electrons. Electron emission from the Kimfol is negligible because it is recessed 6 cm within the hollow cathode. Witness plate and surface damage in the diode indicate that ions striking the cathode before the Rogowski coil represent $< 10\%$ of the total ion current. Computer simulations[12] of the behavior of electrons and ions in the diode suggest that comoving electrons could shield as much as 20% of the total ion current.

The PES system was operated on about half of the shots in this experiment. The amount of plasma in the erosion-switch gap differed from shot to shot depending on the plasma-gun timing. The erosion-switch operation did not affect the inverse dependence of the shunt current on the AK gap (see Fig. 6). On some shots the plasma density was increased

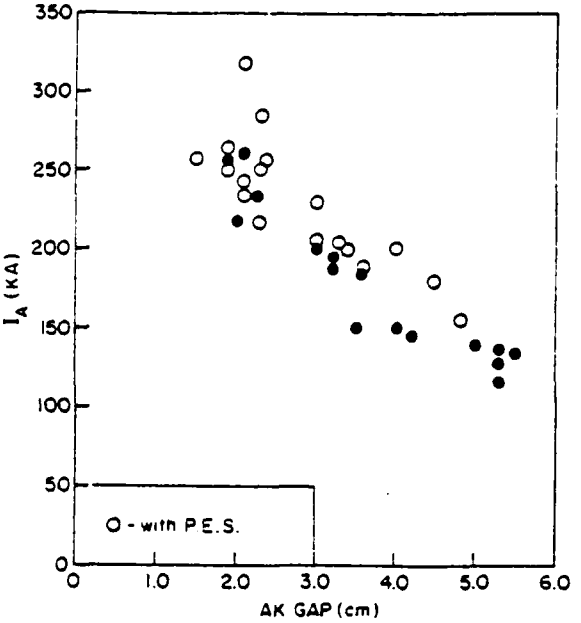

FIG. 6. Dependence of the peak value of the shunt current I_A on the AK gap. Shots with the PES system operating are plotted as open circles.

so that most of the pulse was shunted through the PES system. On these shots the peak shunt-current signal approached 300 kA independent of the AK gap.

The maximum Rogowski current of 65-kA peak value was measured at the smallest AK gap of 2 cm (see Fig. 7). Operation of the PES system did not affect the inverse dependence of the Rogowski current on the AK gap but did sharpen the risetime of this current. This is consistent with suppression of plasma formation in the diode by the PES system early in the voltage pulse.

The diode voltage was inferred from neutron TOF measurements using the ^{7}Li$(p, n)^7$Be reaction. Neutron TOF traces for three different AK gaps are shown in Fig. 8(a). As

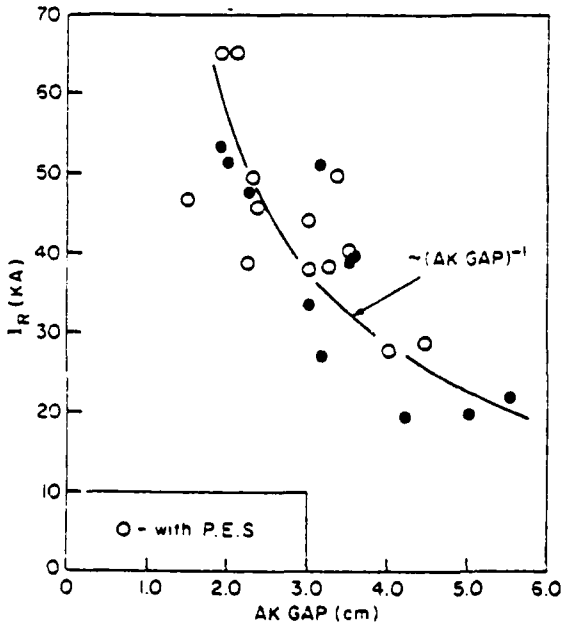

FIG. 7. Dependence of the peak value of the Rogowski-coil current I_R on the AK gap. Shots with the PES system operating are plotted as open circles. The solid curve represents an inverse dependence on the AK gap.

the AK gap is reduced, the neutron signal is delayed in time and is less intense. Measurable neutron traces were observed at small AK gaps by decreasing the neutron flight path. The neutron flight time was determined by measuring from the peak of the x-ray pulse to the leading edge of the neutron signal (50% of the peak) and correcting for the x-ray flight time. This measurement corresponds to the most energetic neutrons and consequently the most energetic protons from the diode. Proton energies extracted from such measurements using the ^{7}Li$(p,n)^7$Be reaction kinematics[21] are shown in Fig. 8(b). These measurements have an uncertainty of ± 0.2 MeV due to the uncertainty in time between the x-ray and neutron signals. This measurement is difficult below 3 MeV because this reaction has a neutron-production threshold of 1.9 MeV. The dependence of the proton energy on AK gap is not sensitive to the use of the PES system [see Fig. 8(b)].

The proton intensity may be deduced from the measured neutron yield for comparison with the Rogowski-current measurements. Yields of 1 to 2×10^{11} neut/sr at 45° were measured with the Rh-activation detector for AK gaps of 2 to 5 cm. This yield is approximately constant as the AK gap is increased because the larger yield expected from increasing proton energy is compensated for by a decreasing proton current. The largest yield in these experiments is 2×10^{12} neutrons/pulse into 4π, which is only 20% of that obtained in the negative-polarity experiments.[5] The proton intensity is determined from the neutron yield by using thick-target yields[5] at 45° for the ^{7}Li$(p,n)^7$Be reaction and the proton energy determined from neutron TOF. Intensities range from 5×10^{15} protons for a 5-cm AK gap to 2×10^{16} protons for a 2-cm AK gap. These intensities correspond to average proton currents of 8 and 30 kA, respectively, for a pulse duration of 100 ns. Since the neutron intensities used to evaluate these currents are time integrated, these currents represent values averaged over the pulse duration. These currents are approximately one-half of the peak Rogowski-current measurements given in Fig. 7. Such a difference is consistent with average currents determined from neutron measurements compared to peak values from Rogowski-coil measurements.

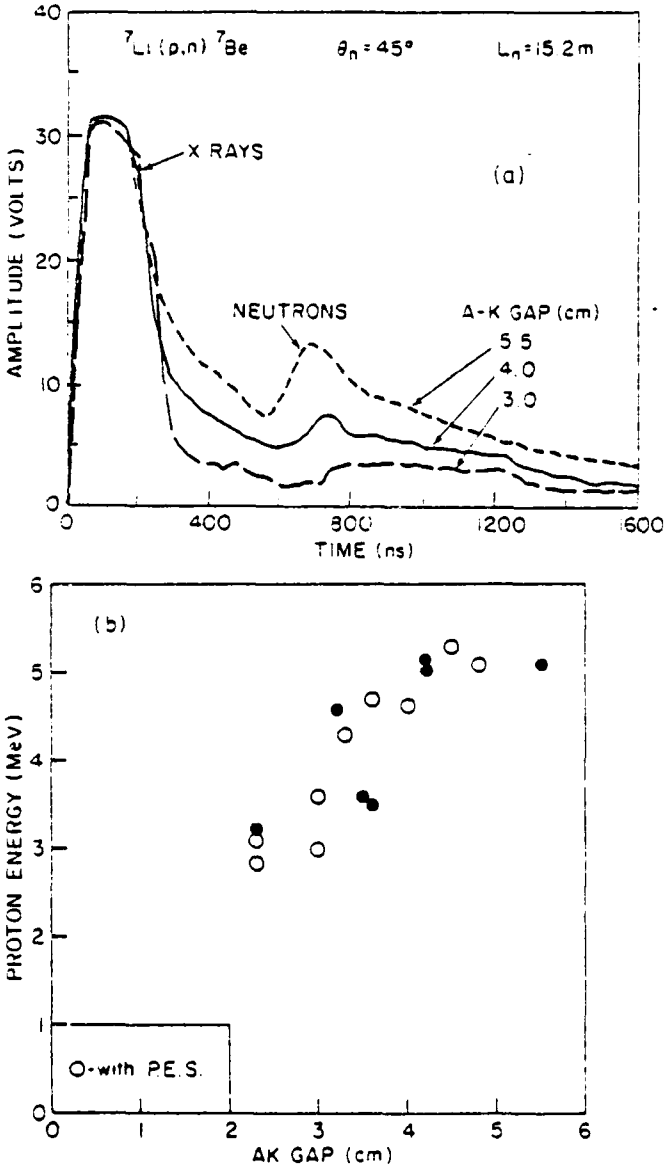

FIG. 8. a) Neutron TOF signals measured for AK gaps of 5.5, 4.0, and 3.0 cm. (b) Dependence of the proton energy, determined from neutron TOF, on the AK gap. Shots with the PES system operating are plotted as open circles.

To provide a representative diode impedance, the diode voltage, derived from a neutron TOF measurement, is divided by the peak diode current, as given by the shunt current I_A. This impedance increases from about 10 Ω at the smallest AK gap to 35 Ω at the largest AK gap. The ion-generation efficiency (I_R/I_A) is 20% for a 2.5-MV, 10-Ω diode with 2-cm AK gap. If the gap is increased to 5 cm, the ion efficiency is still 20% but the diode operates at 5 MV and 35 Ω. These results are similar to negative-polarity experiments[5] for which the ion efficiency was 20% at 5 MV and 25 Ω; however, the negative-polarity experiments were carried out at a higher power level of ~ 1.2 T W.

In order to test the scaling of the ion-beam-generation efficiency, as described in Sec. II, the peak ion current from the Rogowski coil was normalized to the electron current ($I_e = I_A - I_R$) and to the relativistic factor $(\gamma-1)^{1/2}$, where $\gamma = [V_p/M_e c^2) + 1]$ and V_p is the proton energy derived from neutron TOF. The dependence of these normalized quantities on the AK gap is shown in Fig. 9. Shots with the PES system are consistent with an inverse dependence on the AK gap as would be expected from the theory described in Sec. II. The non-PES shots fall to the right of the PES data in Fig. 9. Comparison of these data suggests that without the PES system, anode and cathode plasmas formed early in time result in a 1-cm greater closure of the AK gap than shots with the PES system. Gap closure of 1 cm without the PES is possible due to anode and cathode plasma formation either from the accelerator prepulse or during the rising portion of the diode voltage pulse. The data shown in Fig. 9 correspond to a value of $(I_R/I_e)(\gamma-1)^{-1/2} = 0.09$ for a 2.5-cm AK gap using peak values for the various terms. This value is 2.5 times larger than that predicted for R/D scaling of the pinched-beam diode. Such enhancement factors are consistent with previous experimental results on the other accelerators[11] and are attributed to electron reflexing in the AK gap.

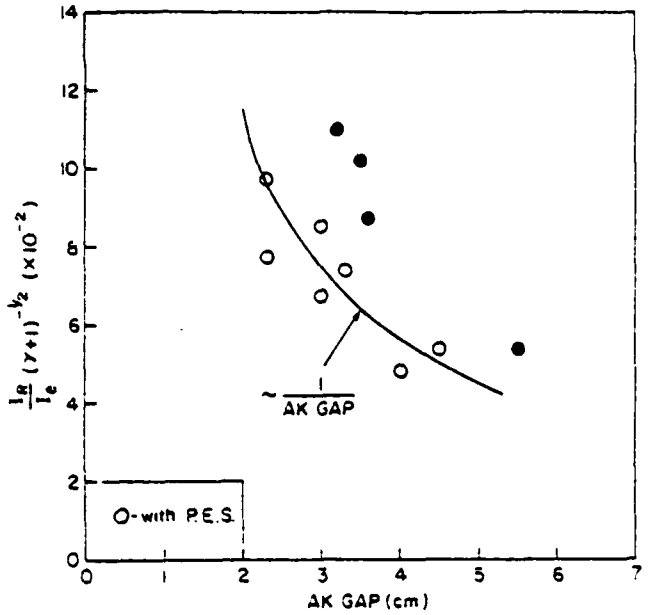

FIG. 9. Dependence of the peak Rogowski-coil current, normalized according to Eq. (1), on the AK gap. Shots with the PES system operating are plotted as open circles. The solid curve represents an inverse dependence on the AK gap.

V. SUMMARY

In these first experiments performed in positive polarity on the Aurora accelerator, the Marx generator and Blumlein operated satisfactorily at + 90-kV Marx charge. A voltage dependent shortening of the pulse across the diode-insulator stack was observed and may be related to insulator flashover. This behavior is dependent on the diode impedance as determined by the AK gap in the pinched-beam-diode geometry used in these experiments.

Plasma erosion switches were used in these experiments to eliminate prepulse at the ion diode. These switches appeared to decrease AK gap closure by 1 cm, thereby allowing smaller AK gaps to be used without gap closure, shorting the pulse prematurely.

Ion beams with peak net currents of 65 kA were measured for a 10-Ω, 2.5-MV diode configuration. The ion current appears to scale inversely with the AK gap. The ion efficiency is constant at 20% over the 10- to 35-Ω impedance range of this experiment. This effect may be due to the poor coupling of the low-impedance pinched-beam diode to the 50-Ω transmission line of the Aurora accelerator which limited peak power levels to less than 1 T W. The ion efficiency of 20% is 2.5 times larger than that expected from pinched-beam-diode theory and agrees with other pinch-reflex-diode experiments and numerical simulations.

ACKNOWLEDGMENTS

The success of this experiment required the support and cooperation of many personnel. The conversion of the Aurora pulser to positive polarity was carried out under the direction of A. Stewart of the Harry Diamond Laboratories (HDL). The modifications to Aurora and the operation of the machine were ably handled by the Operations and Maintenance Staff of HDL under the supervision of A. Pourier or D. Lindsey. J. Shipman of Sachs-Freeman assisted in evaluating power-flow problems in positive polarity. Technical assistance with the experimental setup and data acquisition involved the support of the following personnel: S. Graybill, D. Whittaker, K. Kerris, C. Casaer, T. Cassidy, and R. Bixby of HDL; R. Boller, J. Condon, and T. Robinson of NRL; and D. Bacon of JAYCOR. Guidance and theoretical support were provided by G. Cooperstein of NRL, Shyke A. Goldstein and R. J. Barker of JAYCOR, and A. Drobot of SAI. C. W. Mendel, Jr., of Sandia National Laboratory provided plasma-erosion-switch hardware and technical support for their use. The encouragement and support of R. L. Gullickson of the Defense Nuclear Agency is also gratefully acknowledged. This work was supported by the Defense Nuclear Agency.

[1] P. A. Miller, D. J. Johnson, T. P. Wright, and G. W. Kuswa, Comments Plasma Phys. Controlled Fusion 5, 95 (1979).
[2] G. Cooperstein, Shyke A. Goldstein, D. Mosher, R. J. Barker, J. R. Boller, D. G. Colombant, A. Drobot, R. A. Meger, W. F. Oliphant, P. F. Ottinger, F. L. Sandel, S. J. Stephanakis, and F. C. Young, in *Laser Interaction and Related Plasma Phenomena*, edited by H. Schwarz, H. Hora, M. Lubin, and B. Yaakobi (Plenum, New York, 1981), Vol. 5, p. 105.
[3] S. J. Stephanakis, D. Mosher, G. Cooperstein, J. R. Boller, J. Golden, and Shyke A. Goldstein, Phys. Rev. Lett. 37, 1543 (1976).
[4] S. J. Stephanakis, J. R. Boller, G. Cooperstein, Shyke A. Goldstein, D. D. Hinshelwood, D. Mosher, W. F. Oliphant, F. C. Young, R. D. Genuario, and J. E. Maenchen, Bull. Am. Phys. Soc. 24, 1031 (1979); J. Maenchen, R. Genuario, R. Stringfield, J. Kishi, G. Cooperstein, D. Mosher, S. Stephanakis, F. Young, S. Goldstein, and D. Hinshelwood, Bull. Am. Phys. Soc. 25, 945 (1980).
[5] R. A. Meger, F. C. Young, A. T. Drobot, G. Cooperstein, Shyke A. Goldstein, D. Mosher, S. E. Graybill, G. A. Huttlin, K. G. Kerris, and A. G. Stewart, J. Appl. Phys. 52, 6084 (1981).
[6] N. Camarcat, J. Cortella, C. Patou, and B. Tournier, in *Proceedings of the 4th International Topical Conference on High-Power Electron and Ion-Beam Research and Technology*, edited by H. J. Doucet and J. M. Buzzi (Ecole Polytechnique, Palaiseau, France, 1981), Vol. 1, p. 69, also p. 61.
[7] S. Higaki, S. Ido, K. Imasaki, S. Miyamoto, K. Mima, S. Nagai, K. Nishihara, T. Ozaki, T. Yabe, and C. Yamanaka, in *Proceedings of the 4th International Topical Conference on High-Power Electron and Ion-Beam Research and Technology*, edited by H. J. Doucet and J. M. Buzzi (Ecole Polytechnique, Palaiseau, France, 1981), Vol. 1, p. 11.
[8] B. Bernstein and I. Smith, IEEE Trans. Nucl. Sci. NS-20, 294 (1973).
[9] Shyke A. Goldstein and Roswell Lee, Phys. Rev. Lett. 35, 1079 (1975).
[10] J. W. Poukey, Appl. Phys. Lett. 26, 145 (1975).
[11] S. J. Stephanakis (private communication).
[12] A. T. Drobot, R. A. Meger, and Shyke A. Goldstein, Bull. Am. Phys. Soc., 25, 900 (1980).
[13] R. J. Barker and Shyke A. Goldstein, NRL Memorandum Report No. 4773, April 1982 (unpublished).
[14] C. W. Mendel, Jr., D. M. Zagar, G. S. Mills, S. Humphries, Jr., and S. A. Goldstein, Rev. Sci. Instrum. 51, 1641 (1980).
[15] C. W. Mendel, Jr. and S. A. Goldstein, J. Appl. Phys. 48, 1004 (1977).
[16] R. Stringfield, R. Schneider, R. D. Genuario, I. Roth, K. Childers, C. Stallings, and D. Dakin, J. Appl. Phys. 52, 1278 (1981).
[17] Available from Kimberly Clark Corp., Lee, Mass. 01238.
[18] F. C. Young, IEEE Trans. Nucl. Sci. NS-22, 718 (1975).
[19] R. A. Meger, F. C. Young, A. T. Drobot, G. Cooperstein, Shyke A. Goldstein, D. Mosher, S. E. Graybill, G. A. Huttlin, K. G. Kerris, and A. G. Stewart, NRL Memorandum Report No. 4477, March 1981 (unpublished). Also, F. C. Young and J. G. Pronko, Rev. Sci. Instrum. 53, 1228 (1982).
[20] I. D. Smith, International Symposium on High Voltages in Vacuum, MIT, Cambridge, MA, October 19–21, 1966 (unpublished).
[21] H. Liskien and A. Paulsen, At. Data Nucl. Data Tables 15, 57 (1975).

Production of intense light ion beams on a multiterawatt generator

J. W. Maenchen,[a] F. C. Young,[b] R. Stringfield,[c] S. J. Stephanakis,[b] D. Mosher,[b] Shyke A. Goldstein,[d] R. D. Genuario,[e] and G. Cooperstein[b]
Naval Research Laboratory, Washington, D.C. 20375 and Physics International Company, San Leandro, California 94577

(Received 23 August 1982; accepted for publication 17 September 1982)

The operation of a pinch-reflex diode as an intense pulsed ion-beam source has been scaled up to the multiterawatt PITHON generator. Ion beams with currents of 1 MA at 1.8 MeV have been extracted in a 130 kJ, 100-ns pulse. The corresponding ion production efficiency is 60%. Power losses were observed in interfacing the coaxial diode to the biconic vacuum feed of the generator. By using smaller area diodes, the average current density at the anode source was increased to 20 kA/cm^2. Proton and deuteron beams were studied in both planar and spherical diode geometries. The ion beam is focused predominantly by self-magnetic fields for planar diodes and predominantly by electrode shaping for spherical diodes. Current densities exceeding 150 kA/cm^2 were achieved with spherical diodes. The spatial evolution of the anode and cathode plasmas was studied by laser holographic interferometry. As the peak of the power pulse is approached, plasmas were observed to expand from the electrodes in fairly uniform profiles with steep density gradients and to accelerate across the vacuum gap. After peak power, anode plasma fluctuations and a high-velocity (30 cm/μs) axial plume develop; the latter expands radially coincident with collapse of the power pulse.

PACS numbers: 52.25.Dg, 52.70.c, 29.25.Cy, 29.25.Dz

I. INTRODUCTION

Recent technological advances in the production and focusing of intense pulsed light ion beams[1-3] (hydrogen, deuterium, and carbon) have led to the achievement of intensities approaching 1 MA/cm^2. The present achievements and the potential for continued advancements make light ion beams a prime candidate as a driver for inertial confinement fusion (ICF). Ions can be produced at high efficiency in extraction geometries appropriate to ICF ignition.[4-6] In addition, beam power density delivered on target can be increased over the source density through velocity bunching of the ions during transport,[4] by geometrical shaping of the ion source,[5] or by external magnetic focusing of the extracted ion beam.[7] Energy deposition of the ion beam in target plasmas approaches 100%.[3]

A variety of diode configurations to produce light ion beams for ICF have been discussed in the literature.[1-3] In this paper, experimental investigations into the production and ballistic focusing of proton and deuteron beams from one such diode type are presented. The pinch-reflex diode,[5] developed by the Naval Research Laboratory (NRL), was matched to the Physics International Company PITHON generator.[9] In addition to diode physics studies, the coupling between a biconic magnetically insulated vacuum transmission line and a small pinch-reflex diode at high stress ($E > 2 \times 10^6$ V/cm) has been investigated.

The early motivation for this work stemmed from computational modeling of the pinch-reflex diode for ICF applications. The PITHON generator parameters are similar to those of a single module in a multiion-beam target irradiation concept based on beam bunching during transport in Z pinches[10] and multibeam overlap on target. Two experimental sessions were performed with this generator: The first studied the scaling of diode performance and ballistic focusing at higher powers and longer pulse lengths than previously available[2]; the second studied the detailed evolution of the electrode plasma surfaces—information essential for design of a diode to produce a high-quality focused ion beam.[11] A more detailed report of this work may be obtained by requesting NRL Memorandum Report No. 4726 or PI Report PIIR-2-82.

In this paper, the results of these studies are presented. The generator and diode are discussed in Sec. II. The beam diagnostics employed to evaluate ion species, current-density profile and history, time-integrated beam geometry, and anode plasma surface evolution are described in Sec. III. The principal results of the two experimental sessions are presented and discussed in Sec. IV. Conclusions are presented in Sec. V.

II. EXPERIMENTAL APPARATUS

The negative polarity PITHON generator[9] was used to power these pinch-reflex-diode experiments. The output section of the generator, shown in Fig. 1, is a water-dielectric coaxial transmission line (shaded area) of 0.75 or 1.0-Ω impedance. The line bends radially inward and flares to an epoxy interface which separates the water from vacuum. Interface voltage and current diagnostics are located at several azimuthal positions in the flare. On the vacuum side of this structure the energy pulse is carried both by an electromagnetic wave and by field-emitted drifting electrons. The total current can be measured only on the anode and is monitored

[a] Physics International Co. Present address: Cornell University, Ithaca, NY 14853.
[b] Naval Research Laboratory.
[c] Physics International Co.
[d] JAYCOR, Alexandria, VA 22304.
[e] Physics International Co. Present address: Pulse Sciences, Inc., Oakland, CA 94612.

 0021-8979/83/010089-12$02.40

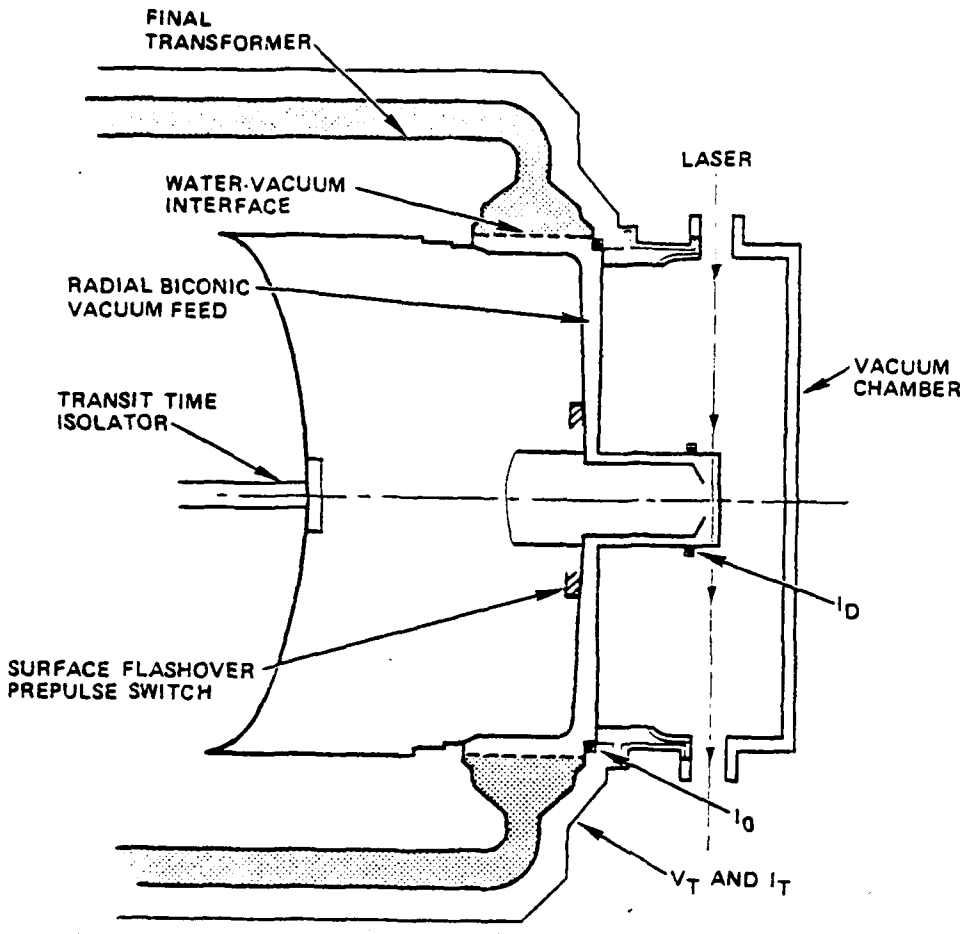

FIG. 1. Schematic of the vacuum-feed interface on PITHON.

by self-integrating Rogowski coils[12] at the vacuum interface (I_0) and at the diode (I_D). A dielectric surface-flashover switch interrupts the cathode feed to reduce the accelerator early-time "prepulse" voltage on the diode to about 5 kV.

Several distinct vacuum-feed and diode configurations were tested in the two experimental sessions reported here. The basic structures for planar and focusing geometry diodes are shown in Fig. 2. Following the vacuum feed from the flashover switch toward the axis, an abrupt transition is made from a radial biconic to a coaxial geometry. The inner coax conductor is rigidly attached to the cathode feed and extends either as a thick stainless steel cylinder or, in later experiments, as a thin disposable aluminum tube which is tapered to give a smaller-diameter cathode emission tip [see Fig. 7(a)]. The outer-coax anode conductor is stainless steel and can be adjusted for concentricity and axial spacing.

For the planar-diode configuration, shown in Fig. 2(a), the anode assembly consists of a 120-μm thick polyethylene (CH_2) disk held 5 mm from a carbon backing plate by a 15-cm-diam insulating ring and central carbon button. When the CH_2 surface flashes early in the electrical pulse, an anode plasma spreads across the foil and expands into the anode-cathode gap. Ions are accelerated toward the cathode from the low-density front of this moving plasma and are deflected radially inward by their self-magnetic field toward a focal position which varies in time. The ion beam current (I_{ion}) is measured by a self-integrating Rogowski coil sheltered behind the cathode tip. The ions pass through a 1.8-μm-thick polycarbonate (Kimfol[13]) pressure-window cathode foil and propagate current and charge neutralized in a 1-Torr-nitrogen drift chamber toward a focus. Several cathode shapes and sizes were studied, including enhanced-emission tip (Fig. 2) and smooth tapered cathodes with hollow inner areas of 100 or 30 cm^2.

The focusing configuration of the pinch-reflex diode is shown in Fig. 2(b). Anode foils of 250-μm-thick polyvinyl acetate (PVA), deformed into spherical sections with a 12.7-cm radius-of-curvature, are mounted onto machined carbon backing plates with similar contours to maintain a 5-mm foil-plate separation. An extended-tip cathode is used to define the 100-cm^2 diode area, and 3- to 4-mm anode-cathode-tip gaps are used for 1-Ω operation. Ions are focused several centimeters inside the center of the sphere defined by the anode because of additional diode B-field bending. The intent of this design is to create a high current-density ion-beam focus which is less sensitive to radial and temporal diode field variations during the pulse.[11]

III. DIAGNOSTICS

In this section beam and plasma diagnostics will be described and data reduction procedures will be discussed. These include: bremsstrahlung diagnostics for the electron-beam dynamic pinch and energy-deposition histories; a Rogowski coil to measure the ion-beam current; a "shadow box" diagnostic for spatial and velocity profiling of the ion beam; nuclear-reaction diagnostics for ion-beam charge and

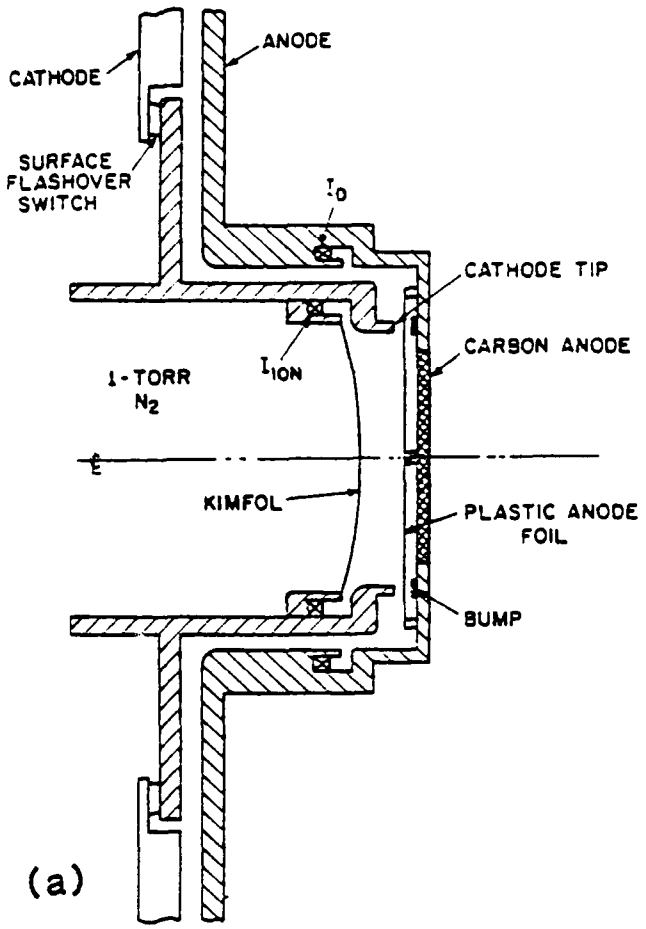

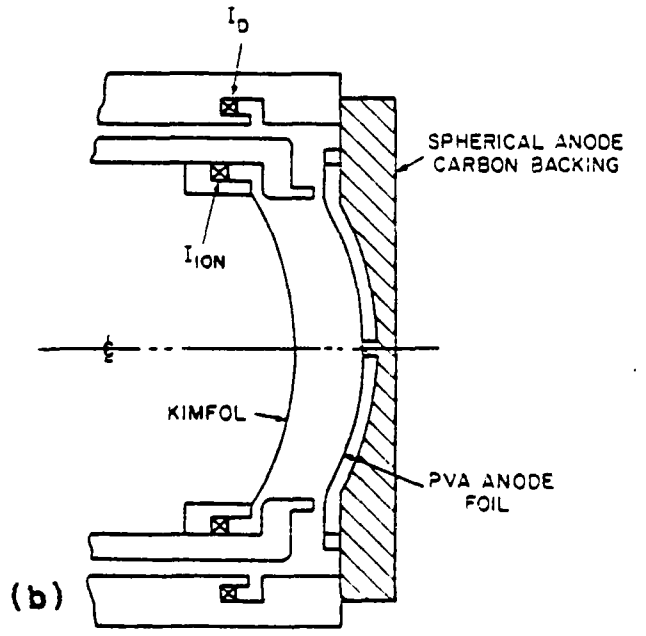

FIG. 2. Pinch-reflex-diode assemblies for the first experimental session in (a) planar geometry and (b) focusing geometry.

current determinations; and a laser holographic interferometry system for studying the evolution of the anode and cathode plasmas.

A. X rays

The ion power and energy on each shot are correlated with the electron bremsstrahlung radiation intensity. The symmetry and size of the electron pinch are determined by imaging this radiation with a pinhole camera which is rigidly mounted outside the vacuum chamber on the diode axis and records photons with energies greater than 30 keV. This camera images the diode with 0.5-mm resolution onto a stack of films with a wide range of x-ray sensitivities to provide good contrast for the variation of bremsstrahlung intensity across the diode image. Lithium fluoride thermoluminescent detector (TLD) capsules monitor the time-integrated bremsstrahlung dose at the camera from the entire anode.

The time-resolved x-ray output from the electron pinch is monitored with an optical photodiode (PDX) coupled to a plastic scintillator. Because the bremsstrahlung intensity scales with electron energy, a large x-ray signal with a large full width at half maximum (FWHM) (40–60 ns) indicates a high-voltage, long-impedance-lifetime shot.

Any serious current losses in the vacuum feed could be correlated with the photographic, TLD, and PDX data as well as with visual hardware damage.

B. Ion imaging

The location of the ion-beam focus was determined by ballistic reconstruction of ion trajectories from ion-induced melt damage patterns on the witness plate of a shadowbox,[2] as illustrated in Fig. 3. The interpretation of this data is based on the following assumptions: Ions are accelerated from a planar anode plasma with initial velocity vectors parallel to the diode axis. As they cross the anode-cathode gap, each ion is magnetically deflected by the magnetic field from a calculated ion-current-density profile.[14] Upon passing

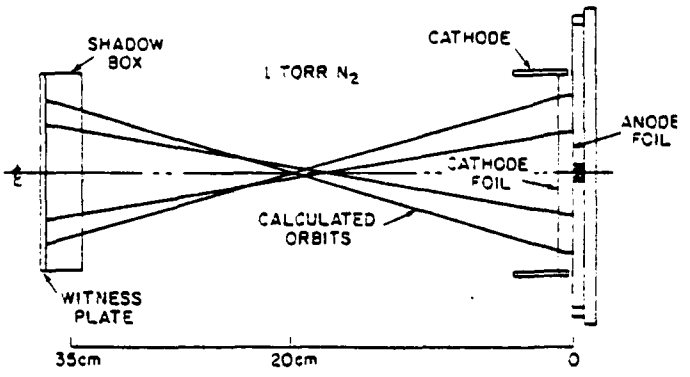

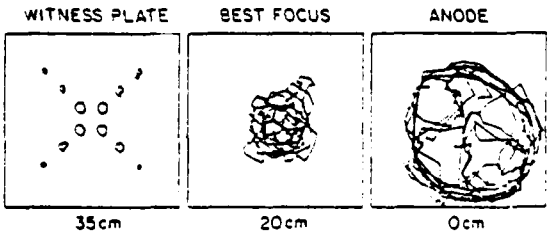

FIG. 3. Shadowbox geometry and reconstruction of ion-beam trajectories for planar-diode Shot 1676.

through the cathode foil and entering the 1-Torr-nitrogen drift chamber, the ions are charge and current neutralized and hence execute straight-line orbits through a focal region and expand into the shadowbox. Current neutrality in the gas region has been measured to be better than 98%. The damage patterns on the witness plate of the shadowbox are projections of the ion beam through the front apertures (see Fig. 3). The patterns, which are time-integrated records, often form teardrop or oval shapes with the long dimension along a radius. The radial extent of the damage is attributed to the change in focal length during the pulse due to time varying diode fields. The azimuthal width of the damage is due to the divergence of the ion beam upon exiting the cathode foil. The computer reconstruction, shown in Fig. 3, traces the recorded damage areas back through the front-plate apertures, through the focus, and onto the anode surface. The large damage patterns at the smallest radii on the witness plate are due to the time varying location of the focal spot moving through the shadowbox position and are not useful in planar geometry reconstructions.

C. Nuclear diagnostics

The intensity and duration of proton or deuteron currents were monitored by nuclear-reaction techniques. For proton beams, a prompt γ-ray diagnostic[15] was employed utilizing the $^{19}F(p,\alpha\gamma)^{16}O$ reaction. Teflon (CF_2) targets were placed in the ion-beam path, and 6-MeV prompt-γ rays were measured with a plastic scintillator and photomultiplier detector housed in a 3.2-cm-thick lead enclosure located 4 m from the ion diode at 95° to the diode axis and behind a 1-m-thick concrete shielding wall. The wall differentially shields the diode bremsstrahlung and improves the γ-ray-to-bremsstrahlung ratio. Measured and calculated signals for this detector on a shot with a CH_2 anode and Teflon target are compared in Fig. 4. The calculated signal shape was obtained from the experimental ion-current and diode-voltage waveforms using the thick-target yield for the $^{19}F(p,\alpha\gamma)^{16}O$ reaction as described in Ref. 15. This detector could not be calibrated absolutely as the attenuation of the prompt-γ signal by the concrete shielding wall is difficult to estimate.

The total yield of deuteron beams was determined by measuring neutrons from the $D(d,n)^3He$ and $^{12}C(d,n)^{13}N$ reactions. Deuteron beams, produced by using CD_2-coated PVA-foil anodes, were directed onto thick CD_2 targets to produce these reactions. Because the ion beam was directed into the generator in these experiments, neutron measurements were confined to angles greater than 90° from the deuteron direction. Total neutron yields were measured with a rhodium-activation detector[16] located 16.8 m from the diode at 175°. This detector viewed the target through a 30-cm-diam hole in the 60-cm-thick concrete shielding wall located midway between the target and detector. This geometry minimized the number of room-scattered neutrons measured and allowed the neutron intensity to be scaled inversely with the square of the source-to-detector distance. The rhodium-activation detector was calibrated with a ^{252}Cf neutron source as described in Ref. 16. Deuteron intensities were inferred from measured neutron intensities by using $D(d,n)^3He$ and $^{12}C(d,n)^{13}N$ reaction yields and deuteron energies from the diode voltage waveform. Thick-target yields for these reactions were calculated from measured cross sections[17,18] and published stopping powers[19] and are presented in Fig. 5. Above 1 MeV, the $^{12}C(d,n)^{13}N$ reaction contributes significantly to the neutron yield.

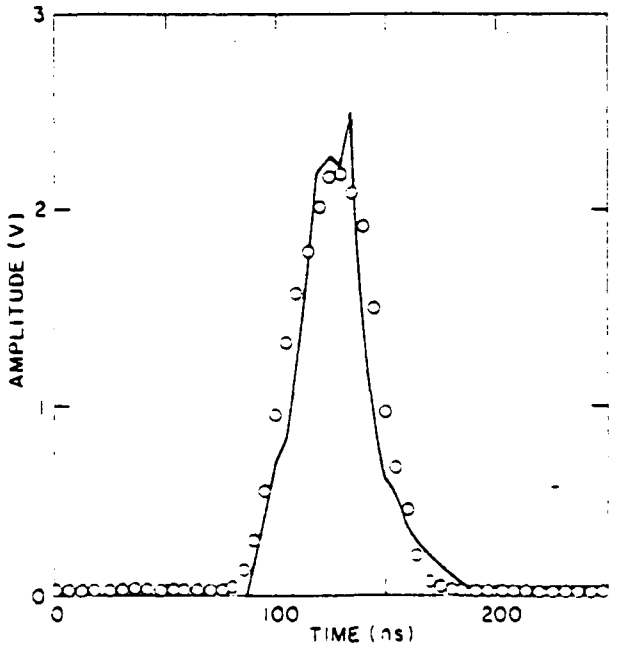

FIG. 4. Prompt-γ signals measured on Shot 1665 (solid line) and calculated (open circles) for protons on a thick CF_2 target. The calculated trace has been normalized in amplitude to the measured signal.

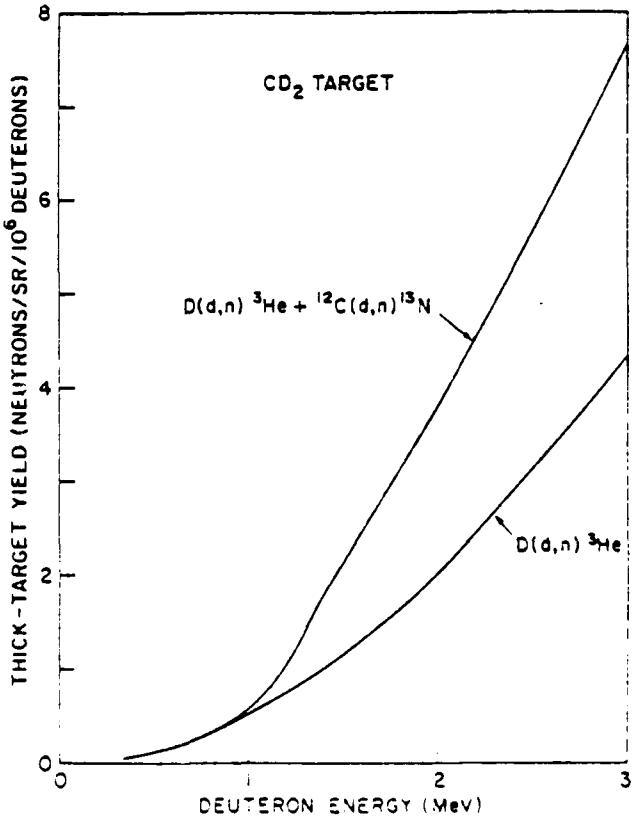

FIG. 5. Thick-target yields for the $D(d,n)^3He$ and $^{12}C(d,n)^{13}N$ reactions at 175°.

The neutron time-of-flight (TOF) technique was used with the $D(d,n)^3He$ reaction to determine neutron energies and to monitor the duration of the deuteron beam. A neutron TOF detector, consisting of a plastic scintillator quenched with 5% piperidine[20] and photomultiplier mounted within a 7.6-cm-thick lead shield, was located next to the rhodium-activation detector. In order to operate the photomultiplier in the linear range, the light emitted from the scintillator was attenuated with an ND-1 filter. The time history of the deuteron beam was determined using a similar TOF detector shielded with 10 cm of lead and located 3.2 m from the diode at 160°.[21] Typical traces from these two TOF detectors are shown in Fig. 6. The time interval from the peak of the bremsstrahlung to the peak of the neutron signal on the far detector was used to determine the neutron kinetic energy of 1.9 ± 0.2 MeV. This measurement could not be used to uniquely determine the deuteron energy (i.e., diode voltage) because the neutron energy is insensitive to the deuteron energy for the d-d reaction at the 175° measurement angle. Furthermore, the variation of deuteron angles incident on the target introduces an uncertainty in the neutron-emission angle. Neutron-energy determinations are, however, consistent with deuteron energies given by the diode voltage. The measured ion current and diode voltage were used to calculate the neutron responses shown in Fig. 6 (Ref. 21). The shapes of the measured and calculated responses are in good agreement. The duration of the neutron signal on the near detector (FWHM of 60 ns) gives a measure of the duration of the deuteron beam, which compares favorably with the duration of the ion pulse based on the measured diode-voltage and ion-current traces for this shot.

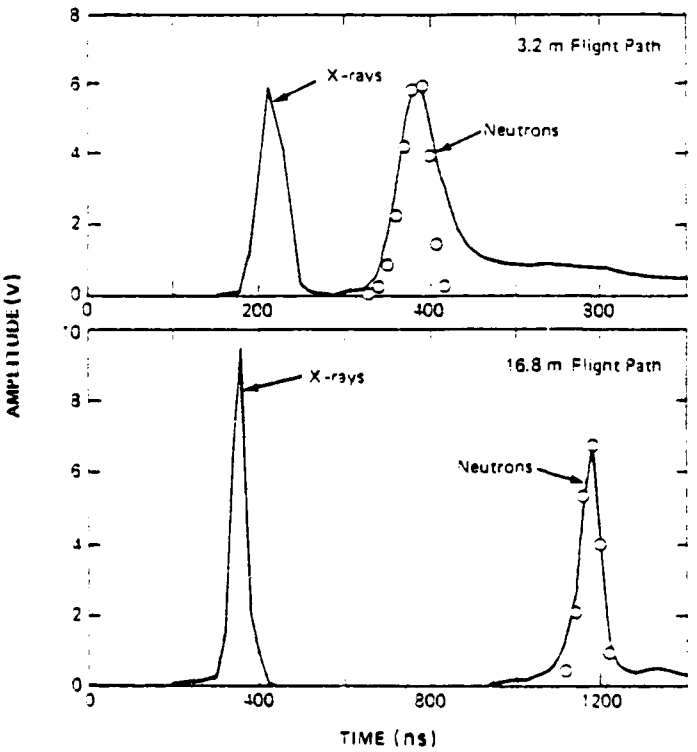

FIG. 6. Neutron TOF traces for Shot 1692. Calculated neutron-pulse shapes at 3.2 and 16.8 m are plotted as open circles. The calculations are normalized in amplitude to the measured neutron responses.

D. Holographic interferometry

The final diagnostic to be described is the holographic-interferometry system[22] used to monitor the anode and cathode plasma motions in the interelectrode gap. The system employs a 6-ns ruby laser pulse which is split into four beams delayed by path length in 10-ns increments to form a train of four laser pulses over a 30-ns interval. Each of these four beams is then split into a scene and a reference beam. The scene beams traverse the pinch-reflex diode through slots on the anode structure and then through lenses and mirrors to form real images of the diode on a glass holographic film plate. The reference beams are directed to the film, overlapping their respective scene beams to produce an array of four holograms on the film plane. Two such sets of holograms are superposed: one made before the shot and the other during the shot.

By shining light through a developed interferometric hologram, both an image of the diode and a series of fringes can be seen (see Fig. 7). Where no plasma is present, uniformly spaced straight fringes are produced on the image by introducing a uniformly changing optical-path-length difference (by slightly tilting a mirror) between the two sets of holograms. Additional changes in the optical path length caused by the presence of plasma result in shifting of the fringes. The shifting of a fringe over the distance of one reference fringe spacing corresponds to an additional wave length of path difference due to the plasma. The corresponding plasma density can be estimated by the relation: $n_e \Delta X = 3.2 \times 10^{17}/\text{cm}^2/\text{fringe shift}$, where ΔX is the total path length through a uniform plasma of density n_e. The largest plasma line density measurable by this technique is that for which the index of refraction equals zero (i.e., $2.3 \times 10^{21}/\text{cm}^2$). The maximum density observable in this experiment is estimated to be between 10^{19} and $10^{20}/\text{cm}^3$ due to ray tracing effects: large-angle refraction of the laser beam by higher-density plasmas reduces the light intensity entering the optical system and the exposure level on the film.

Unfolding the detailed radial-density profile is not possible with this technique. Figure 7(a) shows the diode area with laser viewing slots machined out of the anode: the shaded area is the laser-beam cross section, and the clear holes are the observable regions of the diode. Figure 7(b) shows a reconstructed interferometric hologram. It is important to note that the view through a hole-pair is a chord across a disk system which may not be axially symmetric: a thin plasma ripple in an orientation other than the laser axis will appear to be large-area plasma motion. Further, anode plasma which crosses the visual anode-cathode gap inside the cathode inner radius does not necessarily contact the cathode plasma lifting off the hollow emission ring. Despite these limitations, the system presents new information about the plasma surface evolution which is important for the design of high-focus-quality diodes.[23]

IV. EXPERIMENTAL RESULTS

A variety of technological areas were addressed in two experimental sessions. The first session extended scaling of the pinch-reflex ion diode to the higher power and longer

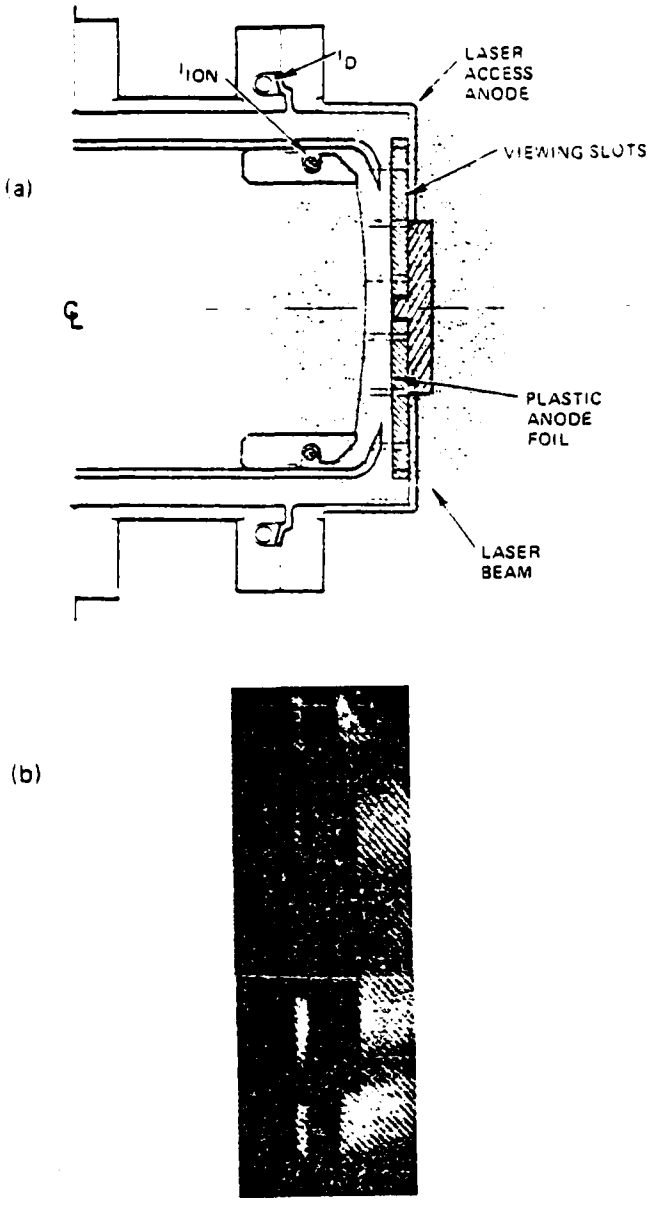

FIG. 7. (a) Ion-diode laser diagnostic detail. (b) Reconstructed holographic interferogram.

pulselength of the PITHON generator. Both planar- and spherical-section anode foils were tested. The second session utilized modified accelerator-impedance and vacuum-feed hardware. Emphasis was placed on determining the evolution of electrode plasmas in the diode, the scaling of diode parameters with cathode radius, and the consequences of diode modifications.

A. Planar diode experiments

The important scaling parameters studied in these experiments were ion efficiency, ion turn-on time, and diode-impedance lifetime. PITHON is similar to the NRL Gamble II generator in impedance (1.0 versus 1.5 Ω) and voltage risetime. These similarities sugggest that the behavior of pinch-reflex diodes would be similar on these generators. Detailed comparisons between equivalent power PITHON and Gamble II shots confirmed these similarities. The scaling variables are the 70% larger and 30% longer FWHM power pulses available on PITHON. Theoretical calculations[5] based on the generator open-circuit-voltage waveforms predicted a doubling of the Gamble II ion currents to about 1.0 MA for a pinch-reflex diode on PITHON.

A typical set of waveforms from the first experimental session (Shot 1662) is shown in Fig. 8. Peak values of the injected voltage (V_T) and current (I_0) measured at the water-vacuum interface (see Fig. 1) are 2.1 MV and 2.0 MA, respectively, at a mean impedance of 1.2 Ω. These signals indicate that a 4-TW power pulse of 88-ns FWHM containing 340 kJ was injected into the vacuum-feed structure. The injected voltage is reduced by the inductive drop in the vacuum feed to give the voltage impressed on the diode (V_D). Current loss in the vacuum feed is indicated by the difference between the interface (I_0) and diode (I_D) current waveforms. The total electron current in the system (I_E) is defined as the difference between the interface (I_0) and ion (I_{ion}) currents. With the losses in the vacuum feed, 2.7 TW and 230 kJ were coupled into the diode on this shot. The ion-beam current entering the 100-cm^2 hollow cathode (0.9 MA at 1.7 MV) begins 22–26 ns after the diode current, a delay characteristic of these PITHON experiments. This delay is associated with the establishment of the electron-pinch flow, the formation of the anode plasma, and the ion flight time in the vacuum region. The resulting peak ion power and energy are 1.6 TW and 125 kJ, respectively. These data correspond to a source-area-averaged ion current density of 9 kA/cm^2 at peak power, which is in agreement with numerical predictions.

The diode-impedance lifetime is an important consideration in scaling the ion diode toward an eventual ICF application. The velocity bunching desired for power multiplication requires carefully programmed voltage and impedance histories. The diode impedance shown in Fig. 8 reaches a plateau near 1.1 Ω for 40 ns then slowly falls until the end of the applied pulse. Accurate impedance control was provided by careful anode-cathode gap adjustment, with shot-to-shot variations of 0.2 Ω obtained throughout the experimental sessions.

The delay of 22–26 ns between the start of the ion current and the total diode current may be due to (a) the time required for the annular electron beam to sweep inward on the anode surface[24,25] to the central button, (b) inherent delay in surface flashover[26] of the anode plastic and corresponding delay in formation of the anode plasma, and (c) a small delay due to ion time-of-flight from the anode to the Rogowski coil (I_{ion}). Experimentally, this delay time did not change discernibly when the cathode area was decreased from 100 to 30 cm^2. This indicates that time delay (a) is not a major contributor to the observed delay. Since time delay (c) only amounts to 1–2 ns, it is likely that the observed delay is due primarily to a delay in surface flashover which should be independent of anode size within the shot-to-shot uncertainty of the observed delay.

The radiation diagnostics provide corroboration of the relative timing and waveshapes of the diode voltage, injected current, and ion current. The x-ray photodiode signal (PDX)

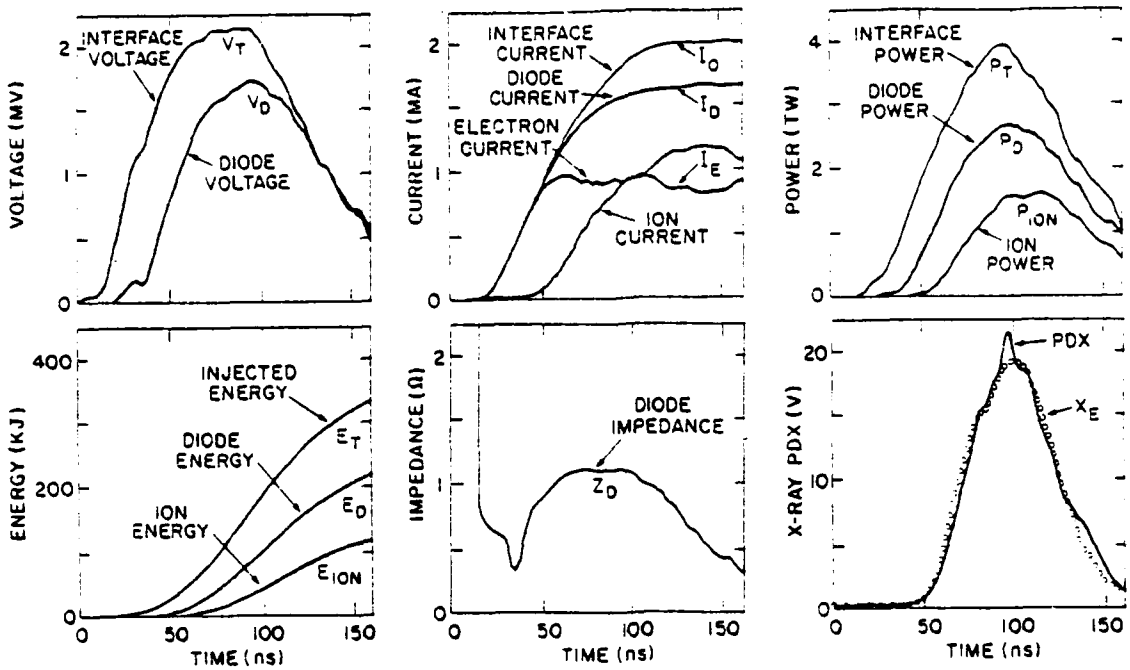

FIG. 8. Measured waveforms for Shot 1662 at 4 TW.

for Shot 1662 is compared in Fig. 8 with a calculated waveform (X_E). The theoretical scaling[27] for x-ray production from electron beams is given by $X_E = I_E(V_D)^{2.8}$, which is a sensitive measure of voltage waveshape. The calculated waveform was normalized in magnitude and shifted in time for the comparison, and the shapes of the two signals agree reasonably well. This agreement provides an independent check on how well the measured voltage and electron current pulse shapes represent the actual wave shapes at the diode. Similarly, the agreement between the measured and calculated prompt-γ nuclear radiation signals, shown in Fig. 4, indicates that the diode voltage and ion current pulse shapes are correctly timed and reasonably shaped.

The ratio of the ion current to the diode current provides a measure of the pinch-reflex-diode efficiency for ion production. At maximum power, the efficiency on Shot 1662 is 60% for an ion current of 900 kA.

Bremsstrahlung diagnostics were used to study the symmetry of power flow and current loss in the vacuum-feed and diode regions. Measurements for two different classes of shots are compared in Fig. 9. A well-centered electron pinch with strong bremsstrahlung from only the central 2 cm of the 12-cm-diam anode is observed in the x-ray pinhole photograph in Fig. 9(a). For this shot, the x-ray photodiode signal (PDX) is elevated for the entire diode pulse duration, and the energy at the vacuum interface (E_T) shows good coupling of

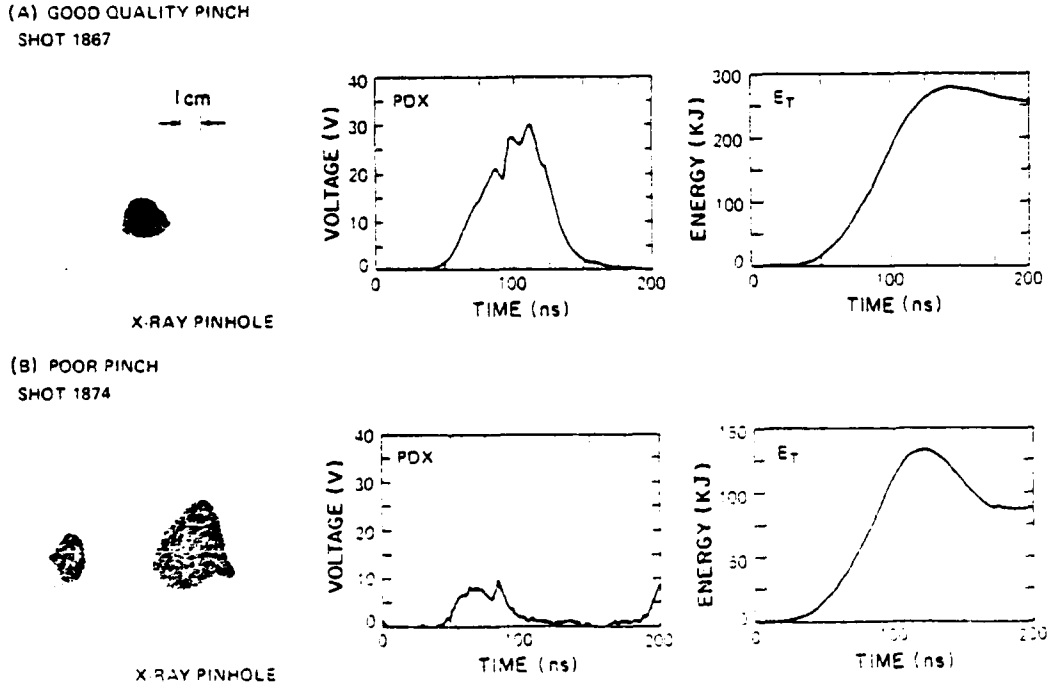

FIG. 9. Comparison of x-ray pinhole images, x-ray photodiode traces, and total energy at the vacuum interface for shots with (a) a good quality pinch and (b) a poor pinch.

the injected power to the diode. A second class of shots is shown in Fig. 9(b), where the power flow is asymmetric and the electron pinch is not well centered. The x-ray pinhole camera shows images extending onto the aluminum backing plate, and bremsstrahlung from the coax feed at 9-cm radius is also seen. More intense bremsstrahlung emission from aluminum and stainless steel, compared to carbon, allows electron losses in the vacuum feed at lower current density to be of comparable intensity to the intense central pinch on carbon. On this shot, the PDX trace is smaller in amplitude and narrower in pulsewidth, indicating a reduction in diode voltage and a short pulse duration. Also, a significant fraction of the injected energy is reflected from the load. Visual damage to the feed hardware was consistent with the origins of x rays indicated in Fig. 9 on these two shots.

The shadowbox diagnostic was used to determine the time-averaged location and size of the focus as indicated previously in Fig. 3. A calculation[11] of the location of best focus based on magnetic bending in the diode gap at peak power predicted best focus at about 18 cm from the anode foil for the voltage and current values of a typical 3-TW shot. The ballistic reconstruction shown in Fig. 3 gives a best focus at 20 cm, in good agreement with this prediction. This agreement substantiates the orbital model of focusing. Witness plate targets placed at this location showed centered front surface damage and backspalls about 1 cm in diameter (see Fig. 10).

B. Focusing diode experiments

Experiments to investigate geometric focusing of high-power ion beams from pinch-reflex ion diodes[3] were extended to higher power in these experiments on PITHON. It is important to note that the voltage, current, and impedance characteristics of the focusing diodes are essentially the same as those of the planar diodes. Ions are launched from a spherical section anode with a 12.7-cm radius of curvature and are then deflected by self B fields in traversing the anode-cathode gap. Upon exiting the cathode foil, they drift ballistically in the 1-Torr gas to a focus at about 8 cm from the anode foil, well inside the geometric focus at the center of the sphere. The shadowbox analysis for a focusing diode (see Fig. 11) indicates that the focus is confined within a 3-cm-diam circle, corresponding to an areal beam reduction from the anode source of a factor of 14. An estimate of the focused current density can be made by assuming that the total measured ion current is uniformly distributed over this circle of least confusion. This yields an ion current density of 150 kA/cm^2 over the 7-cm^2 spot, while peak-focused current densities could be substantially larger. Witness-plate targets of 6.4-mm-thick aluminum (6061-T6) located at the focus exhibit multiple-layered backspalls. This behavior is expected for the high current densities found in these focusing geometry shots.

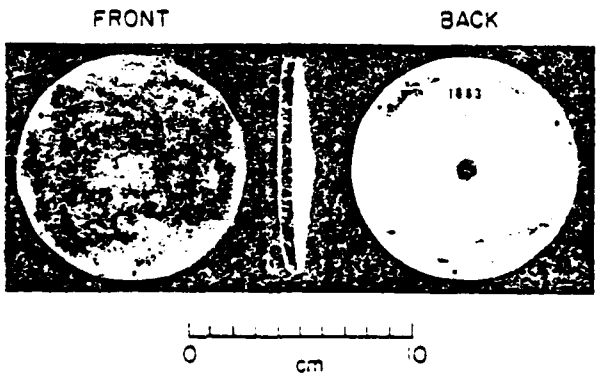

FIG. 10. Witness plate damage on Shot 1663 for a 6.4-mm-thick aluminum (6061-T6) plate located at the approximate proton self-focus of a planar pinch-reflex diode.

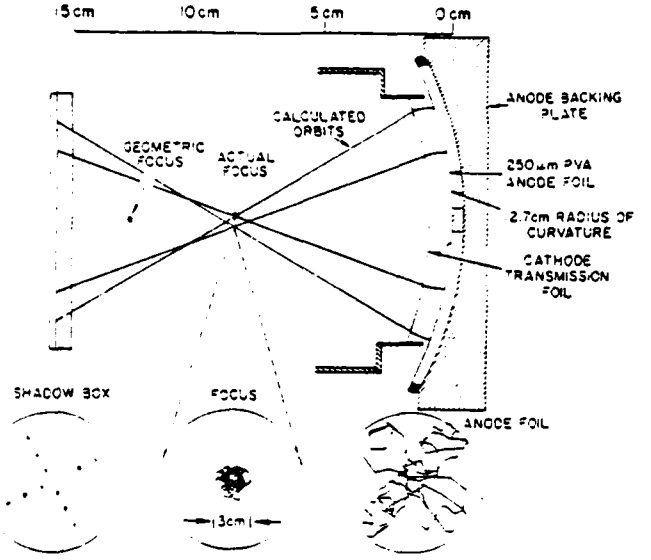

FIG. 11. Shadowbox geometry for a focusing pinch-reflex diode and reconstruction of ion trajectories for Shot 1683.

C. Results from neutron measurements

For both the planar and focusing diode experiments, the measured neutron yields are about 1/3 of yields calculated using the measured ion current and diode voltage corrected for energy loss in the Kimfol. For the planar-diode geometry, the calculated yields are based on the combined thick-target yields for the D(d,n)^{3}He and ^{12}C(d,n)^{13}N reactions at 175° as shown in Fig. 5. For the focusing diode geometry, a broad range of neutron-emission angles (140–180°) exists due to the angular spread of the deuterons incident on the CD_2 target. In this case, the calculated yield is based on thick-target yields at different angles weighted by a radial ion-current-density profile on the anode ($j_i \sim 1/r$) determined from numerical simulations.[14] The difference between the measured and calculated neutron yields may be attributed to several factors: (1) The measured ion current may include significant proton or carbon-ion components which contribute little to the neutron output; (2) ion energy losses, which may occur in the region between the anode and the CD_2 target,[28] have not been taken into account in the neutron-yield calculations; and (3) enhanced deuteron stopping[29] in the hot dense plasma target leads to a reduced neutron output. A quantitative assessment of the importance of these factors in the present experiments is in progress.

The largest neutron yield at 175° was obtained with the planar-diode geometry because the *d-d* neutron yield[17] peaks at 180°. For this diode, neutron yields of up to 4.5×10^{11}/sr were measured. At the diode voltage of 1.7 MeV corresponding to this yield, approximately 50% of these neutrons are from the D(*d*,*n*) reaction (see Fig. 5). The corresponding total neutron yield into 4π sr, corrected for the anisotropy of neutron emission, is 3.7×10^{12} with 50% from the D(*d*,*n*) reaction.

Time-integrated neutron yields were used with the focusing diode geometry to determine the deuteron current density at focus by comparing neutron yields from different area CD_2 targets. For this purpose, the measured neutron output was scaled to the current measured by the ion Rogowski coil. The fraction of deuterons incident on targets as small as 0.75 cm^2 was determined by comparing that neutron yield with the yield measured on 100-cm^2-area targets. On the 0.75-cm^2-area target, the neutron yield was still about 50% greater than that observed without any CD_2 target. To correct for variations in neutron output in these measurements due to shot-to-shot variations in voltage and current, the measured yields were scaled to yields calculated from the measured diode voltages and ion currents. A deuteron current density of 150 kA/cm^2 at peak ion voltage was determined from these measurements. If the ion current is only 1/2 to 1/3 deuterons, as suggested by comparisons between measured and calculated neutron yields, then the total ion current density may be 2 to 3 times larger than this value.

D. Power flow studies

Power dissipation between the PITHON vacuum interface and the pinch-reflex diode occurred in the magnetically insulated biconic line, where some electrons flow across the feed to the anode at large radius before entering the diode. To inhibit electron leakage, the vacuum biconic and coax sections were designed with a characteristic impedance, gradually decreasing to a value several times larger than the ion-diode impedance. A parapotential (Brillouin) flow analysis[30] predicted that the entire electromagnetic-wave energy would be transported as conduction current in the electrodes without vacuum electron flow. This analysis, which was consistent with earlier pinched-electron-beam experiments,[25] was found to be inadequate for larger inductance and higher initial-impedance electron-diode experiments[31] and these ion-diode experiments.

The character of the current loss is seen in Fig. 8. The injected current (I_0) typically separates from the diode current (I_D) when the voltage on the feed exceeds the field-emission threshold. A number of polishing, cleaning, and coating techniques were tried with little improvement in the power flow to the diode. The fraction of current coupled into the diode decreased as the coax section was lengthened to allow access for laser diagnostics.

In experiments with the lengthened coaxial feed, the injected and coupled currents separate immediately as shown in Fig. 12(a). Several vacuum feed modifications were studied to improve power flow to the diode with this coaxial

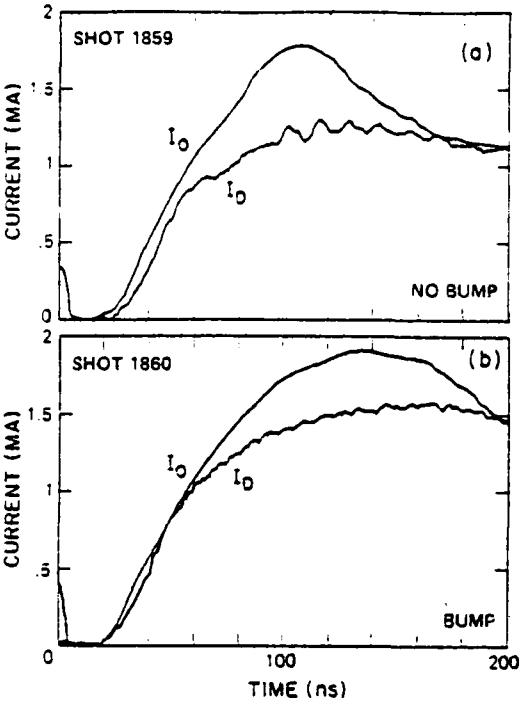

FIG. 12. Comparison of the injected current and diode current (a) on a shot without the bump (No. 1859) and (b) a shot with the bump (No. 1860). Without the bump, the current loss in the vacuum feed is larger.

feed. These include a "bump" behind the anode foil, a smooth conductive covering of the radial-line anode discontinuities, a smooth shorting of the diode current monitor, and an extension to enhance the cathode tip. The "bump" is a grounded aluminum annulus typically 1-cm wide mounted behind the plastic anode foil on the backing plate opposite the cathode tip (see Fig. 2). Its purpose is to lower the early-time pinched-electron-beam diode impedance (before the anode foil becomes conducting) and trap the vacuum flow of electrons emitted in the feed. A sequence of shots taken without the bump, ranging from 2 to 3.5 TW, all showed an early-time current loss between injected (I_0) and diode (I_D) current monitors [see Fig. 12(a)]. Shots with a smoothly curved cathode, as in Fig. 7, produced poor pinches without the bump. Shots taken with a bump did not show the early-time current loss [see Fig. 12(b)]. All low-power (<4 TW) shots taken with the large-area (100 cm^2) cathode and the bump produced excellent pinches.

At the 4.5-TW level, the bump was not sufficient to ensure good electron pinching. Smoothly covering the anode discontinuities in the radial and coax feeds (bypassing I_D) produced better pinches and larger PDX signals of longer duration. No shots without this modification produced good pinches at higher power, while 80% of the shots with the anode discontinuities covered were of high quality.

Comparisons were made between a cathode shank which changed abruptly from the coax vacuum feed to an extended enhanced cathode tip and a smoothly tapered non-enhanced cathode. Early-time current losses were observed with the enhanced tip, but deviations between injected and coupled currents were less than with the tapered cathode. One shot was performed at 5-TW matched-load power to

evaluate the effect of cathode-tip enhancement on power flow: A 1-cm-long, 5-mm-wide enhanced lip was welded to the hollow tapered cathode, a standard bump was employed, and the diode-current monitor was engaged. Power loss in the vacuum feed was observed, but the pinch was quite good, indicating that this configuration compensates at least in part for the anode-discontinuity effect at high power.

Observations from this study indicate that the geometric transition from radial to coax feed is more important to good power flow than a variation of the characteristic impedance. Further, the electrode surfaces are not important, but a well-designed cathode-emission tip and a small diode impedance early in the pulse are essential for good power coupling from the generator to the diode.

E. Small-area diodes

A modification to the diode design was tested to evaluate the performance of smaller-radius diodes with larger ion-current source densities. The hollow-tapered cathode, shown in Fig. 1, was reconfigured with a reduced radius. Shots were taken with 30-cm^2 areas and compared to shots with 100 cm^2, reported above.

Several small-area cathode shots were taken at anode-cathode gaps of 2.6 to 5.6 mm. Shots with small anode-cathode gaps shorted early in the pulse, while the power was dissipated in the lower-impedance vacuum feed for shots with larger gaps. An intermediate gap of 3.5 mm gave efficient coupling of the injected energy into the diode. In this case, the diode-impedance history was 1.4 Ω for 50 ns before collapsing (see Fig. 13). The ion current density averaged over the source area was 20 kA/cm^2 at peak power. The onset time of the ion current for this small-area diode was slightly earlier than for the large-area diode as indicated in Sec. IV A.

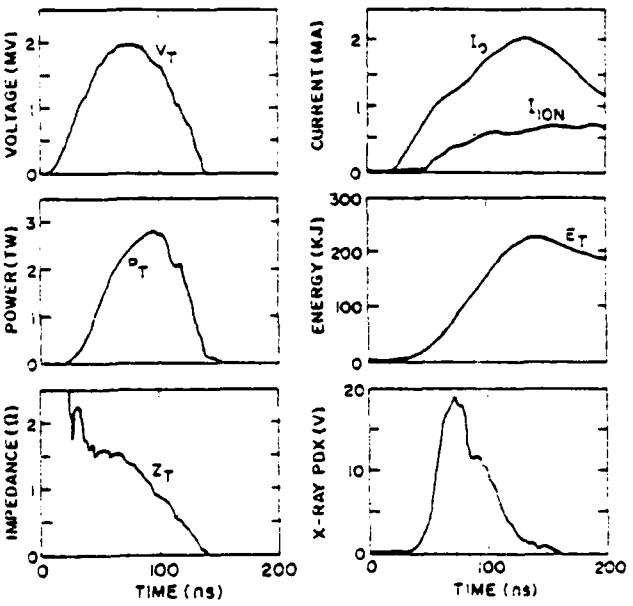

FIG. 13. Measured waveforms for a 3-TW, 30-cm^2-area pinch-reflex diode shot (No. 1884).

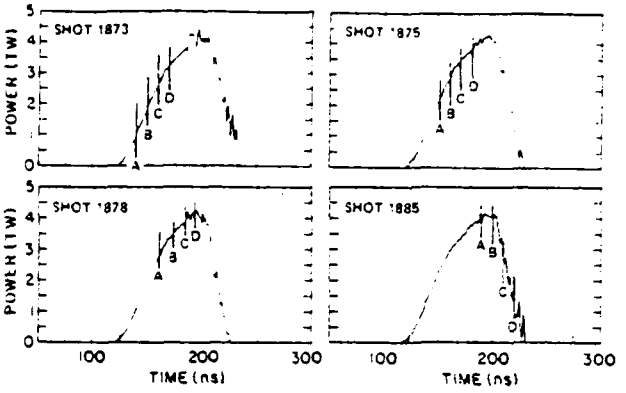

FIG. 14. Timing of the laser-interferometer exposures relative to the power pulse on four different pinch-reflex diode shots. The vertical lines labeled A, B, C, and D indicate the times at which the exposures are recorded on each shot.

F. Interferometric holography

Plasma evolution in the pinch-reflex diode was investigated with the interferometric-holography system. Exposures were made through slots cut in the current-return housing of the anode [Fig. 7(a)] to allow a side view of the cathode and anode. The left side of each rectangular slot is defined by the cathode tip and the right side by the anode foil.

Four-frame holographic measurements were made on the 100-cm^2 diode on four shots to observe plasma motion in the anode-cathode gap throughout the power pulse. The timing of the laser-pulse exposures on these shots is shown in Fig. 14. A tracing of each of the 16 holograms obtained on these shots shows the contour corresponding to a line density of 3.2×10^{17}/cm^2, or one fringe shift. These tracings are shown in Fig. 15. The accuracy of the contour location is estimated to be ± 0.5 mm of the 3.5-mm anode-cathode gap. Contours for larger fringe shifts were difficult to obtain in most cases due to large density gradients behind the plasma front.

The single-fringe-shift reconstructions in Fig. 15 demonstrate that the plasma fronts expanding from the anode foil and cathode tip are fairly uniform with gentle surface fluctuations and are not, in general, cylindrically symmetric. The absence of sharp plasma protrusions is encouraging, although a smoother and more symmetric plasma surface is required to produce high-focus-quality ion beams. The important points to notice are that the plasmas expand from the boundary surfaces as the power pulse approaches its peak, that they are uniform and approach one another with velocities which increase in time, and that the anode velocity on the axis of symmetry appears greater than at larger radii. The observation of an axial plasma plume from the anode can be explained by a time-dependent calculation of magnetic-field penetration into the resistive anode plasma. This calculation[12] predicts a buildup of magnetic pressure behind the plasma front preferentially toward the axis, driving a central plume toward the cathode.

The contours for Shot 1885 [Fig. 15(d)] show the electrode plasma behavior during power collapse. A dramatic

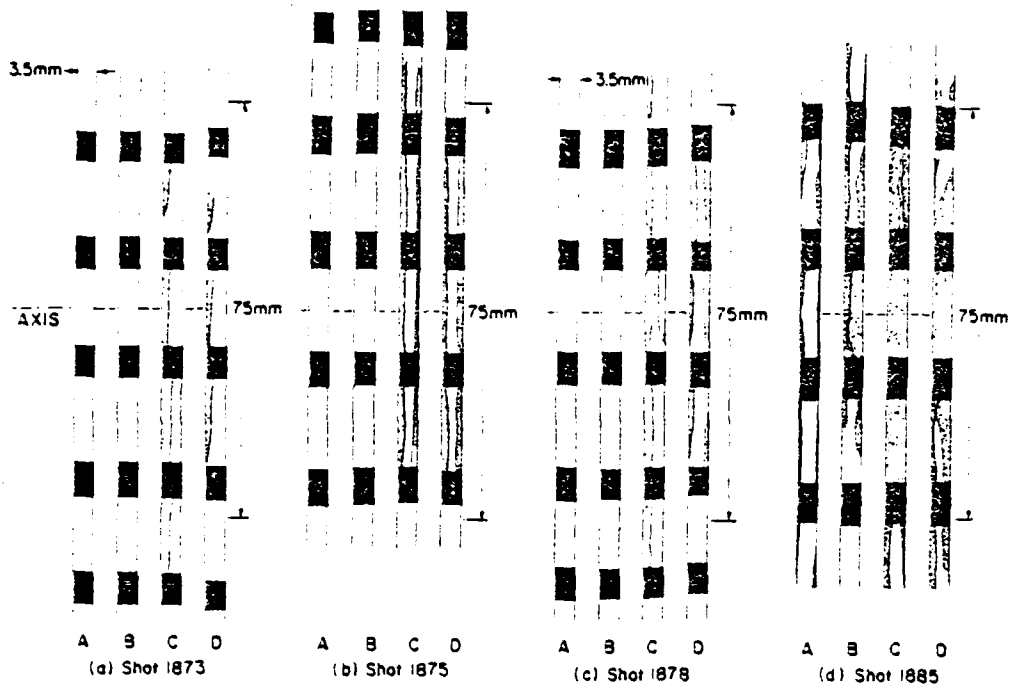

FIG. 15. Single-fringe-shift reconstructions corresponding to the holograms measured on (a) Shot 1873, (b) Shot 1875, (c) Shot 1878, and (d) Shot 1885. The shaded regions indicate plasma line densities greater than $3.2\times10^{17}/\mathrm{cm}^3$.

change was observed between the first (A) and second (B) frames, both of which were taken near peak power. The plasma closure velocity is measured to be 27 cm/μs on axis. Off axis at a radius of 3 cm, the velocity is 7 cm/μs between frames A and B and 10 cm/μs between frames B and C. The line density at a fixed position off axis is seen to decrease in the last frame (D), allowing light to again pass through holes that were formerly opaque. This phenomenon may be due to compression of the anode plasma by magnetic pressure as the diode current grows and the plasma density decreases. Alternatively, the anode and cathode plasmas may never have met in the earlier frames, and the opacity observed may have been caused by surface fluctuations or ripples that blocked the laser line-of-sight.

The plausibility of the magnetic-pressure mechanism can be determined by calculating the time required for the plasma pressure to be overcome by the rising magnetic pressure in the diode gap. Energy is deposited in the anode plasma continuously throughout the pulse by electron deposition and Ohmic heating, thereby increasing the particle kinetic energy. Early in the pulse, the current (and hence magnetic field) is low so that $nkT \gg B^2/2\mu$. As the current increases, the magnetic pressure increases relative to the thermal pressure. Approximate parameters for the diode at the time of the last frame (D) are: 2 MA flowing within a 3-cm radius, a plasma density of about $10^{18}/\mathrm{cm}^3$ of CH_2 components, and a temperature of 5 eV. The magnetic pressure for these values is 67 MPa while the thermal pressure is only 0.75 MPa, so that late in time the electrode plasmas may be compressed by the magnetic field. These figures yield an acceleration of 120 cm/μs^2 and a time of 16 ns for the anode and cathode plasmas to each move 1.5 mm. This value is comparable to the observed plasma motion across the diode.

V. SUMMARY OF RESULTS

In this paper, we have presented recent technological advances in the development of intense pulsed ion beams. The pinch-reflex diode has been successfully scaled up to multiterawatt operation on the PITHON accelerator. Intense proton and deuteron beams have been produced in both planar and spherically focusing geometries with 1.0 MA of 1.8-MeV protons measured (for a peak power of 1.8 TW) yielding a 130-kJ light ion beam in 100 ns.

Focusing of these ion beams by electrode shaping and by self-magnetic field deflection has been shown to follow simple theoretical modeling with several corroborating diagnostics. Spherical-electrode shaping served to compress the ion beam from an 11-cm-diam anode surface to a 3-cm-diam focus located inside the geometric focus by an amount consistent with magnetic bending in the diode gap. Tests of small-area diodes at lower power (< 4 TW) demonstrate that impedance lifetime will not limit the total energy from the diode at a factor-of-3 higher source-current density. Further, these results suggest that a smaller-area pinch-reflex diode of higher power density may be suitable for injection into a plasma transport channel.

The most serious problem encountered in these experiments was independent of the pinch-reflex diode but concerned the coupling of power from the accelerator interface through the vacuum-feed structure to the diode. These losses were found to be geometric, that is, independent of electrode surface, and occurred principally between the biconic-to-coax transition and the diode. Reducing the early-time diode impedance, smoothing the vacuum feed of resonant grooves, and enhancing the cathode-emission tip all served to increase the power flow to the diode.

Beam diagnostics were developed to survive the harsh bremsstrahlung and impulse environment of a 3-TW pinch-reflex diode. Measurements of nuclear-reaction products provided total ion yields and pulse-shape evaluations. Total-beam Rogowski-coil monitors were developed and performed through the time of peak power. The shadowbox technique provided the location and size of the beam focus.

A first study of the spatial evolution of the anode and cathode plasmas was performed on a number of shots spanning the power pulse for a 3-TW pinch-reflex diode. The plasmas are observed to expand from the electrodes before peak power in uniform, though nonsymmetric, profiles and accelerate toward one another. After peak power, anode-plasma surface fluctuations and increased velocities up to 30 cm/μs in axial anode plumes were observed. During the power-pulse collapse, a high-density ($n_e > 10^{18}/cm^3$) plasma bridges the anode-cathode gap over the central 7.5-cm diameter of a 12-cm-diam diode. On some shots, this high-density plasma is observed to be compressed late in the pulse, suggesting magnetic confinement. Knowledge of the shapes of the anode and cathode plasmas at peak power suggests that further research into the formation of more uniform plasmas is necessary to develop more highly focused ion diodes. The measured evolution of the shapes of the anode and cathode plasmas is the information required to design a first-iteration modification to the simple spherically focusing anode.

[1]See for example: G. Yonas, 4th ANS Topical Meeting on Technology of Controlled Nuclear Fusion 1980, Valley Forge, Pennsylvania, Oct. 14–17, 1980; S. Humphries, Jr., Nucl. Fusion 20, 1549 (1980).

[2]G. Cooperstein, S. A. Goldstein, R. A. Meger, D. Mosher, W. F. Oliphant, F. L. Sandel, S. J. Stephanakis, F. C. Young, and H. V. Karow, *Proceedings of the 4th International Topical Conference on High-Power Electron and Ion-Beam Research and Technology*, edited by H. J. Doucet and J. M. Buzzi (Ecole Polytechnique, Palaiseau, France, 1981), p. 53.

[3]V. M. Bystritsky and A. N. Didenko, Uspekhi Fizicheskikh Nauk 132, 91 (1980).

[4]P. F. Ottinger, D. Mosher, and S. A. Goldstein, Phys. Fluids 23, 909 (1980); L. G. Wiley, P. L. Dreike, and D. A. Hammer, LPS 259, Cornell University, Ithaca, October, 1978 (unpublished).

[5]S. A. Goldstein, G. Cooperstein, Roswell Lee, D. Mosher, and S. J. Stephanakis, Phys. Rev. Lett. 40, 1504 (1978).

[6]S. Humphries, Jr., J. Appl. Phys. 51, 1876 (1980).

[7]J. Maenchen, L. Wiley, S. Humphries Jr., E. Peieg, R. N. Sudan, and D. A. Hammer, Phys. Fluids 22, 555 (1979); R. A. Meger, S. A. Goldstein, P. F. Ottinger, D. Mosher, S. J. Stephanakis, and F. C. Young, Bull. Am. Phys. Soc. 26, 921 (1981).

[8]D. Mosher, G. Cooperstein, S. J. Stephanakis, S. A. Goldstein, D. G. Colombant, and Roswell Lee, Report No. 3658, Naval Research Laboratory, 1977.

[9]G. Frazier, in *Proceedings of the NSWC Pulse Power Systems Workshop* (Cornell University, Ithaca, Sept. 1976).

[10]D. Mosher, D. G. Colombant, S. A. Goldstein, and P. F. Ottinger, in *Proceedings of the 4th International Topical Conference on High-Power Electron and Ion-Beam Research and Technology*, edited by H. J. Doucet and J. M. Buzzi (Ecole Polytechnique, Palaiseau, France, 1981), p. 19; also D. Mosher, D. G. Colombant, and S. A. Goldstein, Comments Plasma Phys. 6, 101 (1981).

[11]D. Mosher, Bull. Am. Phys. Soc. 25, 900 (1980).

[12]D. G. Pellinen, Marco S. DiCapua, S. E. Sampayan, H. Gerdracht, and M. Wang, Rev. Sci. Instrum. 51, 1535 (1980).

[13]Available from Kimberly Clark Corp., Lee, MA 01238.

[14]A. Drobot, Roswell Lee, S. A. Goldstein, and G. Cooperstein, 1979 IEEE International Conference on Plasma Science, Montreal, Canada, June 4–6, 1979; Record of Conference Abstracts, IEEE Cat. No. 79CH1410-0, p. 78.

[15]F. C. Young, W. F. Oliphant, S. J. Stephanakis, and A. R. Knudson, IEEE Trans. Plasma Sci. PS-9, 24 (1981).

[16]F. C. Young, IEEE Trans. Nucl. Sci. NS-22, 718 (1975).

[17]H. Liskien and A. Paulsen, Nucl. Data Tables 11, 569 (1973).

[18]H. W. Lefevre, C. A. Burke, and R. M. Bahnsen, Report No. RLO-1925-44, University of Oregon, 1971.

[19]H. H. Andersen and J. F. Ziegler, *Stopping Powers and Ranges in all Elements* (Pergamon, New York, 1977), Vol. 3.

[20]J. G. Pronko, T. R. Fisher, and L. F. Chase, Nucl. Instrum. Methods 163, 227 (1979).

[21]F. C. Young, D. Mosher, S. J. Stephanakis, S. A. Goldstein, and D. Hinshelwood, Memorandum Report No. 3823, Naval Research Laboratory, 1978.

[22]K. Triebes and R. Huff, Bull. Am. Phys. Soc. 19, 976 (1974).

[23]D. Mosher, G. Cooperstein, and S. A. Goldstein, Technical Digest of Conference on Inertial Confinement Fusion, San Diego, California, February 26–28, 1980, IEEE No. 80CH1536-2 QEA, p. 104.

[24]A. E. Blaugrund, G. Cooperstein, and S. A. Goldstein in Proceedings of the International Topical Conference on Electron Beam Research and Technology, SAND76-5122, Albuquerque, New Mexico, Feb., 1976, Vol. I, p. 233.

[25]R. D. Genuario and V. L. Bailey, Appl. Phys. Lett. 33, 694 (1978).

[26]J. C. Martin "Nanosecond Pulse Techniques," SSWA/JCM/704/49, Internal Report, AWRE, Aldermaston, England, 1970.

[27]H. W. Koch and J. W. Motz, Rev. Mod. Phys. 31, 4 (1959).

[28]F. C. Young, S. J. Stephanakis, G. Cooperstein, D. Mosher, F. L. Sandel, P. G. Blauner, and S. A. Goldstein, Memorandum Report No. 4322, Naval Research Laboratory, 1980.

[29]F. C. Young, D. Mosher, S. J. Stephanakis, S. A. Goldstein, and T. H. Mehlhorn, Phys. Rev. Lett. 49, 549 (1982).

[30]J. Creedon, J. Appl. Phys. 48, 2946 (1975).

[31]J. Maenchen, R. D. Genuario, D. Dakin, R. Stringfield, and J. Case, Physics International Report PIIR-9-80, 1980.

[32]D. Colombant and S. A. Goldstein, 1982 IEEE International Conference on Plasma Science, Ottawa, Canada, May 17–19, 1982; Record of Conference Abstracts, IEEE Cat. No. 82CH1770-7, p. 31.

THERMAL-RESISTIVE CURRENT FILAMENTATION IN THE CATHODE PLASMA OF A PINCH-REFLEX DIODE

V. K. Tripathi
Laboratory for Plasma and Fusion Energy Studies
University of Maryland
College Park, Maryland 20742

and

P. F. Ottinger and J. Guillory*
Jaycor, Inc.
205 Whiting St.
Alexandria, Va. 22304

Abstract

Electron current flow drawn off a hollow cylindrical cathode in a pinch-reflex ion diode is observed to have a filamentary structure. Such filamentation can lead to nonuniform anode turn-on and ion emission. Consequently, ion beam brightness is degraded. In this context a purely growing thermal-resistive instability in the cathode plasma is examined. The instability causes current filamentation and grows on a time scale comparable to the electron-ion energy equilibration time. Electron inelastic collisions have a stabilizing influence on the instability.

I. Introduction

In the past few years there has been a great deal of interest in using light-ions for an inertial confinement fusion scheme (ICF).[1] Intense ion beams in the parameter regime required for a modular light-ion ICF device have been generated using the pinch reflex diode (PRD) at the Naval Research Laboratory.[2] The number of modules in such a system can be reduced to less than ten if beams with high brightness can be extracted from such diodes.[3] Beam brightness is most conveniently defined as $J_b/\delta\theta^2$ where J_b is the ion beam current density and $\delta\theta$ is the angular divergence of the beam. Experimentally it has been observed that the ion beam is composed of many beamlets (typically 10-20) and that this filamentation is related to ion beam brightness degradation.[4] It has also been observed that the electron current flow drawn off the hollow cathode in the PRD is filamented. This electron beam filamentation can lead to nonuniform anode turn-on and/or emission possibly causing the filamentary ion beam structure. Electromagnetic field fluctuations due to the electron beam filaments will also enhance the angular divergence of the ion beam and hence decrease beam brightness. In addition, electron beam filamentation is suspected to play an important role in premature gap closure and subsequent impedance collapse in the PRD. In this paper the stability of current flow in the cathode plasma to a transverse temperature perturbation is examined and its relevance to observed current filamentation is discussed.

In order to understand this mechanism, the make-up of the cathode plasma must be understood. The cathode is usually sprayed with Aerodag (Acheson Colloids Co.) which produces a thin layer of micron size

graphite particles on the cathode surface. When the voltage is applied, protrusions from this layer cause local field enhancement and large currents are drawn out of the protrusions by field emission.[5] These protrusions and the surrounding surface through which the current is fed into the protrusions are ohmically heated and are quickly vaporized and subsequently ionized.[6] Within a few nanoseconds a carbon plasma fills in over the cathode surface reaching an equilibrium ion density typically in the 10^{16}-10^{18} cm^{-3} range.[7] The charge state of the plasma will increase in time and will depend on the rising plasma temperature. As the electron current continues to be drawn off the cathode plasma surface, the plasma continues to be heated and eventually expands into the diode gap. Here the concern is with the stability of the current flow in this cathode plasma.

Perturbations in the current flowing in the cathode plasma can be unstable. Because the plasma resistivity decreases with increasing temperature, more current will tend to flow where the temperature is higher. In turn, the higher current will ohmically heat the plasma to even higher temperatures, leading to a thermal-resistive instability. This assumes that the instability grows faster than the thermal conduction time so that local temperature perturbations can be maintained during the growth of the mode. It also assumes that the electron energy loss due to inelastic collisions of electrons with neutrals is less important than that due to coulomb collisons. If these current perturbations grow to significant levels in the cathode plasma, $\underline{j} \times \underline{B}$ pinching of the plasma can cause plasma jetting into the diode gap. Electron emission from these locations would then be higher because of the smaller effective diode gap, thus resulting in filamented electron flow in the

diode vacuum gap. This paper will only deal with the linear stability analysis of the current carrying cathode plasma. The details of the plasma jetting which subsequently develops will be left for a future paper.

Because of the high particle density and low initial temperature of the cathode plasma, the plasma is highly collisional. In this case the thermal-resistive instability mechanism dominates over other current filamentation mechanisms such as the $\vec{V} \times \vec{B}$ pinching forces which drive the filamentation instability in a cold collisionless plasma.[8] A similar mechanism for driving a thermal instability in a laser produced plasma has been documented;[9] however, it is dominated in most laser produced plasmas by another magnetic field-generating thermal instability driven by strong density and temperature gradients.[10] Such an instability exists whenever the equilibrium density and temperature gradients are parallel. A temperature perturbation perpendicular to the density gradient produces a perturbed magnetic field which, in turn, enhances the temperature perturbation through the magnetic field dependence of the thermal conductivity tensor. The growth rate of this instability scales like the electron temperature to the 5/2 power, so that a high electron temperature is required for fast growth ($T_e \gtrsim 1$ keV for a typical laser plasma). For the present cathode plasma problem the electron temperature is initially low ($T_e \sim 2$ eV) so that early in the pulse such a mechanism is unimportant. Another suggested mechanism for filamentation of cathode plasmas, involving an incompressible MHD fluid tearing instability,[10] seems unlikely in this case because the typical growth rate of $\sim 10^7 \text{sec}^{-1}$ derived for the mode is too slow.

In Sec. II of this paper a detailed description of the cathode

plasma equilibrium state will be presented. The linear stability of this equilibrium will be analyzed in Sec. III with the results showing that the system is unstable to current perturbations. The growth rate and typical wavenumber for this thermal-resistive mode will be derived and compared with typical experimental results. Finally, the results of this work and the conclusions which can be drawn from them are summarized in Sec. IV.

II. Equilibrium

The plasma formed at the tip of the cathode in a pinch reflex diode is like a thin cylindrical ring with an initial axial thickness of less than a millimeter, a width, Δr_o, of a few millimeters and a radius, r_o, of 3 cm. After a few nanoseconds into the voltage pulse it is assumed that this plasma has uniformly filled in over the cathode surface and that the plasma has an ion density $n_o \sim 10^{16}$-$10^{18} cm^{-3}$ and an electron temperature $T_{eo} \sim$ 1-10 eV. A uniform axial current flows through the plasma whose value is assumed to be $\lesssim$ 0.5 MA. The uniform current produces a self-magnetic field which for the diode parameters specified gives a peak value of $B_\theta \lesssim$ 30 KG which corresponds to an electron cyclotron frequency of $\omega_c = 5 \times 10^{11} sec^{-1}$. Since this is smaller than the electron-ion collision frequency, ν_o, and much smaller than the electron plasma frequency ω_{pe} ($\omega_{pe} >> \nu_o > \omega_{ce}$), effects of this static B_θ field will not be important and will not be included in the analysis. A sheath is also produced at the boundary of the plasma where electrons are drawn off into the diode vacuum region. These electrons form the diode electron beam. A large fraction of the electrons which enter the sheath, however, will be reflected off the sheath and returned to the plasma. Since the electron mean free path is very small (a few microns) this return current will diffuse before penetrating any great distance back into the dense cathode plasma and hence can also be ignored.

In equilibrium an axial electric field $\vec{E}_o \| \hat{z}$, is present with electrons moving at an average drift velocity $\vec{v}_o$ ($= -\vec{J}_o/n_o eZ$), which is related to E_o through the relation

$$\vec{v}_o = -e\vec{E}_o/m_e\nu_o . \qquad (1)$$

Here $-e$ and m_e are the electronic charge and mass and $\nu_o = 2.9 \times 10^{-6} Z^2 n_o \lambda_{ei}/\theta_{eo}^{3/2}$ with Zn_o being the electron density, λ_{ei} the Coulomb logarithm and θ_{eo} the equilibrium electron temperature in eV. The charge state, Z, will be related to the time history of the density and temperature. In writing Eq. (1) the effects of electron inelastic collisions on momentum transfer has been ignored. The electrons gain thermal energy from the field through ohmic heating at a rate of $-e\vec{E}_o \cdot \vec{v}_o$. In the steady state this is balanced by the loss of energy through collisions with ions, thermal conduction, and inelastic collisions, so that

$$\vec{J}_o \cdot \vec{E}_o/n_o Z = \frac{3}{2}\,\delta\nu_o(T_{eo} - T_{io}) + P/n_o Z + (\chi/Zn_o)\nabla^2 T_{eo} . \qquad (2)$$

In Eq. (2) m_i is the ion mass, $\chi = 3.16\, Zn_o T_{eo}/\nu_o m_e$ is the electron thermal conductivity, T_{eo} is the equilibrium electron temperature, T_{io} is the ion temperature, and $P/n_o Z$ is the energy lost to inelastic collisions in ergs/sec, and is described in more detail in the following paragraph. Here also $\delta = 2\, m_e/m_i$ is the usual mean fraction of electron energy lost in an elastic collision derived from averaging over our ensemble of fast test particles and a Maxwellian field particle distribution.[12]

For the present problem the rate of loss of energy due to thermal conduction is much smaller than the other loss mechanisms for scalelengths greater than 0.01 cm at $n_o \sim 10^{17}$. This claim is justified a posteriori in Eq. (12) where it is found that the wavelength characteristic of maximum growth is much longer than this scalelength.

Equation (2) can then be rewritten as

$$m_e v_o^2 = \frac{3}{2} \delta (T_{eo} - T_{io}) + P/n_o Z \nu_o . \quad (3)$$

For $n_o < 10^{16} cm^{-3}$ the simple corona model is suitable, however, the present analysis applies to a higher density regime. For this regime of $n_o > 10^{16} cm^{-3}$ a collisional radiative equilibrium model is appropriate.[13] Figure (1) shows $P/n_o^2 Z$ as a function of T_r, the ionization temperature for various ion densities. The charge state, $Z(T_r)$, as predicted by this model is shown in Fig. (2) for various densities. With the information displayed in Figs. (1) and (2), Eq. (3) can be used to solve the equilibrium temperature for a given n_o and v_o. This also assumes radiative equilibrium has been reached. If there is not sufficient time to reach radiative equilibrium, an equivalent ionization temperature can be obtained for any assumed Z from Fig. (2). Then Fig. (1) can be used to find P for this equivalent ionization temperature and finally Eq. (3) can be solved for T_{eo}. In all cases the ion temperature T_{io} will be assumed to be on the order of 1 eV.

The early time properties of the plasma are not well understood, however, as the plasma expands and the density decreases the ionization state becomes frozen in with Z most likely between 1 and 4. The current driven in the plasma continues to heat the electrons but the ionization temperature remains at a value determined by the initial plasma formation processes. For $Z > 1$ and $n_o < 10^{19} cm^{-3}$ the ionization temperature only responds on a timescale much slower than an e-folding time for the thermal resistive instability derived in the following sections.

III. Instability Analysis

It is assumed that perturbed quantities vary like $\exp[-i(\omega t-\vec{k}\cdot\vec{x})]$ where $\vec{k}$ has finite θ and z components. Because $\Delta r_o \ll r_o$, a slab model can be used to simplify the analysis. The x direction in this slab model corresponds to the θ direction and k_z is included to model the finite thickness of the plasma. Linearized fluid equations for the response of electrons are

$$\frac{\partial n}{\partial t} + \vec{\nabla}\cdot(Zn_o\vec{v}_e + n\vec{v}_o) = 0 \ , \tag{4}$$

$$\frac{\partial \vec{v}_e}{\partial t} + \vec{v}_o\cdot\vec{\nabla}\vec{v}_e = -\frac{e\vec{E}}{m_e} - \frac{e}{m_e c}(\vec{v}_o \times \vec{B}) - \nu_o(\vec{v}_e-\vec{v}_i)$$

$$- T\vec{v}_o \frac{\partial \nu_o}{\partial T_{eo}} - n\vec{v}_o \frac{\partial \nu_o}{\partial (n_o Z)} \ , \tag{5}$$

$$\frac{3}{2}\frac{\partial T}{\partial t} + \frac{3}{2}\vec{v}_o\cdot\vec{\nabla}T + T_{eo}\vec{\nabla}\cdot\vec{v}_e = -e(\vec{E}_o\cdot\vec{v}_e + \vec{E}\cdot\vec{v}_o)$$

$$- \frac{3}{2}\delta\nu_o T - \frac{3}{2}\delta(T_{eo}-T_{io})\left(\frac{\partial \nu_o}{\partial T_{eo}} T + \frac{\partial \nu_o}{\partial (n_o Z)} n\right)$$

$$- \frac{\partial}{\partial T_{eo}}\left(\frac{P}{n_o Z}\right) T - \frac{\partial}{\partial (n_o Z)}\left(\frac{P}{n_o Z}\right) n \ , \tag{6}$$

where n, $\vec{v}_e$, and T represent the electron density, velocity, and temperature perturbations, $\vec{v}_i$ is the perturbation in ion velocity and $\vec{E}$ and $\vec{B}$ represent the electric and magnetic field perturbations. Faraday's law relates $\vec{B}$ to $\vec{E}$ through $\vec{B} = c\vec{k} \times \vec{E}/\omega$. The pressure term in the equation of motion is not included since $k^2 v_{te}^2/\omega\nu_o \ll 1$. The second and fourth terms on the right-hand side of Eq. (5) drive, respectively, the

conventional Weibel instability and the thermal-resistive instability. The Weibel instability of electrons drifting through a stationary ion background possesses a growth rate of $\gamma \lesssim \omega_{pi} v_o/c$ (ω_{pi} being the ion plasma frequency) which is quite small; hence, the analysis will concentrate on the thermal resistive instability.

Solving Eqs. (4)-(6) one obtains the following expression for the current density

$$\vec{J} = - Zn_o e \vec{v}_e - ne\vec{v}_o = \vec{\vec{\sigma}} \cdot \vec{\vec{E}}, \tag{7}$$

where

$$4\pi\sigma_{xx} = \frac{\omega_{pe}^2}{\nu_o} \left(1 - \frac{k_z v_o}{\omega}\right) ,$$

$$4\pi\sigma_{xz} = \frac{\omega_{pe}^2 k_x v_o}{\nu_o \omega} ,$$

$$4\pi\sigma_{zx} = \frac{\omega_{pe}^2 k_x v_o}{\nu_o \omega} \left(1 - \frac{\omega A}{\Omega}\right) ,$$

$$4\pi\sigma_{zz} = \frac{\omega_{pe}^2 \omega}{\nu_o(\omega - k_z v_o)} \left(\frac{k_x^2 v_o^2}{\omega^2} + \frac{\bar{\Omega} - \frac{k_o^2 v_o^2}{\omega} A}{\Omega}\right) ,$$

and

$$\Omega = \bar{\Omega} + k_z v_o A + \frac{4i}{3} m_e v_o^2 \frac{\partial \nu_o}{\partial T_{eo}} ,$$

$$\bar{\Omega} = \omega - k_z v_o + i\delta\nu_o + \frac{2i\nu_o}{3} \frac{\partial}{\partial T_{eo}} \left(\frac{P}{n_o Z \nu_o}\right) ,$$

$$A = \frac{2T_{eo}}{3\nu_o}\frac{\partial \nu_o}{\partial T_{eo}} + \frac{2iZ\, n_o}{\nu_o(\omega - k_z v_o)}\left[\frac{\partial \nu_o}{\partial (n_o Z)}\frac{\partial}{\partial T_{eo}}\left(\frac{P}{n_o Z}\right) + \frac{\partial \nu_o}{\partial T_{eo}}\frac{\partial}{\partial (n_o Z)}\left(\frac{P}{n_o Z}\right)\right]$$

$$+ \left(1 + \frac{i\delta\nu_o}{\omega - k_z v_o}\right)\frac{n_o Z}{\nu_o}\frac{\partial \nu_o}{\partial (n_o Z)} .$$

Other components of $\overleftrightarrow{\sigma}$ are zero. In writing Eq. (7) the neglegibly small ion contribution (which is the mass ratio times smaller than the electron contribution) has been dropped and $\omega << \nu_o$ has been assumed. Note that σ_{zx} and σ_{xz} depend linearly on k_x; for $k_x = 0$ the x,z coupling vanishes as will the instability.

The wave equation governing the perturbed electric field is given by

$$\nabla^2 \vec{E} - \vec{\nabla}(\vec{\nabla}\cdot\vec{E}) = \frac{4\pi}{c^2}\frac{\partial \vec{J}}{\partial t} + \frac{1}{c^2}\frac{\partial^2 \vec{E}}{\partial t^2} . \qquad (8)$$

The displacement current is assumed to be negligibly small, so that the last term in Eq. (8) may be dropped. Substituting Eq. (7) into Eq. (8) one obtains the dispersion relation

$$(k_x k_z c^2 + 4\pi i\omega\sigma_{zx})(k_x k_z c^2 + 4\pi i\omega\sigma_{xz}) = (c^2 k_x^2 - 4\pi i\omega\sigma_{zz})(c^2 k_z^2 - 4\pi i\omega\sigma_{xx}) . \qquad (9)$$

This equation is quadratic in ω and processes the two complex roots,

$$\omega = k_z v_o - \frac{i}{2}\left[\frac{\nu_o c^2 k^2}{\omega_{pe}^2} + \delta\nu_o + \nu_o \frac{\partial}{\partial T_{eo}}\left(\frac{2P}{3n_o Z\nu_o}\right)\right]$$

$$\pm \frac{i}{2}\left\{\left[\frac{\nu_o c^2 k^2}{\omega_{pe}^2} + \delta\nu_o + \nu_o \frac{\partial}{\partial T_{eo}}\left(\frac{2P}{3n_o Z\nu_o}\right)\right]^2 - \frac{4\nu_o c^2 k^2}{\omega_{pe}^2}\left[\delta\nu_o + \frac{4m_e \nu_o^2 k_x^2}{3k^2}\frac{\partial \nu_o}{\partial T_{eo}} + \frac{2\nu_o}{3}\frac{\partial}{\partial T_{eo}}\left(\frac{P}{n_o Z\nu_o}\right)\right]\right\}^{1/2} , \qquad (10)$$

where $k^2 = k_x^2 + k_z^2$. The upper sign is the root of interest which can lead to unstable growth. The instability exists when

$$\delta\nu_o + \frac{4m_e v_o^2 k_x^2}{3k^2} \frac{\partial \nu_o}{\partial T_{eo}} + \frac{2\nu_o}{3} \frac{\partial}{\partial T_{eo}} \left(\frac{P}{n_o Z \nu_o}\right) < 0 , \qquad (11)$$

where Eq. (3) has been used to eliminate T_{io}. For $k_z = 0$, $P = 0$, and $\partial\nu_o/\partial T_{eo} = -3\nu_o/2 T_{eo}$ Eq. (11) reduces to $m_i v_o^2/T_{eo} > 1$. Ion acoustic instability will not occur under these conditions because of the high collisionality of the dense plasma and the fact that T_{eo} will not greatly exceed T_{io} on these short timescales.[14]

When the threshold of Eq. (11) is exceeded, the growth rate increases monotonically with k for small values of k and then saturates for large values of k. For k = 0, the growth rate is zero. Saturation of the growth rate occurs when

$$k^2 > k_o^2 \equiv \frac{\delta\omega_{pe}^2}{c^2} \left[1 + \frac{2}{3\delta} \frac{\partial}{\partial T_{eo}} \left(\frac{P}{n_o Z \nu_o}\right)\right] . \qquad (12)$$

For a typical density of $Zn_o = 10^{18}$ cm^{-3} and $\delta = 10^{-4}$ one finds $k_o = 25$ which corresponds to a wavelength of a few millimeters. The growth rate of the instability can be approximated by

$$\gamma = -\frac{\nu_o c^2 k^2}{\omega_{pe}^2} \left[1 + \frac{\frac{4k_x^2}{3k^2} m_e v_o^2 \frac{\partial \nu_o}{\partial T_{eo}}}{\delta\nu_o + \frac{2\nu_o}{3} \frac{\partial}{\partial T_{eo}} \left(\frac{P}{n_o Z \nu_o}\right)}\right] \quad \text{for} \quad k < k_o ,$$

$$\gamma = -\left[\frac{4k_x^2}{3k^2} m_e v_o^2 \frac{\partial \nu_o}{\partial T_{eo}} + \delta\nu_o + \frac{2\nu_o}{3} \frac{\partial}{\partial T_{eo}} \left(\frac{P}{n_o Z \nu_o}\right)\right] \equiv \gamma_m \quad \text{for} \quad k > k_o . \qquad (13)$$

For $k_z = 0$, $P = 0$, and $\partial\nu_o/\partial T_{eo} = -3\nu_o/2T_{eo}$ the maximum growth rate

reduces to $\gamma_m = \delta\nu_o(m_i v_o^2/T_{eo} - 1)$ with typical e-folding times of a few nanoseconds.

For $k_z \neq 0$, the mode has a finite real frequency. Furthermore, a threshold k_x for the instability results. From Eq. (11) one finds that growth only occurs for

$$k_x^2 > k_z^2 \left[\frac{\frac{4m_e v_o^2}{3\delta\nu_o}\left|\frac{\partial\nu_o}{\partial T_{eo}}\right|}{1 + \frac{2}{3\delta}\frac{\partial}{\partial T_{eo}}\left(\frac{P}{n_o Z \nu_o}\right)} - 1\right]^{-1} > 0 \ . \qquad (14)$$

In order to model the finite thickness of the cathode plasma, k_z can be estimated to be $\gtrsim \frac{\pi}{2d}$ where d is the plasma scalelength. This introduces a finite k_x required for instability as indicated in Eq. (14) but does not affect the maximum growth rate, γ_m, which occurs at $k_x >> k_z$ for a given k_z.

IV. Results and Discussion

In terms of the current density, J_o, the maximum growth rate of this thermal-resistive instability for $k_x >> k_z$ is

$$\gamma_m = -\left[\frac{4\, m_e\, J_o^2}{3e^2 n_o^2 Z^2}\frac{\partial \nu_o}{\partial T_{eo}} + \delta\nu_o + \frac{2\nu_o}{3}\frac{\partial}{\partial T_{eo}}\left(\frac{P}{n_o Z\, \nu_o}\right)\right], \tag{15}$$

where all quantities are expressed in CGS units. In addition, Eq. (3) can be used to express T_{eo} as

$$T_{eo} = T_{io} + \frac{2}{3\delta}\left(\frac{m_e\, J_o^2}{e^2 n_o^2 Z^2} - \frac{P}{n_o Z\, \nu_o}\right), \tag{16}$$

where the same units as in Eq. (15) are used.

For a given J_o, T_{io} and radiation equilibrium model γ_m can be plotted as function of n_o, the plasma ion density. Three cases are shown in Fig. (3), all of which have $J_o = 0.0125$ MA/cm^2 and $T_{io} = 1$ eV. In one case it is assumed that $Z = 1$ and that the equivalent ionization temperature T_r, radiation rate P, and electron temperature T_e are determined as discussed in Sec. II. The other cases are similar but with $Z = 2$, and 3, respectively. Figs. (4), (5) and (6) show the same plots for $J_o = 0.025$, 0.05 and 0.1 MA/cm^2 respectively. In all cases it is assumed for the instability analysis that T_r does not change on this fast timescale such that $\partial\nu_o/\partial T_{eo} = -3\nu_o/2T_{eo}$ and $\partial(P/n_o Z\, \nu_o)/\partial T_{eo} = 3P/2n_o\nu_o\, Z\, T_{eo}$. This is reasonable since at the densities to be considered the timescale for changes in the ionization temperature is much slower than the growth rate of the instability. If T_r does increase with electron temperature it will tend to slow the growth of the mode.

Mode growth at low ion densities of $\lesssim 10^{16}cm^{-3}$ is very slow because of high T_{eo}. For higher ion densities up to $\sim 10^{17}cm^{-3}$ inelastic collisions prevent growth of the mode. This can be seen from Fig. (2). The dashed and solid curves in Fig. (2) allow one to compare the second and third terms in Eq. (15) which are respectively the elastic-collision-damping term and the inelastic-collision-damping term in the growth rate expression. For $n_o \gtrsim 10^{17}cm^{-3}$ damping due to elastic collisions dominates but does not prevent growth, whereas for $n_o \lesssim 10^{17}cm^{-3}$ damping due to inelastic collisions can dominate and actually prevent mode growth. For very high ion densities $\gtrsim 10^{19}cm^{-3}$ elastic collisions prevent mode growth by dissipating the electron thermal energy to the ions faster than the mode can grow.

One finds from these plots that there is a band between $n_o \sim 10^{17}cm^{-3}$ to $\sim 10^{19}cm^{-3}$ where fast growth can occur. The lower end of this density regime matches that observed experimentally for typical cathode plasmas. Eq. (16) shows that the inclusion of inelastic collisions ($P \neq 0$) allows for slightly higher peak growth rates than for the case with $P = 0$ because of the reduction of T_{eo} for a given n_o, Z, J_o and T_{io}. If the density drops below $\sim 10^{17}cm^{-3}$ due to expansion into the diode gap, growth will essentially cease during the remainder of the pulse. Thus rapid growth of this mode is expected early in the pulse. However any cathode plasma surface bumpiness caused by plasma jetting during this time will persist throughout the pulse and will result in filamented electron flow in the vacuum region.

The wavelength of this thermal-resistive mode also agrees well with experimental data. From Eq. (12) it was found that the number of filaments should be on the order of $m \gtrsim k_o r_o$ or about 75 for $r_o = 3$ cm.

There is evidence of tens of filaments from damage on the cathode which coalesce into 10-20 filaments in the vacuum electron flow. If radial geometry effects were included in the analysis, one might expect to find growth is cut off for $k_x \lesssim 2\pi/\Delta r_o$ or $m \lesssim 2\pi r_o/\Delta r_o$. For $r_o = 3$ cm and $\Delta r_o \sim .3$ cm, this states that $m \lesssim 60$. This is in reasonable agreement with the above result and with experimental observations.

From Figs. (3)-(6) one finds that the peak growth rate scales roughly as $J_o Z^{2.3}/m_i^{1/2}$ and that the ion density at which peak growth occurs scales roughly as $m_i^{1/2} J_o Z$. Since the brightness of ion beams extracted from PRD's seems to be related to filamented flow in the diode, reduction or elimination in the growth of this thermal-resistive instability in the cathode plasma is of great importance. Reducing the current density by increasing the cathode emission area seems to be the easiest way to reduce the mode growth. This may be possible by tapering the cathode such that the inner edge of the cathode is closer to the anode than the outer edge. Simply increasing the thickness of the cathode will not necessarily reduce J_o significantly since the emission from the inner edge of the cathode is reduced by space charge effects produced by electrons flowing inward from the outer edge of the cathode. Reducing the charge state of the plasma or increasing the ion mass may also be possible ways of reducing the growth rate. It should also be noted that shorter pulse beams (e.g. 10 ns pulse duration beams) would be less affected by this instability than the present 50 ns pulse duration beams because of the finite few nanosecond e-folding times.

In summary the thermal resistive filamentation instability described herein could be the cause of the filamentation which is found

to exist in the cathode plasma of a PRD. The e-folding time of a few nanoseconds is fast enough to allow for strong current filamentation which can directly and indirectly affect the brightness of ion beams extracted from such diodes and possibly other diodes.[15]. The optimum density for peak growth of this mode closely matches the experimentally measured cathode plama density and the predicted wavelength of the mode is also roughly equal to that measured experimentally. With this understanding it is hoped that this filamentation can be controlled or eliminated.

Acknowledgements

The authors wish to acknowledge valuable discussions with Drs. Shyke A. Goldstein, C. S. Liu, D. Mosher, and R. Kulsrud. The authors would also like to thank Drs. D. Duston and J. Davis for providing the data for the collisional radiative equilibrium model. This work was supported in part through the University of Maryland - Naval Research Laboratory Joint Program in Plasma Physics. The work was also supported in part by the U.S. Department of Energy and the Defense Nuclear Agency.

References

* Also at the University of Maryland

1. J. P. VanDevender, G. W. Barr, J. T. Crow, S. A. Goldstein, D. H. McDaniel, K. F. McDonald, T. H. Martin, W. B. S. Moore, E. L. Neau, G. D. Peterson, J. F. Seaman, D. B. Seidel, R. B. Spielman, B. N. Turman, and G. Yonas, in Proceedings of the 4th International Topical Conference on High-Power Electron and Ion-Beam Research and Technology, Palaiseau, France (1981), p. 725.
2. G. Cooperstein, Shyke A. Goldstein, R. A. Meger, D. Mosher, W. F. Oliphant, F. L. Sandel, S. J. Stephanakis, F. C. Young, and H. V. Karow, ibid., p. 53.
3. P. F. Ottinger, S. A. Goldstein, and D. Mosher, NRL Memorandum Report 4948, September 1982; D. Mosher, D. G. Colombant, Shyke A. Goldstein, and P. F. Ottinger in Proceedings of the 4th International Topical Conference on High-Power Electron and Ion-Beam Research and Technology, Palaiseau, France (1981), p. 19.
4. S. J. Stephanakis, S. A. Goldstein, P. F. Ottinger, and D. Mosher, Bull. Am. Phys. Soc. 26, 921 (1981).
5. R. K. Parker, R. E. Anderson, and C. V. Duncan, J. Appl. Phys. 45 2463 (1974).
6. G. A. Mesyats, in the Proceedings of the 10th International Conference on Phenomena of Ionized Gases, North Holland, G. A. Mesyats and D. I. Proskurovski, Sov. Phys. Usp. 18, 51 (1975); J. M. Lafferty, "Vacuum Arcs-Theory and Applications" (Wiley, New York, 1980).

7. D. Hinshelwood, 1982 IEEE Int. Conf. on Plasma Science, Ottawa, Canada (1982), p. 138; D. D. Hinshelwood in the Proceedings of the 10th International Symposium on Discharges and Electrical Insulation in Vacuum, Columbia, South Carolina (1982); J. G. Kelly and L. P. Mix, J. Appl. Phs. 46, 1084 (1975).

8. E. S. Weibel, Phys. Rev. Lett. 2, 83 (1959).

9. M. G. Haines, Phys. Rev. Lett. 47, 917 (1981).

10. D. A. Tidman and R. A. Shanny, Phys. Fluids 17, 1207 (1974); A. Z. Dolginov and V. A. Urpin, Sov. Phys. JETP 50, 912 (1979).

11. A. J. Toepfer and L. P. Bradley, J. Appl. Phys. 43, 3033 (1972); A. P. G. Kutty, J. Appl. Phys. 50, 6139 (1979).

12. B. A. Trubnikov, in "Reviews of Plasma Physics", Vol. 1 (Consultants Bureau, New York, 1965), p. 105.

13. R. W. P. McWhister, in "Plasma Diagnostic Techniques", edited by R. H. Huddleston and S. L. Leonard (New York, Academic, 1965), pp. 201-264; D. Duston and J. Davis, Phys. Rev. A 21, 1664 (1980); D. Duston and J. Davis, Phys. Rev. A 23, 2602 (1981).

14. P. F. Ottinger, S. A. Goldstein, and D. Mosher, NRL Memorandum Report 4548, July, 1981.

15. J. N. Olsen, S. E. Rosenthal, L. P. Mix, R. J. Leeper, R. J. Anderson, P. L. Dreikl, D. B. Seidel, J. P. Quintenz and J. W. Poukey, Bull. Am. Phys. Soc. 27, 1120 (1982).

Figure Captions

Fig. 1 Plots of electron energy loss rate due to inelastic collisions versus equivalent ionization temperature for various ion densities from the collisional radiative equilibrium model. The dashed lines are plots of $\delta\nu_o T_{eo}/n_o$ versus temperature with Z = 4 and 1 for the upper and lower curves respectively.

Fig. 2 Plots of average charge state versus equivalent ionization temperature for various ion densities from the collisional radiative equilibrium model.

Fig. 3 Plots of growth rate versus ion density for J_o = 12.5 kA/cm^2 and Z "frozen-in" at 1, 2, and 3.

Fig. 4 Plots of growth rate versus ion density for J_o = 25 kA/cm^2 and Z "frozen-in" at 1, 2, and 3.

Fig. 5 Plots of growth rate versus ion density for J_o = 50 kA/cm^2 and Z "frozen-in" at 1, 2, and 3.

Fig. 6 Plots of growth rate versus ion density for J_o = 100 kA/cm^2 and Z "frozen-in" at 1, 2, and 3.

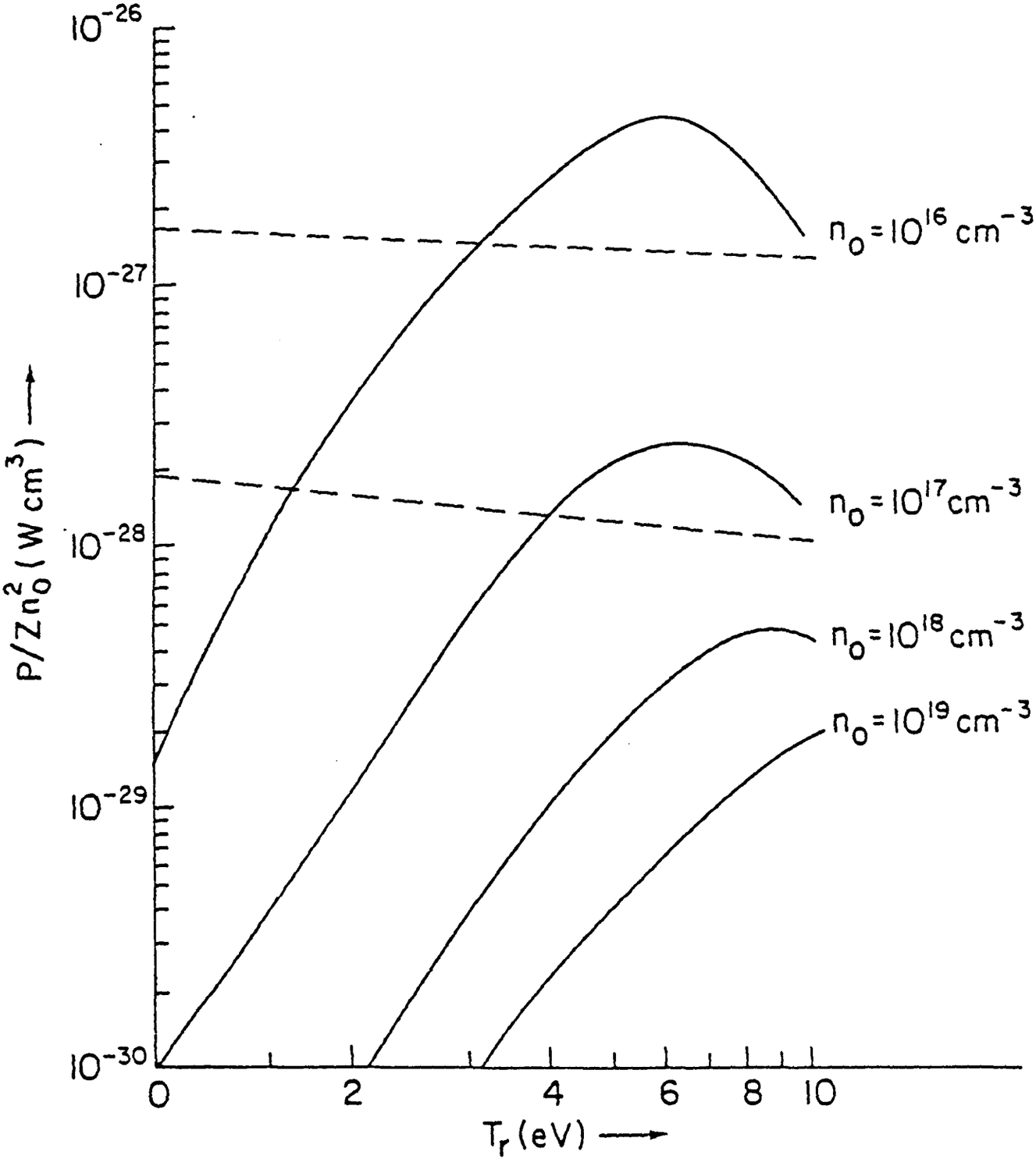
10^{-26}
10^{-27}
10^{-28}
10^{-29}
10^{-30}
P/Zn_0^2 (W cm^3) ⟶
$n_0 = 10^{16}$ cm^{-3}
$n_0 = 10^{17}$ cm^{-3}
$n_0 = 10^{18}$ cm^{-3}
$n_0 = 10^{19}$ cm^{-3}
0
2
4
6
8
10
T_r (eV) ⟶

Figure 1

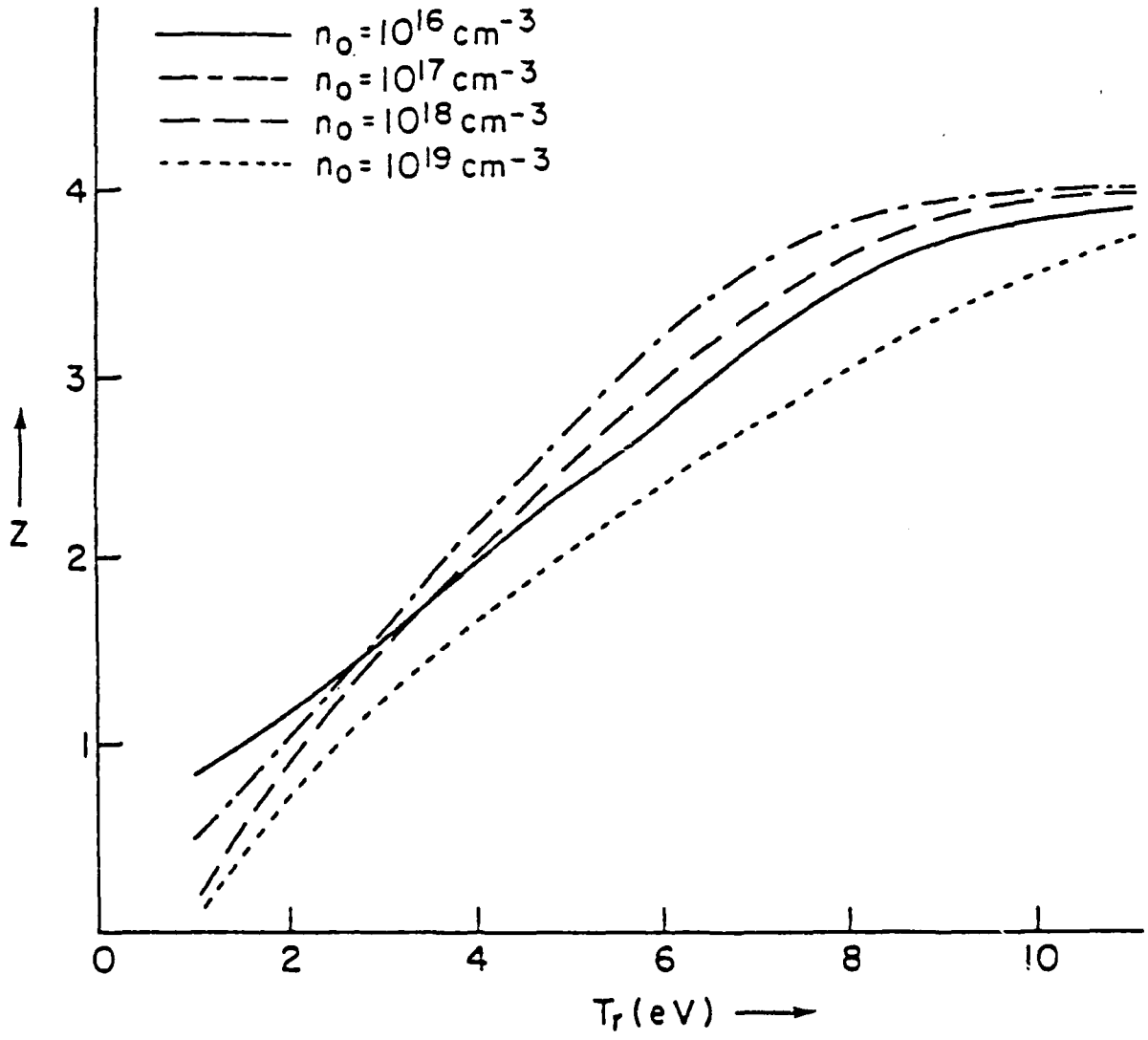
$n_0 = 10^{16}\,cm^{-3}$
$n_0 = 10^{17}\,cm^{-3}$
$n_0 = 10^{18}\,cm^{-3}$
$n_0 = 10^{19}\,cm^{-3}$
Z
1
2
3
4
0
2
4
6
8
10
T_r (eV) ⟶

Figure 2

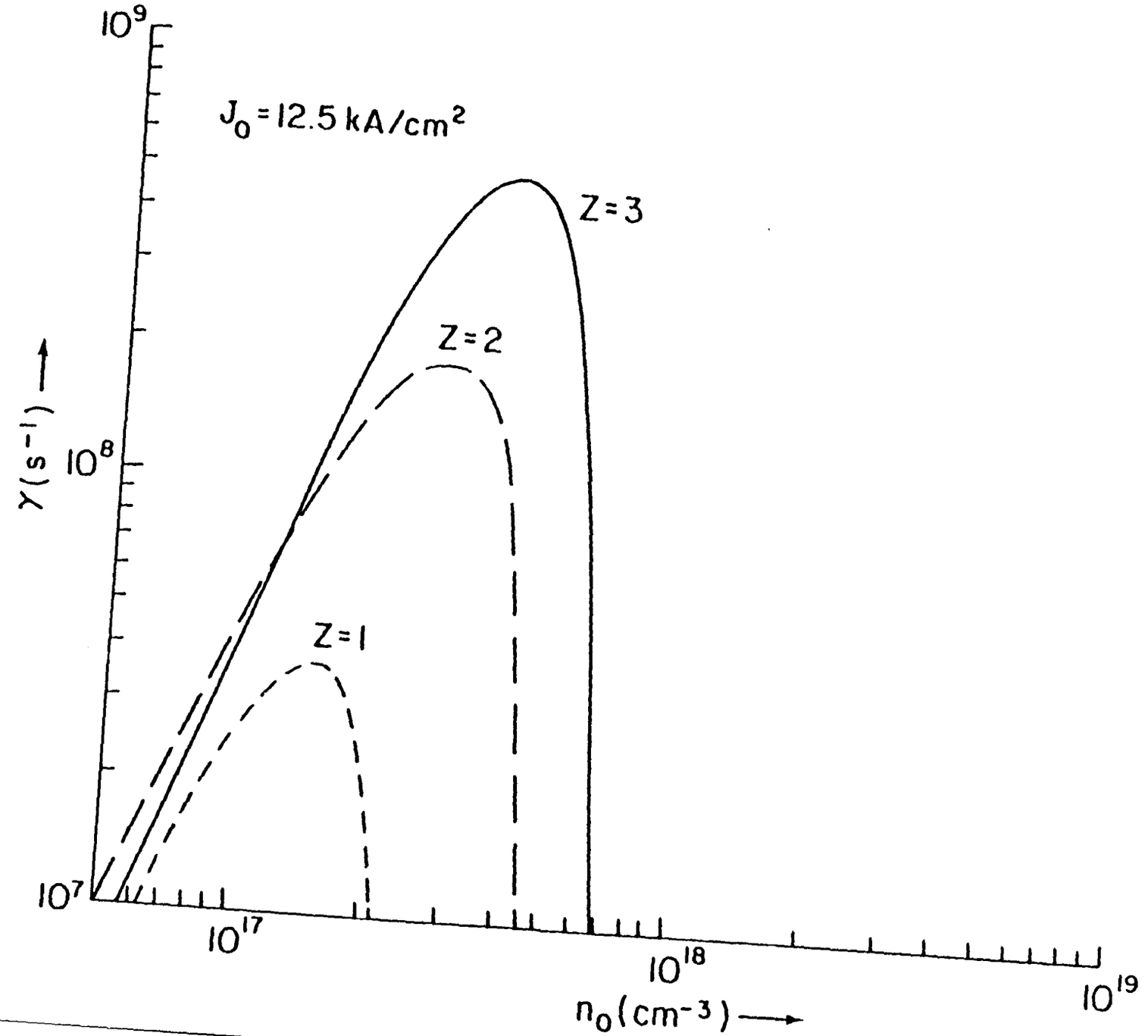

Figure 3

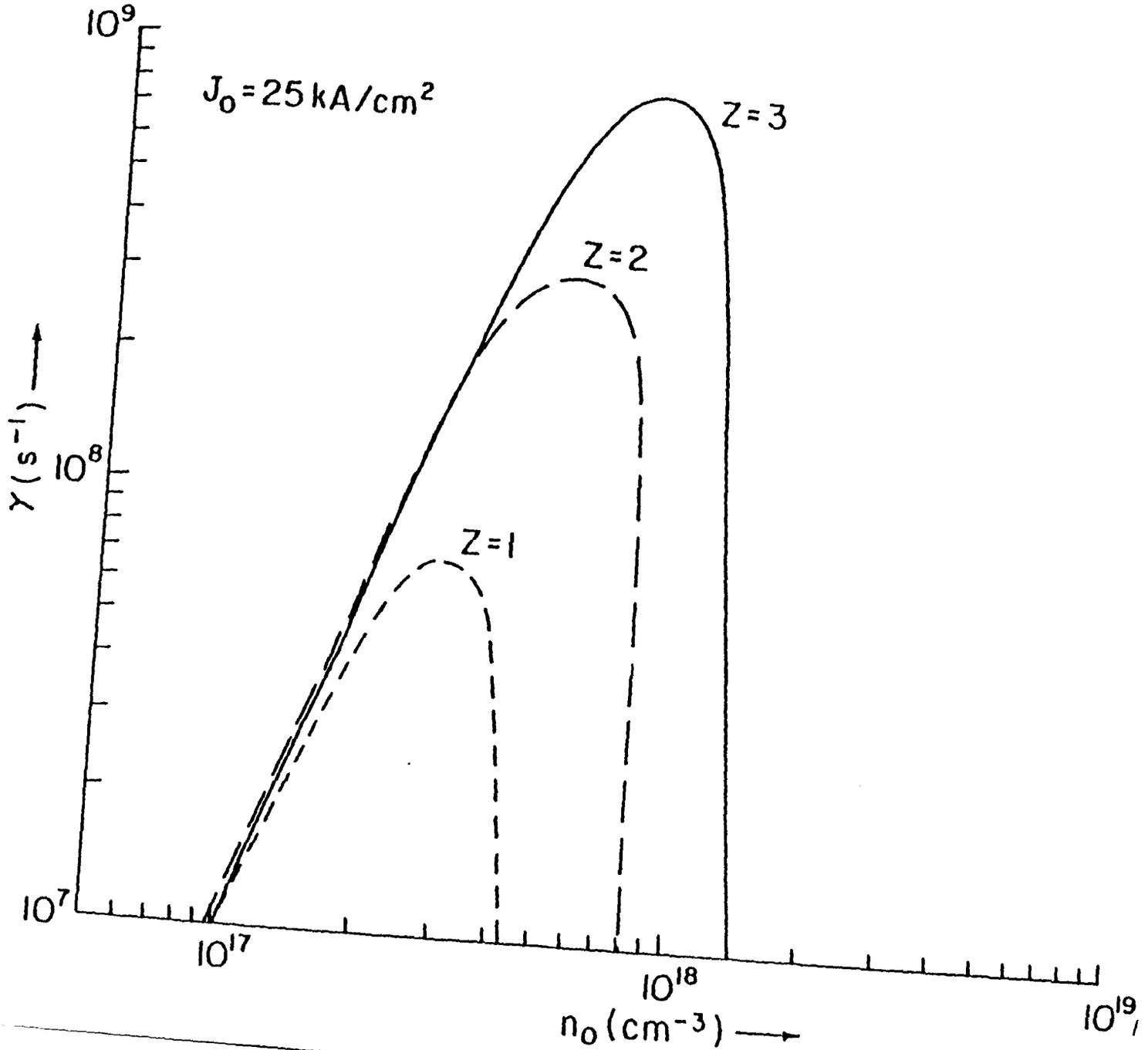

Figure 4

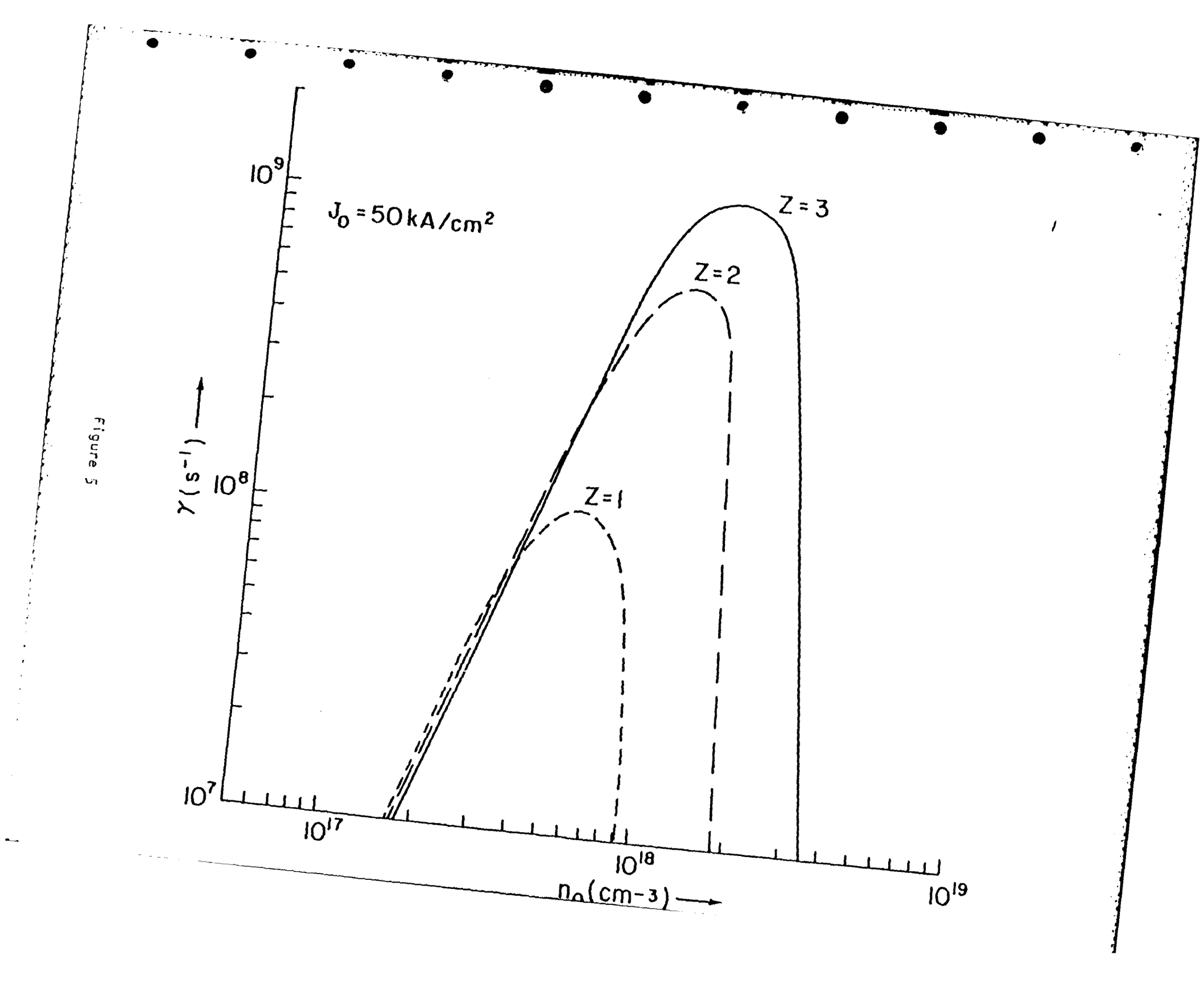

Figure 5

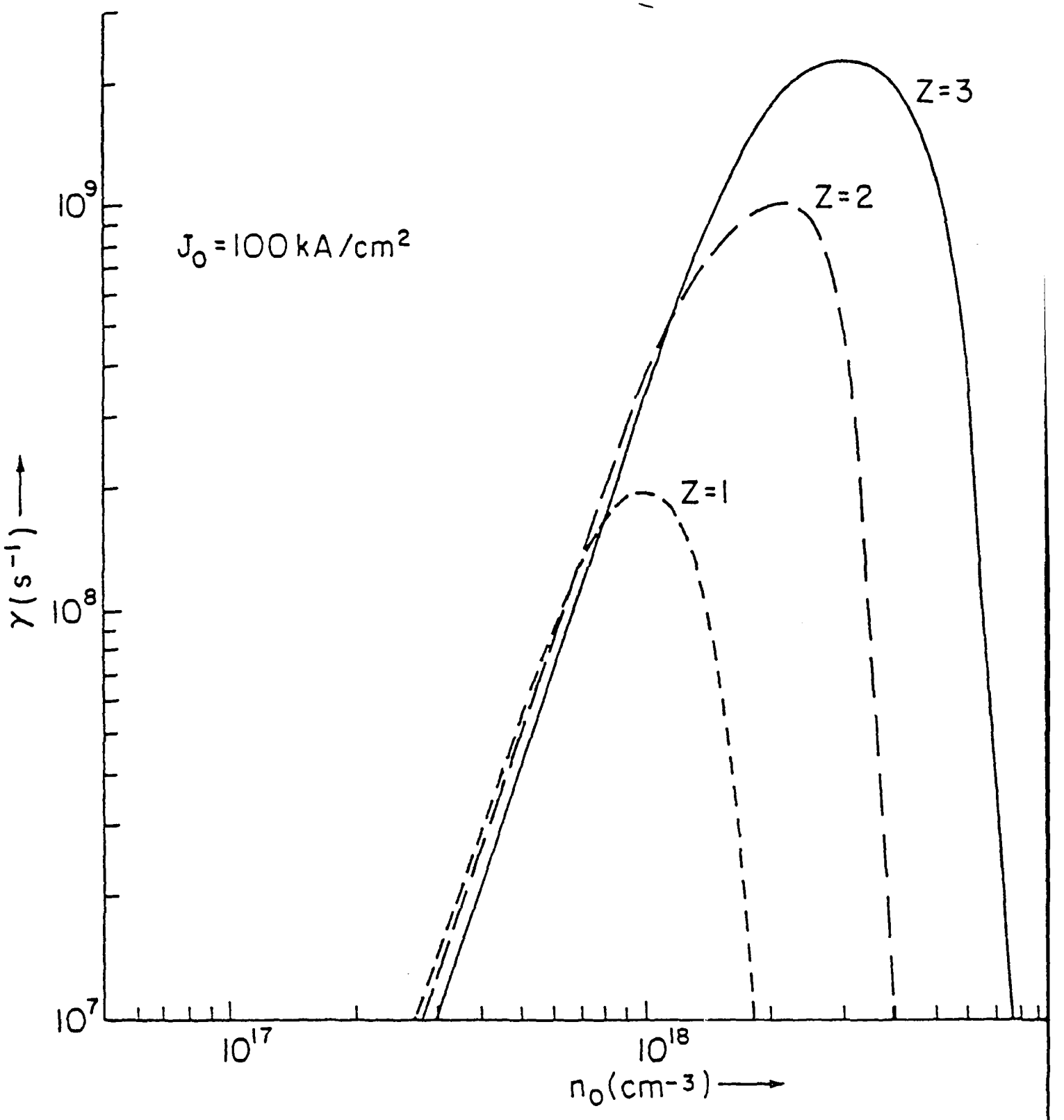

Figure 6

3.0 BEAM TRANSPORT

Beam transport in plasma channels is important in order too provide standoff between the diode and the target region for a survivable diode system. Transport can also be used for TOF beam bunching if an appropriately ramped diode voltage is applied. A considerable effort in the area of beam transport was undertaken under this contract. Extensive experimental and theoretical studies of beam propagation in z-discharge channels were conducted. Some of the issues addressed were the hydrodynamic response of the channel to beam passage, beam particle and energy transport efficiency and the stability of the channel and beam-plasma system. With this understanding it was concluded that large radius (i.e. larger than typical target sizes) transport was most attractive which led to the study of final focusing techniques. System requirements for igniting an ICF target using a multimodular approach with transport bunching, and final focusing were finally considered.

The transport of electron beams was also considered and studied as was enhanced stopping of ions in hot dense plasmas. The results of this beam transport and beam-plasma interaction work is summarized below. Detailed information can be found in the reports which follow.

First consider the transport of intense ion beams over several meters through a z-discharge plasma channel. This technique allows ion beams to be transported and the distance required for reaction-chamber standoff and provides a means of combining beams extracted from many generators onto a single target. The ion beam enters the z-discharge channel at the best beam focus location from the diode. Inside the channel, the ions are confined radially by the azimuthal magnetic field produced by the discharge of an external capacitor bank. The 25-150 kA current in the channel is adjusted to provide radial confinement for ions with the maximum transverse energy. The plasma density in the channel must be sufficiently high to resist expansion forces during beam transit and sufficiently low to prevent excessive energy loss of the beam. A convenient combination of desired transport length (2-5 m), proton or deuteron energy (2-5 MeV), and ion beam pulse duration (50-100 ns) permits axial bunching of the beam during tranport by ramping the accelerator voltage in time. Beam power multiplication of the beam can be achieved in this fashion.

Questions which were addressed during the performance of this contract concerning propagation of beams in such channels included how off-center injection would effect transport, whether efficient transport was possible if the channel were sausage unstable, what effect knock-on

electrons would have at the head of the beam and how would instabilities limit transportable beam power. Answers to these questions were addressed both experimentally and theoretically.

In order to deliver an intense light-ion beam to a target in a z-discharge channel the ions are confined radially by the azimuthal magnetic field in the channel. If the beam is injected on-center and parallel to the axis, transport is azimuthally symmetric and stable. Nonparallel or off-center injection, however, may lead to both particle losses and unstable transport. Results show that after phase-mixing the effect of off-center injection is mainly to increase the beam radius in the channel over that achieved with centered injection. Such a system may also be unstable to growth of hose-like perturbations. Both the self-hose and the resistive hose mechanisms can play important roles. The self-hose mechanism results from the repulsion between the beam current and the oppositely directed return current, whereas the resistive hose mechanism results from the resistive phase lag between oscillations of the beam and magnetic axis. Since off-center injection of the beam into the channel can lead to a finite initial perturbation, growth of the mode on the beam time scale could disrupt transport. Results show that finite velocity spread in the beam axial velocity stabilizes growth of the hose mode.

This result differs from the relativistic e-beam case where the axial velocity spread is very small for relativistic beams.

Beam propagation in an ideal channel has been compared with propagation in non-ideal channels. For an ideal channel $B_\theta \sim r/r_c$ and the channel radius, r_c, does not vary with axial position. If the channel is subject to sausage type instability $[r_c = r_c(z)]$ before beam injection, then radial expansion of the beam can result. The extent of beam expansion is a function of the wavelength and level of bumpiness in the channel. It was found that this expansion will be small because the betatron wavelength is much longer than the typical wavelength of the sausage mode. The effects on beam propagation of steeper magnetic field gradients ($B_\theta \sim (r/r_c)^n, n > 1$), and small electric fields were also considered. These fields arise due to the MHD response of the channel to beam passage and again were found to have little effect on propagation under typical conditions.

Results from micro-stability analysis for both electrostatic and electromagnetic modes show that channel parameters can be chosen which allow beam transport without fast electrostatic wave growth. Slower growing electromagnetic instabilities probably will occur and could lead to plasma current filamentation that could affect the tail of the beam. Conditions for good transport were

derived from these results which point out some of the limiting constraints on transport. The results were derived in a general form so that they may be applied to beams of various species (e.g. H^+, D^+, C^{+4}, etc.).

The effect of knock-on electrons resulting from large angle scattering off beam ions was also studied. Such electrons can obtain velocities up to twice the beam velocity and hence precede the beam into the channel. Significant precursor electron current could degrade the radial confinement of the beam head. It was found, however, that the magnetic field due to the channel current quickly turns the majority of such electrons around before they leave the beam region.

Another important problem which was studied was the magnetohydrodynamic (MHD) response of transport channels to ignition-system-level beams. Simple analytic estimates for channel response agreed with a one-dimensional (1D) radial, two-temperature MHD code for moderate density changes. Results indicated that for 3-5 MeV protons, mega-ampere-level beams can be transported. Starting right after beam injection, the channels expand radially and electromagnetic fields develop inside the channel. Changes in the magnetic field inside the channel are due mainly to convection with the plasma channel. Ion beam energy losses occur because of electric fields which develop inside the

channel and beam intensity losses occur because of changes in the initial magnetic field structure. The electric field inside the channel has three main components: resistive, hydrodynamic and the equivalent field due to collisional slowing-down of the beam ions. An optimum density for the channel density was determined from these considerations.

Initially, the beam current density was assumed to be known as a function of space. In reality however, the beam current spatial distribution depends on the evolution of the electric and magnetic fields in the channel. Refined calculations were performed where the current distribution was obtained by following ion orbits in these macroscopic fields determined from the MHD equations. It is then used as a driving source term in the MHD equations. These refined results were again used to determine the optimum density for transport.

The result that expanding plasma channels decelerated ion beams led to the consideration of using imploding channels to accelerate beams. When magnetized plasmas flow in converging geometries (such as a z-pinch) they generate a combination of $\underline{E}$ and $\underline{B}$ field structures that act on the majority of the plasma particles (trapped, low energy particles) in a self-consistent manner of current and space charge distributions. These fields will, however, act differently on a component of beam particles that are

untrapped. A very fast process of energy delivery from the heavy slow plasma to the beam component will take place when the plasma converges. The inverse is true for plasma expansion. It was found however that special care must be taken to prevent emittance growth during the acceleration process. In fact beam cooling could be achieved if the channel implosion was properly tapered but this required finite length transport sections which would need to be coupled together.

Experiments have been performed on the Gamble I and Gamble II generators at NRL which have demonstrated efficient transport of proton beams of intensities of up to 50 kA/cm^2. The media for beam transport have been wall-stabilized plasma channels performed by capacitor bank discharges of ~50 kA in 1-2 Torr of gas. Channels are formed in a compact, low inductance coaxial geometry with the discharge struck along an aluminum oxide insulating liner. Methods of channel coupling have been developed and tested to allow construction of long modular transport systems. Efficient transport of up to 400 kA of proton current has been observed in channels of 1.6, 2.5 and 4.5 cm diameter over distances up to 1.5 m. Using the channel coupling technique efficient transport over 5 m distances has been achieved.

The time variation of the current of intense bursts of protons has been determined by detecting prompt gamma rays from the $^{19}F(p,\alpha\gamma)^{16}O$ reaction. Detectors have been absolutely calibrated to measure amperes of protons provided the proton energy is known Measurements with this diagnostic on the transort experiments were analyzed to evaluate the proton currents and transport efficiencies discussed above.

The propagation and expansion of beams exiting a transport channel into a field-free, 1 Torr pressure drift space have also been studied. The exiting beams have excellent axisymmetry and uniformity with no evidence of filamentation. Time-integrated and time-resolved photography of beam-channel and target blow-off plasma along with witness-target damage and beam imaging techniques were used to compare the experimental properties of exiting beams with computations of the transported-beam distribution function and ballistic orbits. Both experiment and theory show a dependence of the post-transport expansion on the channel current. Theoretical considerations also emphasize the importance of the radial current distribution on beam expansion, which is controlled by proper plasma engineering in the experiments.

The need for a final focusing cell results from the fact that hydrodynamic and stability constraints associated with transport are considerably relaxed if the beam is transported with a radius a few times larger than the pellet radius (~0.5). A final focusing element consisting of a short (~few cm) 1/2 betatron length high-current (~100-200 kA), z-discharge cell could then radially compress the beam to pellet dimensions after transport. Beam focusing is achieved at the expense of increased angular beam divergence. Detailed calculations of final focusing cells have been done including studies of the effects of focusing geometry for injection into the transport system, and the B_θ-distribution in the transport channel and focusing cell. The B_θ profiles are obtained from MHD code modeling of z-discharges for various gas fill pressures. Standoff for channel packing can be achieved by using a 1/4 betatron length cell. In this case focusing continues for about another 1/4 betatron length beyond the cell.

A proof-of-principle experiment for final focusing was fielded on Gamble II at NRL. Results showed that indeed focusing could be achieved that no significant phase mixing occurred in the short 1/2 betatron length cell.

Stability constraints combined with channel expansion and beam-energy loss constraint define an operational window for ion transport. The stability constraints are derived from the requirements to avoid significant growth of the electron-beam ion two-stream instability the beam filamentation instability and the channel-filamentation instability. The channel-expansion constraint results from demanding the $\underset{\sim}{J}x\underset{\sim}{B}$-driven radial expansion of the channel occurs on a time scale longer than the beam-pulse duration. Finally the beam energy-loss constraint requires that no more than 25% of the beam energy is lost during transport.

The constraints were derived for arbitrary beam-ion species in order to evaluate the advantage of higher-atomic-weight ions. The beam energy, beam radius and channel density are also free parameters which were varied in order to determine their effects on the operational window. In all cases, the channel gas was taken as deuterium. This allows the use of a simple model for channel heating and has the advantage of reduced radial acceleration due to the passing beam at the same stopping-power as hydrogen.

Results for beams of H^+, D^+, He^{+2} and C^{+6} were derived which show that a larger operational window exists for the higher-atomic-weight species. This is a consequence of their lower currents at equivalent transported power levels.

Lower currents relax the filamentation constraints thereby allowing stable transport of lower-angular-divergence, i.e. higher brightness, beams. Raising the channel density above the optimum for minimum beam-energy loss during transport relaxes the two-stream and channel-filamentation stability constraints and the channel-expansion constraint while only slightly modifying the energy-loss constraint. Increasing the beam radius relaxes the two-stream stability constraint and considerably reduces the channel-expansion and beam energy-loss constraint. This results from the reduced $\underset{\sim}{J}x\underset{\sim}{B}$ forces and smaller MHD-generated axial electric fields which are present when the beam current is spread over a larger area. All constraints are relaxed for a higher particle-energy beam because of increased stiffness and lower current. Target-deposition requirements limit the particle-energy range useful for different ion species.

It was determined that multi-terawatt beams can be transported a few meters in large-radius channels. If TOF bunching during transport and final focusing after transport are employed less than 10 (and as few as 4) channels are required to deliver the power needed to ignite a pellet.

Electron beam transport is also of interest, for example, for Bremsstrahlung production. Experimental results of propagating up to 400 kA of relativistic electron beams (~1 MeV) over a distance of 64 cm in a tightly focused

mode were reported. Efficient transport (> 80%) was observed when a channel of plasma containing enough current to confine the hot electrons was used. Theory of the flow includes return current effects, and is in good agreement with experimental results. The theory is used to predict limits of this technique.

A scheme for axial bunching of a REB was also invented and tested in a 1/r azimuthal magnetic field produced by a current driven in a wire, where electrons propagate axially by gradient B drift. Since this gradient B drift velocity $v_{\nabla B}$, is proportioned to $\gamma\beta^2$, axial current bunching can be achieved by appropriate ramping of the diode voltage waveform. In order to reduce the spread in drift velocities due to a dependence of $v_{\nabla B}$ on v_θ, the pinched beam is allowed to expand radially in a narrow gas-filled gap before entering the drift region. In this way azimuthal motion in the beam is reduced and substantial axial bunching is possible. Other electron drift motions and conditions for their neglect were derived. Conditions for efficient beam injection into the magnetic field drift region were also considered as well as other factors which affect transport and bunching of the beam.

A theoretical model was also employed to study the interaction of current and charge neutralized relativistic electron beams with thin targets for a configuration in which the gradient drifts in magnetic fields due to suitably arranged conduction currents used to transport, stagnate and focus the beams. Power deposition of the order of 100 TW/g/MA have been obtained corresponding to enhancements well above 10 times the collisional stopping power. The deposition enhancement is accompanied by the production of an intense component of low-energy Bremsstrahlung.

Finally, the stopping power of deuterons in hot dense plasma is being measured using neutron (TOF) with thin layered targets. Intense beams of 1-MeV deuterons are focused onto subrange thick targets consisting of a stopping foil coated on the front and rear with a thin layer of CD_2. The TOF of d-d neutrons from these two targets is used to determine the deuteron energy loss in the stopping foil which is heated by the focused ion beam ($\sim$50 KA/cm^2). Results indicate that the stopping power is enhanced compared to that of a cold solid target. Alteration of the stopping power is expected when the stopping medium contains a significant ratio of free-to-bound electrons. This ratio may be changed experimentally by using different current-density beams or stopping foils of different atomic number. This result has important implication for target

designs.

The transport work summarized above outlines the development of a significant new technology which has direct application to a multimodule light-ion ICF system. Detailed technical information follows in the attached reports.

3.1 List of Reports of Transport

3.1.a Contributed Papers

1. "Knock-on Electrons in Heavy Ion Beam Fusion Systems," R. F. Hubbard, S. A. Goldstein, S. Slinker, and D. A. Tidman, Bull. Am. Phys. Soc. 24, 1038 (1979).

2. "Gradient Drift Enhancement of Energy Deposition and Bremsstrahlung Production in Thin Targets by Relativistic Electron Beams," J. A. Halbleib, T. P. Wright and Shyke A. Goldstein, Bull. Am. Phys. Soc. 24, 950 (1979).

3. "Ion Beam Transport in Plasma Channels," F. L. Sandel, F. C. Young, S. J. Stephanakis, W. F. Oliphant, G. Cooperstein, S. A. Goldstein and D. Mosher, Bull. Am. Phys. Soc. 24, 1031 (1979).

4. "Analysis of Proton Transport Experiments with a Prompt Gamma Diagnostic," F. C. Young, F. L. Sandel, S. J. Stephanakis, P. G. Blauner, W. F. Oliphant, G. Cooperstein, S. A. Goldstein and D. Mosher Bull. Am. Phys. Soc. 24, 1031 (1979).

5. "Self-Consistent Plasma Channel Response to Propagating Ion Beams," D. G. Colombant, S. A. Goldstein, D. Mosher and W. Manheimer, Bull. Am. Phys. Soc. 24, 1032 (1979).

6. "A Scheme for Axial Bunching of Relativistic Electron Beams" P. F. Ottinger, Shyke A. Goldstein and D. Mosher, Bull. Am. Phys. Soc. 24, 950 (1979).

7. "Final Focusing of an Intense Ion Beam Following Transport Through a Z-Discharge Plasma Channel," P. F. Ottinger, S. A. Goldstein and D. Mosher, 1980 IEEE International Conf. on Plasma Science, (Madison, WN, May 1980), p. 95.

8. "Scaling Laws for Ion Beam Losses in Plasma Channels," D. G. Colombant and Shyke A. Goldstein, 1980 IEEE International Conf. on Plasma Science, (Madison, WN, May 1980), p. 37.

9. "Particle Beam Acceleration in Magnetized Moving Plasma," Shyke A. Goldstein and D. A. Tidman, 1980 IEEE International Conf. on Plasma Science, (Madison, WN, May 1980), p. 96.

10. "Intense Proton Beam Transport in Fast Z-Pinch Plasma Channels," F. L. Sandel, F. C. Young, S. J. Stephanakis, F. W. Oliphant, G. Cooperstein, S. A. Goldstein, and D. Mosher, Bull. Am. Phys. Soc. 25, 900 (1980).

11. "Effects of Off-Center Injection on Intense Ion Beam Transport in Z-Discharge Channels," P. F. Ottinger, S. A. Goldstein, and D. Mosher, Bull. Am. Phys. Soc. 25, 900 (1980).

12. "Optimization of Light-Ion Beam Energy Flux in Low-Z Plasma Channels," D. G. Colombant and Shyke A. Goldstein, Bull. Am. Phys. Soc. 25, 898 (1980).

13. "Post-Transport Propagation and Expansion of Intense Light-Ion Beams," F. L. Sandel, S. J. Stephanakis, D. Mosher, and P. F. Ottinger, Bull. Am. Phys. Soc. 25, 1009 (1981).

14. "Final Focusing of Intense Transported Ion Beams," P. F. Ottinger, D. G. Colombant, Shyke A. Goldstein, R. A. Meger and D. Mosher, Bull. Am. Phys. Soc. 26, 921 (1981).

15. "Proof-of-Principle Experiments for an Ion Beam Final-Focusing Cell," R. A. Meger, Shyke A. Goldstein, P. F. Ottinger, D. Mosher, S. J. Stephanakis and F. C. Young, Bull. Am. Phys. Soc. 26, 921 (1981).

AD-A129 821 DIODE DYNAMICS BEAM GENERATION AND TRANSPORT AND PLASMA 6/8
EROSION OPENING SWITCH DEVELOPMENT(U) JAYCOR ALEXANDRIA
VA P F OTTINGER 17 MAY 83 JAYCOR-J207-83-C-001
UNCLASSIFIED N00173-80-C-0202 F/G 9/1 NL

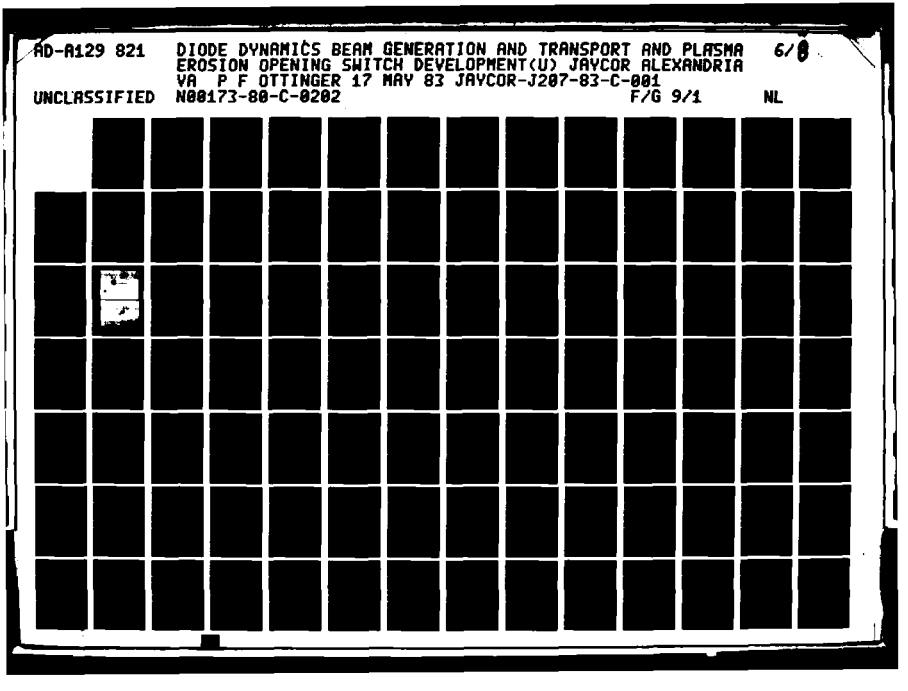

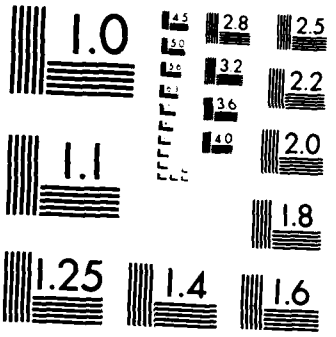

16. "Measurement of the Stopping of Deuterons in Hot Dense Plasmas," F. C. Young, S. J. Stephanakis, Shyke A. Goldstein and D. Mosher, Bull. Am. Phys. Soc. 26, 920 (1981).

17. "Analysis of the Hose instability for Intense Ion Beams Transported in Z-Discharge Channels," P. F. Ottinger and Shyke A. Goldstein, 1981 IEEE International Conference on Plasma Science (Santa Fe, NM, 1981), p. 33.

18. "Modular System Requiements for Light-Ion Inertial-Confinement Fusion," D. Mosher and P. F. Ottinger, 1981 IEEE International Conference on Plasma Science, (Santa Fe, NM, 1981) p. 92.

19. "Determination of the Stopping of Intense Deuteron Beams in Plasma," F. C. Young, S. A. Goldstein, S. J. Stephankis and D. Mosher, 1981 IEEE Interntional Conf. on Plasma Science, (Santa Fe, NM, May 1981), p. 92.

20. "Plasma Channels for Transport of Intense Ion Beams, " F. L. Sandel, 1981 IEEE International Conf. on Plasma Science, (Santa Fe, NM, May 1981), p. 107.

21. "Stability Constraints on Transported Light-Ion Beams," P. F. Ottinger, D. Mosher and Shyke A. Goldstein, 1982 IEEE International Conf. on Plasma Science, (Ottawa, Canda, May 1982), p. 82.

3.1.b Unpublished Technical Reports

1. "Propagation of Relativistic Electron Beams in Current-Carrying Plasma Channels," D. P. Bacon, G. Cooperstein, I. M. Vitkovitsky, S. A. Goldstein, NRL Memorandum Report 4330 (September 1980).

2. "Analysis of Proton Transport Experiments," F. C. Young, S. J. Stephanakis, G. Cooperstein, F. L. Sndel, P. G. Blauner, S. A. Goldstein and D.

Mosher, NRL Memorandum Report 4322 (1980).

3. "Stability Consideration for Light-Ion Beam Transport in Z-Discharge Channels," P. F. Ottinger, S. A. Goldstein and D. Mosher, NRL Memorandum Report 4548 (1981).

4. "Constraints on Transportable Ion Beam Power," P. F. Ottinger, Shyke A. Goldstein and D. Mosher, NRL Memorandum Report 4948 (November 1982).

3.1.c Published Papers

1. "Transport and Bunching of Light-Ion Beams for Pellet Fusion," D. Mosher, G. Cooperstein, Shyke A. Goldstein, D. G. Colombant, P. F. Ottinger, F. L. Sandel, S. J. Stephanakis, and F. C. Young, Proc. of the Third International Topical Conf. on High Power Electron and Ion Beam Research and Tech., (Novosibirsk, USSR, July 3-6, 1979), p. 576.

2. "Hydrodynamic Plasma Channel Response to Propagating Ion Beams," D. Mosher, D. G. Colombant and S. A. Goldstein, Phys. Rev. Lett. 45, 1253 (1980).

3. "Self-Consistent Propagation of Light-Ion Beams in Plasma Channels," Proc. of the Topical Meeting on Inertial Confinement Fusion, (San Diego, CA, Feb. 26-28, 1980), p. 103.

4. "Beam Requirements For Light-Ion-Driven Inertial Confinement Fusion," D. Mosher, D. G. Colombant and S. A. Goldstein, Comments on Plasma Physics and Controlled Fusion 6, 101 (1981).

5. "Intense Ion Beam Handling in Preformed Magnetized Plasma," S. A. Goldstein, D. G. Colombant, D. Mosher, P. F. Ottinger, and F. L. Sandel, Proc. of the 4th International Topical Conf. on High-Power Electron and Ion-Beam Research and Technology Palaiseau, France, June 29-July 3,

1981), p. 113.

6. "System Requirements for Light-Ion ICF," D. Mosher, D. G. Colombant, S. A. Goldstein and P. F. Ottinger, Proc. of the 4th International Topical Conf. on High-Power Electron and Ion-Beam Research and Technology, (Palaiseau, France, June 29-July 3, 1981), p. 19.

7. "A Time Resolved Beam Profile Monitor for Intense Ion Beams," A. E. Blaugrund, S. J. Stephanakis, and S. A. Goldstein, Proc. of the 4th International Topical Conf. on High-Power Electron and Ion Beam Research and Technology, (Palaiseau, France, June 29-July 3, 1981), p. 955.

8. "Experimental Studies of Intense Light-Ion Beam Transport," F. L. Sandel, Proc. of the 4th International Conf. on High-Power Electron and Ion-Beam Research and Technology, (Palaiseau, France, June 29-July 3, 1981), p. 19.

9. "Measurements of Enhanced Stopping of 1-MeV Deuterons in Target-Ablation Plasma," F. C. Young D. Mosher, S. J. Stephanakis, S. A. Goldstein and T. A. Mehlhorn, Phys. Rev. Lett. 849, 549 (1982).

3.1.d Invited Papers

1. "Some Theoretical Aspects of Light-Ion Beam Transport in Z-Discharge Channels," P. O. Ottinger, 1980 IEEE International Conference on Plasma Science, (Madison WI, May 1980), p. 57.

2. "Intense Light-Ion Beam Transport in Z-Discharge Plasma Channels," F. L. Sandel, Bull. Am. Phys. Soc. 26, 998 (1981).

3. "Hydrodynamics of Fast Z-Pinches Interacting with Propagating Ion Beams," D. G. Colombant, S. A. Goldstein, D. Mosher and F. L. Sandel, 1981 IEEE International Conference on Plasma Science, (May 18-20, 1981, Sante Fe), p. 33.

6R1 Knock-on Electrons in Heavy Ion Beam Fusion Systems, R. F. HUBBARD, S. A. GOLDSTEIN, S. SLINKER, and D. A. TIDMAN, JAYCOR*,--For typical reactor chamber conditions ($\beta_b \sim 0.4$, 1 kA per beam, $\rho \sim 1$ corr), the high current heavy ion beams proposed as drivers for pellet fusion will produce large currents of knock-on electrons with $v \geq 3\beta_b c$, the beam velocity. The current carried by these "electrons," which are produced by nearly head-on collisions between beam ions and ambient electrons, usually exceeds the beam particle current and can exceed the ~10 kA Alfven limiting current. Some of these electrons form a broad self-pinched "beam" which outruns the ions and creates a plasma channel whose magnetic field deflects some (or probably all) of the beam ions outward. Based on simple estimates of the knock-on "beam" radius, those deflections lead to a serious increase in spot size for $\rho \geq$ a few corr in fe. Results from a numerical classical beam transport model incorporating these effects will be presented.

*Supported by DOE contract DE-AC08-79DP40101.

2P11 Gradient Drift Enhancement of Energy Deposition and Bremsstrahlung Production in Thin Targets by Relativistic Electron Beams.* J. A. HALBLEIB and T. P. WRIGHT, Sandia Laboratories, and S. A. Goldstein, JAYCOR--A theoretical model has been employed to study the interaction of current and charge neutralized relativistic electron beams with thin targets for a configuration in which the gradient drifts in magnetic fields due to suitably arranged conduction currents are used to transport, stagnate, and focus the beams. Power deposition of the order of 100 TW/g/MA have been obtained, corresponding to enhancements well above 10 times the collisional stopping power. The deposition enhancement is accompanied by the production of an intense component of low-energy bremsstrahlung.

*Work supported by the U. S. Department of Energy and the Naval Research Laboratory.

6D2 Ion Beam Transport in Plasma Channels.* F. L. SANDELF, F. C. YOUNG, S. J. STEPHANAKIS, F. W. OLIPHANT, G. COOPERSTEIN, SHYKE A. GOLDSTEINT, and D. MOSHER, Naval Research Laboratory--Intense proton beams produced in the GAMBLE II generator have been efficiently transported over distances greater than one meter in wall-stabilized current-carrying plasma channels. Ion beams are allowed to ballistically focus in a neutral gas background so that a fully current neutralized beam is injected into the plasma channel, which begins at the ion focus. Channel diameters of 1.6 cm and 4.5 cm have been studied with channel gas pressures in the range .2-2 Torr. Efficient transport has been observed except above a well defined channel current in the 1.6 cm channel, indicating possible instability. The primary diagnostic has been the observation of gamma rays from nuclear reactions in fluorine targets. The detailed analysis of these data will be presented in the following paper. Continuing experiments will be discussed.

*Work supported by the Department of Energy.
†JAYCOR, Inc., Alexandria, VA 22304

6D3 Analysis of Proton Transport Experiments with a Prompt Gamma Diagnostic.* F. C. YOUNG, F. L. SANDELF, S. J. STEPHANAKIS, P. G. BLASNERT, F. W. OLIPHANT, G. COOPERSTEIN, S. A. GOLDSTEINT, and D. MOSHER, Naval Research Laboratory.--The time variation of the current of intense bursts of protons has been determined by detecting prompt gamma rays from the $^{19}F(p,\alpha\gamma)^{16}O$ reaction. Detectors have been absolutely calibrated to measure Amperes of protons provided the proton energy is known. Measurements with this diagnostic on the transport experiments described in the previous talk were analyzed to evaluate proton currents and transport efficiencies. The dependence of these measurements on proton energy losses due to resistive and inductive effects in the diode and proton deceleration due to the return current electric field will be discussed. For energy losses of a few hundred keV, peak proton currents of ~0.3 MA are focussed and transported 1 meter with ~50% efficiency.

*Work supported by the Department of Energy
†JAYCOR, Inc., Alexandria, VA 22304

6D4 Self-Consistent Plasma Channel Response to Propagating Ion Beams. D. G. COLOMBANT, S. GOLDSTEIN,* D. MOSHER, and W. MANHEIMER, Naval Research Lab.--Results have been presented previously[1] for the radial plasma channel response to the passage of a 0.2-1 MA/cm^2, 2-5 MeV proton beam. In those studies, the beam current density was assumed to be known as a function of space. In reality however, the beam current spacial distribution depends on the evolution of the electric and magnetic fields in the channel. The current distribution is now obtained by following ion orbits in these macroscopic fields determined from the MHD equations. It is then used as a driving source term in the MHD equations. Typical cases will be presented. Beam rippling effects will be discussed as well as comparisons with solutions obtained in ref. 1.

[1]D. Colombant, S. Goldstein, D. Mosher, IEEE Inc. Conf. Plasma Science, Montreal (1979), paper 4C4.
*Jaycor, Alexandria, Va.

2P10 A Scheme for Axial Bunching of Relativistic Electron Beams*. P. F. OTTINGER and SHYKE A. GOLDSTEIN, JAYCOR.--In a 1/r azimuthal magnetic field, produced by a current driven in a wire, electrons propagate axially by gradient B drift. Since this gradient B drift velocity, $v_{\nabla B}$, is proportioned to β^2, axial current bunching can be achieved by appropriate ramping of the diode voltage waveform. In order to reduce the spread in drift velocities due to a dependence of $v_{\nabla B}$ on v_z, the pinched beam is allowed to expand radially in a narrow gas-filled gap before entering the drift region. In this way azimuthal motion in the beam is reduced and substantial axial bunching is possible. Other electron drift motions will be discussed and conditions for their neglect will be presented. Conditions for efficient beam injection into the magnetic field drift region will also be discussed as well as other factors which affect transport and bunching of the beam.

*Work performed at Naval Research Laboratory

4C1 Final Focusing of an Intense Ion Beam Following Transport Through a Z-Discharge Plasma Channel.* P. F. OTTINGER†, SHYKE A. GOLDSTEIN†, and D. MOSHER, Naval Research Laboratory. -- Megampere-level light-ion beams appropriate for inertial confinement studies have been generated and focused down to square-centimeter areas.[1] Presently, experiments are underway to study transport and time-of-flight bunching of these focused beams in z-discharge plasma channels.[2] Ions are radially confined by the azimuthal magnetic field produced by the channel current established on a microsecond time scale. For uniform current densities in the channel and small injection angles (e.g. $\alpha \lesssim 0.2$ rad), the beam ions follow nearly sinusoidal betatron orbits in the r-z plane. Bunching is achieved by proper shaping of the diode voltage waveform such that ions generated late in the pulse catch up to ions generated early in the pulse over 2-5 meter channel lengths.[3]

On exiting the channel, the beam must be delivered to a target. Here, a scheme which passes the beam through a short final focusing section is evaluated. Focusing is achieved by increasing the channel current from I_0 to I_1 over the last few centimeters of the transport channel before radially extracting the channel current. As the ion beam propagates forward into the field-free region, the beam will continue to pinch down for a short distance before expanding. Such a scheme containing a final focusing stage is of interest since it allows one to transport beams in a larger radius channel and thus reduces the plasma density (i.e. inertia) required to prevent rapid radial expansion of the channel due to $\underline{J}_0 \times \underline{B}$ forces. Lower plasma densities, in turn, mean less beam energy is lost in traversing the channel. Also, the beam current that can be propagated scales* as r^2 and thus one gains in current density using larger channels.

First, we will consider the matched beam case (i.e. $V_0 \alpha_m / r_s \omega_\beta = 1$), which corresponds to the case where beam rippling near the front of the transport channel does not occur. Here, V_0 is the beam velocity, ω_β is the betatron frequency and r_s and α_m are respectively the beam spot size and the maximum ion injection angle. For a monoenergetic matched beam, the additional channel current, $I_1 - I_0$, should be introduced a distance $(\pi r_s / 4\alpha_m)(I_0/I_1)^{\frac{1}{2}}$ from the end of the channel. The beam ions, following betatron orbits in the now enhanced magnetic field, will begin to pinch down. Upon exiting the channel, focusing continues for a distance $(r_s/\alpha_m) \times (I_0/I_1)^{\frac{1}{2}}(I_1-I_0)/(I_1+I_0)$ before the beam begins to expand in the field-free region. This will be the ideal target position with the minimum beam radius given by $(r_b/r_s)^2 = 2I_0/(I_1+I_0)$. Results will also be presented for a bunched beam with an appropriate distribution of ion energies.

*Work supported by U.S. Department of Energy.
†Present address: JAYCOR, Inc., Alexandria VA 22304

[1] G. Cooperstein, S. A. Goldstein, D. Mosher, W. F. Oliphant, F. L. Sandel, S. J. Stephanakis, and F. C. Young, in Proceedings of the 3rd International Topical Conference on High Power Electron and Ion Beams Research and Technology, Novosibirsk, USSR, 1979, (to be published).
[2] D. Mosher, G. Cooperstein, S. A. Goldstein, D. G. Colombant, P. F. Ottinger, F. L. Sandel, S. J. Stephanakis, F. C. Young, in Proceedings of the 3rd International Topical Conference on High Power Electron and Ion Beam Research and Technology, Novosibirsk, USSR, 1979 (to be published).
[3] P. F. Ottinger, D. Mosher, S. A. Goldstein, to be published in Phys. Fluids.
[4] D. Colombant, et al, these proceedings.

4C1 Scaling Laws for Ion Beam Losses in Plasma Channels. D. G. COLOMBANT and SHYKE A. GOLDSTEIN,*, Naval Res. Lab.--Plasma channels have been proposed for the transport of light ion beams from their sources to the target through a gas blanket medium. These channels are formed by a gas discharge in a dense gas and the channel current gives rise to an azimuthal magnetic field which provides the initial confinement for the beam light ions. Starting right after beam injection, the channels expand radially and electromagnetic fields develop inside the channel.

Ion beam energy losses occur because of electric fields which develop inside the channel and beam intensity losses occur because of changes in the initial magnetic field structure.

The electric field inside the channel has three main components: resistive, hydrodynamic and the equivalent field due to collisional slowing-down of the beam ions. Estimates for the magnitude of these various components will be given and their implication for transport of the beam discussed. In particular, an optimum density for the channel density will be determined from these considerations.

Changes in the magnetic field inside the channel are due mainly to convection with the plasma channel. Estimate of these changes will be made and their effects on the deconfinement of the ion beam discussed. Limits of applicability of the various scaling laws derived will also be presented.

* JAYCOR, Alexandria, Va. 22304.

4C2 Particle Beam Acceleration in Magnetized Moving Plasma*. SHYKE A GOLDSTEIN and DEREK A. TIDMAN, JAYCOR, Inc., Alexandria, VA -- When magnetized plasmas flow in converging geometries (such as a z-pinch) they generate a combination of $\underline{E}$, $\underline{B}$ field structure that acts on the majority of the plasma particles (trapped, low energy) in a self-consistent manner of current and space charge distributions. These fields will, however, act differently on a component of beam particles that are untrapped. A very fast process of energy delivery from the heavy, slow plasma to the beam component will take place when the plasma converges. The inverse is true for plasma expansion. The relevant length and time scales for laboratory plasmas and astrophysical plasmas will be discussed. These include the possibility of a new accelerator scheme to accelerate currents of 10^5-10^6 A (electrons or ions) to very high energies. Structure of needed plasmas in order to provide beam emittance cooling will be discussed.

*Part of the NRL Light Ion Beam work supported by the U.S. Department of Energy.

4F 16 Intense Proton Beam Transport in Fast Z-Pinch Plasma Channels.* F.L. SANDEL†, F.C. YOUNG, S.J. STEPHANAKIS, W.F. OLIPHANT, G. COOPERSTEIN, SHYKE A. GOLDSTEIN† and D. MOSHER, Naval Research Laboratory.--Continuing experiments in intense proton beam transport have concentrated on propagation in wall-stabilized plasma channels consisting of Z-pinches formed on a time scale (500 ns) an order-of-magnitude faster than in previous experiments.[1] Using this new system, efficient transport of up to 400 kA of proton current has been observed in channels of 1.6, 2.5 and 4.5 cm diameter over distances up to 1.5 m. Careful analysis of prompt-γ signals from fluorine targets in the channel indicates minimal particle and energy losses within the channel but has uncovered as yet unexplained proton energy losses in the diode and focusing regions. Present experiments on transport in longer channels and new channel diagnostics will be discussed.

*Work supported by the Department of Energy.
†JAYCOR, Inc., Alexandria, VA 22304
[1]F.L. Sandel, et al., Bull. Am. Phys. Soc. 24, 8, 1031 (1979).

4F 13 Effects of Off-Center Injection on Intense Ion Beam Transport in Z-Discharge Channels.* P.F. OTTINGER,† SHYKE A. GOLDSTEIN,† and D. MOSHER, Naval Research Laboratory.--In order to deliver an intense light ion beam to a target, a z-discharge channel can be used for transporting the beam. The ions are confined radially by the azimuthal magnetic field in the channel. If the beam is injected on-center and parallel to the axis, transport is azimuthally symmetric and stable. Non-parallel or off-center injection, however, may lead to both particle losses and unstable transport. Results will be presented which will relate the severity of these problems to the extent of the nonparallel or off-center injection. Effects on beam bunching and on the radial profile of the beam current density in the channel will also be discussed.

*Work supported by the Department of Energy
†JAYCOR, Alexandria, VA 22304

4F 1 Optimization of Light Ion Beam Energy Flux in Low-z Plasma Channels. D. G. COLOMBANT and SHYKE A. GOLDSTEIN*, Naval Research Lab.---Overall transport efficiency of ion beams in channels can be defined as the product of energy and current density transport efficiencies in the channels. The energy transport efficiency is relatively easy to determine using binary stopping power and E-fields generated in the channel. Current density efficiency is related to the decrease in confinement and is not as easily calculated. Attempts at formulating current density efficiency will be described based on changes in magnetic field profile in the channel. Consequencies for overall transport efficiency will be discussed.

*Jaycor, Alexandria, VA 22304

7R 17 Post-Transport Propagation and Expansion of Intense Light-Ion Beams.* F.L. SANDEL†, S.J. STEPHANAKIS, D. MOSHER, and P.F. OTTINGER†, Naval Research Lab.--Intense proton beams (1 Mev, 50 ns) extracted from pinch-reflex diodes and self-focused to 30-50 kA/cm^2 have been confined in wall-stabilized z-discharge channels and efficiently transported up to 5 m. Recently the propagation and expansion of beams exiting the channel into a field-free, 1 Torr pressure drift space have been studied. The exiting beams have excellent axisymmetry and uniformity with no evidence of filamentation. Time-integrated and time-resolved photography of beam-channel and target blow-off plasma, along with witness-target damage and beam imaging techniques were used to compare the experimental properties of exiting beams with computations of the transported-beam distribution function and ballistic orbits. Both experiment and theory show a dependence of the post-transport expansion on the channel current. Theoretical considerations also emphasize the importance of the radial current distribution on beam expansion, which is controlled by proper plasma engineering in the experiments.

*Work supported by DOE and DNA
†JAYCOR, Inc., Alexandria, VA 22304

4E 3 Final Focusing of Intense Transported Ion Beams* P.F. OTTINGER†, D.G. COLOMBANT, SHYKE A GOLDSTEIN†, R.A. MEGER†, and D. MOSHER, Naval Research Laboratory--Intense light-ion beams appropriate for ICF studies can be individually transported to a common target in wall stabilized z-discharge channels. With voltage ramping transport also permits beam bunching. Hydrodynamic and stability constraints associated with transport are considerably relaxed if the beam is transported with a radius a few times larger than the pellet radius (~ 0.5). A final focusing element consisting of a short (~ few cm), high-current (~ 100-200 kA), tapered z-discharge cell could then radially compress the beam to pellet dimensions after transport. Beam focusing is achieved at the expense of increased angular beam divergence. Detailed calculations of final focusing cells will be presented including studies of the effects of focusing geometry for injection into the transport system, and the βg-distribution in the transport channel and focusing cell. The βg profiles are obtained from MHD code modeling of z-discharges for various gas fill pressures.

*Work supported by the Defense Nuclear Agency and the Department of Energy.
†JAYCOR, Inc., Alexandria, VA 22304

4E 4 Proof-of-Principle Experiments for an Ion Beam Final-Focusing Cell.* R.A. MEGER†, SHYKE A. GOLDSTEIN†, P.F. OTTINGER†, D. MOSHER, S.J. STEPHANAKIS, F.C. YOUNG, Naval Research Laboratory -- An experiment using an ion beam final-focusing cell is being fielded on the NRL Gamble II accelerator. The design is based on modeling of ion beams extracted from pinch-reflex diodes injected into various focusing cells.[1] An increase in peak current density of at least a factor of four is predicted for the experimental parameters. The focusing cell consists of a z-discharge plasma channel tapered from a 4-cm dia. entrance aperture to 1 or 2-cm dia. over an 8-cm length. Up to 100 kA discharge currents will be driven in the channel. Witness plates and shadowbox techniques will be used to diagnose beam focusing and x-ray diode measurements of Au-target foil radiation and Al K-alpha x-ray imaging will be used to determine focused current density.

*Work supported by the Department of Energy and the Defense Nuclear Agency
†JAYCOR, Inc., Alexandria, VA 22304
[1]See previous abstract

4E 2 Measurements of the Stopping of Deuterons in Hot Dense Plasmas.* F. C. YOUNG, S. J. STEPHANAKIS, SHYKE A. GOLDSTEIN†, and D. MOSHER, Naval Research Lab. The stopping power of deuterons in hot dense plasmas is being measured using neutron time-of-flight (TOF) with thin layered targets.[1] Intense beams of 1-MeV deuterons are focused onto subrange thick targets consisting of a stopping foil coated on the front and rear with a thin layer of CD_2. The TOF of the neutrons from these two targets is used to determine the deuteron energy loss in the stopping foil which is heated by the focused ion beam (~ 50 kA/cm^2). Preliminary results indicate that the stopping power is enhanced compared to that of a cold solid target. Alteration of the stopping power is expected when the stopping medium contains a significant ratio of free-to-bound electrons. This ratio may be changed experimentally by using different current-density beams or stopping foils of different atomic number. The results of such experiments will be presented and compared.

*Work supported by the Defense Nuclear Agency.
†JAYCOR, Inc., Alexandria, VA 22304
[1]F. C. Young, S. A. Goldstein, S. J. Stephanakis and D. Mosher, IEEE Int. Conf. On Plasma Science, Santa Fe, NM, May 1981.

2C5 Analysis of the Hose Instability for Intense Ion Beams Transported in Z-Discharge Channels.*
P. F. OTTINGER† and SHYKE A. GOLDSTEIN†, Naval Research Laboratory -- In order to deliver an intense light ion beam to a target, a z-discharge channel can be used for transporting the beam. The B_θ field generated by the net current in the channel (~ initial channel current) provides for radial confinement of the beam. Such a system may be unstable to growth of hose-like perturbations. Both the self-hose and the resistive hose mechanisms can play important roles. The self-hose mechanism results from the repulsion between the beam current and the oppositely directed return current, whereas the resistive hose mechanism results from the resistive phase lag between oscillations of the beam and magnetic axis. Since off-center injection of the beam into the channel can lead to a finite initial perturbation[1], growth of the mode on the beam time scale could disrupt transport. Results will be presented from a stability analysis of the beam-plasma system including the effects of conducting walls, radial motion of the channel plasma, perturbations of the channel conductivity and beam velocity spread. Each of these effects will be discussed independently in order to clearly determine how each alters the behavior of the mode. Conditions for good beam transport will be identified from these results and compared with other transport constraints.[2]

*Work supported by the Department of Energy
†JAYCOR, Alexandria, VA 22304
[1]P.F. Ottinger, S.A. Goldstein and D. Mosher, Bull. Am. Phys. Soc. 25, 900 (1980).
[2]D. Mosher, D.G. Colombant and S.A. Goldstein to be published in Comments on Plasma Physics and Controlled Fusion.

4C5 Modular System Requirements for Light- or Inertial-Confinement Fusion.*, D. MOSHER, Naval Research Laboratory, P.F. OTTINGER, Jaycor, Inc. -- A modular approach to light-ion ICF employs a large number of multi-TW pulsed-power generators driving individual ion diodes. The diodes are designed to focus the beams into 1-cm dia. z-discharge plasma channels which transport them several meters to the vicinity of the pellet. By ramping the accelerating-voltage pulse, the transporting beams are bunched from the ~ 40 ns generator pulse to ~ 10 ns pellet-driver times.

A range of acceptable modular system parameters has been defined[1] by combining constraints associated with focusability, transport, MHD-channel response[2], beam-target overlap and deposition. Here the analysis is

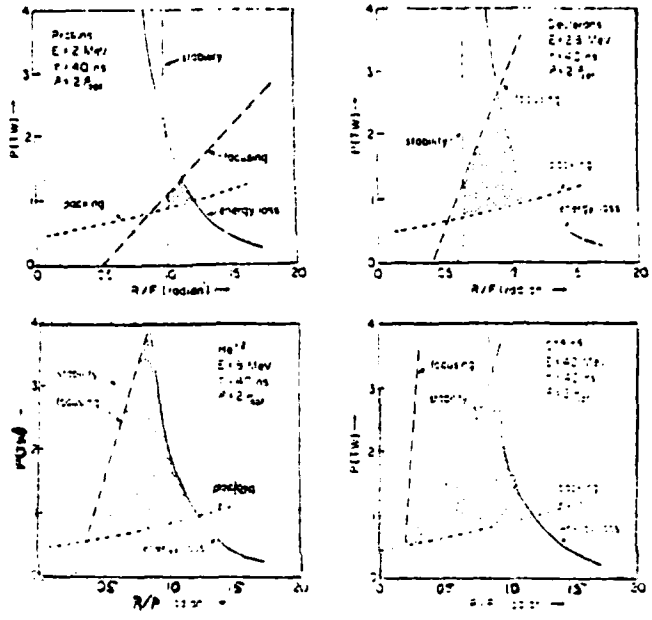

refined by including stability effects[3] and cathode-foil scattering. Collisional stabilization of beam-plasma two-stream modes requires a factor-of-two increase in channel density above that desired for minimum beam energy loss during transport. The shaded region in the figures indicates the parameter space which satisfies the full set of constraints. The quantity P is the modular-beam power at the diode and R/F (the ratio of anode radius to focal length) is the maximum ion injection angle into the transport channel. The beam divergence for focusing from R to spot radius r_s is determined from $\delta\theta = 2\,(r_s/R)(R/F)$ so that multi-TW focusing diodes must achieve $\delta\theta \leq .02$ radian. Diodes with poorer focusing qualities may be adequate if the transporting-beam energy-loss constraint can be relaxed using dynamically-imploding channels[4] rather than those which are static at the time of beam injection.

*Supported by the Defense Nuclear Agency and the Department of Energy
[1]D. Mosher, D. G. Colombant, and Shyke A. Goldstein, Comments in Plasma Physics 6, No. 3 (1980).
[2]D. G. Colombant, Shyke A. Goldstein and D. Mosher, PRL 45, 1253 (1980).
[3]P. F. Ottinger, D. Mosher and Shyke A. Goldstein, Phys. Fl. 22, 332 (1979) and 24, 164 (1981).
[4]Shyke A. Goldstein and D. A. Tidman, Proc. IEEE International Conf. on Plasma Sci., May 1980, Madison, WI, p. 96. Also, D. G. Colombant, these proceedings.

4C3 Determination of the Stopping of Intense Deuteron Beams in a Plasma.* F. C. YOUNG, SHYKE A. GOLDSTEIN†, S. J. STEPHANAKIS, and D. MOSHER, Naval Research Laboratory — The stopping power of intense ion beams in a plasma target may differ significantly from the stopping power of single particles in a cold target. As the plasma is heated, the number of free electrons in the plasma increases, thereby altering the energy loss of energetic ions in the plasma. For high current density beams, the overlap of wakes that single ions generate in the plasma may result in enhanced stopping. The increased stopping power expected under these conditions may produce energy deposition profiles different from those previously assumed for intense ion-beam drivers of inertial-confinement-fusion targets. In this presentation, a technique for measuring the energy loss of intense deuteron beams in heated plasmas will be presented. Also, the results of feasibility experiments and preliminary energy-loss measurements will be described.

The technique is based on using neutron time-of-flight (TOF) with the $d(d,n)^3He$ reaction to determine the deuteron energy. An intense burst of 1 to 2 MeV deuterons is focused to 10^2 to 10^3 kA/cm^2 onto a sub-range layered target. The target consists of a stopping foil which is coated on front and rear with a thin layer of deuterated polyethylene (CD_2). The TOF of neutrons from these two CD_2 targets is used to determine the deuteron energy loss in the stopping foil which has been heated by the intense ion beam.

This technique has several attractive features. 1)Because neutron signals from the two CD_2 targets can be separated by TOF, the energy loss can be measured with only one shot. 2)If the deuteron energy loss increases in the heated plasma (as expected), the neutron signals will be easier to resolve because their separation in time will increase. 3)Contributions to the neutron signals from the low intensity outer region of the beam are reduced because the neutron output scales with the deuteron intensity. 4)Finally, the ratio of neutron yields from the two CD_2 targets can provide an independent determination of the energy loss if the thickness of these two targets is known.

Feasibility experiments with layered targets have been carried out on the Gamble II generator at NRL. The interaction of a deuteron beam with a 1.3-μm thick CD_2 target has produced a neutron TOF pulse of 30 ns FWHM, which is characteristic of the duration of deuteron emission from the ion diode. For such pulse widths, neutron signals from CD_2-layered targets can be resolved for stopping-foil thicknesses corresponding to several hundred keV energy loss. The results of preliminary experiments with such CD_2-layered mylar targets will be discussed.

*Work supported by the Defense Nuclear Agency
†JAYCOR, Inc., Alexandria, VA 22304

4C4 Plasma Channels for Transport of Intense Ion Beams.* F. L. SANDEL, JAYCOR, Inc., Alexandria, VA 22304 — Experiments have been performed[1-3] at the Naval Research Laboratory on the Gamble I and Gamble II generators which have demonstrated efficient transport of proton beams of intensities of up to 50 kA/cm^2. The media for beam transport have been wall-stabilized plasma channels preformed by capacitor bank discharges of ~ 50 kA in 1-2 T of gas. Channels are formed in a compact, low inductance coaxial geometry with the discharge struck along an aluminum oxide insulating liner. Methods of channel coupling have been developed and tested to allow future construction of long modular transport systems.

Transport has been studied in channels of 1.6 cm to 4.5 cm dia. and over distances of 2.5 m. Since the dynamic state of the channel (which is in actuality a long z-pinch) may be extremely important to the transport process[4], recent work has been expanded to include detailed study of the plasma physics of the channels. Ultimately a complete picture of plasma current, density, and temperature profiles and plasma conductivity in the channels is anticipated. First efforts have concentrated on examining the time dependent magnetic field structure of the channel over a wide range of fill pressures and capacitor bank voltages. The z-pinch implosions have been found to be remarkably reproducible and symmetric without resort to preionization or precise mechanical tolerances.

For sufficiently intense ion beams, a strong channel response is expected. In experiments to date, beam passage has had only minor effects on the channel properties. These measurements are being continued with improved diodes which allow ion beams of higher intensity to be injected into the channels.

*Work performed at the Naval Research Laboratory and supported by the Department of Energy
[1]F. L. Sandel, et al, Bull. Am. Phys. Soc. 24, 8, 1031 (1979).
[2]F. C. Young, et al, Bull. Am. Phys. Soc. 24, 8, 1031 (1979).
[3]F. L. Sandel, et al, Bull. Am. Phys. Soc. 25, 8, 900 (1980).
[4]D. C. Colombant, et al, these proceedings.

4A8 Stability Constraints on Transported Light-Ion Beams.* P. F. OTTINGER†, D. MOSHER AND STEVE A. GOLDSTEIN†, Naval Research Laboratory, Washington, DC 20375--Intense light-ion beam transport in z-discharge channels provides accelerator standoff from ICF targets and allows time-of-flight bunching of the beam to higher intensity. Stability constraints combined with channel expansion and beam-energy loss constraint define an operational window for ion transport. The stability constraints are derived from the requirement to avoid significant growth of the electron-beam ion two-stream instability, the beam-filamentation instability and the channel-filamentation instability.[1] The channel-expansion constraint result from demanding that the $J \times B$-driven radial expansion of the channel occurs on a time scale longer than the beam-pulse duration.[2] Finally, the beam energy-loss constraint requires that no more than 25% of the beam energy is lost during transport.

The constraints have been derived for arbitrary beam-ion species in order to evaluate the advantages of higher-atomic-weight ions. The beam energy, beam radius and channel density are also free parameters which have been varied in order to determine their effects on the operational window. In all cases, the channel gas was taken as deuterium. This allows the use of a simple model for channel heating and has the advantage of reduced radial acceleration due to the passing beam at the same stopping-power as hydrogen.

Results for beams of H^+, O^+, He^{+2} and C^{+2} will be presented which show that a larger operational window exists for the higher-atomic-weight species. This is a consequence of their lower currents at equivalent transported power levels. Lower currents relax the filamentation constraints thereby allowing stable transport of lower-angular-divergence, i.e. higher brightness, beams. Raising the channel density above the optimum for minimum beam-energy loss during transport relaxes the two-stream and channel-filamentation stability constraints and the channel-expansion constraint while only slightly modifying the energy-loss constraint. Increasing the beam radius relaxes the two-stream stability constraint and considerably reduces the channel-expansion and beam energy-loss constraint. This results from the reduced $J \times B$ forces and smaller MHD-generated axial electric fields which are present when the beam current is spread over a larger area. All constraints are relaxed for a higher particle-energy beam because of increased stiffness and lower current. Target-deposition requirements limit the particle-energy range useful for different ion species.

It is determined that multi-terawatt beams can be transported a few meters in large-radius channels. If time-of-flight bunching during transport and final focusing after transport are employed, less than 10 (and as few as 4) channels are required to deliver the power needed to ignite a pellet.

---

* Work supported by the Defense Nuclear Agency and the Department of Energy, Washington, DC

† Present address: SAYCOR, Inc., Alexandria, VA 22304

1 P. F. Ottinger, S. A. Goldstein and D. Mosher, NRL Memo Report 4548, July 1981.

2 D. Mosher, D. G. Colombant and S. A. Goldstein, Comments Plasma Physics, 6, 101 (1981).

3A3-4 INVITED PAPER

Some Theoretical Aspects of Light Ion Beam Transport in Z-Discharge Channel*. P. F. OTTINGER, JAYCOR, Alexandria, VA -- The use of light ion beams for inertial confinement fusion has recently drawn a great deal of interest. Target designs for light ion beam drivers call for delivery of several megajoules to a centimeter diameter pellet on a 10 ns time scale in order to achieve high-gain thermonuclear ignition. Present pulsed-power technology can provide 10 TW generator modules, each capable of delivering 300 kJ of light ions in 50-100 ns. Thus, a large number of modules and the means to transport energy from these modules onto the pellet are needed. Additionally, compression of pulses to the pellet-implosion time scale is required.

One method for transporting ions involves the injection of focused ion beams extracted from self-insulated pinch-reflex ion diodes into z-discharge transport channels. During transport, time-of-flight bunching of the beam, produced by ramping the accelerating-voltage waveform, can compress the pulse to the pellet-implosion time scale and enhance the beam power. Additional power density multiplication can also be obtained from radial compression of the beam by tapering the channel. Here, some theoretical aspects of light ion beam transport in such z-discharge channels will be discussed. In particular two problem areas will be addressed: (1) possible growth of plasma modes driven unstable by the relative streaming motion of the different plasma species and the beam, and (2) the effects of non-ideal channel structures on beam propagation. The limits set by these considerations on beam focusing, transport and bunching will be of primary interest.

Results from micro-stability analysis for both electrostatic and electromagnetic modes will be presented which show that channel parameters can be chosen which allow beam transport without fast electrostatic wave growth. Slower growing electromagnetic instabilities probably will occur and could lead to plasma current filamentation that could affect the tail of the beam. The extent of this filamentation and the effects it will have on ion beam propagation will be discussed.

Beam propagation in an ideal channel will be described and compared with propagation in non-ideal channels. For an ideal channel $B_\theta \sim r/r_c$ and the channel radius, r_c, does not vary with axial position. If the channel is subject to sausage type instability $[r_c = r_c(z)]$ before beam injection, then radial expansion of the beam can result. The extent of this beam expansion will be discussed as a function of the wavelength and level of bumpiness in the channel. The effects on beam propagation of steeper magnetic field gradients ($B_\theta \sim (r/r_c)^n, n>1$), and small electric fields will also be considered. These fields arise due to the MHD response of the channel to beam passage.

The constraints that will be discussed indicate that ion current densities of 1 MA/cm^2 can be focused and transported in each arm of a modular light ion ignition system. New plasma techniques, which may allow higher current-density transport, include imploding z-pinches[1] and a final focusing stage[2].

*Work supported by U.S. Department of Energy as part of the Naval Research Laboratory Light Ion Beam Program.

[1] S. A. Goldstein and D. Tidman, these proceedings.
[2] P. F. Ottinger, S. A. Goldstein and D. Mosher, these proceedings.

7A 2 Intense Light-ion Beam Transport in Z-discharge Plasma Channels.* F. L. SANDEL, *JAYCOR, Inc., Alexandria, Va.*

For several years the Naval Research Laboratory has studied methods of transporting intense light-ion beams. This work was motivated by the need to a) provide standoff protection for the ion diode(s) b) allow close packing of multiple generators around a common target chamber and c) facilitate time-of-flight bunching of the ion beam. The most successful efforts have used a wall-stabilized Z-discharge plasma channel for transporting focused ion beams.[1] The channel plasma provides for charge and current-neutralization of the beam which is therefore confined in the channel by the azimuthal magnetic field generated by the externally applied channel current. Beams of up to 400 kA total current and up to 50 kA/cm^2 current density have been transported in such channels with essentially no particle loss and only the expected classical particle energy losses. Adoption of a modularized channel configuration has permitted beam transport over distances up to 5 meters. Recent work has included study of the plasma physics of the channel itself and the effect of channel transport on beam quality and brightness. Theoretical work has considered the stability of the beam-channel system and the modification of the channel by the very intense beams during beam passage. Predicted beam intensity levels for strong beam-channel interaction are sufficiently high so that strong interactions are not expected in current experiments or in anticipated modular system designs. Observations of post-transport field-free propagation and expansion of the beam, showing no degradation of beam quality, agree well with theoretical predictions. Continuing and future work beam transport and handling will also discussed.

*Work performed at the Naval Research Laboratory and supported by the Department of Energy and Defense Nuclear Agency.

[1]F. L. Sandel, et al. Proc. 4th Int. Topical Conf. on High-Power Electron and Ion Beam Research and Technology, Palaiseau, France, July 1981.

2C3-4 INVITED PAPER

Hydrodynamics of Fast Z-Pinches Interacting with Propagating Ion Beams*, D. G. COLOMBANT, SHYKE A. GOLDSTEIN†, D. MOSHER and F. L. SANDEL†, Naval Research Laboratory -- The propagation of intense ion beams in plasma channels has a drastically-different character when the plasma medium is a fast z-pinch rather than a diffuse slow pinch at the time of beam injection. In both cases, the ion beam is magnetically confined and can propagate several-meter distances. The ion currents that can propagate and the energetics of the beam-plasma system are, however, different. The fast-imploding pinch can transfer energy to the ion beam via an MHD-induced electric field and its radial momentum delays expansion due to beam pressure so that longer ion-beam pulses can propagate. The diffuse z-pinch expands when the ion beam is injected into the plasma and the expansion produces an electric field which retards the beam. The expanded channel reduces the propagated current density.

A detailed analytic analysis of the diffuse pinch sets limits on the ion beam current and pulse duration which can be propagated. The analysis predicts optimized densities for the background plasma to be used for a given ion beam. Fast z-pinch formation prior to beam injection is studied with an inductive model that couples the capacitive energy store to a radiating, imploding plasma. The results are compared to ongoing pinch experiments. Using an MHD model[1] of the beam-plasma system, an ion beam is injected into the plasma and the dynamic response is determined numerically. Regimes of ion beam acceleration are thus predicted. The detailed structure of the plasma fields will be presented and contrasted with simple analytic theory[2] of ion-beam acceleration in imploding z-pinches. Preliminary experimental data[3] indicating ion beam acceleration will be compared to the theoretical predictions.

*Work supported by the Defense Nuclear Agency and the Department of Energy

†JAYCOR, Inc., Alexandria, VA 22304

[1]D. G. Colombant, Shyke A. Goldstein and D. Mosher Phys. Rev. Lett., 45, 1253 (1980).

[2]Shyke A. Goldstein and Derek A. Tidman, IEEE Int. Conf. on Plasma Sci., 4C2, 96 (1980).

[3]F. L. Sandel, et al, Bull. Am. Phys. Soc. 25, 900 (1980).

PROPAGATION OF RELATIVISTIC ELECTRON BEAMS IN CURRENT-CARRYING PLASMA CHANNELS

I. INTRODUCTION:

The propagation of relativistic electron beams in plasma channels has, in the last decade,[1-7] received considerable interest due to its applications for energy transfer and pellet fusion. A rough division of this effort may be made by characterizing the electron beam as hot or cold. In both cases, the relativistic electron beam propagates in a plasma having a self-consistent azimuthal magnetic field which confines the electrons radially. The necessary magnetic field for hot beam (electrons injected with a large mean angle) propagation is given by Alfvén's treatment of electron orbits which yields the condition that the net current inside the beam radius must be in the same direction as the beam current and nearly equal to the Alfvén current for the energy of the relativistic electrons

$$I_{CH} \simeq I_A = \frac{mc^3}{e} \left(\gamma^2 - 1 \right)^{\frac{1}{2}} = 17(\gamma^2-1)^{\frac{1}{2}} \text{ kA} \qquad (1)$$

On the other hand, for relatively cold beams (mean angle of injection, $\theta << 1$), the same treatment indicates that the current needed is only

$$I_{CH} \simeq (1 - \cos\theta)\, I_A \simeq \frac{1}{2}\theta^2 I_A \qquad (2)$$

In order to propagate 1 MeV electrons with a 10° mean injection angle, one needs only about 1 kA of net current in the channel compared to the 50 kA of net current needed for hot beam propagation.

Manuscript submitted July 16, 1980

For typical beam currents of a few hundred kiloamperes injected into plasmas at densities of the order of 10^{18} cm^{-3}, the return current induced in the plasma is nearly equal to the primary beam current leaving net currents of the order of 1% of the beam currents. The remainder of the return current flows outside of the beam radius. The resulting net current of a few kiloamperes within the beam radius is sufficient to propagate relatively cool beams (as discussed above) but is insufficient for the propagation of a hot beam. Other means for providing the needed net current must therefore be utilized for hot beam propagation. Historically, these included Z-pinch plasmas[5], and axial discharges via exploding wires.[6,7]

In the present work, we describe an experimental and theoretical study into the physics of the propagation of hot beams in plasma discharges driven by an exploding wire. Our work is an extension of previous work at Sandia[6,7] into a regime of higher beam currents (up to 300 kA injected) and investigating the effect of channel current and diode voltage on beam propagation. In the theoretical study, we investigate the effects of scattering and axial electric fields on electron orbits as well as the limitations on the maximum beam current and beam current density that can be propagated.

II. EXPERIMENTAL APPARATUS AND OBSERVATIONS:

The experimental results of the present work were obtained on the GAMBLE I (300 kV, 220 kA, 80 ns FWHM) and GAMBLE II (1000 kV, 420 kA, 50 ns FWHM) electron beam facilities. A schematic of the experimental apparatus is shown in Figure 1. An 84/39 mm (C.D./I.D.)

was used. The anode was a 1.5 mm thick brass plate with a 20 mm diameter hole on axis. The hole was beveled at 30° on the cathode side and sanded to provide a smooth transition region for the radial electron flow. The hole was covered with a 25 μm titanium foil which was both ground plane and vacuum window. Immediately behind this was mounted a 20 μm aluminum foil on which a 51 μm tungsten wire was affixed. The wire was stretched in air from the center of the foil through the aluminum target plate, located 30 to 64 cm away, to a 56 μf, 2.4 μh (total circuit inductance), 20 kV capacitor bank. A "squirrel cage" of aluminum rods and rings served as a symmetric current return for the channel current. This bank could drive a peak current of 50-80 kA (occurring approximately 15 μs into the pulse) in an air plasma surrounding the wire.

The experimental diagnostics included diode voltage and current monitors; time integrated hard x-ray pinhole cameras looking at the anode, plasma channel, and target; open shutter visual photography of the channel; time resolved, calibrated x-ray p-i-n diode detectors; and $\int \dot{B}_\vartheta$ and Rogowski coils monitoring the channel current. In addition, a depth dose stack utilizing thermoluminescent detectors were used to obtain the peak kinetic energy of the transported electrons.

Streak camera measurements of the plasma channel over the times of interest allowed us to determine the channel radius at the time of beam injection. This was verified by the time integrated x-ray photographs of the channel. The channel's resistance was measured by the shift of the frequency of the ringing channel current from its zero resistance value -- measured by replacing the wire with a 1.5 cm diameter, low resistance (< 500 μΩ) conducting rod -- and by the current

decay time. Using an average channel radius ($r \approx 1.6$ cm) allows one to estimate the channel's conductivity, $\sigma \simeq 2 \times 10^{14}$ s^{-1}, from which a temperature, $T \simeq 2$ eV, was inferred. These parameters are consistent with theory.[8] The chemical composition of the plasma channel is however unknown.

On GAMBLE I, the channel current was varied from about $\frac{1}{2} I_\alpha$ to $2 I_\alpha$, while the anode hole (which limited the maximum injection radius) was varied from less than to greater than the channel radius. Propagation was successful only when the channel and beam currents had the same direction, in agreement with the theoretical prediction. In addition, it also became obvious that a crucial element of the experiment was the diode-channel interface. It was observed that any asymmetrical magnetic field at the target location caused a distortion in the electron distribution at the target. The inference to a similar effect at the diode-channel interface is made even more important as any current feed assymetry at the diode-channel interface could result in stray magnetic fields in the diode which could affect not only the beam injection, but also the diode physics.

Table 1 documents some GAMBLE I shots. Shown are the peak diode voltage and current; the channel current and radius (determined from the beam injection time and the plasma expansion velocity - about 0.8 mm/μs - and confirmed by visual streak photography); the next column shows r_α, the radius which enclosed the Alfvén current; the final columns show the radius of front surface damage r_D, and the radius of the back surface spall r_s.

TABLE 1

Shot#	V(kV)	I(kA)	I_{CH}(kA)	r_{CH}(cm)	r_{α}(cm)	r_{D}(cm)	r_{s}(cm)
5693	700	230	80	1.6	1.1	1.1	--
5695	700	230	77	1.4	1.0	1.0	0.7
5700	800	220	68	1.6	1.2	1.2	0.9
5701	700	185	58	1.6	1.3	1.4	1.0
5903	510	205	42	1.4	1.2	1.2	0.8
5955	540	270	38	1.0	0.9	0.9	0.6

Figure 2 shows the diode voltage and current and the target x-rays for Shot 5700 on GAMBLE I. Thermoluminescent detectors allowed us to obtain an electron kinetic energy loss in the anode foil and plasma channel of 80 keV. Using this energy loss and the diode voltage gave the energy of the electrons striking the target. The collimated p-i-n detector looked at the central 3.5 mm radius of the target. From the electron energy and the p-i-n signal we calculate that at 70 ns it saw a current of 22 kA. Extrapolating the inferred current density out to the spall radius implied a propagated current of 145 kA. This is out of 195 kA of electron current in the diode (220 kA total diode current - 25 kA ion current computed using the Goldstein-Lee formula[9]) or a propagation efficiency of 74%.

On GAMBLE II, there was no parameter study done, rather the goal was to propagate a high beam current and beam current density. On four shots, calibrated x-ray p-i-n detectors indicate that more than 200 kA of electrons propagated in the channel. In addition, a fifth shot is believed to have propagated more than 200 kA based on a comparison of target damage with known shots.

On GAMBLE II, we also viewed the wire channel independently with another p-i-n detector. It indicated that an energy equivalent of less than 20 kA of electrons were lost in the plasma channel. This, however, is an upper limit as it assumed that the primary collisions occurred between the electrons and the $Z \approx 7$ plasma channel not the $Z \approx 74$ tungsten wire.

Figure 3 shows the diode voltage and current for GAMBLE II Shot 1799. In addition, the calibrated p-i-n signal is shown. Its peak signal corresponds to a current of approximately 160 kA. Since the p-i-n viewed only the center 5.3 mm radius, this indicates an average current density over this region of about 180 kA/cm^2. From the x-ray pinhole photograph, the area of the target x-rays (FWHM) was determined to be approximately 1.6 cm^2 and the total propagated current to be about 280 kA. This is out of a diode electron current of 330 kA (420 kA total diode current - 90 kA diode ion current) or an efficiency of approximately 85%. Two other shots gave propagation efficiencies over 50%, one of which had the p-i-n looking at the whole target plate and giving 255 kA.

As a final note, Figures 4 and 5 show the respective x-ray pinhole photographs for the shots described above. At the top of Figure 4 is a photograph taken with two different pinholes the lower providing greater resolution. (Since the wire itself appeared as a line source, the size of its image provided a measure of the resolution.) On the left, electrons striking the edge of the hole in the brass anode produced the annulus surrounding the x-ray image of the pinched beam passing through the titanium anode foil. In the top image, the x-rays produced by electrons in the plasma channel can be seen. The target is not seen. At the bottom of Figure 4 is a photograph taken with another pinhole camera which shows the entire system from left to right. Since the target was closer to the camera than the anode, the relative magnifications are different. On the left is

the anode with the inner halo corresponding to an end-on view of the plasma channel. At the center of the anode is an image of the injected pinched beam while at right can be seen the image of the electrons as they strike the target. Figure 5 shows the propagation of electrons for GAMBLE II Shot 1799. The circular ring around the target is pinhole shine-through while the crosshairs used for alignment are seen as an absence of exposure.

III. THEORETICAL CONSIDERATIONS:

The problem of relativistic electron flow in plasmas heated before beam injection has been treated at length in the literature.[10] Most of the treatments were concerned with the plasma current response to the injected beam current. Two effects were neglected.

First, the conducting plasma has a finite radius, outside of which there exist only low conductivity, cool air (theoretical models assumed high conductivity at all radii) and thus the total return current is forced to run in the conducting plasma due to the voltage increase on the target for the relativistic electron beam - this electrostatic effect was not included in previous theoretical work which included inductive effects only. The fact that the return current is forced to run in the plasma also explains why the $\dot{B}_\vartheta$ loop placed outside the plasma (in both our and the Sandia experiments) showed essentially zero current change during beam transport. There may be about 0.1% of the primary beam current going through the capacitor bank and the return current rods connected to the anode plane of the generator[11] but this is too small a current to be detected with the $\dot{B}_\vartheta$ loop in the present experiments.

Second, the hydrodynamics of the plasma has not received proper treatment. Usually magnetic fields are viewed as confining fields because of the pressure tensor. In the case of beam injection into a plasma however, while the beam particles are confined by the magnetic field, the plasma is pushed outwards. The reason is that the return current set up in response to the injected beam is negative so that the $\underset{\sim}{j}_{plasma} \times \underset{\sim}{B}$ force is pushing the plasma out. Note that $\underset{\sim}{j}_{plasma} \simeq -\underset{\sim}{j}_{beam}$. We give below a simple calculation that shows when plasma expansion becomes a significant process. The main effects of this is an increase in the channel radius with its concurrent reduction of the magnetic field and thus the radial expansion of the hot e-beam. The radial expansion is:

$$\ell_{exp} \simeq \frac{1}{2} \left(\frac{\underset{\sim}{j} \times \underset{\sim}{B}}{\rho c} \right) \tau^2 \simeq \frac{I_B I_{CH}}{\pi r^3 \rho} \tau^2 \times 10^{-12} \qquad (3)$$

where the beam and channel currents are given in kA, beam pulse time in 10^{-8} sec, plasma radius (which is also assumed to be the beam radius) in cm, and the plasma mass density in g/cm^3. For the case of our GAMBLE II experiments $I_B \simeq 280$ kA; $I_{CH} \simeq 50$ kA; $\rho \simeq 10^{-4}$ g/cm^3; and $\tau \simeq 5 \times 10^{-8}$ sec we find that the plasma expands less than 10^{-2} cm. If, on the other hand, we had tried to propagate the same beam with a radius of 0.1 cm, the plasma expansion after 50 ns would be many times the initial radius which indicates that plasma MHD effects would start to dominate.

We thus conclude that the present experiments in open air were performed at a high density with little hydrodynamic effects during

the beam propagation while Physics International experiments[5] with tapered Z-pinches and low densities ($\rho \approx 10^{-7}$ g/cm^3) were strongly affected by such effects.

We now point out some limitations on current propagation. The simplest limit is that due to the plasma conductivity. An electric field $\underset{\sim}{E} = \underset{\sim}{J}_{beam}/\sigma_{plasma}$ is needed to drive $\underset{\sim}{J}_{return} \approx \underset{\sim}{J}_{beam}$. An upper limit on this field for our GAMBLE II experiment is

$$\underset{\sim}{E} = \frac{2.80 \times 10^5 \cdot \frac{c}{10}}{\pi(1.6)^2 2 \times 10^{14}} \cdot 3 \times 10^4 \approx 16 \text{ kV/m}$$

We now consider the question of magnetic field diffusion and its effect on electron beam trajectories.

Because of finite channel conductivity the magnetic field profile will change. The time scale for change over a length r in the radial direction is given by

$$\tau = \frac{4\pi\sigma r^2}{c^2}$$

For a length scale of r = 0.5 cm, and plasma conductivity of $\sigma = 2 \times 10^{14}$ sec^{-1}, τ = 750 ns. The plasma temperature of 2 eV is obtained via the heating by the discharge current of 50 kA during 20 μs; very little additional heating is expected due to the 10^5 A/cm^2 primary current for the plasma densities (10^{19} cm^{-3}) in the experiment. During a 100 ns pulse the net current will increase by $\Delta I = I_{beam}(1-e^{-\frac{100}{750}}) = 0.15\ I_b$ which gives ΔI = 30 kA for I_{beam} = 200 kA. The increased magnetic field due to the net current drastically affects the electron orbits. If the beam radius at injection is nearly equal to the plasma

channel radius, the relativistic electrons injected at large angles will be returned back to the diode by this magnetic field and the efficiency of propagation will be reduced. If, however, the beam radius was initially smaller than the channel radius then the electrons will expand radially to fill a radius smaller than the channel radius which encloses the Alfvén current. As the net current increases, this radius will decrease and the beam will propagate at a higher current density. For this case, no reduction in efficiency will be observed. This effect should be more pronounced at higher total beam currents. The experiments on GI, Hydra (at SLA) and GII are characterized by beam currents of 100, 200 and 250 kA accordingly. In view of the above discussion one should observe the tightest pinches propagated on GII as was indeed observed. If one tries to extrapolate into beam currents of a few mega-amperes then the magnetic field diffusion will be too large and extend into radii less than the beam injection radius causing a reduction of efficiency of transport.

We turn now to the effect of time variation of diode voltage. Since a channel current nearly equal to I_α is needed for transport, when diode voltage is reduced the needed current is accordingly reduced. The combination of initial channel current and the increase of the current by magnetic diffusion bring the total current above I_α as diode voltage falls. This is one of the reasons why GI or Hydra which had nearly constant voltage pulses, show almost constant efficiency of transport while fast changing impedance experiments on GII showed a drastic reduction of beam transport efficiency during the 50 ns pulse.

Based on all the preceding discussion we may now put limits on the total current that can be transported using the present technique. First, the conductivity defines an electric field by $j = \sigma E$, which cannot exceed the diode voltage divided by the channel length.

$$J < \sigma \cdot \frac{V}{\ell} = \sigma \frac{V_{MV}}{\ell_m} \times 10^{-8} \left(\frac{A}{cm^2}\right)$$

$$\text{for } V = 1 \text{ MV}, \ \sigma = 2 \times 10^{14}, \ \ell = 1 \text{ meter}$$

$$J < 2 \times 10^{10} \frac{A}{m^2} = 2 \times 10^{6} \ A/cm^2 \ .$$

For a distance of 10 meters only 2×10^5 A/cm^2 can be transported in these channels, however at higher current densities, these estimates will be modified by the higher temperatures and conductivities associated with the primary and return-current heating.

Second, the plasma channel expansion limits the tightness of the transported beam. For example if we take the 2 MA/cm^2 beam of 1 MV electrons discussed above and inject them into a 5 mm radius air channel carrying the Alfvén current, the channel radius will double in 50 ns. Even taking the magnetic diffusion into account the Alfvén radius will still be 1.2 times the original channel radius.

IV. CONCLUSIONS

In summary we have shown experimentally that high power density electron beams may be efficiently transported using these current-carrying air plasma channels. We have shown theoretically that certain restrictions apply to their use - the most restrictive being the limitation on the current density. This restriction may be overcome to a

certain extent by increasing the channel temperature. This might be accomplished by using a lighter background gas.

The self-consistent problem of plasma-channel expansion occurring simultaneously with the magnetic diffusion and its ultimate effect on the transported beam and the transport efficiency must still be studied.

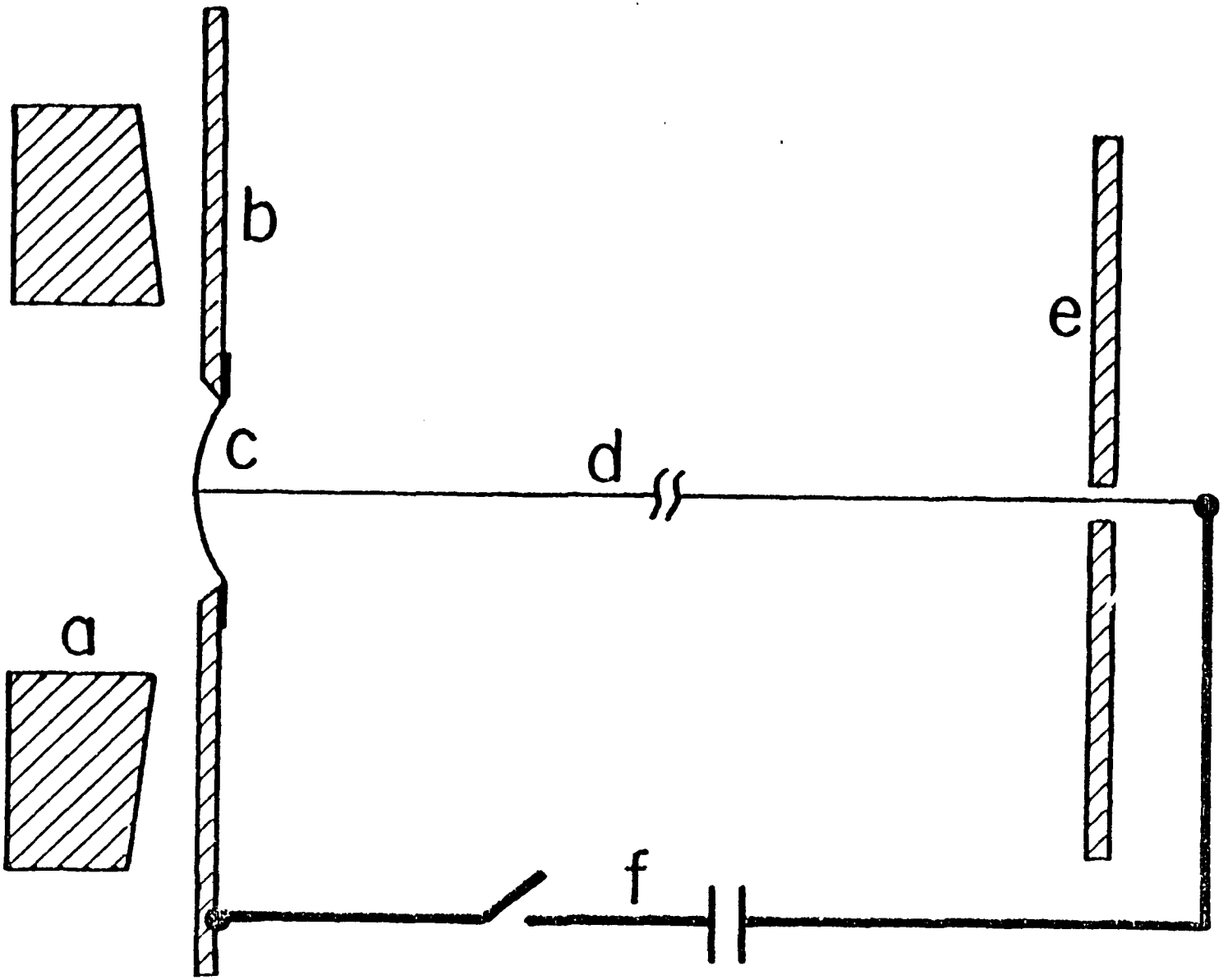

Fig. 1 — This schematic of the experimental apparatus shows: a) the brass cathode; b) the brass anode; c) the titanium/aluminum foils; d) the wire; e) the aluminum target; and f) the switch and capacitor bank which supplies the channel current.

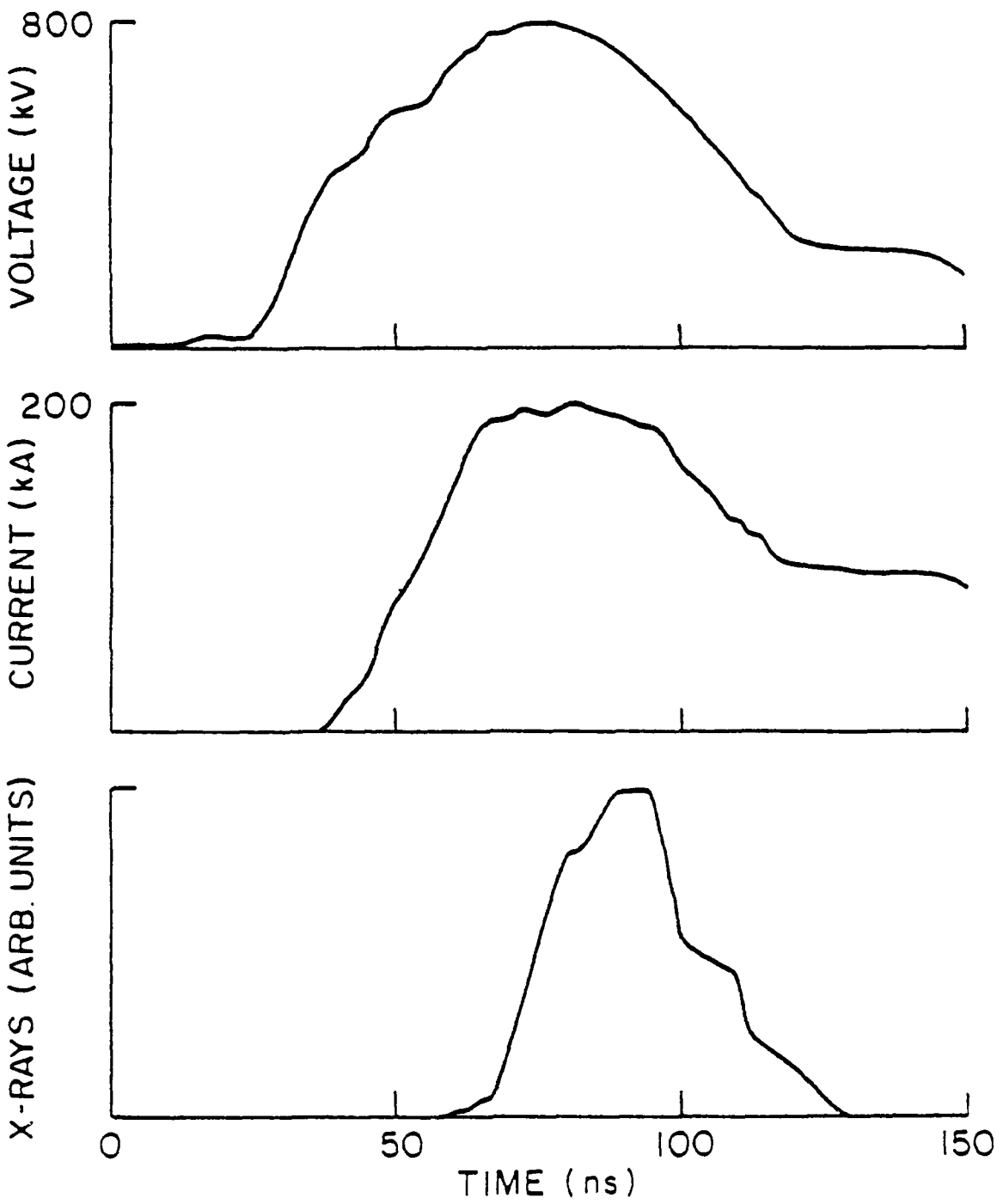

Fig. 2 — Diode voltage, current, and x-rays for GAMBLE I shot 5700.

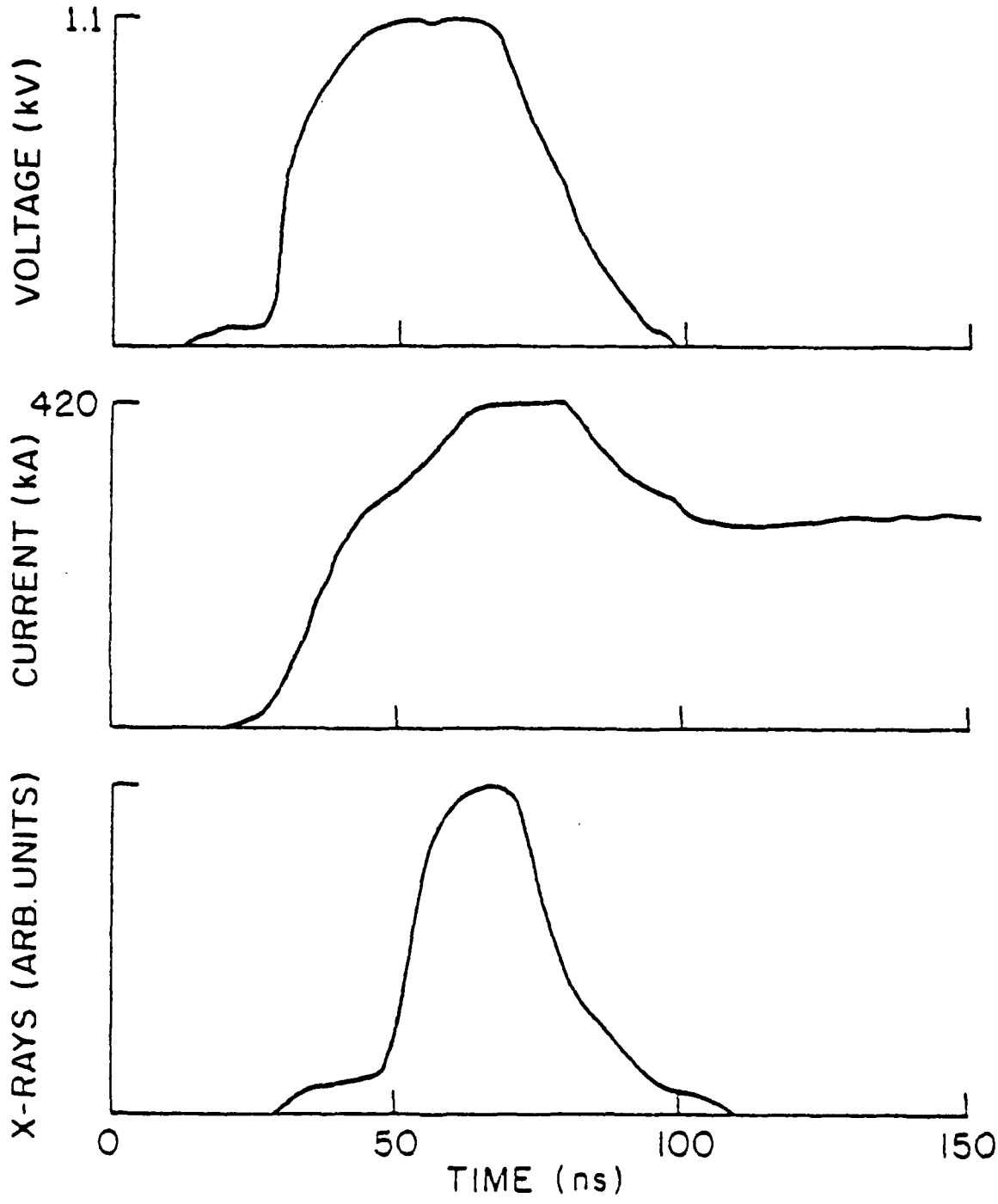

Fig. 3 — Diode voltage, current, and x-rays for GAMBLE II shot 1799.

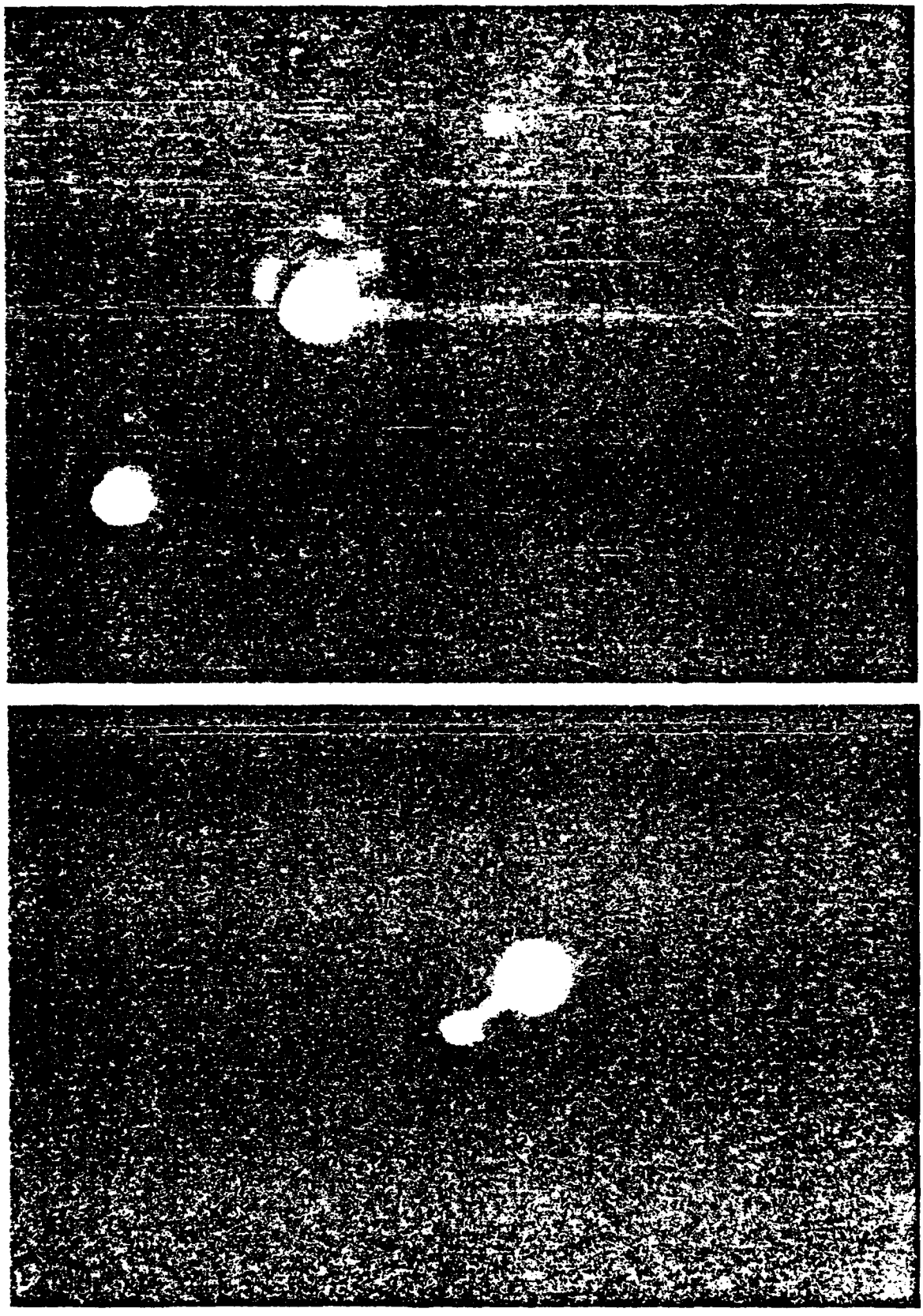

Fig. 4 — X-ray pinhole photographs for Gamble I shot 5700.

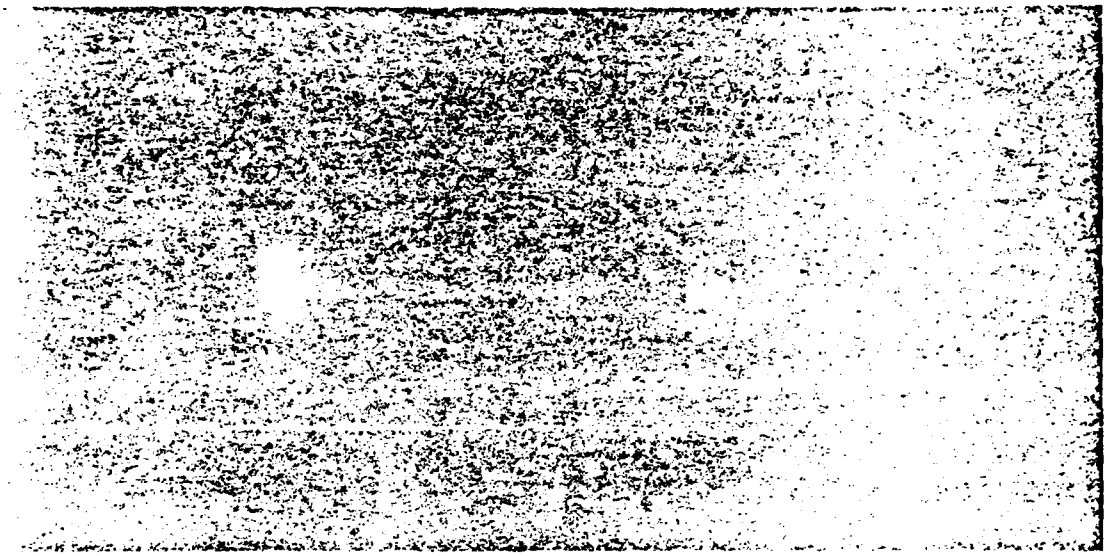

Fig. 5 — X-ray pinhole photograph for GAMBLE II shot 1799.

V. REFERENCES

1. H. Alfven, Phys Rev 55, 425 (1939).
2. D.A. Hammer and N. Rostoker, Phys Fluids 13, 1831 (1970).
3. Roswell Lee and R.N. Sudan, Phys Fluids 14, 1213 (1971).
4. L.S. Levine, et al, J. Appl Phys 42, 1863 (1971).
5. J. Benford and B. Ecker, Phys Rev Lett 26, 1160 (1971); 28, 10 (1972).
6. P.A. Miller, et al, Phys Rev Lett 39, 92 (1977).
7. P.A. Miller, et al, in Proceedings of the 2nd International Topical Conference on High Power Electron and Ion Beam Research and Technology (edited by J.A. Nation and R.N. Sudan), 393 (1977).
8. A.F. Aleksandrov, et al, Zh. Ekop. Teor. Fig. 61, 1841 (1972).
9. S.A. Goldstein and R. Lee, Phys Rev Lett 35, 1079 (1975).
10. See Roswell Lee and R.N. Sudan, Physics of Fluids 14, 1213 (1971) and the references contained therein.
11. Shyke A. Goldstein, et al, in Proceedings of the 2nd International Topical Conference on High Power Electron and Ion Beam Research and Technology, 71 (1977).

ANALYSIS OF PROTON TRANSPORT EXPERIMENTS

I. Introduction

As a part of the NRL light ion beam research program[1], experiments on the transport[2,3] of intense pulsed proton beams have been carried out. The NRL GAMBLE II pulser was used to generate proton beams and the measurement of prompt-gamma rays[4] was the primary diagnostic for proton transport. The first sequence of shots was made using a large-diameter (4.5 cm) transport channel with a 2.5-cm diameter aperture. The transport of 1-MeV proton beams of a few hundred kiloamperes a distance of one meter with efficiencies approaching 100% was achieved in this channel. A second sequence of shots with a smaller-diameter (1.6 cm) channel with a 1.2-cm diameter aperture was much less efficient in transporting the beam. Analysis of the prompt-gamma measurements to determine proton currents in the transport channel and transport efficiencies is presented in this report.

II. Description of Experiment

The proton beam was generated by a planar pinch-reflex diode[5] with a 5.7-cm radius cathode. The beam was brought to a narrow-angle focus 25 cm from the diode and injected into a transport channel. The vacuum diode was separated from the low-pressure-gas-filled transport region by a 1.8-μm thick Kimfol. The proton beam was focused by self B-fields in the 1.9-cm anode-to-Kimfol gap and, after passing through the Kimfol, was ballistically directed toward the focal region. At the expected focus, the beam entered the transport channel which consisted of a wall-stabilized plasma discharge

Manuscript submitted June 24, 1980

typically carrying an externally applied axial current of ~ 50 kA. The B-field from this current was sufficient to confine the injected protons within the larger diameter channel.

The proton beam in the channel was diagnosed by measuring prompt gamma rays[4] from the $^{19}F(p,\alpha\gamma)^{16}O$ reaction. For this diagnostic, Teflon screen targets (50% transparent) were located at the entrance to the channel and one meter into the channel. Two detectors were used to measure prompt gamma rays from these targets as shown in Fig. 1. One detector, which was absolutely calibrated[6], was located 5[illegible] cm from the second target and shielded against radiation from the diode and first target. The other detector was located behind a concrete wall and was equidistant from both targets. The wall differentially shields the diode bremsstrahlung and improves the signal-to-bremmstrahlung ratio for viewing the first target. Measured signals from these two detectors are displayed in Fig. 2. These responses indicate that the inside detector measured signals from the second target while the outside detector recorded signals from both targets. The outside-detector signals are separated in time by the transit of protons from the first to the second target. The detector behind the concrete wall was calibrated absolutely by comparing its response from the second target with that obtained with the inside detector.

For a shot with no Teflon targets, the prompt-gamma responses are given by the dashed curves in Fig. 2. On this background shot, sufficient energy was transported to spall an aluminum plate at the end of the transport system. A small bremsstrahlung signal was measured on the outside detector. The inside detector recorded no bremsstrahlung but did record a small signal probably due to residual Teflon deposited in the transport system from

previous shots. If the apparatus was not cleaned carefully between shots, this background was significantly larger.

Protons injected into the transport channel propagate in the magnetic field associated with the discharge current. The channel is essentially a z-pinch, a radial implosion followed by damped radial oscillations. The confinement of the protons to the channel depends on the radial profiles of the magnetic field, current, and particle density in the channel. These qualities are rapidly varying functions of time and are not known. For the present analysis, the channel is assumed to be of uniform particle and current density and constant in time for the duration of the beam pulse.

Measured prompt-gamma responses were compared to responses calculated using the ion current and proton energy measured on each shot. The charged-particle current incident on the Kimfol was measured with a Rogowski coil. The proton energy was taken to be the voltage determined by correcting the measured diode voltage for inductive effects in the diode and for classical energy loss in the Kimfol. The ion current, presumed to be entirely protons, and the proton energy were combined with the energy dependence of the $^{19}F(p,\alpha\gamma)^{16}O$ reaction and the absolute detector sensitivity[6] to give the expected prompt-gamma response. The energy dependence of this reaction yield is shown in Fig. 3. Corrections for the flight time of protons from the anode to the target were included in the calculations. The shapes and magnitudes of the calculated responses were compared to the measured responses after timing-chain corrections.

III. Large-Transport-Channel Results

Six shots with the large-diameter transport channel were selected for careful analysis. The calculated prompt-gamma responses for these shots are compared with the measured signals in Fig. 4. Here the calculated responses

have been normalized in amplitude to the measured signals. The proton current and energy used for these calculations are also displayed in Fig. 4 for each shot. The current measured on shot 407 was used for shot 406 because that trace was not recorded on shot 406.

The shapes of the calculated responses from the first target agree reasonably well with the measured traces for all the shots except shot 413. Also, the calculated risetimes for responses from the first target agree with the measured traces except for shot 402. The prompt-gamma signals from the first target for shots 402 and 403 were measured at 50 ns/cm and expanded to 20 ns/cm for the comparison in the attached figures. An error of ± 5 ns is inherent in the absolute time scale for these two traces. For shot 413, the calculated response from the first target is narrower in width than the measured trace. The calculated response is narrowed in time due to the peculiar shape of the voltage trace measured on this shot. The narrow peak on the prompt-gamma response is correlated with the narrow peak at the top of the voltage. Explanations for the discrepancy with the measured trace are speculated upon in the discussion (Section VI).

The calculated responses from the second target do not agree with the measured signals in shape or timing. The calculated responses occur too early in time presumably because the proton energy is too high. No energy loss in the focusing region or the transport system has been included in these calculations.

IV. Transport Efficiencies and Energy Losses in the Large Channel

A lower limit on the transport efficiency can be estimated from the ratio of the prompt-gamma signals from the first and second targets. Signals from both targets are recorded with equal sensitivity by the outside detector. The areas of the two peaks in the traces for this detector were used to

evaluate the transport efficiencies given in Table 1. For this evaluation the area of the second peak has been doubled relative to the first peak to correct for the 50% transparent Teflon screen targets. Table 1 also lists the air pressure in the transport channel for each shot. The largest transport efficiency was obtained for 0.5-Torr pressure. At a pressure of 0.12 Torr, the efficiency was reduced to about 20%. These efficiencies are in fact lower limits on the transport efficiency because energy lost by protons in the transport system causes the prompt-gamma signal from the second target to be reduced. The strong energy dependence of this diagnostic is shown in Fig. 3.

To estimate the magnitude of energy losses in these experiments, the average energy of the protons in the transport channel was determined for several shots. The time interval between signals from the two Teflon targets was used to calculate the average proton energy, E_a, in the channel. This energy is compared in Table 2 with the maximum energy of the ions, E_m, after passing through the Kimfol. The difference between E_m and E_a represents an average energy loss and ranges from 100 to 430 keV for these shots. For this comparison, a proton energy extracted from the timing of the maxima of the prompt-gamma responses should correspond to the peak proton energy because this response is strongly energy dependent (see Fig. 3). The average energy losses in Table 2 are larger than one expects from collisional losses in the channel. For example, the classical energy loss for 1.2-MeV protons in 1.5-Torr air is only 50 keV/m. Classical energy losses from the Kimfol to the second target due to the low pressure air in the channel are listed as dE_2 in Table 2. Clearly, energy losses significantly greater than classical collisional losses are reducing the proton energy in these experiments.

Table 1

Large-Channel Transport Results for No Energy Loss

Shot No.	Transport Channel Pressure (Torr)	Minimum Transport Efficiency
402	1.5	0.25
403	1.5	0.12
406	1.5	0.30
407	1.5	0.26
412	0.5	0.47
413	0.28	0.31

Table 2

Energy Loss Estimates

Shot No.	E_m (MeV)	E_a (MeV)	Average Energy Loss (keV)	dE_2 (keV)	ΔE_2 (keV)	dE_1 (keV)
402	0.975	0.88	100	70	300	13
403	1.10	0.93	170	60	--	--
406	1.22	0.96	260	64	--	--
407	1.39	1.01	380	60	600	12
412	1.26	0.93	330	21	500	4
413	1.44	1.01	430	10	700	2

An evaluation of the transport efficiency including energy loss was made for shots 402, 407, 412 and 413. On these shots, efficient transport was observed and all data traces were obtained. For this analysis, the energy loss was assumed to be constant during the beam pulse and was applied directly to the measured voltage to reduce the energy of the protons before time-of-flight corrections thru the focusing and transport sections. The energy loss of the protons after passing through the Kimfol was assumed to consist of a classical energy loss dE due to gas in the channel, and an additional energy loss ΔE to be determined. Subscripts of 1 or 2 will be used on these quantites to denote energy losses from the diode to the first or second Teflon target, respectively. The energy loss of protons from the diode to the Teflon target at the end of the transport system was determined from proton time-of-flight. The energy of the protons after passing through the Kimfol was reduced about an amount $(dE_2 + \Delta E_2)$, and ΔE_2 was adjusted so that the peak of the calculated prompt-gamma signal from the second target agreed in time with the measured signal. Values of dE_2 and ΔE_2 are given in Table 2. An uncertainty of ± 100 keV is assigned to ΔE_2 based on this fitting procedure. The fitting procedure is illustrated in Fig. 6. In all cases the additional energy loss ΔE_2 is much greater than the classical energy loss dE_2. The energy of protons striking the second target is less than the average energy measured in the transport channel, assuming deceleration during transport. Therefore the energy loss from the Kimfol to the second target is larger than the average-energy-loss estimates in Table 2.

The energy loss of the protons is made up of an energy loss in the region from the diode to the first Teflon target (ΔE_1), and an energy loss in the transport channel between the two targets (ΔE_t), where $\Delta E_1 + \Delta E_t = \Delta E_2$. Both ΔE_1 and ΔE_t are not known, but the sum, ΔE_2, was determined above.

A range of values for ΔE_t (and hence ΔE_1) is determined by comparing the intensities of measured and calculated prompt-gamma responses. Prompt-gamma responses were calculated for the first target with protons reduced in energy by $(dE_1 + \Delta E_1)$ and for the second target with protons reduced in energy by $(dE_2 + \Delta E_2)$. The ratio for these results was used to correct the minimum transport efficiencies determined previously for no energy loss. The results are presented in Fig. 5 as a function of ΔE_t. Values of dE_1 are given in Table 2. As ΔE_t increases, the transport efficiency increases until an upper-limit of 100% is reached. Over this range, ΔE_t never exceeds 150 keV and is always less than ΔE_1. For ΔE_t = 100 keV, a likely value, the transport efficiency ranges from 50% to 90%, and ΔE_1 ranges from 200 to 600 keV for these shots.

Only a fraction of the measured ion current is incident on the 2.5-cm diameter Teflon target at the entrance to the transport channel. The fraction of the ion current required to fit the magnitude of the measured prompt-gamma signal from the first target is determined by scaling the measured ion current by the ratio of the measured to calculated prompt-gamma signals. This fraction was determined by integrating the respective signals to eliminate uncertainties due to proton bunching and multiplying by two to correct for the 50% transmission Teflon screen target. This fraction is presented in Fig. 5 as a function of the energy loss in the transport channel, ΔE_t. For less energy loss in the transport channel and more energy loss from the diode to the channel entrance, a larger fraction of the ion current is required to account for the magnitude of the prompt-gamma signal. For ΔE_t = 100 keV, this fraction ranges from 20% to 85% for these shots. Since the measured ion current at peak voltage is about 500 kA for all these

shots (see Fig. 1), currents of 100 to 400 kA at peak voltage were inferred from this analysis.

The inclusion of energy losses in calculating the prompt-gamma responses has minimal effect on the shapes of the calculated responses as illustrated in Fig. 6 for shot 412. The fitting procedure used to determine the energy loss ΔE_2 is shown for the inside detector. If this same energy loss is used for ΔE_1 (i.e. $\Delta E_t = 0$), the timing of the calculated signal from the first target is only slightly delayed because the flight path of protons to the first target is so short.

V. Small-Transport-Channel Results

Measured prompt-gamma signals for two shots with protons injected into the small-diameter transport channel are compared with calculated responses in Fig. 7. These shots were selected because they gave observable transport. Other shots gave unobservable or barely observable transport. The reason for the poor transport in these shots will be discussed later. The proton energy and current used for these calculations are also displayed in Fig. 7. No energy losses have been included in the calculations, and the calculated responses were normalized in amplitude to the measured signals. For shot 419, helium gas was used in the channel instead of air. The channel pressure for each shot is given in Table 3.

The shapes of the calculated responses from the first target compare favorably with the measured traces, but the measured traces occur significantly earlier than the calculated traces. This discrepancy is due to a significant contribution to the first-target signal from diode bremmstrahlung. The measured signals are smaller due to the smaller entrance aperture on the transport channel, and the diode bremsstrahlung is larger in this series of shots so the signal-to-bremsstrahlung ratio is reduced.

The calculated responses from the second target do not agree with the measured signals in shape or absolute time. In fact, for shot 419 the measured response occurs earlier in the time than the calculated response. This suggests that the energy of some protons is greater than the measured diode voltage so that they arrive at the second target earlier in time. One might suspect that this early-time signal is due to protons bombarding a Teflon deposit remaining on the inside walls of the transport channel after previous shots. However, this explanation is unlikely because the channel was carefully cleaned between shots (see Fig. 2).

An analysis including energy loss has not been applied to these small transport channel shots because there are unknown bremsstrahlung contributions to the prompt-gamma signals from the first target and because the proton energy loss from the diode to the second target is poorly determined. Even so, minimum transport efficiencies may be evaluated from the ratio of the measured prompt-gamma signals from the two targets. The results are given in Table 3. These efficiencies are significantly smaller than the results obtained with the larger diameter channel.

Table 3

Small-Channel Transport Results for No Energy Loss

Shot No.	Gas	Transport Channel Pressure (Torr)	Minimum Transport Efficiency
417	Air	0.25	0.06
419	He	1.0	0.09

VI. Discussion

Protons injected into the transport channel propagate in and are confined by the magnetic field produced by the discharge current. Confinement within the channel depends on many factors. If a uniform static discharge current, I, is assumed, then protons entering the channel at angles up to a maximum of θ_m to the channel axis will be confined according to[3]

$$I = \frac{10^{-3} v(1-\cos\theta_m)}{1-(a/R)^2}$$

where I is in amperes, v is the proton speed in cm/s, R is the channel radius and $a < R$ is the radius of the channel entrance aperture. For 1-MeV protons and the maximum possible injection angle in the present experiments, a current of 58 kA in the large channel or 72 kA in the small channel is required.

In the experiments, typically 50 to 60 kA flowed in the large channel, but only ∿ 30 kA flowed in the small channel due to the increased channel resistance and the capacitor bank limitations. In the latter case, the channel current quarter-period rise time was about 15 μs. It is tempting to conclude that the transport efficiencies observed in the small channel were determined principally by the available discharge current. However, it was found in the experiments that observable transport ceased at the highest current levels in the small channel. Transport efficiency was increased by injecting the beam earlier in the rise of the channel current or by shortening the rise time of the channel current, even though the absolute level of channel current decreased.

These observations point to the necessity for a more realistic interpretation of the beam-channel system. The radial profiles of magnetic field, current, and density in the channel are rapidly varying functions of time and depend on such variables as plasma temperature, gas composition, impurity

surprising that the shapes of the calculated prompt-gamma responses do not fit the shapes of the measured signals from the second target even though time-of-flight effects are included in the analysis. As a result, the energy analysis in Section IV is a time-averaged approximation as are the magnitudes of the energy losses.

VII. Conclusions

The best transport results were obtained with the large diameter channel. In this channel, transport efficiencies ranging from 33% to 100% were deduced from this analysis. Total proton currents of a few hundred kiloamperes of 1-MeV protons were calculated to be transported a distance of one meter. There is a trade off between proton current and transport efficiency in the interpretation of these measurements. For 100% transport efficiency in the shots analyzed, the current is $\leq$ 250 kA, but for the smallest transport efficiency (33%) of any of the shots, the current is 300 kA. Energy losses within the transport channel were less than 15% of the maximum proton energy.

gas,[8] and associated losses due to resistive and hydrodynamic electric fields which develop inside the channel during beam transport.[7] Furthermore, since a dynamic plasma exists in the transport system, the beam may lose or gain energy from axial electric fields created from plasma contraction or expansion.[9] This may explain the apparent acceleration of some protons to energies greater than the diode voltage as observed on shot 419. Finally, ions confined to a region close to the axis of the transport channel may sustain enhanced collisional losses if the pinch has compressed the plasma to densities significantly greater than the fill pressure. Wall material brought into the discharge during implosion can also contribute to collisional losses.

The large-diameter-channel measurements indicate that most of the ion beam could be injected into the 2.5-cm diameter aperture and transported. For the small channel, measurements from the first target indicate that less than half of the proton beam is contained within the 1.2-cm diameter aperture. On some shots with the small transport channel, the entrance aperture was increased to 1.6-cm diameter and the first target was removed. Signals from the second target increased by more than the factor-of-two expected by just removing the 50% transmission target. In this case, more protons were injected into the channel and transported. It should be noted that since the voltage and current of the ion beam vary in time, the position of best focus moves axially during the beam pulse. For inertial confinement fusion applications, diodes with improved focusability at long focal lengths are required.[3]

In the large-transport-channel analysis (Section IV), energy losses from the diode to the transport channel and within the channel itself were assumed constant during the beam pulse. For the reasons described above, it is apparent that the energy loss is not constant. Therefore, it is not

surprising that the shapes of the calculated prompt-gamma responses do not fit the shapes of the measured signals from the second target even though time-of-flight effects are included in the analysis. As a result, the energy analysis in Section IV is a time-averaged approximation as are the magnitudes of the energy losses.

VII. Conclusions

The best transport results were obtained with the large diameter channel. In this channel, transport efficiencies ranging from 33% to 100% were deduced from this analysis. Total proton currents of a few hundred kiloamperes of 1-MeV protons were calculated to be transported a distance of one meter. There is a trade off between proton current and transport efficiency in the interpretation of these measurements. For 100% transport efficiency in the shots analyzed, the current is $\leq$ 250 kA, but for the smallest transport efficiency (33%) of any of the shots, the current is 300 kA. Energy losses within the transport channel were less than 15% of the maximum proton energy.

References

1. G. Cooperstein, S. A. Goldstein, D. Mosher, R. J. Barker, J. R. Boller, D. G. Colombant, A. Drobot, R. A. Meger, W. F. Oliphant, P. F. Ottinger, F. L. Sandel, S. J. Stephanakis and F. C. Young, "NRL Light Ion Beam Research for Inertial Confinement Fusion," 5th Workshop on Laser Interaction and Related Plasma Phenomena, Rochester, N.Y., 1979.

2. F. L. Sandel, F. C. Young, S. J. Stephanakis, W. F. Oliphant, G. Cooperstein, S. A. Goldstein, and D. Mosher, Bull. Am. Phys. Soc. 24, 1031 (1979); and F. C. Young, F. L. Sandel, S. J. Stephanakis, P. G. Blauner, W. F. Oliphant, G. Cooperstein, S. A. Goldstein and D. Mosher, ibid. 24, 1031 (1979).

3. D. Mosher, G. Cooperstein, S. A. Goldstein, D. G. Colombant, P. F. Ottinger, F. L. Sandel, S. J. Stephanakis and F. C. Young, "Transport and Bunching of Light Ion Beams for Pellet Fusion," 3rd Inter. Conf. on High Power Electron and Ion Beam Res. and Tech., Novosibirsk, USSR, 1979.

4. J. Golden, R. A. Mahaffey, J. A. Pasour, F. C. Young, C. A. Kapetanakos, Rev. Sci. Instrum. 49, 1384 (1978).

5. D. Mosher, G. Cooperstein, S. J. Stephanakis, S. A. Goldstein, D. G. Colombant and R. Lee, "Intense Focussed Ion Beams and Their Interaction with Matter," 2nd Int. Conf. on High Power Electron and Ion Beam Res. and Tech., Cornell University, Ithaca, N.Y., 1977, p. 257; and S. A. Goldstein, G. Cooperstein, R. Lee, D. Mosher and S. J. Stephanakis, Phys. Rev. Lett. 40, 1504 (1978).

6. F. C. Young, F. Oliphant, S. J. Stephanakis, and A. K. Knudson, "Absolute Calibration of a Prompt Gamma Ray Detector for Intense Bursts of Protons," NRL Memorandum Report 4171, March, 1980.

7. D. G. Colombant and S. A. Goldstein, "Scaling Laws for Ion Beam Losses in Plasma Channels," Conf. Record-1980 IEEE Inter. Conf. on Plasma Science, Madison Wisconsin, 1980, p. 37.

8. P. F. Ottinger, D. Mosher and Shyke A. Goldstein, Phys. Fluids 22, 332 (1979).

9. S. A. Goldstein and D. A. Tidman, "Particle Beam Acceleration in Magnetized Moving Plasma," Conf. Record-1980 IEEE Inter. Conf. on Plasma Science, Madison, Wisconsin, 1980, p. 96.

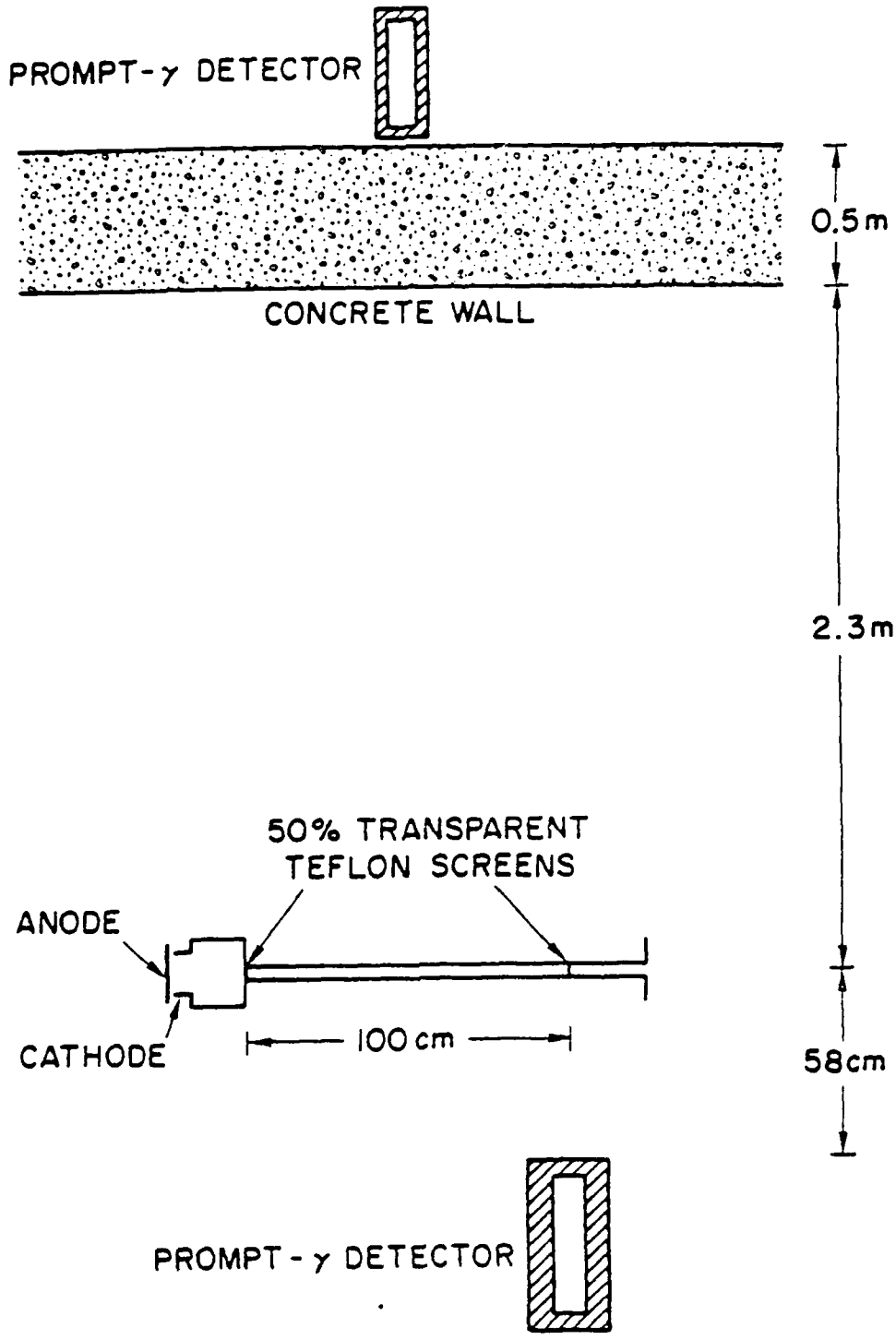

Fig. 1 — Experimental arrangement of the prompt-gamma detectors for the transport experiments.

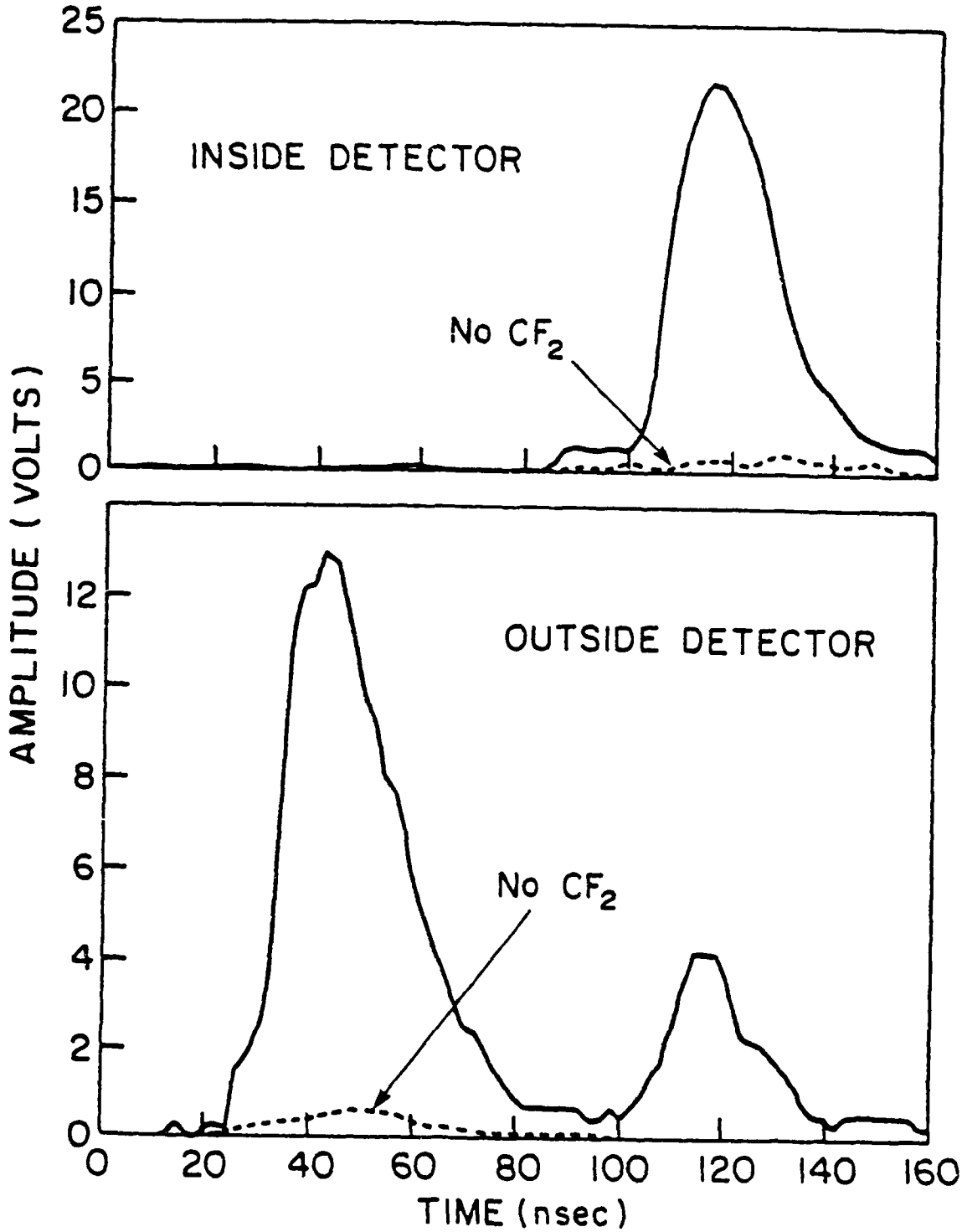

Fig. 2 – Measured traces from the prompt-gamma detectors for Shot 412 with Teflon targets (solid line) and for Shot 411 without Teflon targets (dashed line).

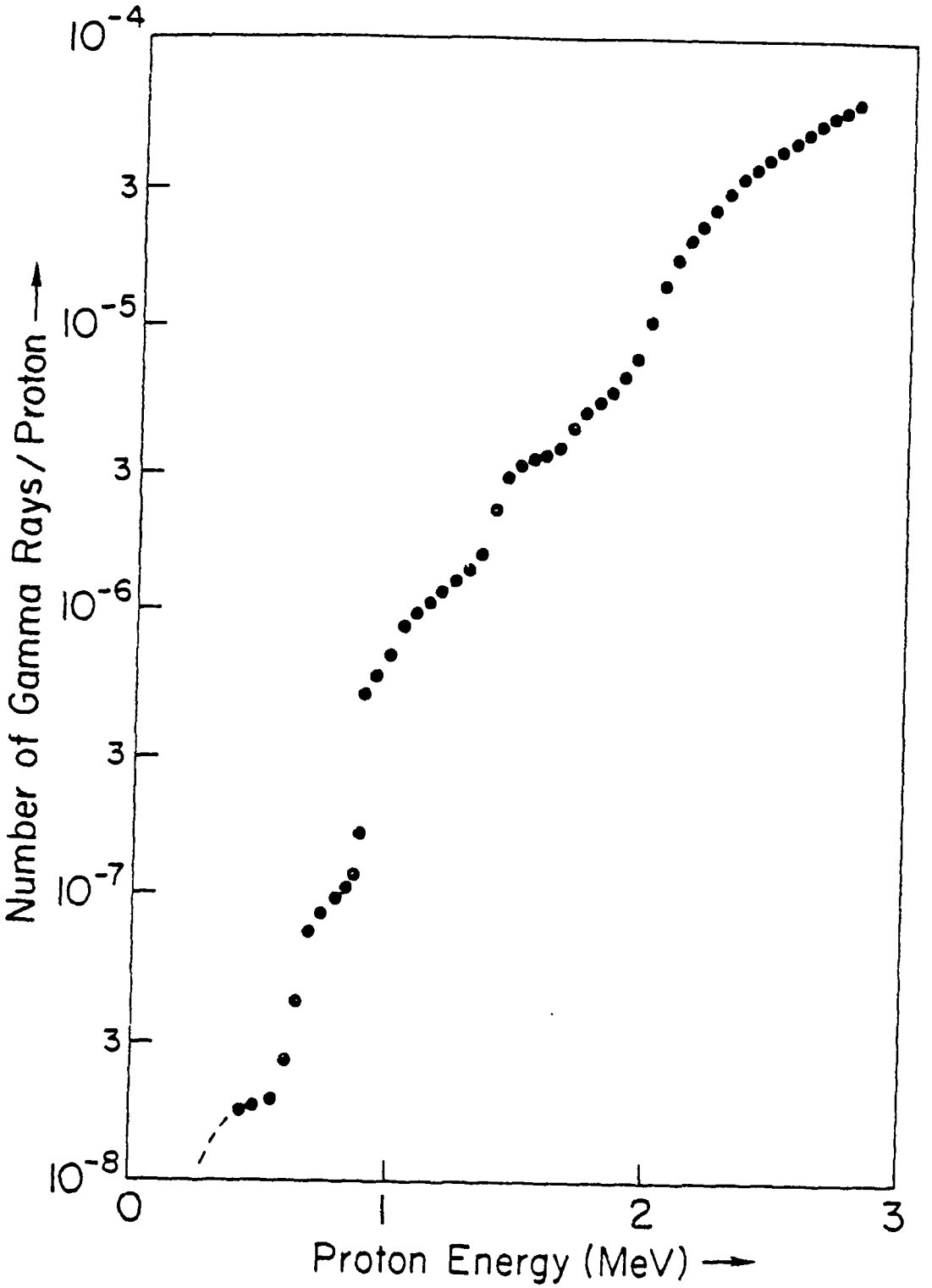

Fig. 3 — Measured thick-target yield for the $^{19}F(p,\alpha\gamma)^{16}O$ reaction on a Teflon target.

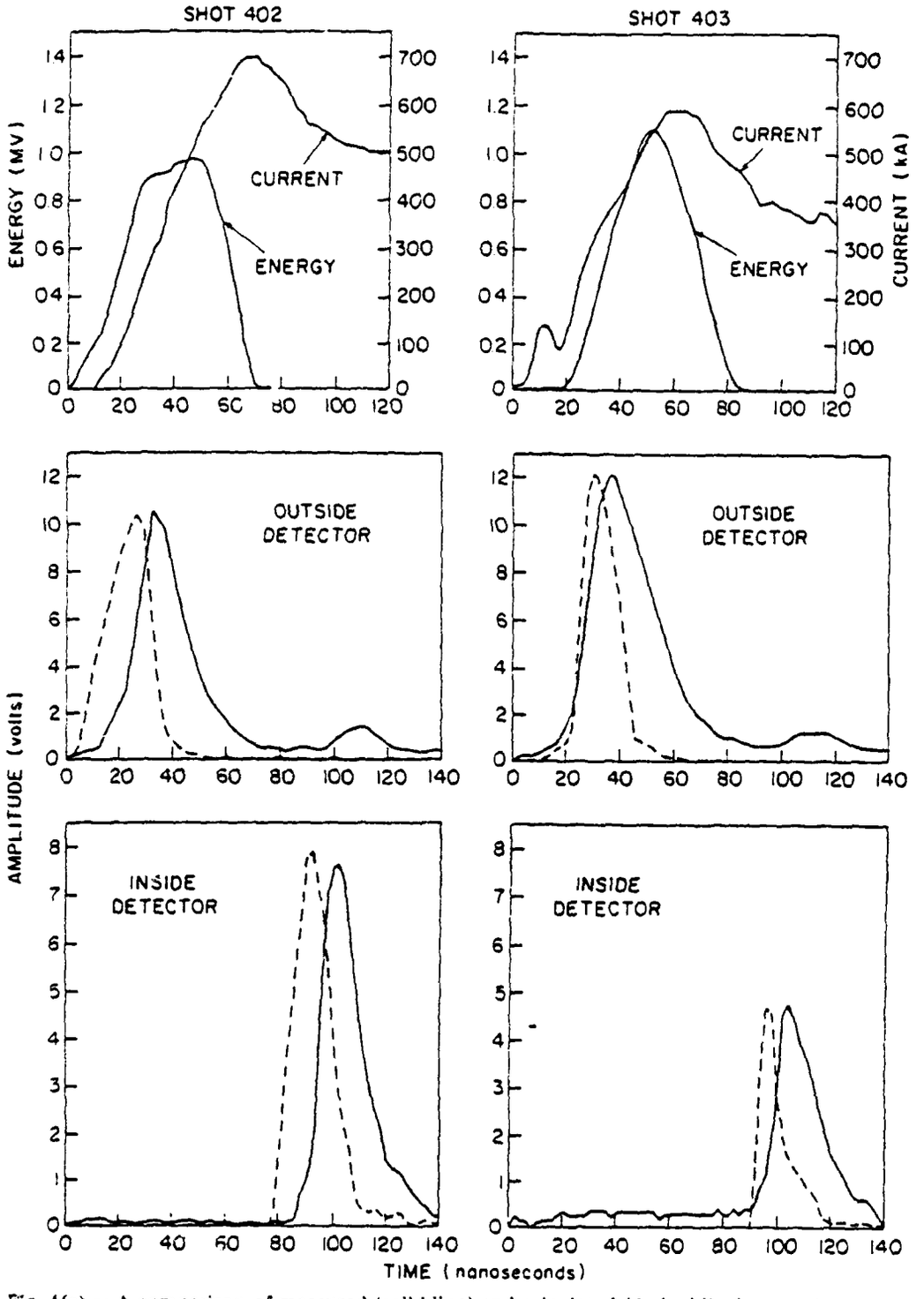

Fig. 4(a) — A comparison of measured (solid line) and calculated (dashed line) prompt-gamma responses for Shots 402 and 403 with the large diameter transport channel. The calculated responses are normalized in amplitude to the measured signals. Also, the proton energy and current which were used to calculate the prompt-gamma responses are displayed. No energy losses are included in these calculations.

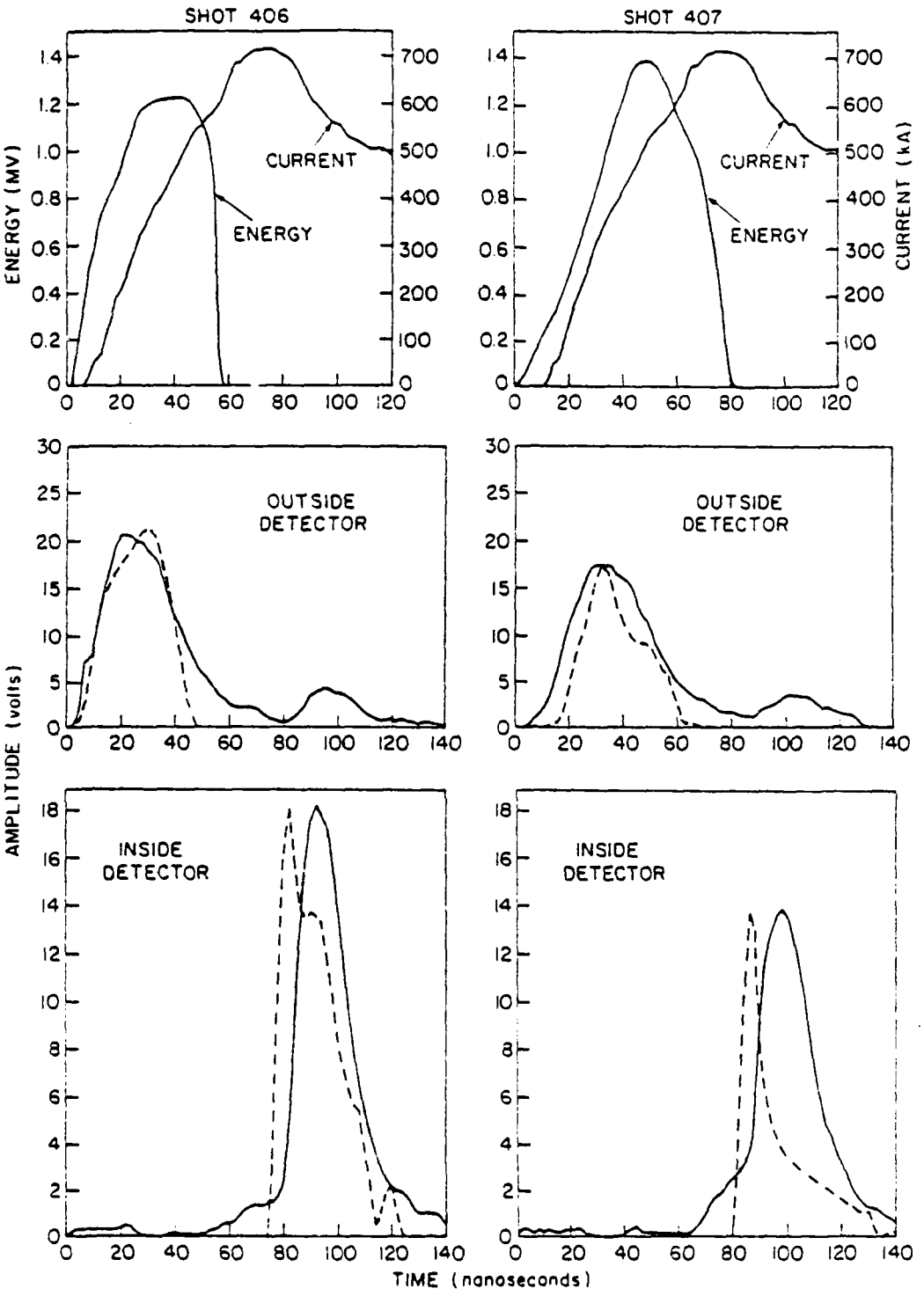

Fig. 4(b) — A comparison of measured (solid line) and calculated (dashed line) prompt-gamma responses for Shots 406 and 407 with the large diameter transport channel. The calculated responses are normalized in amplitude to the measured signals. Also, the proton energy and current which were used to calculate the prompt-gamma responses are displayed. No energy losses are included in these calculations.

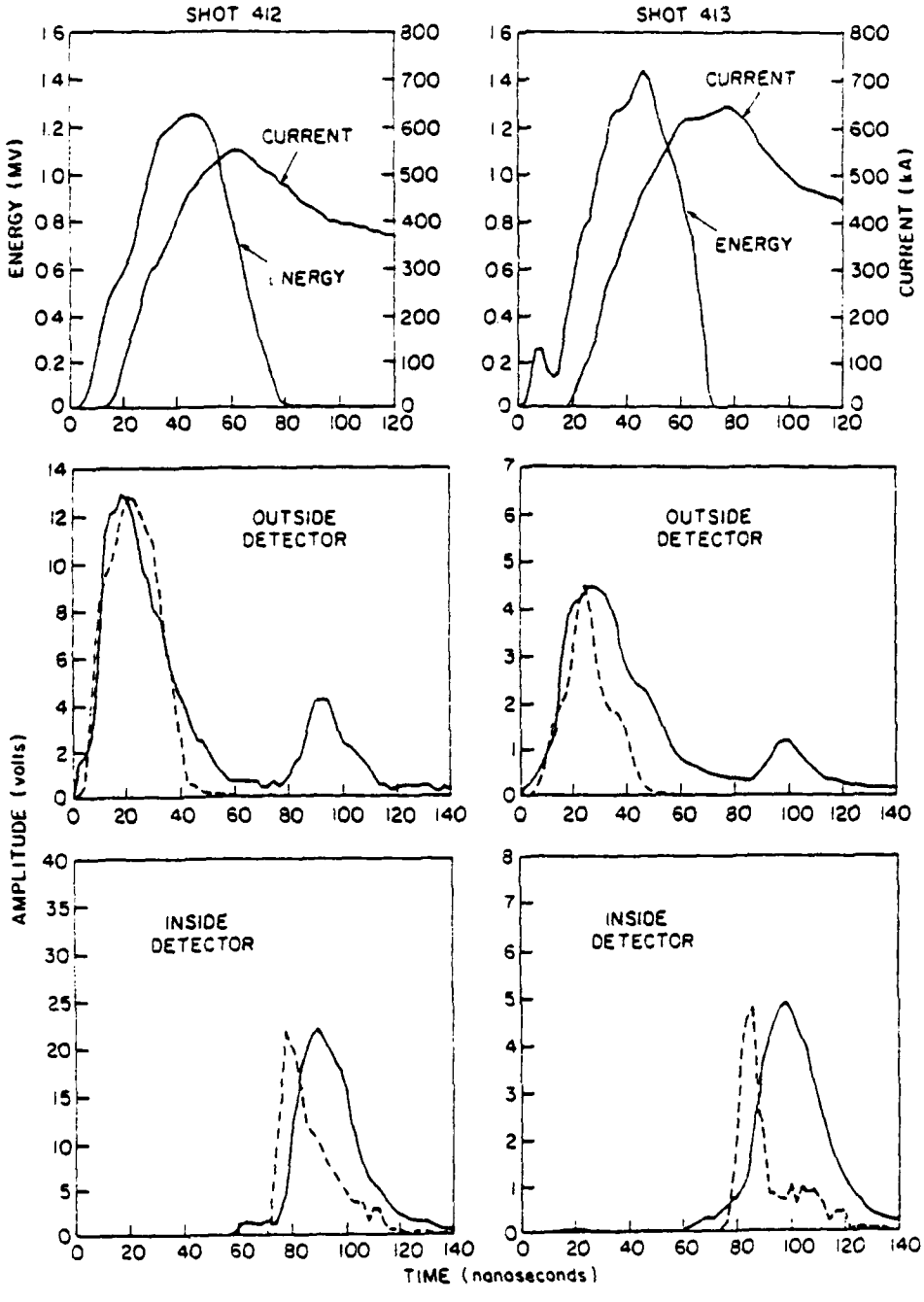

Fig. 4(c) — A comparison of measured (solid line) and calculated (dashed line) prompt-gamma responses for Shots 412 and 413 with the large diameter transport channel. The calculated responses are normalized in amplitude to the measured signals. Also, the proton energy and current which were used to calculate the prompt-gamma responses are displayed. No energy losses are included in these calculations.

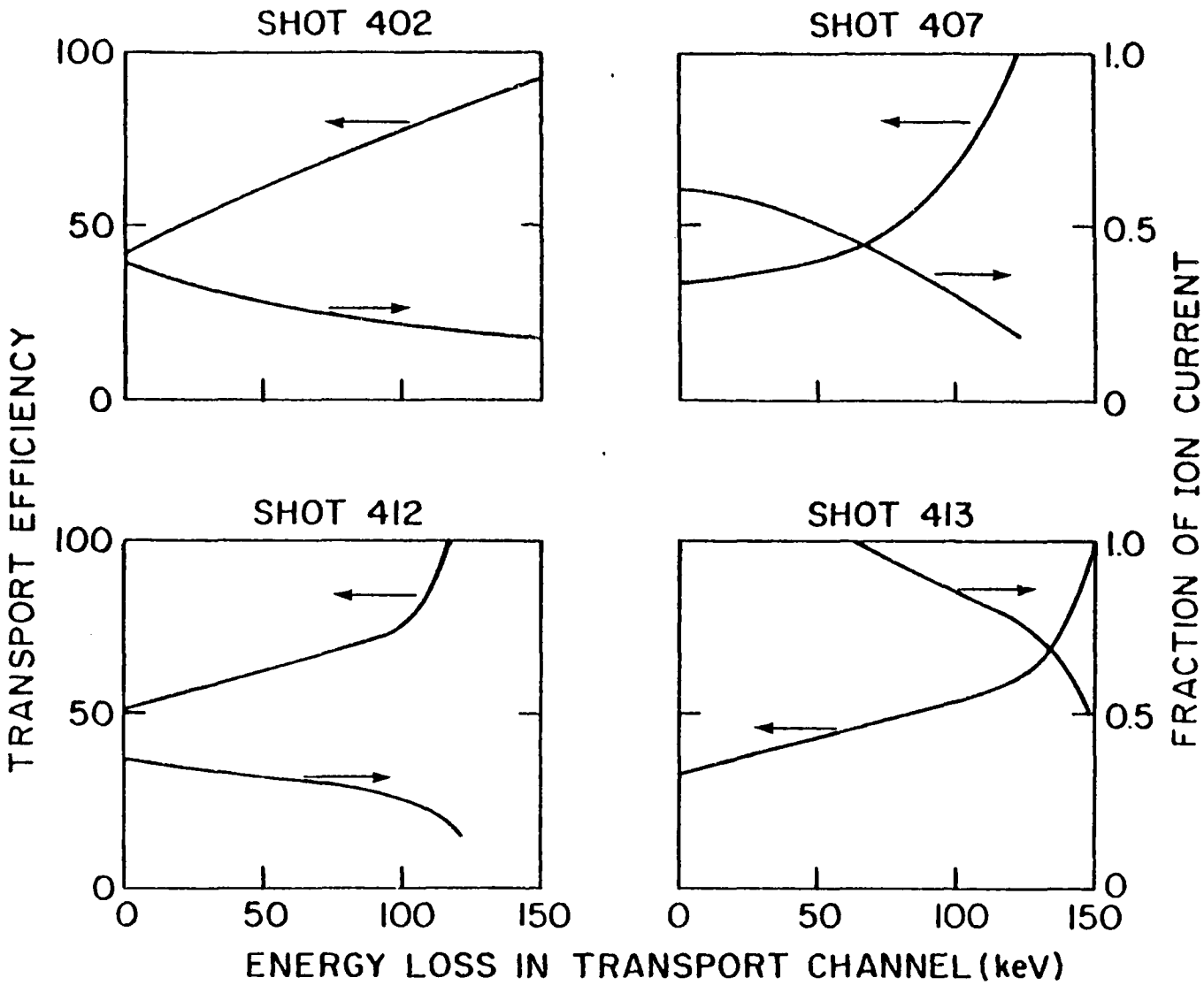

Fig. 5 — Transport efficiencies determined with energy loss included in the analysis. The fraction of ion current required to fit the magnitude of the prompt-gamma response is also given as a function of the energy loss in the transport channel.

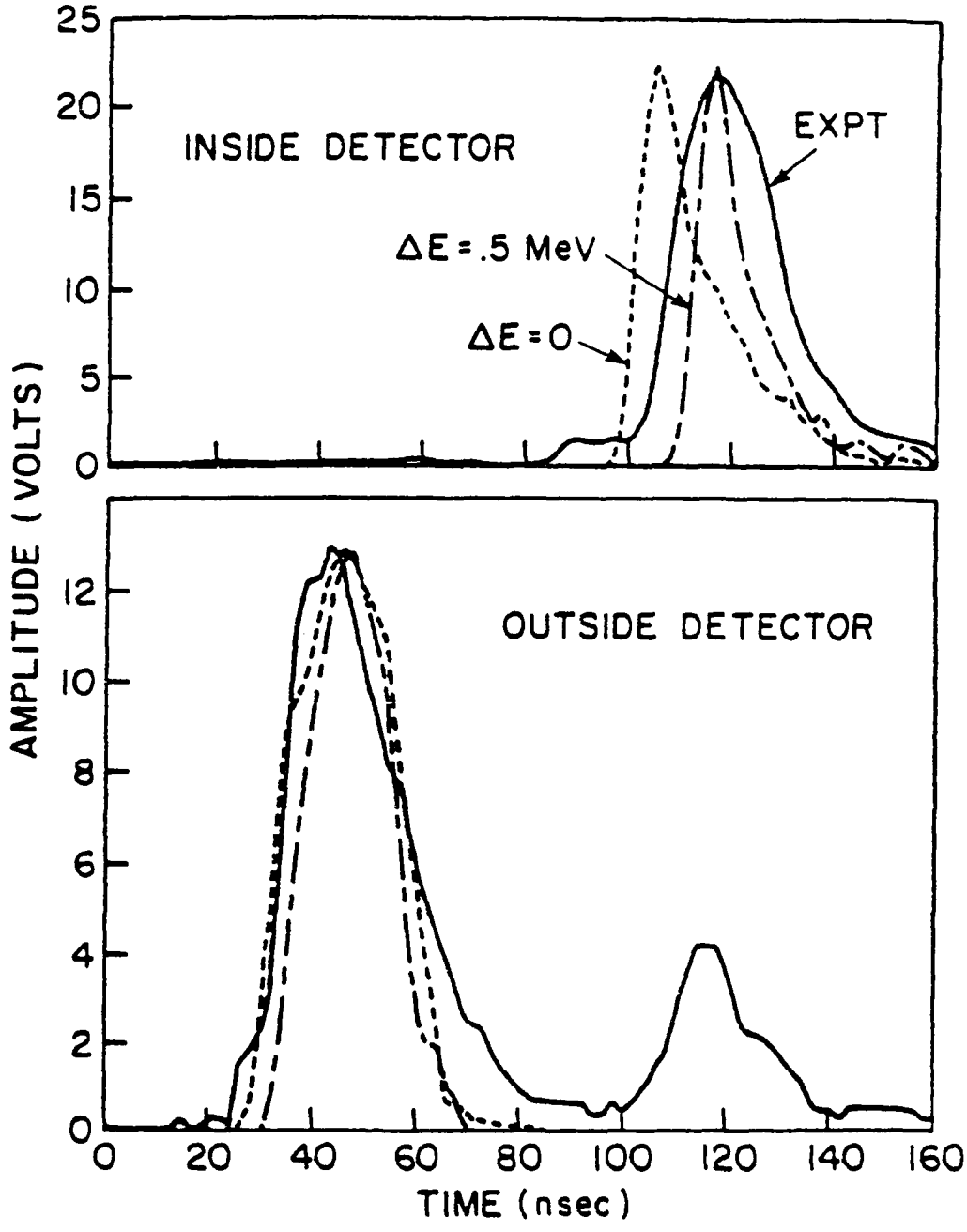

Fig. 6 — A comparison of measured (solid line) and calculated prompt-gamma responses without energy loss (short dashed line) and with 500-keV energy loss (short-long dashed line) for both prompt-gamma detectors. The measured traces correspond to Shot 412.

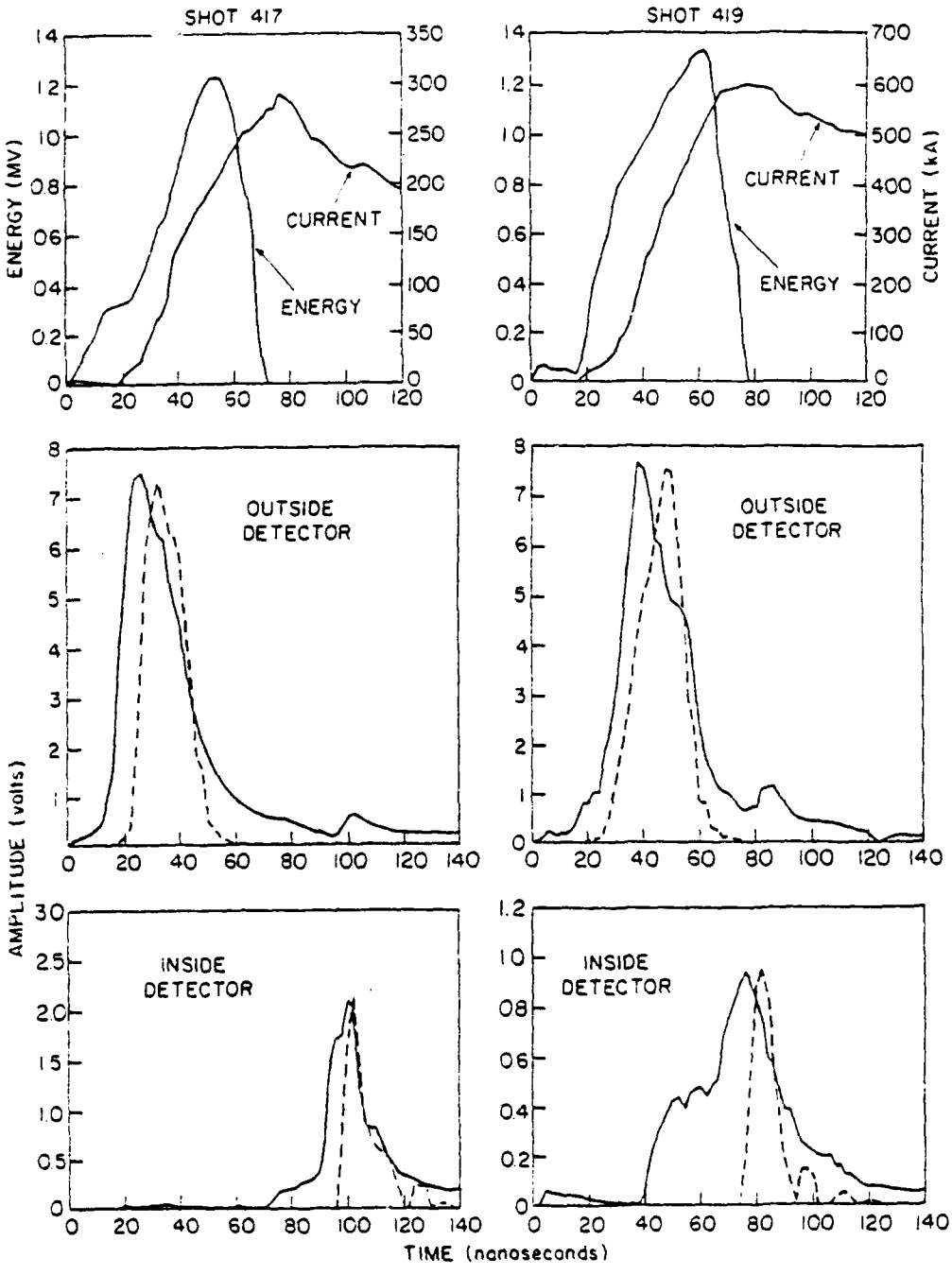

Fig. 7 — A comparison of measured (solid line) and calculated (dashed line) prompt-gamma responses for the small diameter transport channel (Shots 417 and 419). The proton energy and current which were used to calculate the prompt-gamma responses are also displayed. The calculated responses are normalized in amplitude to the measured signals. No energy losses were included in these calculations.

STABILITY CONSIDERATIONS FOR LIGHT-ION BEAM TRANSPORT IN Z-DISCHARGE CHANNELS

1. INTRODUCTION

The development of terawatt-level ion beams has generated a great deal of interest in using light-ion beams to drive thermonuclear pellets.[1-9] Target design studies for light-ion beams indicate that $\sim$ 2 MJ of ions must be delivered in $\sim$ 10 nsec to an $\sim$ 1 cm diameter pellet in order to achieve high-gain thermonuclear ignition.[10] Since present technology can provide up to 5 TW single-generator modules from which up to 200 kJ of ions can be extracted in $\sim$ 50 nsec, a multimodule system is required. In addition, a transport scheme and a method for beam pulse compression are needed.

One possible transport scheme involves the use of a z-discharge channel for transporting a prefocused ion beam (Fig. 1).[11] Focusing is achieved by a combination of geometric and magnetic-field focusing prior to injection into the channel.[12,13] Beam pulse compression results from ramping the diode voltage such that the tail of the beam catches up to the front of the beam.[13,14] The ideal diode voltage waveform is $\phi(t) = \phi_o(1-t/t_a)^{-2}$ for $0 \le t \le \tau_b < t_a$ where τ_b is the beam pulse duration and t_a is the beam arrival time at the target.

Assuming that the z-discharge channel is produced in a MHD stable configuration, the question of the effects that the passage of the beam will have on the equilibrium and stability of the beam-plasma system is an important one. The MHD response of the plasma has been treated elsewhere[15] and will only be briefly reviewed here. Analysis of stable beam propagation in straight and tapered channels, as well as in bumpy channels (subject to sausage instability) has also been done previously.[16] This work shows that, in the absence of microinstabilities driven by the beam, good beam transport and bunching is possible under the conditions set by MHD considerations (which will be outlined in Sec. 2). However, in the presence of microinstabilities, beam transport and bunching can be seriously affected.

Analysis of electrostatic (ES)[17] and electromagnetic (EM)[18] velocity-space instabilities, which can grow on a time scale much faster than the beam pulse duration, will be reviewed in this report. The problem will be considered with the goal of identifying the conditions for good transport and bunching. The results will be presented in a general form so that they may be applied to beams of various low atomic number species propagating in channel plasmas of different compositions.

Manuscript submitted on May 13, 1981.

2. BEAM-PLASMA SYSTEM IN THE TRANSPORT CHANNEL

The beam-plasma system consists of a focused ion beam propagating down the axis of an externally-driven z-discharge plasma channel.[13,19] The ion beam is focused at the entrance to the plasma channel (see Figs. 1 and 2) with velocity components transverse to z given by $V_\perp / V_z = \tan\alpha << 1$. The current being driven in the preformed z-discharge channel provides the radial confinement of the beam. Because of the small perpendicular beam energy, the channel current can be much less than the beam current. A high plasma density in the channel insures good beam charge neutralization.[20] Good beam current neutralization in the interior of the beam also occurs, so that the total magnetic field is comparable to that associated with the preformed channel established before beam injection. Because $J_p = J_{ch} - J_b \approx -J_b$, the electron drift velocity is approximated by $V_e = n_b Z_b V_b / Z_p n_p$, where n_b and n_p are the beam and plasma ion densities, Z_b and Z_p are the beam and plasma ion charge states, and J_p, J_b and J_{ch} are the plasma, beam and preformed channel current densities, respectively. Note that the electron density is $Z_p n_p$.

Hydrodynamic modeling of the background plasma[15] shows that a uniform net-current model is appropriate for the early times associated with passage of the beam front. This is because the low-temperature channel is established microseconds before beam injection so that complete magnetic diffusion occurs. Later in the ion pulse, $J_p \times B$ expansion of the beam-heated high-temperature plasma reduces the magnetic field strength in the interior of the channel. The built-up field in the expanding cylindrical shock wave is also enhanced by significant current non-neutralization in the cool plasma surrounding the beam-heated channel. The maximum field strength just outside the ion-beam radius can exceed that established by the preformed z-discharge current by a large factor. Thus, at late times during beam passage, the magnetic field distribution can be approximated by a surface-current model. Although the induced $V_r \times B_\theta$ electric field is important when considering beam energy losses during transport, at no time does the electric field become large enough to significantly affect the stability analysis.

The linearized stability analysis presented here strictly applies only when the mode under consideration grows on a time scale faster than any changes in the beam-plasma system (i.e., $\gamma > \tau_b^{-1}$). For growth on a time scale slower than the beam pulse duration, the perturbation analysis breaks down since small perturbations will be washed out by the zero-order changes in the system before growth can occur. Thus for those modes which are shown to e-fold less than once during the passage of the beam, the results should be interpreted as showing that significant growth does not occur.

The distribution of particles in axial velocity is illustrated in Fig. 3. The plasma ions form a stationary background while the drift of the plasma electrons provides for beam current neutralization. Because of the high plasma density, this drift velocity, V_e, does not exceed the electron thermal velocity even before the beam heats the plasma. As the beam passes through a given point, the plasma is heated and the conductivity increases. The electron-ion collision frequency, ν_{ei}, decreases but the electrons generally remain collisional ($\nu_{ei} > \omega_{ce}$) at all times during the pulse for purposes of the stability analysis. Since the electron-ion equilibration time is on the order of the beam pulse duration the electron temperature will not exceed the ion temperature by more than a factor of ten.

The ion beam density is typically much less than the plasma density and, beams of interest are nonrelativistic. The spread in axial velocities, designated by V_t in Fig. 3, is on the order of $V_b\alpha_m^2/2$ before beam bunching occurs. Here V_b is the beam velocity and α_m is the maximum ion injection angle into the channel. For α_m = 0.1-0.2 rad, V_t/V_b is relatively small. As the beam bunches, V_t/V_b can increase by an order of magnitude as the faster ions generated later in the pulse catch up to slower ions at the front of the beam. The beam pulse duration, τ_b, decreases and the beam density, n_b, increases as the beam bunches. The dependence of the beam parameters on axial position due to bunching will be expressed explicitly as $V_t(z)$, $\tau_b(z)$, etc.

Since the ES stability analysis depends strongly on the shape of the beam distribution function, it is important to use a theoretical model which contains the appropriate physics. For a distribution in v_z which has a large slope on the low velocity side such as illustrated in Fig. 4a, a resistive instability persists in spite of the thermal spread in v_z and the high frequency of collisions between the plasma electrons and ions.[21,22] However, if the slope of the distribution function is not as sharp, such as for the Gaussian distribution shown in Fig. 4b, electron-ion collision are damping if the thermal spread in v_z is sufficiently large. The slope of the distribution function on the high velocity side does not affect the stability analysis.

Before the beam bunches, the distribution in v_z is determined by the injection condition. Since the ions are injected into the channel nearly uniformly over a range of angles predominately in the r-z plane and since the time-averaged axial velocity for an ion injected at a given α varies like $V_b(1-\alpha^2/2)$, the distribution in v_z rises slowly as indicated in Fig. 4c. Additional smoothing out of the distribution in v_z will result from beam energy spreading due to radial variations in the diode voltage. The stability properties of this distribution closely resemble those of the Gaussian distribution. The beam ion distribution after bunching is also similar in shape to Fig. 4c. Since the ion diodes which are used in the experiments have a constant impedance behavior during the duration of the ion pulse, more ions (higher currents) are generated at higher energies as the diode voltage ramps upward. Thus in the bunched state there are more ions at higher velocities than at lower velocities and the spread in axial velocities is on the order of $(2Z_de/m_i)^{1/2}(\phi_f^{1/2}-\phi_o^{1/2})$. Here Z_d is the charge state of the beam ions in the diode and ϕ_o and ϕ_f are the initial and final diode voltages. This spread can be considerably larger than the initial spread before bunching ($V_t \sim V_b\alpha_m^2/2$).

Thus a Gaussian distribution can be used to properly model the ion beam distribution function both before and after bunching when considering ES modes. When the analysis is not sensitive to the detailed shape of the distribution function (e.g. for analyzing the stability of EM modes), simpler models may be used.

3. LINEAR STABILITY ANALYSIS

The results of linear stability analyses reported previously[17,18,22] are presented here in a more general form so that they may be applied to beams of various species. The composition of the channel plasma is also unspecified. Growth rates will vary as the beam heats the channel plasma and as the channel expands. The changes in the hydrodynamic structures of

the channel occur gradually over the pulse duration of the beam. Growth rate expressions appropriate near both the front and the tail of the beam are presented in order to determine how hydrodynamic changes alter the results. Most notably these changes include (1) a reduction in the e-i collision frequency at the tail of the beam where the plasma is heated, and (2) a reduction in the magnetic field in the interior of the channel at late times in the pulse as the now highly conducting heated plasma expands due to $\underset{\sim}{J} \times \underset{\sim}{B}$ forces. Near the front of the beam, the beam ions follow betatron-like orbits while at the tail of the beam, the beam ions move in more straight line-like orbits with reflections off of the magnetic field piled up at the edge of the channel.

3.1. ES Modes

The ES modes are the fastest growing modes when driven unstable. Unstable growth will generally reach nonlinear saturation on a time scale much faster than the beam pulse duration. These modes involve either charge bunching (e-b and e-i modes) or density bunching (ion-acoustic mode) and generally exhibit their largest growth for $\underset{\sim}{k} = k\hat{e}_z$, which is a result of the small thermal spread in the axial direction before axial beam compression occurs.

3.1a. e-b Two Stream Mode

The e-b two stream instability is driven by the relative streaming between the beam ions and plasma electrons. In general the beam can be considered warm because $V_t(z)/V_b \geq 2\left[m_e Z_b^2 n_b(z)/m_b Z_p n_p\right]^{1/3}$ even before beam bunching occurs. Here m_b is the beam ion mass. Near the front of the beam the betatron motion of the ions can reduce the growth rate of the mode which is given by

$$\gamma_1 = -\frac{\nu_{ei}}{2} + 0.76\,\frac{\omega_{pb}^2(z)}{\omega_{pe}}\left(\frac{V_b}{V_t(z)}\right)^2 R \qquad (1)$$

where $\omega_{pb}^2 = 4\pi e^2 Z_b^2 n_b(z)/m_b$ and $\omega_{pe}^2 = 4\pi e^2 Z_p n_p/m_e$ are the beam and electron plasma frequencies respectively. The electron-ion collision frequency is given by $\nu_{ei} = 1.45\times10^{-6} Z_p^2 n_p \lambda_{ei}/T_e^{3/2}$, where T_e is in eV and λ_{ei} is the Coulomb logarithm. The reduction factor, R, equals the fraction of beam ions which can effectively participate in the wave growth. If $\gamma_1 > 2\omega_\beta$, which is the usual case, all ions can participate and R = 1. Here $\omega_\beta = (V_b\omega_{cb}/r_c)^{\frac{1}{2}}$ is the ion betatron frequency and ω_{cb} is the beam cyclotron frequency. If $\gamma_1 \lesssim 2\omega_\beta$, only those ions with $\Delta z < 1/k$ can participate, where Δz is the amplitude of the betatron oscillations about $z = \bar{v}_z t$ (see Fig. 5). The amplitude, Δz, depends on the ion injection conditions, $r(z=0)$ and $\alpha(z=0)$.[17] If this amplitude is large, the ion moves across many wave fronts before the instability e-folds even once, and thus cannot effectively participate in wave growth. The value of R must be calculated from the actual distribution function. For a Gaussian distribution $R \sim 8\omega_\beta V_b/kV_t^2$ for $k > 8\omega_\beta V_b/V_t^2$ and $R = 1$ for $k < 8\omega_\beta V_b/V_t^2$. At the tail of the beam, betatron effects are less important, so that R = 1 in Eq. (1).

Beam heating of the plasma can considerably reduce the damping term in Eq. (1) as e-i collisions become less frequent. Beam bunching, on the other hand, reduces the driving term in Eq. (1) as V_t increases dramatically. Thus the potentially most dangerous position for wave growth lies at the tail of the beam (R = 1) at the beginning of the transport channel before significant beam bunching occurs.

3.1b. e-i Two Stream Mode

The e-i two stream mode is driven by the relative streaming between the background electrons and ions. The electrons drift with an average velocity $V_e \sim n_b Z_b V_b / Z_p n_p$ relative to the stationary ions and in general $V_e < u_e$. Here u_e is the thermal velocity of the electrons. The expression for the growth (damping) rate is

$$\gamma = -\nu_{ei} - (\pi/8)^{1/2} \frac{kc_s}{(1+k^2\lambda_{De}^2)^2} \left\{ Z_p (T_e/T_i)^{3/2} \exp\left[- \frac{T_e}{2T_i(1-k^2\lambda_{De}^2)} \right] \right.$$

$$\left. + \frac{m_e}{m_i} \left(1 - \frac{V_e}{c_s} \left[1+k^2\lambda_{De}^2 \right]^{1/2} \right) \right\} \qquad (2)$$

where $c_s = (T_e/m_i)^{1/2}$ is the ion sound speed, $\lambda_{De} = (T_e/4\pi e^2 Z_p n_p)^{1/2}$ is the electron Debeye length and where a simple Krook model was used for the collision term. In deriving Eq. (2), it was assumed that $\nu_{ei} < kc_s/(1+k^2\lambda_{De}^2)^{1/2}$. When $T_e \sim T_i$ this reduces to

$$\gamma_2 \approx -\nu_{ei} + (\pi/8)^{1/2} \frac{kc_s}{(1+k^2\lambda_{De}^2)^{3/2}} \left\{ \frac{V_e}{u_e} - \frac{Z_p \exp\left[- \frac{1}{2(1+k^2\lambda_{De}^2)} \right]}{(1+k^2\lambda_{De}^2)^{1/2}} \right\} . \qquad (3)$$

Since V_e is usually less than u_e, the mode is typically stable.

3.1c. Ion-Acoustic Mode

If $T_e >> T_i$, then the drifting electrons can drive an ion-acoustic instability. In this case Eq. (2) reduces to

$$\gamma_3 \approx -\nu_{ei} + \left(\frac{\pi m_e}{8 m_i} \right)^{1/2} \frac{k}{(1+k^2\lambda_{De}^2)^{3/2}} \left[V_e - \frac{c_s}{(1+k^2\lambda_{De}^2)^{1/2}} \right] \qquad (4)$$

This predicts instability ($\gamma > 0$), if $V_e/c_s > (1+k^2\lambda_{De}^2)^{-1/2}$ and if ν_{ei} is sufficiently small. However, the severity of the condition on T_e/T_i is often overlooked. For V_e/c_s as large as 5, T_e/T_i must be greater than 12 for instability even for $k\lambda_{De} << 1$. Figure 6 shows the critical values of T_e/T_i for instability versus k for various values of V_e/c_s (assuming $\nu_{ei} = 0$). Since T_e/T_i is not expected to reach such high levels, in general ion-acoustic turbulence is not expected.

3.1d. ES Stability Conditions

Since the e-b mode is the only ES instability which could be generated, it is important to state under which conditions it may be avoided. For stability ($\gamma_1 \leq 0$) Eq. (1) states that

$$\frac{Z_p^{5/2} n_p^{3/2} \lambda_{ei}}{T_e^{3/2}} \geq 3.2 \times 10^7 \frac{Z_b^2 n_b(z) V_b^2}{\mu_b V_t^2(z)} \tag{5}$$

is required. Here $\mu_b = m_b/m_p$, T_e is measured in eV and all other variables are in Gaussian units. This condition used in conjunction with the condition

$$n_p \approx 1.4 \times 10^{12} I_{ch} r_{ch}^{-2} (I_b(z) \tau_b(z)/S)^{\frac{1}{2}} , \tag{6}$$

derived from MHD considerations[15], set constraints on n_p and T_e for good transport. Here I_{ch} and I_b are measured in amps and S is the beam stopping power of the plasma measured in erg·cm^2/g. Eq. (6) gives the ion density in the channel required for minimum beam energy loss in the channel during transport. Given this required ion density, Eq. (5) sets an upper limit on T_e, beyond which electrostatic turbulence will set in. For good transport both of these conditions must be satisfied. Generally the stability criterion in Eq. (5), is most severely tested at the tail of the beam where T_e is largest and at the beginning of the transport channel before significant bunching occurs where $V_t(z)$ is smallest ($V_t(z)/V_b \sim \alpha_m^2/2$).

3.2 EM Modes

The EM modes are slower growing modes than the ES modes, so that even if the mode is unstable, growth may not have sufficient time to reach nonlinear saturation during the pulse duration of the beam. The modes are nearly purely growing (i.e. do not convect with the beam) and involve current bunching or filamentation of the beam and/or plasma channel. The wave vector, $\underset{\sim}{k}$, is oriented perpendicular to the direction of beam propagation with $\underset{\sim}{k} = k\hat{e}_r$ for the Weibel mode (radial current bunching) and $\underset{\sim}{k} = k\hat{e}_\theta$ for the whistler mode (azimuthal current bunching). In addition, the cylindrical geometry dictates that $k_r \geq 2\pi/r_b$ and $k_\theta \geq \ell/r_b$ where ℓ is an integer.

3.2a. Beam-Whistler Mode

The beam-whistler instability is driven unstable by the relative streaming motion between the beam ions and the channel plasma. Since the wave vector is in the azimuthal direction and the beam ions execute their betatron orbits in the r-z plane, the betatron motion of the beam has little effect on the mode. However, a small spread in angular momentum, which is observed experimentally, can reduce the growth rate significantly. With no spread in angular momentum ($V_\theta^2/c^2 < 2\nu_{ei}\omega_{pb}V_b/c\omega_{pe}^2$) the growth rate is

$$\gamma = \omega_{pb}(z) V_b / c , \tag{7}$$

and with $V_\vartheta^2/c^2 > 2\nu_{ei}\omega_{pb}(z)V_b/c\omega_{pe}^2$ the peak growth rate is

$$\gamma_4 = 2\nu_{ei}\omega_{pb}^2(z)V_b^2/V_\vartheta^2\omega_{pe}^2 \tag{8}$$

at $k \sim \gamma_4/V_b$. Here V_ϑ is a measure of the thermal spread in the azimuthal velocity of the beam ions. If $kr_b < 1$, peak growth rate is reduced to $[1-(k_o r_b)^{-2}]\gamma_4$ because of geometry constraints and if $k_o r_b < 1$, no growth is possible. The critical wavenumber $k_o = \sqrt{2}\omega_{pb}(z)V_b/cV_\vartheta$ [see Eq. (35), Ref. 18].

If there is wave growth at a given point in z, the number of e-folds that occurs is just

$$N = \int_o^{\tau_b(z)} \gamma(t)dt \ , \tag{9}$$

where the time dependence of the plasma parameters must be considered. Most importantly ν_{ei} decreases at $T_e^{-3/2}(t)$ as the plasma is heated by the passing beam. Note that beam thermal effects do not completely quench the instability because of the finite plasma resistivity. Given information from MHD considerations on the time variation of the plasma parameters due to beam passage, one can then determine from Eq. (9) whether significant azimuthal beam current bunching occurs.

3.2b. Beam-Weibel Mode

For the beam-Weibel instability the wave vector is in the radial direction. In this case the spread in perpendicular velocities associated with the betatron motion of the beam ions reduces the growth rate of the instability. A measure of the radial velocity spread is given by $V_o\alpha_m$, so that the peak growth rate is given by

$$\gamma_5 = 2^{4/5}\nu_{ei}\omega_{pb}^2(z)/\omega_{pe}^2\alpha_m^{8/5} \tag{10}$$

at $k \sim \gamma_5/V_b\alpha_m^{7/5}$. Again the number of e-folds that occur at a given point in z can be determined by Eq. (9) and MHD considerations. Since the thermal spread in the radial velocity is typically comparable or larger than the thermal spread in the azimuthal velocity, the beam-Weibel instability is generally less dangerous than the beam-whistler mode. A superposition of both unstable modes, however, will lead to beam filamentation.

3.2c. Plasma-Electron Mode

If beam thermal effects or geometry constraints prevent the beam from driving strong EM wave growth, instability can still result from the electron return current established with the plasma. Because of the high collisionality ($\nu_{ei} > \omega_{ce}$) of the plasma electrons, radial ($\underset{\sim}{k} = \underset{\sim}{k}\hat{e}_r$) and azimuthal ($\underset{\sim}{k} = k\hat{e}_\vartheta$) EM modes driven by the plasma electrons are essentially indistinguishable (aside from small geometric effects). The analysis must include electron thermal effects, as well as collisional effects since the

electron streaming velocity is subthermal even early in the pulse before beam heating occurs.

At early times in the pulse when $\omega_{pe}u_e/cv_{ei} > 1$, the peak growth rate is

$$\gamma = (\omega_{pi}V_e/c)(2-Z_p^{-1})^{\frac{1}{2}} \quad . \tag{11}$$

Later in the pulse after the beam heats the plasma if $\omega_{pe}u_e/cv_{ei} > 1$, then thermal effects slows the growth of the mode. The maximum growth rate is then given by

$$\gamma = 2^{-3/2}\omega_{pe}V_e^2/cu_e \quad . \tag{12}$$

At all times in the pulse geometry constraints prevent wave growth if $k_o r_b < 1$ where in this case $k_o = \omega_{pe}V_e/\sqrt{2}u_e c$. Since again this mode does not convect, the number of e-folds at a given point in z can be obtained from Eqs. (11), (12) and (9) and MHD considerations.

3.2d. EM Stability Conditions

If the growth rates of the EM instabilities are slow enough such that less than one e-fold (N<1) occurs during beam passage, wave growth will be washed out by the MHD changes in the beam-plasma system. Only wave growth with N>1 will affect beam transport. In order to prevent the beam from filamenting, the beam should then have

$$\alpha_m^2 \geq V_\theta^2/V_b^2 > 1.6\times10^{-9}\,\frac{n_b(z)}{\mu_b}\int_o^{\tau_b(z)}\left(\frac{Z_p\lambda_{ei}}{T_e^{3/2}}\right)dt \quad , \tag{13}$$

where again T_e is in eV's and n_b is measured in cm^{-3}. This condition is derived from Eq. (8) for azimuthal current bunching which is typically more severe than the condition for radial current bunching since α_m is usually greater than V_θ/V_b. Here it is also assumed that $\sqrt{2}\omega_{pb}(Z)r_bV_b/cV_\theta > 1$, which is the usual case. In order to evaluate Eq. (13), a knowledge of the MHD response to beam passage is required, in particular, one must know the time history of the electron temperature.

If the beam is warm enough to prevent beam filamentation (i.e., Eq. (13) is satisfied), it is still possible for the channel to filament. Channel filamentation is avoided if

$$\frac{J_b(z)}{n_p^{\frac{1}{2}}}\left(\frac{9.4\times10^1}{\mu_p^{\frac{1}{2}}}\int_o^{t_1(z)}(2-Z_p^{-1})dt + 6.9\times10^4\,J_b(z)\int_{t_1(z)}^{\tau_b(z)}\frac{dt}{n_pZ_p^{3/2}T_e^{\frac{1}{2}}}\right) \leq 1 \; . \tag{14}$$

Here $\mu_p = m_p/m_H$, $J_b(z)=Z_b e n_b(z)V_b$, J_b is measured in sA/cm^2 and t_1 is defined as the time it takes for the beam to heat the plasma

to $T_e^1 = 1.4\times10^{-4}(Z_p^3(t_1)n_p\lambda_{ei}^2)^{1/4}$ in eV. If $T_e(0) > T_e^1$, then $t_1 = 0$ and the first term in Eq. (14) does not contribute. If $t_1 \geq \tau_b$, then the second term in Eq. (14) does not contribute and the limits on the integration of the first term go from 0 to $\tau_b(Z)$. In Eq. (14) it was assumed the $\mu_{pe}r_bV_e/2u_ec > 1$, which is the usual case. Eq. (14) sets an upper limit on transportable beam current density above which channel filamentation will develop.

4. CONCLUSIONS

The stability conditions in Eqs. (5), (13) and (14), identify important constraints on beam propagation. Eq. (5) together with Eq. (6) states that the plasma cannot be heated above a certain critical temperature without generating electrostatic microturbulence. Such turbulence will degrade beam quality and confinement. In general the most severe constraint on T_e exists at the tail of the beam before bunching occurs where the critical temperature is defined by

$$T_e^c(\text{eV}) \equiv 10^{-6}\left(\frac{\mu_b^2 n_p^3 Z^5 \lambda_{ei}^2 \alpha_m^8}{Z_b^4 n_b^2(z=0)}\right)^{1/3} , \qquad (15)$$

where n_p is given in Eq. (6). By increasing n_p the critical temperature can be raised at the expense of increasing the beam energy loss during transport. Operating at twice the density specified in Eq. (6) increases T_e^c by a factor of two but only increases the beam energy loss by 25%. The actual temperature that the electrons will reach for a given beam and background gas is not always easily estimated and must be calculated on a case to case basis and compared with the critical temperature defined in Eq. (15). Here α_m is a measure of the spread in axial velocities in the beam, which for a monoenergetic beam is given by $\Delta V_z/V_b \sim \alpha_m^2/2$. If the beam has a spread in energy such that $\alpha_m^2 < \Delta E/E$, then α_m^3 in Eq. (15) should be replaced by $(\Delta E/E)^{\frac{3}{2}}$.

Growth of electromagnetic waves can be held to a tolerable level by allowing for a reasonable spread in beam perpendicular energy and limiting the beam current density. If the beam is too cold, beam filamentation can occur during beam transport. The condition for good beam transport is given in Eq. (13). If the beam does not filament but the beam current density is too high, the return current in the channel can cause channel filamentation. In order to prevent this from occurring Eq. (14) should be satisfied. The conditions given in Eqs. (13) and (14) may actually be too severe since channel hydrodynamic effects have not been included self consistently in the analysis. Channel expansion due to $J \times B$ force may tend to prevent growth of these transverse modes. These effects are presently under investigation.

5. REFERENCES

1. S. A. Goldstein and R. Lee, Phys. Rev. Lett. 35, 1079 (1975).

2. J. W. Poukey, J. R. Freeman, M. J. Clauser, and G. Yonas, Phys. Rev. Lett. 35, 1806 (1975).

3. J. W. Poukey, J. Vac. Sci. Technol. 12, 1214 (1975)

4. A. E. Blaugrund, G. Cooperstein, J. R. Boller and S. A. Goldstein Bull. Am. Phys. Soc. 20, 1252 (1975).

5. P. A. Miller, C. W. Mendel, D. W. Swain, and S. A. Goldstein, in Proceedings of the International Topical Conference on Electron Beam Research and Technology, Albuquerque, New Mexico (1975), p. 619.

6. G. Cooperstein, S. J. Stephanakis, J. R. Boller, R. Lee, and S. A. Goldstein, in Proceedings of the 1976 IEEE International Conference on Plasma Science, Austin, Texas (IEEE, New York, 1976), p. 126.

7. D. J. Johnson. G. W. Kuswa, A. V. Farnsworth, Jr., J. P. Quintenz, R. J. Leeper, E. J. T. Burns, and S. Humphries, Jr., Phys. Rev. Lett. 42, 610 (1979); D. J. Johnson, Bull. Am. Phys. Soc. 24, 925 (1979).

8. G. Cooperstein, S. A. Goldstein, D. Mosher, W. F. Oliphant, F. L. Sandel, S. J. Stephanakis and F. C. Young in Proceedings Third International Topical Conference on High Power Electron and Ion Beam Research and Technology, Novosibirsk, USSR (1979).

9. G. Cooperstein, S. A. Goldstein, D. Mosher, R. J. Barker, J. R. Boller, D. G. Colombant, A. Drobot, R. A. Meger, W. F. Oliphant, P. F. Ottinger, F. L. Sandel, S. J. Stephanakis and F. C. Young, in Laser Interaction and Related Plasma Phenomena, edited by H. Schwarz, H. Hora, M. Lubin and B. Yaakobi, (Plenum Press, New York, 1980).

10. R. O. Bangerter and D. J. Meeker, in Proceedings of the Second International Topical Conference on High Power Electron and Ion Beam Research and Technology, Ithaca, New York (1977), p. 183; J. H. Nuckolls, in Proceedings of the Topical Meeting on ICF (Opt. Soc. of Am. Wash., DC, 1978) paper TuA5.

11. S. A. Goldstein, D. P. Bacon, D. Mosher and G. Cooperstein Proceedings of the Second International Topical Conference on High Power Electron and Ion Beam Research and Technology, Ithaca, New York (1977), p. 71.

12. D. Mosher, G. Cooperstein, S. A. Goldstein, in Digest of the Topical Meeting on ICF (Opt. Soc. of Am., Wash., DC, 1980), paper ThC5.

13. D. Mosher, Bull. Am. Phys. Soc. 24, 926 (1979).

14. D. Mosher and S. A. Goldstein, Bull. Am. Phys. Soc. 23, 800 (1978).

15. D. G. Colombant, D. Mosher and S. A. Goldstein, Phys. Rev. Lett. 45, 1253 (1980).

16. P. F. Ottinger, D. Mosher and S. A. Goldstein, Phys. Fluids 23, 909 (1980).

17. P. F. Ottinger, D. Mosher and S. A. Goldstein, Phys. Fluids 22, 332 (1979).

18. P. F. Ottinger, D. Mosher and S. A. Goldstein, Phys. Fluids 24, 164 (1981).

19. F. Sandel. G. Cooperstein, S. A. Goldstein, D. Mosher and S. J. Stephanakis, Bull. Am. Phys. Soc. 24, 1031 (1979).

20. D. A. Hammer and N. Rostoker, Phys. Fluids 13, 1831 (1970).

21. B. S. Newberger and L. E. Thode, Bull. Am. Phys. Soc. 24, 1097 (1979).

22. P. F. Ottinger, Conference Record-Abstracts of the 1980 IEEE International Conference on Plasma Science, Madison, Wisconsin (IEEE, New York, 1980), p. 57.

23. V. U. Abramovich and V. I. Sevchenko. JETP 35, 730 (1972).

24. P. F. Ottinger, S. A. Goldstein and D. Mosher, NRL Memorandum Report 4180 (1980).

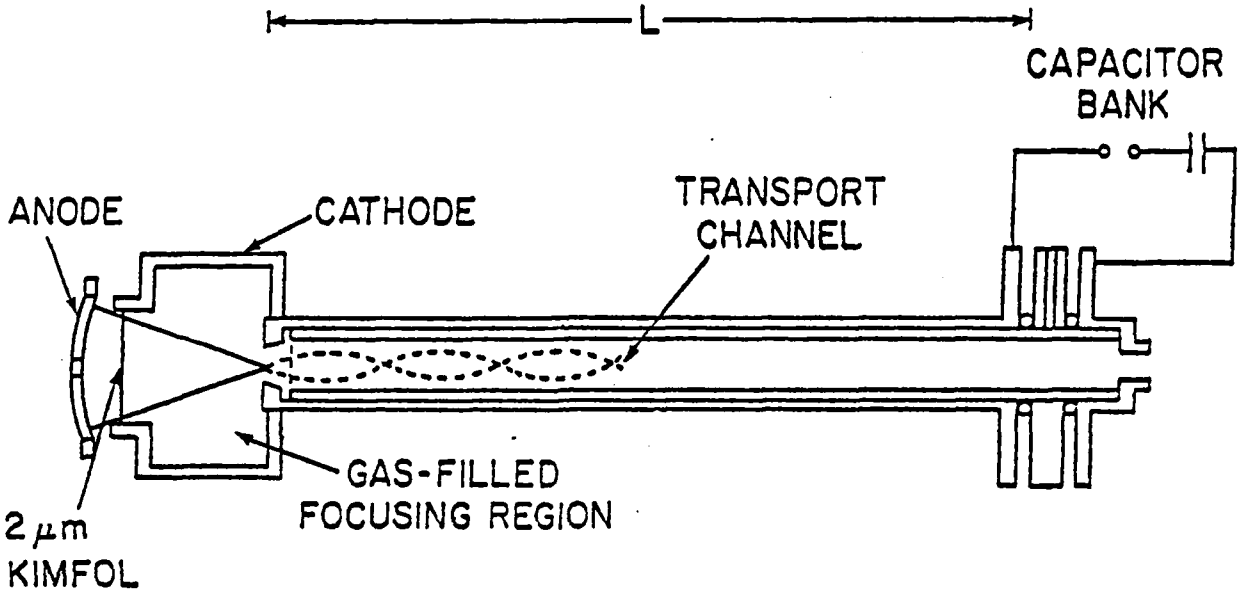

IDEAL DIODE VOLTAGE WAVEFORM:

$$\phi(t) = \frac{\phi_o}{(1 - t/t_a)^2} \; ; \quad 0 \le t \le \tau_b < t_a$$

Fig. 1—Schematic of ion diode, focusing region and transport channel for light ion beam ICF module. The ideal diode voltage waveform for axial bunching is also shown where ϕ_0 in the initial diode voltage, t_a is the beam arrival time at the target and τ_b is the beam pulse duration at injection.

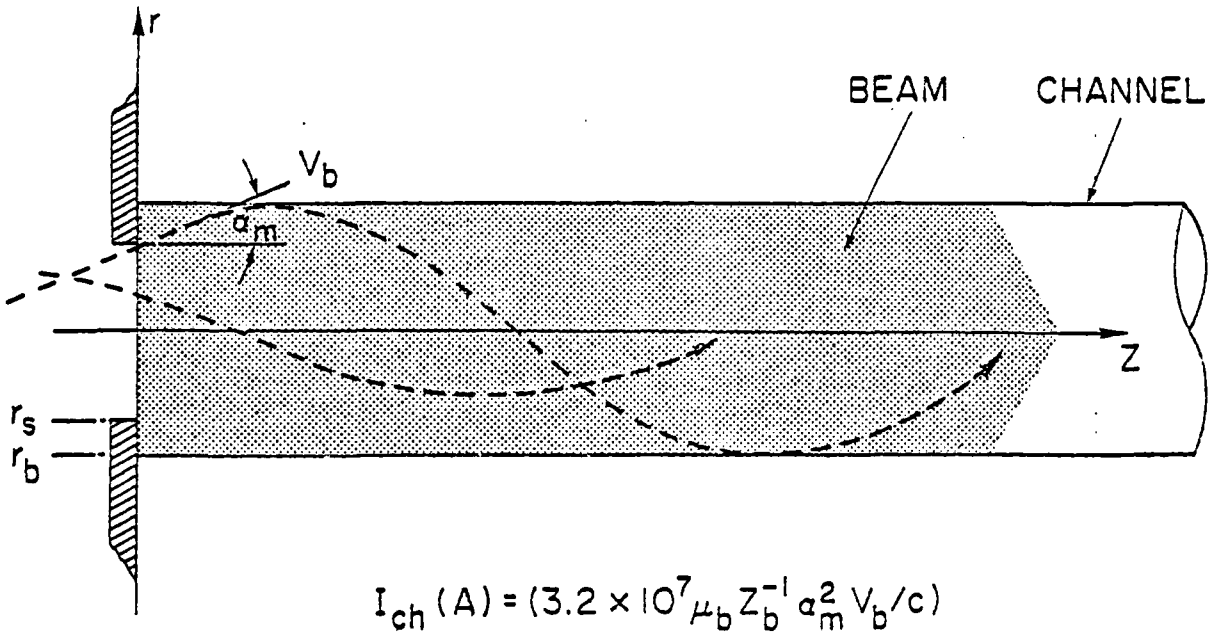

Fig. 2—Schematic of beam propagation in a z-discharge channel. Here $\frac{1}{2}m_i V_b = Z_d e\phi$ (where Z_d is beam ion charge state in the diode and ϕ is the diode voltage), α_m is the maximum injection angle, r_s is the beam spot size (or aperture size) and r_b is the beam radius in the channel. Also shown is the channel current required to confine the beam where Z_b is the charge state of the beam ions in the channel and $\mu_b = m_b/m_H$.

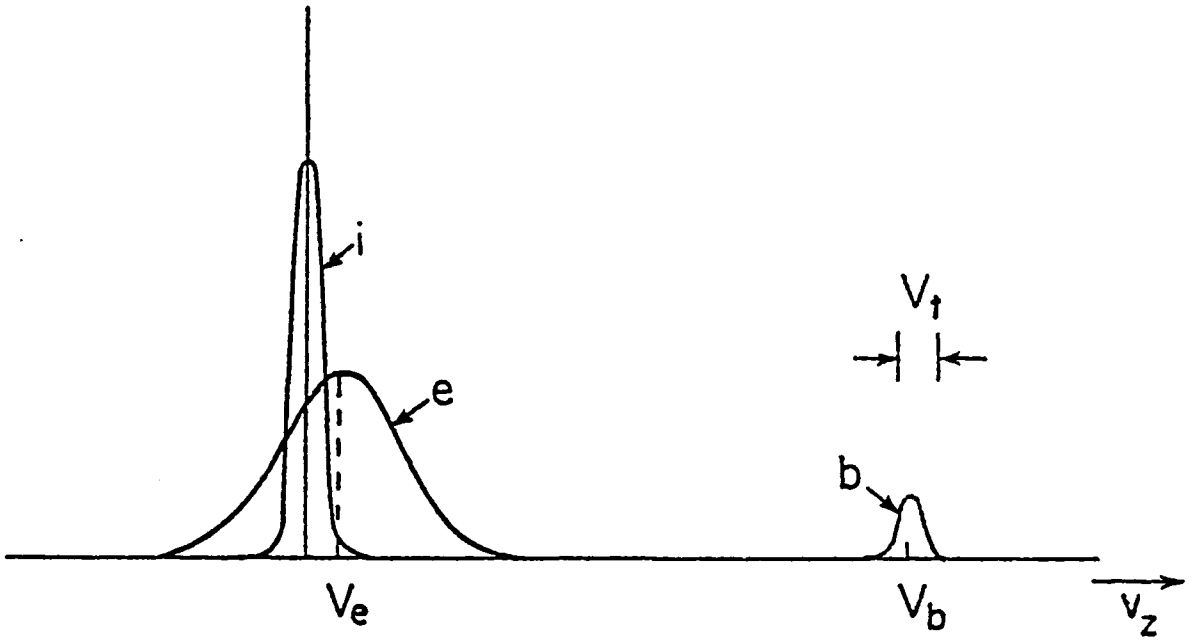

PLASMA:

$T_e \gtrsim T_i$

$\nu_{ei}(T_e) > \omega_{ce}$

$V_e \approx Z_b n_b V_b / Z_p n_p < \left(T_e/m_e\right)^{1/2}$

BEAM:

$V_b/c << 1$

$n_b << n_p$

$\frac{V_t}{V_b} \approx \alpha_m^2$

Fig. 3—Schematic of particle distribution in v_z. Here i, e and b are the plasma ions, plasma electrons and beam ions, respectively, and V_t is the measure of the spread in the beam distribution. Other typical beam-plasma conditions are also listed.

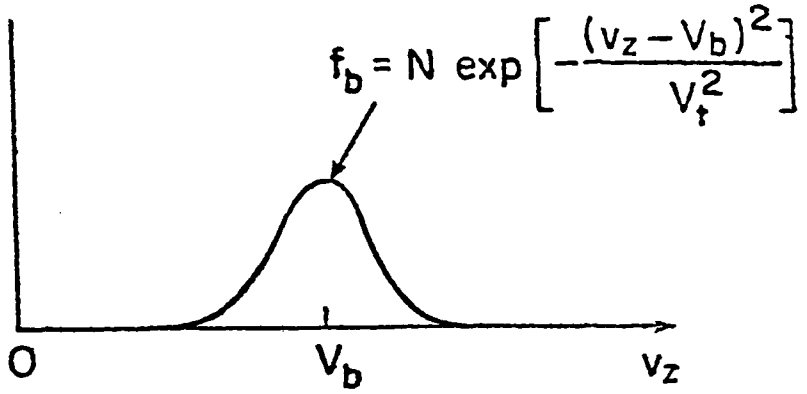

(A)

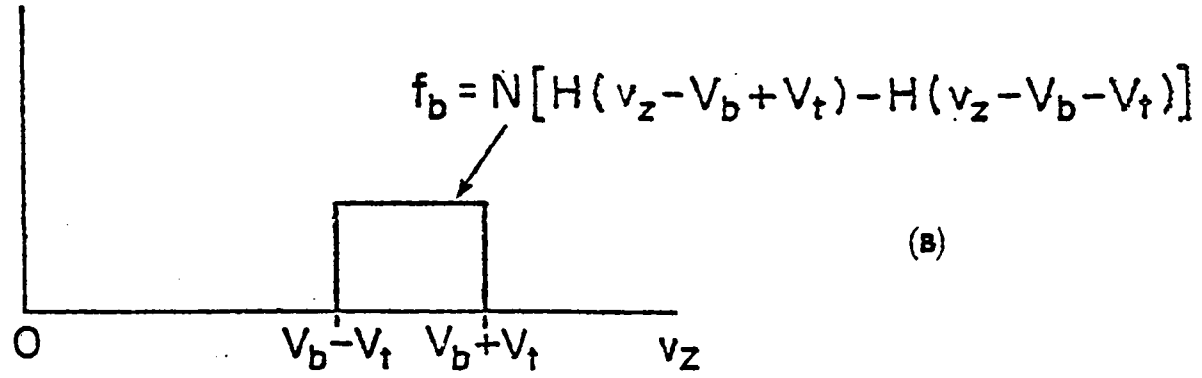

(B)

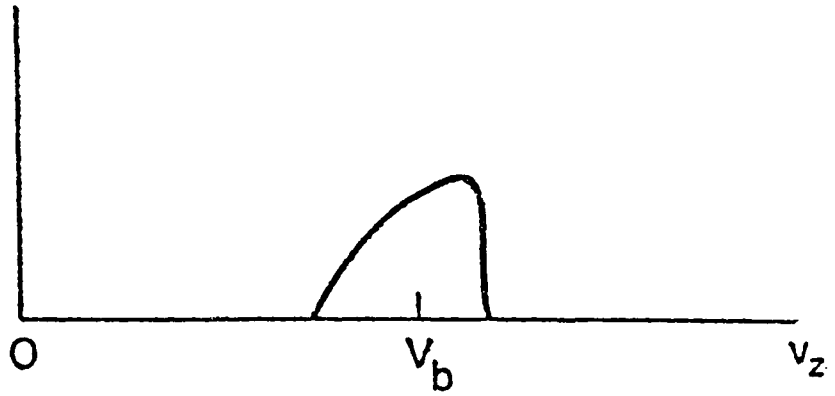

(C)

Fig. 4—Distribution of beam ions in v_z for (a) a uniform distribution, (b) a Gaussian distribution actual distribution and (c)

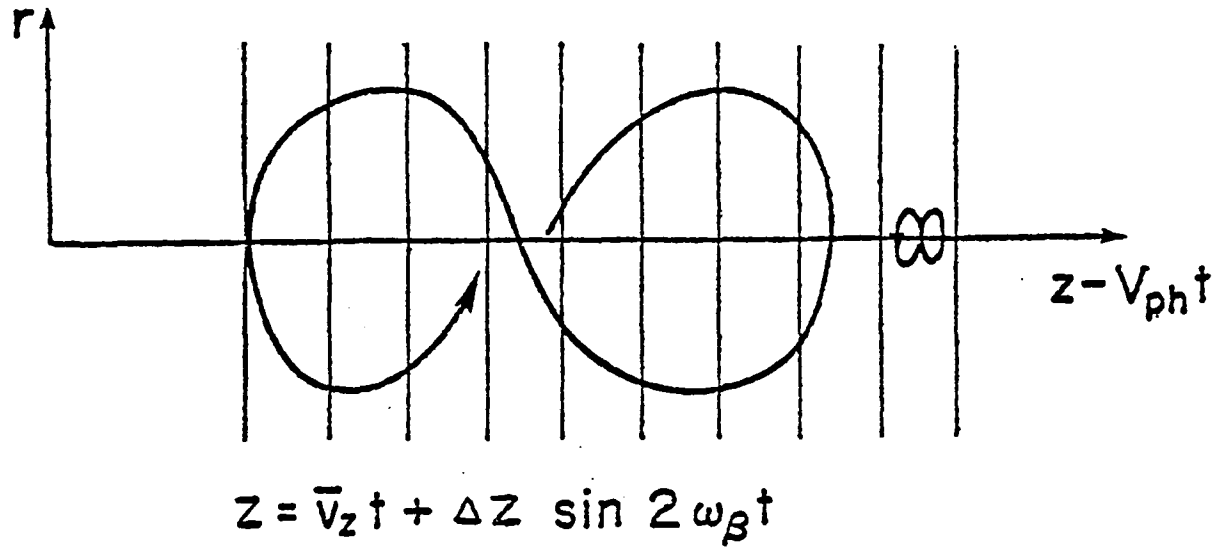

Fig. 5—Beam ion orbits in a frame of reference moving with the phase velocity of an ES wave

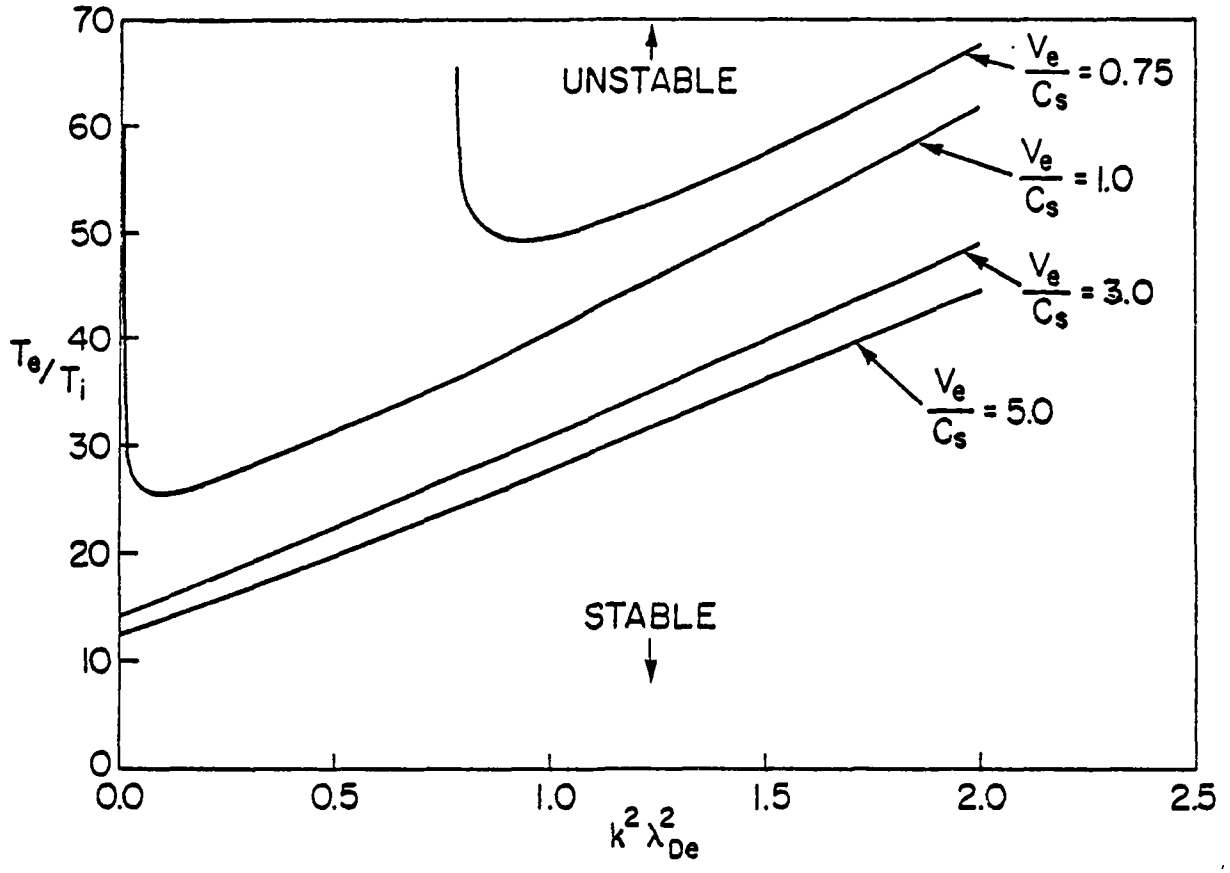

Fig. 6—Critical values of T_e/T_i for ion-acoustic instability (assuming $\nu_{ei} = 0$). Regions above the curves are unstable and below the curves are stable.

CONSTRAINTS ON TRANSPORTABLE ION BEAM POWER

1. INTRODUCTION

The development of terawatt-level ion beams has generated a great deal of interest in using light-ion beams to drive thermonuclear pellets.[1-9] Target design studies for light-ion beams indicate that ~4 MJ of ions must be delivered in ~10 ns to an ~1 cm diameter pellet in order to achieve high gain thermonuclear ignition.[10] Since present technology cannot provide a single-module pulsed-power system from which 4 MJ of ions can be extracted, a multimodule system is required. In addition, a transport scheme and a method for beam pulse compression are needed, since typical pulse durations are on the order of ~50 ns.

One possible transport scheme involves the use of a z-discharge channel for transporting ion beams.[11] Focusing can be achieved by a combination of geometric and magnetic-field focusing prior to injection into the channel.[12,13] Beam-pulse compression results from ramping the diode voltage so that the tail of the beam catches up to the head of the beam.[13,14] In addition, a final focusing cell can be used at the exit of the transport system to radially compress the beam to pellet size.[15] Figure 1 illustrates one module of such a multimodule system.

Assuming that the z-discharge channel is itself produced in the MHD stable configuration, the question of the effects that the passage of the beam will have on the equilibrium and stability of the beam-plasma system is an important one. The MHD response of the plasma has been treated elsewhere[16] and will only be briefly reviewed here. Analyses of stable beam propagation in straight and tapered channels, as well as in bumpy channels (subject to sausage instability), have also been done previously.[17] This work shows that,

Manuscript approved September 20, 1982.

in the absence of microinstabilities driven by the beam, good beam transport and bunching is possible under the conditions set by MHD considerations (which will be outlined in Sec. 3).[18] However, in the presence of microinstabilities, beam transport and bunching can be seriously affected.

Transport constraints arising from electrostatic (ES) and electromagnetic (EM) velocity-space instabilities,[19,23] which can grow on a time scale much faster than the beam pulse duration, will be reviewed in this report. The problem will be considered with the goal of identifying an operational window for good transport and bunching. The results will be presented in a general form so that they may be applied to beams of various low atomic number species propagating in channel plasmas of different compositions.

2. STABILITY CONSTRAINTS

In order to provide stable transport for the beam, certain constraints are put on the transport system. The two-stream instability will rapidly generate electrostatic microturbulence unless growth of the mode is prevented.[19,21,22] Such turbulence will degrade beam quality and confinement. By maintaining the plasma electron temperature below the critical temperature,

$$T_e^c(eV) = 10^{-5}\left(\frac{A_b^2\, n_p^3\, Z_p^5\, \lambda_{ei}^2}{Z_b^4\, n_b^2}\right)^{1/3}\left(\frac{\Delta V_z}{V_b}\right)^{4/3} , \qquad (1)$$

the two-stream mode will remain collisionally stabilized. In Eq. (1) A_b is the atomic weight of the beam ion, n_b and n_p are the beam and plasma ion densities measured in particles/cm^3, Z_b and Z_p are the beam and plasma ion charge states, V_b is the beam velocity, ΔV_z in the axial velocity spread of the beam and λ_{ei} is the Coulomb logarithm. In general, the most severe

constraint on T_e exists at the tail of the beam (after the front of the beam has heated the channel) prior to beam bunching (at the beginning of the transport channel). Note that by increasing n_p, T_e^c can be raised. Operating at twice the density required for minimum beam energy loss during transport, increases T_e^c by a factor of two but only increases the beam energy loss by 25%.[16]

One can estimate the final temperature from the rate of collisional beam deposition in the channel plasma by using[16]

$$T_e^f \text{ (eV)} = T_o + 6.9\times10^9 \, J_b \tau_b / \bar{E} \quad , \tag{2}$$

so that the ES stability constraint is given by

$$T_e^f < T_e^c \quad . \tag{3}$$

Here T_o is the initial electron temperature measured in eV, J_b is the beam current density measured in MA/cm^2, τ_b is the pulse duration of the beam measured in seconds and $\bar{E}$ is the average beam energy measured in MeV. In deriving Eq. (2) it is assumed that $T_e \sim T_i$ since this is the usual case; this also precludes the existence of ion acoustic instability. In plotting constraint curves one-to-two times the density required for minimum beam energy loss is used to calculate n_p and a 10% spread in beam energy is assumed so that $\Delta V_z/V_b = 0.05$ in Eq. (1). T_o was chosen to be ~10 eV in Eq. (2). It will also be assumed in all the stability constraints considerations that

deuterium gas is used to fill the transport system so that Z_p=1 and A_p=2. If the beam is monoenergetic, $\Delta V_z/V_b \sim \theta_m^2$ for the ES stability constraint. Here θ_m is the maximum angle of injection into the transport channel. However, foil scattering and field fluctuations are expected to produce a spread in beam ion energies of about 10% and this spread will be used in the ES stability constraint curves. Energy spreads larger than about 15% at injection into the channel may adversely affect beam bunching.

Growth of electromagnetic waves can be held to a tolerable level by allowing for a reasonable spread in beam perpendicular energy and limiting the beam current density.[20-23] If the beam is too cold, beam filamentation can occur during transport. The condition for good beam transport is

$$\theta_m^2 \sim \frac{V_\phi^2}{V_b^2} > 3.2\times10^{-18}\left(\frac{Z_p \lambda_{ei} n_b \tau_b}{A_b T_e^f T_o^{1/2}}\right) , \qquad (4)$$

where V_ϕ is a measure of azimuthal velocity spread in the beam and T_e^f and T_o are defined in Eq.(2). Here it is assumed that the azimuthal velocity spread is comparable with the radial velocity spread (i.e., $\theta_m \sim V_\phi/V_b$), which is consistent with experimental observations. Note that high electron temperatures are beneficial here, whereas $T_e^f < T_e^c$ is required for two-stream stability.

If the beam does not filament but the beam current density is too high, the return current in the channel can cause channel filamentation. In order to prevent this from occurring requires that[22]

$$J_b < 3.6\times10^{-18}(A_p n_p)^{1/2}\left[(2-Z_p^{-1})t_1 + \frac{1}{n_p Z_p^{3/2} T_e}\frac{.1\times10^{18} J_b \tau_b A_p}{}^{1/2}\left(T_e^{f\,1/2} - [T_o + (T_e^f - T_o)\frac{t_1}{\tau_b}]^{1/2}\right)\right]^{-1}, \quad (5)$$

where t_1 is defined as the time it takes for the beam to heat the plasma to $T_e(t_1) = 1.4\times10^{-4}(Z_p^3 n_p \lambda_{ie}^2)^{1/4}$ in eV. If $T_e(t_1) < T_o$, $t_1 = 0$ and the first term in the large square brackets on the right hand side of Eq. (5) is dropped. If $t_1 > \tau_b$ the last term in the large square brackets is dropped. In the cases considered in Sec. 4, the first term in the square brackets in Eq. (5) can be ignored, since T_o is found to be ~ 10 eV for deuterium discharges which is typically greater than $T_e(t_1)$. For higher Z channel gases this may not be the case.

Eqs. (3)-(5) are the stability constraints which limit the transportable beam power. These constraints along with MHD and energy-loss considerations will determine an operational window for good transport and bunching.

3. MHD AND ENERGY-LOSS CONSTRAINTS

The plasma return current driven in the channel during beam transport results in a radial $\underset{\sim}{J}\times\underset{\sim}{B}$ driven expansion of the channel plasma.[16] Typically, thermal expansion is unimportant. In order to avoid excessive channel expansion, the beam current is limited to

$$I_b < 3\times10^{-10}\ \rho\ r_{ch}^4/\tau_b^2\ I_{ch}\ , \quad (6)$$

where I_b and I_{ch} are the beam and channel current in MA, ρ is the mass density of the channel in g/cm^3 and r_{ch} is the channel radius in cm. Here it is assumed that the beam radius r_b, is equal to r_{ch}. The uniform channel current inside r_{ch} required to confine the beam can be expressed as[17]

$$I_{ch} = 1.3\ \theta_m^2\ A_b^{1/2}\ \bar{E}^{1/2} Z_b\ , \quad (7)$$

where $\bar{E}$ is the beam particle energy in MeV. The strong dependence of I_b on r_{ch} makes large radius transport very attractive, however, a final focusing scheme must then be employed to radially compress the beam to pellet size after transport. A factor of three compression in radius seems easily attainable in the final focusing cell and will be assumed for many of the plots in Sec. 4.

The transport channel length is determined by bunching requirements and is given by[18]

$$L = 1.3\times10^9 \left(1-\frac{1}{\alpha}\right) (\tau_t-\tau_b)\, E(\tau_b)^{1/2} A_b^{1/2}, \qquad (8)$$

where $E(\tau_b)$ is the final ion energy produced at the end of the pulse, α is the bunching factor and τ_t is the transit time of the beam from the diode exit to the bunching location. The transit time is also related to the diode voltage ramp with

$$\phi(t) = \phi(0)/(1-t/\tau_t)^2 \quad , \qquad (9)$$

where $\phi(t)$ is the ideal diode voltage waveform. Here it will be assumed that a factor of 5 bunching is acheived with a beam energy spread at the bunching location of 50%, so that

$$L = 4\times10^9\, \tau_b\, \bar{E}^{1/2} A_b^{1/2} \quad , \qquad (10)$$

where now L is written in terms of the average ion energy, $\bar{E} = [E(0)+E(\tau_b)]/2$. With the assumption of a 50% energy spread at the bunching location, one finds $E(0) = 3\bar{E}/4$ and $E(\tau_o) = 5\bar{E}/4$. This channel length then determines the beam energy lost during transport. It is also assumed that the focusing distance, F, is much shorter than L so that the bunching length and channel length are approximately equal.

The beam losses energy to the channel plasma by collisional slowing down and deceleration in the self-consistent axial electric field generated in the plasma. The electric field results from a resistive J_p/σ component and an inductive $\underline{V}_p x \underline{B}$ component with the latter typically larger. Assuming that the electric field is predominately inductive, the optimum mass density for the channel for minimum energy loss during transport is given by[16,18]

$$\rho_{opt} = 0.167 \frac{\overline{E} I_b^{1/2} \tau_b^{1/2} \theta_m^2}{r_b^2 Z_b^{3/2}} \tag{11}$$

For $\rho = x\rho_{opt}$ and deuterium as the fill gas in the channel, the fraction of beam energy lost during transport over the distance L (defined in Eq.(10)) is expressed as

$$\frac{\delta E}{E} = 6.7 \times 10^{11} \left(x + \frac{1}{x}\right) \frac{\theta_m^2}{r_b^2} \left(\frac{A_b Z_b I_b \tau_b^3}{E}\right)^{1/2} \tag{12}$$

Because Eq. (12) was derived for ions with the average energy, ions at the head of the beam will lose slightly more energy and ions at the tail of the beam will lose slightly less energy. Also, since $\delta E/\overline{E}$ as a function of x has a minimum at x=1, variations of x about x=1 will not change $\delta E/\overline{E}$ dramatically. Operating at twice the optimum mass density, or at x=2, only changes $\delta E/\overline{E}$ by 25% but considerably relieves the stability constraints as will be observed in Sec. 4.

The MHD and energy-loss constraints are then given by Eqs. (6) and (12) when combined with the stability constraints found in Sec. 2, the operational window for good beam transport and bunching is defined.

4. OPERATIONAL TRANSPORT WINDOW

The operational window is defined by the constraints on the transport system derived from ES stability conditions (Eq. (3)), beam and channel filamentation considerations (Eqs. (4) and (5)), MHD considerations (Eq. (6)) and beam energy-loss limitations (Eq. (12)). All constraints are written in terms of the average ion energy $\bar{E}=[E(0)+E(\tau_b)]/2$. Constraints at the head of the beam will be slightly more restrictive while those at the tail of the beam will be slightly more relaxed. For each of these five constraints, a condition on the transportable beam power can be derived as a function of the angular spread in the beam measured by θ_m. For convenience, the conditions will be expressed in terms of $E_o=\bar{E}/A_b^{1/2}Z_b$ which is the energy of an equivalent-range proton. In terms of E_o the beam power can be written as $P=I_b A_b^{1/2} E_o$ where P is in TW, I_b is in MA and E_o is in MeV. It will also be assumed that the channel gas is deuterium. Otherwise, the simple estimate for T_e^f given in Eq. (2) must be replaced by a much more complicated expression because of the more complex chemistry and radiation processes in higher atomic number gases.

The conditions on the transportable beam power will be expressed as functions of R/F where $R/F=\theta_m$ when the beam is focused a distance F downstream from a diode of radius R.[12,18] The transport channel entrance is positioned at the focus and the maximum injection angle into the channel is R/F. This assumes that R/F is much larger than the angular divergence of the beam at the source. If this is not the case, or if a small radius diode is used with no focusing, then P should be plotted as a function of θ_m, the angular divergence of the beam at the channel entrance. In that case, the horizonal axis in the plots should read θ_m rather than R/F and R/F should be replaced by θ_m in Eqs. (13)-(17).

Each of the five conditions on P(R/F) will depend only on the parameters x, E_o, r_b, τ_b, A_b and Z_b. In all that follows it is assumed that $r_{ch} = r_b$, $\rho = x\rho_{opt}$, $\alpha = 5$, $\Delta E/\bar{E}$ before bunching ~ 0.1, $\Delta E/\bar{E}$ after bunching ~ 0.5 and the pellet radius is ~ 0.5 cm. In deriving the constraints due to filamentation considerations, it is assumed that $T_e(t_1) < T_o < 10$ eV so that the first term in Eq. (5) can be dropped. The five conditions are then:

i) ES stability condition before bunching.

$$P < P_{ES} \equiv 1.6\times10^{-3}\left(\frac{x^6 r_b^8 A_b^{13/2}\lambda_{ei}^4 R^{12}}{Z_b^5 \tau_b^3 F^{12}}\right)^{1/7} E_o^3 \quad , \tag{13}$$

where

$$\lambda_{ei} = 24 - \ln\left[\frac{10^2 R\, r_b}{F}\left(\frac{E_o^9 A_b^{1/2} x^2}{Z_b P^3 \tau_b^3}\right)^{1/4}\right] \quad ,$$

and 1.6×10^{-3} is replaced in Eq. (13) by 1×10^{-2} to obtain the ES stability condition after bunching occurs in order to reflect the increased velocity spread in the beam;

ii)beam filamentation condition

$$R/F > \theta_{BF} \equiv 2.5\times10^{-2}\left(\frac{\lambda_{ei}^4 E_o^2}{A_b^5 Z_b^6}\right)^{1/8} \quad , \tag{14}$$

where P only enters weakly through λ_{ei} ;

iii) channel filamentation condition

$$P < P_{CF} \equiv (1.76\times10^5 x^2 R^4/Z_b F^4)\ (E_o^{14}\tau_b^2 A_b^{11})^{1/6}; \tag{15}$$

iv) MHD channel expansion condition

$$P < P_{MHD} \equiv 1.5\times10^{-21} x^2 r_b^4 E_o^2/\tau_b^3 \ ; \qquad (16)$$

and

v) beam energy-loss condition

$$P < P_{\delta E} \equiv \frac{1.36\times10^{-25} r_b^4 E_o^2 F^4}{(x+x^{-1})^2\ \tau_b^3 R^4} \ , \qquad (17)$$

where it is assumed that $\delta E/\overline{E} < 0.25$. In general, the beam ions are fully stripped after passing through the cathode foil, which separates the diode vacuum regime from the gas filled focusing region, and the foil between focusing region and the transport channel.

In the plots that follow, the operational window is defined by the shaded region with the boundaries of the window defined by Eqs. (13)-(17). The two left boundaries are the beam and channel filamentation constraints (ii and iii), the top boundary is the ES stability condition (i) and the right boundary is the energy-loss limitation constraint (v). The MHD-channel-expansion condition (iv) is easily satisfied in all the cases that will be considered and will not play a role in defining the operational windows. In some cases, the channel-filamentation constraints (iii) will be severe enough to dominate over the beam filamentation constraints (ii) or the ES stability condition (i) or both so that the window has only three (e.g., Fig. 5) or two (e.g., Fig. 6) boundaries rather than four.

For a given beam-energy spread and energy-loss limitation, the top and right boundaries are hard boundaries whereas the beam and channel filamentation constraints on the left boundary are somewhat fuzzy. The

filamentation constraints are derived by assuming that less than one e-fold occurs during beam transport but the initial perturbation level is unknown. If the initial perturbation is small, then the filamentation constraints given in Eqs. (14) and (15) are too severe and the left boundaries can be moved further to the left. Channel hydromotion and time variations in the beam distribution function will also tend to relax the filamentation constraints.

The dashed line in the window is the ES stability constraint if the beam were monoenergetic. A beam energy spread of 10%, as assumed in Eq. (13), considerably increases the size of the operational window by moving the ES stability constraint up to the top boundary.

The contours in the plots are lines of constant density. In each plot for a given P and R/F the channel density is defined by $n_p = x\rho_{opt}/2M$ where 2M is the mass of a deuteron and ρ_{opt} is defined in Eq. (11). The upper set of numbers labeling the contours denotes the ion density of the plasma in units of 10^{17} particles/cm^3. The lower set of number in parenthesis is the percentage of the beam energy which is lost during transport at the specified plasma density. The required channel current (Eq. (7)) and the final electron temperature (Eq. (2)) for a given P and R/F can also be determined from each plot by referring to the scale either above or to the right of the plot. The quantity I_{ch} is independent of P and T_e^f is independent of R/F.

In Figs. (2)-(5) the operational window is shown for H^{+1}, D^{+1}, He^{+2} and C^{+6} respectively for E_o=2 MeV, x=1, r_b=0.5 cm and $\tau_b=5\times10^{-8}$s. The size of the window increases with increasing atomic number. Table 1 shows that three of the five constraints are relaxed by increasing A_b while the other two are unchanged. This results from the fact that less beam current is required to transport the same beam power at the same E_o as A_b is increased. Higher A_b

allows transport of both higher power and lower R/F beams, so that the transportable beam power brightness $P/(R/F)^2$, improves considerably.

By increasing x (i.e., the channel plasma density), the ES stability, channel filamentation and channel expansion constraints are relaxed but the beam energy-loss constraint is more severe. Because the beam energy-loss constraint is being varied about a minimum, the change in this constraint is not dramatic. This is shown in Fig. 6 which should be compared with Fig. 2. The real benefit of increasing x is not realized unless r_b and/or E_0 are simultaneously increased in order to relax the energy-loss constraint. This will be shown more clearly in Fig. 9.

In Fig. 7 the parameters are all the same as in Fig. 2 except that the channel and beam radii are increased from 0.5 cm to 1.5 cm. The ES stability channel expansion and beam energy-loss constraints are all relaxed while the filamentation constraints are unchanged. The operational window has increased considerably in size with a maximum transportable power now on the order of 5 TW at R/F of about 0.18 radians. This results from decreasing the beam power density by spreading the beam over an area 9 times larger than in the case considered in Fig. 2. In order to bring R/F to a lower value and improve beam brightness, x and/or E_0 must be increased at the same time as r_b (see Fig. 9) so that the channel filamentation constraint is reduced.

By increasing E_0 all the constraints are relaxed with the exception of the beam filamentation constraint which becomes more severe. This is shown in Fig. 8 where all the parameters are the same as Fig. 2 except that E_0 is increased from 2 MeV to 4 MeV. The maximum transportable power in this case is about 2.8 TW. The increased beam stiffness and lower beam current for a given power level allows higher power transport, however, lower electron temperatures allows the beam filamentation instability to grow at higher R/F

values than in Fig. 2. This is a result of reduced stopping power of the plasma for higher energy beams.

The combination of increased x, r_b and E_o, as evaluated in Fig. 9, improves the transportable power considerably to a peak of about 40 TW at about 0.14 radians for protons. These results should be compared with Fig. 2. At 25 TW the operational transport window has a width in R/F from 0.11 to 0.16 radians. Similar results for D^{+1}, H_e^{+2} and C^{+6} are shown in Figs. 10-12. Once the beam bunches down to a pulse duration of 10 ns, the operational window opens even further as seen in Fig. 13. From Table 1 it can be seen that the ES stability, channel expansion and beam energy-loss constraints all are relaxed when τ_b is decreased. Only the channel filamentation constraint is more severe due to the low plasma temperature attained during the shorter pulse duration. Thus it is possible to transport the high power levels obtained after beam bunching.

5. CONCLUSIONS

By transporting in large-radius channels and ramping the diode-voltage waveforms to take advantage of time-of-flight bunching, high-power, light-ion beams can be delivered to a target a few meters from the diode. The radius of the channel is limited by the ability to compress the beam radially in a short, final-focusing cell positioned at the end of the transport system. Operating at a channel density which is slightly higher than ρ_{opt} and at an ion energy which is close to the high end of the acceptable energy range (defined by target designs) considerably increases the operational transport window for a large radius beam. For r_b = 1.5 cm, x = 2 and 4 MeV protons, it has been shown that a 40 TW beam can be transported with an angular divergence of about 0.14 radians (see Fig. 9). For higher atomic weight beams, such as D^+, He^{+2} and C^{+6}, even higher power levels can be successfully transported

(see Figs. 10-12). The availability of relatively pure source of higher atomic weight ions is still in question. If lighter, faster moving impurities are generated in sufficient quantities in a higher-atomic-weight ion beam, damaging preheat of the pellet may occur.

Although a pulse compression of $\alpha = 5$ was assumed, the actual power multiplication will be less. Comparing the power after bunching $(\alpha/\tau_b) \int_0^{\tau_b} P(t)dt$, with the power at the average energy ($\bar{E}$, as used in Figs. 2-12), one finds a power multiplication of about 4.8. Thus, when comparing the power level before bunching in Fig. 9 with the power level after bunching in Fig. 13, a power multiplication of 4.8 should be used rather than 5. If the figures had been plotted at $E(\tau_b)$, comparison of peak powers before and after bunching would result in a power multiplication factor of only 3.1. In all of these calculations it is assumed that the 10 ns power pulse after bunching is flat topped and that $I \sim E$ at high diode voltages.

From Fig. 13 one finds that propagating a 100 TW, 10 ns beam is feasible at $R/F = 0.15$ radians. This corresponds to about a 20 TW, 50 ns beam before bunching which is easily within the operational window given in Fig. 2. In order to deliver 4 MJ to a pellet in 10 ns, only 4 channels are required. Thus, if time-of-flight bunching of the beam and final focusing can be demonstrated, transport of beams at power levels sufficient to ignite a pellet should be possible in less than 10 and possibly in as few as 4 channels.

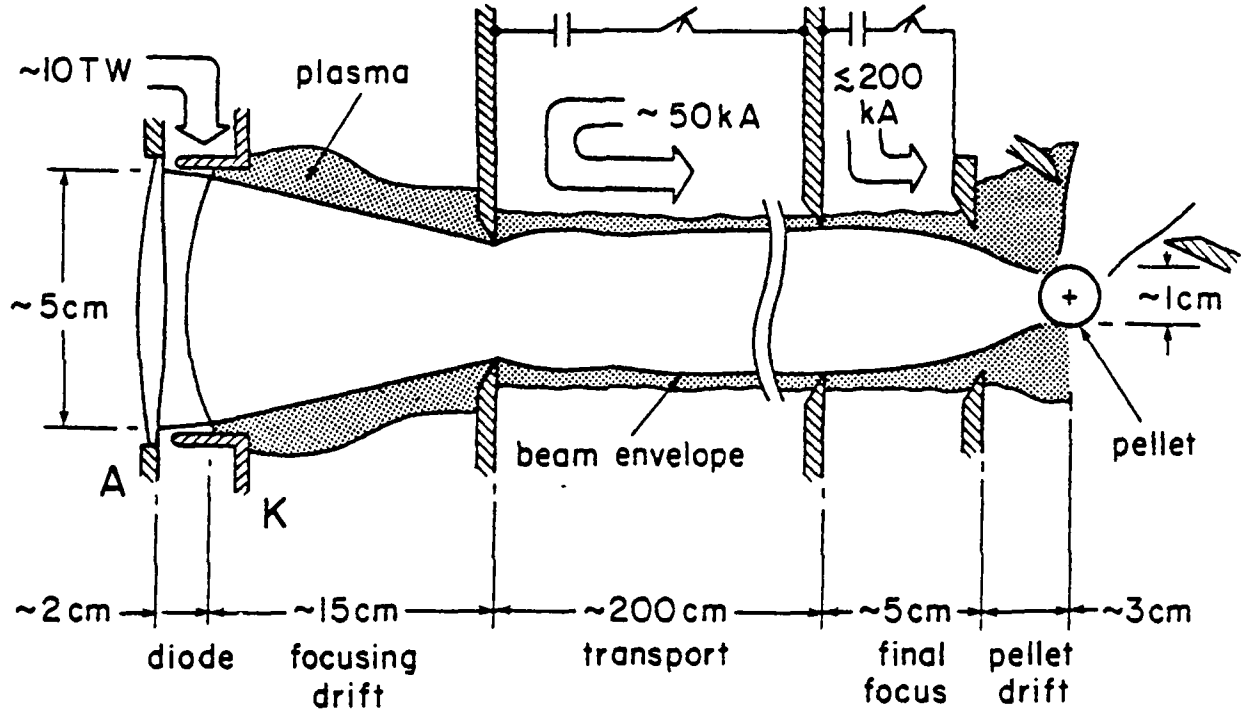

Figure 1 - Schematic of one module of a multimodule light-ion ICF system.

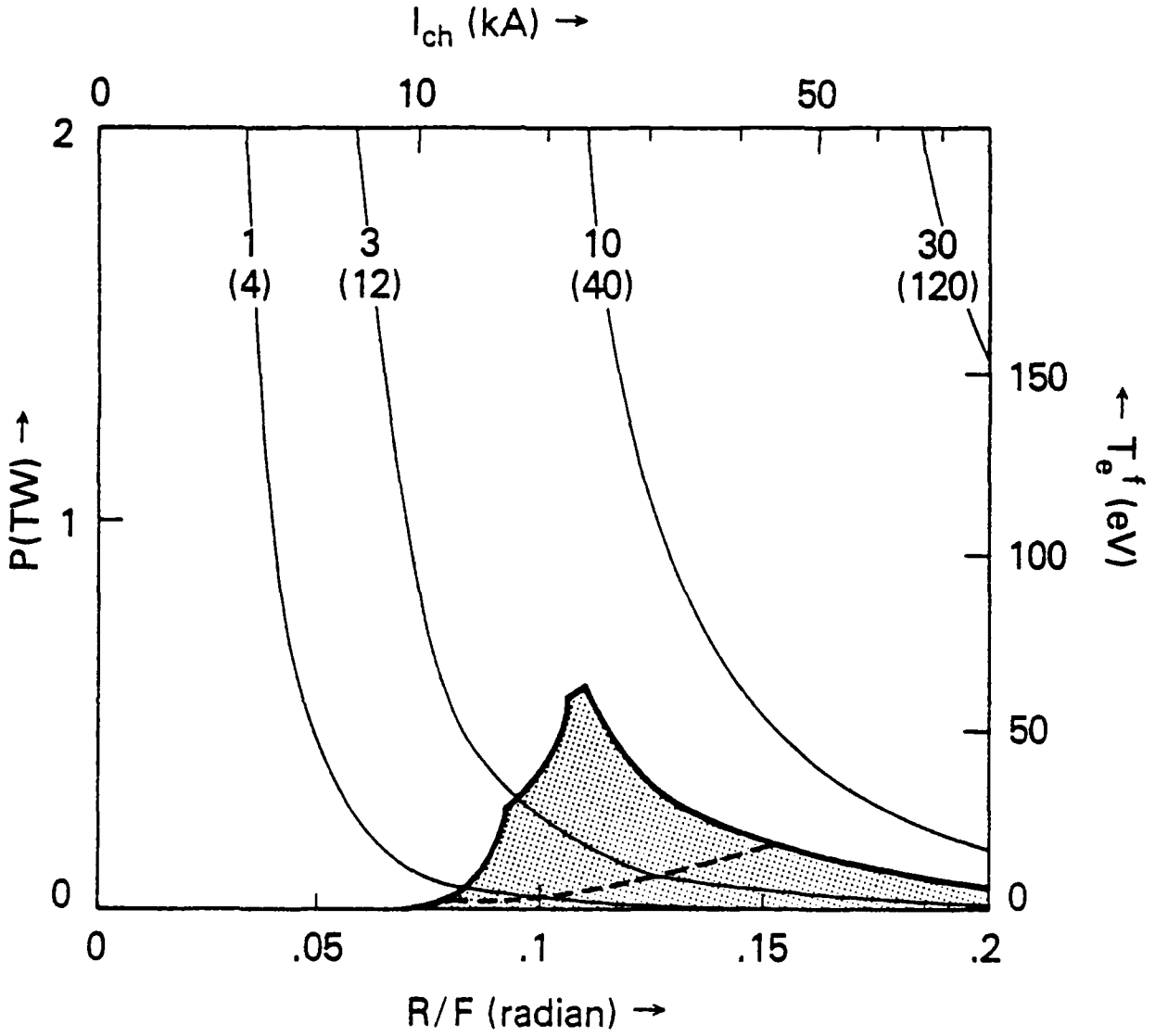

Figure 2 - Operational transport window for a H^{+1} beam with x = 1, r_b = 0.5 cm, E_o = 2 MeV and $\tau_b = 5 \times 10^{-8}$ s.

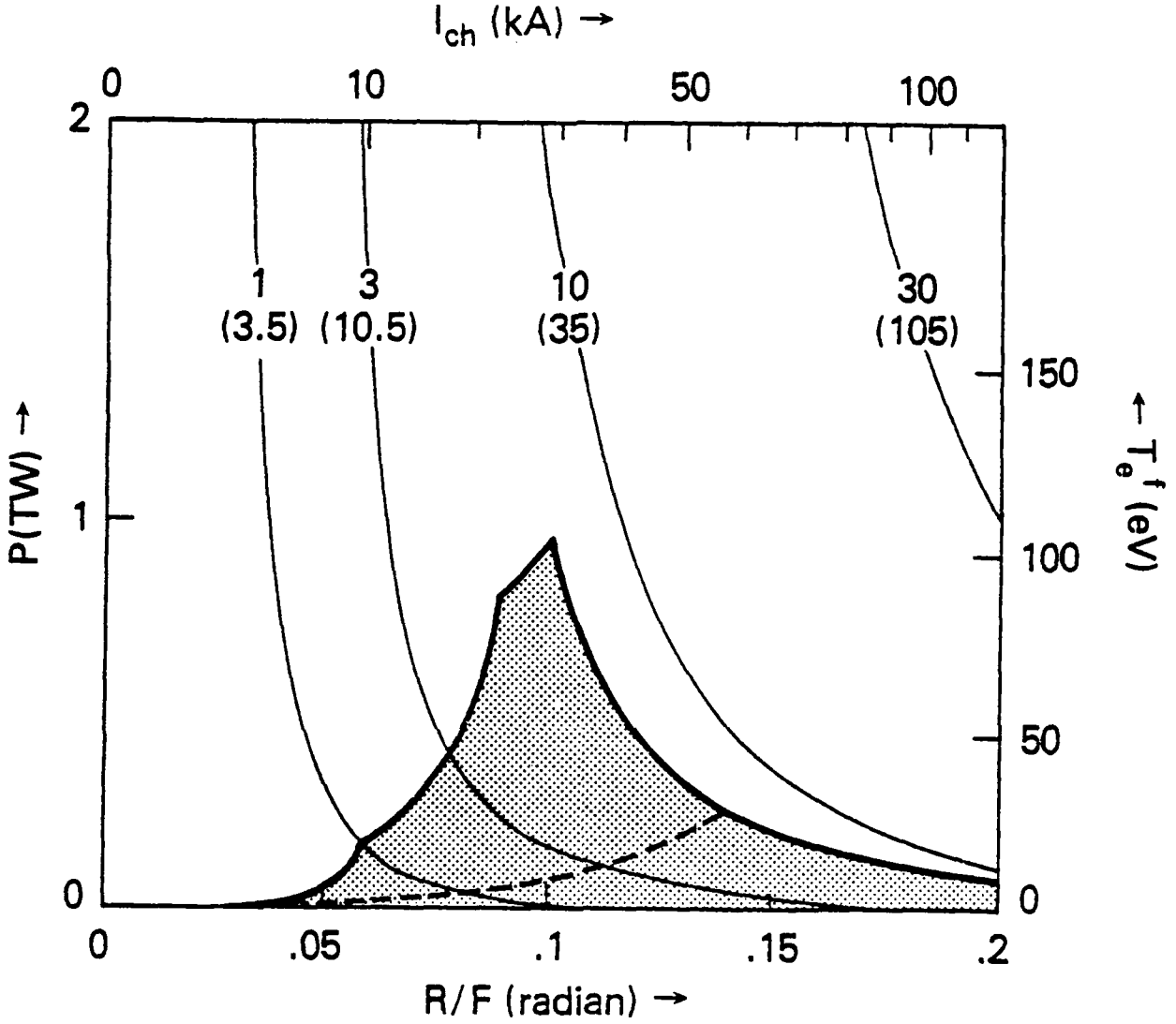

Figure 3 - Operational transport window for a D^{+1} beam with x = 1, r_b = 0.5 cm, E_o = 2 Mev and τ_b = 5×10^{-8} s.

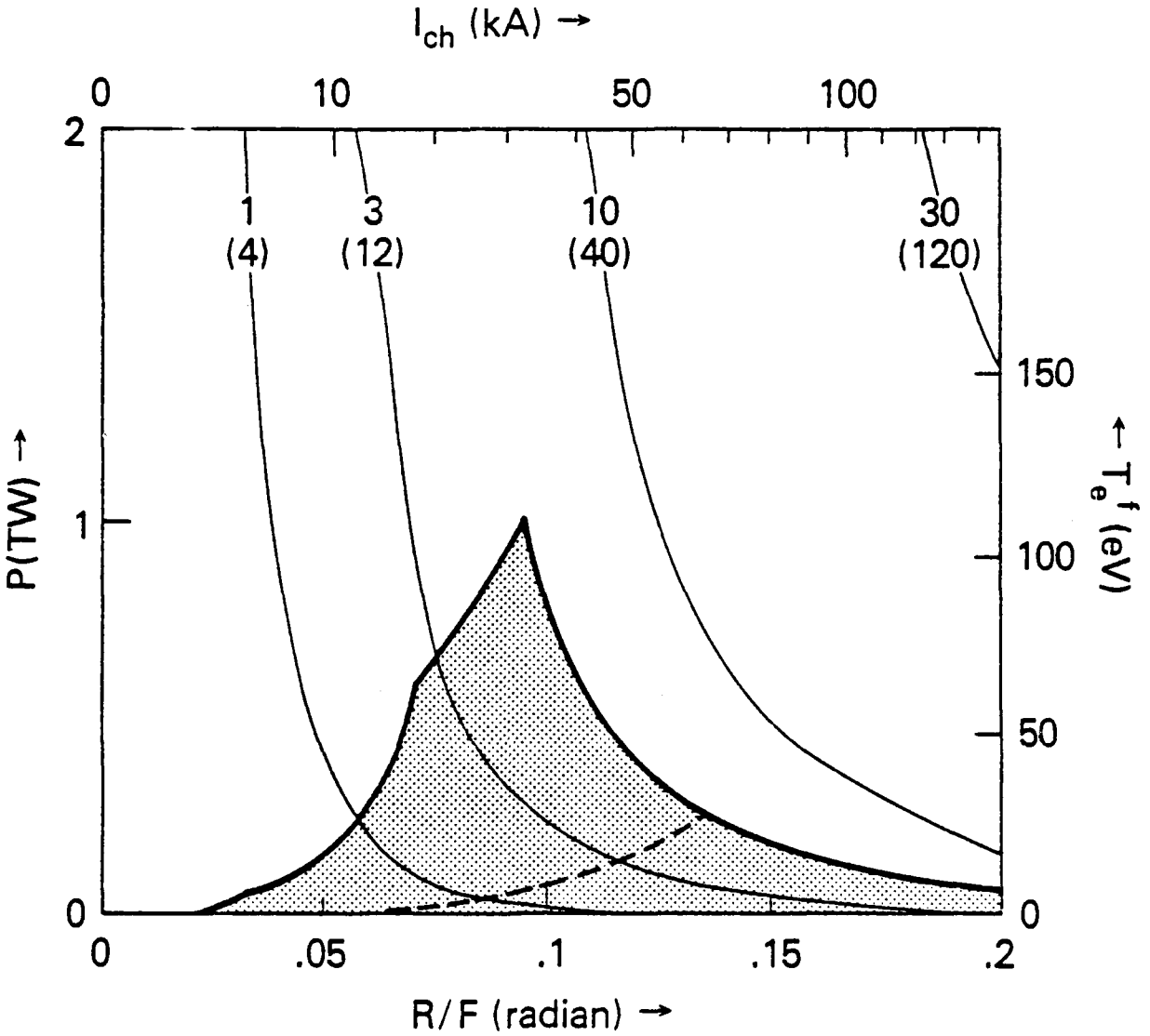

Figure 4 - Operational transport window for a He^{+2} beam with x = 1, r_b = 0.5 cm, E_o = 2 MeV and τ_b = 5×10^{-8} s.

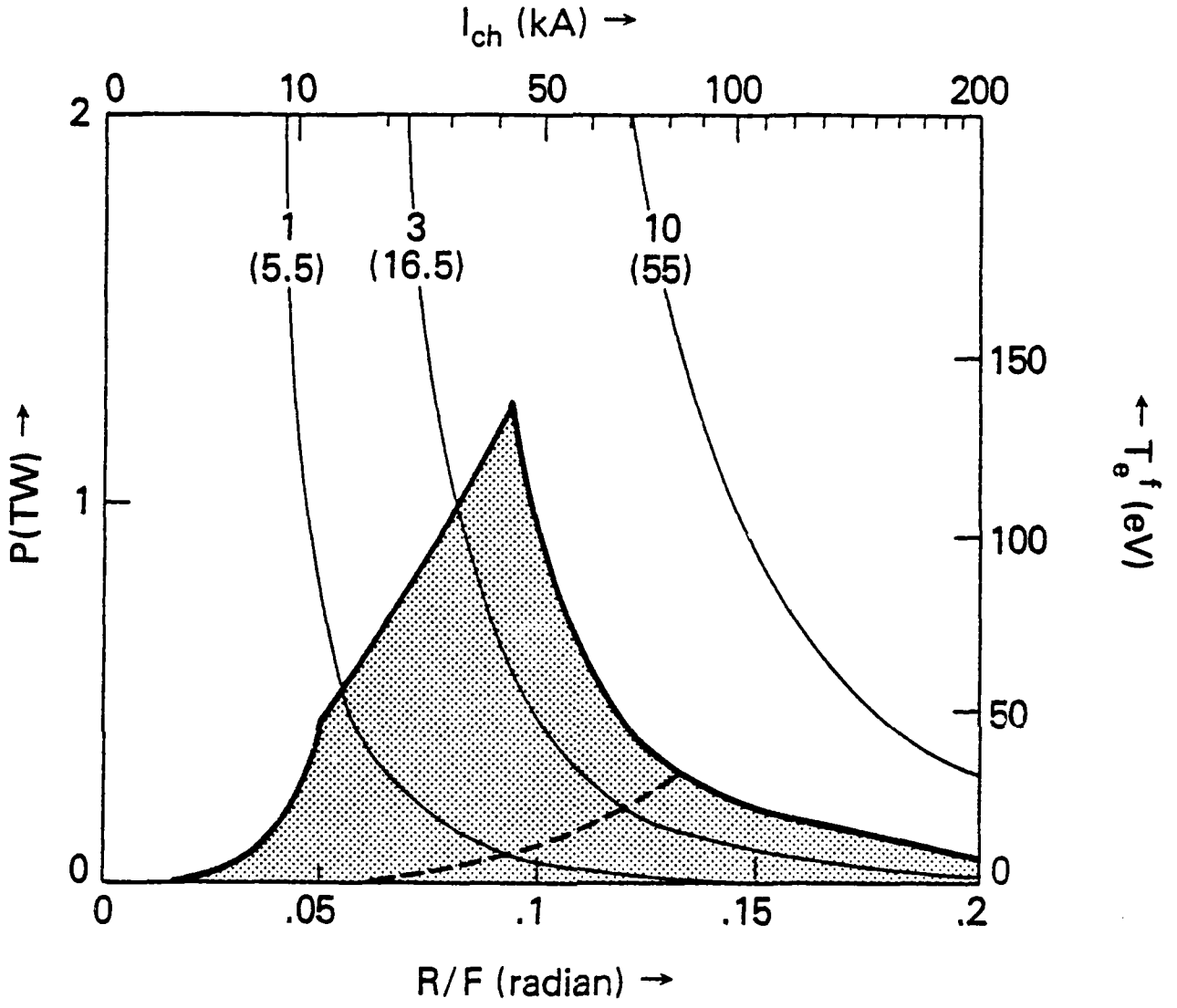

Figure 5 - Operational transport window for a C^{+6} beam with x = 1, r_b = 0.5 cm, E_o = 2 MeV and τ_b = 5×10^{-8} s.

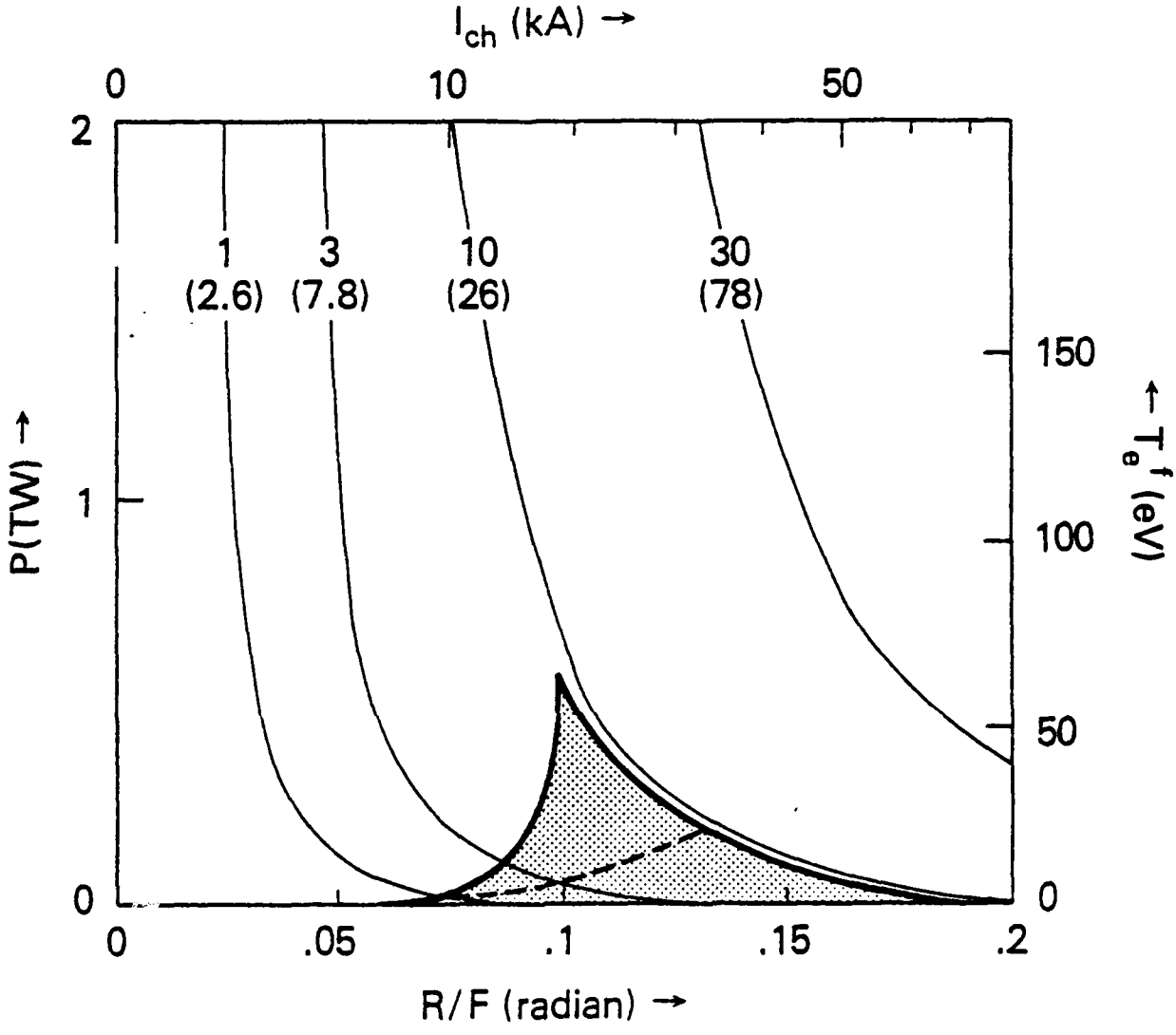

Figure 6 - Operational transport window for a H^{+1} beam with x = 2, r_b = 0.5 cm, E_o = 2 MeV and τ_b = 5×10^{-8} s.

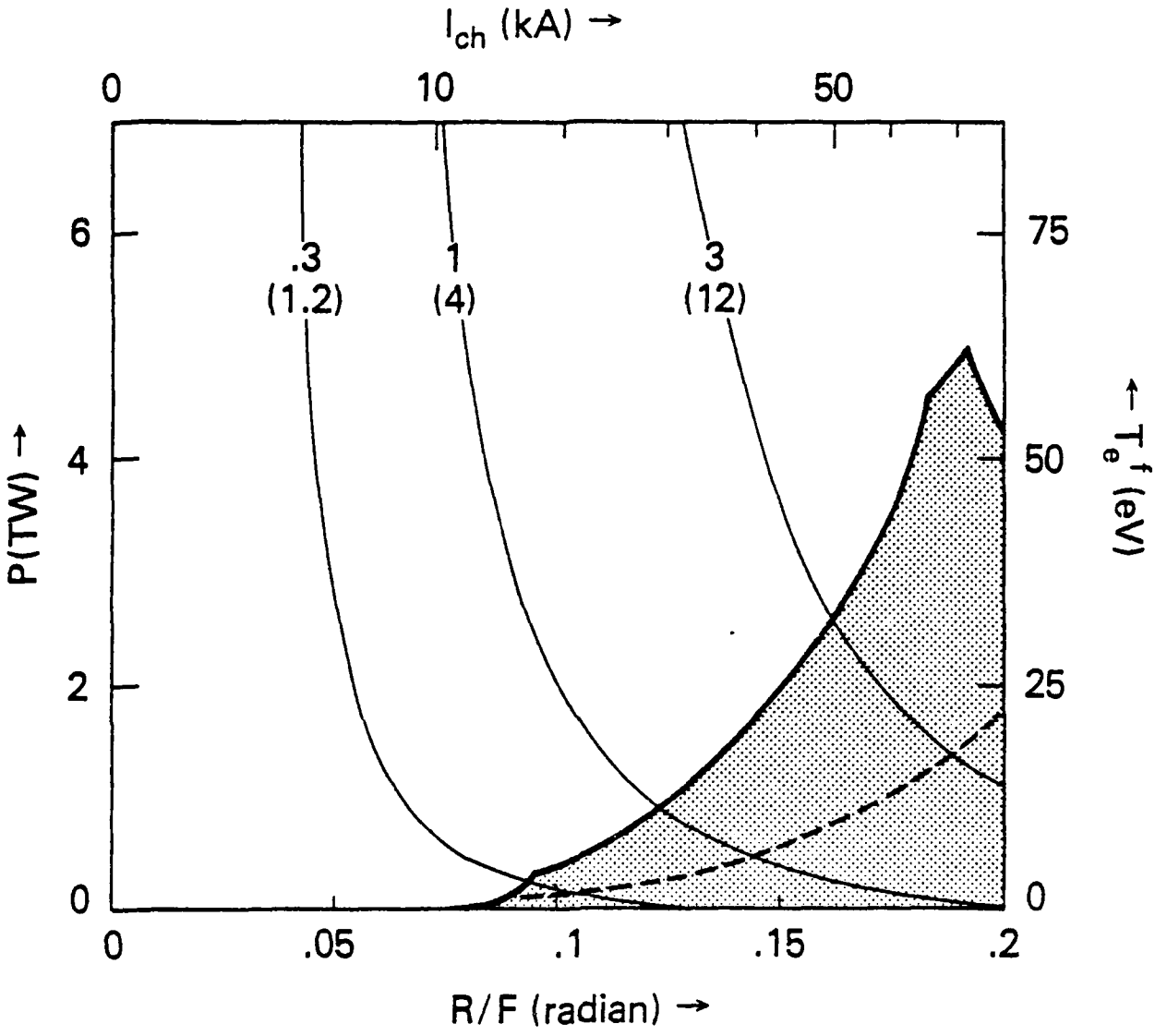

Figure 7 - Operational transport window for a H^{+1} beam with x = 1, r_b = 1.5 cm, E_o = 2 MeV and τ_b = 5×10^{-8} s.

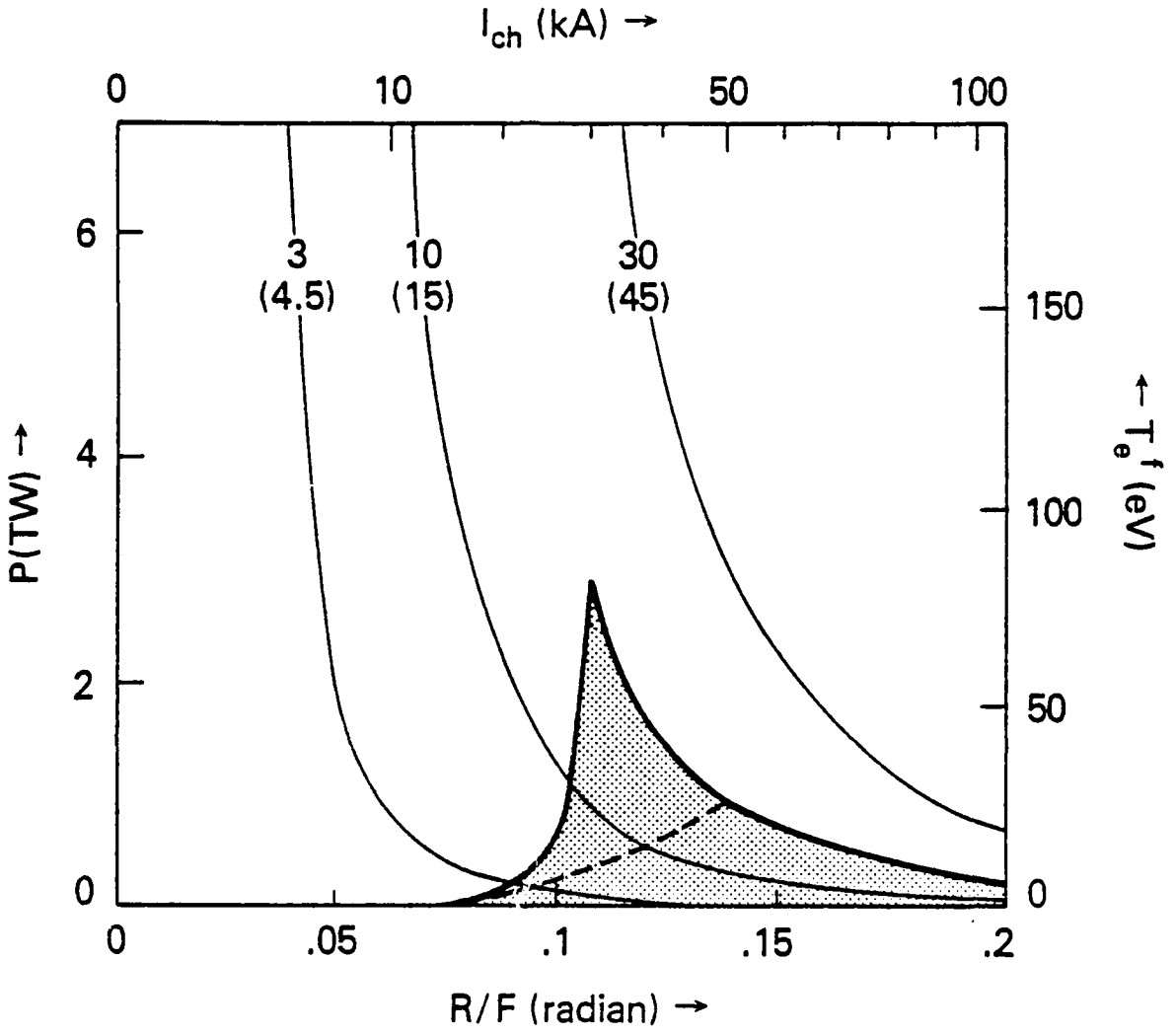

Figure 8 - Operational transport window for a H^{+1} beam with x = 1, r_b = 0.5 cm, E_o = 4 MeV and τ_b = 5×10^{-8} s.

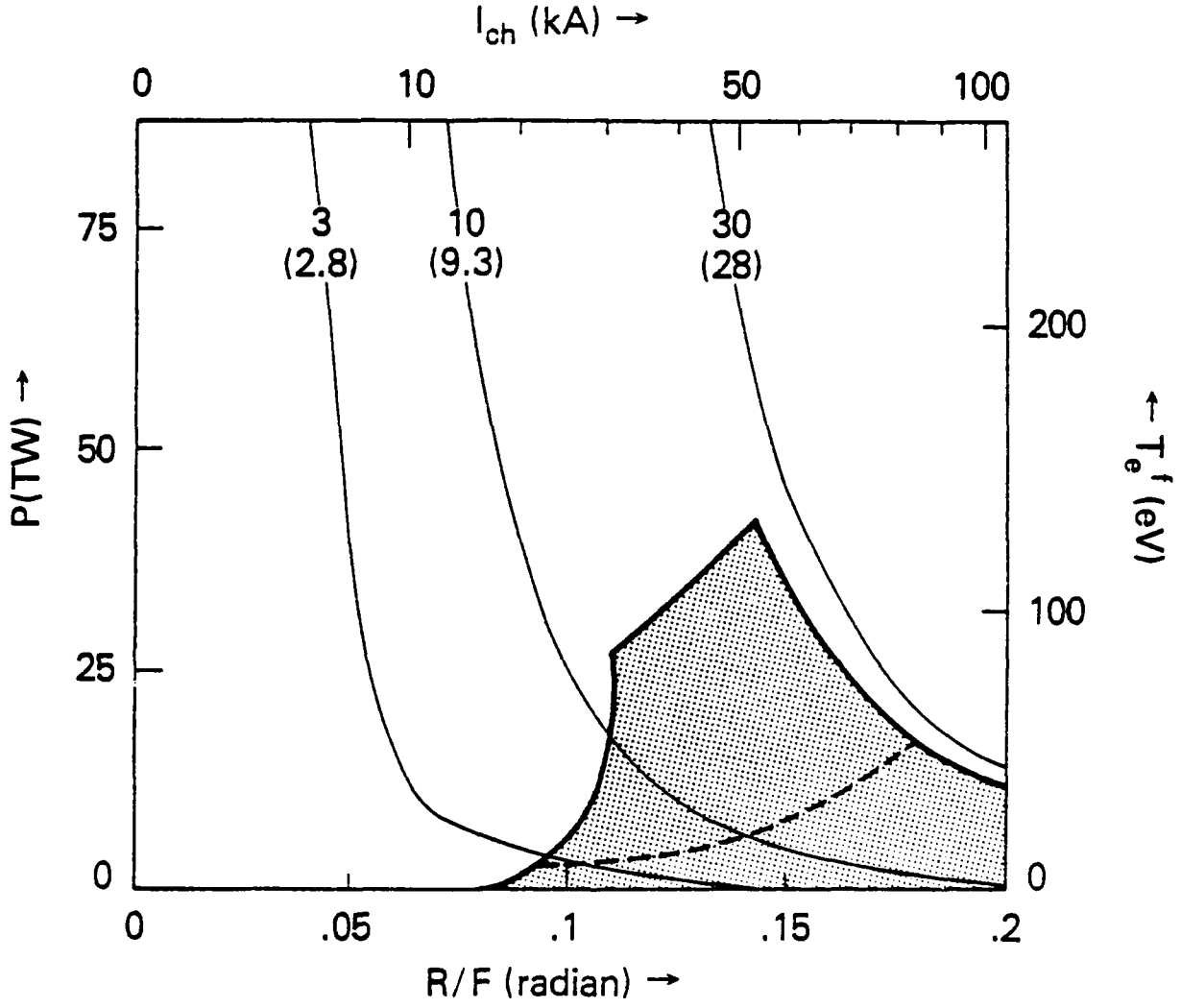

Figure 9 - Operational transport window for a H^{+1} beam with x = 2, r_b = 1.5 cm, E_o = 4 MeV and τ_b = 5×10^{-8} s.

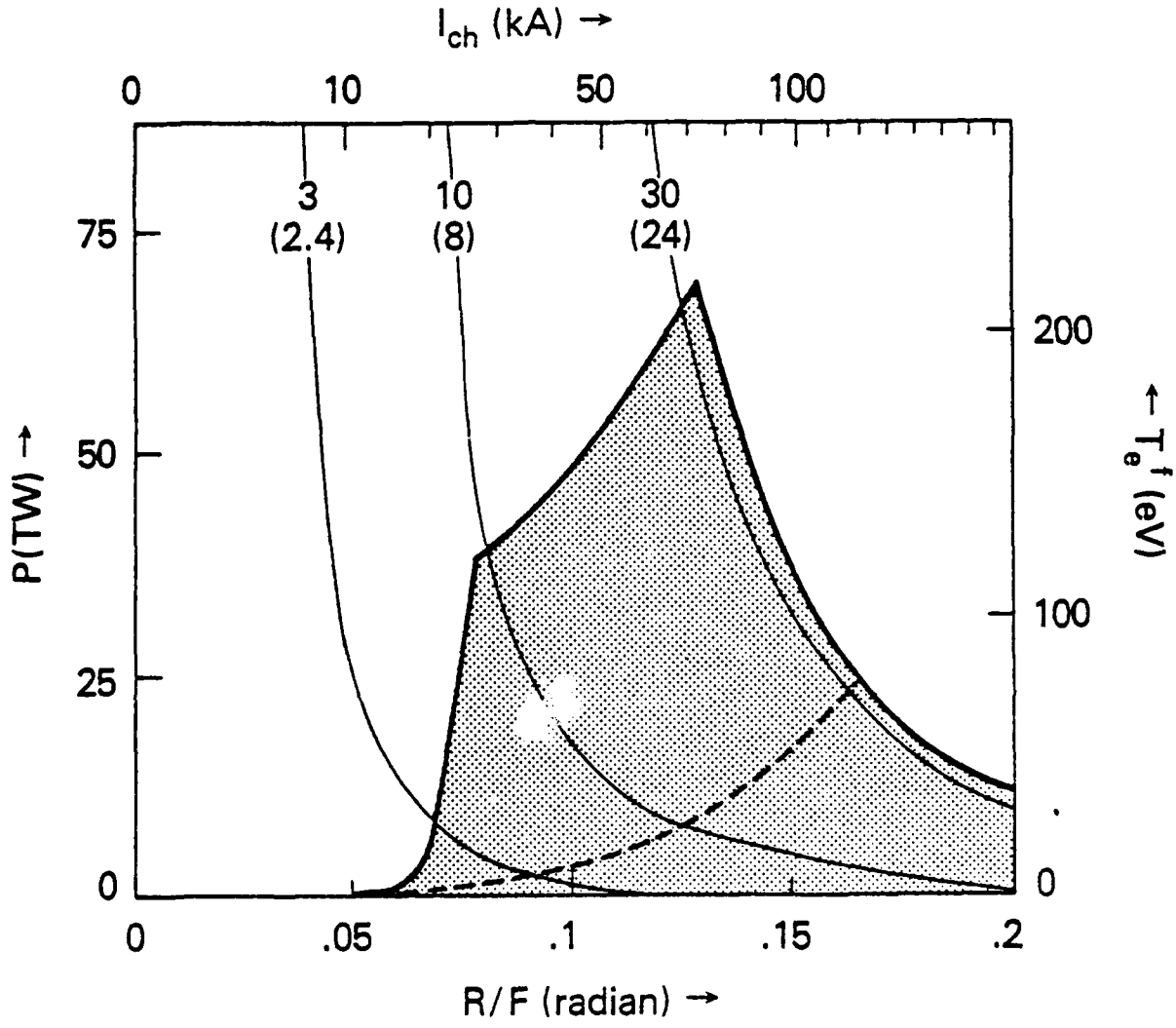

Figure 10 - Operational transport window for a D^{+1} beam with x = 2, r_b = 1.5 cm, E_o = 4 MeV and τ_b = 5×10^{-8} s.

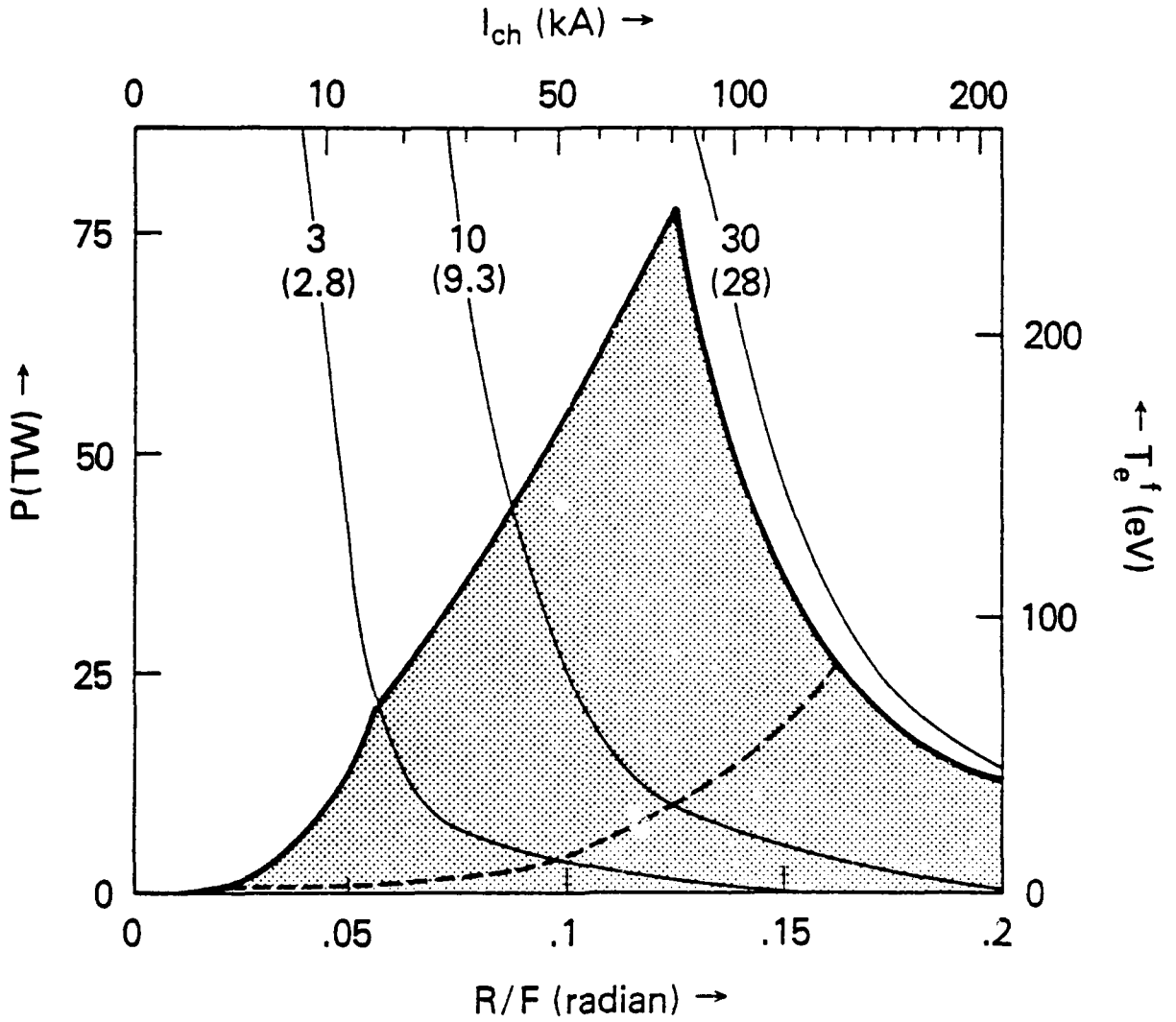

Figure 11 - Operational transport window for a He^{+2} beam with x = 2, r_b = 1.5 cm, E_o = 4 MeV and τ_b = 5×10^{-8} s.

AD-A129 821 DIODE DYNAMICS BEAM GENERATION AND TRANSPORT AND PLASMA EROSION OPENING SWITCH DEVELOPMENT(U) JAYCOR ALEXANDRIA VA P F OTTINGER 17 MAY 83 JAYCOR-J207-83-C-001 7/8

UNCLASSIFIED N00173-80-C-0202 F/G 9/1 NL

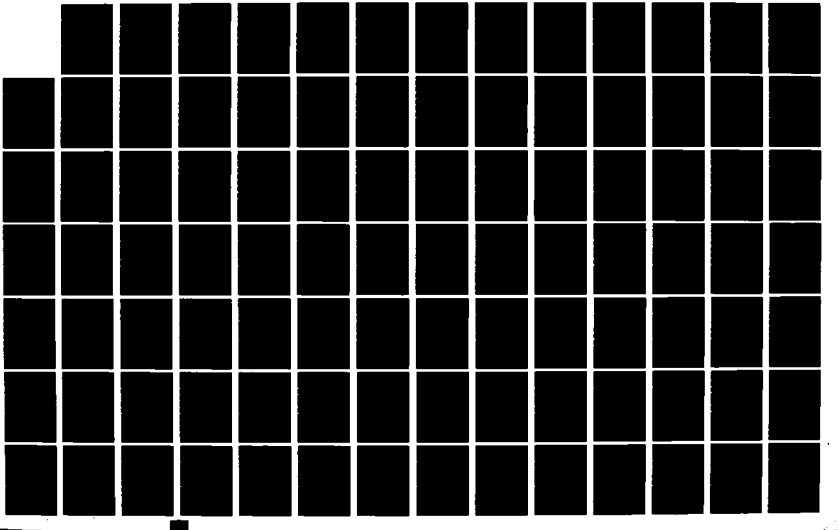

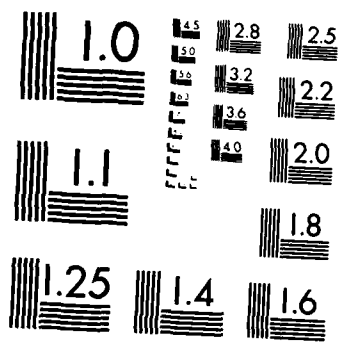

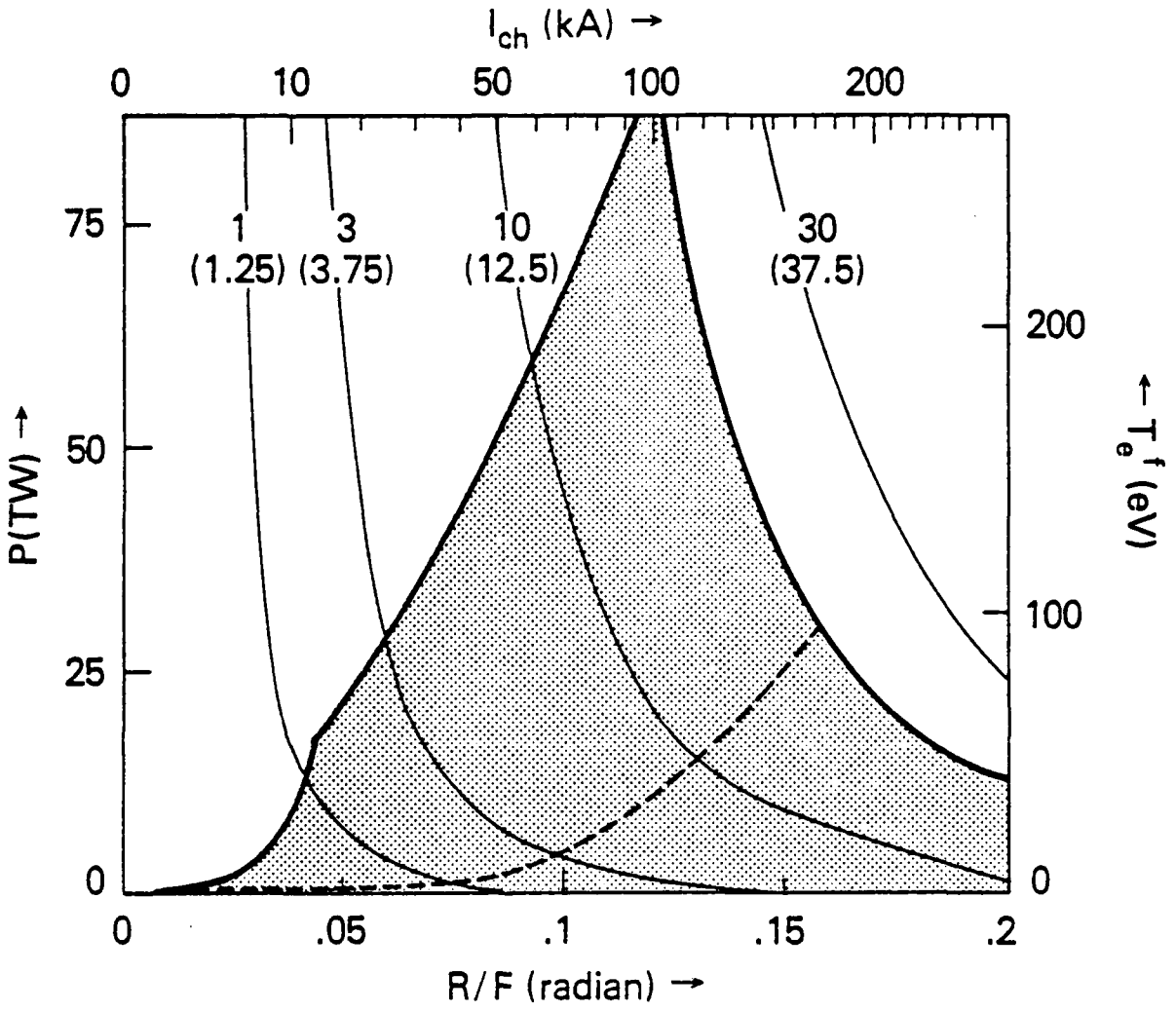

Figure 12 - Operational transport window for a C^{+6} beam with x = 2, r_b = 1.5 cm, E_o = 4 MeV and τ_b = 5×10^{-8} s.

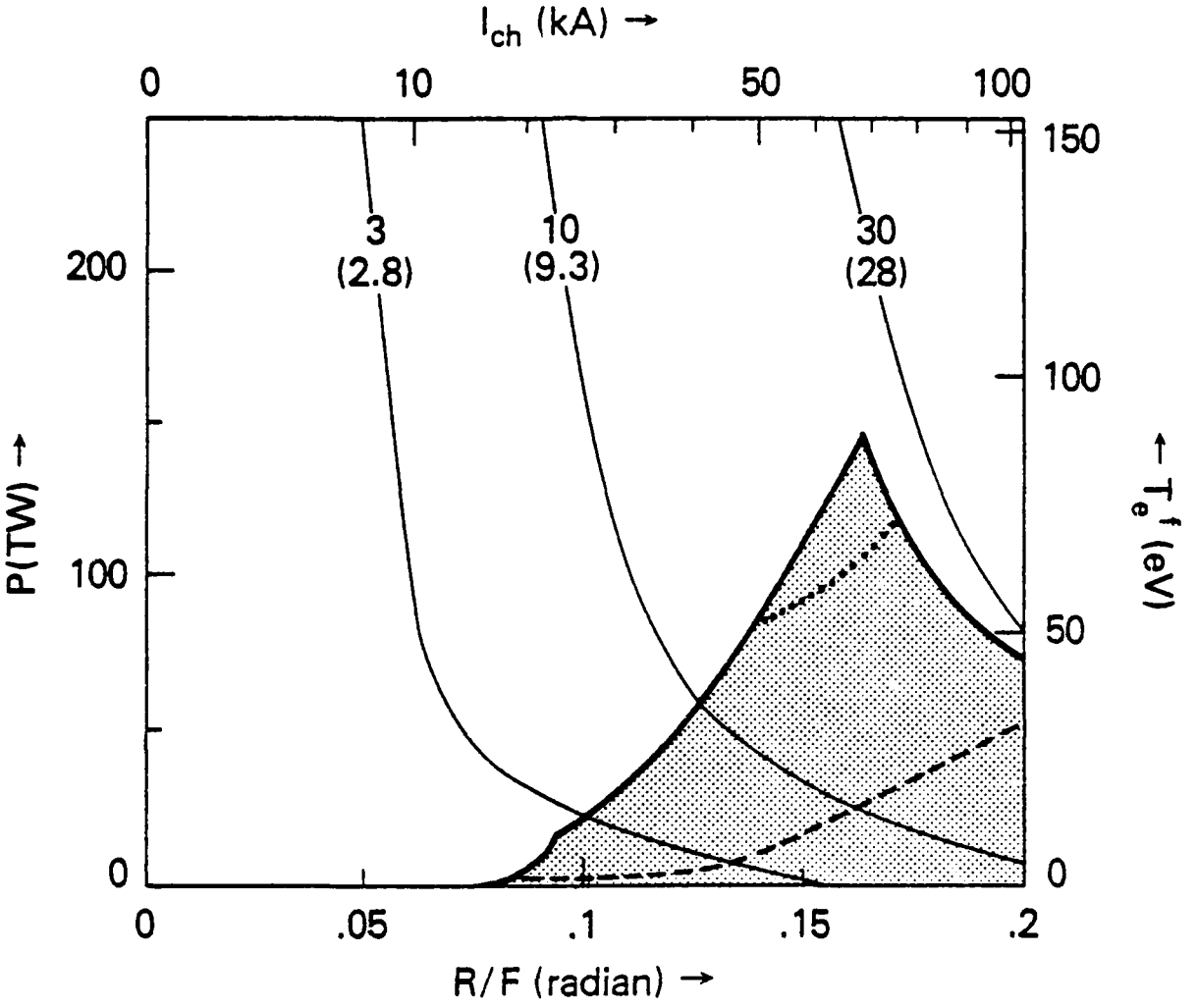

Figure 13 - Operational transport window for a H^{+1} beam with x = 2, r_b = 1.5 cm, E_o = 4 MeV and τ_b = 1×10^{-8} s.

Table I – Variation of the five transport constraints with increasing A_b, x, r_b, E_o, τ_b^{-1} and Z_b. A "+" means the constraint is relaxed, an "0" means there is no change and a "–" means the constraint becomes more severe.

	P_{ES}	θ_{BF}^{-1}	P_{CF}	P_{MHD}	$P_{\delta E}$	Comments
A_b	+	+	+	0	0	source availability and purity limitations
X	+	0	+	+	-	x > 1 is assumed
r_b	+	0	0	+	+	final focusing limitations
E_o	+	-	+	+	+	acceptable range defined by target designs
τ_b^{-1}	+	0	-	+	+	limited to no less than the pellet implosion time
Z_b	-	+	-	0	0	usually fully stripped by foils

6. REFERENCES

1. S. A. Goldstein and R. Lee, Phys. Rev. Lett. 35,1079 (1975).

2. J. W. Poukey, J. R. Freeman, M. J. Clauser, and G. Yonas,. Phys. Rev. Lett. 35,1806 (1975).

3. J. W. Poukey, J. Vac. Sci. Technol. 12, 1214 (1975).

4. A. E. Blaugrund, G. Cooperstein, J. R. Boller and S. A. Goldstein, Bull. Am. Phys. Soc. 20, 1252 (1975).

5. P. A. Miller, C. W. Mendel, D. W. Swain, and S. A. Goldstein, in Proceedings of the International Topical Conference on Electron Beam Research and Technology, Albuquerque, NM (1975), p. 619.

6. G. Cooperstein, S. J. Stephanakis, J. R. Boller, R. Lee, and S. A. Goldstein, in Proceedings of the 1976 IEEE International Conference on Plasma Science, Austin, Texas (IEEE, New York, 1976), p. 126.

7. D. J. Johnson, G. W. Kuswa, A. V. Farnsworth, Jr., J. P. Quintenz, R. J. Leeper, E. J. T. Burns and S. Humphries, Jr., Phys. Rev. Lett. 42, 610 (1979); D. J. Johnson, Bull. Am. Phys. Soc. 24 925 (1979).

8. G. Cooperstein, S. A. Goldstein, D. Mosher, W. F. Oliphant, F. L. Sandel, S. J. Stephanakis and F. C. Young, in Proceedings of the Third International Topical Conference on High Power Electron and Ion Beam Research and Technology, Novosibirsk, USSR (1975).

9. G. Cooperstein, S. A. Goldstein, D. Mosher, R. J. Barker, J. R. Boller, D. G. Colombant, A. Drobot, R. A Meger, W. F. Oliphant, P. F. Ottinger, F. L. Sandel, S. J. Stephanakis and F. C. Young, in Laser Interaction and Related Plasma Phenomena, edited by H. Schwarz, H. Hora, M. Lubin and B. Yaakobi, (Plenum Press, New York, 1980).

10. R. O. Bangerter and D. J. Meeker, in Proceedings of the Second International Topical Conference on High Power Electron and Ion Beam Research and Technology, Ithaca, New York (1977), p. 183; J. H. Nuckolls, in Proceedings of the Topical Meeting on ICF (Opt. Soc. of Am. Wash., DC, 1978) paper TuA5; S. Jorna and N. Metzler, Conference Recond-Abstract of the 1980 IEEE International Conference on Plasma Science, Madison, Wisconsin (IEEE, New York, 1980), p.37.

11. S. A. Goldstein, D. P. Bacon, D. Mosher and G. Cooperstein, in Proceedings of the Second International Topical Conference on High Power Electron and Ion Beam Research and Technology, Ithaca, New York (1977), p. 71; F. L. Sandel, Bull. Am. Phys. Soc. 26, 998 (1981).

12. D. Mosher, G. Cooperstein and S. A. Goldstein, in Proceeding of the Topical Meeting on ICF, San Diego (Opt. Soc. of Am., Wash., DC 1980), p. 104.

13. D. Mosher, Bull. Am. Phys. Soc. 24, 926 (1979).

14. D. Mosher and S. A. Goldstein, Bull. Am. Phys. Soc. 23, 800 (1979).

15. P. F. Ottinger, S. A. Goldstein and D. Mosher, in Conference Record-Abstracts of the 1980 IEEE International Conference on Plasma Science, Madison, Wisconsin (IEEE New York, 1980), p. 95; P. F. Ottinger, D. G. Colombant, S. A. Goldstein, R. A. Meger and D. Mosher, Bull. Am. Phys. Soc. 26, 921 (1981); R. A. Meger, S. A. Goldstein, P. F. Ottinger, D. Mosher, S. J. Stephanakis and F. C. Young, Bull. Am. Phys. Soc. 26, 921 (1981).

16. D. G. Colombant, D. Mosher and S. A. Goldstein, Phys. Rev. Lett. 45, 1253 (1980); D. G. Colombant and S. A. Goldstein, NRL Memorandum Report 4640 (1981).

17. P. F. Ottinger, D. Mosher and S. A. Goldstein, Phys. Fluids 23, 909 (1980).

18. D. Mosher, D. G. Colombant and S. A. Goldstein, Comments Plasma Physics 6, 101 (1981).

19. P. F. Ottinger, D. Mosher and S. A. Goldstein, Phys. Fluids 22, 332 (1979).

20. P. F. Ottinger, D. Mosher and S. A. Goldstein, Phys. Fluids 24, 164 (1981).

21. P. F. Ottinger, in Conference Record-Abstracts of the 1980 IEEE International Conference on Plasma Science, Madison, Wisconsin (IEEE, New York, 1980), p. 57.

22. P. F. Ottinger, S. A. Goldstein and D. Mosher, NRL Memorandum Report 4548 (1981).

23. P. F. Ottinger, S. A. Goldstein and D. Mosher, NRL Memorandum Report 4180 (1980).

TRANSPORT AND BUNCHING OF LIGHT ION BEAMS FOR PELLET FUSION

D. Mosher, G. Cooperstein, Shyke A. Goldstein*
D. G. Colombant, P. F. Ottinger*, F. L. Sandel*
S. J. Stephanakis, F. C. Young

Naval Research Laboratory
Washington, D. C. 20375

I. INTRODUCTION

In the previous paper, Dr. Cooperstein discussed the techniques required to focus TW-level light ion beams extracted from pinch-reflex diodes to high current density [1-3]. In this paper, we consider several-meter transport of the focussed ion beam to inertial-confinement-fusion targets through a Z-discharge transport channel. This technique allows ion beams to be transported the distances required for reaction-chamber standoff and provides a means of combining beams extracted from many generators onto a single target. Referring to Fig. 1, the ion beam enters the Z-discharge channel at the best beam focus location. Inside the channel, the ions are confined radially by the azimuthal magnetic field produced by the discharge of an external capacitor bank. The 25-150 kA current in the channel is adjusted to provide radial confinement for ions with the maximum transverse energy. The plasma density in the channel must be sufficiently high to resist expansion forces during beam transit and sufficiently low to prevent excessive energy loss of the beam. A happy combination of desired transport length (2-5 m), proton or deuteron energy (2-5 MeV), and ion beam pulse duration (50-100 ns) permits axial bunching of the beam during transport by ramping the accelerator voltage in time. Beam power multiplication of the beam can be achieved in this fashion.

The second section of this paper reviews theoretical work on the nature of ion orbits in the transport channel. In Section III, recent transport experimental results are discussed. The MHD response of the channel induced by beam passage is then considered. In Section V, bunching phenomenology of ion beams in transport channels is briefly discussed. Finally, the results of the research are used to determine a range of system parameters which are appropriate for

---

*JAYCOR, Alexandria, VA 22304

driving high-gain pellets with proton or deuteron beams.

II. ION ORBITS IN Z-DISCHARGE CHANNELS

As shown in Fig. 2, ions enter the discharge channel with a range of injection angles up to θ_M determined by the anode radius and distance to the focus. The externally-applied current flowing through the channel must be sufficient to confine ions with maximum transverse kinetic energy, that is, ions which enter the channel with the maximum injection angle at the maximum injection radius, a. The required discharge current can be determined from conservation of ion energy and p_z conical momentum

$$V_r^2 + V_z^2 = V_o^2 ; \qquad V_z = V_o \cos\theta + \frac{q}{m}\int_{r_o}^{r} B_\theta(r')dr'$$

where $\frac{1}{2}mV_o^2$ is the energy of an ion with charge q, θ is the injection angle and r_o is the injection radius. In order for the magnetic field to be just sufficient to confine a maximum-transverse-energy ion to the channel radius, $V_r = 0$ when $r = R$ with the initial conditions $\theta = \theta_M$, $r_o = a$. Substituting into the above, results in the expression

$$q\int_a^R B_\theta dr = mV_o(1-\cos\theta_M) \qquad (1)$$

Defining an ideal channel as one carrying a uniform discharge current so that $B_\theta \sim r$ when $r \le R$, Eq. (1) takes the form

$$I_{ch}(A) = \frac{10^{-3}V_o(1-\cos\theta_M)}{1 - (a/R)^2} \qquad (2)$$

for protons where I_{ch} is in amperes when V_o is in cm/s. This result indicates that megampere discharge currents are required to confine ions injected with large angles. Protons of 5 MeV with $\theta_M = .2$ require about 120 kA for confinement within the channel when $a/R = 2/3$. Because of the large electrical energy investment required to establish larger currents in many small diameter channels, significantly greater injection angles may be impractical.

Analytical and computational techniques have been used to determine the effects of various forms of nonideal channel behavior on ion confinement and beam bunching [4]. Axial electric fields associated with plasma return currents disrupt radial confinement and reduce beam power multiplication due to bunching only if large enough to strongly slow the beam during transport. Radially non-uniform net currents develop as the beam passes through the background because of beam-induced MHD expansion of the channel. The effects of the resulting B_θ

fields on beam confinement are discussed in Section IV. Channels which taper to smaller radius as they approach the pellet were investigated as a means of increasing the beam current density. A WKB-like analysis for the ion motion shows that only a small improvement in current density due to radial beam compression can be achieved before disruption of axial compression by bunching. Both analytic and numerical calculations were performed to determine ion confinement in a channel with a large amplitude m = 0 sausage instability. Fig. 3 shows one result of this work. The channel B_θ was modeled as $\sim r$ inside the channel radius R(z), and $\sim 1/r$ outside. With every change in axial location $\Delta z = \lambda$, the value of R changed abruptly and randomly to simulate the non-linear development of the instability. A large number of ion orbits were numerically determined for a range of injection angles up to θ_M and injection radii up to 'a'. The figure shows a cross-section of beam ion density at various axial locations along the channel. The case shown corresponds to a = .4 cm, R = .6 cm, E_i = 5 MeV, θ_M = .2 radian, I_{ch} = 120 kA, λ = 3.8 cm, $\Delta R_{rms}/\overline{R}$ = 1. This high degree of fluctuation is required for radial loss of half the beam ions after transporting 6 m. When ΔR_{rms} is decreased by about a factor of 2, only about 9% of the beam is lost at 6 m. Good radial confinement is predicted for all cases in which the axial wave length of the instability is much smaller than the betatron wavelength of the ion in the channel.

III. ION TRANSPORT EXPERIMENTS

Fig. 4 illustrates the experimental configuration for transport experiments on the Gamble II device [2]. A planar, pinch-reflex diode configuration is used to bring a .5 MA, 1.4 MV proton beam to a narrow-angle focus 20-30 cm downstream from the diode. The transport section consists of a copper pipe containing an insulating ceramic liner filled to the .2-2 Torr air background pressure of the focussing-drift section. The inside diameter of the ceramic liner defines the diameter of the wall-stabilized discharge. Discharge channel diameters of 4.5 cm and 1.6 cm were employed. The discharge current is provided by a 20 kV, 10 kJ capacitor bank. The current rises to about 50 kA in 15 μs at which time the ion beam is injected into the channel. This current satisfies Eq. (2) for the injection angles employed in the experiment. To date, most experiments have employed the large-diameter transport system due to insufficient voltage for 50 kA with the smaller. Measurements of transport efficiency are provided by diagnosis of 6 MeV gamma rays produced by the interaction of beam protons with fluorine [5]. Collimated scintillator-photodiode detectors are used to detect the gamma rays produced in 50% transparent Teflon screens placed at the entrance and exit apertures of the transport system.

The initial temperature distribution is determined by an equilibrium pressure balance condition. Once the beam enters the channel, the plasma pressure and $\vec{j} \times \vec{B}$ forces acting on the plasma push material out of the channel interior and pile it up against the steep density gradient at the channel edge. The initial magnetic field profile corresponds to uniform current density arising from the long times and the low conductivities associated with channel creation. Once the beam heats the channel, the conductivity rises quickly and magnetic field lines become frozen in the plasma. The magnetic field is then convected out of the center of the channel along with the density.

A primary diagnostic for maintenance of beam confinement is suggested by Eq. (1) and is given by the integral extended foom 0 to R. If the value of the integral is reduced, ions injected with large r_o or θ_o can reach the high density edge of the channel and be lost. Fig. 7 shows the development of the confinement integral with time for low and high beam currents and two values of beam energy. For the low beam current cases, the plasma channel response to the beam is sufficiently gentle not to disrupt confinement. However, in the high-current cases, ions with larger transverse energy are lost. Fig. 7 also shows that the evolution of the confinement integral with time does not depend sensitively on the ion energy. This behavior can be understood qualitatively by examining the plasma equation of motion.

$$\rho \frac{dV_r}{dt} = - \frac{\partial p}{\partial r} - j_z B_\theta \approx j_b B_\theta \qquad (3)$$

In Eq. (3), dominance of the $\vec{j} \times \vec{B}$ term over the pressure term and good beam-current neutralization result in the right-hand side. For a maximum allowed acceleration given by $2R/\tau^2$, where τ is the beam duration, Eq. (3) yields

$$I_b I_{ch} < 300\ \rho\ R^4/\tau^2 \qquad (4)$$

for maintenance of beam confinement. In Eq. (4), the currents are in amperes and the terms of the right-hand-side are in cgs units. This condition is in qualitative agreement with the results of the MHD code. Because of the greater primary beam deposition, lower-voltage ion beams require lower background density. Thus, the maximum allowed value of $I_b I_{ch}$ is reduced with ion voltage. This indicates that less power can be transported in channels carrying lower-voltage ions unless the channel current can be significantly reduced. However, the channel current is determined primarily by the spread of injection angles through Eq. (2), and θ_M is unlikely to be reduced for less-stiff lower-energy ions. Additionally, Eq. (4) is easier to satisfy with the beam in the bunched state since $I_b \tau$ remains constant as τ is reduced.

A second important diagnostic for beam transport in channels is the total

The initial temperature distribution is determined by an equilibrium pressure balance condition. Once the beam enters the channel, the plasma pressure and $\vec{j} \times \vec{B}$ forces acting on the plasma push material out of the channel interior and pile it up against the steep density gradient at the channel edge. The initial magnetic field profile corresponds to uniform current density arising from the long times and the low conductivities associated with channel creation. Once the beam heats the channel, the conductivity rises quickly and magnetic field lines become frozen in the plasma. The magnetic field is then convected out of the center of the channel along with the density.

A primary diagnostic for maintenance of beam confinement is suggested by Eq. (1) and is given by the integral extended foom 0 to R. If the value of the integral is reduced, ions injected with large r_o or θ_o can reach the high density edge of the channel and be lost. Fig. 7 shows the development of the confinement integral with time for low and high beam currents and two values of beam energy. For the low beam current cases, the plasma channel response to the beam is sufficiently gentle not to disrupt confinement. However, in the high-current cases, ions with larger transverse energy are lost. Fig. 7 also shows that the evolution of the confinement integral with time does not depend sensitively on the ion energy. This behavior can be understood qualitatively by examining the plasma equation of motion.

$$\rho \frac{dV_r}{dt} = - \frac{\partial p}{\partial r} - j_z B_\theta \approx j_b B_\theta \qquad (3)$$

In Eq. (3), dominance of the $\vec{j} \times \vec{B}$ term over the pressure term and good beam-current neutralization result in the right-hand side. For a maximum allowed acceleration given by $2R/\tau^2$, where τ is the beam duration, Eq. (3) yields

$$I_b I_{ch} < 300\ \rho\ R^4/\tau^2 \qquad (4)$$

for maintenance of beam confinement. In Eq. (4), the currents are in amperes and the terms of the right-hand-side are in cgs units. This condition is in qualitative agreement with the results of the MHD code. Because of the greater primary beam deposition, lower-voltage ion beams require lower background density. Thus, the maximum allowed value of $I_b I_{ch}$ is reduced with ion voltage. This indicates that less power can be transported in channels carrying lower-voltage ions unless the channel current can be significantly reduced. However, the channel current is determined primarily by the spread of injection angles through Eq. (2), and θ_M is unlikely to be reduced for less-stiff lower-energy ions. Additionally, Eq. (4) is easier to satisfy with the beam in the bunched state since $I_b \tau$ remains constant as τ is reduced.

A second important diagnostic for beam transport in channels is the total

considerations can be combined in order to determine an acceptable set of system parameters for the ignition of a high-gain fusion pellet [9]. High voltage beams are easily focussed because of their relative insensitivity to time-varying magnetic fields in the diode. However, their long range in materials leads to inefficient energy coupling to fusion targets. Low voltage beams suffer from excessive energy loss in the transport channel and difficulty in focussing. For any voltage, channel hydrodynamic response calculations indicate difficulty in transporting ion beams in excess of 1 MA. Thus, for a fixed power and energy requirement delivered to the target, MHD considerations establish a lower limit on the number of channels which can be used to transport ion beams to the target. Table 1 summarizes an acceptable range of system parameters based on the considerations discussed above. Parameters based on two pellet requirements and two ion pulse durations are shown. The stored energy is an estimate of the total electrical energy stored in the Marx generators required to provide the total ion beam energy. The shorter-duration beams require higher powers at the diode but also require less bunching in order to achieve power on target. The focussed power represents the total focussed ion beam power for all the modules into the entrance of all the channels. Focussed current represents the total current transported by all channels. Using 1 MA as an upper limit to the current which can be transported any given channel, the focussed current numbers represent an estimate of the minimum number of channels required to transport the total beam. The minimum channel length (i.e. stand-off distance) is arrived at by determining the smallest transport length which can achieve the desired degree of power multiplication using an accelerating voltage which varies by no more than a factor of 2.

Extension of these results to ion species other than Z = 1 requires further investigation of transport properties. Higher voltage beams can transport at lower beam current to achieve beam powers comparable to Z = 1. Channel currents are uncertain. From Eq. (1), I_{ch} is proportional to the larger values of m/q. However, it tends to be reduced by the smaller values of θ_M permitted by better focussing control [10].

REFERENCES

1 GOLDSTEIN, SHYKE A., COOPERSTEIN, G., LEE, ROSWELL, MOSHER, D., STEPHANAKIS, S. J., PRL 40 (1978) 1504.

2 COOPERSTEIN, G., in Conference Record Abstracts (Proc. 1979 IEEE International Conf. on Plasma Science, Quebec, 1979) IEEE Cat. 79CH1410-ONPS, 80.

3 JOHNSOHN, D. J., FARNSWORTH, A. V., JR., QUINTENZ, J. P., LEEPER, R. J., BURNS, E. J. T., IEEE Quebec, 76.

4 OTTINGER, P. F., MOSHER, D., GOLDSTEIN, SHYKE A., IEEE Quebec, 105.

5 GOLDEN, J., MAHAFFEY, R. A., PASOUR, J. A., YOUNG, F. C., KAPETANAKOS, C. A., Rev. Sci. Instrum. 49 (1978) 1384.

6 COLOMBANT, D. G., GOLDSTEIN, SHYKE A., MOSHER, D., IEEE Quebec, 105.

7 FREEMAN, J. R., BAKER, L., POUKEY, J. W., WIDNER, M. M., Bull. Am. Phys. Soc. 23 (1978) 853.

8 MOSHER, D., GOLDSTEIN, SHYKE A., Bull. Am. Phys. Soc. 23 (1978) 800.

9 MOSHER, D., COOPERSTEIN, G., GOLDSTEIN, SHYKE A., IEEE Quebec, 79.

10 MILLER, PAUL, informal communication.

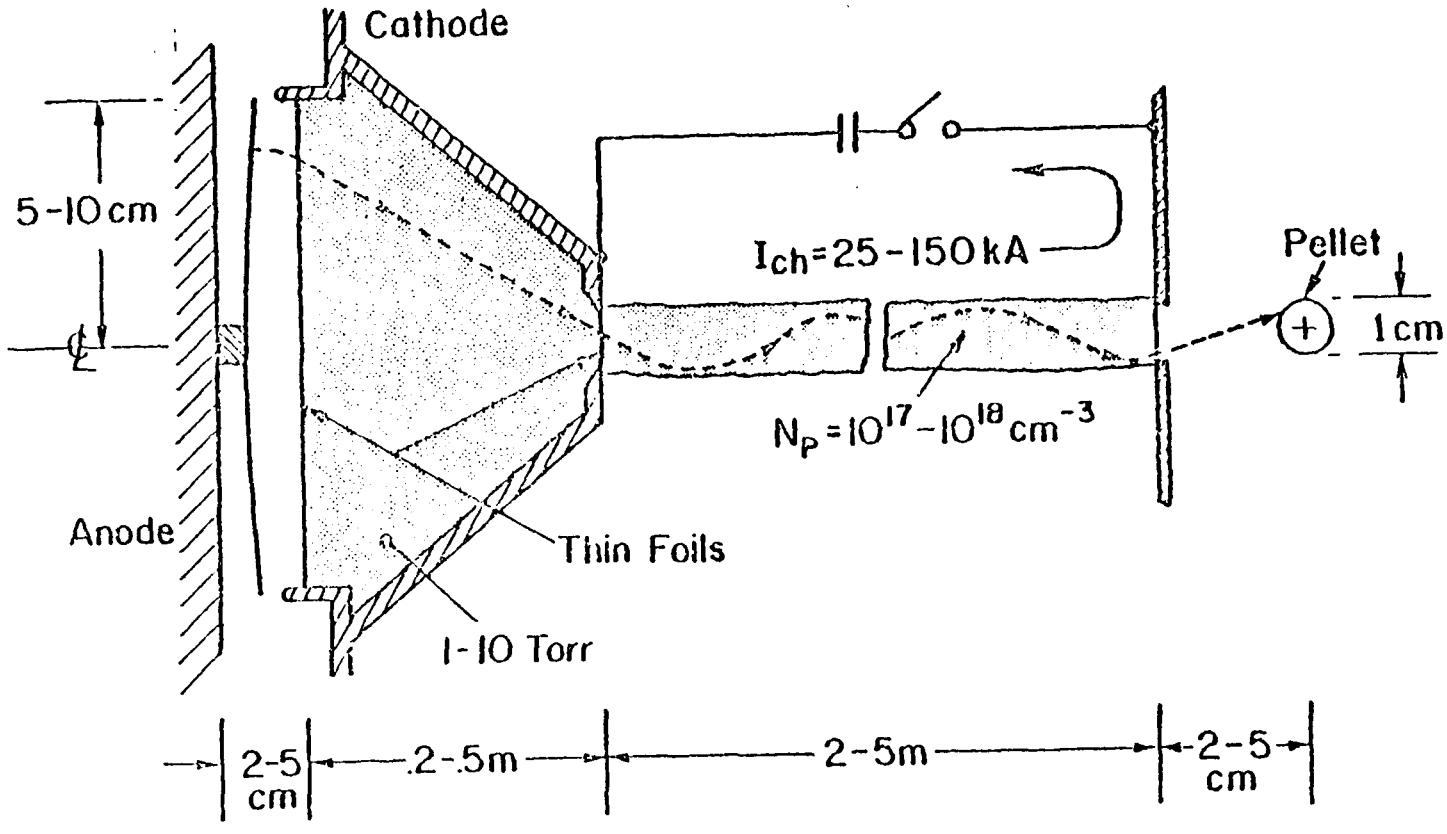
Light-Ion ICF
Cathode
5-10 cm
I_{ch}=25-150 kA
Pellet
1 cm
$N_P = 10^{17}-10^{18}$ cm^{-3}
Anode
Thin Foils
1-10 Torr
2-5 cm
2-5m
2-5m
2-5 cm

Figure 1

Ion Orbits in a Z-Discharge Channel

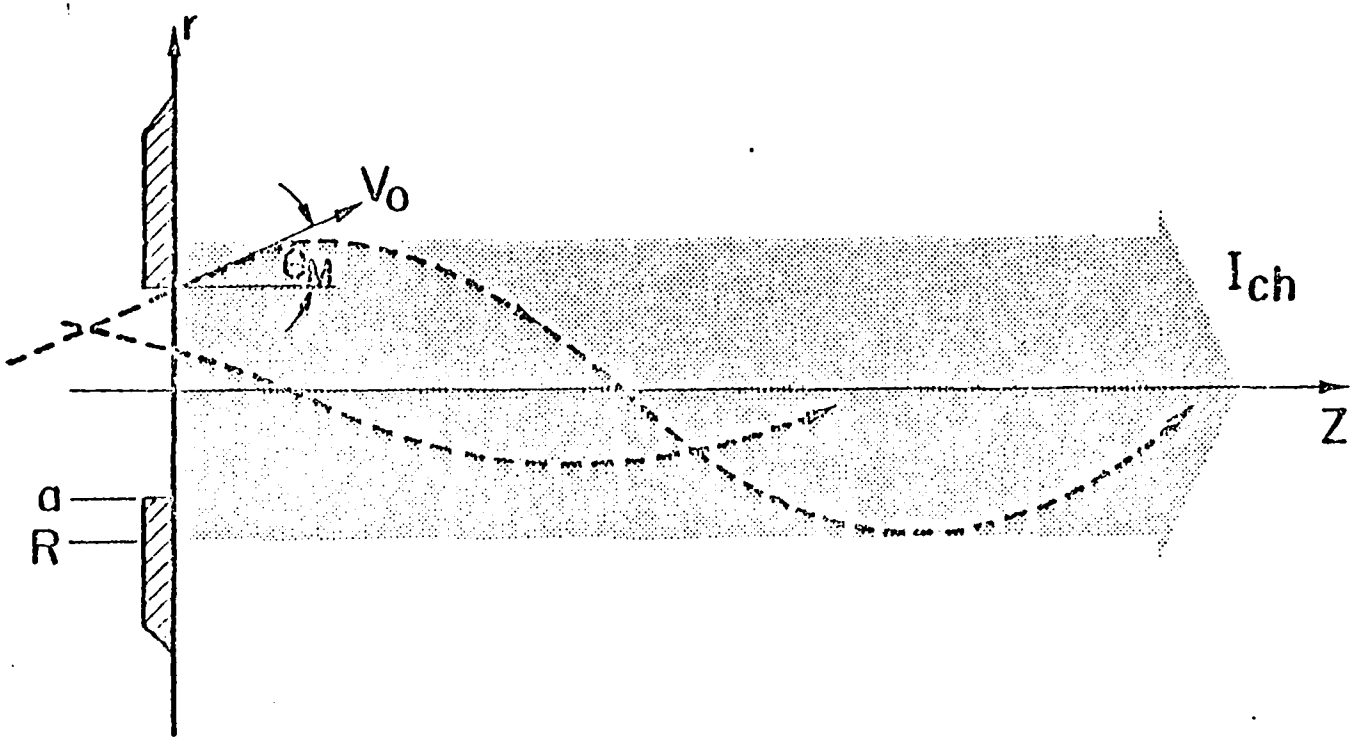

$$\frac{10^3\, I_{ch}}{V_o} = \frac{(1-\cos\theta_M)R^2}{R^2-a^2} = \frac{2\Delta V_z}{V_o}$$

Figure 2

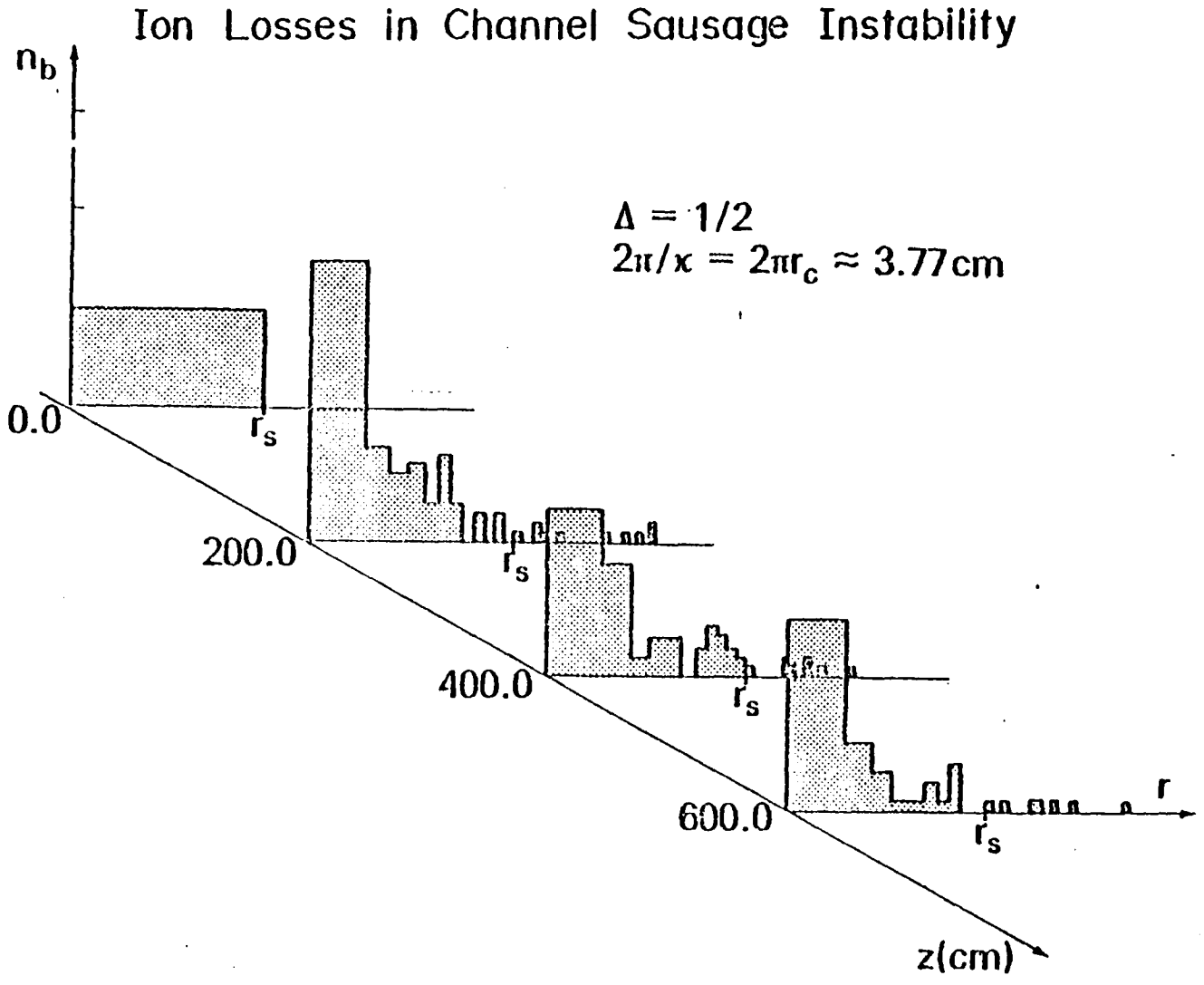
Ion Losses in Channel Sausage Instability
n_b
$\Delta = 1/2$
$2\pi/\kappa = 2\pi r_c \approx 3.77\,cm$
0.0
r_s
200.0
r_s
400.0
r_s
600.0
r_s
r
z(cm)

Figure 3

Ion Transport Experiment

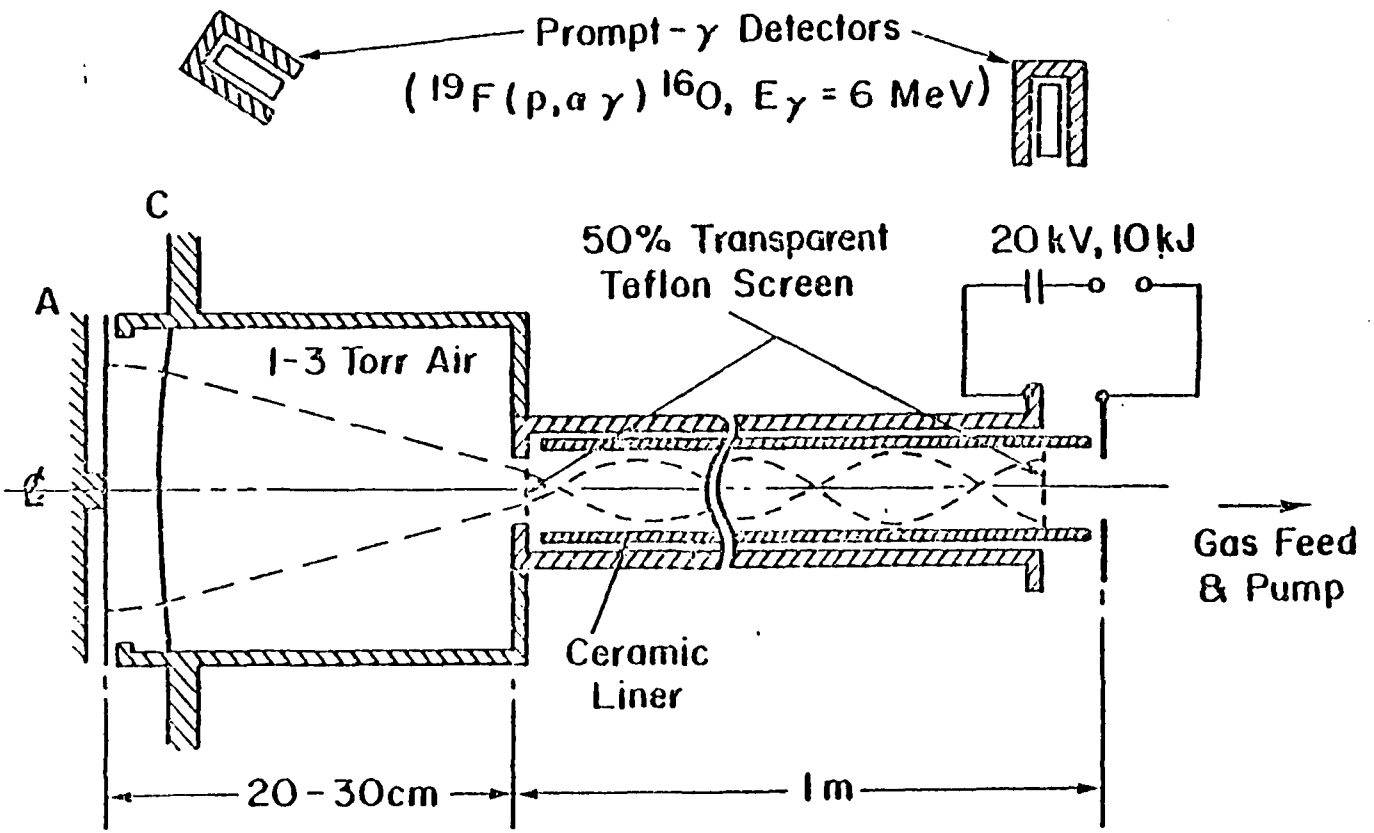

Figure 4

ION TRANSPORT RESULTS

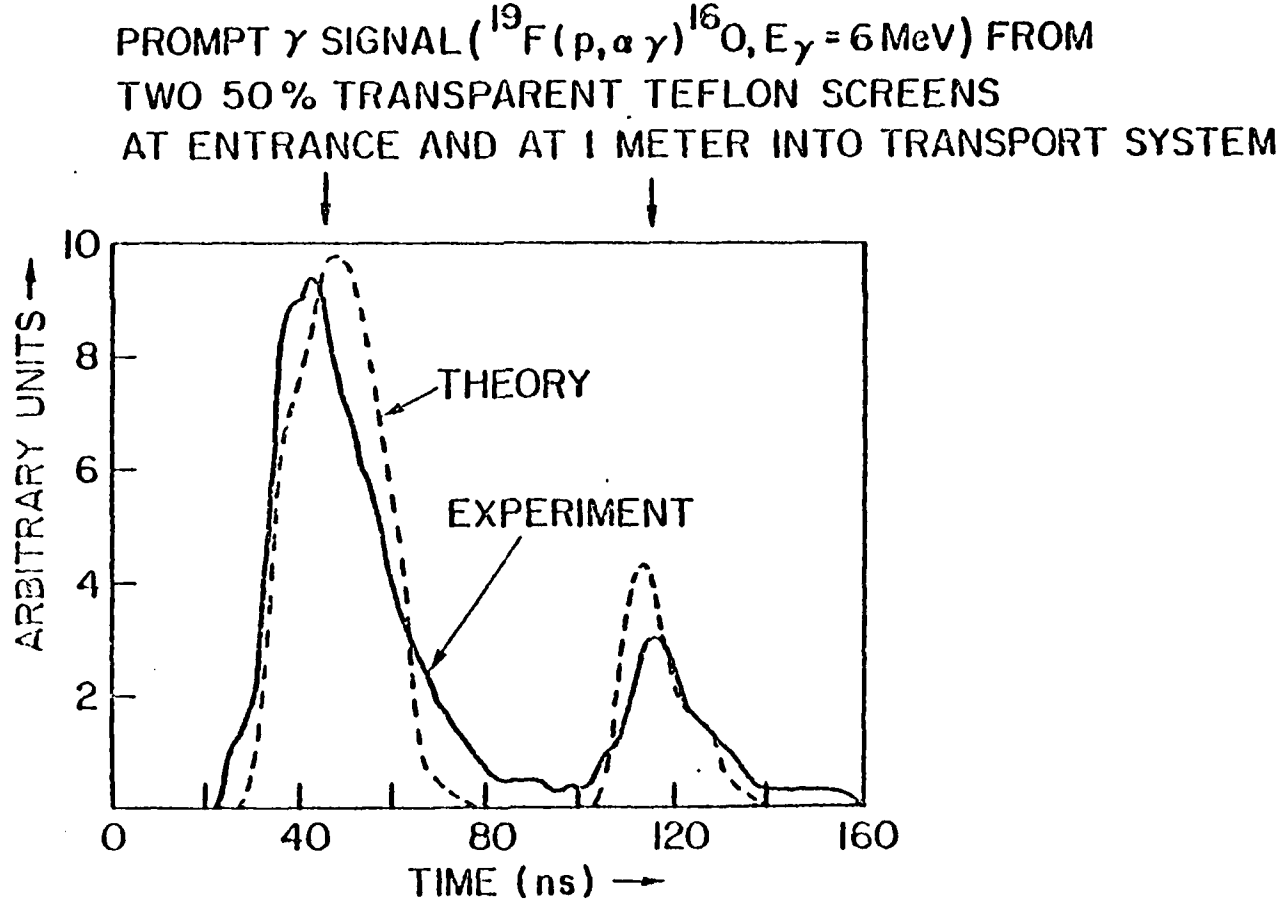

Figure 5

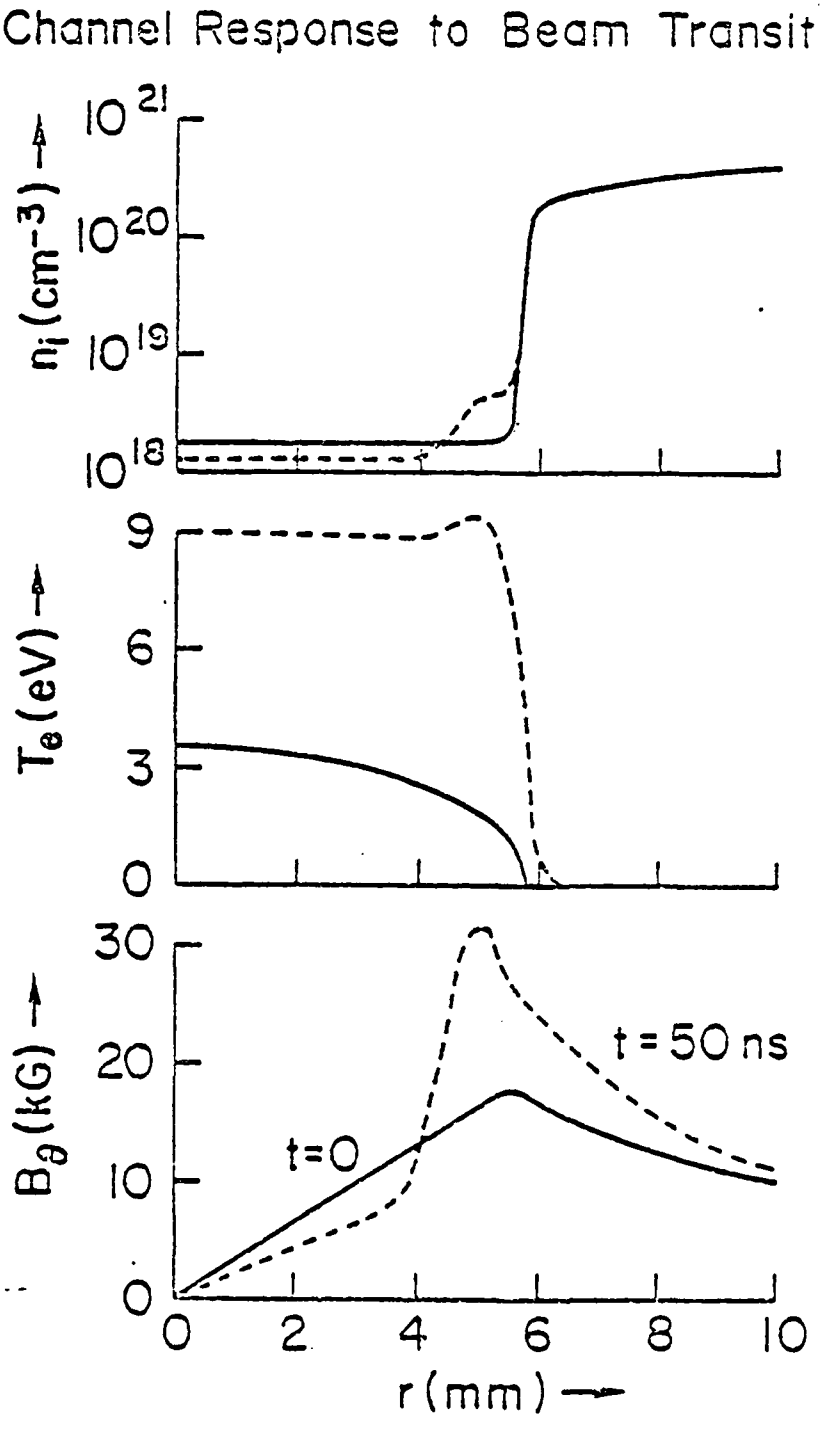
Channel Response to Beam Transit
$n_i\,(cm^{-3})$
10^{21}
10^{20}
10^{19}
10^{18}
$T_e\,(eV)$
9
6
3
0
$B_\theta\,(kG)$
30
20
10
0
t=0
t=50 ns
0
2
4
6
8
10
r(mm)

Figure 6

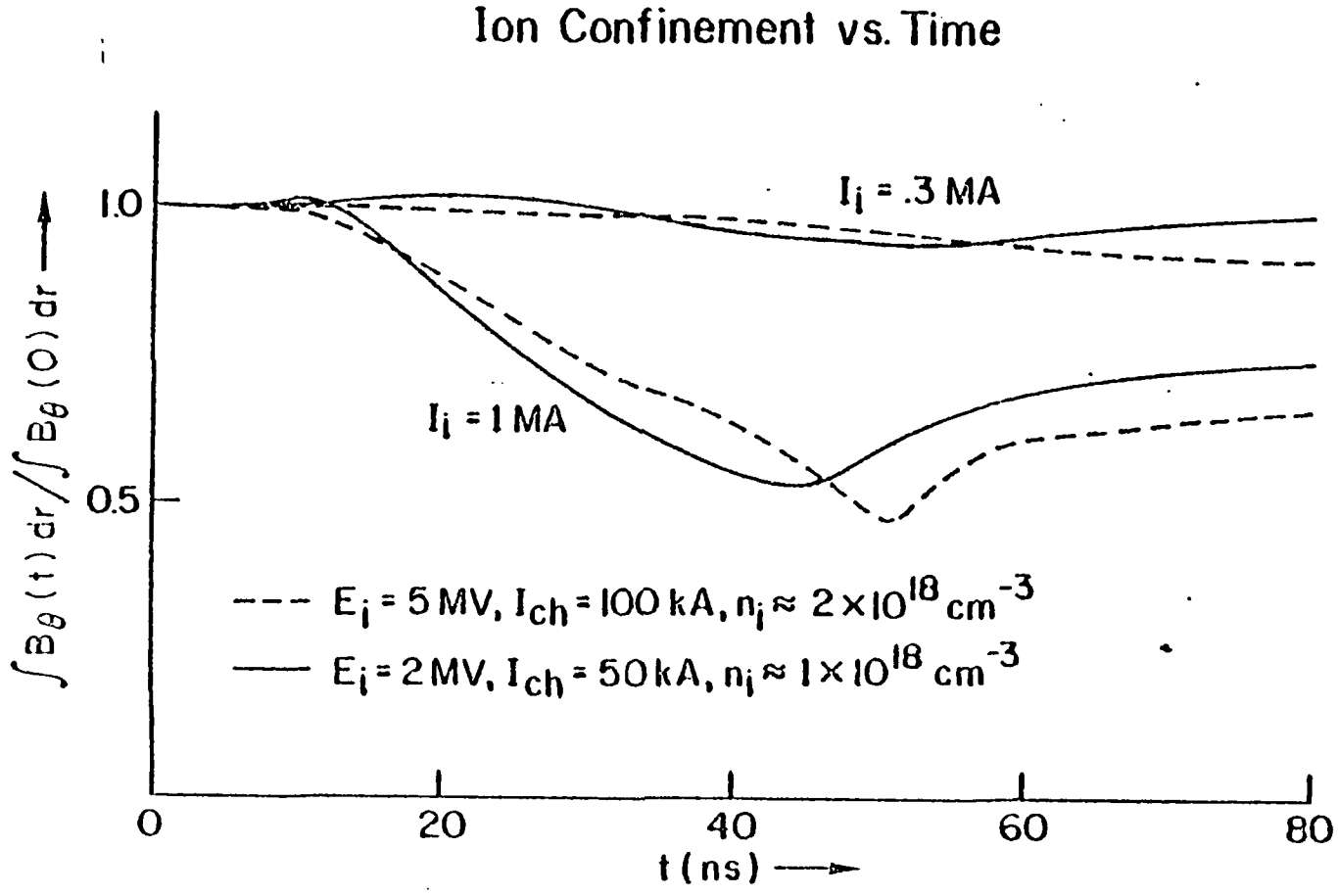
Ion Confinement vs. Time
1.0
0.5
$\int B_\theta(t)\,dr / \int B_\theta(0)\,dr$
I_i = .3 MA
I_i = 1 MA
--- E_i = 5 MV, I_{ch} = 100 kA, $n_i \approx 2\times10^{18}$ cm^{-3}
—— E_i = 2 MV, I_{ch} = 50 kA, $n_i \approx 1\times10^{18}$ cm^{-3}
0
20
40
60
80
t (ns)

Figure 7

Achievable Power Multiplication

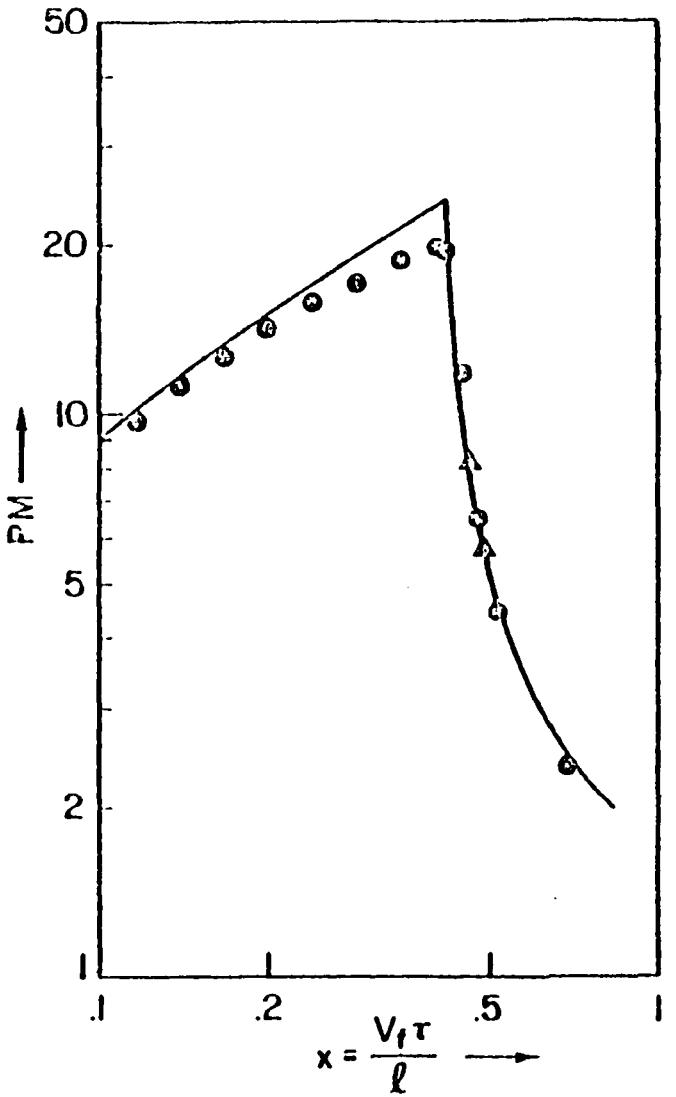

Figure 8

Bunched Pulse Shaping

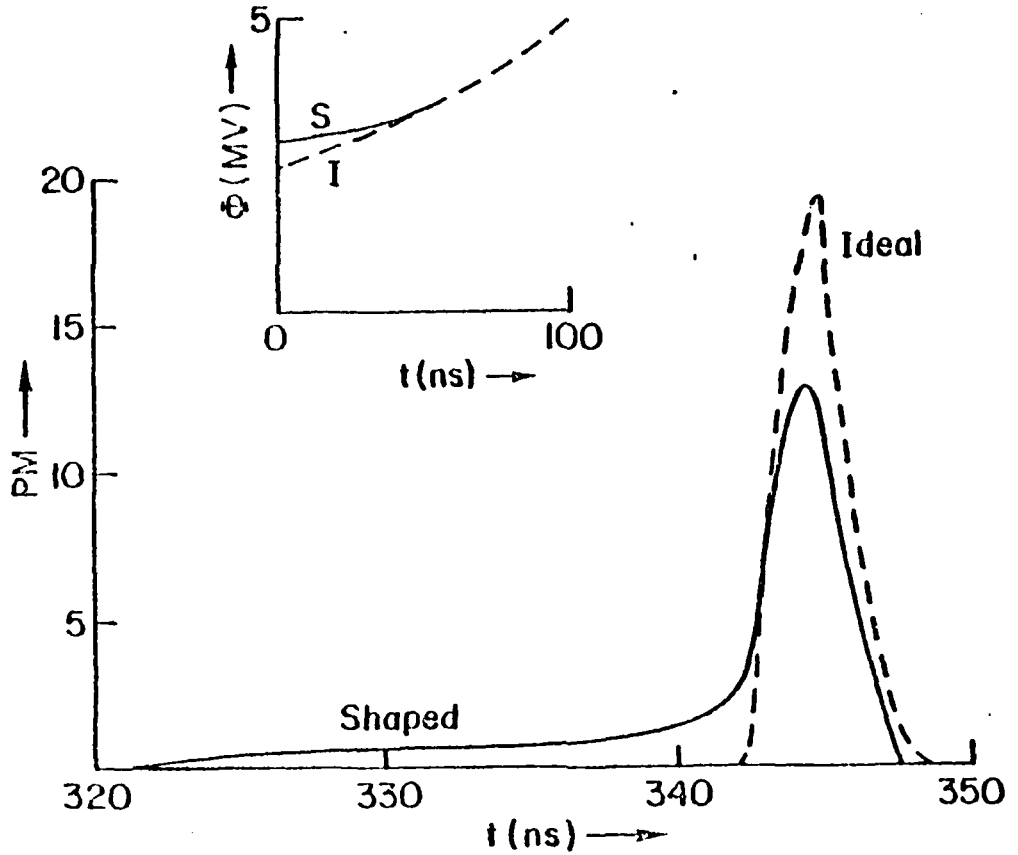

Figure 9

IGNITION SYSTEM PARMETERS

ENERGY ON PELLET (MJ)	3		2	
POWER ON PELLET (TW)	200		100	
STORED ENERGY (MJ)	24		16	
PULSE DURATION (ns)	100	50	100	50
FOCUSED POWER (TW)	35	70	23	45
BUNCHING FACTOR	6	3	4.5	2
FOCUSED CURRENT (MA)				
5 MeV PEAK	7	14	4.5	9
2 MeV PEAK	18	35	12	23
MIN. CHANNEL LENGTH (m)				
5 MeV PROTONS	6	5	6	4
2 MeV DEUTERONS	3	2	3	2

Table 1

Hydrodynamic Response of Plasma Channels to Propagating Ion Beams

D. G. Colombant, Shyke A. Goldstein,[a] and D. Mosher
Naval Research Laboratory, Washington, D. C. 20375
(Received 28 March 1980)

Hydrodynamic response of plasma channels induced by intense propagating ion beams is examined with use of both analytical estimates and a one-dimensional radial numerical model. It is found that mega-ampere, 3–5-MeV proton beams can be propagated in deuterium background over several meters.

PACS numbers: 52.40.Mj, 52.30.+r

Mega-ampere beams of 1–2-MeV protons and deuterons have recently been extracted from 100-cm^2 Pinch Reflex diodes coupled to high-power transmission-line generators. Focusing to 0.4 MA/cm^2 has been reported.[1,2] These light-ion beams are appropriate for inertial-confinement-fusion experiments when a large number of them are individually transported several meters and combined onto a pellet.[3,4] To this end, 100-kA/cm^2 beams have been transported a meter distance through 50-kA discharges in 1 Torr air[5] and 5-kA/cm^2 beams a 50 cm distance in a wire-initiated plasma channel in 40-Torr deuterium gas.[6] The azimuthal magnetic field produced by the discharge current confines the charge- and current-neutralized beam within the discharge diameter. In the present theoretical work, the magnetohydrodynamic (MHD) response of transport channels to ignition-system–level beams is investigated. Simple analytic estimates for channel response agree with a one-dimensional (1D) radial, two-temperature MHD code for moderate density changes. Results indicate that for 3–5-MeV protons, mega-ampere–level beams can be transported. The problem of beam stability has been considered elsewhere.[7]

The discharge current I_{ch} required to transport a beam with given injection conditions is determined from conservation of canonical momentum p_z. For an ion entering a discharge at radius r_0 with speed v_0 at an angle θ to the z axis with no angular momentum,

$$v_z(r) = v_0\cos\theta + (q_i/m_i)\int_{r_0}^{r} B(r)dr, \tag{1}$$

where B is the azimuthal magnetic field. For proton beams and $B(r)\sim r$, $I_{ch}(A) \approx 0.5\times 10^{-3}\theta_m^{\,2} \times v_0(cm/s)$, where θ_m(rad) is the maximum injection angle. For 50-kA discharge currents and several-megaelectronvolt protons, this expression[8] requires $\theta_m \lesssim 10^\circ$. A uniform current distribution is appropriate for few-electronvolt, centimeter-diameter discharges established microseconds before beam injection.[3] Once the beam is injected into the discharge,[10] kinetic pressure and magnetic forces on the plasma return current induced by beam injection drive channel expansion on the 50-ns beam-duration time scale. The expanding plasma convects magnetic field outward, thereby increasing the beam radius. At the same time, the beam experiences energy losses due to collisional deposition and deceleration in induced electric fields. The plasma channel density must be low enough to prevent excessive energy losses but high enough to prevent excessive expansion.

In order to study the response of the channel to injected beams with a 1D radial code, azimuthal symmetry and small axial gradients are assumed.[11] The equations solved in the code include the MHD equations with classical electron transport coefficients and the appropriate Maxwell's equations (the same notation is used as in Braginskii[12]):

$$\partial\rho/\partial t + r^{-1}\partial(\rho r v)/\partial r = 0, \tag{2}$$

$$\partial(\rho v)/\partial t + r^{-1}\partial(\rho r v^2)/\partial r = -\partial p/\partial r - j_b B/c, \tag{3}$$

$$\frac{\partial \epsilon}{\partial t} + \frac{1}{r}\frac{\partial}{\partial r}\{r[(\epsilon + p)v + q_e]\} = Q_e - \frac{vB}{c}j_b, \tag{4}$$

$$\tfrac{3}{2}n_e k\frac{\partial T_e}{\partial t} + \tfrac{3}{2}n_e v k\frac{\partial T_e}{\partial r} + p_e\frac{1}{r}\frac{\partial}{\partial r}rv + \frac{1}{r}\frac{\partial}{\partial r}rq_e = Q_e - \frac{n_e k}{\tau_{ei}}(T_i - T_e), \tag{5}$$

$$\partial B/\partial t = -c\,\partial E/\partial r, \tag{6}$$

$$r^{-1}\partial(rB)/\partial r = (4\pi/c)(j_b + j_p), \tag{7}$$

$$E = \eta j_p - vB/c, \tag{8}$$

with

$$\epsilon = \tfrac{1}{2}\rho v^2 + \tfrac{3}{2}n_i k T_i + \tfrac{3}{2}n_e k T_e, \tag{9}$$

$$p = n_e k T_e + n_i k T_i, \tag{10}$$

$$q_e = -K_e\,\partial T_e/\partial r, \tag{11}$$

$$Q_e = \eta j_p^2 - \rho S j_b - P_{rad}. \tag{12}$$

In the above, j_p and j_b are the plasma and beam current density, τ_{ei} is the electron-ion equipartition time, and P_{rad} is the optically thin radiation loss rate. Finite-$(\omega_{ce}\tau_{ei})$ effects have been included in the calculation of the transport coefficients.

The standard channel prior to beam injection is defined to be 6×10^{-6} g/cm^3 deuterium ($n_i = 2\times10^{18}$ cm^{-3}), with $I_{ch} = 50$ kA, $T_e = T_i \approx 3$ eV inside a channel of radius $r_{ch} = 0.56$ cm. Deuterium is chosen for simplicity of atomic physics—such as ideal-gas law—and radiation processes, and for collisional beam losses lower than a comparable mass density of hydrogen. The plasma channel is surrounded by a cold gas blanket. Radial profiles for the channel prior to beam injection (Fig. 1) are derived from pressure balance for I_{ch} uniformly distributed.[9] The transported beam is modeled by $j_b = j_{b0}(t)$ for $r \le y r_{ch}$, and $j_b = j_{b0}(1 - r/r_{ch})/(1-y)$ for $y r_{ch} < r \le r_{ch}$ with $0.1 \le y \le 0.35$. This distribution simulates an aperture scrapeoff from a larger beam focal-spot size. For beam duration τ, $j_{b0} = j_{bm}(1 + t/\tau)/2$. Ion energy ϵ_b increases in time like j_{b0}, reaching ϵ_{bm} at $t = \tau$. This energy ramp permits beam power multiplication by axial bunching during transport.

In Eq. (3), the magnetic expansion forces usually dominate over kinetic pressure. If we assume constant radial acceleration due to $j_p B/c$, plasma expansion is approximated by

$$\chi \simeq 3\times10^{-2} j_b(\mathrm{A/cm^2})\, j_{ch}(\mathrm{A/cm^2}) \times t^2(\mathrm{s})/\rho(\mathrm{g/cm^2}), \quad (13)$$

where a fluid element initially at radius r is displaced to $(1+\chi)r$ at t, j_{ch} is the discharge current density, and $j_b \simeq -j_p$ is assumed for $j_{ch} \ll j_b$. Radial channel and beam expansion will be small when $\chi \ll 1$. The standard channel parameters give $\chi \simeq \frac{1}{2}$ after 50 ns for a 1-MA/cm^2 beam.

Ion compressional heating in Eq. (4) is always less important than the electron-heating mechanisms on the right-hand side except at the channel boundary. For $\epsilon_b = 5$ MeV and $j_b = 1$ MA/cm^2, collisional deposition dominates over return-current heating above 3 eV. The proton stopping power in deuterium is then $S = 10^3/\epsilon_b$ MeV/(g/cm^2). The associated temperature rise in the plasma is $\delta(T_e + T_i) \sim 7\times10^3 j_b t/\epsilon_b$ and is of order 100 eV for the above beam after 50 ns. For 2.3-m transport, collisional beam-energy losses are less than 20% of the initial beam energy when $\rho \le 9\times10^{-7}\epsilon_b^2$. This criterion combined with that for inertial confinement [Eq. (13) with $\chi \le \frac{1}{2}$] yields $7\times10^{-6} \le \rho \le 9\times10^{-7}\epsilon_b^2$, i.e., $\epsilon_b > 2.8$ MeV. Energy losses due to deceleration in the axial electric field of Eq. (8) must also be considered. Early in time, E is established by return-current flow in the resistive plasma. Later, high plasma conductivity and expansion velocity cause the hydrodynamic term to dominate. Energy losses due to late-time electric field are comparable to collisional losses for the above density regime.

Figure 2 shows the channel at 50 ns for $j_{bm} = 0.6$ MA/cm^2, and $\epsilon_{bm} = 5$ MeV. Expansion has reduced the initial density to $(1.2$–$1.4)\times10^{18}$ cm^{-3}. This agrees with the calculated value of $\chi = 0.3$ from Eq. (13). A figure of merit for ion confinement is defined by the integral in Eq. (1) extended from 0 to r_{ch}. The code calculates a reduction in its value from an initial 5 to 3.3 kG cm for Fig. 2 in agreement with simple scaling. At the conditions shown, transported ions lose about 0.14 MeV/m collisionally and about 0.1 MeV/m because of electric-field deceleration. Early in time, when $\epsilon_b = 2.5$ MeV, corresponding values are 0.28 and 0.03 MeV/m.

Figure 3 illustrates the response of the standard channel to a beam of comparable power density as in Fig. 2 but with $j_{bm} = 2.75$ MA/cm^2 and $\epsilon_{bm} = 3$ MeV. This case is very different from the preceding one since the channel has had time to expand and to bounce from the cold gas blanket.

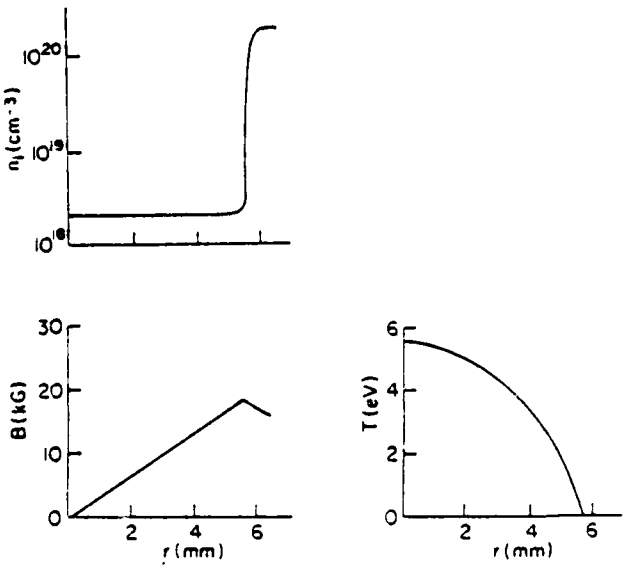

FIG. 1. Initial deuterium plasma channel conditions corresponding to uniform current distribution and to pressure balance between the channel and cold gas blanket.

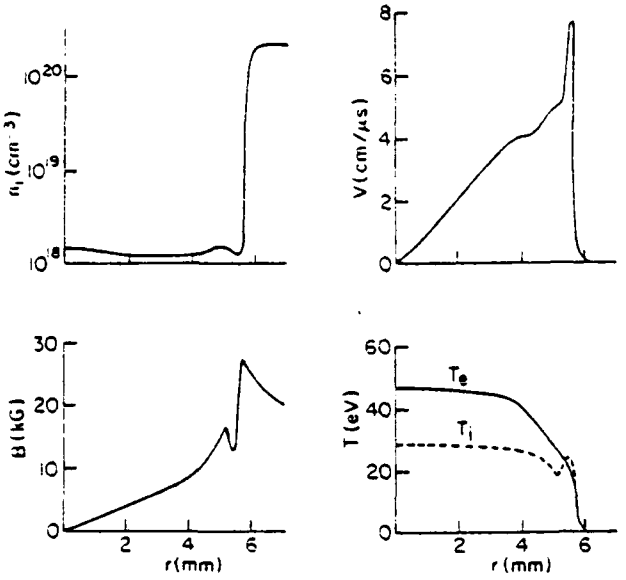

FIG. 2. Plasma channel characteristics at t = 50 ns after injection of a 5-MeV, 400-kA proton beam.

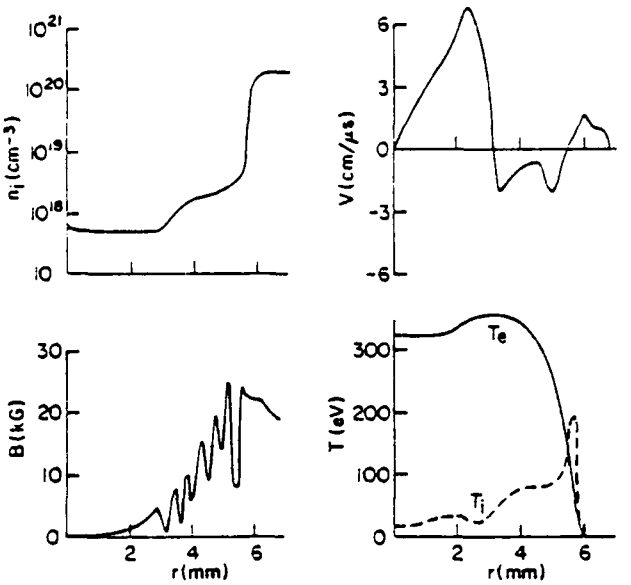

FIG. 3. Plasma channel characteristics at t = 50 ns after injection of a 3-MeV, 2-MA proton beam. Note that the velocity profile indicates reflection from the cold gas blanket.

The structure of the various fluid quantities is much more complicated and indicates that different physics applies. For example, instabilities might play an important role which would change the results quantitatively. Estimates from Eq. (13) can still be made, but only within a radius of about 2 mm where plasma expansion still occurs. In that region, the code is in agreement with simple estimates. An interesting feature of these results is that the vB/c term gives an electric field which will accelerate the ion beam if it exceeds the collisional slowing down (Ohmic electric fields are small because of high conductivity).

In addition to the case of the unbunched beam which prevails at the beginning of the channel, the plasma channel response to a bunched beam near the exit of the channel has been investigated. It is found that a beam of a given current and voltage is more easily transported in its bunched state due to the reduced hydrodynamic expansion. This can be seen from Eq. (13) with $j_b t$ constant so that χ depends only on $j_{ch} t/\rho$. For the 10 ns pulse duration of a bunched beam, the radial expansion is 5 times smaller. Alternatively, the density can be chosen smaller to maintain a constant χ. For constant collisional losses in transit through the channel (i.e., $\int \rho dz$ = const), the density at the beginning of the channel can then be increased to reduce the channel expansion there.

In conclusion, the hydrodynamic plasma response to light-ion beams has been studied with use of simple estimates and numerical solutions. For 3–5-MeV proton-beam propagation, deuterium z discharges were studied for injected, mega-ampere-per-square-centimeter, 50-ns beams. Discharge channel densities $\sim 10^{-5}$ g/cm^3 were found to permit transport of these beams in both unbunched and bunched states over the several-meter distances required for inertial-confinement-fusion ignition experiments.

This work was supported by the U. S. Department of Energy.

---

[a]Permanent address: Jaycor, Inc., Alexandria, Va. 22304.

[1]G. Cooperstein, Shyke A. Goldstein, D. Mosher, F. W. Oliphant, F. L. Sandel, S. J. Stephanakis, and F. C. Young, in Proceedings of the Third International Topical Conference on High Power Electron and Ion Beam Research and Technology, Novosibirsk, 1979 (to be published).

[2]D. J. Johnson, Bull. Am. Phys. Soc. 24, 926 (1979).

[3]D. Mosher, G. Cooperstein, Shyke A. Goldstein, D. G. Colombant, P. F. Ottinger, F. L. Sandel, S. J. Stephanakis, and F. C. Young, in Proceedings of the Third International Conference on High Power Electron and Ion Beam Research and Technology, Novosibirsk, 1979 (to be published).

[4]P. A. Miller, D. J. Johnson, T. P. Wright, and G. W. Kuswa, Comments Plasma Phys. Controlled

Fusion 5, 95 (1979).

[5]F. L. Sandel, F. C. Young, S. J. Stephanakis, F. W. Oliphant, G. Cooperstein, Shyke A. Goldstein, and D. Mosher, Bull. Am. Phys. Soc. 24, 1031 (1979); F. C. Young, F. L. Sandel, S. J. Stephanakis, P. G. Blauner, F. W. Oliphant, G. Cooperstein, S. A. Goldstein, and D. Mosher, Bull. Am. Phys. Soc. 24, 1031 (1979).

[6]J. N. Olsen, D. J. Johnson, and R. J. Leeper, Appl. Phys. Lett. 36, 808 (1980).

[7]P. F. Ottinger, D. Mosher, and S. A. Goldstein, Phys. Fluids 22, 332 (1979), and to be published.

[8]P. F. Ottinger, D. Mosher, and S. A. Goldstein, Phys. Fluids 23, 909 (1980).

[9]J. R. Freeman, private communication; P. A. Miller, L. Baker, J. R. Freeman, L. P. Mix, J. W. Poukey, and T. P. Wright, in *Proceedings of the Second International Topical Conference on High Power Electron and Ion Beam Research and Technology, Ithaca, New York, 1977*, edited by J. A. Nation and R. N. Sudan (Cornell Univ. Press, Ithaca, N.Y., 1977).

[10]S. A. Goldstein, D. P. Bacon, D. Mosher, and G. Cooperstein, in *Proceedings of the Second International Topical Conference on High Power Electron and Ion Beam Research and Technology, Ithaca, New-York, 1977*, edited by J. A. Nation and R. N. Sudan (Cornell Univ. Press, Ithaca, N.Y., 1977).

[11]Azimuthal symmetry applies for symmetric beam injection from Pinch Reflex diodes since no external magnetic fields are employed. Small axial gradients exist because of the shallow injection angles required by modest channel current. Additionally, the channel is kink-mode stabilized by the dense background gas. See, for example, W. M. Manheimer, M. Lampe, and J. P. Boris, Phys. Fluids 16, 1129 (1973).

[12]S. I. Braginskii, in *Reviews of Plasma Physics*, edited by M. A. Leontovich (Consultants Bureau, New York, 1965), p. 205.

THC4 Self-consistent properties of light ion beams in plasma channels

DENIS G. COLOMBANT, WALLACE M. MANHEIMER, D. MOSHER, and SHYKE A. GOLDSTEIN, U.S. Naval Research Laboratory, Plasma Physics Division, Washington, D.C. 20375.

In the light-ion beam fusion schemes, an important problem is the transport of the beam from its production area to the reaction chamber. In a scheme presented previously,[1] the ion beam enters a Z-discharge channel at the best beam focus for better [illegible] inside the channel, the ions are confined radially by the azimuthal magnetic field produced by the discharge of an external capacity bank.

Results for the radial plasma channel response to the passage of 0.3 - 1-MA/cm^2 2-5-MeV proton beams have already been presented.[2] In these studies, the beam current density was assumed to be known as a function of radius. In this paper, the radial current density distribution is obtained by following ion orbits in the macroscopic fields determined from the MHD equations for the plasma channel.

The ions are followed in their 3-D motion, and their current density distribution is determined at the end of each time step. Results are found to depend on the beam initial conditions at their best focus. In particular, the results depend on the ion initial angular momentum distribution.

Calculations are performed for various beam current intensities, beam particle energy, and beam pulse length. Background material for the channel is taken to be hydrogen for simplicity.

Results from this new self-consistent model will be presented, analyzed, and compared with previous results. **(12 min)**

1. S. A. Goldstein, D. P. Bacon, D. Mosher and G. Cooperstein, at Second International Topical Conference on High Power Electron and Ion Beam Research and Technology, Cornell U., Ithaca, N.Y. (1977).
2. D. G. Colombant, S. A. Goldstein, and D. Mosher, in Conference Record, IEEE International Conference on Plasma Science, Montreal (June 1979).

Beam Requirements for Light-ion-driven Inertial-confinement Fusion

Proof-of-principle and scaling experiments for light-ion-driven inertial-confinement fusion are in progress with generators appropriate for use as ignition-system modules.[1,2] Megampere currents of 2-MeV protons and deuterons have recently been extracted in 100-ns pulses from 100-cm^2 pinch-reflex diodes (PRDs) operating at 3-TW diode electric powers.[3] Experiments at the 1-TW level have recorded focused proton-current densities approaching 1 MA/cm^2 with cylindrical magnetically insulated diodes.[4] Deuterons extracted from PRDs have been focused to over 300 kA/cm^2 in a geometry appropriate for injection into transport channels.[3] Proton beams extracted from pinch-reflex diodes have been transported meter distances in the focused state through 50-kA wall-stabilized z-discharges established in 1-torr gas backgrounds.[5] Experiments utilizing laser-initiated discharges are in progress.[6] Several-meter channel transport provides a means of delivering beams extracted from a large number of generators to the vicinity of the pellet. These lengths are sufficient to achieve beam-power multiplication by axial bunching.[7] Computational MHD research[8] and microinstability calculations[9] indicate that individual proton beams with currents approaching 1 MA can be transported.

The cited work indicates that the pulsed-power and ion-beam production and handling techniques are available to assemble a break-even ICF experiment. In this Comment, simple scaling laws for beam focusing, transport, bunching and packaging are combined to define an acceptable range of parameters for ignition-system modules delivering low-atomic-number ($\lesssim 6$) ion beams to a pellet. Techniques for increasing the deliverable beam intensity are then discussed.

Figure 1 illustrates schematically one module for extraction, focusing and transport of an intense ion beam. Ions are accelerated axially across the diode vacuum gap by the applied electric field and are accelerated radially inward by their azimuthal self-magnetic field. The transmission cathode separates the diode region from a low-pressure, gas-filled drift section. Beam-induced breakdown of the gas reduces the self-magnetic field by about two orders of magnitude, so that

Comments Plasma Physics
1981, Vol. 6 No. 3, pp. 101–108

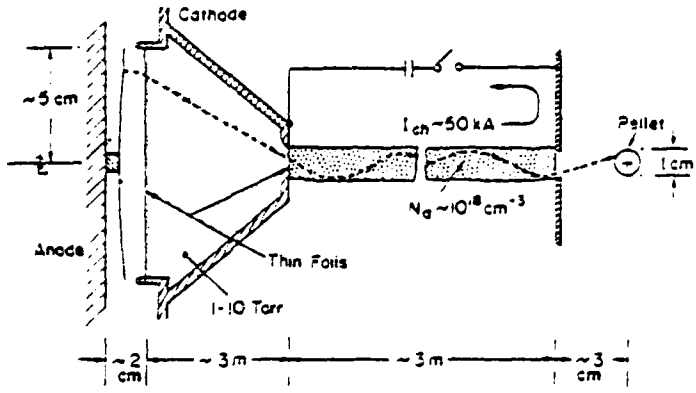

FIGURE 1. Conceptual schematic of one light-ion ICF module, showing a pinch-reflex diode, focusing-drift region and transport channel.

ion orbits in the drift section are nearly ballistic.[3] The anode and cathode structures are shaped so that ions leaving the diode converge to a focus at the entrance of the transport section. Beam ions are magnetically confined in the centimeter-diameter discharge channel and are transported to within a few centimeters of the pellet. The maximum injection angle of ions into the channel must be $\lesssim 0.2$ rad so that modest discharge currents ($\lesssim 50$ kA) suffice for beam confinement[2,7] and excessive expansion between the channel exit and pellet does not occur. For such injection and channel-current conditions, ions of a few MeV/nucleon (which couple efficiently to the pellet[10]) can propagate in a range of channel-plasma densities limited from below by channel expansion during beam transit and from above by excessive collisional beam-energy loss.[3] Increasing the diode accelerating voltage during the ~50-ns injected-ion pulse permits power multiplication during transport by axial bunching down to the ~10 ns required to drive the pellet.[10] Substantial power multiplication can be achieved only when the dispersion in axial ion velocities during transport is small.[7] This condition is also satisfied by small ion-injection angles.

The accelerating-voltage waveform appropriate for beam bunching during transport produces ions which leave the diode with an axial velocity[2,7]

$$v_i(t) = \frac{v_i(0)}{1 - t/T}; \quad 0 \le t \le \tau < T \tag{1}$$

where τ is the ion-pulse duration at the diode and T determines the voltage-ramp steepness. As the beam propagates in z, the beam duration is reduced according to

$$\Delta t = \tau \left[1 - \frac{z}{v_i(\tau)(T - \tau)} \right]. \tag{2}$$

In order to reduce Δt to τ/α, propagation through a distance

$$l = 1.3 \times 10^9 (1 - \alpha^{-1})(T - \tau)\sqrt{(E/A)}\ \text{cm} \tag{3}$$

is required, where E (MeV) is the ion energy at $t = \tau$; A is the atomic weight; α is the power multiplication factor.

The accelerating-voltage ramp required for bunching produces a similarly varying ion current. These time variations cause the magnetic pinch force in the diode to increase with time. In order to minimize defocusing with time at the entrance aperture of the transport section, the diode vacuum gap should decrease with time. With optimal gap-closure velocity,[11] residual time variations produce a focal-spot radius

$$r_s \simeq \frac{0.15 Z_D I}{\sqrt{(AE)}} \frac{(1 - \tau/T)v\tau}{(R/F)}\ \text{cm}. \tag{4}$$

In Eq. (4), Z_D is the ion charge state in the diode; I (MA) is the ion current in the diode; v (cm/s) is the electrode-plasma velocity for cathode or anode; R is the diode radius; and F is the focusing distance from diode to transport entrance aperture. The quantity R/F defines the maximum injection angle of ions into the focus.

The magnetic field produced by the channel current I_{ch} (MA) must confine these ions within the channel radius $r_{ch} > r_s$. From conservation of canonical momentum[2,7]

$$I_{ch} \geq 1.3 \frac{\sqrt{(AE)}}{Z_T} (R/F)^2, \tag{5}$$

where $r_s^2 = r_{ch}^2/2$ has been assumed; Z_T is the beam charge state in the discharge. Collisions with discharge-plasma electrons can produce a charge state different from that in diode.[12] The transporting beam current $I_T = (Z_T/Z_D)I$ produces a plasma-return current of nearly equal magnitude. The channel expands under the influence of the resulting $j_z B_\theta$ force. MHD calculations demonstrate acceptable channel expansion when[2,3]

$$I_T I_{ch} \leq 3 \times 10^{-10} \frac{\rho r_{ch}^4}{\tau^2}, \tag{6}$$

where ρ (g/cm^3) is the channel-plasma mass density.

Channel-response calculations[3] determine the $V_r B_\theta$ electric field which removes energy from the beam as well as collisional energy losses. Minimum beam-energy loss occurs at the plasma density where these two loss rates are equal, since the former is proportional to ρ, while the latter is proportional to ρ^{-1}. For a fully ionized deuterium plasma,[13] this optimum density is given by

$$\rho_{opt} = \frac{0.12 I_{ch}}{r_{ch}^2}\sqrt{\left(\frac{IE\tau}{AZ_D}\right)} \tag{7}$$

and the corresponding total beam-energy loss rate in the channel is

$$\frac{dE}{dz} \simeq \frac{2 \times 10^3 A Z_T^2 \rho_{opt}}{E} \text{ MeV/cm.} \tag{8}$$

Substituting the optimum density into Eq. (6) leads to

$$\frac{Z_T \tau^{3/2}}{r_{ch}^2}\sqrt{\left(\frac{AI}{Z_D E}\right)} \leq 3.5 \times 10^{-11}. \tag{9}$$

An estimate of the minimum total energy loss experienced during transport is

$$\Delta E = l\frac{dE}{dz}. \tag{10}$$

Requiring that ΔE be no more than a quarter of E leads to the condition

$$\frac{Z_T \tau^{3/2}}{r_{ch}^2}\sqrt{\left(\frac{AI}{Z_D E}\right)} \leq \frac{7 \times 10^{-13}}{(1-\alpha^{-1})(T/\tau - 1)(R/F)^2}. \tag{11}$$

A larger energy loss at $t = \tau$ is unacceptable, because lower-energy ions emitted earlier already experience greater losses.

Equation (9) must be satisfied when $(R/F) \leq (R/F)_c$, while Eq. (11) must be satisfied otherwise where

$$(R/F)_c^2 = \frac{0.02}{(1-\alpha^{-1})(T/\tau - 1)}. \tag{12}$$

For the purpose of discussion, the above relations can be simplified by assuming that $Z_D = Z_T = Z$. Also, the beam energy can be eliminated by adjusting E with species to maintain a constant deposition length in the target.[14] Since the stopping power scales roughly like AZ^2/E, constant range results when

$$E^2 = AZ^2 E_0^2. \tag{13}$$

In Eq. (13), E_0 is the proton energy of equivalent range. With this energy scaling, a particularly simple form results when Eqs. (9) and (11) are written in terms of beam power $P(TW) = IE/Z$:

$$P < \frac{1.2 \times 10^{-21} E_0^2 r_{ch}^4}{\tau^3} \times \begin{cases} 1 & \text{when } (R/F) \leq (R/F)_c \\ \dfrac{(R/F)_c^4}{(R/F)^4} & \text{when } (R/F) > (R/F)_c. \end{cases} \tag{14}$$

It is noteworthy that Eq. (14) is species-independent. Note also that P refers to the power extracted from the diode. As the beam bunches, $P\tau$ remains constant so that Eq. (14) becomes easier to satisfy.

Applying the considerations of the previous paragraph to Eq. (4), with $r_s \leq r_{ch}/\sqrt{2}$, leads to

$$P \leq \frac{4.6E_0^2A^{5/4}}{Z^{1/2}} \frac{(R/F)r_{ch}}{(1-\tau/T)\nu\tau} . \tag{15}$$

Equations (14) and (15) are plotted in Figure 2 for E_0 = 2 MeV, r_{ch} = 0.5 cm, τ = 50 ns, $\nu = 1 \times 10^7$ cm/s, α = 5 and τ/T = 0.2. The velocity is consistent with observed electrode-plasma espansion.[15] The τ/T value corresponds to a voltage which rises 50% during the pulse. These results suggest that limits to focusability constrain deliverable modular beam power for protons, while lack of beam confinement and energy loss during transport limit beam power for heavier ions. In either case, very long focal lengths ($R/F \leq 0.1$) are required for transport of maximum beam power. Since focusability may be limited by a number of factors not considered here (electrode-plasma instabilities, asymmetric diode fields, beam–plasma interaction in the focusing drift region or effects peculiar to advanced focusing diode designs not yet discovered), operation at the largest R/F values possible would be desirable. However, increasing R/F increases beam expansion between the channel exit and pellet. Therefore, beam overlap on

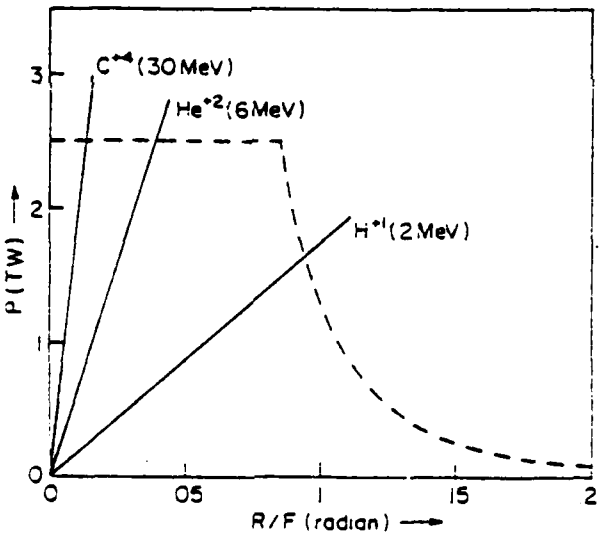

FIGURE 2. Beam-power constraints as a function of the maximum ion-injection angle into the channel. The solid lines represent the maximum focusable power for the species and energies shown. The dashed curve represents the maximum transportable power for all species. The horizontal section of the dashed curve is associated with channel expansion; the curved portion is associated with energy loss. The entire curve scales like $E_0^7 r_{ch}^4/\tau^3$.

target must be considered to determine optimum power and injection-angle regimes of operation.

For channel exits located a distance d from the pellet, each beam expands to a radius $r_{ch} + d(R/F)$ before impacting on target. The average power density on target can then be approximated by

$$p = \frac{NP\alpha}{4\pi [r_{ch} + d(R/F)]^2}, \tag{16}$$

where N is the total number of transported beams. Assuming that no more than 25% of 4π steradians is subtended by the channel-exit aperture area, the maximum number of beams is given by $(d/r_{ch})^2$. The power density on target therefore satisfies

$$p \leq \frac{NP\alpha}{4\pi r_{ch}^2 [1 + N^{1/2}(R/F)]^2}. \tag{17}$$

Since the pellet design specifies p and the facility configuration determines N, Eq. (17) represents an additional constraint which P must satisfy. This constraint is plotted in Figure 3 for N = 36 and 72 modules and two values of p. Other parameters are as in Figure 2. The lower p value corresponds to the incident power density required to drive a 1-cm-diameter break-even pellet of recent design.[16] Acceptable operating ranges are defined by the regions above these curves and below the expansion/energy-loss curve. Thus, operation appears to be limited to the below -0.1-rad regime unless techniques can be employed to

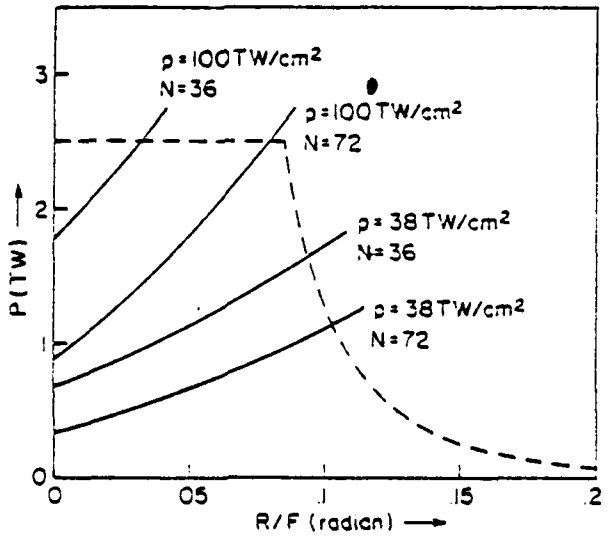

FIGURE 3. Beam-packing constraints for two pellet-irradiance requirements and two ion-module-number values. Acceptable operation is associated with the beam powers above the curves, but subject to the maximum power displayed in Figure 2.

relieve the expansion/energy-loss constraints. Various options to achieve this are now being considered.

Slight increases in $(R/F)_c$ are achieved when the voltage-ramp steepness is increased. This may not be beneficial, since low-energy ions emitted at early times suffer strong energy losses during transport.[5] Low-energy ions do not penetrate deeply enough into the pellet to efficiently couple energy to the fuel. Thus, propagation of several-TW beams at R/F values in excess of 0.1 may require substantial increases in $E_0^2 r_{ch}^4/\tau^3$. A 2-TW beam could be propagated at $R/F = 0.15$ by increasing E_0 to 3 MeV, decreasing τ to 40 ns and increasing r_{ch} to 0.6 cm. The increase in E_0 requires pellets designed for longer deposition lengths. The Sandia National Laboratories PBFA facility is designed with $\tau \lesssim 40$ ns so that the decrease in τ presents no difficulty. The channel radius can be increased provided a final-focusing stage can be added at the channel exit.[7,17] Limitations to deliverable beam power can also be relaxed by employing a discharge channel which is imploding rather than static at the time of beam injection.[18] The MHD expansion constraint is relaxed, since an imploding channel must experience stronger radial acceleration for a longer time before reaching an expanded state. Such dynamic channels have imbedded electric fields which tend to accelerate the beam,[18] thus reducing energy loss as well.

Scale-up of $E_0^2 r_{ch}^4/\tau^3$, dynamic channels or a combination of both techniques can be used to extend allowable R/F values or increase beam power in the transport section. For low pellet irradiance, these techniques may permit delivery of few-TW beams with R/F values as large as 0.15. Proton-beam focusability precludes their use in high-irradiance configurations. When the same focusing constraint is applied to higher-atomic-number beams, high-irradiance operation with a standard, static channel is permitted with $R/F \simeq 0.05$. For reasons discussed in the paragraph following Eq. (15), focusing with such small R/F values is, at best, uncertain. Thus, application of advanced techniques to the transport of nonhydrogenic beams is desirable in order to permit high pellet irradiance at $R/F \simeq 0.1$.

D. MOSHER
D.G. COLOMBANT
Naval Research Laboratory, Washington, DC 20375
and SHYKE A. GOLDSTEIN
Jaycor, Inc., Alexandria, VA 22304

Submitted by Joy Boris
Received October 7, 1980.

References

1. G.W. Kuswa and T.H. Martin, *Proceedings of Meeting on Inertial Confinement Fusion* (San Diego, Feb. 26–28, 1980) p. 32

2. D. Mosher, G. Cooperstein, S.A. Goldstein, D.G. Colombant, P.F. Ottinger, F.L. Sandel, S.J. Stephanakis and F.C. Young, *Proceedings of Third International Conference on High Power Electron and Ion Beam Research and Technology* (Novosibirsk, July 3–6, 1979) p. 576
3. G. Cooperstein, Shyke A. Goldstein, D. Mosher, R.J. Barker, J.R. Boller, D.G. Colombant, A. Drobot, R.A. Meger, W.F. Oliphant, P.F. Ottinger, F.L. Sandel, S.J. Stephanakis and F.C. Young, *Proceedings of Fifth Workshop on Laser Interaction and Related Plasma Phenomena* (Rochester, Nov. 5–9, 1979).
4. D.J. Johnson, G.W. Kuswa, A.V. Farnsworth, Jr., J.P. Quintenz, R.J. Leeper, E.J.T. Burns and S. Humphries, Jr., Phys. Rev. Lett. 42, 610 (1979); D.J. Johnson, Bull. Am. Phys. Soc. 24, 925 (1979).
5. F.L. Sandel, F.C. Young, S.J. Stephanakis, W.F. Oliphant, G. Cooperstein, S.A. Goldstein and D. Mosher, Bull. Am. Phys. Soc. 24, 1031 (1979).
6. J.N. Olsen, D.J. Johnson and L. Baker, Bull. Am. Phys. Soc. 24, 978 (1979).
7. P.F. Ottinger, D. Mosher and Shyke A. Goldstein, Phys. Fluids 23, 909 (1980).
8. D.G. Colombant, D. Mosher and Shyke A. Goldstein, NRL Memorandum Report 4252 (1980, to be published); D.G. Colombant and Shyke A. Goldstein, *Proceedings of IEEE International Conference on Plasma Science* (Madison, May 19–21, 1980) p. 37.
9. P.F. Ottinger, D. Mosher and Shyke A. Goldstein, Phys. Fluids 22, 332 (1980); NRL Memorandum Report 4088 (1980).
10. S. Jorna and N. Metzler, *Proceedings of IEEE International Conference on Plasma Science* (Madison, May 19–21, 1980) p. 37.
11. D. Mosher, G. Cooperstein and Shyke A. Goldstein, *Proceedings of Topical Meeting on Inertial Confinement Fusion* (San Diego, Feb. 26–28, 1980) p. 104.
12. T.A. Mehlhorn, Sandia National Laboratory Report SAND80-0038 (1980).
13. Deuterium plasma has the advantage over hydrogen of half the stopping power.
14. P.A. Miller, informal communication.
15. R.D. Genuario, J. Maenchen, R. Stringfield, G. Cooperstein, D. Mosher, S.J. Stephanakis and S.A. Goldstein, *Proceedings of IEEE International Conference on Plasma Science* (Madison, May 19–21, 1980) p. 13.
16. G.O. Allshouse, informal communication.
17. P.F. Ottinger, Shyke A. Goldstein and D. Mosher, *Proceedings of IEEE International Conference on Plasma Science* (Madison, May 19–21, 1980) p. 95.
18. Shyke A. Goldstein and D.A. Tidman, *Proceedings of IEEE International Conference on Plasma Science* (Madison, May 19–21, 1980) p. 96.

ION BEAM HANDLING IN MAGNETIZED PLASMAS

Shyke A. Goldstein*, D. G. Colombant, D. Mosher,
P. F. Ottinger* and F. Sandel*

Naval Research Laboratory, Washington D.C. 20375 U.S.A.

ABSTRACT. Intense ion beams are shown to behave like weak beams when transported through hot and dense magnetized plasmas. Magnetic diffusion and hydrodynamic motion are shown to be minimized by high plasma conductivity and inertia. Transport and focusing elements are examined for beam brightness effects and attainment of high current density. Beam acceleration and brightness enhancement are shown to occur in imploding channels. Self propagation of ion beams is predicted to happen at beam brightnesses comparable to those needed for fusion.

INTRODUCTION

The physics and technology of intense ion beams at the MA currents and MeV energies is presently undergoing rapid development. The question of handling such very intense beams was raised primarily in connection with reactor scenarios based on Inertial Confinement Fusion (ICF) systems. During the last few years, theoretical and experimental studies have revealed some interesting aspects of the interaction physics of these beams with magnetized plasmas. For clarity, we categorize the systems into two classes involving static and dynamic plasmas. In static plasmas, magnetic field variations are assumed to be small. We show the existence of beam and plasma parameters in which the very intense ion beams behave like weak beams in prescribed electromagnetic fields. As a result, concepts of beam transport, stacking and focusing can be borrowed from weak beam physics. Dynamic plasmas provide a new medium where beam particles can experience time varying forces. An exchange of energy can occur between the plasma and beam systems on a time scale of nanoseconds. The moving plasma can be slowed down, imparting its energy to the beam, or it can be accelerated, slowing down the beam. Similar effects happen to the beam brightness; it can be increased or decreased during propagation in the plasma. Finally, the requirements for self propagating ion beams are shown to be close to those for ICF.

NET CURRENT

The interaction of intense beams with plasmas was first studied for relativistic electron beams (REB) where it was shown[1] that the plasma

responds in such a way as to neutralize both the space charge and the current of the intruding beam. When ion beams are injected into an initially neutral gas, the ionization generates a plasma which responds in a similar fashion. The much slower ion beam, $\beta = v/c \ll 1$, allows for a longer interaction time between any beam ion and plasma electrons. Plasma heating is β^{-2} faster for these ions as compared to REB. In addition, inertia of plasma electrons at the head of the beam is not as important for an ion beam as for the REB since the slower ion beam allows ample time for the plasma electrons to respond. As a result of these effects, electron beams generate net currents which are a few tens of percent of the beam current while ion beams generate about one percent net current when injected into a neutral gas. As a result of the high net current for REB's, they have been shown to self propagate over long distances[2] (up to 7m) while no comparable experiments exist with ion beams. This does not imply that self propagation of ion beams cannot be obtained but rather that special beam parameters discussed later are needed.

The low net current induced by ion beams is further reduced if the plasma is preionized and heated to a few eV prior to beam injection. Additional beam heating of a deuterium plasma was shown[3] to be $\delta T_e \sim 3 \cdot 10^3 \, J_b t/E$ where J_b is the beam current density (A/cm^2), t is the pulse time (sec) and E is the proton beam energy (MeV). This yields a temperature of 5 eV for 3 MeV protons at $10^5 A/cm^2$ during 5 ns. The magnetic field diffusion equations[3] when solved assuming no hydrodynamic effects give a diffusion time $\tau \sim \frac{4\pi\sigma a^2}{c^2}$ where σ is the conductivity and a(cm) is the shortest beam length scale (the radius, for a long beam). The ratio of the net current to the beam current $I_{net}/I_{beam} \sim t/\tau$ is about $10^{-3} \, a^{-2}$. For longer time scales the magnetic field is frozen in the plasma. For typical megampere beams with $a \sim 1$ cm net currents of $10^3 A$ are expected resulting in magnetic fields of ~200G. The magnitude of this time varying magnetic field, if made much smaller than the magnetic field in the plasma prior to beam injection, will thus have a negligible effect on the ion orbits.

PLASMA MOTION

The second effect to consider in addition to diffusion is the motion of the magnetic field with the plasma. Due to the high plasma conductivity any hydrodynamic motion will carry the magnetic flux with it. We now formalize the necessary conditions for small displacements of the plasma. Two major mechanisms accelerate the plasma, pressure gradient and magnetic forces:

$$\rho \frac{d\vec{V}_p}{dt} = -\vec{\nabla}P + \frac{\vec{J}_p \times \vec{B}}{c} \qquad (1)$$

where ρ is the plasma density, J_p the plasma current and V_p the plasma velocity. The thermal pressure results from beam heating and causes plasma expansion from regions of high current density. The J_pxB term is due to the plasma current. The total current density flowing includes also J_b and it is: $J_b + J_p = J_c$, where J_c is the current density in the plasma prior to beam injection. Consider first a weak ion beam $J_b \ll J_c$. The plasma will then continue to undergo pinching by its self-magnetic field with a small reduction in the pinching force since $J_p = J_c - J_b$. If the beam current is increased to $J_b = J_c$, then $J_p = 0$ and no magnetic forces act on the plasma but $B \neq 0$. The pinching force on the plasma is in that case negated by the beam pressure effect which comes about in the following way. The ion beam would have expanded in free flight were it not for the magnetic field bending ion orbits and generating beam pressure. If the magnetic field is focusing the beam, then the beam pushes the magnetic field outward and since the plasma has good conductivity, the plasma electrons are coupled to the magnetic field flux. As the plasma electrons move out, charge separation between them and the plasma ions generates a large radial electric field that holds back the electrons and pulls out the ions coupling the two fluids to move like one. Now consider very high current density beams $|J_b| \gg |J_c|$. In this case $|J_p| \simeq |J_b|$ and the beam will induce plasma expansion if the magnetic field is focusing or plasma compression if it is defocusing. The plasma velocity[3] is simply $V_p \sim J_b\, Bt/\rho c$ and the displacement divided by the plasma radius-a is:

$$\delta a/a \sim 0.03\, J_b\, J_c t^2/\rho \quad . \qquad (2)$$

The relative change induced in the magnetic field will be negligible if the plasma density is large enough to provide inertia against the beam pressure. For example, if one transports a 3 MA, 3 MeV beam in a large, 2 cm radius channel with $J_c \sim 4 \cdot 10^3 A/cm^2$ then for a 50 ns pulse, a density of $2 \cdot 10^{-6}$ g/cm^3 will result in less than 5% change in the magnetic field structure. Also, the energy loss due to the stopping power of 100 MeV/g/cm^2 in such a channel over a 10m distance is about 200 keV which is small compared to the 3-MeV proton energy.

The two conditions for static plasmas are thus high conductivity and inertia. When these two are satisfied the initial magnetic field is frozen

and beam ion orbits can be analyzed in great detail. One should notice, however, that an electric field exists in the plasma and it is important for long distance transport. The electric field is derived[3] from the generalized Ohm's law

$$J_p = \sigma(E + V_p \times B/c) \qquad (3)$$

and since $J_p \simeq - J_b$, $E \sim - J_b/\sigma - \langle V_p \times B/c \rangle$. The expanding plasma channel thus increases the electric field that slows down the ions. This is a coupling mechanism for energy transfer from the ion beam to plasma expansion. For the above plasma transport example $\langle V_p \rangle = 2.10^6$ cm/s and $\sigma \sim 3.10^{15}$ s^{-1} so that E = - 200 V/cm which results in energy loss of 200 keV over 10m in addition to the 200 keV collisional loss. These losses were computed after 50 ns of beam transit when the plasma temperature was 20 eV. At the head of the beam much smaller temperatures, ($\sim$ 5 eV) result in lower plasma conductivity by a factor of 8 so that the total energy loss will be 1100 keV. Even if all the ions started at the same diode voltage they will bunch from 50 ns to a pulse of about 10 ns because of the larger energy loss at the head of the beam than at the tail.

Having established the necessary conditions for treating intense beams much like very weak beams, we now review briefly two systems: straight z-discharges and magnetic lenses.

TRANSPORT IN Z-DISCHARGES

If the beam is not matched to the magnetic structure at injection, the beam distribution function will move in phase space and phase mix during the process, generating filaments that increase the effective phase space volume and decrease brightness. The other effects that will lead to a loss of beam brightness include injection off axis and the hose instability. The worst unmatched magnetic field structure is that of a pinched channel where the high magnetic fields near the transport axis increase sharply the spread in ion divergence angles accompanied with some increase in beam radius. Since the brightness scales as $(r\theta)^{-2}$, the resulting beam brightness is rather poor. Transport in a uniform-current z-discharge[3,4] with $B \sim kr$ results in a smaller loss in beam brightness. The channel current has to be optimized for minimal loss of brightness. If it is too large, ion angles are increased while too small a current allows excessive radial expansion. Using the phase-mixed volume in phase space, one can define the optimum current to minimize that volume. It turns out to be $I = 10^{-3} v_i \theta^2$

with a channel radius, r_c, larger than the beam radius at injection by $\sqrt{2}$.

A completely hollow magnetic field distribution is closer to the optimum for transport. The reason for that is that ion injection angles are conserved and the radius of the beam increases by a small quantity for a large current flowing in a sheath outside the injected beam radius. This type of structure can be obtained experimentally in long wall confined z-pinch channels. The plasma shape is stabilized by the conducting wall symmetry at radii close to the plasma radius. Up to 400 kA proton beams have been successfully transported[5] in such channels with current efficiencies close to 100%. The beam brightness issue was also addressed and more details can be found in these proceedings.

The beam may be injected either off axis or its current density vector can point off axis. In either case and independent of the magnetic field distribution, the beam will ripple and phase mix resulting in brightness loss. Again, however, the hollow channel distribution has minimum loss. Such off-axis injection is an initial large perturbation for a hose instability. The types of instabilities studied include MHD of the channel, self hose and resistive hose. The MHD of the channel is asymmetric and has a purely growing mode localized in space. Its spatial growth physics is similar to the channel expansion physics described earlier. The whole plasma channel takes the shape of an unstable hose. The radial shift scales like r^{-4} so large channels ($r \geq 1$cm) are barely susceptible to the hose when carrying a few megamperes. Smaller ($r \leq 0.5$ cm) channels can carry only currents of a few hundred kA for 50 ns. Besides the possibility of shifting the whole channel, the magnetic field distribution may also shift. Such an instability can be driven by either the self-hose or the resistive hose mechanisms. Mutual repulsion of beam-plasma currents is responsible for the former and resistive lag between the phases of the beam axis and magnetic axis cause the latter. Assuming real wavenumber, the number of e-foldings is $\omega_i \tau \simeq 3.10^{20} \tau\ I_b/(I_{ch}\ r_b^2 \sigma)$ which again favors larger channels.

MAGNETIC LENSES

The magnetic lens concept[6] is used as an element for trading radial distribution for velocity distribution in phase space. Thus, reduction in beam divergence can be achieved by radial beam expansion and increase in current density can be obtained at the expense of larger angular divergence. In order to avoid problems of matching the beam to the lens, only short

distance (typically one quarter of an orbit in phase space) lenses are allowed. The distribution function does not phase mix and no brightness loss occurs, hence $r\vartheta$=constant. The simplest lens to achieve beam cooling is a z-discharge where the current is distributed uniformly up to a desired radius r_c. The total current for a beam having maximum angle θ_1 at injection is: $I_c = 5\cdot10^{-4} v_i \theta_1^2$ Amperes. The ion beam will expand from its initial radius r_1 to the channel radius r_c forming a paraxial beam after one quarter betatron distance. The angular divergence there will be $\theta = \theta_1 \cdot r_1/r_c$. This technique is of importance for achieving cool beam conditions for propagating beams. The same concept works also for focusing. Starting with θ_1, the goal is now to increase ϑ with a reduction in r. The larger current needed $I_c \sim \vartheta^2 \sim r^{-2}$ is proportional to the current density enhancement. For example, a current of 200 kA will increase the current density of a 3 MeV proton beam with θ_1 = 0.1 radians, by an order of magnitude. The increased current in the plasma increases beam pressure significantly and using the logic of Eq. (2), we find that the plasma density should be increased like $J_b \cdot J_c$. A special foil is thus needed to separate focusing elements from the lower-density long transport systems. The use of a tapered focusing element results in another gain of a factor of 3 in current density using the same plasma current for the simple reason that the magnetic field increases along the ion orbits.

DYNAMIC PLASMAS

Fast moving plasmas constitute a special domain for beam handling. The electric field derived from the moving plasma[7] as shown by Eq. (3) can be substantial. Consider first the case of low plasma density. The beam pressure can now induce motion with $v_p \sim 10^3$cm/s and since magnetic fields of 10^6G are technically realizable the ions will be slowed down by $E \simeq 10^6$ V/cm in a low density plasma. This constitutes a special way of heating plasmas to very high temperatures. In the above example for $\rho_p = 10^{-6}$g/cm^3 $J_b = 10^7$A/cm^2 can heat the plasma to 10 keV temperatures. In general, the special effect of enhanced stopping presented here acts in a pronounced way in low density plasmas.

When the plasma has an initial inward velocity the electric field becomes positive and the beam may be accelerated. The plasma is slowed down by the beam pressure. A transfer of energy occurs from the slow-moving plasma into a fast moving beam. Also, this transfer is very efficient since slowing down the plasma by a factor of 2 already transfers 75% of the plasma

energy. A very simple way of understanding the complicated acceleration physics is to note that an imploding z-pinch behaves to first order like moving rigid walls against the confined beam. The beam particles are deflected back into the channel by these walls and thus gain energy. This energy would all be in the perpendicular direction save for the fact that the channel can be tapered. The plasma thus is a long sequence of z-pinches starting sequentially and imploding with a phase velocity equal to the ion axial velocity. The head of the beam is accelerated less than the tail. We solve for the ion orbits using the equation of motion of a single ion:

$$\ddot{r} = -\frac{ev_z \times B}{mc} \tag{4}$$

where the axial velocity $v_z = v_z^o + bt$ is in phase with the imploding plasma so that in the ion beam frame of reference the same magnetic field profile is observed. We further assume $B=B_o r/R_o$ and also neglect any relativistic effects. Multiple time scale analysis is now applied to Eq. (4) giving the amplitude and frequency of the accelerated ion: $A = A_o e^{-at/4v_z}$; $\omega=\omega_o(1 + \frac{1}{4}\frac{bt}{v_z^o})$. The radial velocity $v_r^{max} = \omega A \sim \omega_o A_o$ is nearly fixed while the axial velocity is increased by the acceleration and the angular divergence is: $\theta = \langle \frac{v_r}{v_z} \rangle \sim \frac{1}{1 + \frac{bt}{vz}} \theta_o$. The beam brightness scales as $(A\cdot\theta)^{-2}$ and is thus enhanced by a factor of $e^{bt/2v_z^o}\cdot\left(1 + \frac{bt}{v_z^o}\right)^2$. This is about 6 for $v_z^o = bt$. As for typical accelerations: $v_p \sim 10^7$cm/s $I_c \sim 10^5$A and $r \sim 0.5$ cm yield about 3 kV/cm and more than 10m is required for a 3 MeV addition to a 1 MeV beam. The total beam-power brightness is $J\cdot V/\theta^2$. The combination of (1) beam brightness enhancement by 6, (2) bunching by 5 and (3) increasing V by 4 results in two orders of magnitude increase over the ion power brightness from a diode. Presently ion diodes generate 5 TW/cm^2 at 1 MeV. Scaling up to 4 MeV and bunching the beam will result in 100 TW/cm^2. The use of imploding channels can further increase the power brightness to 500 TW/cm^2 which exceeds present requirements for ICF.

SELF PROPAGATION

The plasma generated at the head of the beam by beam ionization and avalanche is nearly fixed in temperature and only the fractional ionization increases with time. The conductivity increases to a point where the fractional ionization approaches about 10^{-2} at which point Spitzer conductivity

dominates and is independent of plasma density. This happens for ion beams on a few ns time scale for $J_b > 10^5$ A/cm^2. For air, for example, the ion beam spends about 33 eV/ion pair and about 7.5 eV are left for electron kinetic energy, hence $T_e \simeq 5$ eV. The magnetic diffusion during these early times generates $I_{net}/I_b \hookrightarrow 10^6 t/a^2$. The needed net current to confine the beam was shown[3] to be $I_c \hookrightarrow 5 \cdot 10^5 \theta^2 V^{\frac{1}{2}}$ where V is in megavolts. The necessary condition for self propagation, $I_{net} > I_c$, will be satisfied if $I_b t/a^2 > \theta^2 V^{\frac{1}{2}}/3$. This translates into a beam brightness requirement of

$$J_b/\theta^2 > (10t)^{-1} V^{\frac{1}{2}}. \qquad (5)$$

This is about $3 \cdot 10^7$A/cm^2 which coupled with the fact that 3-MeV protons are envisioned for pellet designs results in 10^{14}W/cm^2. It is mere coincidence that the same power brightness is needed for high gain pellets and for self propagating beams! Any reactor scenario that is based on 10^{14}W/cm^2 power brightness can presently use the notion that high gain pellets go hand in hand with self propagation. The physics of these two notions is presently theoretical, of course, since neither pellet ingition nor self-propagation has been demonstrated. When the high power brightness will be obtained in a few years both concepts should be checked and if the theory will be validated then typical reactor scenarios could include self beam propagation inside the explosion cavity.

REFERENCES

*JAYCOR, Alexandria, VA 22304.

1. D. A. Hammer and N. Rostoker, Phys. Fluids 13, 1831 (1970) and R. Lee and R. Sudan, Phys. Fluids 14, 1213 (1971).

2. R. J. Briggs, J. C. Clark, T. J. Fessenden, R. E. Hester and E. J. Lauer in Proceedings of 2d Int. Top. Conf. on High Power Electron and Ion Beam Res. and Tech., Cornell U., Oct. 1977, p. 319. For theory see E. P. Lee et al, ibid, p. 381. Recent experiments and theory by R. B. Fiorito, R. F. Fernsler, J. R. Greig, M. Herndon, I. M. Vitkovitsky, A. W. Ali and V. E. Scherrer, NRL Memo Report 4405, March 1981.

3. D. Colombant, S. Goldstein, D. Mosher, Phys. Rev. Lett 45, 1253 (1980).

4. P. F. Ottinger, D. Mosher, and Shyke A. Goldstein, Phys. Fluids 23, 909 (1980).

5. F. Sandel, F. C. Young, S. J. Stephanakis, W. F. Oliphant, G. Cooperstein, S. A. Goldstein and D. Mosher. Bull. Am. Phys. Soc. 25, 900 (1980), and F. Sandel, et al, these proceedings.

6. P. F. Ottinger, Shyke A. Goldstein and D. Mosher, 1980 IEEE Int. Conf. on Plasma Science May (1980), p. 95.

7. Shyke A. Goldstein and D. A. Tidman, ibid., p. 96.

SYSTEM REQUIREMENTS FOR LIGHT-ION ICF*

D. Mosher, D. G. Colombant, Shyke A. Goldstein** and P. F. Ottinger**

Naval Research Laboratory
Washington, DC 20375 USA

ABSTRACT

Analyses of the diode-focusing, channel-transport, beam-bunching and pellet-overlap constraints for a modular light-ion ICF system have been performed. Results for the overall system favor a few super-power modules utilizing z-discharge transport channels with diameters several-times that of the pellet. Each channel is terminated in a magnetic-focusing element which brings the beam to pellet dimensions. Configurations such as these relax limitations associated with diode focusability and channel MHD.

I. INTRODUCTION

A modular approach to light-ion ICF involves a number of high-power generators driving individual ion diodes [1, 2]. Each diode focuses the ion beam through a neutralizing-plasma background into a z-discharge channel which transports the beam a few meters to the vicinity of the pellet. The separation provided by transport protects the accelerator from the thermonuclear blast and allows time-of-flight bunching of the beam from the ≈ 40 ns pulsed-power times to ≈ 10 ns pellet-driver times. Basic phenomena associated with beam-focusing, transport, pellet-overlap and beam-plasma interactions have been characterized and used to determine system-module parameters which best satisfy constraints.

One class of systems utilizes transport channels which are comparable in diameter to the pellet (≈ 1 cm). The MHD response of this channel plasma to beam passage limits unbunched beam power to a few TW/module and sets a diode-brightness requirement which has not been achieved in experiments [3]. A second class of systems utilizes larger-diameter channels terminated in magnetic-focusing elements which bring each beam to convergence on the pellet (Fig. 1). The larger-diameter channels can transport ≥ 10 TW beams which are focused by diodes with beam-divergence requirements a factor-of-three less severe than for pellet-diameter channels. This paper describes the phenomena which enter the analysis and determines acceptable parameter sets for both types of systems.

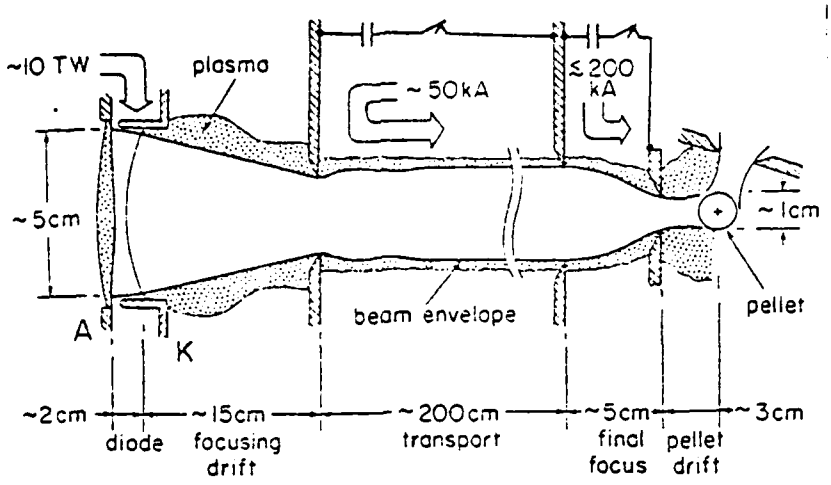

Figure 1

II. DIODE FOCUSING

In a Pinch-Reflex diode, ions extracted from an anode-foil plasma are accelerated axially across the diode vacuum gap by the applied electric field while being accelerated radially inward by the azimuthal self-magnetic field. Once they pass through the cathode-transmission foil into a field-free neutralizing plasma, ions execute straight-line orbits to a focus at the entrance of the transport section. The electrode-foil structures must be shaped so that the sum of the anode-emission and magnetic-bending angles results in ions which exit the diode pointing toward the focus. At high power densities, the emission angle will change with both radius and time as the anode-plasma expands due to non-uniform heating. The magnetic-bending experienced in the vacuum gap also changes with time due to electrode-plasma motion. Additional time-dependence is introduced by applying an accelerating-voltage pulse which is ramped for beam bunching. Diodes can be designed which minimize the time-variation in diode exit angle associated with these effects. This minimum variation [1] is given in radians by

$$\delta\theta_M \approx \frac{.1 Z_D I}{\sqrt{AE}} \frac{v_{cl}\tau}{R} \qquad (1)$$

where Z_D is the beam-ionization level in the diode, I(MA) is the ion current, A is the atomic weight, E(MeV) is the ion energy at the end of a pulse of duration τ(ns), v_{cl}(cm/ns) is the relative closure velocity between electrode plasmas and R(cm) is the diode radius. When E is scaled with species to provide the stopping-power of 2 MeV protons ($E=2\sqrt{A}\,Z$) and scattering in the cathode-plasma ($\delta\theta_S \approx .03\ A/E$) is added to Eq. (1), $\delta\theta_M + \delta\theta_S \lesssim .03$ rad for several-TW beams of deuterons or heavier ions.

If r_s is the focal-spot radius and F is the distance from diode to focus, then $\delta\theta$, the acceptable total beam-divergence at the diode exit must satisfy $2r_s > F\delta\theta$, or

$$\delta\theta < (2r_s/R)\ (R/F) \quad . \tag{2}$$

Centimeter-diameter channels require a spot radius r_s = .35 cm and, as shown below, cannot transport multi-TW beams with maximum injection angles into the channel exceeding R/F = .1 . For R = 2.5 cm, Eq. (2) requires $\delta\theta \lesssim .03$, compatible with $\delta\theta_M + \delta\theta_s$ values.

Recent TW-level experiments on the NRL Gamble II device [3] have measured divergence angles about 3-times higher than calculated above. Electrode damage, anode bremsstrahlung and electromagnetic-code simulation [4] point to the existance of electron-filamentation instabilities as the source of small-scale electric- and magnetic-field structures responsible for enhanced divergence. No power scaling for this process yet exists although it is known to be unimportant at the .1-TW level [5]. It is therefore useful to consider modular systems which are not so strongly constrained by focusability as those with small-diameter channels.

III. BEAM TRANSPORT AND CHANNEL RESPONSE

Once the beam enters the transport channel, the previously-established discharge B_θ field confines ions to betatron-like orbits. The channel current I_{ch}(MA) required to confine ions with maximum transverse energy within the discharge wall radius r_w depends on the radial distribution of I_{ch}. For a uniform current density filling the region $0 < r < r_w$ (a "full" channel) and $r_w = \sqrt{2}r_s$

$$I_{ch} \approx \frac{1.3}{Z_T}\sqrt{AE}\ (R/F)^2 \tag{3}$$

where Z_T is the beam charge state during transport. Gamble II experiments guided by Eq. (3) demonstrated transport [6] of up to 400 kA proton beams over distances up to 2.5 m.

For neutralized transport of multi-TW ion beams, the plasma-electron return current I_p satisfies $-I_p \approx I >> I_{ch} \approx 50$ kA. The $\underset{\sim}{j}_p \times \underset{\sim}{B}_\theta$ force accelerates the plasma radially outward. The $\underset{\sim}{V}_r \times \underset{\sim}{B}_\theta$ electric field induced by this motion decelerates the passing ion beam (the energy source for channel expansion). Since V_r scales inversely with the channel density while collisional losses are proportional to it, the minimum total energy-loss rate for the beam occurs when the field deceleration is equal to the

collisional stopping power [1]. The total beam energy loss during transport is this loss rate multiplied by ℓ(cm), the minimum distance required to bunch the beam from τ to the pellet-driver time t_p. For a beam energy which scales with species as in Sec. II

$$\ell \simeq 6\, Z^{1/4} (\tau - t_p) \quad . \tag{4}$$

This is about 200 cm for cases of interest. The unbunched beam power transportable with energy loss limited to E/4 is then

$$P(TW) = \frac{200 r_w^4}{\tau^3 (R/F)^4} \quad . \tag{5}$$

Since $P\tau$ remains constant as the beam bunches, the MHD constraint becomes easier to satisfy. Eq. (5) indicates that only a few TW of unbunched power can be transported in .5 cm-radius channels when R/F = .1. Large channels can be used to transport much-higher power and somewhat hotter (larger R/F) beams provided final focusing to pellet dimensions can be achieved.

Hotter beams are desirable for suppression of beam-plasma micro-instabilities [7]. The most dangerous electrostatic mode is the beam-plasma 2-stream. It can be stabilized by dispersion in beam-ion axial velocity

$$\left(\frac{\Delta v_{\parallel}}{v_o}\right)^2 \gtrsim \frac{\omega_{pb}^2}{\nu_{ei}\, \omega_{pe}} \quad . \tag{6}$$

The Whister and Weibel instabilities are the fastest-growing electromagnetic modes. Growth can be reduced to a tolarable number of e-folds when

$$\left(\frac{\Delta v_{\perp}}{v_o}\right)^2 \gtrsim \frac{2\, \nu_{ei} \tau\, \omega_{pb}^2}{\omega_{pe}^2} \quad . \tag{7}$$

In these equations, ω_{pb} and ω_{pe} are the beam- and electron-plasma frequencies and ν_{ei} is the electron-plasma collision frequency. Since $v_{\parallel}^2 + v_{\perp}^2 = v_o^2$ is a constant of the beam motion, the left-hand-sides of both equations are about equal to $(R/F)^2$. In general, stability of transporting beams competes with focusability in limiting R/F to about .1 or above.

IV. PELLET OVERLAP

Once the beam exits a pellet-diameter transport section, ions move

ballistically in the plasma surrounding the pellet. Expansion of the beam envelope limits the channel exit-to-pellet separation d to a few centimeters. Countering this small-d advantage is a need for all N of the systems transport sections to fit within the available solid angle surrounding the pellet [8]. This requirement can be expressed

$$N \cdot \pi r_w^2 = f \cdot 4\pi d^2 \tag{8}$$

where f is some fraction determined by hardware-packing limitations.

The character of beam expansion depends on the phase-mixed distribution function for the transporting beam which, in turn, depends on the focusing geometry at injection and the $B_\theta(r)$ distribution within the channel. A 3-dimensional code has been developed which calculates orbits in a specified $B_\theta(r)$ for an ensemble of ions injected according to a specified focusing geometry. The phase-mixed distribution function of the beam is constructed numerically and used to determine radial profiles of ion density $n_i(r,z)$ for the expanding beam where z is the distance from the exit. For a pellet with the same radius as the channel, the fraction of the bunched-beam power incident on the pellet is $P(d)/P(0)$, where

$$P(z) \sim \int_0^{r_w} n_i(r,z) r dr \quad . \tag{9}$$

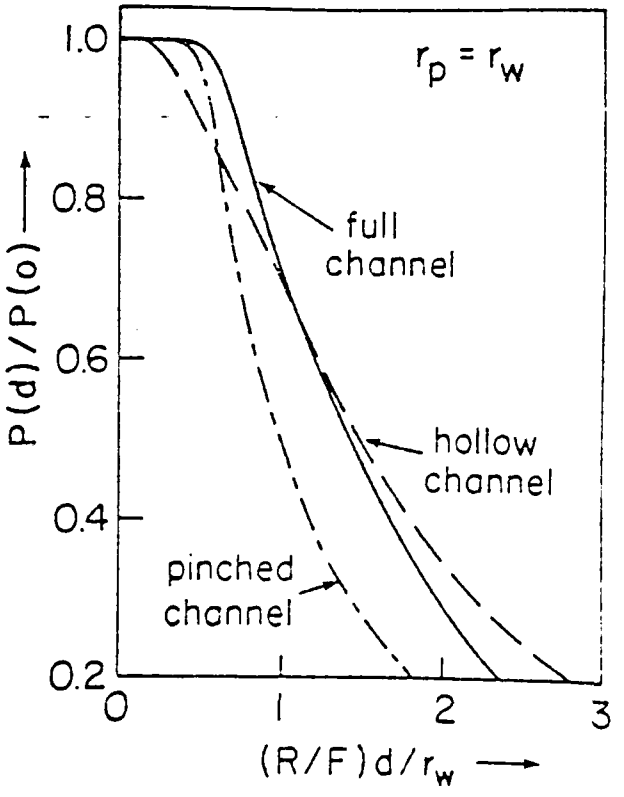

Figure 2

Results of this analysis are shown in Fig. 2 for three channel B-field configurations. The label "pinched" refers to a channel in which current is carried uniformly within $0 \leq r \leq .4\ r_w$ and "hollow" implies one with uniform current in $.6\ r_w \leq r \leq r_w$. In each case, I_{ch} is adjusted to confine all ions within r_w. Large B-fields at small radii in the pinched channel cause ions to cross the axis of symmetry at large angles, thereby producing rapid expansion. For the other two cases, $P(d)/P(0) > 2/3$ for

$$(R/F)d/r_w \leq 1 \quad . \qquad (10)$$

Combination of Eqs. (8) and (10) with f = 1/4 leads to the requirement $R/F \leq 1/\sqrt{N}$.

V. SMALL-DIAMETER-CHANNEL SYSTEMS

The limitations associated with the phenomena described above are satisfied by the shaded region of Fig. 3 for He ions, N = 36 and r_w = .5 cm = r_p (pellet radius) producing 38 TW/cm^2 irradiance on target with 10 ns beams bunched from 40 ns. Diagrams for other light ions are similar in character [1]. Since the focusing limit derives from $\delta\theta_M + \delta\theta_S$ only, present experiments would indicate a shift of the heavy-dashed line to higher R/F. Since multi-TW beams must have $R/F \lesssim .1$ to avoid excessive energy loss, system requirements cannot be satisfied without substantial improvements in *experimental focusability*.

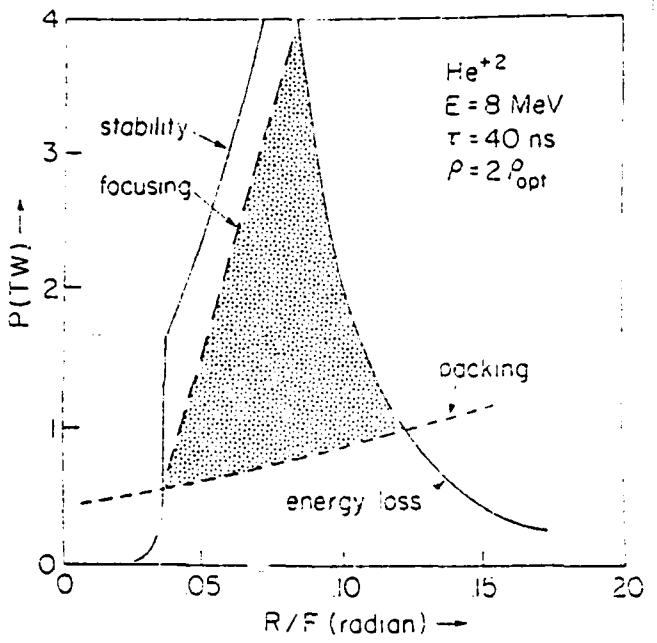

Figure 3

The focusability problem can be resolved with the larger values of r_s and R/F associated with larger-diameter channels terminated in a final-focusing element.

VI. SYSTEMS WITH FINAL-FOCUSING

As demonstrated in these proceedings [9], a transported beam can be manipulated in a short magnetic focusing cell without additional loss of brightness. An increased $B_\theta(r)$ operating over a fraction of an ion betatron wavelength (λ_β) can focus the phase-mixed beam to smaller radius at the expense of increased beam divergence. The channel radius can therefore be increased to a few-times the pellet radius provided a smaller d does not disrupt the pellet. High-density plasma in the cell (> 20 Torr) is required to minimize its MHD response to the strong focusing B_θ field and high-current-density beam. This plasma should remain sufficiently cool to eliminate pellet preheat by plasma expansion from the cell even for d ~ 1 cm.

The simplest final-focusing geometry is a cylindrical region of radius r_w and $\lambda_\beta/4$ long carrying a uniformly-distributed current $I_f(MA) > I_{ch}$. Analytic calculation of ion orbits in the cell demonstrate that all ions leave the cell within radius $r_f = v_o\theta_o/\omega_\beta$ where θ_o is the maximum angle at which ions enter the cell at all radii and ω_β is the betatron frequency. This relation can be written

$$\left(\frac{r_f}{r_w}\right)^2 = \frac{Y}{1-Y} \quad ; \quad Y = \frac{.7\theta_o^2\sqrt{AE}}{I_f Z_T} \quad . \tag{11}$$

For 2 MeV protons, $\theta_o = .15$ and $I_f = .2$ MA, $r_f/r_w \approx 3$ (a factor of 9 compression in beam-current density) is predicted. This might be achieved with a hollow channel for which $\theta_o \approx R/F = .15$. Full channels are characterized by $\theta_o \approx \sqrt{2}\,(R/F)$ on axis so that $r_f/r_w \approx 2$ might be expected.

More precise calculations have been carried out to determine the performance of focusing cells using realistic beam distribution functions and more-complicated field geometries. Of particular interest are full and hollow channels terminated in focusing cells which are tapered towards the pellet to increase the focusing-field strength. These cells are $\lambda_\beta/8$ long so that the best focus is achieved on target beyond the cell. An extension of the code described in Sec. IV was used to determine $n_i(r,z)$ profiles within the cell and in the field-free plasma beyond. In general, variations of θ_o with r result in compression ratios which are smaller than predicted by Eq. (11). For the parameters of the previous paragraph and a full channel of radius $r_w = 1.4$ cm, profiles were calculated for a cell 2.5 cm long which tapered in the second-half of its length to a radius of .7 cm. These are shown in Fig. 4. Current-density compression of 3 was achieved 1 cm beyond the exit of the focusing cell. Hollow channels, because of the associated constancy

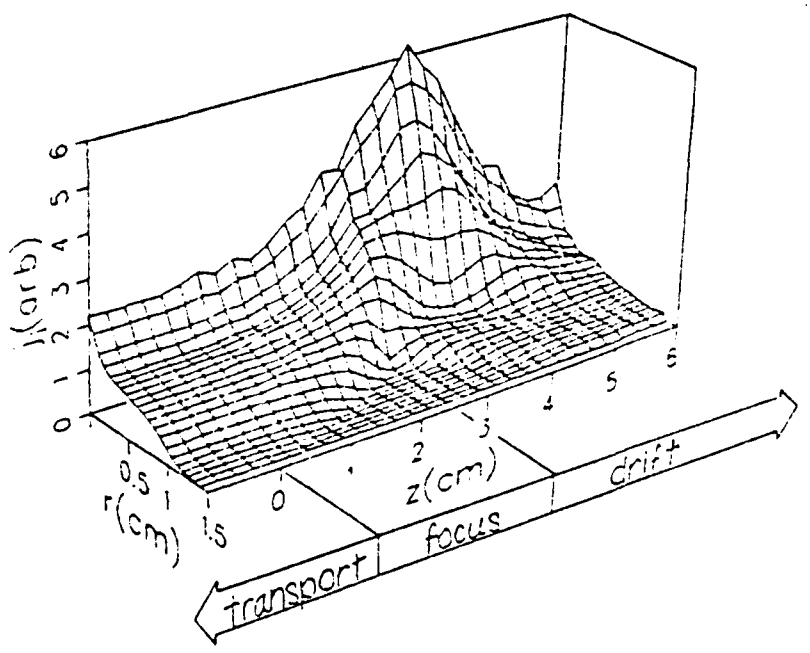

Figure 4

of θ_o in r and minimum loss of beam-brightness during transport [9] achieve larger compression factors and longer stand-off distances to final focus. Factor-of-10 compression 1.5 cm beyond the cell has been calculated with hollow-channel transport.

Consider a beam which can be compressed a factor-of-6 in current density ($r_w/r_f \approx 2.5$) and delivered to a 1-cm-diameter pellet. Transport can then take place in channels with $r_w \approx 1.2$ cm. For R/F = .15, Eq. (5) predicts that unbunched 12.5 TW, 40 ns beams can be transported. After 2 m transport, a bunched 50 TW, 10ns beam enters the final-focusing cell. If most of each compressed beam impacts the pellet, N=4 modules will suffice for ignition. With R = 2.5 cm, Eq. (2) requires $\delta\theta \approx .1$ rad. Provided that the disruptive effects of diode instabilities at the 10 TW-level are comparable to present few-TW experiments, this focusability is achievable.

It is therefore believed that the use of a small number of super-power modules employing large-diameter transport channels terminated in final-focusing elements provides the most practical approach to modular light-ion inertial confinement fusion.

REFERENCES

*Work supported by the Defense Nuclear Agency and the Department of Energy
**Present address: JAYCOR, Inc., Alexandria, VA 22304

[1] D. Mosher, D. G. Colombant and S. A. Goldstein, Comments on Plasma Physics and Controlled Fusion 6, 101 (1981).
[2] J. R. Freeman, L. Baker and D. L. Cook, to be published in Nucl. Fusion.
[3] G. Cooperstein, et.al., these Proceedings.
[4] A. T. Drobot, et.al., these Proceedings.
[5] K. W. Zieher, informal communication.
[6] F. L. Sandel, et.al, these Proceedings.
[7] P. F. Ottinger, D. Mosher and S. A. Goldstein, Phys. Fl. 22, 332 (1979) and 24, 164 (1981).
[8] T. P. Wright and J. A. Halbleib, Phys. Fl. 23, 1603 (1980).
[9] Shyke A. Goldstein, et.al., these Proceedings.

A TIME RESOLVED BEAM PROFILE MONITOR FOR INTENSE ION BEAMS

A.E. Blaugrund[+], S.J. Stephanakis and Shyke A. Goldstein[++]
Naval Research Laboratory, Washington, D.C. 20375

ABSTRACT

An intense ion beam profile monitor employing scintillators and fast photography has been developed. The ion flux reaching the scintillator is reduced by means of Rutherford scattering. Time resolved measurements of the distribution and direction of motion of ion beams as intense as $1 MA/cm^2$ can be made with this diagnostic method. Examples of measurements are presented.

INTRODUCTION

The use of light ion beams for inertial confinement fusion requires extremely powerful beams of particles converging on a small pellet. Present estimates[(1)] indicate that 10-100 TW beams have to be focused onto a pellet a few millimeters in diameter. The first intense ion beams were produced several years ago on the NRL Gamble II accelerator[(2)]. Since then steady progress has been made both in this laboratory[(3)] and elsewhere[(4)]. The most intense beams reported so far have a power of 2 to 3 TW and power densities of $0.3 TW/cm^2$ [(5,6)]. Efforts to improve the performance of light ion generators require diagnostic techniques capable of measuring the ion composition of the beam, the particle energies, the current density and its distribution in space, as well as the directions of motion of the ions. Since the temporal behaviour of these quantities has to be known, the data have to be measured and recorded in a time-resolved way. The large number of parameters necessitates the use of a method in which a large number of data points can be recorded simultaneously. Until now time and space resolved monitoring of intense ($> 1 kA/cm^2$) ion beams presented a problem. Attempts to monitor such beams by observing the light emitted by a scintillator placed in their path failed because the scintillators ceased to function at ion current densitites exceeding a few tens of $amperes/cm^2$. Attempts to attenuate the beam before it reached the scintillator by means of screens or aperture arrays were also unsuccessful.

In this work we present a time resolved ion beam diagnostic method using fast photography and scintillators. The desired reduction in the ion flux incident on the scintillator is achieved by Rutherford scattering: the direct beam hits a scatterer and only deflected ions are allowed

---

[+] Jaycor, Inc., Alexandria, Virginia 22304, Permanent address: The Weizmann Institute of Science, Rehovot, Israel
[++] Jaycor, Inc. Alexandria, Virginia 22304.

to reach the scintillator. The differential scattering cross section for ions scattered through an angle θ is given by $\sigma_R = \sigma_o \sin^{-4}\frac{1}{2}\theta$. σ_o is proportional to $(Z/E)^2$ where Z is the atomic number of the scattering atoms and E the kinetic energy of the ions. The specific functional dependence of σ_R on Z, E and θ can be exploited to obtain desired properties for the diagnostic method. So, for example, an appropriate choice of the scattering angle and of the atomic number of the scatterer will produce the desired flux of ions incident on the scintillator.

Using a simple electronic streaking camera distributions of ions along a beam diameter were measured with a time resolution of about 2 ns and a spatial resolution of 3 to 4 mm. In other experiments the direction of motion of the ions at a few selected radii within the beam was recorded as a function of time.

THE METHOD

The desired reduction in ion flux and the required spatial and temporal resolution can be achieved in a variety of geometrical arrangements. Figure 1 schematically shows three possible geometries. In each case the ion beam passes through a long and narrow slit before impinging on a scatterer. The width d of the slit is chosen as small as possible. However, it should be large enough so that hydrodynamic motion of the slit jaws under beam bombardment does not significantly interfere with the passage of the beam pulse. The length of the slit in the x direction (see fig. 1) should be large enough to let an entire beam diameter reach the scatterer which has the form of a long and narrow strip large enough to intercept the beam passing though the slit. The different geometries can be classified into four general categories: the scattered ions can be observed either in reflection or in transmission and spatial resolution can be achieved either by proximity focusing or by collimation (see fig. 1). Since in reflection the incident and the scattered particles are on the same side of the scatterer, both thin and thick scatterers can be used. In transmission only thin foil scatterers can be employed. In proximity focusing (scintillators I and II in fig. 1) the scintillator is placed as close as possible to the scatterer, while still remaining shielded from the direct beam. The spatial resolution is determined by and is of the order of the distance travelled by the ion from the scatterer to the scintillator. The finite dimension d of the beam puts a limit to the proximity and therefore limits the resolution. In the collimation method the scattered ions reach the scintillator through a row of collimator tubes. Here, the spatial resolution is determined by the size of the collimators in the x direction and by their

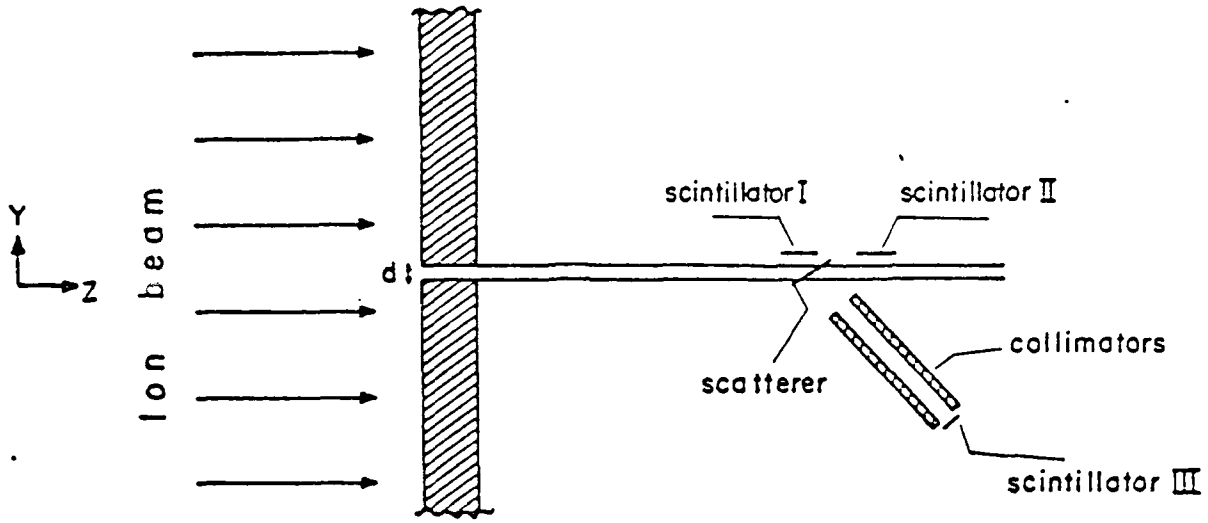

Fig. 1. Schematic diagram of the Rutherford scattering method showing three possible geometries: I - reflection geometry with proximity focusing: II - transmission geometry with proximity focusing; III - transmission geometry with collimation. The entrance slit, the scatterer and the scintillator extend along the x-direction over the entire beam diameter.

length and distance from the scatterer. In principle any desired resolution can be achieved, provided that the flux of ions reaching the scintillator is sufficient for detection.

In the work described here two geometries were tried successfully, viz., transmission scatterer with a collimator array and reflection scatterer with proximity focusing. The latter method offers many practical advantages: 1) One can use a thick scatterer, thus making its mounting and handling easier. 2) When proximity focusing is used there is no need for a rather delicate array of collimator tubes which is easily damaged by the debris produced by a high power ion beam. 3) For a thick reflection scatterer the light output of the scintillator depends only weakly on the ion energy (see below) and is therefore primarily a measure of the ion current density in the beam. This is an advantage when one wants to measure the beam profile as a function of time while the diode voltage is changing.

Since the achievable spatial resolution of a few millimeters was deemed sufficient for our purpose, practically all experiments were done using a thick reflection scatterer in conjunction with proximity focusing.

For low enough ion current densitities incident on the scintillator the light flux produced is approximately proportional to the power density of the ions reaching the scintillator. As the power density rises the scintillator response becomes non linear, reaching saturation and then even declining to zero[7]. The sensitivity of the light recording system should be such that an observable record is produced while the scintillator still functions in its linear range. For any given beam intensity the

desired ion flux on the scintillator can be achieved by choosing the scattering angle and the atomic number of the scattering material.

If one assumes that the light output of the scintillator is porportional to the incident ion power and that the ion range in the scatterer depends linearly on the ion energy E it can easily be shown that, for a thick scatterer operating in reflection, the light output of the scintillator is independent of E. This is so because the change in light output due to the change in ion power ($\sim$E) and due to the change in the number of scattering nuclei ($\sim$E) is compensated by the change in the scattering cross section ($\sim 1/E^2$). Thus, under the above assumptions, the light output of the scintillator is independent of the kinetic energy of the ions and depends linearly on their current.

THE EXPERIMENTAL ARRANGEMENT

Proton beams of several hundreds of kiloamperes at 1 to 1.5 MV were produced in a pinch relex diode[3] on the upgraded Gamble II generator[8] operating in positive polarity. Both planar and curved (focusing) anode foils approximately 10 cm in diameter were used. Figure 2 schematically

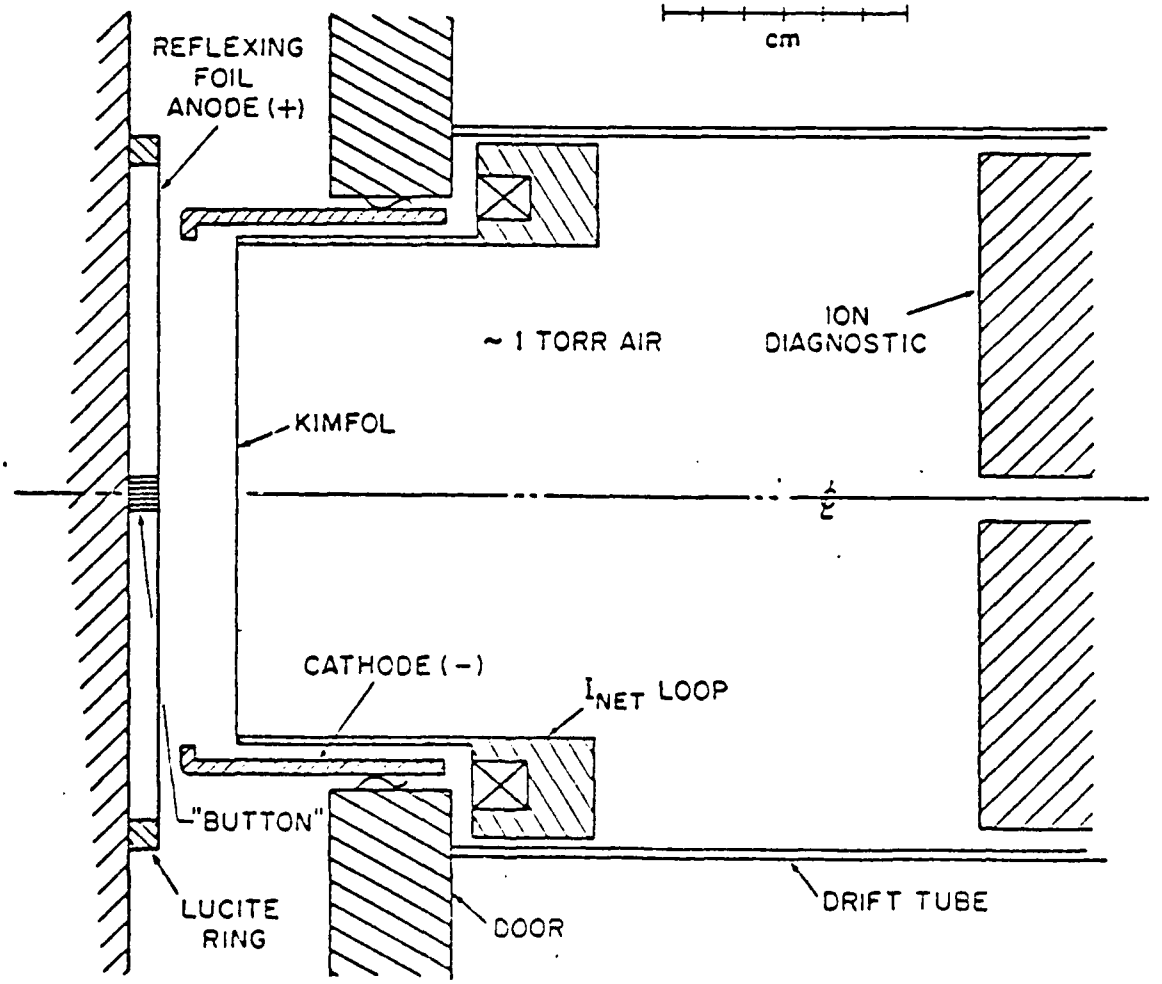

Fig. 2. Schematic diagram of a planar pinch reflex diode.

shows the geometry of a planar diode. The current densities encountered in these experiments ranged from a few kiloamperes per square centimetre to more than 100 kA/cm^2, depending on the diode geometry and on the distance from the diode. The experimental arrangement for detecting the ions by the Rutherford scattering method is shown in fig. 3. The beam aperture, the support for the scatterer, the support for the scintillator and for the optical mirror were machined from two solid blocks of aluminium which together formed the structure shown in fig. 3. This structure could be taken apart for installing the scatterer and the scintillator. The beam aperture had the form of a narrow slit, 1 mm wide and 10 cm long. This aperture extended along a diameter of the circularly symmetric ion beam. The scatterer was an approximately 8 mm wide and 10 cm long strip of metal (usually thicker-than-range copper tape) which intercepted the entire beam passing through the aperture. Its surface made a 30° angle with the beam direction. The NE 102 scintillator was 4.5 mm wide, 10 cm long and 40 μm thick. It was positioned above the scatterer, with its surface parallel to the plane of the incident beam and at a distance of 3.5 mm from it. The

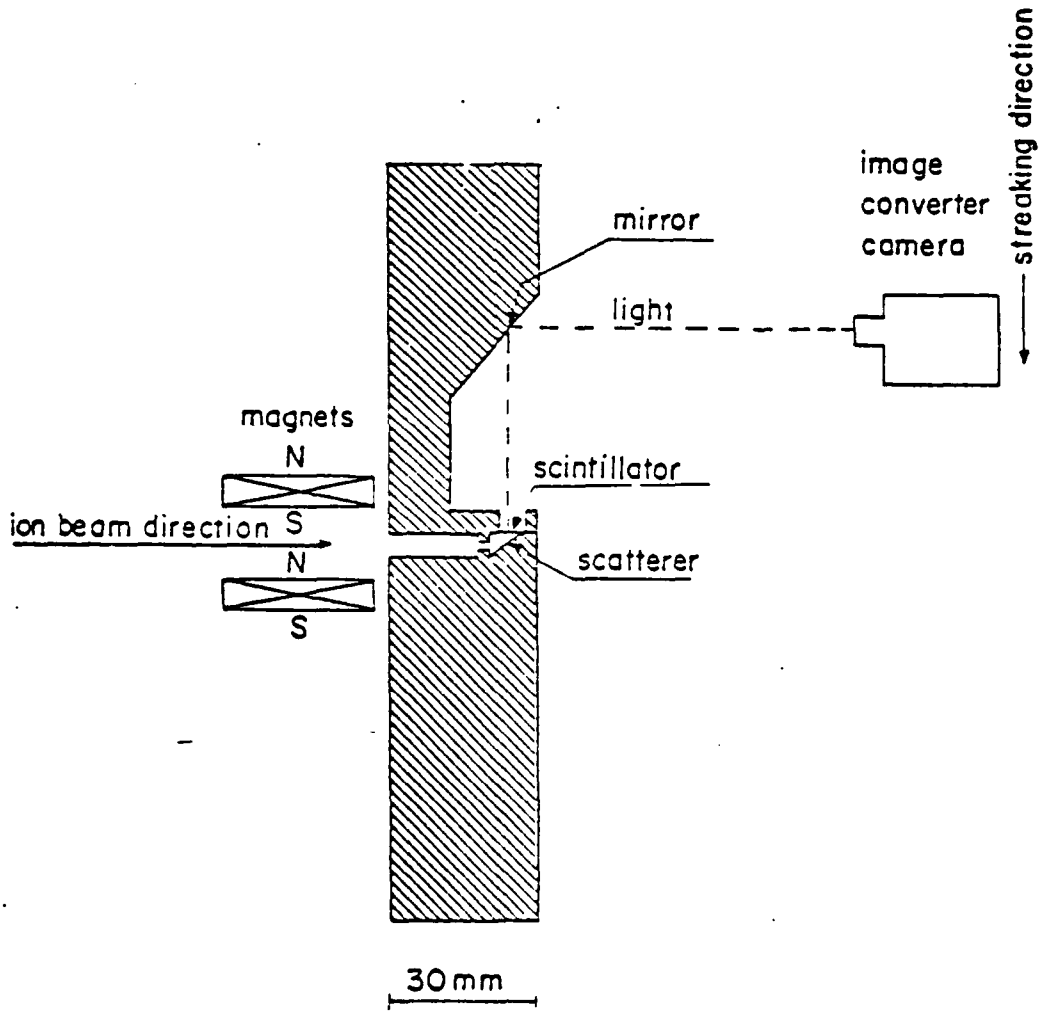

Fig. 3. Cross section through the entrance aperture, the scatterer, and the scintillator support. Note the magnets in front of the entrance aperture.

scattering angles ranged from 30° to 70°. In order to minimize the background due to x-rays and fast electrons the thickness of the scintillator was chosen approximately equal to the range of the protons. On the surface facing the scatterer the scintillator was coated with approximately 1000 Å of aluminium in order to prevent light produced by the ion beam striking the scatterer from reaching the camera. The light of the scintillator was recorded by a TRW model 1D image converter camera with a model 12b streak plug-in unit. The objective lens had an f-number of 2 and the fluorescent screen of the camera was photographed through an f1.4 lens on 3000 ASA Polaroid film. The scintillator-to-film demagnification was approximately 1/4 and the streaking speed was 0.5 mm/ns. The scattering reduced the ion flux incident on the scintillator by a factor of 7×10^{-4} with respect to the flux in the beam.

The diagnostic equipment shown in fig. 3 fitted into a 15 cm diameter drift tube filled with approximately 1 Torr of air (see fig. 2). The air was required to space charge and current neutralize the ion beam and thus facilitate its nearly ballistic propagation down the drift tube.

In most of the experiments a set of permanent magnets were placed before the entrance aperture of the Rutherford diagnostic equipment. These magnets produced a transverse magnetic field of about 1.5 kG over 2 cm which prevented electrons preceding or accompanying the ion beam from reaching the scatterer.

MEASUREMENTS

In the first experiments using the Rutherford diagnostic method it was discovered that the ion beam is preceded by a hollow electron beam. Fig. 4 shows two streak photographs taken at a distance of 20 cm from the anode of a spherical diode under similar experimental conditions except that the

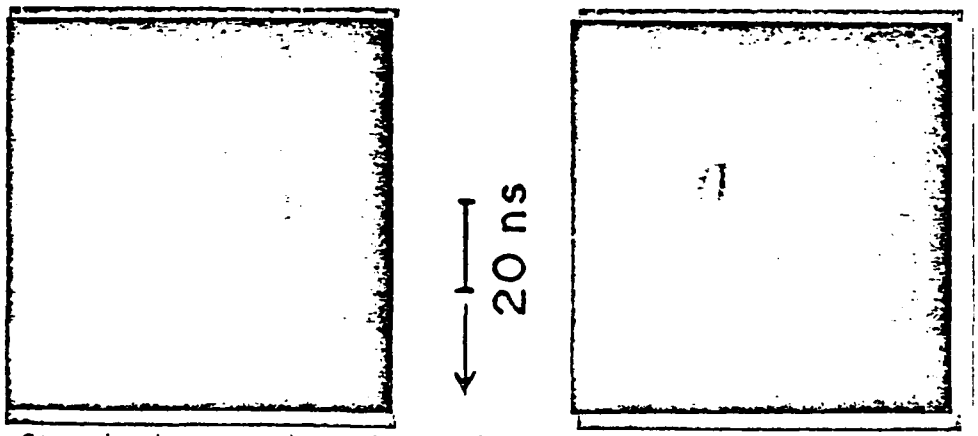

Fig. 4. Streak photographs taken using the Rutherford scattering method: a) without magnetic field; b) with transverse magnetic field. The sharp black lines are fiducial markers. The more diffuse dark bands in b are due to beam stops placed at the entrance aperture.

photograph in fig. 4b was taken with a 1.5 kG transverse magnetic field preceding the entrance aperture of the diagnostic equipment. Figure 4a shows two distinct parts in the signal. In fig. 4b it can clearly be seen that the magnetic field totally removes the early part of the signal without affecting it at later times. This indicates that the first part of the signal in fig. 4a is due to electrons, as opposed to the second part which is due to ions. By covering the scintillator with absorbers of various thicknesses it was determined that these electrons have an energy of 40 to 80 keV.

Placing a narrow beam stop some way upstream (e.g., at the entrance aperture of the equipment) will again produce a distinct shadow on the scintillator, provided the beam particles move along straight lines and the beam is not excessively convergent or divergent at the point of observation. In fig. 4b two such shadows were produced by two 5 mm wide beam stops placed at the entrace aperture of the diagnostic equipment. From the radial position of these shadows, as measured on the scintillator, and from the known radial positions of the beam stops and their distance from the scintillator the direction of motion of the ions at these radii in the beam can be determined. At the same time variations of beam intensity as a function of radius and time can be deduced from the light intensity of the scintillator in the intervals between the shadows of beam stops. This technique very much enhances the power of this diagnostic method.

Figure 5 shows the reconstruction of ion trajectories emerging from a

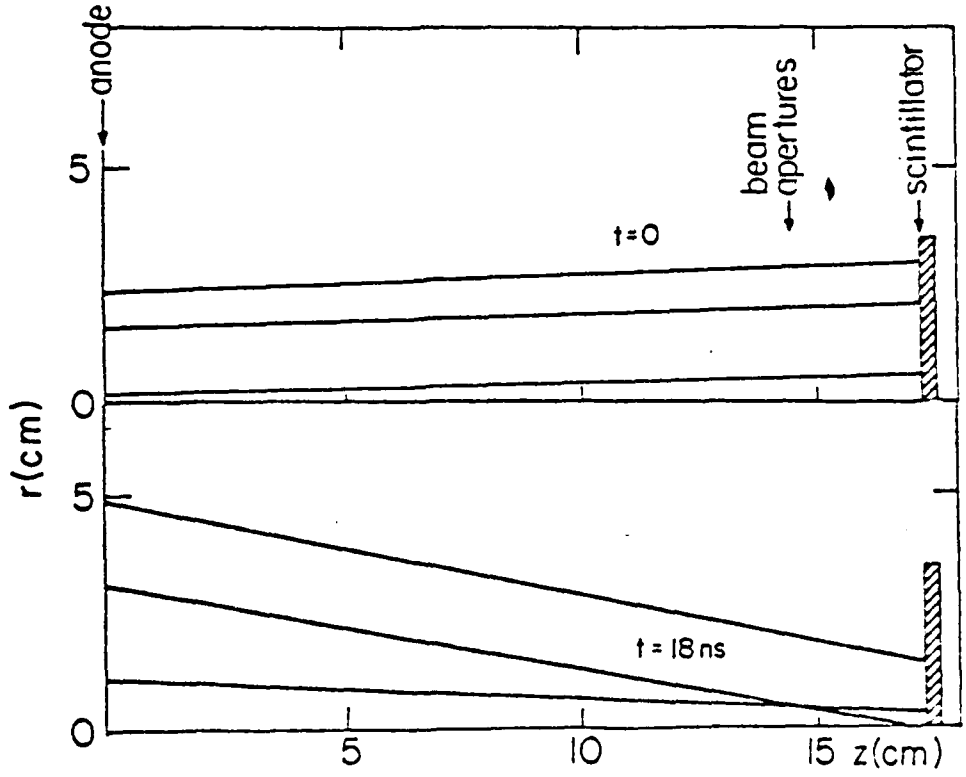

Fig. 5. Ion trajectories from a planar pinch reflex diode

planar pinch reflex diode at the beginning of the ion pulse and 18 ns later. These trajectories were deduced from a streak photograph taken with various beam stops placed at the entrance aperture. The bending and focusing of the ions by the self-magnetic field in the diode at t=18 ns is apparent.

CONCLUSIONS

The Rutherford scattering method presented here is a powerful diagnostic tool which has enabled us to measure current distributions and angular distributions of intense ion beams in a time resolved manner. The method is versatile and can easily be used for current densities of 1 to 1000 kA/cm^2. Nanosecond time resolution and millimeter spatial resolution are readily achievable. Different variants of the method stressing different properties of the ion beams can be used. E.g., focusing by two-dimensional collimator arrays in conjunction with a high speed framing camera can yield time resolved two-dimensional beam profiles. This mode of operation offers very good spatial resolution and may be particularly suitable for investigating focal regions of intense ion beams.

We have used the Rutherford diagnostic methods for investigating ion trajectories and focusing properties of beams emitted by planar and spherical pinch reflex diodes. The results of these measurements as well a more detailed analysis of the diagnostic method will be published elsewhere.

REFERENCES

1. G. Yonas, Proc. 3rd Int. Topical Conf. on High Power Electron and Ion Beams, p. 390, Novosibirsk, July 1979; see also references therein.
2. A.E. Blaugrund, G. Cooperstein, J.R. Boller and S.A. Goldstein, Bull. Am. Phys. Soc. 20 1252 (1975).
3. G. Cooperstein, S.A. Goldstein, D. Mosher, F.W. Oliphant, F.L. Sandel, S.J. Stephanakis, and F.C. Young, Proc. 3rd Int. Topical Conf. on High Power Electron and Ion Beams, p. 567, Novosibirsk, July 1979.
4. D.J. Johnson, Bull. Am. Phys. Soc. 24, 925 (1979).
5. D.G. Colombant, G. Cooperstein, A. Drobot, S.A. Goldstein, R. Meger, D. Mosher, P. Ottinger, F.L. Sandel, S.J. Stephanakis, F.C. Young, J. Maenchen and R. Genuario, Topical Meeting on Inertial Confinement Fusion (Feb. 1980), p. 100, IEEE Catalog Nr. 80 CH1536-2 QEA.
6. D.J. Johnson, R.J. Leeper, and J.P. Quintenz, Bull. Am. Phys. Soc. 25, 899 (1980).
7. J.G. Pronko, D. Kohler, and L.F. Chase, Nucl. Instr. and Meth. 164, 491 (1979).
8. J.R. Boller, J.K. Burton, and J.D. Shipman, Jr., Proc. IEEE Int. Pulsed Power Conf., Lubbock, Texas (1979).

EXPERIMENTAL STUDIES OF INTENSE LIGHT-ION BEAM TRANSPORT†

F. L. Sandel
JAYCOR, Inc.
Alexandria, VA 22304 USA

S. J. Stephanakis, F. C. Young, and W. F. Oliphant
Naval Research Laboratory
Washington, DC 20375 USA

ABSTRACT

Experiments have been performed at the Naval Research Laboratory which have demonstrated the efficient confinement and transport of intense (1 Mev, 30-50 kA/cm^2, 50 ns) light-ion beams in wall-stabilized z-discharge plasma channels up to 5 m long. Measurements of transport efficiency and particle energy loss in the channels have been made and the plasma physics of the channel formation investigated. Recently the field-free propagation and expansion of the transported beams along with the effect of channel transport on beam quality have been studied. These experiments have led to an efficient, modularized, rep-ratable beam transport system design.

Introduction. Large pulse-power generators, such as Gamble II at the Naval Research Laboratory, can be used as sources of intense light-ion beams (1 MeV, 500 kA, 50 ns) [1]. For many applications it is desirable to have a method of transporting these beams at least several meters. In this way beams from several large generators can be combined at a common target, while the generators, due to the large standoff distance, are protected from the target explosion and debris. Also, proper shaping of the ion voltage pulse can lead to time-of-flight bunching in the channel and power multiplication at the target [2].

Concept. All the ion beam transport experiments performed at the Naval Research Laboratory have used the same concept, shown in Figure 1. The intense ion beam is produced in a pinch-reflex diode and is extracted through a hollow cylindrical cathode. A focus is obtained close to the diode by utilizing the self-magnetic field of the beam over a controlled distance or a curved anode or combinations of both. At the focus the beam is injected into a preformed plasma channel which carries an externally supplied axial current. For sufficient channel currents with proper radial current distributions the ions are confined by the azimuthal magnetic field of the channel current and propagate to the target.

Various experiments have used this concept with differing hardware but with several common requirements; sufficient background pressure to provide charge and current neutralization of the beam without excessive ion energy losses between the diode and target and sufficient channel current to confine the beam within a desired diameter channel.

Wall-Stabilized Plasma Channels. A summary of past transport experiments is shown in Figure 2. Early experiments with exploding wire channels and unstabilized low-pressure z-discharges gave poor results and were technically cumbersome. This led to the conception and design of the wall-stabilized channel system, which is an energy efficient, rep-ratable method of producing relatively stable, axially uniform axisymmetric z-discharges without sophisticated biasing or preionization. This technique was refined in further experiments to the optimized modular system now in use. A single module of this system is shown schematically in Figure 3. The coaxial geometry provides low inductance and some stabilization of MHD modes. In typical operation 1-2 kJ/m of energy is invested in the channel with up to 50 kA supplied by the capacitor bank. The channel current rises to peak in 1.5 μs or less and is nearly critically damped. Impurity loading from the walls keeps the plasma temperature low and the channel resistance is typically 0.5 Ω/m for 1 Torr fill pressure. The channel formation is synchronized with the erection of the marx generator with adjustable delay so that the ion beam can be injected at any desired time in the evolution of the channel.

A channel module is mated to the diode and focusing region as shown in the scale drawing of Figure 4. This is the most recently used diode configuration and produces 300 kA of 1 MeV protons [3]. The focused current density at the channel entrance is 30-50 kA/cm^2 with a maximum effective ion entrance angle of 15 degrees.

Beam Transport Diagnosis. The problem of diagnosis is complicated by the necessity of forming the plasma channel in advance of ion beam injection. A primary diagnostic in these experiments has been detection of prompt-γ radiation from teflon targets using the $^{19}F(p,\alpha\gamma)^{16}O$ reaction [4]. Teflon screen targets are placed in the channel as shown in Figure 5. These targets do not interfere with the channel formation and are not damaged by the channel plasma. Absolutely calibrated scintillator-photomultiplier detectors [5] view various targets. A typical configuration is shown in Figure 6 where two channel modules are coupled coupled and driven from a single capacitor bank. Representative signals

from detector 1 are shown in Figure 7. The prompt-γ pulses are separated from the diode bremsstrahlung pulse due to the ion time-of-flight. The temporal separation of the prompt-γ pulses gives the average ion energy in the channel between targets 1 and 2. A simple computer model is used to predict the amplitude, shape and timing of these and subsequent prompt-γ signals from more distant targets based on diode and ion beam voltage and current characteristics, reaction cross sections, experimental geometry and expected ion energy losses. Experimental data is matched to the computer prediction to determine particle transport efficiency and ion energy loss as a function of transport distance. Particle transport efficiencies of up to 100 percent have been observed in these experiments with typical energy losses of order 100keV/m. Up to 400 kA of total ion current has been transported in the largest diameter (4.5 cm) channel. Studies of the modification of channel resistance and redistribution of channel magnetic field structure (using magnetic probes in the diagnostic access shown in Fig. 6) indicated that the ion beam-channel interaction is not strong with available ion beams.

Channel Evolution and Structure. Using the same diagnostic access and magnetic probes cited above, the spatial and temporal evolution of the channel magnetic field structure was investigated. The structure is strongly dependent on gas pressure and composition, capacitor bank parameters and channel geometry. Representative data for a 2.5 m channel at low applied voltage are shown in Figure 8. At a typical ion beam injection time of 1600 ns the magnetic axis has not yet shifted from the geometric axis even with the strong probe perturbation. The current is largely confined to the central two-thirds of the channel diameter where the ion beam would propagate. Because of the complex controlled nature of the channel breakdown and the resulting current flow, strong pinching on axis (detrimental to ion beam propagation) is prevented and a quasi-steady-state magnetic field distribution is obtained as shown.

Post-Transport Beam Quality. The high quality of the transported beam in 1.25m, 2.5m and 5m long channels has been verified using a variety of techniques. Figure 9 shows one simple method. The ion beam exiting the channel is allowed to impact a 0.75 mm thick aluminum plate which has a 2 mm central aperture. The rear surface spall on this plate is well centered, uniform and equal in diameter to the injected ion beam. A beamlet from the central aperture expands and produces uniform front surface damage on a second aluminum plate. The cone angle of the expansion from

the first plate is consistent with the range of injected ion angles and the channel current. Beamlets from the array of apertures on the second plate correctly image the first aperture on infrared sensitive film [6]. The film images confirm the uniformity in angular distribution of the exiting beam and the ballistic nature of its propagation. Similar experiments have been performed with off-axis apertures, multiple apertures and slits in various orientations.

Post-Transport Beam Propagation and Expansion. As the channel current is reduced, the maximum ion injection angle for ion confinement in the channel is expected to decrease. This was confirmed by measurements similar to those described above. Figure 10 shows the expected decrease in exit cone angle of the beam as the channel current is reduced. For further study of the field-free beam propagation the channel was reconfigured as shown in Figure 11. Current was supplied at the channel center, and the beam exited into a large field-free expansion chamber with optical access and target mountings. The channel and chamber were filled with argon to easily distinguish channel plasma from target-blowoff plasma. Open shutter photography (Figure 12) shows a weakly luminous target plasma (expansion velocity ~ 7 mm/μs, measured separately) and an intensely luminous channel plasma (expansion velocity ~ 10 mm/μs, measured separately). The less luminous cone in the argon plasma, denoting the expanded beam channel, is clearly visible, and intense recombination light is observed outside this cone at the walls. A stagnation front between the argon channel plasma and the target blowoff plasma is apparent at the position expected from the different plasma velocities. Target damage was consistent with these observations. Framing-camera photographs of the same events were also taken. Several of these are presented in Figure 13. Of particular interest is the rapid decay of visible emission from the beam channel and the expansion front which moves rapidly radially outward from the beam channel.

Conclusion. A technique for efficiently transporting intense focused ion beams up to 5 meters has been demonstrated. Sufficient knowledge of beam transport and channel formation physics has been obtained to define an optimized systems design of a technologically sound modularized transport system. Transporting beams in this manner has been shown to be non-detrimental to beam quality.

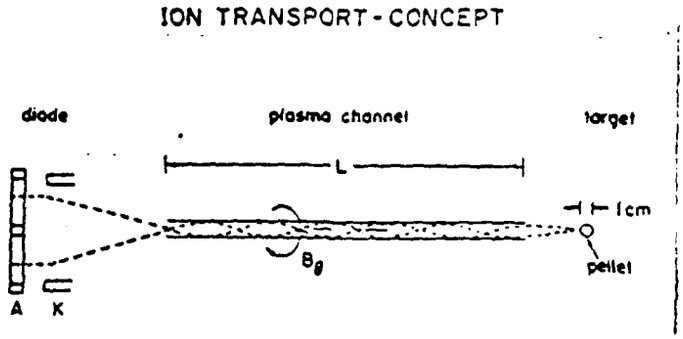

Figure 1

Figure 2

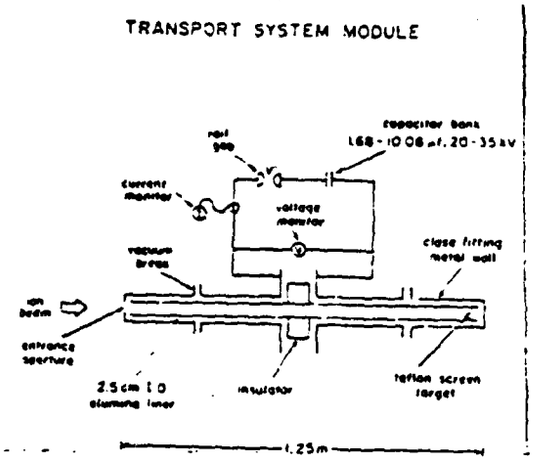

Figure 3

ION TRANSPORT EXPERIMENTS

	method	channel length × dia	efficiency	
1978	• exploding wires	50cm × 2cm	50%	slow capacitor bank $\tau_f \sim 12\,\mu$sec
	• current carrying rods	50cm × 1.6mm	40%	
	• unstabilized plasma channel	50cm × 3cm	10%	
	• stabilized plasma channel	95cm × 1.8cm	not measured	
1979	• stabilized plasma channel	150cm × 4.5cm 100cm × 1.6cm	up to 100% poor	
1980	• stabilized plasma channel	150cm × 4.5cm 100cm × 1.6cm 125cm × 2.5cm	up to 100%	fast capacitor bank $\tau_f \sim 1.2\,\mu$sec
	• tandem plasma channel	250cm × 2.5cm	up to 100%	
1981	• channel diagnostics	250cm × 2.5cm	—	
	• post-transport beam quality and target interaction	125cm × 2.5cm 250cm × 2.5cm	—	
	• tandem plasma channel	500cm × 2.5cm	not measured	

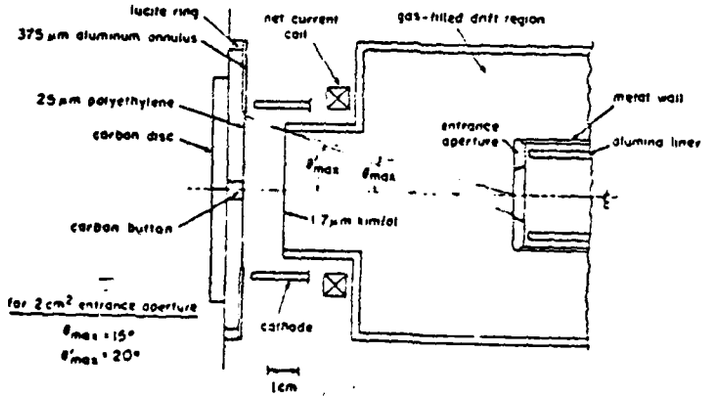

Figure 4

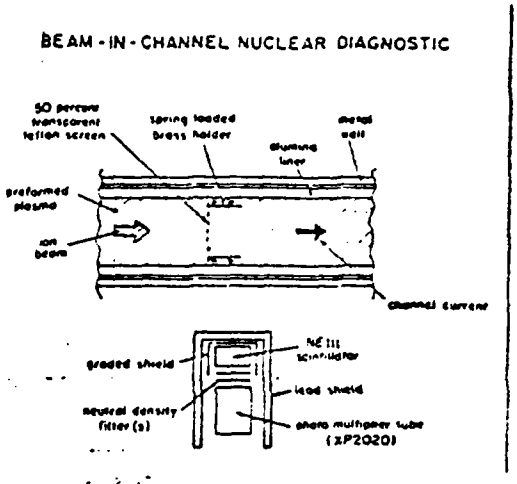

Figure 5

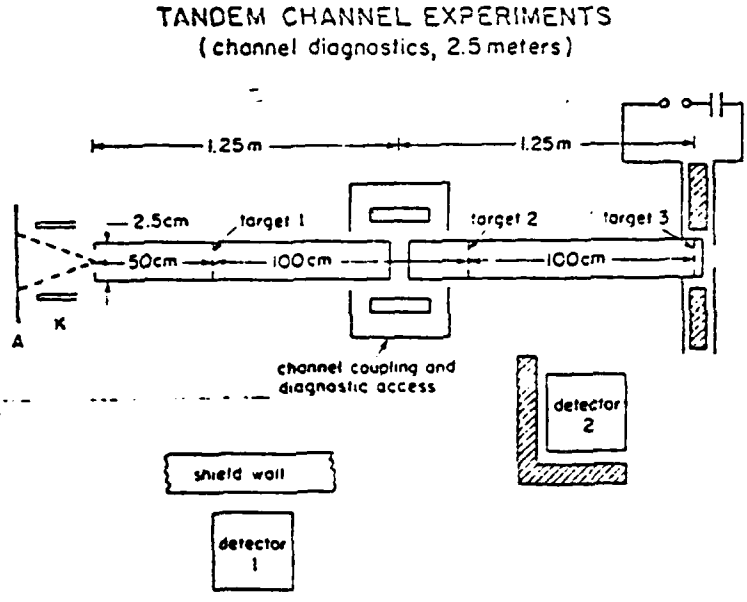

Figure 6

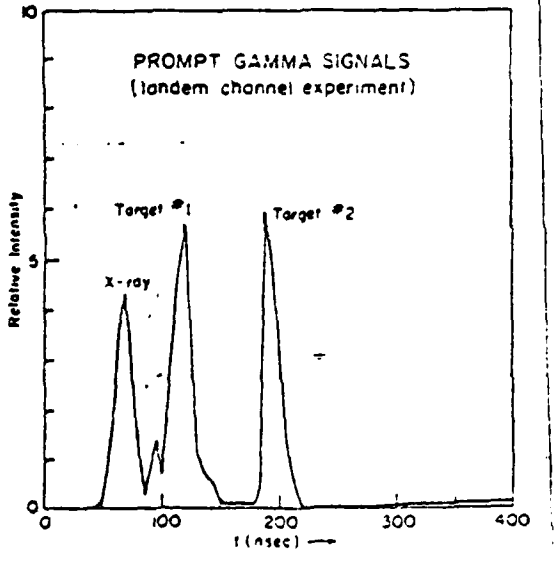

Figure 7

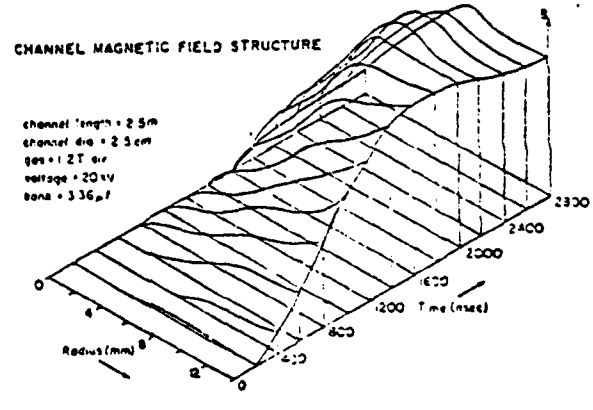

Figure 8

POST-TRANSPORT MULTIPLE-APERTURE TARGET

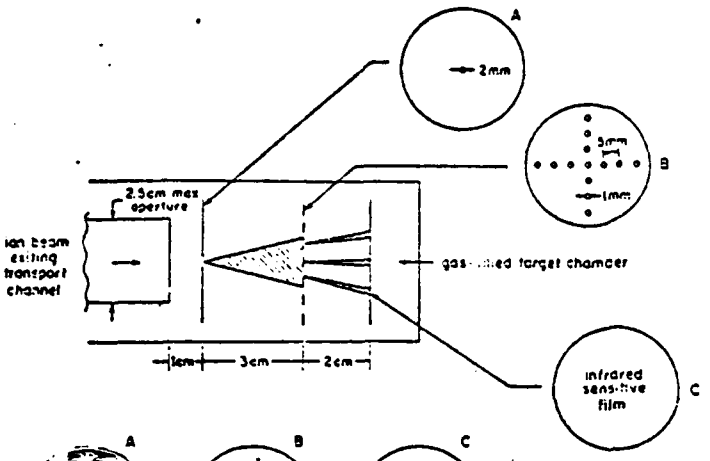

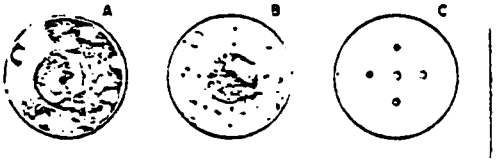

Figure 9

POST-TRANSPORT BEAM EXPANSION

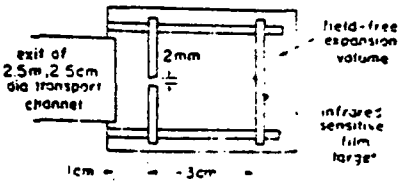

	channel current at beam injection, μA	target spot size, mm	beam half angle, degrees
(a)	4.7	2	1
(b)	21.2	6	3
(c)	23.6	7.5	3.8
(d)	26	9	4.5
(e)	28.3	10	5

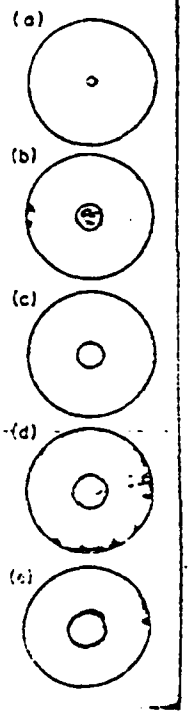

Figure 10

TANDEM CHANNEL EXPERIMENTS
(beam expansion and target interaction, 2.5 meters)

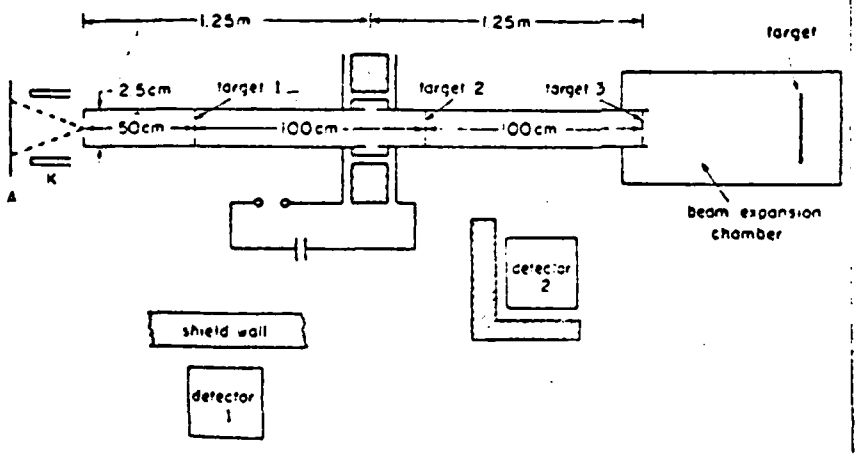

Figure 11

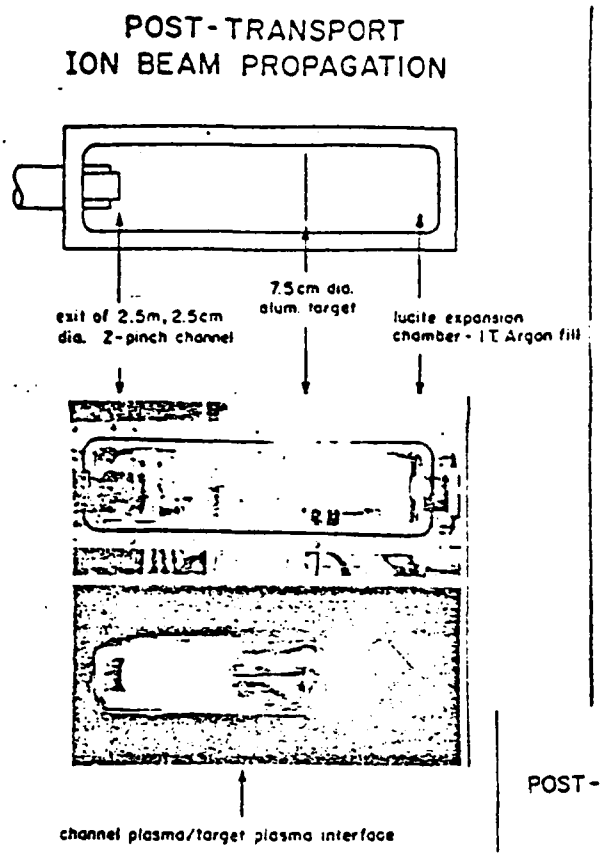

Figure 12

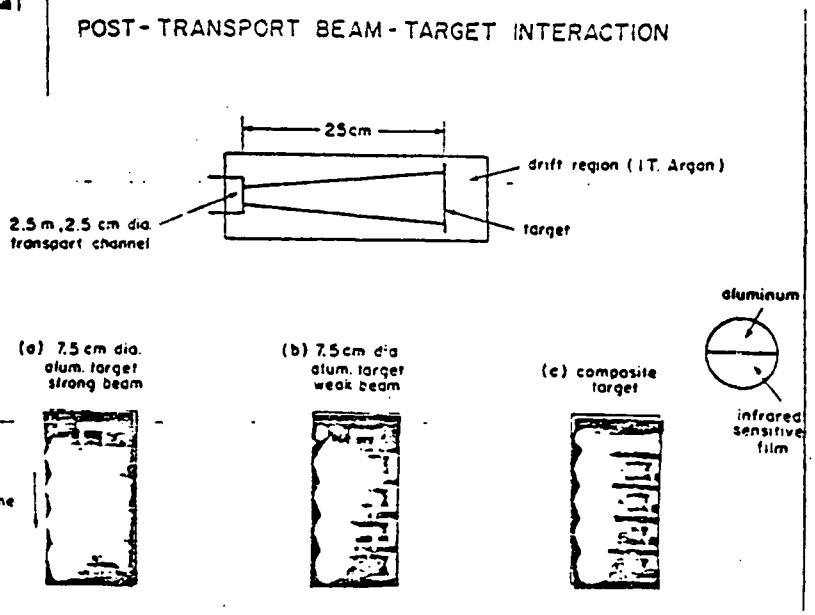

Figure 13

†Work supported by the Department of Energy.

REFERENCES

[1] G. Cooperstein, et.al., Proc. Fifth Workshop on Laser Interaction and Related Plasma Phenomena, Laboratory of Laser Energetics, Rochester, NY, Nov. 5-9, (1979).

[2] For related information and theoretical aspects, see also papers by G. Cooperstein et.al., S. Goldstein, et.al., and D. Mosher, et.al., these proceedings.

[3] S. J. Stephanakis, et.al., Proc. of the IEEE Int. Conf. on Plasma Sci., Madison, Wisconsin, May (1980).

[4] J. Golden, et.al., Rev. Sci. Instr. 49, 1384, Oct. (1978).

[5] F. C. Young, et.al., IEEE Trans. on Plasma Science PS-9, 1, March (1981).

[6] F. Sandel, to be submitted to Rev. Sci. Instr.

Measurements of Enhanced Stopping of 1-MeV Deuterons in Target-Ablation Plasmas

F. C. Young, D. Mosher, S. J. Stephanakis, and Shyke A. Goldstein[a]
Naval Research Laboratory, Washington, D. C. 20375

and

T. A. Mehlhorn
Sandia National Laboratory, Albuquerque, New Mexico 87115
(Received 28 April 1982)

Enhancement of the energy loss of 1-MeV deuterons in target-ablation plasmas over that in cold targets has been observed when significant ionization is present in the plasma. Scaling of enhanced stopping with target ionization is consistent with stopping by free electrons and the remaining bound electrons. Measured energy losses for Mylar and aluminum targets are also in agreement with hydrocode calculations.

PACS numbers: 52.40.Mj, 29.70.Gn, 52.50.Gj, 52.70.Nc

Inertial confinement fusion (ICF) with ion-beam drivers requires high-power-density deposition of ion energy in fusion targets. The beam power density is proportional to the current density focused onto the pellet target and to the stopping power of the beam-heated target material. Calculations[1-3] indicate that at the ionization levels of ICF pellet plasmas, the ion stopping power is enhanced such that the ion range is about half of that in a cold target. In this paper, measurements of the energy loss of megaelectronvolt deuterons in plasmas formed by focusing the beam

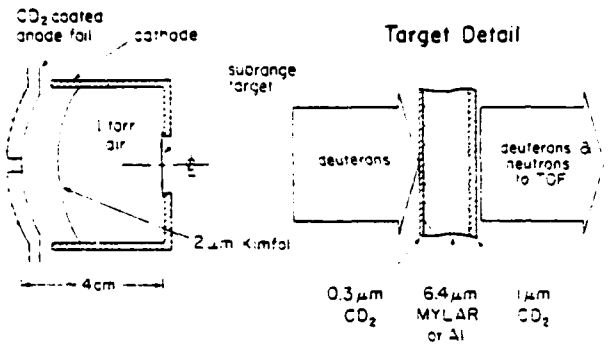

FIG. 1. Conceptual experimental schematic.

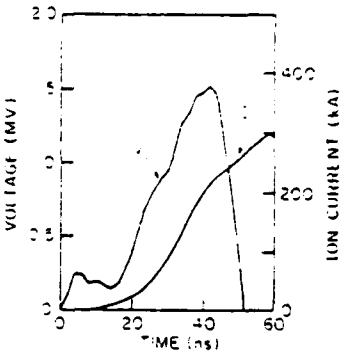

FIG. 2. Diode-voltage and ion-current traces.

(1 MeV, 0.2 MA, 20 ns) onto subrange-thick targets are presented. The results demonstrate that the stopping power is enhanced and confirm theoretical scaling of the stopping power with target ionization.

Recent pulsed-power and diode-physics advances have resulted in the focusing of proton and deuteron beams to several hundred kiloamperes per square centimeter, sufficient for experiments on ion stopping in plasmas.[4] For the present energy-loss experiments, a pinch-reflex diode,[4,5] operating at a peak voltage of about 1.5 MV, is used to produce an intense deuteron beam. A 6-cm-diam annular cathode is employed, and a 100-μm-thick plastic anode, coated with deuterated polyethylene (CD_2), provides the deuteron beam. The ion beam is charge and current neutralized by a 1.8-μm-thick polycarbonate foil at the cathode and 1 Torr air in the focusing-drift region (Fig. 1). The ion current passing through this foil is measured by a Rogowski coil. Typical corrected-voltage and ion-current traces are shown in Fig. 2. After about 40 ns into the pulse, the voltage decreases abruptly due to insulator flashover. Both planar and spherically contoured anodes[4] are used to produce different beam-current densities on target in order to vary target heating. With planar anodes, the beam focus in 10–15 cm from the anode. With spherical anodes, higher current density is achieved about 4 cm from the anode apex.

The experimental technique for determining the deuteron energy loss uses neutron time-of-flight (TOF) with multilayered targets.[6] The beam is focused onto a target consisting of a 6.4-μm-thick subrange stopping foil of Mylar or aluminum sandwiched between 0.3- and 1.0-μm-thick layers of CD_2 (Fig. 1). The TOF of d-d neutrons from the two CD_2 targets determines both the incident deuteron energy and the energy loss in the stopping foil. Neutrons are detected in the forward beam direction, and reaction kinematics[7] are used to extract deuteron energies. Neutrons from the two CD_2 targets are time resolved for a 7.6-m neutron flight path. For planar diodes, the time separation of neutrons from the two targets is increased by locating the rear CD_2 target 21 cm behind the front CD_2 target and stopping foil.

A typical trace from the TOF detector is shown in Fig. 3. The response time (full width at half maximum) of this detector is 4 ns, and its output is linear to 15 V. Bremsstrahlung from the diode saturates the detector, but the neutron pulses are TOF delayed and resolved about 260 ns after the bremsstrahlung pulse. Measurements with just a front or a rear CD_2 target confirm that this neutron response is the superposition of neutrons

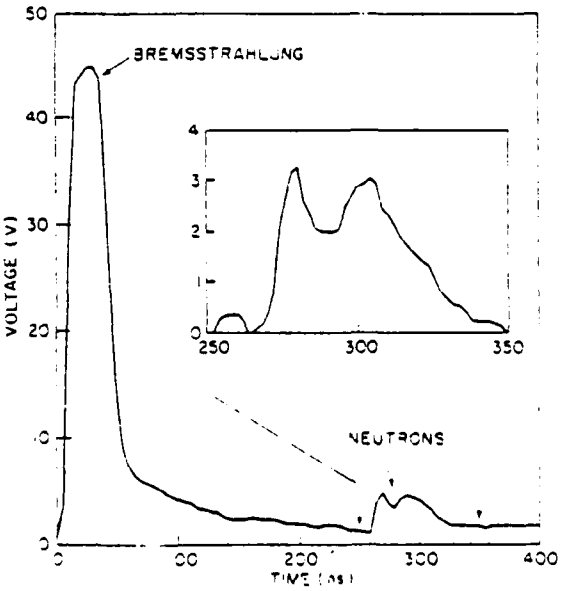

FIG. 3. Neutron TOF trace measured with a Mylar stopping foil and spherical diode.

from the front target (first neutron pulse) and the back target (second neutron pulse), respectively. The bremsstrahlung tail has been subtracted from the neutron signal shown in the inset. Since the neutron output is maximum at peak ion power, the time interval between peak ion power and the peak of the first neutron pulse determines the neutron energy from the front CD_2 target and, by kinematics, the incident deuteron energy. The deuteron energy is determined from the neutron energy and neutron emission angle relative to the deuteron direction. For planar (spherical) diodes, this angle ranges from 0° to about 10° (40°) from the target normal so that an average angle of 5° (20°) is used. A small correction (≤ 5%) is made to the neutron TOF for the TOF of deuterons from the anode to the target. The time separation of the two neutron peaks provides a direct measure of the deuteron energy loss in the stopping foil. This time interval is corrected for the TOF of deuterons from the front to the rear CD_2 target in planar-diode measurements.

Results of energy-loss measurements are presented in Fig. 4. For planar diodes, horizontal errors of ± 0.11 MeV arise from an uncertainty of ± 4 ns in timing neutron signals relative to the peak ion power. Vertical errors of ± 50 keV result from an uncertainty of ± 3 ns in the separation of the two neutron peaks. For spherical diodes, the horizontal and vertical errors include uncertainties due to the large range of deuteron angles on target. Cold-target energy losses, deduced from stopping cross sections[3] using the average angles, are compared with the measurements in Fig. 4. Measured energy losses are significantly larger than cold-target values except for the planar diode with a Mylar target. In that case, measurements are consistent with cold-target values.

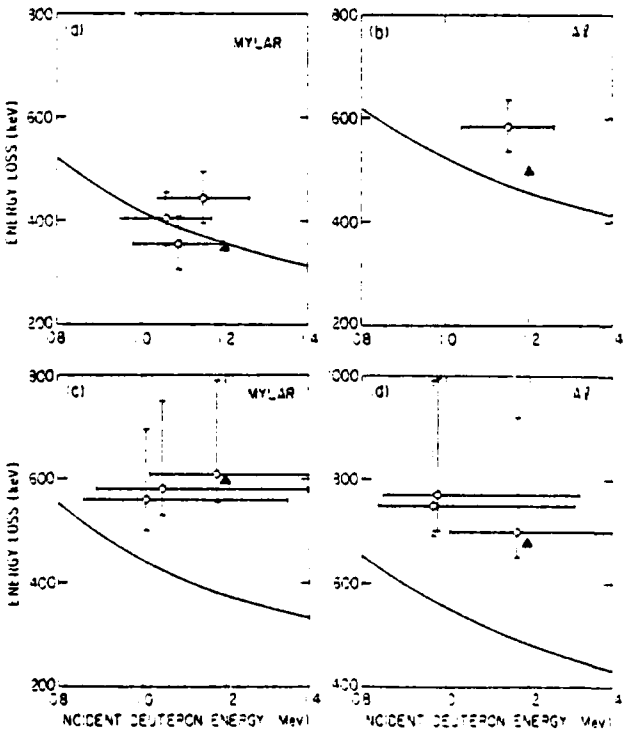

FIG. 4. Comparison of energy-loss measurements for (a) and (b) planar and (c) and (d) spherical diodes with energy-loss curves calculated for solid targets. The triangles are hydrocode results.

The ion-current density on target is required to evaluate target heating. Proton beam-current densities were determined by measuring K-line radiation from aluminum targets.[9] For these measurements the anode was not coated with CD_2, and the proton energy was assumed to be the deuteron energy measured by neutron TOF on similar shots. Proton-current densities at peak power were 30–50 kA/cm² for planar diodes and about 200 kA/cm² for spherical diodes without correction for enhanced proton-energy deposition. An increase in these values can be expected after correction for enhanced stopping. For the energy-loss measurements, deuteron-current densities were scaled from these results using the measured ion currents, and uncertainies of ± 30% were assigned to the values obtained.

The ion energy loss is expected to deviate from that in cold matter when the stopping medium is a dense plasma of significant ionization.[1-3] Variation of the average ionization (Z) with internal energy per gram (e) for aluminum and polyethyl-

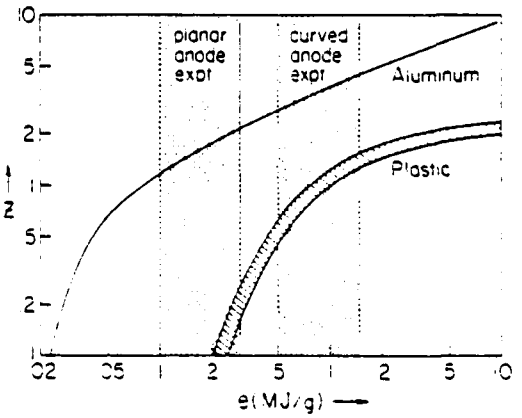

FIG. 5. Dependence of the average ionization on internal energy per gram for aluminum and CH_2 (plastic).

ene (CH_2) from equation-of-state tables[10] is shown in Fig. 5. It is assumed that ionization in Mylar is similar to that in CH_2. The ranges of internal energy per gram corresponding to the experimental conditions are also indicated, where 75% of the deposited energy is converted into internal energy. This partition is determined from hydrocode calculations (to be discussed). The measured deuteron stopping is enhanced [Figs. 4(b)–4(d)] when $Z \gtrsim 1$ from Fig. 5, and is near the cold-target values [Fig. 4(a)] when the ionization is predicted to be low.

Scaling of the stopping power with target ionization can be expressed[3] as

$$S = B[(1 - Z/Z_a)\ln\Lambda_b + (Z/Z_a)\ln\Lambda_f] \quad (1)$$

for a plasma of atomic number Z_a. The quantities $B = 4\pi e^4 N Z_a/mV^2$ and $\Lambda_b = 2mV^2/I_z$ are for nonrelativistic hydrogenic ions. The atomic density of the plasma is N, m is the electron mass, and V is the ion velocity. The average ionization energy for bound electrons (I_z) is Z dependent.[1] The equivalent quantities for free electrons are $\Lambda_f = 2mV^2/I_f$ and $I_f = e^2/\lambda_D$, where λ_D is the plasma Debye length. For target conditions in the present experiment, thermal-electron corrections to Eq. (1) are negligible. For a cold target, $S = S_0$, $I_z = I_0$, $Z = 0$, and $\Lambda_0 = 2mV^2/I_0$ so that

$$\ln\Lambda_0(S - S_0)/S_0 = (Z/Z_a)\ln(I_z/I_f) - \ln(I_z/I_0). \quad (2)$$

The right side of Eq. (2) depends only on the plasma state and is plotted in Fig. 6 against e for aluminum at $\rho = 0.02$ g/cm^3. This is the Al density at peak power based on hydrocode calculations to be discussed. The left side of Eq. (2), evaluated from Figs. 4(b) and 4(d), is also plotted with experimental uncertainties. This comparison of experimental results with calculated ion-stopping enhancement confirms the ionization scaling of Eq. (1).

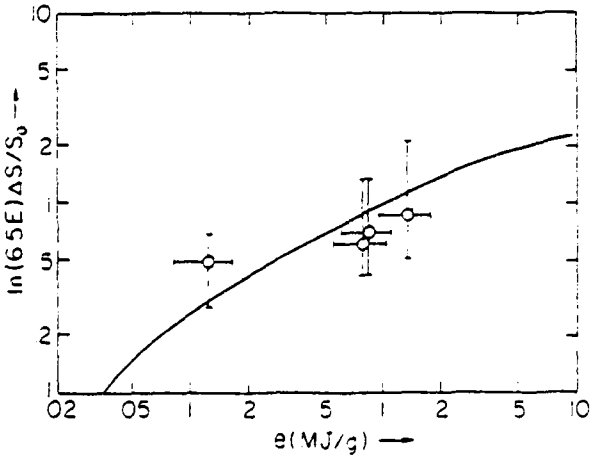

FIG. 6. Comparison of theory and experiment for the dependence of enhancement, $\Delta S/S_0 = (S - S_0)/S_0$, on internal energy per gram for aluminum.

The energy loss of deuterons in the experimental targets was evaluated more precisely by hydrocode simulation with experimental parameters and enhanced stopping.[1] Power on target versus time was based on diode-voltage traces normalized to deuteron energies determined from neutron TOF and ion-current traces normalized to peaks of 50 kA/cm^2 (planar diode) or 250 kA/cm^2 (spherical diode). Target heating was evaluated for a 50-50 mixture of protons and deuterons in the beam based on experimental measurements. These calculations indicate that at peak power, the target has expanded in thickness to about 1 mm at 50 kA/cm^2 and 2 mm at 250 kA/cm^2. In aluminum (Mylar) at peak power, the electron temperature is 4–5 eV (2.5–3.5 eV) at 50 kA/cm^2 and 13–17 eV (9–11 eV) at 250 kA/cm^2. Code-calculated energy losses at peak power, plotted in Fig. 4, agree with most measurements.

In summary, we report measurements of enhanced stopping of ions in dense plasmas. The stopping power of 1-MeV deuterons in aluminum is enhanced by 20% at the 50 kA/cm^2 level and by 40% at the 250 kA/cm^2 level. For Mylar, the stopping power is enhanced by about 45% at the higher current density, but is consistent with cold-target stopping at the lower current density. These results agree with a model of ion-energy deposition which includes stopping by free electrons and the remaining bound electrons in the target.

The work was supported by the U. S. Defense Nuclear Agency and the U. S. Department of Energy.

[a]Permanent address: JAYCOR, Inc., Alexandria, Va. 22304.

[1]T. A. Mehlhorn, J. Appl. Phys. 52, 6522 (1981).

[2]E. Nardi, E. Peleg, and Z. Zinamon, Appl. Phys. Lett. 39, 46 (1981).

[3]D. Mosher, in Proceedings of the U. S. Energy Research and Development Administration Summer Study of Heavy Ions for Inertial Fusion, 1976, Lawrence Berkeley Laboratory Report No. 5543 (unpublished).

[4]G. Cooperstein, Shyke A. Goldstein, D. Mosher,

R. J. Barker, J. R. Boller, D. G. Colombant, A. Drobot, R. A. Meger, W. F. Oliphant, P. F. Ottinger, F. L. Sandel, S. J. Stephanakis, and F. C. Young, in *Laser Interaction and Related Phenomena*, edited by H. Schwarz, H. Hora, M. Lubin, and B. Yaakobi (Plenum, New York, 1981), Vol. 5, p. 105.

[5]Shyke A. Goldstein, G. Cooperstein, Roswell Lee, D. Mosher, and S. J. Stephanakis, Phys. Rev. Lett. 40, 1504 (1978).

[6]F. C. Young, S. A. Goldstein, S. J. Stephanakis, and D. Mosher, in *IEEE International Conference on Plasma Science, Santa Fe, 18–20 May 1981* (IEEE, New York, 1981).

[7]H. Liskien and A. Paulsen, At. Data Nucl. Data Tables 15, 57 (1975).

[8]H. H. Andersen and J. F. Ziegler, *The Stopping and Ranges of Ions in Matter* (Pergamon, New York, 1977), Vol. 3.

[9]R. D. Bleach, D. J. Nagel, D. Mosher, and S. J. Stephanakis, J. Appl. Phys. 54, 3064 (1981).

[10]B. I. Bennett, J. D. Johnson, G. I. Kerley, G. T. Rood, Los Alamos Scientific Laboratory Report No. 7130, 1978 (unpublished). Also data for CH_2 were provided by Andrew Wilson using the CAPO code.

4.0 PLASMA EROSION OPENING SWITCHES

The work with plasma erosion opening switches (PEOS) first began with the Aurora experiments where scaling of PRD operation to high voltage was being tested. At that time the PEOS were being used simply to suppress the prepulse. It was realized, however, that a fast opening switch used in conjunction with inductive storage could provide pulse compression and power multiplication for many existing state-of-the-art pulsed power generators. The development of this new technology could have many applications, the most obvious and immediate one being a short pulse option (10-20 ns) for PBFA-I and PBFA-II, Another obvious application would be to provide a short duration high power Bremsstrahlung source, possibly using the series diode discussed previously if low energy is required. With this potential in mind. A serious program began to develop the PEOS.

The search for reliable opening switches for inductive energy storage devices or other pulse power applications has gone on for many years. Developments in explosive switching and wire fuse technology have been encouraging, but do not provide sufficiently fast opening times (~10 ns) to compete with capacitive pulse line systems. Moreover, they suffer significant joule heating losses and must be physically replaced after each shot. The new experimental program at

NRL with JAYCOR participation has focused on the use of plasma columns as opening switches. Such PEOS's have been employed on several experimnts to date at Sandia National Laboratories (SNL), Physics International and the Naval Research Laboratory (NRL). These experiments used PEOS's to insulate diode loads from prepulse effects to sharpen the beam risetime, and to improve pinch formation. Present experiments at NRL are aimed at understanding the conduction and opening mechanisms of these switches.

This Plasma Erosion Opening Switch (PEOS) utilizes an injected carbon plasma to conduct large currents (~ 1 MA) for up to 100 ns while a vacuum inductor (~ 100 nH) is charged. The switch is then capable of opening on a short (~ 10 ns) timescale and depositing the the stored energy into a load impedance. Output pulse widths and power levels are determined by the storage inductance and the load impedance.

The switch operation has been studied in some detail both analytically and experimentally. The opening process depends on properties of the injected plasma, the switch and inductive store geometry the input voltage waveforms and the load impedance. An analytic model of the switch operation which incorporates these factors has been developed. This model has been used in conjunction with a transmission line code for comparison with experimental results and shows good

agreement.

The theoretical model includes effects due to injected plasma drift motion, surface erosion and the self-consistent magnetic field. Once a voltage is applied across the switch plasma, an anode-cathode gap opens and bipolar electron and ion current flow is established. When ion current is drawn out of the plasma faster than the plasma drift can supply ions, the surface is eroded away causing the gap to open further. This erosion is enhanced by magnetic bending of the electron trajectories when the critical current is reached. Eventually enough current switches to the load to completely insulate the electron flow and the enhanced erosion ceases. The JxB force on the plasma is also important to consider. Since rapid magnetic field penetration into the plasma due to anomalous resistivity occurs on the same timescale as other processes occurring in the switch, its effects have also been studied, however enhanced erosion seems to be the dominate mechanism in causing the rapid opening.

Experiments have been performed at the 5 kJ stored energy level on the Gamble I generator and at the 50 kJ level on the Gamble II generator. Results from both experiments provide scaling of switch operation. Future plans call for fielding experiments on still higher power accelerators including PBFA-I and PBFA-II at Sandia National

Laboratories. Experiments on NRL's Gamble I and Gamble II generators have shown low impedance conduction times of up to 60 nsec followed by opening times of < 10 nsec. The switch has conducted up to 1 MA before opening at switch current densities of < 8 kA/cm^2. Voltage stand-off of greater than 500 kV/cm has been demonstrated. Inductive energy storage has been demonstrated with 3x pulse compressions an ~5x power multiplications.

Other experiments were designed to characterize the initial injected plasma, i.e., density distribution, species, and temperature. Experiments have been carried out using the Gamble I generator (~0.9 MV, ~0.25 MA) to identify some of the important physical mechanisms responsible for the observed switch behavior. Of particular interest are electrode effects, $\vec{J}x\vec{B}$ driven gross plasma motion, and the rate and extent of magnetic field penetration. Diagnostics included streak/framing camera photography, Faraday cups, time and space resolved spectroscopy, Rogowski loops, electric probes, time and space resolved x-ray measurements in the few keV range and internal magnetic field probes.

The results indicate that the plasma is injected at ~7 cm/μs, with a peak in density of ~10^{13} cm^{-3} and a temperature of ~1-5 eV. There appears to be an intense plasma-wall interaction at the switch electrode surfaces with neutrals being generated. Also, there is evidence that

the magnetic field penetrates into the plasma much faster than what is predicted classically.

This program has progressed rapidly and with great success. Many of the technical details not discussed in this summary can be found in the reports that follow.

4.1 List of Reports on Switch Physics

4.1.a Contributed Papers

1. "Small Diameter Pinch-Reflex Diode Behavior with Plasma Erosion Switch Beam-Front Sharpening," W. F. Oliphant, H. U. Karow, S. J. Stephanakis, R. A. Meger, Shyke A. Goldstein and G. Cooperstein, 1981 IEEE International Conf. on Plasma Science, (Santa Fe, NM, May 1981), p. 81.

2. "Plasma Opening Switch Research at NRL," R. A. Meger, R. J. Commisso, A. T. Drobot and Shyke A. Goldstein, 1982 IEEE International Conf. on Plasma Science, (Ottawa, Canada, May 1982), p. 4.

3. "An Inductive Store/Pulse Compression Experiment Using Plasma Opening Switches," R. A. Meger, R. J. Barker, R. J. Commisso, G. Cooperstein, Shyke A. Goldstein, J. M. Neri and P. F. Ottinger, Bull. Am. Phys. Soc. 27, 991 (1982).

4. "Plasma Source Development for Plasma Opening Switches," J. M. Neri, R. J. Commisso and R. A. Meger, Bull. Am. Phys. Soc. 27 1054 (1982).

5. "Scaling Experiment on Plasma Opening Switches for Inductive Energy Storage Applications," R. A. Meger, J. R. Boller, R. J. Commisso, G. Cooperstein, Shyke A. Goldstein, J. M. Neri, P. F. Ottinger, T. J. Renk, J. D. Shipman, Jr., S. J. Stephanakis, F. C. Young, and B. V. Weber, 1983 IEEE International Conf. on Plasma Science, (San Diego, CA, May 1983).

6. "Theoretical Modeling of the Plasma Opening Switch," P. F. Ottinger, Shyke A. Goldstein, R. A. Meger, and S. McDonald, 1983 IEEE International Conf. on Plasma Science, (San Diego, CA, May 1983).

7. "Plasma Opening Switch Studies," J. M. Neri, R. J. Commisso, Shyke A. Goldstein, R. A. Meger, P. F. Ottinger, B. V. Weber and F. C. Young,

1983 IEEE International Conf. on Plasma Science, (San Diego, CA, May 1983).

4.1.b Unpublished Technical Reports

1. "Vacuum Inductive Store/Pulsed Compression Experiments on a High Power Accelerator Using Plasma Opening Switches" R. A. Meger, R. J. Commisso, G. Cooperstein and Shyke A. Goldstein, NRL Memorandum Report 5037 (March, 1983).

4.1.c Published Papers

1. "Pulse Compression/Power Multiplication Experiments Using Plasma Erosion Switches," R. A. Meger, R. J. Commisso, G. Cooperstein and Shyke A. Goldstein, to be published in Appl. Phys. Lett.

3D7 Small Diameter Pinch-Reflex Diode Behavior with Plasma Erosion Switch Beam Front Sharpening.*
W. F. OLIPHANT, H. U. KAROW†, S. J. STEPHANAKIS, R. A. MEGER‡, SHYKE A. GOLDSTEIN‡, G. COOPERSTEIN, Naval Research Laboratory — Experiments are being performed on small diameter (~ 1 cm) low impedance (1-4 Ω) pinch reflex ion diodes in order to increase the ion source current density to ~ 10^5 A/cm^2. Previous unpublished experimental results and theoretical calculations suggest that the very large azimuthal self-magnetic fields associated with these small diameter geometries may retard anode-cathode gap closure due to plasma motion. This should allow the diode impedance to hold up for the duration of the pulse (~ 50 nesc) even at very small anode-cathode gaps (~ 1 mm) with beam voltages of ~ 10^6 volts. However, this effect requires azimuthally symmetric cathode turn on and symmetric electron and ion flow. One method used previously[1,2] to eliminate prepulse, sharpen beam voltage risetime, and to symmetrize pinch beam diodes is to use plasma erosion switches. Preliminary experiments using such switches on the Gamble I accelerator will be described. Diode impedance characteristics will be presented for the small diameter pinch-reflex ion diode with and without plasma erosion.

*Work supported by the Defense Nuclear Agency and the Department of Energy
†Karlsruhe Nuclear Research Institute, Karlsruhe, West Germany
‡JAYCOR, Inc., Alexandria, VA 22304
[1] C. W. Mendel, Jr., and S. A. Goldstein, J. of App. Phys. 48, 1004 (1977).
[2] F. C. Young, et al, Bull. Am. Phys. Soc. 25, 899 (1980).

1A10 Plasma Opening Switch Research at NRL+. R. A MEGER*, R. J. COMMISSO*, G. COOPERSTEIN, A. T. DROBOT**, SHYKE A. GOLDSTEIN*, Naval Research Laboratory, Washington, DC 20375--The search for reliable opening switches for inductive energy storage devices or other pulse power applications has gone on for many years. Developments in explosive switching and wire fuse technology have been encouraging[1] but do not provide sufficiently fast opening times (~ 10 ns) to compete with capacitive pulse line systems. Moreover, they suffer significant joule heating losses and must be physically replaced after each shot. A new experimental program at NRL has focused on the use of plasma columns as opening switches. Such Plasma Erosion Switches (PES's) have been employed on several experiments to date at Sandia National Laboratories[2,3] (SNL), Physics International[4], and the Naval Research Laboratory[5] (NRL). These experiments used PES's to insulate diode loads from prepulse effects, to sharpen the beam risetime, and to improve pinch formation. Present experiments at NRL are aimed at understanding the conduction and opening mechanisms of these switches. Eventually they will be used to current charge a vacuum inductor at low power and then to extract this energy at a significantly higher power level.

All experiments to date have used a carbon plasma gun developed by Mendel and coworkers at SNL[6] which produces carbon plasmas of up to 10^{14} cm^{-3} densities over volumes of 1-2x10^3 cm^3. Several guns have been mounted on the Gamble I accelerator at NRL. The effects of plasma density, plasma injection timing and geometry, output load impedance, and accelerator voltage and polarity on the switch opening are presently under study. The hardware allows changes to be made in the accelerator pulse length and in the vacuum inductance of the transmission line or lumped element load inductance in order to investigate inductive energy storage applications. In conjunction with this work a computer simulation using a 2-D fully electromagnetic particle code is being performed.

Preliminary results to be discussed have shown that a plasma ballast region outside the switch supplies a large fraction of the charge transfered during the conduction and opening phases of the switch operation. This region appears to be charging up to some voltage like a plasma capacitor. Thus far switch opening times have been limited to ~ 20 ns by what may be geometry related effects where the opened switch impedance remains comparable to the load impedance. Up to 10 mCoul of charge from the accelerator pulse has been diverted in present experiments. Magnetic insulation effects also appear to contribute to the opening action with switch electrons joining the diode electron flow.

+ Work supported by the Defense Nuclear Agency
* Present address: JAYCOR, Inc., Alexandria, VA
** Present address: Science Applications, Inc., McLean, VA.

[1] D. Conte, et.al., 2nd IEEE Int. Pulsed Power Conf., Lubbock, TX (1979).
[2] P. Miller, J. W. Poukey, T. P. Wright, PRL 14, 940 (1975).
[3] C. W. Mendel, Jr., S. A. Goldstein, Jour. of Appl. Phys. 48, 1004 (1977).
[4] R. Stringfield, et. al., J. Appl. Phys. 52, 1278 (1981).
[5] F. C. Young, et. al., Bull. Am. Phys. Soc. 25, 899 (1980).
[6] C. W. Mendel, et.al., Rev. Sci. Instrum. 51, 1341 (1980).

4g 7 An Inductive Storage/Pulse Compression Experiment Using Plasma Opening Switches.* R.A. MEGER**, R.J. BARKER**, R.J. COMMISSO**, G. COOPERSTEIN, SHYKE A. GOLDSTEIN**, J.M. NERI**, and P.F. OTTINGER**, Naval Research Laboratory--Plasma erosion switches have been used for prepulse suppression and risetime sharpening on pulsed-power generators at several labs including Sandia, Physics Int., NRL, and Maxwell Labs. Work is presently underway to extend their use to inductive storage. Experiments on NRL's Gamble I and Gamble II generators have shown low impedance conduction times of up to 60 nsec followed by opening times of $\leq$ 10 nsec. The switch has conducted up to 500 kA before opening at switch current densities of $\leq$ 8 kA/cm^2. Voltage stand-off of greater than 500 kV/cm has been demonstrated. Inductive energy storage has been demonstrated with 3x pulse compressions and ~ 5x power multiplications. An analytic model has been developed and coupled to a transmission line code in order to investigate switch operation and a PIC simulation is being used to study the opening process. Results will be presented.

*Work supported by the Defense Nuclear Agency
**JAYCOR, Inc., Alexandria, VA 20305

6s 1 Plasma Source Development for Plasma Opening Switches* J.M. NERI**, R.J. COMMISSO**, and R.A. MEGER**, Naval Research Laboratory--Carbon plasma guns of the type developed by Mendel[1] have been studied for use in plasma erosion switches.[2] Parameters of interest for this application include the plasma density, species, drift velocity and co-moving neutral particle density distribution. Diagnostic techniques include biased Faraday cups, electrostatic energy analysis, and spectroscopy. Measurements show a drift velocity of ~ 10^7 cm/sec, and charge densities of ~ 10^{13}/cm^3 produced by the plasma guns. Attempts to improve the uniformity and reproductibility of the carbon plasma will be reported. Experiments on plasma-wall interactions with regard to ion reflection, recombination and sticking as they affect application to plasma erosion switches will be discussed.

* Work supported by the Defense Nuclear Agency.
**JAYCOR, Inc., Alexandria, VA 20305
[1] C.W. Mendel and S.A. Goldstein, J. Appl. Phys. 48, 1004 (1977).
[2] R.A. Meger, et.al., this conference.

Scaling Experiments on Plasma Opening Switches for Inductive Energy Storage Applications*, R.A. Meger[a], J.R. Boller, R.J. Commisso[a], G. Cooperstein, Shyke A. Goldstein[a], J.M. Neri[a], P.F. Ottinger[a], T.J. Renk[b], J.D. Shipman, Jr.[c], S.J. Stephanakis, F.C. Young, and B.V. Weber[a], Naval Research Laboratory, Washington, DC 20375

A new type of fast opening switch for use with pulsed power accelerators has been developed.[1] This Plasma Opening Switch (POS) utilizes an injected carbon plasma to conduct large currents (~ 1 MA) for up to 100 ns while a vacuum inductor (~ 100 nH) is charged. The switch is then capable of opening on a short (~ 10 ns) timescale and depositing the stored energy into a load impedance. Output pulse widths and power levels are determined by the storage inductance and the load impedance.

The switch operation has been studied in detail both analytically[2] and experimentally.[1,3] The opening process depends on properties of the injected plasma, the switch and inductive store geometry, the input voltage waveforms and the load impedance. An analytic model of the switch operation which incorporates these factors has been developed. This model has been used in conjunction with a transmission line code for comparison with experimental results.

Experiments have been performed at the 5 kJ stored energy level on the Gamble I generator and at the 50 kJ level on the Gamble II generator. Results from both experiments will be reported and the scaling of switch operation discussed. Future plans call for fielding experiments on still higher power accelerators including PBFA I and PBFA II at Sandia National Laboratories.

* Work supported by the Defense Nuclear Agency, the Department of Energy and Sandia National Laboratories.

a) JAYCOR, Inc., Alexandria, Va. 22304
b) NRL/NRC Cooperative Research Associate
c) Sachs/Freeman Associates, Bowie, MD 20715

1 R.A. Meger, R.J. Commisso, G. Cooperstein, Shyke A. Goldstein, NRL Memorandum Report No. 5037, 1983, also submitted to Appl. Phys. Lett., January 1983.
2 P.F. Ottinger, Shyke A. Goldstein, R.A. Meger, S. McDonald, abstract, this conference.
3 J.M. Neri, et.al., abstract, this conference.

Theoretical Modeling of the Plasma Opening Switch†, P.F. Ottinger*, Shyke A. Goldstein*, R.A. Meger*, and S. McDonald**, Naval Research Laboratory, Washington, DC 20375 — Recent experiments at NRL have demonstrated that plasma can be used as the switching medium in a fast opening switch.[1] Pulsed power applications for such switches are manyfold including prepulse suppression, risetime sharpening, inductive storage and pulse compression. Each application, however, requires individual attention to geometry, plasma parameters, timescales, etc. Here theoretical modeling of the basic physical mechanisms involved in the opening process will be described. Emphasis will be placed on relating the model to new experiments at NRL.[2]

The theoretical model includes effects due to injected plasma drift motion, surface erosion and the self-consistent magnetic field. Once a voltage is applied across the switch plasma, an anode-cathode gap opens and bipolar electron and ion current flow is established. When ion current is drawn out of the plasma faster than the plasma drift can supply ions, the surface is eroded away causing the gap to open further. This erosion is enhanced by magnetic bending of the electron trajectories when the critical current is reached. Eventually enough current switches to the load to completely insulate the electron flow and the enhanced erosion ceases. The JxB force on the plasma is also important to consider. Since rapid magnetic field penetration into the plasma due to anomalous resistivity occurs on the same timescale as other processes occurring in the switch, its effects are also studied.

The importance of various aspects of the model will be discussed and scaling laws will be presented. Comparison of the model with specific experimental results will also be presented by incorporating the switch physics into a transmission line code.

† Work supported by the Department of Energy, the Defense Nuclear Agency, Sandia National Laboratory and the University of Maryland/Naval Research Laboratory Joint Program in Plasma Physics.

* JAYCOR, Inc., Alexandria, VA 22304

** University of Maryland, College Park, MD 20742

1 R.A. Meger, R.J. Commisso, G. Cooperstein, and Shyke A. Goldstein, NRL Memorandum Report No. 5037, 1983; also submitted to Appl. Phys. Lett.

2 R.A. Meger, et al., these proceedings; J.M. [illegible] al., these proceedings.

Plasma Opening Switch Studies†, J.M. Neri*, R.J. Commisso*, Shyke A. Goldstein*, R.A. Meger*, P.F. Ottinger*, B.V. Weber*, and F.C. Young, Naval Research Laboratory, Washington, DC 20375 -- Plasma has been successfully used as a switching medium in several particle beam generators. The injected plasma serves as a short circuit that effectively isolates the load from the generator for some period of time. After this time the plasma acts as a fast opening switch, diverting the generator pulse to the load on a short timescale, ~ 5 ns. Depending on the length of time the switch remains closed (short circuit), it can simply serve to suppress prepulse[1] or it can act as an opening switch in inductive storage-pulse compression applications.[2]

We report here on experiments designed to characterize the initial injected plasma, i.e., density distribution, species, and temperature. Experiments are also being carried out using the Gamble I generator (~0.9 MV, ~0.25 MA) to identify some of the important physical mechanisms responsible for the observed switch behavior. Of particular interest are electrode effects, $\vec{J}\times\vec{B}$ driven gross plasma motion, and the rate and extent of magnetic field penetration. Diagnostics include streak/framing camera photography, Faraday cups, time and space resolved spectroscopy, Rogowski loops, electric probes, time and space resolved x-ray measurements in the few keV range, and internal magnetic field probes.

The initial results indicate that the plasma is injected at ~ 7 cm/μs, with a peak ion density of ~ 10^{13} cm^{-3} and a temperature of ~ 1 eV. There appears to be an intense plasma-wall interaction at the switch electrode surfaces with neutrals being generated. Also, there is evidence that the magnetic field penetrates into the plasma much faster than what is predicted classically.

Experimental results will be interpreted in the context of a theoretical model that includes gross plasma motion, microturbulence, magnetic field effects and other opening switch physics.[3]

† Work supported by the Defense Nuclear Agency, the Department of Energy and Sandia National Laboratory.
* JAYCOR Inc., Alexandria, VA 22304

1 C.W. Mendel, Jr., S.A. Goldstein, J. Appl. Phys. 48, 1004 (1977); R. Stringfield, R. Schneider, R.D. Genuario, I. Roth, K. Childers, C. Stallings, and D. Dakin, J. Appl. Phys. 52, 1278 (1981); R.A. Meger and F.C. Young, J. Appl. Phys. 53, 8543 (1982).
2 R.A. Meger, R.J. Commisso, G. Cooperstein, and Shyke A. Goldstein, NRL Memorandum Report No. 5037, 1983.
3 P.F. Ottinger, these proceedings.

VACUUM INDUCTIVE STORE/PULSE COMPRESSION EXPERIMENTS ON A HIGH POWER ACCELERATOR USING PLASMA OPENING SWITCHES

1. Introduction

The use of inductive energy storage for pulsed power production is of great interest to accelerator designers. Inductive storage offers the significant advantage of 10 - 100 times higher energy density than conventional capacitive storage systems, thus making more compact and economical generators possible[1]. Energy can be stored in an inductor at low voltage, relaxing insulator design requirements and extracted on a shorter time scale at a higher power level. Present opening switch technology involves the use of explosively activated circuit breakers,[2] wire fuses,[1,3,4] electron-beam (e-beam) controlled diffuse discharges,[5] and various injected plasma schemes.[6] In this paper we report experiments with a new type of opening switch which operates on a nanosecond timescale. These Plasma Opening Switches (POS's) are used in conjunction with a vacuum inductor and open on a <10 nsec timescale. Similar techniques have been used previously for suppression of prepulse and steepening of pulse risetime on high-power generators[7,8,9,10] as well as in plasma filled diode experiments.[11] The work discussed here is directed at storing energy in a vacuum inductor and then extracting this energy on a shorter time scale through a low inductance, high impedance load thereby pulse compressing and increasing the output power level. Results show the switch remains closed for up to 70 nsec as the vacuum inductor is charged. The switch then opens in <10 nsec and most of the energy in the inductor is delivered to an e-beam diode load. Voltage pulse compressions of a factor of 3 and power multiplications of up to a factor of 4 over non-POS shots have been measured. A model of the switch opening is described which qualitatively agrees with the data.

Manuscript approved January 5, 1983.

2. Apparatus

In these experiments the Gamble I accelerator[12] was used to charge a coaxial vacuum inductor section. A 66-kV charging voltage was used to provide a negative 1-MV, 60 nsec full-width-at-half-maximum (FWHM) sinusoidal open circuit voltage waveform with an effective 2-Ohm source impedance. Figure 1a is a schematic of the inductor section as mated to the Gamble I accelerator. Figure 1b is an equivalent circuit diagram of the system. The experimental hardware consists of three main components: a 40-cm long, 100-Ohm coaxial-vacuum inductor; a switch section; and an e-beam diode section. The ~ 140-nH, high impedance vacuum inductor section and the ~ 30-nH insulator region combine to produce the storage inductance $L_S \sim 175$ nH . The 2.5-nsec electrical length inductor looks like a high impedance lumped element load to the 2-Ohm output impedance accelerator, limiting the energy transferred into the inductor. At 66-kV charge Gamble I can store 250 kA or 6 kJ in the inductor. To the right (downstream) of the inductor in Fig. 1a is the opening switch region. Three plasma guns[13] located 12 cm off axis inject carbon plasma through a 10-cm diam. brass screen toward the inner 5-cm diam. cathode support stalk surface (see Fig. 1a). The plasma strikes the cathode surface over a ~60 cm^2 area. The measured plasma density distribution has a peak density of $\sim 5 \times 10^{12}$ cm^{-3} and moves with a drift velocity of 7.5 cm/μsec.[14] Measurements of the density distribution have shown spatial fluctuations as high as 25% for these guns. The gun plasma has been reported[13] to be comprised of C^+, C^{2+}, C^{3+}, C^{4+} and H^+ with C^+ and C^{2+} dominating. Also, a neutral carbon component with a velocity of ~ 1 cm/μsec has been observed in the switch region arriving after the plasma. No allowance for plasma stagnation near the outer screen and on the

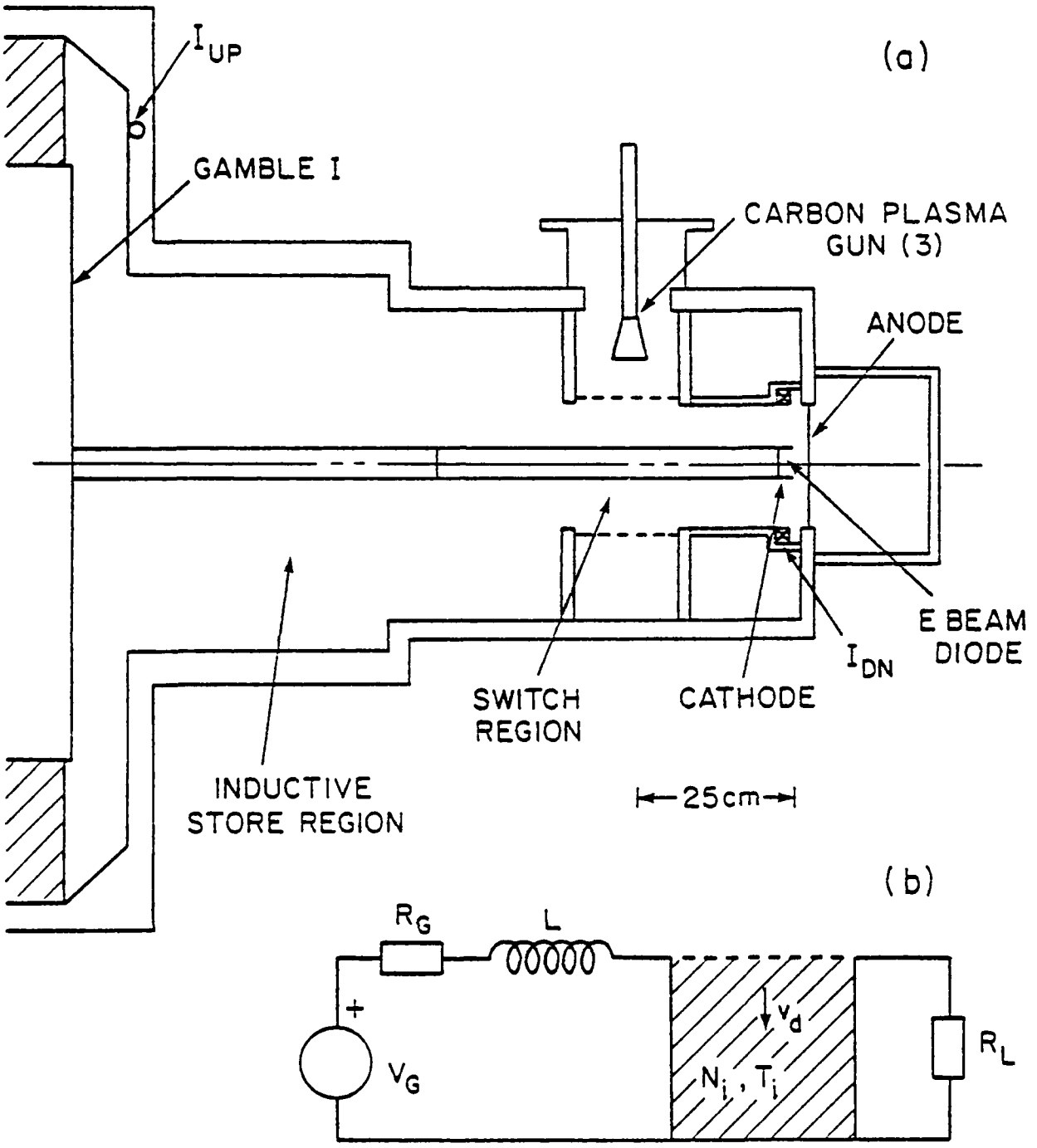

Fig. 1 — (a) A schematic of the Gamble I plasma opening switch experiment. (b) Circuit of the experiment. V_{OC} is the open circuit voltage waveform, R_G is the 2 ohm accelerator impedance, L_S is the inductor, and R_L is the load impedance.

inner cathode surface was made in these experiments. The plasma density in the switch region can be varied by changing the radial location of the gun and the timing relative to the accelerator as well as by changing the screen transmission.

Downstream of the switch region is a 10-cm long, 42-Ohm transmission line segment with inductance L_1 ~14 nH followed by the e-beam diode load. The diode consists of a 6-mm thick rounded edge, hollow cylindrical aluminum cathode opposite a 1.6-mm thick carbon coated aluminum anode. The diode has a critical current impedance of ~ 12 Ohms for the 1-cm anode-cathode (AK) gap used in this experiment.

Diagnostics on this experiment consisted of a voltage monitor upstream (to the left in Fig. 1a) of the Gamble I insulator, a dB/dt current monitor in the inductor section labeled I_{UP} in Fig. 1a and a Rogowski type current monitor downstream of the switch region labeled I_{DN}. In addition, a photodiode with a pilot-B scintillator was located on axis 35-cm downstream of the anode to provide time resolved bremsstrahlung measurements from the e-beam diode.

3. Experimental Measurements

Shown in Fig. 2 is experimental data from two shots, one with the POS and one without. The shots had nearly identical peak accelerator voltage pulses of -960 kV across the inductive store section as measured by the voltage monitor. The accelerator pulse arrived at the inductor 0.5 μsec after the peak of the plasma density as measured by a Faraday cup at the (inner) cathode surface. The currents in the inductor upstream of the switch, I_{UP}, and downstream in the e-beam load section, I_{DN}, are shown in Fig. 2a. The two cases differ dramatically. Without the POS the accelerator sees the full

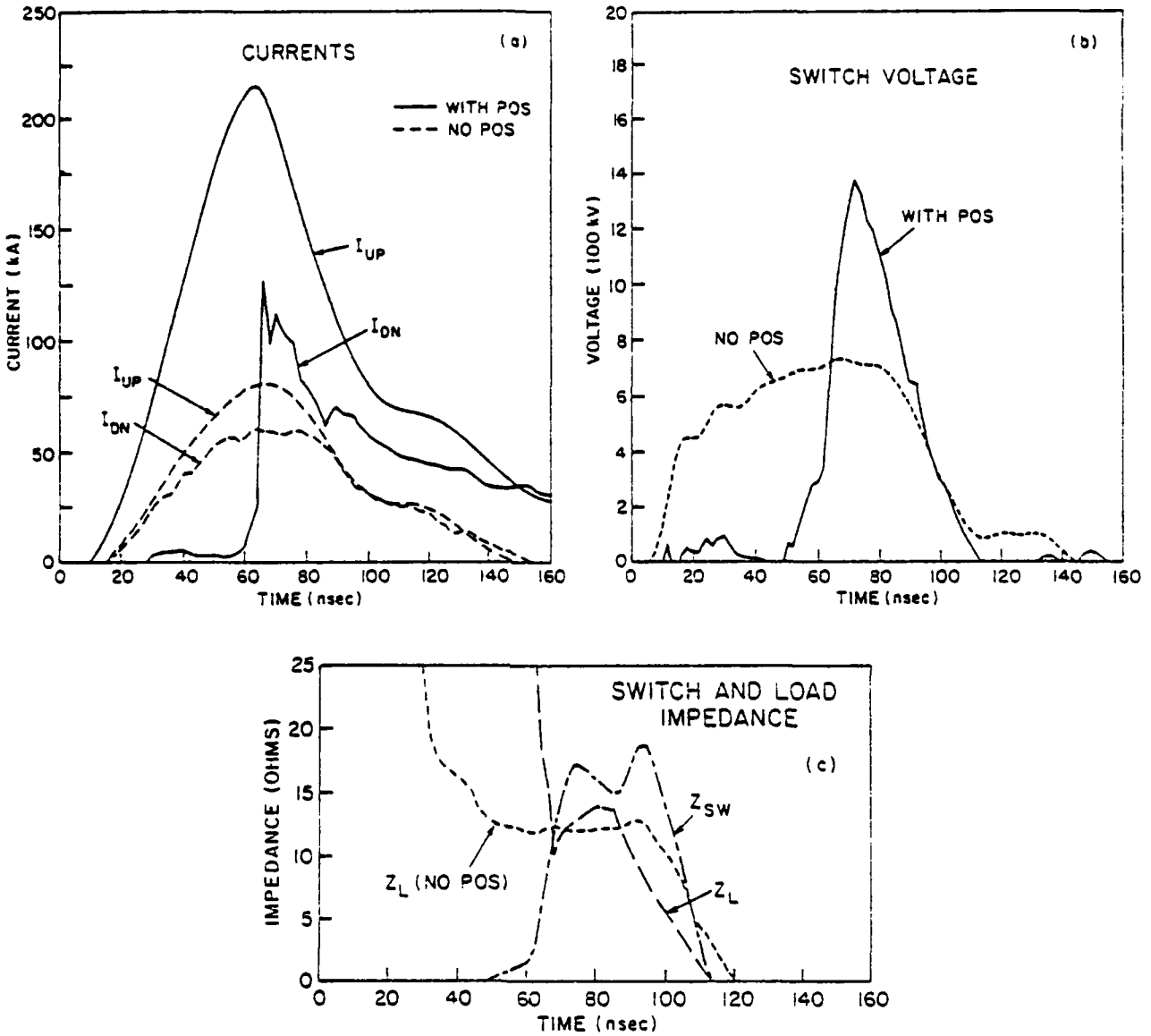

Fig. 2 — (a) Currents upstream I_{UP} and downstream I_{DN} of the switch region, with and without the plasma opening switch. (b) Voltages across the switch for the two cases. (c) Switch impedance Z_{SW} with the POS and load impedance Z_L with and without the POS.

190 nH inductance (inductive store plus transmission line) in series with the ~ 12 ohm e-beam load. Thus the current in the inductor is limited to ~ 80 kA . The downstream current I_{DN} follows the upstream current I_{UP} with some current loss due to cathode stalk emission. With the POS the accelerator sees a 175-nH load inductance into a short circuit for about half of the pulse duration. The switch is closed for the first ~ 50 nsec, as shown in Fig. 2a, during which time it acts as a short circuit, diverting up to 220 kA from the load. When the switch begins to open, the downstream current rises to ~ 130 kA in ~ 6 nsec . The downstream current risetime when the POS opens is $\sim 2.2 \times 10^{13}$ A/sec. An apparent loss of 90 kA occurs in the switch region. This loss is partially in the form of intense beamlets striking the outer conductor just downstream of the switch region and represents a shunt resistance even when the switch has opened. The loss may be related to the geometry of the short line downstream of the switch not properly retrapping the switch electron flow.

Voltages across the switch $V_{SW}=V_D-L_S dI_{UP}/dt$ were computed from the measured insulator voltage V_D and dI_{UP}/dt and are shown in Fig. 2b. The voltage across the load impedance is approximately the same as the switch voltage because $L_1 \ll L_S$. Without the POS the switch voltage peaks at ~ 790 kV and has an 85-nsec FWHM. With the POS the voltage is held near zero during the conduction phase, then rises to 1.4 MV in ~ 20 nsec. The FWHM of the pulse is ~ 25 nsec. The FWHM of the voltage pulse with the POS is reduced by a factor of three and the peak voltage is nearly a factor of two higher than the shot without the POS. The pulse compression and voltage multiplication is a result of the charging of the inductive store and the subsequent extraction of the energy on a shorter time scale. The effective switch shunting resistance $Z_{SW} \equiv V_{SW}/(I_{UP}-I_{DN})$ and the load resistance $Z_L \equiv V_{SW}/I_{DN}$ for the two

cases are shown in Fig. 2c. Without the POS the load impedance is 12 Ohms for most of the pulse. With the POS, the switch looks like a short during the conduction phase, then rises to an effective shunt resistance of ~17 Ohms when the switch opens. The load impedance is ~ 13 Ohms during the output pulse.

Time resolved x-ray signals for both cases are shown in Fig. 3. Without the POS a ~ 35-ns FWHM, 25-V peak photodiode signal is measured compared to a 13-ns FWHM pulse and ~225 V peak with the POS. The shape of the x-ray signal and the factor of 8 signal increase agrees with an $I_{DN}(V_{SW})^{2.8}$ scaling of the data.[15]

The increased current and the higher voltage are corroborated by damage to the anode in these two cases. Without the POS the anode damage is confined within a 6-cm diam. circle opposite the cathode. With the POS the anode damage is confined within 4-cm diam. as would be expected from a higher current in the diode. The rear-surface anode spall is observed to be twice as thick for the POS case as without, which is consistent with a higher voltage.

The peak power into the switch and load combination is 0.065 TW without the POS and 0.28 TW with the POS. The four-fold increase in peak power results from the higher voltage and current in the switch. The higher voltage is due to the inductive energy storage and the fast opening action of the POS. With the POS the power pulse has been reduced to the decay time scale of the inductor through the parallel e-beam and switch load resistances. Another measure of power multiplication is to compare the peak power delivered by the Gamble I accelerator to a matched load to that delivered when an inductive store and POS are used. The open circuit voltage waveform was derived from the data in Fig. 2. A transmission line code[16] was used to reproduce the measured diode waveforms, then to compute output waveforms for a 30-nH, 2-Ohm

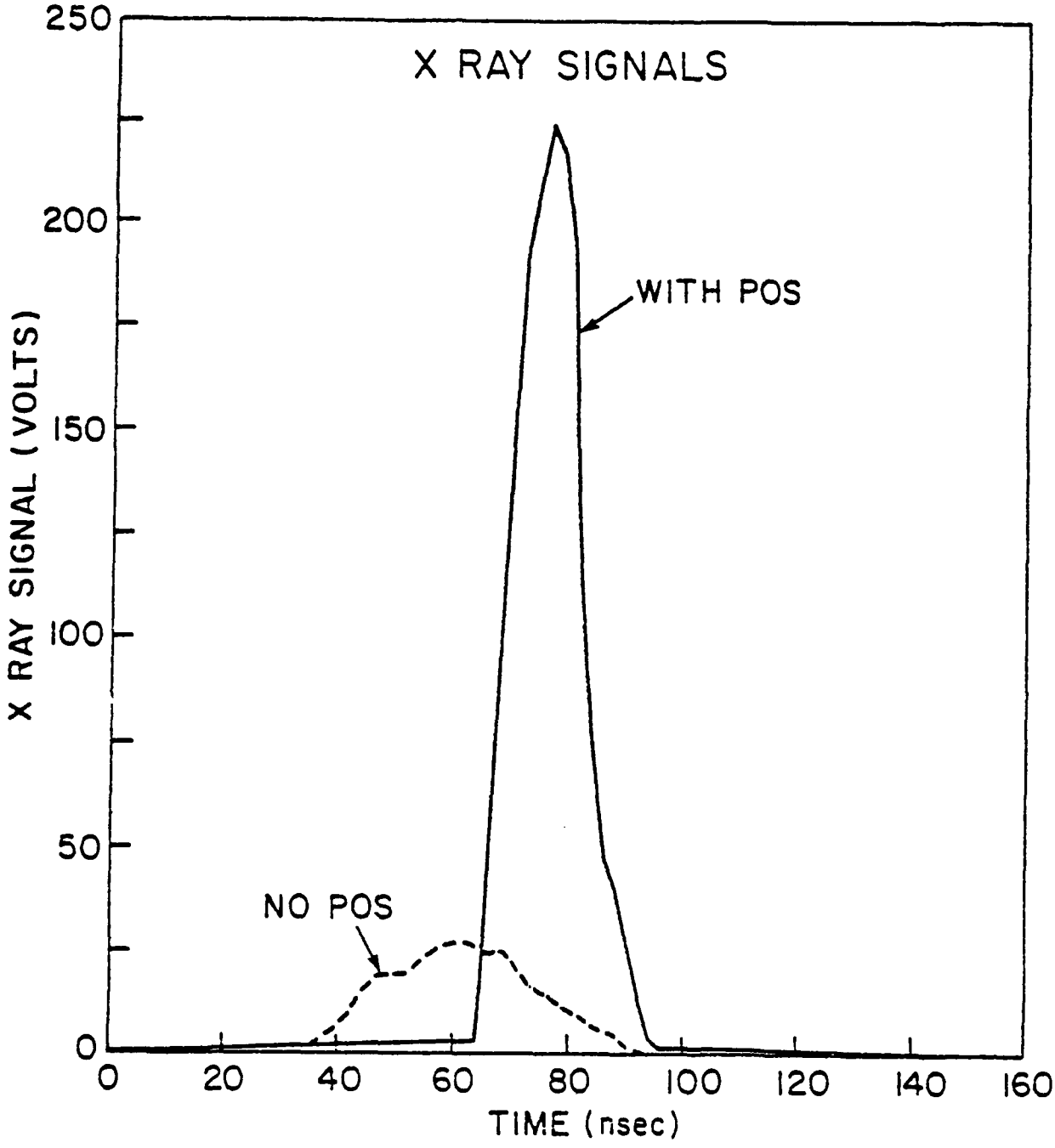

Fig. 3 — X-ray signals as measured by a photodiode with and without the POS.

load which represents the optimum Gamble I load impedance. Peak power for this idealized diode was 0.14 TW which is one-half the measured peak power with the inductive store and POS.

Many shots were taken with different plasma densities in the switch region and with different timing between the arrival of the plasma in the switch region and the arrival of the accelerator pulse. The switch opening was observed to be reproducible within the limits of the plasma gun and accelerator pulse reproducibility. The duration of the conduction phase was reduced if the plasma density in the switch region was decreased by either moving the guns further away from the inner conductor or by injecting the beam earlier in the plasma pulse. With such adjustments the switch could be made to divert only the leading edge of the accelerator pulse as desired for prepulse suppression or to divert as much as 250 kA with the switch still opening in $\sim$ 10 nsec. The conduction time could also be changed with apertures or attenuating screens in front of the guns. If the accelerator pulse was delayed more than one microsecond after the peak plasma density at the inner conductor or if too much plasma was injected, the conduction period increased and the opening time became slower. In the extreme case the switch diverted the entire pulse from the load. Reducing the accelerator voltage increased the switch conduction period. If the conduction time extended beyond the peak inductor current, the switch opening time increased to $\gtrsim$ 25 nsec. An extended parameter study is presently being performed on these variables.

4. Opening Switch Model

A simple model of the opening switch operation will be presented to explain the experimental results. The model is based on bipolar flow in a Child-Langmuir diode and includes magnetic field effects. The model consists of four phases, each of which is treated separately, but the switch progresses from one phase to the next as critical current levels are reached in the switch or load. The four phases are the conduction phase, a simple bipolar-erosion phase similar to previous models,[6,7] an enhanced-erosion phase, and finally a magnetic-insulation phase. The model ignores magnetic-field-pressure effects, surface-physics effects and neutral-background-gas effects.

Phase I of the switch operation begins with a plasma in the switch region of a known species, density, charge state, average drift velocity toward the cathode, and temperature. The switch plasma fills the region uniformly and strikes a finite area on the cathode surface. A schematic representation of the system is shown in Fig. 1b. A load resistance is located downstream of the switch. The accelerator is fired and a voltage appears across the inductor, driving current through the inductor and switch. As a finite voltage appears across the plasma, a sheath forms near the cathode. In this sheath the electrons are swept out producing a planar-diode-like gap with the cathode surface on one side and the edge of the plasma on the other. The gap adjusts itself such that the cathode surface becomes a space-charge-limited-electron emitter while the plasma supplies ions to the opposite side of the gap producing a bipolar current flow across the gap. The current driven through the plasma is limited by the accelerator output driving the entire system and by the series inductor. Ions enter the gap due to their drift velocity and the component of the ion thermal velocity normal to the

cathode. In such a bipolar diode the ion flux necessary to maintain the current flow[17] is

$$j_i/j_e = (m_e/2M_i)^{1/2} (\gamma+1)^{1/2} \qquad (1)$$

where m_e, M_i and $\gamma m_e c^2$ are the electron rest mass, ion rest mass, and maximum electron energy, respectively, and c is the speed of light. The total bipolar current density is

$$j = j_e+j_i = (1+j_i/j_e)\ 4.3\times10^{-6}V^{3/2}/d^2 \qquad (2)$$

where V is the voltage across the gap in volts and d is the gap thickness in cm. For example, according to Eq. (1) a C^+ plasma with a charge flux of 20 A/cm^2 as used in the experiments is sufficient to drive almost 3 kA/cm^2 in total current (electrons and ions) across the gap. If the accelerator current density through the switches is less than this level Eq. (1) is satisfied and the gap will not increas In addition, if the switch plasma becomes resistive so that a finite electric field penetrates the plasma, ions can gain enough energy on the beam timescale to further increase the charge flux into the gap. This allows more current to be driven across the bipolar gap without affecting the gap size. Under these conditions the switch impedance remains low as observed experimentally during the conduction period of switch operation.

Phase II begins when the accelerator current density exceeds the level where the ion flux into the gap is sufficient to maintain bipolar flow across the plasma-gap interface. An additional ion flux is provided by eroding the plasma thereby opening tne gap. The increasing gap raises the effective

resistance of the switch. With the series inductor the system acts like a constant current source, increasing the voltage across the switch impedance which in turn increases the erosion rate. This feedback process produces opening velocities of ~ 10 cm/μsec under the experimental conditions presented in this paper. This process starts the switch opening but can open the gap by only 1 mm in 10 nsec. Phase III begins when electron trajectories are altered significantly by the self-magnetic field associated with the current flow in the switch and the diode load. This field bends the electrons downstream and they travel along the plasma surface for the length of the switch plasma. This increases the electron space charge near the boundary and enhances the ion emission in a manner similar to a pinch-reflex ion diode.[17] This changes Eq. (1) into

$$j_i/j_e = (m_e/2M_i)^{1/2} (\gamma+1)^{1/2} L/d \ , \qquad (3)$$

where L is the axial length of the plasma. For small gaps this L/d enhancement factor can increase the ion flux by a large factor. Opening velocities of ~ 10^2 cm/μsec are obtained so that a gap opening of 1 cm in 10 nsec is expected.

As the switch impedance increases to the load impedance and beyond, the load begins to conduct a larger fraction of the cur ent. Phase IV begins when the diode current exceeds the current $I_i = I_c/\gamma = 8.5\times10^3\ \beta\ R/d$ amp in the switch region, where I_c is the critical current and β is the electron velocity (normalized to the speed of light) at full voltage. The electrons then become magnetically insulated and travel downstream to the load. Since the electrons no longer cross the gap, the switch current becomes that of a single species Child-Langmuir diode pulling carbon ions out of the plasma. Its effective

AD-A129 821 DIODE DYNAMICS BEAM GENERATION AND TRANSPORT AND PLASMA EROSION OPENING SWITCH DEVELOPMENT(U) JAYCOR ALEXANDRIA VA P F OTTINGER 17 MAY 83 JAYCOR-J207-83-C-001 8/8

UNCLASSIFIED N00173-80-C-0202 F/G 9/1 NL

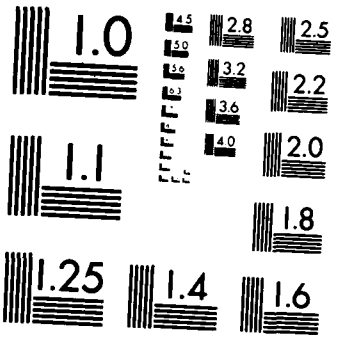

impedance is much higher than for the bipolar case which accounts for the rapid increase in the switch impedance.

The simple switch model described here has all the experimentally observed features. It allows for a conduction period before the switch current exceeds the ion flux criteria. It can explain the observed 10 nsec opening times and shows why the switch impedance increases when magnetic insulation in the switch is obtained. It does not explain the observed losses at the downstream end of the switch region. These losses most likely depend on the impedance mismatch between the opening switch and the downstream section of transmission line.

5. Conclusion

Experimental results have been presented which demonstrate the operation of a Plasma Opening Switch. The switch was shown to conduct current for ~ 50 nsec while a vacuum inductor was charged. Then the switch opened in an interval of ~ 10 ns producing a voltage in excess of 1 MV and delivering a large fraction of the inductively stored energy to an e-beam diode load. The rapid opening is attributed to enhanced erosion effects in the switch due to the beam's self-magnetic field. The output voltage pulse was compressed by a factor of three and increased by a factor of two. The power delivered to the load increased by a factor of four compared to measurements without the switch and by a factor of two compared to the accelerator's matched load peak power. In the closed state the switch successfully diverted > 200 kA of current. A current loss of 90 kA observed in the switch region may be related to electron losses downstream of the switch in the short section of the transmission line.

A simple model of the opening switch was presented which agrees qualitatively with the observed switch operation. This model suggests further experiments which will provide further insight into the operation and improved design of such switches.

The method described here is applicable to many pulsed-power accelerators. It offers a wide range of applications from prepulse suppression to compact inductive energy storage and power multiplication. The POS can lower the inductance between the final energy store and the load which limits the pulse risetime. Applications to multi-line accelerator systems to eliminate line to line jitter are envisioned as well as in other experiments requiring fast risetime, high power pulses. Future experiments will focus on scaling of the switch operation to higher currents and voltages and a better understanding of the opening process.

6. Acknowlegements

The authors would like to acknowledge the technical assistance of M. Sucy, A. Robinson, and J.R. Boller; useful discussions with P.F. Ottinger, R.J. Barker and J.D. Shipman, Jr.; and experimental help from F.C. Young and J.M. Neri. This work was supported by the Defense Nuclear Agency.

7. References

1. R. D. Ford, D. Jenkins, W. H. Lupton, and I. M. Vitkovitsky, Rev. Sci. Inst. 52, 694(1981).

2. I. M. Vitkovitsky, D. Conte, R. D. Ford, and W. H. Lupton, Proceedings of the Seventh Symposium on Engineering Problems of Fusion Research, Vol. 1, IEEE Cat. No. 77-CH-1267-4-NPS (1977), p. 1066.

3. C. Maisonnier, J. G. Linhart, and C. Gourlan, Rev. Sci. Inst. 37, 1380(1966).

4. R. E. Reinovsky, D. L. Smith, W. L. Baker, J. H. Degnan, R. P. Henderson, R. J. Kohn, D. A. Kloc, and N. F. Roderick, IEEE Trans. on Nucl. Sci. NS-10, 73(1982).

5. R. J. Commisso, R. F. Fernsler, V. E. Scherrer, and I. M. Vitkovitsky, accepted for publicaton, IEEE Trans. Plasma Sci. (1982).

6. R. J. Commisso, and I. M. Vitkovitsky, 1982 IEEE International Conf. on Plasma Sci., Ottawa, Canada, IEEE cat. no. 82-CH-1770-7 (1982), p. 154.

7. C. W. Mendel, Jr. and S. A. Goldstein, J. Appl. Phys. 48, 1004 (1977).

8. R. Stringfield, R. Schneider, R.D. Genuario, I. Roth, K. Childers, C. Stallings, and D. Dakin, J. Appl. Phys. 52, 1278 (1981).

9. Rex Richardson, Edd Brown, Jay Pearlman, Maxwell Labs, Inc., March 1982, to be published.

10. R. A. Meger and F. C. Young, Accepted for Publication, J. Appl. Phys., 1982, also NRL Memorandum Report 4838, June, 1982.

11. P.A. Miller, J.W. Poukey, and T.P. Wright, Phys. Rev. Lett. 35, 940 (1975).

12. G. Cooperstein, J.J. Condon, and J.R. Boller, J. Vac. Sci. Technol. 10, 961 (1973).

13. C. W. Mendel, Jr., D. M. Zagar, G. S. Mills, S. Humphries, Jr. and S. A. Goldstein, Rev. Sci. Instrum. 51, 1641 (1980).

14. J. M. Neri, R. J. Commisso, R. A. Meger, Bull, Am. Phys. Soc. 27, 1054 (1982).

15. H. W. Koch and J. W. Motz, Rev. Mod. Phys. 31, 4(1959).

16. D. Hinschelwood, NRL Memorandum Report, to be published.

17. G. Cooperstein, et. al., Laser Interaction and Related Plasma Phenomena, Vol. 5, ed. by H.J. Schwarz, H. Hora, M.J. Lubin, and B. Yaakobi (Plenum, 1981), p. 105.

appla830601L3F811

Vacuum inductive store/pulse compression experiments on a high power accelerator using plasma opening switches

R. A. Meger,[a] R. J. Commisso,[a] G. Cooperstein, and Shyke A. Goldstein[a]
Naval Research Laboratory, Washington, D. C. 20375

(Received 17 January 1983; accepted for publication 14 March 1983)

The first results of experiments using plasma opening switches for inductive energy storage are described. The switch has been shown to conduct up to 200-kA current for ~50 ns then to open in < 10 ns, transferring the current to an electron beam load. Inductive energy storage, pulse compression, and power multiplication are demonstrated. A simple model explaining the switch operation is presented.

PACS numbers: 52.75.Kq, 52.75.Di, 52.80.Vp

The use of inductive energy storage for pulsed power applications is of great interest. It offers the advantage of 10–100 times higher energy density than capacitive storage systems, making more compact and economical generators possible.[1] Present opening switch technology involves the use of explosively activated circuit breakers,[2] wire fuses,[1,3,4] and electron beam (*e*-beam) controlled diffuse discharges.[5] In this letter we report experiments with a new type of opening switch called a plasma opening switch (POS) which operates on a nanosecond timescale. Similar techniques have been used previously for suppression of prepulse and steepening of pulse rise time on high-power generators.[6–10] In this experiment energy from a pulsed power accelerator is first stored in a vacuum inductor and then extracted through a low inductance, high impedance load. Results show the POS remains closed for up to 70 ns as the vacuum inductor is charged then opens in < 10 ns. Most of the energy in the inductor is then delivered to an *e*-beam diode load. Voltage increases by a factor of 2 and power multiplications of up to a factor of 4 over non-POS shots have been measured. A model of the switch opening is described which qualitatively agrees with the data.

In these experiments the Gamble I accelerator[11] was used to charge a coaxial vacuum inductor. At a 66-kV charging voltage, Gamble I provides a negative 1-MV, 60-ns full width at half-maximum (FWHM) sinusoidal open circuit voltage waveform with an effective 2-Ω source impedance. Figure 1 shows a schematic of the experiment and an equivalent circuit diagram. The experimental hardware consists of 40-cm-long, 100-Ω coaxial vacuum inductor, a switch section, and an *e*-beam diode section. The ~140-nH high impedance vacuum inductor section and the ~35-nH insulator provide the $L_S \sim 175$ nH inductive store. The switch section contains three plasma guns of a type described elsewhere.[12] The guns are located 12 cm off axis and inject a carbon plasma (primarily C^+) through a 10-cm-diam brass screen striking the inner 5-cm-diam cathode surface over a ~60 cm^2 area. The plasma density has a peak charge density of $\sim 5\times10^{12}$ cm^{-3} and moves with a drift velocity of 7.5 cm/μs.[13] Neutrals from the guns have a velocity ~1 cm/μs and arrive after the plasma. Downstream of the switch region is a 10-cm-long, 42-Ω transmission line segment with inductance $L_L \sim 14$ nH followed by the *e*-beam diode load. The diode consists of a 6-mm-thick rounded edge, hollow, cylindrical aluminum cathode located 1 cm from a 1.6-mm-thick carbon coated aluminum anode.

Diagnostics included a voltage monitor upstream of the Gamble I insulator, a current monitor in the inductor section labeled I_{UP} and another current monitor downstream of the switch region labeled I_{DN}. A photodiode with a pilot-B scintillator to measure x rays was located on axis 35-cm downstream of the anode.

Shown in Fig. 2 are the experimental data from two shots: one with the POS and one without. The shots had nearly identical peak accelerator voltage pulses of −960 kV across the inductive store section. The accelerator pulse arrived at the inductor 0.5 μs after the peak of the injected plasma density at the cathode surface. The currents in the inductor I_{UP} and in the *e*-beam load section I_{DN} are shown in Fig. 2(a). Without the POS the accelerator sees 190-nH inductance ($L_S + L_L$) in series with the ~12-Ω *e*-beam load. This limits the peak current in the inductor to ~80 kA. I_{DN} follows I_{UP} with some current loss due to cathode stalk emission. With the POS the accelerator sees only the inductive store with $L_S \sim 175$ nH and the closed switch for the first ~50 ns. During this time the switch diverts up to 220 kA from the load. When the switch begins to open, the downstream current rises to ~130 kA in ~6 ns with a maximum $dI_{DN}/dt \sim 2.2\times10^{13}$ A/s. A loss of 90 kA occurs in the switch and downstream of the switch.

Voltages across the switch $V_{SW} = V_D - L_S dI_{UP}/dt$ computed from the measured insulator voltage V_D and dI_{UP}/dt are shown in Fig. 2(b). The voltage across the load impedance is approximately the same as the switch voltage becalue $L_L \ll L_S$. Without the POS the switch voltage peaks at ~790 kV and has an 85-ns FWHM. With the POS the voltage is near zero during the conduction phase, then rises to 1.4 MV in ~20 ns. The FWHM of the pulse is ~25 ns. The FWHM of the voltage pulse with the POS is reduced by a factor of 3 and the peak voltage is a factor of 2 higher than without the POS.

The x-ray signals agree with the pulse compression and voltage multiplication. Without the POS a ~35-ns FWHM, 25-V peak photodiode signal is measured compared to a 13-ns FWHM pulse and ~225-V peak with the POS. The shape of the x-ray signal and the factor of 8 signal increase agrees with an $I_{DN}(V_{SW})^{2.3}$ scaling of the data.[14]

The increased current and the higher voltage in the *e*-beam diode with the POS are corroborated by damage to the anode. Without the POS the anode damage is within a 6-cm-diam circle while with the POS the anode damage is within

tage.

The peak power into the switch and load combination is 0.065 TW without the POS and 0.28 TW with the POS. The fourfold increase in peak power results from the higher voltage and current in the switch. For comparison, the power delivered to a matched (2 Ω) low inductance (30 nH) diode is 0.14 TW for a similar accelerator pulse.

Many shots were taken with different plasma densities in the switch region and with different timing between the arrival of the plasma in the switch region and the arrival of the accelerator pulse. The switch opening was observed to be reproducible within the limits of the plasma gun and accelerator pulse reproducibility. The switch could be made to divert only the leading edge of the accelerator pulse as desired for prepulse suppression or to divert as much as 250 kA with the switch still opening in ~ 10 ns depending on how much plasma was injected. If too much plasma was injected the switch diverted the entire pulse from the load. An extended parameter study of density effects is presently being performed.

A simple model of the opening switch operation has been developed based on erosion of the plasma near the cathode due to the ion current drawn out of the plasma. The model consists of four phases: a conduction phase, a one dimensional bipolar erosion phase,[6-8] a two-dimensional erosion phase, and a magnetic insulation phase. The effects of magnetic pressure due to $J \times B$ forces on the plasma have been neglected in this model. These forces have been studied extensively for the AMPHION ion diode concept[17] and are under active study for their effects.

Phase I of the switch operation begins with the plasma filling the switch region uniformly and striking a finite area on the cathode surface. The accelerator is fired and a voltage appears across the inductor and switch combination. A cathode surface plasma is formed by some process and becomes a space-charge-limited electron emitter. A gap near the cathode plasma forms and a bipolar Child–Langmuir diode is established with the cathode surface on one side and the carbon plasma on the other. Ions enter the gap due to their drift and thermal velocity supplying the $< 1\%$ of the charge flux necessary to maintain a bipolar flow. For example a C^+ plasma with a charge flux of 20 A/cm^2 as used in the experiments is sufficient to drive almost 3 kA/cm^2 (electrons and ions) in the gap region. As long as the switch current density remains below this level the gap will not open and the switch impedance will remain low. Phase II begins when the ion flux into the gap is no longer sufficient to maintain bipolar flow across the plasma-gap interface. The additional ion flux is provided by eroding the plasma and opening the gap. This erosion can produce opening velocities ~ 10 cm/μs. As the gap D increases, the Child–Langmuir switch impedance increases with D^2 giving a rapidly increasing switch resistance. As the current in the switch region increases, the switch electrons are bent downstream by their self-magnetic field and travel along the plasma surface for the length L of the switch plasma. This begins phase III of the opening process. The ion flux and therefore the erosion rate is increased by a factor of L/D in the same way the ion current in a pinched-beam ion diode[16,17] is enhanced. Opening velocities of 10^2 cm/μs are possible with this enhancement leading to very fast increases in switch resistance. As the switch load begins to conduct a larger fraction of the current. Phase IV begins when the diode current exceeds the critical current for magnetic insulation in the switch gap. The electrons no longer interact with the plasma and travel down the final section of transmission line to the load.

This model is very simplistic but does explain the observed operation of the switch. The onset of each phase will not be as clear cut as described here. Further experiments and electromagnetic code simulations are planned to refine the model.

Experimental results have been presented in which a POS was observed to conduct up to 200 kA for ~ 50 ns while a vacuum inductor was charged. The switch then opened in ~ 10 ns producing a voltage in excess of 1 MV and delivering a large fraction of the inductively stored energy to an e-beam diode load. The rapid opening is attributed to two-dimensional enhanced erosion effects in the switch resulting from the beam's self-magnetic field. The output voltage pulse was compressed in time by a factor of 3 and increased in peak value by a factor of 2. The power delivered to the load increased by a factor of 4 as compared to the measured power without the switch and by a factor of 2 compared to the accelerator's matched load peak power. In the closed state the switch successfully diverted > 200 kA of current. A simple model of the opening switch was presented which agrees qualitatively with the observed switch operation. This model suggests further experiments which will provide insight into the operation and improved design of such switches.

The method described here is applicable to many pulsed-power accelerators. It offers a wide range of applications from prepulse suppression to compact inductive energy storage and pulse compression. For existing accelerators the POS can lower the inductance between the final energy store and the load which allows faster risetimes. Applications to multiline accelerator systems to aid in pulse forming and to minimize jitter are currently under investigation. Future experiments will focus on scaling of the switch operation to higher currents and voltages and a better understanding of the opening process.

The authors would like to acknowledge the technical assistance of M. Sucy, A. Robinson, and J. R. Boller, useful discussions with P. F. Ottinger, R. J. Barker, and J. D. Shipman, Jr., and experimental help from F. C. Young and J. M. Neri. This work was supported by the Defense Nuclear Agency.

[a] Permanent address: JAYCOR, Inc., 205 S. Whiting St., Alexandria, Virginia 22304.

[1] R. D. Ford, D. Jenkins, W. H. Lupton, and I. M. Vitkovitsky, Rev. Sci. Instrum. 52, 694 (1981).
[2] I. M. Vitkovitsky, D. Conte, R. D. Ford, and W. H. Lupton, *Procedings of the Seventh Symposium on Engineering Problems of Fusion Research* (IEEE, New York, 1977, Vol. 1, p. 1066.
[3] C. Maisonnier, J. G. Linhard, and C. Gourlan, Rev. Sci. Instrum. 37, 1380 (1966).
[4] R. E. Reinovsky, D. L. Smith, W. L. Baker, J. H. Degnan, R. P. Henderson, R. J. Kohn, D. A. Kloc, and N. F. Roderick, IEEE Trans. Nucl. Sci. NS-10, 73 (1982).
[5] R. J. Commisso, R. F. Fernsler, V. E. Scherrer, and I. M. Vitkovitsky, IEEE Trans. Plasma Sci. PS-10, 241 (1982).

[6]P. A. Miller, J. W. Poukey, and T. P. Wright, Phys. Rev. Lett. 35, 940 (1975).
[7]C. W. Mendel, Jr., and S. A. Goldstein, J. Appl. Phys. 48, 1004 (1977).
[8]R. Stringfield, R. Schneider, R. D. Genuario, I. Roth, K. Childers, C. Stallings, and D. Dakin, J. Appl. Phys. 52, 1278 (1981).
[9]Rex Richardson, Ed Brown, Jap Pearlman, Maxwell Labs, Inc., March 1982 (unpublished).
[10]R. A. Meger and F. C. Young, J. Appl. Phys. 53, 8543 (1982); NRL Memorandum Report 4838, June 1982.
[11]G. Cooperstein, J. J. Condon, and J. R. Boller, J. Vac. Sci. Technol. 10, 961 (1973).
[12]C. W. Mendel, Jr., D. M. Zagar, G. S. Mills, S. Hunphries, Jr., and S. A. Goldstein, Rev. Sci. Instrum. 51, 1641 (1980).
[13]J. M. Neri, R. J. Commisso, and R. A. Meger, Bull. Am. Phys. Soc. 27, 1054 (1982).
[14]H. W. Koch and J. W. Motz, Rev. Mod. Phys. 31, 4 (1959).
[15]C. W. Mendel, Jr., and G. S. Mills, J. Appl. Phys. 53, 7265 (1982).
[16]Shyke A. Goldstein and R. Lee, Phys. Rev. Lett. 35, 1079 (1975).
[17]G. Cooperstein, Shyke A. Goldstein, D. Mosher, R. J. Barker, J. R. Boller, D. G. Colombant, A. Drobot, R. A. Meger, W. F. Oliphant, P. F. Ottinger, F. L. Sandel, S. J. Stephanakis, and F. C. Young, in *Laser Interaction and Related Plasma Phenomena*, edited by H. J. Schwarz, H. Hora, M. Lubin, and B. Yaakobi (Plenum, New York, 1981), Vol. 5, p. 105.

FIG. 1. (a) Schematic of the Gamble I plasma opening switch experiment. (b) Circuit diagram of the experiment. V_{oc} is the open circuit voltage waveform, R_G the 2-Ω accelerator impedance, L_S the inductor, and R_L the load impedance.

FIG. 2. (a) Currents upstream I_{UP} and downstream I_{DN} of the switch region, with and without the plasma opening switch. (b) Voltages across the switch for the two cases.

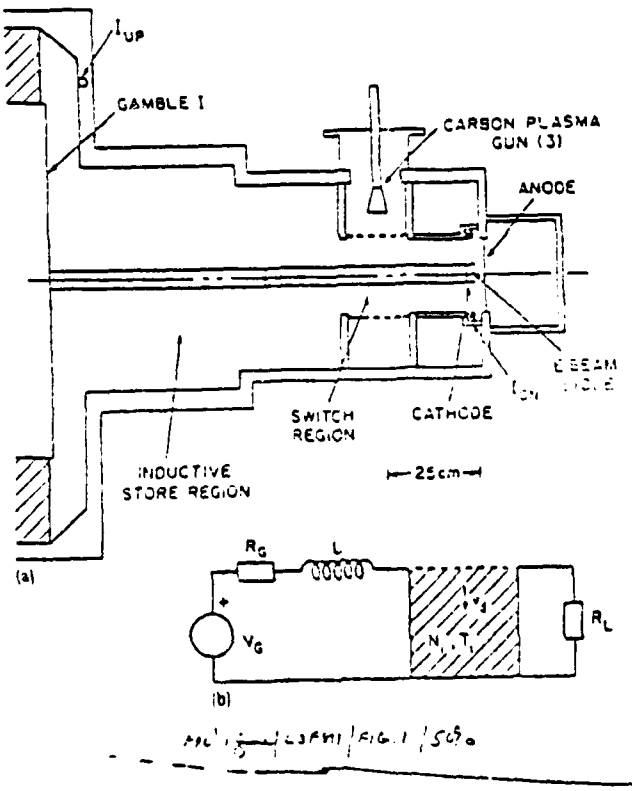

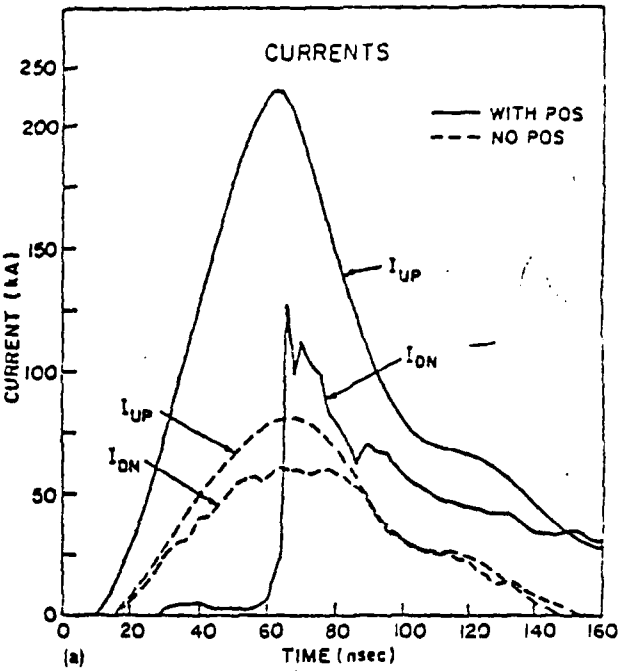
CURRENTS
WITH POS
NO POS
I_{UP}
I_{DN}
I_{UP}
I_{DN}
CURRENT (kA)
TIME (nsec)
(a)

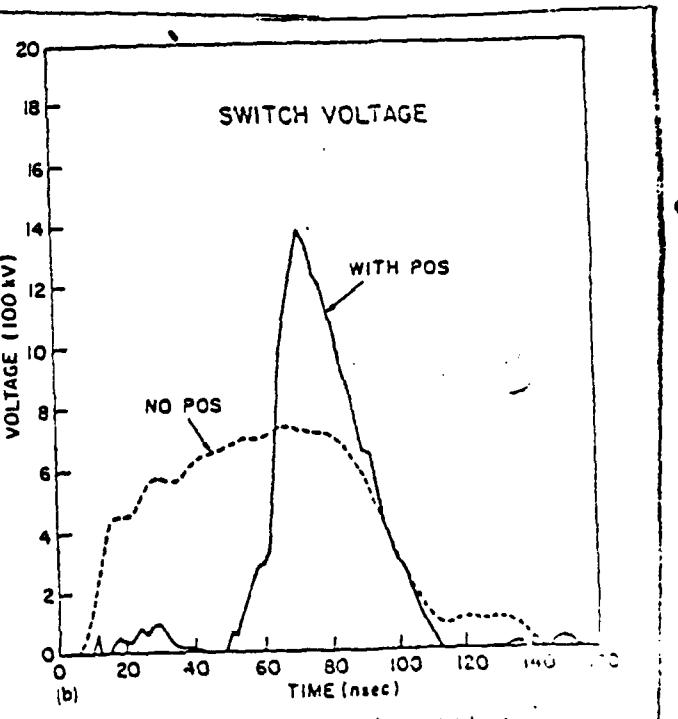
SWITCH VOLTAGE
WITH POS
NO POS
VOLTAGE (100 kV)
TIME (nsec)
(b)

END

FILMED

7-83

DTIC